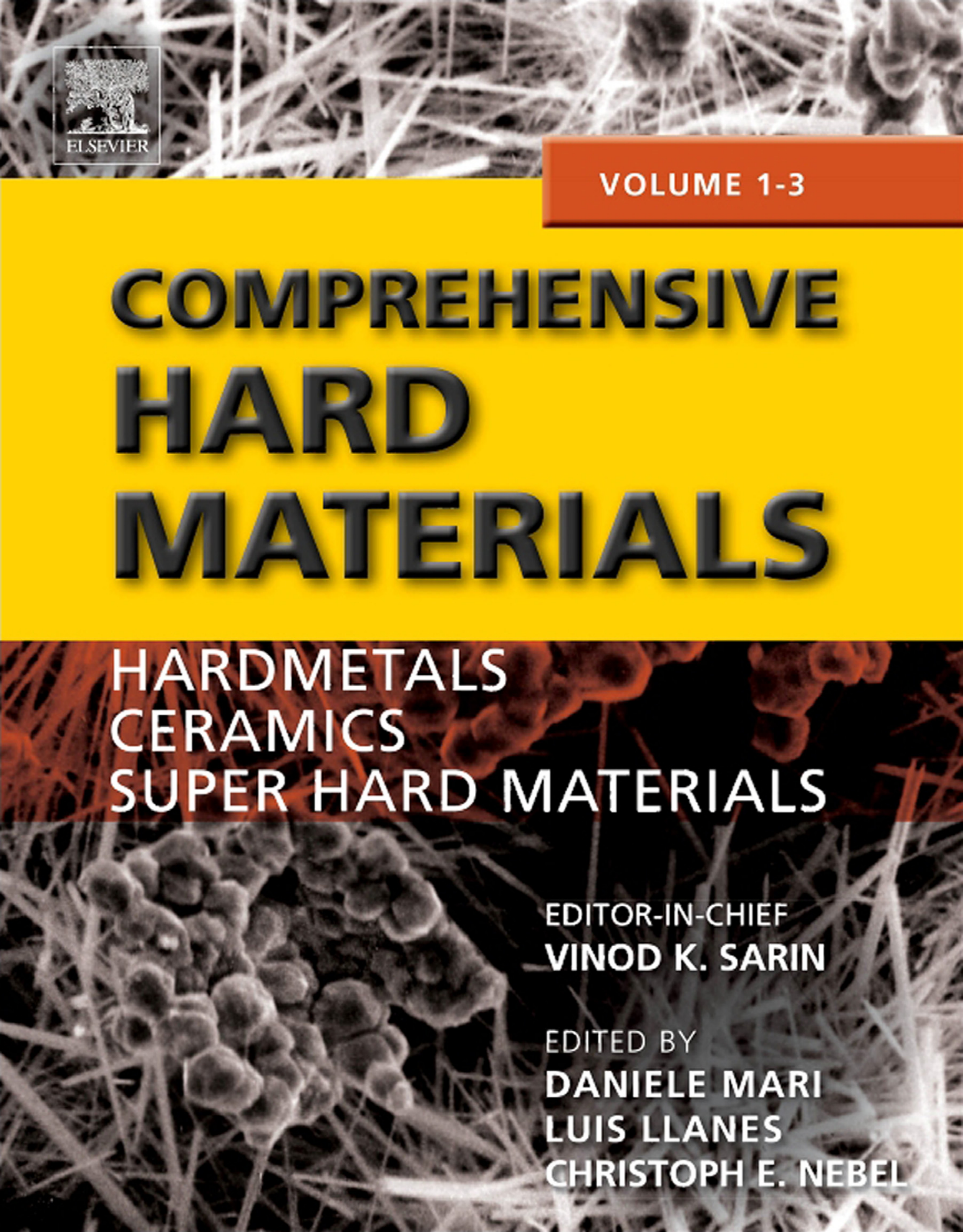

ELSEVIER

VOLUME 1-3

COMPREHENSIVE HARD MATERIALS

HARDMETALS
CERAMICS
SUPER HARD MATERIALS

EDITOR-IN-CHIEF
VINOD K. SARIN

EDITED BY
DANIELE MARI
LUIS LLANES
CHRISTOPH E. NEBEL

COMPREHENSIVE HARD MATERIALS

VOLUME 1

HARDMETALS

COMPREHENSIVE HARD MATERIALS

VOLUME 1

HARDMETALS

EDITOR-IN-CHIEF
VINOD K. SARIN
College of Engineering, Boston University
Boston, MA, USA

EDITED BY
DANIELE MARI
Laboratoire de Physique de la Matière Complexe
Ecole Polytechnique Fédérale de Lausanne, Lausanne, Switzerland

LUIS LLANES
Departament de Ciència dels Materials i Enginyeria Metal·lúrgica
Universitat Politècnica de Catalunya · Barcelona Tech
Barcelona, Spain

ELSEVIER
AMSTERDAM • WALTHAM • HEIDELBERG • LONDON • NEW YORK • OXFORD
PARIS • SAN DIEGO • SAN FRANCISCO • SINGAPORE • SYDNEY • TOKYO

Elsevier
The Boulevard, Langford Lane, Kidlington, Oxford OX5 1GB, UK
225 Wyman Street, Waltham, MA 02451, USA

© 2014 Elsevier Ltd. All rights reserved.

No part of this publication may be reproduced, stored in a retrieval system or transmitted in any form or by any means electronic, mechanical, photocopying, recording or otherwise without the prior written permission of the publisher.

Permissions may be sought directly from Elsevier's Science & Technology Rights Department in Oxford, UK: phone (+44) (0) 1865 843830; fax (+44) (0) 1865 853333; email: permissions@elsevier.com. Alternatively you can submit your request online by visiting the Elsevier web site at http://elsevier.com/ locate/permissions, and selecting Obtaining permission to use Elsevier material.

Notice
No responsibility is assumed by the publisher for any injury and/or damage to persons or property as a matter of products liability, negligence or otherwise, or from any use or operation of any methods, products, instructions or ideas contained in the material herein. Because of rapid advances in the medical sciences, in particular, independent verification of diagnoses and drug dosages should be made.

British Library Cataloguing in Publication Data
A catalogue record for this book is available from the British Library

Library of Congress Cataloging in Publication Data
A catalog record for this book is available from the Library of Congress

Volume 1 ISBN: 978-0-444-63385-9
Volume 2 ISBN: 978-0-444-63384-2
Volume 3 ISBN: 978-0-444-63383-5
SET ISBN: 978-0-08-096527-7

For information on all Elsevier publications
visit our website at www.store.elsevier.com

Printed and bound in UK
14 15 16 17 10 9 8 7 6 5 4 3 2 1

ELSEVIER
Book Aid
International
Working together
to grow libraries in
developing countries
www.elsevier.com • www.bookaid.org

CONTENTS

Volume 1 — Hardmetals

Section I Introduction to Hardmetals

Section II Classes of Materials

Section III Synthesis and Processing

Section IV Mechanical Properties

Section V Applications

Volume 2 - Ceramics

Section I Introduction

Section II Synthesis and Processing

Section III Microstructure and Properties

Section IV Coatings and Applications

Volume 3 - Super Hard Materials

Section I Theory

Section II Materials: Growth, Properties and Applications: Carbon-Based DLC

Section III Nano— and Poly—Diamond

Section IV Single Crystalline Diamond

Section V Selected Properties of Diamond and Applications

Section VI Other Carbon Phases

Section VII III-V Based and Novel Materials

PREFACE

Comprehensive Hard Materials, first reference work of its types, is intended to merge together the myriad facets of this class of materials in a three volume series that reflect the abundance of established and novel uses across industry, from tribology to electronics and from transportation to energy. The range, growth, and innovations of the hard/superhard materials field has become commonplace within materials science as is evident from the vibrant growth of research across and within hardmetals (cemented carbides), ceramics, and superhard materials. Furthermore, the global nature of material science is also reflected by this work and contributors have been drawn from a panorama of global research hubs, with many chapters addressing the specific resource and application challenges within basic research, development, and emergent industrial markets. It is in the true spirit of collaboration across the range of these otherwise hermetically sealed areas of research that this work has been conceived and built. The reader will find original articles covering many relatively unexamined but converging research spaces and the content fully examines the various relationships that focus on fundamentals, properties, characterization, and applications of such materials. It was the objective of the editorial team to assemble a work that would provide strategic insights into hard/superhard materials.

The first volume is devoted to hardmetals, generally known as cemented carbides in the US. This class of materials is composed of unique combinations of carbides and nitrides of transition metals ranging from the fourth to the sixth group of the periodic table and ferrous metals such as Co, Ni, Fe. Since the discovery of WC–Co by Schröter in 1922, they have epitomized a century of industrial applications mainly as cutting tools and wear resistant parts. Probably, without them many challenging enterprises in the field of rock drilling, mechanics or just wire manufacture would not have been possible. Starting from a historical viewpoint the volume contains detailed aspects of manufacturing, composition/structure/properties, and applications. The aim was to define the state of the art in hardmetal manufacturing together with a thorough illustration of the most recent progress obtained by scientific research.

Volume 2 is devoted to hard ceramics—a unique group of materials with a long-standing technical success history but subjected to permanent scientific and technological evolution. Representative ceramics within this subgroup of hard materials are alumina, silicon nitride, silicon carbide, their composites, in the form of bulk material and coatings. Also included are transition metal nitrides, carbides, borides, oxides, and mullite-based environmental barrier coatings. The intention was not only to project the substantial progress achieved in this field, but also to illustrate how scientific research findings are continuously transferred into industrial and technological advances. The overall aim of this volume was to present a critical review of established knowledge and recent advances of hard ceramics covering both their materials science and engineering aspects.

Volume 3 is devoted to superhard materials—materials resistant to a change of shape under applied force, and with a Vickers hardness value exceeding 40 GPa. The strongest of these are composed out of boron, carbon, nitrogen, and oxygen, and can be classified into two categories: intrinsic compounds and extrinsic compounds. The intrinsic group includes diamond as hardest material, cubic boron nitride (c-BN), carbon nitrides and ternary compounds such as B–N–C. Extrinsic materials are those that show super hardness determined by microstructure rather than composition, such as nanocrystalline diamond. These materials are of great interest in many industrial applications such as abrasives, polishing and cutting tools, wear-resistant, and protective coatings. Furthermore, diamond is emerging as an attractive material for new device applications in the field of power electronics, room temperature quantum computing, biosensing, biointerfaces, microelectromechanical systems, color centers and high energy radiation, and particle detectors to name a few. The aim of volume 3 was to present all the critical areas related to superhard materials with an emphasis on recently achieved progress in research, development, and applications.

The Elsevier publication team, especially Paul Prasad Chandramohan, has worked tirelessly to make this publication possible and available in two formats:

- An online version via the Science Direct platform that will guarantee easy worldwide distribution.
- A hard copy version that will be made available based on orders received.

This dual concept readily lends itself to maintaining this reference work current via additions and modifications. Elsevier (Donna de Weerd-Wilson) has discussed this concept with the editors and is in the process of moving on it in the near future.

The idea for this multivolume major reference work originated through discussions at the International Conferences on the Science of Hard Materials. From the outset, David Sleeman and Graham Nisbet (Elsevier) identified not only an overwhelming qualitative demand for extensive, international, innovative, methodologically sound coverage of the subject matter, but also keen interest in a quantitative form as well. Given this encouragement the volume editors Daniele Mari, Luis Miguel Llanes, Christoph E. Nebel, numerous expert contributors and reviewers are responsible for the creation of this definitive publication to encompass the full breadth and considerable depth of the hard/superhard materials field. The editors, contributors, and publishers invested 5 years of time and effort culminating in this, *Comprehensive Hard Materials*, and we are proud to present it to our colleagues and the community it is intended to serve.

Vinod K. Sarin
Boston University
Boston, MA 02215
USA

EDITOR-IN-CHIEF

Prof. Sarin graduated from MIT (Boston, MA) with an Sc.D in material science. He then joined Sandvik's Coromant Research Center, Stockholm, Sweden. Four years later he came back to the US, joined Adamas Carbide and then GTE, where he started an R&D group on hardmetals and ceramics, and was promoted to senior research scientist (Fellow) at GTE. After nearly 20 years of industrial experience he joined academia (Boston University) as professor in the College of Engineering. He has been the recipient of several technical, achievement, and industrial awards, invited distinguished scientist at the Max Planck Institute (Germany), University of Linkoping (Sweden), Visiting Professor, University of Lund (Sweden), Visiting Scholar/Professor Universitat Politècnica de Catalunya (Spain), and a global industrial R&D consultant. He singly or jointly holds over 80 patents, has edited several books, has authored or coauthored several chapters, and over a hundred technical publications. He is a member of the editorial board of several journals, and has chaired several technical sessions and organized several conferences on hard materials.

VOLUME EDITORS

Daniele Mari graduated in physics in 1986, and in 1991 obtained his PhD at the Federal Institute of Technology (EPFL) in Lausanne, Switzerland, with a study on high temperature properties of hardmetals. From 1992 to 1993, he continues his research at the Massachusetts Institute of Technology working in the field of shape memory alloys. In 1993, he joins the company Amysa Yverdon SA (Switzerland) as director of R&D and creates Advanced Composite & Microwave Engineering with activities in the fields of the electromagnetic heating and materials. In 2004, he returns to academia at EPFL with a research group specialized in mechanical spectroscopy. He is the co-author of more than 70 scientific papers and is presently deputy director of the physics section at EPFL. He is a member of the Editorial Board of the International Journal of Refractory Metals and Hard Materials. He has been co-chairman of the last two International Conferences on the Science of Hard Materials (ICSHM).

Luis Llanes is a full professor and current chairman in the Department of Materials Science and Metallurgical Engineering, as well as board member of the Research Center of Nanoengineering in the Technical University of Catalonia (UPC). He graduated in materials engineering from Simon Bolivar University and received his PhD degree in 1992 from the University of Pennsylvania. He carries out his research activities within the Structural Integrity, Micromechanics and Reliability of Engineering Materials (CIEFMA) group at UPC. His research interests include mechanical integrity and damage assessment of structural materials, particularly hardmetals, advanced ceramics, stainless steels, and hard coatings. He is the co-author of more than 70 papers published in top journals in these fields. In addition, he has a track record of technology transfer and consultancy with hard materials industries. He is member of the Editorial Board of the International Journal of Refractory Metals and Hard Materials as well as of the Steering Committee of the European Hard Materials Group within the European Powder Metallurgy Association. He has been co-chairman of the last three ICSHM.

Chrsitoph E. Nebel graduated in electrical engineering at the University of Stuttgart where he also got his PhD in 1989. He became a postdoc at the Xerox Research Center, Palo Alto, USA between 1990 and 1992 funded by the Alexander v. Humboldt Foundation, Germany. He joined the team of Martin Stutzmann at the Walter Schottky Institute of the Technical University Munich in 1993 where he habilitated in 1998. In 2004, he joined the Diamond Research Center of the National Institute of Advanced Industrial Science and Technology, Japan, where he was leading the "Bio-Functionalized Device Team". In 2008, he went back to Germany to become head of the Micro- and Nano-Sensor Department of the Fraunhofer-Institute for Applied Solid State Physics in Freiburg.

LIST OF CONTRIBUTORS

Jocelyn Achard
Laboratoire des Sciences des Procédés et des Matériaux (LSPM), UPR3407 CNRS, Université Paris 13, France; Laboratoire d'Excellence Sciences and Engineering for Advanced Materials and devices (SEAM), Villetaneuse, France

Igor Aharonovich
School of Physics and Advanced Materials, University of Technology Sydney, Ultimo, New South Wales, Australia

Marc Anglada
Departament de Ciència dels Materials i Enginyeria Metal·lúrgica, Universitat Politècnica de Catalunya · Barcelona Tech, Barcelona, Spain

Thomas Babinec
Departments of Electrical Engineering and Applied Physics, Stanford University, CA, USA

Soumendra N. Basu
Division of Materials Science and Engineering, Department of Mechanical Engineering, Boston University, Boston, MA, USA

Bikramjit Basu
Materials Research Center, Indian Institute of Science, Bangalore, India

Carmen Baudín
Instituto de Cerámica y Vidrio, CSIC, Madrid, Spain

I. Bello
Center of Super-Diamond and Advanced Films (COSDAF), and Department of Physics and Materials Sciences, City University of Hong Kong, Tat Chee Avenue, Hong Kong SAR, P.R. China

Eleni Berdermann
GSI Helmholtzzentrum für Schwerionenforschung GmbH, Darmstadt, Germany

Raul Bermejo
Institut für Struktur- und Funktionskeramik, Montanuniversität Leoben, Leoben, Austria

Vladimir Blank
Technological Institute for Superhard and Novel Carbon Materials, Moscow, Russia

Vadim Brazkin
Institute for High Pressure Physics, Russian Academy of Sciences, Troitsk, Moscow, Russia

Ovidiu Brinza
Laboratoire des Sciences des Procédés et des Matériaux (LSPM), UPR3407 CNRS, Université Paris 13, France; Laboratoire d'Excellence Sciences and Engineering for Advanced Materials and devices (SEAM), Villetaneuse, France

Y.M. Chong
Center of Super-Diamond and Advanced Films (COSDAF), and Department of Physics and Materials Sciences, City University of Hong Kong, Tat Chee Avenue, Hong Kong SAR, P.R. China

Marvin L. Cohen
Department of Physics, University of California at Berkeley, Berkeley, CA, USA; Materials Sciences Division, Lawrence Berkeley National Laboratory, Berkeley, CA, USA

Christoph Czettl
CERATIZIT Austria GmbH, Reutte, Austria

Robert Danzer
Institut für Struktur- und Funktionskeramik, Montanuniversität Leoben, Leoben, Austria

Goffredo de Portu
National Research Council of Italy (CNR), Chemical Science & Materials Technology Department, Institute of Science and Technology for Ceramics (ISTEC), Faenza, Italy

Nadira Derkaoui
Laboratoire des Sciences des Procédés et des Matériaux (LSPM), UPR3407 CNRS, Université Paris 13, France; Laboratoire d'Excellence Sciences and Engineering for Advanced Materials and devices (SEAM), Villetaneuse, France

Eric F. Drake
Rice University, Houston, Texas, USA

Yasuaki Einaga
Department of Chemistry, Keio University, Yokohama, Japan

Peter Ettmayer
Vienna University of Technology, Institue of Chemical Technologies and Analytics, Vienna, Austria

Z. Zak Fang
Department of Metallurgical Engineering, University of Utah, Salt Lake City, UT, USA

Gilbert Fantozzi
INSA de Lyon, MATEIS (UMR CNRS 5510), Villeurbanne, France

S.A. Firstov
Department of Physics of Strength and Plasticity of Materials, Frantsevich Institute for Problems of Materials Science, Kiev, Ukraine

Rainer Gadow
University of Stuttgart, Institute for Manufacturing Technology of Ceramic Components and Composites, Stuttgart, Germany

A.J. Gant
National Physical Laboratory, Teddington, Middlesex, TW, UK

Mark G. Gee
National Physical Laboratory, Teddington, Middlesex, TW, UK

Randall M. German
Department of Mechanical Engineering, College of Engineering, San Diego State University, San Diego, CA, USA

Alix Gicquel
Laboratoire des Sciences des Procédés et des Matériaux (LSPM), UPR3407 CNRS, Université Paris 13, France; Laboratoire d'Excellence Sciences and Engineering for Advanced Materials and devices (SEAM), Villetaneuse, France

Brahma Raju Golla
Engineering Ceramics Research Group, Korea Institute of Materials Science, Changwon, Gyeongnam, Korea

Stefano Guicciardi
National Research Council of Italy (CNR), Chemical Science & Materials Technology Department, Institute of Science and Technology for Ceramics (ISTEC), Faenza, Italy

Stuart Hampshire
Materials and Surface Science Institute, University of Limerick, Limerick, Ireland

Khaled Hassouni
Laboratoire des Sciences des Procédés et des Matériaux (LSPM), UPR3407 CNRS, Université Paris 13, France; Laboratoire d'Excellence Sciences and Engineering for Advanced Materials and devices (SEAM), Villetaneuse, France

Bin He
Center of Super-Diamond and Advanced Films (COSDAF), and Department of Physics and Materials Sciences, City University of Hong Kong, Tat Chee Avenue, Hong Kong SAR, P.R. China

Mathias Herrmann
Fraunhofer-Institut für Keramische Technologien und Systeme IKTS, (www.ikts.fraunhofer.de) Dresden, Germany

Jonathan Hird
Schlumberger Gould Research, Cambridge, United Kingdom

Tetsuo Irifune
Geodynamics Research Center, Ehime University, Matsuyama, Japan; Earth-Life Scinece Institute, Tokyo Institute of Technology, Tokyo, Japan

Thomas J. Jewett
Global Tungsten and Powders Corporation, Towanda, Pennsylvania, USA

Emilio Jiménez-Piqué
Departament de Ciència dels Materials i Enginyeria Metal·lúrgica, Universitat Politècnica de Catalunya · Barcelona Tech, Barcelona, Spain

Shinhoo Kang
Department of Materials Science and Engineering, Seoul National University, Gwanak-ku, Seoul, Korea

Hiromitsu Kato
Energy Technology Research Institute, AIST, Japan

Frank Kern
University of Stuttgart, Institute for Manufacturing Technology of Ceramic Components and Composites, Stuttgart, Germany

Hagen Klemm
Fraunhofer-Institut für Keramische Technologien und Systeme IKTS, (www.ikts.fraunhofer.de) Dresden, Germany

Hans Kolaska
Fachverband für Pulvermetallurgie e.V., Hagen, Germany

Igor Konyashin
Element Six Hard Materials, Element Six GmbH, Städeweg, Burghaun, Germany

Mark C. Koopman
Department of Metallurgical Engineering, University of Utah, Salt Lake City, UT, USA

Aaron D. Krawitz
University of Missouri, Columbia, Missouri, USA

Jochen Kriegesmann
Department of Materials Technology, Glass and Ceramics, University of Applied Sciences Koblenz, Höhr-Grenzhausen, Germany

Anke Krueger
Institute for Organic Chemistry, Julius-Maximiliaus University würzburg, Am Hubland, 97074 Würzburg, Germany

Boris Kulnitskiy
Technological Institute for Superhard and Novel Carbon Materials, Moscow, Russia

Sabine Lay
Grenoble Institute of Technology, Saint-Martin d'Hères, France

Shuit-Tong Lee
Center of Super-Diamond and Advanced Films (COSDAF), and Department of Physics and Materials Sciences, City University of Hong Kong, Tat Chee Avenue, Hong Kong SAR, P.R. China

Luis Llanes
Departament de Ciència dels Materials i Enginyeria Metal·lúrgica, Universitat Politècnica de Catalunya · Barcelona Tech, Barcelona, Spain

Kian Ping Loh
Department of Chemistry, National University of Singapore, Singapore

Guillaume Lombardi
Laboratoire des Sciences des Procédés et des Matériaux (LSPM), UPR3407 CNRS, Université Paris 13, France; Laboratoire d'Excellence Sciences and Engineering for Advanced Materials and devices (SEAM), Villetaneuse, France

John E. Lowther
School of Physics and DST/NRF Centre of Excellence in Strong Materials, University of the Witwatersrand, Johannesburg, South Africa

Andriy O. Lyakhov
Department of Geosciences, Stony Brook University, Stony Brook, NY, USA

Alexander Lyapin
Institute for High Pressure Physics, Russian Academy of Sciences, Troitsk, Moscow, Russia

Daniele Mari
Laboratoire de Physique de la Matière Complexe, Ecole Polytechnique Fédérale Lausanne, Lausanne, Switzerland

Julián Martínez-Fernández
Dpto. Física de la Materia Condensada—ICMS, Universidad de Sevilla—CSIC, Sevilla, Spain

Pankaj K. Mehrotra
Kennametal Inc., Latrobe, PA, USA

Jan Meijer
Nuclear Solid State Physics, University Leipzig, Leipzig, Saxony, Germany

Lutz-Michael Berger
Fraunhofer Institute IWS, Dresden, Germany

Armelle Michau
Laboratoire des Sciences des Procédés et des Matériaux (LSPM), UPR3407 CNRS, Université Paris 13, France; Laboratoire d'Excellence Sciences and Engineering for Advanced Materials and devices (SEAM), Villetaneuse, France

Claude Michotte
CERATIZIT Luxembourg S. à. r. l., Route de Holzem, Mamer, Luxembourg

K.P. Mingard
National Physical Laboratory, Teddington, Middlesex, TW, UK

Rosa M. Miranda
UNIDEMI, Departamento de Engenharia Mecânica e Industrial, Faculdade de Ciências e Tecnologia, Universidade Nova de Lisboa, Caparica, Portugal

Pilar Miranzo
Institute of Ceramics and Glass, CSIC. Kelsen, 5, Madrid, Spain

Jean-Michel Missiaen
Grenoble Institute of Technology, Saint-Martin d'Hères, France

Christian Mitterer
Department of Physical Metallurgy and Materials Testing, Montanuniversität Leoben, Leoben, Austria

Michael Moseler
Fraunhofer Institute for Mechanics of Materials IWM, Freiburg, Germany

Christoph E. Nebel
Fraunhofer-Institute for Applied Solid State Physics, Freiburg, Germany

Steffen Nowotny
Fraunhofer Institut IWS, Dresden, Germany

Artem R. Oganov
Department of Geosciences, Center for Materials by Design, Institute for Advanced Computational Science, Stony Brook University, Stony Brook, NY, USA; Moscow Institute of Physics and Technology, Dolgoprudny city, Moscow Region, Russian Federation; Northwestern Polytechnical University, Xi'an, China

Hugo M. Ortner
Darmstadt University of Technology, Department of Material Sciences: Materials Characterization, Darmstadt, Germany

Maria Isabel Osendi
Institute of Ceramics and Glass, CSIC. Kelsen, 5, Madrid, Spain

Lars Pastewka
Fraunhofer Institute for Mechanics of Materials IWM, Freiburg, Germany

Arvid Eric Pasto
Retired from Sparks, NV, USA

Sébastien Pezzagna
Nuclear Solid State Physics, University Leipzig, Leipzig, Saxony, Germany

S.S. Ponomarev
Department of Physics of Strength and Plasticity of Materials, Frantsevich Institute for Problems of Materials Science, Kiev, Ukraine

Michail Popov
Technological Institute for Superhard and Novel Carbon Materials, Moscow, Russia

Leo Prakash
Kyocera Unimerco Tooling A/S, Sunds, Denmark

Joaquin Ramírez-Rico
Dpto. Física de la Materia Condensada—ICMS, Universidad de Sevilla—CSIC, Sevilla, Spain

Pascal Reynaud
INSA de Lyon, MATEIS (UMR CNRS 5510), Villeurbanne, France

John Robertson
Department of Engineering, Cambridge University, Cambridge, UK

B. Roebuck
National Physical Laboratory, TW, UK

Gregory S. Rohrer
Department of Materials Science and Engineering, Carnegie Mellon University, Pittsburgh, PA, USA

Catherine Rond
Laboratoire des Sciences des Procédés et des Matériaux (LSPM), UPR3407 CNRS, Université Paris 13, France; Laboratoire d'Excellence Sciences and Engineering for Advanced Materials and devices (SEAM), Villetaneuse, France

Malika Saâdaoui
LERSIM Ecole Mohammadia d'Ingénieurs, Université Mohamed V Agdal, Rabat, Morocco

Vinod K. Sarin
Division of Materials Science and Engineering, Department of Mechanical Engineering, Boston University, Boston, MA, USA

Uwe Schleinkofer
CERATIZIT Austria GmbH, Reutte, Austria

Matthias Schreck
Universität Augsburg, Institut für Physik, Augsburg, Germany

Alex V. Shatov
8 Parkside Drive, Jamesburg, NJ, USA

Olga A. Shenderova
International Technology Center, Raleigh, NC, USA; Adámas Nanotechnologies, NC, USA

François Silva
Laboratoire des Sciences des Procédés et des Matériaux (LSPM), UPR3407 CNRS, Université Paris 13, France; Laboratoire d'Excellence Sciences and Engineering for Advanced Materials and devices (SEAM), Villetaneuse, France

Raj P. Singh Gaur
Global Tungsten and Powders Corporation, Towanda, Pennsylvania, USA

Vladimir L. Solozhenko
LSPM–CNRS, Université Paris 13, Villetaneuse, France

Jörg Spatzier
Fraunhofer Institut IWS, Dresden, Germany

Hitoshi Sumiya
Electronics Materials R&D Laboratories, Sumitomo Electric Industries Ltd, Itami, Japan

Alexandre Tallaire
Laboratoire des Sciences des Procédés et des Matériaux (LSPM), UPR3407 CNRS, Université Paris 13, France; Laboratoire d'Excellence Sciences and Engineering for Advanced Materials and devices (SEAM), Villetaneuse, France

Takashi Taniguchi
Advanced Key Technology Division, National Institute for Materials Science, Tsukuba, Ibaraki, Japan

Shi Wun Tong
Department of Chemistry, National University of Singapore, Singapore

Yadir Torres
Universidad de Sevilla, Department of Mechanical and Materials Engineering—ETSI, Sevilla, Spain

Vladimir Turkevich
Synthesis and Sintering of Superhard Materials at High Pressures and High Temperatures, Institute for Superhard Materials of the Ukrainian National Academy of Sciences, Kiev, Ukraine

Hongtao Wang
Kennametal Inc., Rogers, AR, USA

Maxime Wartel
Laboratoire des Sciences des Procédés et des Matériaux (LSPM), UPR3407 CNRS, Université Paris 13, France; Laboratoire d'Excellence Sciences and Engineering for Advanced Materials and devices (SEAM), Villetaneuse, France

Dow Whitney
Retired from Department of Materials Science and Engineering at the University of Florida, Gainesville, Florida, USA

Christoph Wild
Diamond Materials GmbH, Freiburg, Germany

Thomas A. Wolfe
Global Tungsten and Powders Corporation, Towanda, Pennsylvania, USA

Eckhard Wörner
Diamond Materials GmbH, Freiburg, Germany

Wenjun J. Zhang
Center of Super-Diamond and Advanced Films (COSDAF), and Department of Physics and Materials Sciences, City University of Hong Kong, Tat Chee Avenue, Hong Kong SAR, P.R. China

Qiang Zhu
Department of Geosciences, Stony Brook University, Stony Brook, NY, USA

SECTION I

INTRODUCTION TO HARDMETALS

1.01 History of Hardmetals

Peter Ettmayer, Vienna University of Technology, Institue of Chemical Technologies and Analytics, Vienna, Austria
Hans Kolaska, Fachverband für Pulvermetallurgie e.V., Hagen, Germany
Hugo M. Ortner, Darmstadt University of Technology, Department of Material Sciences: Materials Characterization, Darmstadt, Germany

1.01.1 Introduction to Hardmetals—Definitions and Classification

1.01.1.1 Definitions

1.01.1.1.1 Hardmetals and Cemented Carbides

The two terms are completely equivalent. However, "hardmetals" is preferably used in Europe (in German, only the word "Hartmetall" is used) while in USA and in European English literature, "cemented carbides" is used.

http://dx.doi.org/10.1016/B978-0-08-096527-7.00001-5

Since their discovery by Schröter in 1922, in the machining industry, hardmetals that contain a dominant WC-phase are generally termed as "cemented carbides". The term "hardmetals" is also used for the binder-free and cemented materials.

1.01.1.1.2 Cermets

There are several definitions of cermets in use. According to German (2005), a cermet is a particulate composite consisting of ceramic particles bonded with metal matrix. The original term was coined by joining ceramic and metal into a single word to describe a composite.

Kolaska and Ettmayer (in preparation) define cermets shortly as sintered hardmetals containing TiC and TiN with exclusion of WC–Co hardmetals.

Mari (2001), pp. 1118–1123 defines cermets as follows. The designation "cermet" has been historically reserved for TiC-based hardmetals to specify the ceramic character (lower electrical conductivity) of TiC in comparison with WC. Among cemented carbides, those based on the system WC–Co are the most widespread, while the most used system among TiC-based cermets is TiC_xN_{1-x} – Mo – Ni.

Finally Lengauer (2012) gives a more precise definition. Cermets are based on Ti(C,N) and exhibit, therefore, a purely cubic-face centered (fcc) hard material phase. They exhibit high wear resistance at high cutting rates if compared to conventional WC–Co hardmetals. They also show high life times and a good surface quality of machined materials. The hard material particles of cermets show a typical core-rim structure which is formed by the varying chemical stability of its components as well as by interaction between the molten binder metal and the hard phases during liquid phase sintering. The hard material particles are rich in nitrogen and are surrounded by a coating phase which is rich in the alloying elements Mo and W. This coating improves the wettability by the binder and thereby causes the superior properties.

1.01.1.2 Classification of Hardmetals

The broad variability of hardmetals concerning their composition and properties has on the one hand led to a very wide field of application; on the other hand, however, to a puzzling multitude of hardmetal grades.

This has led to various classification systems of which the most important are the following:

The classification according to the ISO committee TC 29 of April 1958
The classification according to the US Industrial Code (Buick-Hardmetal-Classification)
The classification according to the DIN 4990 of 1948.

Further relevant information can be found in Schedler (1988) and in Trent (1991).

1.01.2 History of Hardmetals

1.01.2.1 Introduction: Aim and Disposition

Few factors have played a more critical role in global industrial economic growth during the latest centuries than the drastically reduced cost of making products that we need in our daily life. What one man can produce in a couple of minutes today would have been an impossible task for our ancestors for most of the 5000 generations man has existed. It is only in the latest 300 years that any significant process has been made and this applies in particular to the central areas of mining and manufacturing. The important events in the latter activity were for a long time associated with the invention of new tool steel for metal cutting, of which the optimized grades of high-speed steel introduced in the early 1900s were considered by many authorities to be the ultimate tool material. However, like so many other predictions, this turned out to be wrong. Never in the history of tools was there a more rapid revolutionary change than in the 1940s, when what could be achieved with the best high-speed steel was radically outperformed. Thus, the output of the American metal working industry was increased by a factor of three with the same amount of machines and manpower during the short period 1939–1945. And at the same time, a similar change took place in the mines and at major construction sites.

Why this sudden increase in productivity in just a few years? The answer is the general introduction of a new synthetic tool material, cemented carbide, by means of which the costs of manufacturing by turning, milling and other machining (cutting) operations were drastically reduced. Without cemented carbide tools we would have to spend much more than the roughly $750G that is now annually required for making all the drilling in rocks, which is a major operation in the mining and construction companies (Aronsson, 2005).

1.01.2.2 The Birth of Hardmetals—The Schröter Patent

The Viennese Franz Skaupy (Figure 1) obtained his PhD in chemistry under the guidance of Prof. Wegscheider and was then employed at the Auer Gesellschaft in Berlin in 1906. From 1907 until 1928, he was the head of the "study group for electrical fluorescent tubes" which was later changed as "study group for electrical lighting".

Apart from the development of fluorescent tubes, he was also in charge of the production of lamp wires of non-sag tungsten (NS-W). The development of the latter was largely solved by the respective work of Coolidge at General Electric (Schade, 2010b). The study group for electrical lighting was also in search of a proper material to substitute diamond as drawing die for NS-W after the First World War. Skaupy had to devote himself to the refractory metal tungsten within the frame of his research activities. He directed his coworkers to use the sinter technology for the production of solid WC. He attempted to transform the brittle carbide by sintering into a ductile material similarly to tungsten. WC can be melted in the electric arc, the reaction products consisted of a mixture of tungsten monocarbide WC and tungsten subcarbide W_2C. These reaction products were hard but also extremely brittle due to the very fine cracks which formed during cooling. Hence, the material could hardly be used as drawing die. Owing to H. Wolff (Wolff, 1941) who was employed at the study group for electrical lighting m.b.H. in Berlin at that time, WC powder was synthesized by the reaction of tungsten powder with a stoichiometric amount of carbon. The obtained product powder was then pressed and was tried to sinter in the same way as tungsten powder had been successfully sintered for the production of W wire. However, this did not work at all with WC. Hence, all respective work was nearly given up when a coworker with the name Matthieú got the idea to admix some iron powder to the tungsten carbide powder as it was done for tungsten before the introduction of the Coolidge process: 10% nickel powder had been added to the tungsten powder to make the sintered product ductile. The admixed nickel evaporated during sintering at high temperature in vacuum. The first respective experiments of Schröter to sinter WC with Ni additions obviously resulted in varying results which were not really conclusive and satisfactory. These iron and nickel additions to the WC powder were then substituted by cobalt powder—probably due to a proposition by Prof. Guertler. Herewith the today's WC–Co hardmetal had been invented in its present form (Skaupy, 1951). This metal ceramic alloy was indeed proper for the production of drawing dies of relatively coarse W wires which had to be drawn at a slow rate for technical reasons. However, the new materials could not be used for the drawing of fine W wires. Somewhat earlier, Dr Heinrich Baumhauer had infiltrated porous bodies of WC with liquid iron and hereby closed the pores. He was not employed at the study group but in the tungsten production of the former Siemens lamp factory in Charlottenburg (Berlin). Hereby it was possible for the first time to produce drawing dies of good quality. On March 18 1922, Dr Baumhauer applied for the issue of the patent for this procedure (Baumhauer, 1922). Later on, he was the long-term head of the production. Most interesting is the fact that this patent was applied for earlier than the basic patent of Schröter DRP 420.689 (1923), but it was granted later than the Schröter patent.

Figure 1 Prof. Dr Franz Skaupy (about 1950).

Today, almost 100 years after the granting of these patents, it is impossible to find out which personal relations and circumstances had finally led to the famous basic patent DRP 420.689 which carries the name of Karl Schröter as the only inventor. The latter, who had joined the chemical department of the German Gas-Glühlicht Gesellschaft in 1902 as a chemist, changed over to the OSRAM Studiengesellschaft in 1908. Here he was engaged in the fabrication of metal wires for incandescent lamps made of osmium or tungsten. In the 1920s, he was searching for materials for drawing dies for tungsten wires which could be used as substitutes for the very costly diamond which in addition was difficult to obtain in the years during and after the First World War due to the world economic crisis. To reach this goal, Schröter had tried to realize the patent ideas of Lohmann and Voigtlaender (1914). After Skaupy had taken over the research department for incandescent lamps in the enlarged study group of OSRAM in 1921, Schröter tried to develop the manufacture of fused hard carbide materials. Since Schröter did not want to discontinue this work, Dr Skaupy asked Dr Wilhelm Jenssen to start experiments to sinter tungsten carbide to dense bodies. Subsequently, Dr Jenssen produced drawing dies made of pure tungsten powder by pressing and sintering at high temperatures. He then tried to carburize these sinterings with a gas mixture of hydrogen and methane at relatively low temperatures in order to arrive at hard and abrasion-resistant drawing dies. However, the slugs had only been carburized down to a depth of 1–2 mm and the carbide layer exhibited a lot of cracks. Hence, the bodies were useless as drawing dies. Nevertheless, an American patent was claimed by Dr W. Jenssen and K. Schroeter (Jenssen and Schroeter, 1925): US Pat. 1.551.333. Soon afterwards, Dr Jenssen became seriously sick. Hence, further developments had to be continued by K. Schröter and A. Fehse. The first subsequent experiments were started upon Skaupy's urging with small nickel additions to the tungsten carbide. These experiments yielded quite varying results until it turned out—maybe by lucky coincidence—that only tungsten monocarbide with an exact stoichiometric carbon content must be mixed with the metal powder (Co or Ni) and after being pressed and sintered yielding a hard but not too brittle material. This is indicated by a passage in Schröter's patent (Schröter, 1923): a tungsten carbide must be used as starting material for the new alloy which can be obtained either by carburizing the tungsten powder with a proper gas phase or by mixing the tungsten powder with elemental carbon in form of soot, sugar-coal or graphite, etc. and subsequent heating of the mixture to high temperatures. The optimum carbon content turned out to be 7%, but it can be also smaller and vary between 3 and 7% (w/w). However, the carbon content can be also a bit greater up to about 10%. This broad range of carbon might have been given because of reasons concerning the patent; it can be anticipated that Schröter knew already that only tungsten monocarbide with a stoichiometric carbon content yields products of sufficient toughness. Today we know that only the very exact content of carbon is of primary importance to obtain a sufficient hardness without losses of toughness. A carbon deficiency leads to the formation of brittle complex carbides (eta-carbides) and a carbon excess results in porosity which also reduces the toughness of the hardmetal.

The surprising fact that the patent of 1923 carries only the name of Schröter as the inventor is probably due to the fact that at that time patents (developed in a company) only carried the name of the respective company as patent owner but not names of the working group who was responsible for the formulation of the patent (Skaupy's working group). At that time it was not a rule in Germany that one or more inventors had to be named on a patent contrary to the effective patent laws in USA. However, it could also be that the society of electrical incandescent lamps under the leadership of Skaupy was not aware of the significance of the invention of "hardmetal" for the technology of machining, milling and turning. It could be due to an error of judgment that the Schröter patent had only been applied for in England and USA while for all other countries, the timely priority claim was missed. However, the patent was offered to the Krupp company and in the same year (1925), intensive discussions took place between Mr Blau and Meinhard of OSRAM and Mr Strauss and Preussing of Krupp.

The result was an agreement which granted Krupp the exclusive license as well as the right of granting sublicenses. On the other hand, OSRAM was supposed to continue with respective research and development activities and was also allowed to produce hardmetals for their own need free of license payments. The ASKO-Patent-Administration m.b.H. was responsible for managing the Schröter patent and was supposed to receive one-third of the license payments which Krupp might receive from royalties as licensee.

The question of a proper brand name was intensively discussed at Krupp and the following proposals were put forward: WIDIA, DICAR, CARDIA, CARDI and WOCAR. On December 17, 1925, these trademarks were applied for at the Reichspatentamt of Berlin for examination and protection. The trademarks CARDIA and DICAR were turned down due to already existing older trademarks. Hence, the trademark "WIDIA" was chosen. It was created from German words "wie" and "Diamant", meaning "like Diamond" which survived until today.

1.01.2.3 The Development of a Production Technology for the Manufacture of Hardmetals at Krupp-WIDIA

In the basement and on the ground floor of the Chemical Laboratory of Krupp Essen in the Frohnhauserstraβe, construction and furnishing activities started on April 1, 1926. A few weeks later, production started. Eighteen people had been employed for this purpose and the first yearly production amounted to about 1000 kg under strictest secrecy. Of course, the way from production on a laboratory scale to an industrial production was difficult and costly. However, the necessary investments were granted quickly by the Krupp management. Already in February 1926, 70,000 Reichsmark had been made available for the purchase of necessary apparatus. Dipl. Ing. Heinrich Thümling was responsible for the development of a proper new sinter technology. He was previously operations assistant in the mechanical engineering 15 department at Krupp Essen.

The quality testing of the initial sinter products was rather simple. The toughness/brittleness test consisted of a beat with the hammer onto a sintered tip which had been fastened in a vice. The hardness test was performed by scratching of glass. It is reported that after a while no more window glass without scratches was available for this purpose in the quality testing laboratory. The microstructure of the sintered hardmetal was inspected by optical microscopy of respective fracture surfaces especially concerning residual porosity (Klink & Weidenfeld, 1951). One can learn about the serious problems with which the starting production of hardmetals had been confronted in the years 1926 and 1927 from respective reports of Klink and Weidenfeld 1951 and Weidenfeld (1951). The starting materials in the form of powders of tungsten, tungsten carbide, and cobalt had to be produced from tungsten- and cobalt oxides in self-developed installations. Subsequently, they were mixed and pressed. The pieces were sintered in electrically heated graphite tube furnaces under the application of coal gas as protecting atmosphere. This yielded little satisfying results. Only after substitution of coal gas by hydrogen which was recommended by Schröter, proper results could be achieved. Of course, the application of hydrogen was dangerous and a catastrophic hydrogen explosion had been reported by Weidenfeld within a gas purification unit which caused a heavy damage but fortunately no casualties (Weidenfeld, 1951) (**Figure 2**).

The sintered WIDIA hardmetal tips were then soldered onto steel carriers with a brass solder and subsequently ground and polished. Since hardmetal cannot be worked with the then usual polishing disks for steel, experiences had to be gathered for the polishing of hardmetals (**Figure 3**).

Within the frame of the Spring Fair of Leipzig 1927, tools with WIDIA hardmetal inserts for the turning and milling of cast iron and hardened steels (12% manganese steel) had been shown to international public for the first time (**Figure 4**).

It generated a lot of attention and admiration. The new cutting material was extremely precious. At the beginning of the 1930s, 1 g WIDIA hardmetal costs US $1.00, which was more costly than 1 g of gold!

1.01.2.4 The Foundation of WIMET

One of the attentive visitors of the Leipzig Spring Fair 1927 was an engineer with German–Polish parents, Mr Axel Wickman who shortly before started a business with machinery in Coventry. Mr Wickman wanted to gather information about the new material "hardmetal of WIDIA" and supposedly succeeded to obtain such a piece of hardmetal (private communication of Jack Sandford to H. Kolaska). He tested it in his company in Coventry under harsh conditions. In order to get into contact with the Friedrich Krupp AG in Germany, he succeeded to obtain a recommendation letter of the German company Schutte which produced automated instrumentation for turning. In spite of this letter, he experienced great difficulties to be allowed into the headquarters of Krupp at Essen and to have a discussion with the managing director Dr Preussing. Mr Wickman spoke German fluently and after many discussions and negotiations, he finally succeeded to obtain the exclusive commercial rights for WIDIA hardmetals and respective tools for Great Britain in 1928. In 1931, he was so successful in selling WIDIA hardmetal that he was allowed to found a production site for the sintering of WIDIA parts from pressed preforms which were provided by Krupp-WIDIA. He therefore founded the company "Tool Metal Manufacturing Co. Ltd Coventry" which was owned by Krupp AG to 51% and by Wickman to 49%. The name "WIMET" was then introduced, which is an abbreviation of Wickman and Metal.

1.01.2.5 The Foundation of CARBOLOY

Samuel Hoyt was the chief metallurgist of General Electric USA. In 1925, he visited Europe and at OSRAM, he came to know the new material hardmetal. After returning to the USA, he immediately started with experiments

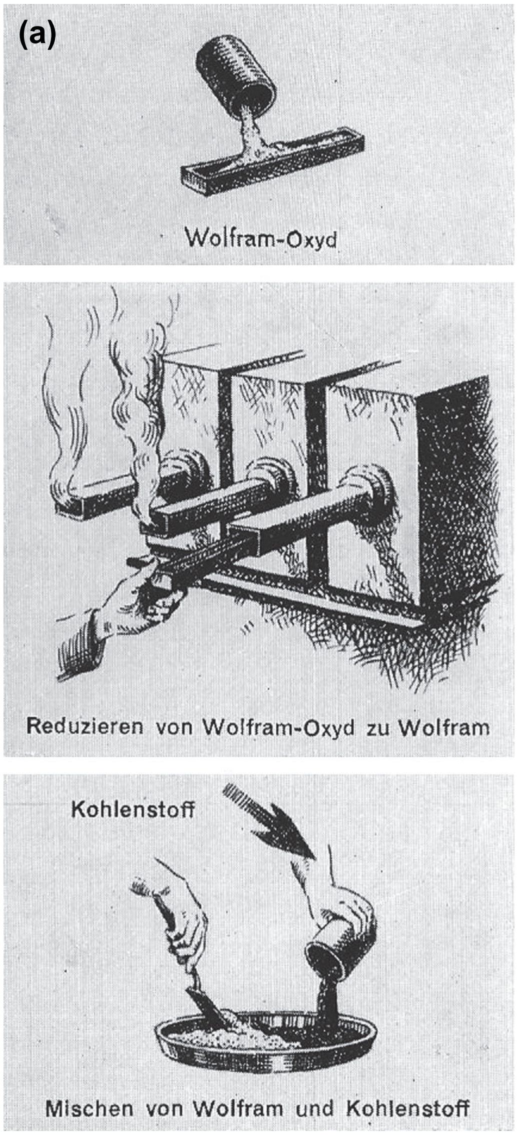

Figure 2 The production of hardmetal "WIDIA" (from the WIDIA-Handbook 1936), English titles to the pictures of the workflow. (a) Tungsten oxide—reduction of tungsten oxide to metallic tungsten and mixing of tungsten with carbon. (b) Carburization to tungsten carbide—mixing of tungsten carbide with cobalt, milling of tungsten carbide and cobalt, and pressing to rods. (c) Presintering of rods—forming of inserts from the presintered rods, finalization of inserts-forming, and sintering of the inserts. (d) Quality control by milling or turning—dimensional end control.

to machine Silumin (an AlSi-alloy). Negotiations with Krupp were initiated and it took 2 years until an agreement was reached. At that time, Krupp already had agreements with Firth Sterling Steel Corp. and Ludlum Steel Corp. Hence, General Electric had to accept these two companies as sublicensees. GE founded a subcompany, the CARBOLOY Corp. Inc. to organize the hardmetal business. In spite of the relatively high price of WC–Co hardmetals, CARBOLOY was not able to come out with profits for the first 5 years and the production volume was smaller than that of Krupp-WIDIA.

1.01.2.6 The Foundation of Montanwerke Walter

During the First World War, Richard Walter (born 1883 in Nürnberg) served in the Austrian Army in Pula in what is now northwestern Croatia. He was in charge of the service of Diesel motors. These exhibited problems with the wear of exhaust valves. He mastered this with the application of stellites, which are alloys with relatively high contents of tungsten, molybdenum, chromium and cobalt. This was presumably his first contact with hard

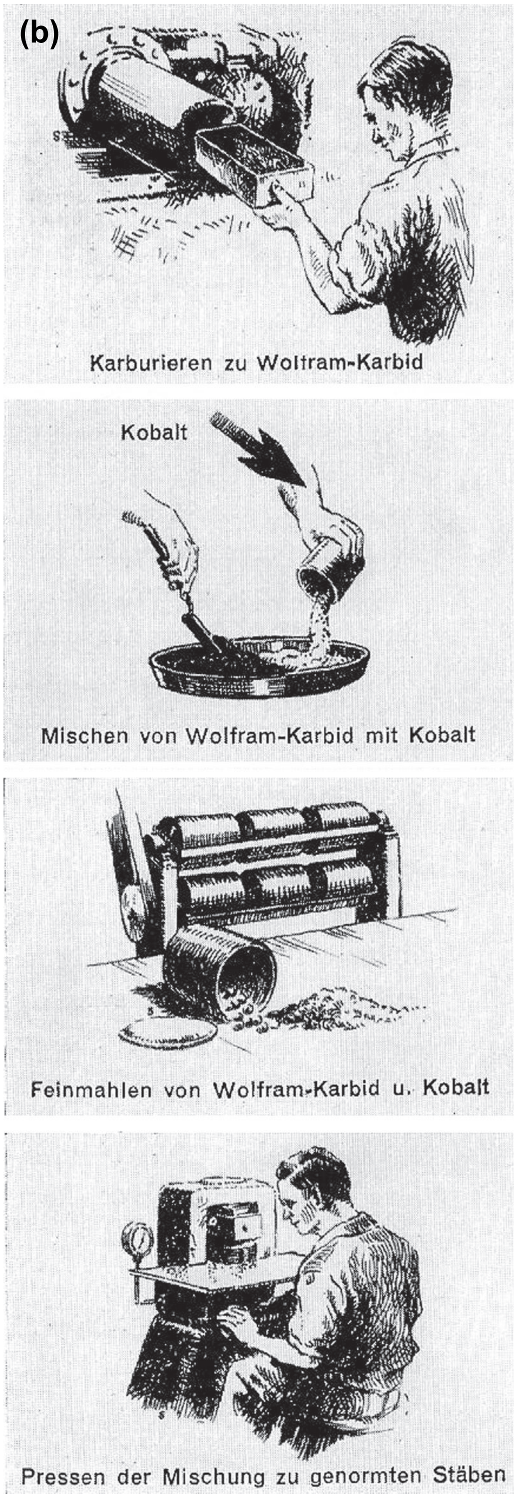

Figure 2 (*continued*).

and wear-resistant materials. After the war, he returned to Germany and bought a small company which he named "Montanwerke Walter" in 1924. Here he engaged himself with the chip forming of metals because he realized that this area will continuously gain importance in modern technology. He produced a hardmetal which he named "Dynit" which was quite successful in milling operations. However, in 1929, the Krupp AG in Essen accused the Montanwerke Walter because of violation against the Schröter Patent DRP 420 689 (1923).

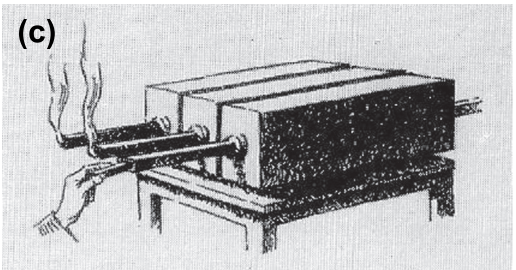

Vorsintern der genormten Stäbe

Ausarbeiten des Plättchens nach Rohmaßen

Fertigstellen des Plättchens

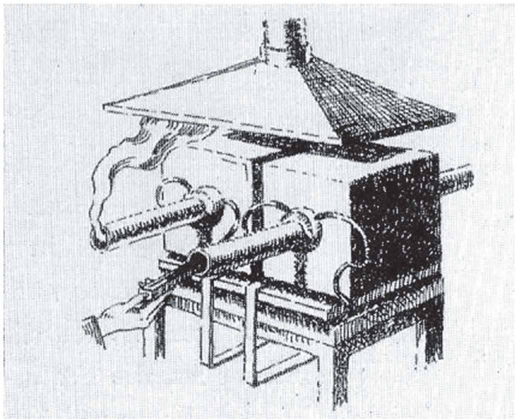

Fertigsintern

Figure 2 (*continued*).

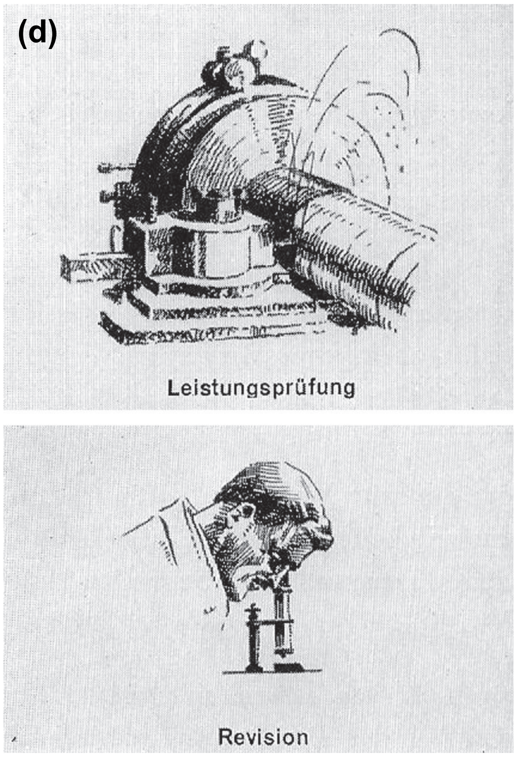

Figure 2 (*continued*).

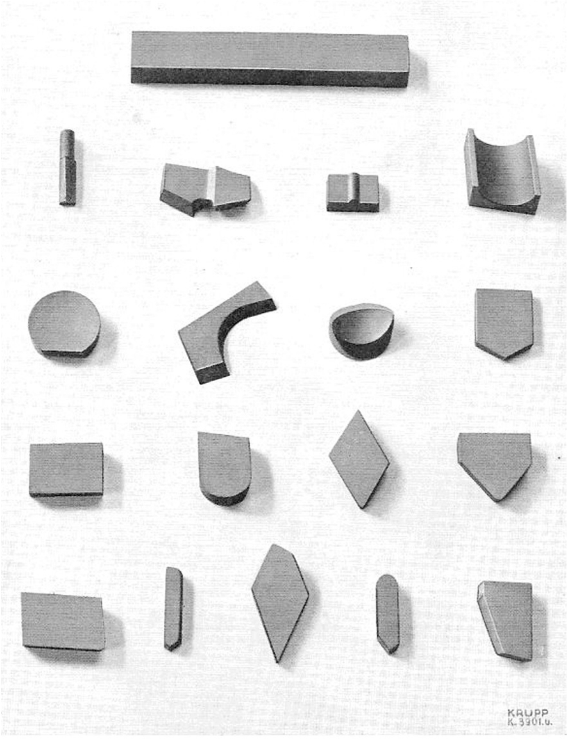

Bild 5. Widia-Formstücke.

Figure 3 WIDIA hardmetal pieces. From the WIDIA-Handbook 1936.

Figure 4 Exhibition of WIDIA hardmetal tools at the Leipzig Spring Fair 1927.

The consequence was that the Montanwerke Walter was not any more allowed to produce and sell tungsten-carbide-containing sintered hardmetals.

The suitability of hardmetals not only for turning operations but also for mining operations, especially drilling as well as for various wear parts resulted in quite a few new companies in all industrialized countries worldwide. In the USSR, a hardmetal was developed in 1929 for the manufacture of cutting tools by a company with the name POBEDIT. This company is still active (2010).

1.01.2.7 Dr Agte and the Company DEHAWE: A Typical German Fate of the Twentieth Century

In 1931, the Fried. Krupp AG started with the production of WIDIA X, a hardmetal based on WC/TiC/Co according to patents of Schröter, Agte, Moers and Wolff (DRP 1931/35 and US Pat. 1932/35). The development of this hardmetal had been carried out at OSRAM because of a deal between OSRAM and KRUPP AG. Presumably the development was performed under the leadership of Curt Agte who worked at OSRAM since 1922 under the guidance of Prof. Dr Franz Skaupy. Agte obtained his PhD in 1931 with a thesis on "Contributions to the knowledge of very high melting materials". In 1932, Dr Agte founded a company with the name "Deutsche Hartmetall-Werkzeug Gesellschaft Dr Agte Berlin/DEHAWE". This company produced hardmetal tools from pressed or presintered hardmetal pieces from various companies. C. Agte and his friend Dr Karl Becker developed hardmetal tools for various applications like drilling, turning, milling, grinding, etc. At the beginning of the Second World War, DEHAWE employed already about 300 workers. During the following years, a subsidiary company was founded in Teschen/Decin in what is now the Czech Republic. At the end of the war, this company had 1400 employees. K. Becker died during an air raid and C. Agte was in Decin when the Germans surrendered. The company was expropriated and nationalized. However, C. Agte and his family were allowed to remain in Decin upon the intervention of his coworkers. After about 10 years, Agte was allowed to return to the former GDR and he became the head of the hardmetal company in Immelborn near Eisenach where he died in 1972.

1.01.2.8 The Foundation of Further Important Hardmetal Companies

Quite a series of today's important hardmetal companies had been founded in the years after the issue of the Schröter patent in 1923 as is shown in Table 1.

It is difficult in many cases to find out the exact starting times for various companies and sometimes the available literature is even contradictory. In such cases, a respective time period is given. Most of the pertinent literature on companies stems from Aronsson (2005).

1.01.2.9 The Further Development of Krupp-WIDIA

In spite of the great attention which the new hardmetal had received during the Spring Fair at Leipzig in 1927, the production volume of about 10 ton/year was moderate in the years 1928–1932. This led to the derisive labeling of that plant as "confectionary company" (Konfektfabrik) by Gustav Krupp. In 1929, the WIDIA

Table 1 The foundation of important hardmetal companies

1924 Montanwerke Walter, Germany
1926 Krupp-WIDIA, Germany
1928 Carboloy Corp. by General Electric, USA
From 1929 onwards: Sumitomo, Japan
1930 Plansee Titanit, Austria
1931 WIMET, Great Britain
From 1931 onwards: Mitsubishi, Japan
1938 Kennametal Inc., USA
From 1942 onwards: Sandvik Coromantfabriken, Sweden

production was moved to the Sälzerstraße in Essen and in 1930, WIDIA was presented at the World Exhibition in Lüttich (Liege). Up to 1931/1932, WIDIA hardmetals were exclusively WC–Co based. In 1932, the introduction of TiC-containing hardmetals took place at WIDIA with the designation "WIDIA X". This material was better suited for the turning of steels than "WIDIA N".

Until 1935, sintered hardmetal on the basis of WC–Co and WC–TiC–Co were manufactured exclusively by Krupp-WIDIA. Then, licenses were given to the Deutsche Edelstahlwerke (DEW) in Krefeld, to the Stahlwerke Böhler in Düsseldorf and to the Rheinmetall Borsig in Berlin. Eighty four percent of the total amount of hardmetal produced in Germany during the war years 1939–1945 was from Krupp-WIDIA (Hobein, 1986). The production of hardmetal projectiles had become successful in 1929 and the respective mass production was taken up at Krupp-WIDIA beginning with November 1935 after a drastic reduction of the production costs. Until the end of the Second World War, it was the third main production branch behind the manufacture of hardmetal tools and respective tips. The rapid rise of Krupp-WIDIA until the end of the war is visible from Figure 5. Figure 6 shows the available hardmetal qualities of Krupp-WIDIA for the various areas of application. The text of this figure is unfortunately in German. However, the authors of this chapter wanted to show it in its original form. It should demonstrate the following:

a) The predominance of the German hardmetal industry in the late thirties of the 20th century.
b) The already developing of a multitude of hardmetal grades for certain areas of application.

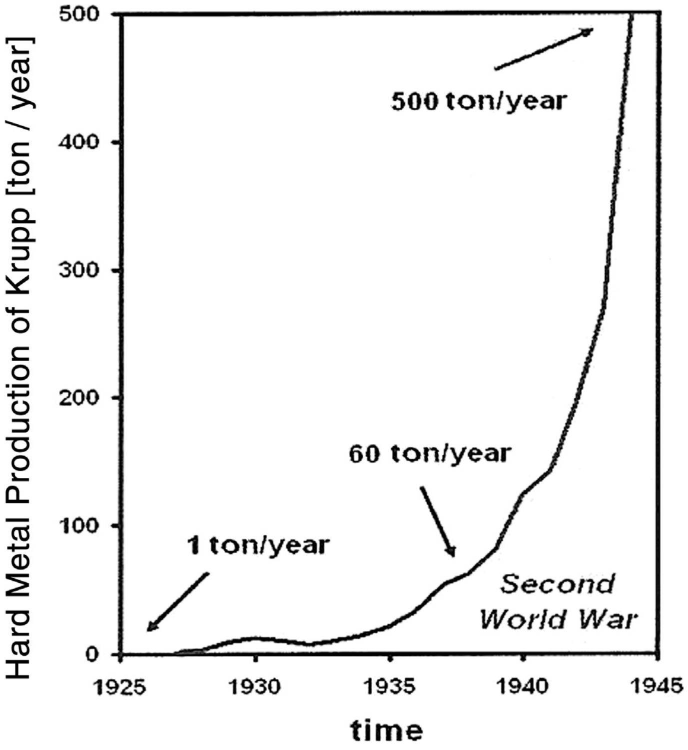

Figure 5 The hardmetal production of Krupp-WIDIA in the years 1926–1945.

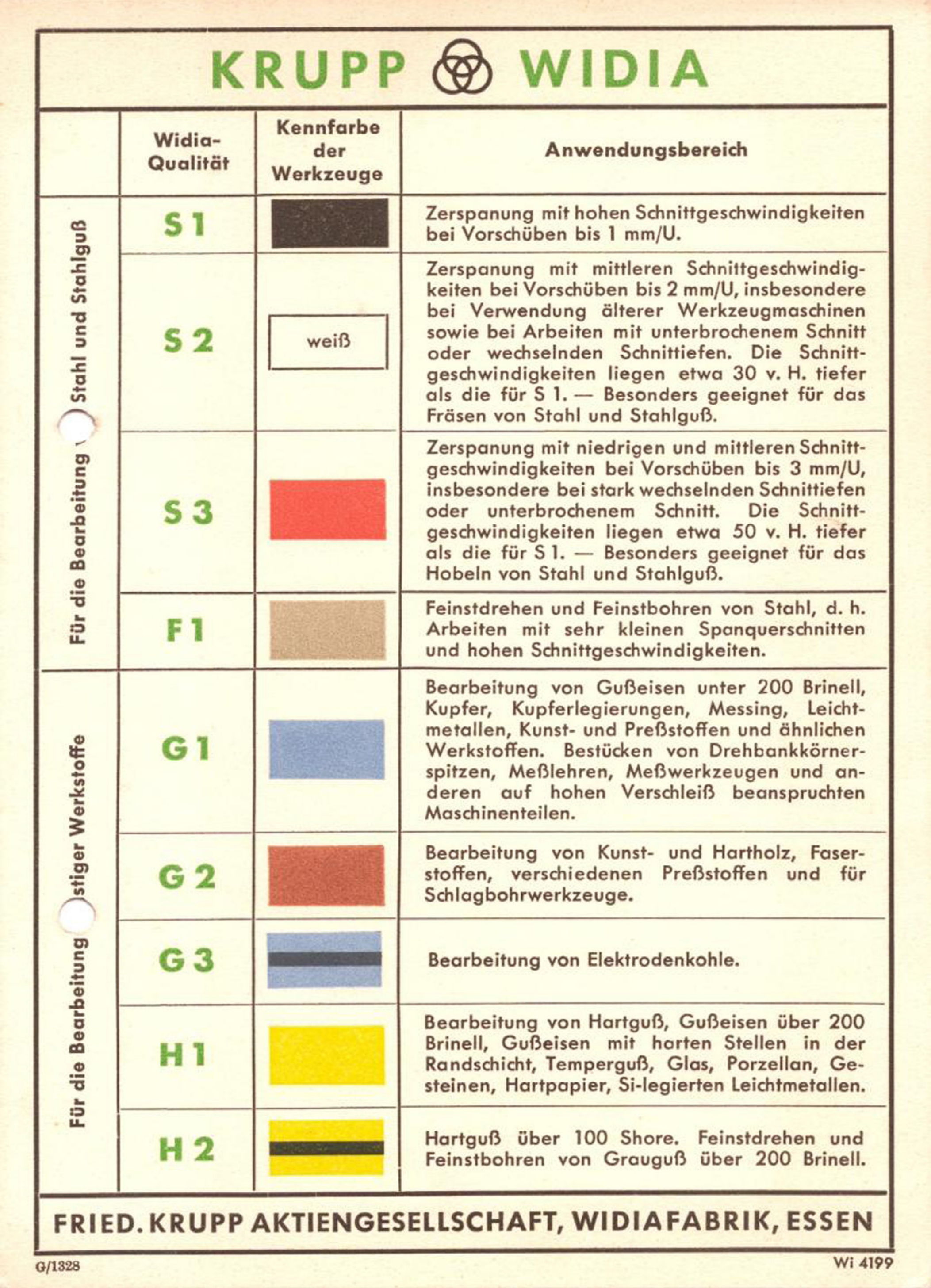

KRUPP WIDIA

	Widia-Qualität	Kennfarbe der Werkzeuge	Anwendungsbereich
Für die Bearbeitung Stahl und Stahlguß	S 1	⬛	Zerspanung mit hohen Schnittgeschwindigkeiten bei Vorschüben bis 1 mm/U.
	S 2	weiß	Zerspanung mit mittleren Schnittgeschwindigkeiten bei Vorschüben bis 2 mm/U, insbesondere bei Verwendung älterer Werkzeugmaschinen sowie bei Arbeiten mit unterbrochenem Schnitt oder wechselnden Schnittiefen. Die Schnittgeschwindigkeiten liegen etwa 30 v. H. tiefer als die für S 1. — Besonders geeignet für das Fräsen von Stahl und Stahlguß.
	S 3	🟥	Zerspanung mit niedrigen und mittleren Schnittgeschwindigkeiten bei Vorschüben bis 3 mm/U, insbesondere bei stark wechselnden Schnittiefen oder unterbrochenem Schnitt. Die Schnittgeschwindigkeiten liegen etwa 50 v. H. tiefer als die für S 1. — Besonders geeignet für das Hobeln von Stahl und Stahlguß.
	F 1	🟫	Feinstdrehen und Feinstbohren von Stahl, d. h. Arbeiten mit sehr kleinen Spanquerschnitten und hohen Schnittgeschwindigkeiten.
Für die Bearbeitung stiger Werkstoffe	G 1	🟦	Bearbeitung von Gußeisen unter 200 Brinell, Kupfer, Kupferlegierungen, Messing, Leichtmetallen, Kunst- und Preßstoffen und ähnlichen Werkstoffen. Bestücken von Drehbankkörnerspitzen, Meßlehren, Meßwerkzeugen und anderen auf hohen Verschleiß beanspruchten Maschinenteilen.
	G 2	🟥	Bearbeitung von Kunst- und Hartholz, Faserstoffen, verschiedenen Preßstoffen und für Schlagbohrwerkzeuge.
	G 3	🟦	Bearbeitung von Elektrodenkohle.
	H 1	🟨	Bearbeitung von Hartguß, Gußeisen über 200 Brinell, Gußeisen mit harten Stellen in der Randschicht, Temperguß, Glas, Porzellan, Gesteinen, Hartpapier, Si-legierten Leichtmetallen.
	H 2	🟨	Hartguß über 100 Shore. Feinstdrehen und Feinstbohren von Grauguß über 200 Brinell.

FRIED. KRUPP AKTIENGESELLSCHAFT, WIDIAFABRIK, ESSEN

G/1328 Wi 4199

Figure 6 Hardmetal qualities of Krupp-WIDIA (around 1937).

The manufacturing plant of Krupp was heavily bombed by the Allied Air Forces within the last years of the Second World War. In October 1944, the production of WIDIA hardmetal had to be discontinued. However, the reconstruction of the WIDIA plant was started directly after the entry of Allied Forces in April 1945. The destructions turned out to be less dramatic than initially anticipated. Much of the machinery could be used after short repairs and the installations for the productions of hydrogen and coal gas were also soon ready for the ongoing production. Only with the electrical and water supply facilities, there were great damages to be fixed. After the occupation of Essen by American Troops in April 1945, the reconstruction work was started immediately and in quite a series of production facilities, the production was resumed. A serious change, however, occurred with the change from the American occupation to the British one. A British "Controller" was installed as the Commander-in-Chief. He issued only part-time working permissions for relatively short time intervals. Only in 1946, a general full-time working permit was issued and the production of hardmetal and hardmetal tools was possible again with full force. Even a selling department was installed. In February 1947, the British Controller allowed to use the official company name "WIDIA-Fabrik, Essen" instead of the previous designation "Krupp-WIDIA Fabrik, Essen". However, with the end of the year 1994, WIDIA was sold to the US company "Cincinnati Milacron" for 180 million D-marks. The respective new management planned a drastic reduction of personnel against which the WIDIA staff demonstrated. In 2002, the US company Kennametal Inc. bought WIDIA for 188 millions of Euro.

1.01.2.10 The Rise of Metallwerk Plansee under Paul Schwarzkopf

Dr Paul Schwarzkopf was born in Prague in 1873. He studied chemistry at the German Prague University of Technology. In 1911, he worked for the Italian company "Lampada Zeta" in Alpignano near Turin which produced incandescent lamps. There he succeeded in producing fine tungsten wires. After this success, he returned to Berlin and founded a company engaged with the production of drawn tungsten wires together with his friend Karl Chvalov in 1913. Already in the successive year, this company employed 400 workers. However, the production was discontinued when the two owners had to join the German army at the beginning of the First World War. Only in November 1918, Paul Schwarzkopf returned to Berlin where his company had gone broke. Hence he became a partner of the German factory for incandescent lamps at Rummelsberg near Berlin (Figure 7).

However, he wanted to become independent again and since the production of ductile tungsten wire needed a respectable amount of electrical energy, he was searching for places where this energy would be cheaper than in a big city. In 1921, he received a favorable offer from Reutte in Tyrol which he accepted together with his partner Richard Kurtz. On July 23, 1921, a respective contract was signed. This was the start of the "Metallwerk Plansee". For the economically poor area "Außerfern" of the province of Tyrol, this was the beginning of an impressive economic rise. It should be mentioned that the foundation of the Metallwerke Plansee GmbH in Reutte was based on a geographical error of Paul Schwarzkopf: He intended to travel to Reith (near Seefeld in Tyrol) but landed in Reutte where he immediately valued the beautiful area along the Plansee. He consequently built his house on the "Kaiserbrunnen" directly on the shore of the Plansee (Schwarzkopf, 1955, Vol. 1).

Figure 7 Dr Paul Schwarzkopf.

In 1923, the production primarily of molybdenum is started. In 1930, Paul Schwarzkopf employed the young chemist Richard Kieffer as head of his research and development department. Dr Kieffer had collected his first experiences with refractory metals at the Bavarian metal works in Dachau which he had joined directly after obtaining his PhD. Already during the years 1932/1934, Dr Kieffer became the director of the hardmetal production "Titanit" which Dr Paul Schwarzkopf had founded together with the head of the DEW, Dr Heinz Gehm. In 1929, Paul Schwarzkopf founded a subsidiary company in the USA which also started with the production of molybdenum and hardmetals. After the seizure of power by the Nazis in Germany in 1933, it was to be expected that they would seize power in Austria as well. Hence, the situation for Paul Schwarzkopf who was of Jewish origin became precarious. Yet he succeeded to sell Metallwerk Plansee to the DEW with the help of his friend Dr Gehm in 1937 in spite of the fact that this deal was theoretically not any more possible and forbidden. The management of the Metallwerk Plansee was taken over by R. Kieffer who succeeded to maneuver the factory through all the confusions of the Second World War. After the war, the French army occupied the Außerfern and planned to dismantle the factory. Kieffer was able to prevent this due to his excellent knowledge of the French language (personal information of R. Kieffer to P. Ettmayer) (Figure 8).

Metallwerk Plansee was not restored to its rightful owner until 1952. A wonderful overview of the achievements, awards and misfortunes of the great pioneer of the powder metallurgy of refractory metals and hard materials, Paul Schwarzkopf, was given by his son, Walter M. Schwarzkopf (1971).

During the first post-war years, much of the know-how had been passed to UGICARB in France. The later head of the laboratory at UGICARB, Dr O. Foglar, has started his career at Plansee (Aronsson, 2005). Since these most difficult post-war times, Plansee has developed remarkably from a small company to an international Plansee Group made up of three divisions with a total of 62 companies operating in 22 countries (Plansee Group, 2010). More than 6700 employees are active in the Plansee Group worldwide, 2000 in Reutte/Tyrol, Austria. The turnover of the Plansee Group reached 1.2 billion of Euros in the business year 2010/2011 and 50% of it were made in countries outside of Europe (Schwarzkopf, 2011, p. 21).

In 2002, the Plansee Group contributes its Tizit activities to a joint venture with the Luxembourg-based CERAMETAL Group. The CERATIZIT division is formed (Plansee Group, 2010).

Some data should now be given on the largest companies active in the production and supply of hardmetals and hard materials.

Figure 8 Dr Richard Kieffer.

1.01.2.11 Some Data on Kennametal Inc

Kennametal Inc. ranks as the largest manufacturer of metal-cutting tools in North America and as the second largest competitor worldwide. Kennametal also ranks as the world's leading manufacturer of tools used by the mining and highway construction industries. Kennametal's tools and tooling systems utilize complex metallurgy and material science in tungsten carbide powders, high-speed steels, ceramics, industrial diamonds and other materials resistant to heat, abrasion, pressure and wear. The recent statistics show that the company employs 11,000 persons and sales are about US $2.4 billion (2011). Since 2003, the company's president is Carlos Cardoso. The company's headquarters remained in Latrobe, PA, since its foundation by Philip McKenna in 1938. Company perspectives: Kennametal's aspiration is to be the premier tooling solution supplier in the world with operational excellence throughout the value claim and best-in-class technology.

From the 1990s onward, acquisitions highlight the success of Kennametal:

1990: Kennametal acquires J&L Industrial Supply.
1991: Kennametal spends $27 million to build its Corporate Technology Center.
1993: Kennametal acquires German toolmaker, Hertel AG.
1997: Kennametal acquires Greenfield Industries Inc.
2002: Kennametal acquires WIDIA in Germany

The company markets its products under various brand names, including Kennametal, Hertel, Rubig, Widia, Cleveland twist Drill, Greenfield, Hanita, Circle Machine, and Disston. Kennametal markets its products in more than 60 countries, deriving nearly half its sales from outside the United States. Overseas, the company's European operations are based in Furth, Germany, and its Asian operations are based in Singapore. Kennametal operates 28 manufacturing plants in the USA and 25 production facilities overseas (Kennametal.com).

1.01.2.12 Some Data on Sandvik

The production of cemented carbide tools at Sandvik was begun in 1942 and the Coromant brand name was established. In 1943, the first cemented carbide tools for metal working were manufactured. In the 1950s, ceramic cutting materials were introduced. Sandvik was first in the world with surface-coated cemented carbide inserts in 1969. In 1994, Sandvik was the first in the world to introduce industry-scale produced diamond-coated carbide cutting inserts. The Sandvik machining business unit that includes Sandvik Coromant employs 12,600 people worldwide with sales of US $2.7 billion (2010). Moreover, hardmetal production represents a significant part of Sandvik mining activities. The head office is located in Sandviken, Sweden.

It cannot be the aim of this chapter to give a full account of the multitude of hardmetal companies worldwide. Some more information of important hardmetal producers are found in Aronsson (2005) and Brookes (1995, 1996).

1.01.2.13 A Project Aimed to Find the Solution to a Specific Problem can Unexpectedly Lead to Much More Important Applications

As stated above, the primary aim of the members of the OSRAM team was to find a substitute for diamond in the dies for tungsten filament production. However, it was soon realized that in addition to achieving this, they had—quite outside the original plan—invented a material that would revolutionize the performance of metal cutting and rock drilling tools. Measures were taken without delay to find ways to exploit these applications more efficiently than would be possible within the companies behind OSRAM Studiengesellschaft.

Cemented carbide is a striking example of the successful transfer of a new technology from one industry to another. It also illustrates how an R&D project with the aim to find the solution to one problem (in this case a new material for advanced drawing dies) unexpectedly can result in much more important applications outside the original aim (Aronsson, 2005, p. 13 and 15). Figure 9 demonstrates the multitude of companies who were active in this technology in the second half of the twentieth century worldwide. Since many hardmetal companies were founded within the twentieth century, it is not surprising that a lot of quarrels about patents also occurred. Aronsson's (2005) book gives an overview on patent situations and respective controversies between 1925 and the Second World War.

Figure 9 Title pages of early brochures of the cemented carbide industry from the second part of the twentieth century.

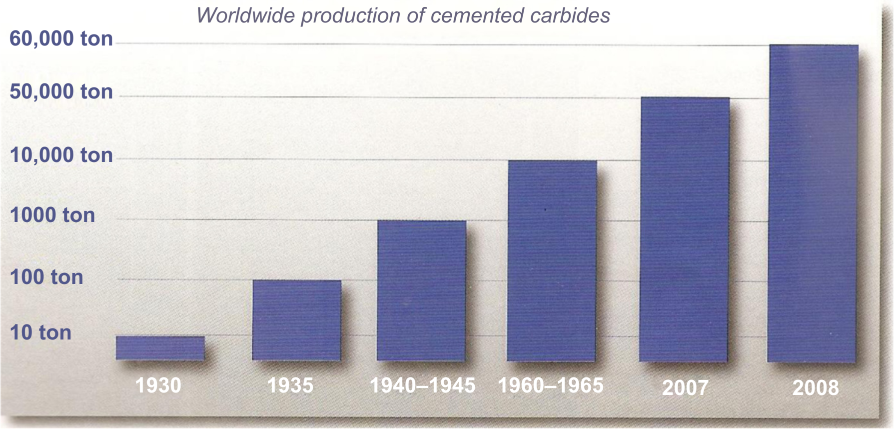

Figure 10 Estimated worldwide production of hardmetals in the years 1930–2008.

Another incidence of the post-war turbulences is worthy to be mentioned:

The "Team of Intelligence" of the Allied Forces forced Krupp to publish almost all details of Krupp-WIDIA products as, e.g. hardmetal compositions, techniques of production, quality control methods for hardmetals and all R&D product reports. All this was published by British Intelligence Objectives Subcommittee. It soon became a very cheap and popular book on how to produce and test hardmetals, which was used worldwide and at least for 10 years.

The development of hardmetals for diverse areas of application led to an impressive and steady rise of the worldwide hardmetal production as can be seen in Figure 10.

The rise of the worldwide consumption of hardmetals is partly due to the rising tendency of automation in metal working: turning, milling, drilling, and forming had dramatically risen in the second half of the twentieth century. The development of automation under the influence of numerical control of single steps of metal working had led to the development of indexable inserts. Here, the cratering wear is not corrected by grinding of the soldered hardmetal inserts but by clamping of the tips with partly quite complex geometries and with very tight tolerances. These tips today are mostly throw away inserts. This way, a lot of costly human working time is spared by computer numerical control (CNC) and working with indexable inserts. Especially, the automobile industry has decisively furthered this development by the necessity to manufacture metal parts of complex geometries in great quantities.

1.01.3 Alloyed WC-Hardmetals and Patent Controversies

1.01.3.1 TiC-Based Hardmetals

As already mentioned, the hard material basis of the Schröter patent was exclusively the tungsten monocarbide. The hard material titanium carbide, TiC, which became important for the turning of materials with continuous chip formation, had been only formed in the melted alloys of the Fuchs and Kopietz patents (Fuchs & Kopietz, 1917, 1918). These alloys exhibited a lower hardness as compared to the tungsten/molybdenum carbide-based alloys patented by Lohmann and Voigtländer (1914) but they exhibited higher tensile strength and toughness values. The DEW AG had applied for a patent for TiC-based hardmetals (Titanit, Cutanit) already in 1929. However, the patent DRP 720502 was granted only in 1942 after long and tedious patent conflicts with Fried. Krupp AG. In the USA, the patent with P. Schwarzkopf and I. Hirschl as inventors had been applied for in November 1931 and was granted in 1933 (Schwarzkopf and Hirschl, 1931/1933). Only in 1934, there was an agreement about the mutual bestowal from patents as well as the mutual participation on payments from licensees.

> "The steel cutting grades of carbide which contain large percentages of TiC are difficult to braze and were unpopular for this reason when brazed tools were the norm. With throw-away tool tips, alloys with higher proportions of TiC could more readily be used and consideration was given to tools based on TiC instead of WC, because of its resistance to diffusion wear in steel cutting. Cemented TiC alloys can be made by a powder metallurgy process differing only in detail from that used for the production of the WC-based alloys. The most useful bonding metal has been nickel and usually the alloys for cutting contain 10–20% Ni. The difficult problems of producing a fine-grained alloy of consistently high quality, free from porosity, have largely been overcome. The addition of about 10% molybdenum carbide (Mo2C) is often made to facilitate sintering to a good quality." (Trent, 1991)

1.01.3.2 Fine-Grained Hardmetals

The further development of hardmetals is characterized by developments which were aimed to improve some of the properties. It was found that the spectrum of hardmetal properties is not only defined by the properties of Co, WC, TiC, TaC and possibly further carbides and the degree of carburization but that the grain size of the main component WC plays an essential role. Already in 1929, the Fried. Krupp AG introduced a new hardmetal WIDIA H1 with a fine-grained WC which exhibited a high hardness although the nominal composition had not been changed. In 1939, WIDIA H2 was introduced with still finer grains. This had been accomplished by the addition of low amounts of the grain growth inhibitors chromium and vanadium. This was a knowledge which is still of great technical and scientific interest even today!

> "Fine-grained cemented carbides have been the fastest growing segment of the cemented carbide industry over 1990–2010, due to their high strength (compressive strength up to 8000 MPa), hardness and microstructural uniformity at still moderate toughness. They are used for round tools (drills, threaders, reamers, and routers), tools for the electronic industries (micro tools), as wear parts, chipless forming tools, circular shearing tools, wood machining tools, for can tooling and more recently, also in the form of a variety of coated and uncoated metal cutting inserts of complex geometries." (Schubert, Lassner, & Böhlke, 2010)

1.01.4 The Coating of Hardmetals

1.01.4.1 Chemical Vapor Deposition: TiC, TiN, Ti(C,N)-Coatings

A quantum jump in the development of efficient cutting materials for the machining of materials with continuous chip formation was the introduction of a new technology "chemical vapor deposition" (CVD) in the years 1968/1969 almost simultaneously at Sandvik in Sweden and at Krupp-WIDIA in Germany. The first experiment to deposit refractory metals and their compounds from the gas phase onto substrates can be traced back to van Arkel and de Boer (1925) as well as to K. Moers (1931), and later on to Campbell, Pavell, Nowitzki, and Gonser (1948). The substrate was usually molybdenum. Münster and Ruppert (1953) critically investigated the deposition of TiC and TiN on the basis of thermodynamics. These two authors and also Wiegand informed about procedures for the deposition of TiC and TiN on iron and steel (Wiegand & Ruppert, 1960). In 1953, patents were applied for these procedures by the Deutsche Metallgesellsschaft (DBP 1056 449). Surprisingly, in the German Patent DPB 1 165 377 (1956) by Ruppert and Schwendler, there is no mention of hardmetals as possible substrates (Ruppert and Schwendler, 1956, 1957). There was no reaction upon this patent in the hardmetal industry. Another patent for the coating of hardmetals was issued for Rix and Dix (1969). An employee of Krupp-WIDIA published a paper on "Hardmetal inserts with a coating of TiC (Schumacher, 1969). The work was financed by Krupp-WIDIA and was presumably the trigger for the impressive victory of coated hardmetals. However, the success was slow. In the excellent paper of Exner and Gurland (1970) there was just one single reference in the respective voluminous list of references. The reason why the coating of hardmetals with hard coatings had been accepted only very gradually by the hardmetal industry might have to do with the fact that the cutting technology at that time was based on hardmetal tips soldered to steel tools which could be ground several times. Throw-away tips were just in the stage of introduction. Coated hardmetals, however, cannot be ground and soldered but have to be fastened by clamping. Further details on the patent situation with respect to CVD-coated hardmetals around 1969 can be found in Aronsson (2005). After first successful attempts to coat hardmetals with TiC, Sandvik reacted quickly. These first experiments had been carried out at "Laboratoire Suisse de Recherche Horlógere" (LSRH). It was found feasible to reduce crater wear dramatically. In 1968, Sandvik acquired the exclusive rights for the LSRH patents and also purchased the coating equipment from LSHR. Most interestingly, LSRH had developed a process of coating the steel cases of wristwatches with TiC in order to make them resistant against scratches in the early 1960s. This was considerably cheaper than to manufacture such cases from sintered hardmetals. Dr Richard Kieffer who had become professor at the Vienna University of Technology after being the managing director of Metallwerk Plansee had heard early about the successful attempts to produce coated hardmetals and also about the introduction of the latter to the hardmetal market. He instructed one of his PhD students, Dietmar Fister, to start with first experiments to coat hardmetals with TiN layers. This worked out excellently and the produced yellow to golden colored TiN layers on hardmetals of the STi 15 type exhibited a lower crater and flank wear even than the TiC-coated hardmetal tips of

Figure 11 Hardmetal parts, partly coated with TiN.

Krupp-WIDIA (carrying the designation WIDIA extra TT 15e). The results of these coating experiments can be found in Fister's PhD thesis (Fister, 1970). Based on those results, the patent DE 1 959 690 was applied for by the DEW and granted in 1971 (Kieffer, Mariacher, & Schoff, 1971).

Since the TiN layers are golden, Plansee named their TiN-coated hardmetals "Goldmaster", cf. to Figure 11.

The CVD coating technology bears an essential disadvantage. The process temperature lies higher than 1000 °C and the adjustment of the carbon activity of the gas phase in dependence of the temperature is somewhat tricky. For the TiC coating, the gaseous atmosphere contains $TiCl_4$, H_2, and CH_4. If the CH_4 content is too high, it is likely that a deposition of graphite occurs between the TiC coating and the substrate. This has a negative effect on the adhesion of the coating. If the CH_4 content is too low, a brittle eta-carbide layer can be formed between the TiC coating and the hardmetal substrate. This has negative consequences especially at interrupted cut and for milling operations. Similar problems exist for the coating with TiN and Ti(C,N).

1.01.4.2 Physical Vapor Deposition

These problems can be prevented by another coating technology, the "physical vapor deposition" (PVD). There exist a series of different PVD procedures but they all work in vacuum and at significantly lower temperatures than the CVD technology applies (Schedler, 1988, pp. 214–220). This is especially important if the thermal coefficients of expansion between the substrate and the layer differ greatly. On the other hand, the CVD coating results in more homogeneous layer deposition especially with greater deposition volumes and layer thickness values and the deposition is independent of the flow direction of the gas mixture. In PVD recipients, the homogeneity of layer deposition has to be affected by a permanent positional change of the substrates, e.g. by rotation.

1.01.4.3 Aluminum Oxide Coatings

The supreme hardness of aluminum oxide and its resistance against oxidative attack and diffusion processes has led to efforts to study the possibility to coat hardmetals with aluminum oxide. However, the adhesion of such layers on hardmetals is low. Hence, this must be counterbalanced by intermediate layers of TiC or Ti(C,N) as was demonstrated by respective developmental work at Batelle Geneve (Lux, Funk, Schachner, & Triquet, 1974).

1.01.4.4 Diamond Coatings

There are only very few substances which are even harder than aluminum oxide. The hardest material is, of course, diamond, the high-pressure modification of carbon. Research of a Russian group of Derjagin et al. (1976) could demonstrate that PVD deposition of cubic diamond layers is principally possible on various substrates, if the carbon deposition from carbon-containing gases (hydrocarbon compounds) is performed in the presence of atomic hydrogen. The generally accepted mechanism is the fact that atomic hydrogen reacts faster with pyrolytically deposited graphite than does diamond. Hence, the formed graphite nuclei are removed faster than respective diamond nuclei which can further grow. The atomic hydrogen can be formed by gas discharge and the latter can be effected by

- activation by high temperatures (TA-CVD),
- activation by electric or electromagnetic gas discharge (PA-CVD),
- combined activation,
- jet methods.

Further details can be found in the excellent article by Lux and Haubner (1989), pp. 615–660.

The formed diamond layers are, of course, extremely hard and wear resistant at ambient temperature. At higher temperatures which usually occur during metal chipping at the cutting edge of coated hardmetal inserts, the diamond starts to react with the oxygen of the air and its tendency to form solid solutions of carbon with hot metals leads to a partial loss in wear resistance. Nevertheless, diamond tools in various forms as polycrystalline diamond tools, single crystal cutting/dressing tools as well as wire drawing die blanks and bonded diamond grits as well as loose diamond abrasives and CVD-diamond-coated tools are in wide use today (Konstanty, 2005; Riedel, 2000).

1.01.4.5 Cubic Boron Nitride

Another very interesting material would be cubic boron nitride (c-BN). It exhibits an extreme inertness against hot steel surfaces under conditions where diamond would be violently attacked. However, the deposition of thin layers of c-BN is still an unsolved problem (Lux & Haubner, 1989, pp. 615–660).

1.01.4.6 Functionally Graded Coatings

There have been lately some scientific publications which focus on mechanisms that govern the formation of graded surface structures on cemented carbides in the form of thin film layers for the production of novel cutting tools with tailored properties. A respective overview is given in a Special Section of the International Journal of Refractory Metals and Hard Materials with Zhigang Zak Fang as the editor (Fang, 2013)

1.01.5 Cermets

The name "cermets" was introduced in the years after the Second World War. It is composed of the syllables "cer" from ceramics and "met" from metal. Originally this new expression was supposed to describe materials which combine the favorable materials properties of ceramics (hardness and wear resistance) with those of metals (toughness especially). Petzow, Clausen, and Exner (1968) had proposed to define with the words "ceramic phase" all sorts of hard and brittle materials. However, this would also include the metallic hard materials TiC, TaC and WC. Hence, the classical Schröter hardmetal WC–Co would also be a cermet. According to today's use of the term "cermet" the sintered hardmetals containing only fcc TiC, TiN-based solid solutions are understood under this word with exclusion of WC–Co hardmetals. According to this understanding, the hardmetals on the basis of molybdenum-containing titanium carbide (Titanit S) of P. Schwarzkopf would have been the very first cermets. A good up-to-date overview on cermets (and hardmetals) is given by Lengauer (2012).

More than a dozen hardmetal producers accepted this material for the chipping of steel in the 1930s due to its superior wear properties and in spite of the fact that its bending strength reaches only about 70% of that of WC–Co hardmetals. A further disadvantage in the application of TiC-based hardmetals was due to their apparently unsatisfactory solderability onto steel carriers as compared to standard hardmetals. Even in the years of the Second World War in Germany, the embargo of the Allied Forces for raw materials was quite efficient and the tungsten supply became a problem, the Titanit–Cermets did not succeed. Possibly, the metal cutting machines were not stable enough at that time so that the lower bending strength of the cermets during chipping operations led to thermal cracks and edge breakage. In the 1950s, the Ford Motor Company introduced cermets which contained unalloyed TiC particles in an Ni–Mo binder unlike the Titanit alloys. The molybdenum content of the binder caused a reaction of TiC particles with the molybdenum of the binder so that a fringe was formed on the surface of the TiC particles consisting of (TiMo)C. This fringe decisively improved the wettability of the TiC particles without deteriorating the high hardness and wear resistance of the TiC nucleus. In spite of their improved strength, the Ford cermets exhibited a tendency to suffer from edge chipping during chipping operations on steels.

The nitrides and carbonitrides of the transition metals were only of scientific concern in the late 1960s. Their presence in hardmetals and cermets was considered to be harmful. A contamination of respective starting products by nitrogen or the presence of nitrides was prevented if possible. Only in the years 1968–1970, Richard Kieffer and his coworkers were able to demonstrate that titanium nitride and titanium carbonitrides could be used as proper hard materials for the production of novel hardmetals. A necessary prerequisite was, however, to improve the lacking wettability of their hard materials by the liquid binder metal during sintering. An addition of molybdenum or molybdenum carbide to the binder metal (usually nickel) has the effect that the oxygen which is present in the form of oxides on the surface of the nitride or carbonitride particles can be removed by reaction with the carbon of the molybdenum carbide.

Rudy (1973) was able to demonstrate that in the mixed crystal range of (Ti,Mo)(C,N), the metal positions are occupied by titanium and molybdenum in the partial metal crystal lattice of the fcc mixed crystal. In the partial nonmetal crystal lattice, carbon and nitrogen atoms occupy the nonmetal positions. During sintering, a demixing reaction is taking place concerning the homogeneous mixed crystal with the metal and nonmetal atoms distributed statistically on the crystal lattice places. Thereby, two isostructural phases α' and α'' are formed. The α'-phase is rich in nitrogen and low in molybdenum whereas α'' is rich in molybdenum and low in nitrogen. Rudy has used this "spinoidal" demixing of the mixed crystal (Ti,Mo)(C,N) to produce cermets. The microstructure of these exhibit hard material phases which consist of a nucleus of a nitrogen-rich titanium carbonitride and a rim of a molybdenum-rich but nitrogen-depleted titanium–molybdenum–carbonitride which is well wetted by the metallic binder. The famous patent of Rudy (Rudy, 1976) covered a broad range of interesting compositions.

In spite of the promising properties with respect to the cutting properties of these cermets, they did not find a respective acceptance in Europe and the USA. However, in Japan the R&D activities in the area of nitride-containing cermets were encouraged. The interest in these tungsten-free cutting materials could have been enhanced by the raw material shortage of tungsten as a consequence of the oil crisis in 1975, whereas titanium was and is available in almost inexhaustible quantities due to its occurrence as an abundant element of the Earth's crust.

The second circumstance has possibly contributed to the success of cermets in Japan. The development of electronically steered great metal cutting machines and the automation of cutting processes have caused a substitution of tougher WC-based hardmetals by the more wear-resistant cermets. This also caused an increase in cutting velocity and a decrease in strain by vibration. The development of the clamping technology substituting the soldering technology also furthered the use of cermets.

The further development of the technique of die casting and the "Near Net Technology" of powder metallurgical processes as well as the drop forging and the herewith connected necessity to perform the chipping operations with higher velocity and with diminished chipping depth led to the effect that the superior edge sharpness of the cermets as compared to coated hardmetals proved to be advantageous.

1.01.6 Cutting Tool Materials, Ceramic and Ultrahard

It goes without saying that ceramics are not only used as coating materials on hardmetal substrates but are also used as matrix materials for cutting operations (Trent, 1991; Riedel, 2000).

1.01.6.1 Alumina and Alumina-Based Composites

Experiments with compact alumina started already before the Second World War. Throw-away tool tips consisting basically of Al_2O_3 have been available commercially for more than 30 years, and have been used in many countries for machining steel and cast iron. Alumina-based composites with, e.g. 30% TiC or (Ta,Ti)C, 10% ZrO_2 or up to 25% SiC (whiskers) are also in use (Trent, 1991).

1.01.6.2 SIALON

A group of ceramics known as "SIALON" has been intensively investigated because of their outstanding properties as high-strength refractory materials. Since 1976, their use as cutting tools has been explored and they have been successful in several applications (Riedel, 2000).

SIALON (Si-Al-O-N) are silicon nitride-based materials with aluminum and oxygen additions (Trent, 1991).

1.01.6.3 Diamond

Single-crystal, natural diamonds have been used in many industrial applications, e.g. as dies for drawing fine wires. For cutting operations, large natural diamonds are used as single-point tools in specialized fields. The optimum orientation is selected and they are lapped to required shape and mounted in tool holders. The tool edges can be prepared to quite exceptional accuracy of form and edge perfection and are capable of producing surfaces of extremely high accuracy and finish. They are used for this purpose in production of optical instruments and gold jewelry (Trent, 1991). Due to technical advances in single crystal diamond syntheses, it has been possible for De Beers to develop a wide range of monocrystalline diamond products to meet the exacting requirements of many different industries (Seb, 1994).

1.01.6.4 Cubic Boron Nitride

The synthesis of compact diamond was made possible by the engineering development of ultra-high-pressure processing units in which temperatures and pressures of the order of 1500 °C and 8 GPa could be maintained for a sufficient time to transform carbon into diamond structure and to grow diamond crystals of usable size. These processing units also made possible the transformation of another substance—BN—from a hexagonal form to a structure akin to diamond. c-BN is not found in nature and there were theoretical considerations which led to the creation of this new substance. Like diamond, c-BN consists of two interpenetrating face-centered lattices, but one of the face-centered sets consists of boron atoms and the other of nitrogen atoms. Like diamond, this is a very rigid structure but in this case not all the bonds between neighboring atoms are covalent. It has been stated that 25% of the bonding is ionic. The resultant c-BN is the next hardest substance to diamond and has many similar, but not identical properties. The hardness varies with the orientation of the test surface relative to the crystal lattice between 40 and 55 GPa (4000 and 5500 HV). It is thus much harder than any of the metallic carbides. A major advantage of c-BN compared with diamond is its greater stability at high temperatures in air or in contact with iron and other metals. It is stable in air for long periods at temperatures above 1000 °C and its behavior as a cutting tool for machining steel at high speed suggests that it does not react rapidly with steel at considerably higher temperatures (Trent, 1991).

1.01.7 A Short Survey of the Literature of Hardmetals and Hard Materials

Of all hardmetal production sites, Plansee has the most impressive record of books and the worldwide-known Plansee Seminars. It started already in 1955 with the founder of Plansee GmbH, Paul Schwarzkopf, who wrote two volumes of "Stories of Molybdenmark" (in German). They give a vivid and often humorous account of the initial difficulties and successes of founding of "Plansee" and the early happenings in the developing world of refractory metals. Many related problems and questions are actually as had they been written yesterday (Schwarzkopf, 1955; Vols 1 and 2). In 1960, Paul Schwarzkopf and Richard Kieffer authored the presumably first book on cemented carbides worldwide (Schwarzkopf & Kieffer, 1960). In 1965, a book on hardmetals in German followed (Kieffer & Benesovsky, 1965). The probably most detailed book on hardmetals was written by Schedler in 1988 in German (Schedler, 1988).

Also in German, Kolaska (1992) wrote an extensive paper on "Powder Metallurgy of Hardmetals". In 2007, Kolaska wrote an excellent article on "Hartmetall – gestern, heute und morgen" (Kolaska, 2007). In 1997, Ortner compiled a book on *The Influence of Trace Elements on the Properties of Hardmetals*. This was a final report on the work performed under the COST 503 Action of the European Commission with a special reference to the phenomenon of heterogeneous impurities in hardmetals (Ortner, 1997). In 1998, G.S. Upadhyaya published a book on *Cemented Tungsten Carbides: Production, Properties and Testing* (Upadhyaya, 1998). Finally in 2008, Novikov edited a book on *Modern Hardmetals, Collection of Proceedings*, which is mostly written in Russian but also with excellent English contributions of Liu Sha, W. Böhlke, R. Bauer, H.E. Exner, G.S. Upadhyaya, W.D. Schubert, B. Roebuck and collaborators of these first authors (Novikov, 2008).

In 1997, R. Telle compiled a book on *Ceramics for High-Tech Applications*. This also is a final report on the respective work performed under the COST 503 Action of the European Commission (Telle, 1997).

A very valuable and rich source of information on ceramic hard materials is the *Handbook of Ceramic Hard Materials* of Ralf Riedel (2 volumes, 1020 pages, Riedel, 2000).

Benesovsky edited a well-known and much read journal *Planseeberichte für Pulvermetallurgie*. This was discontinued by Plansee due to the unexpected death of Benesovsky in 1981. MPR Publishing Services in 1982 purchased the rights of this journal from Plansee and continued with a new title *International Journal of Refractory and Hardmetals*. Editorial Director was Bernard Williams. In 1990, the journal was purchased by Elsevier and in 1991, Hugo Ortner became the Managing Editor of the journal which again changed its title to *International Journal of Refractory Metals and Hard Materials (IJRMHM)*. Benno Lux was the Editor-in-Chief until 2007 when he handed over the responsibility to Ortner (Ortner, 2005, 2009).

There are, of course, quite a number of further journals in which work on hardmetals is reported, like the *International Journal of Powder Metallurgy*, *Acta Materialia*, *Journal of Materials Science*, *Scripta Materialia*, etc.

As to Conferences on hardmetals and hard materials, the Plansee Seminars in Reutte, Tyrol, Austria were already mentioned. The first of these seminars took place in 1952 and now we are looking forward to the Eighteenth Plansee Seminar had taken place in June 2013. Starting with the Sixteenth Plansee Seminar, some selected papers presented at these seminars were also published in IJRMHM, e.g. special topics on molybdenum and tungsten were published in a Special Issue of IJRMHM (Schade, 2010a).

A further series of conferences on hard materials are the International Conferences on the Science of Hard Materials initiated by Vinod Sarin (Boston) in 1981 (Moran, 1981, Rhodos 1984, Nassau 1987, Madeira 1991, Maui 1995, Lanzarote 1998, Ixtapa (Mexico) 2001, San Juan (Puerto Rico) 2004, Montego Bay (Jamaica) 2008). Since the ICSHM 6 in Lanzarote, the respective proceedings have been published as Special Issues of IJRMHM.

A world-known series of Reference books must be mentioned which are edited by Kenneth J.A. Brookes, *The World Directory and Handbook of Hardmetals* (Copyright by International Carbide Data). They are a necessary prerequisite for all using hardmetals for machining, rock drilling, wood cutting and other applications (Brookes, 1996).

Papers dealing with the history of hardmetals are rather scarce. Huppmann (2006), pp. 97–106 reported on the historical roots of the powder metallurgical industry in Germany (in German). Brookes (1995) wrote about *Half a Century of Hardmetals*. Kolaska wrote an article on *Hardmetal – Yesterday, Today and Tomorrow* in German (Kolaska, 2007). Kolaska and Ettmayer are preparing a book on the *History of Hardmetals* (2012). This is the onset of this article.

The wonderful book of Bertil Aronsson, *The Origins and Growth of Cemented Carbide* (Aronsson, 2005) has been cited and mentioned several times already. It also contains a wealth of citations of scientific and technical papers in chronological order hardly found anywhere else.

A very important topic which has not yet been mentioned is *Phase Diagrams of Cemented Carbides*. They have been reviewed recently by Ferdandez and Senos (2011). Mention should also be made in this connection to the "Calphad"-computer program for phase diagram calculations at the Institute of Technology in Stockholm (Sundmann, Jansson, & Andersson 1985).

1.01.8 Conclusion

Cemented carbides remain a growing market. There has been a continuous expansion in the consumption, from an annual world total of 10 ton in 1930 to about 50,000 ton in 2008. As the world's economics grow, cemented carbides will play their part in the progress of technology.

New technologies and new materials will demand new tooling solutions, and cemented carbide tools will provide a cost-effective option due to their attractive properties. Modern recycling technologies and a more efficient collection system of scrap material will contribute in this regard, driven by both the price and the need to maintain and save natural resources. In the long term, recycling will inevitably become the key strategic factor for sustained economic growth, and the respective recycling strategies of cemented carbides are in the line.

So, after a period of almost 90 years, cemented carbides have developed from a temporary solution in industry (as a substitute for diamond in wire drawing in the lighting industry) to a very successful and almost irreplaceable material for the manufacturing industry (Schubert et al., 2010).

The authors of this chapter consider it as being very remarkable that from the very beginning of the hardmetals the optimal combination of WC and Co was chosen. Even by 2013, 90 years later, there is no better combination of hard carbide and metallic binder in sight.

References

Aronsson, B. (2005). *The origins and growth of cemented carbide* (2nd revised ed.). Uppsala: Sandvik.

Baumhauer, H. (1922). DRP 443.911 Patent owner: Patent Treuhand Gesellschaft für elektrische Glühbirnen m.b.H., Berlin Inventor: Dr Heinrich Baumhauer in Berlin, Charlottenburg Title: Procedure for the fabrication of pieces and tools, especially drawing dies issue of letters patent: March 19, 1922.

Brookes, K. J. A. (1995). Half a century of hard metals. *Metal Powder Report*, 22–28.

Brookes, K. J. A. (1996). *The world directory and handbook of hard metals* (6th ed.). International Carbide Data.

Campbell, J. E., Powell, C. F., Nowicky, D. H., & Gonser, B. W. (1948). The vapour-phase deposition of refractory materials; I. General conditions and apparatus. *Journal of the Electrochemical Society, 96*, 318.

Derjagin, B. W., Spitsyn, B. V., Builov, L. L., Klochkov, A. A., Gorodetskii, A. E., & Smol'yaninov, A. V. (1976). Synthesis of diamond on non-diamond substrates. *Doklady Akademii Nauk SSSR, 231*, 333–335.

Exner, H. E., & Gurland, J. (1970). A guide to the literature on tungsten carbide-cobalt alloys. *Powder Metallurgy International, 59–63*, 104–105, 147.

Fang, Z. Z. (2013). Guest editor: Special Section: Recent advances of functionally graded hard materials. *International Journal of Refractory Metals and Hard Materials, 36*, 1–75.

Fernandez, C. M., & Senos, A. M. R. (2011). Cemented carbide phase diagrams: a review. *International Journal of Refractory Metals and Hard Materials, 29*, 405–418.

Fister, D. (1970). About the influence of carbon deficit of the hard material phase on the properties of TiC-VC(TaC, NbC)-Mo2C-Ni hard metals and about the coating of hardmetal plates with TiN.

Fuchs, G., Kopietz, A. (1917). DRP 30 77 64. Metallegierung.

Fuchs, G., Kopietz, A. (1918). DRP 31 00 41. Metallegierung.

German, R. M. (2005). *A-Z of powder metallurgy.* Oxford, UK: Elsevier Advances Techology.

Hobein, D. (1986). The reconstruction of the WIDIA-factory in Essen 1945–1949 (in German). *Technikgeschichte, 53*(4).

Huppmann, W. J. (2006). The historical roots of the powder metallurgical industry in Germany (in German). In *Pulvermetallurgie in Wissenschaft und Praxis, 22*. Hagen: Fachverband Pulvermetallurgie.

Jenssen, W., Schroeter, K. (1925). US Pat. 1.551.333. Tool and die, Kennametal: http://www.kennametal.com.

Kieffer, R., & Benesovsky, F. (1965). *Hartmetalle*. Wien: Springer Verlag.

Kieffer, R., Mariacher, H., Schoff, H. (1971). DE 195 96 90: Überzugsschicht, auf Hartmetallteilen für die spanende and spanlose Formgebung und Verfahren zu ihrer Herstellung [Coating on hard metal parts for the shaping, with continuous and discontinuous chip formation and procedures to their fabrication].

Klink, J., & Weidenfeld, H. (1951). *Mitteilungen der fried.* Krupp WIDIA-Fabrik, Essen (News of the ….)

Kolaska, H. (1992). *Pulvermetallurgie der hartmetalle.* Hagen: Fachverband Pulvermetallurgie (Powder metallurgy of hard metals).

Kolaska, H. (2007). Hard metal – yesterday, today and tomorrow (in German). Metall 12/2007, 825–832.

Kolaska, H., & Ettmayer, P. (in press). Geschichte der hartmetalle (History of Hard Metals).

Konstanty, J. (2005). *Powder metallurgy diamond tools.* Amsterdam, Boston: Elsevier.

Lengauer, W. (2012). Hard metals and cermets; actual tendencies of development (in German); contribution to the planned book of Kolaska and Ettmayer.

Lohmann, Voigtländer. (1914). Metall-fabrikationsges, m.b.H., Essen, DRP 286.184: procedure for the fabrication of pieces of tungsten – and molybdenum carbides of varying size (in German).

Lux, B., Funk, B., Schachner, H., Triquet, C. (1974). US Pat. 3.836.392. Process for increasing the resistance to wear of the surface of cemented carbide parts subject to wear.

Lux, B., & Haubner, R. (1989). Low pressure synthesis of superhard coatings. In H. Bildstein, & H. M. Ortner (Eds.), *Proceedings of the 12th Int. Plansee Seminar '89* (Vol. 3). Innsbruck: Tyrolia (C2).

Mari, D. (2001). *Cermets and hard metals, encyclopedia of materials: science and technology.* Elsevier Science Ltd.

Moers, K. (1931). I. Methods for the preparation of pure high-melting carbides, nitrides and borides and a description of a few of their properties. II. The preparation of pure carbides, nitrides and borides by the method of growth and a description of a few of their properties. *Zeitschrift für anorganische und allgemeine Chemie, 198*, 243–261.

Muenster, A., & Ruppert, W. (1953). Thermodynamics of some reactions of titanium tetrachloride. *Zeitschrift für Elektrochemie, 57*(7), 558–564.

Novikov, N.V. (2008). Modern hard metals, collection of proceedings, Kiev, ISBN 978-966-02-4718-5.

Ortner, H. M. (1997). The influence of trace elements on the properties of hard metals, Vol. IV of the European concerted action COST 503: Powder metallurgy – powder based materials of the European Commission. T. Valente (Ed.), *Directorate – General, Science, Research and Development*, Brussels.

Ortner, H. M. (2005). Trials and tribulations in editing the IJ RMHM for 13 years (1991–2004). *International Journal of Refractory Metals and Hard Materials, 23*, 3–16.

Ortner, H. M. (2009). The International Journal of Refractory Metals and Hard Materials – present state, future and retrospective view. *International Journal of Refractory Metals and Hard Materials, 27*, 513–519.

Petzow, G., Claussen, N., & Exner, H. E. (1968). Structure and properties of cermets. *Zeitschrift für Metallkunde, 59*, 170–179.

Plansee Group. (2010). http://www.plansee-group.com/history_ENG_HTML.htm.

Riedel, R. (Ed.). (2000). *Handbook of ceramic hard materials.* Weinheim: Wiley-VCH.

Rix, E. F. G., Dix, G. E. (1969). DBP 1 521166: *Verfahren zum Herstellen von Überzügen auf Hartmetallkörpern* [Procedure for the fabrication of coatings on hard metals].

Rudy, E. (1973). Boundary phase stability and critical phenomena in higher order solid solution systems. *Journal of the Less Common Metals, 33*, 43–70.

Rudy, E. (1976). US 3971656. Spinodal carbonitride alloys for tool and wear applications.

Ruppert, W., Schwendler, G. (1956). DBP 1 165 377: *Verfahren zur Herstellung von Titankarbidüberzügen durch Gasplattieren.*

Ruppert, W., Schwendler, G. (1957). US Pat. 2, 962. 399. Process for deposition of titanium carbide coatings, Sandvik: http://www.hardmaterials.sandvik.com/sandvik/0130/Internet/SEO3459.NSF.

Schade, P. (2010a). Guest editor of special issue. Selected papers of the 17th Int. Plansee Seminar 2009 in Reutte, Austria: Tungsten and molybdenum. *International Journal of Refractory Metals and Hard Materials, 28*(6).

Schade, P. (2010b). 100 years of doped tungsten wire, as above, 648–660.

Schedler, W. (1988). *Hartmetall für den Praktiker* [Hard metal for the practitioner]. Düsseldorf: VDI-Verlag GmbH.

Schröter, K. (1923). DRP 420.689: sintered hard metal alloy and procedure for its fabrication. Inventor: Karl Schroeter in Berlin-Lichtenberg. Patent owner: Patent-Treuhand-Gesellschaft für Elektrische Glühlampen, mbH, Berlin issue of letters patent: March 30, 1923.

Schröter, K., Agte, C., Moers, K. Wolff, H. DE 622.347 (1931) and US Pat. 2.015.536 (1932/35). *Verfahren zur Herstellung von Hartmetall-Legierungen für Arbeitsgeräte und Werkzeuge aus Wolframkarbid und einem zusätzlichen Hilfsmetall* [Procedure for the fabrication of hard metal alloys for working vessels and, tools made of tungsten carbide and an additional metal].

Schubert, W.-D., Lassner, E., & Boehlke, W. (June 2010). *Cemented carbides – a success story, in Tungsten, Int*. Tungsten Industry Association (ITIA).

Schuhmacher, G. (1969). *Wendeschneidplatten aus Hartmetall mit Titankarbidschicht* (Inserts made of hardmetal with a titanium carbide coating) TZ Prakt. *Metallbearb, 63*, 275–278.

Schwarzkopf, P. (1955). *Geschichten aus Molybdänemark* (Vol. 1). Füssen, Germany: C.F. Wintersche Verlagshandlung.

Schwarzkopf, P. (1955). *Geschichten aus Molybdänemark* (Vol. 2). Austria: Bergland, Verlag Wien.

Schwarzkopf, W. M., (Ed.). (1971). Paul Schwarzkopf – Zur Erinnerung an Prof. Dr. Paul Schwarzkopf anläßliich des ersten Jaherstages seines Ablebens, Metallwerk Plansee AG α Co KG [in memory of Prof. Dr. Paul Schwarzkopf on the occasion of the first anniversary of his demise].

Schwarzkopf, M. (Friday, July 8, 2011). *Plansee celebrates with records (in German)*. Tiroler Tageszeitung. Wirtschaft.

Schwarzkopf, P., Hirschl, I. (1931). US Pat. 1.925.910. Production of hard metal alloys, especially for tools.

Schwarzkopf, P., & Kieffer, R. (1960). *Cemented carbides*. New York: The Macmillan Co.

Seb, P. K. (1994). De Beers Monodite – a performance evaluation. *Industrial Diamond Review, 54*(560), 13–20, 1/94.

Skaupy, F. (1951). Memorandum about the development of hardmetal in the OSRAM-Studiengesellschaft, later named WIDIA from August 15, 1951 [personal information of W. Skaupy to H. Kolaska August 28, 1992].

Sundmann, B., Jansson, B., & Andersson, J. O. (1985). *Calphad, 9*.

Telle, R. (1997). Ceramics for high-tech applications, Vol. V of the European concerted action COST 503 (COST-subgroup hard materials): Powder metallurgy – powder based materials of the European Commission. In T. Valente (Ed.), *Directorate – General, Science, Research and Development*, Brussels.

Trent, E. M. (1991). *Metal cutting* (3rd ed.). Oxford, London: Butterworth-Heinemann Ltd.

Upadhyaya, G. S. (1998). *Cemented tungsten carbides: Production, properties and testing*. New Jersey, USA: Noyes.

van Arkel, A. E., & De Boer, J. H. (1925). Preparation of pure titanium, zirconium, hafnium and thorium metal. *Zeitschrift für Anorganische und Allgemeine Chemie, 148*, 345–350.

Weidenfeld, H. (October 1951). *Heinrich Weidenfeld erzählt (in German). Der Sinterling*. Essen: Mitteilungen der Friedr.-Krupp WIDIA Fabrik.

Wiegand, H., & Ruppert, W. (1960). Some properties of the material combination, steel with titanium carbide coating. *Metalloberfläche, 14*(7), 193 (8) 229–235.

Wolff, H. (1941). Hardmetalltillverknigens utveckling, Teknisk Tidskrift, Arg 71, Häfte 52, 549–551.

1.02 Fundamentals and General Applications of Hardmetals

Leo Prakash, Kyocera Unimerco Tooling A/S, Sunds, Denmark

1.02.1 Introduction

Hardmetals or cemented carbides are a mature class of 90-year-old powder metallurgical, liquid-phase sintered composite materials consisting of at least one hard and wear-resistant phase; in the majority of cases, this being tungsten carbide (WC), and a ductile and softer metallic phase from the iron group of metals (mainly cobalt and its alloys). The invention of hardmetals dates back to the beginning of the twentieth century and is generally attributed to Karl Schröter who disclosed his invention in 1923 in a patent application (Schroeter, 1923). The first products were wire drawing dies and these were quickly followed by cutting tools for the machine tool industry. Cemented carbides today form the backbone of the tool manufacturing industry with such diverse applications as machining of metallic and nonmetallic materials, chipless forming (wire drawing, can tooling, forging, stamping, mill rolls, powder compacting punches and dies, high-pressure dies and anvils), mining

http://dx.doi.org/10.1016/B978-0-08-096527-7.00002-7

(oil well drill bits and rock drill bits), industrial nozzles (sand blasting, water jet cutting, painting, and glue dispensers), industrial wear parts (dental and medical tools), paper, plastic and textile knives, guide rolls, seal rings, road planing knives, tire studs, forestry tools, earth moving and consolidation tools and for functional applications (watch cases and bracelets).

Hardmetals are the material of choice in all applications where wear resistance combined with toughness and strength is required at ambient and elevated temperatures. Figure 1 shows the wide range of properties of cemented carbides in use today. A typical microstructure of WC–cobalt-bonded hardmetals shown in Figure 2 consists of the hard and wear-resistant WC phase embedded in a ductile metallic matrix of cobalt. The unique properties of the cemented carbides can be varied in a wide range by the proper choice of the grain size of the carbide (submicrometer to tens of micrometers) and the amount of binder phase (2–30 wt%). Whereas, in the majority of applications (Figure 3) mainly straight grades of WC–Co are used, metal-cutting grades generally contain a minor amount of around 8–20% of titanium and tantalum carbide to improve the hot hardness and creep resistance of the cemented carbides at service temperatures. Strategic and economic drivers have always been responsible to develop superior hardmetals. One route has been to replace WC at least partly

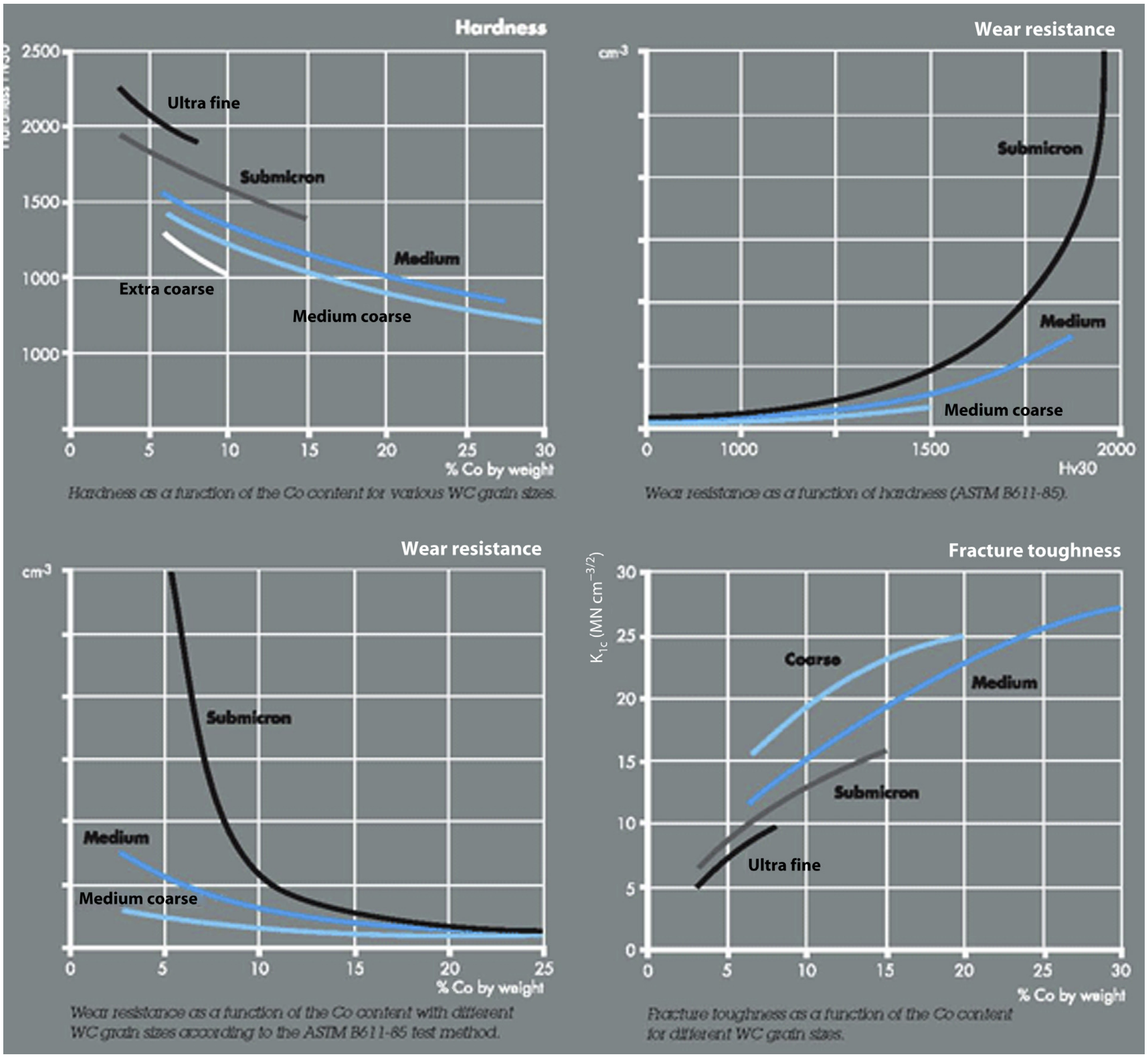

Figure 1 Hardness, wear resistance and fracture toughness of straight WC–Co cemented carbides as a function of WC grain size and cobalt content (Sandvik Hardmaterials).

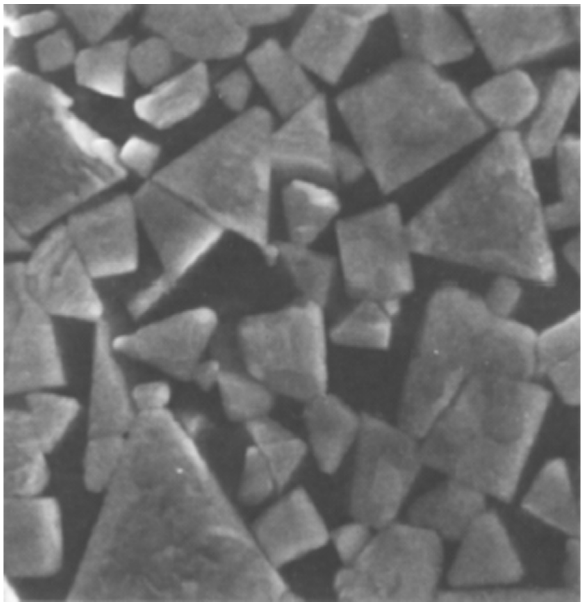

Figure 2 Typical microstructure of a WC–Co hardmetal (SEM image Andren, 2001).

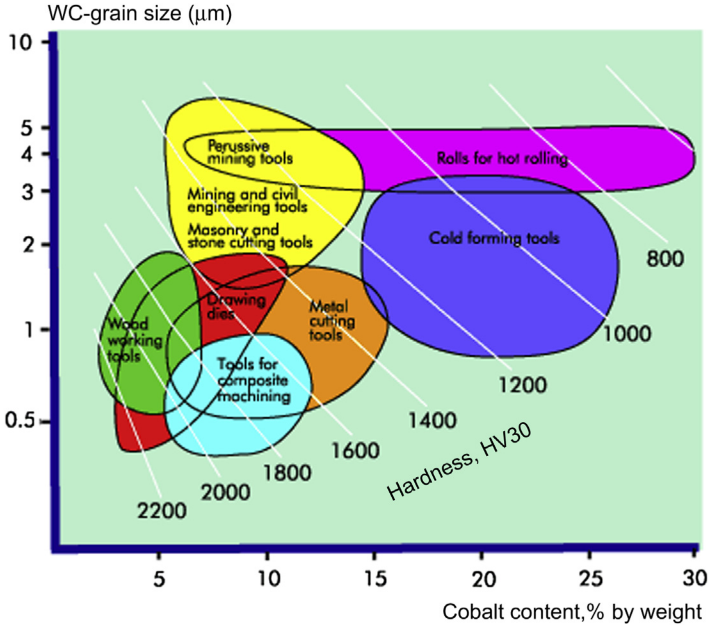

Figure 3 Application range of straight cemented carbide grades (Sandvik Hardmaterials).

through other refractory carbides, nitrides or carbonitrides of titanium, tantalum, molybdenum, etc. This class of materials is frequently called *cermets* and has until now captured only niche markets for metal-cutting and general engineering applications. However, recent developments in coated fine-grained and gradient structured cermets have shown them to be on a par with conventional WC–Co cutting tool materials not only for finishing operations. Figure 4 is a typical microstructure of a multicomponent cermet with a core rim structure. A general breakthrough for the use of hardmetals in machining and milling applications occurred in the 1970s, when chemical vapor deposition (CVD) and later physical vapor deposition (PVD) methods for the deposition of

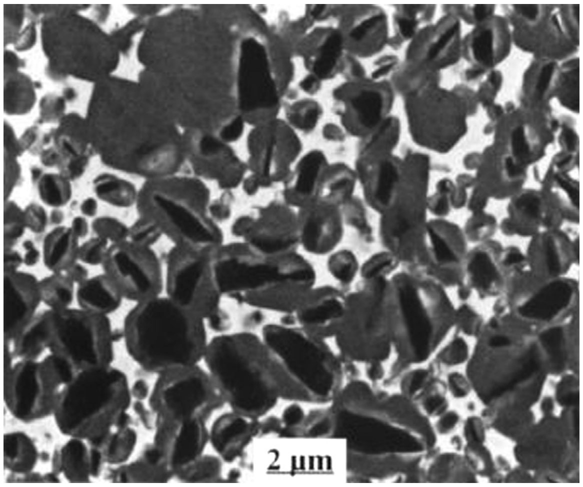

Figure 4 Microstructure of a 10 vol% TiN-10% Mo_2C-65% TiC-15% nickel cermet. TiCN cores (dark) are surrounded by a (TiCMo)(CN) rim (gray) and the nickel-rich binder (bright) (SEM (BSE) image, Andren, 2001).

thin-film hard coatings like TiN, TiC, TiCN, Al_2O_3, TiAlN, etc. became available. This has led to large increases of productivity especially in machining applications (Prakash & Roebuck, 2013).

1.02.1.1 Market Size of WC-Co Hardmetals

Currently about 50–55 GT of WC/cobalt is manufactured globally (2012). About 14 GT is manufactured in western Europe and almost 20 GT in China. The production market share for Europe is about 28%, China 39%, NAFTA 13%, Japan 10% and 10% for the rest of the world. The global market sales volume (2011) for hardmetal goods is in excess of €22 billion. In terms of global turnover and global consumption, the following distribution is estimated (**Table 1**).

The range of cutting-tool material classes with an optimal combination of hardness and toughness is shown schematically in **Figure 5** and a comparison of typical properties of some hard materials in **Table 2** (Schedler, 1988).

Table 1 Market share of hardmetal products by application (Williams, 2012)

Worldwide application area	*Worldwide turnover (%)*	*Worldwide consumption by weight (%)*
Metal cutting	65	22
Wood and plastics	10	26
Wear applications[a]	10	17
Stone working	10	26
Chipless forming	5	9

[a] *The definitions of application areas for wear parts are not well defined; sometimes products in chipless forming, stone working as well as in wood and plastics are partially clubbed together as wear parts.*

1.02.2 Metallurgy of Hardmetals

The strength of a hardmetal is controlled by the properties of the hard phases, the softer metallic binder and the carbide–carbide and carbide–binder interfaces. The strength of the carbide phase is dependent on the grain size as well as the chemical composition and stoichiometry. WC has a rather narrow stoichiometry window for carbon, which calls for utmost production process stability. The binder of choice for WC-based hardmetals is cobalt, although nickel and its alloys are prevalent for niche applications calling for corrosion resistance. There is a growing interest in evaluating alternate binders for enhanced properties as well as health and safety issues. The most advanced alternative for the (partial) replacement of cobalt are alloys based

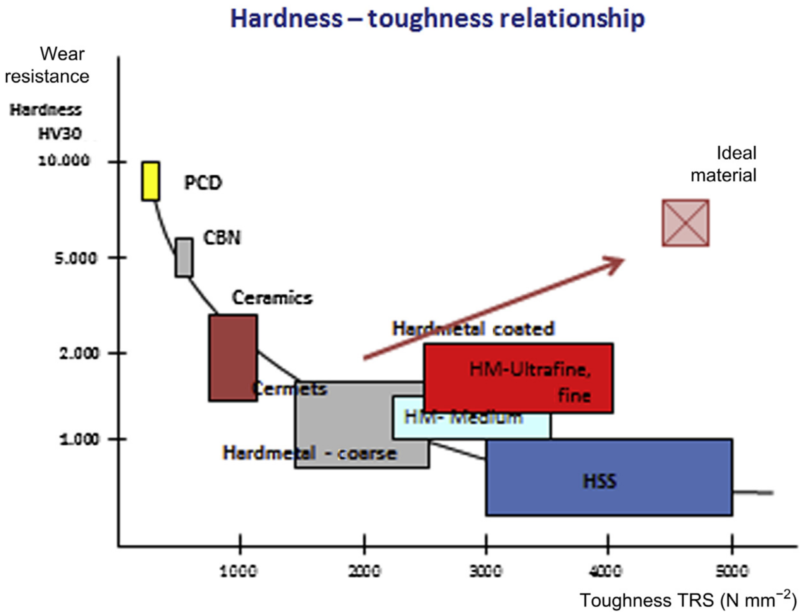

Figure 5 Schematic wear resistance–toughness relationship for cutting tool material classes.

Table 2 Properties of important wear-resistant hard materials (Schedler, 1988)

Property	*High-speed steel*	*WC–Co cemented carbides*	*TiC-based cermets*	*Ceramics (oxides, nitrides)*	*Polycrystalline cubic BN*	*Polycrystalline diamond*
Density, g/cm^3	8.0–9.0	9.0–15.0	5.0–9.0	3.2–5.0	3.45	3.5
Vickers hardness, HV	750–800	800–1900	1500–2200	1500–2500	4000	8000
Transverse rupture strength, N/mm^2	3000–4000	1000–3000	900–1800	400–600	500–800	600–1100
Hot transverse rupture strength (1000 °C), N/mm^2	500	900–1500	600–1500	400–600	500–700	600–1000
Compressive strength, N/mm^2	3500–4000	4000–7000	3000–5000	3000–4000	6000	7600
Modulus of elasticity, kN/mm^2	210	400–680	300–450	300–400	680	850
Thermal expansion coefficient, 10^{-6}/K^{-1}	12	5.0–7.0	6.0–8.0	2.5–7.5	3.5	1.2

in the iron–cobalt–nickel system with properties equivalent to, or superior to conventional cobalt-bonded materials (Prakash & Gries, 2009).

The calculated ternary phase diagram of the WC–Co system at 1350 C is shown in **Figures 6 and 7**. It is apparent that the two-phase region of WC–Co is quite narrow and bordered with three phase regions that contain carbon-deficient complex mixed carbides of type M6C or free carbon at carbon-rich compositions. Third phases are to be avoided to prevent undue loss of strength. **Figure 6** highlights the narrow carbon range for a WC-10% Co as a function of temperature. The stoichiometric carbon content corresponds to 5.52 mass% C. The two-phase regions are limited to 5.38 to 5.54 mass% carbon. If additional carbides such as TiC, TaC, NbC, Cr_3C_2, etc. are added, the cobalt-rich liquid becomes stable at lower temperatures.

Even within the two-phase region of WC–Co, the amount of dissolved tungsten in the binder phase after sintering depends primarily on the carbon content. Higher tungsten contents have been measured in the binder phase at low carbon contents and vice versa. At 1250 °C, it is predicted that the content of W and C in the solid binder at equilibrium with WC varies between approximately (at%) 9W + 1C and 3W + 3C when the total C is increased in the material (Andren, 2001). The amount of dissolved tungsten has a major influence on the strength and ductility of the binder phase at ambient and elevated temperatures. It is well accepted that the solubility of tungsten in the binder is higher in the case of fine-grained WC hardmetals compared with coarse-grained ones. It is also now accepted that WC–Co hardmetals consist of two

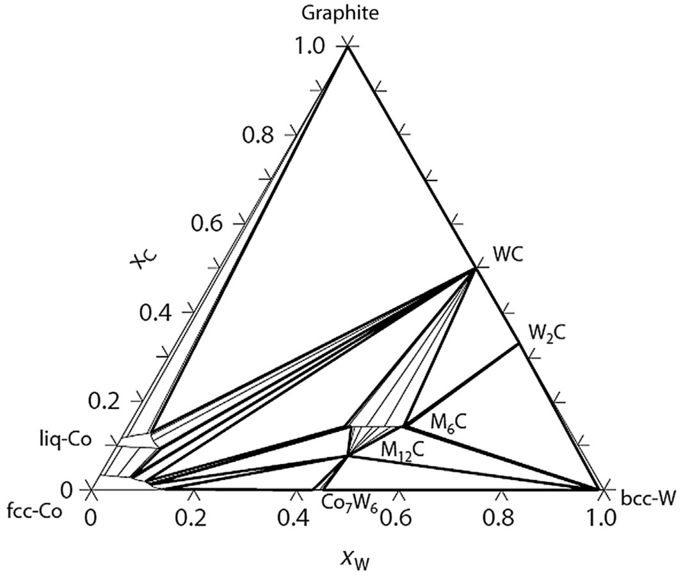

Figure 6 Calculated ternary phase diagram of the WC–Co system at 1350 C (Petersson, 2004).

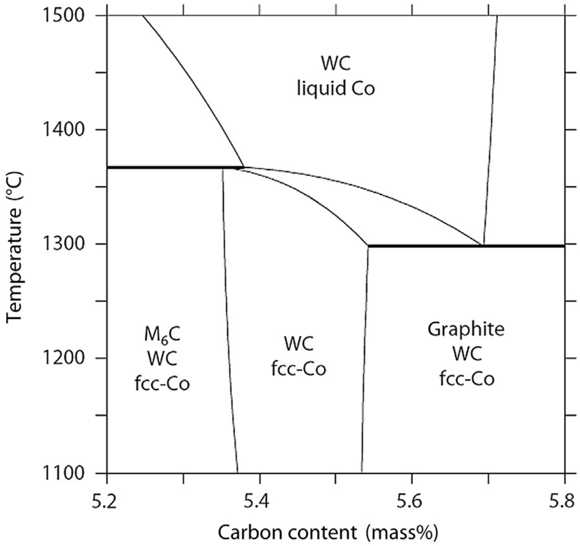

Figure 7 Calculated vertical section of the ternary phase diagram Co–W–C at 10 mass% Co (Petersson, 2004).

interconnected skeletons of the hard carbide phase and the ductile cobalt phase. The grain boundaries between the carbide grains can have up to a 0.5 monolayer of cobalt between them.

Variations in the carbon content of the sintered alloys influence the physical, mechanical, electrical and thermal properties as well as the shrinkage (warpage) after sintering (Table 3).

The manufacturing performance and product reliability of hardmetal components has profited by combining experimental approaches as well as simulation and modelling approaches. Currently phase diagrams and diffusion kinetics can be calculated based on available thermodynamic data (Frisk et al., 2001).

As it has been discussed in literature, the carbide grain size has a strong influence on material properties (Table 4). The "run of mill" hardmetals have an average grain size of 1–2 μm. The tendency to decrease the grain size of the WC and thus improve on properties has been ongoing work in the past decades. **Figures 8** and **9** are the examples that show the influence of grain size on properties.

Table 3 Example of typical WC–Co hardmetal grades and properties (Element Six)

					Hardness		
HM Code	*Cobalt (%)*	*Grain size*	*Density (g cm^{-3} ± 0.10)*	*Coercivity (Oe)*	*HV10 ± 50*	*HRA ± 0.3*	*TRS (MPa)*
T6	6	Coarse	14.95	130–160	1450	90.6	2800
B20	8		14.7	90–110	1250	88.7	2800
B25	10		14.5	75–110	1230	88.5	2900
B30	11		14.4	75–100	1150	87.7	2900
B40	15		14	65–90	1050	86.5	2800
B15N	6.5	Extra coarse	14.9	55–75	1100	87.2	2200
B20N	8.6		14.65	45–60	1050	86.5	2300
B25SN	9.5		14.55	50–64	1050	86.5	2300
G10	6	Medium	14.95	190–220	1600	91.9	2800
G15	8		14.7	160–200	1480	90.9	3000
G20	11		14.4	130–170	1320	89.4	3300
G30	15		14	110–150	1200	88.2	3200
G40	20		13.5	90–120	1050	86.5	3100
G55	26		13	70–100	870	84.4	2900
K04	4	Submicron	15.1	350–450	1850	93.4	2000
K05	5		15	310–360	1800	93	
K06	6		14.9	270–350	1750	92.7	
K07	7		14.7	260–320	1700	92.5	
K010	10		14.4	21–290	1620	92	
K015	15		13.9	190–250	1400	90.2	3700

Table 4 Classification WC grain size

Grain Size (μm)	*Designation*
<0.2	Nano
0.2–0.5	Ultrafine
0.5–0.8	Submicron
0.8–1.3	Fine
1.3–2.5	Medium
2.5–6.0	Coarse
>6.0	Extra coarse

The main advantage of a submicron grain size is the high hardness as well as toughness combined with a high compressive strength, high edge strength and superior abrasive wear resistance. Currently the proportion of submicron and smaller grained WC usage is in excess of 30% of all WC used. This is especially true for applications using round tools in metal, nonferrous, wood composites and man-made industrial materials.

During manufacture of hardmetal parts, WC grain growth occurs during sintering, which is nominally in the range of 1400–1500 °C. Grain growth inhibitors such as tantalum, chromium or vanadium as carbides are commonly used either individually or in varying combinations to design microstructure and properties of submicrometer hardmetals. The large body of research published by Chinese researchers (Liu, 2009) clearly points out that rare-earth additions are also beneficial for WC grain growth retardation. Even though WC–Co materials are a prime example of liquid-phase sintered composites, a major part of densification proceeds during heating up in the solid state. The sintering behavior is dependent on material composition such as carbide grain size, cubic carbide additions, binder volume fraction, carbon content and previous milling history of the powder raw materials. Details about sintering mechanisms will be dealt with in Chapter 1.08. A typical sintering cycle showing general sintering mechanisms is shown in Figure 10.

The advent of electrically resistance heated sintering furnaces of batch type that permit the use of vacuum or protective gases as sintering atmospheres until almost full density of the sintered compacts combined with a gas overpressure consolidation step (between 1 and 10 MPa) have led to a quantum leap in the quality and reliability of hardmetal products. The overpressure treatment (mainly using Argon gas), also termed Sinterhip, practically eliminates bulk residual porosity and leads to more uniform product properties on an industrial

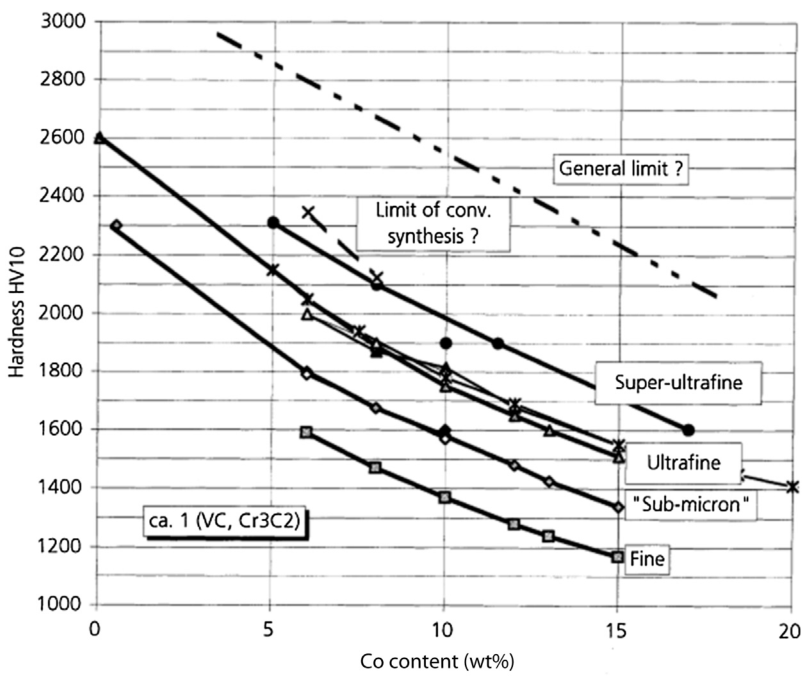

Figure 8 Influence of WC grain size on hardness of WC–Co hardmetals (Richter & Ruthendorf, 1999).

scale. This has been especially of advantage for applications involving chipless forming tools such as Sendzimer rolls, wire rolls, wire-drawing dies and stamping and punching tools.

Since sintering is mainly a diffusion-controlled process that is time dependent, the incentive to control WC grain growth and also improve production productivity by using rapid sintering techniques such as microwave sintering, spark plasma sintering, electric discharge sintering, etc. has been innovative. These processes though not as mature as conventional sintering processes are making production headway in a number of niche applications.

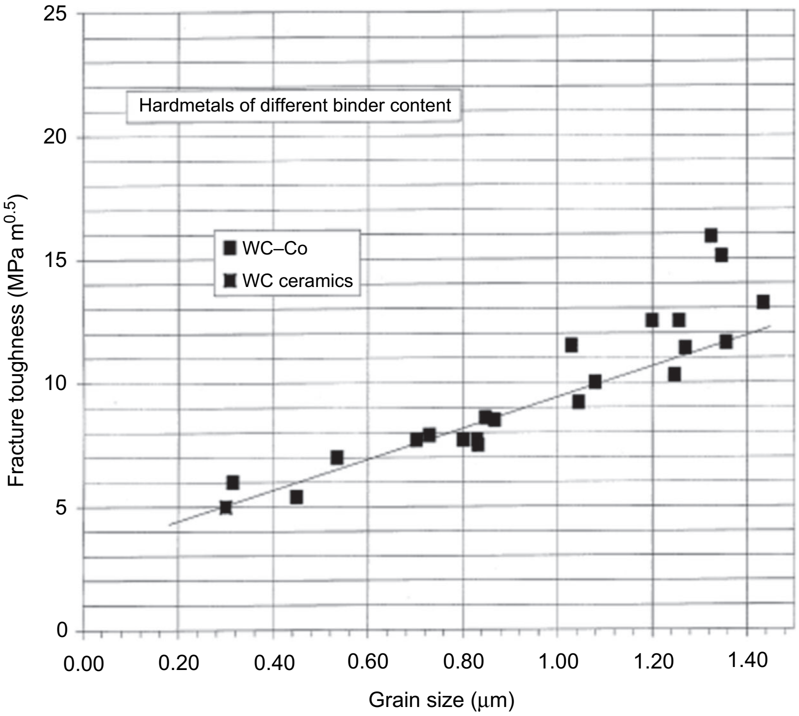

Figure 9 Influence of WC grain size on fracture toughness of WC–Co (Richter & Ruthendorf, 1999).

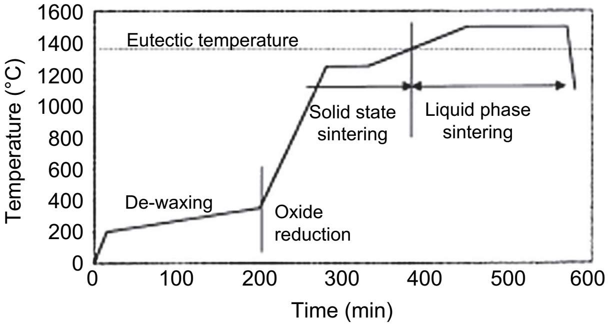

Figure 10 Schematic WC–Co sintering process. Cycle time 12 to >24 h (Andren, 2001).

1.02.2.1 Hardmetals for Metal Cutting

To improve the steel machining performance of WC–Co hardmetals, cubic transition metal carbides (TiC, TaC, and NbC) were added to the basic WC–Co composition even as early as in the 1930s. WC does not dissolve any of these transition metal carbides, but forms a solid solution with these carbides. This leads to a microstructure with an enhanced creep resistance, higher oxidation resistance and higher adhesive wear resistance against long-chipping materials. In practice, this increased the productivity of machining operations since the tool was capable of resisting higher temperatures without suffering catastrophic crater wear. The ISO classification of cutting tools that is summarized in Tables 5 and 6 shows an example of some hardmetal compositions prevalent in metal cutting (Böhlerit). In applications that call for higher toughness, higher binder contents (mainly Cobalt) were chosen. Further productivity improvements in metal cutting have been achieved since the 1970s by coating the hardmetal substrates with a thin wear-resistant film of TiN, TiC, TiCN, TiAlN, Al_2O_3, etc. by CVD or PVD. Nitride and carbonitride layers possess high hardness and high oxidation resistance, whereas the chemically inert Al_2O_3 layer serves as an oxidation-resistant heat barrier to avoid excessive heating and subsequent softening of the substrate.

Table 5 ISO 513 classification of cutting tools according to use

Symbol	*Workpiece material*	*Color code*	*Designation in increasing order of wear resistance and decreasing order of toughness in each category (in increments of 5)*
P	Ferrous metals with long chips	Blue	P01, P10–P 40
M	Ferrous metals with long or short chips, nonferrous metals	Yellow	M10–M40
K	Ferrous metals with short chips, nonferrous metals, non metallic materials	Red	K01, K10–K40

Table 6 Typical compositions and properties of metal cutting grades Type P (Böhlerit)

Grade	*ISO appl. code ISO 513*	*WC (wt%)*	*TiC + Tac (wt%)*	*Co (wt%)*	*WC grain size (μm)*	*Density (g/cm^3) ISO 3369*	*Hardness HV30 ISO 3878*	*Comp. strength (N/mm^2) ISO 4506*	*TRS (N/mm^2) ISO 3327*	*Fracture toughness, K_{1c} (MPa m$^{-0.5}$)*	*Modulus of elasticity (kN/mm^2) ISO 3312*
SB10	P05–P15	57.5	33	9.5	2.5	10.3	1575	5300	2000	9.3	530
SB20	P15–P25	69	22	9	2.5	11.20	1550	5200	2000	9.3	540
LW225	P20–P40	72.7	17.3	10	1.25	12.55	1525	5100	2300	9.8	550
SB29	P20–P40	74.1	15.9	10	1.25	12.35	1525	5100	2200	9.8	550
SB30	P25–P30	69	21	10	2.5	11.60	1500	5100	2200	10.0	550
SB40	P35–P45	77	12	11	5.3	13.15	1400	5000	2400	12.0	560

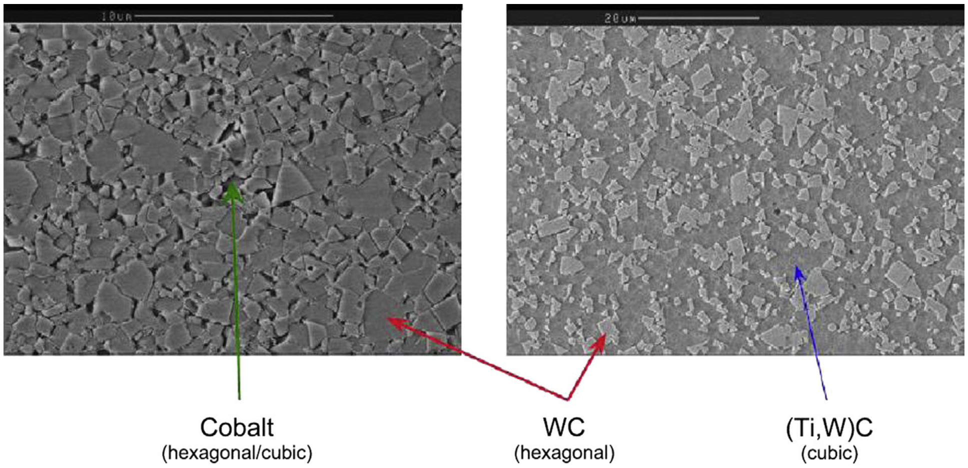

Figure 11 Example for microstructural features of a WC–Co (left) compared to a WC–TiC–TaC–Co HM (right) (SEM micrograph (EPMA)).

1.02.2.2 Cermets

Another important family of wear-resistant cutting tool alloys, also developed in the early days of hardmetals and which is very popular (more than 30% usage) in Japan, is based on TiC, but alloyed with a number of other elements like Ta, Nb, V, Cr, and Mo with the binder alloy being nickel with cobalt and Al.

The name cermet has been coined from the syllables "Cer" from ceramics and "met" from metals and connotes a wide range of materials consisting of hard ceramic phases bonded by metal with properties superior to that attained by any one single component.

Modern cermet alloys exhibit multicomponent microstructures based on titanium carbonitride and varying amounts of Mo, W, Ta, Nb, V, and perhaps other elements. The binder is an NiCo alloy and contains considerable amounts (20–40 mass%) of Ti, Mo, W, V and other metals like Al in solution, depending on composition and sintering conditions. Earlier TiC-based cermets were created to conserve the strategic important metal tungsten in WC–Co. However, the thermal conductivity, thermal shock resistance, toughness, bending strength and fatigue resistance of these TiC-based materials were inferior to WC–Co. The breakthrough in cermet properties to be on a par with WC–Co was achieved only after the introduction of TiN to the basic Ti, MoC–NiMo alloys (**Figure 11**).

The microstructures of cermets, whose hard particles often have a "core–rim" structure, are much more complex than those of relatively straightforward WC–Co hardmetals (**Figure 4**). The core is essentially undissolved TiCN and/or TiN. The rim is enriched in heavier elements W, Ta/Nb and Mo and has the same cubic crystal structure as the core. With increasing nitrogen content in cermets, the grain size of the hard particles and the thickness of the rim generally decrease. The performance of modern cermets to machine steels at high speed is as good as or even better than that of coated hardmetals.

Nitrogen also plays an important role as far as coated hardmetals are concerned. The microstructure in the surface region of coated substrates has been modified by introducing nitrogen to develop a cobalt-enriched, cubic-carbide-free layer (CFL) (Schwarzkopf, Exner, & Fischmeister, 1988). The lifetime of coated hardmetals using CFL substrates can be significantly extended due to increased toughness beneath coating layers. In the mid 1990s, functionally graded material (FGM) cermet was developed by sintering of TiCN + WC + Co/Ni under nitrogen atmosphere (Tsuda, Ikegaya, Isobe, Kitagawa, & Nomura, 1996). The FGM cermet consists of a high wear-resistant cubic-carbide-enriched surface layer, a tough core containing WC, cubic carbides/carbonitrides and CoNi binder and an intermediate zone with graded compositions. The FGM cermet displays better wear resistance compared to standard cermet and coated hardmetals (Chen, Lengauer, & Dreyer, 2000; Glühmann et al., 2013).

The main binder used in cermets has been alloys of nickel and cobalt. Interest in perhaps using steel binders has been growing. **Figure 12** shows an example of a calculated phase diagram (Alvaredo, P., Mari, D., & Gordo, E. (2013)).

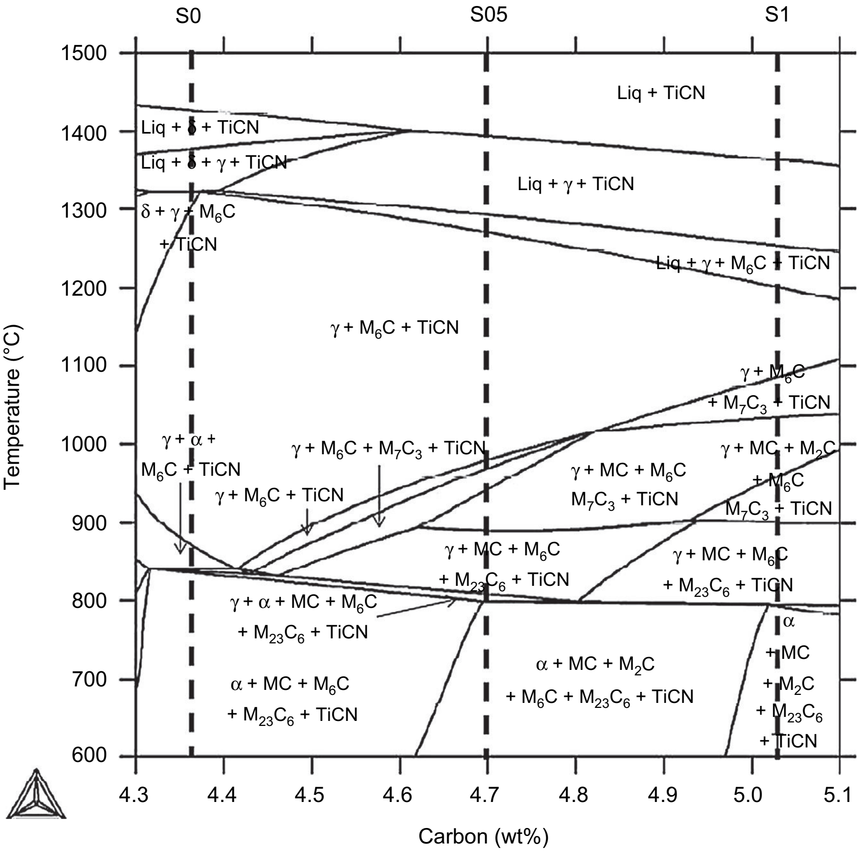

Figure 12 Theoretical Thermocalc calculated phase diagram (Alvaredo, Mari, & Gordo, (2013)) for TiC cermets with steel binders.

1.02.3 Role of the Binder

The most commonly used binder in WC hardmetals is cobalt, though in some applications which demand acidic corrosion resistance, nickel is widely used.

Iron-based binders have been extensively studied, but are only used in selected niche applications such as woodworking. Cobalt is the favorite binder in WC hardmetals since it wets WC readily, exhibits a temperature-dependent solubility that aids sintering and leads to products with excellent strength and ductility. Cobalt as a ferromagnetic binder also facilitates the magnetic nondestructive evaluation of the metallurgical alloy composition by the measurement of coercitivity and magnetic saturation. Nickel-bonded hardmetals are in most cases nonmagnetic and can only be evaluated metallographically. The strength of nickel-bonded hardmetals can be influenced by using metallurgical alloying techniques such as solid solution strengthening or dispersion hardening.

It has been reported (Konyashin et al., 2005) that the binder of ultracoarse WC–Co grades can be reinforced and hardened effectively by nanoparticles of the θ-phase leading to significant improvements in their transverse rupture strength and hardness. The novel MASTER GRADES® with the nanograin-reinforced binder have a dramatically enhanced wear resistance and toughness resulting in a considerable life prolongation of mining and construction tools (Table 7).

It is generally agreed that the binder phase composition in commercially sintered hardmetals is in a thermodynamic nonequilibrium state and that composition gradients are to be expected in the binder phase regions. Researchers in Chalmers University have clearly shown proof of the nonhomogeneity of the binder phase in WC–Co hardmetals (Andren, 2001). Auger electron spectroscopy results lead one to the conclusion that the binder–carbide interfaces have a higher tungsten content than the bulk. The mechanism of WC grain growth inhibitions, e.g. by vanadium or chromium, has been attributed to the segregation of solute atoms of V and/or Cr to the WC–binder interfaces that decrease the propensity for WC grain growth by grain boundary pinning also as a function of the dissolved tungsten contents.

Table 7 Comparison of properties of conventional coarse WC–Co grades with those with a nano reinforced binder (Konyashin et al., 2005)

Grade	*TRS (MPa)*	*HV30*	K_{1c} *(MPa* $m^{-0,5}$*)*
Standard grade for coal cutting	1990	1050	16.0
MASTER GRADE® for coal cutting	2300	1130	16.4
Standard grade for road planing	2010	1100	12.3
MASTER GRADE® for road planing	2330	1150	12.6

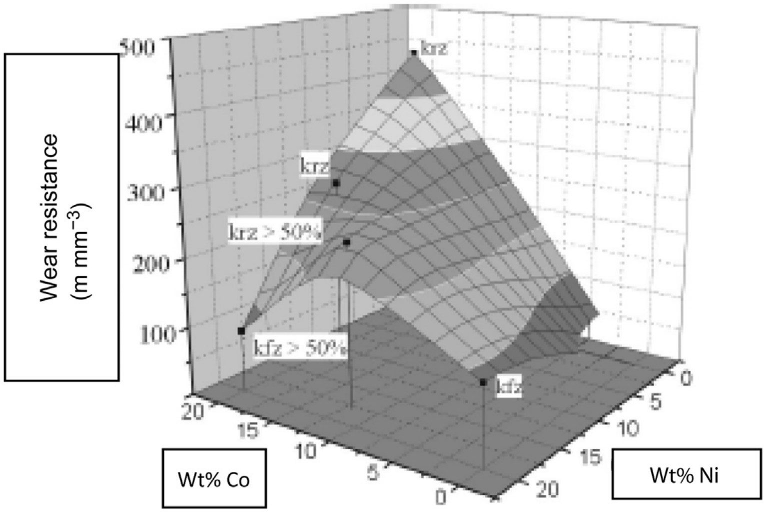

Figure 13 Abrasive wear resistance of nanograined WC-10 wt% FeCoNi bonded hardmetals for different binder compositions and resultant binder phase structures (krz = bcc; kfz = fcc) (Herr, Sailer, Sockel, et al., 2001).

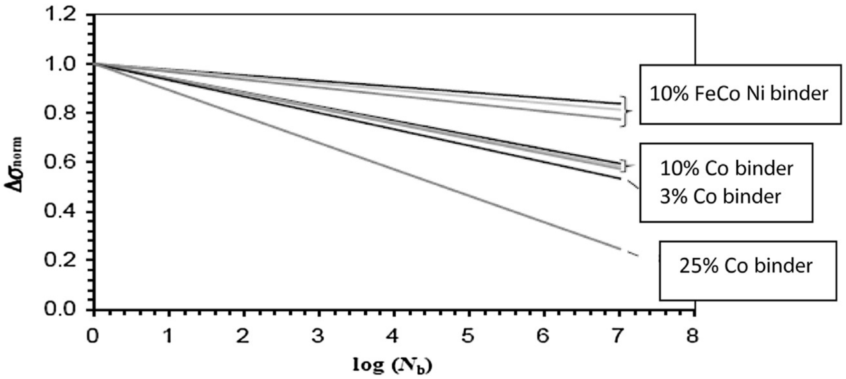

Figure 14 Normalized Wöhler plots of WC–Co and WC–FeCoNi HM for evaluating fatigue sensitivity (Sailer, Herr, Sockel, et al., 2001).

1.02.3.1 Alternate Binders

More than 50 years after Agte pointed out the critical influence of the carbon content for Fe-based binders for WC-based hardmetals, now data on raw materials, phase diagrams, processing, material properties and applications have become available. Research work on new alloy compositions and processing and applications is being carried out at a brisk pace (**Figures 13** and **14**). Annual industrial production though miniscule in the range of less than a hundred tons of hardmetal with Fe-based binders to date is projected to grow based on application superiority in the areas of metal cutting, nonferrous and wood machining, processing of stone, road planing, mining, chipless forming and wear parts. The relative benevolent nature of iron-bonded hardmetals on the environment should be a further driver for more widespread acceptance of this class of materials in the near future (Prakash & Gries, 2009).

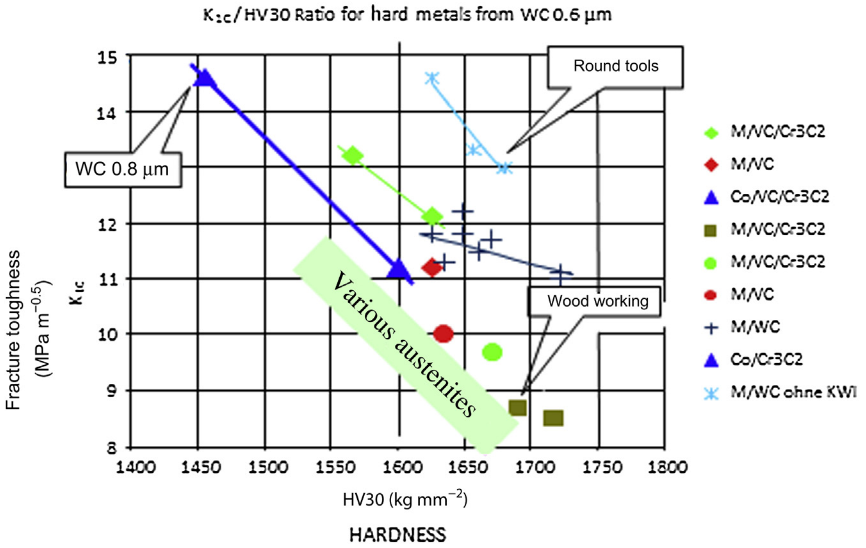

Figure 15 Comparison of fracture toughness to hardness ratio of various fine-grained iron-bonded hardmetals to cobalt-bonded hardmetals (Prakash & Gries, 2009).

The influence of the strength and ductility of the binder phase, achieved by choice of the FeCoNi alloy binder composition regarding transverse rupture strength, hardness, fracture toughness and hot hardness has been published by Prakash, 1979 and subsequently confirmed by Sailer (2001) also as regards fatigue strength in monotonic bending (**Figure 15**). The brittle ordered 50Fe50Co binder phase leads to an inferior transverse rupture test (TRS), fracture toughness and fatigue strength in comparison to a binder composition of 65Fe20Co15Ni with a martensitic/austenitic binder structure that facilities transformation induced plasticity at higher yield stress of the binder phase in comparison to cobalt at ambient temperatures.

Some of these selected data are reproduced in the following diagrams as illustrative examples.

Iron-bonded WC hardmetals also show a better oxidation resistance than Co-bonded hardmetals and this can be further improved by alloying of the binder phase with Cr/Mo as shown in **Table 8**.

Figure 15 shows that various iron-bonded hardmetals with an austenitic binder are superior to cobalt bonded ones as regards fracture toughness at the same hardness level using VC and/or Cr_3C_2 as grain growth inhibitors.

Coarse-grained WC–FeCoNi alloys with an austenitic structure also show an attractive combination of hardness/toughness ratios in comparison with cobalt-bonded hardmetals (**Table 9**) and have been successfully tested for impact applications.

Fe-based binders are also used extensively for metal-rich TiC-based hard materials (e.g. under the tradename "Ferrotic"). Work on TiB_2-based composites has shown the capabilities and suitability of Fe-based binders

Table 8 Enhanced oxidation resistance of WC hardmetals with iron-based binders in air at 850 °C (Wittmann, Schubert, & Lux, 2002)

Composition	*Weight gain (mg cm^{-2})*
WC–10Co	84.1
WC–10Co–1Cr_3C_2	63.3
WC–9Fe–1Ni	36.4
WC–8.5Fe–1.5Ni	41.2
WC–8.5Fe–1.5Ni–0.5Cr_3C_2–0.25Mo_2C	58.9
WC–8Fe–2Ni	75.7
WC–10(FeCoNi)	82.1
WC–10(FeCoNi)–Cr/Mo	27.5
WC–20(FeCoNi)	10.0
WC–20(FeCoNi)–1Cr_3C_2–0.5Mo_2C	6.9

Table 9 Properties of coarse grained WC–FeCoNi hardmetals with an austenitic binder

WC grain size/binder type	*Sintering atmosphere*	*Hardness (HV30/HRA)*	*Fracture toughness K_{1c} (MPa $m^{-0,5}$)*
9 μm + 10% Co (G20)	Vacuum	1203/88.2	18
9 μm + 10% A2500 (G25)	Vacuum	1150/87.6	>20
9 μm + 9% A2500 (G20)	Vacuum	1200–1274/88.2–89	17.4–20

(Jüngling, Oberacker, Thümmler, Sigl, & Schwetz, 1991). Fe alloyed with Mn and/or Al also show potential as binders for WC hardmetals in selected application areas (Bolton, 1992), but problems in processing and mechanical properties have to be addressed for this class of alloys. Other applications (Deshpande, Saxena, & Basu, 1992) of Fe-based binders are in the diamond abrasive industries as well as in thermal spraying. Just as for conventional hardmetals, hard coatings including diamond coatings have been successfully implemented. The outlook for Fe-based binder alloys in hard materials applications is indeed optimistic.

1.02.4 Functional Gradient Hardmetals

A hard and wear-resistant surface combined with a ductile tough core should be an ideal solution to offset the inherent hardness/toughness tradeoff of hardmetals. The success of thin film coatings as practiced in metal cutting applications is based on this philosophy.

The well-established route of surface modification of WC–TiC–TaC–Co hardmetal metal cutting inserts to reap the benefits of a wear-resistant but brittle coating has been developed across many years and profusely studied (Grab & Nemeth, 1982; Spacil, 1997; Nicolae & Nita, 2001). The two routes of surface modification have been to either create a cubic carbide-free tough surface layer or a cubic carbide-rich wear-resistant layer as the substrate for a CVD thin layer coating (Garcia & Pitonak, 2013) (**Figure 16**).

The metallurgical driving force for generating these diffusion controlled surface layers is the interaction of nitrogen with the Ti(Ta,Nb) cubic carbides. The composition of the bulk carbide product as well as the processing parameters such as temperature and pressure of nitrogen determines the type of gradient that is formed. The choice of the suitable variant for the particular application depends not only on the design of the functionally graded microstructure but also on the operating conditions of metal cutting (Garcia & Pitonak, 2013).

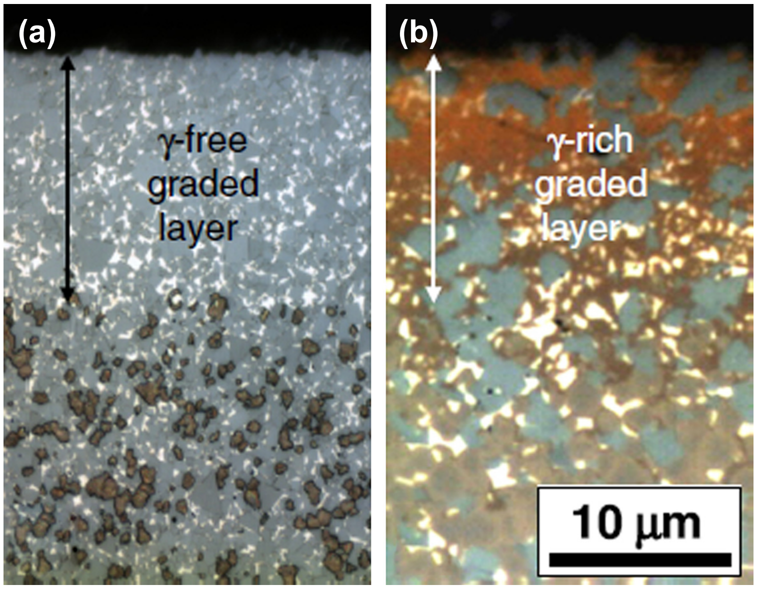

Figure 16 Microstructures (LOM) (Murakami etched) of FG graded surface layers on cemented carbides (gamma phase = TiTaNbC mixed carbides) (Garcia and Pitonak, 2013).

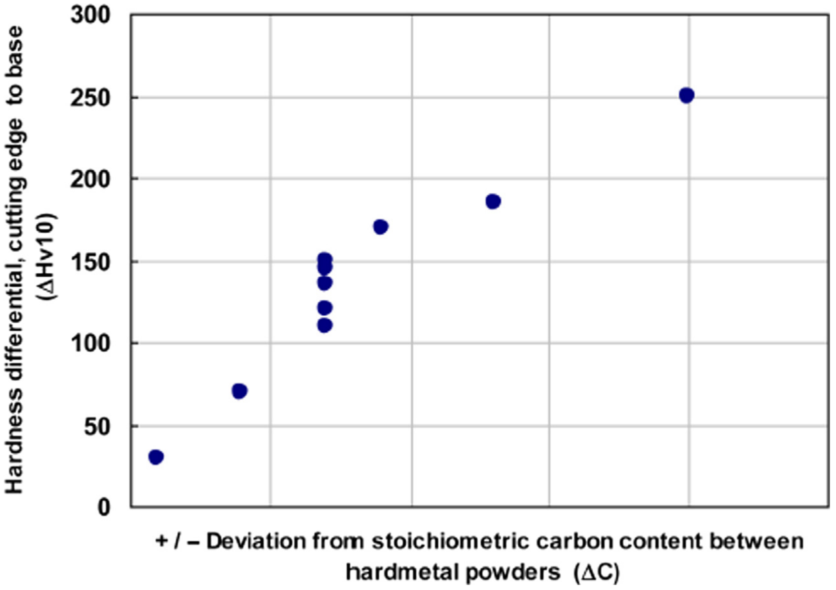

Figure 17 Carbon differential to tailor hardmetal gradient (EPMA, 2006).

The other major area where functional gradient (FG) hardmetals would be of importance where extreme wear resistance as well as toughness is required for applications such as mining, oil and gas exploration, construction and metal forming. In these applications, mainly straight WC–Co grades are used. The earliest reported application of successful FG hardmetals is the dual property carbide process of Sandvik AB / that creates a cobalt depleted surface zone in rock drilling or other inserts of WC–Co.

Other examples of FG hardmetals have also been reported in the literature (EPMA, 2006). A significant cobalt gradient produced by selective carburization of near-surface layers before liquid phase sintering of up to 7 wt% and a hardness differential of up to 250 HV has been reported by Konyashin, Ries, Lachmann, and Fry (2013). The surface is characterized by high compressive residual stresses in both the WC and Co phases that lead to an exceptional combination of hardness and toughness. The authors report that the wear resistance of such gradient hardmetals in percussive drilling of quartzite or cutting of concrete has been found to be improved by a factor between 2 and 4 in comparison with hardmetals with a uniform cobalt distribution (**Figure 17**).

In all cases, the graded structure formation is attributed to the mechanism of liquid phase migration pressure driven by the reduction of the total interfacial energy of the system, due to the difference in the interfacial energies between the solid–solid (WC–WC) interface and the solid–liquid (WC–liquid Co) interface. The establishment of the dependence of liquid phase migration dependent on key material parameters such as WC grain size and the Co and C contents prove to be useful for the design of FG WC–Co (Fan, Zak Fang, & Guo, 2013).

1.02.5 Key Properties of Hardmetals

The various attributes of hardmetals can be summarized as follows:

Compressive strength: Compressive strength values of 4–8 kN mm^{-2} make hardmetals one of the strongest materials available, witness their use in diamond manufacture as anvils and in hot rolls for metallic materials.

Tensile strength: Usually measured in a bend test. Surface condition (grinding stresses) can have a significant effect on measured values. Less than compressive strength, typically 2.4 kN mm^{-2}, but still much stronger than most other materials. Processing route is very important. HIPping or SINTERHIP required for highest values of strength (Chapter 1.10).

Hardness: Defined as the resistance to indenter penetration. It correlates directly with the strength of the cutting tool material. It is measured using either a Vickers test (HV), or the Rockwell test (HRA). It can easily be varied between 1000 and 2000 HV30 by changing cobalt content and WC grain size. Like many other properties of hardmetal, there is the flexibility to design specific hardness values by changing composition (Chapter 1.09). The ability to maintain high hardness at elevated temperatures is called *hot hardness* (**Figure 18**).

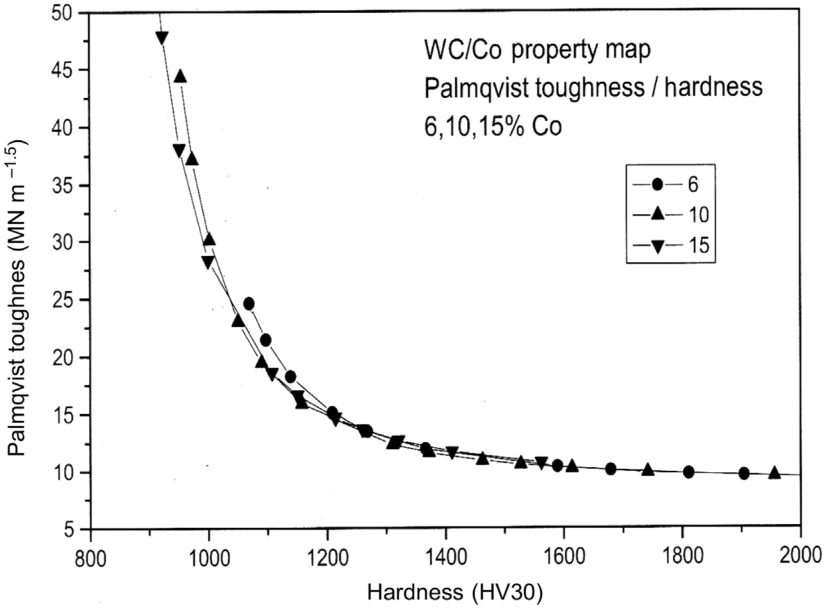

Figure 18 Palmqvist fracture toughness relationship to hardness (Gee et al., 2007).

Toughness: Defined as the ability of a material to absorb energy before fracture. The greater the fracture toughness of a tool material, the better it resists shock load, chipping and fracturing, vibration, misalignments, runouts and other imperfections in the machining system.

The fracture toughness of a hard tool material is measured using the Palmqvist Vickers indentation test. It is difficult to measure due to difficulties in introducing cracks with a known geometry. Typical values of plane strain fracture toughness lie in the range 7–25 m$^{-3/2}$ MPa m$^{-0,5}$. These values are much higher than for similar hard materials like ceramics which have fracture toughnesses of 2–8 MN m$^{-3/2}$. Unfortunately this test is not truly characteristic since the testing conditions of the tool materials is not determined using loading conditions (stress state, strain rate and temperature) similar to that occurring in machining. The validity of such a test is discussed in Chapter 1.10.

Fatigue strength: Limited data available to judge properties but likely to be quite good in the absence of strength-limiting defects, as this property usually correlates with strength (Chapter 1.11).

High-temperature strength: Excellent, although decreases steadily with increasing temperature. Sensitive to choice of hard phase. Cubic carbide additions such as (Ta,Nb)C and (Ta,Ti)C increase elevated temperature strength significantly.

Low temperatures: Hardmetals retain a good combination of properties at temperatures down to as low as that of liquid nitrogen. Hardness increases by about 20–30% with a concomitant decrease in fracture toughness.

Impact strength: Not well understood, probably related to tensile strength and fracture toughness. No standard test method available.

Wear resistance: In general, wear resistance is defined as the attainment of acceptable tool life before tools need to be replaced. Although seemingly very simple, this characteristic is the least understood. Wear resistance is not a defined characteristic of the tool material and the methodology of its measurement. The nature of tool wear, unfortunately, is not yet sufficiently clear despite numerous theoretical and experimental studies. Cutting tool wear is a result of complicated physical, chemical, and thermomechanical phenomena. Because various simple mechanisms of wear (adhesion, abrasion, diffusion, oxidation, etc.) act simultaneously with a predominant influence of one or more of them in different situations, identification of the dominant mechanism is far from simple, and most interpretations are subject to controversy (**Figure 19**).

Abrasion and erosion resistance: In severe abrasion and erosion environments, it is the most wear-resistant material available. This is because it has a unique combination of strength, hardness and fracture toughness compared with other hard materials (**Figure 20**) (Chapter 1.12).

Stiffness: It is one of the stiffest materials known, after diamond, with a Young's modulus about three times that of steel and six times that of aluminum (Chapter 1.09).

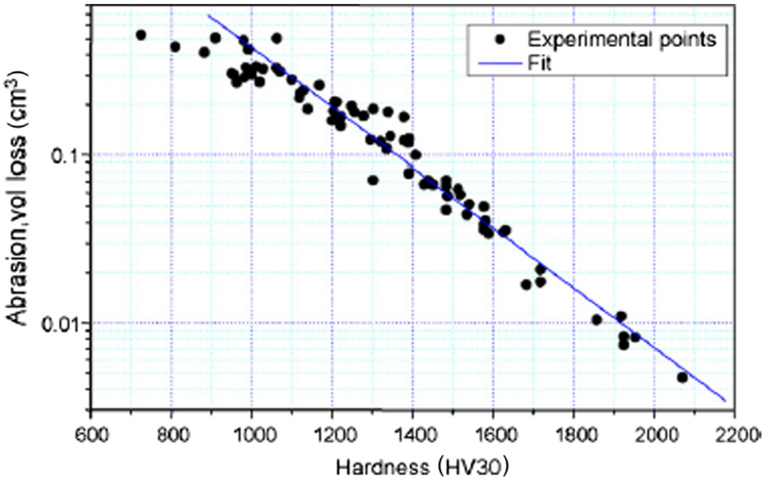

Figure 19 Variation of wear volume with hardness for ASTM B611 tests on range of Hardmetals (Gee, Gant, & Roebuck, 2007).

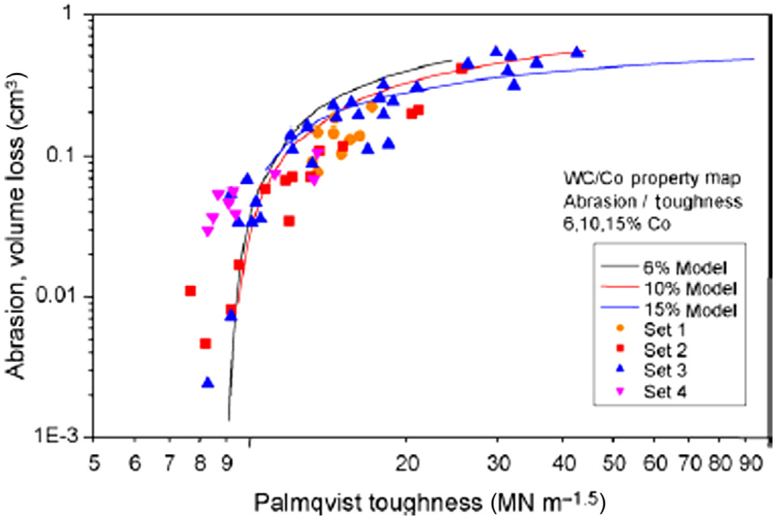

Figure 20 Dependence of abrasive wear volume (ASTM B611 tests) on Palmqvist toughness. The different colored points are different sets of WC–Co (Gee et al., 2007).

Density: Hardmetals are very dense if they contain significant amounts of WC; up to 15 Mg m^{-3} is possible. Lower densities down to 4–5 Mg m^{-3} can be tailored by using higher Co contents or additions of cubic carbides and carbonitrides for the hard phase. The high density endows hardmetal with a very satisfying feel when handling products but if specific properties (i.e. properties per unit weight) are required, it is a disadvantage.

Surface finish: Hardmetal can take a superb mirror finish, a consequence of its defect-free fine-scale structure. It has a deep gray luster, which is particularly attractive.

Coefficient of friction: Hardmetals have a relatively low coefficient of friction, about 0.2, in unlubricated tests in contact with steel, as compared with typical steel against steel values of about 0.4. There is little systematic data of the effects of surface roughness, composition variations and temperature effects.

Coatings: Hardmetals easily take a variety of coatings, e.g. electroless, electroplate, chemical or physical vapor or spray deposited. Both wear resistance and cosmetic coatings of many types are cheap and effective.

Shape: Since hardmetals are manufactured by a powder metallurgy route, there are few restrictions on shape and mass production technologies are possible. However, postmanufacture shape changes can be expensive if extensive diamond grinding is required.

Dimensional stability: Their use as high-quality slip gauges indicates exceptional dimensional stability, provided grinding stresses are stress-relieved. The microstructures are inherently stable since they are formed by an equilibrium process at very high temperatures and are cooled to room temperature relatively slowly.

Table 10 Corrosion resistance of cemented carbides with Co, Ni, and Ni–Cr binders (Kny et al., 1986)

	Corrosion resistance[b]						
Medium	*Temperature (°C)*[a]	*Concentration (mol/l)*	*WC–6Co*	*WC–12Co*	*WC–6Ni*[c]	*WC–9Ni*[c]	*TiC–16Mo$_2$C–18Ni*
Acetic acid	RT	1	2	2	1	1	1
	100	1	3	3	2	2	2
Hydrochloric acid	RT	6	2	3	2	2	2
	100	6	4	4	4	4	4
Nitric acid	RT	6	2	3	1	1	4
	100	6	4	4	4	4	4
Phosphoric acid	RT	0.67	3	3	2	2	2
	100	0.67	4	4	3	3	2
Sodium chloride	RT	0.5	2	2	1	1	1
Sodium hydroxide	RT	1	1	1	1	1	1
Seawater	RT		2	2	1	1	1
Sulfuric acid	RT	1	3	3	2	2	2
	100	1	4	4	3	4	3
Water, tap	RT		1	2	1	1	1
Water, pure	RT		1	1	1	1	1
	100		1	1	1	1	1

[a] *RT, room temperature.*

[b] *1 = negligible attack; 2 = light attack; 3 = medium attack; 4 = strong attack.*

[c] *Ni–Cr alloy with 5% Cr.*

Edge retention and sharpness: The fine scale of the microstructure and the high strength of the hardmetal enable very sharp edges and corners to be manufactured which have myriad uses in cutting and shaping processes.

Corrosion resistance: Corrosion resistance in nonacids is excellent for all hardmetals. However, if a cobalt binder phase is used, they can be prone to dissolution in even mildly acidic environments. This can be mitigated by using Ni-base or alloy binder-phases which are inherently corrosion resistant (**Table 10**).

Joining: Brazing is relatively straightforward as hardmetals are readily wetted if clean. However, care has to be taken to minimize thermal residual stresses because the thermal expansion coefficient is quite low, about half that of high-speed steel. Welding is not always possible but adhesives can be used in some circumstances if care is taken with surface preparation (**Figure 21**) (Chapter 1.19).

Thermal expansion and conductivity: The thermal conductivity of standard WC/Co hardmetals is about twice as high as that of high-speed steel. Both conductivity and expansion can be tailored by changing the volume fraction of binder phase and type of carbide/carbonitride hard phase.

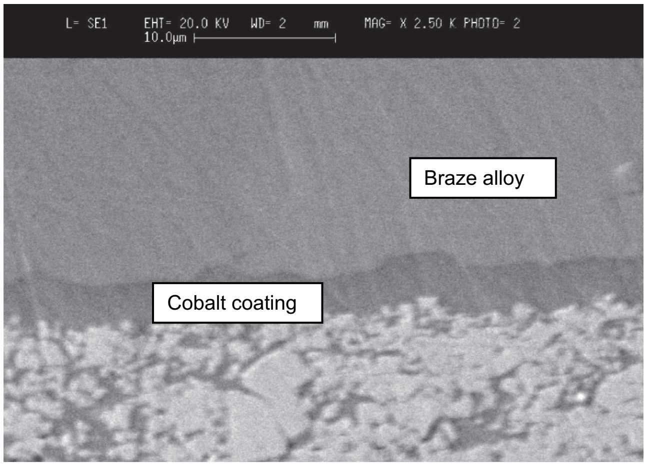

Figure 21 Hardmetal with cobalt surface coating and braze alloy (Konyashin, Hlawatschek, Ries, 2014).

Electrical and magnetic properties: Hardmetals usually have transition metal binder phases and consequently are slightly ferromagnetic, with coercive force values between 5 and 30 kA m^{-1}, depending on the binder-phase content. Nonmagnetic hardmetals can be made using Ni or alloy binder-phases as an alternative to the more common cobalt. Electrical conductivity is good with values of resistivity in the range of 150–250 nm. Higher values of up to 1000 nm can be produced if cubic carbides such as TiC substitute for the WC (Roebuck, 2012).

1.02.5.1 Hardmetal Standards

The ISO subcommittee on hardmetal standards, TC119/SC4, has in recent years developed a number of new standards as well as reviewing some of the more long-standing documents.

1.02.5.1.1 Metallographic Determination of Microstructure—ISO 4499: 2008

The first two parts of this new and revised standard were published as ISO 4499-1 and -2 in 2008.

- Part 1: specifies the methods of metallographic determination of the microstructure.
- Part 2: gives the guidelines for the measurement of hardmetal grain size by metallographic techniques using optical or electron microscopy. It is intended for sintered WC/Co hardmetals containing primarily WC as the hard phase. It is also intended for measurement of the grain size by the linear intercept technique.

Further parts to the standard are under consideration:

ISO 4499-3 hardmetals—metallographic determination of microstructure

- Part 3: measurement of microstructural features in Ti(C,N) and WC/cubic carbide-based hardmetals.

ISO 4499-4 hardmetals—metallographic determination of microstructure

- Part 4: characterization of porosity, carbon defects and eta-phase content.

ISO 4499-5 hardmetals—metallographic determination of microstructure

- Part 5: characterization and measurement of miscellaneous microstructural features.

1.02.5.1.2 Palmqvist Toughness Test for Hardmetals—ISO 28079: 2009

This standard describes a method for measuring the Palmqvist toughness of hardmetals and cermets at room temperature by an indentation method. The standard recommends good practice to minimize levels of uncertainty in the measurement process. The procedure was validated through underpinning technical work within an interlaboratory exercise conducted to generate underpinning technical information.

1.02.5.1.3 Abrasion Tests for Hardmetals—ISO 28080: 2011

This ISO standard provides new and improved methods for testing the abrasion characteristics of hardmetals using rotating wheel systems. There has been a number of abrasion test methods that have been developed that use this type of geometry including the ASTM G65 dry sand rubber wheel test, the ASTM G105 wet rubber wheel test and the ASTM B611 steel wheel test. Other variants of these tests have also been developed for specific applications in various institutes. Because of a fundamental commonality, much of the methodology is the same for the different tests. However, they do differ in the details of how the abrasive is fed to the interface between the wheel and the test sample if the test can be carried out in the presence of fluids and if the abrasive is only used once and passes through the test system, or is reused multiple times. This new standard gives results that indicate how comparable the different tests are, and also gives information on their reproducibility and repeatability.

This new standard is in three parts. Part 1 updates the ASTM B611 test method for abrasion wear with information on testing uncertainties and a common reporting format with Parts 2 and 3. In Part 2, a section is included for the measurement of abrasion wear bases on the ASTM G65 test method, again with new information on testing uncertainties, while Part 3 arises from new studies in Germany that provide a combination of the principles of B611 and G65 with additional instrumentation.

1.02.5.1.4 Determination of Transverse Rupture Strength—ISO 3327: 2009

Historically the TRS standard allowed two sample geometries to be tested in 3pt bend: type A and type B. Type A is 5 × 5 mm in cross-section and 35 mm long, whereas type B is 6.5 mm wide by 5.25 mm high and 20 mm long. Recent work by SC4 has revised the standard to allow a round geometry, 25 mm long and 3.3 ± 0.5 mm diameter, type C to be used as well. This revision was supported by an international interlaboratory exercise to compare the properties of various geometries (Roebuck, 1997).

1.02.5.1.5 Vickers and Rockwell Hardness Tests—ISO 3878 and ISO 3738-1

ISO/TC 119/SC4 has decided that an NWIP for Revision of ISO 3878 and ISO 3738-1 will be instigated in order to provide supporting data for annexes regarding the uncertainties of measurement data. An intercomparison is planned between Rockwell A and Vickers, HV30, for basic WC/Co hardmetals with hardness >1600 HV30. (NB—good data already exists for hardmetal grades with HV30 <1600 and >1100.)

1.02.5.1.6 Knoop Hardness Test—ISO 22394: 2011

A Knoop hardness test method for hardmetals has been introduced because many metallurgical problems require the determination of hardness over very small areas. The special shape of the Knoop indenter makes it possible to place indentations much closer together than with a square Vickers indentation, e.g. to measure a steep hardness gradient. For a given long diagonal length, the depth and area of the Knoop indentation are known to be only 15% of what they would be for a Vickers indentation with the same diagonal length.

1.02.5.1.7 Other Topics

In addition, several other topics are being considered by the committee, including magnetic saturation measurements; characterization of surface condition and semiquantitative identification of binder type. Also, progress is being made with standards for chemical analysis (i.e. total carbon content—gravimetric method; insoluble carbon content—gravimetric method; atomic absorption spectrometric methods and determination of lead and cadmium).

1.02.5.2 Future Needs—Characterization of Hardmetals

The performance and reliability of hardmetal components will, in the future, certainly benefit from combining modelling and experimental approaches through a wide length scale range. Economic drivers and health concerns are continually putting demands on producers and users to optimize, or even consider the replacement, of current binder phase constituents. The majority of the world's production of hard tool materials are multiphase with the predominant hard carbide or carbonitride phase toughened by a secondary binder-phase. For the most part, this binder phase is based on a transition metal or alloy using Fe, Co and Ni as the major constituents. Detailed knowledge of the in-service degradation mechanisms will clearly lead to improved performance. Effective implementation of relevant microstructural effects on critical design parameters requires further research and applied work, *both experimental and modelling*, on *damage and damage evolution*, particularly as related to behavior of intrinsic (short) flaws and surface behavior. The criteria for material selection, in terms of binder content and/or carbide grain size, for many applications with respect to wear, fracture and fatigue mechanisms need further clarification. Cemented carbides are heterogeneous in nature, and modeling of their mechanical behavior (especially in the presence of damage) will require a *multiscale approach*. At the microscale, the initial processes relate to the size dependence and discrete behavior of plastic deformation (often under constraint), strain hardening and fracture within individual phases. At the macroscale, continuum mechanical models are based on homogenized material parameters. At all levels, molecular dynamics, crystal plasticity models and finite element approaches may be effective tools for quantifying the relevance of representative size effects. Capturing microscopic phenomena and bringing them to the macroscale will be essential for the correct simulation of wear, fracture and fatigue degradation phenomena in hardmetals. It is particularly important to take advantage of advanced characterization techniques such as in situ scanning electron microscopy (SEM) testing, nanoindentation, electron backscatter diffraction, transmission electron microscopy (TEM), focused ion beam, and 3-D tomography to provide equivalent information to that yielded by electron microscopy (mainly by means of fractographic analysis) to current knowledge. Extensive and detailed use of these techniques will help to characterize the deformation behavior and operative mechanisms at the microstructural scale for cemented carbides (**Figure 22**).

A major part of the world's production of hardmetals is manufactured with a coating or an engineered surface. Coatings and surface layers are generally thin (of the order 10 μm) and usually multiphased with

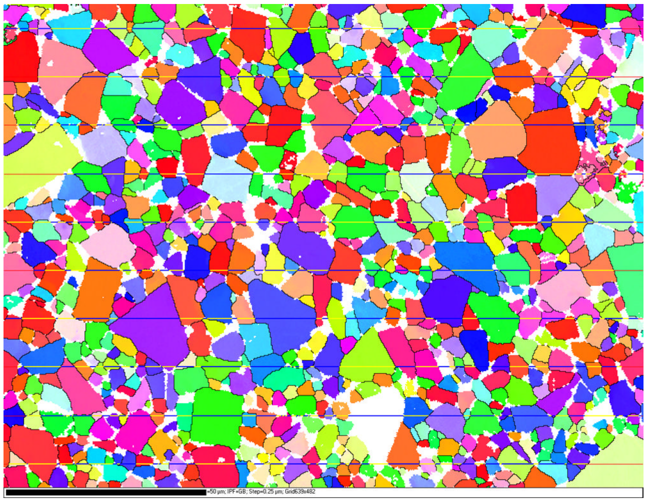

Figure 22 EBSD image of WC grain structure with superimposed lines for intercept measurements. The different colors of each grain correspond to differences in crystal orientation and thus provide a mechanism for automation of the grain recognition process (Roebuck, 2012).

microstructural features in the nano range (20–200 nm). Characterization of these zones, whether it be by phase analysis or through mechanical behavior, provides significant challenges for the science and engineering community. Coatings are multiphase and can contain carbides, carbonitrides, ceramic phases, transition metals and alloy binders. To assess performance and confirm processing quality and consistency, it is necessary to be able to measure the size, shape, composition and distribution of each constituent, as well as characterizing the scale dependence of their physical and mechanical properties in combination. Clearly no one technique is sufficient for this purpose and it is necessary to use a range of complementary methods. For microstructural purposes, the science community has used Transmission Electron Microscopy (TEM), Field Emission Gun Scanning Electron Microscopy (FEGSEM), optical, X-ray, Glow Discharge optical emission spectroscopy (GDS) and other advanced instruments such as Secondary Ion Mass Spectroscopy (SIMS) and Electron Energy Loss Spectroscopy (EELS) for examination of these small regions of material. Each instrument provides unique information on a specific attribute; for example, TEM for internal defects/dislocations/boundaries, FEGSEM for high-resolution measurements of phase size, shape and distribution, X-ray for phase composition and optical for more macroscopic issues, like reproducibility over large areas and gross defect characterization.

Mechanical properties are determined by the material microstructure and WC grain size is significant in this respect. Mechanical properties can be usefully assessed by methods such as hardness and toughness for bulk properties, but is there sufficient knowledge to mechanically interrogate near-surface regions with the same confidence? For mechanical characterization there are, again, many options open to the researcher. For example, indentation methods for plastic and fracture behavior (often on a very fine scale and depth sensing, such as microscratch and nanoindentation testing methods), surface acoustic waves for elastic property measurement, beam bending for joint substrate/coating characterization and, in principle, micro hot hardness for high-temperature studies (although this is not often reported due its challenging nature). Also, knowledge of residual stresses is vital in interpreting the performance of coatings.

Magnetic coercivity provides a characterization tool for indirectly checking the WC grain size and magnetic saturation measurements can be used to investigate differences in binder phase chemistry. But, how do these techniques cope with more complex (i.e. hybrid, gradient or composite), or finer or coarser structures with perhaps alloyed binder phases? Structure–property relations allow the effects of differences in structure and properties to be compared and provide a baseline for the evaluation of new materials and coatings. Measurements on materials with a low Co content have indicated that current understanding is probably suitable only for specified composition ranges. New models are needed for materials outside these limits, and these should be underpinned by further work investigating the nature of the cobalt distribution (Roebuck & Prakash, 2013).

1.02.6 General Applications of Hardmetals

1.02.6.1 Machining

1.02.6.1.1 Introduction

Machining is the broad term used to describe the removal of material from a workpiece and is one of the most important manufacturing processes. Components manufactured by other processes often require further operations before the product is ready for application. Machining operations can be applied to work metallic and nonmetallic materials such as polymers, wood, ceramics, composites and exotic materials.

"Today in industrialized countries, the cost of machining amounts to more than 15% of the value of all manufactured products in those countries." For this reason and others, machining as part of manufacturing science and technology is very important for modern manufacturing industries (Davim, 2008).

This section gives a very brief overview about machining of metals and points out to general trends. Reference handbooks need to be consulted for an in-depth review of the subject.

1.02.6.1.1.1 Cutting Tool geometry

The cutting tool geometry is of prime importance because it directly affects the following:

Chip control. The tool geometry defines the direction of chip flow. This direction is important to control chip breakage and evacuation.

Productivity of machining. The cutting feed per revolution is considered the major resource in increasing productivity. This feed can be significantly increased by adjusting the tool cutting edge angle. For example, the most common use of this feature is found in milling, where increasing the lead angle to 45° allows the feed rate to be increased 1.4-fold. As such, a wiper insert is introduced to reduce the feed marks left on the machined surface due to the increased feed.

Tool life. The geometry of the cutting tool directly affects tool life as this geometry defines the magnitude and direction of the cutting force and its components, the sliding velocity at the tool–chip interface, the distribution of the thermal energy released in machining, the temperature distribution in the cutting wedge, etc.

The direction and magnitude of the cutting force and thus its components. Four components of the cutting tool geometry, namely, the rake angle, the tool cutting edge angle, the tool minor cutting edge angle and the inclination angle, define the magnitudes of the orthogonal components of the cutting force.

Quality (surface integrity and machining residual stress) of machining. The correlation between tool geometry and the theoretical topography of the machined surface is common knowledge. The influence of the cutting geometry on the machining residual stress is easily realized if one recalls that this geometry defines to a great extent the state of stress in the deformation zone, i.e. around the tool (Davim, 2008).

1.02.6.1.1.2 Tool Material Properties

The three prime properties of a tool material are hardness, toughness and wear resistance (Section 1.02.5)

1.02.6.1.1.3 Selection of Carbide Grades

The selection of the most advantageous carbide grade has become as sophisticated a factor as the design of the tooling itself. A wide variety of new carbide grades and coatings available today continue to complicate the manufacturing engineer's task of selecting the optimum grade as it relates to work material machinability, hardness and desired productivity, efficiency and quality. Coupled with newer, high-speed, powerful machines and coolant types and supply techniques, this selection has created a real cutting tool insert selection dilemma for many specialists in the field. Because many manufacturing facilities do not have the luxury of a machining laboratory or even the time to carry out machining evaluations for different cutting parameters, cutting tool manufacturers offer a guide for the initial selection, as shown in **Table 11** (Astakhov & Davim, 2008).

1.02.6.1.1.4 Coating

One of the most revolutionary changes in the metal cutting industry over 1980–2010 has been thin-film hard coatings and thermal diffusion processes. These methods found ever-increasing applications and brought significant advantages to their users. Today, 50% of HSS, 85% of carbide and 40% of superhard tools used in industry are coated (Astakhov, 2006). A great number of coating materials, methods (CVD and PVD) and regimes of application on substrates or whole tools and multilayer coating combinations are used.

Carbides are excellent substrates for all coatings such as TiN, TiAlN, TiCN, solid lubricant coatings and multilayer coatings. Coatings considerably improve tool life and boost the performance of carbide tools in

Table 11 Rough guide for selection of carbide grades for metal cutting applications

Cutting conditions	*ISO code*
Finishing steels, high cutting speeds, light cutting feeds, favorable work conditions	P01
Finishing and light roughing of steels and castings with no coolant	P10
Medium roughing of steels, less favorable conditions. Moderate cutting feeds and speeds	P20
General purpose turning of steels and castings, medium roughing	P30
Heavy roughing of steels and castings, intermittent cutting, low cutting feeds and speeds	P40
Difficult conditions, heavy roughing/intermittent cutting, low cutting feeds and speeds	P50
Finishing stainless steels at high cutting speeds	M10
Finishing and medium roughing of alloy steels	M20
Light to heavy roughing of stainless steels and difficult to cut materials	M30
Roughing tough skinned materials at low cutting speeds	M40
Finishing plastics and cast iron	K01
Finishing brass and bronze at high cutting speeds and feeds	K10
Roughing cast irons, intermittent cutting, low speeds and high feeds	K20
Roughing and finishing cast irons and nonferrous materials. Favorable conditions	K30

high-productivity, high-speed and high-feed cutting or in dry machining, and when machining of difficult to-machine materials.

Coatings: (a) provide increased surface hardness, for greater wear resistance; (b) increase resistance (abrasive and adhesive wear, flank or crater wear); (c) reduce friction coefficients to ease chip sliding, reduce cutting forces, prevent adhesion to the contact surfaces, reduce heat generated due to chip sliding, etc.; (d) reduce the portion of the thermal energy that flows into the tool; (e) increase corrosion and oxidation resistance; (f) improve crater wear resistance and (g) improve the surface quality of finished parts.

The common coatings for carbides that are applied in single- or multilayers are the following:

TiN: General-purpose coating for improved abrasion resistance. Color, gold; hardness HV (0.05), 2300; friction coefficient, 0.3; thermal stability, 600 °C.

TiCN: Multipurpose coating intended for steel machining. Higher wear resistance than TiN. Available in mono- and multilayer. Color, gray-violet; hardness HV (0.05), 3000; friction coefficient, 0.4; thermal stability, 750 °C.

TiAlN and TiAlCN: High-performance coating for increased cutting parameters and higher tool life; also suitable for dry machining. Reduces heating of the tool. Multilayered, nanostructured or alloyed versions offer even better performance. Color, black-violet; hardness HV (0.05), 3000–3500; friction coefficient, 0.45; thermal stability, 800–900 °C.

WC–C and MoS_2: Provides solid lubrication at the tool–chip interface that significantly reduces heat due to friction. Has limited temperature resistance. Recommended for high-adhesive work materials such as aluminum and copper alloys and also for nonmetallic materials. Color, gray-black; hardness HV (0.05), 1000–3000; friction coefficient, 0.1; thermal stability, 300 °C.

CrN: Intended for copper alloys such as brass, bronze, etc. Color, metallic. Coating fracture toughness is as important as coating hardness in crack retardation. Balance between high compressive stress (poor adhesion) and low residual stress (no crack retardation) is necessary.

Al_2O_3: High inertness against workpiece materials, high hot hardness, low thermal conductivity, limited toughness, thermally stable >1200 °C, mainly used for cast iron and steel machining due to the high abrasion resistance. Black color.

Diamond: Mainly used for nonferrous, aluminum, composite, wood and graphite machining. Highest hardness and abrasive wear resistance, but limited toughness which can be compensated by using multilayer coatings. Black color, thermally stable until about 800 °C (Figure 23).

A great attempt to correlate the cutting materials and their performance was made by Klocke and Krieg (1999). It was pointed out that there are basically four major groups of coating materials on the market. The most popular group is titanium-based coating materials as TiN, TiC and Ti(C,N). The metallic phase is often supplemented by other metals such as Al and Cr, which are added to improve particular properties such as hardness or oxidation resistance. The second group represents ceramic-type coatings as Al_2O_3 (alumina oxide). The third group includes superhard coatings, such as CVD diamond. The fourth group includes solid lubricant coating such as amorphous metal carbon. Additionally, to reduce extensive tool wear during cut-in periods, some soft coatings

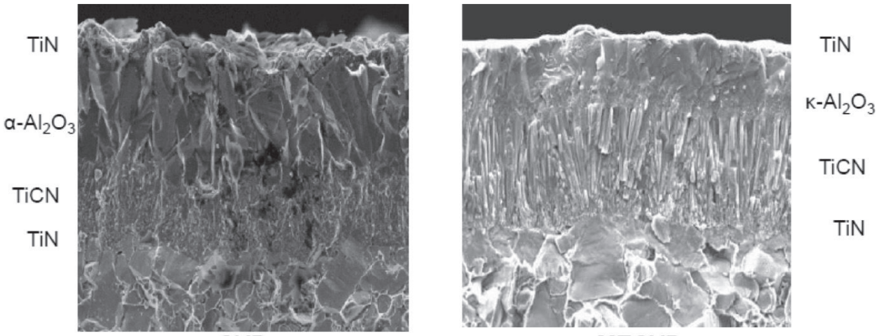

CVD
Hardness 28.8±2.3 GPa
Youngs modulus: 444.4±20.1GPa
Grain size: 500–1000 nm

MTCVD
Hardness 24.7±2.5 GPa
Youngs modulus: 244.3±15.2 GPa
Grain size: 50–100 nm

Figure 23 Example of two multilayer CVD coatings for steel machining (Ruppi, Larsson, & Flink, 2008).

as MoS_2 or pure graphite are deposited on top of these hard coatings. The basic PVD coatings are listed in **Table 12**. The effectiveness of various coatings on cutting tools is discussed by Bushmann and Gupta (1991).

1.02.6.1.1.5 Tool Wear

Tool wear leads to tool failure. According to many authors, the failure of cutting tool occurs as premature tool failure (i.e. tool breakage) and progressive tool wear. **Figure 24** shows some types of failures and wear on cutting tools.

Generally, wear of cutting tools depends on tool material and geometry, workpiece materials, cutting parameters (cutting speed, feed rate and depth of cut), cutting fluids and machine-tool characteristics.

Normally, tool wear is a gradual process. There are two basics zones of wear in cutting tools: flank wear and crater wear.

Flank and crater wear are the most important measured forms of tool wear.

Flank wear is most commonly used for wear monitoring. According to the standard ISO 3685:1993 for wear measurements, the major cutting edge is considered to be divided into four regions, as shown in **Figure 25**:

- Region C is the curved part of the cutting edge at the tool corner.
- Region B is the remaining straight part of the cutting edge in zone C.
- Region A is the quarter of the worn cutting edge length *b* farthest away from the tool corner.

Table 12 Basic PVD coating characteristics

Coating	*Characteristics*
Titanium nitride, TiN	This gold-colored coating offers excellent wear resistance with a wide range of materials, and allows the use of higher feeds and speeds. Forming operations can expect a decrease in galling and welding of workpiece material with a corresponding improvement in the surface finish of the formed part. A conservative estimate of tool life increase is 200–300%, although some applications see as high as 800%.
Titanium carbonitride, Ti(C, N)	Bronze-colored Ti(C, N) offers improved wear resistance with abrasive, adhesive or difficult-to-machine materials such as cast iron, alloys, tool steels, copper and its alloys, inconel and titanium alloys. As with TiN, feeds and speeds can be increased and tool life can improve by as much as 800%. Forming operations with abrasive materials should see improvements beyond those experienced with TiN.
Titanium aluminum nitride, (Ti, Al)N	Purple/black in color, (Ti, Al)N is a high-performance coating which excels at machining of abrasive and difficult-to-machine materials such as cast iron, aluminum alloys, tool steels and nickel alloys. (Ti, Al)N's improved ductility makes it an excellent choice for interrupted operations, while its superior oxidation resistance provides unparalleled performance in high-temperature machining.
Chromium nitride, CrN	Silver in color, CrN offers high thermal stability, which in turn helps in the aluminum die casting and deep-draw applications. It can also reduce edge build-up commonly associated with machining titanium alloys with Ti-based coatings.

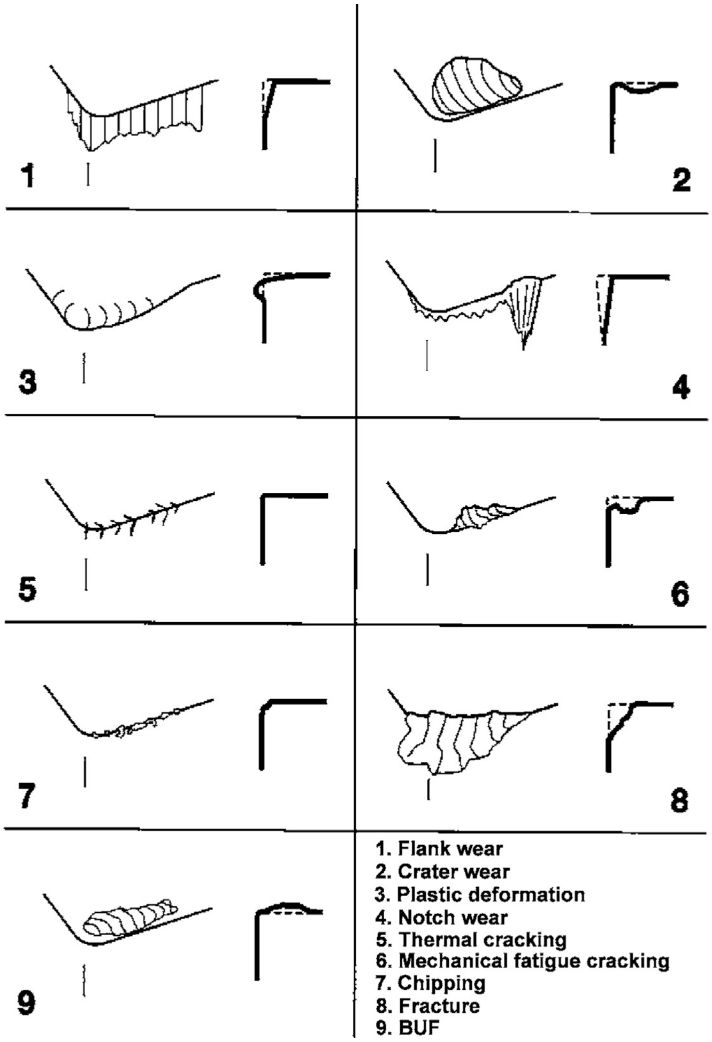

Figure 24 Wear characteristics of cutting tools (Sandvik Coromant, 1995).

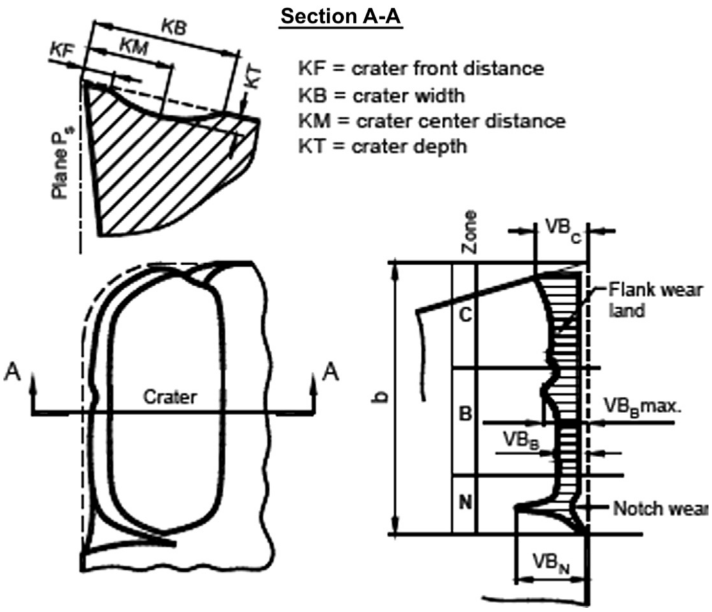

Figure 25 Types of tool wear according to standard ISO 3685:1993.

The width of the flank wear land, VB_B, is measured from the position of the original major cutting edge. The crater depth, *KT*, is measured as the maximum distance between the crater bottom and the original face.

1.02.6.1.1.6 Tool Wear Evolution

Tool wear curves illustrate the relationship between the amount of flank (rake) wear and the cutting time, T_m, or the overall length of the cutting path, *L*. **Figure 26(a)** shows the evolution of flank wear VB_Bmax, as measured after a certain length of cutting path. Normally, there are three distinctive regions that can be observed in such curves. The first region (region I in **Figure 26(a)**) is the region of primary or initial wear. The relatively high wear rate (an increase of tool wear per unit time or length of the cutting path) in this region is explained by accelerated wear of the tool layers damaged during manufacturing or resharpening.

The second region (region II in **Figure 26(a)**) is the region of steady-state wear. This is the normal operating region for the cutting tool. The third region (region III in **Figure 26(a)**) is known as the tertiary or accelerated wear region. Accelerated tool wear in this region is usually accompanied by high cutting forces, temperatures and severe tool vibrations. Normally, the tool should not be used in this region (**Figure 26**).

In practice, the cutting speed is of prime concern in the consideration of tool wear. As such, tool wear curves are constructed for different cutting speeds keeping other machining parameters constant. In **Figure 26(b)**, three characteristic tool wear curves (mean values) are shown for three different cutting speeds, v_1, v_2, and v_3. Because v_3 is greater than the other two, it corresponds to the fastest wear rate. When the amount of wear reaches the permissible tool wear VB_{Bc}, the tool is said to be worn out.

Typically VB_{Bc} is selected from the range 0.15–1.00 mm depending upon the type of machining operation, the condition of the machine tool and the quality requirements of the operation. It is often selected on the grounds of process efficiency and often called the *criterion of tool life*. In **Figure 26(b)**, T_1 is the tool life when the cutting speed v_1 is used, T_2, when v_2, and T_3, when v_3 is the case. When the integrity of the machined surface permits, the curve of maximum wear instead of the line of equal wear should be used (**Figure 26(b)**). As such, the spread in tool life between lower and higher cutting speeds becomes less significant. As a result, a higher productivity rate can be achieved, which is particularly important when high-speed computerized numerical control (CNC) machines are used.

The criteria recommended by ISO 3685:1993 to define the effective tool life for cemented carbides tools:

1. $VB_B = 0.3$ mm, or
2. $VB_B\text{max} = 0.6$ mm, if the flank is irregularly worn, or;
3. $KT = 0.06 + 0.3\,f$, where f is the feed.

1.02.6.1.1.7 Tool Wear Mechanisms

The general mechanisms that generate tool wear are abrasion, diffusion, fatigue and adhesion. The wear is accelerated at higher speeds and the higher temperatures associated with them. The fundamentals of tool wear have been summarized by Shaw (1984) and Trent and Wright (2000).

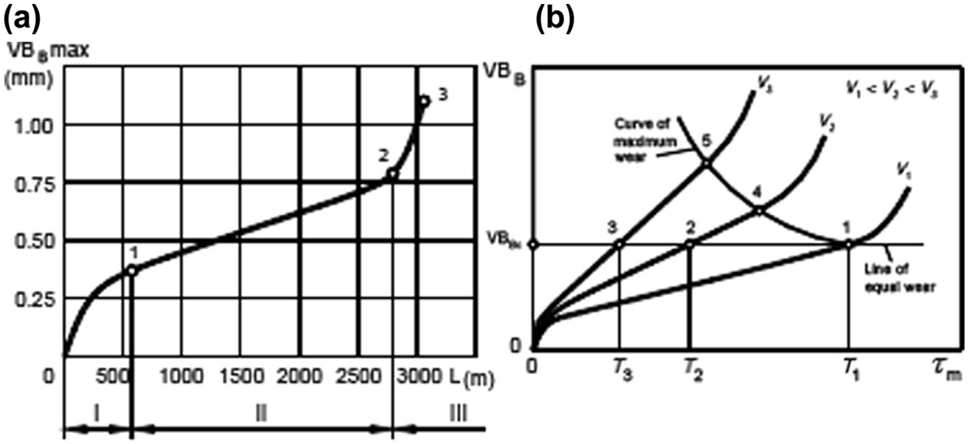

Figure 26 Wear curves (a) normal wear curve, (b) evolution of flank wear land VB_B as a function of cutting time for different cutting speeds.

1.02.6.1.1.8 Tool Life

Tool life is important in machining since considerable time is lost whenever a tool is replaced and reset. Tool life is the time a tool will cut satisfactorily and is expressed as the minutes between changes of the cutting tool. The process of wear and failures of cutting tools increases the surface roughness, and the dimensional accuracy of the workpiece deteriorates.

1.02.6.1.1.9 Expanded Taylor's Tool Life Formula

According to the original Taylor tool life formula, the cutting speed is the only parameter that affects tool life. This is because this formula was obtained using high-carbon and high-speed steels as tool materials. With the further development of carbides and other tool materials, it was found that the cutting feed and the depth of cut are also significant. As a result, the Taylor's tool life formula was modified to accommodate these changes as

$$V_e T^n f^a d^b = C \tag{1}$$

where d is the depth of cut (mm) and f is the feed (mm/rev). The exponents a and b are to be determined experimentally for each combination of the cutting conditions. The order of importance of the parameters is cutting speed, feed, and then depth of cut. Using these parameters, Eqn (1) for the expanded Taylor tool life formula model can be rewritten as

$$T = C^{\frac{1}{n}} V^{\frac{1}{n}} f^{\frac{-a}{n}} d^{\frac{-b}{n}} \quad \text{or} \quad T = C^{5.83} V^{-5.88} f^{-4.53} d^{-2.18} \tag{2}$$

Although cutting speed is the most important cutting parameter in the tool life equation, the cutting feed and the depth of cut can also be the significant factors. Finally, the tool life depends on the tool (material and geometry); the cutting parameters (cutting speed, feed, and depth of cut); the type and conditions of the cutting fluid used; the work material (chemical composition, hardness, strength, toughness, homogeneity and inclusions); the machining operation (turning, drilling, and milling), the machine tool (for example, stiffness, runout and maintenance) and other machining parameters. As a result, it is nearly impossible to develop a universal tool life criterion.

1.02.6.1.1.10 Recent Trends in Tool Life Evaluation

Although Taylor's tool life formula is still in wide use today and lies at the very core of many studies on metal cutting, including at the level of national and international standards, one should remember that it was introduced in 1907 as a generalization of many years of experimental studies conducted in the nineteenth century using work and tool materials and experimental technique available at that time. Since then, each of these three components has undergone dramatic charges. Unfortunately, the validity of the formula has never been verified for these new conditions. The validity of the equations for cemented carbide is discussed in Chapter 1.14 (Mari & Gonseth, 1993). Moreover, one should clearly realize that tool life is not an absolute concept but depends on what is selected as the tool life criteria. In finishing operations, surface integrity and dimensional accuracy are of primary concern, while in roughing operations, the excessive cutting force and chatter are limiting factors. In both applications, material removal rate and chip breaking could be critical factors. These criteria, while important from the operational point of view, have little to do with the physical conditions of the cutting tool.

To analyze the performance of cutting tools on CNC machines, production cells and manufacturing lines, the dimension tool life is understood to be the time period within which the cutting tool assures the required dimensional accuracy and required surface integrity of the machined parts.

Although there are a number of representations of the dimension tool life, three of them are the most adequate (Astakhov, 2006). The dimension wear rate is the rate of shortening of the cutting tip in the direction perpendicular to the machined surface taken within the normal wear period (region II in **Figure 26(a)**), i.e.

$$v_h = \frac{dv_r}{dT} = \frac{h_r - h_{r-i}}{T - T_i} = \frac{v h_{l-r}}{1000} = \frac{v f h_s}{100} (\mu\text{m/min}) \tag{3}$$

where h_r and h_{r-i} are the current and initial radial wear, respectively, T and T_i are the total and initial operating time, respectively, and h_s is the surface wear rate. It follows from Eqn (3) that the dimension wear rate is inversely proportional to the tool life but does not depend on the selected wear criterion (a particular width of the flank wear land, for example).

The surface wear rate is the radial wear per 1000 cm^2 of the machined area (S)

$$h_\mathrm{s} = \frac{\mathrm{d}h_\mathrm{r}}{\mathrm{d}S} = \frac{(h_\mathrm{r} - h_{\mathrm{r-i}})100}{(l - l_\mathrm{i})f}\left(\mu\mathrm{m}/10^3\mathrm{cm}^2\right) \tag{4}$$

where $h_{\mathrm{r-i}}$ and l_i are the initial radial wear and initial length of the tool path, respectively, and l is the total length of the tool path. It follows from Eqn (4) that the surface wear rate is reverse proportional to the overall machined area and, in contrast, does not depend on the selected wear criterion.

The specific dimension tool life is the area of the workpiece machined by the tool per micron of radial wear.

$$T_\mathrm{UD} = \frac{\mathrm{d}S}{\mathrm{d}h_\mathrm{r}} = \frac{1}{h_\mathrm{s}} = \frac{(l - l_\mathrm{i})f}{(h_\mathrm{r} - h_{\mathrm{r-i}})100}\left(10^3\mathrm{cm}^2/\mu\mathrm{m}\right) \tag{5}$$

The surface wear rate and the specific dimension tool life are versatile tool wear characteristics because they allow the comparison of different tool materials for different combinations of the cutting speeds and feeds using different criteria selected for the assessment of tool life.

1.02.6.1.2 Machining Applications

At the advent of the hardmetal age, hardmetal bits were brazed onto steel bodies and ground to the desired shape. Today most inserts are clamped mechanically onto the tool body and have multiple cutting edges shapes and geometries and are termed "throwaway" inserts. The cutting tool bodies are made from hardened steels. In the case of drills, reamers and sometimes gear hobs, the tools can be made of solid carbide, though the tendency here is also to use replaceable carbide heads or inserts to save on hardmetal costs. All insert types and tools are standardized, but each supplier of tools does have some special types to augment their standard tools.

The number of alternate insert products in metal cutting applications cannot be exactly quantified due to the large number of permutations and combinations that are theoretically and practically possible. Some of the parameters that play a critical role are the following:

- Substrate properties (WC grain size and binder content)
- Coating types, coating composition and coating thickness
- Insert geometry
- Geometry of the cutting edge
- Chip breaker geometry
- Tool holder geometry.

Added to this, the workpiece material and geometrical attributes, jigs and fixturing of the workpiece, machining parameters such as feed, speed, depth of cut, coolant type and delivery, machine tool stability (vibrations, elastic deformation under loads), tool holder characteristics (e.g. stiffness, runout, repeatability), and production strategy all have just as much influence on the productivity as the choice of the optimal insert type.

1.02.6.1.3 Machining Trends

The trend in modern machining is toward one of part production lot size, reduced part tolerance, near net shaping capabilities coupled with an increasing number of workpiece materials with enhanced mechanical properties that earn the description "difficult-to-machine".

Whereas mass-produced dedicated inserts are predestined for large production run lots, there is a sizeable demand in general machining applications, that call for a reduction in the complexity of insert choice and insert logistics by engineering "universal inserts" with optimized insert geometry, coating and substrate that could be used for machining a variety of workpiece materials by the proper choice of the cutting parameters like feed, speed and depth of cut. This dedicated "Multimat" universal insert concept was successfully introduced more than a decade ago, e.g. by Lamina Technologies SA and also reported (Prakash, 2010).

This concept foresees just one submicron straight WC–Co carbide substrate for turning applications and one straight WC–Co submicron substrate for milling and drilling applications, with a proprietary nanostructured PVD coating based on the TiAlN family with high hardness, toughness and oxidation resistance coupled with an optimized edge and chip breaker geometry that can handle a wide range of materials like brass, cast iron, stainless steels, nickel based alloys and other exotic materials. The number of insert types required to handle a majority of machining applications is rather limited to about perhaps 100 standard ISO insert styles compared to the thousands of types offered by dedicated insert manufacturers.

The growth in demand of such "universal" inserts for general machining applications is reflected by the fact that many major insert manufacturers like Böhlerit, Ceratizit, Kennametal, Safety, Sandvik, Taegutec amongst others have refined this concept and offer similar types of inserts for turning, milling, drilling, parting, etc. of standard and exotic workpiece materials under dry and wet machining conditions for medium to low chip load applications. This concept of universal types of tools has been also extended to drills and routers (Sandvik Coromant).

1.02.6.1.4 Special Tools

As machining conditions such as machining speed, feed rate, depth of cut, etc. are being driven to even higher benchmarks, the actual machining time is just a fraction of the total machining time for component production time, since tool and component set up times play the lions share in each machining operation using standard tools. This can be combated by the use of tailored, multimachining operation capability of specially engineered complex tools designed to combine many machining operations into a few. Such specialized tooling are offered by many tool suppliers, e.g. Kyocera Unimerco (Figure 28), Walter, Komet, Mapal, Rübig, etc. just to mention a few big players in Europe and a very large number of small specialized tool manufacturers. The higher purchasing price of such special tooling is offset by the possibility of increased productivity as well as the possibility of regrinding and recoating (ReNew) of such "specials" leading to a better utilization of material resources compared to the "once use" and throwaway concept.

As a rule of thumb, the tooling cost makes up only about 3–4% of total machining costs (Figure 29), but proper choice of tools, cutting parameters, machine tools, production engineering concepts, etc. could lead to large cost savings of 40% and more.

1.02.6.1.5 High-Pressure Coolant Supply

As early as 1950, the idea of delivering coolant under high pressure to the cutting region in order to increase tool life during machining was born. The primary objective of this machining technique is to reduce the tool–-workpiece and tool–chip interface temperatures during machining. This can be achieved by directing high-pressure coolant at the chip–tool interface. This can also aid chip breakages and control by chip curl and compressive stress. Flood cooling of the cutting zone should reduce the interface temperatures when machining at lower speeds with significant sliding region and where relatively low cutting temperatures are generated. The coolant also has the function of a lubricant to minimize friction and lower component forces (Figure 30). In addition to the primary function of workpiece cooling, lubrication and chip transport, it also affects the productivity and process reliability. Concepts of high-pressure cooling as well as cyrocooling (using liquid nitrogen or carbon dioxide) have been introduced to improve productivity and process reliability for difficult-to-machine materials. This is reflected in an improvement in chip fracture and longer tool life.

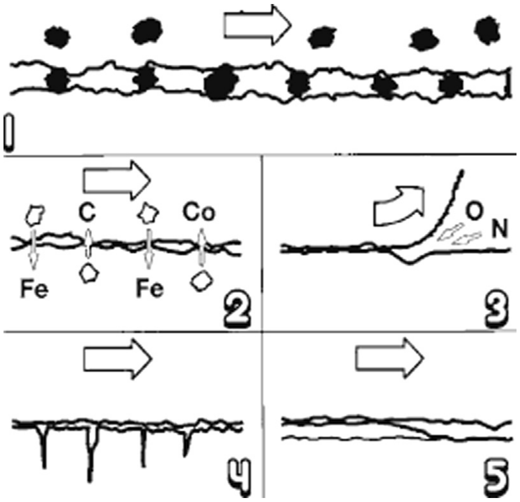

Figure 27 Evolution of the flank wear land VB_B as a function of cutting time for different cutting speeds (Sandvik Coromant, 1995).

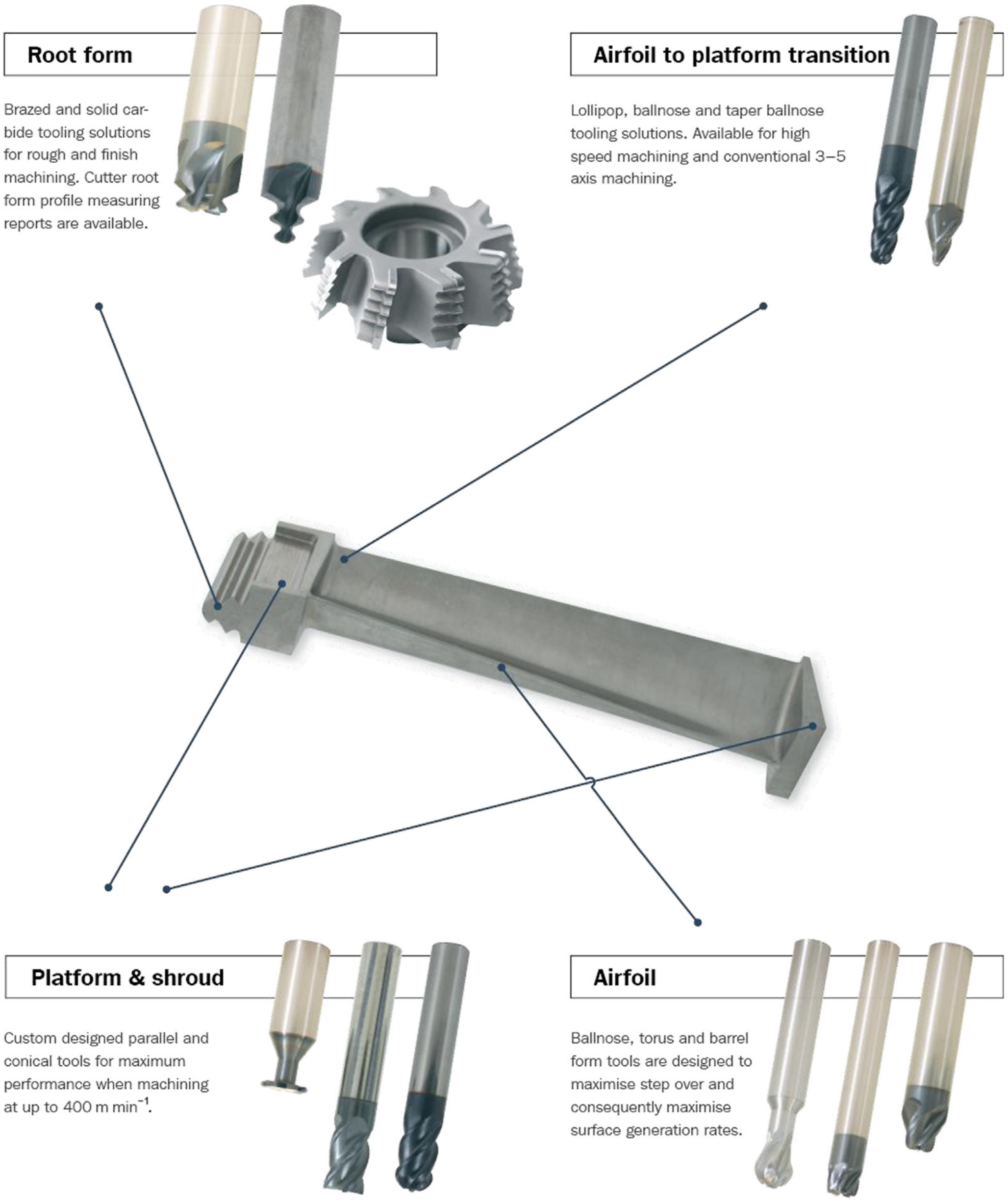

Root form

Brazed and solid carbide tooling solutions for rough and finish machining. Cutter root form profile measuring reports are available.

Airfoil to platform transition

Lollipop, ballnose and taper ballnose tooling solutions. Available for high speed machining and conventional 3–5 axis machining.

Platform & shroud

Custom designed parallel and conical tools for maximum performance when machining at up to 400 m min^{-1}.

Airfoil

Ballnose, torus and barrel form tools are designed to maximise step over and consequently maximise surface generation rates.

Figure 28 Special “Renewable” tools used for the turbine blade machining (Kyocera Unimerco).

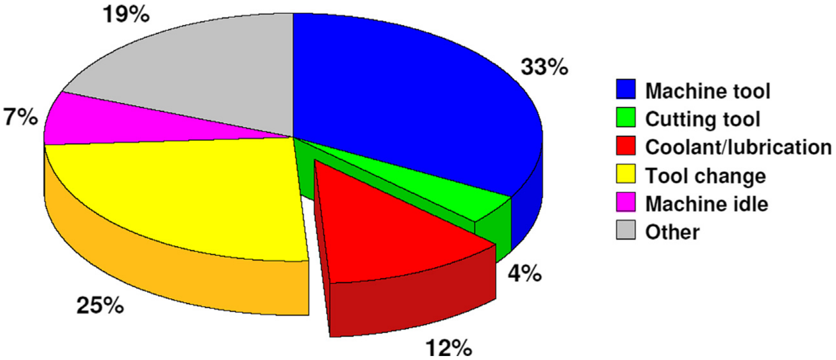

Figure 29 General cost breakdown in machining. www.kyocera-unimerco.com.

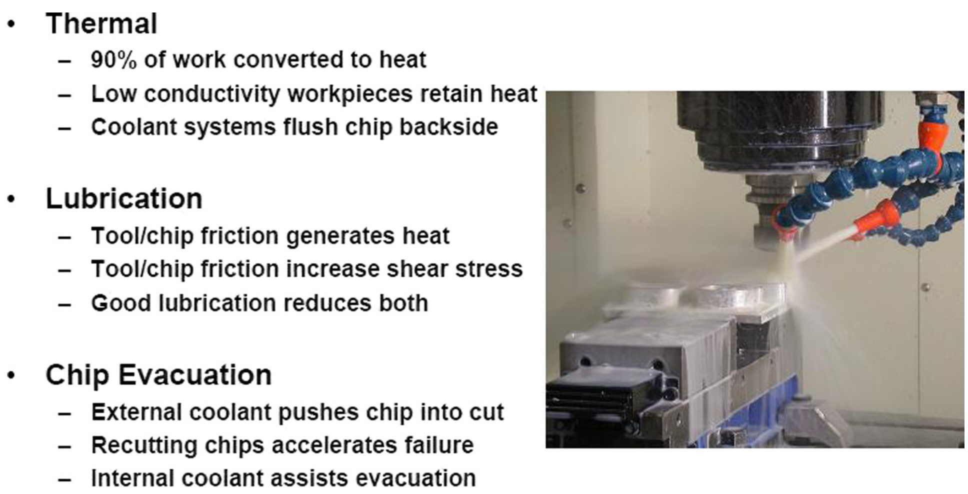

- Thermal
  - 90% of work converted to heat
  - Low conductivity workpieces retain heat
  - Coolant systems flush chip backside
- Lubrication
  - Tool/chip friction generates heat
  - Tool/chip friction increase shear stress
  - Good lubrication reduces both
- Chip Evacuation
  - External coolant pushes chip into cut
  - Recutting chips accelerates failure
  - Internal coolant assists evacuation

Figure 30 Summary influence of COOLANT on metal cutting performance (North, 2011).

1.02.6.1.6 Minimum Quantity Lubricant

In utter disregard to the advantages of machining with coolants, a new technology using no or very little lubricant has established itself in many applications. This has been made possible by tailoring substrates and coatings to withstand high cutting speeds and temperatures.

It is not only cost that drives this new technology but also environmental issues.

A solution to tackle these "costs" is by the use of minimum quantity lubrication (MQL). MQL is also known as near-dry machining. In this process, a controlled amount of focused lubricant mist is delivered to the cutting zone by mixing oil mist with pressurized air. This mixture of oil and air can be sprayed either externally at the cutting edge or through internal coolant holes in the tool similar to conventional lubrication. The oil mist mixture is delivered typically at a pressure of 3–7 bars, the oil consumption is typically 10–100 ml/h. The objectives of the MQL technology are to maintain optimum lubrication at the cutting zone and minimize cutting temperatures.

Other proven advantages are the following:

Improved workpiece surface quality
No recycled chips in coolant
No recycled Si in coolant (aluminum machining)
Protects workpiece from oxidation
Cleaner production
Dry chips and workpiece allow easy cleanup
Environmentally friendly
Usually use vegetable or ester oil which are biodegradable
Improved working environment and reduced health risks
No fungi or bacterial growth found in oil sumps
No dermatitis, respiratory or digestive problems
No odor
No oil hazards on shop floors from dripping workpieces, etc.

The two basic types of MQL systems available today: 1-channel and 2-channel systems are basically differentiated by the location where the oil mist and pressurized air are mixed. The oil aerosol pressure and air pressure are controlled to produce the correct volume of oil in the oil/air mixture (Kyocera Unimerco).

1.02.6.1.7 Modelling and Simulation in Metal cutting

The existence of scatter in metal cutting experiments, it appears, has now been widely accepted and is no longer under discussion. The uncertainty behind work and tool materials properties, working loads, boundary conditions at the tool–chip and tool–workpiece interfaces and other particularities of the machining system is the main reason why two supposedly identical machining operations will yield different results in terms of tool life, quality of the machined part and achievable production rate. This fact is well known and yet, surprisingly, engineers are involved in building very detailed models with the intention of capturing the results of one particular test. It is difficult to understand what exactly is detailed in these models, given the fact that the real world is neither detailed, nor accurate, nor precise. Now, since tests are, for very good physical reasons, nonrepeatable, this race for accuracy is lost from the very beginning.

The results obtained using FEA strongly depend on the experience and judgment of the engineers involved in the analysis of the problem and definition of a simulation model. It should be clear that FEM makes sense if and only if a physically sound and adequate model of the metal cutting process is included at the very foundation of this modelling. Therefore, the construction of such a model, careful selection and justification of the proper boundary conditions and then model validation should be the cornerstone of FEM. The market is over-populated with FE codes and tools for metal cutting simulations, but the issue of model validity is silently set aside. How can one seriously propose to eliminate a physical test with a digital simulation if one cannot say that his model has, say, a 95% level of confidence, or credibility, attached to it? However most modern tools are successfully designed and implemented using C-Technologies, but only after test-bed validation.

1.02.6.1.7.1 Machining Outlook

In the race between work materials and tools, the laurels still go to the tools. The cutting ability of the tool is still slightly ahead of the applications (including available machine tools and their relevant characteristics) because there is a reluctance to apply the available cutting tool technology. However, when one moves to high-speed machining, major changes to the existing machining operation, including fixturing, chucks, guards, programming, coolants and a lot of other housekeeping issues are relevant. Not everyone wants to take the trouble, or spend the money, to do this. In making the ultimate decision, lot size determines to a large extent whether high speed, standard tools, universal tools or special tools are practical (Davim, 2008). The driver for innovation in the tooling sector is to increase productivity and reduce costs whilst conserving resources and decreasing environmental impact, whereas the range of materials as well as the size range of products is continuously rising. New workpiece materials and the continued drive for increased productivity and sustainability of machining will lead to further dynamic improvements.

1.02.6.2 Wear Parts

1.02.6.2.1 Introduction

The unique combination of toughness and wear resistance properties of hardmetals has been dealt with in the chapter on fundamentals. Just as in machining applications, hardmetals can be tailored to meet the individual requirements of a wide range of engineered products that operate under harsh conditions. In almost all applications where the very best solution to an impact, corrosion and wear problem is sought, hardmetals can be found at the forefront of such cases. Hardmetal products help to increase performance, productivity and lifetime and as such help to use all available resources more efficiently. This is the reason that there is an ongoing strong growth in innovations for hardmetal applications to combat wear in such varied industries as agriculture, aerospace, metal, construction, mining, transportation, etc. just to name a few.

The increase in the commercial availability of WC in a wider grain size range from nano (about 0, 2 μm) to extra coarse (up to 40 μm) and the development of binders with higher corrosion resistance have increased the scope of applications of hardmetals as wear parts. Smaller WC grain sizes increase the abrasive wear resistance, whereas coarser grain size is more sought after to increase toughness. The improvements in hardmetal manufacturing processes have also been beneficial, since near-net shape products with improved reliability could be manufactured. This applies to direct shaping processes such as die pressing, cold isostatic pressing, extrusion, injection molding as well as green part machining as an indirect process. Finishing processes such as grinding, lapping, polishing as well as electric discharge machining (EDM) have made great strides in the past decades.

Processes for joining of hardmetal parts to steel substrates—like brazing, adhesive joining, electric resistance welding in casting, etc.—are gaining continued importance since the optimum utilization of the hardmetal and substrate properties can be thus achieved. Computer-based simulation is a strong tool to engineer joint strength not only in mechanical joining (shrink fit) but also in every other joining process as well as in products with gradient structure.

Hardmetal wear parts are made as one off items to items in many millions. The shape and weights of wear parts also vary in many degrees of magnitude. A small hardmetal ball point for a pen weighs a fraction of a gram, whereas a hardmetal roll or a hardmetal plunger could weigh many hundreds of kilograms and could be more than a meter long. The maximum diameter of a commercial hardmetal ring is about 500 mm and the maximum length of a hardmetal blank about 2500 mm.

The criteria for the choice of hardmetal as wear parts could be generalized as the following:

Wear resistance (hardness)
Compressive strength
Fracture toughness
Transverse rupture strength
Fatigue strength
Specific weight
Magnetic properties
Modulus of elasticity, rigidity
Thermal properties
Corrosion resistance
Oxidation resistance
Joinability (mechanical or metallurgical)
Manufacturing capabilities (near-net PM process, grindability, EDM, ECM, etc.).

According to Ceratizit, one of the leading manufacturers of hardmetal wear parts, the following products are termed "wear parts" (nonexclusive). The types of WC used are given in brackets.

Carbide blanks for hobs, slitting knives and circular shear knives (mainly submicron)
Blanks for printed circuit boards (nano to submicron)
Carbide drawing tools (mainly submicron)
Carbide tools for cold forming (mainly medium to coarse)
Carbide tools for cold-heading die nibs (mainly medium to coarse)
Carbide blanks for the die and mold industry (e.g. EDM blanks) (fine to medium)
Knives for paper cutting (mainly submicron)
Carbide blanks for the tool and die industry (submicron to medium)
Carbide blanks for the glass industry (nano to submicron)
Water jet nozzles (nano to submicron)
Carbide rolls (for steel, etc.) (medium to extra coarse)
High-pressure tools (dies and anvils) (submicron to fine)
Carbide engineered parts for automotive industry (nano to fine)
Blanks for ball pens (submicron to fine)
Individual customized engineering blanks (nano to extra coarse).

Examples of industries which use hardmetal wear parts:

(Source: http://www2.hardmaterials.sandvik.com/industry. A click on the links will direct the user to the relevant online detailed information available on the site.)

- Metal
- Food
- Chemical
- Construction
- Agriculture/forestry
- Recycling
- Aerospace
- Automotive
- Medical
- Oil and gas
- Road maintenance
- Iron and steel
- Electronics.

Examples of hardmetal product types and applications:

- Three pieces-can tooling
- Aggregate processing
- Bearing tooling
- Belt scraper cleaner

- Bevel knives
- Brazing tips
- Cold rolls for strips
- Decanter
- Dental burs
- Extrusion dies for ceramic industries
- Fastener die blanks
- Flux-cored wire tooling
- Homogenizers
- Knives for pellets
- Lock blocks
- Pin for milling
- Pin for security lock
- Plastic pelletizing
- Rail clip forming
- Recycling waste
- Scraper
- Seats and ball joint
- Solid carbide hobs
- Solid carbide roller
- Solid carbide slipper
- Stamping tool blanks
- Thin discs
- Tile parts
- Tips
- Tool blanks
- Welding electrodes tooling

The following table shows as an example the wide range of typical hardmetal compositions that are used for wear parts (Ceratizit) (**Figure 31**). This can only be a sampling since the number of application-defined grades offered by various manufacturers is too specialized to be dealt with in this introductory chapter(**Table 13**).

1.02.6.2.2 Applications by Grain size

The choice of a hardmetal grade for an application is governed by its physical, mechanical and chemical properties at ambient and at operating temperatures.

Wear resistance, toughness, corrosion and oxidation resistance and shaping capability are main criteria for the choice of a suitable grade. These properties can be tailored by choosing the appropriate WC grain size, the binder content and the binder type. There is more than just one solution to choose from. Presented here are illustrative examples of appropriate hardmetal choices prevalent in the general industry in Europe in particular. An arbitrary attempt has been made, however feeble it may be, to classify the application of hardmetals based on WC grain size. As will be seen, there are several WC grain sizes that are suitable for any one application.

1. NANO, submicron and fine-grained hardmetals
    a. Wood machining
    b. Electronic industry
    c. Dental and medical applications
    d. Food industry
    e. Water jet nozzles
    f. Circular shearing and cutting blades
    g. Hardmetal blanks for precision tools.
2. Medium- to coarse-grained hardmetals
    a. Stone and masonry tools
    b. Road planning and mining
    c. Rolls
    d. General.

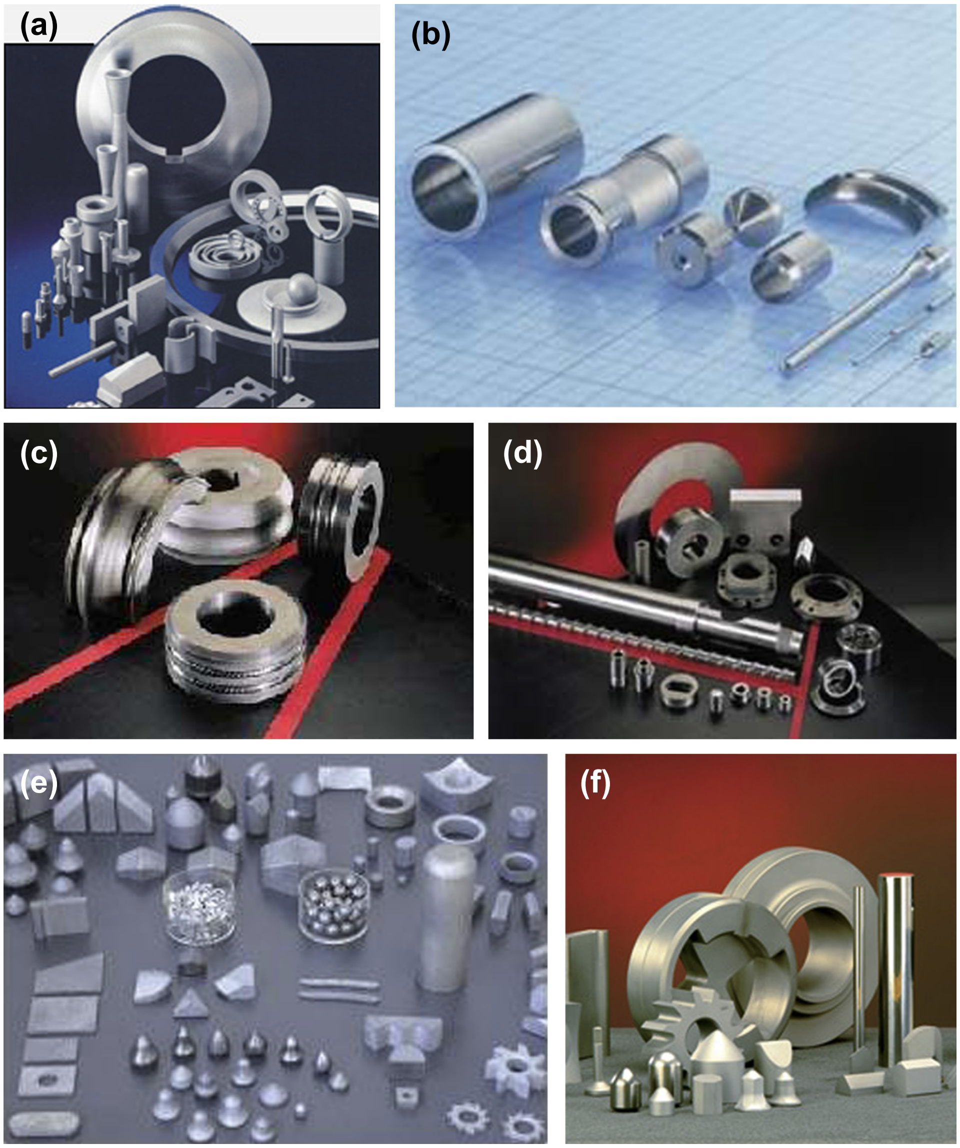

Figure 31 Some examples of typical hardmetal wear parts: (a) Max. part size about 400 mm diameter (www.broda-hartmetall.de). (b) Small parts (min. size 1 mm) precision ground with tight tolerances (www.broda-hartmetall.de). (c) Rolls for the steel industry (www.saar-hartmetall.de/english/produkte/produkte.html). (d) Cold heading tools (cores, dies), drawing tools (jacks, cutting rings, deep drawing and extrusion tools), bordering and shaping tools, cylinders and extrusion screws made of tungsten carbide for the plastic industry, hot cutting tools for roll mills, pressing rings and pressing molds for the manufacture of diamond grinding wheels, and cutting disks and shaping tools for the glass industry. (e) Products from Betek for road planing and construction industry as well as agricultural wear parts (www.betek.de). (f) Element Six wear parts (www.e6.com).

1.02.6.2.2.1 Wood Machining

WC-tipped tools were introduced to the woodworking industry in the early 1950s. Circular saw blades, milling cutters and routers account for the main share of carbide usage in this industry. Figures 32–34 show some typical tools for woodworking. The cutting speed in industrial wood machining ranges from 30 to 100 m s^{-1}, the feed being 1–2 mm per tooth. The cutting forces are comparatively low, but due to the inhomogeneous structure of natural wood, the tools are subjected to high impact forces during the intermittent machining of the wood. Toughness is of utmost priority, not only due to the impact forces but also due to the high centrifugal forces during the high-speed machining. Man-made woods, such as chipboard, contain a large amount of inorganic matter. This, combined with the decorative plastic laminates on

Table 13 Overview of hardmetal grades for wear parts (www.ceratizit.com)

CT grade code	*ISO K*	*Application range*	*Binder (%)*	*HV10*	*HRA*	*TRS (MPa)*
Medium to coarse grain size						
CTM12	K20	G10	6	1520	91.1	2200
CTM14	K25	G10	7	1550	91.4	2600
CTM17	K30–K40	G15	8.5	1420	90.4	2800
CTC12	K30	G10–G20	6	1350	89.9	2800
CTC20	K40	G20–G30	10	1170	88.2	3000
CTC25	>K40	G20–G30	12.5	1080	87.2	3100
CTC30	–	G30–G40	15	1020	86.5	3150
CTC35	–	G40–G50	17.5	950	85.6	3200
CTC40	–	G40–G50	20	900	84.9	3200
CTC50	–	>G50	25	810	83.5	3200
CTC60	–	>G50	30	730	82.2	3200
Fine grain size						
CTF08	K05–K10	G01	4	1850	93.2	2100
CTF11	K10	G05	5.5	1760	92.7	2300
CTF12	K20	G10	6	1630	91.9	2300
CTF18	K30	G15	9	1490	91.1	2800
CTF24	K40	G20	12	1350	89.8	3000
CTF30	>K40	G30	15	1240	88.8	3100
CTF40	–	G40	20	1050	86.7	3400
CTF50	–	G50	25	950	85.4	3400
CTF54	–	>G50	27	920	85	3200
Submicron grain size						
CTS06	K01	–	3.3	2020	93.9	3300
CTS10	K05	–	4.8	1980	93.8	3300
CTS12	K05–K10	–	6	1850	93.3	3500
CTS15	K10–K30	–	7.5	1740	92.6	3600
CTS20	K20–K40	–	10	1650	92.1	3700
CTS24	K40	–	12	1490	90.9	4000
CTS30	>K40	–	15	1330	89.7	3800
Ultrafine grain size						
CTU05	<K01	–	2.4	2300	94.8	3500
CTU13	–	–	6.5	2050	94.1	3800
CTU16	–	–	8	1940	93.6	4300
CTU24	–	–	12	1760	92.7	4500
CTU30	–	–	15	1590	91.7	3900
CTU44	–	–	22	1300	89.4	4000
CTU40S	–	–	20(FeCoNi)	1250	88.9	3500

CT grade code	*ISO K*	*Application range*	*Binder (%)*	*HV10*	*HRA*	*TRS (MPa)*	*Grain size*
Corrosion resistant grades							
CTU05R	–	–	2.5(NiCr)	2350	95	2000	Ultrafine
CTU06M	–	–	2.8(CoNiCr)	2150	94.5	2500	Ultrafine
CTS06M	–	–	3.0(CoNiCr)	1950	93.6	2300	Submicron
CTU12R	–	–	6.0(NiCr)	1750	92.6	2600	Ultrafine
CTU17R	–	–	8.5(NiCr)	1760	92.7	2500	Ultrafine
CTS17R	–	–	8.5(NiCr)	1600	91.7	2800	Submicron
CTF16R	–	–	8.0(NiCr)	1480	90.8	2900	Fine
CTM16N	–	–	8.0(Ni)	1300	89.4	2400	Medium
CTC20M	–	–	10.0(CoNiCr)	1100	87.3	2600	Coarse
CTC30M	–	–	15.0(CoNiCr)	970	85.6	2700	Medium
CTC40M	–	–	20.0(CoNiCr)	850	84	2800	Coarse
CTC60M	–	–	30.0(CoNiCr)	650	80.9	2700	Coarse

CT grade code	*Density*	*Binder (%)*	*HV10*	*HRA*	*TRS (MPa)*	*Grain size*
Cermet grades						
CTF28T	6.4	14.0(CoNi)	1550	91.4	2400	Fine
CTF36T	5.9	18(Ni)	1470	90.8	1800	Fine

Figure 32 Saw blade for wood cutting. Type multirip (www.kyocera-unimerco.com).

Figure 33 Special tool combining edge and ornamental operations into one tool in order to minimize number of tool changes and increase output (www.kyocera-unimerco.com).

Figure 34 Window tooling cutter (www.kyocera-unimerco.com).

chipboards, causes severe abrasive wear of the tools. Resins and glues are a prime source of corrosion of the binder phase. In addition to the material properties, toughness and abrasive wear resistance, the cutting tools must have a sharp cutting edge to produce a product with a good surface finish. In the light of these requirements, nano to submicron cemented carbides are ideal candidates for this application. A range of different alloys have been developed for various woodworking applications with binder contents between 2 and 20 wt% have been developed and their nominal properties as shown in Table 14. The alloys with a fine grain size and a low binder content are used to machine laminated chipboard and medium density fiberboard. The wear of a milling cutter carbide blade is to be seen in Figures 35(a–c). The initial sharp cutting edge is rounded and carbide, as well as cobalt, is being abraded during machining. Figure 35(c) clearly shows that large carbide grains tend to fracture during use and this leads to a poor surface integrity of the finished product. By a proper combination of carbide grain size, binder content and processing parameters to prevent coarse grain growth, nanograined cemented carbides with a hardness above 2000 HV10 are being used, that on average have a 30% higher wear resistance than standard grades. This applies not only for milling cutters but also for saw teeth for circular saws.

Submicron cemented carbide is also being successfully used to machine complicated profiles in natural wood, where it has been replacing stellites and high-speed steels. In this case, a binder content of around 10 wt% and a hardness level of 1600 HV10 has led to optimal tool life, the tool life criterion being chipping, and not wear, as the primary factor.

Corrosion is also encountered during wood machining and modern standard hardmetal grades are now to be found with a corrosion-resistant nickel–cobalt–chromium binder. An iron-based binder is especially favorable in cutting wet woods.

Table 14 Example of the wide range of hardmetals used in wood cutting (www.ceratizit.com)

Grade	*ISO Code*	*USA Code*	*Binder (%)*	*Density (g/cm^3)*	*Hardness (HV10)*	*TRS (MPa)*
Nano grade						
UMG04			2.0	15.30	2550	3200
Ultrafine grade						
SMG02			2.4	15.25	2300	3500
Grades containing chromium in the binder						
CTU05-KC			2.8	15.20	2250	2200
KCR05			2.8	15.20	2150	2500
KCR06			3.0	15.25	1950	2300
KCR08			3.2	15.20	1920	2300
CTE30M			15.0	14.10	960	2700
Submicron grades						
MG06	K01	C4	3.3	15.20	2020	3300
MG18	K20	C2	10	14.45	1680	3700
Grades with cobalt binder						
HC03	K01	C4	4.0	15.15	1840	2200
HC05	K10	C3	4.0	15.15	1730	2100
HC10	K10	C3	5.6	15.00	1760	2300
HC20	K20	C2	6.0	14.95	1640	2300
HC25	K20	C2	7.0	14.90	1550	2600
HC30	K30	C1	8.5	14.65	1420	3000
HC35	K30	C1	9.0	14.60	1400	2800
HC40	K40		12.0	14.30	1330	3200
GC32	>K40		10.0	14.55	1170	3000
GC40	>K40		15.0	14.05	990	3150
Grade with FeCoNi binder						
HE40	>K40		20.0	13.15	1250	3500

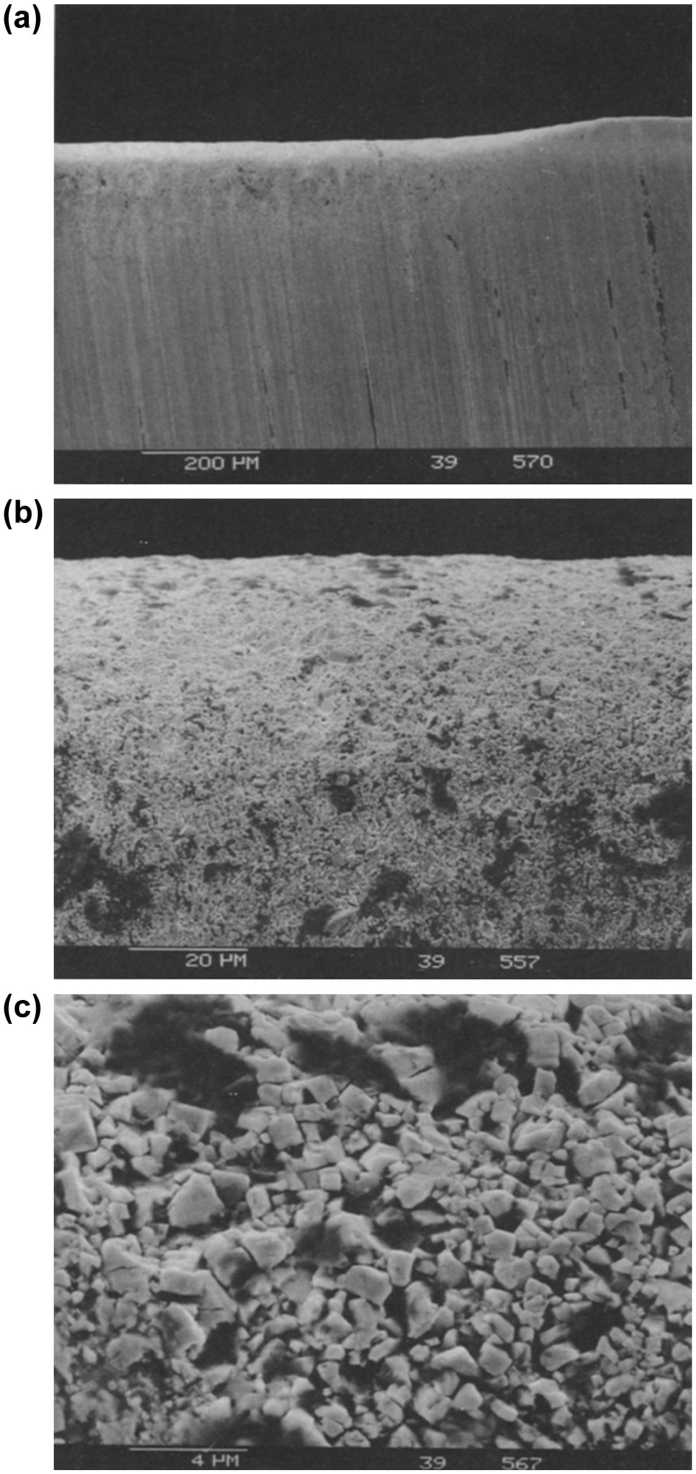

Figure 35 (a–c) Worn cutting edge of a hardmetal planar knife after machining chipboard (Prakash, 1995).

Grade	*Soft wood*	*Hard wood*	*Chipboard*	*MDF*	*HDF*
UMG04			++	+++	++++
SMG02			+++	++++	+++
KCR08	+++	++++	+++	+++	+++
MG06		+++	++++	++	++
MG18	+++	+++	++	+	
HC05	++	++	++	++	++
HC20	+	++			
HC35	++	+			
HE40	++++				

General application chart for Hardmetals in wood machining (Ceratizit)
Legend:

	Not suitable
+	Acceptable
++	Good
+++	Very good
++++	Optimal

1.02.6.2.2.2 Tools for the Electronic Industry

Every printed circuit board contains a large number of holes that have been mechanically drilled using carbide tools. Routers used for sizing or shaping of the boards are also carbide tipped. As in any other machining operation, it is just not the tool material alone that determines the productivity of the process. Whereas before 1990, a drill tool of around 1000 holes at a cutting speed of 20,000 rpm and a tool diameter of 1 mm was considered standard, today's tools have an average diameter of below 0·4 mm, are used at above 100,000 rpm and have a tool life of up to 10,000 holes. One of the major factors that have made this productivity surge possible is truly submicron cemented WC alloys with a homogeneous structure and a high reliability factor. Today's top notch pcb microdrills use a submicron carbide with an average grain size of $<0{\cdot}5\ \mu\text{m}$ and a cobalt content of around 8 wt%. The transverse rupture strength requirements are above $3500\ \text{N mm}^{-2}$ and the hardness level often exceeds 2000 HV10.

Figure 36 shows an example of a pcb drill and a router; the wear on the cutting edge of a drill is shown in **Figure 37(a–c)**. However, it is not primarily wear that is of utmost importance but chipping of the cutting

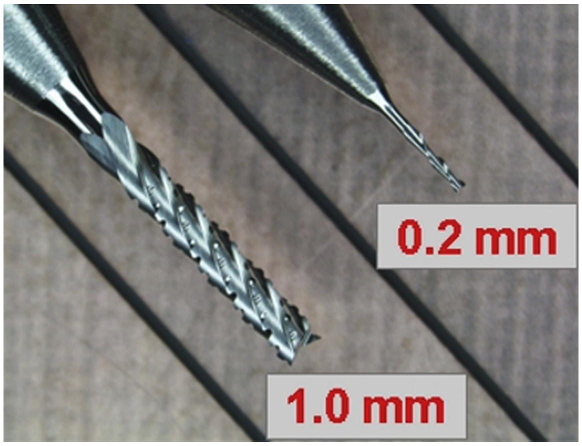

Figure 36 A typical router and a typical drill for machining printed circuit boards (Hptec).

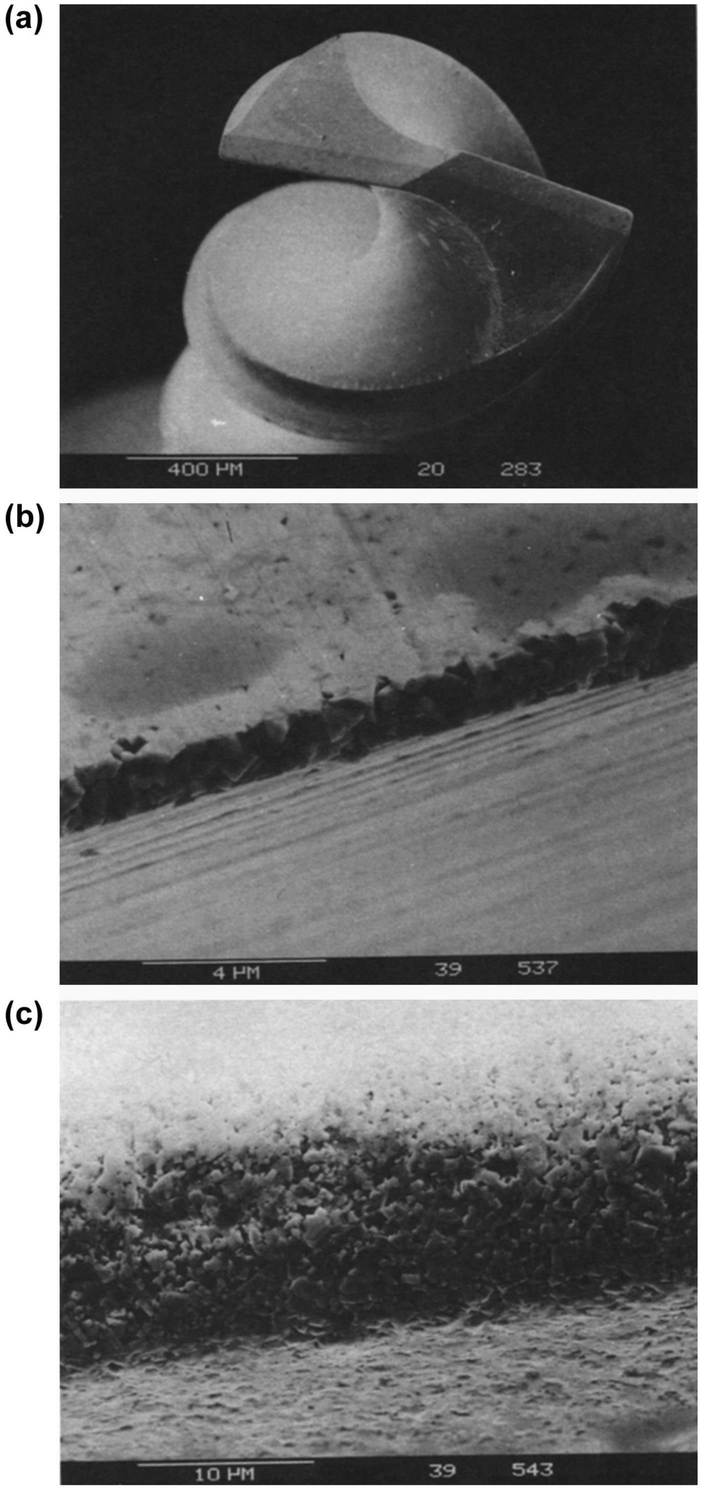

Figure 37 (a–c) PCB drill: (a) overview, (b) middle new cutting lip, and (c) bottom worn cutting lip (Prakash, 1995).

Table 15 Miniaturization of pcb drill sizes in the last decades (Hptec)

Region *Year*	*Asia* *Main diameter (large production quantities)*	*Europe* *Main diameter (large production quantities*	*World* *Min. diameter*
1995	0.5	0.5	0.15
1996	0.4	0.4	0.15
1997	0.35	0.35	0.15
1998	0.35	0.35	0.1
1999	0.3	0.3	0.1
2000	0.3	0.3	0.1
2001	0.3	0.3	0.1
2002	0.3	0.3	0.09
2003	0.25	0.25	0.09
2004	0.2	0.2	0.09
2005	0.2	0.3	0.075
2006	0.2	0.3	0.075
2007	0.15	0.3	0.075
2008	0.15	0.3	0.075
2009	0.12	0.3	0.05
2010	0.105	0.3	0.05
2011	0.105	0.3	0.03
2012	0.105	0.3	0.03
2013	0.105	0.3	0.03

tool edges in today's automated multispindled drilling machines. Chipping and wear greatly influence the quality of the drilled hole surface. Irregularities enhance premature failure of the brazed electrical contact surfaces, which means that the reliability factor is greatly reduced. Other tools in the electronic industry using fine-grained carbides are punches and dies for the boards as well as circular lead cutter knives.

The use of the tools for the electronic industries is still growing, mainly in Asia and there is no abatement in the requirements for miniaturization dictated by consumer and industry demand (Table 15).

1.02.6.2.2.3 Dental and Medical Applications

Most of the modern drilling and shaping tools used by the dentists are carbide tipped. Some examples of such tools can be seen in Figure 38. Fine-grained cemented carbide is preferred as the tool material due to its high wear resistance and toughness characteristics. The preferable alloy contains approximately 10% cobalt as the binder. Since the dentist drills are precision instruments, absolute reliability of the tools is a must. The delicate

Figure 38 Examples of carbide-tipped dentists tools (HAM).

Table 16 FDA-approved hardmetal grades for the food industry. Grade selection is dependent on the pH value of the food (Ceratizit)

pH value	*Grade*	*Composition*	*Grain size classification*	*Binder (%)*	*Density ($g\ cm^{-3}$)*	*Hardness (HV10)*	*TRS (MPa)*	*Toughness ($MPa\ m^{0.5}$)*
>2	CTF00Q	WC–(TiTaNb)C	Fine	5.60	14.40	1900	1600	6.6
>3	CTU05R	WC–Ni	Ultrafine	2.2	15.20	2350	2000	–
	CTF16R	WC–Ni	Fine	8.0	14.80	1480	2900	11.4
	CTM16N	WC–Ni	Medium	8.0	14.85	1300	2400	10.5
	CTS17R	WC–Ni	Submicron	8.5	14.55	1600	2800	8.7
	CTU17R	WC–Ni	Ultrafine	8.5	14.55	1760	2500	8.0
	CTF21N	WC–Ni	Fine	10.5	14.50	1280	2600	11.9
>4	CTS12D	WC–Co	Submicron	6.0	14.80	1820	3500	8.2
	CTS20L	WC–Co	Submicron	10.0	14.45	1680	3700	9.4
>7		WC–Co	Fine	5.6	14.95	1760	2150	9.2
		WC–Co	Fine	6.0	14.95	1640	2200	9.9
		WC–Co	Fine	6.0	14.90	1730	2500	9.0
		WC–Co	Fine	12.0	14.30	1330	3000	12.0
		WC–Co	Coarse	15.0	14.05	1020	3150	17.3

and sharp cutting edges must possess adequate wear resistance and toughness to prevent wear, as well as chipping, in order to keep cutting forces low and minimize heat generation. Cutting forces are of the order of 0.5–2 N and the tool speed is 2000–250,000 rpm. Submicron cemented carbides with a binder content of about 10% and a hardness of around 1600 HV10 are best suited for this application.

As medical technology moves forward and the population matures, the possibilities for replacing teeth with implants as well as advanced surgical techniques allow for replacement or mending of worn bone structures in our bodies. Special tools are required for this purpose to machine bone structures as well as implants of titanium, cobalt base alloys, etc. Most of these precision tools are carbide tipped.

1.02.6.2.2.4 Food Industry

The soft stainless steel tools used in the food industry are being replaced mainly by nickel-bonded highly wear-resistant hardmetal grades for choppers, cutters, knives, etc. The following table is an example of FDA-approved hardmetal grades for the food industry (**Table 16**).

1.02.6.2.2.5 Water Jet Nozzles

High-pressure (up to 6200 bar) water jet cutting is a well-established process in aerospace, automotive, medical, electrical, packaging and general sheet metal and general mechanical industries (**Figure 39**). Profile machining of green hardmetal blanks prior to sintering is also "state of the art". During this clean and contamination-free process, there is no thermal energy input involved. Virtually all materials to a thickness up to about 150 mm can be cut—metals, ceramics, composites, plastics, leather and even food.

The requirement on the nozzle material is high abrasion, erosion and corrosion resistance, which is best met with low binder nanostructured hardmetals with sufficient strength as shown in **Table 17**.

1.02.6.2.2.6 Circular Shearing and Cutting Blades

Submicron hardmetal is also used to manufacture circular shearing blades, as used in the paper, plastics as well as the magnetic tape industry. Whereas steel blades used in the paper industry had to be replaced every couple of weeks, the tool life of carbide blades could be up to a year between regrinds. Other productivity gains are better edge quality of the cut surfaces (less roughness and less dust) and higher cutting speeds.

Magnetic tape cutting causes much more abrasive wear than paper on cemented carbide. When high-speed steel blades were first replaced by cemented carbide in the late 1970s, medium-grained WC (grain size 1–2 μm) was used. The tool life between regrinds was around 100 km of audio tape. With the advent of video tape, the demands on the edge quality of the tape became very stringent and improvements in the magnetic media led to more wear of the slitter blades. Through the use of submicron cemented carbide and optimal grinding conditions, slitter blades with a reliable sharp edge free of chipping could be produced. Tool life between regrinds is

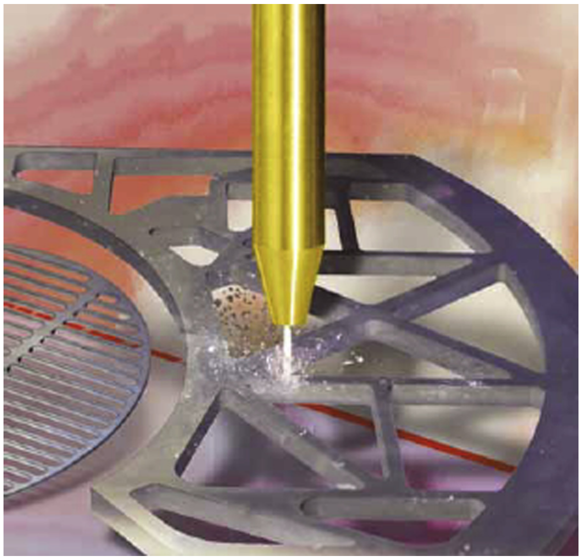

Figure 39 Example of a water jet cutting nozzle (Ceratizit).

Table 17 Hardmetal characteristics for water jet cutting nozzles (Ceratizit)

Grades	*Binder (wt%)*	*Density (g cm^{-3})*	*Hardness (HV10)*	*TRS (MPa)*	*WC designation*
Ultramant 2000	0.4	15.55	2675	2400	Nano
Ultramant 3000	0.5	15.60	2825	2000	Nano

in excess of 400 km. Figure 40 shows the wear of a submicron carbide slitter knife. The cutting edge is still intact in spite of the wear on the radial and flank surfaces. Due to less wear, regrinding stock removal has been minimized.

The reduced demand for audio–video tapes has however been more than offset by demands for cutting plastic, paper and metallic thin foils.

Products used in the paper industry are guillotine knives, cross-cutters, corrugated board cutters, top and bottom knives.

In the plastics industry, hardmetal knives are used for shredding and recycling, for machines and mills. Roll shear knives are used in the sheet metals industry (Figure 41).

Compared to standard steel knives, the life of a hardmetal knife could be 10 times longer. Hardmetal knives are also used in machines with table knives, truncheons, pressing and profile scissors, scrap cutting knives and as tools for chamfering presses (Schoenenberger).

Table 18 Grade recommendations for slitting knives (Ceratizit)

Submicron grades	
6% binder	Machining of nonferrous metals, aluminum alloys, carbon fiber-reinforced plastics, artificial carbon, graphite, cast irons of low and medium hardness, chilled castings hardened steels.
7.5% binder	For machining gray cast iron, tempered iron, nonalloyed steels, super alloys, titanium and tantalum alloys, copper, graphite, aluminum, heat-resistant steels, plastics
10% binder	Machining of corrosion, acid and heat resistant steels, chromium alloyed steels, nickel and cobalt alloyed steels, titanium alloys, nonferrous metals, plastics
12% binder	High toughness grade for unfavorable machining conditions
Fine-grained grades	
6–7% binder	For machining gray cast iron, tempered iron, nonalloyed steels, super alloys, titanium and tantalum alloys, copper, graphite, aluminum, heat-resistant steels, plastics
10–12% binder	Cutting paper, cardboard and plastics

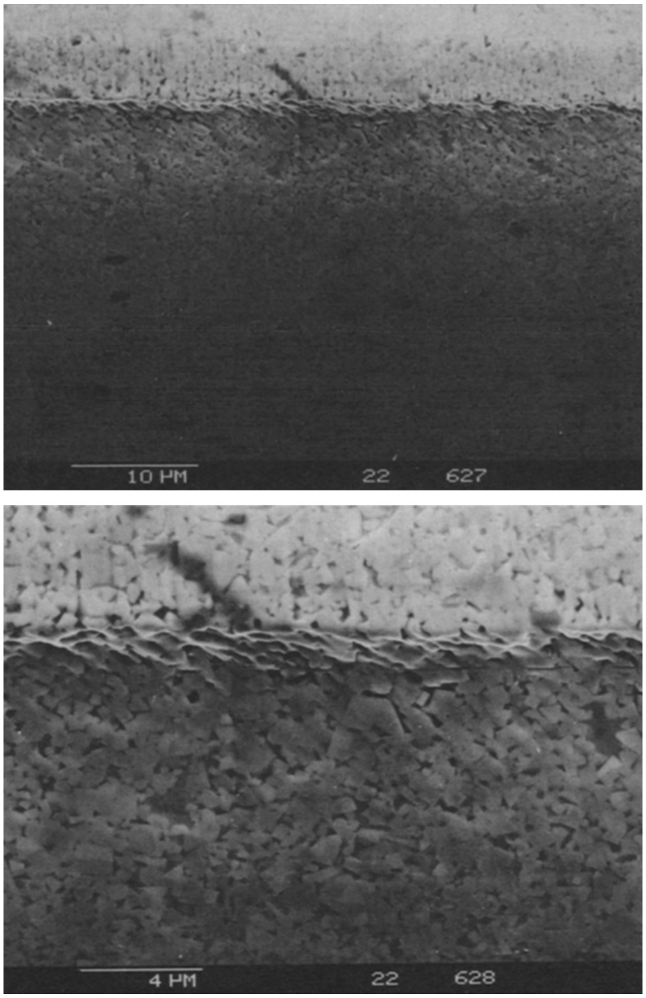

Figure 40 Wear scar of a hardmetal circular knife after cutting magnetic tape (Prakash, 1995).

The optimum carbide choice depends on the application parameters, the type of coatings used and first and foremost the geometry of the tool (**Table 18**).

1.02.6.2.2.7 Hardmetal Blanks for Precision Tools

Hardmetal blanks in small to large numbers are required for manufacturing tools and dies for many standard and specialized applications. Round rods, with and without coolant holes, flat profiles, strips, blocks and shaped parts are used in many industries and applications. Reduction in grinding costs and materials usage can be achieved by soft machining of the blanks before final sintering. In applications involving machining, mainly submicron and fine-grained carbides are materials of choice, the binder content rarely exceeds 10%. The hardness range for such hardmetals is between 1550 and 2300 HV10 (**Figure 42**).

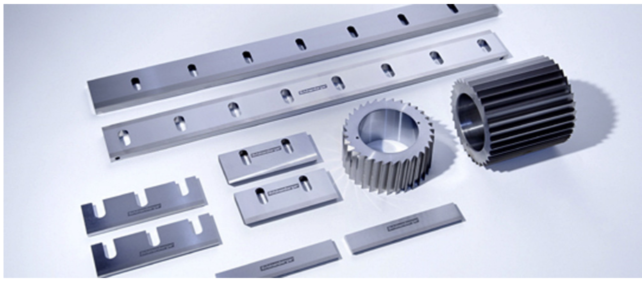

Figure 41 Knives for the plastics industry (Schoenenberger).

Figure 42 Blanks for precision tools (Ceratizit).

1.02.6.2.2.8 Chipless Forming, Blanking and Piercing Tools

1.02.6.2.2.8.1 Cold Forming

Today's cold forming technology is a materials saving, near-net process used to make products at the rate of tens to hundreds per minute. The tool sets cost anywhere between €5000 and 25,000 depending on the part complexity and hardmetal is the tool material of choice for many applications. High impact strength and wear resistance are mandatory for the tool materials used (Figure 43).

Selection of carbide grades depends upon the size of the dies and the severity of their application. Grades having high cobalt contents (9–13%) are often preferable for cold-drawing dies. These grades can withstand greater stock reductions per pass without breaking than can grades having low cobalt contents. For optimum performance and maximum wear resistance, however, it is generally preferable to use grades with low cobalt contents (6–9%) for small-sized dies. Good results, in respect to reduced wear and longer life, are being obtained for some applications by coating carbide dies with titanium nitride (SME).

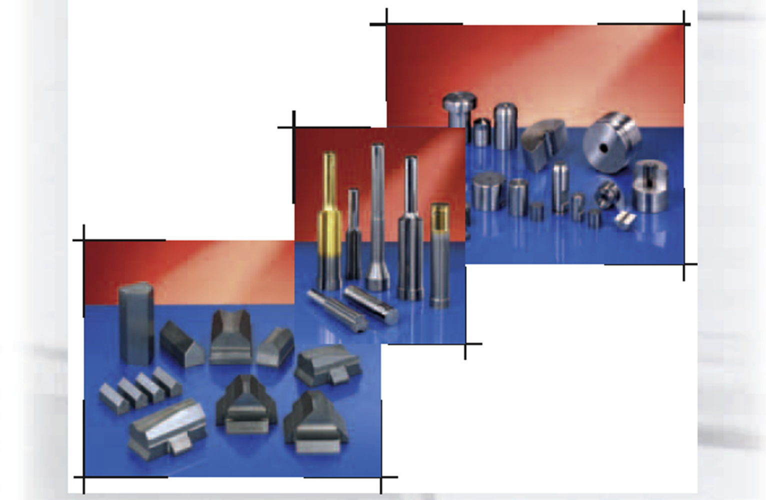

Figure 43 Examples of cold forming tools (Ceratizit).

Figure 44 Drawing dies—for tubing, profiles, rods and wire, e.g. nibs, plugs, drawing jaws, drawing mandrels, straightening tools, infeed tools, peeling inserts for welded seams (Durit).

1.02.6.2.2.8.2 Drawing Dies for Tube, Bar and Special Profiles and Mandrels

Tool steel for machine tools, copper profiles for special cables and motor collectors as well as brass for industrial or decorative uses as well as precious metals are shaped by drawing (Ceratizit) (**Figure 44**).

1.02.6.2.2.8.3 Carbide Grades for Cold Forming

The binder composition of the hardmetals range from 5 to 25% with submicron, fine and medium grain-sized carbides being used. The hardness range lies between 850 HV10 and 1940 HV10.

1.02.6.2.2.8.4 Drawing Dies for Wire

The search for better wire drawing tool materials for tungsten wire for electrical lamps led to the invention of hardmetal about 90 years ago. Wire drawing dies are thus the cradle of hardmetals and are still used in many applications including electrical wiring, cables, springs, paper clips, wheel spokes, strings for musical instruments, steel cord for tyres as well as all other high-tensile strength wires at drawing speeds ranging from 10 m s^{-1} for ferrous materials to 30 m s^{-1} for nonferrous materials (**Figure 45**).

Hardmetals with a submicron or fine carbide grain size and a binder content between 5 and 9% are common in these applications.

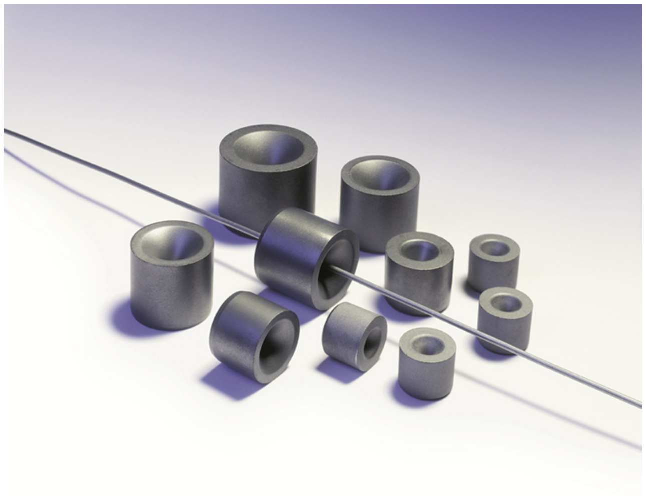

Figure 45 Examples of hardmetal wire drawing dies (Sandvik Hard Materials).

Figure 46 Tool and die blanking (Ceratizit).

1.02.6.2.2.9 Tool and Die Industry

1.02.6.2.2.9.1 Sheet Metal Blanking and Forming

Metal stamping is an indispensable part of the contemporary industrialized manufacturing. An examination of most machines and products would disclose metal stampings in the assembly. Currently, stampings are widely used in machines, tools, vehicles of all kinds, household appliances, hardware, office equipment, electrical and electronic equipment, containers, buildings, clothing, and most manufactured products (SME) (**Figure 46**) (**Table 19**).

As a rule of thumb, the binder content should be as low as possible (to reduce adhesion and corrosion) and the grain size as large as possible (to increase fracture toughness and stabilize the cutting edge).

The widespread use of wire EDM in water-based electrolytes to produce hardmetal blanking tools and dies has called for improving the corrosion resistance of the die blanks. Corrosion-resistant grades are now offered by all major hardmetal manufacturers. The enhanced corrosion resistance is achieved by many proprietary developments; one common method is to alloy the cobalt binder with chromium to reduce binder leaching during processing.

1.02.6.2.2.9.2 Powder Metallurgy Tooling

Most dies and punches used for compaction in the powder metallurgy industry, especially in the hardmetals industry, are themselves made using hardmetals, for long production lot runs. Nonmagnetic nickel-bonded hardmetal dies are used when pm magnets with a special orientation need to be pressed. **Figure 47** shows some typical examples of pm tooling.

The hardmetals used in these applications need a high wear resistance as well as sufficient bulk and edge toughness. Submicron to medium grain-sized hardmetals are chosen here.

The high stiffness of hardmetals is an added advantage for precision part production.

1.02.6.2.2.10 Automotive Wear Parts

Reliable fuel injectors are decisive for emission levels and consumption of diesel engines. Three carbide components for next-generation injectors are lever, bell and pin. In the injection nozzle, these components ensure precise and consistent direct injection of the diesel.

Table 19 Hardmetal grades for the tool and die industry—composition and properties (Ceratizit)

Code ISO K	*Application field*	*Binder content (%)*	*Hardness (HV10)*	*Hardness (HRa)*	*TRS (MPa)*	*Fracture toughness (MPa m$^{-0.5}$)*
Corrosion-resistant fine/medium grades						
K20–K30		8.5	1640	92.1	2600	10.1
K40	C11/C12	12	1400	90.3	3000	12.0
Ultrafine grades						
		8.0	1930	93.7	4000	7.5
K10–K20	C3	12.0	1970	92.4	4600	7.8
Submicron grades						
K10–K20	C3	7.5	1780	92.8	3600	8.6
K20–K40	C2	10.0	1660	92.2	3700	9.4
K40	C1/C10	12.0	1540	91.4	4000	9.9
>K40		15.0	1410	90.4	3800	11.9
Fine/medium grades						
K20	C2	6.0	1660	92.2	2200	9.9
K30	C1	9.0	1450	90.6	2800	10.9
K40	C11/C12	12.0	1330	89.7	3000	12.0
>K40	C13	15.0	1230	88.6	3100	13.1
Coarse grades						
		12.5	1070	86.6	3050	16.3
Nonmagnetic grades						
		8.5	1580			8.7

The requirements regarding such components are particularly high in the automotive industry. The blank must have a high surface quality, low tolerances are required and it is essential that ruptures do not occur. In order to achieve this, the three components are provided with a special coating which makes them particularly hard and wear resistant. At the same time, they have a very high elastic modulus and deform only slightly when exposed to high pressure. Thanks to the high-performance carbide components, the highest current standards such as EURO 6 can be met (Ceratizit, Impact 12/13).

Other automotive applications of hardmetals are valve seats, fuel pump rollers, cam rollers, roller bearings, engine valves, solenoid valve, seats inserts, injector levers, axes, valve pistons, and polygon.

1.02.6.2.2.11 Wear Parts Oil Industry

Hardmetals used in the oil and gas industry could vary from submicron grain sizes to coarse, the binder content from 3 to 30% depending on the particular application (**Figure 48**), (North, 2011). In addition to the cobalt

Figure 47 Tools for powder compaction (Durit).

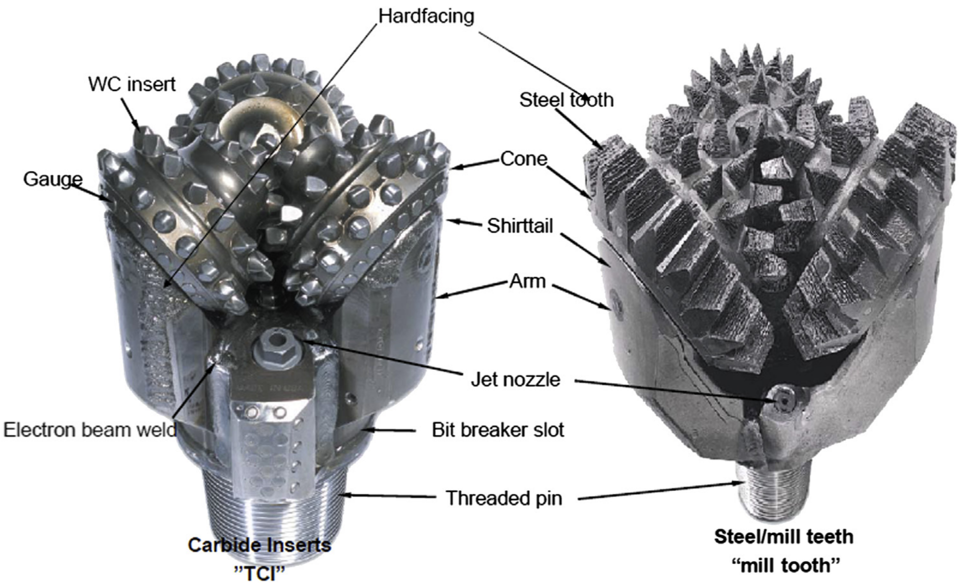

Figure 48 Tailoring of tool bits in the gas and oil industry against wear (North, 2011).

binder, specialty hardmetals with a CoNiCr binder have been developed to improve corrosion resistance. The hardness could range from 700 to 1900 HV10.

1.02.6.2.2.11.1 Subsea Application Example (Ceratizit)

Recent industry technology developments have allowed drilling engineers to venture deeper to explore for oil and gas.

One of the major failure modes is corrosion of components in electrohydraulic control systems, which is particularly prevalent subsea in water depths >150 m. Directional control valves are normally the most susceptible components to corrosion in an open loop hydraulic system that controls subsea operations and uses water–glycol hydraulic fluid.

Research investigations undertaken have concluded that the primary failure can be associated with seawater ingress that may degrade the fluid and can be highly corrosive when in contact with stainless steel 316L.

Even though 316L is usually regarded as the standard "marine grade stainless steel," it is however not resistant to warm seawater where pitting and crevice corrosion can be prevalent.

Given that seawater ingress is hard to avoid in water depths >150 m, nickel WC is the alternative to stainless steel 316L as it is seawater tolerant and gives optimized performance compared to stainless steel 316L at increased temperatures (50–70 °C). The best solution with water–glycol hydraulic fluid in combination with nickel WC is the HW540 from Macdermid Offshore. The higher glycol content in the fluid slows down the corrosion process of nickel WC through the increase of the viscosity of the medium (**Figure 49**).

In summary, seawater ingress is extremely detrimental to stainless steel 316L, but with the use of nickel WC grades, it is possible to significantly improve valve life. The new generation nickel WC gives improved protection against erosion, being a common wear mode during the pumping process of sand water (Zheng, Neville, Gledhill, & Johnston, 2009).

1.02.6.2.2.11.2 General Wear Parts

There are a multitude of cemented carbide parts with a fine to medium grain size used in almost every industry to combat abrasive, erosive and even corrosive wear. Most alloys used here are tailor-made for the particular application; the binder content could range from 4 to 25 wt%, the hardness from 2200 to 1000 HV10. In some cases, the cobalt binder is also replaced by nickel. Textile knives, mud nozzles, belt scrapers, extruder screws, liners, strippers, perforated plates, milling media, burr blanks, paint nozzles, valves, high pressure pistons, glass cutters, paper punches and guides, ball point pen tips, safety lock parts, watch cases and bracelets, etc. are just a few examples.

Figure 49 Application examples for hardmetals for chemical, gas and oil industries (Durit). For example, seal rings, valve seats and cones, valve parts, pistons, plungers, sleeves, and needles.

1.02.6.2.3 Application: Medium- to Coarse-Grained Hardmetals

1.02.6.2.3.1 Stone Working

Hardmetal-tipped tools are used extensively in the construction and stone industry. The superior wear resistance and toughness of hardmetal tools has greatly increased productivity and reduced the intensity of manual labor in working stone and other building materials.

The lion's share of the industrial hardmetal tools in this application are medium grain sized with hardness around HV1400. Table 20 shows a range of hardmetal grades used in the construction industry. Standard DIY hardmetal-tipped tools tend to be fine grained and of a higher hardness.

As in all other cutting tools, the design of the tool bit plays a critical role in tool performance (Table 21).

Table 20 Hardmetal grades for construction tool industry (Ceratizit)

Grade	*Grain*	*Code*	*Binder (%)*	*Density (g/cm^3)*	*Hardness (HV10)*	*TRS (MPa)*
WC–Co grades						
CTF12-BC	F	C2	6.0	14.95	1640	2200
CTM14-BC	M	C2	7.0	14.90	1550	2600
CTM17-BC	M	C1	8.5	14.65	1420	2800
CTF24-BC	F	C11	12.0	14.30	1330	3000

F, fine; M, medium.

Table 21 Application chart for hardmetal grades for electrical power tools (Ceratizit)

	Hammer drills					*Masonry drills*				
Standard grade	*Grades*	*Grain*	*%Co*	*HV10*	*TRS*	*Grades*	*Grain*	*%Co*	*HV10*	*TRS*
Small diameter	CTM17-BC (BC20)	M	8.5	1420	3000	CTF11-BC (BC03)	F	5.6	1760	2300
Large diameter	CTM17-BC (BC20)	M	8.5	1420	3000	CTF12-BC (BC05)	F	6.0	1640	2300
Special for low impact	CTM14-BC (BC10)	M	7	1550	2600	CTF08-BC (BC01)	F	4.0	1840	2200
Special for heavy duty	CTF24-BC (BC30)	F	12	1330	3200	CTM14-BC (BC10)	M	7.0	1550	2600

F, fine; M, medium.

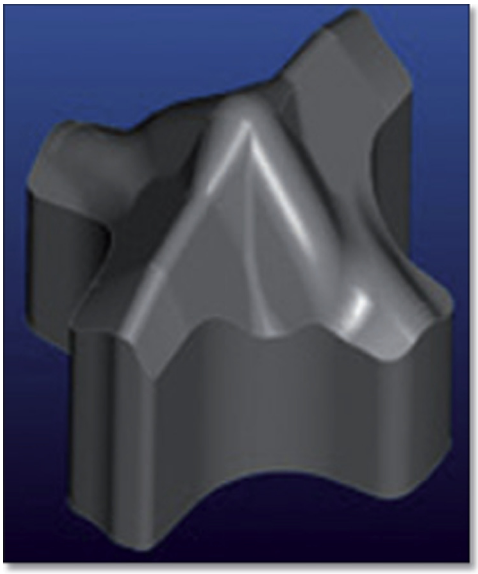

Figure 50 Gradient hardmetal tool bit optimized for optimum performance and production ease (EPMA, 2006).

Figure 50 is a picture of a gradient hardmetal bit optimized for optimum performance in industrial drilling.

Stonemasons, sculptors and engravers have to deal with a range of different types of stone like marble, sandstone, granite, etc. and there are a range of manual and electrically powered tools that require a wider range of hardmetal grades with binder contents up to 17% and a hardness range between HV 920 and 1900 to be able to handle different stone types and detail of engraving.

1.02.6.2.3.2 Mining, Road Planning, Earth moving

That wear is not only dependent on the material properties but also on service conditions is shown in the following diagrams as an example for mining bits of the same grade and design. Wear rate increases with increasing rock hardness, tool velocity and temperature and is primarily abrasive at low wear rates (Sandvik, EPMA, Winterrev 2012).

The typical snakeskin surface appears during the course of service and the surface morphology is shown in **Figure 51(b)**.

There is a strong increase in wear rate once the wear mechanism evolves from abrasion to adhesion. Rock constituents and wear debris can be embedded into the hardmetal surface and the tool material suffers a loss of integrity.

Ultracoarse-grained WC–Co cemented carbides are widely employed in mining and construction; however, there is an ongoing need for improvement. A new development is a novel hardmetal with a nano reinforced binder which has been implemented in industry on a large scale (Konyashin, Ries, Lachmann, Mazilkin, & Straumal, 2012). The microstructure of the novel cemented carbides consists of rounded WC grains with thick and uniform interlayers of the binder among them, which allows lower internal stresses and high fracture toughness to be obtained. The Co-based binder of the novel cemented carbides is reinforced and hardened by nanoparticles of the θ-phase (Co_2W_4C) of nearly 1–8 nm in size. The binder nano reinforcement leads to a noticeable increase of its nanohardness resulting in significantly improved wear resistance of the novel cemented carbides without sacrificing their toughness. Lifetime of mining and construction tools with inserts of the novel cemented carbides is dramatically extended. Usually, an increase of carbide fracture toughness or transverse rupture strength can be achieved only at the expense of hardness and wear resistance, and vice versa (**Table 22**).

The approach of the binder nano reinforcement can presumably be effectively employed mainly for hardmetals with relatively thick Co interlayers and large cobalt mean free path values. In fine-grained carbide grades, when the binder forms very thin Co interlayers, its hardness should not presumably play an important role with respect to abrasive wear. **Figure 52** shows an increase in wear resistance measured by use of the ASTM B611 test depending on the carbide Co mean free path as well as the corresponding microstructures of the cemented

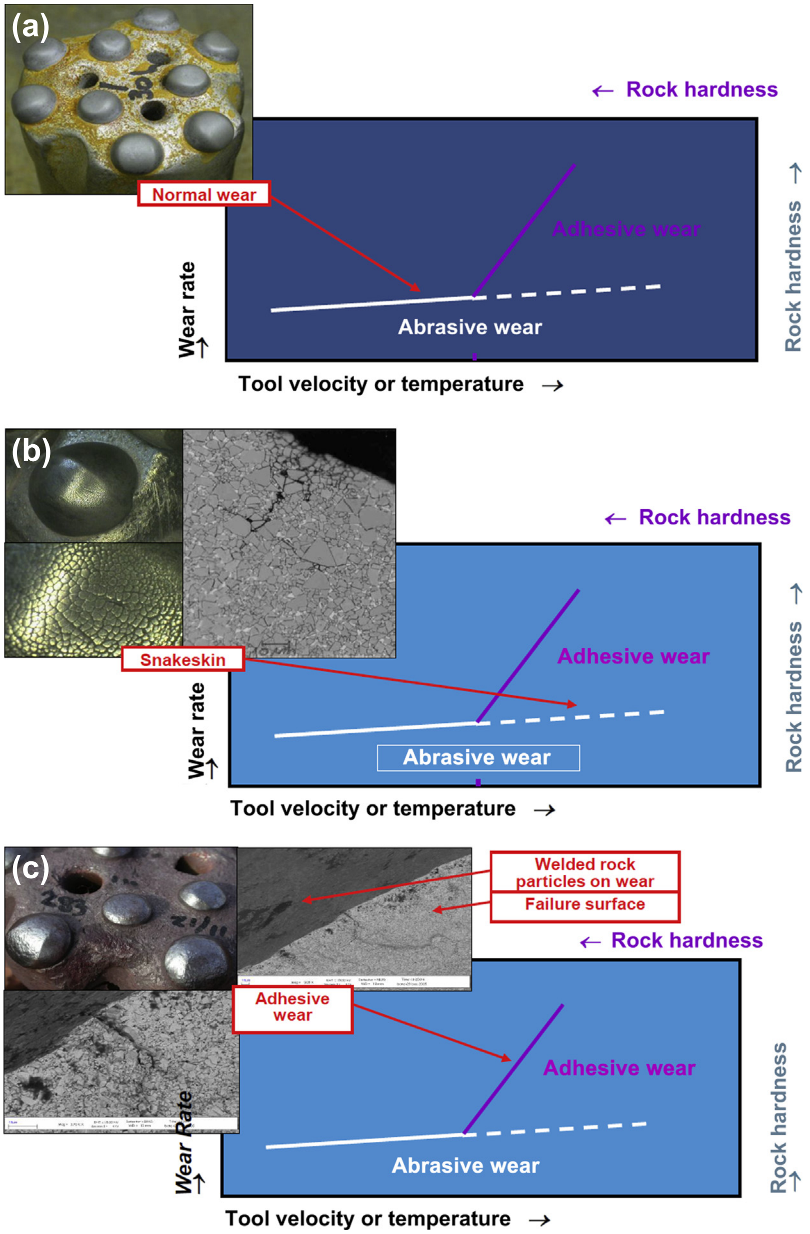

Figure 51 (a) Typical trendlines for hardmetal wear rates. (b) Snakeskin surface morphology detected after extended abrasive wear. (c) Typical trendlines for cemented carbide wear (Sandvik, EPMA, Winterrev 2012).

Table 22 Comparison of properties of ultracoarse 6.5% binder hardmetal with standard and nano reinforced binder (Konyashin et al., 2012)

Ultracoarse grade	*HV30*	*TRS (MPa)*	K_{1c} *(MPa* $m^{-0.5}$*)*	*Wear* cm^3*;* $rev^{-1} \times 10^{-4}$	*Binder microhardness (GPa)*	*Binder nanohardness (GPa)*	*Mean tool lifetime (%)*	*Mean breakage number (%)*
Standard	1100	2010	17.7	2.1	4.7	7.5	100	100
Nano reinforced binder	1130	2330	18.2	1.1	7.8	10.2	190	80

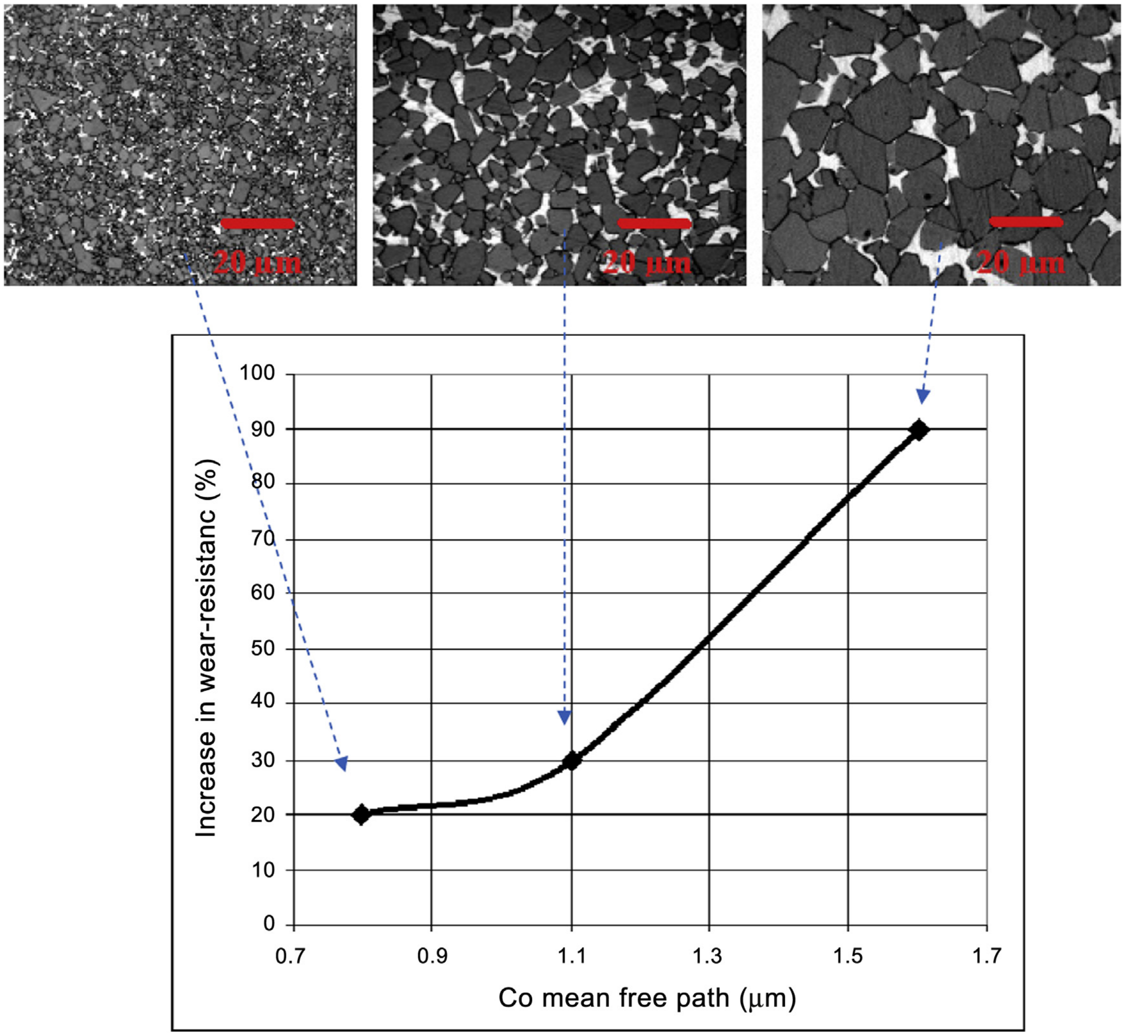

Figure 52 Increase in wear resistance (ASTM B611) of WC–Co cemented carbides with various Co mean free paths as a result of the binder nano reinforcement as well as the microstructures of the cemented carbides (Konyashin et al., 2012).

carbides. It can be seen that the effectiveness of the nano reinforcement is relatively insignificant for the cemented carbides with small WC grain size and correspondingly low values of Co mean free paths (**Figure 53**).

Medium- to coarse-grade tough hardmetals are particularly useful in combating wear in industries such as chrome, manganese and iron ore mining, coal and ash handling and loading, raise boring, blast hole and water drilling, brick and construction industry, waste processing and shredding, road construction and civil engineering, alluvial mining and earth moving, dredging and reclamation, crushing and screening, continuous mining, foundry sand mixing, brick and tile fabrication, concrete mixing and pumping, clay quarrying, and graphite regeneration.

Some application examples and innovative tool systems and hardmetals for road construction, tunneling, excavation, surface mining, crushing operations of all kinds, recycling, soil cultivation and biomass production, are given below.

- Surface mining

As is the case of any application, it is mandatory in surface mining too that special demands need special solutions. Success is then achieved above all if not only the product works really well but also the partnership between toolmaker, machine manufacturer and user.

Surface mining replaces the method of quarrying otherwise used, namely blasting, which not only causes noise, dust and ground vibrations, but also makes it impossible to mine the required material with any degree of precision. Selective extraction of the limestone, on the other hand, enables a higher proportion of the deposit

Figure 53 Miner's milling drum (Betek).

Figure 54 Reinforced bit with a wear-resistant plasma coating on the bit body below the carbide tip (Betek).

Figure 55 New and worn carbide-tipped bits.

to be mined. The miner glides slowly on the limestone bed and eats through the rock. Though it may appear leisurely, it is in fact an act of great force and involves "surgical precision". Optimization of the machine and fine tuning of the cutting system and the tools led to maximum performance as the machine worked on the stone. It was then possible to extract over 1000 m^3 of limestone in one 8-h day (Betek) (Figures 53 and 54).

- Underground mining

In underground mining particularly difficult conditions prevail. Coal mining in particular makes great demands of man and machine. It is very important when mining coal that dust formation is kept as low as possible in order to minimize the risk of coal dust explosion—a much-feared explosive reaction in coal mining between coal dust powder and oxygen in the air. To reduce the amount of coal dust, special shaped slim tools are used with excellent penetration efficiency. Figure 55 is an example of such a tool (Betek).

Figure 56 Tungsten carbide brazed blade (Betek).

- Road milling

The key tool of a milling machine is the milling drum rotating against the direction of feed. Tool holders are mounted on the drum bodies for the rotating round shank cutter bit. During the milling process, the bits loosen the surface and granulate the surface to a reusable material of small pieces.

The round shank hardmetal cutter bit is able to show its strengths especially when milling with a large depth of cut in the surface with a large number of bits on the drum. This bit type also performs excellently when milling asphalt on the top layer, where WC wear tends to be the key criterion for wear and the long, slim tips ensure a high degree of effectiveness. Perfect rotation characteristics for the round shank cutter bit are the prerequisites for optimum usage of the WC tip and the complete bit (Betek).

1.02.6.2.3.3 Agricultural Wear Parts

1.02.6.2.3.3.1 Cultivator Blades

The cultivator blades were developed by arming the blade with appropriate hardmetal. In a practical test, after 2500 ha, seven sets of traditional steel blades had been worn away, while the WC blades still had enough in reserve to outlast a further two sets of standard steel ones. The WC blades proved themselves a worthwhile investment in terms of both cost and efficiency (Betek) (Figure 56).

Other wear parts for agricultural applications are scrapers, rotary cultivators, deep soil looseners, drilling accessories, beets technology, lawn care, ploughs, power harrows, liquid manure accessories, just to name a few.

Snow ploughers and graders are also tipped with coarse-grained tough hardmetals.

1.02.6.2.3.4 All Purpose Antiwear Solutions

Many machines are subjected to great strains and high levels of wear. Sections of plants where abrasive materials are conveyed or processed are always particularly susceptible to this and the plants also often run nonstop. Without special protection against wear, such machines and plant sections can only be operated for short periods. A lack of antiwear protection can lead to greatly reduced hours of operation, high maintenance costs and even to expensive machine failure. Compared to that the capital expenditure costs for a suitable antiwear solution are in most cases very modest. It is clear that a suitable antiwear solution can substantially improve a plant's operational reliability and cost efficiency.

A new composite solution based on a hardmetal core and a weldable steel casing has launched (Betek TungStud) (Figure 57) that is simple and effective. They can even be easily welded onto unevenly formed metallic surfaces and, if necessary, replaced time and again. The problem of wear is often countered using aids such as welded reinforcement panels. In the case of applications with a particular susceptibility to wear it pays, however, to use WC wear protection as the longer lasting alternative (Figure 58). The possible applications are many and varied:

On machines for extracting, handling and working abrasive materials, e.g. gravel, sand, ore, coal, etc.
On shredders and recycling machines
On crushers, grinders and mixers

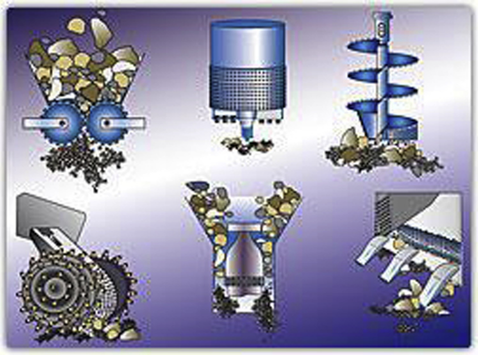

Figure 57 An overview of a few examples of uses for Betek TungStuds (Betek).

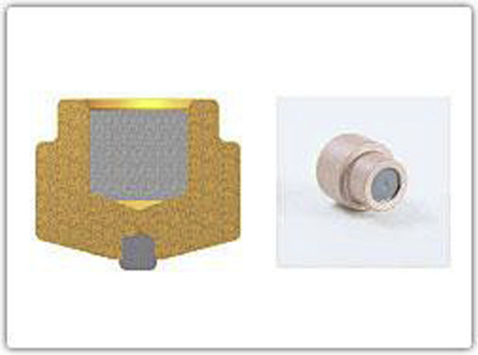

Figure 58 Cross-section drawing and photo of the steel hardmetal wear element (Betek TungStud).

On digger buckets
On road headers
On augers and bucket drills
On surface miners

1.02.6.2.3.5 Hardmetal Rolls

Rolling is a continuous forming process that is done either hot or cold. The rolls shape and orientation determines the type of products such as plates, bars, rods and structural shapes that can be produced (Figure 59).

Hardmetals with a high toughness and good thermal shock resistance, mainly coarse to medium grain size with binder contents between 6 to 30 wt% are used in these applications.

Coarse-grained hardmetals are typically used under very demanding mechanical, thermal and often chemical operating conditions. Mechanical and thermal loads in these applications are highly dynamic. There is an increasing trend toward coarser WC grains in mining and construction applications to profit from higher fracture toughness and thermal conductivity (Table 23).

Figure 59 Tungsten carbide roll (Sandvik).

Table 23 Extra coarse grade properties (Ceratizit)

Binder (wt%)	*Density (g/cm^3)*	*Hardness*		*Transverse rupture strength (N/mm^2)*	*Compr. strength (N/mm^2)*	*Young's modulus elasticity (N/mm^2)*	*Thermal conductivity (Wm/K)*	*Coeff. thermal expansion (K/1000)*
		HV10	*HRA*					
Cobalt Binder								
6	15.0	1300	89.4	2400	4300	630	115	4700
10	14.60	1130	87.6	2600	4000	580	110	5100
12.5	14.30	1050	86.6	2700	3800	540	107	5300
15	14.05	970	85.6	2800	3600	530	105	5600
17.5	13.80	910	84.8	2850	3500	520	103	5900
20	13.60	850	84.2	2900	3400	500	100	6300
22	13.40	810	83.6	2900	3300	490	100	6500
25	13.15	760	82.6	2800	3200	470	97	6800
30.0	12.75	690	81.4	2700	3100	450	95	7300
CoNiCr Binder								
10	14.50	1140	87.7	2600	3600	560	110	5100
15	14.05	960	85.5	2900	3400	530	105	5600
20	13.50	810	83.6	2800	3200	495	100	6300
25	13.15	710	81.7	2700	3100	460	97	7000
30	12.70	610	80.0	2700	3000	420	95	7400

The basic roll failure causes in service are the following:

1. Cracking due to friction and alternating loads and thermal shock caused by alternating thermal loads and nonstationary coolant delivery.
2. Roll fracture due to mechanical overloading, e.g. shock when the workpiece enters the stand, fatigue fracture and/or corrosion (electrochemical/tribochemical wear). The selective loss of the cobalt binder matrix leads to increased wear rates and can serve as the origin of mechanical and thermal cracks, the surface roughness increases (Magin, EPMA, Winterrev 2012).

Alloying of the binder phase to increase dynamic and static strength as well as to increase corrosion resistance and a reduction of flaws and flaw size to improve fatigue strength could be used to increase service life and reliability.

1.02.6.2.4 Modeling and Simulation in Wear Parts Applications

As demands on resource and energy conservation in a growing world with growing standard of life accelerates, society in general and manufacturing and design in particular has to move to a knowledge based society. Computer-aided design and manufacturing are already household words, the computer aided modeling and simulation of material and product properties under service conditions now lead to better resource and design utilization.

As an example, innovative applications of metal forming simulation have led to better and more reliable tooling. Increased competition and the need to control costs have demanded that die designs generate dependable tooling that produces good parts starting almost with the first hit. Metal forming simulation technology is minimizing these risks of errors in die design that cause delays in production. Metal forming simulation can provide early results to designers for changes in part design before the tooling is actually built—predict production problems, such as sheet metal tearing and wrinkling; predict thickness variation and strain; help fabricators reduce their material costs and naturally choose the appropriate tool material (SME) (**Figures 60** and **61**).

The same is true for many other manufacturing processes such as machining, casting, forging, welding, brazing, injection molding, and so on.

The hardmetals industry has also been using modeling and simulation for material, process and product development for quite a while and engineering designers now have reliable access to hardmetal property databases too. This will certainly improve the productivity and scope of hardmetal tools and wear parts.

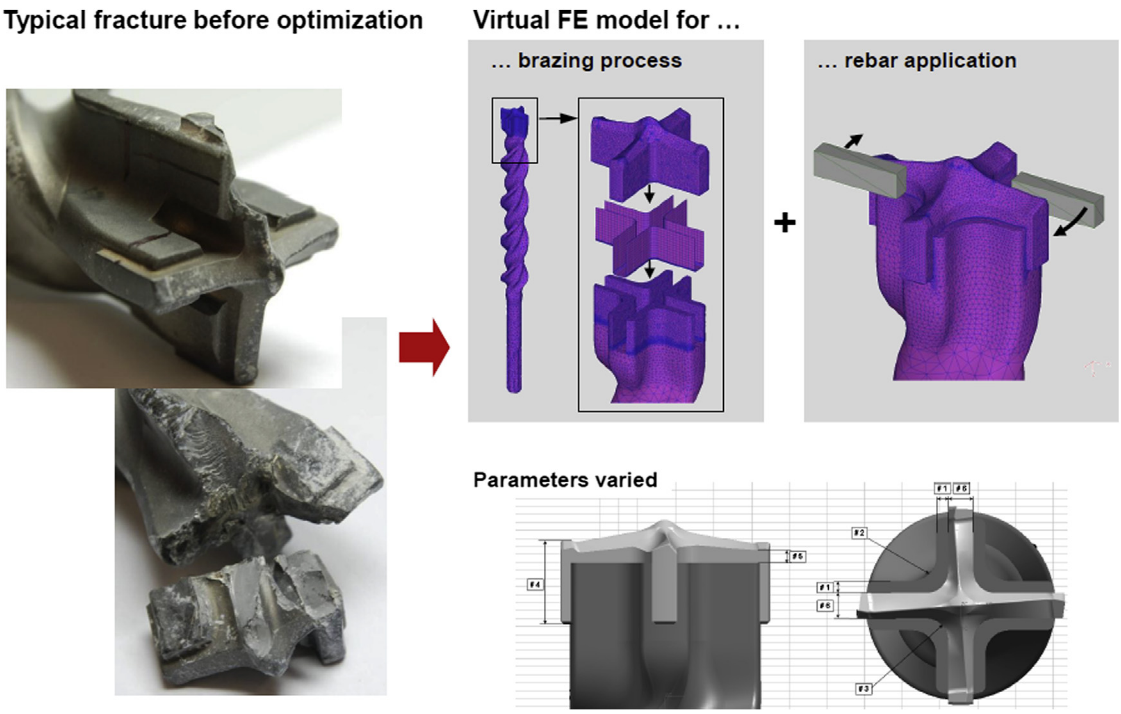

Figure 60 Virtual DoE to improve drill bit robustness (Hilti).

1.02.6.2.4.1 Outlook

Two hundred and fifty years after the discovery of tungsten in Sweden, 120 years after publication of the process to make WC by Moisson, 90 years after the first patents were granted for hardmetals, research and development is still continuing at a brisk pace to improve material properties and widen the application scope of this special class of tough wear-resistant material. The average expected growth rate in the future is also expected to be around 3–4% as in the past and the estimated market value of hard material products (including superhard

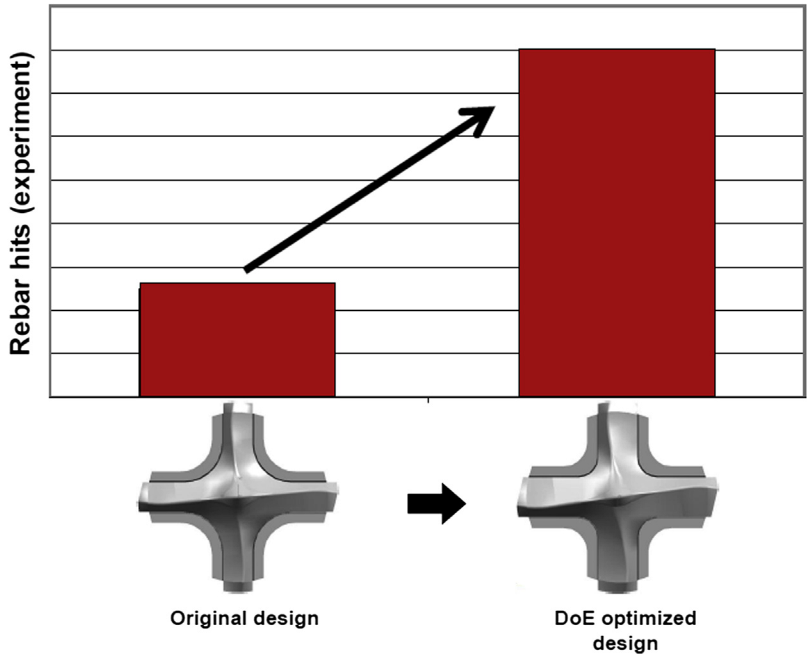

Figure 61 Drill bit robustness is significantly improved by DoE optimized design (Peters & Moseley, 2012).

materials) in the range of US$ 22 billion in 2018. Tools are and have always been a prerequisite for product innovation and improvement in the quality of life of mankind and it can be safely assumed that hardmetal products will continue to have a bright future.

Acknowledgments

My special thanks goes to Dr Bryan Roebuck for critical evaluation and advice for a part of this publication and the many institutions who have granted permission to use their published data.

I would also like to thank my educators, my colleagues and the hardmetal community and customers who have with their guidance and encouragement helped me to gain more insight and offer solutions to solving problems in this area. Last but not least, I would place my deep appreciation to the editors and publishers for giving me the opportunity to write this paper and for their support and patience.

References

Alvaredo, P., Mari, D., & Gordo, E. (2013). High temperature transformations in a steel – TiCN cermet. *International Journal of Refractory Metals and Hard Materials, 41*, 115–120.

Andren, H.-O. (2001). Microstructures of cemented carbides. *Materials and Design, 22*, 491–498.

Astakhov, J. P. (2006). *Tribology of metal cutting*. London, UK: Elsevier.

Bolton, J. D. (1992). In *Proc. int. conf. advances in hard materials production*. Shrewsbury: MPR Publishing Services Ltd., 21-1 – 21-15.

Bushmann, B., & Gupta, B. K. (1991). *Handbook of tribology materials, coatings and surface treatments*. Westwood, USA: Noyes.

Chen, L. M., Lengauer, W., & Dreyer, K. (2000). Advances in modern nitrogen containing hardmetals and cermets. *International Journal of Refractory Metals and Hard Materials, 18*, 153–161.

Davim, P. J. (Ed.). (2008). *Machining fundamentals and recent advances*. Springer. http://dx.doi.org/10.1007/978-1-84800-213-5. ISBN: 978-1-84800-212-8, e-ISBN: 978-1-84800-213-5.

Deshpande, M. V., Saxena, J. P., & Basu, S. (1992), 22-1 – 22-13 *Proc. int. conf. advances in hard materials production*. Shrewsbury, UK: MPR Publishing Services Ltd..

EPMA. (2006). *EPMA award for excellence in PM: TEC C3X Drill Bit*. Liechtenstein: Hilti AG.

EPMA. (2012). Magin, Ceratizit, EPMA, Winterrev workshop. San Sebastian.

Fan, P., Zak Fang, Z., & Guo, J. (2013). A review of liquid phase migration and methods for fabrication of functionally graded cemented tungsten carbide. *International Journal of Refractory Metals and Hard Materials, 36*, 2–9.

Frisk, K., Dumitrescu, L., Ekroth, M., Jansson, B., Kruse, O., & Sundman, B. (2001). Development of a database for cemented carbides; thermodynamic modeling and experiments. *Journal of Phase Equilibria, 22*(6), 645–655.

Garcia, J., & Pitonak, R. (2013). The role of cemented carbide functionally graded outer layers on the wear performance of coated cutting tools. *International Journal of Refractory Metals and Hard Materials, 36*, 52–59.

Gee, M. G., Gant, A., & Roebuck, B. (2007). Wear mechanisms in abrasion and erosion of WC-Co and related hardmetals. *Wear, 263*, 137–148.

Glühmann, J., Schneeweiß, M., van den Berg, H., Kassel, D., Rödiger, K., Dreyer, K., et al. (2013). Functionally graded WC–Ti(C, N)–(Ta, Nb)C–Co hardmetals: metallurgy and performance. *International Journal of Refractory Metals and Hard Materials, 36*, 38–45.

Grab, G. P. & Nemeth, B. J. (1982). Cemented carbide with binder enriched surface. US Patent 2095702 (March 2, 1982), Appl. March 27, 1981.

Herr, M., Sailer, T., Sockel, H. G., Schulte, R., Feld, H., & Prakash, L. J. (2001). Characterisation of wear properties of ultrafine-grained hardmetals using a special abrasive wheel test. *International Journal of Refractory Metals and Hard Materials, 19*, 371–379.

ISO 3685:1993. Tool life testing with single point turning tools.

Jüngling, Th., Oberacker, R., Thümmler, F., Sigl, L. S., & Schwetz, K. A. (1991). *Powder Metallurgy International, 23*, 296–299.

Klocke, F., & Krieg, T. (1999). Coated tools for metal cutting – features and applications. *CIRP Annals, 48*, 515–525.

Kny, E., et al. (1986). *Werkstoffe und Korrosion, 37*, 230–235.

Konyashin, I., Schäfer, F., Cooper, R., Ries, B., Mayer, J., & Weirich, T. (2005). Novel ultra-coarse hardmetal grades with reinforced binder for mining and construction. *International Journal of Refractory Metals and Hard Materials, 23*(4–6)), 225–232.

Konyashin, I., Hlawatschek, S., Ries, B., Lachmann, F., & Vukovic, M. (2014). Cobalt capping on WC–Co hard metals. Part II: A technology for fabrication of Co coated articles during sintering. *International Journal of Refractory Metals and Hard Materials, 42*, 136–141.

Konyashin, I., Hlawatschek, S., Ries, B., Lachmann, F., Sologubenko, A., & Weirich, T. (2010). A new approach to fabrication of gradient WC–Co hardmetals. *International Journal of Refractory Metals and Hard Materials, 28*(2), 228–237.

Konyashin, I., Ries, B., Lachmann, F., Mazilkin, A., & Straumal, B. (2012). Cemented carbides with nano reinforced binder – a new class of metal/ceramic composites. In *Proceedings PM2012, Yokohama, Japan*.

Konyashin, I., Ries, B., Lachmann, F., & Fry, A. T. (2013). Gradient WC-Co hardmetals, theory and practice. *International Journal of Refractory Metals and Hard Materials, 36*, 10–21.

Liu, S. (2009). Study on rare earth doped cemented carbides in China. *International Journal of Refractory Metals and Hard Materials, 27*(3), 528–534.

Mari, D., & Gonseth, D. R. (1993). A new look at carbide tool life. *Wear, 165*, 9–17.

Nicolae, P., & Nita, P. (2001). WC-Co functionally graded materials. In *Proc. 15th int. plansee seminar* (Vol. 2; pp. 332–341). HM54.

North, B. (2011). Developments in the world of hardmetals. In *Proc. ITIA 24th annual general meeting, 2011*. Kennametal.

Peters & Moseley, S. (2012). EPMA Winterrev 2012.

Petersson, A. (2004). *Cemented carbide sintering: constitutive relations and microstructural evolution* (Ph.D. thesis). Stockholm: Royal Institute of Technology.

Prakash, L. (1979). *Weiterentwicklung von WC Hartmetallen mit Eisenbasis Binder*. Ph.D. Thesis. Technical University Karlsruhe.

Prakash, L., & Gries, B. (2009). WC hardmetals with iron based binders. In *Proc.17th int. plansee seminar* (Vol. 2; pp. 1–14). HM 5.

Prakash, L. (1995). Application of fine grained tungsten carbide based cemented carbides. *International Journal of Refractory Metals and Hard Materials, 13*, 257–264.

Prakash, L. (2010). Fine grained cemented carbides – an update. In *Proc. world PM 2010 congress* (Vol. 3; pp. 669–676). Shrewsbury, UK: EPMA.

Richter, V., & Ruthendorf, M. (1999). On hardness and toughness of ultrafine and nanocrystalline hard materials. *International Journal of Refractory Metals and Hard Materials, 17*, 141–152.

Roebuck, B. (1997). Effect of Testpiece Geometry on the Flexure Strength of Representative Hardmetals and Cermets. In *Proc. 14th Int Plansee Seminar* (pp. 352–365). Austria, V2: Reutte.

Roebuck, B., & Prakash, L. (2012). Innovations in tungsten carbide-cobalt hardmetal technology. In *International powder metallurgy directory* (pp. 107–126). UK: Innovar Communications Ltd.

Ruppi, S., Larsson, A., & Flink, A. (2008). Nanoindentation hardness, texture and microstructure of α-Al$_2$O$_3$ and κ-Al$_2$O$_3$ coatings. *Thin Solid Films, 516*, 5959–5966.

Sailer, T., Herr, M., Sockel, H.-G., Schulte, R., Feld, H., & Prakash, L. J. (2001). *International Journal of Refractory Metals and Hard Materials, 19*, 553–559.

Sailer, T. (2002). *Ultrafeinkörnige Hartmetalle mit Co-Binder und alternative Bindersysteme* (Ph.D. Dissertation). University Erlangen – Nürnberg.

Sandvik Coromant. (1995). *Modern metal cutting, a practical handbook*. Sandvik Coromant.

Schedler, W. (1988). *Hartmetalle für den Praktiker*. Düsseldorf: VDI-Verlag.

Schröter, K. (1923). *German Patent D.R.P.420689*.

Schwarzkopf, M., Exner, H. E., & Fischmeister, H. F. (1988). Kinetics of compositional modification of (W, Ti)C–WC–Co alloy surfaces. *Materials Science Engineering, A, 105/106*, 225–231.

Shaw, M. C. (1984). *Metal cutting principles*. Oxford, UK: Oxford Science.

Spriggs, G. E. (1979). In *Conf. recent advances in hardmetal production, 14.1*. Shrewsbury, UK: MPR Publishing Services Ltd.

Trent, E. M., & Wright, P. K. (2000). *Metal cutting*. Boston, USA: Butterworth-Heinemann.

Tsuda, K., Ikegaya, A., Isobe, K., Kitagawa, N., & Nomura, T. (1996). Development of functionally graded sintered hard materials. *Powder Metallurgy, 39*(4), 296–300.

Williams, B. (2012). Powder metallurgy: A global market review. In *International Powder Metallurgy* (15th ed.). UK: Innovar Communications Ltd.

Wittmann, B., Schubert, W.-D., & Lux, B. (Eds.). (2002). *Proc. PM 2002, Lausanne* (pp. 303–308). EPMA.

Zheng, L., Neville, A., A. Gledhill, & Johnston, D. (2009). An experimental study of the corrosion behaviour of nickel tungsten carbide in some water-glycol hydraulic fluids for subsea applications. *Journal of Materials Engineering and Performance*. Published online 27 March, 2009.

Website Resources

www.betek.com
www.broda-hartmetall.de
www.ceratizit.com
www.durit.com
www.e6.com
www.kyocera-unimerco.com
www.ham-dental.com
www.hptec.de
www.saar-hartmetall.de
www.sandvik.com
www.schoenenberger-messer.de/eng/

Multimedia Annexes

Short Product Videos

http://www.durit.com/en/service-and-faq/video/precision-tools.html
http://www.durit.com/en/service-and-faq/video/tooling-for-metal-packing.html
http://www.durit.com/en/service-and-faq/video/high-performance-plugs-and-drawing-dies.html
http://www.durit.com/en/about-us/video/engineering-components.html
http://www.durit.com/en/about-us/video/tools-for-fasteners.html
http://www.kyoceramicrotools.com/Movie/Movie.htm
Agricultural product armament https://www.youtube.com/watch?feature=player_embedded&v=VfccV87_QJM
BETEK TungStuds tutorial HD: https://www.youtube.com/watch?v=OQ4S4r-jq0Q
BETEK TungStuds: Equipping of an auger: https://www.youtube.com/watch?v=e33YfG7NoNM
Trenching solution from Betek: https://www.youtube.com/watch?v=GCUCF0q-RgI
Inline roller blades with tungsten carbide wheels for use on ice!! https://www.youtube.com/watch?v=5JZU458gsFI
How tungsten carbide inserts are made: Sandvik Coromant: https://www.youtube.com/watch?v=aI0xryL1vjI
Sandvik Coromant CoroMill 300 for heavy roughing https://www.youtube.com/watch?v=ffkGizDy2GY
Windmill production technology – Sandvik Coromant https://www.youtube.com/watch?v=eo4kGrx4NrM
Simple demonstration of turning, facing, parting: https://www.youtube.com/watch?v=ffkGizDy2GY

High-Performance geometry turning inserts http://www.youtube.com/watch?v=fnRtw82i55M
Cutting tool design – milling (SME) http://www.youtube.com/watch?v=0ROfDww8UVM
Milling and machining center basics (SME) http://www.youtube.com/watch?v=SeGQ91FKTNg&feature=endscreen
Threading basics (SME) http://www.youtube.com/watch?v=vCHQLFZHHJc
Gear machining Basics (SME) http://www.youtube.com/watch?v=2K45B6tDqsg
Workholding (SME) http://www.youtube.com/watch?v=d7M_bcKjkGw
Holemaking (SME) http://www.youtube.com/watch?v=ul20R32HJ3E
Holemaking basics (SME) http://www.youtube.com/watch?v=bRXUVhubo7g
Metal cutting fluids (SME) http://www.youtube.com/watch?v=ivsigqntxno
Minimum quantity lubrication (SME) http://www.youtube.com/watch?v=djcPbdXFnll
http://www.sandvik.coromant.com/en-gb/video/pages/default.aspx

1.03 Microstructure and Morphology of Hardmetals

Sabine Lay and Jean-Michel Missiaen, Grenoble Institute of Technology, Saint-Martin d'Hères, France

1.03.1 Introduction

Mechanical properties of hard materials are closely related to their microstructure, especially the phase composition, phase distribution and grain size. The phase distribution is to a large extent monitored by the relative energy of the grain boundaries and interfaces. In what follows, interfacial structures and energetics will be the connecting thread to get a comprehensive overview of the microstructure in cemented carbides. These quantities will be described using available experimental or calculated data of the literature. While few experimental data are available, atomistic calculations are helpful to interpret the microstructure and predict the effect of additional elements.

This chapter will focus mainly on WC–Co alloys which were studied extensively for nearly one century at different scales. The microstructure of the binder phase will first be discussed. Then properties of WC/Co interfaces and WC/WC grain boundaries will be described together with their consequences on the grain morphology and on the structure of the hard-phase skeleton. Finally, the state of the art about mechanisms and microstructural evolution related to grain coarsening will be presented. In an additional section, the microstructure of TiC-containing cemented carbides and of Ti(C,N)-based cermets will be briefly addressed.

1.03.2 WC–Co (Ni) Alloys

WC-based cemented carbides were mainly developed with cobalt as binder phase because it gives rise to a dense material with excellent mechanical properties. Nickel and iron were also considered as alternative binders but cobalt is the most common binder. The microstructure of WC–Co (Ni) alloys consists of facetted WC grains

http://dx.doi.org/10.1016/B978-0-08-096527-7.00003-9

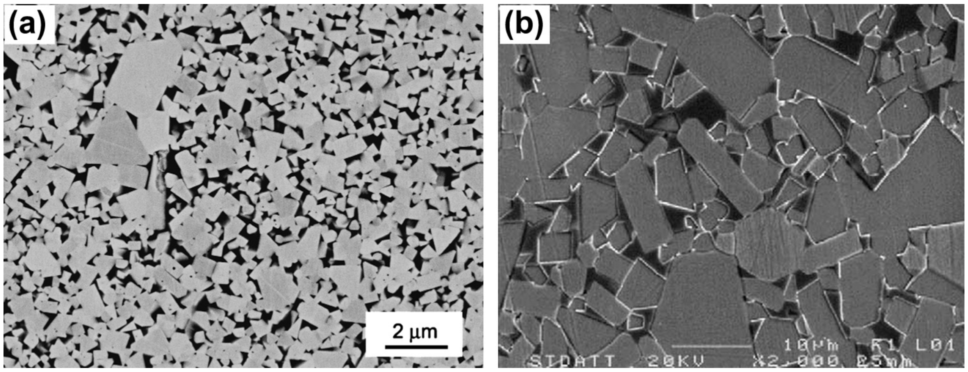

Figure 1 (a) Scanning electron microscopy (SEM) micrograph showing the typical microstructure of a WC–12Co alloy (at%) prepared from a WC powder with a median size of 0.85 µm and sintered at 1450 °C for 1 h (WC in bright grey and Co in dark). (b) SEM image of a high-carbon WC–10 wt% Ni alloy sintered for 1 h at 1480 °C from a starting WC grain size of 0.35 µm (Wittmann et al., 2002).

embedded in a Co(Ni)-rich binder as illustrated in **Figure 1**. WC grains are not completely surrounded by the binder but always form contacts with other WC grains. The microstructure depends to a large extent on the interfacial energy relationships. In what follows, the binder phase will be first described. Then available data on WC/binder interfaces and WC/WC grain boundaries will be given. Finally, the contiguity which quantifies the relative amount of grain boundaries and interfaces will be discussed.

1.03.2.1 Microstructure of the Co-Rich (Ni) Binder

The mechanical properties of the binder are controlled by its composition and its distribution in the alloy after sintering (Almond & Roebuck, 1988). There is no solubility of cobalt in WC while cobalt dissolves a high amount of WC at high temperature. The solubility of W and C atoms in cobalt depends both on the temperature and on the total content of carbon in the material (Akesson, 1982). At 1425 °C, the C and W amount in the binder in equilibrium with WC ranges from about 9C + 13W to 16C + 6W (at%) when the carbon content increases from the η-phase limit to the graphite limit. On cooling, the solubility in the cobalt is reduced and W and C atoms reprecipitate on WC grains. The diffusion rate of W atoms decreases, so a gradient of concentration forms over a distance of about 0.1 µm close to the WC grains (Andrén, 2001). For a slow cooling rate, the W amount remaining in the cobalt at room temperature reflects the composition of the binder at approximately 1000 °C. On the other hand, nearly no carbon is found in the binder likely due to the fast diffusion of this element in the cobalt.

The crystallographic structure of the Co-rich binder is mostly face-centered cubic (fcc) while some hexagonal close-packed (hcp) pools resulting from the fcc–hcp transformation are also present. The fcc high-temperature form of Co is probably stabilized by residual stresses and the presence of dissolved atoms (Almond & Roebuck, 1982). However, a systematic characterization of the binder using the electron backscatter diffraction (EBSD) technique indicates that in some specimens, the hcp form is predominant while no relationship with the composition or with the WC grain size could be established (Mingard, Roebuck, Marshall, & Sweetman, 2011). Although Co grains are interpenetrated, they can be delimited according to their orientation and they attain sizes much larger than the WC grain size (**Figure 2**). This size is influenced by the cooling rate, the amount of W dissolved in the binder and the cobalt content in the alloy (Weidow & Andrén, 2010a). It is also dependent on the WC grain size as cobalt likely nucleates on the surface of some WC grains, adopting a particular orientation relationship (Bounhoure, Lay, Loubradou, & Missiaen, 2008). Small fcc cobalt inclusions are also found in the WC grains with a shape and an orientation that minimize the interface energy (Mohan & Strutt, 1996).

Less data are available for the Ni-based binder since WC–Ni alloys represent a minor part of the cemented carbides. At the sintering temperatures, the two-phase field (WC + binder) is less extended than for WC–Co alloys and the solubility of WC is reduced compared to Co (Gabriel, Pastor, Deo, Basu, & Allibert, 1986; Wittmann, Schubert, & Lux, 2002). Concerning the size of the Ni-based pools, microstructural investigations reported in the literature indicate that both small and large binder grains relative to the WC structure are encountered in such alloys (Mingard et al., 2011).

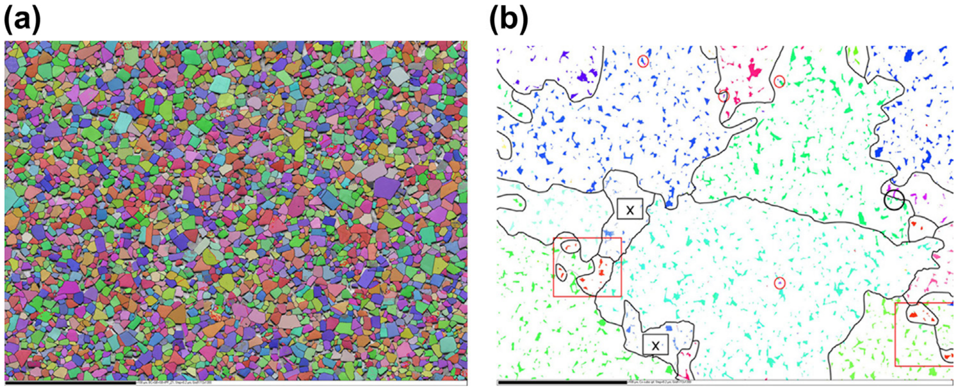

Figure 2 (a) EBSD orientation map of a WC–11Co (wt%) alloy and (b) corresponding fcc Co binder EBSD map where black lines delineate Co regions with the same orientation (scale marker = 100 μm) (Mingard et al., 2011).

1.03.2.2 Interface and Grain Morphology

The facetted shape of WC grains in WC–Co alloys is due to the development of low-energy habit planes. The stability of these facets is related to their relative energy. In what follows, present knowledge on WC/Co interfaces is reviewed with a special emphasis on the energies. The energy calculations are achieved using density functional theory (DFT) that is based on the determination of the ground-state electron density of the system. This approach may be very useful to compare different atomic configurations.

1.03.2.2.1 Wetting of WC

During liquid-phase sintering, the full densification can be achieved only if a good wetting of the hard phase by the binder occurs. The cohesion of the resulting WC–Co alloys is also related to the wetting behavior through the work of adhesion (Eqn (3)). The degree of wetting results from the energy balance between the surfaces of the system. It can be represented by the contact angle θ of the liquid on the solid surface under thermodynamical equilibrium:

$$\gamma_{SV} = \gamma_{SL} + \gamma_{LV} \cos\theta \tag{1}$$

where γ_{SV} and γ_{LV} refer to the surface energies of the solid and liquid, respectively, and γ_{SL} to the solid–liquid interface energy (Figure 3).

The magnitude of the contact angle can be obtained from the geometry of the drop. A small contact angle characterizes a good wetting of the solid by the liquid phase. Although sintering of a powder mixture requires an optimal wetting, few experimental data are available on wetting angles, surface and interface energies for carbides and metals used in the fabrication of cemented carbides. Only the surface energy of the liquid can be measured directly by different methods and the value determined for Co at 1420 °C is 1.91 J m^{-2} and for Ni at 1380 °C is 1.81 J m^{-2} (Ramqvist, 1965).

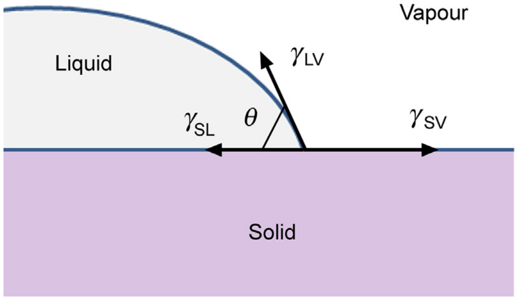

Figure 3 Contact angle θ of a liquid drop deposited on a solid for a solid–liquid–vapor equilibrium.

Table 1 Experimental values of wetting angles θ (°) and adhesion energies W_{ad} (J m^{-2}) for a range of materials used in the cemented carbide industry. The wetting experiments in Ramqvist (1965) were conducted at 1420 °C for Co, and at 1380 °C for Ni, in Warren and Waldron (1972a) between 1380 °C and 1450 °C

		WC	*TiC*	*TaC*	*VC*	*NbC*	*TiC–22WC*	*Mo_2C*
Co wetting	θ_{Co} (°)	0[a]	25[a] 26 ± 2[b]	13[a]	13[a] 13[b]	14[a] 11.5 ± 1[b]	21[a] 24.5[b]	0[a]
	W_{ad}[a]	3.82	3.64	3.77	3.77	3.76	3.69	3.82
Ni wetting	θ_{Ni} (°)[a]	0	23	16	17	18		0
	W_{ad}[a]	3.62	3.47	3.55	3.54	3.53		3.62

[a] *Ramqvist (1965).*

[b] *Warren and Waldron (1972a).*

The wetting angle of WC by molten Co was experimentally found to be close to zero, which indicates a complete wetting of WC grains by Co (Ramqvist, 1965) and participated to the success of this metal as a binder in the cemented carbide industry. The prevalence of Co as a binder is not only related to its wetting behavior. Other binders like Fe or Ni or combined with Co also offer a good wetting of WC (**Table 1**) and similar or superior mechanical properties were found for (Co–Ni–Fe)–WC alloys (Almond & Roebuck, 1988; Gille, Bredthauer, Gries, Mende, & Heinrich, 2000; Prakash, Holleck, Thümmler, & Walter, 1981). The main obstacle in the use of these alternative binders is the higher accuracy needed to control the carbon content of such alloys and to avoid the formation of complex carbides (Pastor, 1999). However, this difficulty should be overcome by choosing suitable compositions (Uhrenius, Pastor, & Pauty, 1997).

The wettability of a solid can also be quantified by the work of adhesion, W_{ad}. This quantity represents the external work required to separate the two crystals and create free surfaces of solid and liquid phases as expressed by the Dupré equation:

$$W_{ad} = \gamma_{LV} + \gamma_{SV} - \gamma_{SL} \tag{2}$$

By combining Eqns (1) and (2), the work of adhesion can be conveniently determined from the contact angle and the surface energy of the liquid:

$$W_{ad} = \gamma_{LV}(1 + \cos\theta) \tag{3}$$

Hence, in early studies of cemented carbides, the work of adhesion of the WC/Co interface was estimated to 3.82 J m^{-2} (Ramqvist, 1965). This high value emphasizes the good wettability of the carbide by the cobalt. A slightly lower value is found for the WC/Ni interface (**Table 1**).

Bonding at an interface can be quantified using DFT calculations by the work of separation W_{sep} that is the work to separate the interface between two solid phases into two free surfaces, without relaxation processes (Finnis, 1996, p. 422). According to the definition, the calculated values should be higher than the work of adhesion. As a consequence, the comparison between W_{ad} and W_{sep} should be only qualitative. DFT calculations were used to evaluate the work of separation of the WC{100}/Co{100} interface assuming the cubic NaCl crystallographic structure for WC, that is stable only at very high temperatures (Christensen, Dudiy, & Wahnström, 2002). A value close to 3.7 J m^{-2} was determined in the same range as the adhesion work found for this interface.

1.03.2.2.2 Interface Energy

WC has a hexagonal unit cell with the P-6m^2 space group and close lattice parameters $a = 0.2906$ nm, $c = 0.2837$ nm. Its stability is due to the formation of strong nearest-neighbor W–C bonds (Mattheiss & Hamann, 1984). Tungsten and carbon atoms lie at (000) and at (1/3, 2/3, 1/2) positions, respectively, so the structure of WC consists of alternate layers of tungsten and carbon atoms along [0001] or [10-10] directions (**Figure 4**). Each carbon atom lies in the centre of a trigonal prism delineated by six tungsten atoms and reversely. As seen on the drawing, carbon atoms occupy the γ sites and the β sites are empty. Consequently, the structure is not centrosymmetric such as (10-10) and (-1010) surfaces are not equivalent. Experiments including etching, sessile-drop wetting and hardness behavior have revealed this polar character of the prismatic surfaces of WC grains (French, 1969).

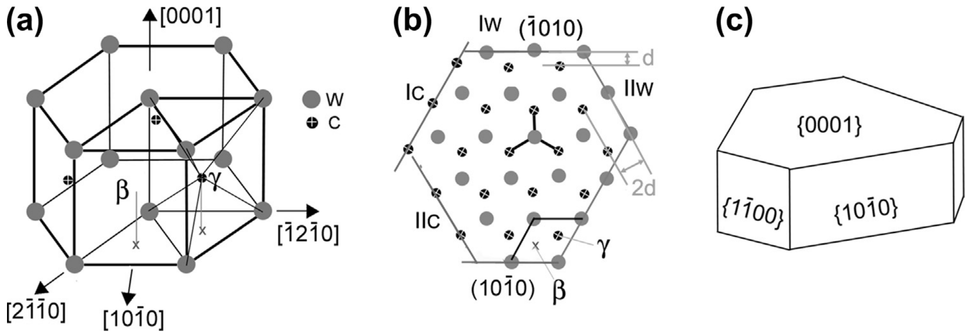

Figure 4 (a) Hexagonal unit cell of WC, (b) atomic projection along [0001] showing the four types of (10-10) prismatic facets denoted IW, IC, IIW and IIC on the drawing, and (c) morphology of WC grains in WC–Co alloys.

In WC–Co alloys, WC grains adopt the shape of a triangular prism with truncated corners delimited by {0001} basal and {10-10} prismatic facets (Exner, 1979) (**Figure 4(c)**). The grain shape is influenced by the carbon potential in the alloy, showing flat facets in C-rich alloys and some rounded parts and steps at WC/Co interfaces in W-rich alloys (Wang, Heusch, Lay, & Allibert, 2002) (**Figure 5**) (Kim, Han, Park, & Kim, 2003). The basal and prismatic planes play a major role in the microstructure formation of WC–Co alloys. According to the crystallographic structure of WC, two kinds of basal surfaces can arise, they can be carbon or tungsten terminated. On the other hand, there are two types of WC(10-10) surface, denoted I and II. For type I surface, the closest atoms lie at an interplane spacing of 0.084 nm while for type II, they lie at 0.168 nm (**Figure 4(b)**). Each type of facet can be carbon or tungsten terminated which leads to four candidate WC(10-10)/Co interfaces.

This faceted shape of carbide grains is caused by the anisotropy in WC/Co interface energy. The equilibrium shape corresponds to the minimal interface energy of the grain and reflects the relative stability of the habit planes (Herring, 1951). A theoretical estimation of the energy γ_{SL} of the WC/Co interface was carried out on the basis of thermodynamic considerations and a value of 0.5 J m^{-2} was deduced (Warren, 1980) (**Table 2**). Quantities like interface energies are difficult to get experimentally. For example, deducing the interface energy from wetting experiments requires the knowledge of the solid surface energy (Eqn (1)). However, unlike liquid surface energies, solid surface energies cannot be measured directly and only estimates are available. Moreover, in the case of ideal wetting in the WC/Co system, a lower bound can only be obtained. Estimates of surface energy were determined for several carbides using wetting data but these later caused controversies (Livey & Murray, 1956). Warren (Warren, 1976) has also determined lower values of the average energies γ_{SV}, γ_{SL} and of the average grain boundary energy γ_{SS} in systems with a continuous WC skeleton (Section 1.03.2.3.2). According to this study, a lower bound of 0.575 J m^{-2} is obtained for the WC/Co interface energy, which is a little higher than the thermodynamic calculation (**Table 2**). All these values do not account for the anisotropy of the interface energies.

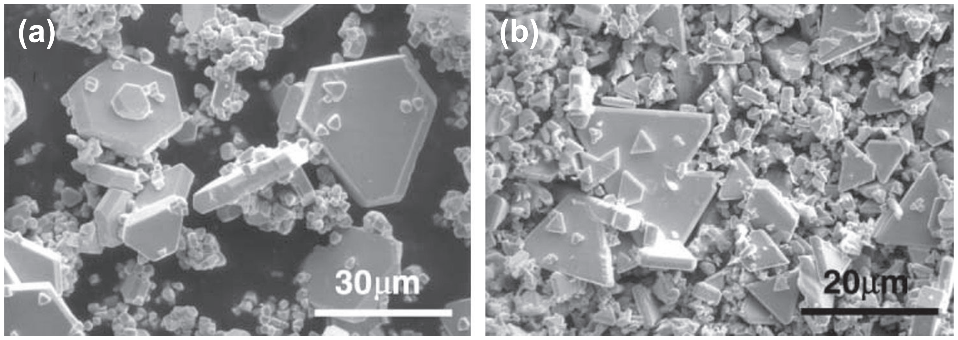

Figure 5 Morphology of WC grains extracted from specimens (a) WC–35%Co–0.7%C (1500 °C, 2 h) and (b) WC–35%Co–0.7%C (1500 °C, 5 h). The compact in (b) corresponds to the compact of (a) embedded in a pack of carbon-black powder and resintered in order to increase the carbon content of the alloy (Kim, Han, et al., 2003).

Table 2 Solid surface energy (γ_{SV}), interface energy (γ_{SL}) and grain boundary energy (γ_{SS}) estimates (expressed in J m^{-2}) based on experimental measurements (exp), thermodynamic calculations (therm) or calculated by DFT techniques as well as grain boundary energy variation due to Co segregation ($\Delta\gamma_{SS}$) (J m^{-2}) and dihedral angle (ϕ_{exp}) available for WC–Co and MC–Co alloys

	WC		*TiC*	*TaC*	*VC*
γ_{SV} exp	$>2.47 \pm 0.2$[a]		1.19 ± 0.35[b] 2.21 ± 0.2[a]	1.29 ± 0.39[b] 2.40 ± 0.2[a]	1.67 ± 0.5[b]
γ_{SL} exp	$>0.57 \pm 0.2$[a]		0.44[c]	0.47[c]	0.46[c]
γ_{SL} therm	0.5[d]				
γ_{SL} DFT	WC(10-10)/Co 0.7–2.9[e]	WC(0001)/Co 0.7–2.3[e]			
γ_{SS} exp	$>0.99 \pm 0.3$[a]		0.88 ± 0.3[a]	0.96 ± 0.3[a]	
γ_{SS} DFT clean boundary	0.03–7.41 1.9 (mean value) ($\Sigma = 2$ twist)[f] 2.1–2.6 ($\Sigma = 2$ tilt)[g] 2.7 (mean value) (generic)[f]				
$\Delta\gamma_{SS}$ DFT Co segregation	-0.4 ($\Sigma = 2$ tilt)[g]				
ϕ exp (°)	≈ 60[h]		25–27[i]		6–8[i]

[a] *Warren (1976).*

[b] *Livey and Murray (1956).*

[c] *Warren and Waldron (1972b).*

[d] *Warren (1980).*

[e] *Christensen et al. (2007).*

[f] *Christensen and Wahnström (2003).*

[g] *Christensen and Wahnström (2004).*

[h] *Deshmukh and Gurland (1986).*

[i] *Warren and Waldron (1972a).*

The measurements of the interface energy of each facet would be extremely tricky. DFT calculations were used for assessing the energy of the different types of habit planes. At the sintering temperature, the binder is liquid so cobalt atoms are mobile and the atomic structure of the interface is constantly changing. In order to get reasonable quantities for the energy, an upper and a lower limit were defined and inside the interval of energy, the parameter α was used to characterize the degree of coherency at the interface (Christensen, Wahnström, Lay, & Allibert, 2007):

$$\gamma = \gamma_{\min} + \alpha(\gamma_{\max} - \gamma_{\min}) \text{ with } 0 < \alpha < 1 \tag{4}$$

For $\alpha = 0$, the energy is minimum and the interface is assumed to be coherent, while for $\alpha = 1$, the interface is completely incoherent. In these calculations, the effect of carbon chemical potential was also taken into account.

The four types of (10-10) facets, denoted I and II, terminated by W or carbon atoms, were examined (Christensen et al., 2007; Christensen, Wahnström, Allibert, & Lay, 2005). For each type of facet, three atomic configurations at the interface were considered (**Figure 6**) and their energy was calculated. Values in the range of 0.7–2.9 J m^{-2} were found (**Figure 7(a)**) (**Table 2**). Most stable interfaces are determined to be W-terminated whatever the carbon content of the alloy. This is due to the formation of metal--metal bonding across the interface. Moreover, type I facets have a lower energy. According to these results, the set of most developed facets are expected to be of type I. Both types of facets are W-terminated independently on the carbon content. High-resolution transmission electron microscopy (HRTEM) characterization of the prismatic facets is in agreement with these calculations (Lay, Donnadieu, & Loubradou, 2010).

The same approach was used to model the WC(0001)/Co interface (Christensen et al., 2007). C- and W-terminated basal facets were considered and in each case, four atomic configurations were assumed. An upper and a lower limit of the energy were deduced as a function of the coherency parameter in a W- or C-rich alloy.

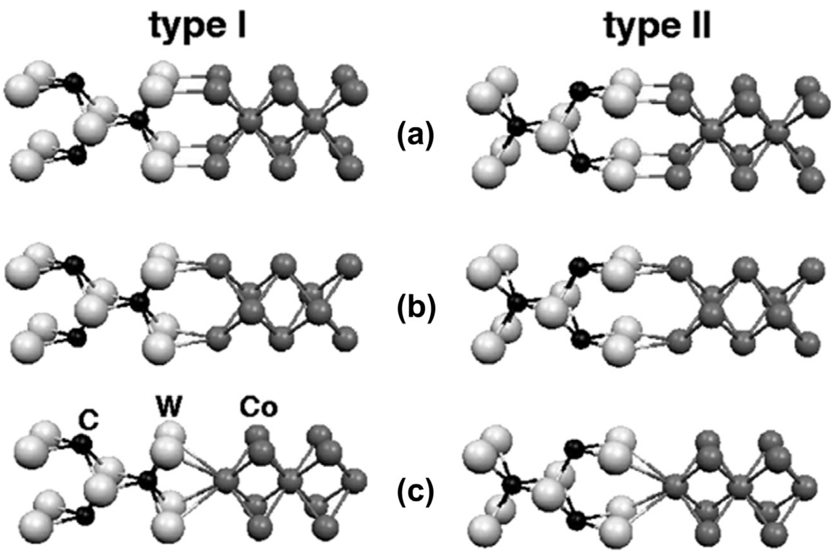

Figure 6 Models of WC(10-10)/Co facets terminated by tungsten atoms used to calculate the interface energy. Three relative positions (a-c) of the cobalt atoms at the interface were considered.

The energy of the basal facets is in the same range as the prismatic facets, between 0.7 and 2.3 J m^{-2} (**Figure 7(b)**; **Table 2**). In the W-rich alloy, the most stable interface is W-terminated while in the C-rich limit, the basal facet is C- or W-terminated depending on the degree of coherency. These energy values were used as shown in the following to predict the WC grain morphology as a function of the carbon content.

Interface energy values deduced from DFT calculations are significantly higher than the values obtained by Warren (1976) (**Table 2**).

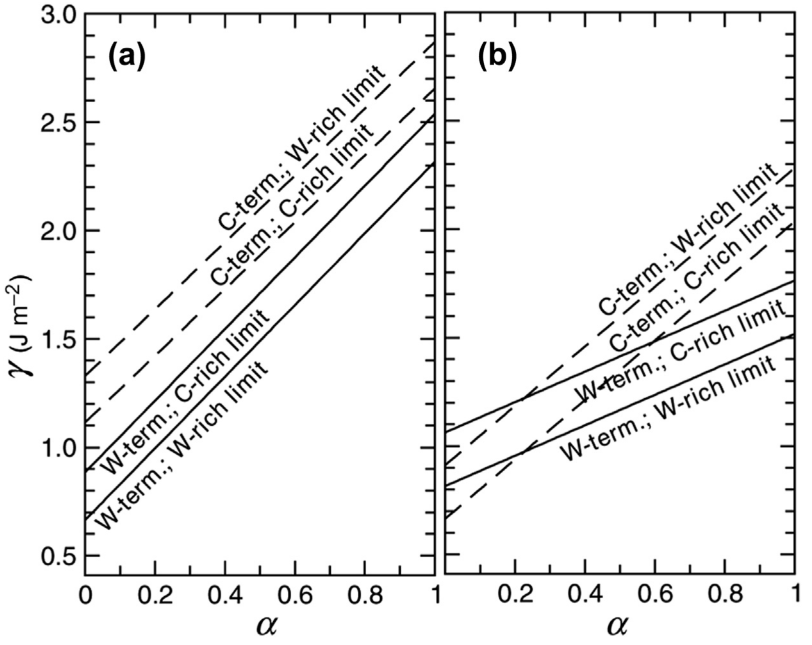

Figure 7 Interface energy of W- or C-terminated (a) prismatic and (b) basal facets as a function of the coherency parameter α for a WC–Co alloy lying in the C-rich or W-rich limit. For sake of clarity, an average value for type I and II facets is plotted for prismatic interfaces (Christensen et al., 2007).

1.03.2.2.3 WC Grain Shape Quantification

In the condition of an equilibrium shape, the energy ratio between the facets can be deduced from the shape of the WC grains. This requires a large volume of Co to decrease the effect of WC/WC contacts and long sintering times to get the equilibrium shape. Two parameters were defined to characterize the facetted shape of WC grains: the truncation and the elongation factors. The truncation factor r is the ratio between the lengths of the two types of facets: it expresses the anisotropy between the two sets of prismatic facets. The elongation factor k is the ratio of the thickness of the prism, t, over the height, h, of the truncated triangle. It measures the anisotropy between the prismatic facets and the basal facet (**Figure 8**).

$$r = \sum a_{\text{short}} / \sum a_{\text{long}} \tag{5}$$

$$k = t/h \tag{6}$$

If the shape is governed by the minimization of the energy, the shape parameters are related to the interface energies:

$$r = \frac{\dfrac{2\gamma_{\text{Plong}}}{\gamma_{\text{Pshort}}} - 1}{\left(2 - \dfrac{\gamma_{\text{Plong}}}{\gamma_{\text{Pshort}}}\right)} \tag{7}$$

$$k = \frac{2\gamma_{\text{B}}(2r+1)}{3\gamma_{\text{Plong}}(r+1)} \tag{8}$$

where γ_{Plong} (γ_{Pshort}) is the energy of the largest (smallest) prismatic facets and γ_{B} the energy of the basal facet.

Using the calculated energies of the facets, the shape parameters were determined including the effect of carbon chemical potential for WC–Co alloys (Christensen et al., 2007) (**Figure 9**). For simplicity, the same α value was chosen for basal and prismatic interfaces. The calculation results in a truncation and elongation factor close to 0.2 and 0.7, respectively, in the incoherent limit whatever the carbon content. However, the atomic

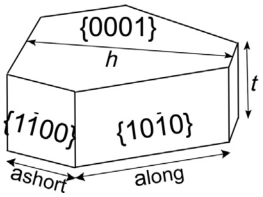

Figure 8 Parameters used for the determination of the shape factors.

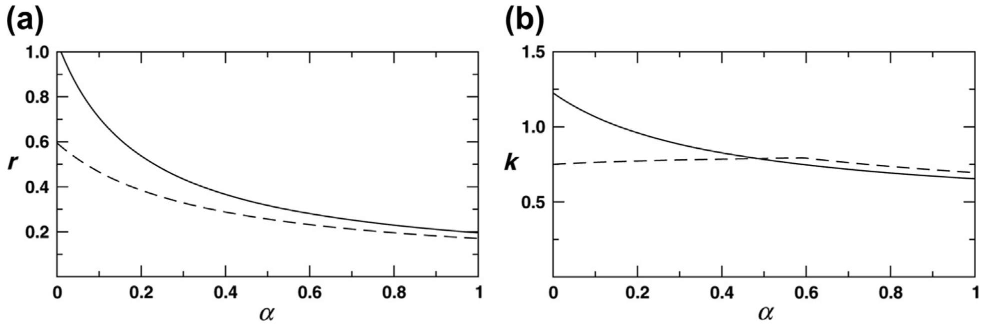

Figure 9 (a) Truncation parameter and (b) elongation parameter as a function of the parameter α. Solid and dashed lines correspond to W-rich and C-rich WC–Co alloys, respectively (Christensen et al., 2007).

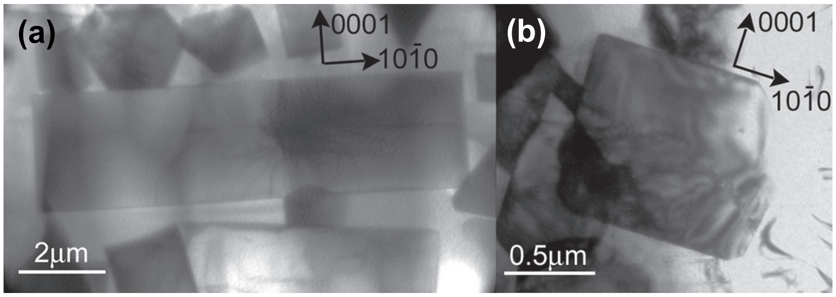

Figure 10 TEM images of WC grains viewed along [1-210] direction (a) in a C-rich alloy ($k = 0.27$), (b) in a W-rich WC–Co alloy ($k = 0.87$) (Lay et al., 2008).

configurations at basal and prismatic habit planes are different. Hence, preferential orientations of cobalt exist at basal facets so the coherency could be higher than for the prismatic facet (Bounhoure et al., 2008).

Up to now, few attempts were devoted to the experimental quantification of the WC grain shape and the question remains opened. In a systematic work conducted in commercial alloys by combining atomic force microscopy and EBSD techniques, elongation values in the range 1–1.4 were found for alloys with various Co contents, smallest values corresponding to the largest Co contents (Kim, Massa, & Rohrer, 2008). Note that in this study, the shape of the grains was assumed to be a triangular prism and the composition of the alloy, especially the carbon content, was not mentioned. Moreover, due to the short sintering durations, the equilibrium shape for the WC grains may not be achieved.

From transmission electron microscopy (TEM) investigations in alloys containing a large amount of cobalt and sintered for a long time, rather similar truncation factors, 0.14 and 0.25, were found in the C-rich and W-rich alloy, respectively, in agreement with DFT calculations, while very different values were deduced for the elongation factor, 0.25 and 0.82, respectively (**Figure 10**) (Lay, Allibert, Christensen, & Wahnström, 2008). These later disagree with the work conducted by Kim et al. (2008). Otherwise, the elongation value matches well with calculations in the W-rich alloy but not in the C-rich alloy. In the C-rich limit, grain growth behavior is much increased (Chabretou, Allibert, & Missiaen, 2003), so grain morphology can be influenced by the dissolution/growth rate of the facets (Shatov, Firstov, & Shatova, 1998). The elongation factor could characterize a growth shape while in the W-rich limit, the grain shape should be closer to the equilibrium. These studies confirm that the grain morphology strongly depends on the carbon content.

1.03.2.2.4 Effect of Transition Metals Addition

Carbides of transition metals like VC, Cr_3C_2, NbC, and TaC are added in the cemented carbides in small quantities to act as grain growth inhibitors as first reported in Suzuki, Fuke, and Hayashi (1972) and Hayashi, Fuke, and Suzuki (1972). Detailed microstructural investigations have shown that not only the carbon content but also the addition of transition metals influences the WC grain shape. The WC grain morphology and therefore the relative stability of the facets are modified by these additives. When VC or Cr_3C_2 is used, WC grains are less truncated and steps are observed at the interface (Delanoë & Lay, 2009; Lee, Kim, Hwang, & Kim, 2003; Wang, Pauty, Lay, & Allibert, 2002; Yamamoto, Ikuhara, & Sakuma, 2000) while the addition of TiC in WC–Ni alloys induces grains with a lower elongation (Shatov et al., 1998). After cooling, some transition metal atoms are detected at WC/Co interfaces and thin (M,W)C cubic carbide films (M being V, Cr, and Ti) can be observed on the surface of the WC grains (**Figure 11**) (Delanoë, Bacia, Pauty, Lay, & Allibert, 2004; Kawakami, Terada, & Hayashi, 2006; Lay, Hamar-Thibault, & Lackner, 2002; Weidow & Andrén, 2010b; Weidow & Andrén, 2011; Yamamoto et al., 2000; Yamamoto et al., 2001).

The propensity for thin cubic film formation in the WC/Co interface at the sintering temperature and the associated change in energy was investigated by DFT calculations (Johansson & Wahnström, 2011). According to this approach, VC, MoC, TiC and CrC cubic carbide films may form at high temperature on the basal facet of WC with a decreasing stability from VC to CrC. The tendency for film formation is much smaller for MoC, VC and CrC on the type I prismatic facet and only MoC is expected on the type II prismatic facet. The calculations predict only very thin films of one or two atomic layers at high temperature. Upon cooling, the solubility of the transition element in the binder decreases and as a result, the thickness of the (M,W)C layer is expected to increase. The film thickness will therefore depend on the amount of additives and on the cooling rate as pointed

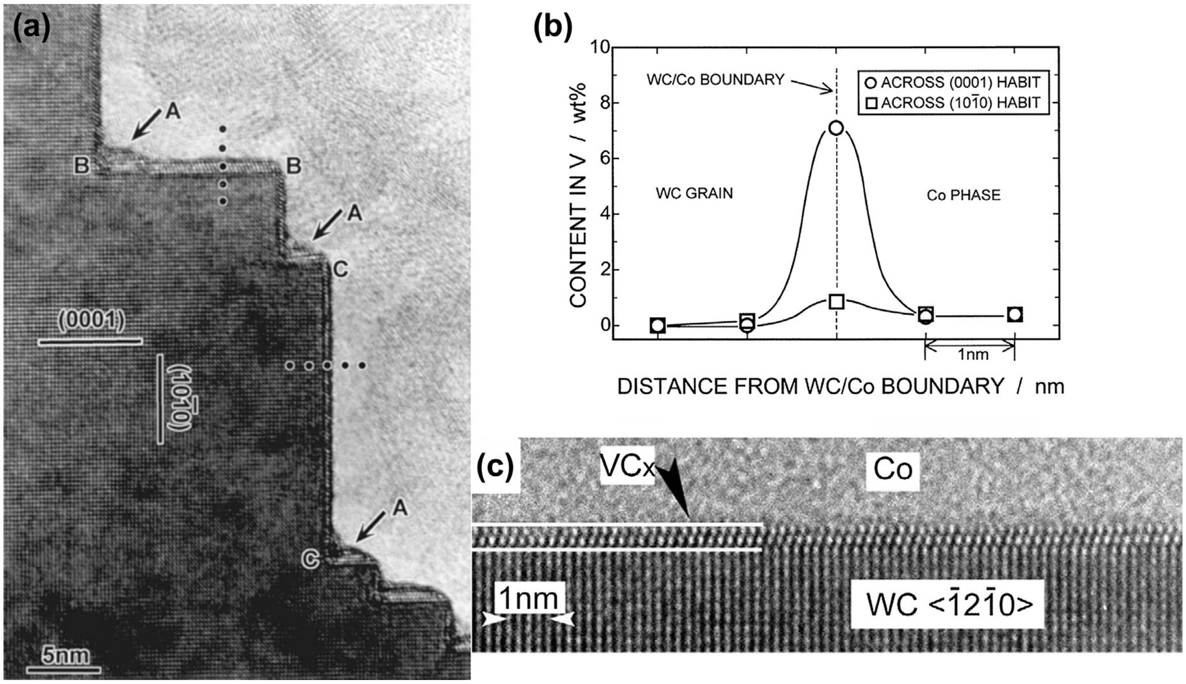

Figure 11 (a) HRTEM image in the WC–12Co–0.5VC (wt%) alloy after liquid-phase sintering. The WC grain shows a stepped interface with Co that consists of (0001) and (10-10) habit planes and a compound is visible on the (0001) facets. (b) V concentration profile carried out across the (0001) facet (denoted B–B in (a)) and (10-10) facet (C–C) (Yamamoto et al., 2000). (c) Image of the cubic MC layer on the basal habit plane in a WC–9.5Co–0.5VC (wt%) alloy (Lay, Hamar-Thibault, & Loubradou, 2004).

out by Kawakami, Terada, and Hayashi (2004). The shape changes of WC grains recorded in alloys containing grain growth inhibitors are consistent with the film formation. For example, VC is expected to form on only one of the two types of prismatic facets, thus increasing the energy anisotropy between them (Johansson & Wahnström, 2011).

1.03.2.3 Microstructure of the WC Hard Phase

Mechanical properties of hardmetals are monitored by the properties of the hard phase and of the binder as well as by their distribution in the alloy. Whether the hard phase is dispersed in the binder or forms a skeleton through the alloy will influence the mechanical behavior of the alloy. The existence of a hardmetal skeleton was investigated in the cemented carbide WC–Co. This part is first devoted to the orientation relationships and atomic configurations at WC/WC grain boundaries. Then, aspects of energy, segregation and infiltration of grain boundaries will be presented. Finally, the existence of a carbide skeleton will be discussed as well as main factors influencing its formation and stabilization.

1.03.2.3.1 Orientation and Structure of WC/WC Grain Boundaries

Several works performed at different scales were devoted to the study of WC/WC grain boundaries. The mutual orientation relationships and the habit plane of the boundaries were first characterized by TEM and HRTEM and more recently by EBSD. The EBSD analyses have the advantage to quantify the relative frequency of boundaries according to their misorientation angle. The distribution of orientation of habit planes can also be deduced after a statistical treatment (Saylor & Rohrer, 2002).

The EBSD studies performed in WC–Co alloys with different Co contents and grain sizes indicate that some mutual misorientations are favored (Farooq & Klement, 2004; Kumar, Fang, Wright, & Nowell, 2006; Kim & Rohrer, 2004; Kim et al., 2008). Three types of special grain boundaries are found in all alloys: mainly 90° rotations about the [10-10] axis are encountered, making up 11–14% of the grain boundaries, then rotations close to 30° about the [0001] axis correspond to 2–3% of the population and finally 90° rotations about [2-1-10] occur in a much smaller amount.

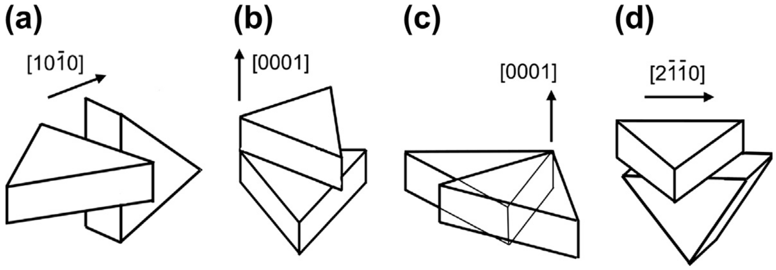

Figure 12 Geometry of the four most common types of WC/WC special grain boundaries in WC–Co. (a) 90°/[10-10] with a (10-10)$_{1,2}$ habit plane (b) 30°/[0001] boundary with a (0001)$_{1,2}$ habit plane (c) 30°/[0001] boundary with a (2-1-10)$_1$(10-10)$_2$ habit plane and (d) 90°/[2-1-10] boundary with a (0001)$_1$(01-10)$_2$ habit plane.

The 90°/[10-10] boundaries are twist boundaries with a (10-10)$_{1,2}$ habit plane. The 30°/[0001] boundaries are either twist boundaries with a (0001)$_{1,2}$ habit plane or asymmetrical tilt boundaries with the (2-1-10)$_1$(10-10)$_2$ habit plane. The 90°/[2-1-10] boundaries are asymmetrical tilt boundaries with a (0001)$_1$(01-10)$_2$ habit plane (**Figure 12**). The special grain boundaries identified by EBSD account for <20% grain boundaries. However, the remaining 80% grain boundaries are not random as pointed out by TEM observations.

TEM studies have used the concept of coincidence site lattice (CSL) to characterize the grain boundaries (Bollmann, 1970). In this approach, the lattices of the crystals meeting at the boundary are interpenetrated. For some relative orientations, common lattice nodes exist forming the CSL. A coincidence index, Σ, is associated with the CSL, and characterizes the density of coincidence sites relative to the lattice of the crystals. In hexagonal materials, exact CSLs only arise for rotations about [0001] axis. Near CSLs can be defined by approximating the $(c/a)^2$ value (where a and c are the lattice parameters of the material) by a rational number (Grimmer, 1989). For WC, a list of CSLs was established for $(c/a)^2 = 1$ to describe and classify the grain boundaries (Hagége, Nouet, & Delavignette, 1980). Owing to the hexagonal symmetry, each CSL can be described by 12 rotation angle/axis pairs. In **Table 3**, only the rotation pair with the smallest rotation angle is given for Σ values lower than 26.

Table 4 summarizes the orientation relationships that were determined by TEM in WC–Co alloys (Benjdir, 1991; Vicens, Benjdir, Nouet, Dubon, & Laval, 1994; Vicens, Lay, Benjdir, & Nouet, 1990; Yamamoto et al., 2001). Mainly three families of grain boundary orientations were found. The first family, independent on the $(c/a)^2$ value, with a [0001] rotation axis and a (0001)$_{1,2}$ habit plane, consists in grain boundaries with a twist character. Compared to **Table 3**, other CSLs are expected like $\Sigma = 7$a, 19a, … In the second family ($\Sigma = 2$, 5 …), the rotation axis is [10-10] and the habit plane is usually (10-10)$_{1,2}$, so the grain boundaries have also a twist character. The third family ($\Sigma = 4$, 28a …) is described by a rotation about [2-1-10]. These grain boundaries have an asymmetrical tilt character with a (01-10)$_1$(0kil)$_2$ or (0001)$_1$(0kil)$_2$ habit plane.

When analyzing the EBSD results using the CSL approach, the 90°/[10-10] twist boundaries correspond to the $\Sigma = 2$ grain boundaries, the 30°/[0001] twist or asymmetrical tilt boundaries to the $\Sigma = 13$a grain boundaries and the 90°/[2-1-10] asymmetrical tilt boundaries to the $\Sigma = 97$ grain boundaries.

Table 3 List of the rotations leading to exact coincidence established for $(c/a)^2 = 1$ and $\Sigma \leq 26$. The angle/axis pair is expressed in the standard stereographic triangle [2-1-10], [10-10], and [0001] (Hagége et al., 1980)

Σ	α (°)	[uvtw]	Σ	α (°)	[uvtw]	Σ	α (°)	[uvtw]	Σ	α (°)	[uvtw]	Σ	α (°)	[uvtw]
2	90	10-10	10b	69.51	20-21	16a	57.91	4-2-23	20a	28.96	4-2-23	25a	51.68	40-43
4	60	2-1-10	11	76.86	8-4-43	16b	82.82	3-1-20	20b	77.00	6-2-43	25b	73.74	10-10
5	53.13	10-10	13a	27.80	0001	17a	28.07	10-10	22a	32.76	20-23	25c	91.15	8-4-43
7a	21.79	0001	13b	32.20	2-1-10	17b	63.82	40-43	22b	45.21	20-21	26a	22.62	10-10
7b	81.79	2-1-10	13c	67.38	10-10	19a	13.17	0001	22c	83.47	20-21	26b	63.75	10-2-83
8	46.57	4-2-23	14a	41.41	20-23	19b	46.83	2-1-10	23a	50.92	8-4-43	26c	93.31	8-2-63
10a	36.87	10-10	14b	92.05	10-2-83	19c	74.74	5-1-40	23b	66.96	3-1-20			

Table 4 Grain boundaries in WC–Co alloys observed by Benjdir (1991), Vicens et al. (1990), Vicens et al. (1994) and Yamamoto et al. (2001) classified according to the CSL approach. The rotation angle/axis pair is recalled for each CSL as well as the observed grain boundary plane. The angular deviation from the reference CSL is mostly below 3°. For the rotations about the [2-1-10] axis, a (0kil) plane of crystal 2 found close to the (0001) or (10-10) plane of crystal 1 has been determined

CSL			*Experimental*
Σ	α(°)	*[uvtw]*	*Boundary plane (hkil)$_1$(hkil)$_2$*
13a	27.80	[0001]	(0001)$_{1,2}$
67e	24.43	"	(0001)$_{1,2}$
2	90	[10-10]	(10-10)$_{1,2}$
2	"	"	(0001)$_1$(1-210)$_2$
5	53.13	"	(10-10)$_{1,2}$
26a	22.62	"	(10-10)$_{1,2}$
4	60	[2-1-10]	(0001)$_1$(0-332)$_2$
28a	21.79	"	(0001)$_1$(0-113)$_2$
37d	69.43	"	(01-10)$_1$(01-13)$_2$
			(03-31)$_1$(0001)$_2$
43d	75.18	"	(0001)$_1$(0-331)$_2$
49a	16.43	"	(01-10)$_1$(03-31)$_2$
61j	52.66	"	(0001)$_1$(0-111)$_2$
67f	24.42	"	(0001)$_1$(0-113)$_2$
97	89.41	"	(0001)$_1$(0-110)$_2$
14b	92.05	[10-2-83]	(0001)$_1$
32b	55.77	[31-20]	(10-11)$_1$
40e	89.28	[10-4-63]	(1-2-31)$_1$(1-102)$_2$
50b	23.07	[2-1-13]	(10-11)$_{1,2}$

Some grain boundaries have been characterized at the atom scale like the $\Sigma = 2$ twist boundary (**Figure 13**). This grain boundary shows a very good continuity of the crystal lattices across the habit plane except at the level of regularly spaced steps and is considered to be the most stable boundary, as will be discussed later. These steps reveal an array of dislocations that compensate for the difference between a and c lattice parameters according to the relationship $41a = 42c$. The dislocations are usually associated with a step height of one (10-10) plane and have a Burgers vector of 1/6[-12-13] type. Consequently, the spacing between the dislocations is close to $21c$, i.e. 5.95 nm. Other dislocations with a step of two (10-10) planes have a Burgers vector equal to 1/3[-12-10]$_1$ or

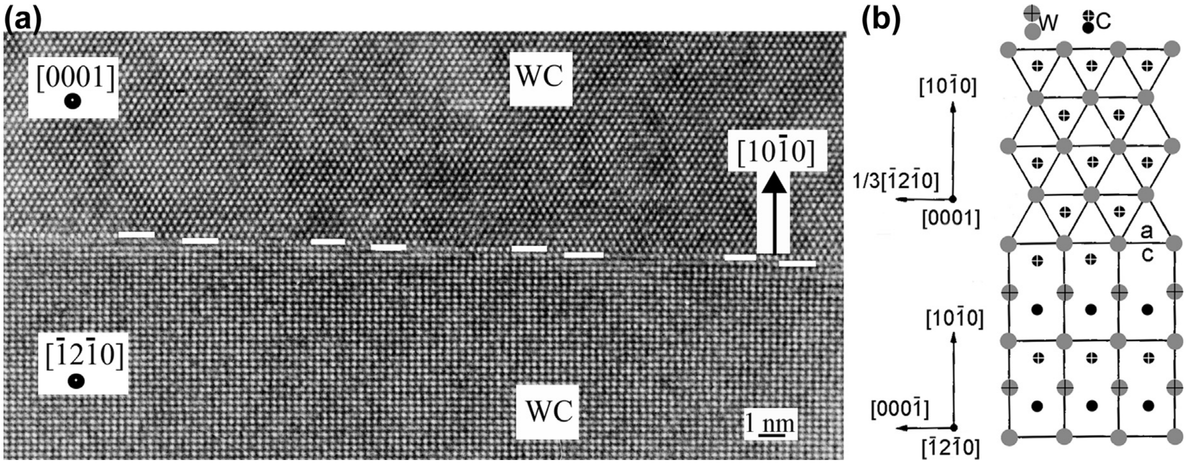

Figure 13 (a) HRTEM image of the $\Sigma = 2$ twist boundary showing regularly spaced steps compensating for the parametric mismatch at the interface. (b) Projection of the crystal lattices assuming $c/a = 1$.

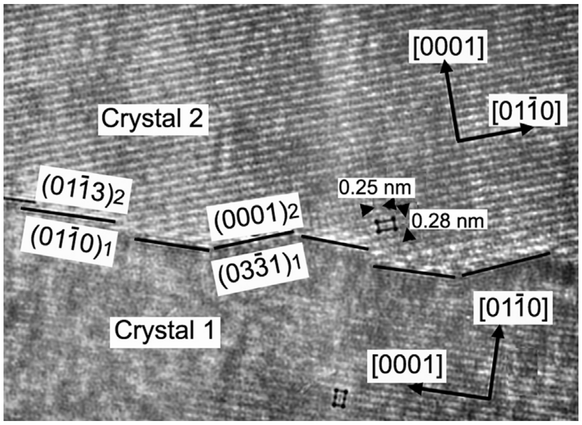

Figure 14 HRTEM micrograph of the $\Sigma = 37$d grain boundary viewed along [2-1-10]$_{1,2}$ direction (Benjdir, 1991).

[000-1]$_2$ (Vicens, Laurent-Pinson, Chermant, & Nouet, 1988). Note that the $\Sigma = 2$ tilt asymmetric boundary with a (0001)$_1$(1-210)$_2$ habit plane is also sometimes encountered but with a much smaller frequency than the $\Sigma = 2$ twist boundary. The presence of many $\Sigma = 2$ grain boundaries in WC–Co alloys questions about their origin. TEM and EBSD observations have revealed that a large amount of these boundaries already exists in WC powder (Kim, Kang, & Lee, 2005; Kumar et al., 2006; Lay & Loubradou, 2003; Mannesson, Elfwing, Kusoffsky, Norgren, & Ägren, 2008).

All grain boundaries cannot be observed by HRTEM because most of the time, there is no observation direction parallel to the boundary plane giving rise to an atomic resolution in both crystals. Fortunately, the tilt [2-1-10] boundaries have a suitable geometry and could be examined by this method. They reveal the faceting of the boundary habit plane to get parallel to (0001) or (10-10) densest planes of WC (**Figure 14**).

More generally, TEM observations indicate that the habit plane of grain boundaries is usually a basal or prismatic facet at least for one grain. EBSD measurements detect about 60% of the grain boundary habit planes to be basal or prismatic planes. As grain boundary faceting occurs at a nanometer scale, this amount is probably larger.

1.03.2.3.2 Grain Boundary Energy

Only scarce experimental data of the grain boundary energy γ_{SS} are available in the literature. Warren has determined lower values of γ_{SV}, γ_{SS} and γ_{SL} using contiguity measurements associated to a microstructural model and assuming a constant value of 0.4 for γ_{SS}/γ_{SV} (Warren, 1976) (**Table 2**). Experimental conditions were designed to get equilibrium microstructures, by preparing alloys with a liquid fraction as high as 50 vol% and a holding time as long as 7 h. These data were deduced from measurements performed on random metallographic sections of WC–Co alloys and provide an average value of the energies. A lower limit of the WC grain boundary energy close to 1 J m^{-2} was obtained.

Grain boundary energy is a quantity that can be calculated by DFT from the work of separation and surface energies. Data are available for three types of grain boundaries, the $\Sigma = 2$ twist boundary (Christensen & Wahnström, 2003), the $\Sigma = 2$ asymmetrical tilt boundary (Christensen & Wahnström, 2004), and the 27°/[10-10] model twist boundary (Christensen & Wahnström, 2003). The first one, often observed, is considered to be a stable boundary and to represent the lowest energy, the second one, much more seldom, is probably less stable while the last one is assumed to be representative of a generic grain boundary.

The comparison of the works of separation indicate that the $\Sigma = 2$ asymmetrical tilt boundary is much weaker than the $\Sigma = 2$ twist boundary and somewhat weaker than the generic grain boundary. For the $\Sigma = 2$ twist boundary, minima in energy are obtained for relative positions of the atoms corresponding to the bulk and a mean energy value of this boundary was evaluated to 1.9 J m^{-2} (values in the range 0.03–7.41 J m^{-2}) (**Table 2**). For the $\Sigma = 2$ asymmetrical tilt boundary, the energy depends on the termination of the (0001) plane. It is in the range 2.1–2.6 J m^{-2} and 3.7–4.4 J m^{-2} when the (0001) plane is W- and C-terminated, respectively. According to these calculations, only W-terminated grain boundaries are expected to be stable. A value of 2.69 J m^{-2} is found for the [10-10] 27° twist boundary. These calculated values are higher than the value of Warren. Note that they were obtained for clean grain boundaries. They can be slightly lowered by the segregation of cobalt as will be seen below.

1.03.2.3.3 Segregation of 3D-Transition Metals to WC/WC Grain Boundaries

The existence of cobalt films in WC/WC grain boundaries has been a debate for a long time in the community of cemented carbides, the history of which is detailed in (Henjered, Hellsing, Andrén, & Norden, 1986). In the 1980's, a consensus was established that the grain boundaries do not contain a continuous film but half a monolayer of segregated cobalt instead (Henjered et al., 1986). More detailed analyses indicate that the amount depends on the geometry of the grain boundary. A higher amount of segregated cobalt is detected when the grain boundary habit plane is not the basal or the prismatic plane of one of the adjacent grains or when dislocations are present (Vicens et al., 1994).

The effect of cobalt segregation on the work of separation of grain boundaries was investigated using DFT (Christensen & Wahnström, 2004). Calculations were carried out for various atomic configurations of the $\Sigma = 2$ asymmetrical tilt WC(0001)/WC(1-210) boundary, using also the geometries with the highest energies in order to evaluate the ability of Co to stabilize generic grain boundaries. Only substitutional segregation was considered because of the restricted number of interstitial positions large enough to accommodate the segregated atoms. For the most stable atomic configuration where the basal plane at the boundary is W-terminated, it was observed that the replacement of both carbon and tungsten atoms in the WC(1-210) boundary plane by cobalt atoms in a proportion of half a monolayer is energetically favorable and induces a reduction of the boundary energy of about 0.4 J m^{-2} (**Table 2**). On the other hand, the segregation of a complete Co monolayer decreases the stability of the boundary. Using the less stable atomic configurations of this grain boundary to stand for generic boundaries, the same result is obtained in agreement with experiments (Henjered et al., 1986).

Calculations emphasize similar effects for the other 3d-transition metals Ti, V, Cr and Mn. For these metals, the propensity for segregation is unfavorable in the most stable configurations of the $\Sigma = 2$ asymmetrical tilt boundary but highly favorable in the less stable ones. In the latter, interfacial carbon–carbon bonds are replaced by stronger metal–carbon bonds that strengthen the grain boundary cohesion (Christensen & Wahnström, 2006). The segregation of V and Cr atoms was experimentally verified (Henjered et al., 1986; Weidow & Andrén, 2010b; Yamamoto et al., 2000; Yamamoto et al., 2001). Moreover, Ti, Zr, and Nb were also shown to segregate in grain boundaries unlike Ta (**Figure 15**) (Weidow & Andrén, 2011).

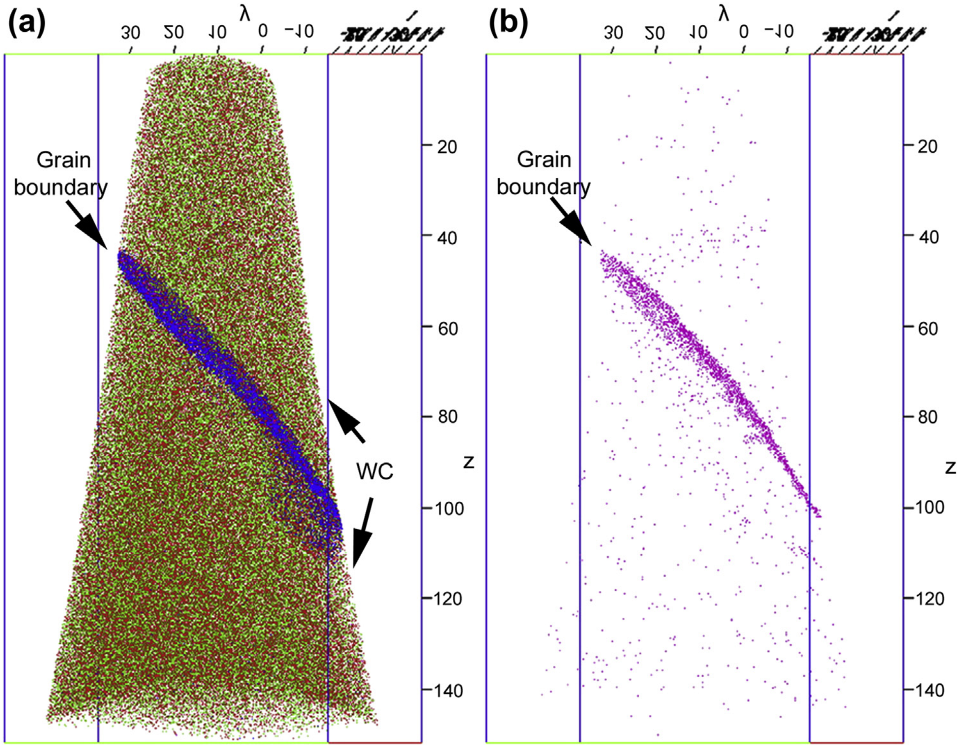

Figure 15 Analysis of a WC/WC grain boundary in a WC–TiC–Co alloy by atom probe tomography showing the presence of Co and Ti atoms. (a) Green dots = W atoms, red = C, blue = Co, pink = Ti. (b) Pink dots = Ti atoms (Weidow & Andrén, 2011).

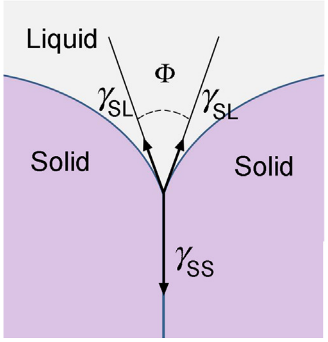

Figure 16 Dihedral angle between contacting grains at equilibrium with a liquid phase.

1.03.2.3.4 Stability of WC/WC Grain Boundaries and Infiltration by Co

Microstructural investigations of WC–Co alloys have revealed the diversity of WC/WC grain boundary geometries with the prevalence of some special boundaries. DFT calculations indicate that these boundaries have different energy levels. During sintering, the formation of contacts between WC grains and the resistance to infiltration of grain boundaries present in the powder depend on the energy ratio of the solid/solid grain boundaries and solid/liquid interfaces. Assuming isotropic interface energies and the equilibrium state, the grain boundary energy γ_{SS} is related to the interface energy γ_{SL} by the relationship

$$\gamma_{SS} = 2\gamma_{SL}(\cos \phi/2) \tag{9}$$

where ϕ is the dihedral angle formed at the intersection of the liquid with the grain boundary (**Figure 16**). If γ_{SS}/γ_{SL} energy ratio is larger than 2, the boundary is infiltrated by the liquid so the solid/solid grain boundary is replaced by two solid/liquid interfaces and the dihedral angle is equal to 0.

Using the estimate of 1.7 for the energy ratio in conditions close to equilibrium (Warren, 1976), a dihedral angle close to 60° may be deduced according to relation (9). Besides dihedral angles between faces of contacting grains were measured on cross-sections of samples sintered for 100 h at 1450 °C with about 40 vol% liquid (Deshmukh & Gurland, 1986). The distribution of dihedral angles shows pronounced peaks at 60° and 90° and a median value close to 60° (**Figure 17**). This distribution was shown to reflect the anisotropic shape of WC grains and the orientation relationships between grains as the most frequent dihedral angles are compatible with special grain boundary geometries already detected by TEM and EBSD.

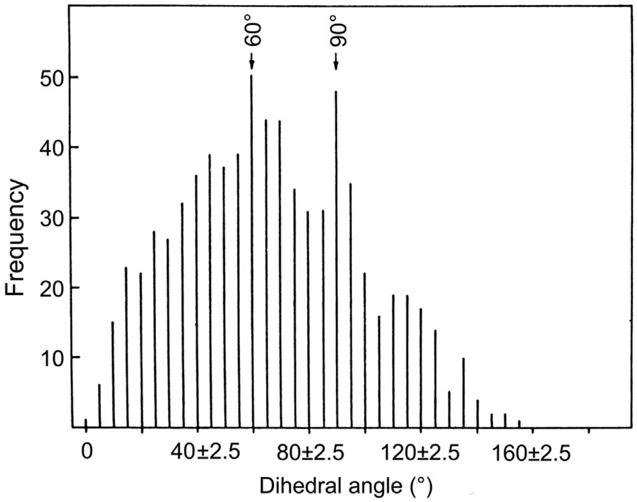

Figure 17 Measured dihedral angles of contact between WC grains in WC–25 wt% Co sintered 100 h at 1450 °C (from Deshmukh & Gurland, 1986).

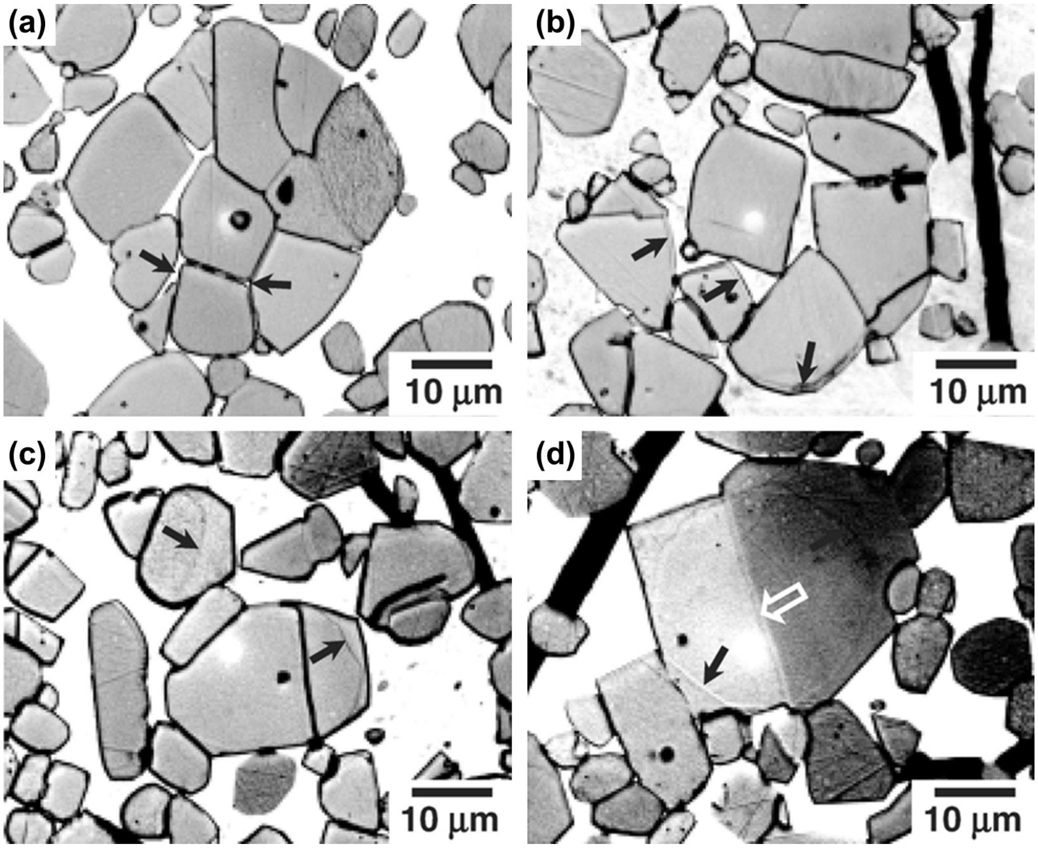

Figure 18 Microstructure of the WC–0.75 wt% Mo2C–25 wt% Co–0.2wt% C alloy sintered at 1450 °C for (a) 1 min, (b) 1 h, (c) 3 h, and (d) 27 h. The black arrows indicate, in (a) the infiltration of Co in the grain boundaries, and in (b–d) the position of the (W,Mo)C layer. The open white arrow in (d) points a grain boundary that arises from the powder (Kim et al., 2005).

Evidence for cobalt infiltration in grain boundaries preexisting in the powder was given during sintering of coarse WC powder with a small addition of Mo_2C (Kim et al., 2005). On heating, Mo_2C dissolves in the binder together with WC and owing to the solubility of Mo atoms in WC (Schubert, Ettmayer, Lux, & Ohlsson, 1981), the (W,Mo)C phase reprecipitates on WC grains thus revealing the growth layer. It was shown that many grain boundaries are already penetrated at the start of the liquid-phase sintering, and finally most of them are destroyed (**Figure 18**). Note that these observations cannot strictly apply for WC–Co alloys since the introduction of Mo modifies the interface energies. Lisovsky (2009) also indicates that many grain boundaries are unstable in sintered materials and may be penetrated by the liquid in imbibition experiments (Section 1.03.2.3.5).

The ability of WC grain boundaries to resist to infiltration may be investigated by comparing the energy of the interfaces and grain boundaries. The condition for the liquid phase to penetrate the grain boundary may be expressed as follows:

$$\gamma_{SS} - 2\gamma_{SL} > 0 \tag{10}$$

The behavior of the $\Sigma = 2$ twist boundary (Christensen & Wahnström, 2003), $\Sigma = 2$ asymmetrical tilt boundary (Christensen & Wahnström, 2004), and 27°/[10-10] model twist boundary (Christensen & Wahnström, 2003) was analyzed. It was found that among the whole set of atomic configurations considered for the $\Sigma = 2$ twist boundary, some geometries were favorable to the infiltration of Co, but not the most stable geometries. On the other hand, the generic 27°/[10-10] twist boundary and the clean $\Sigma = 2$ asymmetrical tilt boundary are expected to be penetrated by Co (**Figure 19(a),(b)**). For this latter, the resistance to infiltration is slightly enhanced by Co segregation in submonolayer proportion (**Figure 19(c),(d)**). This enhancement should apply to all grain boundaries observed in WC–Co alloys (Christensen & Wahnström, 2004). The calculations

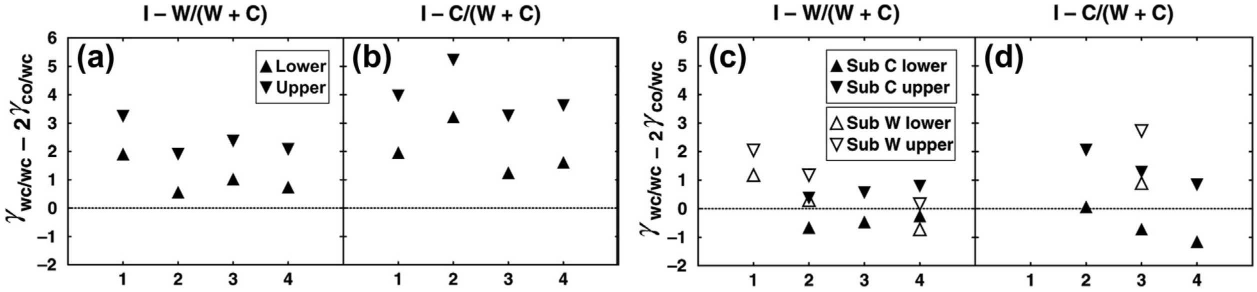

Figure 19 Driving force for grain boundary infiltration of the $\Sigma = 2$ asymmetrical tilt WC(0001)/WC(1-210) boundary (a,b) for a clean boundary and (c,d) with Co segregated atoms. The (1-210) boundary plane has a mixed (W + C) composition while the (0001) plane can be W-terminated (I – W/(W + C)) or C-terminated (I – C/(W + C)). Four geometries denoted 1–4 were considered in each case. In (c,d) a filled (unfilled) symbol indicates the substitution of carbon (tungsten) atoms by cobalt. An upper and a lower limit are given for the driving force. Infiltration is favorable for positive values (Christensen & Wahnström, 2004).

are in qualitative agreement with the experimental evidence of the destruction of WC grain boundaries arising from the powder or present in sintered compacts (Kim et al., 2005; Lisovsky, 2009) and the decrease of $\Sigma = 2$ boundary ratio as the temperature or sintering time increases (Kumar et al., 2006; Mannesson et al., 2008).

1.03.2.3.5 Mean Free Path in the Binder Phase

The mean free path l_{Co} in the binder phase represents the average linear distance between WC grains and may be related to the ductility of the materials (Volume 1, Section 1.10). Assuming isotropic microstructure, this parameter can be easily estimated in image analysis by measuring the length of linear intercepts of the binder phase with a set of parallel lines in a planar section.

Luyckx et al. (Luyckx & Love, 2006) have shown that the mean free path is, in a first approximation, proportional to the WC grain size at fixed Co volume fraction. They checked on a large variety of grades that the ratio of the mean free path in the binder phase l_{Co} and in WC grains $l^{\mathrm{G}}_{\mathrm{WC}}$ may be approximated as a function of the Co volume fraction V_{Co}:

$$\frac{l_{\mathrm{Co}}}{l^{\mathrm{G}}_{\mathrm{WC}}} = f(V_{\mathrm{Co}}) \approx 5.975 V_{\mathrm{Co}}^2 - 0.691 V_{\mathrm{Co}} + 0.214 \quad [11]$$

Microstructures are then more or less homothetic at fixed Co volume fractions, which explains that the mechanical properties of stoichiometric WC–Co mixtures are essentially controlled by the grain size and by the binder phase content. However, deviation to Eqn (11) may be observed in case of the presence of secondary carbides, or with a broad particle size distribution or with ultrafine powders.

1.03.2.3.6 Contiguity

Contiguity of the carbide phase in WC–Co materials can be defined as the ratio of the grain boundary area to the total interface area of carbide grains (Gurland, 1958). It is related to the WC/WC grain boundary and WC/Co interface areas, $S_{\mathrm{WC/WC}}$ and $S_{\mathrm{WC/Co}}$, respectively:

$$C = \frac{2S_{\mathrm{WC/WC}}}{2S_{\mathrm{WC/WC}} + S_{\mathrm{WC/Co}}} \quad (12)$$

where the factor of 2 accounts for the fact that grain boundaries are shared by two adjacent grains. Contiguity of the carbide phase is an important characteristic to control since it determines the rigidity and hence the mechanical strength of the composite material (Volume 1, Section 1.10).

Contiguity is a rather easy accessible parameter since it can be determined by counting the corresponding number of intersections $N_{\mathrm{WC/WC}}$ and $N_{\mathrm{WC/Co}}$ of grain boundaries and interfaces with a set of parallel lines in a plane section (Smith & Guttman, 1953):

$$C = \frac{2N_{\mathrm{WC/WC}}}{2N_{\mathrm{WC/WC}} + N_{\mathrm{WC/Co}}} \quad (13)$$

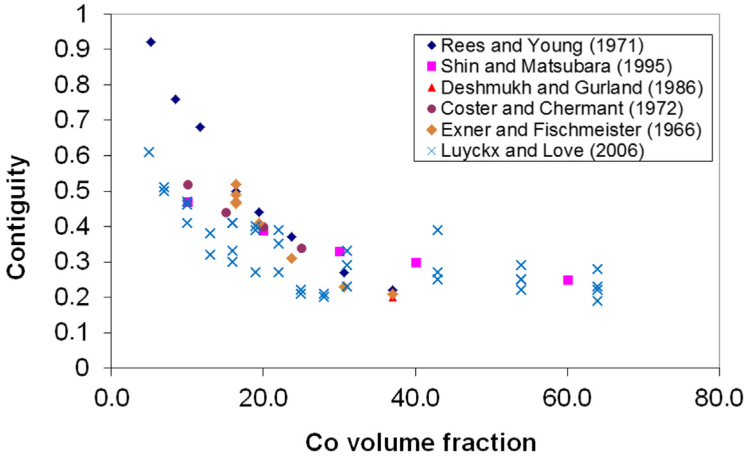

Figure 20 Variation of the contiguity with the Co volume fraction from different authors (Coster et al., 1972; Exner & Fischmeister, 1966; Luyckx & Love, 2006; Rees & Young, 1971; Shin & Matsubara, 1995).

Equation (13) is simply a stereological relation, making no other assumption about the microstructure than isotropy of the surfaces, which can be checked by counting the number of intersections in different directions. The contiguity is also simply related to the Co volume fraction and to the mean free path in the binder phase l_{Co} and in WC grains l_{WC}^{G} defined above (Lee & Gurland, 1978):

$$C = 1 - \frac{V_{Co}}{\frac{l_{Co}}{l_{WC}^{G}}(1 - V_{Co})} \tag{14}$$

Assuming homothetic microstructures, as defined by Eqn (11), the contiguity is then, in a first approximation, only function of the binder phase content.

The contiguity decreases as the amount of binder phase increases (Coster, Chermant, & Deschanvres, 1972; Exner & Fischmeister, 1966; Luyckx & Love, 2006; Rees & Young, 1971; Shin & Matsubara, 1995) (**Figure 20**). This is easily understood since the number of contacts and hence of grain boundaries decreases, as the fraction of carbide phase decreases.

Two different approaches are classically used to analyze the contiguity in cemented carbides: the equilibrium contiguity and the geometrical contiguity (Shatov, Ponomarev, Firstov, & Warren, 2006). The equilibrium contiguity approach considers that contacts develop to minimize the total interface energy of the system while the geometrical contiguity approach assumes that contacts are the result of the necessary overlapping of crystals to fill a given volume. The equilibrium approach dominates in systems with rounded particles and high binder volume fraction where particles are free to adjust their shape to minimize the global interface energy. The geometrical approach dominates with faceted particles and high carbide volume fraction, where steric constraints prevent the system to form only low-energy facets and grain boundaries. However, both aspects are concomitant in real systems and as far as microstructural evolution is possible, any system will tend to optimize the geometry in order to minimize its interface energy.

The equilibrium contiguity approach determines the goal toward which the microstructure should tend and it is therefore important to consider. From DFT calculations of interface energies, all grain boundaries but a few special $\Sigma = 2$ boundaries are not stable (**Figure 19**). One could object that DFT calculations do not exactly capture all ingredients to correctly describe the grain boundary and interface energy. However, the grain boundary energy value obtained by Warren ($\approx 1\ \mathrm{J\ m^{-2}}$) in alloys with a microstructure close to equilibrium probably corresponds to the most stable CSL grain boundaries and it is in the range of energies calculated for the $\Sigma = 2$ boundaries (**Table 2**). In usual sintered compacts, steric effects may force the creation of grain boundaries which could explain the large variety of grain boundaries observed experimentally (Section 1.03.2.3.1). The history of materials processing must be considered to understand the presence of grain boundaries in sintered specimen (Warren & Waldron, 1972a). Grain boundaries are usually present in the initial powder (Section 1.03.2.3.1) and their formation during solid-state sintering is

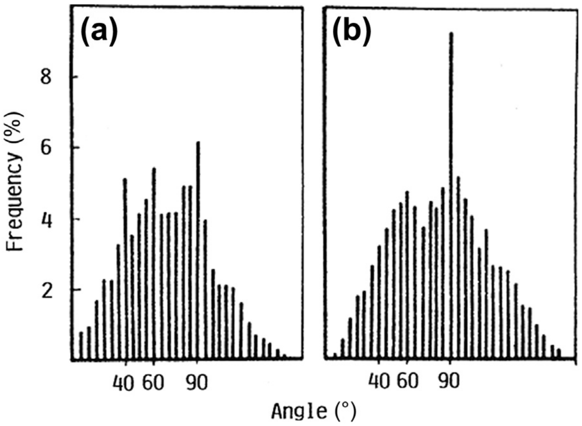

Figure 21 Distribution of dihedral angle cross-sections within a WC–6 wt% Co sintered compact in its initial state (a) and after imbibition by its eutectic melt at 1350 °C (b). The volume fraction of liquid varies from about 14 to 60% during the experiment (Lisovsky, 2009).

favorable since the solid–vapor interface energy γ_{SV} is much larger than the interface energy γ_{SL} which is involved in Eqn (9). In addition, a lot of contacts are created during sintering due to shrinkage, which facilitates the formation of new grain boundaries. Therefore, the initial contiguity as the liquid phase forms is probably larger than the equilibrium value. The contiguity usually decreases during isothermal holding of dense specimens to minimize the interface energy, as observed by most authors (Coster et al., 1972; Deshmukh & Gurland, 1986; Exner & Fischmeister, 1966; Warren & Waldron, 1972b). This evolution toward equilibrium is however very slow in usual sintering experiments since it necessitates the deconstruction and reconstruction of the particle skeleton to optimize grain boundary configurations. It may be accelerated in experiments where liquid migration is involved, such as imbibition of a WC–Co sintered compact by its eutectic melt. Lisovsky (1987) has shown that a WC–6 wt% Co compact can be imbibed by its eutectic melt in a few minutes at 1350 °C, with an increase of the volume fraction of liquid from 14 to 60%. The contiguity naturally decreases in such an experiment but the interesting point is that the distribution of dihedral angles shows a significant reduction in the fraction of low dihedral angles, which are observed on sintering samples (**Figure 17**) and a significant increase of 90° dihedral angles (**Figure 21**). The latter are among others characteristic of $\Sigma = 2$ grain boundaries. This means that the interface energy is minimized not only by reducing the number of grain boundaries but also by a preferential elimination of high-energy (low-dihedral angle) boundaries. In another experiment, Lisovsky (1991) shows that the contiguity of a mixture with 9 wt% Co obtained by partial imbibition of a 6 wt% Co mixture is significantly lower (0.53) than the contiguity of a 9 wt% Co obtained by sintering (0.65) with a similar grain size. This demonstrates the potential for a sintered material with a fixed liquid-phase fraction to minimize its interface energy by optimizing the packing geometry in order to reduce the contiguity.

A last issue remains as far as DFT energetic calculations are assumed to give a correct estimation of interface and grain boundary energies. Increasing the carbide volume fraction undoubtedly forces the system to create contacts, but a particular grain boundary is not stable if its replacement by a thin liquid film with the creation of two interfaces is energetically more favorable, which would be the case for most grain boundaries (**Figure 19**). Other effects may oppose to the infiltration of grain boundaries. Segregation may stabilize grain boundaries as discussed in Section 1.03.2.3.3. Another effect which is not often discussed is the possible role of the capillary force that liquid menisci at the external surface exert on the sintered compact (Park, Kang, & Yoon, 1986). The pressure induced on the grain boundaries may oppose to infiltration by the liquid. The elimination of this capillary force by immersing the specimen in its eutectic liquid could allow infiltration of the less stable grain boundaries and explain the rapid liquid migration observed in imbibition experiments. This could also facilitate the infiltration of large agglomerates embedded in the liquid as observed in the early stage of liquid-phase sintering (**Figure 18**).

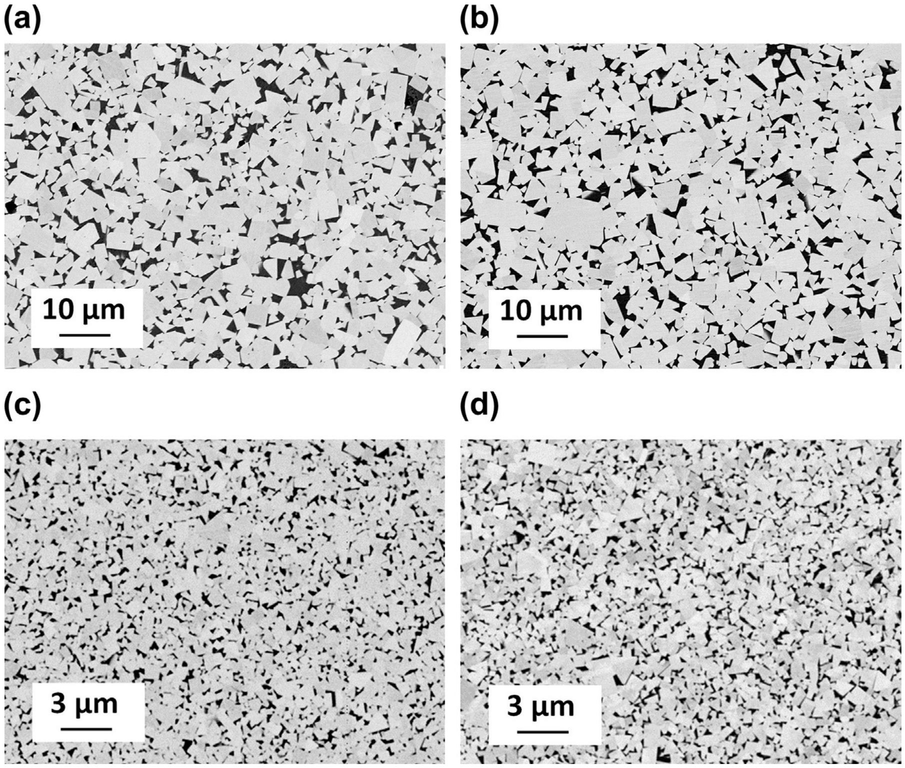

Figure 22 Microstructural evolution of WC–8 wt% Co mixtures during isothermal holding micronic powder for (a) 1450 °C 1 h, (b) 1450 °C 8 h and submicronic powder for (c) 1450 °C 1 h, and (d) 1450 °C 8 h.

1.03.2.4 Grain Growth

1.03.2.4.1 Mechanisms and Kinetics of Grain Growth in WC–Co Alloys

Grain growth in cemented carbides is essentially due to Ostwald ripening, i.e. the dissolution of smaller grains and the growth of larger grains to reduce the total interface energy in the system. A typical evolution of the microstructure is shown in Figure 22 for micronic and submicronic powders. The growth kinetics is very low with micronic powders. It becomes significant with submicronic powders, with a relatively broad particle size distribution.

Different authors have proposed a cubic law for the variation of the average 3D equivalent diameter (Chermant, Coster, Deschanvres, & Iost, 1977; Exner & Fischmeister, 1966; Shin & Matsubara, 1995; Warren & Waldron, 1972b):

$$D^3 = D_0^3 + Kt. \tag{15}$$

The experimental kinetic constant K has the order of magnitude 10^{-21}–10^{-20} $m^3\,s^{-1}$ in the temperature range 1400–1450 °C, depending on the experimental conditions (Figure 23). Especially the C content has a significant influence on grain growth kinetics (Section 1.03.2.4.2) and this parameter is not always controlled or specified in the literature. The C content in Gurland's and in Shin and Matsubara's experiments was in the two-phase region at the limit with the WC–Co–C domain, which may explain the higher kinetic constant in these studies. Equation (15) would be consistent with a limitation of the kinetics by the solute diffusion in the liquid, from the classical Lifshitz-Slyozov-Wagner (LSW) theory (Lifshitz & Slyozov, 1961; Wagner, 1961). However, on one hand, the experimental value of constant K is orders of magnitude too low compared to the theoretical value for diffusion-controlled growth (Warren & Waldron, 1972b) and on the other hand, the constant should decrease as the volume fraction of liquid increases which is not consistent with the observations (Figure 23). In fact, due to the rather slow grain growth, variation of the grain size could as well be described with a parabolic equation and the kinetics is probably limited by a reaction step at the interface.

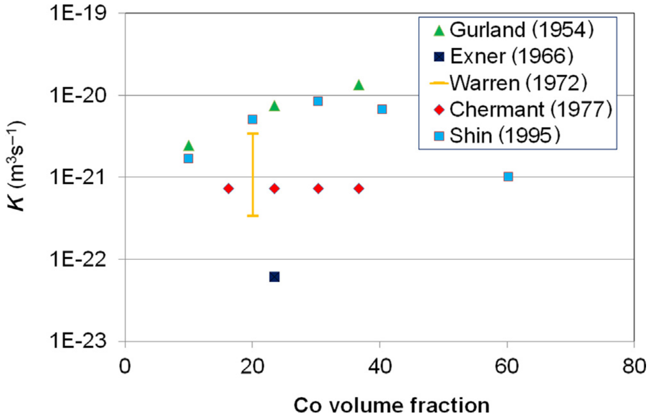

Figure 23 Variation of the kinetic constant K of grain growth (Eqn (15)).

As the sintering time increases, the microstructure evolves to a more or less monodisperse particle size distribution (Coster et al., 1972; Exner & Fischmeister, 1966; Mannesson et al., 2008; Warren & Waldron, 1972b) but it is significantly broader than the theoretical LSW-predicted particle size distribution, with a 3D size dispersion of about one decade (Coster et al., 1972; Park, Hwang, & Yoon, 1996b). This means that the growth rate of large grains relative to medium-sized grains is much larger than in the reaction-limited LSW model. Park et al. (1996b) explained this effect by the fact that precipitation is not continuous on the faceted grain surfaces in the WC–Co system, but would be limited by a 2D-nucleation step. **Figure 24** represents the growth rate by 2D-nucleation as a function of the curvature-induced supersaturation Δg^*. 2D-nucleation is, however, a very slow process owing to the weak curvature-induced driving force and other mechanisms may accelerate the precipitation on particles surfaces. Park invokes that surface defects may be preferential nucleation sites and the kinetics would gradually tend to the linear variation with the supersaturation, which is characteristic of continuous precipitation, as the density of defects increases. This could explain the very slow growth observed with micronic powders, as the curvature-induced supersaturation is rather small, and the significant grain growth with broadening of the particle size distribution with ultrafine powders, as the driving force is larger. The steep variation of the nucleation rate above the critical driving force (**Figure 24**) may even cause the abnormal grain growth of a few very large grains at the expense of the fine grain matrix (Park et al., 1996b). Since nucleation is very sensitive to local defects, chemical heterogeneity, to the width of the initial particle size distribution or to the thermal cycle, abnormal grain growth is a highly unpredictable phenomenon but it can be usually avoided with ultrafine powder by the proper addition of inhibitors (Adorjan, Schubert, Schon, Bock, & Zeiler, 2006).

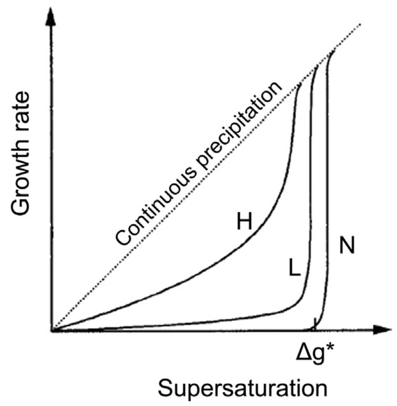

Figure 24 Schematic variation of the growth rate of faceted particles with supersaturation Δg^* at high (H), low (L), and zero (N)-nucleation defect density (from Park, Hwang, & Yoon, 1996a).

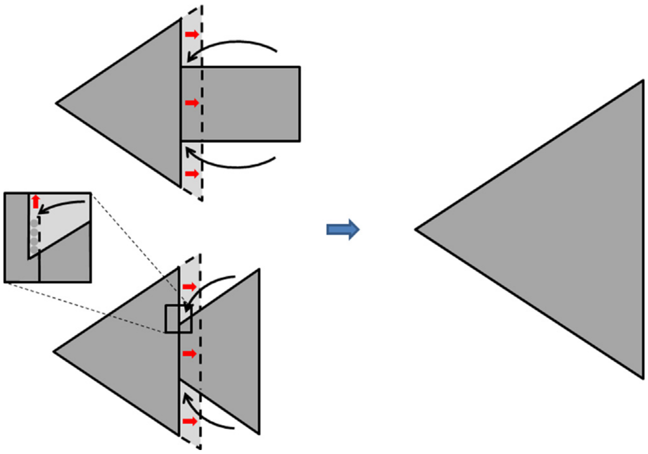

Figure 25 Schematic representation of the coalescence/coarsening mixed process for two grains.

Another aspect to take into consideration is the effect of WC/WC grain boundaries on grain growth. As discussed by Warren (Warren & Waldron, 1972b), depending on the relative migration rate of grain boundaries relative to WC/Co interfaces, grain boundaries may either impede or enhance grain growth. From experiments, the contiguity increases as the liquid volume fraction decreases (**Figure 20**), whereas the experimental grain growth rate decreases or does not change (**Figure 23**). Therefore, grain boundaries, if they have an effect, would rather impede grain growth in the WC–Co system. In fact, the growth of a large grain in a high solid content system causes the creation and growth of contacts with the surrounding grains, which is not energetically favorable compared to the same grain growing freely in the liquid (Shatov et al., 2006) since the energy of general grain boundaries is relatively high (**Table 2**). However, the migration may be energetically more favorable for some specific low-energy grain boundaries and/or for grain boundaries able to migrate without increasing their area (**Figure 25**). From the kinetic point of view, the energy barrier for nucleation may be decreased if the nucleation occurs at the grain boundary triple line, followed by lateral growth of the new solid layers (**Figure 25**). This simultaneous migration of the grain boundary and interface results in a mixed process of coalescence/coarsening of adjacent grains with special geometric or interfacial configurations. Once created, such grains several times larger than the initial grains and without internal grain boundaries can be so energetically advantageous over other smaller carbide crystals that they will continue to grow faster. This preferential growth of grains with a specific environment is probably one of the reasons for the broadening of the particle size distribution in the system. This is to be compared to the broadening of the particle size distribution as the grain boundary energy dispersion increases, observed on Monte-Carlo simulations of grain growth in a polycrystalline material (Grest, Srolovitz, & Anderson, 1985). Grain growth is also slightly anisotropic (Chermant et al., 1977), in particular due to the coalescence of prismatic grains. Large grains are indeed more anisotropic, with a side-to-height length ratio of 4–5 instead of 2 for grains of the main population (Ryoo & Hwang, 1998). This coalescence/coarsening process is facilitated by the presence of a high quantity of $\Sigma = 2$ grain boundaries in the powder (Section 1.03.2.3.1) and it explains the elimination of a large part of these latter (Kumar et al., 2006; Mannesson et al., 2008) and the rapid grain growth observed in the early stage of sintering (Kumar et al., 2006; Mannesson et al., 2008; Wang, Fang, & Sohn, 2008).

In addition to the interface driving force for grain growth, the mechanical driving force may be responsible for the growth of WC grains. Very large anisotropic grains may form by recrystallization during heating after long milling time of the powder (Schön, Schubert, & Lux, 2001). Also a chemical driving force may play a role in case the composition is not at equilibrium within the system. For example, if η-phase is formed during heating, due to local heterogeneity in the composition, the decomposition and growth of WC grains may result from carburization at higher temperature, according to the balance reaction (Gurland, 1954): $\eta + 2C \rightarrow 3WC + 3Co$.

This growth may already occur in the solid-state or during liquid-phase sintering due to the homogenization of the composition by liquid migration (Adorjan et al., 2006; Yang, Kim, & Eun, 1986) and results in the formation of local clusters of very large grains isolated in a fine grain matrix (**Figure 26**). These mechanical or chemical effects are then alternative causes of abnormal grain growth in the WC–Co system.

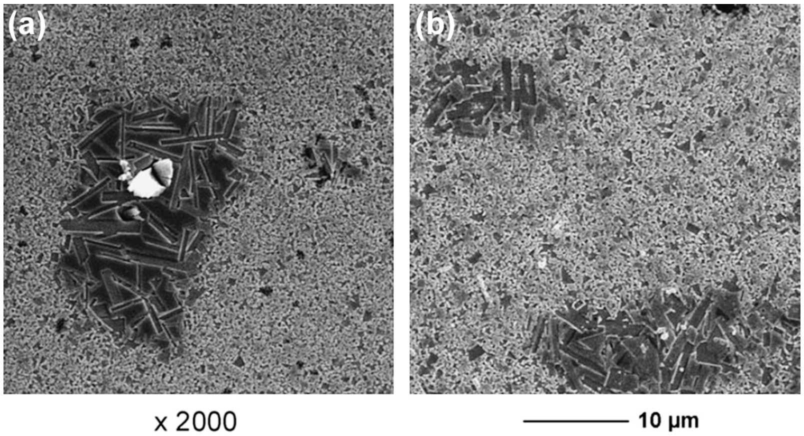

Figure 26 Example of the local formation of abnormal grains by the carburization of previously formed η-phase. (a) Interrupted at 1350 °C; (b) 1450 °C, 1 h (from Adorjan et al., 2006).

1.03.2.4.2 Effect of C Content

Grain growth is enhanced when the C/W ratio is increased in the two-phase field {WC + liquid} and up to the three-phase field {WC + C + liquid} (Chabretou et al., 2003; Gurland, 1954). The earlier formation of the eutectic liquid during heating in C-rich alloys may play a role (Bock, 1992) but grain growth enhancement is also observed during isothermal holding. The decrease of the liquid content associated with the formation of η-phase in the {WC + η + liquid} three-phase field may also have an effect but it cannot explain the growth enhancement in the two-phase field, where the liquid content is practically unchanged. Differences in interface morphology are noticed, with more steps and rounded corners in W-rich mixtures (Section 1.03.2.2.2). This suggests a different growth mechanism but it is still an open question.

1.03.2.4.3 Effect of Inhibitors

An extensive analysis of elements inhibiting grain growth was performed by Tulhoff (1980) who showed that most inhibiting elements are carbide formers (V, Cr, Ti, Ta, Mo, ...). The inhibiting effect increases with the additive content in the liquid phase, until the solubility limit (Hayashi et al., 1972), when secondary carbides containing the inhibitor element are observed. The higher efficiency of V and Cr is related to their higher solubility at the same temperature (Bock, 1992). The morphology of interfaces is generally modified by the addition of inhibitors (Section 1.03.2.2.4), with more steps at the interface (V, Cr) and the local precipitation of a cubic carbide layer at the WC–Co interface (V, Cr, Ti). This may limit the solution or precipitation of W and C atoms at WC/Co interfaces and then explain the grain growth inhibition, although no direct evidence was made up to now.

1.03.3 Other Cemented Carbides and Cermets

MC cubic carbide additions are used to increase the hardness and the wear resistance of WC–Co alloys for applications like high-speed machining of steels. The metals M belonging to the group IV (Ti, Zr, Hf) or to the group V (V, Nb, Ta) of the periodic table were considered because the corresponding carbides are harder than WC (Exner, 1979). Among them, TiC is the hardest and mainly mixtures of WC–TiC carbides with additions of (Ta,Nb)C were selected. Besides, much harder TiC-based cemented carbides like TiC–Mo_2C–Ni alloys were developed for their higher tool life in specific operations like fine turning (Pastor, 1987). Then further improvements mainly on toughness and wear resistance of hardmetals were obtained by introducing TiN in TiC–Ni/Mo alloys and thus developing titanium carbonitride-based cermets (Pastor, 1999). The available data of the literature on the wetting behavior and on the interface energies in these systems will be first briefly presented before describing the microstructure.

1.03.3.1 Wetting of TiC and TiN

Compared to WC, the wetting angle of the transition-metal carbides by Co is found higher especially for TiC what reflects the more difficult densification of TiC–Co alloys (Warren & Waldron, 1972c) (**Table 1**). In early studies of cemented carbides, the poorer strength of the TiC/Co interface was pointed out by a lower value of the work of adhesion (3.64 J m^{-2}) relative to WC/Co. The analysis of the electronic structure of TiC/Co and WC/Co interfaces indicates that strong covalent Co–C bonds form at both interfaces (Christensen et al., 2002; Dudiy & Lundqvist, 2001). However, the enhanced strength of WC/Co interface originates from a larger contribution of metal–metal Co–W bonds. In agreement with the experiments, a lower value of the separation work is obtained for the TiC/Co interface ($W_{sep} = 3.25–3.45$ J m^{-2}) (Dudiy & Lundqvist, 2001). The poorer wettability of TiC by Co results in the formation of pores and worsens the mechanical properties of WC–TiC–Co alloys (Bhaumik, Upadhyaya, & Vaidya, 1991). In TiC-based grades, nickel proved to be more suitable than cobalt as a binder (Brookes, 1992) and wetting was improved by the addition of Mo or Mo_2C (Exner, 1979).

Compared to WC and TiC carbides, scarce experimental data on the wetting behavior of TiN by Co or Ni are available although it is admitted that wetting is not so good but does not limit the densification of these alloys. The adhesion properties of the Co/TiN interface were investigated by means of DFT calculations (Dudiy & Lundqvist, 2001). It was found that the adhesion of the interface is provided by strong covalent Co–N bonds comparable to Co–C bonds occurring at TiC/Co interface. However, the extra electron of the N atom induces a reduction of the strength of these bonds resulting in a weaker adhesion in the Co/TiN case. This analysis is consistent with the practice that a higher sintering temperature is needed as the TiN content increases to get full densification of the cermets (Ettmayer, Kolaska, Lengauer, & Dreyer, 1995).

1.03.3.2 WC–TiC–Co Alloys

As TiC carbide is much more brittle than WC, the TiC content of WC–TiC–Co alloys usually does not exceed 18 wt% (Brookes, 1992). After sintering, the microstructure consists in a mixture of angular WC grains and TiC rounded grains embedded in the Co-rich binder. The TiC grains, called γ phase, usually show a core–rim structure (**Figure 27**), with the core having the composition of the initial TiC or (Ti,W)C powder and the rim being a (Ti,W)C phase with a higher amount of W. Solubility of WC in TiC is significant, whereas it is negligible for TiC in WC. At 1400 °C, the equilibrium composition of the cubic carbide varies from $W_{0.35}Ti_{0.65}C$ in η containing alloys to $W_{0.40}Ti_{0.60}C$ when graphite is present (Kruse, Jansson, & Frisk, 2001). The formation of the rim around TiC grains arises from the partial dissolution of TiC and WC in the binder/liquid followed by the epitaxial precipitation of the (Ti,W)C solid solution onto undissolved TiC grains (Andrén, 2001). For low TiC additions, all TiC raw grains are dissolved in the binder and only (Ti,W)C grains are present (Weidow, Zackrisson, Jansson, & Andrén, 2009). The distribution of the elements in the core–rim structure of the γ phase was accurately determined using atom probe field ion microscopy (Rolander & Andrén, 1988). It was found that the diffusion distance of W atoms from the rim to the core is only a few nanometers because of the low mobility of W atoms in TiC (**Figure 28**). The Ti content of the binder is low and depends on the carbon content during sintering. For example, at 1450 °C, the solubility of Ti is expected to be 2.4 wt% in carbon-rich alloys and 1.0 wt % in tungsten-rich alloys (Frisk et al., 2001). As for WC–Co alloys, a low carbon content was found in the binder after sintering.

The inspection of the microstructure (**Figure 27**) shows the formation of (Ti,W)C/WC phase boundaries and (Ti,W)C/(Ti,W)C grain boundaries where segregated cobalt was detected (Henjered et al., 1986; Weidow & Andrén, 2011). These observations confirm the formation of a WC–MC skeleton (Andrén, 2001). The overall microstructure is however highly dependent on the amount of TiC and on the WC/TiC grain size ratio and

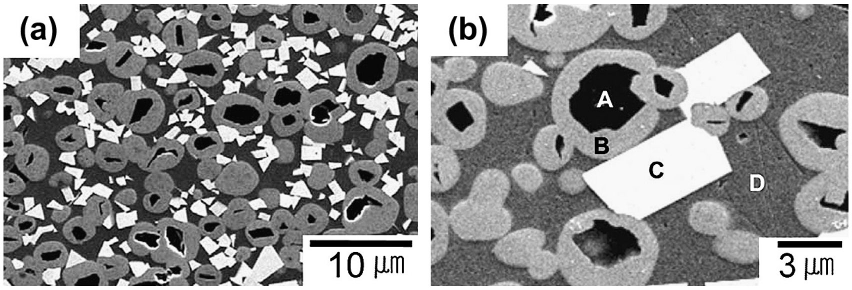

Figure 27 Microstructure of 70(25TiC–75WC)–30Co (wt%) samples sintered at 1450 °C for (a) 2 h and a starting size of powder of 1.3 μm (b) sintered for 5 h with a starting size of 4.1 μm, (A) TiC core, (B) (Ti,W)C grain, (C) WC grain, (D) Co-based matrix (Yoon, Lee, & Kang, 2005).

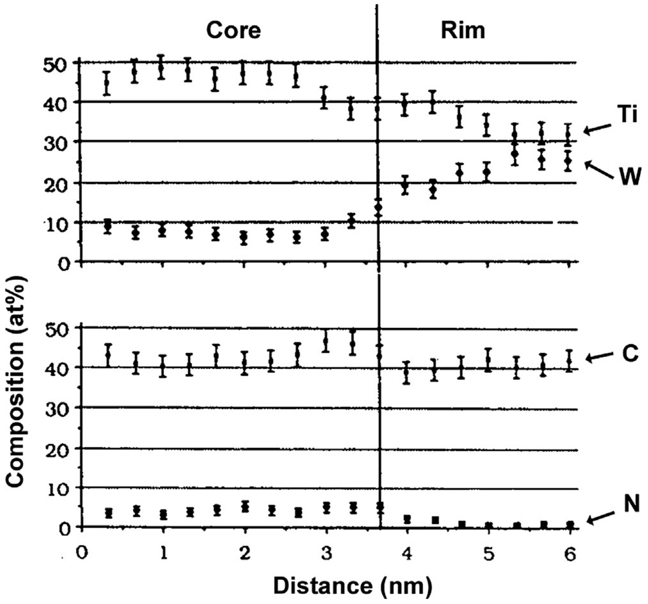

Figure 28 Atom probe field ion microscopy (APFIM) composition profile through a core–rim boundary in an 85WC–7.7(Ti,W)C–7.3Co (wt%) material. Some impurity nitrogen was found in the core (Andrén, 2001).

finally greatly influences the mechanical properties (Lee, Cha, Kim, & Hong, 2006). In some grades containing high percentages of TiC, nickel is used as an entire or partial replacement of cobalt.

1.03.3.3 TiC–Mo_2C–Ni Alloys

The addition of Mo_2C to TiC–Ni alloys induces the formation of the characteristic core–rim structure of the carbide grains, the rim having the same crystallographic orientation than the core. The composition of the core corresponds to the initial TiC powder while the rim is a (Ti,Mo)C solid solution and a rather abrupt change in composition occurs at the core–rim interface (**Figure 29**) (Yamamoto, Jaroenworaluck, Ikuhara, & Sakuma, 1999). The mechanism of the rim formation is not completely assessed (Pastor, 1999). The rim formation would start at the solid state by the diffusion of Mo into TiC grains. Moreover, a (Ti,Mo)C solid solution likely precipitates on TiC grains from the eutectic liquid with a composition in equilibrium with the melt. The

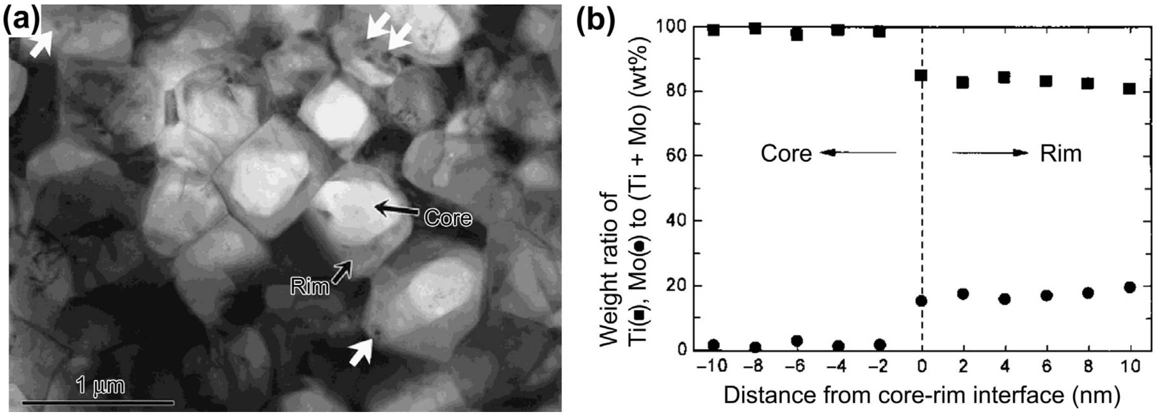

Figure 29 (a) Bright-field TEM image in TiC–20 wt% Mo_2C–20 wt% Ni sintered at 1370 °C for 1 h, showing the typical core–rim structure. The white arrows indicate Ni phases included into carbide grains during sintering. (b) Plots of Ti and Mo weight ratio estimated from EDS analysis across the interface. The weight ratio shown is calculated from the ratio of Ti or Mo to (Ti + Mo) (Yamamoto et al., 1999).

composition of the liquid binder depends on the carbon content of the alloy. For specimens sintered between 1300 °C and 1450 °C, the Ti and Mo binder content was found to range from about 3 wt% Ti and 0 wt% Mo for high-carbon alloys to about 10 wt% Ti and 6 wt% Mo for low-carbon alloys (Suzuki, Hayashi, & Terada, 1971). The Mo enrichment of the rim at the surface of the TiC grains is likely to be responsible for the better wetting of the carbide grains when Mo_2C is present in the alloy. Moreover, the addition of Mo can limit grain growth (Barranco & Warenchak, 1989). Development of this grade of alloys by changing the composition is still a topical field of research (Guo, Xiong, Yang, & Jiang, 2008).

1.03.3.4 Ti(C,N)-Based Cermets

Cermets are prepared from a mixture of TiC and TiN hard phases or from the Ti(C,N) compound, with nickel or/and cobalt as a binder. This class of materials also contains WC or Mo_2C to improve the wetting of the hard phase and increase the mechanical performance of the alloys interfaces (Brookes, 1992; Ettmayer et al., 1995). The microstructures are usually complex, depending on the composition, starting powders and sintering treatment. The hard-phase particles are embedded in the binder and show the characteristic core–rim structure while the rim may be divided into the inner and outer rims that have different compositions (**Figure 30**). The microstructure has been carefully characterized in various cermets and at different stages of the sintering cycle and processes leading to the formation of the complex structure could be identified. Among the variety of starting materials, the Ti(C,N)–TiN–Co–WC or Ti(C,N)–Ni–WC model alloys are chosen to illustrate the microstructure evolution on sintering and to get a better insight on the core/rim structure formation (Ahn & Kang, 2000; Zackrisson, Rolander, & Andrén, 2001; Kim, Min, & Kang, 2003).

On heating, the hard-phase particles start to dissolve in the binder and the (Ti,W)(C,N) inner rim with a high amount of tungsten precipitates epitaxially onto undissolved Ti(C,N) particles. The thickness of the inner rim is not uniform what could be related to the difficulty for this phase to nucleate. The outer rim forms after melting of the binder by precipitation of a (Ti,W)(C,N) solid solution from the liquid. The outer rim has a smaller tungsten content and higher nitrogen content than the inner rim. The composition of the core of the carbonitride grains evolves during sintering due to the diffusion of carbon and nitrogen atoms. They do not contain tungsten atoms except at the level of crystal defects where the diffusion is enhanced. The onset of formation of the inner rim is not fully established. It could form on heating at the solid state by diffusion through the solid binder with a composition close to the equilibrium (Zackrisson et al., 2001). The difference between inner and outer rims would be due to a change of the chemical equilibrium as the temperature increases and as the nitrogen activity is enhanced due to the closure of the porosity. On the other hand, it is also assumed that the inner rim forms at the onset of binder melting and the outer rim when sintering proceeds (Ahn & Kang, 2000). The composition change would be related to the difference in dissolution rate of the WC and Ti(C,N) phases at higher temperature. The dissolution rate is higher for WC and the relative rates vary as a function of the temperature. As the solute content of the binder determines the composition of the rim, the inner rim is enriched in W atoms compared to the outer rim.

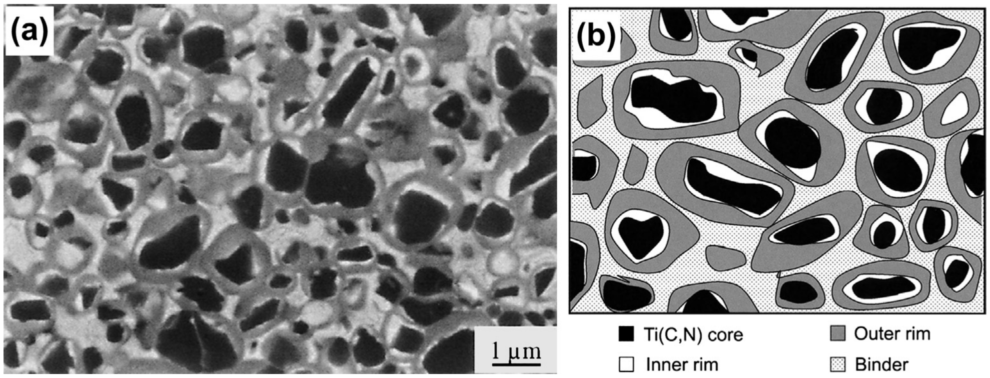

Figure 30 (a) SEM micrograph of a Ti(C,N)–TiN–Co–WC cermet sintered at 1430 °C for 90 min showing the typical core/rim structure, where the inner rim close to the core has a bright contrast and the outer rim a darkest contrast (Zackrisson et al., 2001). (b) Schema of the microstructure of a Ti(C,N)-based cermet (Ahn & Kang, 2000).

Very similar microstructures are observed in Mo_2C-containing cermets with the formation of the core/rims structure, the core and the rims having the Ti(C,N) and the (Ti,Mo)(C,N) composition, respectively, the inner rim being richer in Mo atoms than the outer rim (Andrén, 2001; Lindahl, Gustafson, Rolander, Stals, & Andrén, 1999).

References

Adorjan, A., Schubert, W. D., Schon, A., Bock, A., & Zeiler, B. (2006). WC grain growth during the early stages of sintering. *International Journal of Refractory Metals and Hard Materials, 24*, 365–373.

Ahn, S.-Y., & Kang, S. (2000). Formation of Core/Rim structures in Ti(C, N)-WC-Ni cermets via a dissolution and precipitation process. *Journal of the American Ceramic Society, 83*, 1489–1494.

Akesson, L. (1982). *An experimental and thermodynamic study of the Co-W-C system in the temperature range 1473–1698 K*. Thesis. Sweden: University of Stockholm.

Almond, E. A., & Roebuck, B. (1982). The origin of WC substructure and the effect of processing on the microstructure of WC-Co hardmetals. *High Temperatures – High Pressures, 14*, 143–154.

Almond, E. A., & Roebuck, B. (1988). Identification of optimum binder phase compositions for improved tungsten carbide hard metals. *Materials Science and Engineering A, 105–106*, 237–248.

Andrén, H. O. (2001). Microstructures of cemented carbides. *Materials and Design, 22*, 491–498.

Barranco, J. M., & Warenchak, R. A. (1989). Liquid-phase sintering of carbides using a nickel-molybdenum alloy. *International Journal of Refractory Metals and Hard Materials, 8*, 102–110.

Benjdir, M. (1991). *Analyses cristallographiques et chimiques des joints de grains du carbure de tungstène dans le composite WC-Co. Etudes en microscopie électronique en transmission*. Thesis. France: University of Caen.

Bhaumik, S. K., Upadhyaya, G. S., & Vaidya, M. L. (1991). Properties and microstructure of tungsten carbide-titanium carbide-cobalt and tungsten carbide-titanium carbide-molybdenum carbide-cobalt(nickel) cemented carbides. *Materials Science and Technology, 7*, 723–727.

Bock, A. (1992). Inhibition of grain growth on submicron cemented carbides. *Powder Metallurgy International, 24*, 20–26.

Bollmann, W. (1970). *Crystal defects and crystalline interfaces*. Berlin: Springer-Verlag.

Bounhoure, V., Lay, S., Loubradou, M., & Missiaen, J. M. (2008). Special WC/Co orientation relationships at basal facets of WC grains in WC-Co alloys. *Journal of Materials Science, 43*, 892–899.

Brookes, K. J. A. (1992). *Hardmetals and other hard materials*. International Carbide Data.

Chabretou, V., Allibert, C. H., & Missiaen, J. M. (2003). Quantitative analysis of the effect of the binder phase composition on grain growth in WC-Co sintered materials. *Journal of Materials Science, 38*, 2581–2590.

Chermant, J. L., Coster, M., Deschanvres, A., & Iost, A. (1977). Etude de la cinétique de croissance de systèmes carbure - métal. *Journal of the Less-common Metals, 52*, 177–196.

Christensen, M., Dudiy, S., & Wahnström, G. (2002). First-principles simulations of metal-ceramic interface adhesion: Co/WC versus Co/TiC. *Physical Review B, 65*, 045408.

Christensen, M., & Wahnström, G. (2003). Co-phase penetration of WC(10-10)/WC(10-10) grain boundaries from first principles. *Physical Review B, 67*, 115415.

Christensen, M., & Wahnström, G. (2004). Effects of cobalt intergranular segregation on interface energetics in WC-Co. *Acta Materialia, 52*, 2199–2207.

Christensen, M., & Wahnström, G. (2006). Strength and reinforcement of interfaces in cemented carbides. *International Journal of Refractory Metals and Hard Materials, 24*, 80–88.

Christensen, M., Wahnström, G., Allibert, C., & Lay, S. (2005). Quantitative analysis of WC grain shape in sintered WC-Co cemented carbides. *Physical Review Letters, 94*, 066105.

Christensen, M., Wahnström, G., Lay, S., & Allibert, C. H. (2007). Morphology of WC grains in WC-Co alloys: theoretical determination of grain shape. *Acta Materialia, 55*, 1515–1521.

Coster, M., Chermant, J. L., & Deschanvres, A. (1972). Cinétique de croissance des cristaux de CW dans le cobalt. *Memoires Scientifiques de la Revue de Métallurgie, LXIX*, 465–478.

Delanoë, A., Bacia, M., Pauty, E., Lay, S., & Allibert, C. H. (2004). Cr-rich layer at the WC/Co interface in Cr-doped WC-Co cermets: segregation or metastable carbide? *Journal of Crystal Growth, 270*, 219–227.

Delanoë, A., & Lay, S. (2009). Evolution of the WC grain shape in WC-Co alloys during sintering: cumulated effect of the Cr addition and of the C content. *International Journal of Refractory Metals and Hard Materials, 27*, 189–197.

Deshmukh, R., & Gurland, J. (1986). A study of microstructural development during the liquid-phase sintering of tungsten carbide-cobalt (WC-Co) alloys. Proceedings of the international Conference on the Science of Hard Materials, *Institute of Physics Conference Series,* 75 (Sci. Hard Mater.), 347–358.

Dudiy, S. V., & Lundqvist, B. I. (2001). First-principles density-functional study of metal-carbonitride interface adhesion: Co/TiC(001) and Co/TiN(001). *Physical Review B, 64*, 045403.

Ettmayer, P., Kolaska, H., Lengauer, W., & Dreyer, K. (1995). Ti(C, N) cermets – metallurgy and properties. *International Journal of Refractory Metals and Hard Materials, 13*, 343–351.

Exner, H. E. (1979). Physical and chemical nature of cemented carbides. *International Journal of Metals Reviews*, 149–173.

Exner, H. E., & Fischmeister, H. (1966). Gefüge Ausbildung von gesinterten Wolframkarbid-Kobalt-Hartlegierungen. *Archiv für das Eisenhüttenwesen, 37*, 417–426.

Farooq, M. U., & Klement, U. (2004). EBSD characterization of carbide–carbide boundaries in WC–Co composites. *Journal of Microscopy, 213*, 306–312.

Finnis, M. W. (1996). The theory of metal – ceramic interfaces. *Journal of Physics: Condensed Matter, 8*, 5811.

French, D. N. (1969). The microstructure and properties of WC-Co alloys. *International Journal of Powder Metallurgy, 5*, 47–60.

Frisk, K., Dumitrescu, L., Ekroth, M., Sunduman, B., Jansson, B., & Kruse, O. (2001). Development of a database for cemented carbides: thermodynamic modeling and experiments. *Journal of Phase Equilibria, 22*, 645–655.

Gabriel, A., Pastor, H., Deo, D. M., Basu, S., & Allibert, C. H. (1986). New experimental data in the C-Fe-W, C-Co-W, C-Ni-W, C-Fe-Ni-W and C-Co-Ni-W cemented carbides systems and their application to sintering conditions. *International Journal of Refractory Metals and Hard Materials, 5*, 215–221.

Gille, G., Bredthauer, J., Gries, B., Mende, B., & Heinrich, W. (2000). Advanced and new grades of WC and binder powder – their properties and application. *International Journal of Refractory Metals and Hard Materials, 18*, 87–102.

Grest, G. S., Srolovitz, D. J., & Anderson, M. P. (1985). Computer simulation of grain growth. IV. Anisotropic grain boundary energies. *Acta Metallurgica, 33*, 509–520.

Grimmer, H. (1989). Coincidence orientations of grains in rhombohedral materials. *Acta Crystallographica Section A, 45*, 505–523.

Guo, Z., Xiong, J., Yang, M., & Jiang, C. (2008). WC-TiC-Ni cemented carbide with enhanced properties. *Journal of Alloys and Compounds, 465*, 157–162.

Gurland, J. (1954). A study of the effect of carbon content on the structure and properties of sintered WC-Co alloys. *Journal of Metals*, 285–290.

Gurland, J. (August 1958). The measurement of grain contiguity in two-phase alloys. *Transactions of the AIME*, 452–455.

Hagége, S., Nouet, G., & Delavignette, P. (1980). Grain boundary analysis in TEM. IV. Coincidence and the associated defect structure in tungsten carbide. *Physica Status Solidi (a), 62*, 97–107.

Hayashi, K., Fuke, Y., & Suzuki, H. (1972). Effects of addition carbides on the grain size of WC-Co alloy. *Journal of the Japan Society of Powder and Powder Metallurgy, 19*, 67–71.

Henjered, A., Hellsing, M., Andrén, H. O., & Norden, H. (1986). Quantitative microanalysis of carbide/carbide interfaces in tungsten carbide-cobalt-base cemented carbides. *Materials Science & Technology, 2*, 847–855.

Herring, C. (1951). Some theorems on the free energies of crystal surfaces. *Physical Review, 82*, 87–93.

Johansson, S. A. E., & Wahnström, G. (2011). A computational study of thin cubic carbide films in WC/Co interfaces. *Acta Materialia, 59*, 171–181.

Kawakami, M., Terada, O., & Hayashi, K. (2004). Effect of sintering cooling Rate on V Segregation amount at WC/Co interface in VC-doped WC-Co fine-grained Hardmetal. *Journal of the Japan Society of Powder and Powder Metallurgy, 51*, 576–585.

Kawakami, M., Terada, O., & Hayashi, K. (2006). HRTEM microstructure and segregation amount of dopants at WC/Co interfaces in TiC and TaC Mono-doped WC-Co submicro-grained hardmetals. *Journal of the Japan Society of Powder and Powder Metallurgy, 53*, 166–171.

Kim, S., Han, S.-H., Park, J.-K., & Kim, H.-E. (2003). Variation of WC grain shape with carbon content in the WC-Co alloys during liquid-phase sintering. *Scripta Materialia, 48*, 635–639.

Kim, J.-D., Kang, S.-J. L., & Lee, J.-W. (2005). Formation of grain boundaries in liquid-phase-sintered WC–Co alloys. *Journal of the American Ceramic Society, 88*, 500–503.

Kim, C.-S., Massa, T. R., & Rohrer, G. S. (2008). Interface character distributions in WC-Co composites. *Journal of the American Ceramic Society, 91*, 996–1001.

Kim, S., Min, K.-h., & Kang, S. (2003). Rim structure in Ti(C0.7N0.3)–WC–Ni cermets. *Journal of the American Ceramic Society, 86*, 1761–1766.

Kim, C.-S., & Rohrer, G. S. (2004). Geometric and crystallographic characterization of WC surfaces and grain boundaries in WC-Co composites. *Interface Science, 12*, 19–27.

Kruse, O., Jansson, B., & Frisk, K. (2001). Experimental study of invariant equilibria in the Co-W-C and Co-W-C-M (M = Ti, Ta, Nb) systems. *Journal of Phase Equilibria, 22*, 552–555.

Kumar, V., Fang, Z., Wright, S., & Nowell, M. (2006). An analysis of grain boundaries and grain growth in cemented tungsten carbide using orientation imaging microscopy. *Metallurgical and Materials Transactions A, 37*, 599–607.

Lay, S., Allibert, C. H., Christensen, M., & Wahnström, G. (2008). Morphology of WC grains in WC-Co alloys. *Materials Science and Engineering: A, 486*, 253–261.

Lay, S., Donnadieu, P., & Loubradou, M. (2010). Polarity of prismatic facets delimiting WC grains in WC-Co alloys. *Micron, 41*, 472–477.

Lay, S., Hamar-Thibault, S., & Lackner, A. (2002). Location of VC in VC, Cr_3C_2 codoped WC-Co cermets by HREM and EELS. *International Journal of Refractory Metals & Hard Materials, 20*, 61–69.

Lay, S., Hamar-Thibault, S., & Loubradou, M. (2004). Accommodation of the lattice mismatch at the VCx-WC interface. *Interface Science, 12*, 187–195.

Lay, S., & Loubradou, M. (2003). Characteristics and origin of clusters in submicron WC-Co cermets. *Philosophical Magazine, 83*, 2669–2679.

Lee, K. H., Cha, S. I., Kim, B. K., & Hong, S. H. (2006). Effect of WC/TiC grain size ratio on microstructure and mechanical properties of WC-TiC-Co cemented carbides. *International Journal of Refractory Metals and Hard Materials, 24*, 109–114.

Lee, H. C., & Gurland, J. (1978). Hardness and deformation of cemented tungsten carbide. *Materials Science and Engineering, 33*, 125–133.

Lee, H. R., Kim, D. J., Hwang, N. M., & Kim, D.-Y. (2003). Role of vanadium carbide additive during sintering of WC–Co: mechanism of grain growth inhibition. *Journal of the American Ceramic Society, 86*, 152–154.

Lifshitz, I. M., & Slyozov, V. V. (1961). The kinetics of precipitation from supersaturated solid solutions. *Journal of Physics and Chemistry of Solids, 19*, 35–50.

Lindahl, P., Gustafson, P., Rolander, U., Stals, L., & Andrén, H. O. (1999). Microstructure of model cermets with high Mo or W content. *International Journal of Refractory Metals and Hard Materials, 17*, 411–421.

Lisovsky, A. (1987). On the imbibition of metal melts by sintered carbides. *Powder Metallurgy International, 19*, 18–21.

Lisovsky, A. (1991). Composition and structure of cemented carbides produced by MMT-process. *Powder Metallurgy International, 23*, 157–161.

Lisovsky, A. F. (2009). Deconsolidation of polycrystalline skeletons in sintered composite materials. *Materials Science Forum, 624*, 43–56.

Livey, D. T., & Murray, P. (1956). The wetting properties of solid oxides and carbides by liquid metals. *Plansee Proc. Sintered High-temperature and Corrosion-resistant Materials 19–23 June 1955*, 375–404.

Luyckx, S., & Love, A. (2006). The dependence of the contiguity of WC on Co content and its independence from WC grain size in WC-Co alloys. *International Journal of Refractory Metals and Hard Materials, 24*, 75–79.

Mannesson, K., Elfwing, M., Kusoffsky, A., Norgren, S., & Ägren, J. (2008). Analysis of WC grain growth during sintering using electron backscatter diffraction and image analysis. *International Journal of Refractory Metals and Hard Materials, 26*, 449–455.

Mattheiss, L. F., & Hamann, D. R. (1984). Bulk and surface electronic structure of hexagonal WC. *Physical Review B, 30*, 1731–1738.

Mingard, K. P., Roebuck, B., Marshall, J., & Sweetman, G. (2011). Some aspects of the structure of cobalt and nickel binder phases in hardmetals. *Acta Materialia, 59*, 2277–2290.

Mohan, K., & Strutt, P. R. (1996). Microstructure of spray converted nanostructured tungsten carbide-cobalt composite. *Materials Science and Engineering: A, 209*, 237–242.

Park, Y. J., Hwang, N. M., & Yoon, D. Y. (1996a). Abnormal growth of faceted grains in liquid matrix. *Materials Science Forum, 204–206*, 411–416.

Park, Y. J., Hwang, N. M., & Yoon, D. Y. (1996b). Abnormal growth of faceted (WC) grains in a (Co) liquid matrix. *Metallurgical Transactions A, 27*, 2809–2819.

Park, H. H., Kang, S. J. L., & Yoon, D. N. (1986). An analysis of the surface meniscii in a mixture of liquid and deformable grains. *Metallurgical Transactions A-physical Metallurgy & Materials Science, 17*, 325–330.

Pastor, H. (1987). Etat actuel et développement des matériaux durs et superdurs. *Matériaux et Techniques, 1–2*, 5–11.

Pastor, H. (1999). Developments in the powder metallurgy of non-oxide cermets. In B. D. Stojanović, V. V. Skorokhod, & M. V. Nikolić (Eds.), *Advanced science and technology of sintering*. New York: Kluwer Academic/Plenum Publishers.

Prakash, L., Holleck, H., Thümmler, F., & Walter, P. (1981). The influence of the binder composition on the properties of WC-Fe/Co/Ni cemented carbides. *Modern Developments in Powder Metallurgy, 14*, 255–268.

Ramqvist, L. (1965). Wetting of metallic carbides by liquid copper, nickel, cobalt, and iron. *International Journal of Powder Metallurgy, 1*, 2–21.

Rees, G. J., & Young, B. (1971). A study of the factors controlling grain size in sintered hard-metal. *Powder Metallurgy, 14*, 185–198.

Rolander, U., & Andrén, H.-O. (1988). Atom probe microanalysis of the γ phase in cemented carbide materials. *Materials Science and Engineering: A, 105–106*, 283–287.

Ryoo, H. S., & Hwang, S. K. (1998). Anisotropic atomic packing model for abnormal grain growth mechanism of WC-25%Co alloy. *Scripta Materialia, 39*, 1577–1583.

Saylor, D. M., & Rohrer, G. S. (2002). Determining crystal habits from observations of planar sections. *Journal of the American Ceramic Society, 85*, 2799–2804.

Schön, A., Schubert, W. D., & Lux, B. (2001). WC platelet-containing Hardmetals. *Proceedings of the 15th International Plansee Seminar, 4*, 322–336.

Schubert, W. D., Ettmayer, P., Lux, B., & Ohlsson, W. (1981). Phase equilibriums in the cobalt-molybdenum-tungsten-carbon and nickel-molybdenum-tungsten-carbon systems. *Proceedings of the 10th Plansee Seminar, 2*, 871–897.

Shatov, A. V., Firstov, S. A., & Shatova, I. V. (1998). The shape of WC crystals in cemented carbides. *Materials Science & Engineering A, 242*, 7–14.

Shatov, A. V., Ponomarev, S. S., Firstov, S. A., & Warren, R. (2006). The contiguity of carbide crystals of different shapes in cemented carbides. *International Journal of Refractory Metals and Hard Materials, 24*, 61–74.

Shin, S. G., & Matsubara, H. (1995). Grain growth of carbide based cermets during liquid phase sintering. In R. M. German, G. L. Messing, & R. G. Cornwall (Eds.), *Sintering technology* (pp. 157–164). New York: Dekker.

Smith, C. S., & Guttman, L. (1953). Measurement of internal boundaries in three-dimensional structures by random sectioning. *Trans AIME, 197*, 81–87.

Suzuki, H., Fuke, Y., & Hayashi, K. (1972). Grain size of WC in sintered WC-VC-Co alloys. *Journal of the Japan Society of Powder and Powder Metallurgy, 19*, 106–112.

Suzuki, H., Hayashi, K., & Terada, O. (1971). The two-phase region in TiC-Mo-30%Ni alloys. *Journal of the Japan Institute of Metals, 35*, 146–150.

Tulhoff, H. (1980). On the grain growth of WC in cemented carbides. *Modern Developments in Powder Metallurgy, 14*, 269–279.

Uhrenius, B. R., Pastor, H., & Pauty, E. (1997). On the composition of Fe-Ni-Co-WC-based cemented carbides. *International Journal of Refractory Metals and Hard Materials, 15*, 139–149.

Vicens, J., Benjdir, M., Nouet, G., Dubon, A., & Laval, J. Y. (1994). Cobalt intergranular segregation in WC-Co composites. *Journal of Materials Science, 29*, 987–994.

Vicens, J., Laurent-Pinson, E., Chermant, J. L., & Nouet, G. (1988). Structural analysis and properties of grain boundaries in hexagonal carbides. *Journal de Physique, C5*, 271–276.

Vicens, J., Lay, S., Benjdir, M., & Nouet, G. (1990). Nature of the boundary planes in tungsten carbide-cobalt composites. *Journal de Physique, C1*, 353–358.

Wagner, C. (1961). Theory of precipitate change by redissolution. *Zeitschrift fuer Elektrochemie, 65*, 581–590.

Wang, X., Fang, Z. Z., & Sohn, H. Y. (2008). Grain growth during the early stage of sintering of nanosized WC-Co powder. *International Journal of Refractory Metals and Hard Materials, 26*, 232–241.

Wang, Y., Heusch, M., Lay, S., & Allibert, C. H. (2002). Microstructure evolution in the cemented carbides WC-Co. I – effect of the C/W ratio on the morphology and defects of the WC grains. *Physica Status Solidi (a), 193*, 271–283.

Wang, Y., Pauty, E., Lay, S., & Allibert, C. H. (2002). Microstructure evolution in the cemented carbides WC-CoII. Cumulated effects of Cr additions and of the C/W ratio on the crystal features of the WC grains. *Physica Status Solidi (a), 193*, 284–293.

Warren, R. (1976). Determination of the interfacial energy ratio in two-phase systems by measurement of interphase contact. *Metallography, 9*, 183–191.

Warren, R. (1980). Solid-liquid interfacial energies in binary and pseudo-binary systems. *Journal of Materials Science, 15*, 2489–2496.

Warren, R., & Waldron, M. B. (1972a). Microstructural development during the liquid-phase sintering of cemented carbides. I. Wettability and grain contact. *Powder Metallurgy, 15*, 166–180.

Warren, R., & Waldron, M. B. (1972b). Microstructural development during the liquid-phase sintering of cemented carbides. II. Carbide grain growth. *Powder Metallurgy, 15*, 180–201.

Warren, R., & Waldron, M. B. (1972c). Surface and interfacial energies in systems of certain refractory-metal monocarbides with liquid cobalt. *Nature (London), Physical Science, 235*, 73–74.

Weidow, J., & Andrén, H.-O. (2010a). Binder phase grain size in WC-Co-based cemented carbides. *Scripta Materialia, 63*, 1165–1168.

Weidow, J., & Andrén, H.-O. (2010b). Grain and phase boundary segregation in WC-Co with small V, Cr or Mn additions. *Acta Materialia, 58*, 3888–3894.

Weidow, J., & Andrén, H.-O. (2011). Grain and phase boundary segregation in WC-Co with TiC, ZrC, NbC or TaC additions. *International Journal of Refractory Metals and Hard Materials, 29*, 38–43.

Weidow, J., Zackrisson, J., Jansson, B., & Andrén, H.-O. (2009). Characterisation of WC-Co with cubic carbide additions. *International Journal of Refractory Metals and Hard Materials, 27*, 244–248.

Wittmann, B., Schubert, W.-D., & Lux, B. (2002). WC grain growth and grain growth inhibition in nickel and iron binder hardmetals. *International Journal of Refractory Metals and Hard Materials, 20*, 51–60.

Yamamoto, T., Ikuhara, Y., & Sakuma, T. (2000). High resolution transmission electron microscopy study in VC-doped WC–Co compound. *Science and Technology of Advanced Materials, 1*, 97–104.

Yamamoto, T., Ikuhara, Y., Watanabe, T., Sakuma, T., Taniuchi, Y., Okada, K., et al. (2001). High resolution microscopy study in Cr_3C_2-doped WC-Co. *Journal of Materials Science, 36*, 3885–3890.

Yamamoto, T., Jaroenworaluck, A., Ikuhara, Y., & Sakuma, T. (1999). Nanoprobe analysis of core-rim structure of carbides in TiC-20Mo2C-20 wt.% Ni cermet. *Journal of Materials Research, 14*, 4129–4131.

Yang, J., Kim, D.-Y., & Eun, K.-Y. (1986). Formation of anomalous large grains in WC-Co alloy observed by Co infiltration. *Powder Metallurgy International, 18*, 62–64.

Yoon, B.-K., Lee, B.-A., & Kang, S.-J. L. (2005). Growth behavior of rounded (Ti, W)C and faceted WC grains in a Co matrix during liquid phase sintering. *Acta Materialia, 53*, 4677–4685.

Zackrisson, J., Rolander, U., & Andrén, H. O. (2001). Development of cermet microstructures during sintering. *Metallurgical and Materials Transactions A, 32*, 85–94.

SECTION II

CLASSES OF MATERIALS

1.04 Cemented Tungsten Carbide Hardmetal—An Introduction

1.05 Cermets

1.04 Cemented Tungsten Carbide Hardmetal—An Introduction

Z. Zak Fang and Mark C. Koopman, Department of Metallurgical Engineering, University of Utah, Salt Lake City, UT, USA
Hongtao Wang, Kennametal Inc., Rogers, AR, USA

1.04.1 Introduction

Although sixteenth century smelters of tin had noticed its presence, another 200 years would pass before the pure element tungsten would be isolated. The mineral *wolframite* was sometimes found with the tin-bearing ores that the Renaissance smelters used, and the *wolframite* devoured part of their precious tin yield. They could see the tiny droplets of tin trapped in the foam on the slag's surface, and, hence, the name "wolf". Tungsten's chemical symbol, W, derives from this historical connection, and the element is still known as "wolfram" in a number of languages around the world. Tungsten in its metallic form was first isolated in the early 1780s by the Spanish nobleman, Juan José D'Elhuyar, a student of the Swedish metallurgical chemist Torbern Bergman.

The synthesis of tungsten carbide (WC) was accomplished by the French chemist Henri Moissan in the 1890s, and WC was subsequently combined with a ductile matrix to make cemented carbides in the early 1920s by researchers at Osram Studiengesellschaft in Germany. The initial application employed the new material to replace diamond in the nozzle tips of extruders for drawing tungsten filaments for incandescent light bulbs, but over the coming decades, WC would see a dramatic expansion in a range of applications. High hardness and wear resistance, coupled with better fracture toughness than most hard materials, has led to cemented carbides becoming integral in manufacturing fields ranging from plastics to metal forming, as well as in construction and specialized structural components. Cemented carbides are the material of choice for many applications involving high abrasive wear, such as in rock and earth drilling for the mining, oil and gas industries, and is also used to make tool bits for precision drilling. In the fabrication of integrated circuit boards, for example, holes as small as 150 μm are drilled at speeds up to 300,000 rpm. After nearly a century of research and development, cemented WC is now the most important industrial tool material.

Because of its historical significance in manufacturing and its extensive capabilities, there have been several dedicated monographs on cemented WC. Early texts solely on cemented carbides were published by Dawihl and Dinglinger (1953), and also by Schwarzkopf and Kieffer (1960). Following several other authors in intervening years, a more recent and very thorough volume was published by Upadhyaya (1998). Readers interested in a historical perspective or a more detailed view of cemented carbides may consult these texts, as well as the extensive literature available from relevant journals and conference proceedings.

As a part of this comprehensive handbook on hard materials, this chapter will focus on the uniqueness of cemented WC, and we will highlight the properties of cemented WC from the backdrop of the vast universe of materials. As the following will show, cemented WC is truly an indispensable material. There are currently no

http://dx.doi.org/10.1016/B978-0-08-096527-7.00004-0

alternatives that could conceivably replace cemented WC in manufacturing and industry, and the prospects for the future of the cemented WC industry appear solid and reliable.

1.04.2 Processing of Cemented WC

Cemented WC is a composite of WC and cobalt metal (Co). In most commercially available grades of WC–Co, cobalt content ranges from 6.0 to 16.0%. There are applications using as low as 3% cobalt or as high as 25% cobalt, but the use of the more extreme compositions is not common. WC grain sizes range from submicron (0.2 μm) to 10 μm in the fully sintered solid state. The manufacturing processes of cemented WC from ore to powder and from powder to products are illustrated in Figures 1 and 2.

As Figure 1 shows, WC powders are made through the carburizing of metal tungsten powder, which is, itself, produced from either Wolframite [$(FeMn)WO_4$] or Sheelite ($CaWO_4$) tungsten ores via multiple steps of chemical extractive metallurgical processes. Key intermediate products are ammonium paratungstate (APT) and either tungsten blue oxide (WO_2) or yellow oxide (WO_3). Tungsten oxides are produced from APT by calcination. These tungsten oxides are subsequently reduced in hydrogen in order to produce tungsten metal powder (TMP), which is then carburized in mixtures with carbon at high temperatures under hydrogen atmosphere to form WC. The calcination of APT and the reduction of tungsten oxides are critical steps of the overall process because the size of tungsten oxide particles has a strong effect on the size of resulting metal tungsten powders, and, therefore, the size of subsequent WC powders. Particle sizes of WC produced via the processes described above can range from 0.1 to tens of microns.

The processes transforming WC powder to tools and other products are typical for powder metallurgy processes. They involve milling of blended WC and metal binder powders, such as Co, shaping through various powder compaction techniques, and liquid phase sintering in vacuum with or without a final step of low pressure hot isostatic pressing (sinter-HIP). The processes from powder to products are illustrated in Figure 2.

Milling serves several purposes, including the mixing of WC and binder powders with a desired composition, reducing WC agglomeration and WC particle size, and to get a uniform distribution of binder powders among WC particles. Typical milling equipment includes rolling ball mills and attritor mills, and each method has particular milling characteristics. Rolling ball mills are effective in reducing the size of large particles (>2 μm) to fine particles, and can produce narrow particle size distributions, which have a lower tendency toward grain growth during sintering, thus leading to a uniform sintered microstructure. When the particle size is <2 μm, ball mills are less effective at further reducing the particle size.

Attritor mills are more aggressive than rolling ball mills, and are approximately 11 times more effective than ball mills with respect to particle size reduction. Fine particles (<2 μm) can also be milled; however, attritor mills have a tendency to produce very fine particles and sometimes wide and/or bimodal particle size

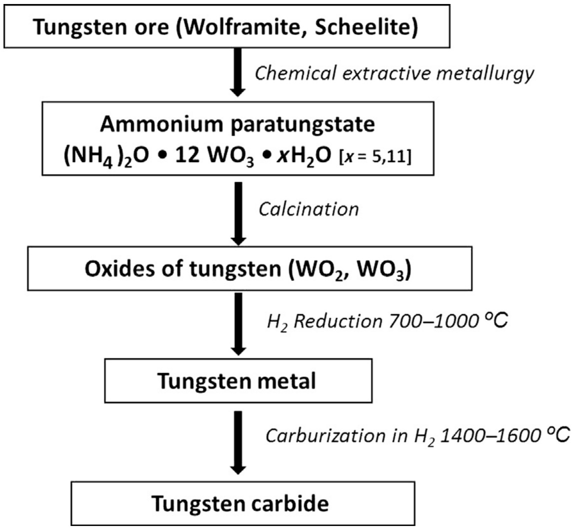

Figure 1 General manufacturing process for tungsten carbide powder.

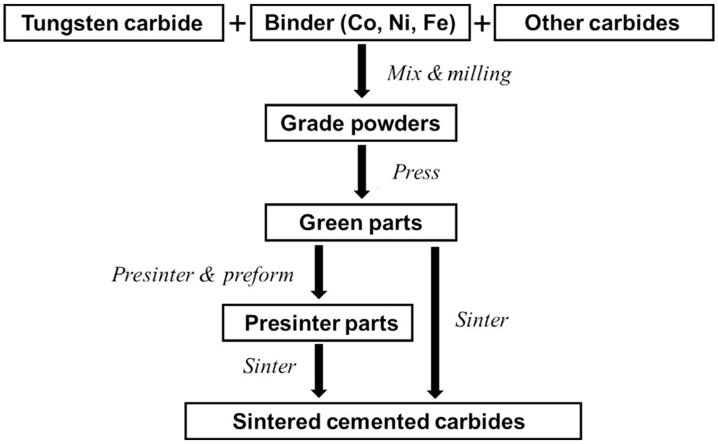

Figure 2 Typical powder metallurgy processes of producing cemented carbides.

distributions. Such particle distributions are prone to grain growth during sintering and result in a less uniform sintered microstructure. Both methods are currently used in the industry, depending on the required microstructure of the final sintered product.

After milling, the powders are dried and granulated for compaction. The consolidation of cemented carbide powders into different shapes can be achieved by die pressing, cold isostatic pressing, extrusion, or powder injection molding. Die pressing is still the most widely used and economical shaping method in the cemented carbide industry. Extrusion of cemented carbide powders mixed with a plasticizing binder is typical for the production of rods, strips, etc., especially for round rotary tools such as drilling and milling tools produced in large quantities. Cold isostatic pressing is mainly used to produce large blanks in smaller numbers. The large blanks usually need to be further machined in either the green state or presintered state in order to obtain parts close to their final sintered size and shape. Powder injection molding is used to fabricate very small parts with complex geometries that cannot be readily machined.

All cemented carbides are generally sintered in the liquid phase state under vacuum conditions. Sintering is the critical step for the determination of the final properties of cemented carbide. One of the key innovations of the industry in the past two decades is the sinter-HIP process. Sinter-HIP is now a mature process that has been replacing the standard vacuum sintering method gradually since the late 1980s to the early 1990s. The pressure of the sinter-HIPing step ranges from 3 to 10 MPa, and the profound benefit of sinter-HIP over standard vacuum sintering is the elimination of residual porosity. This has resulted in a significant increase in the transverse rapture strength of the material, as well as improving the consistency of the strength of the material.

Figure 3 shows a typical sinter-HIP furnace. The typical capacity of production furnaces ranges from 300 to 500 kg per charge. However, furnaces up to 1000 kg per charge are also available. One of the key issues for

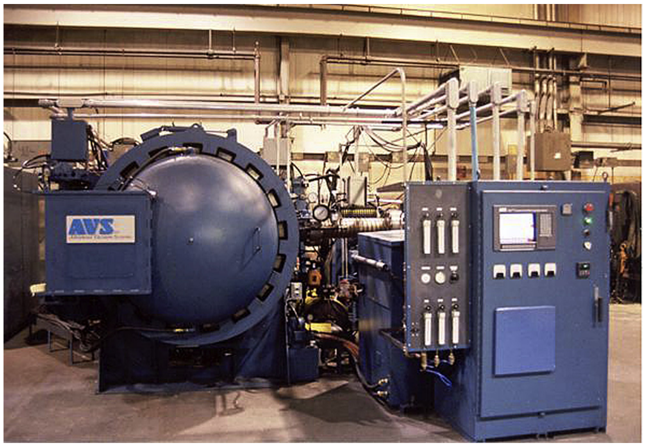

Figure 3 A typical tungsten carbide sintering HIP furnace.

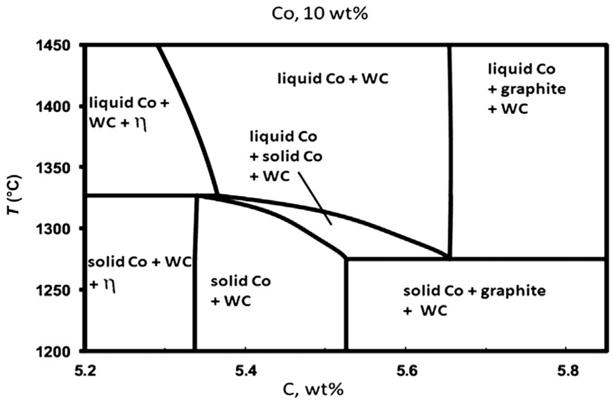

Figure 4 Phase diagram of the WC–10 wt% Co system with varying carbon content. From Mahale (1994).

sintering cemented WC is carbon content control. The carbon content has a strong effect on mechanical properties. Figure 4 shows a phase diagram of the WC–Co system with 10 wt% Co, but varying carbon content. When the carbon content is too low, the material will form the eta phase, η, which can be complex carbides of W–Co–C. Typical formulas of the eta phase include $Co_{3.2}W_{2.8}C$ and Co_2W_4C. The eta phase is characterized as brittle, and consequently, detrimental to mechanical properties. It is generally avoided in the final microstructure of WC–Co. When the carbon content is too high, uncombined carbon forms a free graphite phase in the microstructure. Particles of uncombined graphite phase are also considered undesirable from the standpoint of mechanical strength, although the graphite phase is not perceived as being as detrimental as the eta phase in WC–Co microstructures.

Even when the carbon content is within the two-phase field of WC and Co, it still has a significant effect on mechanical properties. When the carbon content is lower than the stoichiometric content of 5.52 wt% C for WC–10 wt% Co, and higher than the level that would induce the eta phase, the density and hardness of cemented carbides increase when the carbon level decreases. In this region of the phase diagram, a lower carbon level induces more W solution in the Co phase, and not only increases the density of cobalt phase but also slows down the solution–reprecipitation process during sintering and, thus, results in a smaller grain size and higher hardness in the sintered parts.

Many processing variables affect the carbon content in the final sintered material. Powder milling and sintering are the two critical processes that determine the final carbon content in the sintered parts. During powder milling, the carbon content is primarily dependent on raw WC materials, and can be adjusted by either graphite addition or TMP addition to increase or decrease the carbon balance in the sintered parts. During sintering, the dewax step and tungsten/cobalt oxide reduction process can also affect the carbon content in the sintered parts. For example, improper dewax may leave free carbon in the sintered parts, and excessive oxide reductions can cause an issue with carbon deficiency. Other factors, such as furnace load volume, plate tray coating, and vacuum leaks can also have distinct influences on the carbon level in the sintered parts.

Conventional sintering of cemented carbide is a long thermal cycle process (18–24 h including heating and cooling), which favors undesirable WC grain growth. In recent years, in order to control grain growth during sintering and shorten the sintering cycle, several new sintering techniques have emerged. One of these techniques is microwave sintering. Microwave heating requires little time to obtain nearly full densification, and, therefore, grain growth is relatively suppressed and a fine microstructure is generally obtained. Some reports have shown that cemented carbide parts produced by microwave sintering can exhibit an improvement in abrasion resistance, erosion resistance, and corrosion resistance without any noticeable loss in hardness or fracture toughness. These improvements in the properties are believed to be due to the fine microstructure, uniform cobalt phase distribution, and pure cobalt phase in microwave-sintered samples. Microwave sintering of cemented carbide is now under commercial exploitation for specialty carbide products.

The quality of sintered products is generally characterized and monitored by measuring density, porosity, magnetic saturation, coercive force (H_c), and hardness of the sintered products. Other inspection and characterization techniques, such as cobalt pools, grain size distribution, and maximum grain size may also be required to evaluate some sintered products. The measurements of these properties should conform to American Society for Testing and Materials (ASTM) standards. Different specifications are defined with respect to the target and/or tolerance of the above-mentioned properties for the different sintered products, and the quality of the sintered products is basically controlled per these specifications.

1.04.3 Mechanical Properties and the Role of Microstructure in Cemented WC

1.04.3.1 General Properties

The basic physical and mechanical properties of WC include high elastic modulus, high hardness, and high thermal conductivity. Table 1 lists the values of these basic properties along with those for several other common hard materials for comparison.

Figure 5 displays the elastic modulus versus compressive strength of different families of materials, putting WC in a perspective relative to other superhard, hard, ceramic, and metallic materials. It shows WC as the hardest material, although diamond and cubic boron nitride would be above WC if included in the database used for this figure. WC exceeds the hardness range for many common hard ceramic materials, such as SiC and alumina (Al_2O_3). The elastic modulus and hardness of cemented WC (WC–Co) are lower than for pure WC, due to the effects of Co in the composite microstructure. However, the elastic modulus and hardness of WC–Co are

Table 1 Selected mechanical properties of WC and other common hard materials

Material	*Young's modulus, E (GPa)*	*Hardness* (H_V)	*Compressive strength (MPa)*	*Thermal conductivity* ($W\,m^{-1}\,°C^{-1}$)	*Electrical resistivity* (μ*ohm cm*)
WC	625–700[a]	2200–3600[a]	3350–6830[a]	55–80[a]	20–100[a]
Diamond	1220[b]	10,000[c]	9000[d]	2000[d]	1e19–1e22[e]
WC–Co (cemented WC)	400–650[f]	700–2200[f]	3000–9000[f]	70–120[f]	16–20[f]
Steel (typical)	150–200[f]	240–300[f]	250–1760[a]	15–65[f]	15–120[f]
SiC	400–460[a]	2300–2600[a]	1000–4500[f]	80–130[a]	1e9–1e12[a]
Al_2O_3	343–390[a]	1200–2060[a]	500–2700[f]	26–38.5[a]	1e20–1e22[a]

[a] *CES Edupack, Cambridge, UK.*

[b] *Spear and Dismukes (1994).* Synthetic diamond—emerging CVD science and technology. *Wiley, NY. ISBN 978-0-471-53589-8.*

[c] Smithells metals reference book *(8th ed.), chap. 22.*

[d] *CVD Diamond, http://www.e6cvd.com/cvd/page.jsp?pageid=349.*

[e] *CVD Diamond, http://www.e6cvd.com/cvd/page.jsp?pageid=348.*

[f] *Understanding Cemented Carbides, Sandvik Coromant.*

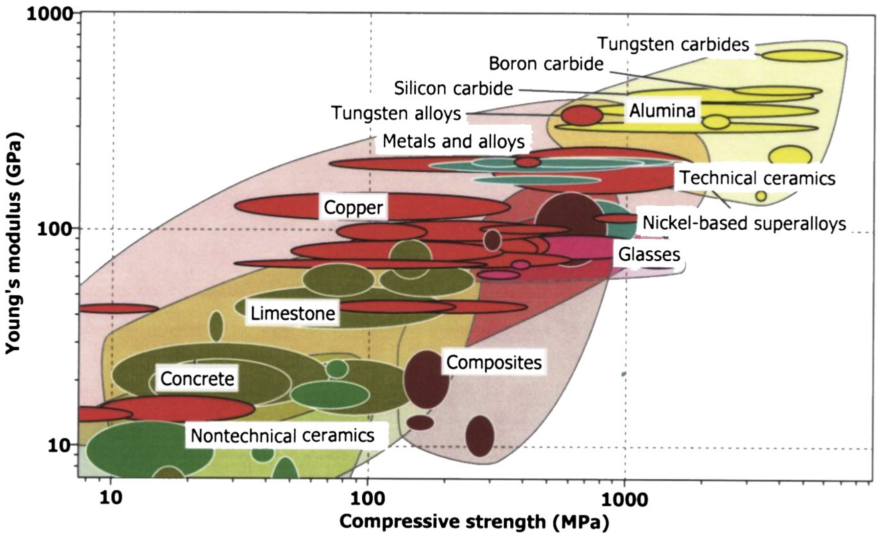

Figure 5 Ashby plot of Young's modulus versus strength, illustrating relative comparison of WC to other families of materials (created with CES Edupack).

still much higher than for many other widely used engineering materials, and in this system the Co significantly improves fracture toughness. The range of Co composition within the WC–Co system provides this material with its exceptional range in mechanical properties, and hence its broad utility.

Another very important difference between WC and other ceramic materials is that WC is an excellent thermal conductor, while most ceramics are thermal insulators. A less known fact is that the thermal conductivity of WC is higher than for most metals, including Fe, Ni, and Co. Consequently, the higher the content of the Co binder phase in cemented carbides, the lower the thermal conductivity (Frandsen & Williams, 1991; Percherla & Williams, 1988). Additionally, WC–Co shows a higher thermal conductivity than TiC–Co or mixed carbide systems (Frandsen & Williams, 1991). The high thermal conductivity of WC is due to the lower phonon scattering in the hexagonal crystal structure, which shows a low incidence of point defects (Frandsen & Williams, 1991; Percherla & Williams, 1988), whereas TiC with its cubic structure tends to have missing C atoms in the structure that increase phonon scattering at room temperature (Frandsen & Williams, 1991) thus, decreasing thermal conductivity. The superior thermal properties of WC play an important role in separating it from typical ceramic materials, opening applications that require good heat flow in addition to high hardness and/or modulus.

1.04.3.2 Engineering Properties and Dependence on Microstructure

The primary industrial applications of WC–Co put it in the category of structural materials. The most important mechanical properties of WC–Co include hardness, transverse rupture strength (TRS), fracture toughness, impact resistance, and wear resistance. Table 2 lists out the ranges of these properties for metal alloys and ceramics, and for typical WC–Co, considering cobalt contents from 3 to 30% by weight.

TRS measurements are sensitive to porosity and other defects, particularly in the near surface region. TRS can be measured according to ASTM B406, using a three-point bending flexural strength test that puts the test surface under tensile stress. Since retained porosity in sintered WC–Co was often a limiting factor in the microstructure of these materials and how they would respond to various applications, TRS was used extensively in evaluating these materials during their development. The test continues to be widely used as a quality control indicator today despite the fact that porosity levels have dropped significantly in the commercial grades of WC–Co due to the advances of modernized manufacturing processes. Historically, cemented carbides tended to have a large scatter in TRS data (Exner & Gurland, 1970). With appreciable porosity, TRS and fracture toughness tend to track one another closely, since the pores act as defects of a critical size for fracture toughness, governed by $K_{IC} = A\sigma_r(a_c)^{0.5}$, where A is a geometrical constant, σ_r is the rupture strength and a_c is the defect or pore size. With negligible porosity, however, the static tensile state in TRS measurements can be more contingent on the intrinsic mechanical properties of the WC–Co system.

Detailed examination has revealed a complex relationship between TRS, hardness, and fracture toughness, even though TRS has sometimes been regarded as having a simple inverse relationship with hardness. An examination of samples with various Co contents and grain sizes, but excluding the hardest samples with very low Co or submicron grain sizes, showed a bell-shaped curve of TRS versus hardness with maximum TRS values occurring between hardness values from 1100 to 1300 kg mm^{-2} (Fang, 2005). The same study showed a high scatter of very hard samples, correspondingly with a very low fracture toughness, at hardness values >1600 kg mm^{-2}. The relationship between TRS and hardness can also be analyzed by examining its dependence on cobalt content and grain size separately. TRS values are highly contingent on Co content with a maximum value at approximately 20 wt% Co. Exner and Gurland (1970) also showed variation of TRS with WC grain size, again with a bell-shaped curve, and with a maximum TRS in the WC grain size range of 3–4 μm.

In terms of fracture toughness, cemented WC is generally considered a brittle material, and the primary failure mode for most tool applications involves chipping or fracturing. In order to minimize and eliminate the

Table 2 Comparison of ranges for mechanical properties of WC–Co with those of ceramics and metal alloys

Material	*Hardness (H_v N mm^{-1})*	*TRS (MPa)*	*Fracture toughness (MPa$\sqrt{m}$)*	*Impact resistance*	*Wear resistance*
WC–Co	1000–2300	2000–4000	9–20	Moderate	High
Ceramics		500–2000	3–7	Low	Moderate
Metal alloy	300–900	<5000	20–100	High	Low

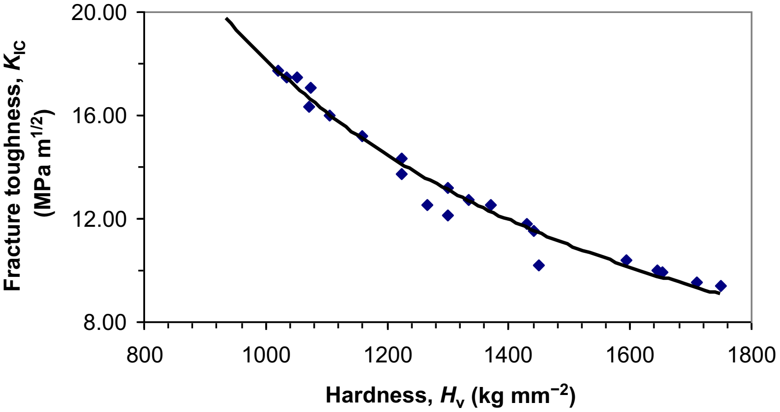

Figure 6 Fracture toughness versus hardness for a range of cemented carbide compositions.

possibility of catastrophic failure during service, fracture toughness (K_{IC}) of WC–Co must be considered a key mechanical property, dictating the selection of different grades of WC–Co materials.

A large body of literature is available on the fracture toughness of cemented WCs: Peters (1979), Bolton and Keely (1982), Sigl, Exner, and Fischmeister (1986), p. 631, Sigl and Exner (1987), Ravichandran (1994), Luyckx, Sacks, and Love (2007), and Zhang, Fang, and Belnap (2007). A. Shatov also further addresses an examination of fracture toughness within this volume in Chapter 1.10. Fracture toughness differs from TRS in that it is essentially a measurement of the materials resistance to crack propagation. It is well established that the fracture toughness is inversely proportional to the hardness of the material as shown in Figure 6, and both hardness and toughness are functions of the cobalt content and grain size of the material. For a given grain size, K_{IC} increases with cobalt content, and for a given Co%, K_{IC} increases as grain size increases (Luyckx et al., 2007). The combined effects of grain size and cobalt can be expressed by the dependence of K_{IC} on the mean free path (MFP) between WC grains, which is effectively the size of cobalt pools between WC grains. Figure 7 shows the dependence of both hardness and fracture toughness on MFP. MFP is related to grain size and cobalt content by the following equation:

$$\lambda = \frac{4(1 - V_V)}{S_V}$$

where λ is MFP, V_V is the volume fraction of WC particles, and S_V is the total surface area of WC grains which is determined by the grain size as well as cobalt content.

In the WC–Co system, the dependence of fracture toughness on microstructure is indicative of the toughening mechanisms in cemented carbides by the addition of Co. Sigl et al. systematically studied the propagation

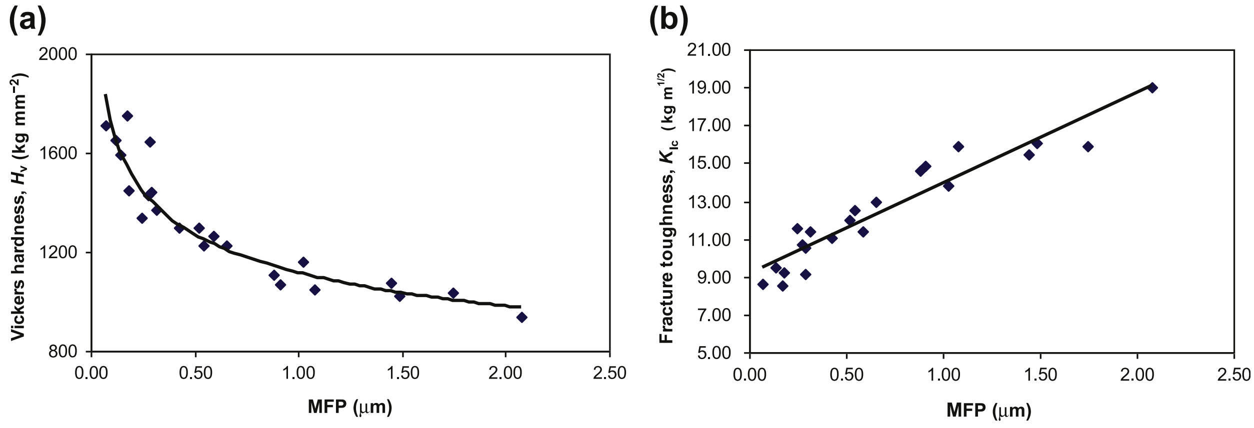

Figure 7 Mean free path for a range of cemented carbide compositions plotted against (a) hardness and (b) fracture toughness.

of cracks in a WC–Co composite and found that 90% of the energy consumed during fracture of WC–Co is attributable to the plastic deformation of the cobalt phase in the path of the crack tip movement (Sigl et al., 1986, p. 631). The ductile tearing and crack bridging of cobalt is the primary mechanism for toughness in the WC–Co composite microstructure.

In testing procedures for fracture toughness, it is generally necessary to introduce sharp preexisting cracks of a known length to the samples before testing. Due to the principally brittle nature of cemented carbides, the introduction of precracks is not trivial, although a number of techniques have been successfully developed (Bolton & Keely, 1982). Consequently, TRS experiments are favored over fracture toughness in some cases, although the two tests do not investigate precisely the same materials phenomenon.

Early analyses of the plastic deformation process in WC–Co proposed that the ductile Co phase was completely responsible for plasticity in this system, and that the WC particles acted solely as dispersion strengthening agents (Doi, Fujiwara, & Miyake, 1969). Other researchers have noted the contribution of WC deformation in relation to the deformation of the composite structure: Takahashi and Freise (1965), Hibbs and Sinclair (1981), Chernyavsky (1986), and Sarin and Johannesson (1975). Chernyavsky noted contributions from the slip within WC grains, as well as the slip along intercarbide grain boundaries.

Damage evolution has been investigated using a Hertzian indentation technique, which uses a near frictionless spherical indenter loaded normal to a polished surface (Zhang, Fang, et al., 2007). In addition to obtaining stress–strain curves in this work, Zhang measured and evaluated surface and subsurface microscopic and macroscopic cracking. The material response was categorized into three regions with increasing stress: a pseudoelastic region with an initial linear stress–strain response; a quasiplastic zone characterized by Co-binder deformation, as well as slip within WC grains and evidence of microcracking; and a fully plastic zone where the stress–strain curve reaches a plateau and the skeleton of interconnected WC grains is broken (Zhang, Fang, et al., 2007).

1.04.3.3 Wear Resistance

Owing to its very high hardness and strength, cemented WC has excellent wear resistance, which is the primary reason why WC–Co is chosen for most applications. For any given wear environment, the mechanisms of wear loss may be different, and the wear resistance of the material may vary. The main wear applications include

1. Adhesive and chemical wear during metal cutting
2. Abrasive wear during rock drilling
3. Sliding wear when used as machine rotational components

Similar to other materials used for wear applications, the wear resistance of WC–Co is determined by three categories of factors: mechanical properties, microstructure features, and the wear environment. The most important and primary factor that determines the wear resistance of WC–Co is the hardness. Figure 8 shows the dependence of high stress abrasive wear resistance of WC–Co as a function of hardness as measured by the standard method prescribed in ASTM-B611. Figure 8 also shows that wear resistance is inversely proportional to

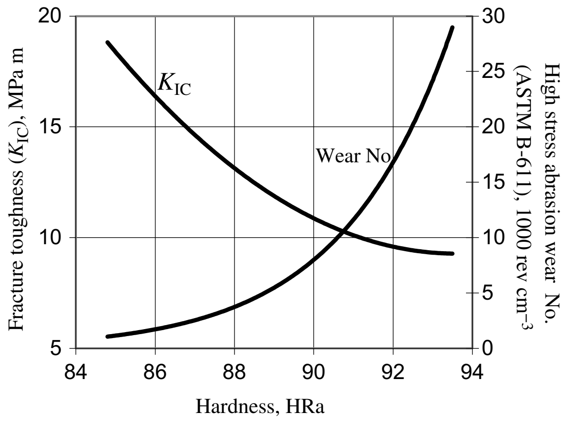

Figure 8 Wear resistance and fracture toughness versus hardness for WC–Co materials. After Fang (1998).

the fracture toughness, which is directly a result of the inverse relationship between the hardness and the fracture toughness.

The same trend also applies to other types of wear environments. However, in addition to hardness, other factors must also be considered, such as mechanical loading conditions, wear mechanisms, harshness of abrasive particles, and hardness and size/shape of abrasive particles. In cases of abrasive wear, the relative size between the hard phase particles, d_c, and abrasive particles, d_a, is an important factor. In general, if $d_c < d_a$, the rate of wear is greater than it would be if $d_c > d_a$. In cases of sliding wear, relative hardness between the two mating surfaces, the chemical affinity between the two mating surfaces, and abrasive particles contained in the materials are all important factors that affect the wear behavior and wear rate. Depending on the wearing system, different mechanical properties (e.g. resistance to plastic deformation, crack formation, or crack propagation) have to be considered. Depending on which wear mechanism is dominant, different material properties and microstructure may be desired. Other environmental factors such as corrosive fluids and potential chemical interactions need to also be considered. Chapter 1.12 by M. Gee sheds further illumination on the mechanisms and effects of wear in this system.

1.04.3.4 Interrelationship between TRS, Hardness, Wear Resistance, and Fracture Toughness and Comparison with Ceramics and Metals

The interrelationship between hardness, wear resistance, and fracture toughness is, in general, consistent with the fundamentals of structural metal alloys. The relationship between TRS, hardness, and fracture toughness is, however, not straightforward.

Historically, the industry has considered TRS as a measure of the "toughness" of the material. The perceptions are that the higher the cobalt content or the lower the hardness, the higher the TRS. Fang examined the relationships between TRS, hardness, and fracture toughness and found that the relationship between TRS and hardness is not a monotonic one as was perceived (Fang, 2005). Figure 9 shows that TRS decreases as hardness increases from HRa 87 to 92, but, it increases as hardness increases from HRa 85 to 87. When hardness is >HRa 93, the corresponding TRS values increase dramatically. In recent years with the advent of commercial ultrafine grain-cemented WC products with hardness equal or greater than HRa 93, TRS values are typically reported to be ≥4000 MPa. This is understood on the basis that TRS is essentially a tensile strength property. As hardness increases, the yield strength of the material increases proportionally. However, TRS is sensitive to defects, including microcracks. In the medium hardness range, the fracture toughness becomes the dominating factor; hence, TRS decreases as hardness increases and toughness decreases.

The relationship between hardness, fracture toughness, and wear resistance (Fang, 1998, pp. 965–977) is shown in Figure 8. Due to the inverse relationship between hardness and toughness, and the proportional relative relationship between wear resistance and hardness, the wear resistance and fracture toughness are inversely related. This is the trade-off between wear resistance and toughness that engineers must make when selecting a particular grade for a specific application.

The role of cemented WC tools in the industry is dictated by cemented carbides' mechanical properties relative to those of metal alloys and ceramics. The performance of cemented WC is determined by a

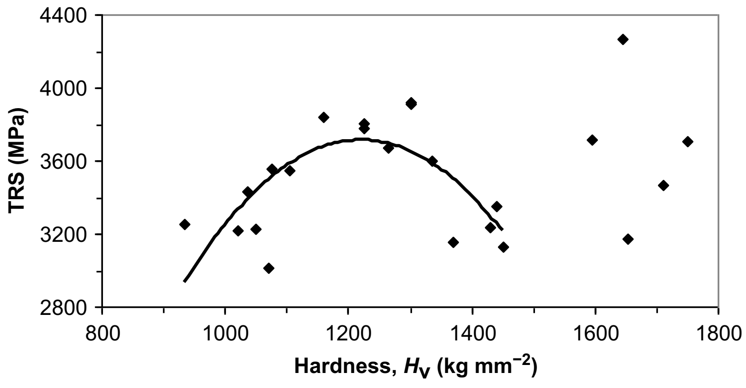

Figure 9 Transverse rupture strength versus hardness for cemented carbides. From Fang, 2005.

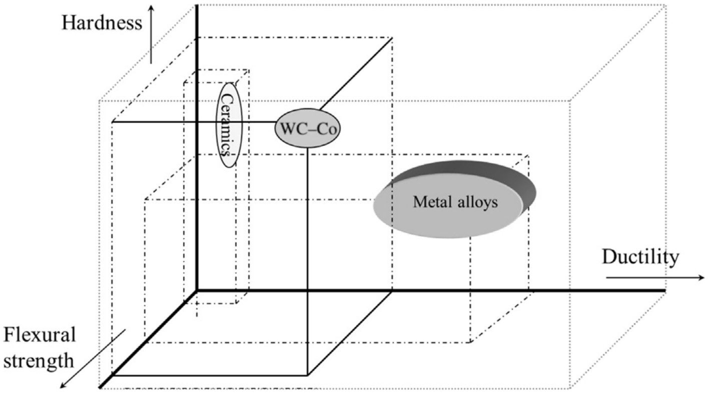

Figure 10 The relationship between hardness, ductility, and flexural strength; comparing metal alloys, ceramics and WC–Co.

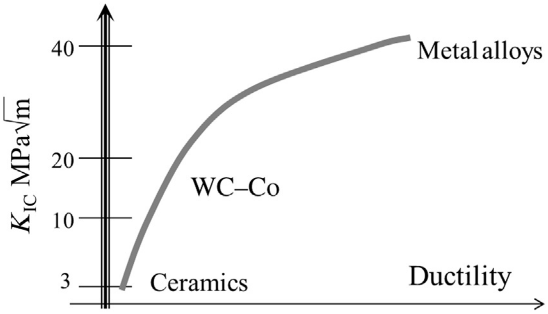

Figure 11 Relative placement of ceramics, WC–Co, and metal alloys, showing the relationship between fracture toughness, K_{IC}, versus ductility.

combination of mechanical properties that set it apart from metal alloys and ceramics. Figure 10 illustrates that WC–Co is equivalent to ceramic materials in terms of hardness. WC–Co, however, has a much higher flexural strength and ductility than traditional ceramic materials. In contrast, WC–Co does not have the exceptional ductility of metal alloys, but has a much higher hardness and strength. Therefore, WC–Co is a material that spans the spectrum of mechanical properties between ceramic and metals. Figure 11 further shows the unique position of WC–Co relative to metals and ceramics when considering ductility and toughness. Once again, it is the unique combination of mechanical properties that has determined the specific applications and broad role of WC–Co in manufacturing industries; a range of applications that cannot be matched or replaced by any metal or ceramic material currently known.

1.04.3.5 The Role of Coatings

Approximately 50% of all sintered WC–Co materials are used as cutting tools for the machining of metals and other materials. Since the 1980s, and continuing through current use, the majority of WC–Co cutting tools are coated by a thin film of ceramic material, using either chemical vapor deposition (CVD) or physical vapor deposition (PVD) methods. Major PVD techniques include sputtering and evaporation methods, while CVD describes methods involving reactions between gases at the surfaces of heated substrates. While PVD coatings are applied under partial vacuum, CVD processes involve elevated temperature and pressure. The ceramic coating materials are typically carbides, nitrides, or carbonitrides of Ti, Cr, Al, Hf, or Ta, although aluminum oxide is also widely used and diamond coatings are becoming more readily available. Coatings of nanocomposite microstructure are also being investigated (Chen, Du, Wang, Wang, & Xu, 2009; Wang et al., 2010). The thin film coatings range from a few micrometers to several tens of micrometers. Often the thin film consists of multiple layers of nanometer thicknesses, with different alternating coating compositions. Generally, it is desired to select coatings composed of materials with a low chemical affinity to the materials being machined or worked, in order to minimize adhesion wear and favor abrasive wear as the primary wear mechanism. In Chapter 1.16 by U. Schleinkofer, the role of coatings is examined in further detail.

There are a number of advantages of coated WC–Co over conventional uncoated WC–Co materials, including higher wear resistance, potentially better chemical stability, and some coatings also provide higher potential tool speeds, which result in faster cutting or machining operations. Many of these attributes result in cost savings in manufacturing processes, which accounts for their high market share. Additionally, by maintaining dimensional integrity of the tools during operation (by virtue of the high wear resistance), greater dimensional accuracy can be obtained in difficult to machine alloys like Inconel 718, other high nickel alloys and Al_6Ti_4V. This is particularly useful in parts produced for certain aerospace applications, as well as other applications requiring high precision machining (Biksa et al., 2010; Fox-Rabinovich et al., 2010).

Cemented carbides provide a high modulus–high hardness substrate for these hard wear-resistant coatings, but care must be taken in both the design and fabrication of the coated materials in order to obtain maximum wear efficiency. Normally, it is desired to have coatings with similar thermal conductivity and coefficient of thermal expansion (CTE) to that of the cemented carbide. A large mismatch in CTE between the coating and substrate can promote loss of the coating due to high shear stresses generated at the coating–substrate interface, depending on the temperature range of the coating process or the temperature of the in-service application. This is among the reasons for multilayer coatings, where both intermediate layer thickness and composition can minimize residual shear stresses during temperature variation. Most coatings are also designed to be under residual compressive stress, which contributes to coating retention during use.

Coating retention is a major consideration in the design, production, and application of coated cemented carbides. To this end, cleaning of the surfaces is often done by ion etching, solvent, or chemical processes to prevent debonding or inadvertent porosity at the coating–substrate interface. Subsequently, surface pretreatments are often employed in both PVD and CVD processes to modify the chemistry, morphology, or roughness of the WC–Co surfaces. These pretreatments are sometimes used in combination, and include mechanical, chemical, and thermal methodologies, as well as laser ablation and the application of interlayers (Arroyo, Diniz, & Fernandes de Lima, 2010). As an example, Bouzakis et al. recently investigated the effects of different nanointerlayers (W, Cr, and Ti deposited by high-power pulsed magnetron sputtering) for PVD coatings of AlTi(N) with varied surface roughness (Bouzakis, Skordaris, et al., 2010). Their results indicated that a Cr-adhesive nanolayer and a polished and microblasted surface finish gave the best tool life in this coating system. Because the microscopic stress states at the interface play an integral role in coating adhesion, the thickness of interlayers must be considered in relation to the roughness of the substrate surface (Bouzakis, Makrimallakis, et al., 2010). Both testing and finite element analysis can be useful in such efforts to obtain the best coating adherence and, therefore, tool life.

A number of coating compositions with Vicker's hardness values, as high as 8000 H_V, are being studied or have been introduced to the marketplace in recent years (Upadhyaya, 1998). These include TiB_2, BN, TiB_XN_Y, diamond, and diamond-like carbon.

1.04.3.6 Novel Microstructures

Over the past half century, great strides have been made in the science of cemented carbides to understand the relationships between the chemical constituents, and to improve processing technology. These efforts have resulted in low-porosity materials suitable for a wide variety of tool applications, and the advent of coatings has pushed their utility further still. The desire to increase wear performance without sacrificing fracture toughness, or to improve fracture toughness without decreasing wear resistance, has led to several innovative microstructures, including functionally graded (FG) and double cemented carbides (DCCs).

DCCs describe a microstructure whereby granules of high WC content are dispersed in a continuous Co matrix, resulting in a much higher MFP within the Co matrix compared to conventional cemented carbides (Deng et al., 2001; Fang, Lockwood, & Griffo, 1999; Fang & Sue, 2005). The much larger regions of Co between granules serve to improve fracture toughness, while the hard granules support load during wear, thus resulting in a material that performed particularly well under conditions of high stress wear.

FG microstructures have been introduced in other composite systems, and involve a variation from overall chemistry at the surface, and a gradual change in chemistry moving away from the surface into the bulk of the material. This gradual change in chemistry results in a corresponding gradual change of material properties from the surface into the interior, and consequently avoids the discrete change in properties, as well as the level of residual shear stresses, encountered at the interface of many coated materials.

Although FG cemented carbides have been fabricated with excess Co at the surface (Nemeth & Grab, 1986), most efforts have been toward producing materials with higher concentrations of WC at the surface and a zone of decreasing WC into the sample. The high WC at the surface creates tools with a higher wear resistance, but with a higher Co interior that possesses a better fracture toughness than the wear surface.

The dual property FG cemented carbides employ a low C matrix containing eta phase, and carburization during a second sintering process to force Co to migrate away from the surface (Fisher, Hartzell, & Akerman, 1988; Liu et al., 2006; Zhang, Chen, et al., 2007). Several groups have worked on other methods (Konyashin et al., 2010; Larsson & Odén, 2004). Work by Fang et al. has developed a method whereby materials are carburized within the 3-phase region of the ternary W–C–Co phase diagram, producing linear composition gradients without the presence of eta phase (Fang & Eso, 2005; Eso, Fang & Griffo, 2005; Fan, Guo, Fang, & Prichard, 2009; Guo, Fan, Wang, & Fang, 2011; Guo et al., 2012). The eta phase can have negative impact on mechanical properties, and is often avoided in conventional microstructures (Upadhyaya, 1998). Measurements of fatigue, impact, and wear properties indicate a significant improvement in properties for a range of potential applications (Wang, Hwang, Koopman, Fang, & Zhang, 2013). In addition to outperforming traditional microstructures, FG materials have recently been studied as a hybrid structure where the FG surface was shown to be a superior platform for ultrahard coatings in cutting tests (Glühmann et al., 2010). It seems highly probable that although the cemented carbide industry has achieved a mature status, innovations in processing and technology will continue to drive advances in these materials.

1.04.4 Industrial Applications

Prior to the widespread use of cemented WC, high-speed steels and tool steels were the primary materials for making cutting, drilling, and fabrication tools. Over the past several decades, however, the applications of cemented WC have increased so consistently and so broadly that it has become the most dominant tool material today. Approximately 70% of metal cutting tools, for example, are made from WC, with 20% of high-speed steels, and 10% of titanium carbide-based cermets and other advanced ceramic materials. Using tonnage of production as a metric, approximately 40,000 MT of WC powder was produced globally in 2011, and that quantity is increasing at about 3% annually. Although the use of WC–Co is very diverse, the majority of applications can be classified into three major categories: machining, rock drilling, and wear parts.

1.04.4.1 Metal-Cutting Tools

Metal cutting is the largest market for WC tools. The term “cutting tools” generally refers to a vast variety of tools for machining. Although the majority of cutting tools are for machining of metals, they are also used for other materials such as plastics, wood, composites, and ceramic preforms. Main types of cutting tools include inserts that are indexed for use in lathes, end mills, and rotary drilling tools. Owing to the huge advances of computer numerical controlled machines and systems that integrate multiple machining procedures into one device, termed a “machine center”, the developers of metal-cutting tools have invested huge resources on developing total solutions, i.e. methods of machining in addition to developing new materials technologies for WCs and coatings. The topic of the methods of machining is an extremely important component of manufacturing technology, but a thorough examination is, however, beyond the scope of this chapter.

There are two unique phenomena that are noteworthy regarding metal cutting. One is that the temperature at the cutting tip, between the cutting tool and the workpiece, can be as high as 1000 °C, or sometimes higher. This puts a stringent requirement on high-temperature strength, or hot hardness of the WC–Co cutting tool material. The hot hardness of WC–Co decreases as temperature increases as do many other materials. The addition of titanium, tantalum, chromium carbide, and vanadium carbide is known to improve the high-temperature properties of WC–Co.

The second phenomena is that the interactions between the cutting tool and the metal chips that are formed during the cutting process can lead to chemical adhesion and wear of the tool, especially at the high temperatures at the cutting tip. A special wear phenomenon called “crater” wear is usually the result of the chemical interaction between the cutting tool and the workpiece. Titanium carbide and tantalum carbide are usually added to WC–Co to reduce crater wear.

As discussed earlier, ceramic coatings are used on a large majority of WC–Co cutting tools today. The coatings provide cutting tools not only with increased wear resistance but also thermal insulation so that the substrate will remain at lower temperatures than that of the cutting edge, thus maintaining the integrity of the tool. Additionally, the coatings are often more resistant to chemical interactions with the workpiece materials, such as steel. With the rapid advancement of coating technologies, the role of WC–Co material as a substrate has evolved in conjunction. For example, due to lower chemical interactions between the tool and workpieces, the need for TaC and TiC has become less important, and the need for high-temperature strength has become even more important. Modern manufacturing operations are pushing for higher and higher productivity. It is often said that the "durability" of a cutting tool is not as important as the ability of a tool to cut at extremely high speed, which leads to extremely high temperatures. Thus, the priorities for optimizing properties of WC–Co substrates are evolving accordingly.

1.04.4.2 Rock Drilling Tools

Rock drilling tools include those used for oil and natural gas exploration, mining, construction, and all other industrial operations that need to excavate or drill through natural rocks, concrete, and masonry. This is the second largest market segment that uses WC tools.

Different from metal cutting, there is no forming of continuous metallic chips during rock drilling. The temperature at the cutting edge is, consequently, much lower than that of metal cutting. In some cases, for example, in oil and gas drilling, the compressive strength of the rock formations can be extremely high, and proportionally increases as the depth of the well increases. The cutting mechanism of crushing rock is mostly by indentation of the rock, followed by fracture of the rock and removal of crushed debris. The rock drilling tools take advantage of the high compressive strength, high hardness, high bending strength, and moderately high fracture toughness of WC–Co materials. There is no other material that has the same combination of mechanical properties, which makes WC–Co the only viable material for such industrial operations.

The fracture toughness versus hardness (thus wear resistance) relationship of WC–Co materials, as shown in Figure 8 is particularly important for rock drilling tools. Failure modes of rock-drilling tools usually include abrasive wear or breakage. To avoid breakage, application engineers usually select grades with high cobalt content and coarse grains, in order to achieve a high toughness at the expense of wear resistance. A particular trend in the development of new grades of WC–Co materials for rock-drilling applications is to use ultracoarse grains. At a given hardness level, large grain sizes usually yield better abrasive wear resistance than a fine grain grade with an equivalent hardness.

1.04.4.3 Wear Parts

Wear parts are the third major segment of industrial applications for WC–Co. Common characteristics of wear parts, distinguished from metal cutting and rock drilling, are those involving relative motion of the carbide tool surface and a mating surface or particles. Carbides, in this case, are not directly involved in cutting or crushing of the mating material. Typical examples of this category include metal forming dies, powder forming dies, wire drawing dies, plastic extrusion dies, metal working roll mills, abrasive fluid handling nozzles, mechanical seals, paper or plastic cutting tools, food processing tools, and special applications, such as ammunitions for fire arms. These applications are often low volume, but high margin, for manufacturers. The readers may wish to consult Section 1.20 by I. Konyashin for further information on wear parts.

1.04.5 Conclusions

The unique thermodynamic and intrinsic mechanical properties of WC have provided the essential qualities that, when combined with Co and other materials, encompass a class of composite materials critical to modern industries. Advancements in manufacturing processes have resulted in fully dense materials, as well as in specialized microstructures, that address crucial industrial needs and which substantively benefit society. The current state of the cemented carbide industry is quite mature, and is a cornerstone of modern manufacturing. Efforts are ongoing to further bolster surface hardness and wear resistance, while maintaining good fracture toughness, and continued investigations promise expansion of the range of ultimate properties and applications.

References

Arroyo, J. M., Diniz, A. E., & Fernandes de Lima, M. S. (2010). Cemented carbide surface modifications using laser treatment and its effects on hard coating adhesion. *Surface and Coatings Technology*, *204*, 2410–2416.

Biksa, A., Yamamoto, K., Dosbaeva, G., Veldhuis, S. C., Fox-Rabinovich, G. S., Elfizy, A., et al. (2010). Wear behavior of adaptive nano-multilayered AlTiN/Me_xN PVD coatings during machining of aerospace alloys. *Tribology International, 43*, 1491–1499.

Bolton, D., & Keely, R. J. (1982). Effects of nonstoichiometric carbon contents on the fracture toughness of WC–Co hardmetal alloys. *International Journal of Refractory Metals and Hard Materials, 3*, 103–111.

Bouzakis, K.-D., Makrimallakis, S., Katirtzoglou, G., Skordaris, G., Gerardis, S., Bouzakis, E., et al. (2010). Adaption of graded Cr/CrN-interlayer thickness to cemented carbide substrates' roughness for improving the adhesion of HPPMS PVD films and the cutting performance. *Surface and Coatings Technology, 205*, 1564–1570.

Bouzakis, K.-D., Skordaris, G., Gerardis, S., Katirtzoglou, G., Makrimallakis, S., Pappa, M., et al. (2010). The effect of substrate pretreatments and HPPMS-deposited adhesive interlayers' materials on the cutting performance of coated cemented carbide inserts. *CIRP Annals – Manufacturing Technology, 59*, 73–76.

Chen, L., Du, Y., Wang, S., Wang, J., & Xu, H. (2009). Mechanical properties and microstructural evolution of TiN coatings alloyed with Al and Si. *Materials Science and Engineering A, 502*, 139–143.

Chernyavsky, K. S. (1986). Stereological analysis of structure formation for solid WC–Co alloys in the process of carbide powder consolidation. *Poroshkovaga Metallurgiya, 3*, 65–69.

Dawihl, W., & Dinglinger, E. (1953). *Handbuch der hartmetallwerkzeuge.* Germany: Springer.

Deng, X., Patterson, B. R., Chawla, K. K., Koopman, M. C., Fang, Z., Lockwood, G., et al. (2001). Mechanical properties of a hybrid cemented carbide composite. *International Journal of Refractory Metals and Hard Materials, 19*, 547–552.

Doi, H., Fujiwara, Y., & Miyake, K. (1969). Mechanism of plastic deformation and dislocation damping of cemented carbides. *Transactions of the Metallurgical Society AIME, 245*, 1457–1470.

Eso, O., Fang, Z. Z., & Griffo, A. (2005). Liquid phase sintering of functionally graded WC–Co composites. *International Journal of Refractory Metals and Hard Materials, 23*, 233–241.

Exner, H. E., & Gurland, J. (1970). A review of parameters influencing some mechanical properties of tungsten carbide–cobalt alloys. *Powder Metallurgy, 13*, 13–31.

Fan, P., Guo, J., Fang, Z. Z., & Prichard, P. (2009). Effects of liquid phase composition on its migration during liquid-phase sintering of cemented carbide. *Metallurgical and Materials Transactions, 40A*, 1995–2006.

Fang, Z. (1998). Wear resistance of powder metallurgy alloys. *ASM handbook* (Vol. 7).

Fang, Z. Z. (2005). Correlation of transverse rupture strength of WC–Co with hardness. *International Journal of Refractory Metals and Hard Materials, 23*, 119–127.

Fang, Z. Z., & Eso, O. (2005). Liquid phase sintering of functionally graded WC–Co composites. *Scripta Materiala, 52*, 785–791.

Fang, Z., Lockwood, G., & Griffo, A. (1999). A dual composite of WC–Co. *Metallurgical and Materials Transactions A, 30*, 3231–3323.

Fang, Z., & Sue, J. (2005). US Patent No. 5880382.

Fisher, U. K. R., Hartzell, E. T., & Akerman, J. G. H. (1988). US Patent No. 4,743,515.

Fox-Rabinovich, G. S., Yamamoto, K., Aguirre, M. H., Cahill, D. G., Veldhuis, S. C., Biksa, A., et al. (2010). Multi-functional nano-multilayered AlTiN/Cu PVD coating for machining of Inconel 718 superalloy. *Surface and Coatings Technology, 204*, 2465–2471.

Frandsen, M. V., & Williams, W. S. (1991). Thermal conductivity and electrical resistivity of cemented transition-metal carbides at low temperatures. *Journal of the American Ceramic Society, 74*, 1411–1416.

Glühmann, J., Schneeweiß, M., van den Berg, H., Kassel, D., Rödiger, K., Dreyer, K., et al. (2010). Functionally graded WC–Ti(C, N)–(Ta, Nb)C–Co hardmetals: metallurgy and performance. *International Journal of Refractory Metals and Hard Materials*.

Guo, J., Fan, P., Wang, X., & Fang, Z. Z. (2011). A novel approach for manufacturing functionally graded cemented tungsten carbide. *International Journal of Powder Metallurgy, 47*, 55–62.

Guo, J., Koopman, M., Fang, Z. Z., Wang, X., Fan, P., & Rowe, M. C. (2012). FE–EPMA measurements of compositional gradients in cemented tungsten carbides. *International Journal of Refractory Metals and Hard Materials, 36*, 265–270.

Hibbs, M. K., & Sinclair, R. (1981). Room-temperature deformation mechanisms and the defect structure of tungsten carbide. *Acta Metallurgica, 29*, 1645–1654.

Konyashin, I., Hlawatschek, S., Ries, B., Lachmann, F., Sologubenko, A., & Weirich, T. (2010). A new approach to fabrication of gradient WC–Co hardmetals. *International Journal Refractory Metals and Hard Materials, 28*, 228–237.

Larsson, C., & Odén, M. (2004). Hardness profile measurements in functionally graded WC–Co composites. *Materials Science and Engineering A, 382*, 141–149.

Liu, Y., Wang, H., Long, Z., Liaw, P., Yang, J., & Huang, B. (2006). Microstructural evolution and mechanical behaviors of graded cemented carbides. *Materials Science and Engineering A, 426*, 346–354.

Luyckx, S., Sacks, N., & Love, A. (2007). Increasing the abrasion resistance without decreasing the toughness of WC–Co of a wide range of compositions and grain sizes. *International Journal of Refractory Metals and Hard Materials, 25*, 57–61.

Mahale, A. E. (1994). *Phase diagrams for ceramists, X*. USA: American Ceramic Society.

Nemeth, B. J., & Grab, G. P. (1986). US Patent No. 4,610,931.

Percherla, A., & Williams, W. S. (1988). Room-temperature thermal conductivity of cemented transition-metal carbides. *Journal of the American Ceramic Society, 71*, 1130–1133.

Peters, C. T. (1979). The relationship between Palmqvist indentation toughness and bulk fracture toughness for some WC–Co cemented carbides. *Journal of Materials Science, 14*, 1619–1623.

Ravichandran, K. S. (1994). Fracture toughness of two phase WC–Co cermets. *Acta Metallurgica et Materialia, 42*, 143–150.

Sarin, V. K., & Johannesson, T. (1975). On the deformation of WC–Co cemented carbides. *Metal Science, 9*, 472–476.

Schwartzkopf, P., & Kieffer, R. (1960). *Cemented carbides.* New York, USA: The Macmillan Company.

Sigl, L. S., & Exner, H. E. (1987). Experimental study of the mechanics of fracture in WC–Co alloys. *Metallurgical and Materials Transactions A, 18*, 1299–1308.

Sigl, L. S., Exner, H. E., & Fischmeister, H. F. (1986). In E. A. Almond, C. A. Brookes, & R. Warren (Eds.), *Science of hard metals.* Bristol, UK: Adam Hilger.

Takahashi, T., & Freise, E. J. (1965). Determination of the slip systems in single crystals of tungsten monocarbide. *Philosophical Magazine, 12*, 1–8.

Upadhyaya, G. S. (1998). *Cemented tungsten carbides; production, properties and testing*. Westwood, New Jersey, USA: Noyes Publications.

Wang, S., Chen, L., Yang, B., Chang, K., Du, Y., Li, J., et al. (2010). Effect of Si addition on microstructure and mechanical properties of Ti–Al–N coating. *International Journal of Refractory Metals and Hard Materials, 28*, 593–596.

Wang, X., Hwang, K. S., Koopman, M., Fang, Z., & Zhang, L. (2013). Mechanical properties and wear resistance of functionally graded WC–Co. *International Journal of Refractory Metals and Hard Materials, 36*, 46–51.

Zhang, L., Chen, S., Xiong, X., He, Y., Huang, B., & Zhang, C. (2007). Phase composition, transition and structure stability of functionally graded cemented carbide with dual phase structure. *Journal of the Central South University of Technology, 14*, 149–152.

Zhang, H., Fang, Z. Z., & Belnap, J. D. (2007). Quasi-plastic deformation of WC–Co composites loaded with a spherical indenter. *Metallurgical and Materials Transactions A, 38*, 552–561.

1.05 Cermets

Shinhoo Kang, Department of Materials Science and Engineering, Seoul National University, Gwanak-ku, Seoul, Korea

Glossary

Cermet abbreviation of **cer**amic–**met**al composites.

Dissolution a decomposing phenomenon of a solid phase in a liquid phase at a much lower temperature than its melting temperature.

1.05.1 Thermodynamics of Hard Phases

Ti(CN)-based cermets have gained considerable attention from researchers since TiC emerged as a potential replacement for WC in the cutting tool field (Graham, 1953; Kieffer, Ettmayer, & Freudhofmeier, 1971a, 1971b, pp. 201; Kieffer & Fister, 1970). Furthermore, the beneficial effects of N in TiC systems have spurred research into the design of materials for new cermet systems. It is known that the presence of N in the form of Ti(CN) refines the microstructure and improves the mechanical properties of TiC-based cermets (Fukuhara & Mitani, 1982; Nishigaki & Doi, 1980; Suzuki, Hayashi, Matsubara, & Tokumoto, 1983).

As the use of Ti(CN) becomes more extensive for cermet applications, phase stability during high-temperature processing has become an important issue. The compositions have been known to be sensitive to the changes in temperature and pressure. An ideal solution model is commonly employed to explain the compositional changes in the formation or dissociation of the Ti(CN) solid solution (Doi, Nomura, Tobioka, Takahashi, & Hara, 1985; Kieffer et al., 1971a, 1971b; Pastor, 1988). In this section, the characteristics, formation energy and stability domain of the Ti(CN) phase are explained.

1.05.1.1 Characteristics of Ti(CN)

The characteristics of the Ti(CN) phase were analyzed and discussed extensively based on the experimental results (Kieffer et al., 1971b; Schick, 1966). Even if an ideal solution model was proposed previously, other

http://dx.doi.org/10.1016/B978-0-08-096527-7.00005-2

studies (Jung & Kang, 2000; Jung, Kang, Jhi, & Ihm, 1999; Kang, 1997) concluded that the mixing reaction of TiC and TiN or mixing of C and N in TiC (B1) structure does not happen ideally. Details to understand the characteristics of the Ti(CN) phase are as follows.

The standard state formation reaction of Ti(C_xN_y), at any temperature, from Ti, C and $P_{N_2} = 1$ atm can be expressed as

$$\mathrm{Ti} + x\mathrm{C} + y/2\mathrm{N_2} \rightarrow \mathrm{Ti}(\mathrm{C}_x\mathrm{N}_y) \quad \Delta_f G^o_{\mathrm{Ti(CN)}} \tag{i}$$

where $x + y = 1$ and x and y are the mole fractions of carbon and nitrogen, respectively, and $\Delta_f G^o_{\mathrm{Ti(CN)}}$ is the free energy of Ti(CN) formation at standard state. This reaction is virtually the sum of the following three reactions:

$$\mathrm{Ti} + \mathrm{C} \rightarrow \mathrm{TiC} \quad \Delta_f G^o_{\mathrm{TiC}} \tag{ii}$$

$$\mathrm{Ti} + 1/2\mathrm{N_2} \rightarrow \mathrm{TiN} \quad \Delta_f G^o_{\mathrm{TiN}} \tag{iii}$$

$$x\mathrm{TiC} + y\mathrm{TiN} \rightarrow \mathrm{Ti}(\mathrm{C}_x\mathrm{N}_y) \quad \Delta_f G^M_{\mathrm{Ti(CN)}} \tag{iv}$$

Thus, the free-energy change in the formation of a new solid solution at a particular temperature and any N_2 pressure, i.e. non-standard state, $\Delta_f G^M_{\mathrm{Ti(CN)}} (= G^M_{\mathrm{Ti(CN)}})$, is the sum of the proportioned free-energy changes to form each component, $x\Delta_f G^o_{\mathrm{TiC}}$ and $y\Delta_f G^o_{\mathrm{TiN}}$ and the free-energy change in mixing to produce a complete solid solution. Therefore, in any N_2 partial pressure, if ideal mixing is assumed,

$$G^M_{\mathrm{Ti(CN)}} = \Delta_f G^M_{\mathrm{Ti(CN)}} = x\left(\Delta_f G^o_{\mathrm{TiC}} + RT \ln x\right) + y\left(\Delta_f G^o_{\mathrm{TiN}} - \frac{1}{2} RT \ln P_{N_2} + RT \ln y\right) \tag{1}$$

The composition of the most stable carbonitride can be determined where the partial differential of $\Delta_f G^M_{\mathrm{Ti(CN)}}$ with respect to x (or y) is zero. The formation energy of the most stable phase should be the lowest. From this calculation, a simple relationship can be derived for ideal mixing, between P_{N_2} and the C:N ratio, (x/y), in the equilibrium carbonitrides.

$$RT \ln\left[\left(\frac{x}{y}\right) P_{N_2}^{\frac{1}{2}}\right] = \left(\Delta_f G^o_{\mathrm{TiN}} - \Delta_f G^o_{\mathrm{TiC}}\right) \tag{2}$$

Table 1 lists the calculated N contents, y, in the Ti(C_xN_y) solid solution based on the ideal model. A significant loss of N from the carbonitride phase is predicted as the reaction temperature increases or as the N_2 pressure decreases. The values are compared with experimental results to examine the validity of the ideal solution model and the results are summarized in **Table 2** (Kang, 1997).

The equilibrium N content predicted by Eqn (2) is 0.016 at 1500 °C and 10^{-4} atm. However, the amounts of C and N lost in the various Ti(C_xN_y) compositions during vacuum processing are insignificant compared with the starting compositions. Also, the C:N ratio remains, more or less, constant regardless of the exposure time

Table 1 Variation of N content, y, in Ti(C_xN_y) solid solutions with N_2 partial pressure and processing temperature. The values are calculated based on an ideal solution model: note decrease in cubic phase N content with decreasing N_2 pressure

Processing temperature (°C)	*N_2 pressure (atm)*	*N content*
1500	0.01	0.14
	0.1	0.33
	1	0.61
	10	0.83
1800	0.01	0.04
	0.1	0.11
	1	0.29
	10	0.56

Table 2 Variation of N content, y, in $Ti(C_xN_y)$ as a function of maximum processing temperature and holding time

		TiC		*$Ti(C_{0.7}N_{0.3})$*		*$Ti(C_{0.5}N_{0.5})$*		*$Ti(C_{0.3}N_{0.7})$*		*TiN*	
Maximum processing temperature (°C)	*Holding time (h)*	u	v	u	v	u	v	u	v	u	v
As received	–	0.97	0.01	0.68	0.28	0.51	0.46	0.31	0.64	0.03	0.95
800	0	–	–	0.67	0.28	0.49	0.45	0.30	0.65	–	–
1200	0	–	–	0.66	0.27	0.49	0.46	0.30	0.65	–	–
1200	1	0.96	0.02	0.66	0.28	0.49	0.46	0.30	0.65	0.02	0.94
1500	0	0.96	0.02	0.66	0.27	0.49	0.46	0.30	0.65	0.01	0.97
1500	1	0.96	0.02	0.66	0.27	0.50	0.45	0.30	0.65	0.02	0.98
1500	5	0.95	0.02	0.66	0.27	0.50	0.46	0.29	0.64	0.02	0.91

and processing temperature. This discrepancy limits the relevance of many estimates derived from an ideal solution approach to actual processing.

Another interesting observation made from this experiment is that the relative stability or loss of C and N depended on the composition, i.e. C:N ratio. As the processing time and temperature increases, the C content in the system continues to decrease gradually even though it looks like a minor quantity in terms of atomic percentage. This becomes obvious when the C:N ratio approaches zero. It implies that C is less stable in $Ti(C_xN_y)$ than N in this temperature range. A measurable C and/or N loss of about 2 at% is noted in all cases except $Ti(C_{0.5}N_{0.5})$. Thus, the gas evolution during sintering with these solid solutions might be linked closely to the escape of C in the system. The highest stability is obtained from an equiatomic C:N ratio, as observed by other researchers (Nishigaki & Doi, 1980; Nishigaki, Ohnishi, Shiokawa, & Doi, 1974). Similar observations to those given in **Table 2** have also been made with Ti(CN)–WC–TaC–Ni–Co (Kang, 1996) and Ti(CN)–Mo_2C–Ni–Co (Park, 1994) systems. The level of O in all samples varied in the range 0.01–0.02 at%. A particularly high level of O (0.02–0.04 at%) was observed in TiN. The role of oxygen in the system has not yet been identified.

In a non-ideal solution case, Eqns (1) and (2) above can be changed as follows:

$$\Delta_f G^M_{Ti(CN)} = x\left(\Delta_f G^o_{TiC} + RT\ln\gamma_{TiC}x\right) + y\left(\Delta_f G^o_{TiN} - \frac{1}{2}RT\ln P_{N_2} + RT\ln\gamma_{TiN}y\right) \tag{3}$$

$$RT\ln\left[\left(\frac{x}{y}\right)P_{N_2}^{\frac{1}{2}}\left(\frac{\gamma_{TiC}}{\gamma_{TiN}}\right)\right] = \left(\Delta_f G^o_{TiN} - \Delta_f G^o_{TiC}\right), \tag{4}$$

where γ_{TiC} and γ_{TiN} are the activity coefficients. These equations enable us to measure the deviation of this solid solution from the ideality. Thus, using Eqn (4) and the experimental data (Kieffer et al., 1971b; Schick, 1966) shown in **Figure 1**, the values of the term $(\gamma_{TiC}/\gamma_{TiN})$ are estimated as a function of x $(=1-y)$. An integration method (Belton & Fruehan, 1967) derived from the Gibbs–Duhem equation for a binary system is used to calculate the activities of TiC and TiN as a function of x or y. A variation of the Gibbs–Duhem equation is written as below:

$$x\mathrm{d}(\ln a_A) + y\mathrm{d}(\ln a_B) - \mathrm{d}(\ln a_B) = -\mathrm{d}(\ln a_B) \tag{5}$$

where a_i is the activity of ith component. When Eqn (5) is rearranged by replacing A and B with TiC and TiN, the following equations can be obtained:

$$\ln\gamma_{TiC}|X_{TiC} = -\int_{X_{TiC}=1}^{X_{TiC}} X_{TiN}\mathrm{d}\left[\ln\left(\frac{\gamma_{TiN}}{\gamma_{TiC}}\right)\right], \tag{6}$$

$$\ln\gamma_{TiN}|X_{TiN} = -\int_{X_{TiN}=1}^{X_{TiN}} X_{TiC}\mathrm{d}\left[\ln\left(\frac{\gamma_{TiC}}{\gamma_{TiN}}\right)\right], \tag{7}$$

where X_{TiC} and X_{TiN} are the same as x and y in Eqn (1) or (2), respectively.

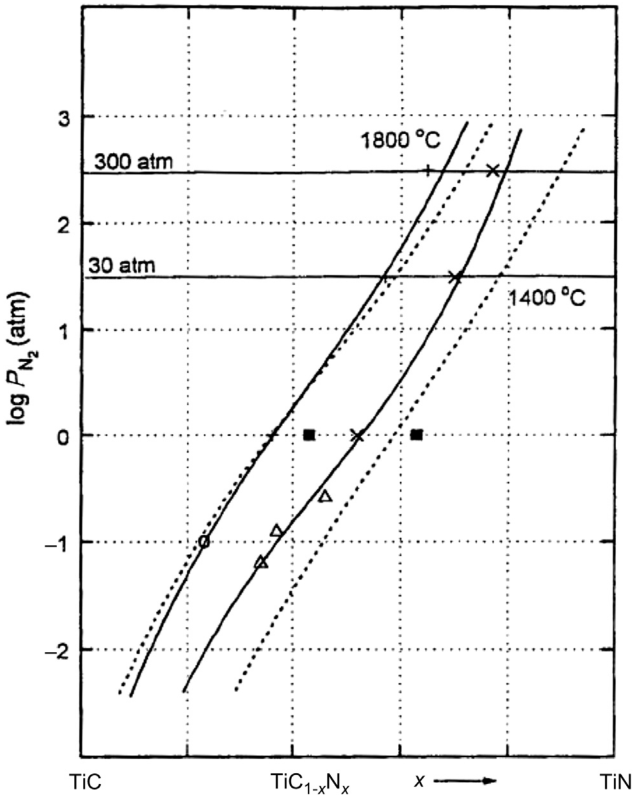

Figure 1 Variation of Ti(CuNv) composition with N_2 partial pressure.

Based on these equations, the activity coefficients for the TiC–TiN mixture are calculated; these are presented graphically in Figure 2, showing a strong negative deviation from ideality (non-ideal behavior) regardless of reaction temperature. This means that the formation of Ti(CN) occurs more readily than an ideal mixing of TiC and TiN. As expected, the tendency to form the Ti(CN) solid solution is much stronger at low temperatures (1400 °C) than at high temperatures (1800 °C). The activity coefficients of TiC vary from 0.04 to 0.3 at 1400–1500 °C as the N_2 pressure changes while high coefficients (0.2–0.7) are found at 1800 °C. The

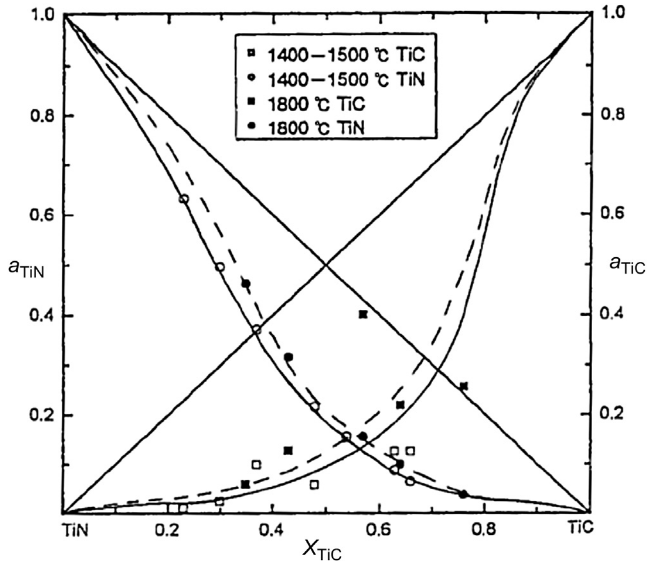

Figure 2 Activities *a* of TiC and TiN in Ti(CN) solid solution at 1400 and 1800 °C: values obtained from **Figure 1**.

coefficients of TiN remained in the same range (0.2–0.8) for both temperatures. This result suggests that TiC has a higher tendency to form a solid solution than TiN. This analysis confirms a higher thermal stability of C and N in Ti(CN) than expected by an ideal solid-solution model.

The diffusivity of C in $TiC_{0.89-0.97}$ is reported to be in the range 10^{-11}–10^{-12} $cm^2\ s^{-1}$ at 1500 °C. The extrapolation of these data results in C diffusivity of 10^{-12}–10^{-13} $cm^2\ s^{-1}$ at 1350 °C. Diffusivity increases as the non-stoichiometry of TiC increases (Matzke, 1989). Similarly, the diffusivity of N in TiN has been reported to be of the order 10^{-14} $cm^2\ s^{-1}$ at 0.5 T_m (1350 °C). Nitrogen atoms move in the TiN matrix at a rate equivalent to or slower than C atoms in TiC at 1500 °C. Since the diffusivity of a species in a system is proportional to the gradient of the activity coefficient (affinity) with respect to concentration, the diffusivity data are in agreement with the activity data. It suggests further that the diffusivity of N remains low compared with that of C in the Ti(CN) solid solution. This accounts for the low dissociation rate of N observed. A similar diffusion behavior of C and N is expected to occur in complex carbonitride systems such as $(Ti,M_1,M_2)(CN)$ solid solutions as long as the second and third metallic phases are minor (<20%) (Kang, 1996; Park, 1994).

Basically, the diffusivity and dissociation rate of nitrogen in Ti(CN)-based systems are largely controlled by the Ti–N bond strength in the structure. The strengths are normally quantified by measurements of enthalpy for the dissociation reaction. Some work has been done to estimate the Ti–C and Ti–N bond strengths in TiC and TiN (Gingerich, 1979, pp. 289–300; Kohl & Stearns, 1970), but this needs more investigation. However, the bond strengths in diatomic molecules have been measured spectroscopically for Ti–C and Ti–N bonds and the room temperature strengths are reported to be 423 and 476 kJ mol^{-1}, respectively (Bilz, 1958; Gupta & Gingerich, 1980; Kohl & Stearns, 1974; Rundle, 1948). All this evidence indicates a stronger Ti–N bond than Ti–C bond in B1 (NaCl) structure. Overall results confirm that the reaction between TiC and TiN exhibits a strong negative deviation from the ideal solid-solution behavior in the formation of Ti(CN). The formation of Ti(CN) occurs more readily than an ideal mixing of TiC and TiN.

With the formation energy values of various $Ti(C_xN_y)$ in the following section (Jung et al., 1999; Jung & Kang, 2000), a regular solution model, which is not a function of temperature, is examined for its applicability to Ti(CN) solid solutions. The variation of free energy with temperature can be obtained as long as the excess Gibbs free energy, G^{XS}, is known (Darken, 1967; Gaskell, 2003). In order to obtain $G^M (= \Delta_f G^M_{Ti(CN)})$ as a function of temperature, G^{XS} is calculated by means of the results in the previous section. The heat of mixing for a regular solution is expressed by the equation below:

$$\Delta H^M = G^{XS} = \alpha' X_{TiC} X_{TiN}, \tag{8}$$

where $\Delta G^M = \Delta H^M + T\Delta S^M$ and α' must be a constant which is independent of temperature and where X_{TiC} and X_{TiN} are the same as x and y in Eqn (1) or (2), respectively. However, the data shown in previous work (Jung & Kang, 2000) did not show that α' is a single value as required in the case of a regular solution, showing temperature dependence. Thus, it is concluded that the Ti(CN) solid solution fails to be a regular solution.

The G^{XS} of the solution is expressed as a temperature function to see if a sub-regular solution model works. By the addition of a temperature function, G^{XS} can be represented as in Eqn (5). The coefficient, a, is related to the extent of deviation from ideal behavior. The value of τ indicates the degree of sensitivity of G^{XS} to temperature dependence. The larger the absolute value of τ, the weaker is its dependence with temperature. As τ increases, G^{XS} in Eqn (5) becomes close to that of a regular solution. In fitting the data using Eqn (4), the values of a and τ were calculated to be −6.94 and 889.9 K, respectively (Jung & Kang, 2000).

$$G^{XS} = a X_{TiC} X_{TiN} \left(1 + \frac{T}{\tau}\right) \tag{9}$$

A general function of G^M can be expressed in the incorporation of G^{XS} into Eqn (6) and the relative stability can be estimated as a function of temperature. The G^M curves at various temperatures are shown in **Figure 3**.

$$G^M = G^o + \Delta G^M = X_{TiC}\Delta_f G^o_{TiC} + X_{TiN}\Delta_f G^o_{TiN} + \left(\Delta G^{M,id} + G^{XS}\right) \tag{10}$$

As is seen in **Figure 3**, the free energy near the TiN composition is lower than that of TiC at low temperatures (below 1500 K), whereas TiC tends to have lower values at higher temperatures (above 2500 K). It means that the relative stability among Ti(CN) solid solutions is strongly dependent on temperature. Based on the above

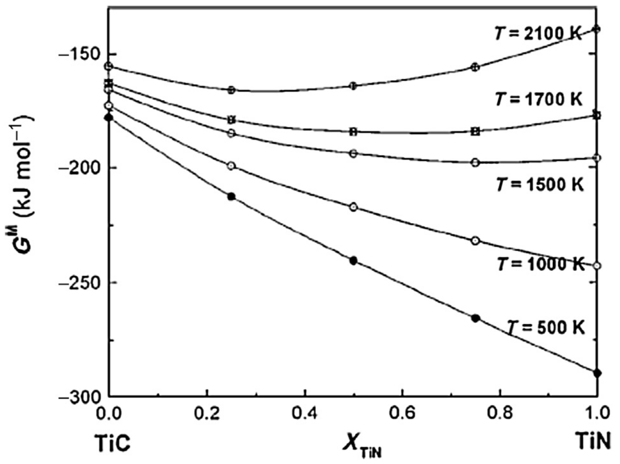

Figure 3 Curves of the free energy of a solid solution of Ti(CN) calculated from a subregular solution model.

analysis, the solution behavior is found to be beyond a regular solution range and it could show ordering tendency to some extent as reported.

1.05.1.2 Formation Energy of Ti(CN), G^M

Based on the TiC–TiN solution model, a value for the free energy of formation of Ti(CN) was obtained using the following equations and the data from JANAF tables (Jung & Kang, 2000).

$$G^M = \Delta_f G^M_{Ti(CN)} = X_{TiC}\Delta_f G^o_{TiC} + X_{TiN}\Delta_f G^o_{TiN} + \Delta G^M, \qquad (11)$$

where ΔG^M, the change in the free energy of mixing, is equal to entropy of mixing, $RT\{X_{TiC}\ \ln_{TiC} + X_{TiN}\ \ln_{TiN}\}$. In Figure 4, $G^{M,id}$ and $G^{M,real}$ represent the absolute free energy of formation based on ideal mixing of TiC with TiN, and that obtained by using the derived activity coefficients in previous section, respectively. The G^M graphs of 1700 and 2100 K were drawn as a solid and dashed curve, respectively. The data in the figure are those calculated by means of pathwise integration.

Each curve for $G^{M,real}$ has a unique minima at certain compositions. At 1700 K, this minimum is located in the nitrogen-rich composition ($X_{TiN} = 0.6$–0.7). However, the minimum point swings to carbon-rich composition ($X_{TiN} = 0.3$–0.4) at 2100 K. This plot demonstrates that a stable composition exists for various temperatures. G^M is an indicator of the phase stability of a material. The solid solution with high nitrogen content would be expected to be more stable at 1700 K, while that with high carbon content to be more stable at 2100 K.

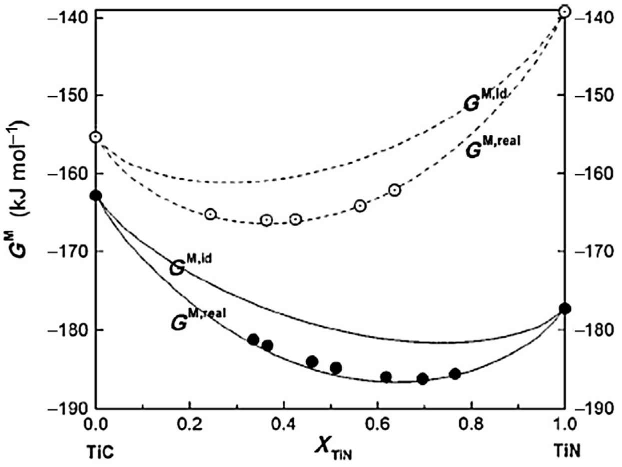

Figure 4 The Gibbs free energy of formation of, G^M, Ti(CN)(kJ mol^{-1}): the minimum points of $G^{M,real}$ are at $X_{TiN} \sim 0.7$ and 0.4 for the temperature of 1700 and 2100 K, respectively.

The behavior of the solid solution is in line with previous findings, ruling out the previous understanding that nitrogen in Ti(CN)-based cermets has a destabilizing effect by dissociating in sintering at 1400–1500 °C. However, the more negative is G^{M}, the less a substance evaporates or reacts. Thus, the composition with a minimum G^{M} value would be expected to be the most stable, even if the stability region were to be extended further to the compositions in the vicinity of the minimum point.

The free energy of mixing for Ti(CN) solid solutions is calculated using theoretical models to obtain the free energies of the formation of various Ti(CN) at specific temperatures of interest (Jung et al., 1999). The stability regions of such solid solutions are then compared with empirical data obtained at 1700 and 2100 K (Jung & Kang, 2000). Previous reports have discussed the relative strength of the chemical bonding in Ti(CN) solutions compared with TiC and TiN phases (Zhukov, Gubanov, Jepsen, Christensen, & Andersen, 1988; Zhukov, Medvedeva, & Gubanov, 1989). The maximum energy of formation of carbonitrides was calculated to be -10 kJ mol^{-1} at 0 K. These values deviate from linear behavior at varying nitrogen contents when the linear muffin-tin orbital method is used. Although the magnitude of the energy of formation itself shows some discrepancy relative to a recent pseudopotential method (Jhi & Ihm, 1997), the trend is consistent in both calculations.

Using the first-principles pseudopotential total energy method, the internal energy of various Ti(CN) solutions was calculated. Since the calculated equilibrium volume of a Ti(CN) solid solution nearly obeys Vegard's law (Jhi & Ihm, 1997), the internal energy can be regarded as the enthalpies of formation. Hence the enthalpy change of mixing at 0 K is expressed as below:

$$\Delta H_{0\mathrm{k}}^{\mathrm{M}} = U_{0\mathrm{k}}^{\mathrm{M}}(\mathrm{TiC}_{1-x}\mathrm{N}_x) - xU_{0\mathrm{k}}^{\mathrm{o}}(\mathrm{TiN}) - (1-x)U_{0\mathrm{k}}^{\mathrm{o}}(\mathrm{TiC}) \tag{12}$$

where U^{M} and U^{o} represent the internal energies of the Ti(CN), TiC or TiN phases, respectively. As the temperature increases, the entropy contribution to phase stability becomes important. The lattice vibration energy and the electronic excitation energy as well as the configuration term all influence phase stability. A conventional approach was taken to estimate the thermal effect of lattice vibrations and electronic excitations. This was carried out within the framework of frozen-ion motion and the rigid band model (Ashcroft & Mermin, 1976; Lebacq, Pasturel, Manh, et al., 1996). The free energy induced by lattice vibrations was calculated using the Debye model:

$$G_{\mathrm{vib}}(T) = H_{\mathrm{vib}}(T) - TS_{\mathrm{vib}} = 3RTD(\theta_{\mathrm{D}}) - 3RT\left[\frac{4}{3}D(\theta_{\mathrm{D}}) - \log\left\{1 - \exp\left(-\frac{\theta_{\mathrm{D}}}{T}\right)\right\}\right] \tag{13}$$

where θ_{D} and $D(\theta_{\mathrm{D}})$ are the Debye temperature and its function, respectively. With the help of the rigid-band model and the density of states at a given temperature, the free energy of electrons at a given temperature, T, can be expressed as follows:

$$G_{\mathrm{el}}(T) = H_{\mathrm{el}}(T) - TS_{\mathrm{el}} = \frac{1}{2}\gamma T^2 + T\int_{-\infty}^{\infty} N(\varepsilon,T)[F(\varepsilon,T)\log F(\varepsilon,T) + \{1 - F(\varepsilon,T)\}\log\{1 - F(\varepsilon,\mathrm{T})\}]\mathrm{d}\varepsilon \tag{14}$$

where γ represents the constant which is proportional to the density of states at the Fermi level (Guillermet, Haglund, & Grimvall, 1993), while $N(\varepsilon,T)$ and $F(\varepsilon,T)$ represent the density of states and the Fermi–Dirac distribution function, respectively. For the density of states, $N(e, 0)$ was used in place of $N(e, T)$. The results indicate that the electronic part provides a significant contribution to the energy change of mixing although the absolute value itself is smaller than that of the lattice vibrations. The thermal excitation of electrons depends on the available states existing above the Fermi level as represented in the density of states. The electronic structure calculation shows that the density of states increases rapidly up to a nitrogen content of 0.5 in the Ti(CN) solution from the linearly interpolated values, thus resulting in a large electronic thermal energy. This behavior of the density of states is also found in other transition metal carbonitrides, e.g. Hf(CN) (Jhi, 1998).

Based on these models, the enthalpy of formation for various Ti($\mathrm{C}_{1-x}\mathrm{N}_x$) solid solutions was calculated at 0, 1700 and 2100 K. It was found an exothermic reaction, which indicates that it is energetically favorable for the mixture of TiC and TiN to form a solid solution. The maximum reduction in the energy of formation was obtained at nitrogen concentrations in the range of 0.2–0.4 with a value of approximately -4.5 kJ mol^{-1}. With an increase in temperature, $\Delta H_{\mathrm{T}}^{\mathrm{M}}$ increases by 1 kJ mol^{-1} at 2100 K, maintaining the original shape of the curve at 0 K.

1.05.1.2.1 Modeling Real Solution

In a real solution, the atomic distributions will be gradually randomized with increasing temperature (Christian, 1975). Hence, the configurational entropy change of mixing is different from that of ideal mixing. It is controlled by the heat of mixing in that a negative or positive H_T^M value signifies a deviation from random mixing with a tendency toward ordering or segregation. Therefore, the entropy change in mixing requires modification by a parameter, β, which should be a function of temperature and ΔH_T^M. The parameter, β, may be expressed as an exponential function with some constants, ε and n, as below. In a high-temperature range, a realistic ΔS_{conf}^M can be obtained by means of proper constants:

$$\beta = \exp\left(-\frac{\varepsilon\left|\Delta H_T^M\right|^n}{RT}\right) \quad (\varepsilon, n \geq 0) \tag{15}$$

$$\Delta S_{\text{conf}}^M = \beta \times \Delta S^{\text{M,ideal}} \tag{16}$$

With Eqn (1)–(9), it is possible to obtain the enthalpy and entropy change for the mixing of TiC with TiN as well as the absolute enthalpy and entropy. Finally, the free-energy change of mixing, ΔG_T^M, at any temperature can be obtained using the equations below:

$$\Delta H_T^M = \Delta H_{0K}^M + \Delta H_{\text{vib}}^M + \Delta H_{\text{el}}^M \tag{17}$$

$$\Delta S_T^M = \Delta S_{\text{conf}}^M + \Delta S_{\text{thermal}}^M \tag{18}$$

The value for β was plotted with respect to temperature at nitrogen contents of 0.25, 0.50, and 0.75 where ε and n are given as unity using the ΔH_T^M values obtained as a function of temperature (Jung et al., 1999). The condition that ε and n are equal to unity is arbitrarily chosen as a case of ordering since no experimental data are available for the determination of the upper bounds for ordering. β is found to constantly increase from zero and the curve for $\text{Ti(C}_{0.25}\text{N}_{0.75})$ provides the highest values for β because of its small heat of mixing. That is, the tendency to have random mixing increases with temperature and nitrogen contents in Ti(CN).

The total free energy of a solid solution, G^M, then, is expressed as below:

$$G^M = \Delta_f G_{\text{Ti(CN)}} = X_{\text{TiC}}\Delta_f G_{\text{TiC}}^o + X_{\text{TiN}}\Delta_f G_{\text{TiN}}^o + \Delta G^M \tag{19}$$

$\Delta_f G_{\text{TiC}}^o$ and $\Delta_f G_{\text{TiN}}^o$ are the standard-state energies of the formation of TiC and TiN, respectively (Chase, Davies, Downey, et al., 1985). The free energy of mixing, G^M, for the formation of Ti(CN) at various temperatures is plotted and found the same as in **Figure 4**.

The stability region at 1700 K, where the values of G^M are close to the minimum value, is predicted near 0.6 when ε and n are equal to unity in the study (Jung et al., 1999). In contrast, the experimental value is 0.7 while the ideal mixing (entropy) model ($\varepsilon = 0$) predicts 0.75. When the temperature reaches 2100 K, the equilibrium nitrogen content moves to ~0.3 while the experimental results indicate a value of 0.4. Considering the limited number of data points, the predicted values do not differ greatly from the experimental value, 0.7. With changes in the ε value for the model, the stability regions of Ti(CN) cover a wide area with respect to nitrogen content, resulting in less dramatic differences in practical processing than expected.

Based on the observation above, it can be concluded that the stability region of the $\text{Ti(C}_{1-x}\text{N}_x)$ solid solution tends to shift toward $\text{Ti(C}_{0.5}\text{N}_{0.5})$ at temperatures higher than 1000 °C. The change in the compositions of the highest stability is less rapid than predicted by the ideal mixing model. This appears to be due to the strong affinity of carbon and nitrogen in the octahedral sites of the B1 structure as nearest neighbors. Because of the interactions between interstitial atoms, the free energy for Ti(CN) becomes more negative and provides an extra measure of stability to its elements in Ti(CN). The affinity of carbon and nitrogen as neighbors should affect the atomic arrangement to some extent at 1700 and 2100 K. Thus, the value for ε cannot be zero, i.e. a complete random mixing is not guaranteed. Even in such a case, however, the degree of discrepancy in the G^M values between theoretical and empirical results appears to be within acceptable limits. In other words, the sums of the inharmonic effect of lattice vibrations, deviations from the rigid-band model, the correction in the density of states at high temperatures, and experimental errors might mutually compensate one another.

1.05.1.3 Stability Domain for Ti(CN)

There is an alternative way to examine the phase stability other than free energy of formation. That is stability domain of a certain compound, which is in our case, Ti(CN). This method is more useful when the compound is exposed to nitrogen, oxygen and/or carbon environment. We will briefly look at the stability domains of Ti(CN) based on different solution models.

Three stability diagrams are possible based on ideal mixing of TiC and TiN with/without the formation of Ti(CN) solid solution and the exothermic reaction to form Ti(CN) at 1673 K as reported (Jung et al., 1999; Jung & Kang, 2000; Kang, 1997). The results are compared in terms of characteristics of each solution proposed. Two independent variables—carbon activity and nitrogen partial pressure—are used for the diagrams based on experimental and thermodynamic data (Kieffer et al., 1971a, 1971b; Kwon & Kang, 2012).

Commonly, Ti(CN) powders have been produced in a nitrogen atmosphere either by nitriding TiC or by reduction and carburization of TiO_2 in the presence of carbon. If TiC and TiN do not form a solid-solution phase, three reactions prevail as below:

$$\mathrm{Ti_{(s)}} + \mathrm{C_{(s)}} = \mathrm{TiC_{(s)}} \tag{v}$$

$$\mathrm{Ti_{(s)}} + \frac{1}{2}\mathrm{N_{2(g)}} = \mathrm{TiN_{(s)}} \tag{vi}$$

$$\mathrm{TiC_{(s)}} + \frac{1}{2}\mathrm{N_{2(g)}} = \mathrm{TiN_{(s)}} + \mathrm{C_{(s)}} \tag{vii}$$

These equations provide domain boundaries for Ti–TiN, Ti–TiC and TiC–TiN. In case of ideal mixing of TiC and TiN, Eqn (vii) changes to Eqn (viii) as below. **Figure 5(a)** is the result obtained using the formation energies of TiC and TiN, $\Delta_f G^\circ_{\mathrm{TiC}}$ and $\Delta_f G^\circ_{\mathrm{TiN}}$, respectively.

$$\mathrm{Ti_{(s)}} + x\mathrm{C_{(s)}} + \frac{y}{2}\mathrm{N_{2(g)}} = x\mathrm{TiC} + y\mathrm{TiN} = \mathrm{Ti}\left(\mathrm{C}_x\mathrm{N}_y\right)_{(s)} \tag{viii}$$

It was assumed that the formation energies of Ti(CN) change proportionally to the relative amounts of TiC and TiN in Ti(CN).

In case of non-ideal solutions, the formation energies of Ti(CN) was calculated from the activities of TiC and TiN using the following equation and experimental data (Jung et al., 1999; Jung & Kang, 2000; Kang, 1997):

$$G^{\mathrm{M}} = \Delta_f G^{\mathrm{M}}_{\mathrm{Ti(CN)}} = X_{\mathrm{TiC}}\Delta_f G^{\mathrm{o}}_{\mathrm{TiC}} + X_{\mathrm{TiN}}\Delta_f G^{\mathrm{o}}_{\mathrm{TiN}} + RT\{X_{\mathrm{TiC}} \ln a_{\mathrm{TiC}} + X_{\mathrm{TiN}} \ln a_{\mathrm{TiN}}\}, \tag{20}$$

Table 3 lists the activities of TiC and TiN in $\mathrm{Ti(C}_x\mathrm{N}_y)$ and the formation energies of $\mathrm{Ti(C}_x\mathrm{N}_y)$ at 1673 K (Kwon & Kang, 2012).

In this case, the Ti(CN) phase exists alone without the TiC and TiN phases. Therefore, Ti, Ti(CN), C and gas phase (N_2) are the equilibrium phases present after the complete reaction among Ti, TiC and C under nitrogen atmosphere at 1673 K. The equilibrium Ti–$\mathrm{Ti(C}_x\mathrm{N}_y)$-gas phase ($x + y = 1$) reacts as below:

$$\mathrm{Ti_{(s)}} + x\mathrm{C_{(s)}} + \frac{y}{2}\mathrm{N_{2(g)}} = \mathrm{Ti}\left(\mathrm{C}_x\mathrm{N}_y\right)_{(s)} \tag{21}$$

$$\Delta G_{1673\ \mathrm{K,Ti}\left(\mathrm{C}_x\mathrm{N}_y\right)} = -RT \ln \frac{1}{a_{\mathrm{C}}{}^{x} \cdot P_{\mathrm{N_2}}{}^{\frac{y}{2}}} \tag{22}$$

Using the formation energies, $\Delta G^{\mathrm{o}}_{1673\ \mathrm{K,Ti(C}_x\mathrm{N}_y)}$, in **Table 3**, the phase domains between Ti and Ti(CN) can be constructed at 1673 K with respect to a_{c} and $P_{\mathrm{N_2}}$. **Figure 5(b)** is the final stability domains for Ti and Ti(CN) along with that of ideal mixing case (dotted line). It demonstrates the conditions for Ti(CN) synthesis, such as carbon activity and nitrogen pressure, at a given temperature (1673 K). Further, it is to be noted that the stable domain for Ti(CN) is much larger than that of ideal mixing case bound by dotted lines. It is because the mixing reaction of TiC and TiN or nitriding of TiC occurs exothermically.

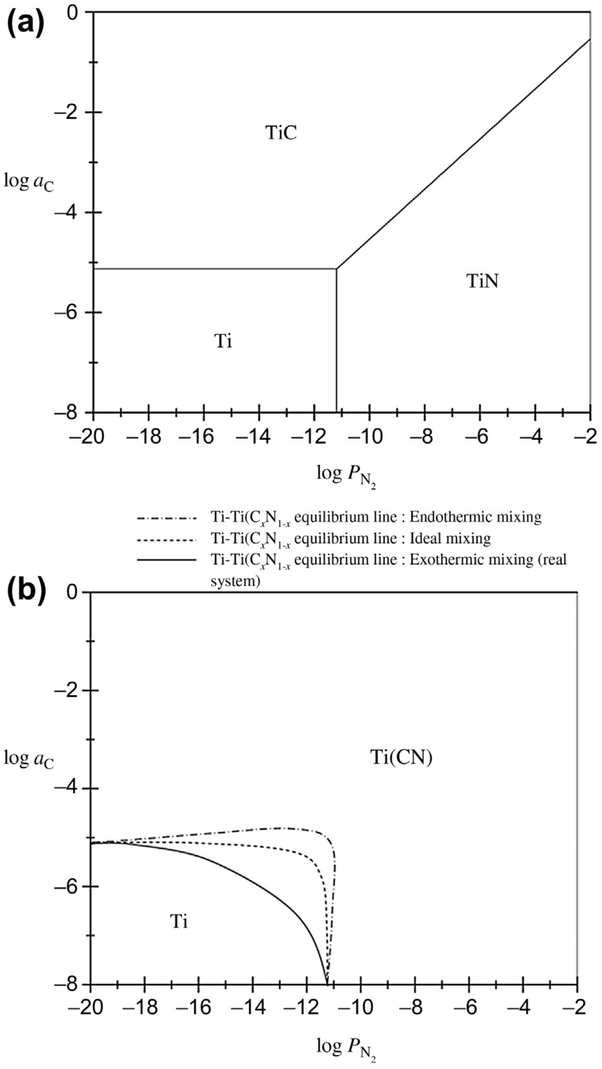

Figure 5 (a) Ti–TiC–TiN phase domains at 1673 K and (b) Ti–Ti(CN) phase domains at 1673 K.

Table 3 Activities and Gibbs formation energies of Ti(C_xN_y) at 1673 K (Nishigaki et al., 1974)

x in Ti(C_xN_y)	Activity of TiC (a_{TiC})	Activity of TiN (a_{TiN})	Formation energies of Ti(C_xN_y) (KJ mol^{-1})
0.23	0.01	0.65	−197.2
0.25	0.02	0.50	−197.1
0.48	0.06	0.22	−203.2
0.63	0.13	0.08	−201.4

This diagram is also instructive in the shape of the domain and domain boundaries. The size of Ti domain changes depending on the affinity between TiC and TiN in mixing. That is, if TiC and TiN mix endothermically, the Ti domain is expected to increase along the TiC–TiN boundary line drawn in **Figure 5(a)**. The trend in the domain size is shown according to the characteristics of the solutions in **Figure 5(b)**.

Early work showed the stability domains for TiN–C, Ti(CN)–Ti and Ti(CN)–C based on ideal solution model (Pastor, 1988). **Figure 6** is the result obtained as a function of temperature, P_{N_2} and Ti(CN) composition. However, it seems more plausible to interpret differently when two dependent variables such as Ti($C_{1-x}N_x$) composition and P_{N_2} are used at a given temperature; the Ti($C_{1-x}N_x$) composition changes as a function of P_{N_2}. That is, based on the Gibbs phase rule, the stability regions should be expressed only by lines in this diagram.

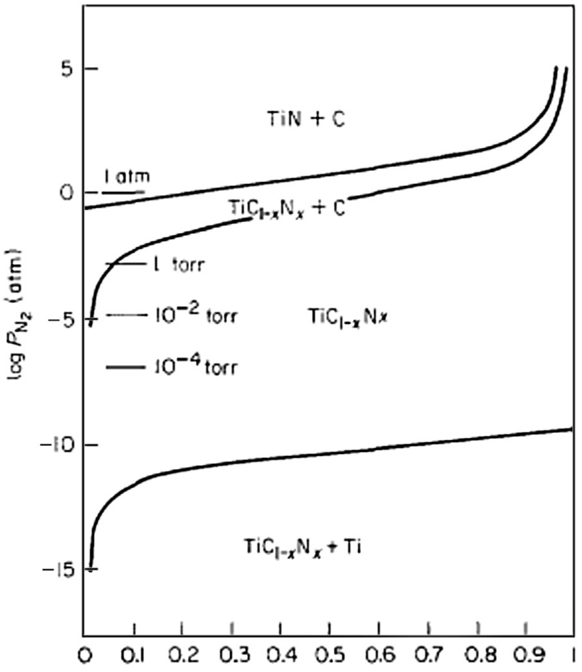

Figure 6 Ti(CN)–TiN–C–Ti equilibrium lines at 1673 K (Jung & Kang, 2000).

The boundary lines presented in Pastor (1988) are the equilibrium coexistence lines of Ti(CN)–C, Ti(CN) or Ti(CN)–Ti, which is in contrast with **Figure 5(b)**. Further, the regions between the lines should not be interpreted as stability domains. The domains are unstable because carbon and nitrogen interact in Ti(CN). In **Figure 6**, the experimental results (Kang, 1997) from various sources are also plotted. The results were approximated in the previous work as an ideal solution. Obviously, this resulted in a significant difference in interpreting the solution behavior of Ti(CN).

(Ti,W)C solid-solution materials are usually detected from TiC–WC–Ni/Co systems as a solid-solution rim phase. $(Ti_{1-x}W_x)C$ solid solutions show a solubility limit because TiC and WC have a different crystal structure, i.e. B1 and hexagonal, respectively. Both carbides are not easy to be sintered, if without binder metals, through normal vacuum sintering. Sometimes, $(Ti_{1-x}W_x)C$ solid solutions are found with $Ti_{1-x}W_x$ intermetallic. Recently, Kim (2011) investigated thermodynamic properties of (Ti,W)C and (Ti,W)(C,N) solid solutions using empirical equation of state, Debye approximation and first-principle calculation methods as done for Ti(CN) solid solutions in preceding section.

In order to measure the phase stability of (Ti,W)C solid solutions, the Gibbs free energy of formation is calculated (Kim, 2011). The phase stability of TiC is relatively high compared to those of WC (B1). WC of B1 structure is found unstable even up to 2500 K. As the tungsten content increases in (Ti,W)C solid solutions, the phase stability of (Ti,W)C decreases in the temperature range of 0–1000 K. On the other hand, the phase stability of (Ti,W)C solid solutions increases at high temperatures. At high temperatures, $(Ti_{0.75}W_{0.25})C$ solid-solution phase has maximum stability among the solid solutions. However, after the tungsten content, x, exceeds 0.25 in mole fraction, the phase stability of (Ti,W)C solid solutions decreases again.

1.05.1.4 Carbothermal Reduction

1.05.1.4.1 Equilibrium Reduction

TiC and Ti(CN) show excellent hardness, wear resistance, and thermal stability at high temperature (Toth, 1971). These materials, when combined with a metal binder and secondary carbides (termed titanium carbide-based cermets), offer a wide range of cutting-tool materials. Thus, many studies have focused on synthesizing TiC, TiN, Ti(C,N) or (Ti,W)C (Berger, Ettmayer, & Schultrich, 1994; Berger, Langholf, Jaenicke-Robler, & Leitner, 1999; Koc, 1998; Koc & Folmer, 1997; Kwon & Kang, 2008a; Park & Kang, 2005; Shaviv, 1996; Swift & Koc, 1999; White, Mackenzie, & Johnston, 1992). In this section, we will consider thermodynamics of powder synthesis with/without enhanced kinetics. For powder production, TiO_2 is the main raw material and reduced carbothermally in the presence of carbon for the synthesis of TiC and Ti(CN) (Berger et al., 1994; Berger et al., 1999; Koc, 1998; Koc & Folmer, 1997; Kwon & Kang, 2008a; Park & Kang, 2005; Shaviv, 1996; Swift & Koc, 1999; White et al., 1992). In this process, the reduction sequence of TiO_2 often became an issue for research in order to control the process effectively. Koc et al. (Koc & Folmer, 1997; Swift & Koc, 1999) summarized the carbothermal reduction sequence of TiO_2 in a nitrogen-free atmosphere as follows: $TiO_2 \rightarrow Ti_4O_7 \rightarrow Ti_3O_5 \rightarrow (Ti_2O_3) \rightarrow Ti(C_xO_y)$. Ti_3O_5 is the oxide phase with the lowest oxidation state, before forming the oxycarbide phase when coated pyrolytic carbon is used as carbon source while Ti_2O_3 is the lowest oxide phase in carbon black. The $Ti(C_xO_y)$ phase is reduced further under vacuum, yielding TiC as an end product. The crystal structure of TiC, TiO, and $Ti(C_xO_y)$ is known to be B1 (Toth, 1971).

The characteristics of the TiO and $Ti(C_xO_y)$ phases and the phase-stability domains of various oxides, carbide and nitride were thermodynamically evaluated during the reduction process by Kwon and Kang (2008b) and Kwon and Kang (2009b). When TiO was placed with carbon, it changed into TiC and Ti_2O_3 simultaneously at low temperatures. This change was ascribed to the low thermodynamic stability of TiO compared with that of Ti_2O_3, indicating that no TiO forms during the reduction process (Kwon & Kang, 2008b).

Further, the affinity of TiC and TiO was calculated to determine the tendency to form $Ti(C_xO_y)$ solid solution based on the result of Ouensanga (1981). The activities and Gibbs formation energies of $Ti(C_xO_y)$ at 1580 K are shown in **Table 4**. TiC and TiO showed a small positive deviation in mixing from the ideal solid-solution behavior, not readily forming Ti(CO) solid solution thermodynamically. For the two possible cases with and without the formation of Ti(CO), the phase domains of Ti_3O_5–Ti_2O_3–Ti(CO)–TiC and Ti_3O_5–Ti_2O_3–TiO–TiC were constructed at 1580 K with respect to carbon activity, a_c, and oxygen partial pressure, P_{O_2}, as shown in **Figure 7**. They indicate that the phase domain for TiO does not exist in the presence of carbon ($a_c = 1$) and that the carbothermal reduction sequence follows $TiO_2 \rightarrow Ti_3O_5 \rightarrow Ti_2O_3 \rightarrow TiC$. However, due to various kinetic factors in the process, it is highly possible to follow the sequence observed from experiments: $TiO_2 \rightarrow Ti_3O_5 \rightarrow Ti_2O_3 \rightarrow Ti(C_xO_y) \rightarrow TiC$.

Ti(CN) is generally synthesized by heat treatment of TiC in an N_2 atmosphere or by direct reaction between TiC and TiN. In addition, carbonitridation of Ti can be accomplished by reducing oxide in the presence of carbon and nitrogen flow. Berger et al. (1994, 1999) found that TiO_x and Ti_2O_3 phases are absent when TiO_2 is reduced carbothermally under nitrogen. In the context of thermodynamics (Kwon & Kang, 2009b), activities and Gibbs formation energies of $Ti(C_xN_y)$ at 1673 K are shown in **Tables 3** and **5** (Kang, 1997). The stable region for Ti_2O_3 is much smaller in the TiO_2–Ti_3O_5–Ti_2O_3–Ti(CN) phase domains in comparison with Ti(CN), and decreases with increasing nitrogen pressure as shown in **Figure 8**. This finding explains the apparent absence of the Ti_2O_3 phase during the carbothermal reduction of TiO_2 under nitrogen atmosphere.

1.05.1.4.2 Kinetic-Assisted Reduction

The energy of formation of TiC through carbothermal reduction is quite large as shown in Eqn (23).

$$TiO_2 + 3C = TiC + 2CO \quad \Delta G_T = 378.6 - 0.2424T\left[\mathrm{J\ mol^{-1}}\right] \tag{23}$$

Therefore, based on equilibrium reaction, the majority of industrial titanium carbide powders are currently produced by the carbothermal reduction of TiO_2 with carbon at temperatures ranging from 1700 to 2100 °C for 10–20 h (Toth, 1971). Meanwhile, the direct reaction between Ti and C has a strong driving force to form TiC, as shown in Eqn (24).

$$Ti + C = TiC \quad \Delta G_T = -10,550 + 0.8386T\left[\mathrm{J\ mol^{-1}}\right] \tag{24}$$

In order to increase the reaction kinetics, it is common to find that the mixtures of oxide and carbon are normally prepared by low- or high-energy milling and reduced carbothermally. Many studies (Berger et al.,

Table 4 Activities and Gibbs formation energies of $Ti(C_xO_y)$ at 1580 K

x in $Ti(C_xO_y)$	Activity of TiC (a_{TiC})	Activity of TiO (a_{TiO})	Formation energies of $Ti(C_xO_y)$ (KJ mol^{-1})
0.67	0.74	0.41	−248.7
0.72	0.78	0.36	−236.6
0.85	0.89	0.23	−204.6
0.90	0.93	0.17	−192.0
0.96	0.97	0.09	−176.5

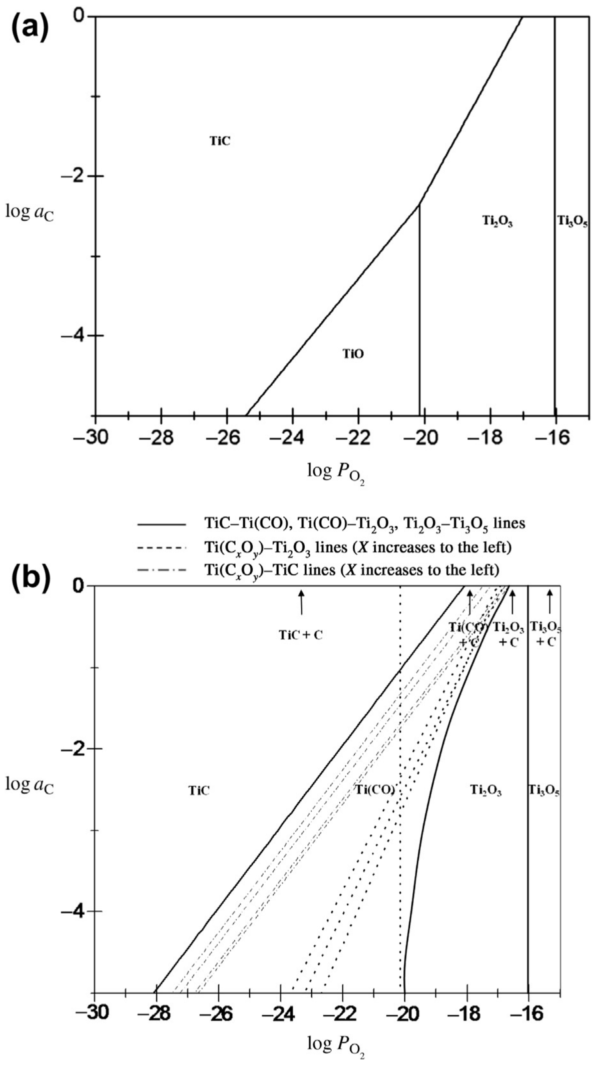

Figure 7 Phase domains of (a) Ti_3O_5–Ti_2O_3–TiO–TiC (without solid-solution formation) and (b) Ti_3O_5–Ti_2O_3–Ti(CO)–TiC (with solid-solution formation) at 1580 K.

Table 5 Activities and Gibbs formation energies of Ti(C_xO_y) at 1673 K (using regular solution model)

x in Ti(C_xO_y)	Activity of TiC (a_{TiC})	Activity of TiO (a_{TiO})	Formation energies of Ti(C_xO_y) (KJ mol^{-1})
0.67	0.74	0.40	−246.0
0.72	0.78	0.36	−234.2
0.85	0.89	0.22	−202.9
0.90	0.92	0.16	−190.5
0.96	0.97	0.08	−175.2

1994; Koc, 1998; Koc & Folmer, 1997; Park, Kang, Kwon, & Kang, 2006) performed a series of reduction/carburization experiments to produce single-phase carbides such as TiC and WC by low- or high-energy milling process. For example, carbothermal reduction of an amorphous mixture of ($TiO_2 + C$) can be complete at 1300 °C within 2 h if high-energy milling is employed. This is a much lower temperature than is typically used in a conventional carbothermal reduction (1700–2000 °C). The synthesis of nanocrystalline TiC at a low temperature is possible only because of the enhanced reactivity of the amorphous phase of $TiO_2 + C$ mixtures (Berger, 2001; Stull, 1971).

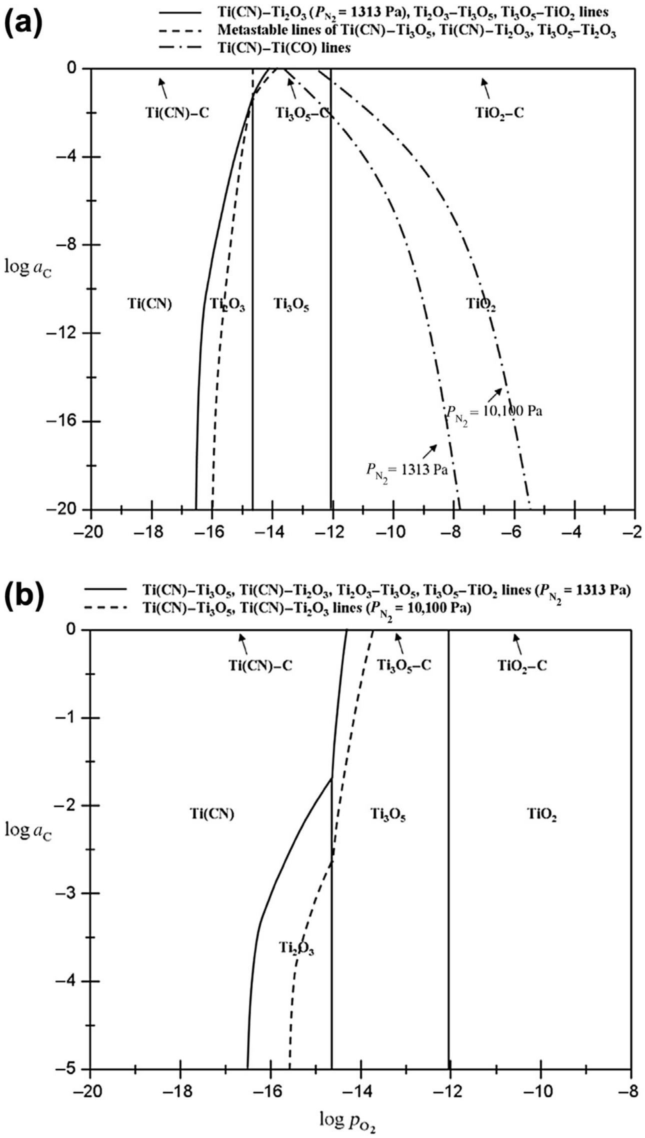

Figure 8 (a) Domain boundaries in Ti(CN)–Ti(CO), Ti(CN)–Ti_2O_3–Ti_3O_5, Ti_3O_5–TiO_2 and (b) stability domain of Ti(CN)–Ti_2O_3–Ti_3O_5–TiO_2 ($P_{N_2} = 1313, 10,100$ Pa).

The milled mixture of $WO_3 + C$ converts to a $W_2C + WC$ mixture at 1300 °C. The presence of W_2C is attributed to the lack of carbon during the carbothermal reduction and powder handling. In order to understand the high reactivity of high-energy milled oxide powders, Kwon et al. investigated the effect of other oxides in inducing relevant transformations by examining the milling behavior of the individual oxides with carbon (Kwon & Kang, 2008a; Park et al., 2006). The same amount of the individual oxide, such as TiO_2, WO_3 and NiO along with C, was milled with the same amount of carbon as that of the oxide mixture in the investigation.

When a mixture of TiO_2/C was milled for 20 h, anatase phase transformed completely to rutile. However, the crystallinity was much higher than that of the oxide mixture with partial reduction oxides, resulting in WO_2 and hexagonal Ni. WO_3 can be alloyed effectively in the form of nanocrystalline or amorphous phases in the presence of other oxides such as TiO_2. The milling result also confirms that the NiO/C mixture has the least milling and miscibility among oxides. The presence of WC found in this system was due to contamination from the milling media.

There are many studies that report a phase transformation with only one or two milled compounds such as TiO_2, V_2O_5, ZrO_2, and metals (Ni, Al, and Ti) using high-energy milling (Dutta & Pradhan, 2002; Dutta, Pradhan, & De, 2002; Manik, Dutta, & Pradhan, 2003; Shau, De, & Zdujic, 2003). The effect of high-energy milling on the phase transformation of a milled oxide mixture, TiO_2–WO_3–NiO–C was studied by Kwon et al. (Kwon & Kang, 2008a; Park et al., 2006).

High-energy milling enables raw anatase TiO_2 to transform first to TiO_2-II and then to rutile in the form of a nanocrystalline phase, while WO_3 transforms to a high-pressure WO_3-HP and hexagonal WO_3. The presence of the WO_3 phase is reported to help form a nanocrystalline or amorphous phase with TiO_2 due to its low bond strength and brittle nature. TiC begins to form in the vicinity of 1000 °C while the formation of WC is almost complete at ~800 °C. (Ti,W)C formation occurs mainly at 1150 °C from TiC and WC, which have formed previously.

Figure 9 is the sequential X-ray diffraction (XRD) profiles of TiO_2–WO_3–NiO–C mixtures with respect to the high-energy milling time. In the initial stage of milling, new phases appear, such as rutile TiO_2 and a high-pressure TiO_2-II phase (**Figure 9(a) and (b)**). In addition, TiO2-II forms preferentially over rutile. In the late stage, rutile grows dominantly by consuming TiO_2-II (**Figure 9(b) and (c)**). Apparently, raw anatase TiO_2 transformed to two new phases that are stable at high temperature and/or high pressure. The impact induced from the milling actions is regarded as the main reason for high-pressure TiO_2-II synthesized during milling (Begin-Colin, Girot, Le Caer, & Mocellin, 2000; Coste, Bertrand, Coddet, et al., 2007; Gajovic, Furic, Tomasic, et al., 2005). This result is consistent with the phase diagram shown in **Figure 10** where the anatase and TiO_2-II phases change into rutile under high pressures and temperatures. This result implies that high pressures (>2500 MPa) and temperatures (>500 °C) prevail during milling, which allows such transformations. **Figure 9(d)** demonstrates the formation of (Ti,W)C–Ni by carbothermal reduction.

The result of Rietveld analysis is summarized in **Table 6**, which shows the phases present in the powder milled by the attrition and planetary mills for 20 h. It also lists their space group, crystal structure and final grain size of the phases found from the planetary mill. This analysis indicates that there are three different types of TiO_2 in the system. The possible presence of srilankite TiO_2 was also noted in the powder milled using the planetary mill. WO_3 transforms to a high-pressure WO_3-HP and hexagonal WO_3 in the planetary mill, whereas $W(CO)_6$ was found in the attrition mill. The transformation can vary significantly according to the milling techniques or impact. The results of the Scherrer's method revealed that the size of crystallites milled using the attrition technique exceeds the limit of the method (>100 nm). However, the average size of rutile in the planetary mill was under 10 nm while that of raw anatase was milled to 30 nm (**Table 6**).

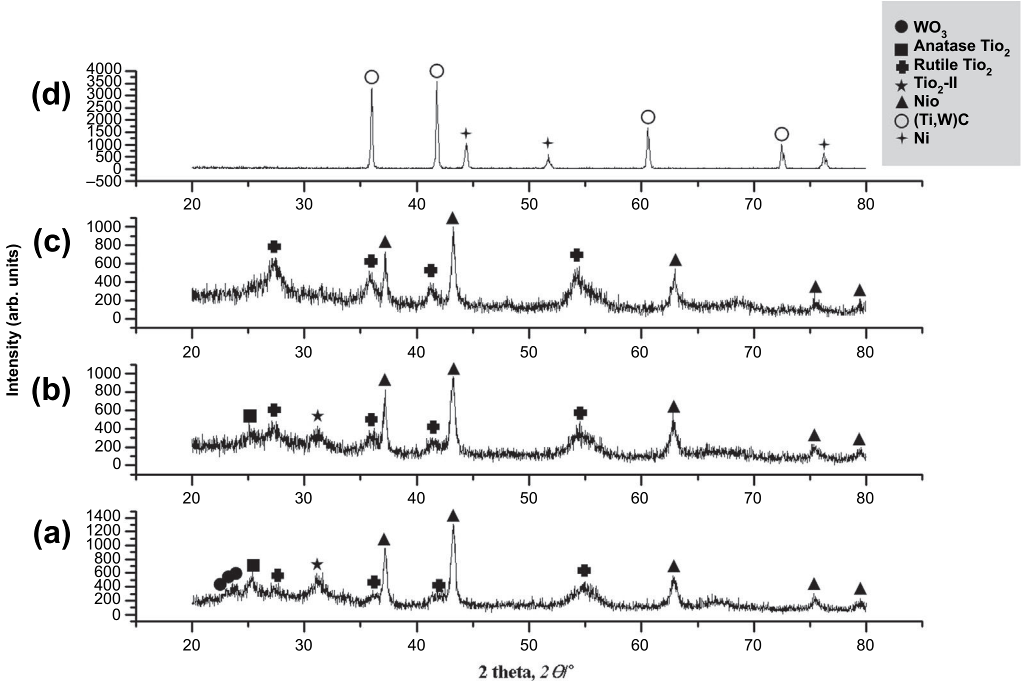

Figure 9 XRD profiles of TiO_2–WO_3–NiO–C mixtures after planetary milling for (a) 5 h, (b) 10 h, (c) 20 h, and (d) after carbothermal reduction of (c) at 1300 °C for 1 h.

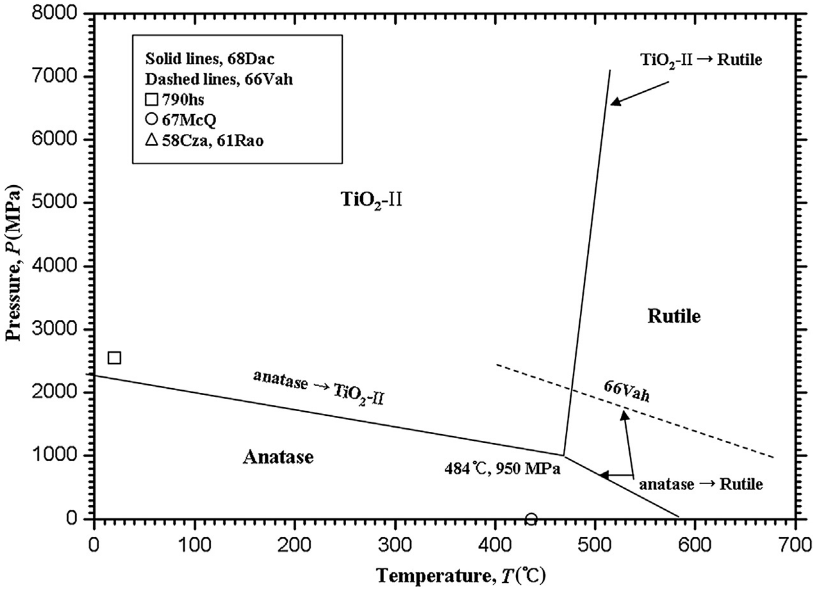

Figure 10 Phase diagram of TiO_2 as a function of temperature and pressure.

Table 6 Microstructural parameters of the powder after attrition and planetary milling for 20 h

Starting materials		*Powder after attrition milling*	*Powder after planetary milling*			
Phase	*Crystallite size (µm)*	*Phase*	*Phase*	*Crystallite size (nm)*	*Crystal system*	*Space group*
TiO_2 anatase	43	TiO_2 anatase	TiO_2 anatase	21.7	Tetragonal	I41/amd
		TiO_2-II	TiO_2-II	31.2	Orthorhombic	Pbcn
		TiO_2 rutile	TiO_2 rutile	7.6	Tetragonal	P42/mn
WO_3 mono	20	WO_3 mono	WO_3 mono	*a*	Monoclinic	P21/n
		$W(CO)_6$ Pnma	WO_3-HP	*a*	Monoclinic	P21/c
			WO_3-hex	*a*	Hexagonal	P6/mmm
NiO	45	NiO	NiO	52.7	Cubic	Fm3m
C	1.65	C	C	3.3	Hexagonal	P63mc

[a] *Fraction of the phase was <5 wt% and therefore the grain value is not reliable.*

BPR, ball-to-powder weight ratio.

Figure 11 shows the evolution of CO/CO_2 gas measured using a mass spectrometer from the oxide mixtures milled for 5, 10, and 20 h. The temperature range for the reduction was varied with respect to the milling time. While the onset temperature of the CO/CO_2 gas evolution is ~530 °C for the powder milled for 5 h, CO/CO_2 gas is released at ~500 and 450 °C in case of 10 and 20 h milling, respectively. A thermodynamic calculation shows that CO_2 is more stable at a lower temperature than CO. According to the Ellingham diagram (Gaskell, 2003), the coexistence of CO and CO_2 gases prevails up to ~1130 °C with unmilled oxides if the total pressure is maintained at 1×10^5 Pa. In this case, the temperature decreases to ~500 °C, even if the reduction environment is much different from the standard state. With the milled powder, the CO evolution was completed at a lower temperature, 1200 °C, with increasing milling time (Figure 11(c)). Table 7 summarizes the XRD results of the mixture. The results show that the rutile phase was continuously reduced into a suboxide, TiO_{2-x}, until it reached 1000 °C. Various suboxides appeared and were reduced at a faster rate than rutile. This can indicate the relative stability of the oxides examined in this study.

Prealloyed powder mixtures, which are composed of nanocrystalline $(Ti,M_1,M_2)(CN)$ and Ni, were prepared by Park et al. (2006). For uniform distribution of Ni in the cermet powder, NiO was added to the oxide mixture with carbon and the mixture was then reduced in a vacuum. The reduction and carburization were performed in one step at 1300 °C for 2 h. For the final production of $(Ti,M_1,M_2)(CN)$–Ni powders, the mixture was exposed to a nitrogen atmosphere at the temperature used for carburization. This made it possible to synthesize well-dispersed solid-solution powder with an Ni binder.

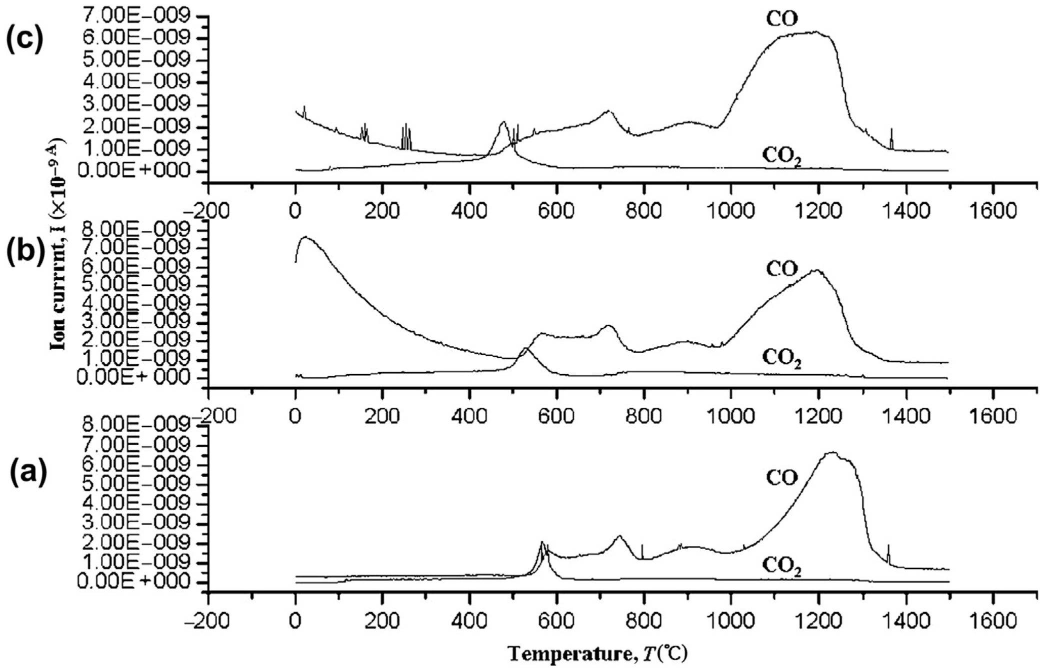

Figure 11 Gas evolution of CO/CO_2 during carbothermal reduction of $TiO_2 + WO_3 + NiO + C$ mixture after high-energy milling for (a) 5 h, (b) 10 h, and (c) 20 h.

Table 7 The phases observed after carbothermal reduction at various temperatures for 1 h

	500 °C	*800 °C*	*1000 °C*	*1100 °C*	*1150 °C*
Phases confirmed from XRD analysis	TiO_2 rutile WC Ni	TiO_2 rutile Ti_4O_7 Ti_3O_5 WC Ni	TiC Ti_4O_7 Ti_3O_5 WC Ni	TiC Ti_3O_5 Ti_2O_3 WC Ni	(Ti,W)C WC Ni

Figures 12 and 13 show the XRD results for the powders synthesized, in the temperature range of 900–1300 °C for 2 h, from various mixtures of milled oxides. No other phase is present, except the solid-solution phases of (Ti,W)(CN) and (Ti,W,Mo)(CN) with Ni after the heat treatment at 1300 °C for 2 h. In a separated experiment, the XRD results indicate that NbC and Mo_2C are formed at 1000–1100 °C during the reduction/carburization process while TiC/Ti(CN) and WC form at 1100–1200 °C. The formation of the final solid-solution phases is complete at a temperature, ~100 °C higher than the formation temperature of individual carbides. Individual carbides such as WC, Mo_2C and NbC begin to form at low temperatures. This indicates that the solid-solution phases are more stable, in terms of free energy of formation, than the mixture of individual carbides. Thus, the solid solutions begin to form in the vicinity of the formation temperature of Ti(CN). These individual carbides are known to be less stable than Ti(CN) in terms of free energy of formation and melting points (Chase, 1998; Lide & Frederikse, 1994). The observation is attributed to the thermal stability of the additive carbides. The mechanism of formation of the solid-solution phases is yet to be understood.

The condition for the reduction of NiO was found by performing a separate synthesis of Ni nanocrystalline particles from NiO. This permits (Ti,M)C–Ni or a (Ti,M)(CN)–Ni system to be prepared in one step. The NiO was reduced under a hydrogen atmosphere. Although Ni was obtained from unmilled NiO at temperatures above 700 °C, milled NiO was reduced to Ni under a hydrogen atmosphere at temperatures >500 °C. The reduction of NiO was also facilitated by the presence of carbon. The synthesized Ni nanopowders were typically in the form of large agglomerates of ~30 μm. However, the Ni agglomerate consisted of fine crystallites, with a particle size of ~200 nm. This extensive agglomeration can be attributed, in part, to the strong magnetic properties of Ni.

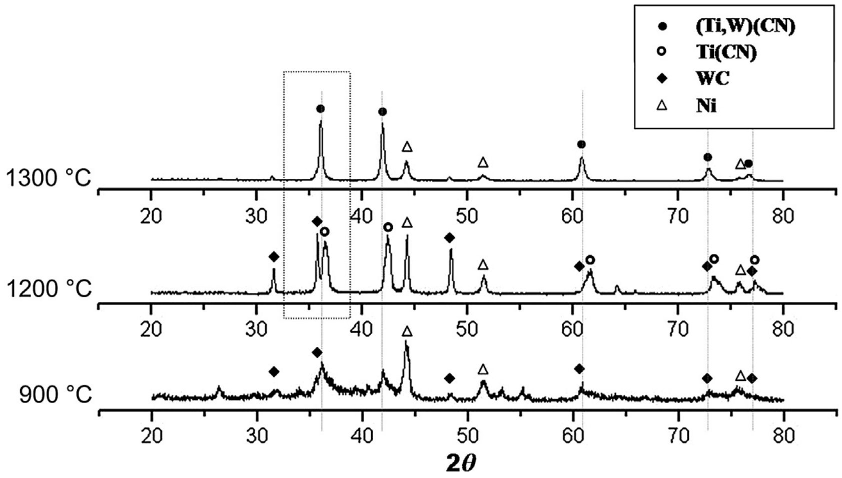

Figure 12 XRD of phase formation of (Ti,30W)(CN)–Ni: WC and Ti(CN) formed first at low temperatures.

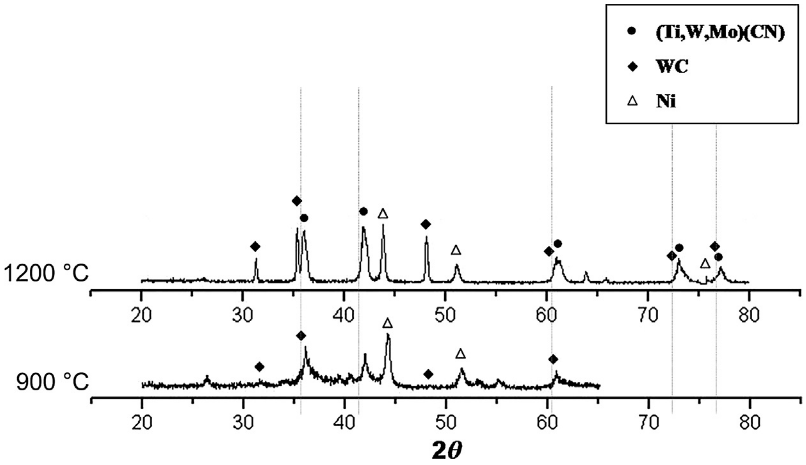

Figure 13 XRD of phase formation of (Ti,10W,5Mo)(CN)–Ni.

The average size of the powder agglomerates was in the range of 200–400 nm, depending on the type of carbides added. Crystallite size measured by the Scherrer's method is estimated to be ~30 nm. However, the TEM image of synthesized powders, in our previous study for (Ti,W)C–Ni and (Ti,W)(CN)–Ni (Park & Kang, 2005), shows that the agglomerates are composed of small crystallites in the range of ~50 nm.

A carbon/nitrogen/oxygen analysis was done on the nanopowders to confirm that the carbothermal reduction was complete. The results were compared with commercial micron-sized powders, as shown in Table 8. The oxygen level is much lower than that of commercial powders as long as the reduction/carburization is performed at >1200 °C. It was noted that the presence of nitrogen in the solid-solution phase significantly reduces the level of oxygen, compared with solid solutions of carbide (Park & Kang, 2005). It seems that the nitrogen destabilizes the presence of oxygen or oxides in carbonitride solid solutions.

The nitrogen content depends on the type of solute used and their content in the solid solutions (Table 8). Further, it has been reported that the thermal stability of Ti(CN) increases when the composition moves toward the high carbon side from 1200 °C (Jung et al., 1999). The results for (Ti,Mo)(CN) and (Ti,Mo,Nb)(CN) indicate that Nb has a higher affinity for nitrogen than Mo. W and Mo in the VIa group in the periodic table behave similarly with respect to nitrogen in the Ti(CN) phase of the B1 structure. In general, (Ti,15W)(CN)–Ni and (Ti,10Mo,5Nb)(CN)–Ni have a ratio of 2:1 (C/N), whereas other compositions tend to be on the high carbon side.

Table 8 Chemical analysis of synthesized powders (in wt% balanced by Ti and W)

Compositions	*Processing temperature (°C)*	*Carbon (wt%)*	*Nitrogen (wt%)*	*Oxygen (wt%)*
(Ti,15Mo)(CN)–Ni	1200	10.37	2.70	0.12
	1300	5.64	1.59	0
(Ti,10Mo,5Nb)(CN)–Ni	1200	12.00	5.68	0.27
	1300	11.31	3.90	0
(Ti,15W)C–Ni	1200	14.99	0.13	0.05
	1300	12.14	0.52	1.14
(Ti,15W)(CN)–Ni	1300	11.45	5.58	0.36
(Ti,15W,5Mo)(CN)	1300	7.61	1.65	0.05
(Ti,15W,5Nb)(CN)	1300	15.22	4.28	0.05
(Ti,30W)C–Ni	1300	10.65	0.38	1.08
(Ti,30W)(CN)–Ni	1300	10.39	3.66	0.08
$Ti(C_{0.7}N_{0.3})$–15WC–20Ni	Commercial	10.10	4.44	0.81
$Ti(C_{0.7}N_{0.3})$–30WC–20Ni	Commercial	9.00	3.39	0.83

1.05.2 Microstructure of Ti-Based Cermets

1.05.2.1 Instability Issues of TiC-Based Cermets

In transitional metal carbides, the interface stability between carbide and the binder metal is an important issue in determining the microstructure of cermets. Especially, it is so with TiC and Ti(CN). The tendency to reduce surface energy is a major driving force in the sintering of a single-phase system. Therefore, grain morphologies are typically spherical or at least flat. However, in some special cases, negative curvatures are also found. This phenomenon is referred to as chemically induced grain migration (CIGM) and especially in the liquid-phase sintering, it is called instability of the solid–liquid interface (ISLI).

Many reports have appeared on the driving force for CIGM (Ahn, Kim, & Kang, 2001; Hillert, 1983; Lee, Baik, & Yoon, 1987; Park, Park, Kang, & Kim, 1998; Song & Yoon, 1984; Yoon, 1995). These studies indicate that a large part of the total driving force for CIGM can be attributed to the presence of strain energy at the coherent interface layer. Chae, Chun, Kim, Baik, and Eun (1990) reported ISLI in a TiC–Fe system. Later Chun, Kim, and Eun (1993) also studied ISLI using a TiC–Mo–Ni system. They concluded that the strain was induced by the formation of a coherent layer, which is a solid-solution rim formed from the carbide and binder phases. However, CIGM is not always observed in all systems.

It was found that CIGM, narrowly speaking, ISLI is not commonly observed in carbide–metal systems during sintering. It is generally thought that the formation of a solid-solution rim is a necessary condition for ISLI. Kwon and Kang (2006) investigated the microstructures of various carbide–Ni composites in terms of the parameters in Hume–Rothery rules such as atomic size, electronegativity, electron valence, and crystal structure. Average size and manufacturers of initial powders are listed in **Table 9**. Of fourth period transition-metal carbides, TiC is the only carbide that exhibits a strong ISLI with negative curvatures in molten Ni (Kwon & Kang, 2006). No ISLI was observed for other carbides of the fifth and sixth period elements.

Table 9 Average particle size and manufacturers of initial powders (Kwon & Kang, 2006)

	Particle size (μm)	*Manufacturer*
TiC	1.00	Treibacher
ZrC	2.40	H. C. Starck
HfC	1.61	Kennametal
VC	1.10	HCST
NbC	1.75	Treibacher
TaC	1.12	Treibacher
Cr_3C_2	1.75	Kennametal
Mo_2C	1.42	Kennametal
WC	1.88	Xiamen
Ni	4.00	INCO

The origin of ISLI is strain developed at the interface between the carbides and the newly formed solid solutions. The difference in the size of the atoms involved can be used to predict the formation of a carbide–Ni solid solution when the Hume–Rothery rules are applied. Aside from the size factor, other factors in the rules are not found effective in predicting this phenomenon. Figure 14 shows the microstructures of the specimens without ISLI, which were obtained after infiltration and heat treatment at 1510 °C for 1 h. All those were from fifth period metal-carbide systems. Similar microstructures were obtained from sixth period carbides.

Figure 15 shows the microstructures of the specimens obtained from the fourth period transitional-metal carbides. In these systems, carbide particles (TiC and Cr_3C_2) with negative curvatures can be seen. The IVB, VB, and VIB transitional-metal carbides in the fourth period were found to grow much faster (30–100 μm) than the other carbides in the fifth and sixth periods (5–10 μm). An XRD analysis was done to better understand the tendency toward solid-solution formation by measuring the shifts in the main peaks. As summarized in Table 10, all carbide systems demonstrate clear peak shifts. The peak shifts to high diffraction angles (2θ) were observed for TiC, Cr_3C_2, and WC. The shifts to high angles, which indicate the decrease of lattice parameters, could be interpreted as a tendency of the carbides to form solid solutions or compounds readily with solutes such as Ni in these cases. The TiC–Ni system, which demonstrates a strong ISLI, shows a decrease in lattice constants as the result of forming a solid solution, (Ti,Ni)C. Other carbides such as VC, ZrC, NbC, HfC, TaC, and Mo_2C showed peak shifts to low angles. This implies a low affinity between these transition metals and Ni in their crystal structure.

In Table 11, the differences in atom size between carbides and nickel are shown under a size factor. Other factors are also listed for comparison. The size factor was determined by the following formula: (atomic size of the metal in the carbide – atomic size of nickel)/(atomic size of the metal in the carbide). The size difference between impurity and host atoms must be under $\sim$15% for a solid solution to form. The fifth and sixth period metal atoms (Zr, Hf, Mo, Nb, Ta, and W) have size factors of over 15% with nickel while fourth period metal atoms (Ti, V and Cr) have size factors under $\sim$15%. VC has the best conditions among the carbides of this study to form a solid solution with Ni. However, the tendency of VC to form a solid solution with Ni was small from XRD data and this system failed to show ISLI. Main peak of VC in XRD data is from (400) plane and (400) plane's lattice parameter is smaller than that of other planes. This can be why the tendency to form a solid solution with Ni is not big as much as the case of TiC, Cr_3C_2 and ISLI is not observed in VC–Ni system. However, all these factors including electronegativity, electron valence and crystal structure do not provide clear predictive information on the formation of solid solutions.

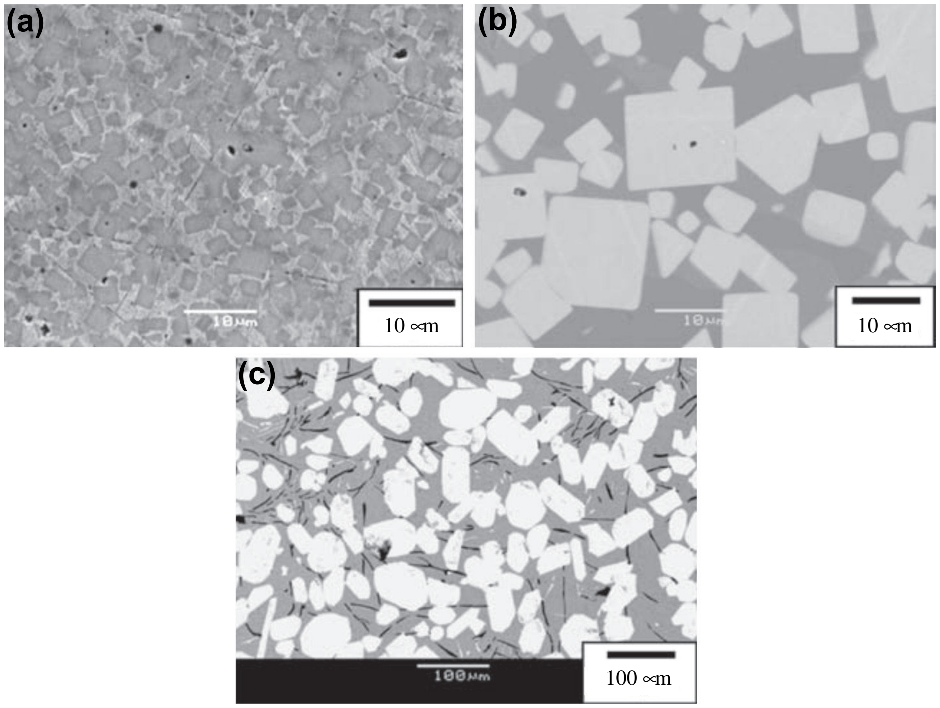

Figure 14 SEM micrographs of (a) ZrC–50Ni, (b) NbC–50Ni, and (c) Mo2C–50Ni (vol%), heat treated at 1510 °C for 1 h.

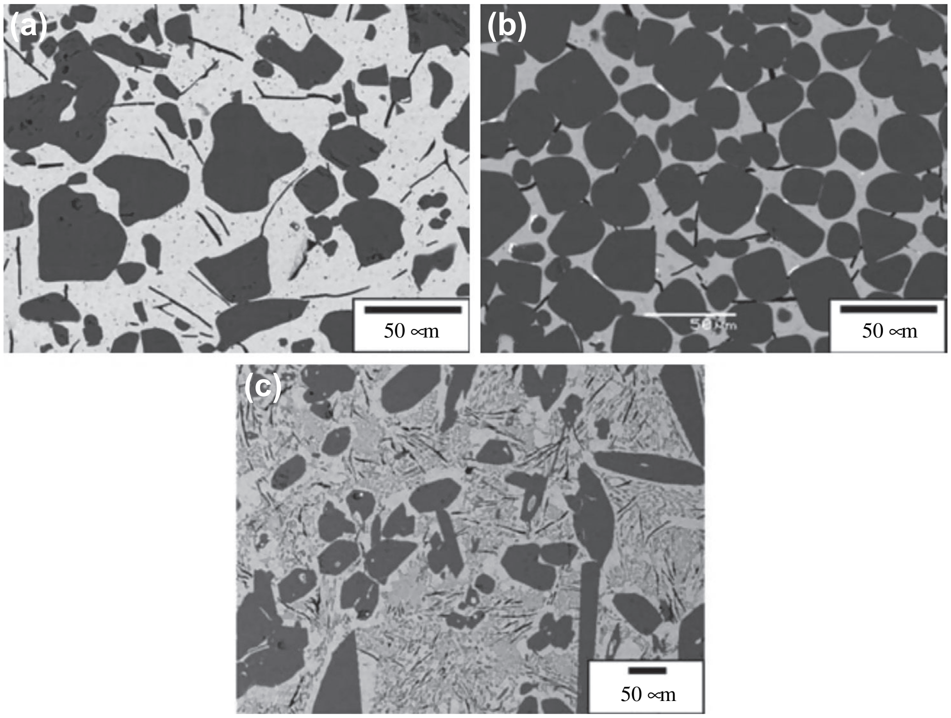

Figure 15 SEM micrographs of (a) TiC–50Ni, (b) VC–50Ni, and (c) Cr_3C_2–50Ni (vol%) heat treated at 1510 °C for 1 h under vacuum.

Table 10 Peak shifts of major peaks of various carbide–metal systems (2θ) (Kwon & Kang, 2006)

Carbides	*A* *JCPDS*	*B* *Raw powder*	*C* *1510 °C heat treatment w/o Ni (C-B)*	*D* *1510 °C sintering with Ni (D-C)*
TiC	41.710	41.673	41.400 (−0.273)	41.657 **(+0.257)**
VC	43.490	43.415	43.360 (−0.055)	43.340 (−0.020)
Cr_3C_2	50.077	50.051	50.027 (−0.024)	50.054 **(+0.027)**
ZrC	33.040	33.054	33.034 (−0.020)	32.755 (−0.279)
NbC	34.730	34.822	34.633 (−0.189)	34.458 (−0.175)
Mo_2C	39.392	39.530	39.466 (−0.064)	39.229 (−0.237)
HfC	33.437	33.456	33.213 (−0.243)	33.212 (−0.001)
TaC	34.855	34.927	35.065 (0.138)	34.607 (−0.458)
WC	48.266	48.355	48.118 (−0.237)	48.550 **(+0.432)**

Table 11 Atomic radii and size factors of 4, 5, and 6 group transition-metal atoms and nickel atom (Kwon and Kang, 2006)

	Atomic radius (nm) (A)	*Most common valence (V)*	*Crystal structure of carbide*	*Electronegativity (E)*	*ΔA (nm)*	*ΔV*	*ΔE*	*Atomic size factor (%)*
Ni	0.149	2	FCC	1.91	–	–	–	–
Ti	0.176	4	B1	1.54	0.027	2	0.37	15.34
Zr	0.206	4	B1	1.33	0.057	2	0.58	27.67
Hf	0.208	4	B1	1.3	0.059	2	0.61	28.37
V	0.171	5	B1	1.63	0.022	3	0.28	12.87
Nb	0.198	5	B1	1.6	0.049	3	0.31	24.75
Ta	0.200	5	B1	1.5	0.051	3	0.41	25.5
Cr	0.166	3	Orthorhombic	1.66	0.017	1	0.25	10.24
Mo	0.190	4	Hexagonal	2.16	0.041	2	0.25	21.58
W	0.193	4	Hexagonal	2.36	0.044	2	0.45	22.8

1.05.2.2 Dissolution/Precipitation: Ti(CN)–MC–Ni

TiC- and Ti(C,N)-based cermets possess a fine and stable microstructure. Such microstructure, when formed during liquid-phase sintering shows a typical core/rim structure where the cores are partially dissolved raw material particles on which the rim structure has grown through a dissolution–precipitation process (Ahn & Kang, 1998; Ettmayer, Kolaska, Lengauer & Dreyer, 1995; Ettmayer & Lengauer, 1989; Qi & Kang, 1998). **Figure 16** is a schematic of a scanning electron microscopy (SEM) microstructure for commercial cermets. In general, most of the particles in the microstructure consist of black TiC or Ti(C,N) cores and gray (Ti,W,...)C or (Ti,W,...)(C,N) solid-solution rims.

WC, secondary carbide, is a necessary carbide component in a cermet system which serves to improve mechanical and functional properties. The general role of added WC in a cermet system is to enhance density via improving wetting and sinterability (Matsubara, Shin, & Sakuma, 1992). It has also been reported that the addition of WC to a TiC–Ni or Ti(C,N)–Ni system improves toughness and decreases particle growth rate (Suzuki et al., 1983; Suzuki & Matsubara, 1986). Finally, it has been noted that WC, which forms a solid solution with TiC or Ti(C,N), remains as an independent phase with increasing nitrogen content of a Ti(C,N)–Ni system. However, to date, few studies of the dissolution and precipitation behavior of Ti(C,N) and WC in a Ti(C,N)–Ni system have been reported (Rynemark, 1991). In the following, the discussion will be limited to Ti(CN) as an exemplary major carbide component.

1.05.2.2.1 Core/Rim Structure

There are numerous studies on core/rim microstructure of Ti(CN)-based cermets. As an example, Ahn and Kang (2000) investigated the core/rim structures of Ti(C,N)–xWC–20Ni in order to determine the effect of WC and nitrogen content on the microstructure of the system. In addition, the relative dissolution rate of WC to Ti(C,N) in the system was studied by analyzing the rim compositions which, to a large extent, reflects the equilibrium reaction during liquid-phase sintering.

Variations in WC content had a much less influence, as an additive, on the rim microstructure than that of other carbides (Ahn & Kang, 2000; Yang & Lee, 1996). This is attributed to the low dissolution rate of Ti(C,N) as compared to that of WC in the Ni melt. The known effect of particle refinement as the result of added WC to Ti(C,N)–Ni cermets was not evident sometimes (Matsubara et al., 1992).

1.05.2.2.2 Nitrogen Effect on Dissolution of Ti(CN)

The nitrogen content in $\mathrm{Ti(C_{1-x}N_x)}$, however, had a significant effect on the microstructure by changing the stability of $\mathrm{Ti(C_{1-x}N_x)}$, resulting in different rates of dissolution. It has been reported that the dissolution of WC in the Ni binder phase can be limited if the total nitrogen concentration is high in a cermet (Doi et al., 1985). This can be attributed to the low chemical affinity between W and N. **Figure 17** shows the microstructures of the systems composed of the $\mathrm{Ti(C_{0.7}N_{0.3})}$, $\mathrm{Ti(C_{0.5}N_{0.5})}$ and $\mathrm{Ti(C_{0.3}N_{0.7})}$ phases, respectively, and it demonstrates the

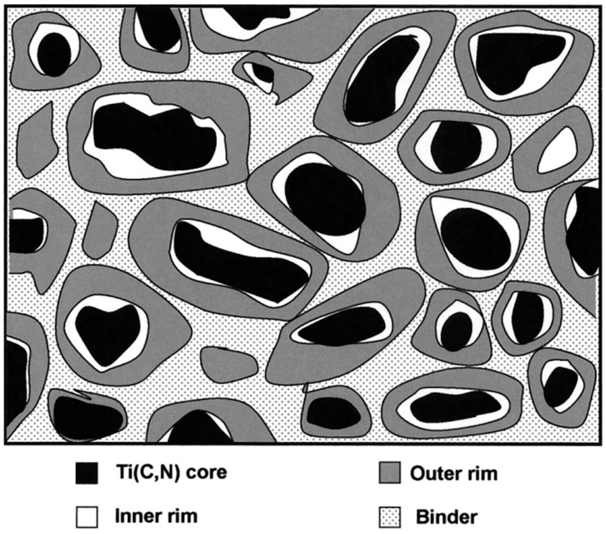

Figure 16 An SEM schematic of Ti(C,N)-based cermets.

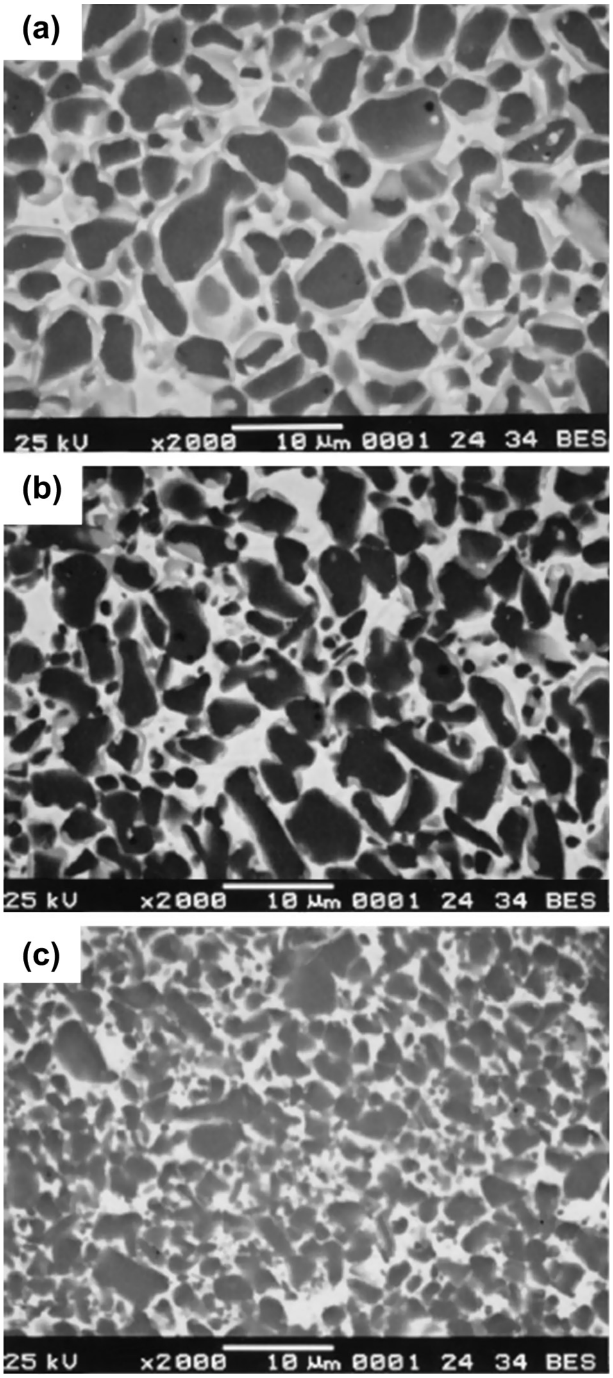

Figure 17 SEM/BSE micrographs of Ti($C_{1-x}N_x$)–10WC–20Ni systems sintered at 1510 °C in vacuum for 1 h: (a) $x = 0.3$ (b) $x = 0.5$ (c) $x = 0.7$.

influence of N in Ti($C_{1-x}N_x$) on the microstructure. For other systems (Ahn & Kang, 1998; Fukuhara & Mitani, 1982; Jung et al., 1999; Mun & Kang, 1999), it has been reported that the microstructure is strongly affected by the nitrogen content of Ti(C,N). Somewhat different results were reported by Fukuhara and Mitani (1982) for a Ti(C,N)–Mo–Ni system via the P/M technique and by Qi and Kang (1998) from a Ti(C,N)–NbC–Ni system via infiltration techniques. Both investigators showed that when Mo or NbC were added to Ti(C,N)–Ni, the Ti($C_{0.5}N_{0.5}$) phase exhibited the slowest dissolution rate among the various Ti($C_{1-x}N_x$) phases. Based on thermodynamic calculations for Ti(C,N) stability (Jung et al., 1999), it has been reported that Ti($C_{0.3}N_{0.7}$) is the most stable compound in the 1400–1600 °C range and it is consistent with the result from Figure 17.

1.05.2.2.3 Dissolution Rates of Secondary Carbides

The cores of undissolved Ti(C,N) particles act as nucleation sites for the rim structure. The rims are forming when oversaturated solutes precipitate out from the melt on the Ti(C,N) particles (Gee, Reece, & Roebuck, 1992). Thus, the equilibrium reactions in the dissolution and precipitation of the hard phase during sintering can be inferred from the composition analysis of the core/rim structure as long as the solute content is within solubility limit in a carbide system (Doi et al., 1985; Mun & Kang, 1999). It has been regarded that the inner rim forms during the heating stage from the onset temperature for liquid forming (~1300 °C), whereas the outer rim forms at the sintering temperature (1510 °C) (Doi et al., 1985; Gee et al., 1992).

The dissolution rate of WC was measured to be approximately two and five times faster than that of Ti(C,N) in the system at 1300 and 1510 °C, respectively (Ahn & Kang, 2000). The results were interpreted in terms of phase stability and precipitation phenomena. Ahn and Kang (2001) reported the dissolution behaviors of $Ti(C_{0.7}N_{0.3})$ with various secondary carbides such as HfC, TaC and WC. The average dissolution rate of $Ti(C_{0.7}N_{0.3})$ in the HfC-containing system is found ~1.6 and 1.9 times higher than those for $Ti(C_{0.7}N_{0.3})$ in the TaC- and WC-containing systems at the same sintering conditions. **Figure 18** shows the SEM/backscattered electron micrographs of $Ti(C_{0.7}N_{0.3})$–10 MC–30Ni systems sintered at 1510 °C in vacuum for 1 h. MC is (a) HfC, (b) TaC, and (c) WC, which are the basis for the measurement of dissolution rate.

1.05.2.2.4 Factors Influencing Dissolution Behavior

The particle dissolution is an interesting issue, which is complicated by various thermodynamics and kinetics factors. In practice, the dissolution phenomena of a compound in a liquid melt can be considered as two separate steps: if the dissolution of the particle is limited to its surface or in the neighborhood of the surface, (1) the elemental dissociation of a compound and (2) mixing between the dissociated species and the surrounding materials, such as a liquid melt. The first step, the dissociation of a compound particle, can be described as below:

$$J = A\,n\,v\,\exp(-Q/RT)\exp\left(-\Delta G_f/RT\right), \qquad (25)$$

where J is the flux of dissociating species from the particle to the melts, A is the probability of available jump sites in the melt for the elements, n is the number of possible unit compounds to be dissociated, v is the Debye

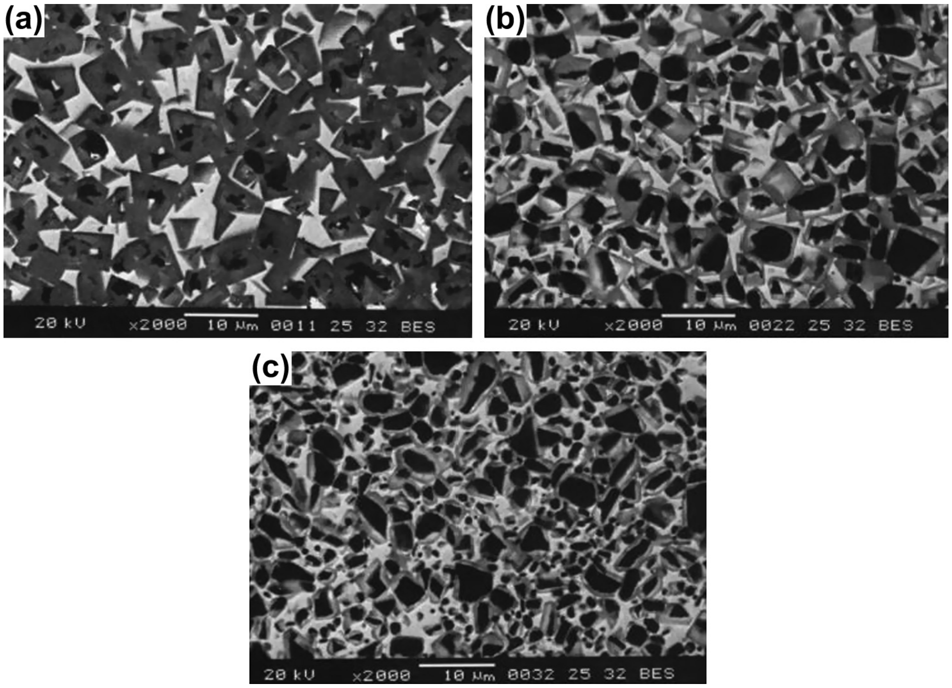

Figure 18 SEM/BSE micrographs of $Ti(C_{0.7}N_{0.3})$–10 MC–30Ni systems sintered at 1510 °C in vacuum for 1 h. MC is (a) HfC, (b) TaC, and (c) WC.

frequency, Q is the activation energy for particle dissociation, and ΔG_f is the energy of formation of the compound from the elements. In the case of carbide dissolution in Ni melts, the reverse reaction can be assumed to be negligible. In Eqn (25), the probability of available jump sites, A, is closely related to the solubility of the dissolving species in the liquid melt. This is, in turn, determined by interactions (coefficients) among species in the melts as the number of elements involved in the system increases. This issue has been well documented for the effect of secondary solutes on the solubility of a primary solute in the field of steel production (Pehlke & Elliot, 1960). A similar approach as shown in Eqn (25) can be found to describe the migration of grain boundaries (Crank, 1956; Shewman, 1989). The equation indicates that little dissociation would occur due to the high energy of formation term unless it is in a liquid melt.

The driving force for the dissolution of dissociated elements in the melt is the reduction in total free energy of the system, as the result of the entropy of mixing and solid–liquid instability. Thus, for the case of (1) the free energy of mixing, ΔG^M, and (2) strain energy, ΔG^ε, due to the instability of the solid–liquid interface and (3) a surface-related term, ΔG^γ (Park et al., 1998; Chun et al., 1993; Rhee and Yoon, 1987) are additional thermodynamic factors that are needed to describe the dissolution behavior. Thus, Eqn (25) can be expressed as below:

$$J = \alpha A n \nu \exp(-Q/RT)\exp(-\Delta G_f/RT), \tag{26}$$

where $\Delta G_{rxn} = \Delta G_f + \Delta G^M + \Delta G^\gamma + \Delta G^\varepsilon + \ldots$ and α is a constant. The surface energy not only determines particle morphology but also influences the level of strain energy at the solid–liquid interface in a complicated manner. Different shapes of a compound particle in a solution with slightly different compositions are not uncommon.

Further, the transport of the species is often described by the mobility and a gradient of activity coefficient of the diffusing species with respect to concentrations. The product of these factors determines the diffusivity of the species at a given temperature. Therefore, at a given temperature, the rate-limiting step in the transport for dissolution–precipitation or coarsening is generally determined by a dominating factor between (1) the thermal stability of the compounds to be dissolved (interface-controlled) and (2) difficulties in transport due to interactions among the diffusing species and the melts (diffusion-controlled).

The above factors show that the dissolution phenomena involve many intricate thermodynamic and kinetic factors and that the accurate quantification of these factors is not an easy task.

1.05.2.2.5 Onset of Core/Rim Structure Formation

A number of studies related to the microstructure of Ti(C,N)-based cermets have appeared (Suzuki et al., 1971; Zhang, 1993). However, issues regarding the final microstructures, especially regarding the onset of formation, remain ambiguous and controversial. Some studies suggest that the final rim structure is formed during the final sintering step via dissolution of constituent carbides into the liquid binder and its reprecipitation in the form of a solid solution onto the Ti(C,N) particles (Ahn et al., 2001; Ahn & Kang, 2000; Ettmayer et al., 1995). Early studies have proposed that the inner rims are formed by solid-state reactions or during an early stage of sintering (~1300 °C) while the outer rims form thereafter via a dissolution/reprecipitation process (Doi et al., 1985; Lihndahl, Gustafson, Rolander, Stals, & Andrén, 1999; Zackrisson & Andrén, 1999). An extensive investigation was made on this issue to clarify the onset time for formation of the final rim structure with $\mathrm{Ti(C_{0.7}N_{0.3})}$–$x$WC–20Ni ($x = 5$–25 wt%) systems (Kim, Min, & Kang, 2003). The study concluded that the inner rim forms at sintering temperature and the outer rim forms thereafter during the sintering or cooling stage of sintering.

It would be anticipated that rim structures start forming on the Ti(C,N) particles when liquid Ni becomes saturated with solutes (Pehlke & Elliot, 1960). Assuming that the rim phase forms at compositional equilibrium, the solid solution of the rim should have the same Ti/W ratio in composition as that in the liquid Ni. Thus, reactions occurring during the dissolution/reprecipitation process could also be inferred from the composition analysis of the core/rim structure (**Figure 19(b)**) (Ahn et al., 2001; Ahn & Kang, 2000; Doi et al., 1985; Lihndahl et al., 1999; Qi & Kang, 1998; Zackrisson & Andrén, 1999). In the figure, 1510 °C/0 h stands for immediate cooling after furnace temperature reaches to 1510 °C.

The increase in the solubility of W in liquid Ni with temperature is consistent with thermodynamic principles and phase diagrams for W–Ni and WC–Ni(Co) (Exner, 1979; Ettmayer et al., 1995). The relation between sintering temperature and W content in the rim phase, as shown in **Figure 19**, reveals that the solid solution in the outer rim could be formed at lower temperatures than that in the inner rim or at the same sintering temperature by the dissolution of Ti(CN) cores and inner rim phase at the sintering temperature. In

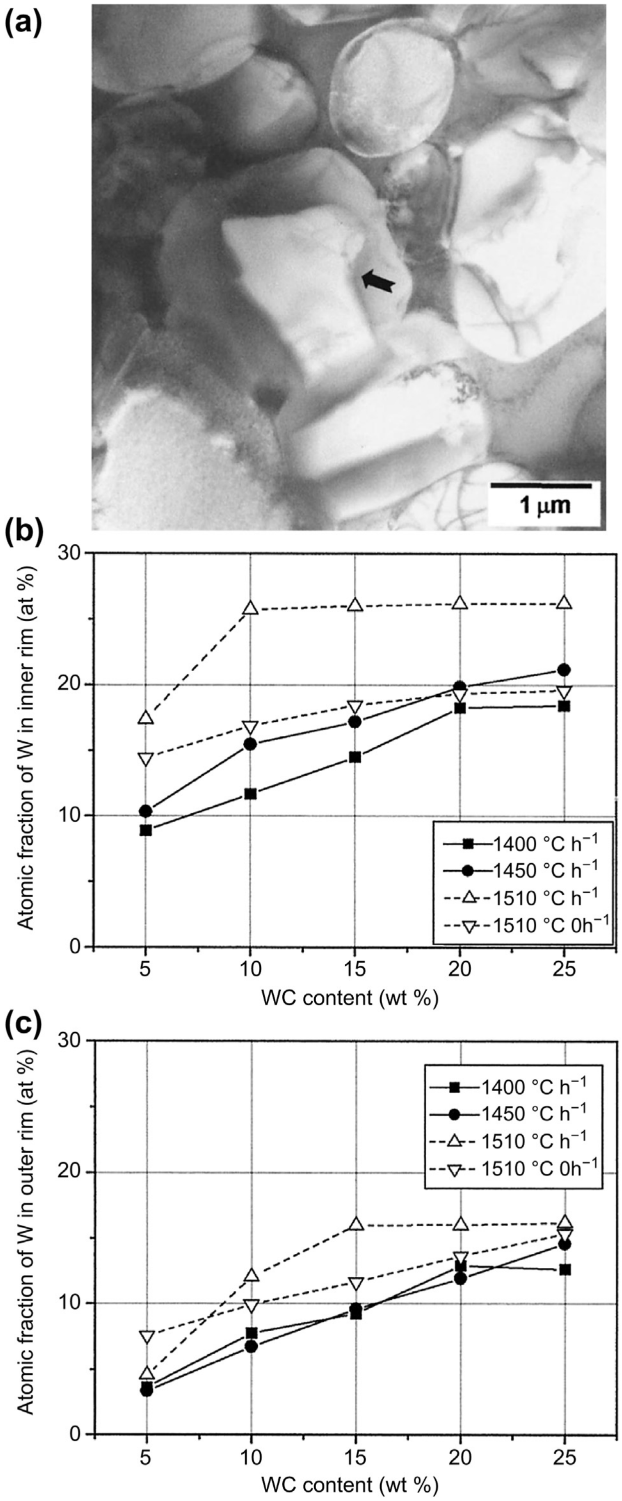

Figure 19 (a) TEM micrograph of a Ti($C_{0.7}N_{0.3}$)–15WC–20Ni system; (b,c) TEM/EDS concentrations of tungsten, for Ti($C_{0.7}N_{0.3}$)–*x*WC–20Ni systems for various sintering temperatures: (b) inner rim (c) outer rim.

addition, from a location point of view, the outer rim forms at a later time than the inner rim. Based on these two facts, it can be concluded that the onset of inner rim formation in "the final microstructure" takes place at the sintering temperature, 1510 °C. A portion of outer rim or the entire outer rim forms thereafter near or at the cooling stage, depending on the initial WC content. The unusually high amount of W in the

Ti(C,N)–5WC–20Ni sintered at 1510 °C for 0 h in **Figure 19** might be due to the combined effect of the short time for carbide dissolution and the high dissolution rate of WC compared to that of Ti(C,N) (Ahn & Kang, 2000; Shewman, 1989).

It is possible for the solid solution to form inner rim at any temperature. However, the rim phases formed at low temperatures in early stages become thermodynamically unstable and tend to redissolve at high temperatures. Thus, the rim phases formed by solid-state diffusion or during the early stage of sintering (~<1400 °C) with the initial liquid Ni cannot constitute the final rim structure. **Figure 20** is the microstructure of a Ti(C,N)–25WC–20Ni system infiltrated at 1510 °C for 0, 10, 30, 60 min (Kim et al., 2003). The change in the inner rim compositions of the infiltrated samples is shown in **Figure 21**. Based on the information in **Figure 22**, the coalescence of Ti(C,N) is likely to occur at the sintering temperature to a great extent prior to the formation of the final rim phases.

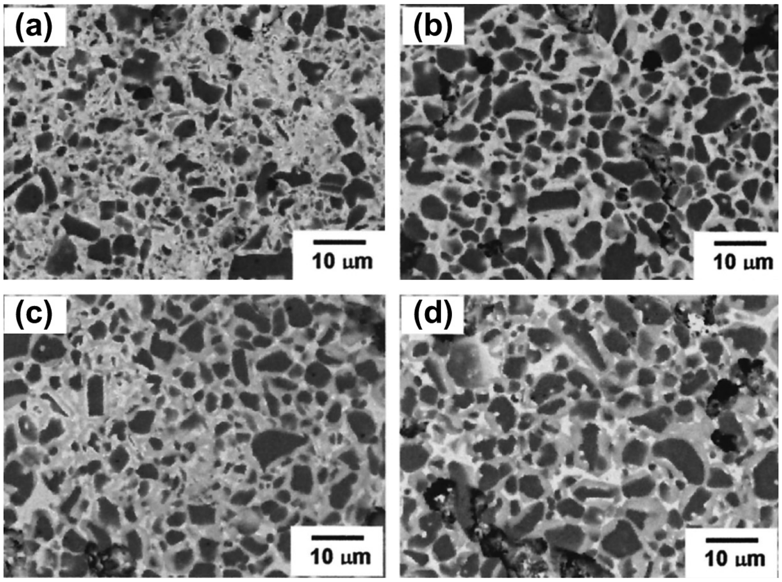

Figure 20 SEM/BSE micrographs of Ti($C_{0.7}N_{0.3}$)–25WC–20Ni systems infiltrated at 1510 °C for (a) 0 min, (b) 10 min, (c) 30 min, and (d) 60 min in vacuum.

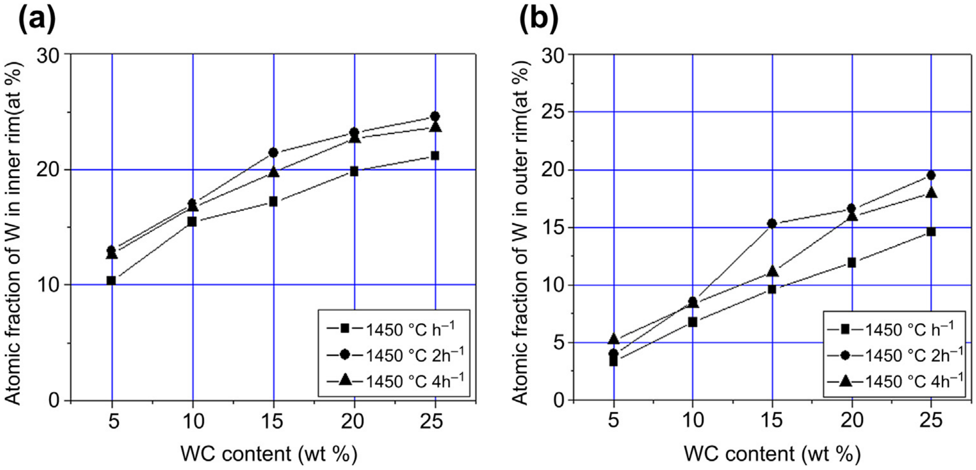

Figure 21 TEM/EDS concentrations of tungsten, for Ti($C_{0.7}N_{0.3}$)–*x*WC–20Ni systems for various sintering times, (a) inner rim and (b) outer rim.

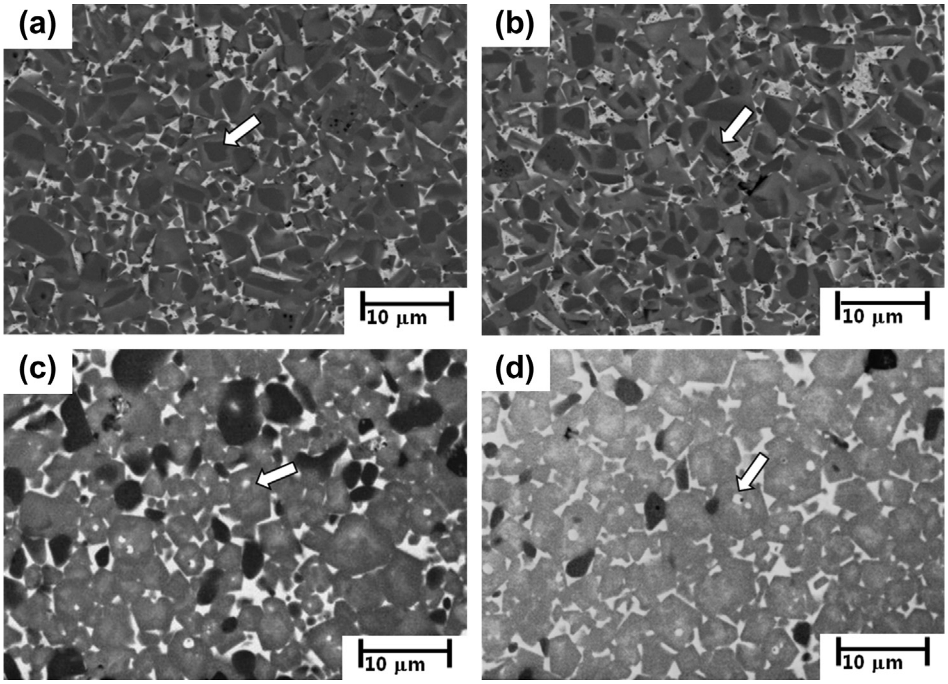

Figure 22 SEM/BSE micrographs of Ti($C_{0.7}N_{0.3}$)–xNbC–20Ni systems (for $x=$ (a) 5, (b) 10, (c) 15, and (d) 25 wt%) sintered at 1510 °C in vacuum for 1 h. Arrows indicate black Ti(CN) cores in (a), (b) and white Nb-rich (Ti,Nb)(CN) cores in (c), (d).

1.05.2.3 Strain Effect on Core/Rim Structure

It is known that dissolution–reprecipitation is involved in the mechanism of the formation of the core/rim structure, ruling out other processes such as spinodal decomposition (Rudy, 1973) and diffusion process (Moskowitz & Humenik, 1966). One of the major interests we have in cermets is to develop an understanding of the formation process of the core/rim structure when various carbides are, individually or multiply, added to Ti(CN)–Ni system. The rim phases present in the final microstructure have been observed to form and grow largely during liquid-phase sintering (Kim et al., 2003; Lihndahl et al., 1999). Variations in the compositions of rim phases have been reported to be dependent on the formation temperature and the relative dissolution rates among carbides in the system (Ahn & Kang, 2000; Kim et al., 2003). This compositional variation would be expected to change the interface energy and lattice parameters of the rim phases, resulting in changes in microstructure and, subsequently, mechanical properties such as wear and fracture behavior. In many SiC-based systems (Lee, Tanaka, & Kim, 1996; Naoto, Yoshio, & Mamoru, 1994; Padture, 1994; She & Ueno, 1999), which also retain a solid-solution rim phase around SiC particles, fracture paths along the rim phase are often observed. Similarly, the property or composition of the rim phase might be closely related to the mechanical behavior of cermets in cutting performance.

In order to study the formation process of the rim phase, the main cause of the change in the microstructures of Ti($C_{0.7}N_{0.3}$)–WC–Ni, Ti($C_{0.7}N_{0.3}$)–NbC–Ni and Ti($C_{0.7}N_{0.3}$)–WC–NbC–Ni systems was investigated extensively (Ahn et al., 2001). The compositions and lattice parameters of the rim structures have also been characterized using energy-dispersive spectrometry (EDS) and XRD (Chen et al., 2000; Kim, Zuo, Kang, 2010), respectively. In Ti($C_{0.7}N_{0.3}$)–NbC–20Ni systems, a phase separation occurred between the Ti(CN) core and (Ti,Nb)(CN) rim phases when a system contains more than 15 wt% NbC. This is due to the increase of misfit between the cores and solid-solution rim phases with the addition of NbC (**Figures 22** and **23**) (Ahn & Kang, 2000; Ahn et al., 2001). The lattice parameter of Ti(C,N) core in the alloys above was measured 43.02 nm by conversion beam electron diffraction while that of (Ti,Nb)(CN) rim in the range of 43.338–43.361 nm (**Table 12**) The critical unconstrained misfit, which causes the separation of the inner rim in the Ti(C,N)–MC–Ni systems, is in the vicinity of 1.38% (Ahn & Kang, 2000). In Ti($C_{0.7}N_{0.3}$)–WC–10NbC–20Ni systems, a phase separation does not occur between the Ti(CN) core and (Ti,Nb)(CN) rim phases.

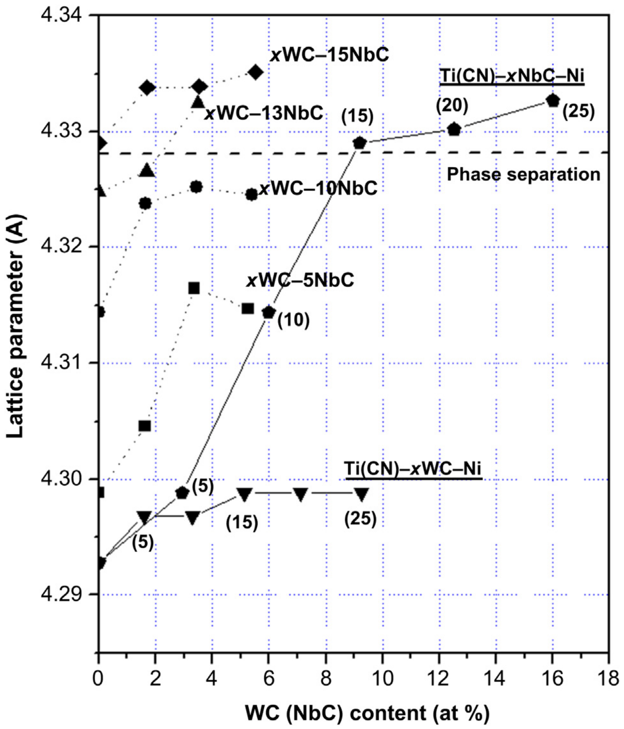

Figure 23 The lattice parameters of the solid-solution phase in the Ti($C_{0.7}N_{0.3}$)–*x*WC–*y*NbC–20Ni system as a function of carbide. The numbers in () indicate the carbide content in wt%.

Table 12 Lattice parameters and strain level in Ti(C,N)–*x*NbC–Ni core/rim structure by CBED in STEM mode

	Outer rim (Zhang, 1993)		*Inner rim (Qi & Kang, 1998)*		*Level of strain (mm mm^{-1})*	
Alloy	*Composition via TEM/EDS*	*HOLZ Analysis (nm)*	*Composition via TEM/EDS*	*Lattice Parameter by Extrapolation (nm)*	*δ at interface between core and inner rim*	*δ between inner and outer rims*
Ti(C,N)–10NbC	($Ti_{0.92}Nb_{0.08}$)(C,N)	43.23	($Ti_{0.83}Nb_{0.17}$)(C,N)	4.3381	0.0084	0.0035
Ti(C,N)–15NbC	($Ti_{0.89}Nb_{0.11}$)(C,N)	43.23	($Ti_{0.71}Nb_{0.29}$)(C,N)	4.3612	0.0138	0.0067
	($Ti_{0.87}Nb_{0.13}$)(C,N)	43.32				
Ti(C,N)–20NbC	($Ti_{0.83}Nb_{0.17}$)(C,N)	43.36	($Ti_{0.71}Nb_{0.29}$)(C,N)	4.3612	0.0138	0.004
	($Ti_{0.81}Nb_{0.19}$)(C,N)	43.44				

1.05.2.4 Carbide Size Effect

Powder size strongly affects the dissolution and precipitation of particles and is a major determinant of the final microstructure and compositions of the rims. Microstructural and compositional analyses have been reported for Ti(CN)–*x*WC–20Ni cermets to understand the dissolution behavior of Ti(CN) as a function of particle size: micron, submicron and nano size (Saidi & Barati, 2002; Jung & Kang, 2004; Jung & Kang, 2007; Yoon, Kang, & Kim, 1997). The WC content was varied from 10 to 70 wt%. As the size of Ti(CN) decreases, the rate of dissolution and reprecipitation increases.

In case of nano-sized Ti(CN), the rapid dissolution and reprecipitation of nano-Ti(C,N) powders induced the formation of a coreless microstructure. With an increase in the amount of WC, the concentration of W in the rims increased but was low compared to the ultrafine or micron system. An inversion in W concentration between inner rim and outer rim occurred at ~40 wt% added WC. That is, the outer rim was richer in W than the inner rim. Following are the details of carbide size effect on dissolution and microstructure.

In Ti(CN)–WC–Ni systems with micron-size Ti(CN), it is common to observe two different (Ti,W)(C,N) solid-solution rim phases as shown in Figure 24. As mentioned, one of the rims is a W-rich inner rim and the other is a relatively W-poor outer rim. In both cases, the W content is much higher than the average amount of W

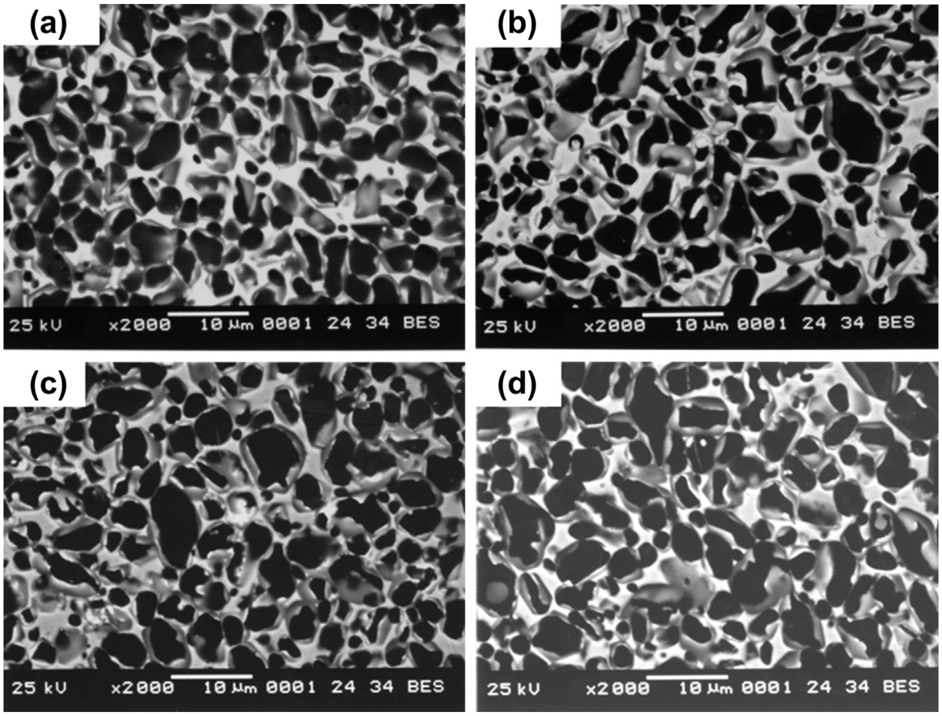

Figure 24 SEM/BSE micrographs of micron-sized Ti($C_{0.7}N_{0.3}$)–*x*WC–20Ni systems sintered at 1510 °C in vacuum for 1 h: (a) $x=5$, (b) $x=10$, (c) $x=15$, and (d) $x=20$.

in the system of interest (Ahn & Kang, 2000; Chen et al., 2000). In ultrafine Ti(CN) system, the core is difficult to detect and the contrast between the outer rim and inner rim is inverted when more than 50 wt% WC was added. This can be clearly seen in **Figures 25** and **26**. In general, the microstructure is uniform and refined in size compared to those of micron systems. It is known that nano-Ti(C,N) particles in Ti(C,N)–Ni systems grow rapidly in an Ni melt, resulting in abnormal growth with Ti(C,N) particles of ~50 μm in the final

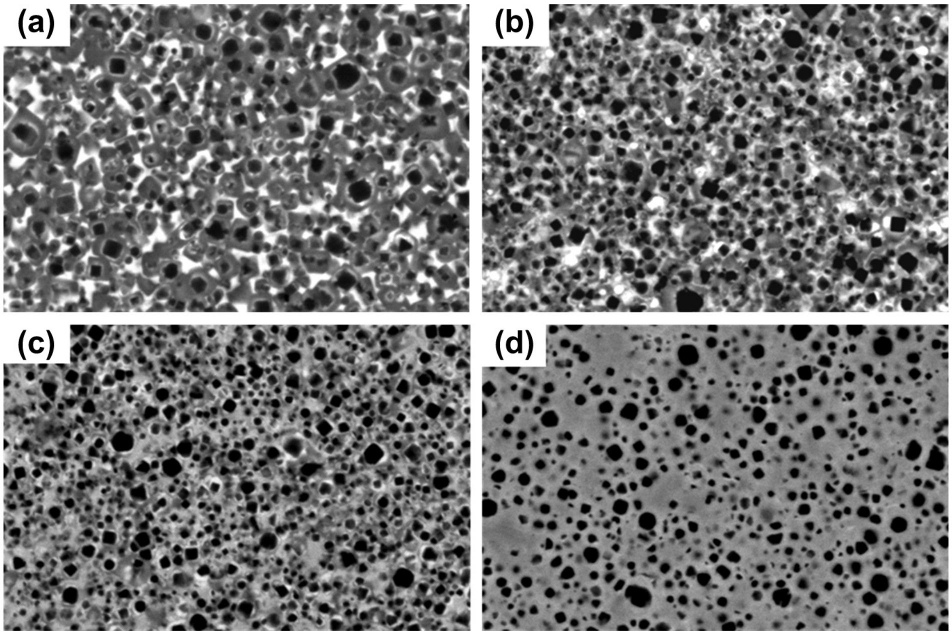

Figure 25 SEM/BSE micrographs of ultrafine Ti(C,N)–*x*WC–20i systems, *x* in wt%: (a) $x=10$, (b) $x=20$, (c) $x=30$, and (d) $x=50$.

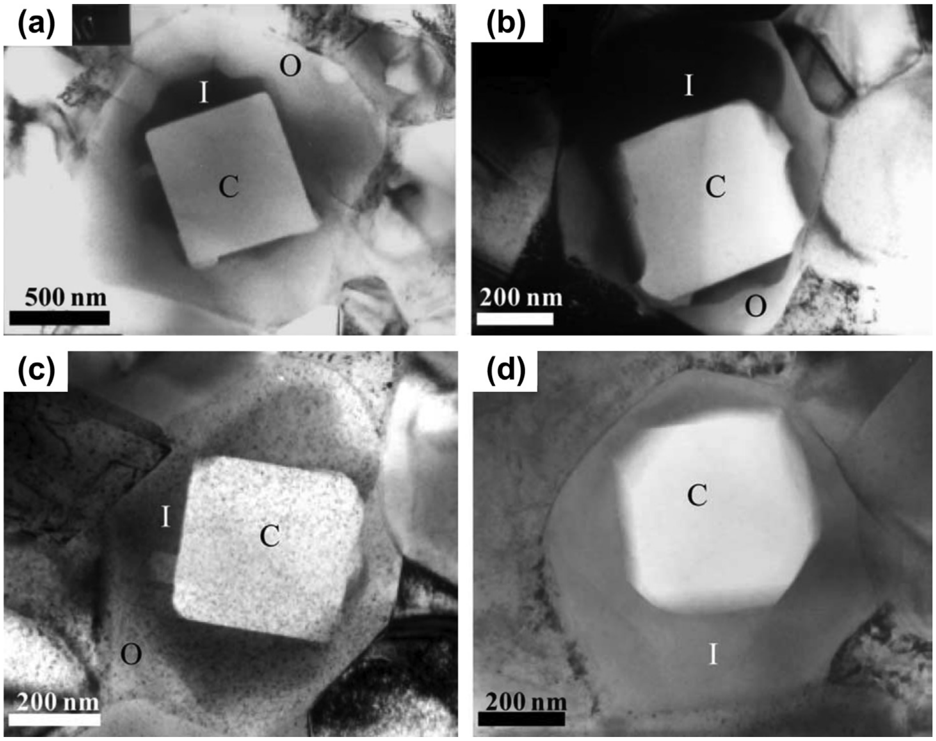

Figure 26 TEM bright-field micrograph of ultrafine Ti(C,N)–*x*WC–Ni system: (a) $x=20$, (b) $x=25$, (c) $x=30$, and (d) $x=50$ (C, I and O represent core, inner rim and outer rim, respectively).

microstructures. It should also be noted that once the WC is added, such growth is effectively suppressed (Ahn & Kang, 2000).

In all compositions of nano systems of this study, the amount of WC was not found to have any particular effect on particle growth. There is no refinement in the microstructure with added WC as observed from micron system (Ahn & Kang, 2000). Furthermore, the final particle size is not much smaller than those of ultrafine systems with high WC contents. This indicates that the refinement of the particle size in Ti(C,N)–WC–Ni systems is not strongly related to the compositions, but rather to the kinetics of dissolution and precipitation. The kinetics will be determined by the initial particle size and the stability of the carbides involved in the systems (Ahn & Kang, 2000). That is, the use of nano-sized Ti(C,N) facilitates the dissolution of Ti(C,N), which is thermodynamically more stable than WC. This enables more normal growth of the (Ti,W)(C,N) solid solution in a nano system than in a micron system.

The inversion of W concentration in rims has not been observed in ultrafine or micron Ti(C,N)–WC–Ni systems. This can be explained rather simply by kinetic and thermodynamic factors. In the case of 30 wt% added WC, Ti(C,N) and a high fraction of WC, which is relatively less stable than Ti(C,N), immediately dissolve and form the inner rim rich in W. For the outer rim, the remaining Ti(C,N) and WC dissolve and form the rim outside the inner rim with a lower content of W. Since nano Ti(C,N) has a large surface area, it dissolves at a faster rate than micron or ultrafine Ti(C,N). Thus, it is easier to produce a high amount of solid-solution phase in the nano system with WC. With more WC, the size of the inner rim phase becomes larger and W concentration increases due to the increase in WC content and the decrease in Ti(C,N). The W concentration in (Ti,W)(C,N) reaches a maximum value within the availability of W in the melt. The W concentration in the outer rim also increases. In Figure 27, inner and outer rims formed in such a manner are observed for 20–40 wt% WC.

In the case of the high amounts of WC, in other words, less Ti(C,N), the same procedure occurs. Initially, Ti(C,N) dissolves in the Ni binder to form an inner rim phase with WC. After most of the Ti(C,N) participates in forming a solid solution with WC, the remaining WC phase begins to form a different solid solution with the inner rim phase available in the system. It is by the dissolution of the remaining WC and the inner rim phase formed previously that the dissolution and precipitation continue. Thus, the outer rim of the (Ti,W)(C,N) solid solution has a higher W content than the inner rim and the inversion of the W concentration occurs. In Figures

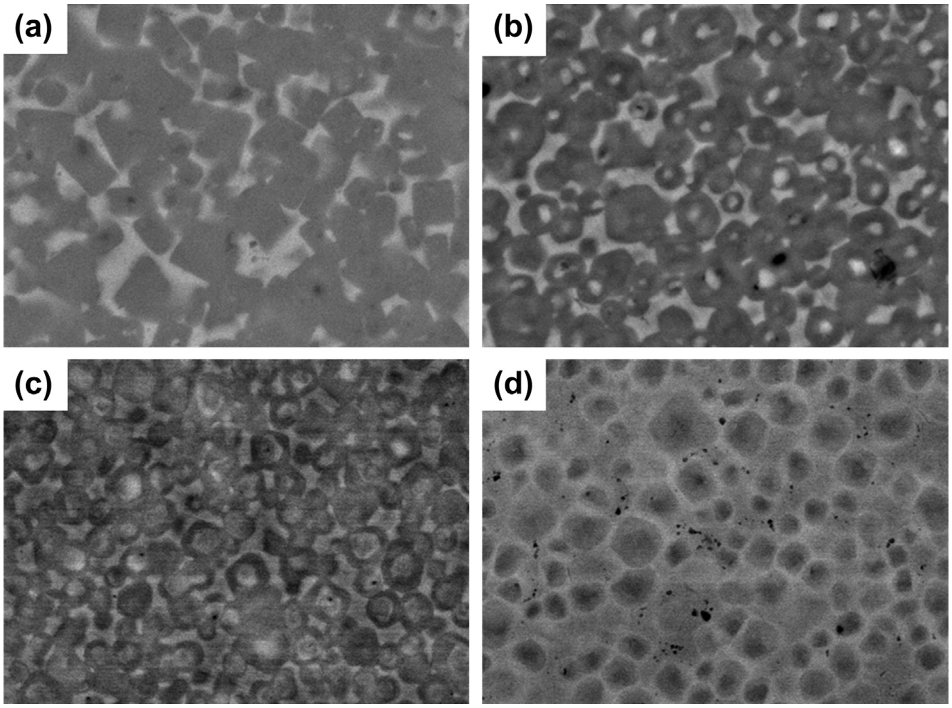

Figure 27 SEM/BSE micrographs of nano Ti(C,N)–*x*WC–20i systems, *x* in wt%: (a) $x=10$, (b) $x=30$, (c) $x=40$, and (d) $x=50$.

27(d) and 28(c), (d), the inner and outer rims formed by this procedure are observed at 50 wt% WC or more. If the inner rim reaches a maximum value of W in (Ti,W)(C,N), the outer rim will no longer form. However, this was not observed in the case of the nano system. When the system does not consume the entire WC within the sintering time, it will contain undissolved WC particles in the microstructure.

Figure 29 shows the results of the compositional analysis of the rim phases for nano systems along with those of the micron-sized and ultrafine systems. They differ to a great extent among them. The W contents in the inner rim phase of the micron systems are the highest among the three systems in the 10–20 wt% WC ranges. The W contents in the inner rims of the nano systems do not exceed those of the inner rim in micron system until the composition reaches 60 wt% WC. In all compositions, the W content of the outer rim in the nano system is lower than the ultrafine system.

Further, the micron size system and ultrafine system exhibit saturation at a maximum value of the rim compositions even though the values are different from one another. On the other hand, the nano systems do not appear to have a saturation point in rim composition. For the ultrafine system (Chae et al., 1990), the W concentrations in the outer and inner rims increase. However, the W-poor outer rim phase disappears and only the inner rim is present with >50 wt% WC. The concentration of W in the rim remains constant at ∼45 at% regardless of the amount of added WC. Therefore, it can be concluded that the maximum solubility of W in (Ti,W)(C,N) is close to ∼45 at% at the given conditions of rim formation. In contrast, the W concentration in the nano system never reaches maximum value, 45 at%.

In a typical microstructure of most Ti(C,N)–WC–Ni systems, Ti(C,N) cores are always observed. This indicates that WC dissolves faster than Ti(C,N) since Ti(C,N) is thermodynamically more stable than WC. A similar observation has been reported for a TiC–TiN–Ni system (Kang, Lee, & Kang, 2007; Qi & Kang, 1998). That is, large TiC particles (∼14 μm) dissolve completely and precipitate around small TiN particles of 1–3 μm. Regardless of their sizes, the relatively unstable carbide dissolves preferentially and precipitates around the stable carbides when both carbides are present in a system during liquid-phase sintering. However, when the size of the stable phase becomes extremely small and has a very large surface area, a different microstructure would be expected.

It is obvious that as the particle size of WC or Ti(CN) decreases, more W or Ti is available for the formation of the rim phase. In the ultrafine system, the surface area of Ti(C,N) is three times greater than that of WC. In the nano system of this study, Ti(C,N) is much smaller than WC and has a large surface area, as much as eight times that of WC. As most Ti(C,N) particles in the nano system are dissolved to form the rim phase, the system attains

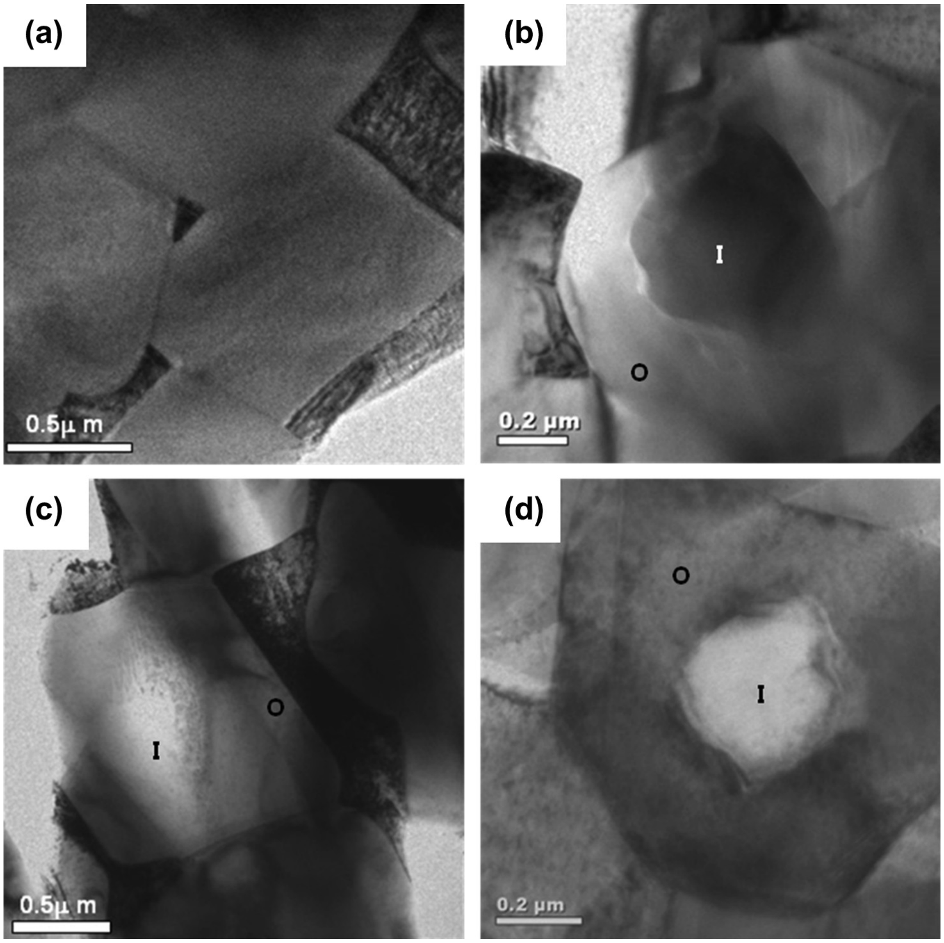

Figure 28 TEM bright-field micrograph of nano Ti(CN)–*x*WC–Ni system: (a) $x = 10$, (b) $x = 30$, (c) $x = 50$, and (d) $x = 60$ (C, I and O represent core, inner rim and outer rim, respectively).

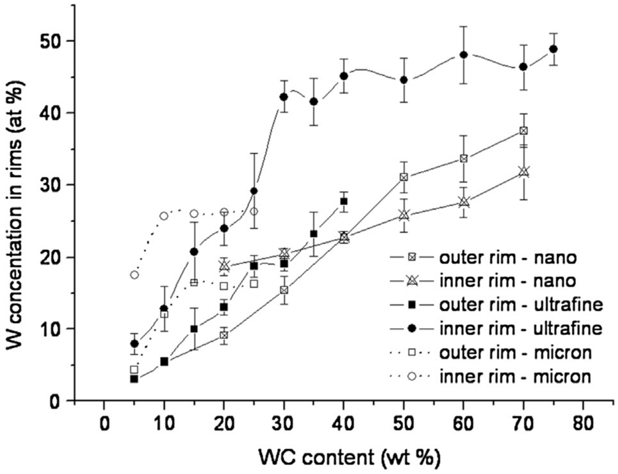

Figure 29 WC Concentrations obtained by TEM/EDS in the rim.

a high volume fraction of rim phase with a low W concentration. This indicates that the W concentration is relatively low in all ranges of WC content. It is supported by the observation that the nano system has no Ti(C,N) cores while a large portion of Ti(C,N) remains in the ultrafine system. Thus, the rim composition of the nano system never reaches a maximum W concentration as in the rim of the ultrafine system. A similar approach can be used to explain the observation of undissolved WC at 60 and 70 wt% of added WC for ultrafine and nano systems, respectively.

In addition, the W concentration in the solid solution could be influenced by nitrogen available in the (Ti,W)(C,N) phase. The nano system would be expected to have a higher nitrogen content in the solid solution due to the rapid and high dissolution of Ti(C,N). Generally, W is known to have a low affinity for nitrogen (Mun & Kang, 1999). The increase of N in the rims might reduce the solubility of W partly in rims compared to the ultrafine system.

1.05.2.5 Effect of Solid Solution Carbides

As mentioned in previous section, the conventional Ti(CN)-based cermets have a core/rim structure. Thus, they have a large area of interfaces in the microstructure such as core–rim, inner rim–outer rim and outer rim–metal binder interfaces. The interface between Ti(CN) core and inner rim phase can be highly strained, depending on the difference in compositions between the core and constituent inner rim phase. These interfaces are potential sites for crack initiation and propagation. The presence of many interfaces in the microstructure results in reduced fracture toughness for cermets, thereby limiting their industrial applications (Ahn & Kang, 2000; Ahn & Kang, 2001; Chae et al., 1990; Chun et al., 1993; Ettmayer et al., 1995; Kang et al., 2007; Kim et al., 2003; Qi & Kang, 1998). To reduce the interfaces, simple microstructure cermets like WC–Co material are desirable.

Recently, many researchers reported Ti-based solid-solution cermets with a simple microstructure (Park et al., 2006; Park & Kang, 2005; Kim, Seo, & Kang, 2011). **Figure 30** shows the microstructures of (Ti,W)C–Ni and (Ti,W)(CN)–Ni sintered at 1510 °C for 1 h (Park & Kang, 2005). They are significantly homogeneous without a core/rim structure, confirming that a complete solid solution is formed. The size of the hard phase is in the range of 100–500 and 200–800 nm for (Ti,W)C–Ni and (Ti,W)(CN)–Ni, respectively. These microstructures are in great contrast to microcrystalline cermets of the same composition. It has been well demonstrated that the growth rate of Ti(CN) is slower than that of TiC (Jeon, Joardar, & Kang, 2002; Jung et al., 1999; Kang, 1997). This high stability is shown to retard the dissolution and subsequently the coarsening of Ti($C_{0.3}N_{0.7}$) in the Ni melt, resulting in a refined microstructure (Park & Kang, 2005).

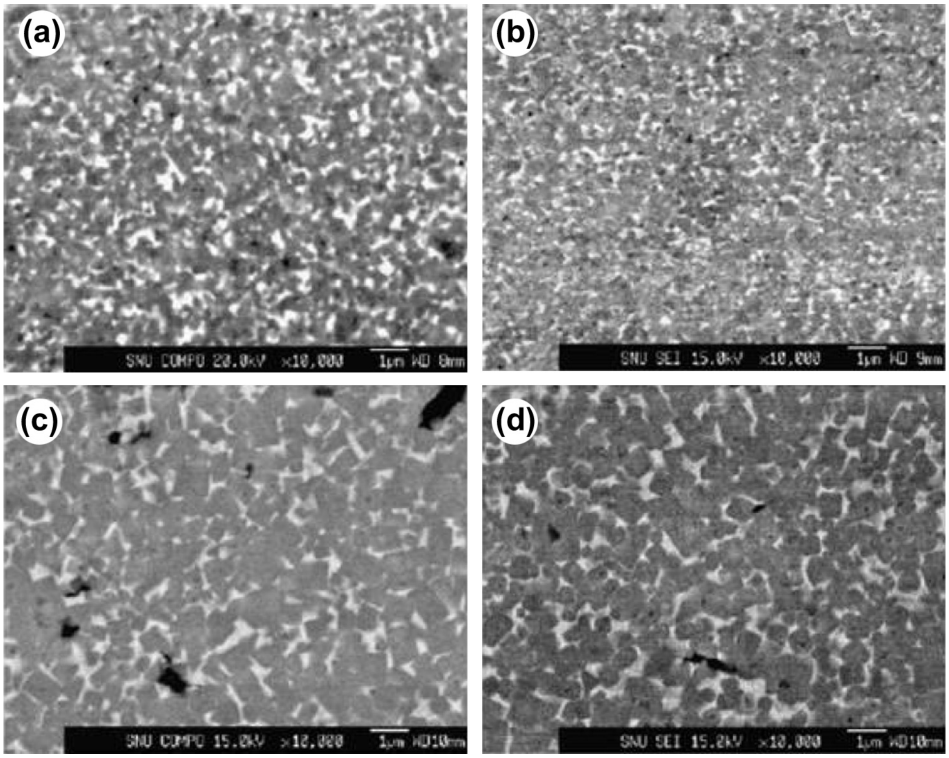

Figure 30 FE-SEM images of the cermets sintered at 1510 °C for 1 h: (a), (b) (Ti,W)C–Ni obtained from 15 and 30 wt% WC, respectively; and (c), (d) (Ti,W)(CN)–Ni obtained from 15 and 30 wt% WC, respectively.

The changes in the microstructure of complete solid-solution cermets—(Ti,W)C–Ni and (Ti,W)(CN)–Ni—were also studied as a function of sintering time at 1510 °C. The two systems are fairly similar in coarsening behavior, even if (Ti,W)C grows rapidly at the initial stage of sintering. This is contrary to microcrystalline Ti($C_{1-x}N_x$). The addition of WC to Ti($C_{1-x}N_x$) might have reduced the stability of the (Ti,W)(CN) phase more than that of (Ti,W)C. This fact is supported by the calculated free energy of formation in previous section (Kim, 2011). W is known to have less affinity for nitrogen than for carbon. Thus, the coarsening tendency of (Ti,W)(CN) increases with an increase in W content.

Figure 31 shows the microstructures of various Ti-based solid-solution cermets, ($Ti_{1-x}W_x$)C–20 wt%Ni, along with conventional TiC–20Ni. All these samples are sintered at 1510 °C for 1 h in vacuum. The microstructures of all ($Ti_{1-x}W_x$)C–20 wt%Ni (**Figure 31(b)–(d)**) appear extremely simple compared to that of conventional cermets shown in **Figure 31(a)**, resembling a simple microstructure of WC–Co. It is to be noted that the carbide morphology is different from that of conventional cermet. With increase of W content, it changes from faceted to round carbide. Also, the particle size decreases with increase of W content in (Ti,W)C. It means that the thermodynamic stability of the solid-solution phase is increased until certain point (~30 at% of W, at 1500 °C). Moreover, the wettability of W and Ni is found excellent. These properties retard the dissolution of carbides and enable the simple and uniform microstructure to be retained (Kim et al., 2011).

Kang and Kang (2010) reported that (Ti,W)(CN)-based solid-solution carbides could exhibit new microstructures composed of (Ti,W)(CN) with WC platelets when the composition and processing conditions are controlled. The separation of WC from (Ti,W)(CN) is ascribed to the solubility limit. **Figure 32** shows the SEM microstructures of (Ti,W)(CN) as the WC content is varied from 30 to 50 at%. All samples are sintered at 1510 °C for 1 h under a nitrogen pressure of 40 Torr. The platelet phase appears actively as brighter regions when the WC content exceeds 40 at%, which is near solubility limit of WC in Ti(CN). The gray regions in the SEM images are (Ti,W)(CN) solid-solution grains, while the brighter regions are WC precipitates. The high nitrogen pressure and/or insufficient binder phase are responsible for the pores in the microstructures of the (Ti,W)(CN) systems.

The separation of WC from (Ti,W)(CN) can be facilitated in the presence of nitrogen, which limits WC solubility in Ti(CN) (Doi et al., 1985). The (Ti,W)C solid solution is reported to retain up to 52 at% WC based on the result of ThermoCalc at 1500 °C (Jung, 2006). The WC phase separated out more readily due to the low limit of solubility in the presence of nitrogen. Based on the SEM–EDS and Carbon/Nitrogen/Oxygen (CNO)

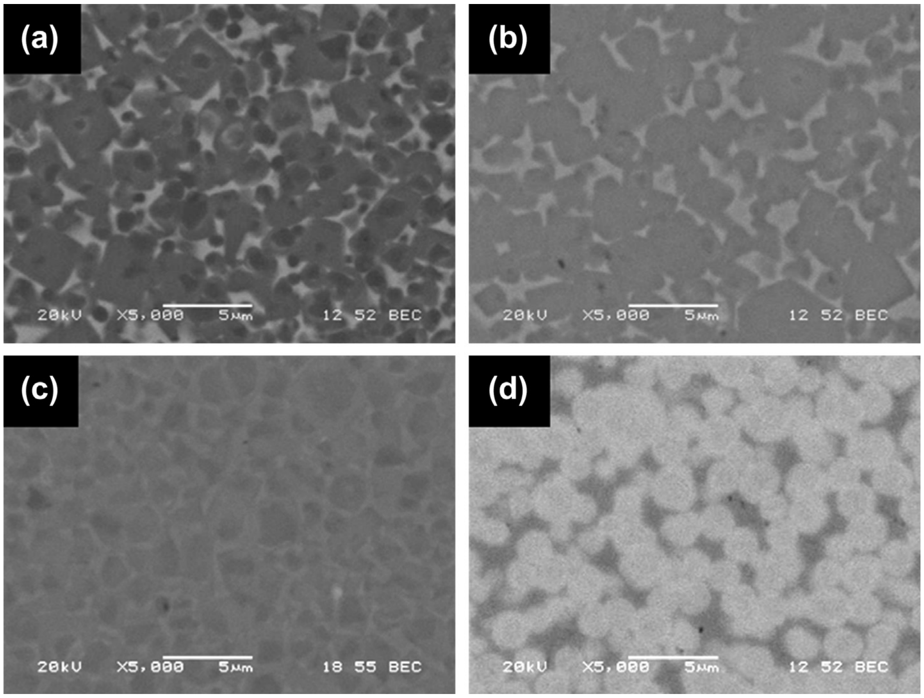

Figure 31 Microstructure of ($Ti_{1-x}W_x$)C–20 wt%Ni solid-solution cermets: x, mole fraction, of (a) 0, (b) 0.07, (c) 0.12, and (d) 0.30.

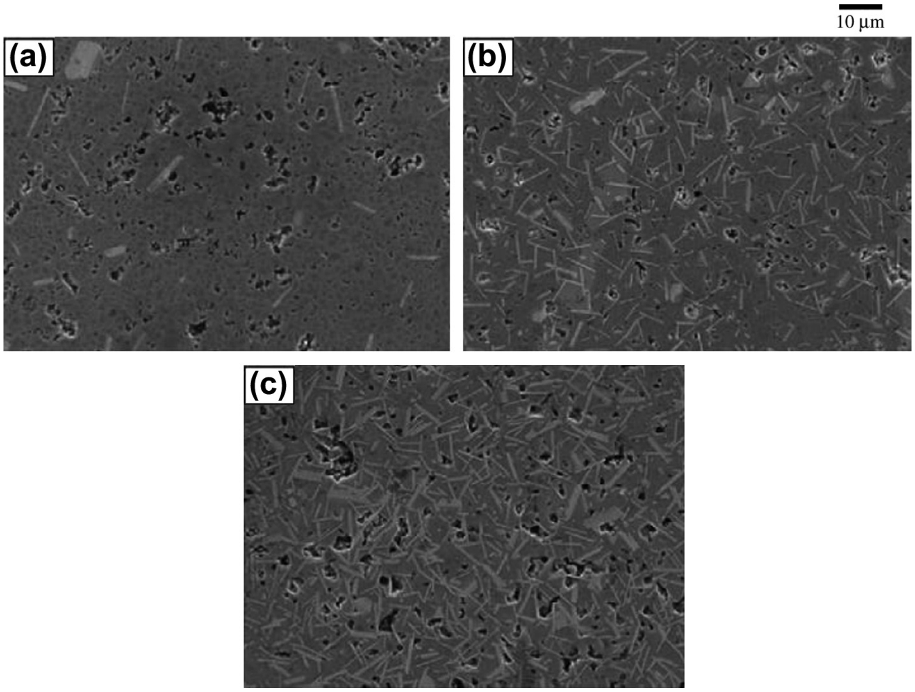

Figure 32 Microstructure of (Ti,W)(CN) sintered at 1510 °C for 1 h in N_2 at 40 Torr: (a) (Ti0.7W0.3)(CN), (b) (Ti0.6W0.4)(CN), and (c) (Ti0.5W0.5)(CN).

analyses, the matrix compositions in **Figure 32(a)–(c)** are found to be $(Ti_{0.68}W_{0.32})(C_{0.87}N_{0.10})$, $(Ti_{0.68}W_{0.32})(C_{0.88}N_{0.07})$ and $(Ti_{0.67}W_{0.33})(C_{0.85}N_{0.05})$, respectively, along with WC. It means that $(Ti_{0.68}W_{0.32})(C_{0.87}N_{0.07})$ is the approximate phase composition at equilibrium with WC in this processing condition. The observation that the WC phase starts separation from the $(Ti_{0.7}W_{0.3})(CN)$ solid solution also supports that the solubility limit of WC in (Ti,W)(CN) is ~30 at% at 1500 °C.

The effect of solid-solution carbides or carbonitrides on the microstructure of conventional cermets is investigated when they are added as secondary carbide (Kim, Ahn, & Kang, 2009; Kwon & Kang, 2009a). **Figure 33** shows the microstructures of a conventional Ti(CN)-based cermet and a Ti-based complete solid-solution carbonitride. **Figure 34** shows the microstructure changes in partially solutionized cermets of $Ti(C_{0.5}N_{0.5})–x(Ti_{0.93}W_{0.07})C–7TaC–3Mo2C–9Co–9Ni$ (in wt%).

Figure 34 shows the microstructures of conventional Ti(CN)-based cermets with the additions of $(Ti_{0.93}W_{0.07})$C. The major findings from these microstructures are (1) the decrease in the number of cores and their size and (2) the increase in the volume fraction of rim phase with increase of $(Ti_{0.93}W_{0.07})C$ content. Those cores apparent in **Figure 34(a)** demonstrate a remarkable decrease when a small amount of $(Ti_{0.93}W_{0.07})C$, 5 wt%, is added. When

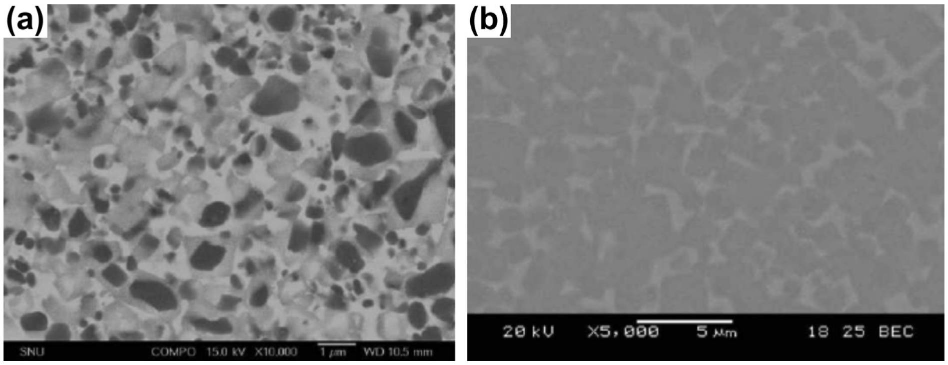

Figure 33 Microstructure of (a) $Ti(C_{0.5}N_{0.5})–7TaC–3Mo_2C–9Co–9Ni$ and (b) $(Ti_{0.93}W_{0.07})C–20Ni$.

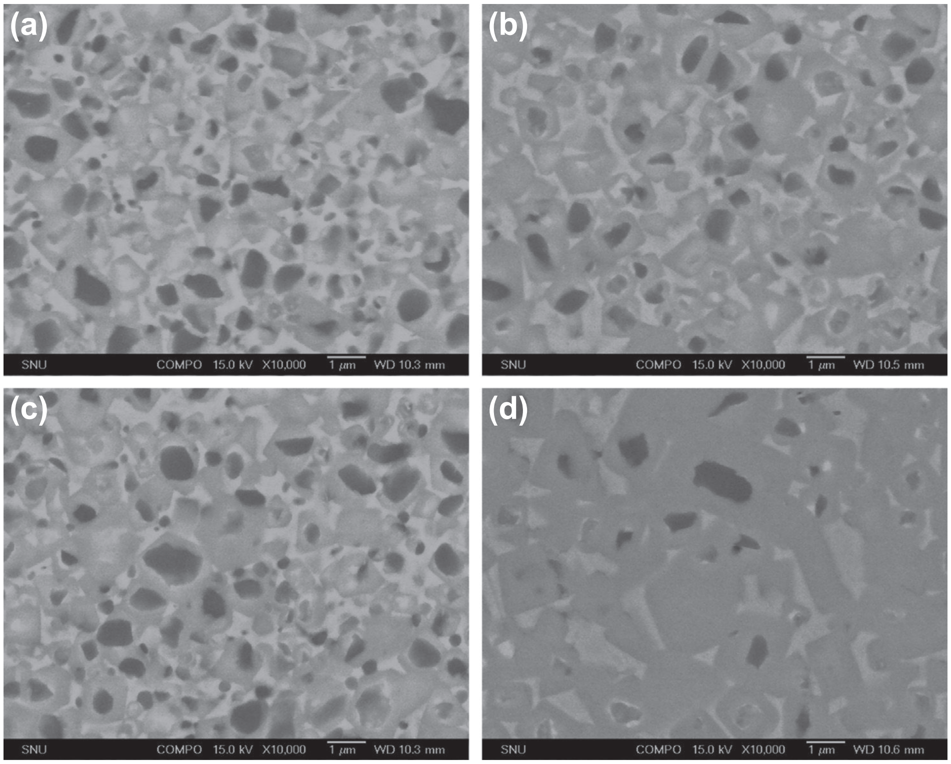

Figure 34 Microstructures of partially solutionized cermets: $Ti(C_{0.5}N_{0.5})–x(Ti_{0.93}W_{0.07})C–7TaC–3Mo_2C–9Co–9Ni$, of (a) $x = 5$, (b) $x = 10$, (c) $x = 20$, (d) $x = 50$.

the content exceeds more than 10 wt%, the microstructure changes significantly. Figure 34(c) shows the decreasing number of Ti(CN) and white cores and increasing number of coreless grains. Most Ti(CN) cores disappeared and decreased in size in Figure 34(d). Compared with Figure 34(a) and (b), Figure 34(c) and (d) shows the simple microstructure with large carbides.

Partially solutionized cermets have an advantage in that a small addition of a solid-solution phase can increase the volume fraction of rim phase dramatically in the microstructure. This enhances toughness of the cermets as reported previously (Kim et al., 2009; Kwon & Kang, 2009a). It means that the microstructure and mechanical properties of cermets can be controlled significantly by simple addition of solid-solution carbide. This allows us great freedom in designing new cermet materials.

1.05.2.6 Effect of Binder Phase

The various binder phases have been used for TiC-based cermets. Fe, Co and Ni are the typical metals for liquid-phase sintering of the cermets. The effects of these binder phases on the cermet microstructure could be explained in terms of composition, surface energy, binder amount, sintering temperature and atmosphere (Daoush, Lee, Park, & Hong, 2009; Joardar, Kim, & Kang, 2003).

Kang and Kang (2010) reported that platelet WC forms in (Ti,W)(CN) solid-solution ceramics, which were synthesized from milled mixtures of oxides with carbon as mentioned before. The WC platelets separated from the (Ti,W)(CN) ceramics changes its morphology, depending on the composition of the binder phase added and the sintering conditions. With increasing binder content, the WC platelet shape became more irregular. This change is attributed largely to surface energy. Similarly, the morphology of Ti(CN) particles in Ti(CN) systems is strongly influenced by the kind and amount of binder phase.

Joardar et al. (2003) investigated high-melting intermetallic binders, namely, NiAl and Ni_3Al to promote high-temperature mechanical properties of the cermets. However, no significant change in the mechanical properties could be detected in the case of nanocrystalline NiAl and Ni_3Al binder addition (Birringer, 1989). Furthermore, the effect of highly deformed nanocrystalline Ni is investigated (Joardar et al., 2003). The mechanically milled nano-Ni contains a mixture of fcc and hexagonal Ni phases. The cermet with nanocrystalline

Ni shows a considerably improved microstructure over cermets with commercial coarse grade Ni and exhibits a high Vickers hardness of ~16.1 GPa, along with a good fracture toughness value of ~9 MPa $m^{1/2}$. The enhanced properties of the cermets containing nano-Ni are attributed to the finer particle size of the hard phase after sintering along with improved particle size distribution caused by rapid dissolution, which prevents excessive coalescence of the hard particles.

The microstructure shows considerably finer and more homogeneously distributed Ti(CN) particles when compared to the one with coarse grade Ni. Such observation suggests that there is more of hard-phase dissolution in the binder phase of the latter, possibly due to the presence of high concentration of defects. The structure is known to promote enhanced rate of bulk diffusion (Birringer, 1989; Suryanarayana, 1995). Furthermore, in the absence of rim structure, hard-phase particle coalescence takes place (Humenik & Parikh, 1957; Jia, Fischer, Gallois, 1998; Parikh & Humenik, 1958). A substantial degree of coarsening of the ultrafine Ti(CN) hard phase, from 0.7 to ~1.5 μm, is observed during sintering of the cermet with coarse Ni. A greater dissolution of carbides in MMed Ni binder, during early stage of sintering, possibly restricted such coalescence of the hard-phase particles by forming rim phase around Ti(CN).

The cermets containing aluminides show microstructures comprising fine and uniformly distributed hard-phase particles enclosed in bright W-rich phase. The outer rim is not well defined and is not visible with SEM particularly at higher WC level of 25%. The MAed nanocrystalline Ni_3Al with relatively low melting point is likely to facilitate easy dissolution of the hard phase when compared to the high-melting NiAl, leading to a finer microstructure. The presence of NiAl in the cermet, on the other hand, causes poor wetting and large fraction of porosity, leading to crack initiation and propagation even at small load, and consequently shows inferior properties.

1.05.2.7 Surface Microstructure

The need for hard-surfaced or toughened cermet tools is largely dependent on the characteristics of the work pieces and machining steps. In fact, the microstructures at the surface and corners of cermet-cutting tools determine both the lifetime and efficiency of a tool. In TiC-based cermets, the addition of nitrogen to TiC-based cermets is now indispensable for these required properties. It is known, however, that the loss of nitrogen from Ti(CN) during processing causes changes in composition, pore level (Suzuki et al., 1983; Suzuki, Hayashi, & Matsubara, 1982), and sometimes gives rise to a microstructurally inhomogeneous surface layer (Gustafson & Ostlund, 1993–1994; Kang & Kang, 2010; Schwarzkopf, Exner, & Fischmeister, 1988; Suzuki, Hayashi, & Taniguchi, 1981).

Extensive studies (Andren, 2001; Chen, Lengauer, & Dreyer, 2000; Frykholm et al., 2001; Lengauer & Dreyer, 2002; Nomura et al., 1999; Park, Kim, & Kang, 2000; Zackrisson et al., 2000) have been done, in attempts to explain these alternations in surface microstructure. Schwarzkopf et al. suggested early an analytical model for surface microstructure in WC–TiN–Co and also reported that the metal-enriched surface area is formed through interdiffusion of Ti and N as rate-controlling factors (Park & Kang, 2005). Gustafason investigated the behavior with respect to thermodynamic calculations and kinetic considerations (Park et al., 2006). However, some discrepancies are found in the interpretations of these phenomena because phase reactions that occur during the sintering process are complex in various systems under different sintering conditions. Further, the formation of solid solutions of carbonitrides in such systems has usually been ignored in these systems.

In this section, the effects of atmospheric conditions and compositions on the surface microstructures are briefly discussed for Ti(CN)–Ni cermets under a variety of sintering conditions. The effects of nitrogen, carbon, carbide addition, and sintering atmosphere on the surface microstructure and on material transport are explained (Andren, 2001; Park et al., 2000; Zackrisson et al., 2000).

Park et al. (2000) reported that the surface microstructure is strongly dependent on the carbides added and the sintering atmosphere in Ti(CN)–MC–Ni systems. They reported vacuum processing is the most effective parameter for the formation of a solid-solution band (carbide-enriched layer) at the surface. In addition, the band size can be extended in the samples which are embedded in the carbon powders, under vacuum. The active dissolution of Ti(CN) at the surface region provides a driving force for Ti and W transport from the interior to the surface.

As to the effect of various carbides on the formation of the band, the TaC phase added to a Ti(CN)-based cermet facilitates the formation near the surface. On the other hand, WC in the cermet system exhibits a significantly reduced tendency to form the band due to its weak affinity for nitrogen (Cheburaeva & Chaporova, 1986; Suzuki et al., 1983; Suzuki & Matsubara, 1986; Ueki, Saito, Saito, Kitamura, & Suzuki, 1988). The fact that a large amount of W is present in the binder phase for the central part of the cermets (Andren, Rolander, & Lindahl, 1994; Kang, 1996; Lindahl, Rolander, & Andren, 1991; Suzuki & Matsubara, 1986) is in agreement with this observation. The addition of both TaC and WC to Ti(CN)–Ni–Co cermet did not give rise to a synergy effect in forming the solid-solution band. The nitrogen concentration appears to significantly affect the carbon concentration in the liquid binder phase and vice versa; the carbon concentration might vary inversely proportionally to that of nitrogen (Park & Kang, 2005).

All atmospheric conditions resulted in a binder-depleted region near the surface except for the nitrogen atmosphere in Ti(CN)–TaC–Ni–Co. Their influence on the solid-solution band size is limited to approximately 200 mm at 1510 °C. In their work, Ti(CN) content was fixed at 50 wt% and the total amount of additives such as TaC and WC are at 20 wt% for the compositions of the cermets under investigation. As shown in **Figure 35(a)**, the Ti(CN) cores, which display a black contrast disappeared and a band consisting largely of a solid solution of (Ti, M)(CN), are observed near the surface of the sintered specimen. **Figure 35(b)** is a schematic for the surface microstructure at a high magnification. In region A, most of the Ti(CN) phase disappeared, as compared to region C. In an adjacent region (region B), Ti(CN) remains partially. The combined regions, A and B, are referred to as the solid-solution band in this investigation.

Kim and Kang (2007) investigated in detail the effect of nitrogen introduced at different stages during sintering on the formation of the surface gradient zone for Ti(C,N)-based cermets. WC is used as a secondary carbide in a Ti(C,N)–Ni/Co system, and processing is carried out in a vacuum or nitrogen pressure at 1 Torr. Nitrogen is introduced during various stages of the sintering above 1300 °C. The introduction of nitrogen during the heating stage facilitated the formation of a (Ti,W)(C,N)-enriched layer (a solid-solution band) to a greater extent than the vacuum conditions as shown in **Figure 36**.

With a subsequent heating process at the sintering temperature, the dissolution of constituent particles, which is delayed by the previous nitriding atmosphere, is intensified and the denitriding conditions become more severe enhancing the (Ti,W)(C,N) solid solution. The enrichment with the binder at the surface was observed in cases where the samples were sintered with the introduction of nitrogen during the holding or cooling stages. From the results of interrupted sintering with various cooling rates, it is found that the binder-enriched layer is formed during the cooling stage.

Kang and Kang (2010) reported the effects of nitrogen, Ti(CN) particle size and presence of solid-solution carbide on the surface microstructure. In their study, complete solid-solution carbides, $(Ti_{0.93}W_{0.07})C$, are mixed in powder form with micron- or nano-sized carbides and Ni powders. The mixed powder is sintered in various nitrogen atmospheres (5–40 Torr). They report that with increase in the nitrogen pressure, the depth of Ni-enriched layer is increased, but the size of the (Ti,W)(CN) formed at the surface is decreased. The changes in the depth of the enriched layer and the size of the cubic phase are ascribed to the concentration gradient of the constituent elements between surface and interior and nitrogen content in (Ti,W)(CN), respectively.

In the nano-sized TiC system, the depth of the layer and the size of the cubic phase were decreased together due to rapid dissolution of TiC powders. Dissolution kinetics of constituent carbides affects the microstructural changes in this system. As the $(Ti_{0.93}W_{0.07})C$ content increases, the influence of nitrogen on the surface microstructure and concentration profile becomes less significant in all systems. It is due to the highest stability

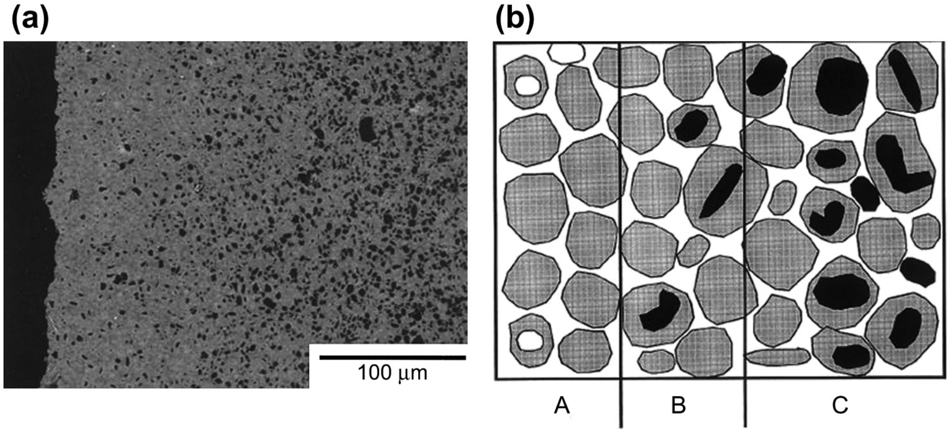

Figure 35 A typical solid-solution band formed at the cermet surface: (a) SEM micrograph (250×) and (b) schematic illustration.

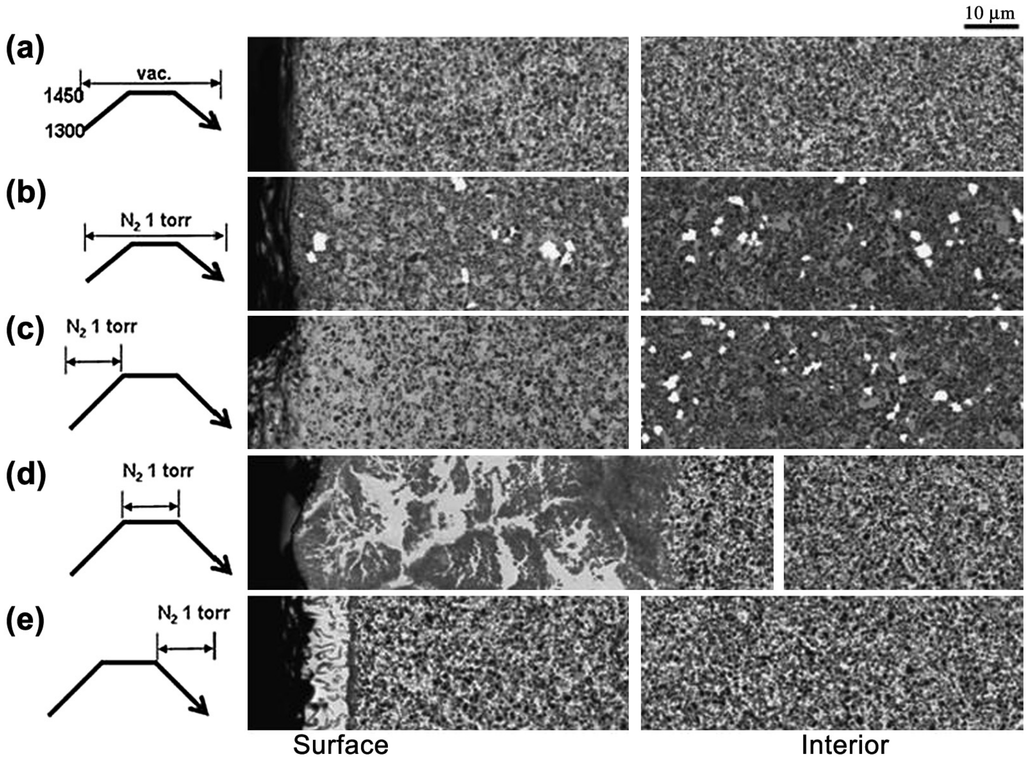

Figure 36 Microstructure of Ti($C_{0.5}N_{0.5}$)–20WC–10Ni–10Co sintered at 14,501 °C for 1 h in (a) vacuum, (b) N_2 at 1 Torr during all stages above 13,001 °C, (c) N_2 at 1 Torr during the heating stage, (d) N_2 at 1 Torr during the holding stage, and (e) N_2 at 1 Torr during the cooling stage with the cooling rate of 51 °C/min. (Black particles represent Ti(C,N) and white particles in (b) or (c) represent WC; meanwhile, (Ti,W)(C,N) solid solution appears to be in gray contrast and binder phase turns out to be brighter gray contrast.)

of ($Ti_{0.93}W_{0.07}$)C among the carbides in the systems. The ($Ti_{0.93}W_{0.07}$)C content and size of TiC were found to be most controlling factors in determining the surface microstructure of the systems.

References

Ahn, S. Y., & Kang, S. (1998). Effect of VC addition on the microstructure & mechanical properties. *Journal of the Korean Ceramic Society, 35*(12), 1316–1322.

Ahn, S. Y., & Kang, S. (2000). Formation of core/rim structures in Ti(C, N)-WC-Ni cermets via a dissolution and precipitation process. *Journal of the American Ceramic Society, 83*, 1489–1494.

Ahn, S. Y., & Kang, S. (2001). Effect of various carbides on the dissolution behavior of Ti($C_{0.7}N_{0.3}$) in a Ti($C_{0.7}N_{0.3}$)–30Ni system. *International Journal of Refractory Metals and Hard Materials, 19*, 539–545.

Ahn, S. Y., Kim, S. W., & Kang, S. (2001). Microstructure of Ti(CN)-WC-NbC-Ni cermets. *Journal of the American Ceramic Society, 84*(4), 843–849.

Andren, H.-O. (2001). Microstructure development during sintering and heat-treatment of cemented carbides and cermets. *Materials Chemistry and Physics, 67*(1–3), 209–213.

Andren, H. O., Rolander, U., & Lindahl, P. (1994). Atom-probe analysis of cemented carbides and cermets. *Applied Surface Science, 76–77*, 278–284.

Ashcroft, N. W., & Mermin, N. D. (1976). *Solid state physics*. New York: Holt, Rinehan and Winston.

Begin-Colin, S., Girot, T., Le Caer, G., & Mocellin, A. (2000). Kinetics and mechanisms of phase transformations induced by ball-milling in anatase TiO_2. *Journal of Solid State Chemistry, 149*, 41–48.

Belton, G. R., & Fruehan, R. J. (1967). Determination of activities by mass spectrometry. I. The liquid metallic systems iron-nickel and iron-cobalt. *The Journal of Physical Chemistry, 71*, 1403–1409.

Berger, L. M. (2001). Investigation of the carbothermal reduction of Ti_2O_3 in argon and nitrogen atmospheres. *Journal of Materials Science Letters, 20*, 1845–1848.

Berger, L. M., Ettmayer, P., & Schultrich, B. (1994). Influencing factors on the carbothermal reduction of titanium dioxide without and with simultaneous nitridation. *International Journal of Refractory Metals and Hard Materials, 12*, 161–172.

Berger, L. M., Langholf, E., Jaenicke-Robler, K., & Leitner, G. (1999). Mass spectrometric investigations on the carbothermal reduction of titanium dioxide. *Journal of Materials Science Letters, 18*, 1409–1412.

Bilz, H. (1958). Uber elektronenzustande von hartstoffen mit natriumchloridstruktur. *Zeitschrift fur Physik A Hadrons and Nuclei, 153*, 338–358.

Birringer, R. (1989). Nanocrystalline materials. *Materials Science and Engineering: A, 117*, 33–43.

Chae, K.-W., Chun, D.-I., Kim, D.-Y., Baik, Y.-J., & Eun, K.-Y. (1990). Microstructural evolution during the infiltration treatment of titanium carbide-iron composite. *Journal of the American Ceramic Society, 73*(7), 1979–1982.

Chase, M., Jr (1998). *Nist-janaf thermochemical tables*.

Chase, M. W., Davies, J. R., & Downey, J. R., et al. (1985). Janaf thermochemical tables, 3rd ed. J. Phys. Chem. Ref. Data 14.

Cheburaeva, F. F., & Chaporova, I. N. (1986). The role of tantalum in TiC-WC-TaC-Co sintered carbides. II. Influence of tantalum content on the structure and properties of TiC-WC-TaC-Co three-phase sintered carbides. *Poroshkovaga Metallurgiya, 4*(281), 89–93.

Chen, L., Lengauer, W., & Dreyer, K. (2000). Advances in modern nitrogen-containing hardmetals and cermets. *International Journal of Refractory Metals and Hard Materials, 18*(2–3), 153–161.

Chen, L., Lengauer, W., Ettmayer, P., Dreyer, K., Daub, H. W., & Kassel, D. (2000). Fundamentals of liquid phase sintering for modern cermets and functionally graded cemented carbonitrides (FGCC). *International Journal of Refractory Metals and Hard Materials, 18*(6), 307–322.

Christian, J. W. (1975). *The theory of transformations in metals and alloys, part I*. Oxford: Pergamon.

Chun, D.-I., Kim, D.-Y., & Eun, K.-Y. (1993). Microstructural evolution during the sintering of TiC-Mo-Ni cermets. *Journal of the American Ceramic Society, 76*(8), 2049–2052.

Coste, S., Bertrand, G., Coddet, C., Gaffet, E., Hahn, H., Sieger, H., et al. (2007). High-energy ball milling of Al_2O_3-TiO_2 powders. *Journal of Alloys and Compounds, 434*, 489–492.

Crank, J. (1956). *The mathematics of diffusion*. Oxford University Press.

Daoush, W. M., Lee, K. H., Park, H. S., & Hong, S. H. (2009). Effect of liquid phase composition on the microstructure and properties of (W, Ti)C cemented carbide cutting tools. *International Journal of Refractory Metals and Hard Materials, 27*, 83–89.

Darken, L. S. (1967). Thermodynamics of binary metallic solutions. *Transactions of the Metallurgical Society of AIME, 239*, 80–87.

Doi, A., Nomura, T., Tobioka, M., Takahashi, K., & Hara, A. (1985). *Thermodynamic evaluation of equilibrium nitrogen pressure and WC separation in Ti-W-C-N system carbonitride*.

Dutta, H., & Pradhan, S. K. (2002). Microstructure characterization of high energy ball-milled nanocrystalline V_2O_5 by Rietveld analysis. *Materials Chemistry and Physics, 77*, 868–877.

Dutta, H., Pradhan, S. K., & De, M. (2002). Microstructural evolution on ball-milling elemental blends of Ni, Al and Ti by Rietveld's method. *Materials Chemistry and Physics, 74*, 167–176.

Ettmayer, P., & Lengauer, W. (1989). The story of cermets. *Powder Metallurgy International, 21*, 37–38.

Ettmayer, P., Kolaska, H., Lengauer, W., & Dreyer, K. (1995). Ti(C, N) cermets – metallurgy and properties. *International Journal of Refractory Metals and Hard Materials, 13*, 343–351.

Exner, H. E. (1979). Physical chemical nature of cemented carbides. *International Metals Reviews, 243*(4), 149–171.

Frykholm, R., Ekroth, M., Jansson, B., Andrén, H.-O., & Ågren, J. (2001). Effect of cubic phase composition on gradient zone formation in cemented carbides. *International Journal of Refractory Metals and Hard Materials, 19*(4–6), 527–538.

Fukuhara, M., & Mitani, H. (1982). Effect of nitrogen content on grain growth in Ti/C, N/-Ni-Mo sintered alloy. *Powder Metallurgy International, 14*, 196–200.

Gajović, A., Furić, K., Tomašić, N., Popović, S., Skoko, Ž., Musić, S., et al. (2005). Mechanochemical preparation of nanocrystalline TiO_2 powders and their behavior at high temperatures. *Journal of Alloys and Compounds, 398*, 188–199.

Gaskell, D. R. (2003). *Introduction to the thermodynamics of materials* (4th ed.). Hemisphere Pub.

Gee, M. G., Reece, M. J., & Roebuck, B. (1992). High resolution electron microscopy of Ti(C, N) cermets. *Journal of Hard Materials, 3*(2), 119–143.

Gingerich, K. A. (1979). *Proc. 10th materials research symposium on characterization of high temperature vapors and gases*. Gaithersburg, MD: NBS. Special publ. 651.

Graham, J. W. (1953). Sintered titanium carbide. *Iron Age, 172*(7), 148–152.

Guillermet, A. F., Haglund, J., & Grimvall, G. (1993). Cohesive properties and electronic structure of 5d-transition-metal carbides and nitrides in the NaCl structure. *Physical Review B, 48*, 11673.

Gupta, S. K., & Gingerich, K. (1980). Identification and the thermodynamic stabilities of titanium carbide species in the vapor above the titanium-iridium-graphite system. *High Temperatures – High Pressures, 12*, 273–280.

Gustafson, P., & Ostlund, A. (1993–1994). Binder-phase enrichment by dissolution of cubic carbides. *International Journal of Refractory Metals and Hard Materials, 12*, 129–136.

Hillert, M. (1983). On the driving force for diffusion induced grain boundary migration. *Scripta Materialia, 17*, 237–240.

Humenik, M., & Parikh, N. M. (1957). I. Fundamental concepts related to microstructure and physical properties of cermet systems. *Journal of the American Ceramic Society, 39*(2), 60–63.

Jeon, E. T., Joardar, J., & Kang, S. (2002). Microstructure and tribo-mechanical properties, of ultrafine Ti(CN) cermets. *International Journal of Refractory Metals and Hard Materials, 20*, 207–221.

Jhi, S. H., & Ihm, J. (1997). Electronic structure and structural stability of TiC_x N_{1-x} alloys. *Physical Review B, 56*, 13826.

Jhi, S. H. (1998). *Study on the hardness of transition metal compounds and alloys through electronic structure calculations* (Ph.D. thesis). Seoul, Korea: Seoul National University.

Jia, K., Fischer, T. E., & Gallois, B. (1998). Microstructure, hardness and toughness of nanostructured and conventional WC-Co composites. *Nanostructured Materials, 10*, 875–891.

Joardar, J., Kim, S. W., & Kang, S. (2003). Effect of nanocrystalline binder on the microstructure and mechanical properties of ultrafine Ti(CN) cermets. *Materials Science and Engineering: A, 360*, 385–389.

Jung, J., (2006). *A study of the formation and thermo-properties of (Ti, W)(CN)* (Ph.D. thesis). Korea: Seoul National University.

Jung, I. J., & Kang, S. (2000). A study of the characteristics of Ti(CN) solid solutions. *Journal of Materials Science, 35*, 87–90.

Jung, J., & Kang, S. (2004). Effect of ultra-fine powders on the microstructure of Ti(CN)-xWC-Ni cermets. *Acta Materialia, 52*, 1379–1386.

Jung, J., & Kang, S. (2007). Effect of nano-size powders on the microstructure of Ti(C, N)-xWC-Ni cermets. *Journal of the American Ceramic Society, 90*(7), 2178–2183.

Jung, I. J., Kang, S., Jhi, S. H., & Ihm, J. (1999). A study of the formation of Ti(CN) solid solutions. *Acta Materialia, 47*, 3241–3245.

Kang, S. (1996). Some issues in Ti (CN)-WC-TaC cermets. *Materials Science and Engineering: A, 209*, 306–312.

Kang, S. (1997). Stability of N in Ti(CN) solid solutions for cermet applications. *Powder Metallurgy, 40*, 139–142.

Kang, Y., & Kang, S. (2010). The surface microstructure of TiC-(Ti, W)C-WC-Ni cermets sintered in a nitrogen atmosphere. *Materials Science and Engineering: A, 527*, 7241–7246.

Kang, Y., & Kang, S. (2010). Wc-reinforced (Ti, W)(CN). *Journal of the European Ceramic Society, 30*, 793–798.

Kang, Y., Lee, G., & Kang, S. (2007). Growth of ultra-fine Ti(CN) particles in Ti(CN)-Ni cermets. *Scripta, 56*, 133–136.

Kieffer, R., & Fister, D. (1970). Effect of a hypo-stoichiometric carbon content of the carbide phase on the properties of TiC-Mo_2. Planseeber Pulvermet 18.

Kieffer, R., Ettmayer, P., & Freudhofmeier, M. (1971a). Novel types of nitrides and carbonitrides of hard metals. *Metal, 25*, 1335–1342.

Kieffer, R., Ettmayer, P., & Freudhofmeier, M. (1971b). *About nitrides and carbonitrides and nitride-based cemented hard alloys.* Vienna: Technical Univ., 5.

Kim, J. (2011). *Mechanical, thermo-physical and thermodynamic properties of Ti-based solid solution materials and their behavior with Ni binder: experimental and theoretical approaches* (Ph. D. thesis). Seoul, Korea: Seoul National University.

Kim, J. W., Ahn, S. Y., & Kang, S. (2009). Effect of the complete solid solution phase on the microstructure of Ti(CN)-based cermet. *International Journal of Refractory Metals and Hard Materials, 27*, 224–228.

Kim, S. W., & Kang, S. (2007). Change in the surface microstructure of Ti($C_{0.5}N_{0.5}$)-20WC-10Ni-10Co cermets during sintering in a nitrogen atmosphere. *Journal of the American Ceramic Society, 90*(9), 2974–2979.

Kim, S., Min, K., & Kang, S. (2003). Rim structure in Ti ($C_{0.7}N_{0.3}$)-WC-Ni cermets. *Journal of the American Ceramic Society, 86*, 1761–1766.

Kim, J., Seo, M., & Kang, S. (2011). Microstructure and mechanical properties of Ti-based solid solution cermets. *Materials Science and Engineering: A, 528*, 2517–2521.

Kim, S. W., Zuo, J., & Kang, S. (2010). Effect of WC of NbC addition on lattice parameter of surrounding structure in Ti($C_{0.7}N_{0.3}$). Ni cermets investigated by TEM/CBED. *Journal of the European Ceramic Society, 30*, 2131–2138.

Koc, R. (1998). Kinetics and phase evolution during carbothermal synthesis of titanium carbide from ultrafine titania/carbon mixture. *Journal of Materials Science, 33*, 1049–1055.

Koc, R., & Folmer, J. (1997). Carbothermal synthesis of titanium carbide using ultrafine titania powders. *Journal of Materials Science, 32*, 3101–3111.

Kohl, F. J., & Stearns, C. A. (1970). The dissociation energy of gaseous titanium mononitride (dissociation energy of gaseous tin molecule at high temperature). *High Temperature Science, 2*, 146–153.

Kohl, F. J., & Stearns, C. A. (1974). Vaporization dissociation energies of the molecular carbides of titanium, zirconium, hafnium, and thorium. *High Temperature Science, 6*, 284–302.

Kwon, H., & Kang, S. (2006). Instability of solid-liquid interface in transitional metal-carbide system. *Journal of Material Science, 41*, 4649–4653.

Kwon, H., & Kang, S. (2008a). Effect of milling on the carbothermal reduction of oxide mixture for (Ti, W) C-Ni. *Materials Transactions, 49*, 1594–1599.

Kwon, H., & Kang, S. (2008b). Carbothermal reduction of titanium monoxide (TiO). *Journal of the Ceramic Society of Japan, 116*, 1154–1158.

Kwon, H., & Kang, S. (2009a). Microstructure and mechanical properties of TiC-WC-(Ti, W)C-Ni cermets. *Materials Science and Engineering: A, 520*, 75–79.

Kwon, H., & Kang, S. (2009b). Stability domains of TiO_2-Ti_3O_5-Ti_2O_3-TiC/Ti(CN) systems during reduction process. *Journal of the American Ceramic Society, 92*, 272–275.

Kwon, H., & Kang, S. (2012) Stability domain of Ti(CN) in Ti-TiC-TiN. *Materials Letters, 68,* 426–428

Lebacq, O., Pasturel, A., Manh, D. N., Finel, A, Caudron, R;, Barrachin, M., et al. (1996). Ab initio analysis of structural stability in the compound Ni_3V. *Physical Review B, 53*, 6203.

Lee, K.-R., Baik, Y.-J., & Yoon, D. N. (1987). A critical test for the coherency strain energy as the driving force for the discontinuous precipitation in Mo-Ni alloy. *Acta Materialia, 35*(8), 2145–2150.

Lee, J. K., Tanaka, H., & Kim, H. (1996). Formation of solid solutions between SiC and AlN during liquid-phase sintering. *Materials Letters, 29*(1–3), 1–6.

Lengauer, W., & Dreyer, K. (2002). Functionally graded hardmetals. *Journal of Alloys and Compounds, 338*(1–2), 194–212.

Lide, D., & Frederikse, H. (1994). *CRC handbook of chemistry and physics* (75th ed.). Florida: CRC Press. Inc.

Lihndahl, P., Gustafson, P., Rolander, U., Stals, L., & Andrén, H.-O. (1999). Microstructure of model cermets with high Mo or W content. *International Journal of Refractory Metals & Hard Materials, 17*, 411–421.

Lindahl, P., Rolander, U., & Andren, H. O. (1991). Atom-probe analysis of a commercial cermet. *Surface Science, 246*, 319–322.

Manik, S. K., Dutta, H., & Pradhan, S. K. (2003). Microstructure characterization and phase transformation kinetics of polymorphic transformed ball milled a-TiO_2-10 mol% m-ZrO_2 mixture by Rietveld method. *Materials Chemistry and Physics, 82*, 848–859.

Matsubara, H., Shin, S., & Sakuma, T. (1992). Grain growth of TiC and Ti(C, N) base cermet during liquid phase sintering. *Solid State Phenomena, 25 & 26*, 551–558.

Matzke, H. J. (1989). In R. Freer (Ed.), *The physics and chemistry of carbides, nitrides, and borides.* Kluwer Academic Pub.

Moskowitz, D., & Humenik, M., Jr (1966). Cemented titanium carbide cutting tools. *Modern Developments in Powder Metallurgy, 3*, 83–94.

Mun, S., & Kang, S. (1999). The effect of HfC addition on the microstructure of Ti(C, N)-Ni cermet system. *Powder Metallurgy, 42*(3), 251–256.

Naoto, H., Yoshio, A., & Mamoru, M. (1994). Microstructure characterization of gas-pressure-sintered -silicon nitride containing large-silicon nitride seeds. *Journal of the American Ceramic Society, 77*(4), 1093–1097.

Nishigaki, K., & Doi, H. (1980). Effect of additional carbon content on mechanical and cutting properties of $TiC_{0.7}N_{0.3}$-15Ni-8Mo alloy. *Japan Society of Powder and Powder Metallurgy, 27*, 130–136.

Nishigaki, K., Ohnishi, T., Shiokawa, J., & Doi, H. (1974). Ti(CN)-based cermets. *Modern Developments in Powder Metallurgy, 8*, 627–643.

Nomura, T., Moriguchi, H., Tsuda, K., Isobe, K., Ikegaya, A., Moriyama, K., et al. (1999). Material design method for the functionally graded cemented carbide tool. *International Journal of Refractory Metals and Hard Materials, 17*(6), 397–404.

Ouensanga, A. (1981). Thermodynamics of the Ti-Co system at 1580 K. *Journal of the Less Common Metals, 79*, 237–241.

Padture, N. (1994). In situ-toughened silicon carbide. *Journal of the American Ceramic Society, 77*(2), 619–523.

Parikh, N. M., & Humenik, M. (1958). Cermets: II, wettability and microstructure studies in liquid phase sintering. *Journal of the American Ceramic Society, 40*(9), 315–322.

Park, J. S. (1994). *Effects of nitrogen partial pressure sintering on the mechanical properties and microstructure of Ti(C, N)-based cermets* (Ph.D. thesis). Seoul, Korea: Seoul National University.

Park, S., & Kang, S. (2005). Toughened ultra-fine (Ti, W)(Cn)-Ni cermets. *Scripta Materialia, 52*, 129–133.

Park, S., Kang, Y., Kwon, H., & Kang, S. (2006). Synthesis of (Ti, M_1, M_2)(CN)-Ni nanocrystalline powders. *International Journal of Refractory Metals and Hard Materials, 24*, 115–121.

Park, Y. J., Kim, S. W., & Kang, S. (2000). The formation of a solid solution band at the surface of Ti(CN)-based cermets. *Materials Science and Engineering: A, 291*, 198–206.

Park, S.-D., Park, J.-K., Kang, S., & Kim, D.-Y. (1998). Instability of solid-liquid interfaces in TiC-Ni ceramics. *Journal of Materials Synthesis and Processing, 6*(4), 255–259.

Pastor, H. (1988). Titanium-carbonitride-based hard alloys for cutting tools. *Materials Science and Engineering: A, 105*, 401–409.

Pehlke, R. D., & Elliot, J. F. (1960). Solubility of iron alloys: 1, Thermodynamics. *Transactions of the Metallurgical Society of AIME, 218*, 1088–1101.

Qi, F., & Kang, S. (1998). A study on microstructural changes in Ti(C, N)-NbC-Ni cermets. *Materials Science and Engineering: A, 251*, 276–285.

Rhee, W. H., & Yoon, D. N. (1987). The instability of solid-liquid interface in Mo-Ni alloy induced by diffusional coherency strain. *Acta Materialia, 35*(7), 1447–1451.

Rudy, E. (1973). Constitution of ternary titanium-tungsten-carbon alloys. *Journal of the Less-Common Metals, 33*, 24–5247.

Rundle, R. E. (1948). A new interpretation of interstitial compounds-metallic carbides, nitrides and oxides of composition Mx. *Acta Crystallographica, 1*, 180–187.

Rynemark, M. (1991). Investigation of equilibria in the Ti-W-C-N system at 1750 °C. *Refractory Metals and Hard Materials, 10*, 185–193.

Saidi, A., & Barati, M. (2002). Production of (W, Ti)C reinforced Ni-Ti matrix composites. *Journal of Materials Processing Technology, 124*(1–2), 166–170.

Schick, H. L. (1966). *Thermodynamics of certain refractory compounds* (Vol. 1). 111 Fifth Avenue, New York, N. Y., 10003: Academic Press, 632 pp.

Schwarzkopf, M., Exner, H. E., & Fischmeister, H. F. (1988). Kinetics of compositional modification of (W, Ti)C-WC-Co alloy surfaces. *Materials Science and Engineering: A, 105/106*, 225–231.

Shau, P., De, M., & Zdujic, M. (2003). Microstructural characterization of the evoluted phases of ball-milled α-Fe_2O_3 powder in air and oxygen atmosphere by Rietveld analysis. *Materials Chemistry and Physics, 82*, 864–876.

Shaviv, R. (1996). Synthesis of tin and TiN_xC_y: optimization of reaction parameters. *Materials Science and Engineering: A, 209*, 345–352.

She, J., & Ueno, K. (1999). Effect of additive content on liquid-phase sintering on silicon carbide ceramics. *Materials Research Bulletin, 34*(10–11), 1629–1636.

Shewman, P. G. (1989). *Diffusion in solids* (2nd ed.). New York: McGraw Hill.

Song, Y.-D., & Yoon, D. N. (1984). The driving force for chemically induced migration of molten Ni Films between W Grains. *Metallurgical and Materials Transactions A, 15A*, 1503–1504.

Stull, D. R. (1971). Janaf thermochemical tables. DTIC Document.

Suryanarayana, C. (1995). Nanocrystalline materials. *International Materials Reviews, 40*, 41–64.

Suzuki, H., Hayashi, K., & Matsubara, H. (1982). The microstructural change near the surface of Ti(C, N)-Mo_2C-Ni sintered compacts. *Japan Society of Powder and Powder Metallurgy, 29*(2), 58–61.

Suzuki, H., Hayashi, K., Matsubara, H., & Tokumoto, K. (1983). High temperature strength of TiC–Mo_2C–Ni alloys containing nitrogen. *Japan Society of Powder and Powder Metallurgy, 30*, 106–111.

Suzuki, H., Hayashi, K., & Taniguchi, Y. (1981). The b-free layer formed near the surface of vacuum-sintered WC-b-Co alloys containing nitrogen. *Transactions of the Japan Institute of Metals, 22*(11), 753–764.

Suzuki, H., Hayashi, K., & Terada, O. (1971). The two-phase region in TiC-Mo-30% Ni alloys. *Journal of the Japan Institute of Metals, 35*, 146–150.

Suzuki, H., & Matsubara, H. (1986). Some properties of Ti(C, N)-WC-Ni alloy. *Japan Society of Powder and Powder Metallurgy, 33*(4), 199–203.

Suzuki, H., Matsubara, H., & Saitoh, T. (1983). The microstructures of Ti(C, N)-Mo_2C-Ni cermet affected by WC addition. *Japan Society of Powder and Powder Metallurgy, 31*(7), 236–240.

Swift, G., & Koc, R. (1999). Formation studies of TiC from carbon coated Tio_2. *Journal of Materials Science, 34*, 3083–3093.

Toth, L. E. (1971). *Transition metal carbides and nitrides*. New York: Academic Press.

Ueki, M., Saito, T., Saito, T., Kitamura, K., & Suzuki, H. (1988). Properties of TiC-TiN-Mo_2C-Ni alloy affected mainly by additional tantalum or Tungsten carbide. *Japan Society of Powder and Powder Metallurgy, 35*(1), 27–32.

White, G., Mackenzie, K., & Johnston, J. (1992). Carbothermal synthesis of titanium nitride. *Journal of Materials Science, 27*, 4287–4293.

Yang, J. K., & Lee, Hu-C. (1996). Microstructural evaluation during the sintering of Ti(C, N)-Mo_2C-Ni alloy. *Materials Science and Engineering: A, 209*, 213–217.

Yoon, D. Y. (1995). Theories and observations of chemically induced interface migration. *International Materials Reviews, 40*(4), 149–179.

Yoon, C. S., Kang, S., & Kim, D. Y. (1997). Dissolution and reprecipitation behavior of TiC-tin-Ni cermets during liquid-phase sintering. *Korean Journal of Ceramics, 2*, 124–128.

Zackrisson, J., Rolander, U., & Jansson, B. (2000). Microstructure and performance of a cermet material heat-treated in nitrogen. *Acta Materialia, 48*(17), 4281–4291.

Zackrisson, J., & Andrén, H.-O. (1999). Effect of carbon content on the microstructure and mechanical properties of (Ti, W, Ta, Mo)(C, N)-(Co, Ni) cermets. *International Journal of Refractory Metals and Hard Materials, 17*, 265–273.

Zhang, S. (1993). Titanium carbonitride-based cermets: process and properties. *Materials Science and Engineering: A, 163*, 141–148.

Zhukov, V. P., Gubanov, V. A., Jepsen, O., Christensen, N. E., & Andersen, O. K. (1988). Calculated electronic properties of titanium carbonitrides TiC_xn_{1-x}. *Philosophical magazine B. Physics of Condensed Matter Electronic, Optical and Magnetic Properties, 58*, 139–152.

Zhukov, V. P., Medvedeva, N. I., & Gubanov, V. A. (1989). The electronic band structure and non empirical calculations of cohesive properties of refractory compounds. *Physica Status Solidi (B), 151*, 407–440.

SECTION III

SYNTHESIS AND PROCESSING

1.06 Powder Synthesis

Thomas A. Wolfe, Thomas J. Jewett, and Raj P. Singh Gaur, Global Tungsten and Powders Corporation, Towanda, Pennsylvania, USA

1.06.1 Tungsten Carbide

Tungsten carbide, or "carbide" as it is often historically referred to, is a compound composed of one atom of tungsten and one atom of carbon. Tungsten carbide synthesis has been covered previously in several comprehensive books over the years (Brooks, 1996; Lassner & Schubert, 1999; Yih & Wang, 1979). In this chapter, we cover the basics and expand on modern trends and techniques. The synthesis of tungsten carbide starts with the recovery and purification of tungsten and/or tungsten compounds from various ores and secondary sources.

1.06.1.1 Preparation of Ammonium Paratungstate

Ammonium paratungstate (APT) is the main tungsten compound used in the manufacturing of tungsten metal powder. From tungsten ore concentrates and various tungsten-containing scraps, APT is made via a hydrometallurgical route (Lassner & Schubert, 1999; Shamsuddin & Sohn, 1981; Singh Gaur, 2006a; Songina, 1970; Yih & Wang, 1981, chap. 2, pp. 79–128). During the last 100 years, there have been significant scientific and technological developments in the processing of APT. This chapter reviews the modern hydrometallurgical methods for APT production.

APT is a white crystalline salt of ammonium and tungsten, with the generally accepted formula $(NH_4)_{10}(H_2W_{12}O_{42})\cdot 4H_2O$ (van Put & Zegers, 1991). Other formula $(NH_4)_{10}(W_{12}O_{41})\cdot 5H_2O$ and $5(NH_4)_2O\cdot 12WO_3\cdot 5H_2O$ were noted by Songina (1970). APT from tungsten feed materials is produced by hydrometallurgical methods. The hydrometallurgical methods for APT production have been known for a long time. In the old methods of hydrometallurgical processing of APT (Lassner & Schubert, 1999), scheelite was mainly processed by acid digestion. During this digestion reaction, scheelite ($CaWO_4$) is converted into tungstic acid. Tungstic acid, thus obtained, was dissolved in ammonium hydroxide and the solution after purification was crystallized to APT

http://dx.doi.org/10.1016/B978-0-08-096527-7.00006-4

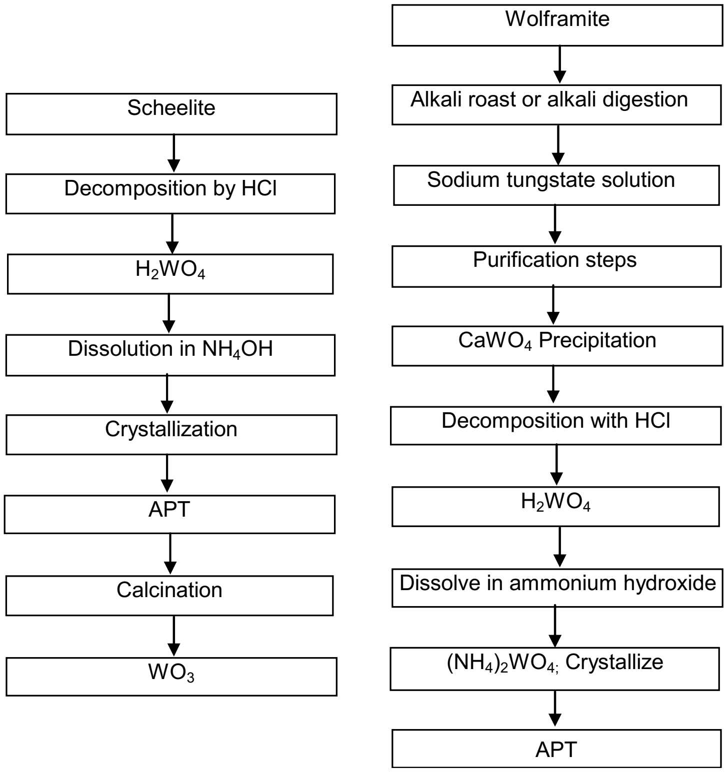

Figure 1 General flow diagrams for the processing of scheelite and wolframite ores by the acid process.

via evaporation crystallization. A similar procedure was also used for wolframite, which initially was digested in an alkali solution, but then the resulting sodium tungstate solution was converted into $CaWO_4$. $CaWO_4$ was then processed via acid digestion as described above. Figure 1 presents the general flow diagrams for the processing of scheelite and wolframite by the acid process. The acid process to make APT from both the ore concentrates can be represented by the following chemical reactions.

$$MnWO_4 + 2NaOH \rightarrow Mn(OH)_2 + Na_2WO_4 \qquad \text{(i)}$$

$$FeWO_4 + 2NaOH \rightarrow Fe(OH)_2 + Na_2WO_4 \qquad \text{(ii)}$$

$$Na_2WO_4 + CaCO_3 \rightarrow CaWO_4 + Na_2CO_3 \qquad \text{(iii)}$$

$$CaWO_4 + 2HCl \rightarrow CaCl_2 + H_2WO_4 \qquad \text{(iv)}$$

$$H_2WO_4 + 2NH_4OH \rightarrow (NH_4)_2WO_4 + 2H_2O \qquad \text{(v)}$$

$$12(NH_4)_2WO_4 \rightarrow (NH_4)_{10}(H_2W_{12}O_{42})\cdot 4H_2O + 2H_2O + 14NH_3 \qquad \text{(vi)}$$

In the modern methods of hydrometallurgical processing of APT, all the tungsten feeds are digested in sodium hydroxide (or sodium carbonate) at high temperature. After purification steps, the sodium is separated from the sodium tungstate solution via liquid ion exchange (LIX) and finally converted into APT. Figure 2 illustrates the LIX process.

As mentioned above, in the modern methods of APT processing, separation of sodium from purified sodium tungstate solution is largely carried out by solvent extraction; however, in some plants (especially in China), solid ion exchange (SIX) is also used for the separation of sodium and other impurities from sodium tungstate solution (Lassner & Schubert, 1999).

1.06.1.1.1 Tungsten Feeds

Most of the raw material used in tungsten production today comprises high-grade tungsten ore concentrates and synthetic concentrates obtained from tungsten scraps.

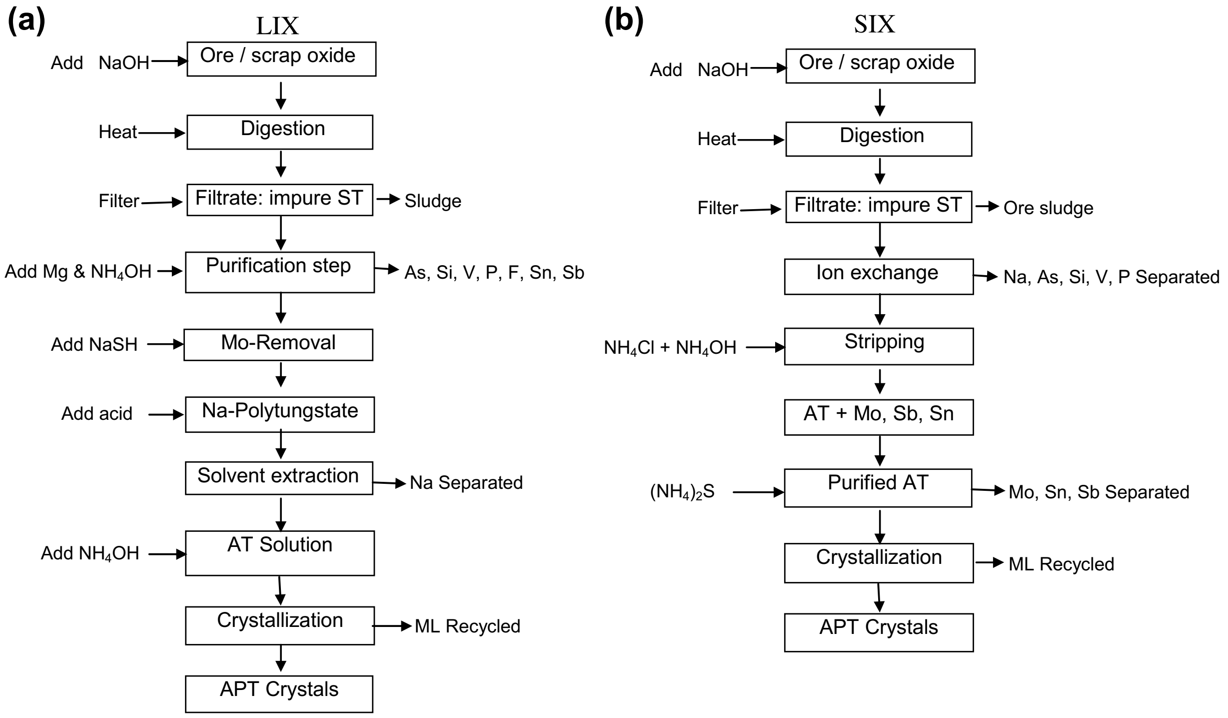

Figure 2 General flow diagrams for the (a) LIX and (b) SIX processes.

1.06.1.1.1.1 Ores

Tungsten minerals that occur in sufficient abundance to be of economic significance and can be used in the production of APT are divided into two groups: scheelite ores and the wolframite ores (Lassner & Schubert, 1999).

1.06.1.1.1.1.1 Scheelite Ores

The mineral scheelite (calcium tungstate, $CaWO_4$) is normally found in quartz veins and in contact with scarn ores of complex mineralogical composition (Lassner & Schubert, 1999; Singh & Miller, 1998; Singh, Miller, & Wolfe, 1999, 2000). These scarn minerals include garnets, pyroxene, and amphibole, and other minerals such as calcite, apatite, and quartz. Figure 3 depicts a picture of a scheelite tungsten mine. Scheelite ores can be classified

Figure 3 Picture of a scheelite tungsten mine.

Table 1 Mineralogical composition of one high-grade ore concentrate and one low-grade ore concentrate

Component	*Low-grade ore (%weight)*	*High-grade ore (%weight)*
$CaWO_4$ (scheelite)	32	88
Phlogopite and talc	33	8
Calcite ($CaCO_3$)	14	1–2
Apatite	4	–
$Fe_{1-x}S + CuFeS_2$	17	2–3

into five different categories: (1) simple scheelite ore, (2) scheelite–sulfides ore, (3) scheelite–cassiterite ore, (4) scheelite–calcite–apatite ore, and (5) scheelite–powellite ore.

Table 1 presents the mineralogical composition of one high-grade ore concentrate and one low-grade ore concentrate.

The analytical data of two high-grade scheelite ore concentrates and one low-grade ore concentrate are presented in Table 2. Figure 4 depicts the X-ray diffractogram of a low-grade ore concentrate.

From an ore, scheelite is typically concentrated via a flotation process (Agar, 1984; Lassner & Schubert, 1999; Vedova & Grauerholz, 1977; Zajic & Kosaric, 1977). In a typical scheelite ore concentration process (Figure 5), the ore (containing 0.4–0.6 %W) from the mine is brought to the plant and fed to the grinders to grind below 200 mesh. Ground ore is slurried in water and the slurried ore is cycloned. Overflow from the cyclone goes for talc flotation; concentrates from talc flotation cells go to tailings (reject); and tail from the cell is screened: oversized concentrates go to tailings (reject) and undersized concentrates go to low-grade ore thickeners for reclaim as low-grade ore. The underflow from the cyclone is screened and the oversized concentrates are returned for regrinding. The undersized concentrate goes to high-grade ore feed to the thickener. The ground material goes back to cyclone. The thickened mud is conditioned for sulfide flotation. Concentrate from the flotation cell (mainly sulfides) goes to the tailings (reject). The tailing of sulfide flotation cells goes to the tables (rougher and cleaner) for high-grade ore concentrate separation. The ore portion collected at the corners of the high-grade ore separation tables is the low-grade ore feed and goes to the thickeners.

Table 2 Analytical data of two high-grade scheelite ore concentrates and one low-grade ore concentrate

Elements	*(A) High-grade scheelite ore concentrate (%weight)*	*(B) High-grade scheelite ore concentrate (%weight)*	*Low-grade scheelite ore concentrate (%weight)*
Al	0.21	0.4	0.5
As	0.2	–	–
Ba	0.41	–	–
Bi	0.06	0.4	0.08
Ca	12	13	10
Cl	0.01	–	–
Cr	0.05	–	–
Cu	0.03	–	1.6
Fe	2.5	1.8	8.8
K	0.26	0.05	0.44
Mg	0.14	0.5	4.5
Mn	0.13	0.2	0.12
Mo	0.22	0.04	<0.01
Na	1.6	–	–
P	0.16	0.14	0.74
Pb	0.05	–	–
S	–	2.0	8.6
Si	1	2.0	6.6
Sn	0.13	–	–
Sr	0.23	–	–
Ti	–	0.05	–
W	58	56	20.6

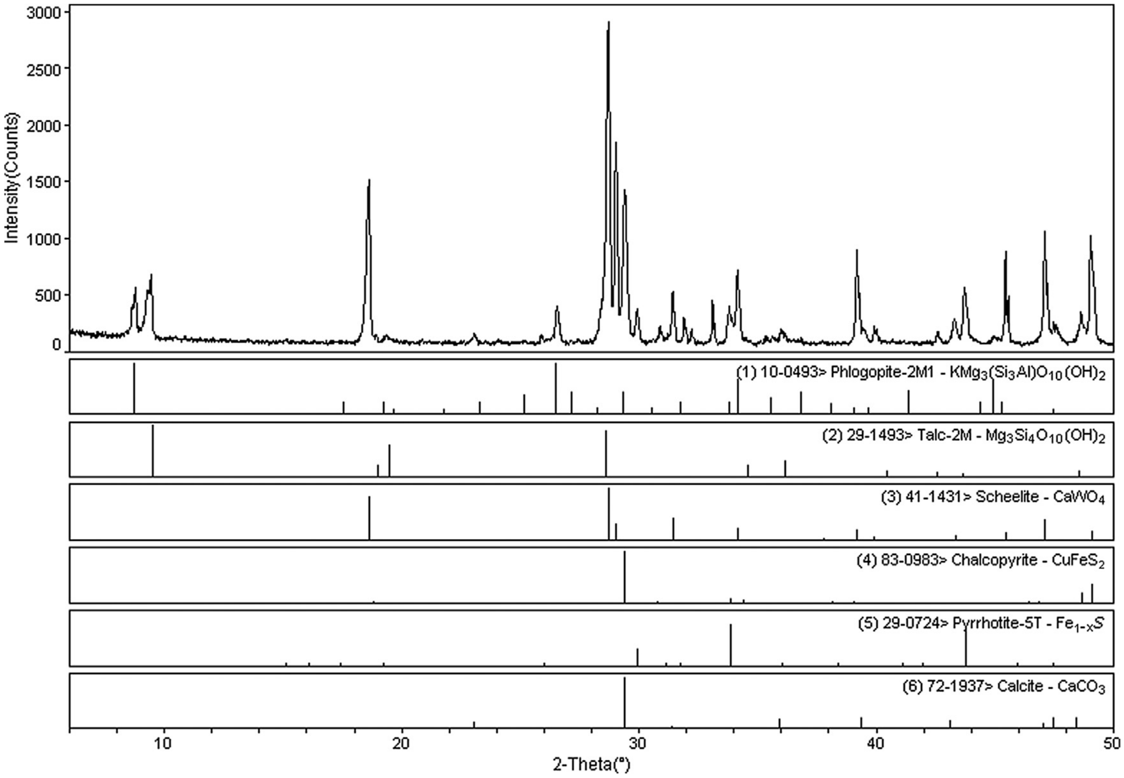

Figure 4 X-ray diffractogram of a low-grade ore concentrate.

High-grade ore concentrate, collected from the tables, goes to the roaster and is roasted at about 540°C to remove organics. The roasted high-grade ore goes to magnetic separator for final sulfide cleaning. Clean ore is bagged and shipped. The magnetically separated material goes for another magnetic separation. Rejects from this magnetic separator go back to the cleaner tables.

In high-grade ore separation tables, rougher tables pull (concentrate) scheelite, which then goes to the cleaner tables. Tailings from the rougher go for scheelite scavenging. The scavenged scheelite goes back to the rougher tables. Scheelite from the cleaner tables goes to high-grade ore collection. All the tailings from the rougher and cleaner tables are the feed for low-grade ore and go to low-grade ore thickeners. Coarser material from the high-grade rougher tables goes for cyclone separation. Underflow from the cyclone goes for ball milling and secondary sulfide flotation and back to high-grade ore tables; overflow goes to thickener for low-grade ore feed. Figure 5 presents the general flow diagram of the scheelite concentration process.

1.06.1.1.1.1.2 Wolframite Ores

The wolframite ores consist of three minerals: ferberite, wolframite, and hubnerite. The iron-rich tungstate ($FeWO_4$; WO_3 content 76.3%) is ferberite, the manganese-rich tungstate ($MnWO_4$; WO_3 content 76.6%) is hubnerite, and the iron–manganese-mixed tungstate ($(Fe,Mn)WO_4$; WO_3 content 76.5%) is wolframite. Wolframite contains between 20% and 80% each of $FeWO_4$ and $MnWO_4$ in their pure form. Table 3 presents the composition of three wolframite ore concentrates. Concentration of wolframite from its ores is typically carried out by gravity and magnetic methods, as wolframite occurs mainly in vein-type deposits whose mineralization is much coarser than most of the scheelite ores (Lassner & Schubert, 1999). Figure 6 depicts wolframite ore in a tungsten mine.

1.06.1.1.1.2 Scrap

There are two types of tungsten carbide scraps available in the market (Singh & Miller, 1997). Typically, these are known as hard scrap and soft scrap.

Hard scrap commonly consists of worn tools such as cemented carbide cutting and drilling tool bits. Although the major component of hard scrap is tungsten carbide, it can be best represented by a solid solution

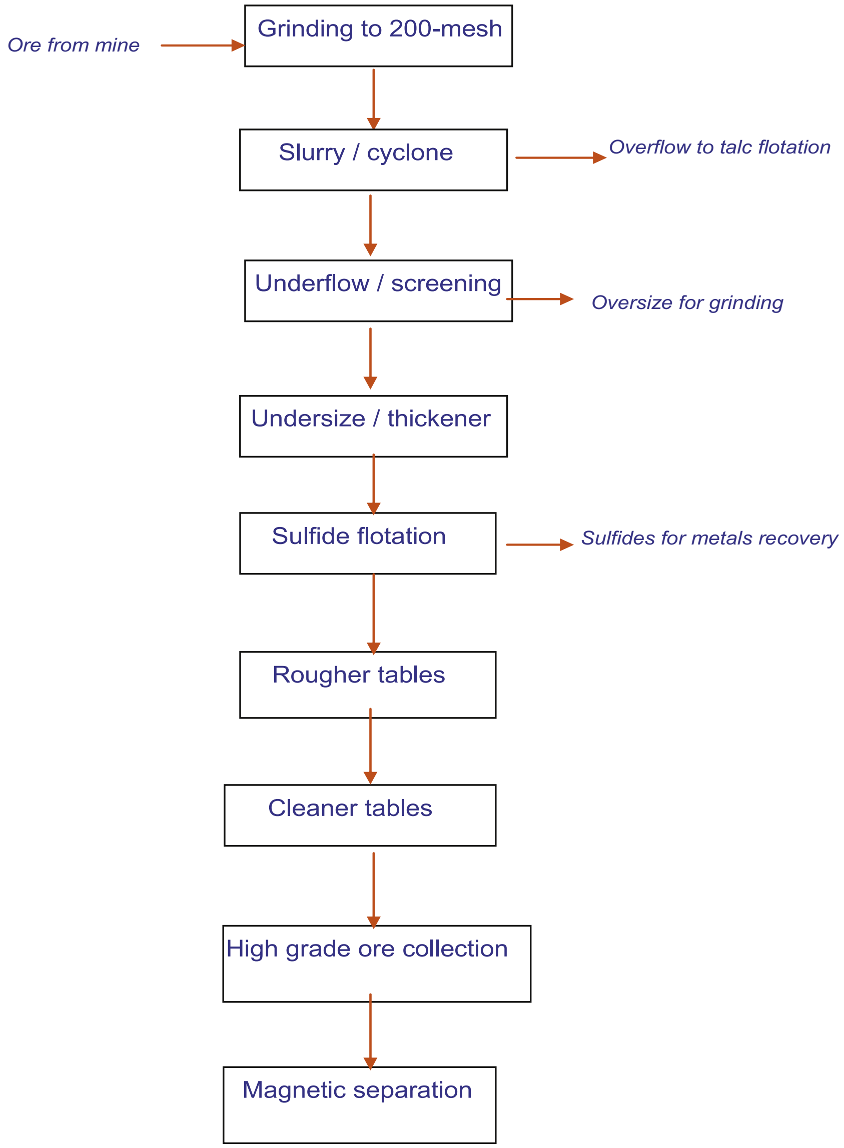

Figure 5 General flow diagram of the scheelite concentration process.

Table 3 Composition of the three wolframite ore concentrates

Parameter	*Typical high-grade wolframite ore concentrate (%weight)*	*High Sn–containing high-grade wolframite ore concentrate (%weight)*	*High Sb–containing high-grade wolframite ore concentrate (%weight)*
Al	0.19	1.1	0.19
Ca	0.84	–	0.9
Fe	12	15	12
Mn	2.4	5.5	2.5
Nb	–	0.45	–
Sb	–	–	1.4
Si	3.9	0.6	4.0
Sn	–	9.2	–
Ti	–	0.3	–
W	52	42	53

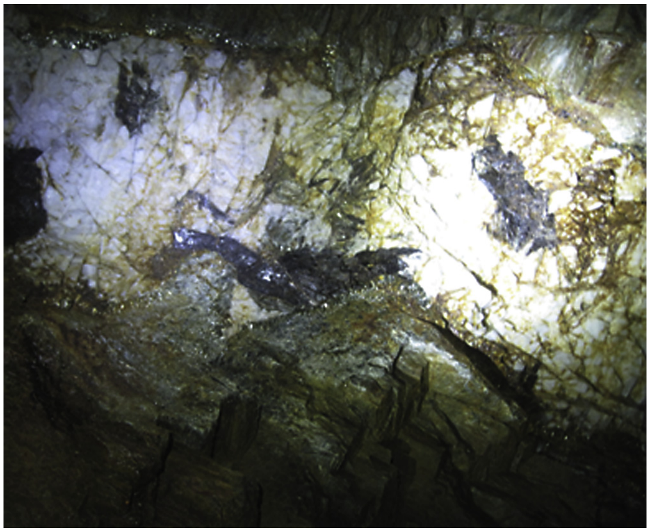

Figure 6 Wolframite ore in a tungsten mine.

Figure 7 Different types of hard tungsten carbide scraps.

of (W,Ti,Ta,Nb)C–Co type. In cemented carbides, Co is used as a binder and TiC, TaC, and/or (Ta,Nb)C is used to modify the properties of the hardmetals. Tool bits are normally coated to resist wear to have high hardness, a good chemical stability, and resistance to oxidation, as well as a smooth surface to reduce friction. Figure 7 depicts the picture of hard scraps.

Soft scrap pertains to all tungsten-containing scraps that do not have a defined shape. Typically, this scrap contains the rejects of the manufacturing of tungsten products such as wires, coils, powders, turnings. Soft scrap, typically, contains more metallic impurities than hard scrap. Table 4 presents the composition of one hard scrap oxide and one soft scrap oxide. Hard tungsten carbide scrap, typically, contains more Ta than soft scrap.

Non-tungsten carbide scrap (e.g. tungsten copper, tungsten heavy alloys) is also available; however, some of these tungsten-containing scraps are very difficult to process.

1.06.1.1.2 Digestion of Ore Concentrates and Oxidized Scraps

In the basic process, the ore concentrate is digested in alkali solutions such as NaOH and/or Na_2CO_3 at a high temperature of 150–250 °C to produce a mixture comprising soluble sodium tungstate and an insoluble sludge (residue) (MacInnis & Kim, 1985; Quatrini, 1982; Quatrini & Martin, 1982; Quatrini, Terlizzi, & Martin, 1982; Quatrini, Vogt, & Martin, 1982; Queneau & Huggins, 1982).

Table 4 Composition of one hard scrap oxide and one soft scrap oxide

Element	*Hard WC scrap oxide (%weight)*	*Soft WC scrap oxide (%weight)*
Al	–	0.23
Co	6.0	7.5
Cr	–	0.4
Fe	0.6	0.3
Nb	0.4	0.11
Ni	0.2	0.5
Si	–	1.1
Ta	2.8	0.29
Ti	1.8	0.14
W	67.9	68

The following chemical equations illustrate the digestion of ore concentrates and scraps.

$$CaWO_4 + 2NaOH \rightarrow Ca(OH)_2 + Na_2WO_4 \tag{1}$$

$$CaWO_4 + Na_2CO_3 \rightarrow CaCO_3 + Na_2WO_4 \tag{2}$$

$$MnWO_4 + 2NaOH \rightarrow Mn(OH)_2 + Na_2WO_4 \tag{3}$$

$$FeWO_4 + 2NaOH \rightarrow Fe(OH)_2 + Na_2WO_4 \tag{4}$$

$$WO_3 + 2NaOH \rightarrow H_2O + Na_2WO_4 \tag{5}$$

$$CoWO_4 + 2NaOH \rightarrow Co(OH)_2 + Na_2WO_4 \tag{6}$$

Much of the tungsten production results from the high-grade tungsten ore concentrates (such as wolframite and scheelite) and synthetic concentrates obtained from tungsten scraps (Lassner & Schubert, 1999; Singh Gaur, 2006a). The obtained mixture is then diluted to form an aqueous portion containing dissolved sodium tungstate, which is separated from an insoluble sludge portion via filtration (Singh Gaur, 2006b). The impure sodium tungstate is purified by the below-mentioned procedures.

1.06.1.1.3 Purification of Impure Sodium Tungstate Solution

1.06.1.1.3.1 Separation of Si, As, Sn, P, and F

The impurities Si, As, Sn, P, and F are present as anions and are separated by suitable precipitation methods (Lassner, 1995; Miller, Vogt, & Scheithauer, 1985; Queneau, Beckstead, & Huggins, 1982). For example, P, Si, and As are precipitated by the addition of a magnesium compound and ammonium hydroxide into impure sodium tungstate solution. To ascertain maximum separation of impurity elements, a much larger concentration of magnesium compound and ammonium hydroxide than stoichiometrically required amounts is added. The following chemical reactions typically occur in the separation of Si, P, and As.

$$MgSO_4 + Na_2SiO_3 \rightarrow MgSiO_3 + Na_2SO_4 \tag{7}$$

$$MgSO_4 + NH_4OH + Na_3PO_4 \rightarrow MgNH_4PO_4 + NaOH + Na_2SO_4 \tag{8}$$

$$MgSO_4 + NH_4OH + Na_3AsO_4 \rightarrow MgNH_4AsO_4 + NaOH + Na_2SO_4 \tag{9}$$

Magnesium compounds in combination with an aluminum compound are also used for the separation of Si, P, and F (Queneau et al., 1982). Sn can also be separated using magnesium compound and ammonium hydroxide (Miller et al., 1985).

1.06.1.1.3.2 Separation of Molybdenum

Small concentration of molybdenum can be separated from concentrated sodium tungstate solution by treating alkaline or neutral tungstate solution with NaHS (Bellingham, 1976; Huggins & Queneau, 1981a, 1981b; Kurtak, 1965; Smith, 1944). Under these conditions, molybdate ions are converted into thiomolybdate. The chemical reactions that describe the preferential precipitation of molybdenum trisulfide in the separation of molybdenum from tungsten are given below. Sodium hydrogen sulfide at a basic pH reacts with sodium molybdate to form sodium thiomolybdate.

$$4NaHS + Na_2MoO_4 \rightarrow Na_2MoS_4 + 4NaOH \tag{10}$$

The addition of sulfuric acid to the alkaline thiomolybdate solution neutralizes the sodium hydroxide and excess sodium carbonate coming from the digestion step.

$$2NaOH + H_2SO_4 \rightarrow Na_2SO_4 + H_2O \quad (11)$$

$$Na_2CO_3 + H_2SO_4 \rightarrow Na_2SO_4 + H_2O + CO_2 \quad (12)$$

Carbon dioxide released in this step slows down the addition of sulfuric acid due to the foam generation (therefore, carbonate should be separated from the solution before this step to prevent the foam generation). The continued addition of sulfuric acid decomposes the thiomolybdate ion to precipitate molybdenum trisulfide and release hydrogen sulfide.

$$Na_2MoS_4 + H_2SO_4 \rightarrow MoS_3 + H_2S + Na_2SO_4 \quad (13)$$

The minimum quantity of NaSH used in this step is critical for the complete removal of molybdenum. Typically, 2.0–2.5 times the required concentration of NaSH based on the above chemical equations is added, as tungsten and other impurities (such as Co and As) also consume sulfide.

1.06.1.1.3.3 Separation of Sodium

After the separation of molybdenum, the sodium tungstate solution is treated by LIX or SIX resins for the separation of sodium (Boyer & Christini, 1982; Kim, MacInnis, McClintic, & Vogt, 1983; Kulkarni, Montclair, & Cleary, 1978; Lassner & Schubert, 1999; MacInnis, McClintic, & Kim, 1982). In the old process, separation of sodium was carried out via its conversion to calcium tungstate: $Na_2WO_4 + Ca(OH)_2 \rightarrow CaWO_4 + 2NaOH$, which was processed via acid digestion: $CaWO_4 + 2HCl \rightarrow CaCl_2 + H_2WO_4$. Tungstic acid, thus obtained, was dissolved in ammonium hydroxide and the solution was crystallized to produce APT. In a modern solvent extraction method, tungsten is extracted from slightly acidic sodium tungstate solution by aliphatic amines dissolved in an organic solvent. The solvent extraction of tungstate ionic species from acidic solution occurs in four main (continuous) steps: extraction, scrubbing, stripping, and regeneration of amine.

The extracting reagents are long-chained primary, secondary, tertiary, and quaternary ammonium compounds (with chain length of C8–C10) such as trioctylamine and tridecylamine (Lassner & Schubert, 1999). Commercial products are Primene JMC (primary amine), Amberlite LA-1 or Adogen 283 (secondary amine), Trioctylamine (tertiary amine), and (quaternary ammonium compound). Depending on the process conditions, either secondary or tertiary amines are preferred. Primary amines are advantageous for higher condensed tungstate solutions that are derived from the electrodialytic process.

The concentration of the reagent varies between 1% and 22% as reported in the literature (Boyer & Christini, 1982; Kim et al., 1983; Kulkarni et al., 1978; Laferty, Queneau, & Beckstead, 1984; MacInnis et al., 1982). The organic phase consists of two or three components: reagent (amine), modifier, and solvent. Solvent is either kerosene or mixtures of alkyl benzenes like toluene or xylene. Modifiers are necessary when kerosene is used as the solvent. Modifier such as isodecanol (5%) or tributyl phosphate (12%) increases the solubility of the isopoly tungstate–amine complex, which is low in kerosene.

Before extraction, the organic amine is converted into its salt by the reaction of acid. For example, reaction of amine with sulfuric acid will convert it into sulfate salt. Reaction of salted amine with isopoly tungstate (main tungsten species at low pH) typically occurs as follows:

$$10(R_3NH)^+ + 5SO_4^{2-} + 2HW_6O_{21}^{5-} + 10Na^+ \rightarrow 2(R_3NH)_5HW_6O_{21} + 5Na_2SO_4 \quad (14)$$

As the organic reagent (amine) extracts only tungsten species, sodium, sulfate, and other cations report to the aqueous phase (raffinate), which is recycled or discarded.

The loaded organic after scrubbing (washing) is stripped in ammonium hydroxide, leaving tungsten in the aqueous phase as ammonium tungstate.

$$(R_3NH)_5HW_6O_{21} + 5NH_4OH \rightarrow (NH_4)_5HW_6O_{21} + 5(R_3NH)OH \quad (15)$$

$$2(NH_4)_5HW_6O_{21} + 14NH_4OH \rightarrow 12(NH_4)_2WO_4 + 8H_2O \quad (16)$$

Stripping (Laferty et al., 1984) is typically carried out in concentrated (1–10%) ammonia solution ($pH = 8–13$). For APT crystallization, highly concentrated ammonium tungstate solution is desired from the stripping step. Stripped amine is regenerated by sulfuric acid into sulfate form for its continuous reuse in LIX step. The sodium-free ammonium tungstate solution is crystallized to form APT. The LIX process is illustrated in **Figure 8**.

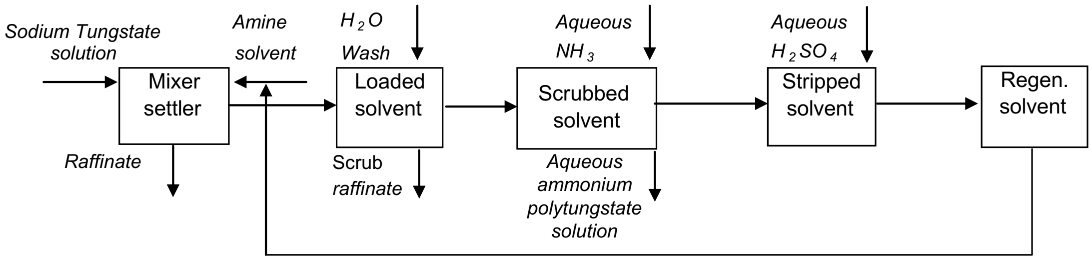

Figure 8 Representation of LIX process for sodium separation.

Figure 9 Morphology of APT.

1.06.1.1.3.4 Crystallization of Ammonium Tungstate Solution to APT

Concentrated ammonium tungstate solution is crystallized via evaporation crystallization as shown in the following chemical equation.

$$12(NH_4)_2WO_4 \rightarrow (NH_4)_{10}H_2W_{12}O_{42}4H_2O + 2H_2O + 14NH_3 \tag{17}$$

During and after crystallization of APT, a further separation of impurities is achieved (Gingerich, Christini, Vogt, Vanderpool, & Miller, 1995; Goddard, 1982).

1.06.1.1.3.5 Purity and Typical Morphology of Industrially Produced APT

APT separated after crystallization is dried and blended. The size and morphology of APT crystals depend on the purity of the ammonium tungstate solution and crystallization and other parameters (Wolfe, 1996). Industrially produced APT consists of faceted crystals (Figure 9). Purity of a typical APT production batch is presented in Table 5.

1.06.1.2 Conversion of APT to Tungsten Oxides

APT is the main compound for the production of tungsten powders and tungsten carbide. For these applications, APT is converted into different tungsten oxides: tungsten yellow oxide (WO_3), tungsten blue oxide (TBO), and tungsten violet oxide (TVO or $WO_{2.72}$).

For the production of WO_3, APT is thermally (500–700 °C) decomposed in the air (Lassner & Schubert, 1999; Schubert & Lassner, 1991). WO_3 is produced by calcination of APT in the air, typically in rotary furnaces operating at 500–700 °C. Other oxides are formed via the high-temperature reduction of APT in hydrogen.

Table 5 Purity of a typical lot of APT

Element	*APT (ppm)*
Al	0.4
As	1.5
B	<0.1
Ba	0.9
Bi	<0.1
Ca	0.7
Cd	<0.5
Co	<0.1
Cr	0.2
Cu	0.5
F	<1.0
Fe	<0.5
K	<0.2
La	<0.1
Li	<0.1
Mg	0.1
Mn	<0.1
Mo	<0.5
Na	0.1
Ni	<0.1
P	0.7
Pb	<0.1
S	<0.5
Sb	<0.1
Sc	<0.1
Si	1.1
Sn	<0.1
Sr	<0.1
Th	<0.1
Ti	<0.1
U	<0.1
V	1.2
Zn	<0.2
Zr	<0.1

Van Put and Zegers (1991) reviewed the hydrogen reduction of APT into TBO (Schubert & Lassner, 1991). Investigations by Ziemer and Lunk (1989), pp. 471–481 determined that TBO consists of a hexagonal ammonia–hydronium–tungsten bronze, $(NH_4)_x(H_3O)_yWO_3$, amorphous oxide, γ-oxide, and WO_2. They define an overall formula for TBO, $(NH_4)_x(H_3O)_yWO_z$, and determined the values of x, y, and z at various temperatures. At 517 °C, for example, TBO consists of 23% crystalline bronze and 77% of an amorphous phase. It was concluded that ammonium hydronium and hydrogen tungsten bronzes are the main constituents of TBO in the temperature range of 300–600 °C. The β-oxide coexists with these phases at these temperatures, and γ-oxide, WO_2, and β-W can also coexist.

On the basis of their experimental work, van Put, Zegers, and Liu (1991) concluded that hydrogen reduction of APT to TBO occurs in four steps. The first three steps are endothermic, while the fourth step is an exothermic reaction. The transition temperatures may shift depending on the reduction time, hydrogen gas pressure, and the amount of APT in the boat. The reaction sequence for the reduction of APT to TBO is provided below.

$$\approx 220\,^{\circ}\mathrm{C}: \mathrm{APT} \rightarrow \mathrm{Amorphous\ APT}$$

$$\approx 300\,^{\circ}\mathrm{C}: \mathrm{Amorphous\ APT} \rightarrow \mathrm{y(NH_4)_2O \cdot WO_3 \cdot zH_2O}$$

$$\approx 420\,^{\circ}\mathrm{C}: \mathrm{y(NH_4)_2O \cdot WO_3 \cdot zH_2O} \rightarrow \mathrm{((x/2)(NH_4)_2) \cdot WO_{3-x/2}} + \mathrm{W_{20}O_{58}}$$

$$\approx 480\,^{\circ}\mathrm{C}: \mathrm{((x/2)(NH_4)_2) \cdot WO_{3-x/2}} + \mathrm{W_{20}O_{58}} \rightarrow \mathrm{((x/2)(NH_4)_2O) \cdot WO_{3-x/2}} + \mathrm{W_{20}O_{58}} + \mathrm{lower\ oxides}$$

Table 6 Properties of tungsten metal

Atomic number	74
Average atomic mass	183.85 g mol^{-1}
Melting point	$3422 \pm 15\,°C$
Boiling point	$5700 \pm 200\,°C$
Vapor pressure (2000 °C)	8.15×10^{-8} pa
Density	19.25 g cm^{-3}
Crystal structure	Body center cubic (A2)
Lattice parameter	$a = 3.16524$ Å (298 K)
Atomic radius	137 pm
Electrical resistivity	5.28 $\mu\Omega \cdot$cm (298 K)
Thermal conductivity	1.75 W $(cm \cdot K)^{-1}$ (298 K)
Coefficient of thermal expansion	$4.32–4.68 \times 10^{-6}$ K^{-1} (298 K)
Modulus of elasticity	390–410 GPa (298 K)
Hardness	300–650 HV30
Enthalpy of fusion	46 kJ mol^{-1}

In China (Zhang, Wu, & Wu, 2011), TVO is used for the production of tungsten powders and tungsten carbide. The advantage of using TVO is that it can be prepared in pure phase and as nano-sized rods (Liao, Chen, Zou, Lu, & Huang, 1999; Liao, Huang, & Zou, 2001).

1.06.1.3 Reduction to Metallic Tungsten

In its refined form, tungsten metal is a shiny white metal. In pure form, the metal has a good ductility; however, contamination with small concentrations of impurities, such as oxygen and carbon, will imbue the metal with considerable hardness and embrittle it. Standard properties of the pure metal are listed in Table 6; these were taken from the International Tungsten Industry Association, ITIA (2011).

The conversion of tungsten oxides or ores to metallic tungsten is a mature process that can be controlled to deliver specific grain sizes and/or a desired particle size distribution. Other properties of interest include purity, the presence and level of doping agents, shape, and degree of agglomeration. Today, a handful of processing methods account for nearly all of the commercially produced tungsten powder; these are hydrogen reduction and carbothermal reduction. Other emerging technologies such as fluidized bed reactors, laminar flow processing, and the FCC-Cambridge method offer potential alternatives. In addition, there are numerous variations of the above-mentioned methods and some novel techniques that are at present still limited to the laboratory bench.

1.06.1.3.1 Hydrogen Reduction

The predominant industrial method in use today for the conversion of tungsten oxide to tungsten metal is hydrogen reduction, utilizing multi-zone, multi-tube horizontal pusher-type furnaces. The oxide powder is loaded into metal boats and then stoked into the furnace via corrosion-resistant tubes. Reduction temperatures typical of commercial production range from 700 to 1000 °C (Brooks, 1996), although it has been noted that the reduction processes may range from 500 to 1100 °C under nonstandard conditions (Lassner & Schubert, 1999; ITIA, 2011). As the boats progress through the furnace, they are subjected to a flow of excess hydrogen that may be co- or countercurrent to the direction of the travel of the boats. The hydrogen serves as the primary reduction species and also acts to remove the water vapor generated during the reduction process. Tungsten powders produced by this method range from 0.1 µm to up to 100 µm in size (ITIA, 2011).

The rate at which the reduction occurs is dependent on several variables, including the powder bed depth, furnace temperature, hydrogen flow rate and direction, hydrogen humidity, and desired powder size. The conversion of WO_3 to metallic tungsten takes place in a complex multi-step process, which is controlled by both diffusion and chemical reaction at the interface between species (Hellmer, Schubert, Lassner, & Lux, 1985, pp. 43–86). The reduction sequence for commercially produced tungsten metal is generally accepted to proceed as $WO_3 \rightarrow WO_{2.9} \rightarrow WO_{2.72} \rightarrow WO_2 \rightarrow$ W metal. Alternate reaction paths may exist depending on nonstandard reduction conditions, as well as the formation of the metastable β-W (Figure 10) (Schubert, 1990; Wilken, Morcom, Wert, & Woodhouse, 1976).

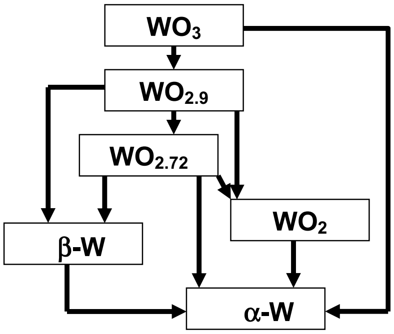

Figure 10 Possible reduction reactions for the reduction of tungsten oxide (Schubert, 1990).

The transformations can be understood to proceed via the following chemical reactions (Lassner & Schubert, 1999).

$$WO_3 + H_2 = WO_{2.9} + H_2O$$
$$WO_{2.9} + 0.6H_2 = WO_{2.72} + 0.6H_2O$$
$$WO_{2.72} + 0.75H_2 = WO_2 + 0.75H_2O$$
$$WO_2 + 2H_2 = W + 2H_2O$$

The reduction reaction is easily followed by monitoring the color change of the powder as it progresses from yellow (WO_3) to bright blue ($WO_{2.9}$) to purple ($WO_{2.72}$) to brown (WO_2) to gray for tungsten metal. Along with the change in color, the reduction process can be tracked by the change in particle morphology (Sarin, 1975).

The particle morphology of WO_3 is pseudomorphous with the morphology of the APT feedstock. Under standard production conditions, the conversion of WO_3 to $WO_{2.9}$ does not result in any identifiable structural changes. The particle shape is still pseudomorphous with the original APT. The only change is the development of surface cracks. The conversion of $WO_{2.9}$ to $WO_{2.72}$ does not alter the overall particle shape; however, the crystal structure changes significantly. Across the surface of the $WO_{2.9}$, particles column or needlelike structures form. Their shape and the speed at which they form strongly suggest a gas-phase transport mechanism. Eventually, the entire particle is transformed into a large cluster of needles. Transformation of $WO_{2.72}$ into WO_2 begins with the formation of small, circular clusters/rosettes of WO_2. A gap between the $WO_{2.72}$ and WO_2 regions suggests that a gas-phase transport mechanism is also at work here. The particles will eventually transform into clusters of large grains of WO_2. The final transformation of WO_2 into W metal begins with a breakdown in the WO_2 structure to a coral-like skeleton, from which small, faceted grains of W metal form. Once again, the growth mechanism appears to have a gas-phase transport component. The reaction continues until the prior WO_2 particles have been converted into several highly faceted W metal particles (Haubner, Schubert, Hellmer, Lassner, & Lux, 1983; Schubert, 1990; Wilken et al., 1976; Zhengji, 1989).

Reduction of WO_3 to $WO_{2.9}$ or $WO_{2.72}$ occurs very easily, such that the majority of the reduction process is occupied with the conversion of $WO_{2.72}$ to WO_2, and subsequently from WO_2 to W. In addition to the primary reactions, there is a pair of minor reactions involving the formation of an intermediate tungsten oxide-hydroxide species. These reactions are critical for the complete understanding of reduction process, especially in reference to particle growth by chemical vapor transport (CVT) and dopant entrapment (Haubner et al., 1983).

$$H_2O + WO_3 = WO_2(OH)_2$$
$$3H_2 + WO_2(OH)_2 = W + 4H_2O$$

$WO_2(OH)_2$ is a gaseous species that forms at elevated temperatures when tungsten oxide is in contact with water. Taking these reactions into account, for the reduction of WO_2, one can identify a pair of simultaneous

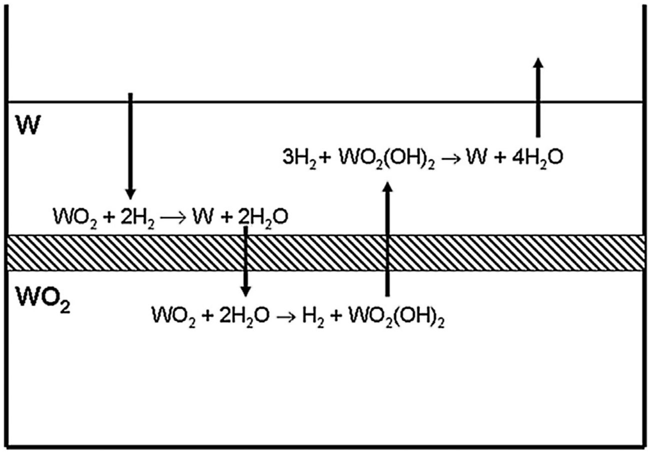

Figure 11 Depiction of reduction reaction involving $WO_2(OH)_2$.

processes, both of which result in the formation of metallic tungsten. The preferred pathway is governed by the H_2:H_2O ratio, with the gas ratio governed in part by the speed at which H_2O vapor can escape from the powder bed (Haubner, Schubert, Lassner, & Lux, 1985, pp. 69–97).

Process 1:

$$WO_2 + 2H_2 = W + 2H_2O$$

Process 2:

$$WO_2 + 2H_2O = WO_2(OH)_2 + H_2$$
$$WO_2(OH)_2 + 3H_2 = W + 4H_2O$$

The reduction of WO_2 to tungsten metal is schematically represented in Figure 11. The direct formation of tungsten metal, Process 1, occurs within the reaction interface of the powder bed where the local H_2:H_2O equilibria allow the reduction to take place. The formation of tungsten metal is accompanied by the formation of water vapor, which diffuses through the powder bed both upward, out of the bed, and downward, into the WO_2 layer. The H_2O that travels downward can then oxidize the WO_2 to the volatile $WO_2(OH)_2$. The $WO_2(OH)_2$ vapor then migrates upward in the powder bed until it reaches a site where the local H_2:H_2O ratio allows reduction of the species and the deposition of tungsten metal on the already reduced tungsten particles. It is understood that the reduction of the volatile species is responsible for particle coarsening.

The rates of the two processes are heavily influenced by the temperature, H_2:H_2O ratio, particle size and surface area, bed depth, and the presence of dopants. Dopant activity varies by species, with some dopants such as the alkali metals promoting the formation of the volatile $WO_2(OH)_2$, leading to an increase in average grain size (Haubner et al., 1985, pp. 69–97).

Understanding the role of the H_2:H_2O ratio in the reduction process reveals several practical effects. Complete reduction of the oxide species becomes more difficult as the water vapor content of the incoming hydrogen is increased. Furthermore, the reduction process can be slowed by using a countercurrent hydrogen flow, such that the gas flowing over freshly stoked boats of powder has the highest water content. Increasing the rate of hydrogen flow through the furnace increases the rate of removal of water vapor. Faster removal of water vapor will allow for an increase in the powder bed depth at the same processing conditions. In general, however, deeper bed depths will require longer reduction times and/or higher temperatures.

In order to consistently produce standard powder grades, the average particle size must be controlled. Although not ideal, much of the industry still defines the average particle size based on the Fisher Sub-Sieve Sizer (FSSS). Among the variables responsible for control of the tungsten particle size, FSSS, are: the reduction time, furnace temperature, and a factor related to the particle size of the starting oxide (Parsons, 1965).

Additional factors include the degree of dopants and the H_2:H_2O ratio. As noted by Ji (1986), the production of submicron tungsten powder is highly dependent on the H_2:H_2O ratio, noting the necessity to carry out the reduction at the lowest possible ratio as well as using a low furnace temperature.

As with submicron tungsten powder, the production of coarse tungsten powder requires the tailoring of the reduction parameters (high temperatures, long dwell times, a low H_2 flow, high H_2:H_2O ratio, deep bed depth). Beyond the adjustment of processing parameters, tungsten particle growth can also be enhanced through the use of dopants, specifically salts of alkali metals (Bleecker, 1974; Kronenwetter, Harris, & Kimmel, 1983; Millner, 1957). Dopant additions are blended into the starting oxides at concentrations ranging from 50 to 500 ppm (Kronenwetter et al., 1983). The alkali metal dopants act to catalyze the WO_2 to tungsten metal reduction by increasing the formation of the volatile $WO_2(OH)_2$ phase (Haubner et al., 1985, pp. 69–97). Work by Lunk, Newman, Gonzalez, and He (2010) suggests that the alkali dopants are more potent when added to WO_3 than to $WO_{2.9}$. The dopants react with the oxide to produce an alkali tungstate, which is then reduced by hydrogen to tungsten metal.

$$WO_3 + MX + H_2O = M_2WO_4 + 2HX$$

$$M_2WO_4 + 4H_2 = 2M + W + 4H_2O$$

In addition to the effects on grain size, dopants are also added prior to the reduction process to improve the properties of the end products, i.e. tungsten wire and cemented carbides (Zeiler, Schubert, & Lux, 1991).

An alternate method of producing metallic tungsten from WO_3 via hydrogen reduction is the use of a rotary furnace (Lassner & Schubert, 1999). The primary benefit of using a rotary furnace is the removal of the static powder bed. The powder in the rotary furnace tube is constantly tumbled as it progresses through the furnace, constantly exposing fresh oxide to the hydrogen stream. In doing so, the retention of water vapor within the powder bed is decreased, thus reducing the prevalence of the volatile $WO_2(OH)_2$ phase. By facilitating the removal of water vapor, the powder bed reduces under drier conditions and will tend to produce a finer tungsten metal powder as well as a narrow particle size distribution. Dwell time in the furnace is controlled by a combination of the furnace rotation speed and the incline of the furnace. In order to produce coarse tungsten, the rotary furnace must be adjusted to simulate a pusher-type furnace by using a low rotational speed and low incline, as well as a high powder feed rate and high temperature.

WO_3 may also be reduced by hydrogen, utilizing a fluidized bed reactor (Buerkel, Wightman, & Tomalin, 1992). Reduction of WO_3, $WO_{2.9}$, or $WO_{2.72}$ is achieved by passing hydrogen gas through the powder bed. Reduction generally takes place between 650 and 1000 °C. In order to speed up the reaction, it is suggested that the gas initially have a H_2:H_2O ratio set at the equilibrium partial pressure for the formation of WO_2. When the bulk of the powder bed has been converted into WO_2, it is recommended that the fluidizing gas be changed to dry hydrogen. The benefits of fluidized bed processing is the production of a narrow particle size distribution and the potential for production of fine particles due to the avoidance of growth due to CVT. Recently, Powdermet (Euclid, OH, USA) has reported the ability to use fluidized bed technology in the fabrication of nanometer-sized W particles in quantities of tens of kilos per run (Sherman, Doud, & Hardy, 2011). The resulting powder is highly agglomerated but has an average grain size near 50 nm and a specific surface area of approximately 15 $m^2\ g^{-1}$. Through the addition of carbon to the system, the nanometer-sized tungsten metal can be converted into WC. Kemp Development (Houston, TX, USA) has combined the fluidized bed and rotary furnace technologies to conduct reduction under hydrogen (Kemp, 1995).

1.06.1.3.2 Reduction by Carbon

Prior to the development of hydrogen reduction, production of tungsten metal from WO_3 was carried out via a carbothermal reduction process. The process consists of blending WO_3 with fine carbon powder in a sealed carbon boat and then heating the boat between 650 and 1050 °C. A thermogravimetric study by Venables and Brown (1996a) indicated that the reaction between WO_3 and graphite is sluggish up to about 900 °C. Reduction with carbon was observed to follow the same basic stepwise reduction as noted with hydrogen reduction; WO_3 to $WO_{2.9}$ to $WO_{2.72}$ to WO_2 and then to W metal (Venables & Brown, 1996b). A by-product of the WO_3 reduction with carbon is CO_2, with the CO_2 reacting with additional carbon to form CO. Complicating the reduction process is that temperatures above 1050 °C are necessary to fully reduce WO_3 to tungsten metal. However, at temperatures above 850 °C, tungsten metal will react with carbon to form W_2C and WC, with full saturation occurring rapidly at about 1400 °C. As such, the tungsten metal produced via carbon reduction will always contain some fraction of carbide.

1.06.1.3.3 Emerging Bulk Reduction Technologies

Tungsten powder can also be produced from oxide by an electrolytic process referred to as the FCC-Cambridge method (Parker, 2005). Developed in 1997 at Cambridge University, the process is touted as being a green technology due to the lower energy usage in the reduction process as compared to thermally reducing oxides at elevated temperatures. Another aspect of its green ability is that it uses only benign salts for the electrolytic solution. The technology is indeed intriguing at a time with rising energy costs and heightened concerns over the impact of industrial chemicals, in light of the EU-REACH legislation; however, an insufficient number of studies have been conducted to allow for a full assessment on the ability of this process to produce tungsten metal powder with tailored particle sizes or distributions. Information on the ability to pre-dope the oxide prior to reduction or on retention of unwanted impurities is also lacking. Until a greater body of work fully explores the benefits and limits of the system, this technology will remain unproven.

As reported by Lackner, Filzwieser, and Paschen (1996), the reduction rate can be increased substantially by injecting the oxide powder directly into a flowing stream of hydrogen at temperatures above 1000 °C. The "laminar flow furnace" allows for maximum separation of the entrained oxide particles, essentially preventing particle growth due to CVT. It was noted that shortly after introduction of the powder into the furnace, the oxide particles crack due to the surface stress of oxygen depletion at the particle surface. On initiation of the reduction process, the cracked particles will fracture, creating a finer product than the initial feedstock. Although the laboratory scale production was limited, 1–2 g min^{-1}, the processing method has the potential to yield both narrow particle size distributions and fine particle sizes.

1.06.1.3.4 Emerging Submicron Reduction Technologies

As applications develop for ever smaller WC-based tools, the need for particles approaching the nanoscale has required novel production techniques (Fang, Wang, Ryu, Hwang, & Sohn, 2009; Gille et al., 2002). One such technique is the use of sol–gel synthesis for the production of particles in the range of 10–30 nm (Raghunathan & Bourell, 1999). The synthesis mixed sodium tungstate with a gel, forming material such as alcoholized cupric acetate hydrate. The mixture was then reduced in a hydrogen environment to produce a nanoscale aerogel.

Plasma Processes Inc. (Huntsville, AL, USA) has developed a technique for producing nanometer-sized tungsten powders (McKechnie, Antony, O'Dell, Power, & Tabor, 2009). Proprietary tungsten precursors were processed through a plasma flame that vaporized the feedstock. On exiting the plasma, the nanometer-sized tungsten particles nucleated from the vapor. The rapidly quenched particles were collected in a controlled atmosphere to prevent oxidation. While the majority of the collected powder was determined to be metallic tungsten by X-ray Diffraction Spectroscopy, a small fraction of WO_3 was also present. In order to remove any remaining WO_3, the powder was then heat-treated in hydrogen. A 1 h hydrogen treatment results in XRD traces with only tungsten metal peaks; however, the oxygen level is still high. Longer hydrogen treatments, up to 10 h, reduce the oxygen content to levels commonly seen for ultrafine tungsten powder. Average powder particle sizes were found to be approximately 40 nm for the test lots. The process has been upscaled to produce in excess of 5 kg h^{-1}.

Gao and Kear (1996) stepped even further back in the process by proposing the direct reduction of ammonium metatungstate (AMT). Reductive decomposition of AMT in flowing hydrogen at temperatures of 450–500 °C utilizing a controlled stepwise heating program allowed the formation of tungsten metal without the formation of any tungsten oxide intermediates. Average particle sizes were in the order of 30 nm, with actual grain sizes in the range of 5–7 nm. The method was expanded to include other reducible tungsten compounds and was patented by Nanodyne (New Brunswick, NJ, USA) (Gao, Kear, & Seegopaul, 1999).

Slightly larger but still ultrafine tungsten powder was fabricated by Kim, Kim, and Kwon (2005) using an electrical explosion of wires technique. The technique used a high voltage discharge to evaporate fine tungsten wire. The vaporized tungsten condensed into ultrafine powder as it cooled in an argon environment. Continual production was achieved with wire being supplied by a spool delivery system. The resulting particles were smooth spheres less than 0.5 μm. Air passivation was used to stabilize the product.

Nanostructured tungsten metal powder can also be obtained through the high-energy milling of larger metal particles (Bose, Klotz, Kellogg, Cho, & Dowding, 2008). A horizontal high energy mill was used to produce the nanostructured powder. The reduction in the powder structure required extensive milling, greater than 20 h. The extended milling resulted in a high level of contamination from the milling media and container. This method can also be used to incorporate small amounts of dopant particles into the metal.

Table 7 Physical properties of WC

Property	*WC*
Molecular weight	195.87
Crystal structure	Hex (Bh)
Lattice constants	$a = 0.29065$ nm; $c = 0.28366$ nm
Density	15.7 g cm^{-3}
Melting point	2720 °C
Microhardness	1200–2500
Modulus of elasticity	696,000 N mm^{-2}
Transverse rupture strength	550–600 N mm^{-2}
Coefficient of thermal expansion	$a = 5.2° \times 10^{-6}\ \text{K}^{-1}$; $c = 7.3 \times 10^{-6}\ \text{K}^{-1}$
Thermal conductivity	121 W $(\text{m}\cdot\text{K})^{-1}$

1.06.1.4 Tungsten Carbide Production

Tungsten forms two distinct carbide compounds: a monocarbide, WC, and a subcarbide, W_2C. Of the two phases, WC has the greatest industrial interest due its ubiquitous use in hardmetal applications. WC appears as a dull gray powder. WC has a small range of homogeneity, extending from 6.13 wt% C to down to about 6.00 wt % C at elevated temperatures (Exner, 1979). Selected properties of WC are presented in Table 7 (Kirk-Othmer, 1978a, p. 492).

WC is produced by a handful of industrial techniques, with the method depending on both the desired size of the particles and the end application. Among the most common carburization methods are carburization of W metal in static bed boats, or rotary furnace, the Menstruum process, reduction/carburization of WO_3. Other techniques with industrial potential include fluidized bed carburization and chemical vapor reaction. Numerous other techniques have been developed, especially for the production of submicron and nanocarbides, with some enjoying a degree of industrial acceptance.

Post carburization processing of the WC powder generally needs mechanical deagglomeration. The deagglomeration, especially for traditional carburized powder, is necessary so that an accurate sizing of the powder can be conducted. The WC particle size is the primary powder property used in specifying materials. The average particle size is reported based on the FSSS measurement of the as supplied powder. FSSS values on laboratory milled powder provide information on the degree of agglomeration. Based on the FSSS values, WC powder is divided into defined particle size ranges, with a classification designation indicated in Table 8.

While the average particle size, FSSS, is the defining property in terms of differentiating between powder grades, significantly dissimilar powders can yield the comparable FSSS values. In order to obtain the desired property in the final sintered product, other properties need to be taken into consideration.

The particle size distribution will partially determine the homogeneity of the final sintered microstructure. A narrow distribution of particles may yield the same FSSS value as a powder comprising a broad distribution centered on that same value, or even a powder consisting of a multi-modal distribution of particles. However, the sintered microstructures will be substantially different. The distribution can be controlled partially through reduction conditions, especially the bed depth or through post-processing classification.

While the grain size distribution is important in determining the final sintered grain size, it is also necessary to consider the WC grain size within the particles. Each WC powder particle is composed of several individual

Table 8 Industry designation of WC particle sizes

Mean particle size (μm)	*Designation*
<0.1	Nano
0.1–0.5	Ultrafine
0.5–0.8	Submicron
0.8–2.1	Fine
2.1–5.0	Medium
5.0–11.0	Coarse
>11.0	Extra coarse

WC grains of potentially differing sizes. Nucleation and growth kinetics will, in part, determine the degree of poly-crystallinity of the particles. The key factors in determining the WC grain size are the carburization temperature and dwell time at temperature. Carburization is essentially a diffusion-controlled process, with an exponential dependence on the carburizing temperature, followed by coarsening of the individual WC grains based on free energy. Higher carburization temperatures and longer dwell times will yield particles with a limited number of large WC grains, while low temperatures and short cycle times will produce particles with numerous small grains.

Additional properties of interest are specific surface area, apparent density of the powder, press density, carbon content, presence and concentration of grain growth inhibitors, and the level of trace impurities, including oxygen.

1.06.1.4.1 Standard Tungsten Carbide Production

The most common method used to produce WC, referred to as traditional carburization or fusion and used for most WC powder types, consists of pushing a graphite boat of blended tungsten metal and carbon powders through a furnace at elevated temperatures, 1200–2000 °C, in a reducing atmosphere. Carburization takes place in a diffusion-controlled process via a shrinking core mechanism. According to Zhengji (1987), the carburization process begins with the formation of a thin surface layer of WC. After the initial WC formation, carbon diffusion into the particle results in the formation of W_2C, which grows inward to consume the tungsten metal core (Figure 12). As the reaction progresses, the outer layer of WC will grow inward following and eventually consuming the W_2C. Stages 2 and 3 will take place concurrently until such time as the tungsten metal core is consumed.

Stage 1 (initial layer formation):

$$W + C = WC$$

Stage 2 (W core consumption):

$$WC + W = W_2C$$

Stage 3 (W_2C consumption):

$$W_2C + C = WC$$

Owing to the high melting temperature of tungsten metal powder, and the associated carbides, and the lack of a CVT mechanism, particle growth during the carburization process is generally minimal. Some particle growth can be expected for particle sizes below 0.8 µm and at carburization temperatures above 2000 °C, both of which are related to the time the powder spends at the elevated temperature. An issue of greater concern is the average WC grain size within the individual particles. The average WC grain size is influenced by several factors, including temperature, carbon content, dopant levels, and dwell time (Lassner, 1989; Zhengji, 1987).

Basu and Sale (1978) presented a reduction–carburization process using CO to convert various tungsten oxides to WC. The study confirmed the aforementioned conversion pathways to convert WO_3 to tungsten metal and subsequently tungsten metal to WC. One of the more interesting findings is that the morphology of the WC can be altered based on which oxide is used as a feedstock. Reduction–carburization of $WO_{2.72}$ will result in the formation of WC whiskers with a thickness of 0.2–0.5 µm. This pathway opens up the potential for the preparation of very fine WC particles. In a related study, the production of WC with a variety of $CO:CO_2$ ratio was investigated (Alonso, Morales, Sales, & Becerril, 1987). The study determined that the reduction–carburization reaction proceeds best with a 100% CO atmosphere, as the CO_2 level increased, the reaction rate decreased.

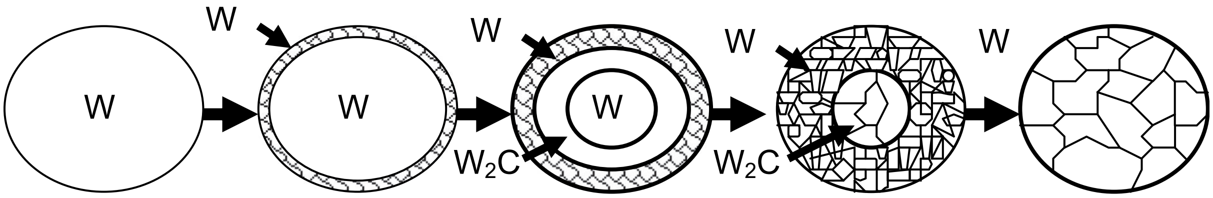

Figure 12 Schematic representation of W metal carburization.

WC can also be produced from a reduction–carburization of WO_3 or tungsten metal from a mixture of CH_4 and H_2 (Leclercq et al., 1996). The study indicated that carburization takes place in two stages, with W_2C forming first, followed by WC. Based on specific conditions, it should be possible to select the final product. The rate of reaction was highly dependent on the total pressure. The authors also determined that WO_3 was not directly carburized but was rather converted into tungsten metal prior to carburization.

Alternate methods for producing WC include the use of scheelite as the feedstock. Gomes, Raddatz, and Carnahan (1985) heated a mixture of scheelite concentrate, NaCl, and sodium metasilicate at 1100 °C. A decantation removed the slag, and then, CO or methane was introduced to the remaining halide-tungstate phase to form WC. Another scheelite reduction–carburization reaction was detailed by Johnston and Nguyen, whereby scheelite was blended with carbon and reacted at 1224 °C (Johnston & Nguyen, 1996). Complete carburization was found to be dependent on the initial scheelite particle size. Carburization occurred via a three-stage reaction pathways, which take place simultaneously. The reactions governing the stages were found to proceed as follows.

$$3CaWO_4 + 6C = CaWO_6 + 2W + 6CO$$

$$CaWO_6 + 3C = 3CaO + W + 3CO$$

$$2W + 2CO = W_2C + CO_2$$

$$W_2C + 2CO = 2WC + CO_2$$

For very coarse powders, an alternate technique referred to as a macro process can be utilized. The macro process is derived from the Menstruum process developed by McKenna in 1937. The original process was established to produce mixed carbides, specifically (W,Ti)C from a nickel melt (Schwarzkopf & Kieffer, 1953). The present process combines an aluminothermic reduction and carburization of tungsten ores at temperatures above 2500 °C to yield WC crystals well in excess of 40 μm (Smith, 1980). The reaction is carried out in a graphite kiln, constructed to withstand the heat of the thermic reaction. The kiln is loaded with a predetermined ratio of tungsten ore, iron oxide, aluminum metal, and calcium carbide to initiate the reaction. Once the reaction becomes self-sustaining, the remaining of the reactants is added. The reactions involved in the process are as follows.

$$3Fe_3O_4 + 8Al = 9Al + 4Al_2O_3$$

$$MeWO_4 + CaC_2 + 2Al = WC + Me + CaO + Al_2O_3$$

The reaction takes only about 1 h, after which the products are left to cool prior to post-processing. Approximately 22 tons of stoichiometric WC will be formed that needs to be removed from the crystal mass after the slag layer has been separated. The unwanted elements are removed through a combination of dissolution by water and acid.

WC can also be produced in a rotary furnace from direct carburization of tungsten metal powder with carbon or in a two-step process involving the carbothermal reduction of a tungsten oxide, followed by the complete carburization of the products to WC (Hara & Miyaka, 1974). As in the production of tungsten metal, the constant motion of the powder bed limits particle growth due to CVT as well as agglomeration due to contact sintering. This technique is ideally suited for the production of submicron and finer WC.

As noted above, Powdermet utilized fluidized bed technology in the fabrication of nanometer-sized WC particles from WO_3 in quantities of tens of kilos per run (Sherman et al., 2011). The resulting powder was determined to have a particle size less than 100 nm. The particles were highly agglomerated but were said to be easily separated on milling. Production of submicron WC in a fluidized bed has also been detailed for the conversion of $WO_{2.9}$ under an atmosphere of H_2 and CO (Luidold & Antrekowitsch, 2008).

1.06.1.4.2 Submicron (0.8–0.2 μm) Tungsten Carbide Production

Production of uniform-sized WC in the range of 0.2–0.8 μm requires tight control on the production parameters of traditional carbide production from the initial calcination steps through to carburization, with parameters such as grain size, size distribution, trace element concentration, addition of grain growth inhibitors, and impurities tightly controlled (Bock & Zeiler, 2002). The importance of the WC production was illustrated by Caspers, Sauberlich, and Reiss (2008) in a study examining the effects of carburization properties on powder properties and subsequently on the properties of WC-Co–sintered bodies. Standard production and laboratory WC powders in the range of 86–200 nm were produced in a range of temperatures. The greatest effect on the powder was the change in specific surface area, which then influenced key properties in the final sintered hardmetal, such as the hardness.

Alternate methods to produce WC in this size range include a two-stage carbothermal reduction process (Kimmel, Shaffer, Pinkowski, & Harris, 1987). The first stage of the process carbothermally reduces a blend of WO_3 and carbon to a mixture of W, W_2C, and WC. The carbon balance is then adjusted to full saturation prior to the second carburization stage where the powder is traditionally carburized. The key benefit with this method is the avoidance of tungsten particle growth via CVT. As an alternative to blending with carbon, Koc and Kodambaka (2000) devised a carbothermal reduction–carburization process that utilizes carbon-coated WO_3 as the feedstock. The WO_3 was pyrolytically coated with carbon in a furnace at 600 °C using propylene as the carbon source. The carbon-coated powder was then heat-treated at various temperatures, up to 1400 °C, to yield WC powder. WC particle size was generally less than 200 nm, with numerous particles in the range of 50 nm.

A report by Welham (2000) detailed the process, whereby WC of approximately 0.3 μm was produced from scheelite which was ball-milled with carbon and then carbothermally reduced. Evidence of W_2C formation was partially offset by the fact that extended ball milling decreased the WC formation temperature by about 300 °C.

Dow Chemical Company (Midland, MI, USA) developed a method of producing submicron WC referred to as rapid carbothermal reduction (Dunmead, Moore, Weimer, Eisman, & Henley, 1995). Tungsten oxide and carbon black are milled together to produce a fine mixture. The invention allows for two methods of production. Process 1 is referred to as the drop method, whereby the blended powder is allowed to drop into a preheated graphite crucible in the hot zone of an induction furnace. The temperature is typically 1500 °C, and the reaction time can range from 5 min to 2 h. The heating rate for the drop method is estimated to be between 100 and 10,000 $K\,s^{-1}$. The progress of the reaction is followed by monitoring the CO level, so as to determine the completion of the reaction. The second process is referred to as the entrainment method. In this method the blended powder is entrained in a stream of non-oxidizing gas as it flows into a vertical graphite furnace. According to the patent, the heating rate is between 10,000 and 100,000,000 $K\,s^{-1}$, with residence time in the furnace of up to 10 s. The entrainment gas expands outward as it enters the furnace column, spreading the powder stream into a diffuse cloud. By separating the powder particles, agglomeration and particle growth are minimized. The reacted powder exits the reaction chamber and is collected in a cooled stainless steel chamber. If the powder produced via the entrainment method is not fully carburized, it can then be milled with carbon to bring it up to stoichiometric levels and then processed via the drop method or simply put into graphite boats and processed through a standard pusher-type furnace.

1.06.1.4.3 Nano (<0.2 μm) Tungsten Carbide Production

Production of nanoscale WC represents a challenge beyond those inherent in the production of submicron WC.

One method for nanoscale WC powder production is the use of high-energy ball mills to mechanically reduce the size of larger WC (Butler, Lu, Fang, & Rajammani, 2007). In order to improve the milling efficiency and decrease the milling time, a planetary mill can be used to increase the then kinetic energy of the milling media. Using a planetary ball mill, Butler et al. (2007) produced 6 nm size particles in 24 h, as compared to 300 h as required for standard ball mills. The study revealed that the bulk of the size reduction takes place within the first 12 h, with only moderate particle reduction in the following 12 h. Although the powders possessed a high level of lattice stress, a post-production annealing of the powder did not result in significant particle growth below 600 °C.

Attempts to directly synthesize nanoscale WC include the use of high-energy ball milling of WO_3, Mg, and C powders to produce a mixture of MgO and WC in a process termed mechanical solid-state reduction (El-Eskandarany et al., 1996). After completion of the reaction, the MgO is acidically leached to leave the nanoscale WC.

Nanograined WC has also been prepared by combining the reduction and carburization reactions using a mixture of hydrogen and CO (Seegopaul, Gao, & Kear, 1998). The powder is heated slowly to about 700 °C in order to avoid the formation of W_2C.

Nanostructured WC can also be prepared through the reduction–carburization of APT with a gaseous mixture of H_2 and CH_4 (Medeiros, da Silva, Sasakic, Souza, & Gomes, 2005). The use of APT as a starting material allows the reaction temperature to be reduced to 850 °C. The resulting powder has a highly porous structure, with a crystallite size of 18 nm and a specific surface area of 35 $m^2\,g^{-1}$. The reaction sequence was determined to proceed as: $APT \rightarrow WO_3 \rightarrow WO_2 \rightarrow W \rightarrow W_2C \rightarrow WC$.

Rather than the use of WC to produce a dense structure, Zhang et al. (2005) used spark plasma sintering to reduce, carburize, and sinter a blend of WO_3 and carbon. In order to allow complete reaction, the process was carried out at 1300 °C for 3 min. The resulting structures were 99.8% dense and had a grain size of 500 nm. The reaction process was found to progress as standard reduction and carburization reactions detailed above.

Nanocrystalline WC has also been prepared using an ion arc method (Li, Zhang, Zhang, Wang, & Wu, 1998). Utilizing a tungsten rod as the cathode and a graphite block as the anode, an arc was struck between the two poles under a nitrogen environment. Characterization revealed the powder to be a mixture of WC and W_2C, both of which were encapsulated in crystalline graphite. The graphite encapsulation renders the nanoparticles stable in air at room temperature. The average grain size was determined to be about 12 nm.

WC has also been synthesized by gas-phase reactions of tungsten halides with hydrogen and methane (Lamprey, Culbertson, & Ripley, 1966). The process consists of introducing a tungsten halide, such as WCl_6, into a vaporizing zone to create a gaseous species, which is then blended with H_2 and CH_4 and preheated to between 450 and 1300 °C inside an argon-shrouded reaction region. A spontaneous and self-sustaining reaction results in the creation of uniform WC and W_2C particles of size less than 100 nm. An investigation by Hojo, Oku, and Kato (1978) was undertaken to determine the reaction pathways. It was discovered that the carbon to tungsten ratio in the products increased with an increase in the reaction temperature and/or an increase in the methane concentration. Nearly pure WC was formed at a reaction temperature of 1400 °C. The final particle size was also observed to be dependent on the reaction temperature, with low temperatures yielding particles in the size range of 40–50 nm and higher reaction temperatures producing particles in the range of 80–110 nm. The reaction sequence was observed to follow a two-step process, with the first step being the formation of tungsten metal and then the subsequent carburization. For high temperature mixing of the reactants, the two stages occur simultaneously, whereas at low temperatures, they are unique stages.

$$3WCl_6 + 3H_2 = 3W + 6HCl$$

$$W + CH_4 = WC + 2H_2(\text{also} W, W_2C)$$

1.06.2 Other Refractory Carbide Species

WC–Co hardmetal grades often make use of additives to provide enhanced performance. Among the more common carbide additives are vanadium carbide, Cr_3C_2, TiC, NbC, and TaC, and some combinations thereof. These carbide additions may be admixed to the WC powder when it is blended with wax, or in some cases may be co-carburized with the WC (Johnson, Runyon, & Morton, 2008). Many of the species act as grain growth inhibitors for WC, while others provide direct machining benefits. NbC and TaC are added to WC–Co grades primarily to provide enhanced impact resistance and reduce cyclic fatigue, especially at elevated temperatures. The production methods for several species are detailed in the following sections. Although numerous experimental techniques have been established, only the primary methods are presented in this chapter. Material properties for those same materials are presented in Table 9 (Kirk-Othmer, 1978a, p. 492).

1.06.2.1 Titanium Carbide Production

Titanium carbide, TiC, is generally prepared from high-purity titanium dioxide blended with carbon black between 1700 and 2100 °C (Schwarzkopf & Kieffer, 1953; Kirk-Othmer, 1978b, pp. 133–135). The

Table 9 Physical properties of various carbides

Property	*TiC*	*NbC*	*TaC*
Molecular weight	59.91	104.92	192.96
Crystal structure	FCC (B1)	FCC (B1)	FCC (B1)
Lattice constants (nm)	0.43305	0.4470	0.4454
Density (g cm^{-3})	4.93	7.78	14.48
Melting point (°C)	2940	3613	3825
Microhardness	3000	2000	1800
Modulus of elasticity (N mm^{-2})	451,000	338,000	285,000
Transverse rupture strength (N mm^{-2})	200–400	300–400	350–450
Coefficient of thermal expansion (K^{-1})	7.74×10^{-6}	6.65×10^{-6}	6.29×10^{-6}
Thermal conductivity (W (m·K)$^{-1}$)	21	14	22

reduction–carburization reaction can be conducted in vacuum or argon, where the reaction proceeds as $TiO_2 \rightarrow Ti_3O_5 \rightarrow Ti_2O_3 \rightarrow TiO \rightarrow TiC$. In the case of a reduction using hydrogen, a reaction with liberated CO is expected to form hydrocarbons, specifically C_2H_4, which may then react with the titanium oxide species in another reduction pathway (Schwarzkopf & Kieffer, 1953).

Large-scale TiC particles can be produced if the oxides or ores are blended with carbon in a Menstruum process (Kirk-Othmer, 1978c, pp. 826–834).

TiC has also been synthesized by gas-phase reactions of titanium halides with hydrogen and methane (Lamprey et al., 1966). The reaction is analogous with that described above for the formation of WC, only that the precursor here is $TiCl_4$. This method may be used for the formation of submicron- and nanometer-sized particles.

1.06.2.2 Niobium Carbide Production

Niobium carbide, NbC, can be produced via a number of processes, some of which are detailed below. The primary method for producing NbC is through a reduction–carburization reaction of Nb_2O_5 with carbon, between 1600 and 2000 °C (Schwarzkopf & Kieffer, 1953; Kirk-Othmer, 1978c, pp. 826–834; Miller, 1959; Gupta & Suri, 1994). The reaction can be carried out under vacuum, argon, or hydrogen. The reaction most likely proceeds through a series of niobium oxide species, with the overall reaction appearing as follows.

$$Nb_2O_5 + 7C = 2NbC + 5CO$$

Shimizu, Sasaki, and Morita (2005) used Nb_2O_5 blended with carbon under flowing hydrogen to generate ultrafine NbC. The reaction pathway did not identify the intermediates of NbO or Nb metal and was observed to be as follows.

$$Nb_2O_5 + 3H_2 = 2NbO_2 + 3H_2O$$

$$NbO_2 + 3C = NbC + 2CO$$

NbC has been carbothermally produced from the reduction–carburization of Nb_2O_5 in a flowing gas mixture of $CH_4 + H_2$ (Kim, Bugli, & Djega-Mariadassou, 1999). The reaction, with a catalyst, was found to take place between 800 and 1000 °C, although the reaction times were fairly lengthy. The investigation determined the reaction from NbO_2 to NbC to have the form shown below. Carbothermal reduction of NbC can also be produced in a rotary furnace with a flowing gas mixture of $CH_4 + H_2$ (Fontes, Gomes, Olivera, Souza, & Sousa, 2004). The study suggests that the use of a rotary furnace can substantially reduce the total reaction time, as compared to the carbothermal reduction conducted using a static bed process.

$$NbO_2 + 3CH_4 = NbC + 2CO + 6H_2$$

Teixeira da Silva, Schmal, and Oyama (1996) conducted an investigation into the reaction mechanism for the reduction–carburization of Nb_2O_5 to NbC in an atmosphere of $CH_4 + H_2$. Their findings indicated that the first stage of the reaction Nb_2O_5 to NbO_2 was kinetically fast. The subsequent reaction from NbO_2 to NbC was the rate-limiting step and involved the formation of a niobium oxycarbide, $Nb(O_xC_y)$, intermediate. The intermediate phase was not detectable by bulk XRD; however, the phase was identified by X-ray Photoelectron Spectroscopy. The authors also determined that NbO was not an intermediate in the transformation.

NbC has also been synthesized by gas-phase reactions of niobium halides with hydrogen and methane (Lamprey et al., 1966). The reaction is analogous with that described above for the formation of WC, only that the precursor here is $NbCl_5$. This method may be used for the formation of submicron- and nanometer-sized particles.

1.06.2.3 Tantalum Carbide Production

Tantalum carbide, TaC, is primarily produced through the reduction–carburization of Ta_2O_5 with carbon at temperatures from 1600 to 2000 °C (Kirk-Othmer, 1978d, pp. 547–560; Miller, 1959; Schwarzkopf & Kieffer, 1953). The general form of the reaction is (Shimada, Koyama, Kodaira, & Matsushita, 1983) as follows.

$$Ta_2O_5 + 7C = 2TaC + 5CO$$

Similar to W and Nb, TaC has also been synthesized by gas-phase reactions of tantalum halides with hydrogen and methane (Lamprey et al., 1966). The reaction is analogous with that described above for the formation of WC, only that the precursor here is $TaCl_5$. This method may be used for the formation of submicron- and nanometer-sized particles. A subsequent investigation determined that the minimum temperature for the reaction to proceed was 1400 °C. Increasing the reaction temperature to 1600 °C had no appreciable effect on the particle size range, with an estimate that 80% of the particles produced were between 30 and 50 nm (Crayton & Gridley, 1971).

1.06.2.4 Mixed Carbide Production

Numerous mixed carbides are known to exist, including WC–TiC, WC–TaC, NbC–TaC, and TiC–NbC–TaC. Although some species such as WC–TiC can be used directly with a binder material to produce cutting tools, others are formed to be used as additives to WC–Co hardmetal grades (see section on cutting tools). Mixed carbide species can be prepared from several of the aforementioned techniques for producing WC (Kirk-Othmer, 1978e, pp. 501–503). One technique, utilized for making species such as (W,Ti)C and (W,Ti,Ta)C, is co-carburization of mixed metal oxides with carbon black. Carburization usually takes place under hydrogen at temperatures from 1600 to 1800 °C. The most common method for producing mixed NbC–TaC carbides is direct reduction–carburization of blended oxides as per the standard process for the individual species (Schwarzkopf & Kieffer, 1953). Alternately, the individual metal powders can be blended along with carbon and then carburized under hydrogen at temperatures from 1500 to 1800 °C. Or, a refractory oxide such as TiO_2 can be added to a blend of W metal or WC and carbon and then reduced under hydrogen (Kirk-Othmer, 1978e, pp. 501–503).

WC–TiC was first claimed to have been produced by McKenna from the Menstruum process (Schwarzkopf & Kieffer, 1953). The Menstruum process can also be used to produce a variety of other carbide species, depending on the mix of ores, metals, or carbide additives.

Finally, mixed carbides can be prepared by diffusion annealing of mixed preformed carbides at elevated temperatures of 1500–1900 °C. The diffusion process is often aided through the addition of Co, Fe, or Ni, in order to promote diffusion (Kirk-Othmer, 1978e, pp. 501–503).

1.06.3 Titanium Carbonitride

Titanium carbonitride, TiCN, is a cermet material with a wide composition range dependent on the ratio of C:N, usually expressed as $TiC_{1-x}N_x$. TiCN has several properties that make it of interest to the cutting tool industries. These properties include high hardness, high wear resistance, and chemical inertness. Typical properties of TiCN are listed in Table 10 (Clark & Roebuck, 1992; Jha & Yoon, 1999).

Hard TiCN particles are combined with a ductile binder phase to yield a cutting tool for applications beyond the capabilities of standard WC–Co grades. Applications using TiCN powder require very fine particle sizes and narrow particle size distributions. Various processing strategies are currently used to produce TiCN powder, with powder currently available in the market in the size range of 0.5–2.0 μm. Among the more commercial methods are plasma reaction, carbothermal reduction of TiO_2, solid-state diffusion of carbon and nitrogen into Ti metal of carbide and nitride blends, self-propagating high-temperature synthesis, and titanium halide reactions involving $TiCl_4$ (Davidson, Shirts, & Harbuck, 1989; Leparoux, Kihn, Paris, & Schreuders, 2008).

Plasma synthesis of TiCN powders utilizes Radio Frequency inductively coupled plasma to control the stoichiometry and size of the powder. Precursors such as Ti metal or TiH are injected into the plasma, where they

Table 10 Physical properties of TiCN

Property	*TiCN*
Molecular weight	59.9–61.9
Crystal structure	FCC (B1)
Density (g cm^{-3})	6.0–6.8
Melting point (°C)	2950
Microhardness HV30	1400–1750
Transverse rupture strength (N mm^{-2})	1400–1900
Coefficient of thermal expansion (K^{-1})	9.0×10^{-6}
Thermal conductivity (W (m·K)$^{-1}$)	10

are evaporated in an RF plasma. The vaporized species are then reacted with a hydrocarbon source to form TiCN (Davidson et al., 1989). Work by Grabis and Zalite (2005) demonstrated the ability to produce TiCN nanoparticles with an average grain size below 30 nm over a wide range in composition.

The carbothermal reduction of TiO_2 accompanied by the simultaneous carbonitridation is considered to be the high-volume, low-cost synthesis process in an industry. The oxide feedstock is blended with carbon and reduced at elevated temperatures of 1300–1700 °C. The reduction of TiO_2 liberates CO, with further reactions producing a locally equilibrated amount of CO_2. The nitrogen flow will serve as a sweep gas for the CO/CO_2 species and will also provide the reactant for the nitridation process (Berger, Gruner, Langholf, & Stolle, 1999; Monteverde, Medri, & Bellosi, 2001). The reaction sequence is as follows.

$$TiO_2 \rightarrow Ti_nO_{2n-1} \rightarrow Ti_3O_5 \rightarrow TiC_xN_yO_z \rightarrow TiC_xN_y$$

Jha and Yoon (1999) have studied the carbothermal reaction in which the atmosphere ranged from pure N_2 to blends of $N_2 + H_2 + CO$ or $NH_3 + H_2 + Ar$. The time required for complete conversion is dependent on the reaction temperature. Alteration of the initial TiO_2:C ratio or the ratio of the gases will also affect the degree of completion and mixture of phases formed in addition to TiCN, primarily Ti_3O_5 and C.

The high temperature diffusion process of preparing submicron TiCN can proceed with either TiN or TiC as feedstock (Monteverde et al., 2001; Pastor, 1987). Three reaction sequences are available depending on the feedstock. When TiN is one of the starting materials, it is blended with TiC powder and then mixed by ball milling. The powder blend is then diffusion-treated under flowing nitrogen to yield TiCN, with the ratio of C:N determined by the ratio of the initial powders. Or, the TiN can be blended with carbon between 1300 and 1700 °C. If TiN is not used as one of the starting materials, then Ti metal and TiC can be blended by ball milling and then nitrided in flowing nitrogen at elevated temperatures.

A self-propagating, high-temperature synthesis of TiCN has been reported by Eslamloo-Grami and Munir (1994). The process combines titanium and carbon, pressed into cylinders, with either nitrogen gas or liquid nitrogen. Combustion of the cylinder is initiated with radiant heat from a tungsten coil. On initiation of the reaction, the reaction front progresses to the opposite end of the compact, with temperatures in the range of 2100–2600 °C. It has been proposed that the reaction takes place in a two-step process. The first step being a partial carburization of Ti metal, followed by the nitidation to produce the TiCN.

Halide production of TiCN uses an oxidizing vapor such as magnesium or sodium to reduce the $TiCl_4$ in a reaction vessel at elevated temperatures of 500–1250 °C. The reduced Ti vapor condenses to form very fine metal powder, which rapidly reacts with any reactive species introduced into the reaction zone, such as nitrogen, ammonia, and methane (Davidson et al., 1989). As of 1999, H. C. Starck (Goslar, Germany) was known to be using this method on a pilot plant scale to produce nanophase TiCN (Lassner & Schubert, 1999).

1.06.4 Cobalt

Cemented carbides combine the hardness and strength of metallic carbide WC, TiC, TaC, or carbonitrides (e.g. TiCN) with the toughness of a metallic alloy binder (Co, Ni, Fe) in which hard particles are evenly distributed to form a metallic composite. Although other binder metals such as Ni and Fe widen the scope of carbides in certain area, cobalt is still the main binder metal for carbides used in tooling industry. Cobalt fulfills all the needs of a binder metals, while others like Ni, Fe, etc. only fulfill some of the desired attributes of a binder metal.

Due to limited availability of cobalt ores, it is mainly produced as the by-product of more abundant copper and nickel metals. Cobalt-processing developments are recently reviewed by Fisher (2011). The other source of cobalt production is cemented carbide scrap. Hydrometallurgical processing of cobalt from the ores and scrap typically produces pure cobalt compounds such as cobalt oxides: Co_3O_4, CoO, cobalt hydroxides: $Co(OH)_2$, $Co(OH)_3$, $HCoO_2$, $CoCO_3$, which are typically used as the feed for cobalt metal powder production. Cobalt oxalate and basic cobalt carbonate are also used as the feeds for making submicron cobalt metal powders. From these compounds, cobalt powder is made via hydrogen reduction in the temperature range of 350–600 °C. For carbide production, submicron (<1 μm) to extra fine (1–2 μm) size powders are typically made.

Sha, Kai-hua, and Min (2006) have reviewed methods of making cobalt metal powders in China. It is reported that there are two processes for preparing cobalt powders: (1) direct reduction of cobalt oxalate in hydrogen (one-step method) and (2) cobalt oxalate is calcined into Co_2O_3 or Co_3O_4 in the air and then cobalt oxide is reduced in hydrogen.

In other methods (Cheresnowsky & Vanderpool, 1984; Ehrreich & Reti, 1974; Gingerich & McClintic, 1980; Matti et al., 1980), aqueous solution of cobalt chloride is oxidized in the presence of ammonia and respective ammonium salt and a catalyst to convert cobalt(II) to cobalt(III) hexammine chloride. During this conversion, cobalt is purified from nickel. Cobalt hexammine chloride solution is decomposed in caustic to make $Co(OH)_3$, which is converted into Co_3O_4 for reduction in hydrogen to make extra fine cobalt metal powder.

Submicron cobalt metal powders are made via thermal decomposition of cobalt oxalate, $CoC_2O_4 \cdot 2H_2O$ (Baco-Carles, Arnal, Poquillon, & Tailhades, 2008; Gingerich & McClintic, 1980). Gorge, Meese-Marktscheffel, Naumann, Olbrich, and Schrumpf (2004) patented conversion of spheroidally agglomerated basic cobalt(II) carbonate and spheroidally agglomerated cobalt(II) hydroxide, process for making submicron cobalt metal powder.

References

Agar, G. E. (1984). Scheelite flotation process, United States Patent No. 4,488,959.

Alonso, F. C. N., Zambrano Morales, M. L., Uribe Sales, A., & Bedolla Becerril, J. E. (1987). Tungsten trioxide reduction-carburization with carbon monoxide-carbon dioxide mixtures. *International Journal of Mineral Processing, 20*, 137–151.

Baco-Carles, V., Arnal, A., Poquillon, D., & Tailhades, P. (2008). Correlation between the morphology of cobalt oxalate precursors and the microstructure of metal powders and compacts. *Powder Technology, 185*, 231–238.

Basu, A. K., & Sale, F. R. (1978). A morphological study of the carburization/reduction of tungsten oxides with carbon monoxide. *Metallurgical Transactions B, 9B*, 603–613.

Bellingham, A. I. (1976). Process for the separation of tungsten and molybdenum, United States Patent 3,939,245.

Berger, L. M., Gruner, W., Langholf, E., & Stolle, S. (1999). On the mechanism of carbothermal reduction processes of TiO_2 and ZrO_2. *International Journal of Refractory Metals and Hard Materials, 17*, 235–243.

Bleecker, W. H. (1974). Production of tungsten and carbide powder, United States Patent 3,850,614.

Bock, A., & Zeiler, B. (2002). Production and characterization of ultrafine WC powders. *International Journal of Refractory Metals and Hard Materials, 20*, 23–30.

Bose, A., Klotz, B. R., Kellogg, F. R., Cho, K. C., & Dowding, R. J. (2008). Nanocrystalline tungsten powder synthesis using high energy milling. *Proceedings of the 2008 international conference on tungsten, refractory & hardmaterials VII* (pp. 5.35–5.48).

Boyer, C. W., & Christini, J. N. (1982). Recovery of tungsten values from alkali-tungstate solutions by solvent extraction, United States Patent 4,360,503.

Brooks, K. J. A. (1996). *World directory and handbook of hardmetals and hard materials* (6th ed.). East Barnet, England: International Carbide Data.

Buerkel, W. A., Wightman, S. R., & Tomalin, D. S. (1992). Fluidized bed process for preparing tungsten powder, U.S. Patent No. 5,125,964.

Butler, B. G., Lu, J., Fang, Z. Z., & Rajammani, R. K. (2007). Production of nanometric tungsten carbide powders by planetary milling. *International Journal of Powder Metallurgy, 43*, 35–43.

Caspers, B., Sauberlich, T., & Reiss, M. (2008). Influence of manufacturing parameteres on properties of nano tungsten carbide. In: *Proceedings of the 2008 international conference on tungsten, refractory and hardmaterials VII* (pp. 5.27–5.34). MPIF.

Cheresnowsky, M. J., & Vanderpool, C. D. (1984). Method for producing cobalt metal powder, U.S. Patent No. 4,469,505.

Clark, E. B., & Roebuck, B. (1992). Extending the application areas for titanium carbonitride cermets. *Refractory Metals and Hard Materials, 11*, 23–33.

Crayton, P. H., & Gridley, M. C. (1971). Vapour-phase synthesis of submicron tantalum carbide. *Powder Metallurgy, 14*, 78–85.

Davidson, C. F., Shirts, M. B., & Harbuck, D. D. (1989). Production of titanium nitride, carbide, and carbonitride powders, United States Patent 4,812,301.

Dunmead, S. D., Moore, W. G, Weimer, A. W., Eisman, G. A., & Henley, J. P. (1995). Method for making submicrometer carbides, submicrometer solid solution carbides, and the material resulting therefrom, United States Patent 5,380,688.

Ehrreich, J. E., & Reti, A. R. (1974). Acicular cobalt powders having high squareness ratios, U.S. Patent No. 3,855,016.

El-Eskandarany, M. S., Omori, M., Ishikuro, M., Konno, T. J., Takada, K., Sumiyama, K., et al. (1996). Synthesis of full-density nanocrystalline tungsten carbide by reduction of tungstic oxide at room temperature. *Metallurgical and Materials Transactions A, 27A*, 4210–4213.

Eslamloo-Grami, M., & Munir, Z. A. (1994). The mechanism of combustion synthesis of titanium carbonitride. *Materials Research Society, 9*, 431–435.

Exner, H. E. (1979). Physical and chemical nature of cemented carbides. *International Metals Reviews, 4*, 149–173.

Fang, Z. Z., Wang, X., Ryu, T., Hwang, K. S., & Sohn, H. Y. (2009). Synthesis, sintering, and mechanical properties of nanocrystalline cemented tungsten carbide – a review. *International Journal of Refractory & Hard Materials, 27*, 288–299.

Fisher, K. G. (2011). Cobalt processing developments. *Proceedings of the Southern African Institute of Mining and Metallurgy 6th Southern African Base Metals Conference* (pp. 237–257).

Fontes, F. A. O., Gomes, K. K. P., Olivera, S. A., Souza, C. P., & Sousa, J. F. (2004). Niobium carbide synthesis by solid-gas reaction using a rotating cylinder reactor. *Brazilian Journal of Chemical Engineering, 21*, 393–403.

Gao, L., & Kear, B. H. (1996). In: *Proceedings of the 1995 international. conference on tungsten and refractory metals* (pp. 247–256). MPIF.

Gao, L., Kear, B., & Seegopaul, P. (1999). Method of forming tungsten carbide particles, United States Patent, 5,919,428.

Gille, G., Szesny, B., Dreyer, K., van den Berg, H., Schmidt, J., Gestrich, T., et al. (2002). Submicron and ultrafine grained hardmetals for microdrills and metal cutting inserts. *International Journal of Refractory Metals and Hard Materials, 20*, 3–22.

Gingerich, R. G. W., Christini, J. N., Vogt, M. C., Vanderpool, C. D., & Miller, M. J. (1995). Process for recovering tungsten as an ammoniacal tungstate compound in which ammoniacal tungstate liquors are reclaimed, States Patent 5,417,945.

Gingerich, R. G. W, & McClintic, R. P. (1980). Method for producing cobaltic hexammine compounds and cobalt metal powder, U.S. Patent No. 4,218,240.

Goddard, J. H. (1982). Purification of ammonium tungstate solutions, United States Patent 4,346,061.

Gomes, J. M., Raddatz, A. E., & Carnahan, T. G. (1985). Preparation of tungsten carbide by gas sparging tungstate melts. *Journal of Metals, 12*, 29–32.

Gorge, A., Meese-Marktscheffel, J., Naumann, D., Olbrich, A., & Schrumpf, A. F. (2004). Spheroidally agglomerated basic cobalt(II) carbonate and spheroidally agglomerated cobalt(II) hydroxide, process for their production and their use, U.S. Patent No. 6,699,453.

Grabis, J., & Zalite, I. (2005). Preparation of Ti(N,C) based nanosized powders and their densification. *Material Science, 11*, 372–375.

Gupta, C. K., & Suri, A. K. (1994). *Extractive metallurgy of niobium*. Ann Arbor: CRC Press.

Hara, A., & Miyaka, M. (1974). Rotary furnace for carburization, United States Patent 3,802,847.

Haubner, R., Schubert, W. D., Hellmer, H., Lassner, E., & Lux, B. (1983). Mechanism of technical reduction of tungsten: Part 2 hydrogen reduction of tungsten blue oxide to tungsten powder. *Refractory Metals and Hard Materials, 12*, 156–163.

Haubner, R., Schubert, W. D., Lassner, E., & Lux, B. (1985). *Einfluss von alkalidotierungen auf die reduktion von WO_3 zu wolfram mit wasserstoff*. In *Proceedings of the 11th international Plansee seminar* (Vol. 2).

Hellmer, H., Schubert, W. D., Lassner, E., & Lux, B. (1985). *Kinetik der wolfamoxidreduktion*. In *Proceedings of the 11th international Plansee seminar* (Vol. 3).

Hojo, J., Oku, T., & Kato, A. (1978). Tungsten carbide powders produced by the vapor phase reaction of the WCl_6-CH_4-H_2 System. *Journal of Less-common Metals, 59*, 85–95.

Huggins, D. K., & Queneau, P.B. (1981a). Separation of trace molybdenum from tungsten solutions, United States Patent 4,303,623.

Huggins, D. K., & Queneau, P. B. (1981b). Chemical treatment of low-grade wolframite concentrate having high Mo/WO3 ratio, United States Patent 4,303,622.

International Tungsten Industry Association. (2011). London, England, http://www.itia.info/.

Jha, A., & Yoon, S. J. (1999). Formation of titanium carbonitride phases via the reduction of TiO_2 with carbon in the presence of nitrogen. *Journal of Material Science, 34*, 307–322.

Ji, T. Z. (June 1986). Production of submicron tungsten powder by hydrogen reduction of tungsten trioxide. *International Journal of Refractory Metals and Hard Materials*, 108–112.

Johnson, J. L., Runyon, & Morton, C. (2008). Powder power. *Cutting Tool Engineering, 60*, 76–83.

Johnston, R. F., & Nguyen, H. T. (1996). Direct carbursation of scheelite with carbon. *Minerals Engineering, 9*, 765–773.

Kemp, W. E. (1995). Mechanically fluidized retort and method for treating particles therein, United States Patent 5,407,498.

Kim, H. S., Bugli, G., & Djega-Mariadassou, G. (1999). Preparation and characterization of niobium carbide and carbonitride. *Journal of Solid State Chemistry, 142*, 100–107.

Kim, H. T., Kim, J. S., & Kwon, Y. S. (2005). Production and characterization of ultrafine tungsten powder by electrical explosion of wires method. *Proceedings of the 16th Plansee seminar* (pp. 470–480).

Kim, T. K., MacInnis, M. B., McClintic, R. P., & Vogt, M. C. (1983). Recovery of tungsten values from alkali-tungstate solutions by solvent extraction, United States Patent 4,374,099.

Kimmel, E. R., Shaffer, M. E., Pinkowski, T. R., & Harris, G. L. (1987). Method of producing monotungsten carbide powder, United States Patent 4,664,899.

Kirk-Othmer encyclopedia of chemical technology. 3rd ed., (1978a) Vol. 4.

Kirk-Othmer encyclopedia of chemical technology. 3rd ed., (1978b) Vol. 23.

Kirk-Othmer encyclopedia of chemical technology. 3rd ed., (1978c) Vol. 15.

Kirk-Othmer encyclopedia of chemical technology. 3rd ed., (1978d) Vol. 22.

Kirk-Othmer encyclopedia of chemical technology. 3rd ed., (1978e) Vol. 4.

Koc, R., & Kodambaka, K. (2000). Tungsten carbide (WC) synthesis from novel precursors. *Journal of the European Ceramic Society, 20*, 1859–1869.

Kronenwetter, C. A., Harris, G. L., & Kimmel, E. R. (1983). Method of producing tungsten and tungsten carbide powder, United States Patnet 4,402,737.

Kulkarni, A. D., Montclair, N. J., & Cleary, J. G. (1978). Processing of ammonium paratungstate from tungsten ores, United States Patent 4,115,513.

Kurtak, C. R. (1965). Separation of molybdenum from tungsten values, United States Patent 3,173,754.

Lackner, A., Filzwieser, A., & Paschen, P. (1996). On the reduction of tungsten blue oxide in a stream of hydrogen. 14, 383–391.

Laferty, J. M., Queneau, P. B., & Beckstead, L. W. (1984). Ammonium hydroxide stripping of tungstate from organic solvent, United States Patent 4,450,144.

Lamprey, H., Culbertson, J. B., & Ripley, R. L. (1966). Process for producing ultrafine powder of refractory materials, United States Patent 3,253,886.

Lassner, E. (1989). Influence of carburization temperature on tungsten carbide properties. *Refractory Metals and Hard Materials*, 185–188.

Lassner, E. (1995). From tungsten concentrates and scrap to highly pure ammonium paratungstate (APT). *International Journal of Refractory Metals and Hard Materials, 13*, 35–44.

Lassner, E., & Schubert, W.-D. (1999). *Tungsten, properties, chemistry, technology of the element, alloys, and chemical compounds*. New York: Kluwer Academic/Plenum Publishers.

Leclercq, G., Kamal, M., Giraudon, J. M., Devassine, P., Feigenbaum, L., Leclercq, L., et al. (1996). Study of the preparation of bulk powder tungsten carbides by temperature programmed reaction with $CH_4 + H_2$ mixtures. *Journal of Catalysis, 158*, 142–169.

Leparoux, M., Kihn, Y., Paris, S., & Schreuders, C. (2008). Microstructure analysis of RF plasma synthesized TiCN nanopowders.

Liao, J.-q., Chen, S.-y., Zou, Z.-q., Lu, H.-b., & Huang, B.-y. (1999). Influence of tungsten oxides characteristics on fineness, homogeneity and looseness of reduced ultrafine tungsten powder. *International Journal of Refractory Metals and Hard Materials, 17*, 423–429.

Liao, J.-q, Huang, B.-y, & Zou, Z.-q (2001). Determination of physical characterization of tungsten oxides. *International Journal of Refractory Metals and Hard Materials, 19*, 79–84.

Li, Z. Q., Zhang, H. F., Zhang, X. B., Wang, Y. Q., & Wu, X. J. (1998). Nanocrystalline tungsten carbide encapsulated in carbon shells. *NanoStructured Materials, 10*, 179–184.

Luidold, S., & Antrekowitsch, H. (2008). Direct carburetion of tungsten blue oxide in a fluidized bed reactor. *International Journal of Refractory and Hard Materials, 26*, 324–328.

Lunk, H.-J., Newman, K. E. Gonzales, J. M., He, J. (2010). Study of the reduction of tungsten trioxide and tungsten blue oxide doped with NaX (X=Cl, Br, NO_2, NO_3), Na_2CO and KY (Y=Cl, Br). *Proceedings of the 2010 International Conference on Powder Metallurgy and Particulate Materials* (pp. 2.101–2.111).

MacInnis, M. B., & Kim, T. K. (1985). Impact of solvent extraction on the tungsten industry. In: *Proceedings of the third international tungsten symposium* (pp. 41–51). MPR Publishing Services Ltd.

MacInnis, M. B., McClintic, R. P., & Kim, T. K. (1982). Recovery of tungsten values from alkali-tungstate solutions by solvent extraction, United States Patent 4,360,502.

Matti, K., Hamalainen, J., Jussi, P., Rastas, K., Heikki, U., Tiitinen, A., Tom, O., & Niemi, O. (1980). Process for the recovery of cobalt from impure aqueous in particular nickel bearing solutions and catalyst therefore, U.S. Patent No. 4,208,380.

McKechnie, T. N., Antony, L. V. M., O'Dell, J. S., Power, C., & Tabor, T. (2009). Nano powders, components and coatings by plasma technique, U.S. Patent 7, 615097.

Medeiros, F. F. P., da Silva, A. G. P., Sasakic, J. M., Souza, C. P., & Gomes, U. U. (2005). Synthesis and characterization of nanostructured tungsten carbide (WC) prepared from ammonium paratungstate (APT) under CH_4/H_2 atmosphere. *Proceedings of the 16th Plansee seminar* (pp. 481–491).

Miller, G. L. (1959). *Tantalum and niobium*. London: Butterworths Scientific Publications.

Miller, M. J., Vogt, M. C., & Scheithauer, R. A. (1985). Method for removing tin from sodium tungstate solution, United States Patent 4,552,729.

Millner, T. (1957). Scientific background of the production of metallic tungsten for the electrical lamp industry and factors influencing its quality. *Acta Technica, 17*, 67–111.

Monteverde, F., Medri, V., & Bellosi, A. (2001). Synthesis of ultrafine titanium carbonitride powders. *Applied Organometallic Chemistry, 15*, 421–429.

Parker, D. (2005). FFC-Cambridge – a new, low energy, low environmental impact route to powder metals. *Proceedings of the 16th Plansee Seminar* (pp. 24–36).

Parsons, D. S. (1965). The reduction of tungsten oxides by hydrogen. *Electrochemical Technology, 3*, 280–283.

Pastor, H. (1987). Titanium-carbonitride-based hard alloys for cutting tools. *Materials Science and Engineering, A105/106*, 401–409.

Quatrini, L. R. (1982). Tungsten recovery from tungsten ore concentrates by caustic digestion, United States Patent 4,353,880.

Quatrini, L. R., Terlizzi, M. B., & Martin, B. E. (1982). Tungsten recovery from tungsten ore concentrates by caustic digestion, United States Patent 4,353,878.

Quatrini, L. R., Vogt, M. C., & Martin, B. E. (1982). Tungsten recovery from tungsten ore concentrates by caustic digestion, United States Patent No. 4,353,881.

Quatrini, L. R., & Martin, B. E. (1982). Tungsten recovery from tungsten ore concentrates by caustic digestion, United States Patent 4,353,879.

Queneau, P. B., Beckstead, L. W., & Huggins, D. K. (1982). Treatment of sodium tungstate liquor containing dissolved silica, phosphorous and fluorine impurities, United States Patent 4,311,679.

Queneau, P. B., & Huggins, D. K. (1982). Autoclave soda digestion of refractory scheelite concentrates, United States Patent 4,320,095.

Raghunathan, S., & Bourell, D. L. (1999). Synthesis and evaluation of advanced nanocrystalline tungsten-based materials. *P/M Science & Technology Briefs, 1*, 9–14.

Sarin, V. K. (1975). Morphological Changes Occurring During the Reduction of WO3. *J. Mater. Sci., 10*, 593–598.

Schubert, W. D. (1990). Kinetics of the hydrogen reduction of tungsten oxides. *Refractory Metals and Hard Materials, 6*, 178–191.

Schubert, W. D., & Lassner, E. (1991). Production and characterization of hydrogen reduced submicron tungsten powders – part 1: state of art in research, production and characterization of raw materials and tungsten powders. *Refractory Metals and Hard Materials, 10*, 133–144.

Schwarzkopf, P., & Kieffer, R. (1953). *Refractory hardmetals: borides, carbides, nitrides and silicides*.

Seegopaul, P., Gao, L., & Kear, B. (1998). Method of forming tungsten carbide particles, European Patent EP0846659.

Sha, L., Kai-hua, X., & Min, W. (2006). Preparation of Co powders for cemented carbides in China. *International Journal of Refractory Metals and Hard Matererials, 24*, 405–412.

Shamsuddin, M., & Sohn, H. Y. (1981). Extractive metallurgy of tungsten. Extractive metallurgy of refractory metals. In H. Y. Sohn, O. Norman Carlson, & J. Thomas Smith (Eds.), *Proceedings of 110th AIME annual meeting* (pp. 205–230). A Publication of The Metallurgical Society of AIME.

Sherman, A. J., Doud, B., & Hardy, D. (2011). Powder properties of nanocrystalline, fluidized bed reduced tungsten, tungsten carbide and tungsten rare-earth alloy powders. *Proceedings of the international conference on tungsten, refractory and hard materials VIII* (pp. 2.47–2.57).

Shimada, S., Koyama, T., Kodaira, K., & Matsushita, T. (1983). Formation of NbC and TaC by solid state reaction. *Journal of Materials Science, 18*, 1291–1296.

Shimizu, H., Sasaki, K., & Morita, S. (2005). Studies on synthetic processes and properties of ultrafine niobium carbide powders. *Proceedings of the 16th Plansee seminar* (pp. 506–518).

Singh Gaur, R. P. (2006a). Modern hydrometallurgical production for tungsten. *Journal of Metals, 58*, 45–49.

Singh Gaur, R. P. (2006b). Effect of normality, temperature and time on the tungsten losses in the residue separated from diluted scheelite-slurry-in-NaOH after digestion. In S. M. Howard, R. L. Stephens, C. J. Newman, J.-Y. J. Hwang, A. M. Gokhale, T. T. Chen, et al. (Eds.), *EDP Congress 2006* (pp. 1097–1109). TMS (The Minerals, Metals & Materials Society).

Singh, R. P., & Miller, M. J. (1997). Speciation of titanium in tungsten carbide scrap, before, during and after its processing fir tungsten and cobalt recovery. In B. Mishra, & G. J. Kiouros (Eds.), *Titanium extraction and processing* (pp. 31–43). The Minerals, Metals & Materials Society.

Singh, R. P., & Miller, M. J. (1998). Characterization and purification of a phosphorous containing scheelite ore concentrate, Light Metals 1998. In B. J. Welch (Ed.), *Proceedings of the technical sessions presented by the TMS aluminum committee* (pp. 1343–1347). A Publication of TMS.

Singh, R. P., Miller, M. J., & Wolfe, T. A. (1999). Purification of a phosphorous –containing scheelite ore concentrate: a design-of-experiment study. *Separation Science & Technology, 34*, 1679–1688.

Singh, R. P., Miller, M. J., & Wolfe, T. A. (2000). Purification of phosphrous containing scheelite ore, United States Patent No. 6,051,196.

Smith, G. S. (1944). Recovery of molybdenum and tungsten from ores, United States Patent 2,339,888.

Smith, E. N. (1980). MACRO process for direct production of tungsten monocarbide. *Metal Powder Report, 35*, 53–54.

Rhenium, molybdenum, and tungsten (Chapter I). In Songina, O. A. (Ed.), *Rare earths* (3rd ed.). (pp. 15–71) Jerusalem: Israel Program for Scientific Translation. (Translated from Russian).

Teixeira da Silva, V. L. S., Schmal, M., & Oyama, S. T. (1996). Niobium carbide synthesis from niobium oxide: study of the synthesis conditions, kinetics, and solid-state transformation mechanism. *Journal of Solid State Chemistry, 123*, 168–182.

van Put, J. W., & Zegers, T. W. (1991). Hydrogen reduction of ammonium paratungstate into tungsten blue oxide – part I: literature review. *International Journal of Refractory Metals and Hard Materials, 16*, 115–122.

van Put, J. W., Zegers, T. W., & Liu, H. (1991). Hydrogen reduction of ammonium paratungstate into tungsten blue oxide – part II: experimental. *Refractory Metals and Hard Materials, 10*, 123–131.

Vedova, R., & Grauerholz, N. L. (1977). Method for recovering scheelite from tungsten ores by flotation, United States Patent No. 4,054,442.

Venables, D. S., & Brown, M. W. (1996a). Reduction of tungsten oxides with carbon. Part 1: thermal analyses. *Thermochimica Acta, 282/283*, 251–264.

Venables, D. S., & Brown, M. W. (1996b). Reduction of tungsten oxides with carbon. Part 2: tube furnace experiments. *Thermochimica Acta, 282/283*, 265–276.

Welham, N. J. (2000). Novel route to submicrometer tungsten carbide. *Journal of the American Institute of Chemical Engineering, 46*, 68–71.

Wilken, T. R., Morcom, W. R., Wert, C. A., & Woodhouse, J. B. (1976). Reduction of tungsten oxide to tungsten metal. *Metallurgical Transactions B, 7B*, 589–597.

Wolfe, T. (1996). Process for reducing the average size of ammonium paratungstate powders, United States Patent 5,578,285.

Yih, S. W. H., & Wang, C. T. (1979). *Tungsten: sources, metallurgy, properties, and applications*. New York: Plenum Press.

Yih, S. W. H., & Wang, C. T. (1981). *Tungsten: sources, metallurgy, properties and applications*. New York: Plenum Press.

Zajic, J. E., & Kosaric, N. (1977). Flotation of scheelite from calcite with a microbial based collector, United States Patent No. 4,046,678.

Zeiler, B., Schubert, W. D., & Lux, B. (1991). On the reduction of NS-doped tungsten blue oxide – part I: literature reveiw. *Refractory Metals and Hard Materials, 10*, 83–90.

Zhang, L., Wu, C.-h., & Wu, H-p. (2011). Some aspects of technology progresses in China's cemented carbide industry. In: *Proceedings of tungsten, refractory & hardmetals VIII*. San Francisco, CA: MPIF.

Zhang, J., Zhang, G., Zhang, L., Wang, C., Zhou, M., & Zou, T. (2005). SPS in situ synthesis of WC compact by tungsten oxide direct carbonization. *Proceedings of the 16th Plansee Seminar* (pp. 588–594).

Zhengji, T. (1987). Study of carburization of coarse tungsten powder. *Refractory Metals and Hard Materials*, 221–225.

Zhengji, T. (1989). Investigation of hydrogen reduction process for blue tungstic oxide. *Refractory Metals and Hard Materials, 5*, 179–184.

Ziemer, B., & Lunk, H.-J. (1989). *Quantitative X-ray powder diffraction of reduction products formed in the manufacturing process of tungsten wire*. In *Proceedings of the 12th international plansee seminar* (Vol. 1).

1.07 Powder Processing and Green Shaping

Pankaj K. Mehrotra, Kennametal Inc., Latrobe, PA, USA

Glossary

Binder The metallic part of the hardmetal which cements the hard particles together.

Coercivity Magnetic field needed to bring the induced magnetization to zero after saturation; it is an indirect measure of Co mean free path or WC grain size.

Core rod Rod used to create an internal cylindrical cavity during green forming.

Crater wear Tool wear at the chip–tool interface, caused primarily by chemical reaction at high temperature.

Cubic carbides Single or solid solution carbides of Ti, Ta, Nb, Zr, and Hf with cubic structure.

Deflash Removal of flash.

Delamination Cracks in uniaxially pressed green parts tending to separate a thin layer near one of the surfaces.

Delubing Removal of binders, surfactants and other organic materials from the part prior to sintering.

Eta phase Porous compound of C–W–Co generated due to carbon deficiency.

Extrudate Green formed rod exiting the die in an extrusion press.

Flash Thin slivers of powder attached to the part created by powder extrusion between two mating surfaces of tooling.

Fugitive binder, organic binder Organic substances used to impart green strength to powder compact. These are removed prior to sintering during delubing.

Granule satellites Projections from the surface of granules which may interfere with granule flow.

Granules Agglomerates of individual particles to facilitate powder handling.

Green shaping Forming of powder into desired shapes.

Green strength Strength of a part when it is still green (compressed powder) prior to sintering.

Hone Rounding of cutting corner to strengthen the cutting edge.

Magnetic saturation Induced saturation magnetization is an indirect measure of C and W content of Co.

http://dx.doi.org/10.1016/B978-0-08-096527-7.00007-6

Menstruum This refers to a mass of material created during metallocarbothermic reduction of WC-based precursor, resulting in WC particles imbedded in a matrix.

Picker A mechanical device used to automatically pick green parts as they are pressed.

Positive cutting edge Two surfaces of the cutting corner making an acute angle scrapings. Powder that is not converted to product during various processes which can be recycled.

Shrinkage Reduction in size of a green part caused by sintering, as porosity is removed.

Shrinkage factor Ratio of green to sintered part size, also expressed as a percentage.

Solvent Liquid medium used to disperse powder for processing, including milling.

Surfactants, lubricants Organic compounds active on particle surfaces used to facilitate powder processing and green shaping.

Nomenclature

Coercivity Magnetic field needed to bring induced magnetization to zero after saturation, measured in Oersted.

Magnetic saturation Induced saturation magnetization, measured in μT, $m^3\ kg^{-1}$ or Gauss. It is also expressed as a percentage of the magnetic saturation of pure Co.

Powder flow Time taken for a specified amount of powder to flow through a specified orifice opening, measured in seconds.

Scott density Powder bulk density measured in $g\ cm^{-3}$ or $g\ in^{-3}$.

Shrinkage factor Shrinkage caused by sintering, measured as (Green dimension−sintered dimension)/Green dimension, expressed as a percentage; also Green dimension/sintered dimension.

1.07.1 Introduction

Powder processing to manufacture green parts ready to be sintered is a critical and integral part of hardmetal technology. This chapter gives an overview of different process steps required for hardmetal powder processing from WC production, composition selection, powder preparation and finally to green part making. A qualitative description of most common variants of different process steps and related equipment are presented, and the reader is referred to additional material for more details and specifics for individual processes of interest.

Raw materials are a critical component of powder processing since they determine not only the hardmetal composition but also specific processes and features to be used to ensure quality. Composition of hardmetal is most commonly selected by the intended application and related material or part properties. Powder processing steps and quality control features are greatly influenced by the starting raw materials, hardmetal composition and properties to be achieved. In this chapter, a brief overview of hardmetal composition selection is followed by a summary of WC production methods, powder selection, milling for powder mixing and particle size control, drying for obtaining granulated powder mix, green shaping by many common methods to achieve desired shapes ready to be sintered, and finally, a brief description of environmental, health and safety (EHS) issues to be considered during powder processing of hardmetals.

1.07.2 Hardmetal Compositions

Hardmetals are composed of a large group of compositions based on hard particles bonded with a metallic binder. Typically, carbides of W, Ti, Ta, and Nb comprise the hard particles. Nitride or carbonitride of Ti is sometimes added to modify the properties or impart specific processing options. The most commonly used metal binder compositions are based on Co, but those based on Ni, Fe or their alloys have also been commercialized. Metal binder is further modified with minor amounts of C and W to affect properties of the sintered compact. Small amounts of carbides of Mo, V and Cr are commonly added to further achieve specific microstructure and properties. Although hardmetals can also be described as cermets (**cer**amic + **met**al), this designation is commonly used in the industry to refer to compositions based on carbides, nitrides or borides of Ti bonded with Ni- or Fe-based metals (Santhanam, Tierney, & Hunt, 1990, pp. 950–977). See Chapters 1.04 Cemented Tungsten Carbide Hardmetal—An Introduction and 1.05 Class of Materials—Cermets for more details on hardmetal and cermet compositions.

The most common hardmetal compositions are based on WC–Co. Carbides of Ti, Ta, Nb, Zr and Hf, together known as cubic carbides, are optionally added to improve wear resistance and thermal deformation resistance,

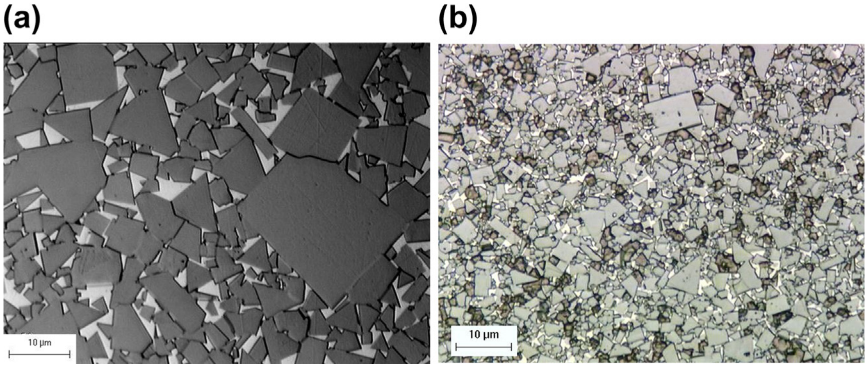

Figure 1 Microstructure of (a) WC–Co and (b) WC–Co with cubic carbides.

however, generally at the expense of thermal conductivity and thermal shock resistance (Mehrotra, Mizgalski, & Santhanam, 2006; Santhanam et al., 1990, pp. 950–977). On sintering, cubic carbides make solid solution carbide in combination with WC, with the final microstructure depending on the starting composition and particle size. **Figures 1(a) and 1(b)** shows microstructures of WC–Co and WC–Co with cubic carbide compositions, respectively. Prereacted carbides are sometimes used to facilitate the solid solution formation. Nitrides or carbonitrides of Ti can be added to WC–Co-based compositions to further modify sintering behavior and generate unique microstructures, such as binder-enriched surface zone, as shown in **Figure 2** (Mehrotra, Santhanam, Mizgalski, Roediger, & VanDenBerg, 2008). Typically, cubic carbide content may range from 0 to 15 wt%, but it may extend to as high as 50% for specific applications. Carbide of Mo has also been used to improve thermal deformation resistance.

Co is the most common metallic binder used in the manufacture of hardmetals, typically in the 5–20 wt% of the hardmetal. The binder in hardmetal serves the dual purpose of cementing the hard particles together and imparting ductility and toughness to the otherwise brittle hard particles. Co also provides a medium for dissolution and reprecipitation of hard particles during the sintering process. As a result, the metallic binder system is based on a Co–C–W alloy, whose composition needs to be controlled with precision to obtain desired microstructure and properties of the sintered structure. Too high a C content of the Co binder will lead to free carbon; on the other hand, carbon lean composition will result in brittle eta phase, which occurs as a porous compound of Co–W–C. Ferromagnetic properties of Co have been extensively used for nondestructive quality control in hardmetals. Most commonly, magnetic saturation has been used to estimate the composition of the Co–C–W binder alloy, and coercivity gives an indication of the carbide grain size (Upadhyaya, 1998). Ni and Fe are also used as part of the binder system for specific applications, such as improved corrosion resistance and deformation resistance.

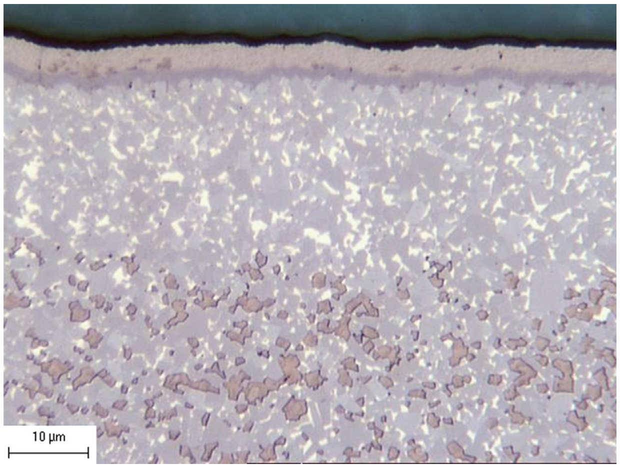

Figure 2 Microstructure of a hardmetal composition with binder-enriched surface zone.

Table 1 Grain size type designation convention based on sintered mean grain size

Mean Sintered Grain Size (μm)	*Type Designation*
<0.2	Nano
0.2-0.5	Ultrafine
0.5-0.8	Submicron
0.8-1.3	Fine
1.3-2.5	Medium
2.5-6.0	Coarse
>6.0	Extra coarse

Grain size control in hardmetals is commonly affected by minor additions of carbides of V and Cr. Of these, VC is the most effective grain growth inhibitor, however, at the expense of toughness. Typically, 0 to less than 1 wt% of these carbides may be added based on the overall hardmetal composition. VC is insoluble in Co, and therefore does not affect its magnetic properties. However, Cr_3C_2 is partially soluble and affects magnetic saturation of Co. Although not as affective, TaC has also been used for grain size control (Bose, 2011). **Table 1** shows commonly accepted designation for grain sizes.

The primary reason for composition selection is suitability for application. Compositions with fine grain size and low binder content are commonly used for applications requiring high wear resistance, whereas higher binder content and relatively coarse grain size compositions are more suitable for applications requiring high toughness. Relatively finer grain sizes increase transverse rupture strength due to smaller flaw size but reduce facture toughness due to relatively straighter crack path. Therefore, an optimum combination of wear resistance and toughness for a given application is obtained by proper selection of binder content and grain size of the hardmetal. This is represented in **Figure 3** as hardness values for different Co contents and grain size of the hardmetal. High corrosion resistance is obtained by incorporating Ni in the binder composition, whereas

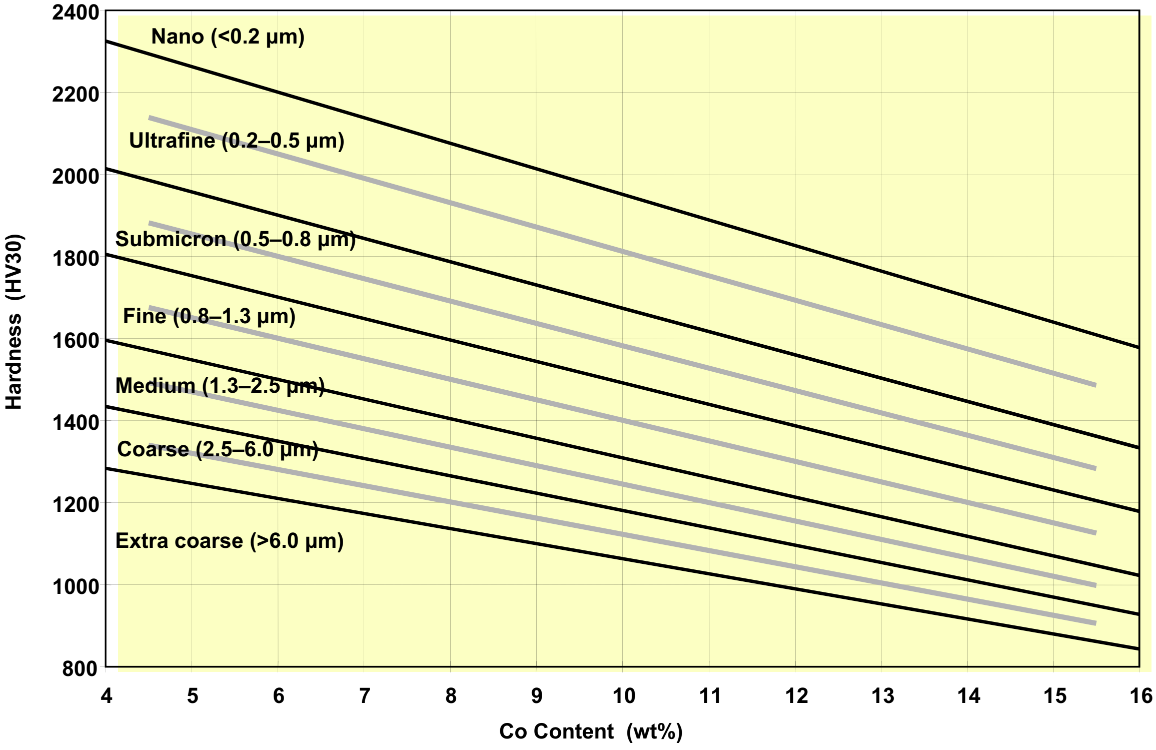

Figure 3 Hardness, Co content and WC grain size relationships for hardmetals.

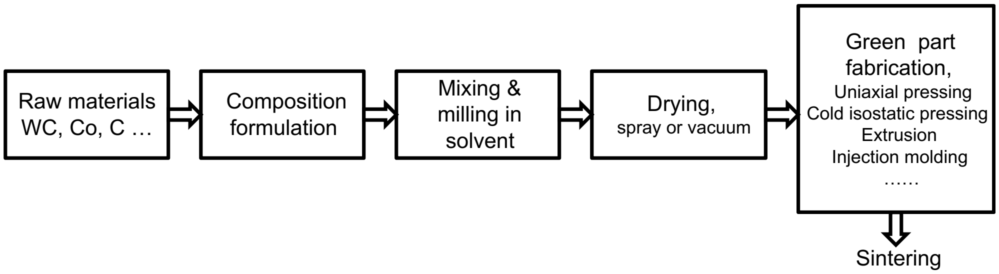

Figure 4 Schematic process flow diagram from raw material to green consolidation of hardmetals.

addition of Fe can improve deformation resistance for selected applications. Another application of hardmetals is as coatings deposited by thermal spray processes, used to enhance wear resistance of many critical components in mining and oil drilling industries. Thermal spray processes require superior powder flow for handling and consistent feed rates. Powder flow rates improve with increasing particle size and particle shape, with spherical shape being preferred (Mehrotra et al., 2006; Santhanam et al., 1990, pp. 950–977).

Crater wear in metal cutting tools is commonly resisted by cubic carbides due to their chemical inertness; however, coatings provide this protection in modern cutting tool materials. See Chapter 1.16 Coating Applications for Cutting Tools of this book for more details. Cubic carbides also provide high-temperature deformation resistance needed for turning applications where high temperatures are produced at the cutting edge. Unique compositions, where a binder-enriched surface zone is used to improve crack resistance in compositions with relatively low Co content for high bulk deformation resistance, require careful control of starting powder composition. In milling and drilling applications, where cutting temperatures are moderate, toughness and thermal shock resistance are required due to the interrupted nature of the cuts. This can be provided by using moderate grain size with relatively high amount of Co heavily alloyed with W without creating eta or other brittle phases (Santhanam et al., 1990, pp. 950–977).

Submicron- and nano-sized tungsten carbide powders have attracted special attention due to the perceived promise of high hardness in nanostructured tungsten carbide-cobalt-based alloys. Manufacturing these compositions involves the twin challenge of producing nanograined starting powders and retaining such a structure during sintering, when grain growth and densification occur simultaneously (Bose, 2011).

The entire manufacturing process and related costs also need to be considered in selecting compositions and powder formulation. Figure 4 schematically shows process flow from raw material to green consolidation. In addition to the raw material cost, overall cost is determined by process steps needed for manufacturing the final product. Powder formulations, therefore, are also attuned to the subsequent processes of powder consolidation, sintering and postsintering process. Low binder content, fine grain size and requirement for high reliability necessitate pressure-assisted sintering or hot isostatic pressing, which adds cost to the final product. Similarly, part size, required size control, powder consolidation processes, etc. determine powder formulation. This may dictate the equipment to be employed and influence scrap produced in individual processes.

1.07.3 Tungsten Carbide Powder

A great variety of methods have been used to produce tungsten carbide powders, driven by the availability of the starting raw materials and the structure and properties desired in the final product (Mehrotra et al., 2006; Stoll & Santhanam, 1992, pp. 861–878). The most common way to manufacture WC powder is stepwise reduction of oxide-based tungsten ore concentrates first to W and then to WC. As shown in Figure 5, tungsten ore

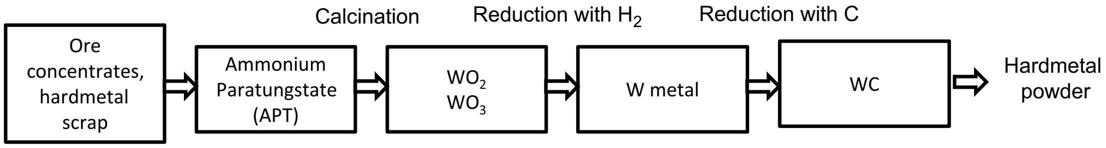

Figure 5 Schematic representation of process flow for making WC powder.

concentrates or recycled hardmetal scrap are the raw material sources for making ammonium paratungstate (APT), the form in which tungsten commodity is most commonly bought and sold.

APT is calcined to make one of the tungsten oxides, which is reduced to tungsten metal in the presence of dry hydrogen at 700–1000 °C.

$$WO_3 + 3H_2 \xrightarrow{(700-1000\ \ ^\circ C)} W + 3H_2O$$

Control of moisture content of H_2 gas is critical to the success of this process. The next step of carburization involves heating a mixture of tungsten metal and carbon powder in a reducing atmosphere to yield tungsten carbide powder. The purity and grain size of the resulting powder are determined by the composition and surface area of the starting materials, powder bed height, reaction conditions, temperature, etc.

$$W + C \xrightarrow{(1400-1600\ \ ^\circ C, H_2)} WC$$

Additives can also be used to control the particle size of WC (Upadhyaya, 1998). W may be cocarburized with V or Cr to obtain a more uniform distribution of the grain growth inhibitors to reduce grain size of the sintered hardmetal. WC grain size can also be reduced to submicron range by high-energy milling and controlled by screening. An example of WC produced by this process is shown in **Figure 6 (a)**.

The alternate menstruum process of tungsten carbide powder production combines the oxide reduction and carburization process in a single carbothermic reduction process step, whereby the oxide precursor and a carbon source are reacted in the presence of an auxiliary metal–metal alloy or menstruum at high temperature. A variant of this process involves simultaneous aluminothermic reduction and carburization in an exothermic reaction.

$$6Fe(Mn)WO_4 + 22Al + 3CaC_2 + 3Fe_3O_4 \xrightarrow{2500-3000\ \ ^\circ C} 6WC + 6Fe(Mn) + 9Fe + 3CaO + 11Al_2O_3$$

The resulting metallic mass contains dispersed tungsten carbide crystals, which are isolated by chemically dissolving the menstruum. Tungsten carbide powder produced by the menstruum process is macrocrystalline and highly stoichiometric. **Figure 6 (b)** shows an example of the coarse WC powder particles produced by the menstruum process.

Manufacture of submicron and nanograined hardmetal powders can be accomplished by mechanical alloying using high-energy milling (Zhang, Wang, & Zhu, 2003). This method suffers from a high energy requirement and poor chemical purity and chemical homogeneity. As noted earlier, in situ grain size reduction of tungsten carbide can be accomplished by the addition of tantalum carbide, chromium carbide and vanadium carbide; however, it generally leads to some loss in strength. Their effectiveness increases if they are added during the carburization step of the process. The use of lower process temperature and special additives during reduction and/or carburization process also leads to smaller tungsten carbide grain size. Spray conversion processing has also been used to produce nanostructured W-based hardmetals (Kear & Strutt, 1995). Solutions of precursor compounds are mixed and spray dried to form a chemically homogeneous mixture, which is then carburized to obtain nanostructured powder. High-energy milling of the precursor

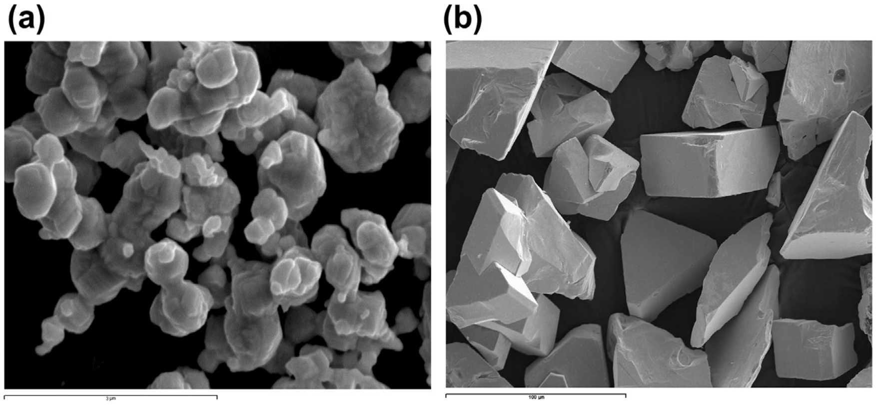

Figure 6 Particle morphologies of WC powders in (a) submicron range and (b) nearly 100 µm range.

mixture followed by carbothermic reduction has been used to obtain chemically homogeneous nano-structured powder (Shaw, Ren, & Yang, 2004).

$$WO_3 + CoO + 5C \rightarrow WC + Co + 4CO$$

1.07.4 Powder Selection

Powder selection is critical to achieving the required quality in the final sintered product, meeting cost targets and accommodating subsequent process requirements. Particle size and quality of hardmetal powders and the metallic binder are of paramount importance to achieving these objectives. Use of recycled powder is commonly employed to reduce cost, minimize energy consumption and utilize existing inventory of powder. Furthermore, paraffin wax and other additives are commonly used to facilitate powder processing and green consolidation.

The quality of selected hardmetal powder is determined by its composition, particle size, morphology, surface chemistry, etc. which, in turn, depend on the raw materials and production manufacturing processes. The composition of starting raw materials is used for mix calculation and determining carbon balance, whereas particle size is critical for selecting milling equipment and conditions, which subsequently determine powder consolidation and sintering characteristics. Particle morphology and particle surface chemistry depend on the manufacturing processes, which affect mix calculation and downstream processes in subtle but critical ways. Carbon balance, in combination with sintering furnace carbon potential, is required to ensure a microstructure without free carbon or eta phase, and it also determines the composition of the binder phase. Carbon balance must also take into account the oxygen inherent in the matrix and at the surface of the carbides of hardmetal powders, and other components of the composition, since it may influence the final composition and microstructure. During sintering, oxygen in the powder combines with carbon to generate CO/CO_2. Carbon thus lost must be compensated for in order to achieve the desired microstructure and binder composition. Consideration must be given to the type of carbide and metal powders, since the reduction of their oxides will depend on the stability of the oxide and the carbon potential and temperature of the sintering process. For example, oxides of Ti are more difficult to reduce than those of W (see Chapter 1.08 Synthesis & Processing—Consolidation Techniques of this volume). Typically, the finer the particle size for a given raw material, higher is the oxygen content due to higher surface area available. Close attention needs to be paid to the composition of powders recycled as scrapings or via the zinc process (Upadhyaya, 1998). These sources of powders are of relatively lower cost compared to the virgin powder; however, their compositions could be variable, depending on their source and the original mix. Therefore, they may already have cubic carbides, binder metal, or other components, along with a relatively higher oxygen content due to prior processing.

Particle size of the starting powder determines if the powder can be milled to the required particle size in an economical time using the available milling equipment. Long milling times may be counterproductive since the efficiency of milling decreases rapidly with time (Upadhyaya, 1998), as schematically shown in **Figure 7**, and reagglomeration of particles may occur. Submicron particles, on the other hand, may not experience any particle size reduction, or only at the expense of substantial milling time.

WC powders in the particle range of 0.2–100 μm are commercially available. Typically, the particle morphology, oxygen content and other impurities of the powder are determined by the manufacturing process for producing the powder. Similarly, composition and particle size of cubic carbides, Co, Ni and Fe, as well as of carbides of V and Cr are selected based on the requirements of the properties needed in the sintered product and the powder consolidation and sintering parameters desired. The source of these powders, especially that of Co, and their characteristics can have significant influence on the success of the green shaping and sintering processes.

An important aspect of hardmetal powder preparation is selection of organic binder, surfactants and other additives. Organic binders, such as wax or poly ethylene glycol, are typically used to provide sufficient green strength to the green consolidated parts so that they can be handled without causing damage prior to sintering. At the same time, they are instrumental in obtaining a sufficiently high green density so that a fully dense product is obtained on sintering. Furthermore, melting/boiling point of the organic binder needs to be considered in selecting the sintering cycle step which is intended to remove it. These organic binder systems may leave behind C and/or O as they are removed, so this must be taken into account for mix calculation. Therefore,

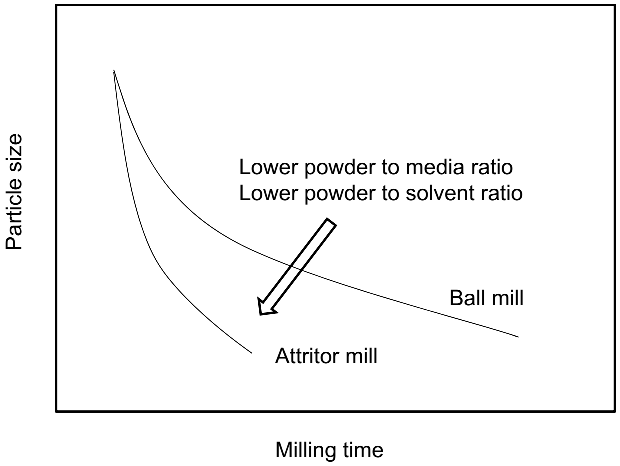

Figure 7 A schematic representation of the effect of various milling parameters on the particle size.

fine tuning is needed between the organic binder characteristics and mix calculation in conjunction with the sintering cycle (German, 1994).

Similarly, characteristics of additives used as surfactants to facilitate milling, powder dispersion or as lubricants to assist green powder consolidation must also be considered, so that the desired effects are achieved with the selected powders and compositions. Any residual impurity needs to be taken account of in formulating the composition in combination with the contribution from the sintering process.

Finally, powder milling is almost always done in a liquid solvent, in the presence of milling media. Liquid solvent improves the efficiency of the milling process for both particle size reduction as well as mixing of different ingredients. Both organic and aqueous media are used as solvents (Soares, Malheiros, Sacramento, Valente, & Oliveira, 2011), with the wax, surfactants and pressing additives being selected based on the solvent type. Another role of solvents in the milling process is to protect powder from oxidation as particle size is reduced and fresh surfaces are exposed, as well as to facilitate discharging of mills and producing suitable slurries for the subsequent drying and pelletizing process. If an aqueous medium is used, oxidation inhibitors are added to minimize oxygen pickup during the milling process. The role of milling media is to facilitate particle deagglomeration and mixing and to reduce particle size via a process of crushing and attrition. But the milling media also suffers attrition in the process and contributes to the mill charge. Therefore, milling media composition, size and type should be selected based on the powder composition of interest, mill type, size and milling parameters.

1.07.5 Powder Mixing and Particle Size Reduction

Hardmetal composition guides the selection of powders and mix composition for processing. Another factor determining the powder selection is the process used to mix various component powders and reducing particle size to a desired value. Powder selection should also take into account minor chemistry changes which occur during powder mixing and milling.

Figure 8 schematically shows an overview of various process steps and considerations for the powder milling process. Powders, based on mix calculation, milling media and solvent are charged in the mill, along with organic binders or other additives. The mill is allowed to run for a predetermined length of time, when it is discharged or a sample taken to determine if appropriate mixing and particle size reduction has taken place. If the milled powder meets this criterion, the powder is ready for the next stage of drying. Otherwise, the milling process may continue or powder may be scrapped if it cannot be reworked.

The objective of powder milling is to provide deagglomeration, uniform mixing of various component powders and reduce particle size to a desired value such that subsequent processes of green body consolidation and sintering can be accomplished with success. Uniformity of mixing is critical since it determines reliability and repeatability of properties and performance achieved. In hardmetals, insufficient mixing may lead to a variety of defects such as porosity, binder metal pools, regions of high concentration of various

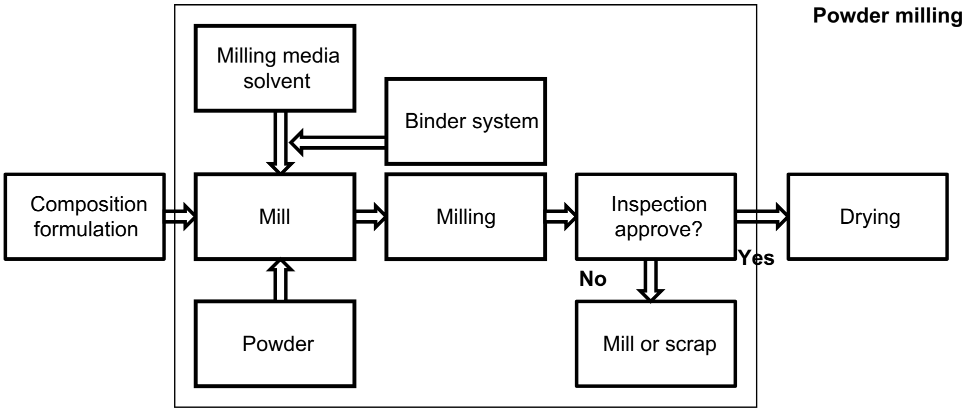

Figure 8 Schematic of powder milling process steps.

components, etc. Improper mixing can also lead to nonuniform distribution of the fugitive binder, which in turn may lead to voids in the microstructure and poor control of downstream processes and properties. Reduction of particle size to a desired value is also critical to controlling subsequent green shaping and sintering processes and resulting properties.

1.07.5.1 Ball Milling

There are many technologies used to achieve the objective of powder mixing and particle size reduction, with the most common being ball milling and attritor milling. As shown in Figure 9(a), ball milling employs a horizontal hollow cylindrical vessel, typically half filled with cycloid-shaped media, a solvent, additives and powder mix. Rotation of this vessel around a horizontal axis causes powder mixing. As media climbs and then cascades down, it breaks agglomerates by shear and crushes individual powder particles trapped between two media balls, causing particle reduction. Ball mill diameter, media size and mill revolutions per minute (rpm) control the process of powder mixing and particle size reduction (Upadhyaya, 1998). For given mill size and

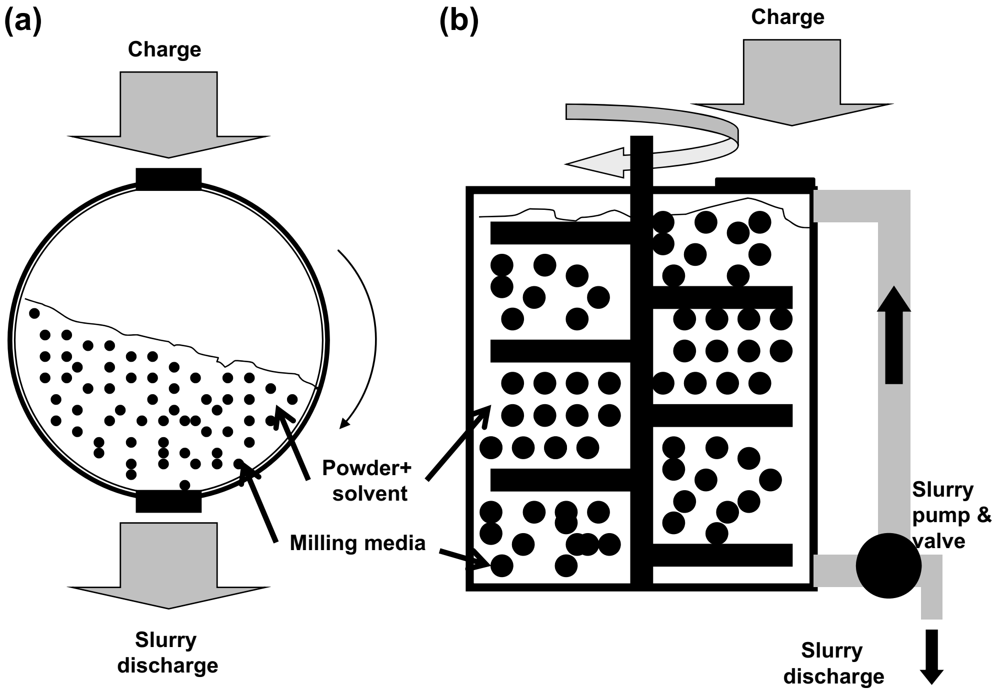

Figure 9 Schematic representation of (a) ball milling and (b) attritor milling.

media, too low an rpm extends the process time, whereas too high an rpm leads to poor cascading of media, leading to inefficient particle size reduction. Other parameters controlling the milling process are powder to media ratio and solids content of the slurry. As shown in **Figure 7**, low powder to media ratio and solid content not only reduce milling time but also reduce productivity of the milling process. Therefore, these parameters need to be optimized based on powder characteristics and desired mix properties. Powder and solvent can be charged from the top of the mill through an opening and discharged through the same opening oriented at the bottom. Slurry is discharged through a screen into a container to keep the milling media in the mill and also to prevent any coarse agglomerates from leaving the mill. From time to time the milling media and mill lining need to be examined for wear and damage and replenished or repaired if needed.

1.07.5.2 Attritor Milling

Attritor milling is a relatively higher energy milling process compared to ball milling, and generally can reduce the milling time significantly (**Figure 7**) (Koch, 1998, pp. 53–66). As shown in **Figure 9(b)**, it employs a vertical hollow cylinder, filled with spherical media, powder and solvent. Arms extending from a central rotating shaft provide mixing and particle size reduction. Considerations of mill and media size, powder to media ratio, and solids content are important in achieving the desired process time and efficiency, as previously discussed with ball milling. During the milling process, the powder has a tendency to settle to the bottom of the mill; therefore, some attritor mills, especially of relatively large size, have a provision for recirculating the slurry from the bottom to the top of the vessel to provide better mixing and improve process and powder uniformity. Both ball mills and attritor mills may require cooling of the mill via double-walled vessels (especially relatively large sizes) to remove the heat generated as a result of the milling process.

Ball milling typically requires a longer process time (up to 100 h) than attritor milling (less than 15 h), as schematically shown in **Figure 7**, but generally gives a narrower particle size distribution. This may influence the subsequent processes of powder consolidation and sintering, but typically, is not a hindrance to using either of the processes; the choice may be more determined by capacity, batch size, and other business requirements. Other issues to consider in the milling process relate to minor changes in powder composition due to the milling process itself, such as media wear, mill lining wear, oxygen pickup due to particle size reduction and contamination caused by poor hygiene. Both milling media and mill wall wear as a result of the milling process, and may contribute to a change in the chemistry of the powder. Therefore, often the milling media and mill lining have a composition similar to that of the powder composition. Alternatively, the small contribution to the chemistry of the powder from wear of milling media and mill lining should be within the desired specifications for the powder. Depending on the powder characteristics, powder size reduction almost always results in oxygen pickup, with the extent of this pickup depending on the powder characteristics. Often organic solvents are used to minimize this oxygen pickup, or, in the case of aqueous solvents, inhibiting agents may be used for the same purpose. Thorough cleaning of mills and milling media is a critical part of maintaining proper hygiene to avoid contamination when changing powder composition or characteristics in the same mill. Failure to adhere to a strict regimen can result in poor control of processes and properties and lead to scrap. Additives to improve the efficiency of the milling process in the form of surfactants, whose type and amount depend on the characteristics of the solvent, affect powder pressing characteristics after drying.

Due to the small particle size of the nanograined powders, the role of milling is limited to deagglomeration for this class of WC powders, with minimal particle size reduction, as suggested by **Figure 7**.

The result of the milling process is a slurry in a solvent with desired powder mix and particle size. This slurry needs to be dried in order to obtain powder with desired characteristics for the subsequent process of powder consolidation.

1.07.6 Production of Dried Powder

The slurry obtained from the powder mixing and particle size reduction process needs to be dried in order for that powder to be made suitable for the next process step of green powder consolidation. This needs to be done while maintaining uniformity of the powder, minimizing contamination and any oxygen pickup, while keeping a high throughput, low cost and minimal powder waste. The process and equipment used for the drying process depend on the solvent and additives used during the powder milling process, as well as the green powder consolidation process for which the powder is intended.

A factor of paramount importance is to keep a uniform distribution of powder in the slurry and avoid powder segregation since WC, Co and the cubic carbides may have very different densities. As a result, slurries are often kept agitated until the drying process begins. This not only ensures a uniform dry powder mix but also keeps the solids content of the slurry stable as it is pumped into the drying chamber thereby keeping the drying process stable. Uniaxial pressing demands powders with excellent flow and specified bulk density in order to keep a high pressing rate while maintaining part to part consistency. Powders intended for consolidation using cold isostatic pressing (CIP) require homogeneity but can tolerate somewhat inferior flow. Postdrying processes involving incorporation of additional binder systems are generally needed for powders destined for extrusion or injection molding. These powders can be dried using either a continuous spray drying process or batch-type vacuum drying process.

Of the many processes used to dry powder slurries, spray drying and vacuum drying are the most common. Spray drying is a continuous process with high throughput and consistent granulated powder quality. However, this requires high capital investment and facility cost as well as the infrastructure to supply a high volume of powder slurry. Vacuum drying, on the other hand, is a batch-type process with limited throughput and generally requires less capital investment. Vacuum-dried powders are suitable for CIP, but generally require additional processes if granulated powders are needed, for example, for uniaxial pressing.

1.07.6.1 Production of Granulated Powder by Spray Drying

The objective of the spray drying process is to dry the milled powder slurry in a continuous process and create granulated powder of desired quality. Some of the basic quality requirements for granulated powder include flow, bulk density, granule shape and size distribution, granule density, etc. within specified limits. These properties determine the process control achievable in subsequent powder consolidation processes.

Figure 10 shows a schematic representation of process flow for the spray drying process, and Figure 11 shows a schematic representation of a spray dryer and its operation. Spray drying process involves pumping the powder/solvent slurry through a nozzle to aerate and create a spray of the slurry in a counter or cocurrent flow of hot gases, such that droplets of the slurry are dried in flight before falling to the bottom of the vessel. It is critical to maintain slurry uniformity from the time slurry is discharged from the mill to the time it is actually sprayed. This is done by maintaining the slurry in a state of constant agitation in a feed tank prior to spraying. Often wax or other additives may be added to the slurry prior to spraying, thus slurry in the feed tank must be kept in constant agitation to mix the ingredients and avoid any sedimentation or separation of different ingredients of the powder. The slurry is pumped into the nozzle using a pump or pressurization of the feed tank.

Although there are many configurations for creating the spray, the most common is the one using a nozzle at the bottom of a vessel. Both pressure and two-fluid nozzles are used depending on the characteristics of the slurry and the dried powder desired. Pressure nozzles create atomization of the slurry via a sudden release of the pressure, whereas two-fluid nozzles use a flowing neutral gas to create the atomization. Nozzle design and

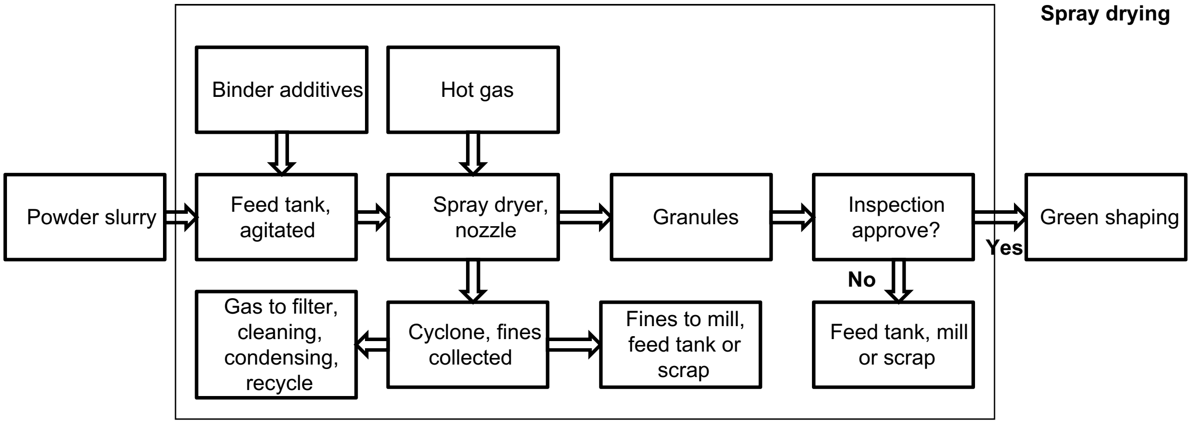

Figure 10 Schematic process flow for the spray drying process.

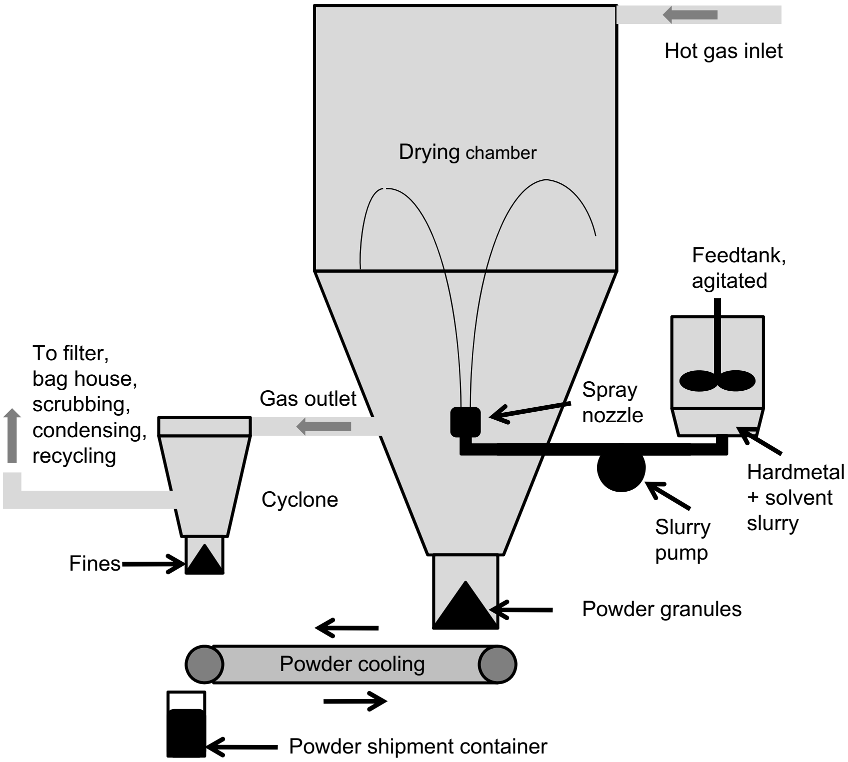

Figure 11 A schematic representation of spray dryer and its operation.

the atomization process are critical to determining the droplet size and structure, which, in turn, determine the quality of the granulated powder. Droplets created by the atomized slurry travel up against a countercurrent of hot neutral gas. N_2 is a common gas for organic solvent evaporation, whereas air with controlled humidity can be used to dry aqueous droplets. As droplets travel up and then fall down at the bottom of the chamber in a hot gas environment, the solvent is evaporated and dried granules are collected. In the process, the hot gas is cooled and exits the chamber. Gas inlet and outlet temperatures are closely controlled, in combination with slurry, nozzle and atomization characteristics. If these parameters are not closely controlled, one of the process problems which arises is splattering of wet granules on the vessel wall. This reduces the yield of the process and gives uncontrolled granule size and size distribution. The exiting gas passes through a cyclone separator to capture fine granules, while the bulk of the granules are collected at the bottom of the chamber. The granules collected at the bottom of the chamber often need to be cooled before further processing. Granule size can be increased by a lower atomizing pressure, larger nozzle size and higher solids content of the slurry (Masters, 2002). Gas exiting from the cyclone needs to be filtered to remove fines and condensed to remove the solvent. Both solvent and gas can be recycled after proper conditioning to ensure quality.

Granules produced by spray drying, such as shown in **Figure 12**, are often characterized using Hall flow, whereby a fixed amount of powder is allowed to flow through a funnel and the time taken for the flow is used as a measure of powder flow (ASTM B213, 2007). Powder flow determines how fast and consistently powder will flow in a press cavity. Bulk or Scott density is a measure of the weight of powder in a given volume, which determines the consistency of die fill (ASTM B329, 2007). Scott density is also an important consideration in die design by ensuring that die cavity is large enough to hold sufficient powder to reach the target weight for the part. Both these properties are influenced by granule size, size distribution, granule structure, granule density and surface characteristics. Larger granule size and more uniform granule size distribution generally lead to faster powder flow but reduced bulk density. Therefore, an optimization is generally needed. Hollow granules, which may be caused by too fast an evaporation of the solvent, reduce bulk density. Granules with smooth surface show faster flow, whereas satellites sticking out from the granule surfaces will slow the powder flow. Another important property of a granule is its crushing strength, which should be sufficiently high to maintain good flow and bulk density, but low enough such that the granule is crushed during green body consolidation. If this crushing is not complete, large porosities may remain in the green body which may not be closed during

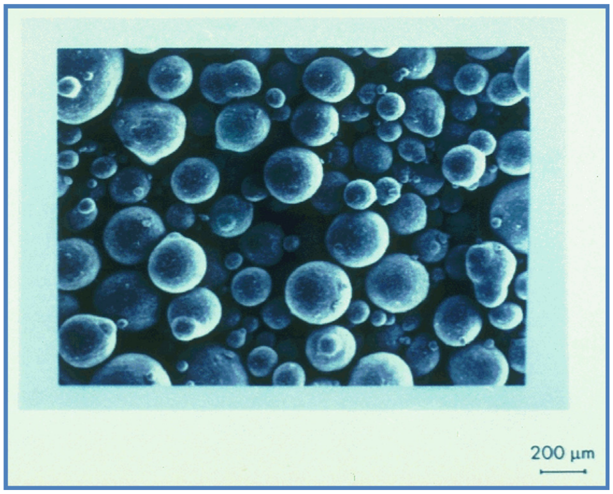

Figure 12 Typical granules created by the spray drying process.

sintering. Granule strength is a result of the choice of the fugitive binder system and drying parameters. Granule wetness is a measure of residual solvent in the granules, and it must be kept low and be closely controlled for superior process control for later processes. Granules which do not meet required properties can be put back in the mill for rework or scrapped depending on the quality standard (Masters, 2002).

Yield of the spray drying process is determined by the amount of powder fed versus collected at the bottom of the vessel. The powder collected in the cyclone is normally recycled into the milling process or scrapped, but if the applications allow, it may also be mixed with the rest of the granules, keeping in mind that it may degrade the powder quality.

1.07.6.2 Production of Dry Powder by Vacuum Drying

Powder slurry produced by the milling process can also be dried using a vacuum drying process. Vacuum drying is a batch process, so its throughput may be limited and process cost may be higher than that of spray drying. However, equipment and operational cost for vacuum drying may be generally lower.

Dried powder produced by vacuum drying is generally poorly pelletized and is therefore not suitable as a free flowing powder for uniaxial pressing. Thus, vacuum-dried powders may be used in applications where free flowing powder is not essential, such as in CIP, or as a feedstock for subsequent powder processes, such as pelletizing or mixing with other additives or components. Wax or other additives may be added either prior to vacuum drying or during the process.

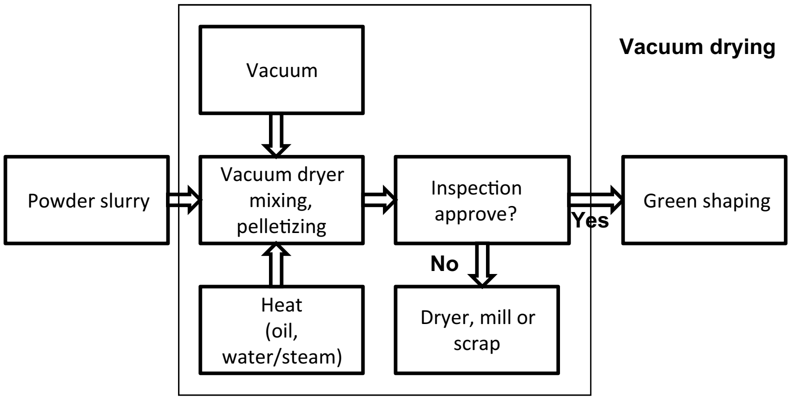

Figure 13 Schematic process flow for vacuum drying of hardmetal powders.

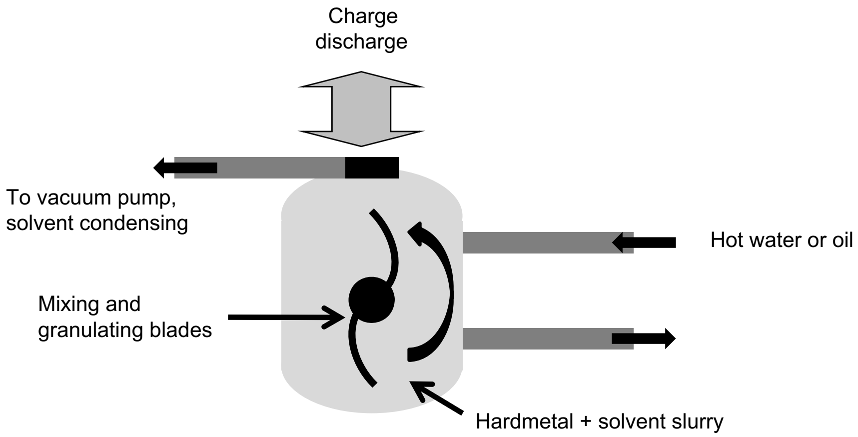

Figure 14 Schematic representation of a vacuum dryer.

Figure 13 shows a schematic representation of process flow steps for vacuum drying and Figure 14 is a schematic representation of a vacuum dryer. Vacuum driers typically consist of a double-walled chamber in which powder slurry is contained. The double walls can be used for heating or cooling the chamber in different process steps. For the purpose of drying slurry, hot water or oil may be used to raise the chamber temperature to promote solvent evaporation, which is aided by the application of a vacuum. For some processes, double walls of the chamber can also be used to control the process temperature, either to take away heat generated due to friction or to heat the contents to maintain certain level of fluidity in the slurry. Mixing blades are often used to continuously mix the powder while it is being dried to minimize powder segregation and to uniformly dry the powder. Mixing blades also help in granulating the powder with the help of a binder after the solvent has been removed. The drying chamber is connected to a vacuum pump to maintain and control chamber pressure. The solvent vapors thus collected can be condensed if needed. Vacuum drying temperature and vacuum level depend on the solvent used and the desired process time. Solids content of the slurry should also be considered in selecting the process parameters so that both quality and cost targets are met.

Mixing and drying uniformity determine the quality of vacuum-dried powder. Since hardmetal powders can be very abrasive, the condition and wear of the vessel and mixing blades are important factors in determining the quality of the powder and the efficiency of the drying process. As mentioned earlier, certain level of granulation can be accomplished in the vacuum drying mixer by controlling the temperature and the mixing process. Typically, granules thus produced are not as spherical as spray drying and therefore, are not as free flowing; however, they tend to be relatively soft. If good flowing powder is needed, vacuum-dried powder can be granulated by a variety of granulation processes after vacuum drying.

1.07.7 Green Shaping

The next powder processing step is green-forming the granulated powder produced by spray drying or vacuum drying into desirable shapes so that they can be sintered to full density. There are a great variety of green shaping processes; however, uniaxial pressing, CIP, extrusion and injection molding are by far the most commonly used, in addition to simple green machining, as shown in the schematic process flow diagram in Figure 15. Powder formulation is specifically tailored for each of these processes. The purpose of green shaping is to form the dried and granulated powder into desired shapes via compaction and get it ready for the next process step of sintering. The green shaping process must take into account not only the flow and sintering characteristics of the powder but also specified dimensional requirements and metallurgical specifications. The shrinkage characteristics of the powder must be measured and compared to the dimensional requirements. All these must be accomplished with the type of green shaping tool at hand.

Common requirements for all green shaping processes are attainment of desired metallurgical quality and dimensional specification on sintering. Metallurgical quality of hardmetal includes density, magnetic saturation, coercive force, microstructure, hardness, etc. These are closely related to the fugitive binder used and the sintering furnace and process employed. The fugitive binder affects granulation and flow characteristics of the

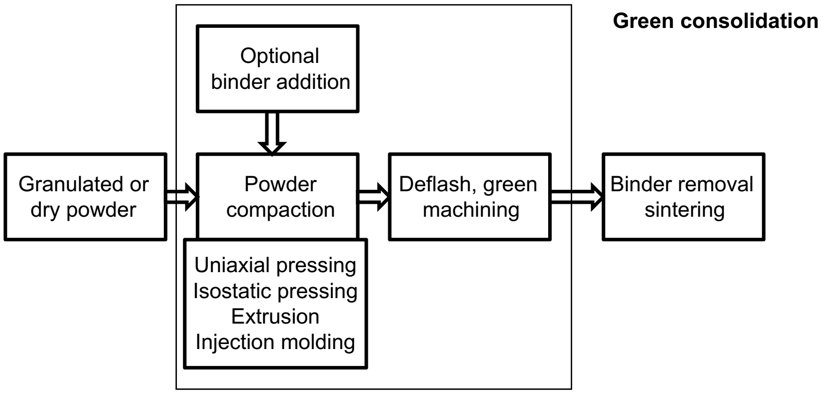

Figure 15 Schematic process flow diagram for green shaping.

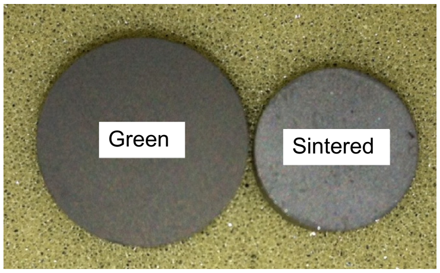

Figure 16 Example of shrinkage in a green part as a result of sintering.

powder, which, in turn, determine the size and weight control of the sintered parts. Furthermore, part green strength should be sufficient so that it can be handled without damage in the green state. At the same time, it should not be so strong that flash created by the tooling seams (fit) during the green shaping operation cannot be removed easily. Green strength is a function of green density, fugitive binder system, pressing pressure, part geometry, etc. Powder and green shaping parameters need to be controlled closely such that an optimum green strength of the part is achieved. In general, the fugitive binder is allowed to be removed in a vapor form during the early stages of sintering. The effectiveness of this process step determines carbon control in the furnace and magnetic saturation of the sintered part. Excessive carbon left behind during the binder burnout may increase magnetic saturation and leave free carbon on sintering. On the other hand, if powder has been exposed to air or humidity for extended length of time, powder or wax may get excessively oxidized, which may, in turn, reduce magnetic saturation or give eta phase on sintering.

On further heating after binder burnout, melting of metallic binder takes place, and causes the composite to shrink between 15% and 20% on a linear basis or 35–50% on a volumetric basis, as shown in Figure 16. This shrinkage is essential for achieving full density. See Chapter 1.08 Synthesis & Processing—Consolidation Techniques of this volume for more details. Thus, the dimensions of the final part are closely controlled by the dimensions of the green part and the shrinkage factor of the powder. By carefully controlling these parameters, sintered dimensions can be controlled to within 1% of dimensional target.

1.07.7.1 Uniaxial and Multiplaten Pressing

Uniaxial pressing is a fairly common method to green-shape parts made from carbide powders. This is possible due to the relative ease of the process, high production rate, and relatively low cost. Depending on the geometry of the part to be made and the cost, pressing can be used for both large- and small-sized parts, with small to large batch sizes.

As shown in schematic diagrams of process flow for uniaxial pressing in Figure 17 and of the pressing operation in Figure 18, uniaxial pressing consists of first setting up the press and die to the required settings and then placing granulated powder in powder hopper. Powder is fed to the die cavity via powder feed shoe.

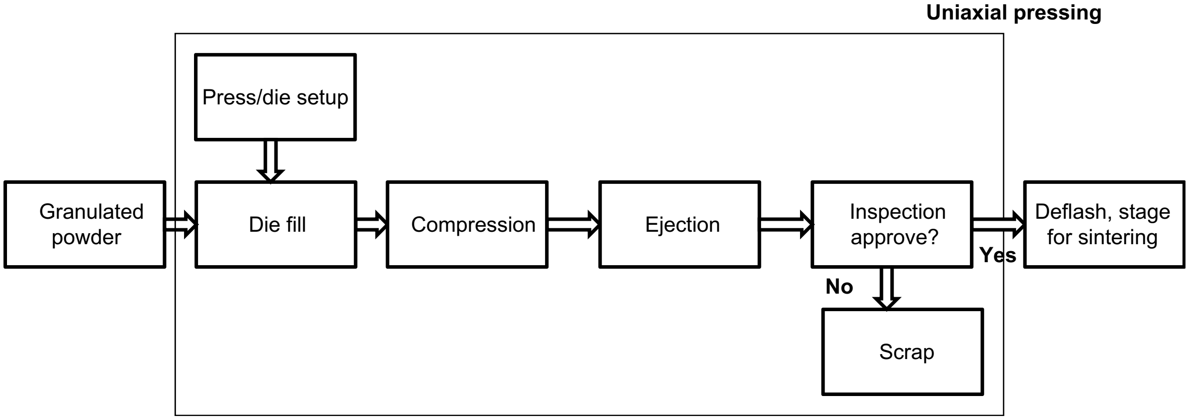

Figure 17 Schematic process flow diagram for uniaxial pressing.

The position of the bottom punch creates a measured cavity for die fill. This is followed by pressing between top and bottom punches to pressures of 30–200 MPa. The pressed part is then ejected by withdrawing the top punch and raising the bottom punch. Often a combination of motion of the two punches and die allow for different pressing cycles to obtain acceptable parts. Geometries of the die cavity and rams are closely controlled, so that the pressed part has the desired green part weight, thickness and dimensions. This ensures a fully dense sintered part with the required dimensions. Dies and rams have high precision and are made of steel body with carbide inserts at the wear surfaces to increase life before replacement in order to maintain dimensional control. They are also made to match the shrinkage factor of the powder, in combination with the intended pressing pressures. Often a core rod is used to generate a central hole through the part during the pressing operation. Significant attention is paid to align the top and bottom rams to avoid chipping and establishing a suitable pressing cycle so that a uniform green density distribution is achieved in the part without cracks and yet obtain an economical throughput. This is accomplished through fine-tuning the timing and speed of ram and die motions during pressing as well as ejection of the part. Both mechanical and hydraulic presses are used in the industry. Modern computer numerical controlled (CNC) presses are equipped with integrated robotic part pickers, which not only pick and place parts on stacked sintering trays but also conduct secondary operations, such as deflasing with a soft brush. CNC controls allow the press to be set up at the center of the allowable green weight and thickness of the part required by sintered dimensions.

During the first stage of pressing, powder granules reorient, followed by crushing and deformation of granules in the second stage. The third and final stage involves densification through continued compaction

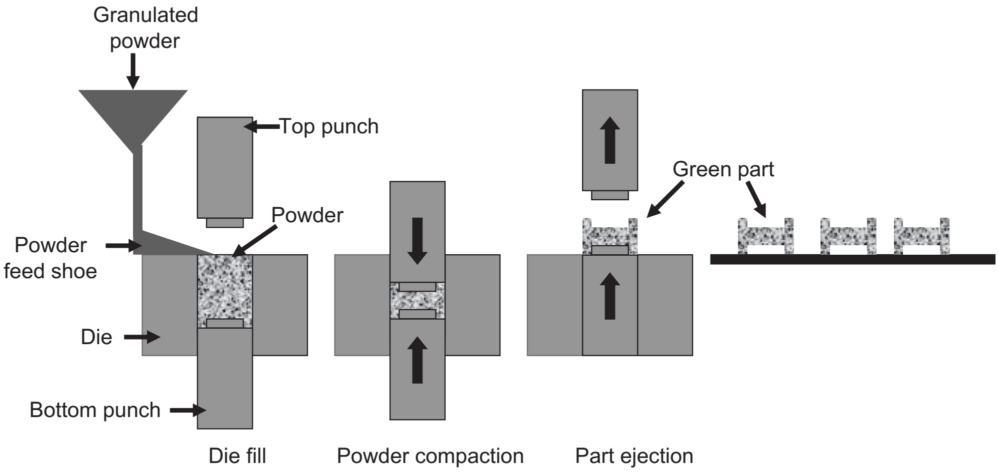

Figure 18 Schematic representation of uniaxial pressing.

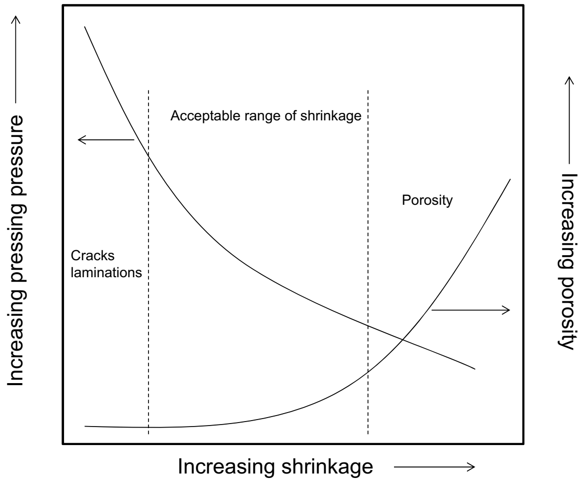

Figure 19 Process of optimization of pressing pressure and shrinkage in uniaxial pressing of carbide powder.

and deaeration of the compact (German, 2005). Significant shear is involved at die walls and between granules, whereas densification by compression is dominant near the top and bottom rams. Thus, control of shear and deformation characteristics of granule is critical to obtaining the desired results. As part ejects, it expands due to elastic recovery, therefore, the part ejection rate and ejection pressure are closely controlled. The density of the powder is typically increased from about 20–30% to 40–60% of the theoretical during the pressing operation.

Repeatable powder flow and Scott density are critical to ensuring an acceptable control of weight and dimensions of both green and sintered parts. Poor powder flow may require longer cycle time on the press and may lead to inconsistent part quality. As indicated before, Scott density is an important factor to consider in die design. The die cavity should be large enough to hold sufficient powder to achieve target part weight. An optimum Scott density is critical to the pressing operation, since too low a Scott density may excessively increase pressing pressure, whereas too high a Scott density may not allow for sufficient shear to take place during compaction. A very low pressing pressure may not give the needed compaction for achieving thickness and weight targets. On the other hand, a very high pressing pressure, in addition to tooling damage, leads to excessive elastic recovery, and cracks. This is sometimes controlled by maintaining an axial pressure during ejection or synchronizing the ejection speed with ejection pressure. Modern CNC presses offer sophisticated decompression motion to remove cracks and delaminations. Flash, as noted earlier, is generated by powder flow between mating tooling surfaces and is difficult to remove once sintered. It can be minimized by reducing the gap between tooling surfaces and keeping tool wear to a minimum. Once formed, it is often removed in the green state using a brush either automatically or manually.

An important aspect of uniaxial pressing is optimization of pressing pressure, shrinkage and powder particle size in order to obtain crack-free parts meeting dimensional and metallurgical requirements. This is schematically shown in Figure 19. With increasing pressing pressures, shrinkage and porosity decrease; however, incidence of cracks and laminations increases. On the other hand, if pressing pressure is too low, shrinkage will be too high, resulting in unacceptable porosity. Thus, an optimum shrinkage is required, which is accomplished by appropriate die design in combination with powder shrinkage characteristics. As powder particle size becomes submicron and nanograined, high-shrinkage dies are used to keep pressing pressures within acceptable limits to avoid pressing cracks. The resulting incidence of unacceptable porosity can be minimized by hot isostatic pressing or hot pressing.

Dies with multiple cavities are used to press multiple parts in each stroke of the press, thus increasing throughput. Top and bottom rams can be split into more than one ram for multiplaten pressing to achieve complex geometries on top and bottom surfaces. Side pressing, provided by transversely acting rams, has also been utilized to achieve complex shapes on the vertical surfaces of the part. Robotic pickers, part handling systems and tool changers have contributed to increasing throughput and reducing cost.

1.07.7.2 Cold Isostatic Pressing

CIP is commonly used for large parts with low volumes, often requiring subsequent green machining for the final shape. Dimensional control in CIP is generally comparable to uniaxial pressing. Dry-bag and wet-bag cold isostatic presses are commonly used, with the former used for large numbers of small volume parts and the latter for small numbers of high-volume parts, which typically may be green machined.

Figures 20 and 21, respectively, show schematic diagrams of process flow and press operation for CIP. Powder is poured into an impervious moldable bag, evacuated, and subjected to 50–200 MPa of isostatic pressure using a water-based liquid medium at ambient temperature. This causes powder compaction to the desired green densities. In the wet-bag CIP operation, the entire bag is removed from the pressure chamber and the part is obtained by cutting open the bag. On the other hand, in dry-bag CIP, the bag remains fixed to the pressure chamber and only the dry part is removed. Shaped bags with cores are commonly used to obtain near-net shapes. Powders with no or low wax may also be used in CIP.

Parts may be machined in a green or presintered state and even after sintering in the hard state. Thus, material yield in CIP may vary from as low as 20–30% to 100% depending on the part. However, material utilization can be improved by making parts as close to the desired size as possible. As with uniaxial pressing, calculation of shrinkage factors helps in estimating the size of the green part for the desired sintered part. Furthermore, extra care needs to be taken, especially for large parts, to minimize variation in powder green density, which may result in deformation or cracking of the sintered part. This can be accomplished by controlling flow characteristics and vibration during powder filling. The applied pressure needs to be high enough to obtain sufficiently high green density and green strength for green machining and obtaining acceptable sintered density and microstructure. One common defect in cold isostatically pressed parts is the formation of "elephant feet", whereby the ends of a cylindrical bar, for example, have a larger diameter compared to the rest of the body. Elephant feet are generally cut off to obtain a part with uniform diameter.

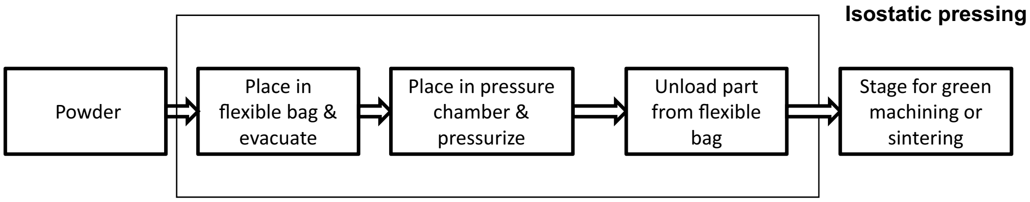

Figure 20 Schematic representation of the cold isostatic pressing (CIP) process.

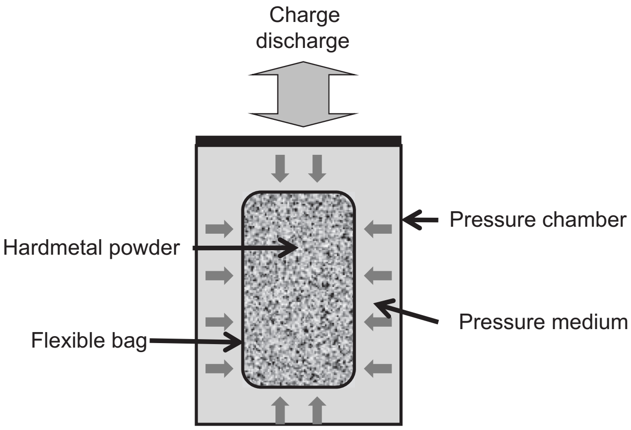

Figure 21 A schematic diagram of a cold isostatic press.

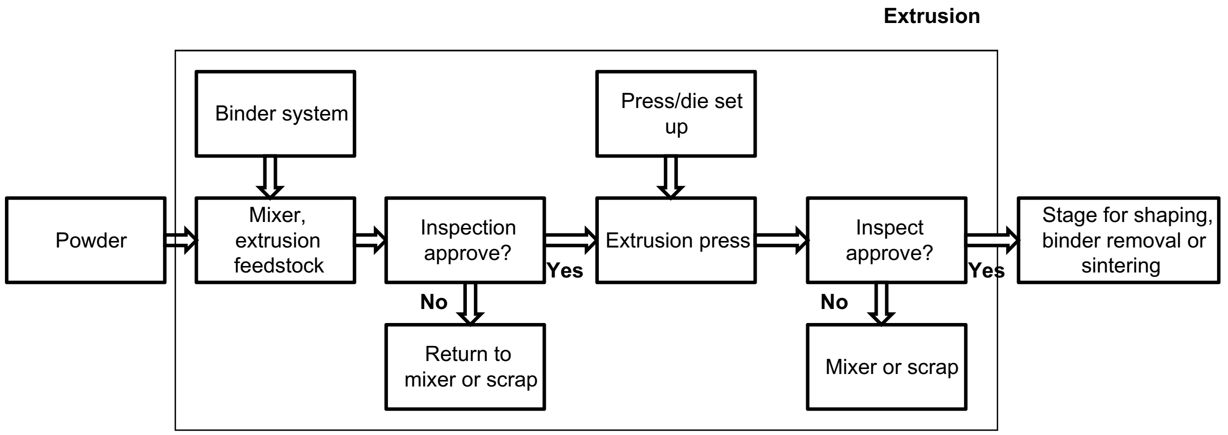

Figure 22 Schematic of process flow diagram for the extrusion process.

1.07.7.3 Powder Extrusion

Many hardmetal parts are in the shape of rods, and these are commonly produced by extrusion. Green shaping of powder to produce solid carbide drills, end mills, boring bars, etc. can be accomplished via the use of powder extrusion. Components having internal structures, such as internal holes for delivering coolant to the cutting edge, are preferentially made by this process.

As shown in Figures 22 and 23, hardmetal powder extrusion is accomplished in an extrusion press, using either a piston-type or a screw-type mechanism to push a powder/binder mix through a die. Spray-dried or vacuum-dried powder is mixed with a binder system, tested for approval, and then placed in the press for extrusion. The most common die shape is round, but a variety of cross-sections can be extruded, as illustrated in Figure 24. Filaments at the center of the die can be used to generate continuous internal holes in the extrudate. Spirals on the die wall, in combination with two or more filaments, can generate rods with spiraling holes with a fixed pitch. The pitch of the holes is determined by the desired pitch of the flutes of the solid rod product (Friedrichs, 1998). Both batch-type and continuous-type extrusion processes are used depending on the volume of individual batch size.

Formulation of the powder/binder mix is critical to the success of the extrusion process, since it determines the pressure at which powder can be extruded. Therefore, good mixing of the powder and the binder system must be accomplished. Generally, binder type and amount, as well as the temperature during extrusion, determine the extrusion pressure and speed. An optimum powder/mix should have a good balance between powder compaction due to compression and powder flow through shear. Powder compaction is needed to remove porosity and achieve sufficiently high green density so that full density is achieved on sintering. On the other hand, powder shear is needed to obtain an economical extrusion rate at an acceptable pressing pressure. The green strength of the extrudate must be sufficiently high so that it can be handled and processed without damage or excessive deformation. The binder system chosen will also determine delubing and sintering cycles needed for full densification.

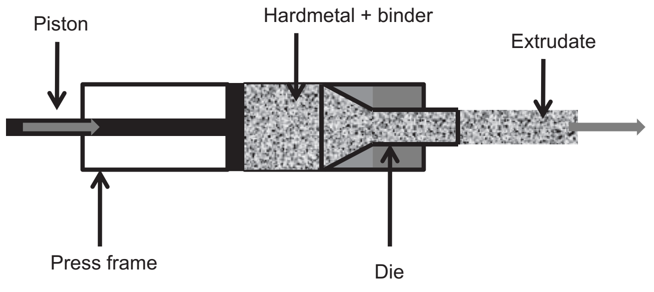

Figure 23 Schematic representation of a piston type extrusion press.

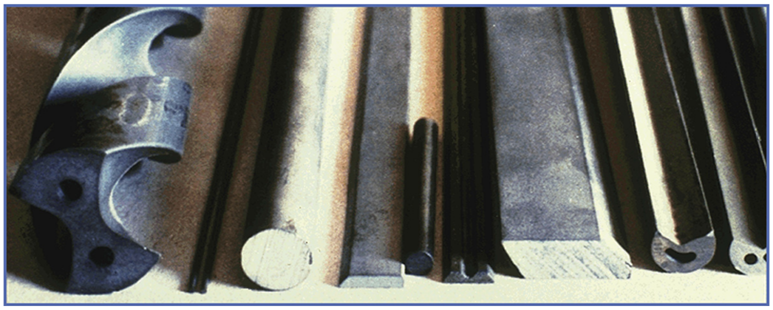

Figure 24 An illustration of various cross-sections of rods made by powder extrusion.

Poor mixing of powder and binder results in binder pools which create surface imperfections or microstructural defects. This can also lead to excessively high variability in the extrudate. Too high a binder content or temperature may cause a high rate of extrusion but without sufficient compaction of powder. On the other hand, too low a binder content may result in excessively high pressing pressures, which can cause surface cracks or damage to tooling or the press. Furthermore, it may also slow down the rate of extrusion, thus making it uneconomical. A consistent pitch of the spiraling holes in rods with coolant holes is critical since it needs to match with the pitch of the flutes which are subsequently ground on the sintered rods. An inconsistent pitch may result in coolant holes opening up in the middle of flutes as they are ground.

1.07.7.4 Powder Injection Molding

Complex hardmetal parts, which cannot be easily made by pressing, are best made by injection molding. Small to medium size parts made by green machining after uniaxial pressing or CIP are good candidates for being made by injection molding.

As illustrated in the schematic diagrams in Figures 25 and 26, the injection molding machine injects a powder/binder mixture, using a screw feed, into a confined cavity formed by tooling, which is opened at the end of each stroke or shot to release the green part. The binder system used for hardmetals typically consists of multiple components, depending on the injection process employed. Wax or wax/polymer systems, with additives to control rheology and overall injection behavior of the feedstock are used as binder systems for carbide powders. Furthermore, selection of the binder system should also consider the method used to remove the binder prior to sintering while retaining sufficient green strength for part handling and size and shape control. One- or two-stage delubing is used depending on the binder system characteristics. The binder system used and delubing method employed generally leave some residual carbon. So, the binder system, delubing method and sintering cycle together should be chosen so as to allow precise and repeatable control of carbon in the sintered product. The screw feed carefully controls time and temperature, speed, pressure and amount of feedstock being

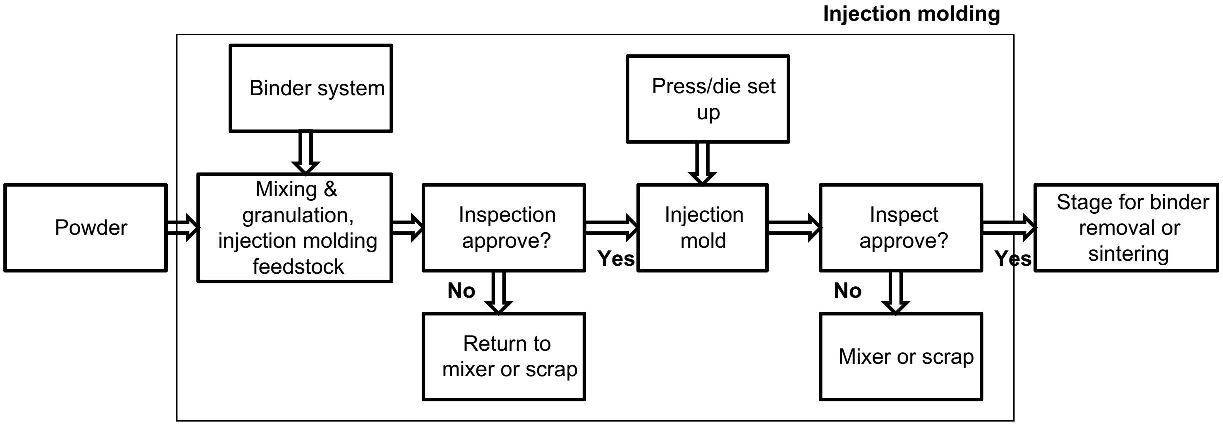

Figure 25 Schematic representation of the injection molding process.

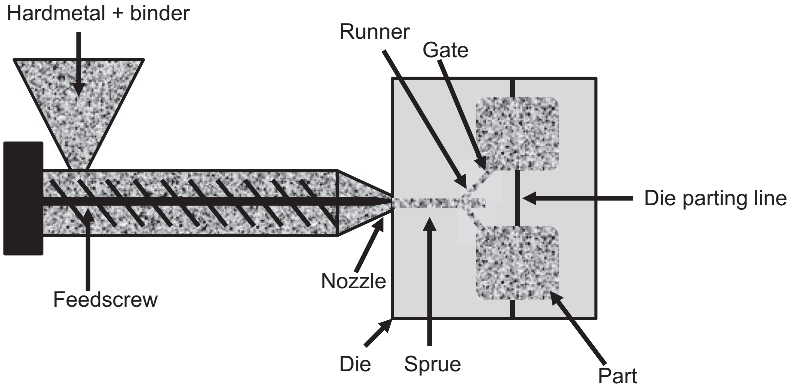

Figure 26 A schematic representation of the injection molding press.

injected in each stroke. These parameters must be carefully optimized in conjunction with feedstock properties, such that defect-free parts can be made in an economical manner. Special considerations need also to be given to tooling design which serves to deliver the feedstock to the die cavity through a system of sprue, runner and gate; remove air from the formed part; as well as allow for a fast release of the part with acceptable surface finish but without cracks, laminations, flashings, and other defects (German, 2011). Often, a robot is used as a part handling system, to pick and place parts for the next operation.

Common defects in injection-molded parts include porosity, surface or internal defects, flash on the surface, cracks, etc. Porosity could be caused by several reasons, including a very high shrinkage factor and/or inadequate removal of air through vents in the die. Surface and internal defects evident as flow marks could be caused by powder/binder separation or insufficient bonding of the two fronts of feedstock as the die is filled. This could be caused by too low a process temperature or pressure. Cracks are formed when part shrinkage after injection is restrained by a die component. It can be minimized by proper die design or feedstock design to minimize shrinkage on cooling. Flash is a common defect produced at the juncture of two tooling components, where a crevice is available for the feedstock to extrude into. A remedy for this type of defect either involves die design to place the flash at a noncritical area or provide a better fit between the die components or involves control feedstock and/or process characteristics to minimize the extrusion through the crevice (German, 2011).

1.07.7.5 Post–Green Forming Operations

Most green parts undergo some form of green shaping operation after green forming by uniaxial pressing, CIP, extrusion or injection molding. These may range from removing small amounts of powder in a flash to significant amounts of material to obtain desired shapes. These operations help reduce the amount of hard grinding needed after sintering, improve sintering yield, and reduce powder cost by making near-net-shape parts.

As discussed earlier, flash is generated at the juncture of two die segments in uniaxial pressing or injection molding. These thin slivers of powder material are removed by a soft brush either manually or by an automated process. Presence of flash (or poorly removed flash) may not allow parts to be placed properly for sintering, and once sintered, its removal may chip the entire edge. Powder particles left over from the deflashing operation should be carefully removed with a brush or blown with air. Leftover loose carbide particles may settle on the surface of parts, creating defects.

Green machining is a common form of making near-net-shape parts fabricated by any of the above green shaping processes. Cold isostatically pressed parts are primary candidates for subsequent green machining; however, parts made by uniaxial pressing, extrusion or injection molding are also green machined. Figure 27 shows a turning operation for a cold isostatically pressed carbide part. Similarly, milling, drilling and other operations are used as green machining processes to achieve desired shape of the part. Swarf produced as a result of the green machining process is in a powder form, is removed using air flow, and is collected in a cyclone separator. The exhausted air is filtered before being released to the atmosphere. Diamond tooling is best suited for these machining operations since the highly abrasive nature of carbide can easily dull the cutting edge of any

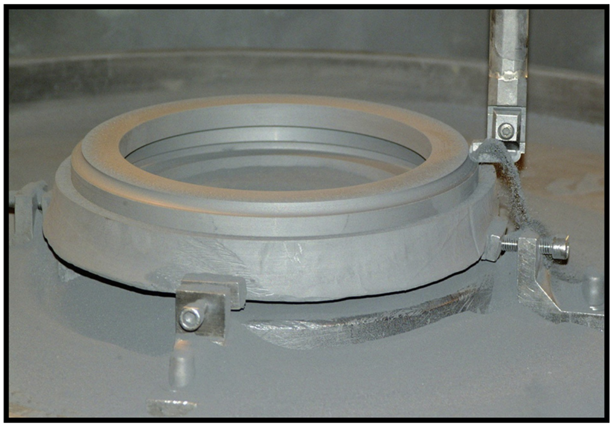

Figure 27 An illustration of a turning operation of a green part made by cold isostatic pressing.

other tool material quickly. Cutting forces and cutting temperatures are modest; nevertheless, positive cutting edges and small to no hones are preferred to keep cutting forces low and generate smooth surfaces without powder pull out (Heath, 1989, pp. 105–117). Clamping systems for parts need to be optimized to ensure positive part holding without crushing the soft carbide green shapes. Due to their high density, carbide parts are relatively heavy and therefore, should be sufficiently supported during machining, and support provided by the part itself, which is common for fully dense parts, should be minimized.

1.07.8 Environmental, Health and Safety

EHS concerns are of paramount importance in handling hardmetal powders. Some of these concerns are common to handling all powders; however, others are specific to hardmetals and related materials used in hardmetal production. All materials should be accompanied by Material Safety Data Sheets (MSDS), which outline long-term and acute exposure limits as well as actions to be taken in case of an accidental spill or release. Work environment should be closely monitored and engineered to ensure that the exposure is within recommended limits.

Exposure to carbide and metal powders should be minimized by maintaining and monitoring the air handling system, using protective clothing and gear, and maintaining good hygiene. As powder particle size becomes submicron or finer, they may become pyrophoric and undergo spontaneous combustion when exposed to air. This can be avoided by keeping these powders under protective cover (neutral gas, solvent or wax). Use of organic solvents brings the risk of explosion of its vapors in the presence of a spark. This can be minimized by using facilities and equipment which do not generate sparks. It is a good practice to familiarize oneself with MSDS of any new material and conduct a Potential Hazard Analysis for any new process.

Acknowledgments

The author wishes to acknowledge support provided by Kennametal Inc. management in preparing the manuscript and colleagues Rich Gubanich, Neal Myers, Anders Petersson and Mark Greenfield in reviewing the manuscript.

References

ASTM B213. (2007). *Standard test method for flow rate of metal powders. Annual book of ASTM standards, Sec. 2* (Vol. 2.05). Conshohocken, PA: ASTM International.

ASTM B329. (2007). *Standard test method for apparent density of metal powders and compounds using the Scott Volumeter. Annual book of ASTM standards, Sec. 2* (Vol. 2.05). Conshohocken, PA: ASTM International.

Bose, A. (2011). A perspective on the earliest commercial PM metal-ceramic composite: cemented tungsten carbide. *International Journal of Powder Metallurgy, 47*(2), 31–50.

Friedrichs, A. (1998). US Patent 5780063. Apparatus for producing a hard metal or ceramic rod having helical bores.

German, R. (1994). *Powder metallurgy science*. Princeton, NJ: Metal Powder Industries Federation.

German, R. (2005). *Powder metallurgy & particulate materials processing*. Princeton, NJ: Metal Powder Industries Federation.

German, R. (2011). *Metal injection molding: A comprehensive MIM designing guide*. Princeton, NJ: Metal Powder Industries Federation.

Heath, P. J. (1989). *Ultrahard tool materials, metals handbook* (9th ed.). *Machining* (Vol. 16) Metals Park, OH: ASM International.

Kear, B. H., & Strutt, P. R. (1995). Chemical processing and applications for nanostructured materials. *Nanostructured Materials, 6*(1–4), 227–236.

Koch, C. C. (1998). *Milling of brittle and ductile materials, ASM handbook*. *Powder metal technologies and applications* (Vol. 7). Metals Park, OH: ASM International.

Masters, K. (2002). *Spray drying in practice*. Denmark: SprayDryConsult International ApS.

Mehrotra, P. K., Mizgalski, K. P., & Santhanam, A. T. (2006). Recent advances in tungsten based hardmetals. In A. Bose, & R. J. Dowding (Eds.), *Proceedings of the 2006 international conference on tungsten, refractory & hardmetals VI* (pp. 1–10). Princeton, NJ: Metal Powder Industries Federation.

Mehrotra, P. K., Santhanam, A. T., Mizgalski, K. P., Roediger, K., & VanDenBerg, H. (2008). Trends in hardmetal gradient microstructures: processing & applications. In A. Bose, R. J. Dowding, & J. A. Shields, Jr. (Eds.), *Proceedings of the 2008 international conference on tungsten, refractory & hardmetals VII*. Princeton, NJ: Metal Powder Industries Federation.

Santhanam, A. T., Tierney, P., & Hunt, J. L. (1990). *Cemented carbides, metals handbook* (10th ed.). *Properties and selection* (Vol. 2) Metals Park, OH: ASM International.

Shaw, L. L., Ren, R., & Yang, Z. (2004). US Patent 6,793,875 B1. Nanostructured carbide cermet powders by high energy ball milling.

Soares, E., Malheiros, L. F., Sacramento, J., Valente, M. A., & Oliveira, F. J. (2011). Ethanol and water processing of submicron cemented carbide powders. *Journal of American Ceramic Society, 94*, 84–91.

Stoll, W. M., & Santhanam, A. T. (1992). *Industrial hard carbides* (4th ed.). *Kirk-Othmer encyclopedia of chemical technology* (Vol. 4) Hoboken, NJ: John Wiley & Sons, Inc.

Upadhyaya, G. S. (1998). *Cemented tungsten carbides: production, properties and testing*. Westwood, NJ: Noyes Publications.

Zhang, F. L., Wang, C. Y., & Zhu, M. (2003). Nanostructured WC/Co composite powder prepared by high energy ball milling. *Scripta Materialia, 49*(11), 1123–1128.

1.08 Consolidation Techniques

Randall M. German, Department of Mechanical Engineering, College of Engineering, San Diego State University, San Diego, CA, USA

Nomenclature

A $N_C \cos(\varphi/2)$, dimensionless
A_{SS} Solid–solid contact area, m^2 (convenient units: μm^2)
C Solid concentration in the matrix, m^3/m^3 or dimensionless
C_G Grain connectivity, dimensionless
C_{SS} Contiguity, dimensionless
D Particle size, m (convenient units: μm)
D_S Temperature-dependent solid diffusivity in the liquid, $m^2\ s^{-1}$
$F(G)$ Cumulative grain size distribution, dimensionless [0,1]
$F(L)$ Cumulative intercept size distribution, dimensionless [0,1]
G Grain size, m (convenient units: μm)
G_{50} Median grain size, m (convenient units: μm)
K Grain growth rate parameter, $m^m\ s^{-1}$ (convenient units: $\mu m^m\ s^{-1}$)
L Intercept size, m (convenient units: μm)
L_0 Initial length, m (convenient units: mm)
L_{50} Median intercept size, m (convenient units: μm)
N_C Three-dimensional grain coordination number, dimensionless
N_L Number of grains per unit line, m^{-1} (convenient units: μm^{-1})
N_{SL} Number of solid–matrix intercepts per unit length of test line, m^{-1} (convenient units: μm^{-1})
N_{SS} Number of solid–solid intercepts per unit length of test line, m^{-1} (convenient units: μm^{-1})
P_G Gas pressure in the pores, Pa
$P(n)$ Probability of finding n contacts, dimensionless
R Universal gas constant, 8.31 $J\ mol^{-1}\ K^{-1}$
S_{SL} Solid–matrix surface area per grain, m^2 (convenient units: μm^2)

http://dx.doi.org/10.1016/B978-0-08-096527-7.00008-8

S_{SS} Solid–solid surface area per grain, m^2 (convenient units: $\mu\mathrm{m}^2$)
T Temperature, K
V_{L} Volume fraction of liquid, dimensionless
V_{S} Volume fraction of solid, dimensionless
X Neck diameter or diameter of the contact, m (convenient units: μm)
c Scale parameter related to the median grain size, m (convenient units: μm)
d Diameter of capillary tube, m (convenient units: μm)
d_{P} Pore size, m (convenient units: μm)
g_1 Geometric constant, near 192, dimensionless
g_2 Geometric constant, near 16, dimensionless
g_3 Geometric constant, near 160, dimensionless
m Mechanism-dependent exponent or shape parameter, dimensionless
n Mechanism-dependent exponent, dimensionless
r Radius of curvature, m (convenient units: μm)
r_{m} Liquid meniscus radius at the pore–liquid–grain contact, m (convenient units: μm)
t Time, s
ΔL Change in a dimension from the size L_0, m (convenient units: mm)
ΔP Pressure difference across a curved liquid surface, Pa
Γ Ratio of densification rates, dimensionless
Ω Atomic volume, $\mathrm{m}^3\ \mathrm{mol}^{-1}$
δ Distance between contacting grain centers, m (convenient units: μm)
φ Dihedral angle, rad (convenient units: degree)
γ_{LV} Liquid–vapor surface energy, $\mathrm{J\ m}^{-2}$
γ_{SL} Solid–liquid surface energy, $\mathrm{J\ m}^{-2}$
γ_{SS} Solid–solid grain boundary energy, $\mathrm{J\ m}^{-2}$
γ_{SV} Solid–vapor surface energy, $\mathrm{J\ m}^{-2}$
κ Reaction rate constant, s^{-1}
λ Mean grain separation, m (convenient units: μm)
θ Contact angle, rad (convenient units: degree)
ρ Instantaneous density, $\mathrm{kg\ m}^{-3}$ (convenient units: $\mathrm{g\ cm}^{-3}$)
ρ_{G} Green density, $\mathrm{kg\ m}^{-3}$ (convenient units: $\mathrm{g\ cm}^{-3}$)
ρ_{S} Sintered density, $\mathrm{kg\ m}^{-3}$ (convenient units: $\mathrm{g\ cm}^{-3}$)
ψ Angle in capillary bonding, rad (convenient units: degree)

1.08.1 Introduction to Sintering Processes

Packed particles heated near their melting temperature bond together by a combination of atomic motion events. The thermally induced bonding of particles is called sintering. The term initially described mineral agglomeration by heating, coming from the "cinder" concept. By the early 1900s, sintering was used to describe the heat treatment of metal powders to form solids. This early work relied on direct current heating (spark sintering) to induce sintering, as evident from several patents on refractory metal lamp filaments. By the 1920s, cemented carbides were sintered with a transition metal (Co, Fe, or Ni) bonding addition. In the late 1930s, ceramic firing began to be termed sintering.

Sintering occurs by atomic motion as induced by high temperatures. Atoms vibrate around their lattice sites and higher temperatures induce more vibrational amplitude and an increase in vacant lattice sites. Thus, atomic diffusion along volume, surface, vapor, and grain boundary pathways accelerates at higher temperatures. These are described by Arrhenius exponential temperature relations. Bond formation between contacting particles initiates at low temperatures, but becomes significant near the material melting temperature. Hence, it is appropriate to think of sintering with respect to the material's melting temperature. Snow sinters to form glacial ice at temperatures near $-15\ ^\circ\mathrm{C}$, while cemented carbides show first signs of sintering beyond $1000\ ^\circ\mathrm{C}$. But both happen as the melting temperature is approached. Additionally, sintering is faster as particle size decreases. This is because diffusion distances are shorter and curvature stresses are larger with small particles. Liquid phases lubricate and enhance sintering, especially since diffusion rates in liquids are 100–1000 times higher than in solids. Likewise, external pressure supplements the inherent sintering event, supplementing the capillary stress with an external stress.

1.08.2 Phenomenological Description of Sintering

Sintering involves the reduction in surface energy initially by the growth of interparticle bonds and later in the cycle by microstructure coarsening. The surface energy per unit volume depends on the inverse of the grain size, so smaller grains have more energy and sinter at lower temperatures. However, not all surface energy is

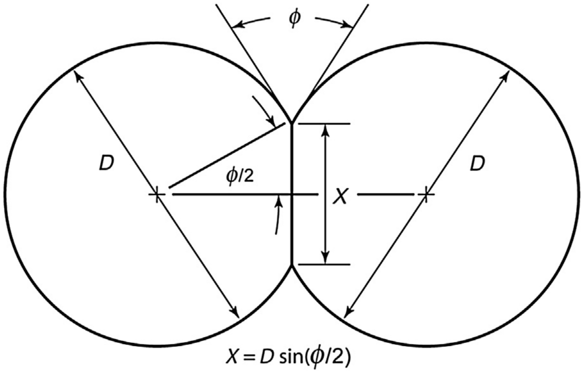

Figure 1 The classical two-sphere sintering model, where particles of diameter *D* grow a bond of diameter *X* with a dihedral angle reflecting the solid–solid and solid–vapor surface energies. Shrinkage occurs as the bond grows.

available for sintering. In crystalline solids, particle contacts from bond that contain grain boundaries consisting of disrupted atomic bonding with an associated grain boundary energy. As illustrated in Figure 1, neck growth between particles of size D removes surface energy (surface area is proportional to X^2) with an offsetting increase in grain boundary energy (boundary area is proportional to X^2). So sintering is favored when the surface energy is larger than the grain boundary energy. The dihedral angle shows where the grain boundary emerges at the surface. Late in sintering, grain growth reduces this grain boundary area. Hence, sintering models embrace surface area elimination via bonding and densification, as well as coarsening via pore and grain growth.

Conceptualizations and mathematical treatments consider the following key factors:

Driving forces arise from the surface energy, grain boundary energy, and curvature, all acting to move the microstructure to lower energies.

Transport mechanisms are the atomic motion paths that respond to the driving forces and include volume diffusion, grain boundary diffusion, surface diffusion, plastic flow, dislocation climb, and evaporation–condensation.

Sintering stages describe the geometric progress resulting from the atomic motion and generally focus on bonding (initial stage), pore rounding and closure (intermediate state), and pore elimination with grain growth (final stage); these stages change the driving forces and dominant transport mechanisms.

The matrix of driving forces, transport mechanisms, and geometric stages, along with microstructure evolution assumptions (such as pores migrating with moving grain boundaries or separating from grain boundaries) give over 100 different combinations that make up the body of sintering theory as reviewed by German (1996) and Kang (2005).

To move an atom inside a crystal requires the atom to break free of its neighbors, which is analogous to evaporation, so it is a difficult process except at high temperatures. The activation energy required to break free an atom generally scales with the absolute melting temperature. Hence, stable high-temperature compounds resist atomic motion and prove difficult to sinter; in other words, sintering scales with the melting temperature. During sintering the population of atoms that have sufficient energy to move is described by statistical concepts captured in the Boltzmann energy distribution and Arrhenius temperature relation—an exponential dependence on the activation energy divided by the absolute temperature. Accordingly, sintering is faster as temperature approaches the melting point where a material exhibits a rate of atomic jumping that is about a million moves per second. Practical sintering is observed when the rate of atomic jumping is just 1% of that.

The moving atoms preferentially deposit at the bond between particles to lower surface area and energy, resulting in neck growth. This bond is irreversible. Each atom is small, so growth of sinter bonds requires many billions of atomic jumps. Along with particle bonding, several other changes occur in the sinter body, including increases in strength, conductivity, hardness, density, and a decrease in dimensions and surface area.

Because of their high melting temperatures, hard materials resist sintering. Thus, extremely high temperatures are required to sinter carbides, borides, and nitrides. There are several problems. First, the compounds can decompose before they sinter. Second, the devices required to reach very high temperatures are quite expensive. Third, although the sintered structures are very hard, they are also brittle. Accordingly, several means exist to improve sintering and to improve toughness and ductility. These are usually composites involving a tough metallic phase that melts, spreads, and cements the hard particles together. Termed cemented carbides, they have benefits of a reduced sintering temperature and improved processing cost. This is done by liquid-phase sintering (LPS), and compositions include most of the hard materials—WC–Co, TiC steel, Si_3N_4–Y_2O_3, and so on.

1.08.3 Liquid-Phase Sintering

Thermodynamic factors make solid-state sintering difficult for the hard materials. A widely applied variant is LPS. It induces lower temperature densification using mixed powders that form a liquid during the heating cycle. As pointed out by German (1985) about 90% of the commercial value of sintered products is formed using a liquid during the heating cycle.

In the typical LPS situation, the solid grains are soluble in the liquid. This solid solubility causes the liquid to spread and wet the solid grains, providing a capillary force that pulls the grains together. Often termed a sintering stress, capillarity is equivalent to about 10 atmospheres external pressure during sintering. Dissolution of solid from the grain surface slightly shrinks the grains and the liquid lubricates the grains to enable rapid repacking. In hot stage microscopy, Froschauer and Fulrath (1976) show the grains literally leaping into new positions on liquid formation. At the same time, the high sintering temperature softens the solid, further assisting densification by diffusional creep. High diffusion rates are associated with liquids, giving fast sintering if the solid is soluble in the liquid. The final product is a composite with solid grains dispersed in a network of solidified liquid, allowing customization of properties depending on the amount and size of each phase.

Early uses of LPS involved firing ceramics with a glass bond, giving porcelain and earthenware. Glass is a viscous liquid at high temperatures. For hard materials, LPS became the mainstay fabrication process for tungsten carbide, abrasives, diamond, and other hard materials starting in the 1920s. The process is used in a diverse range of applications from the fabrication of oil well drill bits to wedding rings.

Conceptualization of how LPS works started with W–Ni–Cu alloys in the 1930s. A first conceptual model was offered by Lenel (1948) based on observations from a variety of systems. From this base, Kingery (1959) created a quantitative three-stage treatment. The current conceptualization is four stages as captured in a recent review by German, Suri, and Park (2009)—solid-state heating, rearrangement, solution-reprecipitation, and solid skeletal sintering. The events taking place during LPS are outlined in **Figure 2**. One powder is more refractory and remains solid, while the other powder melts during the heating cycle (often eutectic melting). On cooling, the solid grains are cemented by the frozen, former liquid phase, thus the term cemented carbides.

Prior to liquid formation, the solid structure solid-state sinters. On first liquid formation, grain surfaces are dissolved, while capillary force from the wetting liquid pulls the solid grains together. This rearrangement event gives a burst of densification that is paced by heat transfer rates and the enthalpy needed to form the liquid. Next, the solid grains undergo dissolution into the fresh liquid. There is a net transport from the smaller grains to the larger grains. As a consequence, over time, the large grains grow at the expense of the small grains. Grain shape accommodation ensures a tight fitting together of the grains to eliminate pores, thereby removing vapor surface energy. This happens by a process termed solution-reprecipitation (solid dissolves into the liquid, diffuses, and precipitates elsewhere as solid). After the liquid reaches saturation, the contacting solid grains grow sinter bonds, giving a rigid three-dimensional (3D) solid skeletal structure with liquid dispersed in the spaces between solid grains. At this point, further densification of the solid skeleton structure occurs slowly in the final stage of LPS. To speed the process, it is common to apply external pressure to squeeze any residual pores closed.

The details behind the stages, mechanisms, and conceptual developments in LPS are detailed in documents by Eremenko, Naidich, and Lavrinenko (1970), German (1996), Kang (2005), German et al. (2009), and German (2010). In recent years, the publication rate on LPS has accelerated as applications emerged; today there are over 200,000 journal articles and another 200,000 conference papers on LPS. Coarsening during sintering is an inherent part of the analysis.

The schematic density map in **Figure 3** suggests how a variety of stages impact LPS. At the start, the body is at the green density (pressed powder condition), at maybe 60% of theoretical. Although the regions are illustrated with hard demarcations, in reality, there is an overlap between events. With no liquid, only solid-phase sintering occurs to reach full density, which is slow and usually requires very small particles, as is typical in ceramics. On the other hand, with a large quantity of wetting liquid, densification is complete once the melt flows to fill the pores between the solid grains. However, such systems are weak at the sintering temperature and easily distort,

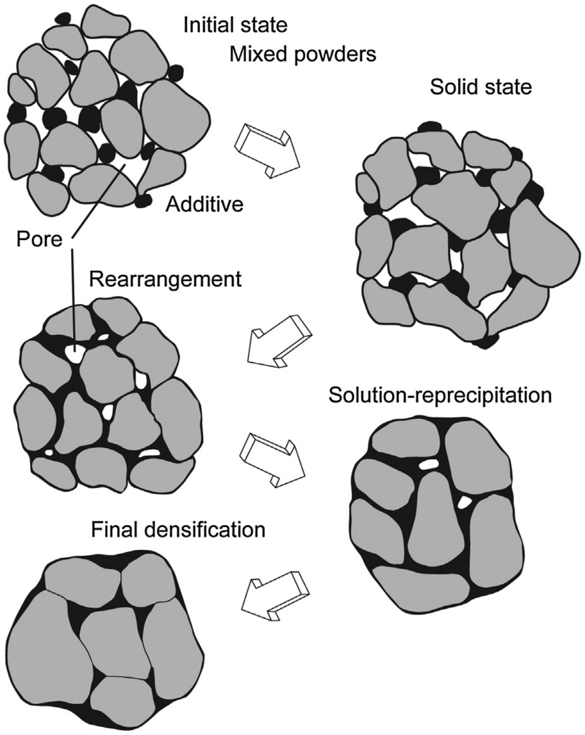

Figure 2 A schematic of the microstructure changes during LPS, starting with mixed powders and pores between the particles. During heating the solid grains sinter, but when a melt forms, it spreads and causes the solid grains to rearrange. Subsequent densification by solution-reprecipitation is accompanied by coarsening. For many products, porosity decreases as grain shape changes, facilitating pore filling.

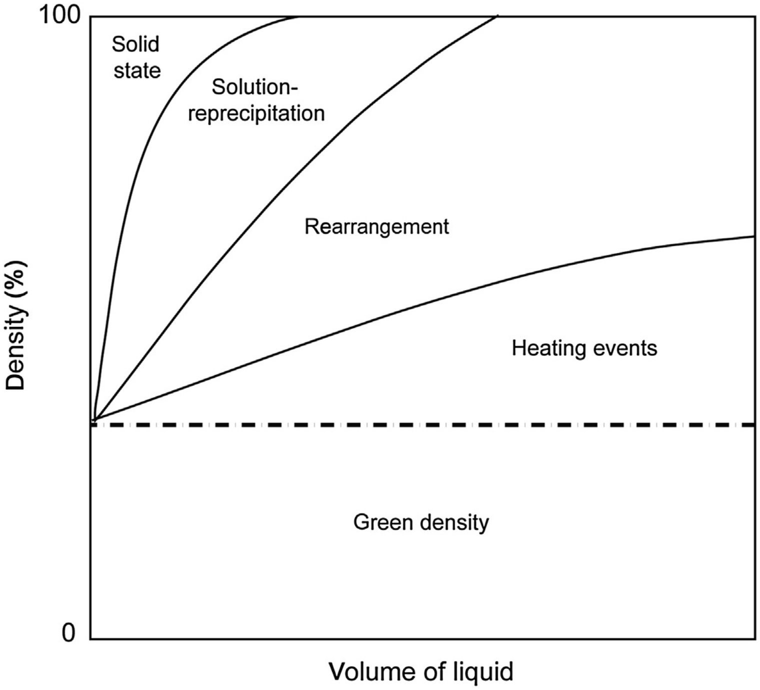

Figure 3 A schematic map illustrating LPS densification events versus liquid volume. With a low liquid content densification is by slow solid-state sintering. With a high liquid content it is possible to reach full density during liquid formation by grain rearrangement. Most LPS compositions require several cooperating mechanisms, with solution-reprecipitation being the most important.

forming a puddle in the furnace. Thus, a typical LPS composition, with 5–15 vol% liquid, requires a combination of four stages to reach full density. Several factors besides composition impact densification, with a dominance by particle size, melting temperature, and solubility.

The LPS details depend on many material parameters, including thermodynamic factors such as solid solubility in the liquid, particle size, and processing factors such as peak temperature and hold time. Different microstructure evolution pathways are possible depending on the system attributes. The common situation is for the newly formed liquid to dissolve some of the solid and spread quickly over the solid. Effectively, the liquid phase provides a fast transport pathway that greatly accelerates sintering. External pressure accentuates sintering and is a means to ensure full density; variants include the following:

Hot pressing in a heated die with uniaxial pressure, good for high solid contents.
Spark sintering with electric discharge heating through the hot pressing punches.
Hot isostatic pressing (*HIP*) in a flexible (glass, metal) container for complex shapes.
Sinter-HIP: vacuum sintering is followed by HIP in one cycle.

The LPS approach is ideal for densifying hard materials. The WC–Co system is a prime example, where the eutectic at 1310 °C enables the bonding of micrometer-sized WC grains into a dense component. Vacuum sintering is followed by backfilling the furnace with pressurized gas to implement sinter-HIP, an approach widely used in the production of metal cutting inserts, drills or milling tools.

1.08.4 Microstructures and Microstructure Development

Composition and processing history determine the sintered microstructure. After initial transients at melt formation, the microstructure coarsens over time. Indeed, a “final” microstructure is not seen in LPS materials. As calculated by Fikes, Park, and German (2011), true equilibrium consists of one single crystal and a surrounding liquid coating. What is seen in LPS is a glimpse of a slowly evolving microstructure that consists of solid grains, liquid, and possibly residual pores.

During LPS, initial densification occurs because of the rapid transport rates; solid interface motion is in the $\mu m\ s^{-1}$ range, grain boundary penetration by liquids is in the $\mu m\ s^{-1}$ range, and solid coarsening in the liquid is in the $\mu m^3\ s^{-1}$ range. However, it takes years to transform micrometer-sized particles into millimeter-sized grains, times much longer than used in practice. Even so, during a typical cycle, thousands of initial particles coalesce to form each grain. After LPS, the microstructure consists of the solid grains with an interlaced solidified liquid network, and possibly residual pores. In some cases, the pores are retained for lubrication, frangibility, or filtration attributes. Thus, sintered microstructures exist in several variants, with differences in the amount, size, shape, and distribution of the phases. Accordingly, substantial performance differences result, especially for cemented carbides.

During the LPS cycle, coarsening gives a change in grain size over time, as illustrated in **Figure 4**. These two micrographs, at the same magnification, show a W–Ni–Cu composition after two isothermal hold times. The structures appear similar except for the 50% difference in grain size, which amounts to a fivefold reduction in the number of grains in 30 min, corresponding to a 3 $\mu m^3\ s^{-1}$ coarsening rate.

Study of LPS focuses on linking composition, processing, and properties and how these factors determine microstructure, since microstructure determines properties. A homogeneous starting structure greatly improves the LPS response. The amount and placement of the liquid phase has significant impact on the sintering trajectory. Most effective is placement of the liquid phase on the interface between the solid grains. As a consequence, coated powders are an ideal starting point. Further, the identification of additives that improve wetting, accelerate diffusion, or harden the composition depend on system-specific phase relations.

1.08.4.1 Contact Angle and Dihedral Angle

When the liquid forms in LPS, the microstructure consists of solid, liquid, and vapor. Liquid spreading on the solid replaces solid–vapor interfaces with liquid–solid and liquid–vapor interfaces. **Figure 5** contrasts good and poor wetting based on the contact angle. In the horizontal plane, the contact angle θ is associated with the balance of three interfacial energies, γ_{SV}, γ_{SL}, and γ_{LV} as follows:

$$\gamma_{SV} = \gamma_{SL} + \gamma_{LV} \cos\theta \tag{1}$$

where the subscripts S, L, and V represent solid, liquid, and vapor, respectively.

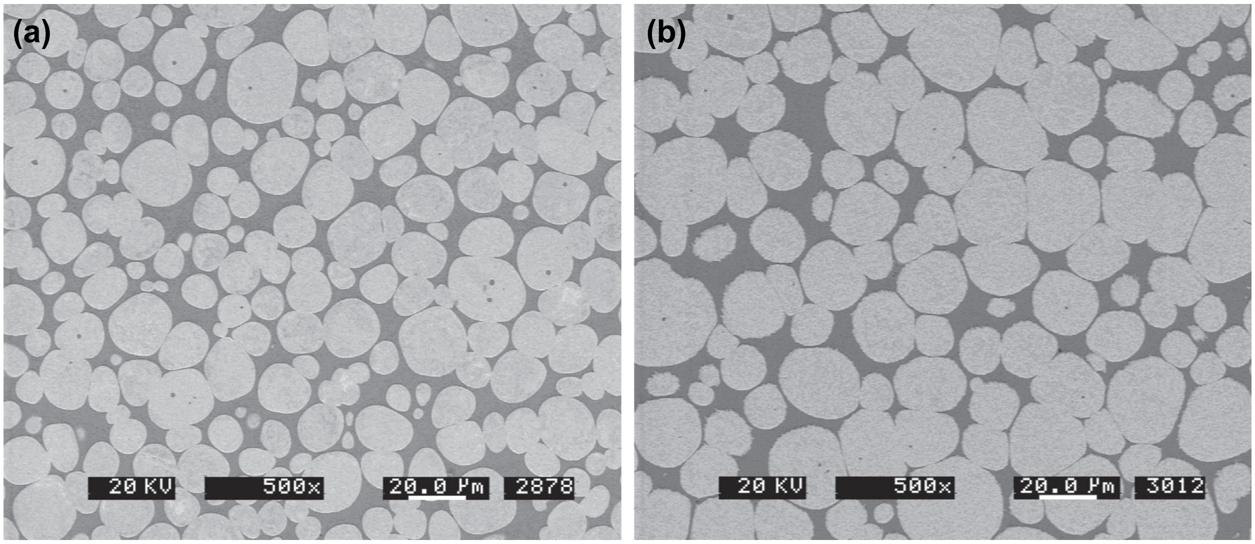

Figure 4 These two micrographs of a tungsten alloy were taken after two different hold times at 1500 °C: (a) 0 min and (b) 30 min. The structure is well developed by the time the sintering temperature is reached. The structures are similar except the grain size is larger for the longer hold time.

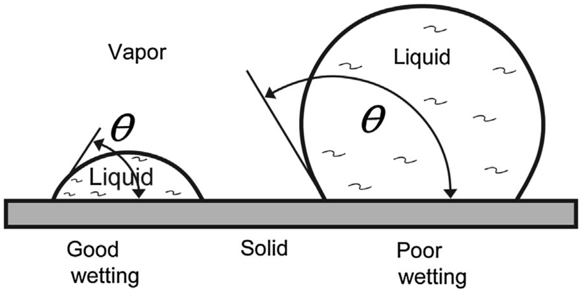

Figure 5 Contrast of wetting behavior for a liquid on a horizontal plane. A low contact angle induces wetting, while a high contact angle resists wetting. Densification in LPS requires a low contact angle to ensure that the grains are pulled together.

Rearrangement of Eqn (1) gives the contact angle as a function of the relative surface energies,

$$\theta = \arccos\left(\frac{\gamma_{SV}}{\gamma_{LV}} - \frac{\gamma_{SL}}{\gamma_{LV}}\right) \tag{2}$$

The contact angle is altered by factors that change solubility or surface chemistry. For example, the addition of Mo to the TiC–Ni system decreases the contact angle from 30° to 0°. Also, surface chemistry depends on the processing atmosphere, but often this is not intentionally controlled.

A low contact angle induces liquid spreading over the solid grains, providing a capillary attraction that helps to densify the system. For small grains, contact stress can rival that seen in pressure-assisted sintering techniques, such as HIP. In practice, a range of capillary conditions exist, since the microstructure is composed of a range of grain sizes, grain shapes, pore sizes, and pore shapes, each with a different capillary condition. A wetting liquid flows to occupy the lowest energy configuration, so it preferentially migrates to the smaller grains and pores, giving rise to rearrangement. A high contact angle indicates poor wetting, resulting in compact swelling and liquid exuding from pores. On the other hand, a low contact angle gives densification. The magnitude of the capillary effect depends on the amount of liquid, particle size, and contact angle.

The dihedral angle is where a grain boundary intersects the liquid phase, as illustrated in Figure 6. The two solid–liquid surface energy components γ_{SL} oppose the solid–solid γ_{SS} grain boundary energy, so a vertical force balance gives the dihedral angle φ as:

$$2\gamma_{SL}\cos\left(\frac{\varphi}{2}\right) = \gamma_{SS} \tag{3}$$

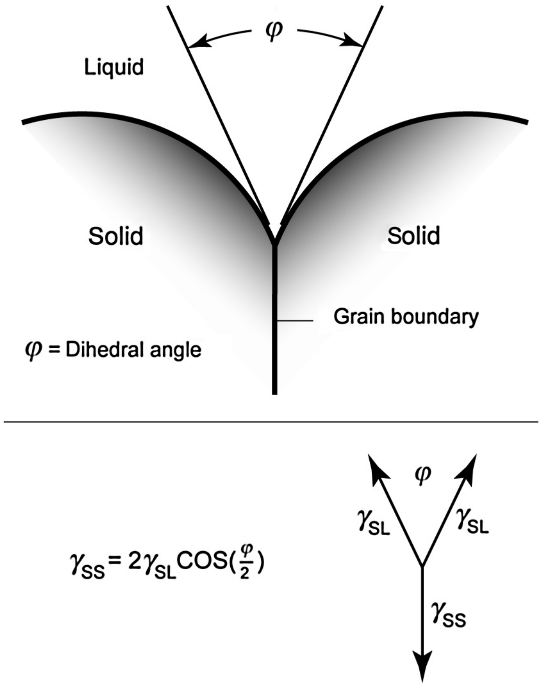

Figure 6 The dihedral angle for a solid–liquid system is evident by the groove that forms where the grain boundary emerges into the liquid. The lower portion of the figure shows the vector equilibrium linking surface energies to the dihedral angle.

Rearrangement gives the dihedral angle as a function of the ratio of the liquid interface energies. A high ratio of the solid–solid to solid–liquid surface energy means that the dihedral angle approaches 0° and liquid separates contacting grains.

In some situations, the solid–solid contacts form low-energy grain boundaries, resulting in large dihedral angles which enhance coarsening by grain coalescence. More typically, the grain boundary energy varies with crystallographic orientation and chemical segregation, so the dihedral angle has a distribution of values. Because of the distribution in contact situations, disagreement exists as to the presence of liquid on the grain boundaries. What is observed depends on several factors, such as impurities, grain misorientation, and cooling rate after sintering—factors often not properly controlled.

The dihedral angle sensitivity to changes in solid–liquid surface energy is,

$$\frac{d\gamma_{SL}}{\gamma_{SL}} = \frac{d\varphi}{\varphi}\frac{\varphi}{2}\tan\left(\frac{\varphi}{2}\right) \tag{4}$$

The relative change in dihedral angle is proportional to the solid–liquid surface energy change associated with solid dissolution into the liquid. Penetration of a grain boundary requires the change in dihedral angle such that $d\varphi = -\varphi$, giving,

$$\frac{d\gamma_{SL}}{\gamma_{SL}} = -\frac{\varphi}{2}\tan\left(\frac{\varphi}{2}\right) \tag{5}$$

Small changes in the solid–liquid surface energy are sufficient to give liquid penetration of grain boundaries. For example, a dihedral angle of 30° requires only a 7% decrease in the solid–liquid surface energy to enable grain boundary penetration. Solid dissolution into the liquid reduces γ_{SL} to enable liquid penetration of grain boundaries since the initial liquid is undersaturated with solid. In the model system for LPS studies, W–Ni–Fe, the solubility of tungsten in the additive phase increases by about 16 at% when the liquid forms. Hence, the newly formed liquid penetrates the solid–solid interfaces, and as shown by Aksay, Hoge, and Pask (1974) the surface energy disappears, thereby reducing the dihedral angle.

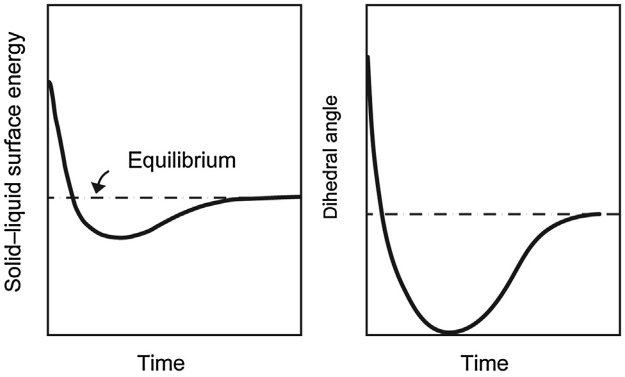

Figure 7 The wetting transient on melt formation leads to a temporary drop in the equilibrium solid–liquid surface energy as solid dissolution occurs. This momentary change gives a transient decrease in the dihedral angle that enables liquid penetration of the solid grain boundaries. Rapid solid grain rearrangement results from this weakening due to liquid penetration.

Accordingly, most hard materials exhibit grain boundary penetration on melt formation. Thus, the γ_{SL} surface energy and dihedral angle variation behave as illustrated in Figure 7. After liquid formation and spreading, the solid–liquid system approaches equilibrium. With a low liquid content, the liquid fills pockets between grains, as depicted in Figure 8. During the liquid flow, the reduction in skeletal strength does not cause distortion if pores are present to generate internal capillary forces. These capillary forces pull the grains into contact and effectively induce resistance to flow. Distortion occurs when solid skeletal bonding is delayed to after densification and pore filling.

The dihedral angle is distributed in a material, reflecting the grain boundary energy variation between grain contacts. This distribution slowly changes due to grain rotation to lower energy values, so it is common to report typical values, such as the median.

1.08.4.2 Volume Fraction

The liquid content in LPS is usually between 5 and 15 vol%. Figure 9 illustrates the microstructure changes expected as the solid-to-liquid ratio varies, notably showing more grain contacts and more grain shape accommodation at higher solid contents.

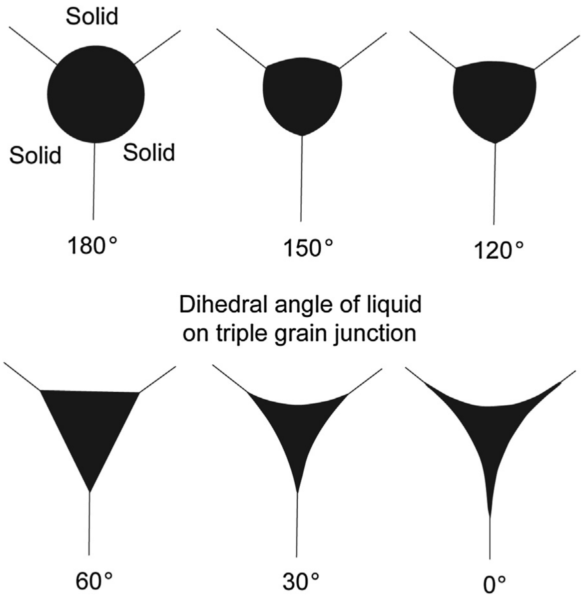

Figure 8 At low liquid contents, the liquid forms pockets at the triple points between grains, where three grain boundaries intersect. The shape of that liquid pocket depends on the dihedral angle.

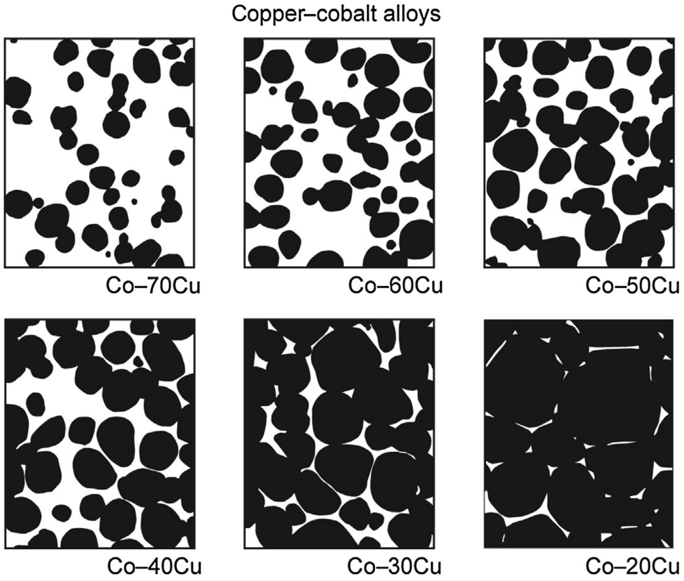

Figure 9 Example drawings taken from Co–Cu microstructures after LPS, where white regions correspond to copper liquid and dark regions correspond to cobalt solid, ranging from 30 to 80 vol% solid.

Gravity causes the solid and liquid to separate over time. Regions low in liquid content exhibit faster grain growth, so not only is there a solid–liquid variation in the sintered body, but also variations in grain size, contiguity, hardness, and other properties. Most reports fail to detail where in a sintered body the microstructure measurements are recorded. Thus, there is much scatter in the reported property data.

For LPS systems, the grain coordination number is over six contacts. The 3D grain coordination N_C (number of touching grains per grain) variation with solid volume fraction V_S is as follows:

$$N_C = -8 \ln(1 - V_S) \tag{6}$$

Further, the distribution of contacts in the body follows a Poisson distribution,

$$P(n) = \frac{N_C^n (1 - V_S)^8}{n!} \tag{7}$$

$P(n)$ is the probability of finding n contacts when the average is N_C. Since the solid grains compress the skeletal structure, there is an increase in grain size with depth.

Once pores are eliminated, the solid and liquid volumes stabilize. In some LPS systems, the sintered density then decreases as evaporation or reaction occurs to form vapor pockets. These are not pores that are shrinking from sintering but pores that are growing due to internal vapor generation, usually from decomposition or reaction at the sintering temperature.

In LPS systems characterized by multiple solid phases, the grains exhibit core–rim gradients. This is because the two solids have differing solubility–temperature relations that result in preferential dissolution of one solid during heating. Subsequent solvation of the second solid at a higher temperature reduces the solubility of the first solid in the liquid. The stepwise solvation and precipitation events influence grain growth and densification that depend on sintering temperature. Control of these events allows manipulation of the sintered microstructure for property optimization.

1.08.4.3 Porosity, Pore Size, and Pore Location

Pores are initially present as voids between the particles. Large pores reflect defects in the green body and greatly lower sintered strength. Usually, residual pores are smaller than the grains. Capillarity drives the liquid to preferentially fill smaller pores. As the smaller pores fill, the mean pore size increases, while the porosity and number of pores decrease. Pore coarsening works against densification, especially in cases where a gas exists in

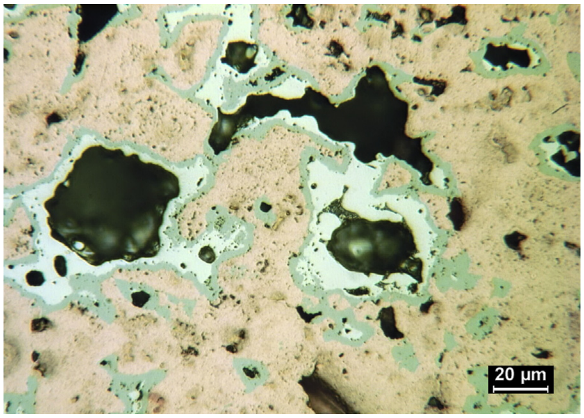

Figure 10 Pore formation due to particle melting and flow into neighboring capillaries. The dark pores exist where the particle melting and liquid formation occurred.

the pores, since the pores will coarsen and enlarge. Further, because of pore buoyancy, there is progressive migration of the pores to the top of the component.

Large melt-forming particles generate pores when they form a liquid. Figure 10 is a micrograph showing pores left behind by outward liquid flow. In cases where the melt-forming particles are large and the compact has a low porosity, this spreading leads to swelling, but densification still occurs at longer sintering times.

Large pores are filled over time by meniscus growth, as long as there is no trapped gas in the pores (vacuum sintering). Grain growth eventually induces pore filling when the ratio of the grain size G to pore size d_P is favorable,

$$\frac{G}{d_P} = \frac{\gamma_{SS}}{2\gamma_{SV}} = \cos\left(\frac{\varphi}{2}\right) \tag{8}$$

where φ is the dihedral angle. Since grain size increases with sintering time, liquid filling of larger pores takes considerable time. Figure 11 is a micrograph of a refilled pore that now appears as a liquid lake in the sintered microstructure.

Trapped gas in the pores inhibits final densification, but the pores can be filled by applying an external pressure, such as encountered during HIP. Curiously, if reheated without an external pressure, the trapped gas reforms the pore. It reflects the external pressure balance against the internal pore pressure. Without an external

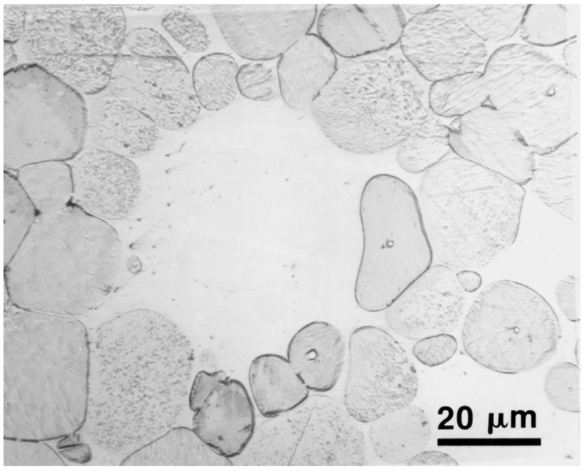

Figure 11 A liquid lake forms with delayed refilling of a large pore during LPS. Grain growth led to a condition that eventually enabled liquid flow into the pore.

pressure such as from HIP, the gas-filled pores are spherical and balance the liquid–vapor surface energy against the internal gas pressure in the pore P_G,

$$P_G = \frac{4\gamma_{LV}}{d_P} \tag{9}$$

At roughly 8% porosity, the pores close and spheroidize. At that point, the pore size is be reduced by supplementing $4\gamma_{LV}$ with an external pressure. Note P_G is typically small, about 8 MPa, so a typical external stress of 15–200 MPa causes a substantial reduction in pore size.

Some LPS systems exhibit delayed pore generation from high-temperature reactions. In such cases the porosity increases over time, contrary to the normal expectation in sintering. The decomposition of one of the hard phases is usually the cause of delayed swelling.

1.08.4.4 Grain Shape

The shape of the solid grain depends on the volume fraction of solid, as well as the dihedral angle and surface energy anisotropy. Contacts between neighboring grains cause the grains to flatten. The effect is most pronounced at low liquid contents. As the dihedral angle increases over 30°, a proportionate increase in liquid content is required to sustain a connected liquid along the grain edges. For a dihedral angle over 60°, the liquid forms isolated pockets at the triple points between grains.

At high solid content, the grains reshape to eliminate pores, termed grain shape accommodation. For isotropic solid–liquid surface energy and liquid contents over about 30 vol%, the grains are spherical with flat contact faces. With lower liquid levels there is insufficient liquid to fill all pores, so densification requires the grains to undergo shape accommodation. Because of coarsening, the starting particle shape has no significant effect on the sintered grain shape. The liquid shape and grain shape are related giving the six structures shown in Figure 12 assuming isotropic surface energies and no porosity.

During sintering the dissolving grains are spherical, while the growing large grains are more flat faced. The grain shape changes to a flat-faced structure with a relatively small change in orientation-dependent surface energy, hence faceting is evident in LPS WC–Co. Chemical additives segregated to interfaces provide a means to grain size or grain shape in sintered products.

1.08.4.5 Grain Size Distribution

Grain size after sintering is reported based on a linear dimension, such as the intercept length. Other measures include the number of grains per unit area or the diameter of a grain with equivalent projected area. Models for

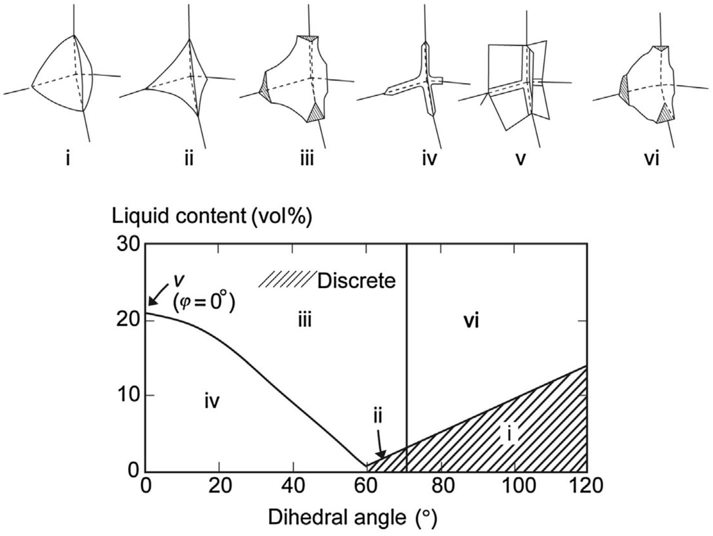

Figure 12 Liquid shape and liquid connectivity for LPS materials at the end of the sintering cycle, showing how microstructure varies with dihedral angle and liquid content. The upper drawings depict the liquid shape for the six regions marked on the lower plot.

the LPS grain size distribution predict the 3D sizes, while most experimental data give the two-dimensional (2D) random intercept size. As detailed by Liu, German, and Iacocca (1999), two transformations are required to pass from the 2D random intercepts to true 3D grain sizes; the first transforms the intercepts into equivalent circles, and the second transforms the circles into equivalent spheres with flat faces at the contacts. Due to the randomness of the section plane with the grain, few grains are sliced at their largest diameter.

The grain size distribution is self-similar, independent of the starting particle size distribution. Mathematical techniques allow extraction of the 3D grain size distribution. When the median 2D intercept is known, the cumulative distribution is given by an exponential distribution:

$$F(L) = 1 - \exp\left[\ln\left(\frac{1}{2}\right)\left(\frac{L}{L_{50}}\right)^{2}\right] \tag{10}$$

where L_{50} is the median intercept size. The mean is 1.06 times the median, while the mode is 0.85 times the median. The intercept size at 99% on the cumulative distribution is about 2.6 times the median. Cumulative grain intercept distributions are shown in **Figure 13** for several LPS materials, where the largest grains are much larger than predicted by early coarsening models.

Johnson, Campbell, Park, and German (2009) determined that the 3D cumulative grain size distribution was a similar function, given as;

$$F(G) = 1 - \exp\left[-\left(\frac{G}{c}\right)^{m}\right] \tag{11}$$

where G is the true grain size, c is a scale parameter related to the median grain size, and m is a shape parameter. The median of this distribution, G_{50}, is given as follows:

$$G_{50} = c(\ln 2)^{1/m} \tag{12}$$

The cumulative 3D distribution in a form similar to Eqn (10) is,

$$F(G) = 1 - \exp\left[\ln\left(\frac{1}{2}\right)\left(\frac{G}{G_{50}}\right)^{m}\right] \tag{13}$$

where G/G_{50} is the grain size normalized to the median size. Since the normalized median is unity, selecting the shape parameter m determines the scale parameter c. For the 2D intercept distribution, the shape parameter

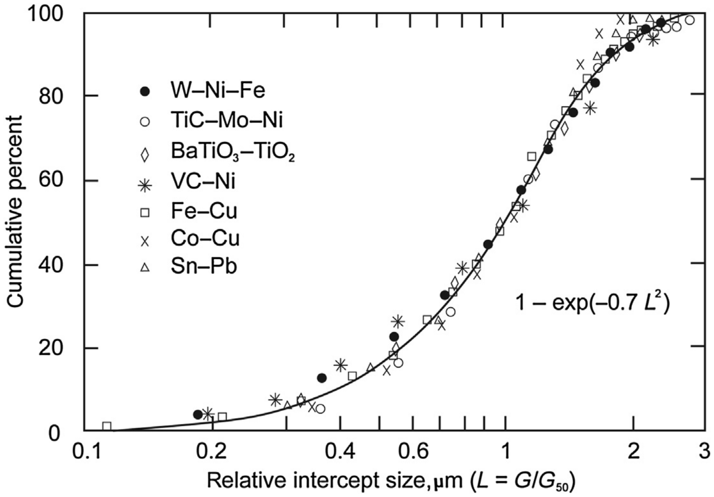

Figure 13 Cumulative grain size distributions based on 2D intercepts for several LPS materials. This self-similar (normalized) plot illustrates how the distributions are the same when normalized to the median size. The exponential function is a Weibull distribution.

$m = 2$ and Eqn (13) reduces to Eqn (10). Experimentally, the shape parameter for the 3D distribution is 2.76. Intuitively a value of $m = 3$ is expected. Kaysser, Takajo, and Petzow (1984) report that coalescence acts to broaden the distribution. The fact that measured distributions are wider than those predicted by diffusion alone is further evidence for coalescence in LPS.

1.08.4.6 Grain Separation

Separation between sintered grains determines the mechanical behavior since the matrix phase resists crack propagation. Grain separation depends on grain size, liquid content, and dihedral angle. The average grain separation λ is a measure of the phase thickness between grains,

$$\lambda = \frac{V_L}{N_L} \tag{14}$$

where V_L is the volume fraction of liquid and N_L is the number of grains per unit line length (effectively related to grain size). Some reports ignore solid–solid grain contacts (zero grain separation) in calculating the mean and are skewed to higher values. Since the grain separation only depends on the number of grains per unit measurement length, it should include zero separation instances. The mean grain intercept size L (proportional to the true 3D grain size) relates to the mean grain separation for zero porosity as follows:

$$L = \frac{1}{N_L} - \lambda \tag{15}$$

Grain separation scales with grain size.

1.08.4.7 Bond Size

Contacts grow between grains to reach a stable bond size X that depends on the dihedral angle φ as and grain size G:

$$X = G \sin\left(\frac{\varphi}{2}\right) \tag{16}$$

Because of the distribution to the grain contact orientations and grain boundary energies, LPS microstructures exhibit contact size distribution.

Similar to the neck size, the distance between contacting grain centers δ depends on the grain size G and dihedral angle φ as follows:

$$\delta = G \cos\left(\frac{\varphi}{2}\right) \tag{17}$$

Assuming that a circular contact gives the solid–solid contact area A_{SS} as,

$$A_{SS} = \frac{\pi}{4}X^2 \tag{18}$$

The contact between grains is not always circular. There are instances where very different contact shapes are evident, including half-moon and donut shapes.

Solid–solid contacts involve grains of differing sizes and the resulting grain boundary curvature favors grain coalescence, with the large grains absorbing the small grains, evident as elongated grains in the sintered microstructure. Coalescence happens from the start of sintering, but is evident even after long sintering times. Since the terminal neck size depends on the grain size, the relative bond size X/G remains constant.

1.08.4.8 Grain Coordination, Contiguity, and Connectivity

The grain coordination is the number of touching grains in three dimensions N_C. At the lower typical solid content of 50 vol% solid, the coordination number ranges from three to six, and it reaches a high range of

12–14 at full density with no liquid. For low dihedral angles, there are approximately 8–12 contacts per grain at 75% solid. Alternatively, for a high dihedral angle, there will be four to six contacts per grain at 75% solid. In the absence of pores, the 3D coordination number N_C relates to the solid volume fraction V_S and the dihedral angle φ by an empirical relation;

$$V_S = -0.83 + 0.81N_C - 0.056N_C^2 + 0.0018N_C^3 - 0.36A + 0.008A^2 \tag{19}$$

with $A = N_C \cos(\varphi/2)$.

3D grain coordination is difficult to measure, so 2D measures are used. Contiguity C_{SS} is the relative solid–solid interface area in the microstructure, defined by the solid–solid contact surface area as a fraction of the total microstructure interfacial area,

$$C_{SS} = \frac{S_{SS}}{S_{SS} + S_{SL}} \tag{20}$$

where the solid–solid surface area per grain is S_{SS} and the solid–matrix surface area per grain is S_{SL}. Usually contiguity is measured in 2D by quantitative microscopy based on the number of intercepts per unit length of test line N,

$$C_{SS} = \frac{2N_{SS}}{2N_{SS} + N_{SL}} \tag{21}$$

The subscript SS denotes the solid–solid intercepts and SL denotes the solid–liquid (solidified) intercepts. The factor 2 is necessary since the solid–solid grain boundaries are only counted once by this technique, but are shared by two grains.

Contiguity varies in LPS due to liquid penetration of the grain boundary followed by subsequent neck growth between contacting grains. After a few minutes, it stabilizes. For spherical grains, Figure 14 plots the relation between these factors and includes data from three carbide systems for comparison. The VC–Co system has a

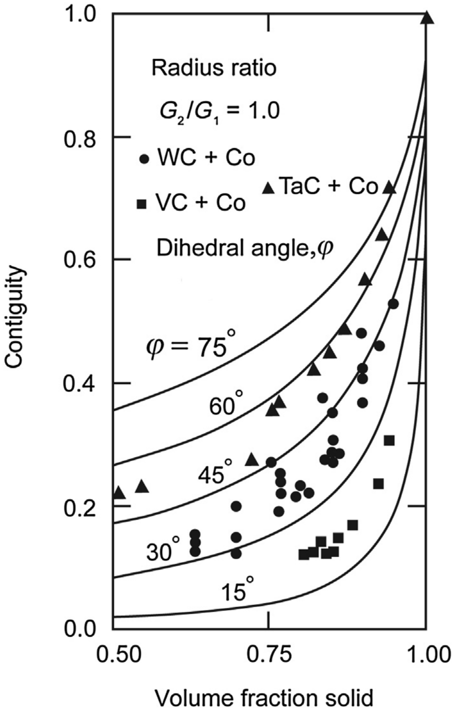

Figure 14 Contiguity versus solid volume fraction for dihedral angles ranging from 15° to 75°. For comparison the experimental results for three carbide systems are included.

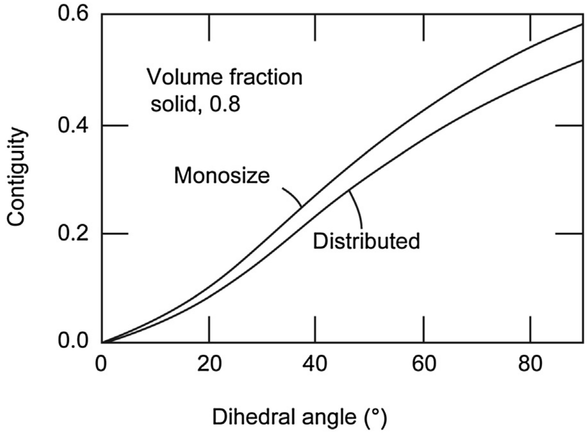

Figure 15 Contiguity variation with dihedral angle at 80 vol% solid. The two curves correspond to the model for monosized grains and the model as applied to a typical LPS grain size distribution.

low dihedral angle, so it has a lower contiguity trace. In the absence of pores, the relation between contiguity C_{SS}, volume fraction of solid V_S, and dihedral angle φ is as follows:

$$C_{SS} = V_S^2\left[0.43\sin(\varphi) + 0.35\sin^2(\varphi)\right] \tag{22}$$

This relation is not accurate at high solid contents since it does not include grain shape. Figure 15 plots the contiguity variation with dihedral angle for a solid volume fraction of 0.8 for a typical grain size distribution. For nonspherical grains, the grain contacts are variable in size and shape, but contiguity exhibits a similar variation with solid content.

Connectivity is a related parameter based on the average number of grain–grain connections per grain as observed on a random 2D cross-section. It is effective in explaining the component's resistance to distortion during LPS. Grain connectivity C_G depends on the 3D grain coordination number N_C and dihedral angle φ as:

$$C_G = \frac{2}{3} N_C \sin\left(\frac{\varphi}{2}\right) \tag{23}$$

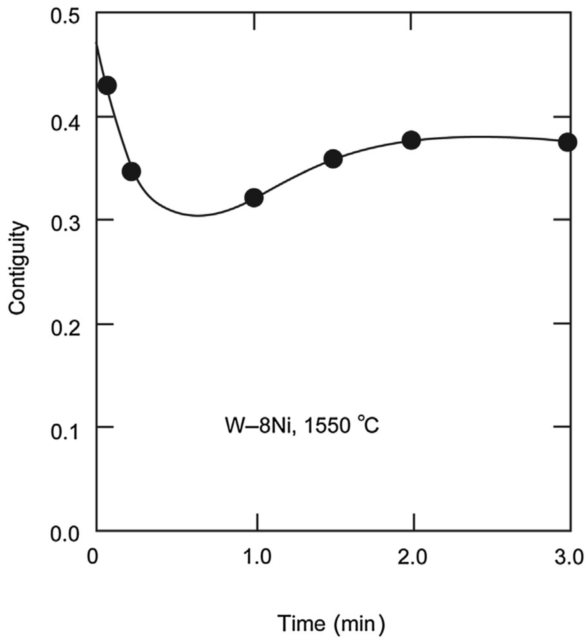

Figure 16 The solid contiguity versus sintering time for a W–8Ni compact sintered at 1550 °C. The transients show how time-dependent surface energy changes give a varying contiguity in the first few minutes of LPS.

For example, a typical 3D grain coordination number is six for a solid content near 60 vol% with a dihedral angle of 60°, giving two contacts per grain in 2D, in agreement with experiment.

Any change in interfacial energies changes the dihedral angle and contiguity; thus, contiguity drops on first melt formation, with a subsequent time-dependent decrease and then recovery, as illustrated in Figure 16. The formation of solid–solid necks leads to generation of a rigid solid skeleton and the final phase of LPS.

The starting point in LPS is defined by the green body porosity, particle size, and phase homogeneity. During sintering the microstructure follows a common pathway. Porosity is decreasing. Pore size remains nearly constant (pore annihilation balanced against microstructure coarsening). The dihedral angle and contiguity vary when the liquid first forms. Then the microstructure converges to self-similar behavior in spite of chemical differences. Anisotropic surface energies are one of the few significant variants in LPS materials. Otherwise, the LPS microstructure parameters are distributed, and the scaling is time dependent. Care is needed to properly freeze microstructures from the sintering temperature, since temperature-dependent solubility changes alter the microstructure during slow cooling. Most reports on the LPS microstructure are for the "sintered" condition and are not relevant to the conditions existing during "sintering". This gives disagreement between studies on factors such as the grain boundary condition.

1.08.5 Solution-Reprecipitation

The most important aspect of LPS is the mass transport through the liquid in the solution-reprecipitation process:

1. Solid dissolves into the liquid, preferentially from higher energy regions, including asperities, convex points in the microstructure, areas under compression, and small grains.
2. Diffusion of the dissolved solid in the liquid.
3. Precipitation of the dissolved solid onto concave regions or larger grains in areas not under compression.

Figure 17 is a microstructure with pores isolated in the liquid, typical to solution-reprecipitation-controlled densification. Pore elimination and microstructure coarsening are key features of solution-reprecipitation-controlled densification. Both depend on the same diffusion steps, as do grain shape changes and the growth of grain bonds.

Usually the controlling step is diffusion through the liquid, but interfacial reaction control is observed sometimes. Rounded grains are characteristic of diffusion control. A curved surface has a high density of atomic-scale surface ledges that provide surface dissolution and precipitation sites. Flat-faced grains indicate reaction control. The low population of defects on planar crystallographic faces limits solution-reprecipitation. Most LPS microstructures evidence rounded grains, indicative of densification by diffusion-controlled solution-reprecipitation.

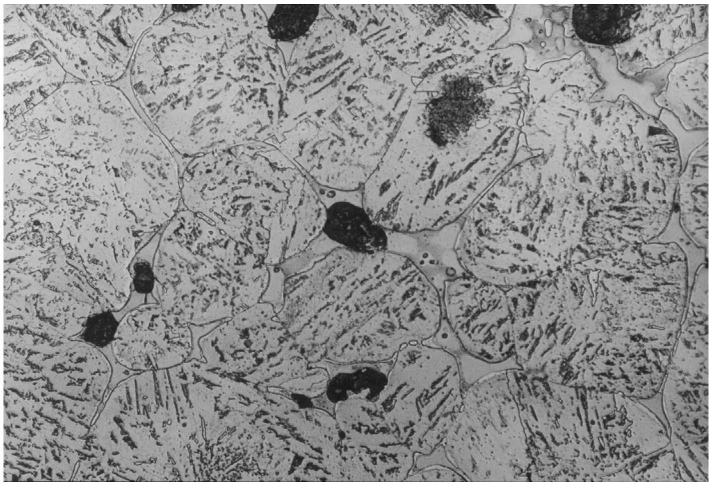

Figure 17 A microstructure typical to solution-reprecipitation-stage densification, consisting of liquid films on the grain boundaries, residual nearly spherical pores, and grains undergoing shape accommodation.

1.08.5.1 Grain Shape Accommodation

Grain shape accommodation via solution-reprecipitation improves grain packing, releasing liquid to fill the pores and reduce the overall interfacial energy. For an isotropic surface energy, the excess energy associated with a nonspherical grain is termed the sphering force. At full density, a low liquid content causes more grain shape accommodation, giving a larger sphering force. A dense compact with shape accommodation is not at the lowest energy condition. This is demonstrated by immersing a full-density compact with grain shape accommodation into a liquid metal reservoir. Additional melt wicks into the compact, allowing the solid–liquid interface to relax toward a lower energy spherical grain shape.

1.08.5.2 Densification

Usually pores remain in the compact after rearrangement, especially since the typical liquid content is below the 30 vol% needed to fill all voids with liquid. Solution-reprecipitation allows substantial densification. Three mechanisms are envisioned as means to densify the structure.

First is contact flattening. A compressive force at the grain contacts from a wetting liquid pulls the grains together. This capillary force causes preferential dissolution of solid at the contact point with reprecipitation at regions away from the contact. Densification results from the grain's center-to-center motion. The key step is diffusion in the liquid. For small grains, the contact zone force is large, so contact flattening tends to dominate LPS. This fails to explain coarsening.

Second is small grain dissolution with reprecipitation on large grains. Small grains disappear, while large grains grow and undergo shape accommodation. Diffusion in the liquid is the controlling transport step. This does not involve shrinkage, so it fails to explain densification, but grain shape accommodation enables better grain packing.

Third is bond growth by diffusion along the liquid-wetted grain boundary. The contact zone enlarges to change the grain shape with simultaneous shrinkage of the grains. This does not involve grain coarsening, but it does require a cooperative redistribution process of the mass deposited where the grain boundary intersects the liquid.

These three mechanisms differ in the source of the solid and the transport path, but together they explain grain shape accommodation, grain growth, and densification. Grain growth follows a common density trajectory, with more rapid grain growth occurring as pores are eliminated. On the other hand, contact flattening and small grain dissolution couple to fully explain the microstructure and density progression typical to LPS.

Reaction control occurs when transport is controlled by interfacial events. It is observed in complex cemented carbides from WC, VC, TiC, to TaC with a cobalt-based liquid. Grain growth inhibitors slow interfacial reaction events. The most effective inhibitors reduce the number of reaction sites, leading to the emergence of flat-faced grains or core–rim grains, where the chemistry changes from the outside to the inside. In diffusion-controlled growth, the grains remain rounded with an abundance of atomic steps, so there is no limitation from the population of interfacial sites available for dissolution or precipitation.

Kingery (1959) gave the sintering shrinkage $\Delta L/L_0$ (change in length divided by the initial length) by diffusion-controlled solution-reprecipitation as follows:

$$\left(\frac{\Delta L}{L_0}\right)^3 = \frac{g_1 \delta_L \Omega \gamma_{LV} D_S t C}{RTG^4} \tag{24}$$

where δ_L is the liquid layer thickness between the grains, γ_{LV} is the liquid–vapor surface energy, Ω is the atomic volume of the solid, D_S is the diffusivity of the solid in the liquid, C is the solid concentration in the liquid, t is the time, R is the gas constant, T is the absolute temperature, G is the solid grain size which changes with sintering time (typically $G^3 \sim t$), and g_1 is a constant. These change with temperature. Figure 18 plots two examples of shrinkage versus time on a log–log basis, giving a slope in agreement with diffusion-controlled solution-reprecipitation.

The force causing shrinkage is the capillary force at the particle contacts, and this force arises from surface energy. The capillary stress is proportional to the surface energy divided by the scale of the microstructure, essentially the grain size G. In various calculations it is estimated at about 1 MPa for micrometer-sized powders. If sintering is slow, then external pressure provides a beneficial supplement. For hot pressing or HIP, this often requires pressures in the 15–200 MPa range.

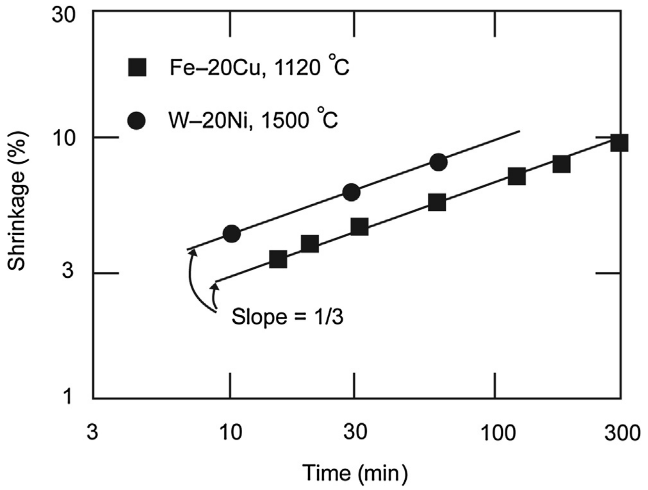

Figure 18 A log–log plot of sintering shrinkage versus sintering time for two liquid phase sintering materials: Fe–20%Cu and W–20% Ni. Both undergo diffusion-controlled solution-reprecipitation densification.

For interface reaction control, there is a similar form:

$$\left(\frac{\Delta L}{L_0}\right)^2 = \frac{g_2 \kappa \Omega \gamma_{\mathrm{LV}} t C}{RTG^2} \tag{25}$$

with κ being the reaction rate constant and g_2 being a constant. Here reaction site availability determines the shrinkage rate.

The sintered density ρ_S is calculated from the shrinkage and green density ρ_G,

$$\rho_S = \frac{\rho_G}{\left(1 - \frac{\Delta L}{L_0}\right)^3} \tag{26}$$

These equations demonstrate the effects of the process variables on shrinkage and density change; densification is faster with higher temperatures, smaller grains, and more solid solubility in the liquid. Note that there is no dependence on the amount of liquid.

Solid-state sintering by grain boundary diffusion is a densification mechanism applicable to systems with no solid solubility in the liquid, such as WC–Cu, Mo–Ag, or W–Cu.

Densification during solution-reprecipitation correlates with grain growth. Densification occurs in parallel with the elimination of the small grains. Likewise, grain shape accommodation occurs by dissolution of the small grains and reprecipitation on the large grains. Letting Γ be the ratio of densification rates due to contact flattening versus that due to small grain dissolution gives:

$$\Gamma = \frac{\lambda}{X} \tag{27}$$

where λ is the width of the liquid layer between grains and X is the diameter of the contact. If the liquid width is small, on the order of a few atomic diameters, then small grain dissolution and precipitation on the large grains is controlling. For systems where the liquid film thickness is on the order of 1–3 µm, contact flattening dominates densification until solid bonds grow between contacting grains.

Accordingly, a few key parameters control sintering densification:

- green density determines the initial number of neighboring grains for bonding;
- temperature controls solubility, wetting, and diffusivity;
- particle and grain size control the curvature, surface area, and diffusion distance; and
- time determines the amount of cumulative change.

1.08.5.3 Neck Growth

Neck growth by solution-reprecipitation occurs after newly formed liquid wets the grain boundaries as:

$$\left(\frac{X}{G}\right)^6 = \frac{g_3 D_S C \gamma_{SL} \Omega t}{G^3 RT} \tag{28}$$

where X is the neck diameter, G is the grain diameter, g_3 is a constant close to 160, D_S is the temperature-dependent diffusivity of the solid in the liquid, C is the solid concentration in the liquid, γ_{SL} is the solid–liquid surface energy, Ω is the atomic volume, t is the sintering time, R is the gas constant, and T is the absolute temperature. The amount of liquid does not significantly change the initial neck growth rate, as long as there is sufficient liquid to cover the neck. Neck growth models ignore the dihedral angle, so they are only useful for initial bonding. While there is a high porosity, grain growth is slow, so neck growth occurs without a change in grain size.

Eventually, the neck size reaches a stable size dictated by the dihedral angle. For grains of size G with a bond of size X, the equilibrium neck size ratio depends on the dihedral angle φ as given in Eqn (16). Once formed, the distributions in grain sizes, contact misorientation angles, and surface energy give a distribution to the neck sizes.

Associated with initial neck growth is shrinkage and densification. As a first approximation, the sintering shrinkage $\Delta L/L_0$ is proportional to the neck size ratio X/G,

$$\frac{\Delta L}{L_0} = \frac{1}{3.6}\left(\frac{X}{G}\right)^2 \tag{29}$$

In an LPS material with a dihedral angle of 60° the neck size ratio grows to a limiting value of $X/G = 0.5$, corresponding to a shrinkage under 7%. But at a dihedral angle of 23° the corresponding shrinkage is just 1%. After the stable neck size ratio is formed, as dictated by the dihedral angle, X/G remains constant and further neck growth depends on grain growth.

1.08.5.4 Coalescence

A wetting liquid induces particle contact due to an attractive capillary force. Amorphous particles will coalesce, since there is no grain boundary. For crystalline solids, there is a 5–10% probability that a random grain contact will form with a low-angle grain boundary that favors coalescence. Figure 19 is a microstructure involved in coalescence. The driving force of coalescence is the grain boundary curvature, and large–small grain combinations naturally favor coalescence. Also, chemical gradients, where the solid grains have differing compositions, accelerate boundary motion and coalescence.

Gas-filled pores also grow in size during LPS. Buoyancy-driven pore migration leads to stratification of larger pores near the top of the component. At the same time, Ostwald ripening of the pores leads to a decrease in the number of pores with a simultaneous increase in the average pore size. Gas-filled pores expand in volume as they grow since the internal pressure inversely depends on the size.

1.08.5.5 Grain Growth

During later stage sintering, smaller grains dissolve and larger grains grow. The local grain environment is important to determining size change. In LPS, some of the larger grains shrink and some of the smaller grains grow. This complication, coupled with coalescence and the absence of solution-reprecipitation over the interfaces coved by pores and solid contacts, makes prediction of grain growth behavior during solution-reprecipitation challenging.

As reviewed by German (2010), grain growth during sintering follows a power law,

$$G^n - G_0^n = Kt \tag{30}$$

where G_0 is the initial grain size after the liquid formation transients, G is the grain size during LPS, and t is the sintering time. Values of $n = 3$ indicate that the mean grain volume increases linearly with time and the number of grains decreases with inverse time. For instances where the grains are flat faced, solution-reprecipitation is limited by a low population of interfacial defect sites and $n = 2$. The grain growth rate parameter K is related to the transport mechanism. Experimental data for diffusion-controlled grain growth show the cubic growth law for rounded grains and the square law for flat-faced grains.

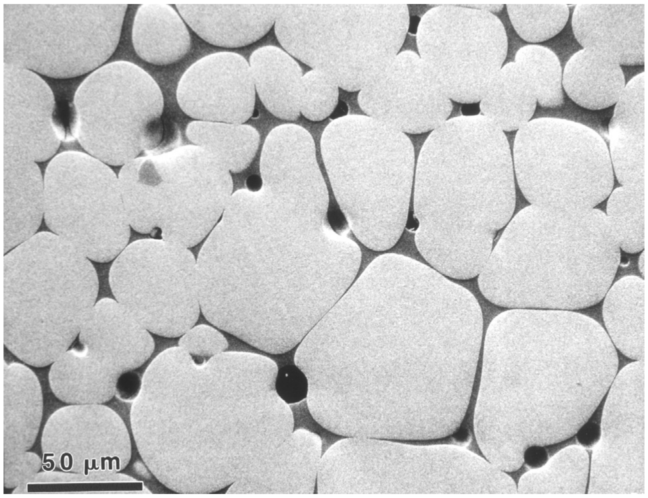

Figure 19 This micrograph captures grain coalescence during liquid-phase sintering, in terms of the elongated grains making contact and fusing without an interparticle grain boundary. Some pores are remaining in this structure. During LPS about 5% of the microstructure is undergoing coalescence at any time.

The grain growth rate parameter is sensitive to several factors, especially temperature. These are lumped into an apparent activation energy and research by German (2010) added the solid volume fraction to the rate parameter.

Grain growth models vary significantly in their predictions of the effect of volume fraction on the grain growth rate parameter. Thus, trials with changes in the solid volume fraction are useful for assessing the grain growth mechanism. In doing this, LPS data support a grain growth rate parameter dependence on the liquid volume fraction raised to the −2/3 power. If the grain growth rate parameter is normalized to the Ostwald ripening model, the grain growth rate parameter is

$$K = \frac{64}{9}\frac{D_S C \Omega \gamma_{SL}}{RT} \tag{31}$$

where D_S is the solid diffusivity in the liquid, C is the solubility of the solid in the liquid, Ω is the solid molar volume, γ_{SL} is the solid–liquid surface energy, R is the gas constant, and T is the absolute temperature.

The LPS grain growth rate parameter is,

$$K_{LPS} = K(1 - V_S)^{-2/3} \tag{32}$$

where V_S is the solid volume fraction. This is valid for the range of situations in LPS. From 5 to 15 vol% liquid, the rate parameter varies by a factor of 2.1. Consequently, a measurable grain size difference is seen from the top to bottom of LPS compacts because solid grain compression changes V_S with position.

1.08.5.6 Pore Filling

Pore filling by liquid preferentially starts at a localized region in the compact and spreads during LPS. Small pores fill first, since they have the highest capillary attraction for the liquid. High-green-density regions correspond to smaller pores, so pore filling naturally favors these regions. As noted earlier, grain growth reduces the capillary gradients and eventually reaches a favorable condition for liquid flow into the pores. This condition is described by the liquid meniscus radius at the pore–liquid–grain contact, r_m, which is given as:

$$r_m = \frac{G}{2}\left[\frac{1 - \cos\alpha}{\cos\alpha}\right] \tag{33}$$

where α is the angle from the grain center to the solid–liquid–vapor contact point. Pore filling occurs when the pore size and meniscus radius are about the same and is favored by a low contact angle. Earlier, Figure 11 shows a refilled pore as a liquid lake surrounded by grains. Grain growth usually follows a cube root dependence on time, so the filling of large pores can be delayed for some time. However, trapped gas in the pores will retard densification.

1.08.5.7 Sintering Atmosphere

The atmosphere used during LPS provides an opportunity to alter the material chemistry and sintering rate. Usually, oxide ceramics are sintered in air, nitride ceramics in nitrogen, and carbides in a carbon-controlled atmosphere. Highly reactive metals are sintered in vacuum. Small changes in the atmospheric composition, such as partial pressure of oxygen or water, produce a measurable change in sintered properties. A completely inert atmosphere, such as argon, inhibits full densification since the trapped argon stabilizes closed pores.

Reactions between impurities and sintering atmosphere might generate insoluble reaction products, leading to stable pores. The internal pressure in the pore increases with temperature, leading to swelling.

1.08.6 Solid Skeletal Sintering

Final-stage LPS corresponds to a microstructure of connected solid grains with liquid occupying the space between the grains. This system is rigid. Grain growth continues while the solid skeleton sinters to full density or to where gas trapped in the pores halts densification. As demonstrated by Johnson and German (1996), for low-solubility systems, such as W–Cu, densification is paced by the solid-phase sintering rate. For systems with solid solubility in the liquid, the solution-reprecipitation events control final densification.

The microstructure continues a slow approach to a minimum energy solid–liquid configuration. Pores become spherical once total porosity is less than 8%, giving an interlaced microstructure of solid grains and liquid, but isolated near-spherical pores. In this case, the densification rate is:

$$\frac{d\rho}{dt} = \frac{12D_S C\,\Omega}{RTG^2}\beta\left(\frac{4\gamma_{LV}}{d_P} - P_G\right) \tag{34}$$

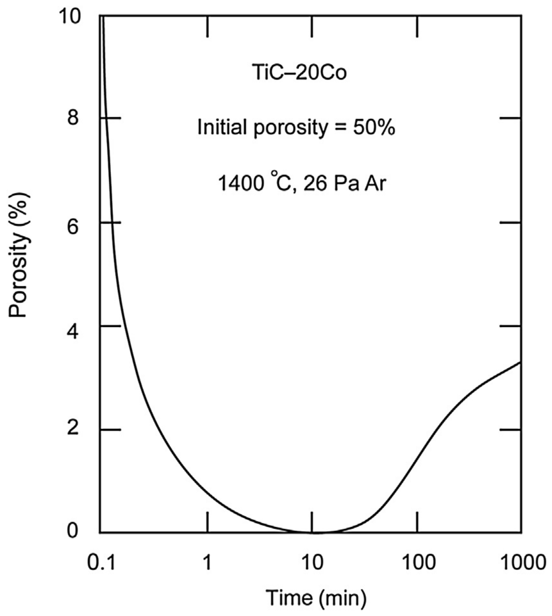

Figure 20 Liquid-phase sintering of a TiC–Co hard material where swelling occurs after reaching full density due to residual argon gas trapped in the pores.

where ρ is the fractional density, t is the time, D_S is the diffusion rate of the solid in the liquid, C is the solubility of the solid in the liquid, Ω is the atomic volume of the solid, R is the gas constant, T is the absolute temperature, G is the grain size, d_P is the pore size, γ_{LV} is the liquid–vapor surface energy, P_G is the gas pressure in the pore, and β is a pore density factor. This factor is given by

$$\beta = \frac{\pi N_V G^2 d_P}{6 + \pi N_V G^2 d_P} \tag{35}$$

where N_V is the number of pores per unit volume. Because trapped gas in the pores inhibits full densification, it is important that final-stage LPS be conducted in vacuum or an atmosphere that diffuses out of the pores. If sintering occurs in an atmosphere that is insoluble in the liquid, then the final product is porous with spherical pores. As illustrated in **Figure 20**, an insoluble gas in the pores results in swelling after densification. The swelling happens in the final stage of LPS. Besides an increase in porosity and pore size, there is a concurrent loss of properties.

1.08.7 Pressure-Assisted Sintering

The driving force for sintering is the surface energy divided by the scale of the microstructure, namely, the particle or grain size. This ratio (J m^{-2} divided by m) has units of stress (N m^{-2}) and is termed the sintering stress. For a liquid such as cobalt and a grain size of 1 μm, the capillary sintering stress is about 8 MPa. This is an internal stress, generated by the wetting liquid bridging between grains. As pore space is filled, the stress falls, while the system becomes rigid and resists further densification. Accordingly, external stress enhances final densification. Thus, pressure-assisted sintering processes arise where heat and pressure are applied simultaneously to the sintering body. These include:

uniaxial hot pressing in a die where the die is usually graphite, externally heated or heated via induction and the die strength limits the maximum applied pressure;

spark sintering, which is very similar to hot pressing with uniaxial pressing and graphite tooling, but heating is via electric discharge through the punches and dies, with some current leakage through the compact;

HIP, where pressure is generated using a gas chamber; since open pores will let in the gas, it is only effective if the material is enclosed in a container or if applied after sintering to about 92% density where pores close;

sinter-HIP, which is simply sintering in vacuum to pore closure, and then pressurizing the furnace to accelerate pore closure.

The mathematics of pressure-assisted densification are the same as in Eqn (34), with a supplemental force added to the surface energy and gas pressure term, proportional to the external pressure. The mechanisms of sintering are the same, but with a larger driving force. One advantage is assurance of full density for components where residual porosity might be detrimental to performance. A second advantage is that lower temperatures can be applied to reduce microstructure coarsening during sintering.

Pressure-assisted sintering of hard materials dates from the late 1890s, based on electric current discharge through the pressurized powder. Goetzel and De Marchi (1971) formally termed the concept spark sintering, since some of the early ideas came from electrodischarge machining. Because of early conjecture on plasma between particles, the name was rephrased spark plasma sintering. Research by Munir, Anselmi-Tamburini, and Ohyanagi (2006) show there is no plasma, so besides spark sintering the approach is also termed field-assisted sintering, pulsed electric current sintering, current-activated pressure-assisted sintering, electric current-assisted sintering, electrical discharge compaction, electroconsolidation, and so on.

Process control during spark sintering is complicated by the substantial shifts in material and tooling conductivity during densification. Generally the consequence is that it is restricted to thin cylinder geometries—poker chip-sized compacts. At the start of the consolidation the powders are poor conductors, but with densification some materials become so conductive that they fail to properly heat. On the other hand, nonconductor materials rely on the graphite die to heat. In several instances where spark sintering is directly compared to hot pressing, there is no difference, as long as the hot press is heated quickly. It is because of rapid heating that spark sintering exhibits the greatest benefit, although this benefit is attainable via exothermic, induction, microwave, laser, or capacitive discharge heating. Likewise, quick HIP uses cycles of just 1 min, but at a high cost.

Spark sintering runs reach into the current density range where electromigration supplements diffusion, usually at current densities near 1000 A cm^{-2}. The resulting electron wind enhances atomic diffusion in proportion to the electric field. Normally, diffusion fluxes during sintering are based on concentration gradients, but electromigration supplements diffusion. The main gains come with DC pulses of 1 s or more and even 15 s pulses are used in diamond sintering. Unfortunately, most commercial spark sintering machines are limited in power and rely on relatively short 2–3 ms pulses that fail to induce electromigration benefits.

For about 60 years there has been speculation on new phenomena in spark sintering. The pending questions include determining if there is a grain boundary structure change or otherwise altered grain boundary via segregation or diffusion. Grain boundary films, such as cobalt in WC–Co, preferentially interact with the electric field. For metastable materials, such as tungsten carbide, diamond, cubic boron nitride, and boron suboxide, decomposition occurs during consolidation. As Ericksson, Radwan, and Shen (2013) show, rapid consolidation is the key benefit of spark sintering. However, the key gain is fast heating, an advantage well known in sintering and pressure-enhanced sintering without the need for electric fields.

There are several variants of the pressure-assisted sintering concept, but generally the added cost results in sinter-HIP being the only one to be widely used in hard materials. Much speculation has been made on possible new mechanisms of sintering using spark sintering, but to date the only significant gains are in mixed phase composites. Indeed, in several comparisons between spark sintering and traditional hot pressing, there is no significant difference in microstructure, density, or properties.

1.08.8 Practical Consolidation Cycles

Much of this article had focused on basic events, driving forces, transport mechanisms, and the geometric progressing and coarsening that make up sintering. For hard materials, these come together in practical cycles for the consolidation of different materials. Since there are tens of thousands of compositions, detailed listings are not useful. However, the intent here is to show a few examples to represent consolidation options for hard materials.

Listed in Table 1 are combinations of various types, sizes, and amounts of hard particles with different matrix phases, consolidation cycle details (peak temperature, pressure, hold time) and die or sintering tray material where reported. These are the conditions used to obtain full density, but other combinations of processing

Table 1 Example Hard Material Consolidation Cycles

hard phase	*matrix phase, %*	*route*	*particle size, μm*	*temperature, °C*	*pressure, MPa*	*time, h*	*die/tray material*
$(Fe,Mo)_6C$	26 Fe	HIP	1	825	250	3	steel
Al_2O_3	20 Mo	HP	30	1700	40	1	graphite
diamond	80 WC	HP	50	1100	75	0.1	graphite
NbC	20 Co	LPS	7	1450	-	2	NbC
SiC	30 TiC	HP	0.6	2150	40	2	graphite
TaC	20 Co	LPS	2	1450	-	2	TaC
Ti_3SiC_2	20 Ti	HP	0.2	1450	50	0.3	graphite
Ti_5Si_3	70 Ti	HP	25	1000	40	0.3	graphite
TiB_2	10 Ni	HP	5	1550	12	2	graphite
TiB_2	80 NiAl	HIP	4	1200	170	1	Ta
TiC	10 Ni	LPS	10	1450	-	2	TiC
TiC	33 Ti	HP	1	1550	24	1.5	graphite
TiC	5 Co	LPS	1	1400	-	1	graphite
TiC	70 Al_2O_3	HIP	1	1935	150	0.3	Mo
TiC	70 Ni	HIP	2	1300	200	2	Al_2O_3
VC	20 Co	LPS	5	1380	-	2	VC
WC	10 Co	HIP	1	1300	200	1.5	graphite
WC	10 Co	LPS	0.5	1400	-	1	graphite
WC	3 Co	HP	0.1	1275	40	0.3	graphite
WC	none	HP	0.4	1700	60	0.1	graphite

(LPS = liquid phase sintering, HP = hot pressing, HIP = hot isostatic pressing) parameters would also be successful. Thousands of reports are available, so this is only a sampling of the practical knowledge about hard material consolidation. Clearly, computer simulations, as discussed below, provide a means to optimize processing if sufficient information is known about the materials and their response to sintering cycles.

1.08.9 Computer Simulation

Historically, sintering has been empirically based, due to both the emphasis on applications and the relative complexity of the field. Further, the large variety of materials processed by sintering requires broad generalizations that degrade model accuracy. It is possible to simulate powder consolidation, including pressing, sintering, injection molding, and HIP, as reviewed by Chung, Kwon, Park, and German (2010). This is facilitated by the growth of computing power in conjunction with refinements to the simulation algorithms.

An early, widely adopted simulation is from Ashby (1974) in the form of sintering diagrams and Helle, Easterling, and Ashby (1985) in the form of HIP diagrams. They assemble various transport equations, allow for an evolving microstructure, include processing parameters, and solve for stages of densification to map sintered density as a function of processing time, temperature, and pressure for a given set of starting conditions, namely, material, material properties, particle size, green density, and assumed system behavior. As an example, **Figure 21** is a map for the hot pressing densification of WC–10Co. The simulation is conducted for 0.1 μm powder starting at a green density of 60% of theoretical with 30 MPa applied pressure. The fractional density is plotted versus temperature for hold times of 10 and 40 min. Densification starts by 900 °C, with a slightly higher density for the longer time. Full density is attained at 1325 °C for 40 min hold time and 1400 °C for 10 min. More than 30 prior reports on hot pressing this hard material generally show that similar combinations give full density usually with temperatures over 1100 °C and pressures up to 75 MPa for short times such as 5 min.

Beyond this single-parameter prediction of density, computer simulations are trying to move into the prediction of industrially relevant aspects, such as the optimal means to form a sintered body, the size and shape of the green body to attain the desired final shape, and how to minimize cost. Computer simulations are struggling in these areas, but progress is afoot.

One area of current research simulation of the time-dependent microstructure evolution in LPS. A variety of approaches are under investigation. For example, Ryoo, Hwang, Kim, and Chung (2000) detailed the use of the Monte Carlo method to track anisotropic grain growth in WC–Co. Unfortunately, most of the simulations are 2D and inherently flawed when compared to 3D microstructures. These simulations tend to be of limited value and have been displaced by newer approaches.

The Potts Monte Carlo model is a discrete, statistical mechanical model. The technique is adaptable to solid grains in a liquid matrix and includes interfaces. It is capable of dealing with the geometric complexity relevant

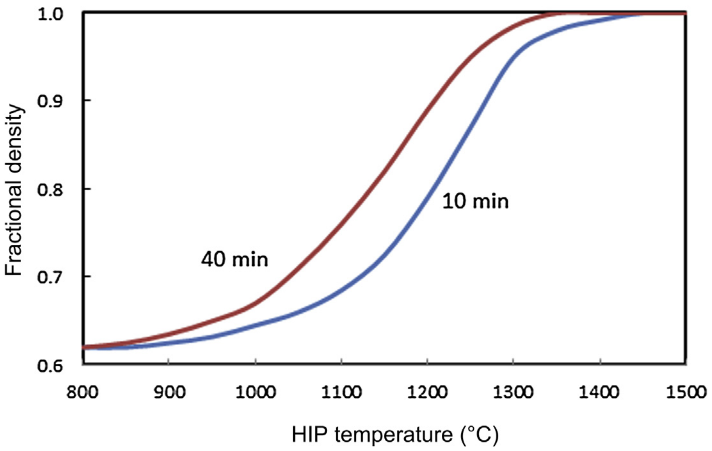

Figure 21 A densification map for HIP WC–10Co, using 0.1 μm powder at 60% green density. Plotted here is the fractional density versus hold temperature at 30 MPa applied pressure for hold times of 10 or 40 min. Densification is predominantly by diffusional creep of WC in the cobalt-rich grain boundaries.

to LPS. It does not rely on explicit input of thermodynamic and kinetic characteristics. The powder is represented on a lattice as an agglomerate of grains with different interface energies, and statistical sampling is performed to find configurations of lower energy. Matsubara (2005) has spearheaded methods for treating grain growth. The limitation of this method is in deciding on the range and relative size of the interface energies.

The discrete element method is a numerical approach suitable for treating a mesoscale problem without restrictive assumptions on grain kinematics. The technique does not include coarsening, so it has limited value. The behavior of each grain is treated using a distinct element (particle) by calculating the interactions between contacting grains. Access to computing power allows practical situations to be tackled using very large particle arrays. It is probably more useful in compaction models versus sintering models.

The finite difference method is a numerical method for solving a system of differential equations through approximation at each mesh point, called pointwise approximation. The primary limitation of this method is in dealing with the complicated geometry, which makes this method of limited use to industry. However, this method is very efficient with respect to other resources.

The finite element method is a popular approach for solving a system of differential equations through approximation functions in each element. As illustrated by Sun and Riedel (1995) this method is powerful for analysis of complex carbide geometries so it is popular with industry. It is widely used to predict the final size and shape of LPS components. Most of the efforts are applied to generation of constitutive relations to support this approach for complex geometry, largely to design compaction tools that deliver the desired final sintered shape.

1.08.10 Summary

Sintered hard materials and LPS emerged from empirical origins traced to the late 1920s and early 1930s. Since the 1950s much progress was made in the quantitative treatment of LPS to where computer simulations integrate the knowledge and enable predictions of microstructure, component size, and component shape. The scientific principles have advanced to include many processing factors and provide a platform for the identification of new systems. Hard materials fabrication and LPS go together. Almost all hard materials are formed via LPS techniques.

Solution-reprecipitation is fundamental to LPS. It occurs with concomitant microstructure coarsening, wherein pores are both annihilated and coarsen, grain size and grain separation increase, and solid–liquid surface area decreases. Solid diffuses through the liquid and deposits on convex surfaces, allowing a grain shape change to give a better packing arrangement, releasing liquid to fill the remaining pores. Accordingly, density increases, grain size increases, and grain bonding and grain shaping occur simultaneously. Much effort has gone into modeling grain growth during LPS. Ostwald ripening notions prove inadequate to explain the experimental observations on LPS systems. Models that combined diffusion-controlled coarsening with coalescence proved capable of explaining the grain size distribution, coarsening kinetics, and sensitivity to liquid content. As the solid contiguity increases, there is more interfacial area over which coalescence occurs and less interfacial area over which solution-reprecipitation occurs.

There is much about LPS that needs attention. From an industrial view, the most pressing need relates to dimensional control. Because of tight industrial tolerances, many LPS hard materials are machined or ground after sintering. These postsintering dimensional adjustments are costly. How can LPS be used to give the final size and shape? How do factors such as gravity, substrate friction, green density gradients, and nonuniform heating contribute to distortion? Can changes in the starting microstructure (via particle size, mixing technology, or compaction conditions) be used to minimize distortion? LPS systems often distort shortly after the liquid forms and continue to distort with a viscous flow or creep behavior. Is it possible to separate densification events from distortion events to improve sintered tolerances? Possibly there are gains from idealized cycles, such as by controlled, slow heating.

Modeling efforts include most of the key concepts. The initial chemical gradients associated with mixed powder are important to the sintering trajectory, as is the green body density homogeneity. As reported by Blaine, Park, Suri, and German (2006), much progress arises from integral work concepts to explain sintering densification, distortion, property evolution, and coarsening. These constitutive equations, derived from simple experimental studies, enable accurate simulations of component density, size, shape, density, microstructure, properties, performance, and cost. Further, equipment optimization is also a reality using objective functions tailored to sintering devices.

References

Aksay, I. A., Hoge, C. E., & Pask, J. A. (1974). Wetting under chemical equilibrium and nonequilibrium conditions. *Journal of Physical Chemistry, 78*, 1178–1183.

Ashby, M. F. (1974). A first report on sintering diagrams. *Acta Metallurgica, 22*, 275–289.

Blaine, D. C., Park, S. J., Suri, P., & German, R. M. (2006). Application of work of sintering concepts in powder metallurgy. *Metallurgical and Materials Transactions, 37A*, 2827–2835.

Chung, S. H., Kwon, Y. S., Park, S. J., & German, R. M. (2010). Modeling and simulation of press and sinter powder metallurgy. In D. U. Furrer, & S. L. Semiatin (Eds.), *ASM handbook: Vol. 33B. Metals process simulation* (pp. 323–334). Materials Park: ASM International.

Eremenko, V. N., Naidich, Y. V., & Lavrinenko, I. A. (1970). *Liquid phase sintering*. New York: Consultants Bureau.

Ericksson, M., Radwan, M., & Shen, Z. (2013). Spark plasma sintering of WC, cemented carbide, and functionally gradient materials. *International Journal of Refractory Metals and Hard Materials, 36*, 31–37.

Fikes, J., Park, S. J., & German, R. M. (2011). Equilibrium states of liquid, solid, and vapor and the configurations for copper, tungsten, and pores in liquid phase sintering. *Metallurgical and Materials Transactions, 42B*, 202–209.

Froschauer, L., & Fulrath, R. M. (1976). Direct observation of liquid-phase sintering in the system tungsten carbide – cobalt. *Journal of Materials Science, 11*, 142–149.

German, R. M. (1985). *Liquid phase sintering*. New York: Plenum.

German, R. M. (1996). *Sintering theory and practice*. New York: Wiley.

German, R. M. (2010). Coarsening in sintering: grain shape distribution, grain size distribution, and grain growth kinetics in solid-pore systems. *Critical Reviews in Solid State and Materials Sciences, 35*, 263–305.

German, R. M., Suri, P., & Park, S. J. (2009). Review: liquid phase sintering. *Journal of Materials Science, 44*, 1–39.

Goetzel, C. G., & De Marchi, V. S. (1971). Electrically activated pressure sintering (spark sintering) of titanium powders. *Powder Metallurgy International, 3*, 80–87 and 134–136.

Helle, A. S., Easterling, K. E., & Ashby, M. F. (1985). Hot isostatic pressing diagrams: new developments. *Acta Metallurgica, 33*, 2163–2174.

Johnson, J. L., Campbell, L. G., Park, S. J., & German, R. M. (2009). Grain growth in dilute tungsten heavy alloys during liquid phase sintering under microgravity conditions. *Metallurgical and Materials Transactions, 40A*, 426–437.

Johnson, J. L., & German, R. M. (1996). Solid-state contributions to densification during liquid phase sintering. *Metallurgical and Materials Transactions, 27B*, 901–909.

Kang, S. J. L. (2005). *Sintering densification, grain growth, and microstructure*. Oxford: Elsevier Butterworth-Heinemann.

Kaysser, W. A., Takajo, S., & Petzow, G. (1984). Particle growth by coalescence during liquid phase sintering of Fe-Cu. *Acta Metallurgica, 32*, 115–122.

Kingery, W. D. (1959). Densification during sintering in the presence of a liquid phase. 1. Theory. *Journal of Applied Physics, 30*, 301–306.

Lenel, F. V. (1948). Sintering in the presence of a liquid phase. *Transactions of the Metallurgical Society of AIME, 175*, 878–896.

Liu, Y., German, R. M., & Iacocca, R. G. (1999). Microstructure quantification procedures in liquid phase sintered materials. *Acta Materialia, 47*, 915–926.

Matsubara, H. (2005). Computer simulation studies on sintering and grain growth. *Journal of the Ceramic Society of Japan, 113*, 263–268.

Munir, Z. A., Anselmi-Tamburini, U., & Ohyanagi, M. (2006). The effect of electric field and pressure on the synthesis and consolidation of materials: a review of the spark plasma sintering method. *Journal of Materials Science, 41*, 763–777.

Ryoo, H. S., Hwang, S. K., Kim, B. K., & Chung, H. S. (2000). Anisotropic grain growth based on the atomic adsorption model in WC-25 pct Co alloy. *Metallurgical and Materials Transactions, 31A*, 1925–1935.

Sun, D. Z., & Riedel, H. (1995). Prediction of shape distortions of hard metal parts by numerical simulation of pressing and sintering. In S. F. Shen, & P. Dawson (Eds.), *Simulation of materials processing* (pp. 881–886). Rotterdam, Netherlands: Balkema.

SECTION IV

MECHANICAL PROPERTIES

1.09 Hardness and Deformation of Hardmetals at Room Temperature

Alex V. Shatov, 8 Parkside Drive, Jamesburg, NJ, USA
S.S. Ponomarev and S.A. Firstov, Department of Physics of Strength and Plasticity of Materials, Frantsevich Institute for Problems of Materials Science, Kiev, Ukraine

http://dx.doi.org/10.1016/B978-0-08-096527-7.00009-X

Glossary

Contiguity of carbide crystals (G) The area fraction of the carbide–carbide contacts in the total surface area of the carbide crystals.

Final chemistry The phase composition and content of the alloy.

Final geometry A geometrical description of the microstructure of the alloy.

Hardness (H) The ability of material to resist localized plastic deformation. For hardmetals, the indentation hardness is referred to as hardness.

Indent size effect (ISE) The increase in indentation hardness when the indent diagonal or diameter is decreased from several hundred microns down to a micron and further to submicrons due to the lower loads on the indenter.

Initial chemistry An initial choice of the main carbide and binder substances, as well as of the optionally added carbides and other chemical element(s).

Initial geometry The size, size distribution, and morphology of the carbide, binder, and other optionally added powders, as well as the uniformity of the powder mixture.

Mean linear intercept of the carbide crystals (mlicc) The stereological measure of carbide crystals size calculated as the average size of randomly oriented chords that cross the carbide crystals at carbide–binder interfaces and carbide–carbide boundaries on the cross-section of the specimen.

Mean linear intercept of the binder phase (mlibp) The stereological measure of binder phase size calculated as the average size of randomly oriented chords that cross the binder phase at carbide–binder interfaces on the cross-section of the specimen.

Microhardness The indentation hardness when the indent diagonal or diameter is about or below one micron.

Poisson's ratio (ν) The relative deformation in two directions perpendicular to the axis of the uniaxial load.

Production technology A process that converts the powders into consolidated material, as well as the subsequent surface and bulk treatments of the alloy.

Residual compressive surface stresses (RCSS) The stresses that occur on the surface of the specimen due to surface preparation treatment like grinding.

Residual thermal stresses (RTS) The stresses on the phases occurring due to the difference in the thermal expansion of the phases.

Shear elastic modulus (μ) The stress-to-strain ratio when the shape is changed at the constant volume of the specimen.

Volumetric elastic modulus (K) The stress-to-strain ratio when the load is uniformly applied in all directions, which changes the volume but preserves the shape of the specimen.

Young's modulus (E) The stress-to-strain ratio in the direction of the uniaxial load.

Nomenclature

AGG Abnormally grown grains

α Ratio between the hardness and the yield stress of WC in the MLN model, or experimental constant in other models

b Burgers vector of the binder phase in the model of Laugier

b_{WC} Basal edge length of the triangular prism of an ideal WC crystal

C_{ij} Elastic constants tensor

d_{α} Mean linear intercept of carbide crystals (mlicc)

d_{WC} Mean linear intercept of WC crystals (mlicc) in cemented carbides

D_{min}, D_{max} Minimal and maximal chord through the center of mass of cross-section of WC crystal in definition of the shape equiaxiality P_{WC}

E Young's elastic modulus

E_C, E_B Young's elastic modulus of the carbide and binder phase, respectively

E_U, E_L Upper and lower bounds, respectively, of Young's elastic modulus

ε_C, ε_B Strain in the carbide and binder phase, respectively

G Contiguity of carbide crystals in hardmetals measured as the area fraction of the carbide–carbide contacts in the total surface area of the carbide crystals

h Indent depth in microhardness test

h^* Characteristic length of the material in microindentation test

h_{WC} Height of the triangular prism of an ideal WC crystal

H_{bulk} Hardness due to the homogeneous bulk strain in microhardness

H_{micro} Microhardness of material

H, HV, HV30 Vickers hardness of hardmetals

H^0 Hardness of the bulk single crystal material in Hall–Petch relation or other experimental constant in hardness expression
H^0_{Binder} Bulk hardness of the binder phase in Hall–Petch relation
$H_{0,\mathrm{Co}}$ Bulk hardness of Co in the CLRH model for hardness
H^{HP} Hall–Petch hardening factor for polycrystalline material
$H^{\mathrm{HP}}_{\mathrm{Binder}}$ Hall–Petch hardening factor for the binder phase
$H^{\mathrm{HP}}_{\mathrm{Ni}}$ Hall–Petch hardening factor for the Ni binder phase
H^0_{WC} Bulk hardness of WC in Hall–Petch relation
$H^{\mathrm{HP}}_{\mathrm{WC}}$ Hall–Petch hardening factor for WC crystals
HFIHS High-frequency induction heating sintering
ISE Indent size effect
K Bulk or volumetric elastic modulus
K_{C}, K_{B} Bulk elastic modulus of the carbide and binder phases, respectively
K_{U}, K_{L} Upper and lower bounds, respectively, of bulk elastic modulus
$K_{1\mathrm{C}}$ Fracture toughness—critical stress intensity factor
LPS Liquid phase sintering
λ Mean linear intercept of binder phase (mlibp)
λ' Noncontiguous mean linear intercept of the binder phase that ignores the contiguity G of carbide crystals. $\lambda' = \lambda(1 - G)$
λ'' Some critical depth of shear stress penetration into the binder phase in the CLRH model for hardness
$\lambda_{\perp}$ Mean distance between carbide crystals in cemented carbides
M Strain-gradient related constant in microhardness
mlicc Mean linear intercept of the carbide crystals d_{α}
mlibp Mean linear intercept of the binder phase λ
MWS Microwave sintering
μ Shear elastic modulus of the alloy
μ_{C}, μ_{B} Shear elastic modulus of the carbide and binder phases, respectively
μ_{U}, μ_{L} Upper and lower bounds of shear elastic modulus
P_{WC} Shape equiaxiality of WC crystals
P^0_{WC} Initial value of the shape equiaxiality P_{WC} before the change of the shape of WC crystals
RCSS Residual compressive surface stresses after grinding
RTS Residual thermal stresses in the carbide and binder phases
SPS Spark plasma sintering
SSS Solid-state sintering
σ_{C}, σ_{B} Stress in the carbide and binder phase, respectively
$\sigma_{0.01}$ Yield stress of the alloy at 0.01%
σ_{y} Yield stress of the polycrystalline material
$\tau_{\mathrm{y}}{}^{\mathrm{WC}}$ Yield stress of WC
U Macroscopic strain energy density in the BK model of the elastic moduli
V_{V} Volume fraction of the carbide phase in cemented carbides
ν Poisson's ratio
γ The size of carbide–carbide neck (contact) in the MLN model of hardness

1.09.1 Introduction

Basic mechanical properties and behavior of hardmetals[1] include hardness, elastic moduli, deformation behavior, fracture modes and stages, fracture toughness, and strength. These properties are usually measured at room temperature and serve as the main quantitative basis for comparison of the materials and their production technologies. The basic mechanical properties can be divided into nondestructive and destructive tests based on their measuring technique. The nondestructive tests measure the elastic and plastic deformation of the material that does not cause the fracture of the specimen into pieces, even though the bulk and surface of the specimen can undergo irreversible strain and cracking. The destructive tests break the specimen into two or more pieces. Elastic moduli, study of deformation behavior, and the measurement of hardness are nondestructive properties and are reviewed in this chapter together with the discussion of the structure–property relation approach. The fracture behavior, fracture toughness, and strength of the material are destructive properties and are discussed in a separate chapter.[2]

---

[1] For more information on the definition and fundamentals of hardmetals, see Chapters 1.1, Introduction to Hardmetals—Definitions, classification and history of hardmetals; 1.2, Introduction to Hardmetals—Fundamentals and general applications of hardmetals; 1.4, Class of Materials—Cemented Carbides; and 1.5, Class of Materials—Cermets.

[2] For more information on the destructive properties, see Chapters 1.10, Fracture and strength of hardmetals at room temperature; 1.11, Mechanical Properties—Fatigue; 1.12, Mechanical Properties—Wear of Hardmetals; 1.14, Mechanical Properties—Plastic, high temperature

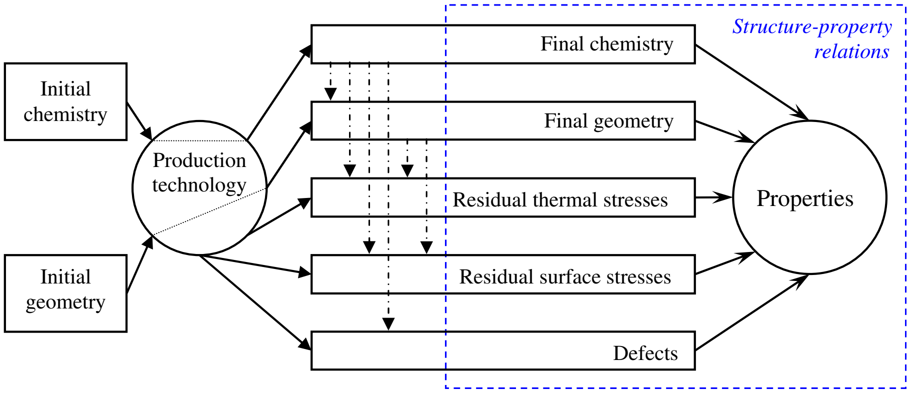

Figure 1 Dependence of properties on chemistry, geometry, residual stresses, defects, and production technology. This chapter mainly focuses on the structure–property relations that are shown inside a dashed blue box. The dependencies of the final chemistry, final geometry, residual stresses, and defects on the production technology and initial chemistry and geometry as well as their interdependencies (dash–dot lines) are also shown, but are out of scope of this chapter.

1.09.2 Structure–Property Relation

The mechanical properties are determined by the chemical state, geometrical structure, mechanical state in terms of residual stresses, and the defects of the materials that are combined under a wide term, the material's structure (Figure 1). Further in the chapter, the chemical state is referred to as chemistry, whereas the geometrical structure is referred to as geometry. To achieve the final chemistry and geometry, the initial substances that constitute the material undergo several steps of chemical and geometrical transitions controlled by the selected production technology. Therefore, the mechanical properties also, even though indirectly, depend on the initial chemistry and initial geometry of the constituting substances and the production technology.

1.09.2.1 Property Dependencies

1.09.2.1.1 Initial Chemistry, Initial Geometry, and Production Technology

Initial chemistry[3] is the choice of the main carbide and binder substances, as well as the optional addition of extra carbides or other chemical element(s). *Initial geometry*[4] is the size, size distribution, and morphology of the initial powders and uniformity of their mixture. There exists a large variety of *production technologies*[5] including liquid phase sintering (LPS), solid state sintering, spark plasma sintering, pulse plasma sintering, microwave sintering, high-frequency induction heating sintering, and other emerging technologies (Fang, Wang, Ryu, Hwang, & Sohn, 2009; Fischmeister, 1983; German, 2005; German, Suri, & Park, 2009; Mukhopadhyay & Basu, 2011). The production can be done under vacuum or selected sintering atmosphere, can often be combined with hot pressing, and can be followed up by additional heat treatments after sintering. All this variety of the initial chemistry, initial geometry, and production technologies is aimed at creating the final chemistry and geometry with minimal defects and optimal combination of mechanical properties.

1.09.2.1.2 Final Chemistry

Final chemistry[6] is the phase composition and content of the alloy. The chemical balance is maintained very well by the classical LPS technologies, but it might become especially important for the new technologies of quick sintering. Carburization or decarburization can cause formation of unwanted phases of free carbon or η-phases, as well as changes in the tungsten content in the binder phase (Andren, 2001a; Exner, 1979, 1983;

---

[3] For more information on the initial chemistry, see Chapters 1.6, Powder Synthesis; 1.7, Synthesis and Processing—Powder Processing and Green Shaping.

[4] For more information on the initial geometry, see Chapters 1.6, Powder Synthesis; 1.7, Synthesis and Processing—Powder Processing and Green Shaping.

[5] For more information on production technologies, see Chapters 1.8, Synthesis and Processing—Consolidation Techniques.

[6] For more information on the final chemistry, see Chapters 1.1, Introduction to Hardmetals—Definitions, classification and history of hardmetals; 1.2, Introduction to Hardmetals—Fundamentals and general applications of hardmetals; 1.3, Introduction to Hardmetals—Microstructure and morphology of hardmetals; 1.4, Class of Materials—Cemented Carbides; 1.5, Class of Materials—Cermets.

Fischmeister, 1983). Cleaning of or penetration into the alloy of the impurities, oxygen, and residual gases affects the final composition. Solution of the carbide in the liquid binder phase followed by binder crystallization and precipitation of the carbide elements back onto the carbide crystals with formation of the diffusional chemical gradient in the binder during cooling affects the binder composition (Almond & Roebuck, 1988; Andren, 2001a, 2001b; Andren, Rolander, & Lindahl, 1994a, 1994b; Hellsing, 1988; Hellsing & Andren, 1986; Mari, Krawitz, Richardson, & Benoit, 1996; Roebuck & Almond, 1988; Roebuck, Almond, & Cottenden, 1984). Nanoparticles can occur in the binder phase (Exner, 1983; Konyashin, Ries, & Lachmann, 2008; Konyashin, Schafer, & Cooper, 2005). Crystallography of Co binder can change showing more or less hexagonal close-packed (hcp) lattice rather than face-centered cubic (fcc) lattice, when the carbide grain size is decreased from micron-sized grains down to nanograins (Cha, Hong, Ha, & Kim, 2001; Jia, Fischer, & Gallois, 1998) or due to chemical doping (Weidow, Norgren, & Andren, 2009) on WC–Co cemented carbides.

Submonolayer of the binder metal and other elements is found at the carbide–carbide contacts (Christensen & Wahnstrom, 2003, 2004, 2006; Elfwing & Norgren, 2005; Henjered, Hellsing, Andren, & Norden, 1986; Ostberg, Buss, & Christensen, 2006; Vicens, Benjdir, Nouet, Dubon, & Laval, 1994; Weidow & Andren, 2010, 2011). Added elements can segregate onto carbide–binder interfaces from the binder phase either during sintering, or cooling (Delanoe, Bacia, Pauty, & Lay, 2004; Lay, Donnadieu, & Loubradou, 2010; Lay, Hamar-Thibault, & Lackner, 2002; Shatov & Firstov, 1995; Shatov, Firstov, & Shatova, 1998; Wang, Pauty, Lay & Allibert, 2002; Weidow & Andren, 2010, 2011; Weidow, Norgren, & Andren, 2009). The added elements can even somewhat dissolve in the growing areas of WC crystals during LPS with the highest measured solubilities being those of Ta, Nb, Cr, and V that ranges from about 1 at% for Ta down to about 0.1 at% for V, whereas the solubilities of other elements including Ti and Co do not exceed 2×10^{-2} at% and are usually neglected (Weidow, Johansson, Andren, & Wahnstrom, 2011). Complex carbides and core-rim structures like TiC/(Ti,W)C with gradients of chemical composition are formed during the sintering of the three- and more-phase cemented carbides (Andren, 2001a; Exner, 1983; Fischmeister, 1983; Mari, 2001).

1.09.2.1.3 Final Geometry

Final geometry[7] of two-phase cemented carbides is usually described by the stereological parameters of volume fraction of the carbide phase V_V, the area fraction of the carbide–carbide contacts in the total surface area of the carbide crystals referred to as the contiguity of the carbide crystals G, the mean linear intercept of the carbide crystals (mlicc) d_α and the mean linear intercept of the binder phase (mlibp) λ, as well as by the shape of carbide crystals (Exner, 1970, 1979, 1983; Exner & Fischmeister, 1966; Fischmeister, 1983; Gurland, 1958, 1959, 1963a, 1963b; Underwood, 1968). The stereological parameters V_V, G, d_α, and λ cannot change independently and are interrelated through the following stereological equation:

$$\frac{\lambda}{d_\alpha} = \frac{1 - V_V}{V_V \cdot (1 - G)} \tag{1}$$

It is a well-known experimental fact for the conventional hardmetals that the contiguity G of the carbide crystals mainly depends on the volume fraction of the carbide phase V_V and does not depend on the mean linear intercepts of the phases when the shape of the carbide crystals is kept unchanged (Deshmukh & Gurland, 1986; Exner, 1979; Exner & Fischmeister, 1966; Lee & Gurland, 1978; Shatov, Ponomarev, Firstov, & Warren, 2006; Warren & Waldron, 1972).

$$G|_{\text{Carbide Shape} = \text{const}} = f(V_V) \tag{2}$$

The interrelation (1) and correlation (2) imply that there are only two independent stereological parameters and one of them is the volume fraction of the carbide phase V_V. The obvious choice for the second independent parameter seems to be the mlicc d_α. Nevertheless, this interdependence often presents a challenge for identifying the main reason of the change of the mechanical properties from the experimental correlations of the mechanical properties versus the stereological parameters.

---

[7] For more information on the final geometry, see Chapters 1.1, Introduction to Hardmetals—Definitions, classification and history of hardmetals; 1.2, Introduction to Hardmetals—Fundamentals and general applications of hardmetals; 1.3, Introduction to Hardmetals—Microstructure and morphology of hardmetals; 1.4, Class of Materials—Cemented Carbides; 1.5, Class of Materials—Cermets.

Despite a seemingly predefined value of contiguity by the experimental correlation (2), the carbide–carbide contacts and their contiguity play an important role for many mechanical properties. Presence of a submonolayer of the binder metal at the carbide–carbide contacts (Christensen & Wahnstrom, 2003, 2004, 2006; Elfwing & Norgren, 2005; Henjered, Hellsing, Andren, & Norden, 1986; Vicens, Benjdir, Nouet, Dubon, & Laval, 1994) splits the size distribution of the binder phase into a bimodal distribution. Carbide crystals can also form high-coincidence and low-energy carbide–carbide contacts (Deshmukh & Gurland, 1982, 1986; Exner, 1983; Kim & Rohrer, 2004; Ostberg, Farooq, & Christensen, 2006; Weidow, Norgren, & Andren, 2009; Weidow, Zackrisson, Jansson, & Andren, 2009).

1.09.2.1.4 Dependence of the Final Geometry on Chemistry

Change of the chemistry affects the final geometry in many ways. Addition of VC, Cr_3C_2, and other carbides inhibits the growth of WC grains (Fang, Wang, Ryu, Hwang, & Sohn, 2009). The shape of WC crystals can be changed to a flatter triangular prism by doping the WC-based cemented carbide with TiC (Shatov, Firstov, & Shatova, 1998; Schon, Schubert, & Lux, 2001; Wittmann, Schubert, & Lux, 2002). Changing the carbon balance or adding VC and Cr_3C_2 carbides changes the truncation and rounding of WC triangular prism (Christensen, Wahnstrom, Allibert, & Lay, 2005; Delanoe & Lay, 2009a, 2009b; Herber, Schubert, & Lux, 2006; Kim, Han, Park, & Kim, 2003; Lee, Kim, Hwang, & Kim, 2003; Wang, Heusch, Lay, & Allibert, 2002; Wang, Pauty, Lay, & Allibert, 2002). Growth steps are observed on the facets of WC crystals when TiC (Shatov, Firstov, & Shatova, 1998), VC (Lay, Hamar-Thibault, & Lackner, 2002), or Cr (Delanoe, Bacia, Pauty, Lay, & Allibert, 2004; Wang, Pauty, Lay, & Allibert, 2002) is added to the cemented carbides. Changing the shape of carbide crystals breaks the correlation of the contiguity G versus the volume fraction V_V (2) and introduces another degree of variation of the final geometry (Shatov, Ponomarev, Firstov, & Warren, 2006; Warren, 1968).

The values of the stereological parameters vary from the surface to the bulk of the specimen on functionally graded materials (Murray, Balogun, Steen, Basu, & Sarin, 2005; Zhang, Lu, Zhang, & Fang, 2010). Introduction of the new phases on three- or more-phase cemented carbides, presence of abnormally grown grains (AGG), as well as formation of the core–rim structures of the carbide grains requires further expansion of the stereological parameters and shape characterization for each carbide phase by measuring their respective microstructure parameters like $V_{V\alpha}$, $V_{V\beta}$, d_α, d_β, $G_{\alpha\alpha}$, $G_{\beta\beta}$, $G_{\alpha\beta}$, shape$_\alpha$, shape$_\beta$; distribution of the linear intercepts of phases; mean core–rim ratio; and so on. Moreover, the dual composites that represent a mixture of two cemented carbides one inside the other (Fang, Lockwood, & Griffo, 1999; Deng, Patterson, & Chawla, 2002) also require some way of microstructure quantification. The added complexity and extra degree of the microstructure variation presents an extra challenge for identifying the correlations and building models for the mechanical properties of these materials.

1.09.2.1.5 Residual Surface and Thermal Stresses

There are two types of residual stresses that change the mechanical state of the constituting phases as well the surface of the specimen after sintering and specimen preparation, namely, the residual thermal stresses (RTS) of phases and the residual surface stresses (Exner, 1979; Fischmeister, 1983). The residual compressive surface stresses (RCSS) are caused by surface preparation treatment like grinding and are compensated by the tensile stresses in the bulk of the specimen. RCSS can increase the compressive stress level in WC phase up to 1.5 GPa and can penetrate up to a depth of 10–100 μm depending on the binder content and the grinding conditions (Exner, 1969, 1979; Jaensson, 1971; Roebuck & Almond, 1988). It is usual practice to reduce or eliminate RCSS by polishing out layers of material from its surface or annealing at temperatures above 800 °C (Exner, 1969, 1979; Jaensson, 1971; Roebuck & Almond, 1988) before testing for transverse rupture strength, Palmqvist toughness, and micro- and nanohardness that are sensitive to the state of the surface of the material.

The RTS[8] of phases are caused by the difference in the thermal expansion of the phases and occur during cooling after the sintering (Coats & Krawitz, 2003; Exner, 1979; Krawitz, Crapenhoft, Reichel, & Warren, 1988; Mari, Clausen, Bourke, & Buss, 2009; Mari, Krawitz, Richardson, & Benoit, 1996; Paggett, Krawitz, & Drake, 2006, 2007). At room temperature, the carbide phase is under triaxial compression stress, whereas the binder phase is under triaxial tensile stress, which is close to the yield stress. Little is known about whether and how the RTS of phases can affect the mechanical properties because there is not much control over or ways to vary the values of RTS. In addition, the RTS are usually changed simultaneously with other parameters of the final geometry and therefore it is hard to pinpoint their effect on the mechanical properties.

---

[8] For more information on the residual thermal stresses, see Chapter 1.13, Mechanical Properties—Residual/thermal stress in hardmetals.

1.09.2.1.6 Defects

Defects of the microstructure include pores, third unwanted phase like free carbon and η-phases, impurities, AGG and large carbide crystals, as well as the so-called binder lakes when the binder is not uniformly distributed between the carbide crystals but is agglomerated into a carbideless area. In general, these defects adversely affect the mechanical properties (Almond, 1983; Exner, 1979, 1983; Fischmeister, 1983; Laptev, Ponomarev, & Ochkas, 2001; Roebuck & Almond, 1988).

1.09.2.2 Two Types of Property Comparability

The vast variety of the initial and final chemistry, geometry, residual stresses, and defects listed above predicates the mechanical properties of the hardmetals. Therefore, finding the main cause among this variety and identifying the mechanism for the property presents a significant challenge. This puzzle is usually approached from two sides: the technology-property comparability and the final structure-property comparability. The main goal of comparing is to find the reason or a set of reasons for the change in the mechanical property. To achieve this, as many as possible input and control parameters that are out of research scope should be kept unchanged. In other words, only the minimal number of the input or control parameters should be varied to study the effect of these selected parameters on the property.

1.09.2.2.1 Technology–Property Comparability

At the first or initial stage of research, the technology–property comparability can bring a quick answer to whether the selected technology increases the property. For pure comparison of the technology and its parameters, both the initial chemistry and initial geometry should be kept unchanged. On the other hand, varying the initial chemistry and/or initial geometry allows comparison of the pretechnology factors when the same technology is used. Simultaneous change of the pretechnology factors and the technology parameters makes the materials practically not comparable, even though the properties of the resulting materials are usually different. In the technology–property comparability approach, the final chemistry and geometry are only used to describe the result of the preproduction conditions and production technology. Final structure and chemistry depend on many input parameters and structure formation mechanisms. Defects of the microstructure can also be introduced by the production technology.

Simultaneous change of multiple structure and chemistry characteristics makes it hard to identify the cause(s) for the affected properties and therefore leaves room for educated guessing about the actual reasons. For instance, adding VC carbide reduces mlicc d_{WC} of WC crystals in cemented carbides. Reduction of d_{WC} increases the hardness of the alloy. Nevertheless, the whole effect of VC on the hardness is not revealed. To fully study how VC affects hardness, it would be necessary to sinter for a longer period to increase d_{WC} to the same value as of the cemented carbides without the addition of VC. Sintering for a longer time might bring decarburization, impurity penetration, AGG, and many other changes in the chemistry and geometry, that will make it even harder to compare the materials. Alternatively, starting with bigger d_{WC} would probably require going through different initial stages of sintering like carbide powder dissolution and powder contact separation by the liquid binder phase, that might also take some time and affect the resulting microstructure in yet another way.

Nevertheless, despite the fact that the technology–property comparability approach cannot be considered as a clear basis for fully understanding the properties, it does point in the right direction for improvement of the properties.

1.09.2.2.2 Structure–Property Comparability

On a more mature stage of research, the materials can be compared based on their final chemistry and geometry and the main reason and mechanisms of the property can be identified. Identification of the mechanism eventually allows the creation of a model that relates the property to the final chemistry and geometry of the material. Practically, the initial chemistry and geometry, as well as the production technology parameters become nonrelevant for this comparability. The final chemistry and geometry have to be very similar with variation of only one parameter or a minimal set of variable parameters. Only then it would be clear whether the property depends on the variable parameter of the final chemistry and geometry or not.

On the other hand, sometimes it might be possible to eliminate even varying parameters that are not related to the property. For example, purely empirical correlations of fracture toughness $K_{1\mathrm{C}}$ versus all the stereological parameters (Bolton & Keely, 1983) or only the mlibp λ and the contiguity G of WC crystals can be measured on cemented carbides (Bolton & Keely, 1983; Chermant & Osterstock, 1976; Sigl & Fischmeister, 1988;

Slesar, Dusza, & Parilak, 1986). Nevertheless, the physics of the fracture process (Gurland, 1988; Sigl & Exner, 1987; Sigl, Exner, & Fischmeister, 1986) and experiments on the cemented carbides with a flatter shape of WC crystals (Shatov, Ponomarev, & Firstov, 2008) indicate that the fracture toughness K_{1C} does not depend on the contiguity G and that contiguity should be excluded from these correlations.

The structure–property comparability approach requires more experimental and production work and it is not always possible to produce the comparable final structures. Nevertheless, the main benefit of the structure–property comparability lies in the ability to build and verify physical models as well as to develop fundamental understanding of the properties. Physical models that are based on the structure–property relations can be transferred, verified, and/or extended to other materials. For example, Lee & Gurland (LG) model of hardness for two-phase cemented carbides (Gurland, 1979; Lee & Gurland, 1978), discussed below, can be considered as an enhancement of the Hall–Petch model (Hall, 1952; Petch, 1953) that is built for single-phase polycrystals. Physical models accelerate and direct further research, as well as form a basis for further exploration of the structure–property and technology–property relations.

1.09.2.3 Modeling the Properties

Assumptions have to be made to create a model. Clear statement of the assumptions allows easier assessment of the validity, applicability, and limitations of the model. In general, the best models have the least number of and simpler assumptions. In other words, when an excessive number of assumptions are made or very specific conditions are imposed on the model, there is a higher chance for the model to either be invalid or have a very limited applicability. At the same time, any model cannot be fully universal and will always have its limitations. For example, as discussed below, moving to nanograined cemented carbides can change the deformation mechanisms from the dislocation-driven mechanism to grain-boundary slippage and other nanospecific nondislocation deformation. This change can break many assumptions and becomes a limiting factor for the regular models of hardness. Extension to other materials can also change the chemistry and geometry outside the applicability limits of the model.

Models can be classified based on their physical ideas and assumptions. The minimal requirement for the model is the ability to *correlate* and predict the value of the studied property from the geometry of a material with the predefined chemistry. For instance, pure empirical correlations can have high correlation factors, but they fail to provide physical reason for property changes. The model that is based on a physical idea should be able to *explain* the correlation by providing the physical reasoning for the property change. When the ideas behind the model are universal and the number of assumptions is low, the model should allow for *generalization* and/or extension to other materials. In other words, the most advanced model should be able to or allow being enhanced to explain the correlations of hardmetals with different carbide phase, with another binder, or with the changed shape of the carbide crystals. It should also be transferrable to other similar composites and be able to provide general indication on how to model the addition of extra carbides. When the model is generalized to the next level of complexity, it is expected to be reducible back to the original form by elimination of this extra complexity. For instance, model for two-phase materials should be reducible to that for one-phase materials that are the binderless cemented carbides by setting the volume fraction of the carbide phase to 1. Models for three-phase materials should be reducible to those of two-phase and even to those of one-phase materials the same way. Models that add the effect of the shape of the carbide crystals should be reducible to the original model when the shape is kept unchanged.

1.09.3 Hardness

1.09.3.1 Hardness Definition

Hardness is the ability of material to resist localized plastic deformation. For hardmetals, the indentation hardness is referred to as hardness. Vickers hardness (HV) test (ISO 3878) is the most common for hardmetals, followed in popularity by Rockwell hardness of scale A test (ISO 3738, ASTM B294). Knoop hardness (HK) test (ISO 22394) is also used when the anisotropy of material is of interest, as it is the case in WC crystals (Exner, 1979; French & Thomas, 1965). A wide variety of load weights of 100, 50, 30, 20, 15, 10, and 1 kg are used for measuring the HV, with the most common load being 30 kg of weight, denoted as HV30. Reduction of the weight load below 1–5 kg qualifies as the test for the microhardness on cemented carbides (Jia, Fischer, & Gallois, 1998; Roebuck, 1995). HV typically ranges from about 7 up to 22 GPa for WC–Co cemented carbides and can reach up to about 24 GPa for binderless WC and nano–grained grades of WC–Co with grain growth inhibitors (Almond, 1983; Ettmayer, 1989; Fang, Wang, Ryu, Hwang, & Sohn, 2009; Gille, Szesny, & Dreyer, 2002; Gurland, 1988; Jia, Fischer, & Gallois, 1998; Michalski & Siemiaszko, 2007; Mukhopadhyay & Basu, 2011; Mukhopadhyay, Chakravarty, & Basu, 2010; Roebuck & Almond, 1988; Sailer, Herr, & Sockel, 2001; Schubert, Neumeister, Kinger, & Lux, 1998; http://www.allaboutcementedcarbide.com/). For the sake of brevity in this chapter, the term hardness is used for HV of hardmetals, whereas indentation tests for Rockwell hardness and HK are specifically denoted by their type when used.

1.09.3.2 Hardness Dependence on Microstructure and Chemistry

Hardness seems to be sensitive to almost all the parameters of chemistry and geometry of hardmetals. Hardness increases with the increase of the volume fraction of the carbide phase V_V and the decrease of the mlicc d_{WC} (Fischmeister, 1983; Gurland, 1979; Lee & Gurland, 1978). It also depends on other microstructure parameters like the contiguity G and the shape of the carbide crystals, plus the mlibp λ (Fischmeister, 1983; Gurland, 1979; Lee & Gurland, 1978; Shatov, Ponomarev, & Firstov, 2009). Doping with carbides like VC, Cr_3C_2, NbC, and TaC increases the hardness of WC-based cemented carbides mainly due to the reduction of the size of WC crystals (Fang, Wang, Ryu, Hwang, & Sohn, 2009; Jia, Fischer, & Gallois, 1998; Li, T., Li, Q., & Fuh, 2006; Mukhopadhyay & Basu, 2011). Doping with TiC carbide can increase the hardness of WC-based cemented carbides due to change of shape of WC crystals (Shatov, Ponomarev, & Firstov, 2009). Adding more TiC changes the microstructure to core-rim type of mixed carbide crystals of TiC/(Ti,W)C that have higher hardness than WC crystals and therefore also increase the total hardness of the WC-based cemented carbides (Almond, 1983; Gurland, 1988). Hardness of TiC-based cermets is usually higher than the hardness of WC-based cemented carbides with similar dependencies on the microstructure parameters (Doi, 1986; Gurland, 1988).

Replacing the binder metal from Co to Ni, Co–Ni, Fe–Co–Ni, Ni–Cr–Mo, Ni–Al, Ni–Cr–Mo–Al, or other combination usually decreases but in some cases can somewhat increase the hardness of WC-based cemented carbides (Almond & Roebuck, 1988; Ekemar, Lindholm, & Hartzell, 1982; Exner, 1979; Fischmeister, 1983; Guilemany, Sanchiz, Mellor, Llorca, & Miguel, 1994; Prakash, 1993; Tracey, 1992). Partial or full substitution of Co with Ni binder phase decreases the hardness of Ti(C,N)-based cermets (Ettmayer, Kolaska, Lengauer, & Dreyert, 1995). Partial or full substitution of Co binder with nanograined ceramics ZrO_2 increases the hardness in comparison to WC–Co (Mukhopadhyay & Basu, 2011; Mukhopadhyay, Chakravarty, & Basu, 2010). Hardness of dual cemented carbides seems to be lower than the hardness of the regular cemented carbides (Deng, Patterson, Chawla, et al., 2002; Fang, Lockwood, & Griffo, 1999). Solid solution and doping of the binder phase are assumed to increase the hardness, but no direct and conclusive experimental evidence is reported as this state of the microstructure is usually accompanied by other microstructure and chemistry changes like the decrease of the mean linear intercepts and/or occurrence of the third phase of the growth inhibitors (Jia, Fischer, & Gallois, 1998; Mukhopadhyay & Basu, 2011). Presence of nanoparticles in binder phase increases the hardness (Konyashin et al., 2005, 2008).

Hardness decreases when AGG is present in the alloy due to the increase of the average mlicc (Li, T., Li, Q., & Fuh, 2007; Schreiner, Schmitt, Lassner, & Lux, 1984; Yang & Kang, 2009). Defects of microstructure like pores, free carbon phase, and/or η-phase reduce the hardness of cemented carbides. Little is known on whether the RTS can affect the hardness; perhaps the nanoindentation tests might reveal some dependence on them. Hardness measured at regular and higher loads is not that sensitive to the RCSS from grinding (Exner, 1979; Exner & Gurland, 1970), but the micro- and nanohardness values are affected and therefore are measured on the polished surface of the specimen.

1.09.3.3 Hardness of Nanograined Cemented Carbides

Many recent research efforts are devoted to achieving the nanosized carbide grains in hardmetals, which promise higher hardness for the alloy (Fang, Wang, Ryu, Hwang, & Sohn, 2009; Jia, Fischer, & Gallois, 1998; Mukhopadhyay & Basu, 2011). This is accomplished through a reduction of the exposure to high temperature and the application of high pressure at sintering by using a variety of new sintering techniques as well as by WC grain growth inhibition by addition of VC, Cr_3C_2 and other carbides and elements to the alloys. Usually, the production methods for nanograined cemented carbides leave some porosity and other impurities that negatively affect the hardness. Moreover, decrease of the mlicc d_{WC} faces the so-called reversed Hall–Petch effect of unexpected decrease of the hardness at nanoscale that is also observed on many other nanograined materials (Fang, Wang, Ryu, Hwang, & Sohn, 2009; Mukhopadhyay & Basu, 2011). At the nanoscale, the relative specific surface area of the carbide–carbide and carbide–binder interfaces increases dramatically and the size of the grains is reduced closer to the Burgers vector of the crystalline lattice of phases. The adhesion between the contacting carbide crystals and between the carbide and binder phases becomes of utmost importance because the deformation mechanism can change from the dislocation pileups in the binder and carbide phase observed in the conventional hardmetals (Gurland, 1979; Lee & Gurland, 1978; Makhele-Lekala, Luyckx, & Nabarro, 2001) to the slippage along the boundary between the grains (Fang, Wang, Ryu, Hwang, & Sohn, 2009; Milman, 2008; Richter & Ruthendorf, 1999), cobalt lattice martensitic transformation from fcc to hcp (Cha, Hong, Ha, & Kim, 2001; Jia, Fischer, & Gallois, 1998), or perhaps even to the transformation of the WC crystal lattice from hcp to fcc (Zavodinsky, 2010) in the nano- and low nano range. Besides, any impurity at the interfaces common to the production of the nanograined cemented carbides can dramatically affect the hardness of the alloy (Fang, Wang, Ryu, Hwang, & Sohn, 2009; Richter & Ruthendorf, 1999).

1.09.3.4 Micro- and Nano Indentation

The indentation hardness increases when the indent diagonal or diameter is decreased from several hundred microns down to a micron and further to submicrons due to the lower loads on the indenter, as it was initially observed for single crystals by Stelmashenko, Walls, Brown and Milman (1993a, 1993b) and De Guzman, Neubauer, Flinn and Nix (1993). The indent size effect (ISE) is also observed at microindentation of hardmetals. For microindentation of WC–Co alloys, the loads should be below 1 kg and down to several grams of weight (Nabarro, Shrivastava, & Luyckx, 2006; Shrivastava & Luyckx, 2008). Jia, Fischer and Gallois (1998) observed almost constant hardness in the load range between 10 and 40 kg of weight, whereas the microhardness of the alloy steeply increases when the loads went below about 2 kg and down to 0.025 kg of weight on a wide variety of regular and nanograined WC–Co cemented carbides (Figure 2).

Gee, Roebuck, Lindahl and Andren (1996) reported that the nanohardness of phases measured by the nanoindentation on WC–Co cemented carbides and Ti(C,N)–Co cermets is about an order of magnitude higher than the hardness values expected for the constituent phases and the regular hardness of these materials. Bonache, Rayon, Salvador and Busquets (2010) reported similar, higher than expected, results of nanoindentation for the phases of WC–Co alloys. Bonache, Rayon, Salvador and Busquets (2010) also found that the nanohardness of the prismatic facet $\{10\bar{1}0\}$ is about two times higher than the nanohardness of the basal facet $\{0001\}$ of WC crystals in WC–Co cemented carbides. This measurement of nano-hardness anisotropy of WC is the opposite of the classic measurement of HK on stand-alone WC crystals made by French and Thomas (1965), where the basal facet is about two times harder than the prismatic facet of WC (Exner, 1979). These observations indicate that the values of the micro- and nano hardness are strongly affected by the indent size.

The explanation of the ISE is based on the idea of separating and comparing the effects of the strain gradient versus the homogeneous bulk strain of the material under indenter (Ashby, 1970, 1971; De Guzman,

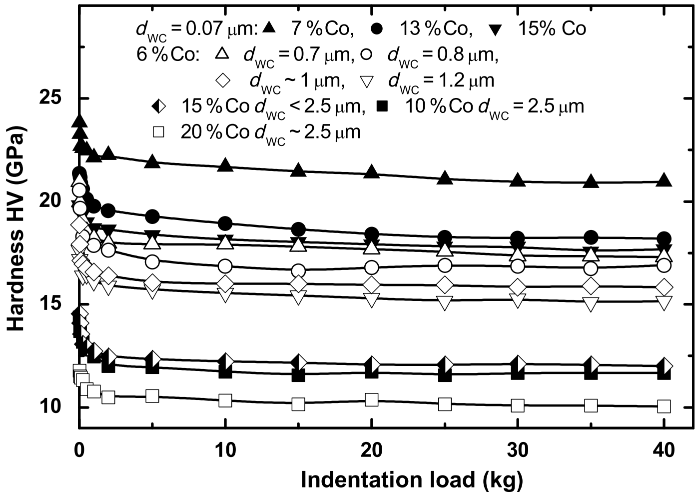

Figure 2 The variation of the hardness of WC–Co cemented carbides with the indentation load between 0.025 and 40 kg of weight. Reproduced from Figure 7 in Jia, Fischer, & Gallois (1998) with permission from Elsevier.

Neubauer, Flinn, & Nix, 1993; Nye, 1953; Stelmashenko, Walls, Brown, & Milman, 1993a, 1993b). The strain gradient is responsible for the localized change of the shape of the surface of crystalline material and therefore is associated with the geometrically necessary dislocations. The homogeneous bulk strain is not localized under indenter; it acts as if the whole surface of the material were pushed to the bulk of the material and therefore is associated with the statistically stored dislocations in the bulk of the material. It is the homogeneous bulk strain that is responsible for the values of the regular hardness under loads of several kilograms of weight.

Strain gradient plasticity theories were developed and applied to a variety of single and polycrystalline materials (De Guzman, Neubauer, Flinn, & Nix, 1993; Fleck & Hutchinson, 1997, 2001; Fleck, Muller, Ashby, & Hutchinson, 1994; Gao, 2001; Nix & Gao, 1998; Stelmashenko, Walls, Brown, & Milman, 1993a, 1993b) as well as to two-phase composites (Fleck & Willis, 2004) and cemented carbides (Nabarro, Shrivastava, & Luyckx, 2006; Shrivastava & Luyckx, 2008). In general, strain gradients are inversely proportional to the length scale over which the plastic deformation occurs (Fleck & Hutchinson, 1997). In some sense, the relative effect of the surface change versus the bulk is proportional to the specific surface area of the indent, which is inversely proportional to the indent size. Therefore, the decrease of the indent size increases the relative density of the geometrically necessary dislocations versus statistically stored dislocations. Hardness is proportional to the square root of the total dislocation density. Theories and experiments produce the following equation for the microhardness H_{micro} versus the indent depth h (De Guzman, Neubauer, Flinn, & Nix, 1993; Fleck, Muller, Ashby, & Hutchinson, 1994; Fleck & Hutchinson, 1997, 2001; Fleck & Willis, 2004; Gao, 2001; Nabarro, Shrivastava, & Luyckx, 2006; Nix & Gao, 1998; Shrivastava & Luyckx, 2008; Stelmashenko, Walls, Brown, & Milman, 1993a, 1993b).

$$H_{\mathrm{micro}}^2 = H_{\mathrm{bulk}}^2 + M \cdot \frac{h^*}{h} \tag{3}$$

where H_{bulk} is the hardness due to the homogeneous bulk strain, M is a constant that is determined by the geometry of indenter, and h^* is a characteristic length that depends on the properties of the material.

Nabarro, Shrivastava and Luyckx (2006) and Shrivastava and Luyckx (2008) go further and introduce an intrinsic length of the material that is equal to the sum of the mlicc d_{WC} and the mlibp λ for WC–Co cemented carbides (**Figure 3**). It is reported that the linear dependence (3) changes its characteristic length h^* at the intrinsic length of $(d_{\mathrm{WC}} + \lambda)$ with lower h^* value at lower indent depths (Nabarro, Shrivastava, & Luyckx, 2006; Shrivastava & Luyckx, 2008). The preliminary physical interpretation of the effect suggests that at the indent depth greater than the intrinsic length of $(d_{\mathrm{WC}} + \lambda)$, the cemented carbide behaves like a homogeneous elastic–plastic material, whereas at the lower indent depth, the combined effect of two separate phases should be taken into account (Nabarro, Shrivastava, & Luyckx, 2006; Shrivastava & Luyckx, 2008).

The microindentation hardening effect has to be taken into account when measuring the micro- and nanohardness of the phases, of the core–rim complex carbides, when studying the gradients and changes of the

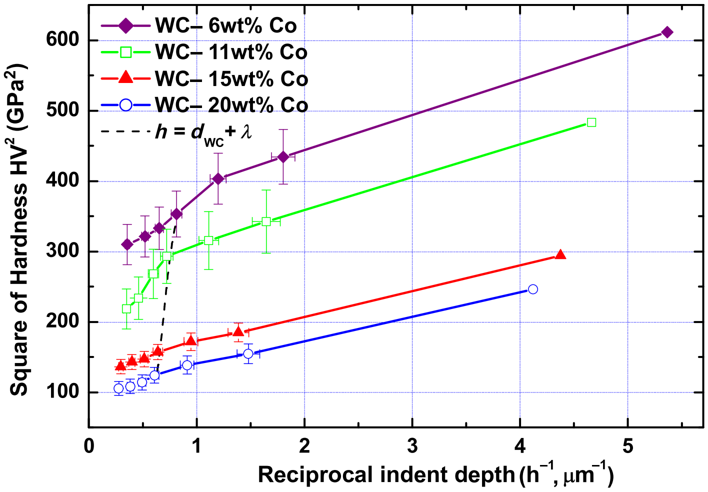

Figure 3 The square of the Vickers hardness as a function of the reciprocal indent depth h^{-1} for WC–Co cemented carbides with four different binder contents. The dashed line corresponds to the indentation depth h equal to the intrinsic length that is the sum of the mean linear intercepts of carbide and binder phases ($d_{\mathrm{WC}} + \lambda$). Reproduced from Figure 2 in Nabarro, Shrivastava, & Luyckx (2006) with permission from Taylor & Francis.

microstructure on the functionally gradient materials, as well as for the comparison of properties of the coatings over the hardmetals.[9]

1.09.3.5 Models for Hardness

A wide variety of models is understandable as the number of parameters that influence the hardness is rather large. The main differences lie in the consideration of the deformation of the carbide phase in addition to or in parallel to the deformation of the binder phase, the mechanical interaction between the phases, and the selection of microstructure parameters that are believed to affect the hardness of the cemented carbides. The most widely accepted LG model extends the Hall–Petch relation of the single-phase polycrystalline materials to two-phase cemented carbides by introducing the term of the contiguous volume fraction of the carbide phase and assuming the independence between the hardness of the carbide and binder phases. Several other semiempirical and pure empirical models make an attempt to avoid using the Hall–Petch relation and/or to reduce the number of parameters and deformation processes that the hardness can relate to. Continuum deformation model attempts to calculate the hardness from continuum elastic deformation with some critical stress for the plastic deformation. The assumptions, applicability, and limitations of the models are discussed.

1.09.3.5.1 Lee & Gurland (LG) Model

1.09.3.5.1.1 LG Model Definition

The LG model (Gurland, 1979; Lee & Gurland, 1978) is based on the calculation of the yield stress of both the carbide and binder phases. Lee and Gurland (Gurland, 1979; Lee & Gurland, 1978) noticed that hardness dependence on the mlicc d_{WC} in cemented carbides resembles the well-accepted Hall–Petch relation for the hardness of single-phase polycrystalline materials (Hall, 1952; Petch, 1953) when the volume fraction of the carbide phase and highly equiaxed shape of WC crystals are kept unchanged. The Hall–Petch relation for single-phase materials is based on a well-defined physical model of dislocation pileups in grains against grain boundary and transfer of the stress through the grain boundary to another grain (Hall, 1952; Petch, 1953). Lee and Gurland (Gurland, 1979; Lee & Gurland, 1978) further observed that the hardness dependence on the volume fraction of the carbide phase V_{V} is below the rule of mixture of hardness values of each phase and that this dependence resembles the dependence of the contiguity G on the volume fraction V_{V} of the carbide phase in addition to the dependence on the mean linear intercepts of the phases (Figure 4).

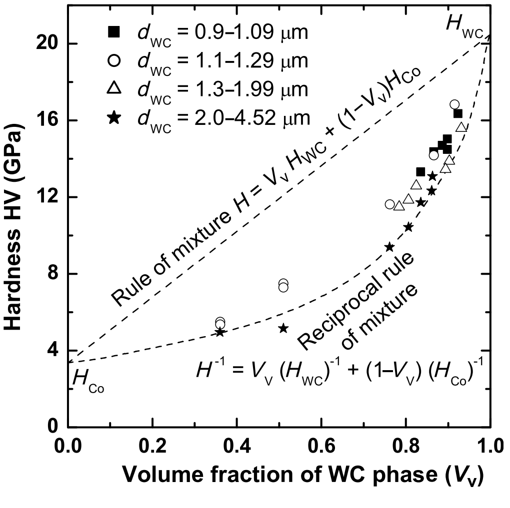

Figure 4 Vickers hardness HV versus carbide volume fraction V_{V} in WC–Co for a wide range of the mlicc $d_{\mathrm{WC}} = 0.9$–4.52 μm. Hardness dependence on the volume fraction of the carbide phase V_{V} is below the rule of mixture (straight line) but in most cases above the reciprocal rule of mixture (curve). Reproduced from Figure 2 in Lee and Gurland (1978) with permission from Elsevier.

---

[9] For more information on the coatings of hardmetals, see Chapters 1.16, Applications - Coating application to cutting tools; 1.17, Applications - Coatings by thermal spray; 1.18, Applications - Coatings by laser cladding.

These observations allowed the LG model to extend the Hall–Petch relation from single-phase polycrystalline materials to two-phase cemented carbides. Assuming that the carbide crystals deform mainly by the slip originated at the carbide–carbide contacts and that the binder deformation is transferred only through the continuous binder, the LG model calculates the hardness of cemented carbides as a superposition of mutually independent hardness values of the phases with relative contribution factors of the contiguous volume fraction $V_V \cdot G$ for the carbide phase and the continuous volume fraction $(1 - V_V \cdot G)$ for the binder phase (Gurland, 1979; Lee & Gurland, 1978).

$$H^{\mathrm{LG}} = \left(H^0_{\mathrm{WC}} + \frac{H^{\mathrm{HP}}_{\mathrm{WC}}}{\sqrt{d_{\mathrm{WC}}}}\right) \cdot V_V \cdot G + \left(H^0_{\mathrm{Binder}} + \frac{H^{\mathrm{HP}}_{\mathrm{Binder}}}{\sqrt{\lambda}}\right) \cdot (1 - V_V \cdot \mathrm{G}) \tag{4}$$

where H^0_{WC} and H^0_{Binder} are the bulk hardness, whereas $H^{\mathrm{HP}}_{\mathrm{WC}}$ and $H^{\mathrm{HP}}_{\mathrm{Binder}}$ are the Hall–Petch factors for the carbide phase of WC and Co-binder phase, respectively (Gurland, 1979; Lee & Gurland, 1978).

$$H^0_{\mathrm{WC}} = 13.54\ \mathrm{GPa}, \qquad \left(1382\ \mathrm{kg} \cdot \mathrm{mm}^{-2}\right) \tag{5}$$

$$H^{\mathrm{HP}}_{\mathrm{WC}} = 7.16\ \mathrm{GPa} \cdot \mu\mathrm{m}^{1/2}, \left(23.1\ \ \mathrm{kg} \cdot \mathrm{mm}^{-3/2}\right) \tag{6}$$

$$H^0_{\mathrm{Binder}} = 2.98\ \mathrm{GPa}, \qquad \left(304\ \mathrm{kg} \cdot \mathrm{mm}^{-2}\right) \tag{7}$$

$$H^{\mathrm{HP}}_{\mathrm{Binder}} = 3.94\ \mathrm{GPa} \cdot \mu\mathrm{m}^{1/2}, \left(12.7\ \mathrm{kg} \cdot \mathrm{mm}^{-3/2}\right) \tag{8}$$

These Hall–Petch parameters are experimentally measured on the binderless WC polycrystals and from the microhardness of the cobalt binder in WC–Co cemented carbides (Lee & Gurland, 1978). Use of the microhardness measurements in Eqns (7) and (8) for the binder phase is dictated by the much higher value of the hardness of the binder layers in the cemented carbides in comparison to the hardness of the pure cobalt with the hardness between 1.37 and 2.06 GPa (140–210 kg·mm^{-2}), or the dilute Co–W–C polycrystals of the same grain-layer size (Lee & Gurland, 1978). These excessive values of microhardness are attributed to the pileup of the dislocations in the binder layer against the much more rigid carbide crystal at the carbide–binder interface in cemented carbides, rather than against the cobalt–cobalt grain boundary with the same plastic properties as the current binder grain (Lee & Gurland, 1978). In other words, the interaction between the binder and carbide phases is implicitly included in the high experimental values of the Hall–Petch parameters of the binder phase in Eqns (7) and (8).

In general, the number of parameters in formula (4) can be reduced by substituting any microstructure parameter of λ, d_{WC}, G, or V_V from stereological relationship (1) into Eqn (4). Interesting enough, this substitution changes the balanced symmetry of the relationship (4) to emphasize the influence of only one of the two phases on the total hardness of the alloy, or to hide the dependence of the hardness on either the contiguity G or the volume fraction of the carbide phase V_V. Nevertheless, it is Eqn (4) that carries the most physical basis for the model, despite its thorough excessiveness on the parameters.

1.09.3.5.1.2 LG Model Applicability

Several experimental results support the LG model through measurement of all the stereological parameters of the microstructure (Fischmeister, 1983; Mari, Bolognini, & Feusier, 2003; Shin, Cao, Sargent, & Conrad, 1988; Sigl & Exner, 1989). Even more results are reported on finding the experimental correlations in the simplified form of Eqn (4) that can be reduced to the Hall-Petch-like relation versus the mlicc d_{WC} with the help of the stereological relationship (1) and Eqn (2) for each fixed volume fraction V_V of the carbide phase (Armstrong, 2011; Armstrong & Cazacu, 2006; Cha, Hong, Ha, & Kim, 2001; Jeong, Kim, & Doh, 2007; Kim, Jeong, Shon, Ko, & Doh, 2007; Lee, Cha, Kim, & Hong, 2006; Milman, Chugunova, Goncharuck, Luyckx, & Northrop, 1997; Milman, Yu, Luyckx, & Northrop, 1999; Roebuck, 1995; Roebuck & Almond, 1988).

$$H^{\mathrm{LG}}\big|_{V_V=\mathrm{const}} = H^0_{\mathrm{CC}}(V_V) + \frac{H^{\mathrm{HP}}_{\mathrm{CC}}(V_V)}{\sqrt{d_{\mathrm{WC}}}} \tag{9}$$

Where $H^0_{\mathrm{CC}}(V_V)$ and $H^{\mathrm{HP}}_{\mathrm{CC}}(V_V)$ are constants experimentally measured for each volume fraction V_V of the carbide phase in cemented carbides.

Furthermore, the LG model (4) can be easily reduced to the binderless cemented carbides that correspond to the polycrystalline WC alloys. Using stereological Eqn (1) and adjusting the carbide phase volume fraction V_V to 100% while simultaneously increasing the contiguity G to the highest value of 1 gives the regular Hall–Petch relation of a single-phase WC polycrystalline material (Hall, 1952; Petch, 1953).

$$H^{LG}\big|_{\text{Binderless}} = H_{WC}^{0} + \frac{H_{WC}^{HP}}{\sqrt{d_{WC}}} \tag{10}$$

Besides being tested on a large variety of hardmetals, the LG model, in its reduced Hall-Petch-like form (9), seems to be also applicable to other two-phase composite materials like FeAl-TiB$_2$ (Matsuura, Obara, & Kojima, 2009) and ZrC-Mo (Landwehr, Hilmas, Fahrenholtz, Talmy, & DiPietro, 2008). This ability to be generalized to other materials makes the LG model very attractive.

1.09.3.5.1.3 LG Model Assumptions

The LG-XA model (Gurland, 1979; Lee & Gurland, 1978) assumes that both the carbide and binder phases, as well as the whole alloy, have the same constraint factor, the ratio of hardness H to the yield stress σ_y, of about 3.

$$H \approx 3 \cdot \sigma_y \tag{11}$$

The LG model assumes that the in situ values of the hardness of the carbide and binder phases follow the Hall–Petch relation (Hall, 1952; Petch, 1953) independently from each other and therefore depend only on their own mean linear intercepts of d_{WC} and λ. In other words, in the light of Hall–Petch physics, the dislocations are assumed to neither cross nor transfer stress through the interphase boundaries between the carbide and binder phases but instead only interact with other grains of the same phase through the carbide–carbide boundaries in cemented carbides. Despite this rather questionable assumption, the LG model closely fits to the experimental data and provides a feasible explanation for all the observed correlations on cemented carbides with unchanged shape of carbide crystals. It might also be that if the dislocations penetrate the interphase boundaries, their effect is proportional and separable into one or two independent Hall–Petch terms—one for each phase or only one selected phase.

On the other hand, the application of the microhardness results of Eqns (7) and (8) also raises some questions about the ISE of Eqn (3) (**Figure 3**). ISE is not accounted for and therefore the values of the binder microhardness from Eqns (7) and (8) seem to overestimate the contribution of the hardness of the binder layers in the LG model. If ISE effect is subtracted from the microhardness of the binder phase, the third term $H'_{WC-Binder}$ should be added to the LG model to compensate for the decrease of the total hardness in Eqn (4).

$$H^{LG*} = \left(H_{WC}^{0} + \frac{H_{WC}^{HP}}{\sqrt{d_{WC}}}\right) \cdot V_V \cdot G + \left(H_{Binder}^{0^*} + \frac{H_{Binder}^{HP^*}}{\sqrt{\lambda}}\right) \cdot (1 - V_V \cdot G) + H'_{WC-Binder} \tag{12}$$

where $H_{Binder}^{0^*}$ and $H_{Binder}^{HP^*}$ are the actual bulk and Hall–Petch factors for the binder phase, respectively, that do not include ISE. The third term $H'_{WC-Binder}$ could then be describing the seemingly lacking interaction of the dislocations between the carbide crystals and the binder layers in cemented carbides.

The LG model assumes an isotropic, highly equiaxed and unchanged shape of WC crystals. The LG model does not take into account the solid solution of carbide in the binder phase, but assumes that the Hall–Petch constants reflect the mechanical properties of the binder. It also assumes that the chemical composition and structure of the constituent phases is not changing with the volume fraction. This seems to be pretty much the case for WC–Co cemented carbides, but it might not be a valid assumption for other composite materials when carbide grains can exhibit core-rim or chemical gradient structure and/or binder material can be dissolved in the harder phase. The LG model is developed for two-phase nonporous cemented carbides. It is unclear how it can be extended to composite materials of three or more phases.

1.09.3.5.1.4 LG Model Limitations

The LG model follows Hall–Petch pattern and predicts an infinite hardness when the mlicc d_{WC} decreases to zero size. It is well known that the Hall–Petch relation is limited to the sizes larger than nanoscale and that the hardness drops for nano-sized grains due to the change of the mechanisms of plastic deformation (Arzt, 1998; Jia, Fischer, & Gallois, 1998; Milman, 2008; Richter & Ruthendorf, 1999). Therefore, the LG model cannot be applied to the nanoscale cemented carbides. The LG model also does not explain the microhardness dependencies of hardmetals.

Nevertheless, the LG model has the least number of assumptions, has the most physical basis and relies on the well-established Hall–Petch relation for the hardness of polycrystals. This is the only model that takes the contiguity *G* of WC crystals into account. On the other hand, it uses the largest number of parameters of the microstructure, except for the shape of the carbide crystals.

1.09.3.5.2 LG Model Enhancement by Shatov, Ponomarev & Firstov (LG-SPF) for the Shape of WC

Shatov, Ponomarev and Firstov (2009) found that the hardness of cemented carbides increases when the shape of WC crystals become a flatter triangular prism, whereas the LG model (4) expects it to decrease due to the decrease of the contiguity *G*. The increase of the relative surface area of the harder basal facets on WC crystals cannot explain the increase of the hardness for alloys with flatter WC crystals, because the hardness of the two and more contacting WC crystals is mainly determined by the softest, rather than by the hardest, facet surface in the contact and by the relative area of the contact. The most common carbide–carbide contact type is between the softer prismatic and the harder basal facets of WC (Shatov, Ponomarev, Firstov, & Warren, 2006). The contiguity *G* of the WC crystals that measures the relative area of the contact decreases for the flatter WC crystals (Shatov, Ponomarev, Firstov, & Warren, 2006) that according to the LG model can only decrease the total hardness of the alloy.

The LG-Shatov, Ponomarev & Firstov (SPF) model (Shatov, Ponomarev, & Firstov, 2009) enhances the LG model and explains the increase of the hardness caused by the change of the WC shape to a flatter triangular prism. The pileups of dislocations in WC can only touch the basal facets of highly anisotropic WC crystals when the shape becomes flatter due to the very limited set of the slip planes with orientation $\{10\bar{1}0\}$ that is parallel to the prismatic facets on WC crystals (Figure 5). Therefore, the Hall–Petch hardening of the carbide phase is determined by the height h_{WC} of WC crystals, that is, the distance between the basal facets of the triangular prism, rather than by the mlicc d_{WC}, as it is stated in the LG model (4).

$$\Delta H_{\mathrm{WC}}^{\mathrm{HP}} \propto \frac{1}{\sqrt{h_{\mathrm{WC}}}} \tag{13}$$

For a similar reason, the Hall–Petch hardening of the binder phase is determined by the mean distance between WC crystals $\lambda_{\perp}$, rather than by the mlibp λ, as it is stated in the LG model (4).

$$\Delta H_{\mathrm{Binder}}^{\mathrm{HP}} \propto \frac{1}{\sqrt{\lambda_{\perp}}} \tag{14}$$

Computer simulation shows that the height h_{WC} of the triangular prism is proportional to the product of the mlicc d_{WC} and the shape equiaxiality P_{WC} of WC crystals (Shatov, Ponomarev, & Firstov, 2009).

$$h_{\mathrm{WC}} \propto P_{\mathrm{WC}} \cdot d_{\mathrm{WC}} \tag{15}$$

where the shape equiaxiality P_{WC} is defined and measured as a mean ratio of the minimal $D_{\min}$ to maximal $D_{\max}$ chords through the center of mass of cross-section of WC crystals (Shatov, Firstov, & Shatova, 1998).

$$P_{\mathrm{WC}} = \langle D_{\min}/D_{\max} \rangle|_{\mathrm{WC\ sections}} \tag{16}$$

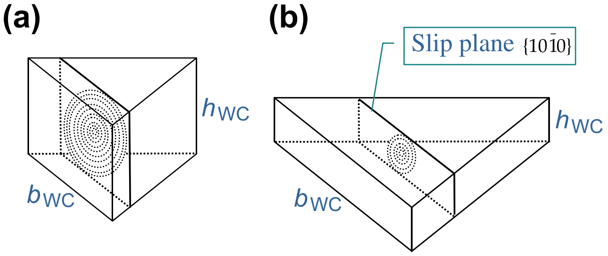

Figure 5 Change of the shape from the highly equiaxed (a) to flatter triangular prism (b) reduces the number of Frank–Read dislocation loops in the pileup along the slip plane $\{10\bar{1}0\}$ on WC crystals due to decrease of the prism height h_{WC}. Reproduced from Figure 9 in Shatov, Ponomarev, & Firstov, (2009) with permission from Elsevier.

The flatter shape of WC crystals corresponds to a lower value of the shape equiaxiality P_{WC}, whereas the ideal sphere has the highest value of $P_{\mathrm{WC}} = 1$ (Shatov, Firstov, & Shatova, 1998).

Similarly, the mean distance between the carbide crystals $\lambda_{\perp}$ can be estimated as being proportional to the product of the mlibp λ and the shape equiaxiality P_{WC} (Shatov, Ponomarev, & Firstov, 2009).

$$\lambda_{\perp} \propto P_{\mathrm{WC}} \cdot \lambda \tag{17}$$

The proportionalities (15) and (17) allow the LG-SPF model to enhance the LG model by the multiplication of the mean linear intercepts with the normalized shape equiaxiality $P_{\mathrm{WC}}/P_{\mathrm{WC}}^{0}$, where P_{WC}^{0} is the initial value of the shape equiaxiality of WC crystals that corresponds to the regular shape of WC crystals in cemented carbides (Shatov, Ponomarev, & Firstov, 2009).

$$H^{\mathrm{LG-SPF}} = \left(H_{\mathrm{WC}}^{0} + \frac{H_{\mathrm{WC}}^{\mathrm{HP}}}{\sqrt{\frac{P_{\mathrm{WC}}}{P_{\mathrm{WC}}^{0}} \cdot d_{\mathrm{WC}}}} \right) \cdot V_{\mathrm{V}} \cdot G + \left(H_{\mathrm{Binder}}^{0} + \frac{H_{\mathrm{Binder}}^{\mathrm{HP}}}{\sqrt{\frac{P_{\mathrm{WC}}}{P_{\mathrm{WC}}^{0}} \cdot \lambda}} \right) \cdot (1 - V_{\mathrm{V}} \cdot G) \tag{18}$$

Decrease of the shape equiaxiality P_{WC} increases the Hall–Petch hardening of both the carbide and the binder phases causing an increase of the hardness for the alloy. The LG-SPF model (18) can be easily reduced to the pure LG model (4) when the shape of WC crystals is not changed and the shape equiaxiality is equal to its initial value, i.e. $P_{\mathrm{WC}} = P_{\mathrm{WC}}^{0}$.

1.09.3.5.3 LG Model Adjustment by Xu & Agren (LG-XA)

The LG-XA model (Xu & Agren, 2004) slightly readjusts the LG model based on the idea that the constraint factor, the ratio of hardness H to the yield stress σ_{y}, differs for the carbide and binder phases and deviates from the constraint factor of 3 that is assumed by the LG model in Eqn (11). The LG-XA model calculates the constraint factors of WC–Co cemented carbides and the WC particles based on nanoindentation experiments and finite element simulations of indentation on WC–Co cemented carbides. This allows the LG-XA model to adjust the LG model by multiplying the terms in Eqn (4) with the factors of 1.205 for WC and of 0.9 for Co binder phases in cemented carbides.

$$H^{\mathrm{LG-XA}} = 1.205 \cdot \left(H_{\mathrm{WC}}^{0} + \frac{H_{\mathrm{WC}}^{\mathrm{HP}}}{\sqrt{d_{\mathrm{WC}}}} \right) \cdot V_{\mathrm{V}} \cdot G + 0.9 \cdot \left(H_{\mathrm{Binder}}^{0} + \frac{H_{\mathrm{Binder}}^{\mathrm{HP}}}{\sqrt{\lambda}} \right) \cdot (1 - V_{\mathrm{V}} \cdot G) \tag{19}$$

Unfortunately, reduction of Eqn (19) to the binderless cemented carbides similar to Eqn (10) produces a 20.5% excess over the hardness of the polycrystalline WC due to the adjustment factor 1.205.

$$H^{\mathrm{LG-XA}}\Big|_{\mathrm{Binderless}} = 1.205 \cdot \left(H_{\mathrm{WC}}^{0} + \frac{H_{\mathrm{WC}}^{\mathrm{HP}}}{\sqrt{d_{\mathrm{WC}}}} \right) \tag{20}$$

This is in contrast to the LG model prediction of pure Hall–Petch relation for the binderless cemented carbides in Eqn (10). The LG-XA model should be readjusted to eliminate this controversy. For instance, LG-XA adjustment could be hidden as a reevaluation of the Hall–Petch constants in Eqn (4) rather than being kept as separate factors in the LG-XA model. Alternatively, the dependence of the adjustment factors on the volume fraction of the carbide phase V_{V} could be introduced and studied.

1.09.3.5.4 LG Model Extension by Lee, Cha, Kim & Hong (LG-LCKH) to 3-Phase Hardmetals

The LG-LCKH model (Lee et al., 2006) makes a first attempt to extend the LG model to three-phase WC–TiC–Co hardmetals. The LG-LCKH model breaks the dependence of hardness into two regions depending on the WC/TiC grain size ratio.

In the region of relatively small WC grains that are about half the size of TiC/(Ti,W)C grains, the LG-LCKH model suggests using the rule of mixture between the regular WC–Co cemented carbide and the reinforcing TiC/(Ti,W)C phase for three-phase WC-TiC-10wt% Co cemented carbides.

$$H_{\mathrm{WC-TiC-Co}}^{\mathrm{LG-LCKH}} = H_{\mathrm{WC-Co}} \cdot \left(1 - V_{\mathrm{V}}^{\mathrm{TiC}}\right) + H_{\mathrm{TiC}} \cdot V_{\mathrm{V}}^{\mathrm{TiC}} \tag{21}$$

where $\mathrm{H}_{\mathrm{WC\text{-}Co}}$ is the hardness of WC-10wt% Co cemented carbide according to the reduced LG model (9), H_{TiC} is the hardness of TiC/(Ti,W)C, $V_{\mathrm{V}}^{\mathrm{TiC}}$ is the volume fraction of TiC/(Ti,W)C phase (Lee, Cha, Kim, & Hong, 2006). It is not clear what value is used for H_{TiC} and whether it depends on the grain size and other microstructure parameters of the alloy in the LG-LCKH model (Lee, Cha, Kim, & Hong, 2006).

In the other region, where the WC grains become relatively bigger and comparable in size to core-rim TiC/(Ti,W)C grains, the TiC/(Ti,W)C phase cannot be considered any longer as just a reinforcing phase for the two-phase WC–Co cemented carbide and the contribution of both carbide phases should be taken into account simultaneously. The LG-LCKH model suggests modifying the LG model in a few steps. In the first step, the LG model is reduced to the simplified version of Eqn (9) that is calculated for a fixed volume fraction V_{V} of WC phase and therefore hides both the dependence of the Hall–Petch factors on V_{V} and the dependence of the contiguity G on V_{V} as is shown in Eqn (2). In the second step, the LG-LCKH model reintroduces the dependence on the volume fraction V_{V} of WC and $V_{\mathrm{V}}^{\mathrm{TiC}}$ of Ti/(Ti,W)C phases with a double mixture rule. Both Hall–Petch factors are mixed between WC and TiC/(Ti,W)C separately.

$$H^{0} = H_{\mathrm{WC-Co}}^{0} \cdot V_{\mathrm{V}} + H_{\mathrm{TiC}}^{0} \cdot V_{\mathrm{V}}^{\mathrm{TiC}} \tag{22}$$

$$H^{\mathrm{HP}} = H_{\mathrm{WC-Co}}^{\mathrm{HP}} \cdot V_{\mathrm{V}} + H_{\mathrm{TiC}}^{\mathrm{HP}} \cdot V_{\mathrm{V}}^{\mathrm{TiC}} \tag{23}$$

Surprisingly, even the grain size of the carbide phases is also calculated as a mix without any explanation and no apparent reason for such a mix between the mean linear intercept of WC d_{WC} and Ti/(Ti,W)C d_{TiC} crystals.

$$d = V_{\mathrm{V}} \cdot d_{\mathrm{WC}} + V_{\mathrm{V}}^{\mathrm{TiC}} \cdot d_{\mathrm{TiC}} \tag{24}$$

Application of these double mixture rules allows the LG-LCKH model to arrive at the following relation for the hardness of the three-phase alloy:

$$H_{\mathrm{WC-TiC-Co}}^{\mathrm{LG-LCKH}} = \left(H_{\mathrm{WC-Co}}^{0} \cdot V_{\mathrm{V}} + H_{\mathrm{TiC}}^{0} \cdot V_{\mathrm{V}}^{\mathrm{TiC}}\right) + \frac{H_{\mathrm{WC-Co}}^{\mathrm{HP}} \cdot V_{\mathrm{V}} + H_{\mathrm{TiC}}^{\mathrm{HP}} \cdot V_{\mathrm{V}}^{\mathrm{TiC}}}{\sqrt{V_{\mathrm{V}} \cdot d_{\mathrm{WC}} + V_{\mathrm{V}}^{\mathrm{TiC}} \cdot d_{\mathrm{TiC}}}} \tag{25}$$

The LG-LCKH model for three phases does not reduce to the pure LG model for two phases. Setting the volume fraction of the TiC phase $V_{\mathrm{V}}^{\mathrm{TiC}}$ to zero produces an unexpected dependency on the volume fraction V_{V} of WC phase.

$$H_{\mathrm{WC-Co}}^{\mathrm{LG-LCKH}} = \left(H_{\mathrm{WC-Co}}^{0} + \frac{H_{\mathrm{WC-Co}}^{\mathrm{HP}}}{\sqrt{V_{\mathrm{V}} \cdot d_{\mathrm{WC}}}}\right) \cdot V_{\mathrm{V}} \tag{26}$$

All the steps in the model development seem to be rather questionable. First, the Hall–Petch factors $H_{\mathrm{WC-Co}}^{0}$ and $H_{\mathrm{WC-Co}}^{\mathrm{HP}}$ in Eqn (22) are not constants and already depend on the volume fraction of the carbide phase $H_{\mathrm{WC-Co}}^{0}(V_{\mathrm{V}})$ and $H_{\mathrm{WC-Co}}^{\mathrm{HP}}(V_{\mathrm{V}})$ as it is shown in Eqn (9). Second, it seems counterintuitive to mix all the terms, the numerator, and the denominator separately instead of breaking the phases into separate terms first and then mixing them with some flavor of contiguous volume factors as it is done in the LG model (4).

The LG-LCKH model does not use the contiguity of carbide crystals (Lee, Cha, Kim, & Hong, 2006). Nevertheless, it seems that the carbide–carbide contacts should be considered in the manner of the LG model (4). Introduction of the second carbide phase with core-rim structure requires the consideration of a new variety of carbide–carbide contacts like WC/WC, WC/(Ti,W)C, and (Ti,W)C/(Ti,W)C. In addition, the effect of the core-rim gradient of the structure and microhardness of TiC/(Ti,W)C grains should be taken into account. It is not clear how the contiguous volume fraction introduced by the LG model in Eqn (4) can be extended to the three-phase materials. Therefore, the LG-LCKH model should not be used as is and more analysis and research is appropriate for the three-phase cemented carbides and composites.

1.09.3.5.5 Model of Makhele-Lekala, Luyckx & Nabarro (MLN)

1.09.3.5.5.1 MLN Model Definition

Makhele-Lekala et al. (Makhele-Lekala, Luyckx, & Nabarro, 2001) found that the hardness linearly correlates with $(d_{\mathrm{WC}})^{0.251}/\lambda^{0.497}$ in a wide range of the volume fractions V_{V} and the mean linear intercepts of phases on WC–Co cemented carbides.

$$H^{\mathrm{MLN}}_{\mathrm{experiment}} = H^0 + B \cdot d_{\mathrm{WC}}^{0.251}/\lambda^{0.497} \tag{27}$$

where $H^0 = 1.7705$ GPa and $B = 1.4015\ \mathrm{GPa \cdot mm^{-0.246}}$ are the experimental constants for WC–Co.

This purely empirical correlation (27) allowed Makhele-Lekala et al. to propose a semiempirical Makhele-Lekala, Luyckx & Nabarro (MLN) model (Makhele-Lekala, Luyckx, & Nabarro, 2001) that is based on the physical approach of mechanical interaction between the binder and carbide phases in contrast to the LG model (4) where no dependency between hardness values of the phases is assumed, even though the phases are interpenetrating each other and there exists a possibility of dislocation transfer from one phase to the other.

The MLN model relates the hardness to d_{WC} and λ without the explicit inclusion of the contiguity G and the volume fraction V_{V} of the carbide phase. The plastic deformation is assumed to start in the binder phase, while the carbide–carbide contacts play the role of an elastic obstacle for the propagation of dislocation pileups from one binder area to another. The MLN model assumes that the plastic deformation of the binder phase is limited to the slip planes that connect the carbide–carbide contacts to each other. The carbide–carbide contact size is assumed to be significantly less than the mean linear intercept of the phases. Therefore, the shear stress from dislocations of the binder phase is assumed to be concentrated at the carbide–carbide contacts.

Furthermore, the MLN model assumes the stress on the other side of the carbide–carbide contact to be inversely proportional to the square root of the contact size. The size of the WC/WC contacts γ is further believed to be proportional to the square root of the mlicc by assumed similarity to the neck size between isotropic cubic crystals with nearly spherical shape in single-phase porous polycrystalline materials (German, 1996).

$$\gamma \propto \sqrt{d_{\mathrm{WC}}} \tag{28}$$

The MLN model postulates that the whole alloy yields only when the stress on the WC/WC contacts from the dislocation pileups in the binder reaches the flow stress of WC. The model produces the following relationship for the hardness:

$$H^{\mathrm{MLN}} = \alpha \cdot \tau_{\gamma}^{\mathrm{WC}} \cdot \left[k \cdot \left(\frac{\lambda}{2 \cdot \sqrt{d_{\mathrm{WC}}}} \right)^{1/2} + 1 \right]^{-1} - A \tag{29}$$

where $\tau_{\gamma}^{\mathrm{WC}} = 6.9$ GPa is the yield stress of WC, $\alpha = 5.9$ is the empirically determined ratio between the hardness and the yield stress of WC that lies in the range between 3 and 5.9 for the cemented carbides (Gurland, 1979; Lee & Gurland, 1978; Makhele-Lekala, Luyckx, & Nabarro, 2001), $k = 22.3\ \mathrm{mm}^{-1/4}$ and $A = 1.3$ GPa are the empirical constants (Makhele-Lekala, Luyckx, & Nabarro, 2001).

Stereological relation (1) allows rewriting the MLN model versus the carbide phase parameters without mlibp λ.

$$H^{\mathrm{MLN}} = \alpha \cdot \tau_{\gamma}^{\mathrm{WC}} \cdot \left[k \cdot \left(\frac{\sqrt{d_{\mathrm{WC}}}}{2} \cdot \frac{1 - V_{\mathrm{V}}}{V_{\mathrm{V}} \cdot (1 - G)} \right)^{1/2} + 1 \right]^{-1} - A \tag{30}$$

The MLN model (30) predicts an increase of the hardness when d_{WC} decreases for the fixed values of the volume fraction V_{V} and the contiguity G of WC crystals. Nevertheless, in contrast to the LG model (4), the MLN hardness (30) does not grow infinitely when the size of the carbide crystals d_{WC} decreases down to nanosizes and approaches zero. Instead, the MLN hardness (30) is limited by some constant value related to the yield stress of WC substance. Furthermore, the MLN model also expects the hardness to reach the same constant highest value for the binderless cemented carbides when λ approaches zero in Eqn (29).

$$H^{\mathrm{MLN}}\Big|_{d_{\mathrm{WC}} \to 0} = H^{\mathrm{MLN}}\Big|_{\mathrm{Binderless}} = \alpha \cdot \tau_{\gamma}^{\mathrm{WC}} - A = 5.9 \cdot \tau_{\gamma}^{\mathrm{WC}} - 1.3 \approx 39.7\ \mathrm{GPa} \tag{31}$$

1.09.3.5.5.2 MLN Model Limitations

The MLN model does not expect the hardness of the binderless cemented carbides in Eqn (31) to depend on the mlicc d_{WC} in contrast to the well-accepted Hall–Petch relation for polycrystalline materials and as it is predicted by the LG model (10). The MLN model is not verified on other hardmetals.

The assumptions made in the MLN model redirect the accent from the plastic deformation of both the carbide and the binder phases, as it is done in the LG model, to the plastic deformation in the binder phase alone as the initial and main source of the plastic deformation in the alloy. The MLN model expects the yield of WC crystals and the carbide–carbide contacts to occur only under an excessive stress from the dislocations in the binder phase, rather than by the dislocations inside WC phase. It is well known that WC crystals exhibit significant plastic deformation when tested for hardness (Exner, 1979; Luyckx, 1989; Roebuck & Almond, 1988; Zhang & Fang, 2008). Perhaps, that is why the MLN model needs to double the multiplication factor α of the yield stress from the typical value of 3 to the highest possible value of 5.9 to fit to the experimental values of hardness.

The assumption that the carbide–carbide contact size is proportional to the square root of the crystal size according to Eqn (28) seems to be rather questionable for WC-based cemented carbides. The contiguity G of WC crystals is a measure of the relative carbide–carbide contact area. It is well known that the contiguity G mainly depends on the volume fraction of the carbide phase V_{V} (see Eqn (2)) and does not depend on the carbide crystals size when the shape of the carbide crystals is kept unchanged (Exner, 1979; Exner & Fischmeister, 1966; Lee & Gurland, 1978; Warren & Waldron, 1972). It would be more natural to expect the ratio of the size of the neck (contact) γ to the mlicc d_{WC} to depend on the contiguity G and therefore on the volume fraction of the carbide phase V_{V}, rather than to be determined by the mlicc d_{WC} alone, as stated in relation (28). In this case, the size of the neck (contact) γ might be proportional to d_{WC} at the constant volume fraction V_{V} and the contiguity G of the carbide phase, rather than being proportional to the square root of the mlicc $(d_{\mathrm{WC}})^{1/2}$ regardless of V_{V} and G.

1.09.3.5.6 Models Based on Noncontiguous Mean Linear Intercept of the Binder Phase λ'

1.09.3.5.6.1 Model of Laugier for the Deformation of the Binder Phase Only

Laugier (1985) proposed a model for hardness under the assumption that it is controlled by the deformation of the binder phase only. Laugier also ignores the contiguity G of carbide crystals and assumes the absence of the carbide crystal contacts in the alloy. This model is based on the purely empirical observation that the hardness is proportional to $(\lambda')^{-1/5}$.

$$H^{\mathrm{Laugier}} = H^{0} + k \cdot \mu_{\mathrm{B}} \cdot \left(\frac{b}{\lambda'}\right)^{0.2} \tag{32}$$

where H^0 and k are empirical constants; μ_{B} is the shear modulus and b is the Burgers vector of the binder phase, whereas λ' relates to the mlibp λ and the contiguity G of the carbide crystals through the following relation that excludes the contiguity from the stereological Eqn (1).

$$\lambda' = \lambda \cdot (1 - G) = d_{\mathrm{WC}} \cdot \frac{1 - V_{\mathrm{V}}}{V_{\mathrm{V}}} \tag{33}$$

The Laugier model predicts an increase in the hardness with the decrease in λ'. It also predicts an infinite value of the hardness both for the binderless cemented carbides with λ' approaching zero value and for the cemented carbides with the mlicc d_{WC} decreased to nanosizes and approaching zero value according to Eqn (33). The Laugier model was not verified on other materials and explains a limited set of observations.

1.09.3.5.6.2 Model of Engqvist, Jacobson & Axen (EJA)

The EJA model (Engqvist, Jacobson, & Axen, 2002) makes an attempt to limit the Hall-Petch-like hardness at nanoscale and for binderless cemented carbides. The authors came up with a rather complicated model based on the assumption that the hardness of the cemented carbides is mainly controlled by the plastic deformation of the binder phase but is limited by the yield stress of the polycrystalline carbide phase. The EJA model states that the noncontiguous mlibp λ' (Eqn (33)) should be used for characterizing the size of the binder phase in cemented carbides because the binder phase is always present at carbide–carbide contacts (Engqvist et al., 2002). The EJA model empirically approximates the hardening of the binder phase due to its size constraint by an arbitrarily chosen exponent function of $\exp(-\lambda'/k)$. The hardening effect of the binder phase is assumed to be limited by the Hall-Petch-type hardness of the polycrystalline WC. Furthermore, the Hall–Petch relation is modified by adding an empirical size shift of $c = 2.1$ μm to the mlicc d_{WC} in attempt to limit the hardness of polycrystalline WC at the nanoscale.

$$H = \left[\left(H_{\mathrm{WC}}^{0} + \frac{H_{\mathrm{WC}}^{\mathrm{HP}}}{\sqrt{c + d_{\mathrm{WC}}}}\right) - H_{\mathrm{Binder}}^{0}\right] \cdot \exp(-\lambda'/k) + H_{\mathrm{Binder}}^{0} \tag{34}$$

where H_{WC}^{0} and $H_{\mathrm{WC}}^{\mathrm{HP}}$ are the empirically modified bulk hardness and Hall–Petch factor of the carbide phase, respectively; H_{Binder}^{0} is the hardness of the bulk binder phase; and $k = 0.35$ μm is an empirical constant.

The EJA model predicts an increase of the hardness when λ' decreases regardless of the volume fraction of the phases. The EJA model gives a slightly worse fit to the experimental data in comparison to the LG model (4) (Engqvist, Jacobson, & Axen, 2002). The exponential hardening and shifted Hall–Petch relations lack physical reasoning.

1.09.3.5.6.3 Bimodal Distribution of the Binder Phase for Modeling the Hardness

Usage of the noncontiguous mlibp $\lambda' = \lambda \cdot (1 - G)$ (Eqn (33)) in the Laugier and the EJA models is questionable. The binder phase is distributed in two modes that differ both in size and properties. One is the bulk binder layers; another is the binder in the form of submonolayer found at the carbide–carbide contacts (Andren, 2001a; Christensen & Wahnstrom, 2003, 2004; Henjered, Hellsing, Andren, & Norden, 1986; Ostberg, Buss, Christensen, et al., 2006; Vicens, Benjdir, Nouet, Dubon, & Laval, 1994; Weidow & Andren, 2010, 2011). These two modes of the binder phase should be considered separately as their properties are expected to differ dramatically (Engqvist et al., 2002; Exner, 1979; Rowcliffe, Jayaram, Hibbs, & Sinclair, 1988; Sigl & Fischmeister, 1988). Presence of the binder submonolayer at carbide–carbide contacts makes these contacts stronger (Christensen & Wahnstrom, 2003, 2004, 2006; Ostberg, Buss, Christensen, et al., 2006; Weidow & Andren, 2010, 2011). Therefore, the submonolayer of the binder should be considered either as the third constituent phase in the alloy or as a part of the carbide–carbide contacts, rather than being intermixed with the bulk binder phase by using the value of λ'.

The value of the contiguity G helps to separate the bulk binder layers from the submonolayers of the binder at the carbide–carbide boundaries. The properties of the bulk binder layers are related to the average size of the bulk mode of the binder phase that is measured by the regular mlibp λ calculated on the basis of the contiguity G according to the stereological relationship (1). The properties of the submonolayer mode of the binder are related directly to the carbide–carbide contacts and are measured by the contiguity G itself. In this light, measuring the average of the bimodal distribution of the binder phase just by ignoring the contiguity G brings a value of λ' (see Eqn (33)) that does not reflect the size of any of the binder modes and therefore cannot represent either of the binder modes.

It would seem only natural to use λ for the bulk binder phase properties and the contiguity G for the submonolayer regions of the binder in all the models that claim the hardness to be controlled by the binder phase only. This is especially true when the hardness is considered to be primarily related to the size of the binder phase. Using an average of two very different modes of the binder phase in these relationships defeats the whole purpose of relating the hardness to the binder phase deformation.

1.09.3.5.7 Empirical Models

Gille, Bredthauer, Gries, Mende and Heinrich (2000) used an empirical polynomial approximation of hardness versus the volume fraction of the binder phase $(1 - V_{\mathrm{V}})$ and the mlicc d_{WC}.

$$H^{\mathrm{GBGMH}} = A \cdot \left(1 - k_1 \cdot (1 - V_{\mathrm{V}}) + k_2 \cdot (1 - V_{\mathrm{V}})^2\right) \cdot (d_{\mathrm{WC}})^{-m} \tag{35}$$

where A, k_1, k_2, and $m = 0.194$ are empirical constants. This empirical relationship is quite similar to the model of Laugier (Laugier, 1985) expressed by the relationship (32) with the difference that the binder phase size λ' (see Eqn (33)) is substituted with the interrelated mlicc d_{WC} (see Eqn (1)) and added dependence on the volume fraction V_{V}.

Roebuck (Roebuck, 2006) questions the Hall–Petch relation both at the nanoscale and at rather high values of d_{WC} and points out that the empirical logarithmic approximation (Fischmeister & Exner, 1966; Gurland &

Bardzil, 1955; Richter & Ruthendorf, 1999; Roebuck, 2006) somewhat better fits the experimental data of WC-6wt% Co and WC-10wt% Co alloys on the whole range of the carbide crystal sizes.

$$H^{\text{Roebuck}} = H_0(V_V) - H_1(V_V) \cdot \log_{10}(d_{WC}) \tag{36}$$

where $H_0(V_V)$ and $H_1(V_V)$ are empirically determined values for each volume fraction of the carbide phase V_V.

As an alternative, a second-order polynomial fit that adjusts the Hall–Petch relationship at lower sizes is also suggested by Gille et al. (Gille, Szesny, & Leitner, 1999) and Roebuck (Roebuck, 2006) to accommodate the decreasing value of the hardness at nanoscale.

$$H^{\text{GSL-R}} = H_0(V_V) + H_1(V_V) \cdot d_{WC}^{-1/2} - H_2(V_V) \cdot d_{WC} \tag{37}$$

where $H_0(V_V)$, $H_1(V_V)$, and $H_2(V_V)$ are empirically determined values for each volume fraction of the carbide phase V_V.

At nanoscale, a change of the plastic deformation mechanism invalidates the Hall–Petch relationship (Arzt, 1998; Fang, Wang, Ryu, Hwang, & Sohn, 2009; Jia, Fischer, & Gallois, 1998; Milman, 2008; Richter & Ruthendorf, 1999). This invalidation implies the need for a different correlation with microstructure parameters. In this light, the attempt to find an empirical approximation that would fit through all the ranges of the carbide sizes with changing mechanism of the deformation seems to promise little benefit for understanding the hardness.

All the empirical models that are based on the pure approximation against an arbitrary chosen set of microstructure parameters lack physical reasoning behind them. In other words, having just a pure approximation does not help in understanding of the mechanism of the hardness change. Usually, it is impossible to adjust or enhance these models for the change of the parameters that had been fixed at the moment of the model creation. Nevertheless, the empirical correlations provide an experimental relation that maps the general direction for the property change and might be the first step in guessing of the mechanism for the property dependencies.

1.09.3.5.8 Continuum Deformation Model of Cha, Lee, Ryu & Hong (CLRH)

The CLRH model (Cha, Lee, Ryu, & Hong, 2008) makes an attempt to analytically calculate the hardness on the basis of the continuum elastic deformation of the binder phase with some critical stress to start the plastic deformation and avoid the infinite hardness at the nanoscale. Many assumptions and simplifications about the microstructure and deformation are made to overcome the mathematical complexity of the task. The presence of carbide–carbide contacts is ignored. The stress transfer from WC crystal to the binder phase is calculated for a single center point load on a flat WC/Co interface.

The CLRH model assumes a shallow penetration of the shear stress into the binder up to only some critical depth of λ'' from the WC/Co interface. The critical depth λ'' is assumed to be less than the mlibp λ. Further assuming that the plastic deformation of the binder phase starts when the shear stress reaches a critical value on the border between some narrow (thinner than λ'') and wide (thicker than λ'') regions of the binder phase at the distance of $((\lambda'')^2 + (d_{WC})^2)^{1/2}$ from the single point of load at the center of the WC/Co interface, the CLRH model arrives at the following expression for the hardness of cemented carbides:

$$H^{\text{CLRH}} = 2 \cdot \pi \cdot H_{0,\text{Co}} \cdot \left[\frac{\lambda''}{\sqrt{(\lambda'')^2 + d_{WC}^2}} + (1 - 2 \cdot \nu) \cdot \ln\left(1 + \frac{\sqrt{(\lambda'')^2 + d_{WC}^2}}{\lambda''}\right) \right]^{-1} \tag{38}$$

where $H_{0,\text{Co}}$ is the hardness and ν is the Poisson's ratio of cobalt. The values for $\lambda'' = 0.06$ μm and $H_{0,\text{Co}} = 291.7$ are empirically determined by fitting the formula (38) to the experimental dependence of the hardness of WC–Co cemented carbides on d_{WC} (Cha, Lee, Ryu, & Hong, 2008).

The CLRH model (38) introduces a steep elastic shear stress gradient in the binder phase of cemented carbides with characteristic depth $\lambda'' = 0.06$ μm from the carbide–binder interface. On one hand, the CLRH model limits the plastic deformation of the binder to this narrow region and does not expect the propagation of the plastic deformation throughout all the binder phase up to the next WC crystal by dislocation sliding. On the other hand, it allows the different regions of the binder to yield against each other that seems as a rather controversial assumption. Furthermore, the CLRH model does not take into account the stress distribution and the possible plastic deformation in the carbide phase but instead assumes that the stress from the carbide crystals is concentrated at a single point at the carbide–binder interface.

The calculation of the CLRH model seems to be closely tailored to the artificial assumptions of the model on the microstructure, single point stress application at the carbide–binder interface, continuum gradient stress and deformation distribution in the binder phase, as well as to the plastic deformation criteria. Emphasizing on the elastic shear stress gradient in the binder phase at very small distances of $\lambda'' = 0.06$ μm but not considering the plastic deformation process and hardening of the binder phase seems to be unreasonable for the model of hardness when the deformation of the whole alloy reaches several percent and all the carbide crystals and binder layers undergo significant plastic deformation under indenter. Nevertheless, the general direction of calculating the stresses and deformation by the continuum deformation approach might still bring some progress in understanding the deformation mechanism of the hardmetals, if more reasonable assumptions and more complex stress distributions could be calculated in the future.

1.09.3.6 Outlook

The physical reasoning for the reverse Hall–Petch relation for nanograined hardmetals constitutes the first biggest challenge. The nanoproblem starts with the new mechanisms of plastic deformation by the grain–boundary sliding and is further complicated by the need to take into account the effect of variety of doping carbides and porosity of the material. In this light, modeling of the hardness of three-phase composite materials and doped cemented carbides gains importance and already starts attracting some attention of researchers.

Can the LG model be extended to hardmetals with three and more phases, as well as to the alloys with AGG by introducing the contiguous volume fractions of two and more carbide phases? The carbide–carbide contacts would need to be classified by different carbides. It should also be considered whether the contiguous substructure is formed for each specific carbide phase or the extra carbide plays the role of disperse hardening phase inside the two-phase cemented carbide similar to the suggestion of the LG-LCKH model (Lee et al., 2006). The main assumption of the LG model of independence of the hardness terms might also need to be reevaluated for the carbide phases in these multiphase materials.

For example, the hardness of multiphase materials like $WC–Co + VC + Cr_3C_2$ and WC–TiC–Co that consist of main carbide phase α and additional carbide phase β might look like this.

$$\begin{aligned} H = {} & H_\alpha \cdot V_{V\alpha} \cdot G_{\alpha\alpha} + H_\beta \cdot V_{V\beta} \cdot G_{\beta\beta} + H_{\alpha\beta} \cdot f\left(G_{\alpha\beta}, V_{V\alpha}, V_{V\beta}\right) \\ & + H_{\text{Binder}} \cdot \left(1 - \left(V_{V\alpha} \cdot G_{\alpha\alpha} + V_{V\beta} \cdot \left(G_{\alpha\beta} + G_{\beta\beta}\right)\right)\right) \end{aligned} \tag{39}$$

where $V_{V\alpha}$ and $G_{\alpha\alpha}$ are the volume fraction and the contiguity of the main carbide like WC, $V_{V\beta}$ and $G_{\beta\beta}$ are the volume fraction and the contiguity of the additional carbide like VC or TiC, and the term $H_{\alpha\beta}^{HP} \cdot f(G_{\alpha\beta}, V_{V\alpha}, V_{V\beta})$ can represent the function of carbide–carbide interaction between the two carbides.

Is it possible to include the carbide composition and carbide crystal structure like core-rim into the LG model? It is not clear how the change in rim-to-core ratio of harder rim-to-softer core versus softer rim-to-harder core complex carbide affects the hardness of the alloy.

It seems the effect of the solid solution of the carbide and other doping elements in the binder phase on the hardness of the cemented carbides waits to be discovered. Is it possible to extend the LG model to consider the solid solution in the binder? For example, the binder term might be multiplied by the normalized concentration of tungsten X_W/X_W^0 or a function of X_W/X_W^0 when the tungsten content changes in the binder phase.

$$H_{\text{Binder}} \cdot (1 - V_V \cdot G) \cdot X_W/X_W^0 \tag{40}$$

Furthermore, it seems that a study of the state of carbide–carbide contacts and carbide–binder interfaces on the hardness and microhardness of the cemented carbides might also be appropriate.

It seems that more research on the nature of the microhardness at indent depth below the intrinsic length of $(d_{WC} + \lambda)$ found by Nabarro et al. (Nabarro, Shrivastava, & Luyckx, 2006) and Shrivastava & Luyckx (Shrivastava & Luyckx, 2008) can bring deeper understanding of the hardness of phases and total hardness of hardmetals. It is not clear whether the micro- and nanohardness of phases could be used to enhance the LG model. It seems that more experiments on wider ranges of all the microstructure and chemical parameters of hardmetals as well as on bigger variety of composite materials would be needed to enhance the existing models or create new models of hardness. Computer simulation for hardness modeling might also facilitate its progress.

1.09.4 Elastic Moduli and Deformation Behavior

1.09.4.1 Elastic Moduli Definition

Elastic moduli measure the stress required to elastically deform the material to a predefined strain. Either of two interdependent pairs of elastic moduli fully describes the elastic behavior of isotropic homogeneous materials. The Young's modulus E measures the stress–strain ratio when the tensile or compression load is applied along one selected axis, whereas the Poisson's ratio ν measures the related deformation in two perpendicular directions versus the axis of the load. The bulk or volumetric modulus K measures the stress–strain ratio when the load is uniformly applied in all directions that changes the volume but preserves the shape of the specimen, whereas the shear modulus μ measures the related change of the shape with unchanged volume of the specimen. The E and ν pair can be calculated from K and μ by the following relation of the linear elasticity theory:

$$E = 9 \cdot K \cdot \mu / (3 \cdot K + \mu) \tag{41}$$

$$\nu = (3 \cdot K - 2 \cdot \mu)/(6 \cdot K + 2 \cdot \mu) \tag{42}$$

There are two ways to measure the elastic moduli of hardmetals, namely, by the direct measurement of the slope of the stress–strain curve during the mechanical load that are referred to as static elastic moduli or by measuring the speed of the ultrasound waves (ISO 3312, ASTM E494) that are referred to as dynamic elastic moduli (Fischmeister, 1983; Koopman, Chawla, & Coffin, 2002; Lee & Gilmore, 1982).

1.09.4.2 Elastic Moduli Dependence on Microstructure and Chemistry of Hardmetals

The static Young's modulus E monotonously decreases with the decrease of the volume fraction of the carbide phase V_V from the Young's modulus of polycrystalline WC (703–707 GPa) toward the Young's modulus of Co (207 GPa) on a wide range of the binder contents in WC–Co alloys (Figure 6) (Doi, Fujiwara, Miyake, & Oosawa, 1970; Exner & Gurland, 1970; Gurland, 1963a; Gurland, 1988; Kieffer & Schwarzkopf, 1953; Nishimatsu & Gurland, 1960; Voronov & Balashov, 1960). Doi et al. (Doi et al., 1970) found that the dynamic elastic moduli depend solely on the volume fraction of the carbide crystals V_V for the WC-(1–30) wt% Co alloys; they neither depend on the mlicc d_{WC} in the range between 0.6 and 5 μm nor do they change with the carbon content in the two-phase region for these alloys (Figure 6). Okamoto et al. (Okamoto, Nakazono, Otsuka, Shimoitani,

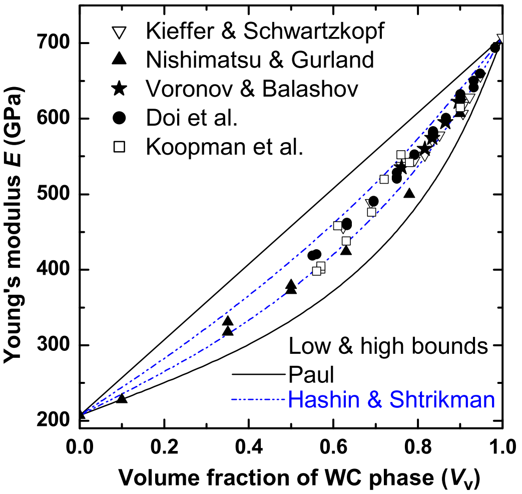

Figure 6 Dependence of Young's modulus E on the volume fraction V_V of the carbide phase in WC–Co cemented carbides. Reproduced from Figure 7 in Doi, Fujiwara, Miyake, & Oosawa, (1970) with kind permission from Springer Science + Business Media B.V.; Figure 5 in Koopman, Chawla, Coffin, et al. (2002) with permission from Wiley—VCHVerlag Gmbh & Co. KGAA.

& Takada, 2005) confirmed that the Young's modulus does not change with the mlicc d_{WC} in a wider range from about 3 μm and up to 20 μm but it reportedly decreases by about 10% at very high $d_{\mathrm{WC}} = 30$ μm. Koopman et al. (Koopman, Chawla, Coffin, et al., 2002) showed that the dependence of the Young's modulus on the volume fraction of the WC phase stays valid even when the binder phase is nonuniformly distributed in the alloy as it is the case in the double cemented carbides that are characterized by geometrical mixture of granules of the conventional cemented carbides dispersed within a continuous matrix of Co (**Figure 6**). Poisson's ratio of WC–Co has similar dependence on the volume fraction of the carbide phase and decreases from 0.31 for pure Co down to about 0.194 for WC with usually measured values between 0.20 and 0.25 on the conventional WC–Co hardmetals (Doi, Fujiwara, Miyake, & Oosawa, 1970).

Appearance of the free graphite or η-phase reduces the Young's modulus due to the occurrence of the softer third phase (Doi, Fujiwara, Miyake, & Oosawa, 1970). For the same reason, the Young's modulus decreases in porous alloys. Changing the shape of WC crystals to flatter triangular prism only slightly increases the Young's modulus by about 1% on WC–Ni cemented carbides (Shatov, Ponomarev, & Firstov, 2006). Young's modulus of the uniaxially hot-pressed double-cemented carbides with somewhat lamellar microstructure also slightly increases compared to the regularly sintered double-cemented carbides (Koopman, Chawla, Coffin, et al. 2002). It is usually assumed that the elastic moduli of other hardmetals have similar dependencies on the volume fraction of the carbide phase and can vary due to the change of the elastic moduli of the phases.

1.09.4.3 Deformation Behavior and Its Dependencies

Aligned with the macroscopically brittle fracture behavior, the WC–Co hardmetals with regular binder phase contents of up to 25 wt% exhibit the close-to-linear stress–strain dependence up to the moment of fracture for the bending and tensile loads (Dusza, Parilak, & Diblk, 1983; Exner & Gurland, 1970; Fischmeister, 1983; Gurland, 1963a; Nishimatsu & Gurland, 1960; Roebuck & Almond, 1988). Initial increase of the binder content reveals the deviation from the linear stress–strain dependence for WC–Co cemented carbides at about 15 wt% of the binder. No obvious choice for the yield stress can be observed on the stress–strain curve, therefore, the yield stress $\sigma_{0.01}$ is usually assumed to be reached when the strain reaches 0.01%. Further increase of the binder phase content beyond the range of the conventional cemented carbides changes the stress–strain curves and introduces visible yielding. The measured proportionality limit stress and the yield stress $\sigma_{0.01}$ decrease but the deformation at fracture increases with the decrease of the volume fraction of the carbide phase V_{V} (Dusza, Parilak, Diblk, & Slesar, 1983; Exner & Gurland, 1970; Gurland, 1963a; Nishimatsu & Gurland, 1960; Roebuck & Almond, 1988). Both the proportionality limit and the yield stress $\sigma_{0.01}$ have a dependence similar to the hardness on the mlicc and mlibp according to the LG model (4) and (11) (Dusza, J., Parilak, L., Diblk, J. & Slesar, M 1983; Gurland, 1979; Lee & Gurland, 1978; Roebuck & Almond, 1988).

Stress–strain hysteresis and deviation from the linear deformation are observed on hardmetals with the unload stress–strain curve being below the load curve and the hysteresis gap increasing with the increase of the binder phase content in the alloy that is either attributed to the difference between the elastic moduli of the phases or to the reduction of the RTS of phases due to the plastic deformation of the binder phase (Jaensson, 1971, 1972; Paggett, Krawitz, Drake, et al., 2006, 2007; Sundstrom, 1973).

Deformation behavior differs under compression in comparison to the bending and tensile load of hardmetals. Higher strains of up to about 1–3% and even higher are achieved under compression with the significant plastic deformation and formation of the stacking faults in the carbide phase in addition to the plastic deformation of the ductile binder phase (Roebuck & Almond, 1988), whereas the fracture of the hardmetals occurs at much lower strains of 0.1–0.5% under bending and tensile loads (Exner & Gurland, 1970; Jaensson, 1971; Nishimatsu & Gurland, 1960).

1.09.4.4 Elastic Moduli for Anisotropic Single Crystal and Isotropic Polycrystalline WC

For anisotropic materials, as it is the case for WC crystals, the Young's modulus E and Poisson's ratio ν become dependent on the orientation in the crystal and therefore the elastic constants tensor C_{ij} has to be used to calculate the elastic behavior (Golovchan, 1998, 2010; Lee & Gilmore, 1982). Here i and j are the Cartesian indexes in the stress–strain tensor with $i = 3$ chosen for the direction perpendicular to the basal plane of WC lattice, $i = 1$ chosen for the direction perpendicular to the prismatic plane, and $i = 2$ direction being perpendicular to both $i = 1$ and $i = 3$ directions. Due to the hexagonal symmetry, only five independent elastic constants C_{11}, C_{33}, C_{44}, C_{12}, and C_{13} are required to fully describe the elastic behavior of WC single crystal.

The anisotropic Young's modulus E_i and Poisson's ratio ν_{ij} are calculated from the elastic constants tensor C_{ij} through the following set of equations (Golovchan, 1998, 2010).

$$E_1 = (C_{11} - C_{12}) \cdot \left(1 + \left(C_{12} \cdot C_{33} - C_{13}^2\right)/\left(C_{11} \cdot C_{33} - C_{13}^2\right)\right) \tag{43}$$

$$E_3 = C_{33} - 2\,C_{13}^2/(C_{11} + C_{12}) \tag{44}$$

$$\nu_{12} = \left(C_{12} \cdot C_{33} - C_{13}^2\right)/\left(C_{11} \cdot C_{33} - C_{13}^2\right) \tag{45}$$

$$\nu_{13} = C_{13}/(C_{11} + C_{12}) \tag{46}$$

$$\nu_{31} = C_{13} \cdot (C_{11} - C_{12})/\left(C_{11} \cdot C_{33} - C_{13}^2\right) \tag{47}$$

The Young's modulus E and Poisson's ratio ν for the polycrystalline WC can now be calculated as an average of the respective anisotropic values for WC single crystals from Eqns (43)–(47) (Golovchan, 1998, 2010).

$$E = (2 \cdot E_1 + E_3)/3 \tag{48}$$

$$\nu = (\nu_{12} + \nu_{31} + \nu_{13})/3 \tag{49}$$

Lee and Gilmore (1982) measured the elastic constants tensor C_{ij} of WC single crystal by using ultrasonic pulse-echo technique of longitudinal and shear sound waves. Golovchan (Golovchan, 1998, 2010) observed the discrepancy between the experimental measurements of elastic moduli on the binderless WC–Co hardmetals and precisely calculated Young's modulus E and Poisson's ratio ν of the polycrystalline WC with Eqns (43)–(49) from the elastic constants tensor C_{ij} for the single crystal WC measured by Lee and Gilmore (1982). To eliminate the discrepancy, Golovchan (Golovchan, 1998, 2010) adjusted the value of C_{13} from 267 GPa to 150 GPa. The resulting values for the elastic constants tensor C_{ij} as well as for the Young's modulus E and Poisson's ratio ν of the single-crystal WC are as follows (Golovchan, 2010).

$$C_{11} = 720\text{ GPa},\ C_{33} = 972\text{ GPa},\ C_{44} = 328\text{ GPa},\ C_{12} = 254\text{ GPa},\ C_{13} = 150\text{ GPa} \tag{50}$$

$$E_1 = 620\text{ GPa},\ E_3 = 925\text{ GPa},\ \nu_{12} = 0.331,\ \nu_{13} = 0.155,\ \nu_{31} = 0.104 \tag{51}$$

The corresponding values of the Young's modulus E and Poisson's ratio ν for WC polycrystals calculated by Eqns (48) and (49) from the adjusted values of Eqn (51) give very close fit to the experimental data (Golovchan, 2010).

$$E = 722\text{ GPa},\ \nu = 0.197 \tag{52}$$

Golovchan (Golovchan, 2010) also points out the striking degree of the anisotropy of Young's modulus E on WC single crystal calculated by Eqn (51), where the ratio of Young's modulus for the stress applied to the basal plane E_3 versus the prismatic plane E_1 $E_3/E_1 = 1.5$ correlates with the ratio of microhardness measured on the basal versus the prismatic facets of WC crystal (Exner, 1979).

1.09.4.5 Models of Elastic Moduli and Deformation Behavior

Calculating the elastic moduli and deformation behavior of the composite material has many challenges due to the complexity of the mechanical interaction between the phases. The main complication is finding the right balance condition between the stresses and strains at the carbide–binder interface that is further convoluted by the anisotropic properties of the carbide phase. Since solving this problem analytically confronts unresolved mathematical obstacles, the upper and lower bounds approach that predicts the range of values for the deformation characteristics is widely and successfully used instead.

1.09.4.5.1 Model of Paul for Parallel and Series Loads

The Paul model (Paul, 1960) suggests calculating the upper and lower bounds for Young's modulus E of the composite material based on the theorem of minimum potential energy and the theorem of least work regardless of the phase shape. The Young's modulus is limited by the upper bound E_{U} when the phases are loaded in parallel to each other under the constant strain $\varepsilon = \mathrm{const}$ and ignoring the Poisson's contractions between the phases, in which case the volume fraction mixture rule can be applied to the load stresses σ_{C} and σ_{B} as well as to the Young's moduli E_{C} and E_{B} of the carbide and the binder phases, respectively.

$$\sigma|_{\varepsilon=\mathrm{const}} = V_{\mathrm{V}} \cdot \sigma_{\mathrm{C}} + (1 - V_{\mathrm{V}}) \cdot \sigma_{\mathrm{B}} \tag{53}$$

$$E_{\mathrm{U}} = V_{\mathrm{V}} \cdot E_{\mathrm{C}} + (1 - V_{\mathrm{V}}) \cdot E_{\mathrm{B}} \tag{54}$$

The lower bound for Young's modulus E_{L} is achieved when the phases are loaded in series under the condition of the constant stress $\sigma = \mathrm{const}$ that is transferred from one phase to the next one. In this case, the volume fraction mixture rule can be applied to the strains and the reciprocal Young's moduli of phases.

$$\varepsilon|_{\sigma=\mathrm{const}} = V_{\mathrm{V}} \cdot \varepsilon_{\mathrm{C}} + (1 - V_{\mathrm{V}}) \cdot \varepsilon_{\mathrm{B}} \tag{55}$$

$$1/E_{\mathrm{L}} = V_{\mathrm{V}}/E_{\mathrm{C}} + (1 - V_{\mathrm{V}})/E_{\mathrm{B}} \tag{56}$$

where ε_{C} and ε_{B} are the strains of the carbide and the binder phases, respectively.

To calculate the actual Young's modulus of the hardmetals, assumptions about the shape and the distribution of the carbide phase has to be made. The Paul model (Paul, 1960) makes simplifying geometrical assumption of the regular equidistant distribution of the identical carbide crystals with the cubic shape and no carbide–carbide contacts and arrives at the approximate "strength of materials" type of formula for the dependence of the Young's modulus of the alloy on the volume fraction of the carbide phase V_{V}.

$$E^{\mathrm{Paul}} = E_{\mathrm{B}} \cdot \left(E_{\mathrm{B}} + (E_{\mathrm{C}} - E_{\mathrm{B}}) \cdot V_{\mathrm{V}}^{2/3}\right) \Big/ \left(E_{\mathrm{B}} + (E_{\mathrm{C}} - E_{\mathrm{B}}) \cdot V_{\mathrm{V}}^{2/3} \cdot \left(1 - V_{\mathrm{V}}^{1/3}\right)\right) \tag{57}$$

The gap between the upper and lower bounds of the Young's modulus calculated by the Paul model is rather wide for WC–Co hardmetals (**Figure 6**) (Doi, Fujiwara, Miyake, & Oosawa, 1970; Gurland, 1988; Paul, 1960). On the other hand, the approximate "strength of materials" Eqn (57) gives relatively close fit to the experimental data on hardmetals (Doi, Fujiwara, Miyake, & Oosawa, 1970; Paul, 1960). The upper and lower bounds of the Paul model can be easily extended to any number of the phases in the alloy by adding new terms with the respective volume fractions of phases to Eqns (53)–(56).

1.09.4.5.2 Hashin & Shtrikman (HS) Model of Upper and Lower Bounds for Composite Materials

The HS model (Hashin & Shtrikman, 1963) reduced the gap between the upper and lower bounds in comparison to the Paul model by introduction of variational principles in the linear theory of elasticity that uses the elastic polarization tensor on quasi-isotropic and quasi-homogeneous multiphase materials of arbitrary phase geometry (**Figure 6**). The HS model minimizes the stored energy with respect to the polarization tensor and arrives at the upper and lower bounds for the bulk modulus $K_{\mathrm{U}}^{\mathrm{HS}}$ and $K_{\mathrm{L}}^{\mathrm{HS}}$ as well as for the shear modulus $\mu_{\mathrm{U}}^{\mathrm{HS}}$ and $\mu_{\mathrm{L}}^{\mathrm{HS}}$.

$$K_{\mathrm{U}}^{\mathrm{HS}} = K_{\mathrm{C}} + (1 - V_{\mathrm{V}}) \cdot \left((K_{\mathrm{B}} - K_{\mathrm{C}})^{-1} + 3 \cdot V_{\mathrm{V}}/(3 \cdot K_{\mathrm{C}} + 4 \cdot \mu_{\mathrm{C}})\right)^{-1} \tag{58}$$

$$K_{\mathrm{L}}^{\mathrm{HS}} = K_{\mathrm{B}} + V_{\mathrm{V}} \cdot \left((K_{\mathrm{C}} - K_{\mathrm{B}})^{-1} + 3 \cdot (1 - V_{\mathrm{V}})/(3 \cdot K_{\mathrm{B}} + 4 \cdot \mu_{\mathrm{B}})\right)^{-1} \tag{59}$$

$$\mu_{\mathrm{U}}^{HS} = \mu_{\mathrm{C}} + (1 - V_{\mathrm{V}}) \cdot \left((\mu_{\mathrm{B}} - \mu_{\mathrm{C}})^{-1} + 6 \cdot (K_{\mathrm{C}} + 2 \cdot \mu_{\mathrm{C}}) \cdot V_{\mathrm{V}}/(5 \cdot \mu_{\mathrm{C}} \cdot (3 \cdot K_{\mathrm{C}} + 4 \cdot \mu_{\mathrm{C}}))\right)^{-1} \tag{60}$$

$$\mu_{\mathrm{L}}^{\mathrm{HS}} = \mu_{\mathrm{B}} + V_{\mathrm{V}} \cdot \left((\mu_{\mathrm{C}} - \mu_{\mathrm{B}})^{-1} + 6 \cdot (K_{\mathrm{B}} + 2 \cdot \mu_{\mathrm{B}}) \cdot (1 - V_{\mathrm{V}})/(5 \cdot \mu_{\mathrm{B}} \cdot (3 \cdot K_{\mathrm{B}} + 4 \cdot \mu_{\mathrm{B}}))\right)^{-1} \tag{61}$$

where K_C and K_B are the bulk moduli and μ_C and μ_B are the shear moduli of the carbide and the binder phases, respectively.

The upper and lower bounds for the Young's modulus E_U^{HS} and E_L^{HS} as well as for the Poisson's ratio υ_U^{HS} and υ_L^{HS} are calculated from Eqns (58)–(61) by substituting them into relations (41) and (42). The HS model does give a much narrower gap between the upper and lower bounds of the elastic moduli in comparison to the Paul model. All the experimental data on WC–Co hardmetals and even on the double cemented carbides fall in this range (Figure 6) (Doi, Fujiwara, Miyake, & Oosawa, 1970; Gurland, 1988; Koopman et al., 2002).

1.09.4.5.3 Model of Wu for Young's Modulus versus the Shape of the Inclusion in Two-Phase Material

Wu (Wu, 1966) calculated the effect of the inclusion shape on the Young's modulus of a two-phase material. The Wu model shows that the Young's modulus of the alloy increases when the shape of the harder phase changes from spheroid to needle and further to disk with most pronounced difference observed at very low volume fractions of the harder phase V_V, whereas at the higher V_V, the effect of the shape essentially disappears (Wu, 1966). On the other hand, when the inclusion is the softer phase or pores, the Young's modulus of the alloy has an opposite dependence and the change of the softer inclusion or pore shape from spheroid to needle or disk decreases the Young's modulus of the alloy with the most pronounced decrease at the low volume fraction of the softer phase or porosity level (Wu, 1966).

The Wu model provides qualitative explanation for the slight increase of the Young's modulus by about 1% when the shape of WC crystals changes from bulky to flatter triangular prism on WC–Ni cemented carbides (Shatov, Ponomarev, & Firstov, 2006) as well as for the reported slight increase of the Young's modulus on the somewhat lamellar microstructure of the uniaxially hot-pressed double cemented carbides versus the regularly sintered double cemented carbides (Koopman, Chawla, Coffin, et al., 2002).

1.09.4.5.4 Lee & Gurland (LG) Model for the Yield Strength

The LG model (Gurland, 1979; Lee & Gurland, 1978) of hardness (4) that is discussed in Section 1.09.3 is actually based on the calculation of the yield stress of both the carbide and binder phases and their combination with the relative contribution factors of the contiguous volume fraction $V_V \cdot G$ for the carbide phase and the continuous volume fraction $(1 - V_V \cdot G)$ for the binder phase. In other words, the yield strength σ_y of the hardmetals can be calculated from Eqns (4) and (11).

1.09.4.5.5 Byun & Kim (BK) Model of Stress–Strain Partitioning

The BK model (Byun & Kim, 1991) is based on the modified rules of mixture initially suggested by Tamura et al. (Tamura, Tomota, & Ozawa, 1973) that assume that the stress σ_{ij} and strain ε_{ij} tensors of the composite material can be separately approximated as a mixture of stress and strain tensors of phases multiplied by the respective volume fractions.

$$\sigma_{ij} = V_V \cdot \sigma_{ij}^C + (1 - V_V) \cdot \sigma_{ij}^B \tag{62}$$

$$\varepsilon_{ij} = V_V \cdot \varepsilon_{ij}^C + (1 - V_V) \cdot \varepsilon_{ij}^B \tag{63}$$

The BK model calculates the macroscopic strain energy density U in the alloy.

$$U = \sum_{ij} \int \sigma_{ij}\, d\varepsilon_{ij} \tag{64}$$

Finding an extremum of the macroscopic strain density U for the volume fraction of the carbide phase under modified rules of mixture (62) and (63) allows the BK model to calculate the elastic moduli of the hardmetals that fall within the upper and low bounds of the HS model.

1.09.4.5.6 Poech & Fischmeister (PF) Model Based on Strain Compatibility of Phases

The PF model (Poech & Fischmeister, 1992) calculates the Young's modulus of two-phase material by taking into account the strain compatibility between the phases. Assuming that the series loading is applicable to hardmetals by applying the basic boundary condition of the constant stress $\sigma = \text{const}$ (55) and introducing the condition of equality between the total Poison's contractions in both phases, the PF model arrives at the dependence of the Young's modulus E of the alloy on the volume fraction of the carbide phase V_V from the Young's moduli E_C and E_B and Poisson's ratios ν_C and ν_B of the carbide and the binder phases, respectively.

$$E^{PF} = \left[\frac{V_V}{E_C} + \frac{(1 - V_V)}{E_B} - 2 \cdot V_V \cdot (1 - V_V) \cdot \left(\frac{\nu_C}{E_C} - \frac{\nu_B}{E_B}\right)^2 \cdot \left((1 - V_V) \cdot \frac{(1 - \nu_C)}{E_C} + V_V \cdot \frac{(1 - \nu_B)}{E_B}\right)^{-1}\right]^{-1} \quad (65)$$

Interestingly enough, the PF model (65) can be reduced to the lower bound of series load in the Paul model (56) when the Poisson's contractions are neglected by setting $\nu_C = \nu_B = 0$. On the opposite side, setting the Poisson's ratios to the maximal possible value of $\nu_C = \nu_B = 0.5$ converts the PF model (65) to the upper bound of parallel load in the Paul model (54) (Poech & Fischmeister, 1992).

The PF model (Poech & Fischmeister, 1992; Poech, Fischmeister, Kaute, & Spiegler, 1993) also applies the same principle of strain compatibility between the phases to the calculation of the dependence of the flow stress on the strain of the alloy by taking into account the increase of the flow stress of the binder phase due to the stress triaxiality caused by the strain equality on both sides of the phase boundary. The PF model approximates the flow stress of the binder phase by a mixture of Hall-Petch-type dependence on the mlibp with an exponential dependence of the strengthening on the plastic strain, and applies the iterative numerical procedure to calculate the flow stress of the alloy.

1.09.4.5.7 Unit Cell Models of Ge & Schmauder (GS) and Ravichandran

The GS (Ge & Schmauder, 1993) and the Ravichandran models (Ravichandran, 1994a) suggest using a unit cell approach to calculate narrow upper and lower bounds of the Young's modulus of two-phase materials. The GS model is using a spherically shaped inclusion, whereas the Ravichandran model is using the cubically shaped inclusion in a cubic unit cell with no contacts between the particles. The GS model assumes a uniform shear stress along the particle–matrix interface and strain compatibility at the particle–matrix interface. The Ravichandran model uses a mixture of the series and parallel loading to calculate the joint effect of the particle and the matrix of the same Poisson's ratio in the unit cell. Both models give a narrower gap in comparison to the Paul model (Eqns (54) and (56)) and a comparable gap to the HS model (Eqns (58)–(61)). Ravichandran (Ravichandran, 1994b) further applies the unit cell model to calculating the flow stress of hardmetals under the assumption that the stress is proportional to an exponent of the plastic strain in the binder phase.

1.09.4.5.8 Computer Simulation of Elastic Moduli

A set of computer simulations by finite element modeling and object-oriented finite element modeling techniques allow calculation of the elastic moduli of hardmetals (Chawla, Patel, Koopman, et al. 2003; Jaensson & Sundstrom, 1972; Xu & Agren, 2004). The computer models allow feeding the realistic microstructure of the cross-section of the specimen that reflects the size, the volume fraction, the contiguity, the geometry of the carbide–binder interfaces, and even the arrangement of the carbide crystals in the hardmetals. The models still require making assumptions on or ignoring the anisotropy, misorientation, shape, and arrangement of the carbide crystals in three-dimensional space from two-dimensional cross-section. Nevertheless, the computed values of the elastic moduli fit very close to the experimental data with usually narrower gap than the Paul and the HS models (Chawla, Patel, Koopman, et al., 2003; Jaensson & Sundstrom, 1972; Xu & Agren, 2004).

1.09.4.6 Outlook

Despite rather deep understanding and strong mathematical background behind the models for the upper and lower bounds of the elastic moduli, direct calculation of the elastic moduli of the multiphase alloy from the constituent phase properties and the microstructure parameters still presents a challenge and requires either making simplifying assumptions or utilization of the computer simulation. Modeling of the deformation behavior and flow stresses even further complicates the problem by introduction of the plastic deformation and strengthening factors.

Cross-references

1.1 Introduction to Hardmetals—Definitions, Classification and History of Hardmetals
1.2 Introduction to Hardmetals—Fundamentals and General Applications of Hardmetals

1.3 Introduction to Hardmetals—Microstructure and Morphology of Hardmetals
1.4 Class of Materials—Cemented Carbides
1.5 Class of Materials—Cermets
1.6 Powder Synthesis
1.7 Synthesis and Processing—Powder Processing and Green Shaping
1.8 Synthesis and Processing—Consolidation Techniques
1.10 Fracture and Strength of Hardmetals at Room Temperature
1.11 Mechanical Properties—Fatigue
1.12 Mechanical Properties—Wear of Hardmetals
1.13 Mechanical Properties—Residual/Thermal Stress in Hardmetals
1.16 Applications—Coating Application to Cutting Tools
1.17 Applications—Coatings by Thermal Spray
1.18 Applications—Coatings by Laser Cladding

References

All about cemented carbide. http://www.allaboutcementedcarbide.com/

Almond, E. A. (1983). Deformation characteristics and mechanical properties of hardmetals. In R. K. Viswanadham, D. Rowcliffe, & J. Gurland (Eds.), *Proceedings of the 1st international conference on the science of hard materials* (pp. 517–561). New York: Plenum Press.

Almond, E. A., & Roebuck, B. (1988). Identification of optimum binder phase compositions for improved WC hard metals. *Materials Science and Engineering: A, 105–106*, 237–248.

Andren, H.-O. (2001a). Microstructures of cemented carbides. *Materials and Design, 22*, 491–498.

Andren, H.-O. (2001b). Microstructure development during sintering and heat-treatment of cemented carbides and cermets. *Materials Chemistry and Physics, 67*, 209–213.

Andren, H.-O., Rolander, U., & Lindahl, P. (1994a). Atom-probe analysis of cemented carbides and cermets. *Applied Surface Science, 76/77*, 278–284.

Andren, H.-O., Rolander, U., & Lindahl, P. (1994b). Phase composition in cemented carbides and cermets. *International Journal of Refractory Metals and Hard Materials, 12*, 107–113.

Armstrong, R. W. (2011). The hardness and strength properties of WC–Co composites. *Materials, 4*, 1287–1308.

Armstrong, R. W., & Cazacu, O. (2006). Indentation fracture mechanics toughness dependence on grain size and crack size: application to alumina and WC–Co. *International Journal of Refractory Metals and Hard Materials, 24*, 129–134.

Arzt, E. (1998). Size effects in materials due to microstructural and dimensional constraints: a comparative review. *Acta Materialia, 46*, 5611–5626.

Ashby, M. F. (1970). The deformation of plastically non-homogeneous alloys. *Philosophical Magazine, 21*, 399–424.

Ashby, M. F. (1971). The deformation of plastically non-homogeneous alloys. In A. Kelly, & R. B. Nicholson (Eds.), *Strengthening methods in crystals* (pp. 137–192). London: Applied Science Publishers Ltd.

Bolton, J. D., & Keely, R. J. (1983). Fracture toughness (K_{IC}) of cemented carbides. *Fibre Science and Technology, 19*, 37–58.

Bonache, V., Rayon, E., Salvador, M. D., & Busquets, D. (2010). Nanoindentation study of WC-12Co hardmetals obtained from nanocrystalline powders: evaluation of hardness and modulus on individual phases. *Materials Science and Engineering: A, 527*, 2935–2941.

Byun, T. S., & Kim, I. S. (1991). Stress and strain partition in elastic and plastic deformation of two phase alloys. *Journal of Materials Science, 26*, 3917–3925.

Cha, S. I., Hong, S. H., Ha, G. H., & Kim, B. K. (2001). Mechanical properties of WC-10Co cemented carbides sintered from nanocrystalline spray conversion processed powders. *International Journal of Refractory Metals and Hard Materials, 19*, 397–403.

Cha, S. I., Lee, K. H., Ryu, H. J., & Hong, S. H. (2008). Analytical modeling to calculate the hardness of ultra-fine WC–Co cemented carbides. *Materials Science and Engineering: A, 489*, 234–244.

Chawla, N., Patel, B. V., Koopman, M., Chawla, K. K., Saha, R., Patterson, B. R., et al. (2003). Microstructure-based simulation of thermomechanical behavior of composite materials by object-oriented finite element analysis. *Materials Characterization, 49*, 395–407.

Chermant, J. L., & Osterstock, F. (1976). Fracture toughness and fracture of WC–Co composites. *Journal of Materials Science, 11*, 1939–1951.

Christensen, M., & Wahnstrom, G. (2003). Co-phase penetration of WC(1010)/WC(1010) grain boundaries from first principles. *Physical Review B, 67*, 115415.

Christensen, M., & Wahnstrom, G. (2004). Effects of cobalt intergranular segregation on interface energetics in WC–Co. *Acta Materialia, 52*, 2199–2207.

Christensen, M., & Wahnstrom, G. (2006). Strength and reinforcement of interfaces in cemented carbides. *International Journal of Refractory Metals and Hard Materials, 24*, 80–88.

Christensen, M., Wahnstrom, G., Allibert, C., & Lay, S. (2005). Quantitative analysis of WC grain shape in sintered WC–Co cemented carbides. *Physical Review Letters, 94*, 066105.

Coats, D. L., & Krawitz, A. D. (2003). Effect of particle size on thermal residual stress in WC–Co composites. *Materials Science and Engineering: A, 359*, 338–342.

De Guzman, M. S., Neubauer, G., Flinn, P., & Nix, W. D. (1993). The role of indentation depth on the measured hardness of materials. *Materials Research Society Symposium Proceedings, 308*, 613–618.

Delanoe, A., Bacia, M., Pauty, E., Lay, S., & Allibert, C. H. (2004). Cr-rich layer at the WC/Co interface in Cr-doped WC–Co cermets: segregation or metastable carbide? *Journal of Crystal Growth, 270*, 219–227.

Delanoe, A., & Lay, S. (2009a). Evolution of the WC grain shape in WC–Co alloys during sintering: effect of C content. *International Journal of Refractory Metals and Hard Materials, 27*, 140–148.

Delanoe, A., & Lay, S. (2009b). Evolution of the WC grain shape in WC–Co alloys during sintering: cumulated effect of the Cr addition and of the C content. *International Journal of Refractory Metals and Hard Materials, 27*, 189–197.

Deng, X., Patterson, B. R., Chawla, K. K., Koopman, M. C., Mackin, C., Fang, Z., et al. (2002). Microstructure/hardness relationship in a dual composite. *Journal of Materials Science Letters, 21*, 707–709.

Deshmukh, R., & Gurland, J. (1982). Orientation of contiguous tungsten carbide crystals in sintered WC–Co as determined from slip line traces. *Metallography, 15*, 383–390.

Deshmukh, R., & Gurland, J. (1986). A study of microstructural development during the liquid-phase sintering of WC–Co alloys. In E. A. Almond, C. A. Brookes, & R. Warren (Eds.), *Proceedings of 2nd international conference on the science of hard materials* (pp. 347–358). Bristol and Boston: Adam Hilger.

Doi, H. (1986). Advanced TiC and TiC-TiN base cermets. In E. A. Almond, C. A. Brookes, & R. Warren (Eds.), *Proceedings of 2nd international conference on the science of hard materials* (pp. 489–523). Bristol and Boston: Adam Hilger.

Doi, H., Fujiwara, Y., Miyake, K., & Oosawa, Y. (1970). A systematic investigation of elastic moduli of WC–Co alloys. *Metallurgical and Materials Transactions B, 1*, 1417–1425.

Dusza, J., Parilak, L., Diblk, J., & Slesar, M. (1983). Elastic and plastic behaviour of WC–Co composites. *Ceramics International, 9*, 144–146.

Ekemar, S., Lindholm, L., & Hartzell, T. (1982). Nickel as a binder in WC-based cemented carbides. *International Journal of Refractory Metals and Hard Materials, 1*, 37–40.

Elfwing, M., & Norgren, S. (2005). Study of solid-state sintered fine-grained cemented carbides. *International Journal of Refractory Metals and Hard Materials, 23*, 242–248.

Engqvist, H., Jacobson, S., & Axen, N. (2002). A model for the hardness of cemented carbides. *Wear, 252*, 384–393.

Ettmayer, P. (1989). Hardmetals and cermets. *Annual Review of Materials Science, 19*, 145–164.

Ettmayer, P., Kolaska, H., Lengauer, W., & Dreyert, K. (1995). Ti(C, N) cermets – metallurgy and properties. *International Journal of Refractory Metals and Hard Materials, 13*, 343–351.

Exner, H. E. (1969). The influence of sample preparation on Palmqvist's method for toughness testing of cemented carbides. *Transactions of the Metallurgical Society of AIME, 245*, 677–683.

Exner, H. E. (1970). Method and significance of particle and grain size control in cemented carbide technology. *Powder Metallurgy, 13*, 429–448.

Exner, H. E. (1979). Physical and chemical nature of cemented carbides. *International Metals Reviews*, 149–173.

Exner, H. E. (1983). Qualitative and quantitative interpretation of microstructures in cemented carbides. In R. K. Viswanadham, D. Rowcliffe, & J. Gurland (Eds.), *Proceedings of the 1st international conference on the science of hard materials* (pp. 233–262). New York: Plenum Press.

Exner, H. E., & Fischmeister, H. F. (1966). Structure of sintered tungsten carbide-cobalt alloys. *Archiv fur das Eisenhuttenwesen, 37*, 417–426.

Exner, H. E., & Gurland, J. (1970). A review of parameters influencing some mechanical properties of tungsten carbide–cobalt alloys. *Powder Metallurgy, 13*, 13–31.

Fang, Z., Lockwood, G., & Griffo, A. (1999). A dual composite of WC–Co. *Metallurgical and Materials Transactions A, 30*, 3231–3238.

Fang, Z. Z., Wang, X., Ryu, T., Hwang, K. S., & Sohn, H. Y. (2009). Synthesis, sintering, and mechanical properties of nanocrystalline cemented tungsten carbide – a review. *International Journal of Refractory Metals and Hard Materials, 27*, 288–299.

Fischmeister, H., & Exner, H. E. (1966). Structural dependence of the properties of tungsten carbide–cobalt alloys. *Archiv fur das Eisenhuttenwesen, 37*, 499–510.

Fischmeister, H. F. (1983). Development and present status of the science and technology of hard materials. In R. K. Viswanadham, D. Rowcliffe, & J. Gurland (Eds.), *Proceedings of the 1st international conference on the science of hard materials* (pp. 1–46). New York: Plenum Press.

Fleck, N. A., & Hutchinson, J. W. (1997). Strain gradient plasticity. *Advances in Applied Mechanics, 33*, 295–362.

Fleck, N. A., & Hutchinson, J. W. (2001). A reformulation of strain gradient plasticity. *Journal of the Mechanics and Physics of Solids, 49*, 2245–2271.

Fleck, N. A., Muller, G. M., Ashby, M. F., & Hutchinson, J. W. (1994). Strain gradient plasticity: theory and experiment. *Acta Metallurgica et Materialia, 42*, 475–487.

Fleck, N. A., & Willis, J. R. (2004). Bounds and estimates for the effect of strain gradients upon the effective plastic properties of an isotropic two-phase composite. *Journal of the Mechanics and Physics of Solids, 52*, 1855–1888.

French, D. N., & Thomas, D. A. (1965). Hardness anisotropy and slip in WC crystals. *Transactions of the Metallurgical Society of AIME, 233*, 950–952.

Gao, H. (2001). Strain gradient plasticity. In K. H. J. Buschow, R. W. Cahn, M. C. Flemings, B. Ilschner, E. J. Kramer, S. Mahajan, et al. (Eds.), *Encyclopedia of materials: science and technology* (pp. 8861–8865). Elsevier.

Ge, X., & Schmauder, S. (1993). Elastic modulus and interface stress constraint of particle-reinforced composites. *Materials Science and Engineering: A, 168*, 93–97.

Gee, M. G., Roebuck, B., Lindahl, P., & Andren, H.-O. (1996). Constituent phase nanoindentation of WC/Co and Ti(C, N) hard metals. *Materials Science and Engineering: A, 209*, 128–136.

German, R. M. (1996). *Sintering theory and practice*. New York: John Wiley & Sons.

German, R. M. (2005). *Powder metallurgy and particulate materials processing*. Princeton: MPIF.

German, R. M., Suri, P., & Park, S. J. (2009). Review: liquid phase sintering. *Journal of Materials Science, 44*, 1–39.

Gille, G., Bredthauer, J., Gries, B., Mende, B., & Heinrich, W. (2000). Advanced and new grades of WC and binder powder – their properties and application. *International Journal of Refractory Metals and Hard Materials, 18*, 87–102.

Gille, G., Szesny, B., Dreyer, K., van den Berg, H., Schmidt, J., Gestrich, T., et al. (2002). Submicron and ultrafine grained hardmetals for microdrills and metal cutting inserts. *International Journal of Refractory Metals and Hard Materials, 20*, 3–22.

Gille, G., Szesny, B., & Leitner, G. (1999). A new 0.4 mm WC powder as well as powder-related properties and sintering behavior of 0.6 to 30 mm WC–Co hardmetals. *Journal of Advanced Materials, 31*, 9–22.

Golovchan, V. T. (1998). Elastic moduli of a tungsten monocarbide crystal. *International Applied Mechanics, 34*, 755–757.

Golovchan, V. T. (2010). On the strength of polycrystalline tungsten monocarbide. *International Journal of Refractory Metals and Hard Materials, 28*, 250–253.

Guilemany, J. M., Sanchiz, I., Mellor, B. G., Llorca, N., & Miguel, J. R. (1994). Mechanical-property relationships of Co/WC and Co–Ni–Fe/WC hard metal alloys. *International Journal of Refractory Metals and Hard Materials, 12*, 199–206.

Gurland, J. (1958). The measurement of grain contiguity in two-phase alloys. *Transactions of the Metallurgical Society of AIME, 212*, 452–455.

Gurland, J. (1959). Observation of the structure and sintering mechanism of cemented carbides. *Transactions of the Metallurgical Society of AIME, 215*, 601–608.

Gurland, J. (1963a). Current views on the structure and properties of cemented carbides. *Jernkontorets Annaler, 147*, 1–18.

Gurland, J. (1963b). The fracture strength of sintered tungsten carbide – cobalt alloys in relation to composition and particle spacing. *Transactions of the Metallurgical Society of AIME, 227*, 1146–1150.

Gurland, J. (1979). A structural approach to the yield strength of two-phase alloys with coarse microstructures. *Materials Science and Engineering, 40*, 59–71.

Gurland, J. (1988). New scientific approaches to development of tool materials. *International Materials Reviews, 33*, 151–166.

Gurland, J., & Bardzil, P. (1955). Relation of strength, composition and grain size of sintered WC–Co alloys. *Transactions of the Metallurgical Society of AIME, 203*, 311–315.

Hall, E. O. (1952). The deformation and ageing of mild steel: III discussion of results. *Proceedings of the Physical Society B, 64*, 747–753.

Hashin, Z., & Shtrikman, S. (1963). A variational approach to the theory of the elastic behaviour of multiphase materials. *Journal of the Mechanics and Physics of Solids, 11*, 127–140.

Hellsing, M. (1988). High resolution microanalysis of binder phase in as sintered WC–Co cemented carbides. *Materials Science and Technology, 4*, 824–829.

Hellsing, M., & Andren, H.-O. (1986). Determination of the binder phase composition in WC–Co cemented carbides. In E. A. Almond, C. A. Brookes, & R. Warren (Eds.), *Proceedings of 2nd international conference on the science of hard materials* (pp. 311–320). Bristol and Boston: Adam Hilger.

Henjered, A., Hellsing, M., Andren, H.-O., & Norden, H. (1986). The presence of cobalt at WC/WC interfaces. In E. A. Almond, C. A. Brookes, & R. Warren (Eds.), *Proceedings of 2nd international conference on the science of hard materials* (pp. 303–309). Bristol and Boston: Adam Hilger.

Herber, R. P., Schubert, W. D., & Lux, B. (2006). Hardmetals with "rounded" WC grains. *International Journal of Refractory Metals and Hard Materials, 24*, 360–364.

Jaensson, B. O. (1971). Residual stresses and stress-strain behaviour of the WC–Co composite material. *Materials Science and Engineering, 8*, 41–53.

Jaensson, B. O. (1972). Microstructural interpretation of the stress-strain behaviour of the WC–Co composite material. *Materials Science and Engineering, 9*, 339–346.

Jaensson, B. O., & Sundstrom, B. O. (1972). Determination of Young's modulus and Poisson's ratio for WC–Co alloys by the finite element method. *Materials Science and Engineering, 9*, 217–222.

Jeong, I. K., Kim, H. C., Doh, J. M., Yoon, J. K., Ko, I. Y., & Shon, I. J. (2007). Mechanical properties and consolidation of WC-8wt%Ni hard materials by HFIHS and PCAS. *Solid State Phenomena, 124–126*, 1153–1156.

Jia, K., Fischer, T. E., & Gallois, B. (1998). Microstructure, hardness and toughness of nanostructured and conventional WC–Co composites. *Nanostructured Materials, 10*, 875–891.

Kieffer, R., & Schwarzkopf, P. (1953). *Hartstoffe und hartmetalle*. Wien, Austria: Springer.

Kim, C. S., & Rohrer, G. S. (2004). Geometric and crystallographic characterization of WC surfaces and grain boundaries in WC–Co composites. *Interface Science, 12*, 19–27.

Kim, H. C., Jeong, I. K., Shon, I. J., Ko, I. Y., & Doh, J. M. (2007). Fabrication of WC-8 wt.% Co hard materials by two rapid sintering processes. *International Journal of Refractory Metals and Hard Materials, 25*, 336–340.

Kim, S., Han, S. H., Park, J. K., & Kim, H. E. (2003). Variation of WC grain shape with carbon content in the WC–Co alloys during liquid-phase sintering. *Scripta Materialia, 48*, 635–639.

Konyashin, I., Ries, B., Lachmann, F., Cooper, R., Mazilkin, A., Straumal, B., et al. (2008). Hardmetals with nanograin reinforced binder: binder fine structure and hardness. *International Journal of Refractory Metals and Hard Materials, 26*, 583–588.

Konyashin, I., Schafer, F., Cooper, R., Ries, B., Mayer, J., & Weirich, T. (2005). Novel ultra-coarse hardmetal grades with reinforced binder for mining and construction. *International Journal of Refractory Metals and Hard Materials, 23*, 225–232.

Koopman, M., Chawla, K. K., Coffin, C., Patterson, B. R., Deng, X., Patel, B. V., et al. (2002). Determination of elastic constants in WC/Co metal matrix composites by resonant ultrasound spectroscopy (RUS) and impulse excitation. *Advanced Engineering Materials, 4*, 37–42.

Krawitz, A. D., Crapenhoft, M. L., Reichel, D. G., & Warren, R. (1988). Residual stress distribution in cermets. *Materials Science and Engineering: A, 105–106*, 275–281.

Landwehr, S. E., Hilmas, G. E., Fahrenholtz, W. G., Talmy, I. G., & DiPietro, S. G. (2008). Microstructure and mechanical characterization of ZrC–Mo cermets produced by hot isostatic pressing. *Materials Science and Engineering: A, 497*, 79–86.

Laptev, A. V., Ponomarev, S. S., & Ochkas, L. F. (2001). Structural features and properties of alloy 84%WC-16% Co obtained by hot pressing in the solid and liquid phases. Part 2. Influence of the temperature at which the specimens are made on their physicomechanical properties. *Powder Metallurgy and Metal Ceramics, 40*, 77–83.

Laugier, M. T. (1985). A microstructural model for hardness in WC–Co composites. *Acta Metallurgica, 33*, 2093–2099.

Lay, S., Donnadieu, P., & Loubradou, M. (2010). Polarity of prismatic facets delimiting WC grains in WC–Co alloys. *Micron, 41*, 472–477.

Lay, S., Hamar-Thibault, S., & Lackner, A. (2002). Location of VC in VC, Cr_3C_2 codoped WC–Co cermets by HREM and EELS. *International Journal of Refractory Metals and Hard Materials, 20*, 61–69.

Lee, H. C., & Gurland, J. (1978). Hardness and deformation of cemented tungsten carbide. *Materials Science and Engineering, 33*, 125–133.

Lee, H. R., Kim, D. J., Hwang, N. M., & Kim, D.-Y. (2003). Role of vanadium carbide additive during sintering of WC–Co: mechanism of grain growth inhibition. *Journal of the American Ceramic Society, 86*, 152–154.

Lee, K. H., Cha, S. I., Kim, B. K., & Hong, S. H. (2006). Effect of WC/TiC grain size ratio on microstructure and mechanical properties of WC–TiC–Co cemented carbides. *International Journal of Refractory Metals and Hard Materials, 24*, 109–114.

Lee, M., & Gilmore, R. S. (1982). Single crystal elastic constants of tungsten monocarbide. *Journal of Materials Science, 17*, 2654–2660.

Li, T., Li, Q., Fuh, J. Y. H., Yu, P. C., Lu, L., & Wu, C. C. (2006). Effects of lower cobalt binder concentrations in sintering of tungsten carbide. *Materials Science and Engineering: A, 430*, 113–119.

Li, T., Li, Q., Fuh, J. Y. H., Yu, P. C., Lu, L., & Wu, C. C. (2007). Effects of AGG on fracture toughness of tungsten carbide. *Materials Science and Engineering: A, 445–446*, 587–592.

Luyckx, S. B. (1989). WC–Co components with textured surfaces. In H. Bildstein, & H. M. Orthner (Eds.), *Proceedings of 12th international plansee seminar* (pp. 215–221). Reutte/Tirol: Metallwerk Plansee.

Makhele-Lekala, L., Luyckx, S., & Nabarro, F. R. N. (2001). Semi-empirical relationship between the hardness, grain size and mean free path of WC–Co. *International Journal of Refractory Metals and Hard Materials, 19*, 245–249.

Mari, D. (2001). Cermets and hardmetals. In K. H. J. Buschow, R. W. Cahn, M. C. Flemings, B. Ilschner, E. J. Kramer, S. Mahajan, et al. (Eds.), *Encyclopedia of materials: science and technology* (pp. 1118–1123). Elsevier.

Mari, D., Bolognini, S., Feusier, G., Cutard, T., Viatte, T., & Benoit, W. (2003). TiMoCN based cermets Part II. Microstructure and room temperature mechanical properties. *International Journal of Refractory Metals and Hard Materials, 21*, 47–53.

Mari, D., Clausen, B., Bourke, M. A. M., & Buss, K. (2009). Measurement of residual thermal stress in WC–Co by neutron diffraction. *International Journal of Refractory Metals and Hard Materials, 27*, 282–287.

Mari, D., Krawitz, A. D., Richardson, J. W., & Benoit, W. (1996). Residual stress in WC–Co measured by neutron diffraction. *Materials Science and Engineering: A, 209*, 197–205.

Matsuura, K., Obara, Y., & Kojima, K. (2009). Combustion synthesis of boride particle dispersed hard metal from elemental powders. *International Journal of Refractory Metals and Hard Materials, 27*, 376–381.

Michalski, A., & Siemiaszko, D. (2007). Nanocrystalline cemented carbides sintered by the pulse plasma method. *International Journal of Refractory Metals and Hard Materials, 25*, 153–158.

Milman, Yu. V. (2008). Plasticity characteristic obtained by indentation. *Journal of Physics D: Applied Physics, 41*, 074013.

Milman, Yu. V., Chugunova, S., Goncharuck, V., Luyckx, S., & Northrop, I. T. (1997). Low and high temperature hardness of WC-6wt% Co alloys. *International Journal of Refractory Metals and Hard Materials, 15*, 97–101.

Milman, Yu. V., Luyckx, S., & Northrop, I. T. (1999). Influence of temperature, grain size and cobalt content on the hardness of WC–Co alloys. *International Journal of Refractory Metals and Hard Materials, 17*, 39–44.

Mukhopadhyay, A., & Basu, B. (2011). Recent developments on WC-based bulk composites. *Journal of Materials Science, 46*, 571–589.

Mukhopadhyay, A., Chakravarty, D., & Basu, B. (2010). Spark plasma-sintered WC–ZrO2–Co nanocomposites with high fracture toughness and strength. *Journal of the American Ceramic Society, 93*, 1754–1763.

Murray, T. W., Balogun, O., Steen, T. L., Basu, S. N., & Sarin, V. K. (2005). Inspection of compositionally graded mullite coatings using laser based ultrasonics. *International Journal of Refractory Metals and Hard Materials, 23*, 322–329.

Nabarro, F. R. N., Shrivastava, S., & Luyckx, S. B. (2006). The size effect in microindentation. *Philosophical Magazine, 86*, 4173–4180.

Nishimatsu, C., & Gurland, J. (1960). Experimental survey of the deformation of the hard-ductile two-phase alloy system WC–Co. *Transactions of ASM, 52*, 469–484.

Nix, W. D., & Gao, H. (1998). Indentation size effects in crystalline materials: a law for strain gradient plasticity. *Journal of the Mechanics and Physics of Solids, 46*, 411–425.

Nye, J. F. (1953). Some geometrical relations in dislocated crystals. *Acta Metallurgica, 1*, 153–162.

Okamoto, S., Nakazono, Y., Otsuka, K., Shimoitani, Y., & Takada, J. (2005). Mechanical properties of WC/Co cemented carbide with larger WC grain size. *Materials Characterization, 55*, 281–287.

Ostberg, G., Buss, K., Christensen, M., Norgren, S., Andren, H.-O., Mari, D., et al. (2006). Mechanisms of plastic deformation of WC–Co and Ti(C, N)–WC–Co. *International Journal of Refractory Metals and Hard Materials, 24*, 135–144.

Ostberg, G., Farooq, M. U., Christensen, M., Andren, H.-O., Klement, U., & Wahnstrom, G. (2006). Effect of $\Sigma 2$ grain boundaries on plastic deformation of WC–Co cemented carbides. *Materials Science and Engineering: A, 416*, 119–125.

Paggett, J. W., Krawitz, A. D., Drake, E. F., Bourke, M. A. M., Livescu, V., Claussen, B., et al. (2006). In situ loading response of WC–Ni: origins of toughness. *International Journal of Refractory Metals and Hard Materials, 24*, 122–128.

Paggett, J. W., Krawitz, A. D., Drake, E. F., Bourke, M. A. M., Claussen, B., & Brown, D. W. (2007). In-situ response of WC–Ni composites under compressive load. *Metallurgical and Materials Transactions A, 38*, 1638–1648.

Paul, B. (1960). Prediction of elastic constants of multiphase materials. *Transactions of the Metallurgical Society of AIME, 218*, 36–41.

Petch, N. J. (1953). The cleavage strength of polycrystals. *The Journal of the Iron and Steel Institute, 174*, 25–28.

Poech, M. H., & Fischmeister, H. F. (1992). Deformation of two-phase materials: a model based on strain compatibility. *Acta Metallurgica et Materialia, 40*, 487–494.

Poech, M. H., Fischmeister, H. F., Kaute, D., & Spiegler, R. (1993). FE-modelling of the deformation behaviour of WC–Co alloys. *Computational Materials Science, 1*, 213–224.

Prakash, L. (1993). A review of the properties of tungsten carbide hardmetals with alternative binder systems. In H. Bildstein, & R. Eck (Eds.), *Proceedings of 13th international plansee seminar* (pp. 80–109). Reutte/Tirol: Metallwerk Plansee.

Ravichandran, K. S. (1994a). Elastic properties of two-phase composites. *Journal of the American Ceramic Society, 77*, 1178–1184.

Ravichandran, K. S. (1994b). A simple model of deformation behavior of two phase composites. *Acta Metallurgica et Materialia, 42*, 1113–1123.

Richter, V., & Ruthendorf, M. V. (1999). On hardness and toughness of ultrafine and nanocrystalline hard materials. *International Journal of Refractory Metals and Hard Materials, 17*, 141–152.

Roebuck, B. (1995). Terminology, testing, properties, imaging and models for fine grained hardmetals. *International Journal of Refractory Metals and Hard Materials, 13*, 265–279.

Roebuck, B. (2006). Extrapolating hardness-structure property maps in WC–Co hardmetals. *International Journal of Refractory Metals and Hard Materials, 24*, 101–108.

Roebuck, B., & Almond, E. A. (1988). Deformation and fracture processes and the physical metallurgy of WC–Co hardmetals. *International Materials Reviews, 33*, 90–110.

Roebuck, B., Almond, E. A., & Cottenden, A. M. (1984). The influence of composition, phase transformation and varying the relative FCC and HCP phase contents on the properties of dilute Co–W–C alloys. *Materials Science and Engineering, 66*, 179–194.

Rowcliffe, D. J., Jayaram, V., Hibbs, M. K., & Sinclair, R. (1988). Compressive deformation and fracture in WC materials. *Materials Science and Engineering: A, 105–106*, 299–303.

Sailer, T., Herr, M., Sockel, H.-G., Schulte, R., Feld, H., & Prakash, L. J. (2001). Microstructure and mechanical properties of ultrafine-grained hardmetals. *International Journal of Refractory Metals and Hard Materials, 19*, 553–559.

Schon, A., Schubert, W. D., & Lux, B. (2001). WC platelet-containing hardmetals. InG. Kneringer, P. Rodhammer, & H. Wildner (Eds.), *Proceedings of 15th international plansee seminar* (Vol. 4; pp. 322–336). Reutte/Tirol: Metallwerk Plansee.

Schreiner, M., Schmitt, Th., Lassner, E., & Lux, B. (1984). On the origins of discontinuous grain growth during liquid phase sintering on WC–Co cemented carbides. *Powder Metallurgy International, 16*, 180–183.

Schubert, W. D., Neumeister, H., Kinger, G., & Lux, B. (1998). Hardness to toughness relationship of fine-grained hardmetals. *International Journal of Refractory Metals and Hard Materials, 16*, 133–142.

Shatov, A. V., & Firstov, S. A. (1995). Variation of WC crystal shape due to Ti segregation onto interphase boundaries in WC–Ni hardmetals. *Physics of Metals, 14*, 789–797.

Shatov, A. V., Firstov, S. A., & Shatova, I. V. (1998). The shape of WC crystals in cemented carbides. *Materials Science and Engineering: A, 242*, 7–14.

Shatov, A. V., Ponomarev, S. S., Firstov, S. A., & Warren, R. (2006). The contiguity of carbide crystals of different shapes in cemented carbides. *International Journal of Refractory Metals and Hard Materials, 24*, 61–74.

Shatov, A. V., Ponomarev, S. S., & Firstov, S. A. (2006). Strength of WC–Ni cemented carbides with different shape of WC crystals. In *Hard materials: Vol. 1. Proceedings of the powder metallurgy congress & exhibition Euro PM2006* (pp. 77–82). Ghent: EPMA.

Shatov, A. V., Ponomarev, S. S., & Firstov, S. A. (2008). Fracture of WC–Ni cemented carbides with different shape of WC crystals. *International Journal of Refractory Metals and Hard Materials, 26*, 68–76.

Shatov, A. V., Ponomarev, S. S., & Firstov, S. A. (2009). Modeling the effect of flatter shape of WC crystals on the hardness of WC–Ni cemented carbides. *International Journal of Refractory Metals and Hard Materials, 27*, 198–212.

Shin, Y., Cao, W., Sargent, G., & Conrad, H. (1988). Effects of microstructure on hardness and Palmqvist fracture toughness of WC–Co alloys. *Materials Science and Engineering: A, 105–106*, 377–382.

Shrivastava, S., & Luyckx, S. (2008). Evidence and importance of an intrinsic length scale in WC–Co. In *Extended abstracts of 9th international conference on the science of hard materials* (pp. 11–12) (Montego Bay, Jamaica).

Sigl, L. S., & Exner, H. E. (1987). Experimental study of the mechanics of fracture in WC–Co alloys. *Metallurgical Transactions A, 18*, 1299–1308.

Sigl, L. S., & Exner, H. E. (1989). The flow stress and hardness of metal-reinforced brittle composites. *Materials Science and Engineering: A, 108*, 121–129.

Sigl, L. S., Exner, H. E., & Fischmeister, H. F. (1986). Characterization of fracture processes and fracture relevant parameters in WC–Co hard metals. In E. A. Almond, C. A. Brookes, & R. Warren (Eds.), *Proceedings of 2nd international conference on the science of hard materials* (pp. 631–644). Bristol and Boston: Adam Hilger.

Sigl, L. S., & Fischmeister, H. F. (1988). On the fracture toughness of cemented carbides. *Acta Metallurgica, 36*, 887–897.

Slesar, M., Dusza, J., & Parilak, L. (1986). Micromechanics of fracture in WC–Co hardmetals. In E. A. Almond, C. A. Brookes, & R. Warren (Eds.), *Proceedings of 2nd international conference on the science of hard materials* (pp. 657–668). Bristol and Boston: Adam Hilger.

Stelmashenko, N. A., Walls, M. G., Brown, L. M., & Milman, Yu. V. (1993a). Microindentations on W and Mo oriented single crystals: an STM study. *Acta Metallurgica et Materialia, 41*, 2855–2865.

Stelmashenko, N. A., Walls, M. G., Brown, L. M., & Milman, Y. V. (1993b). STM study of microindentations on oriented metallic single-crystals. In M. Nastasi, D. M. Parkin, & H. Gleiter (Eds.), *Nato ASI series: Vol. E233. Mechanical properties and deformation behavior of materials having ultra-fine microstructures* (pp. 605–610). Portugal: Springer.

Sundstrom, B. O. (1973). Elastic-plastic behaviour of WC–Co analysed by continuum mechanics. *Materials Science and Engineering, 12*, 265–276.

Tamura, I., Tomota, Y., & Ozawa, M. (1973). Strength and ductility of Fe–Ni–C alloys composed of austenite and martensite with various strengths. In *Proceedings of the third international conference on strength of metals and alloys* (pp. 611–615). London: Institute of Metals, Iron and Steel Institute.

Tracey, V. A. (1992). Nickel in hardmetals. *International Journal of Refractory Metals and Hard Materials, 11*, 137–149.

Underwood, E. E. (1968). *Quantitative stereology*. London: Addison-Wesley.

Vicens, J., Benjdir, M., Nouet, G., Dubon, A., & Laval, J. Y. (1994). Cobalt intergranular segregation in WC–Co composites. *Journal of Materials Science, 29*, 987–994.

Voronov, F. F., & Balashov, D. B. (1960). Adiabatic elastic moduli of tungsten based hardmetals. *Physics of Metals and Metallography, 9*, 616–620.

Wang, Y., Heusch, M., Lay, S., & Allibert, C. H. (2002). Microstructure evolution in the cemented carbides WC–Co. I. Effect of the C/W ratio on the morphology and defects of the WC grains. *Physica Status Solidi (a), 193*, 271–283.

Wang, Y., Pauty, E., Lay, S., & Allibert, C. H. (2002). Microstructure evolution in the cemented carbides WC–Co. II. Cumulated effects of Cr additions and of the C/W ratio on the crystal features of the WC grains. *Physica Status Solidi (a), 193*, 284–293.

Warren, R. (1968). Microstructural development during the liquid-phase sintering of two-phase alloys, with special reference to the NbC/Co system. *Journal of Materials Science, 3*, 471–485.

Warren, R., & Waldron, M. B. (1972). Microstructural development during the liquid-phase sintering of cemented carbides. *Powder Metallurgy, 15*, 166–201.

Weidow, J., & Andren, H.-O. (2010). Grain and phase boundary segregation in WC–Co with small V, Cr or Mn additions. *Acta Materialia, 58*, 3888–3894.

Weidow, J., & Andren, H.-O. (2011). Grain and phase boundary segregation in WC–Co with TiC, ZrC, NbC or TaC additions. *International Journal of Refractory Metals and Hard Materials, 29*, 38–43.

Weidow, J., Johansson, S., Andren, H.-O., & Wahnstrom, G. (2011). Transition metal solubilities in WC in cemented carbide materials. *Journal of the American Ceramic Society, 94*, 605–610.

Weidow, J., Norgren, S., & Andren, H.-O. (2009). Effect of V, Cr and Mn additions on the microstructure of WC–Co. *International Journal of Refractory Metals and Hard Materials, 27*, 817–822.

Weidow, J., Zackrisson, J., Jansson, B., & Andren, H.-O. (2009). Characterisation of WC–Co with cubic carbide additions. *International Journal of Refractory Metals and Hard Materials, 27*, 244–248.

Wittmann, B., Schubert, W. D., & Lux, B. (2002). WC grain growth and grain growth inhibition in nickel and iron binder hardmetals. *International Journal of Refractory Metals and Hard Materials, 20*, 51–60.

Wu, T. T. (1966). The effect of inclusion shape on the elastic moduli of a two-phase material. *International Journal of Solids and Structures, 2*, 1–8.

Xu, Z. H., & Agren, J. (2004). A modified hardness model for WC–Co cemented carbides. *Materials Science and Engineering: A, 386*, 262–268.

Yang, D.-Y., & Kang, S.-J. L. (2009). Suppression of abnormal grain growth in WC–Co via pre-sintering treatment. *International Journal of Refractory Metals and Hard Materials, 27*, 90–94.

Zavodinsky, V. G. (2010). Small tungsten carbide nanoparticles: simulation of structure, energetics, and tensile strength. *International Journal of Refractory Metals and Hard Materials, 28*, 446–450.

Zhang, H., & Fang, Z. Z. (2008). Characterization of quasi-plastic deformation of WC–Co composite using Hertzian indentation technique. *International Journal of Refractory Metals and Hard Materials, 26*, 106–114.

Zhang, H., Lu, Q., Zhang, L., & Fang, Z. Z. (2010). Dependence of microcrack number density on microstructural parameters during plastic deformation of WC–Co composite. *International Journal of Refractory Metals and Hard Materials, 28*, 434–440.

1.10 Fracture and Strength of Hardmetals at Room Temperature

Alex V. Shatov, 8 Parkside Drive, Jamesburg, NJ, USA
S.S. Ponomarev and S.A. Firstov, Department of Physics of Strength and Plasticity of Materials, Frantsevich Institute for Problems of Materials Science, Kiev, Ukraine

http://dx.doi.org/10.1016/B978-0-08-096527-7.00010-6

Glossary

Contiguity of carbide crystals (G) The area fraction of the carbide–carbide contacts in the total surface area of the carbide crystals.

Critical crack The crack is considered to be critical when any increase of its size or stress condition at its tip causes the catastrophic propagation of the crack and failure of the specimen.

Critical defect A defect or fractured microstructure element(s) that causes the creation of the critical crack.

Critical stress intensity factor K_{1C} A stress condition required for an existing crack to become critical and cause its uncontrolled catastrophic propagation and failure of the specimen under plane strain load.

Defects The unintentional elements of the final chemistry and final geometry of the material.

Exner crack resistance (W) The ratio of the load to the length of the cracks emanating from the corners of Vickers indent in Palmqvist toughness test.

Fracture mode A fracture of the phase or phase boundary on the crack path through the material.

Fracture stage A crack evolution period.

Fracture toughness The ability of material to resist the propagation of the crack.

Limiting strength The strength of the material without externally introduced defects. Fracture initiation for the limiting strength occurs in the microstructure.

Mean linear intercept of the carbide crystals (*mlicc*) The stereological measure of carbide crystals size calculated as an average size of randomly oriented chords that cross the carbide crystals at carbide–binder interfaces and carbide–carbide boundaries on the cross-section of the specimen.

Mean linear intercept of the binder phase (*mlibp*) The stereological measure of binder phase size calculated as an average size of randomly oriented chords that cross the binder phase at carbide–binder interfaces on the cross-section of the specimen.

Palmqvist toughness test A toughness of the material measured by the length of the cracks emanating from the corners of Vickers indent.

Strength The stress on the surface of the specimen when the stress condition at the tip of the critical crack causes the uncontrolled catastrophic propagation of the crack and failure of the specimen.

Nomenclature

A Amplitude of double sinusoidal profile for the deflection of the fractured surface in the Kotoul model

$A_A^C, A_A^{C/C}, A_A^{B/C}, A_A^B$ Area fractions of fracture modes in cemented carbides

${}^{f}A_j^i, {}^{p}A_j^i$ Fracture surface area and respective planar projection of each piece j for the fracture mode $i = $ C, C/C, B/C, B

a Half diagonal of the indent from Vickers indenter on the surface of the specimen

a_C Half-diameter of the critical defect or critical defect size

AGG Abnormally grown grains

α Experimental constant

b_{WC} Basal edge length of the triangular prism of an ideal WC crystal

B Ductile fracture mode through the binder phase

B/C Ductile fracture mode along or close to the carbide–binder interfaces

γ_i Free surface energy of the fracture mode i

C Half length of the radial-median (half-penny) crack under indenter

C Transgranular fracture mode through the carbide crystals

C/C Intergranular fracture mode of the carbide phase along the carbide–carbide boundaries

d_{mc} Depth of the micro-cracking for transverse rupture strength test

D_{min}, D_{max} Minimal and maximal chord through the center of mass of cross-section of WC crystal in definition of the shape equiaxiality P_{WC}

d_{WC} Mean linear intercept of WC crystals in cemented carbides (*mlicc*)

D_{WC} Mean diameter of WC crystals in cemented carbides

E Young's elastic modulus of the alloy

E_C, E_B Young's elastic modulus of the carbide and binder phases, respectively

ε Strain in the binder phase

ε_f Strain in the binder phase at critical fracture stress

f^K Multiplication factor for the fracture surface deviation from the orientation of the main crack in the Kotoul model

φ_j^i Angle between the main stress plane and the fracture surface region j of the fracture mode i

G Contiguity of carbide crystals in hardmetals measured as the area fraction of the carbide–carbide contacts in the total surface area of the carbide crystals

G_{1C} Critical strain energy release rate

H, **HV** Vickers hardness of hardmetals

H_0 Constant in the Viswanadham and Venables correlation of the inverse Exner crack resistance W^{-1} versus hardness

H_{Binder}^{0} Bulk hardness of the binder phase in Hall–Petch relation
$H_{\mathrm{Binder}}^{\mathrm{HP}}$ Hall–Petch hardening factor for the binder phase
H_{WC}^{0} Bulk hardness of WC in Hall–Petch relation
$H_{\mathrm{WC}}^{\mathrm{HP}}$ Hall–Petch hardening factor for WC crystals
K^{HP} Hall–Petch strengthening factor
K_{1C} Fracture toughness – critical stress intensity factor
L Period of double sinusoidal profile for the deflection of the fractured surface in the Kotoul model
L, ΣL_{i} Length of the Palmqvist crack and the total length of the Palmqvist cracks on the surface of the specimen, where $i = 1, 2, 3, 4$—four cracks emanating from the corners of Vickers indent
L_{C} Characteristic length for the limiting strength of cemented carbides
λ Mean linear intercept of binder phase (*mlibp*)
λ' Mean linear intercept of the binder phase without contiguity G of carbide crystals. $\lambda' = \lambda(1 - G)$
$\lambda_{\perp}$ Mean distance between carbide crystals in cemented carbides
$\lambda^{\mathrm{maxTRS}}$ Mean linear intercept of binder phase in cemented carbides corresponding to the maximal transverse rupture strength for a given volume fraction of the carbide phase V_{V}
m Number of fracture modes in hardmetals
mlicc Mean linear intercept of the carbide crystals d_{WC}
mlibp Mean linear intercept of the binder phase λ
n Number of phases in hardmetals
P Load value in indentation test
P_{C} Critical value of the indentation load when the cracks are developed on the surface of the specimen
P_{WC} Shape equiaxiality of WC crystals
r Number of cores inside of the core–rim structured phases in hardmetals
RCSS Residual compressive surface stresses after grinding
RTS Residual thermal stresses in the carbide and binder phases
σ_{B} Stress in the binder phase
σ_{f} Fracture stress
σ_{mc} Stress required for the microcracking during the transverse rupture test
σ_{y} Yield stress of the polycrystalline material
$\sigma_{\mathrm{y}}^{\mathrm{B}}$ Yield stress of the binder phase
σ_{0}, σ_{0}^{B} Yield stress of the bulk alloy and bulk binder, respectively
TRS, σ_{TRS} Transverse rupture strength
u Displacement of the binder material under stress
u_{f} Critical displacement of the binder material under fracture stress
V_{A} Volume per unit area of the fracture surface of the deformed binder
V_{V} Volume fraction of the carbide phase in cemented carbides
ν Poisson's ratio
W Exner crack resistance for Palmqvist toughness on hardmetals
$w(x,y)$ Double sinusoidal profile for the deflection of the fractured surface in the Kotoul model

1.10.1 Introduction

Basic mechanical properties and behavior of hardmetals[1] include hardness, elastic moduli, deformation behavior, fracture modes and stages, fracture toughness, and strength. These properties are usually measured at room temperature and serve as the main quantitative basis for comparison of the materials and their production technologies.[2] The properties depend on the chemistry and geometry[3] of the material that is referred to as the structure–property relation. The basic mechanical properties can be divided into two groups of nondestructive and destructive tests by their measuring technique. The nondestructive tests measure the elastic and plastic

---

[1] For more information on the definition and fundamentals of hardmetals, see the following chapters: 1.1 Introduction to Hardmetals—Definitions, classification and history of hardmetals; 1.2 Introduction to Hardmetals—Fundamentals and general applications of hardmetals; 1.4 Class of Materials—Cemented Carbides; 1.5 Class of Materials—Cermets.

[2] For more information on powder preparation and production technologies, see the following chapters: 1.6 Powder Synthesis; 1.7 Synthesis and Processing—Powder Processing and Green Shaping; 1.8 Synthesis and Processing—Consolidation Techniques.

[3] For more information on the chemistry and geometry, see the following chapters: 1.1 Introduction to Hardmetals—Definitions, classification and history of hardmetals; 1.2 Introduction to Hardmetals—Fundamentals and general applications of hardmetals; 1.3 Introduction to Hardmetals—Microstructure and morphology of hardmetals; 1.4 Class of Materials—Cemented Carbides; 1.5 Class of Materials—Cermets; 1.9 Hardness and deformation of hardmetals at room temperature.

deformation of the material that does not cause the fracture of the specimen into pieces, even though the bulk and surface of the specimen can undergo irreversible strain and cracking. The destructive tests break the specimen into two and more pieces. The fracture behavior, fracture toughness, and strength of the material are the destructive properties and are discussed in this chapter. Elastic moduli, study of deformation behavior, and the measurement of hardness are the nondestructive properties and are reviewed together with the discussion of the structure–property approach in a separate chapter.[4]

Fracture of the material occurs in several stages and reveals multiple modes of crack propagation on the multiphase materials. Crack is usually initiated from the fracture of the unintended defects of the material or from the microstructure elements that reach their critical stress or strain condition. Occurrence of the initial cracks does not necessarily cause the fracture of the whole specimen because the material is capable of resisting to the propagation of the crack that is referred to as the fracture toughness of the material. When the stress condition around the crack tip reaches some critical level, the material is fractured in front of the crack that corresponds to the start of crack propagation and further failure of the specimen. The maximal stress level measured at the surface of the specimen at the moment of the fracture is referred to as the strength of the material.

1.10.2 Fracture of Hardmetals

1.10.2.1 Fracture Modes

At room temperature, the hardmetals exhibit brittle fracture behavior on the macrolevel, but on the microlevel both the brittle fracture of the carbide phase and the ductile fracture of the binder phase are observed (Fischmeister, 1983; Gurland, 1988; Johannesson & Warren, 1988; Mari, Bolognini, Feusier, Viatte, & Benoit, 1999; Sigl & Exner, 1987). Two-phase cemented carbides have the following four modes of fracture beside the fracture of defects (**Figure 1**) (Almond, 1983; Chermant & Osterstock, 1976; Hong & Gurland, 1983; Lea & Roebuck, 1981; Luyckx, 1977; Nabarro & Bartolucci Luyckx, 1968):

C: transgranular fracture through the carbide crystals;
C/C: intergranular fracture of the carbide phase along the carbide–carbide boundaries;
B/C: fracture along or close to the carbide–binder interfaces;
B: ductile fracture through the binder phase.

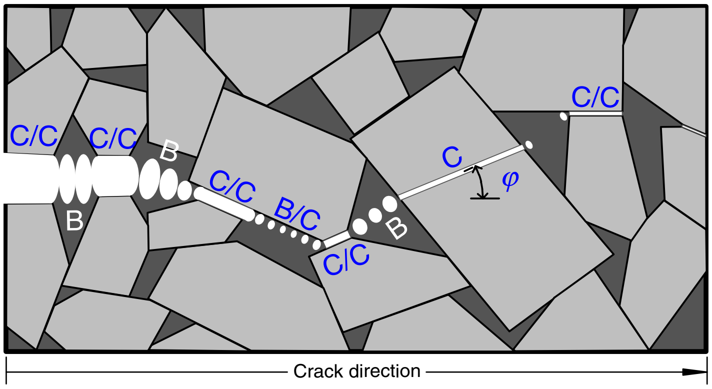

Figure 1 Schematic illustration of four fracture modes in cemented carbides (C, C/C, B/C, B) and of the crack connecting the broken carbide areas C and C/C by the fracture of the ductile binder regions B and along the carbide–binder interfaces B/C in WC–Co. Each fracture surface is slanted against the main stress plane under angle φ.

---

[4] For more information on the nondestructive properties and the discussion of the structure–property approach for hardmetals, see Chapter 1.9, Hardness and deformation of hardmetals at room temperature.

The transgranular fracture through the carbide crystals C is characterized by the typical river-like pattern of the brittle fracture; the intergranular fracture along the carbide–carbide boundary C/C has a smooth surface of the carbide; the fracture along or close to the carbide–binder interface B/C has remnants of the plastically fractured binder phase with shallow dimples on the smooth surface of the carbide; whereas the transgranular ductile fracture through the binder phase B is characterized by deeper dimples with elongated edges of the size comparable to the mean linear intercept of the binder phase (*mlibp*) λ. The intergranular fracture along the grain boundaries of the binder phase B/B is excluded from the above list of the fracture modes because it is not observed on the fracture surface of cemented carbides due to the relatively big size of the binder crystal of about 1 mm (Exner, 1983) that is of several orders of magnitude bigger than the mean linear intercepts of the phases that usually are up to a few microns.

The river-like pattern of the brittle fracture mode C occurs when the crack direction deviates from the crystallographic lattice plane of the carbide. The cleavage fracture path through the carbide can either follow the crystallographic plane with relatively smooth surface that increases the deviation from the crack direction or return closer to the crack direction by jumping between the crystallographic planes that produces the river-like ripples or steps on the fracture surface.

In general, the number of fracture modes m can be calculated from the number of phases n and the number of cores r inside of the core–rim structured phases by the graph theory.

$$m = (2\cdot n - 1) + n\cdot(n - 1)/2 + 2\cdot r \tag{1}$$

Here the first term $(2\cdot n - 1)$ counts the trans- and intergranular fracture modes of each phase except the intergranular fracture of the binder phase B/B. The second term $n\cdot(n - 1)/2$ is the number of fracture modes along all the possible interfaces between the phases. The third term $2\cdot r$ adds the transgranular fracture of the core and fracture along the boundary between the core and the rim of the core–rim structured phase while the core–rim structured phase is counted as a single phase in the first and second terms.

For instance, Eqn (1) gives $m = 4$ modes of fracture for the regular two-phase cemented carbide like WC–Co with $n = 2$ and $r = 0$ (**Figure 2(a)**). For the three-phase hardmetals as it is the case for WC–VC–Co with two carbide phases ($n = 3$) but without the core–rim structure ($r = 0$), the number of the fracture modes becomes $m = 8$ that is C and C/C for WC, C and C/C for VC, B for the binder, plus the fracture along the interfaces between the phases B/C for WC/Co, B/C for VC/Co and C/C for WC/VC (**Figure 2(b)**). The number of fracture modes becomes $m = 10$ for the three-phase ($n = 3$) hardmetals like WC–(TiC+(Ti,W)C)–Co with TiC core ($r = 1$) inside of (Ti,W)C rim of the core–rim structured phase TiC+(Ti,W)C due to the additional fracture modes of the transgranular fracture of the core and the fracture between the core and the rim of TiC+(Ti,W)C phase (**Figure 2(c)**).

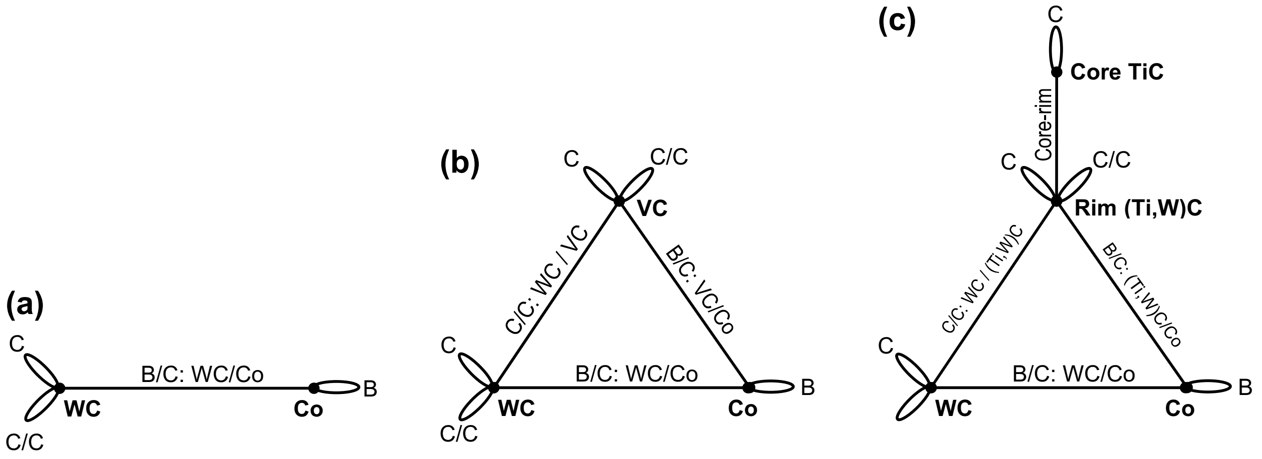

Figure 2 Counting the number of fracture modes (edges and circles) by the graph theory in (a) two-phase cemented carbides WC–Co have four modes, (b) three-phase hardmetals WC–VC–Co have eight modes, (c) three-phase hardmetals WC–(TiC+(Ti,W)C)–Co with TiC core inside of (Ti,W)C rim of the core–rim structured phase TiC+(Ti,W)C have 10 fracture modes.

1.10.2.2 Fracture Stages

In general, there are three stages of fracture, namely, *crack initiation* on defects and/or microstructure; *subcritical crack growth* due to the increase of the load, as well as in fatigue and creep tests[5]; that is followed by the *catastrophic crack propagation* that is usually referred to as *crack propagation* (Chermant & Osterstock, 1976; Exner, Sigl, Fripan, & Pompe, 2001; Hong & Gurland, 1983; Johannesson & Warren, 1988; Osterstock & Chermant, 1983; Sigl & Exner, 1987). The crack is considered to be critical when any increase of its size or stress condition at its tip causes the catastrophic propagation of the crack and failure of the whole specimen.

The subcritical crack growth is usually observed at elevated temperature under fatigue or creep tests and contributes to the deviation from the linear elastic load–displacement curve in addition to the plastic deformation (Johannesson & Warren, 1988; Roebuck & Almond, 1988; Schmid, Mari, Benoit, & Bonjour, 1988). Some limited subcritical crack growth was expected for high binder alloys with at least 25 wt% Co at room temperature and loads close to the critical, but it is not experimentally observed (Johannesson & Warren, 1988). Therefore, the conventional cemented carbides at room temperature under regular loading rates exhibit brittle fracture behavior on the macrolevel with only two fracture stages, where the catastrophic crack propagation originates from the cracks initiated on the fractured defects and/or microstructure elements without any subcritical crack growth (Exner, Sigl, Fripan, & Pompe, 2001; Johannesson & Warren, 1988; Osterstock & Chermant, 1983; Roebuck & Almond, 1988; Sigl & Exner, 1987). Critical defects that cause the crack initiation are further discussed in Section 1.10.4, whereas the crack propagation is the main topic of the current section.

1.10.2.3 Dependencies of Crack Propagation

The total area fraction of crack path through the carbide phase by trans- and intergranular fracture modes ($A_A^C + A_A^{C/C}$) accounts for at least 50–80% of the fracture area of WC–Co cemented carbides and increases with, but always remains below, the volume fraction of the carbide phase V_V in the alloy regardless of the mean linear intercepts of phases (Almond, 1983; Chermant & Osterstock, 1976; Fischmeister, 1983; Gurland, 1988; Hong & Gurland, 1983; Lea & Roebuck, 1981; Mason & Kenny, 1970; Sigl & Exner, 1987; Sigl, Exner, & Fischmeister, 1986; Slesar, Dusza, & Parilak, 1986; Viswanadham, Sun, Drake, & Peck, 1981). The estimated fracture energy of single crystal or polycrystalline WC is about 50 $\mathrm{J\,m^{-2}}$, the surface energy of WC is negligibly low at about 2.8 $\mathrm{J\,m^{-2}}$, whereas the fracture energy of WC–Co cemented carbides is much higher at 10^2–10^3 $\mathrm{J\,m^{-2}}$ (Gurland, 1988; Sigl, Exner, & Fischmeister, 1986; Sigl & Exner, 1987). In other words, crack prefers to fracture the ductile binder, rather than the brittle carbide phase, despite the increase of the total fracture energy. Nevertheless, the excessive ductile fracture through the binder phase on the microlevel does not change the overall brittle character of the fracture on the macrolevel of the cemented carbides at room temperature (Fischmeister, 1983; Gurland, 1988; Johannesson & Warren, 1988; Mari, Bolognini, Feusier, Viatte, & Benoit, 1999; Sigl & Exner, 1987). Crack branching and scattering are extremely rare for hardmetals. The plastic zone in the binder phase extends only through the binder regions directly intersected by and adjacent to the crack (Fischmeister, Exner, Poech, et al., 1989; Fischmeister, Schmauder, & Sigl, 1988; Sigl, Exner, & Fischmeister, 1986; Sigl & Exner, 1987; Spiegler & Fischmeister, 1992).

Hardmetals based on the cubic carbides exhibit similar behavior with excessive ductile fracture through the binder phase on alloys with lower hardness, but the crack propagation preference changes to the dominant brittle fracture through the carbide phase on alloys with higher hardness (Mari, Bolognini, Feusier, Viatte, & Benoit, 1999; Viswanadham & Precht, 1980; Warren & Matzke, 1983).

Quantitative fractography by means of microscopy and Auger-electron spectroscopy reveals the following dependencies for the crack propagation (Almond, 1983; Chermant & Osterstock, 1976; Fischmeister, 1983; Hong & Gurland, 1983; Lea & Roebuck, 1981; Mason & Kenny, 1970; Sigl & Exner, 1987; Slesar, Dusza, & Parilak, 1986; Viswanadham, Sun, Drake, & Peck, 1981). Increasing the mean linear intercept of carbide crystals (*mlicc*) d_{WC} causes the increase of the relative area of transgranular fracture through the carbide crystals C versus the intergranular fracture of the carbide phase C/C and at the same time, the increase of the relative area of the fracture through the binder phase B versus the fracture along the carbide–binder interfaces B/C at any volume

---

[5] For more information on fatigue and creep tests of hardmetals, see the following chapters: 1.11 Mechanical Properties—Fatigue; 1.14 Mechanical Properties—Plastic, high temperature.

fraction of the carbide phase V_V in the alloy. The transgranular fracture of the carbide crystals C is prevailing on the alloys with large carbide crystals with *mlicc* d_{WC} above 5 μm, whereas it is almost not observed on the alloys with smaller WC crystals with d_{WC} below 2 μm, where the intergranular fracture C/C prevails.

Changing the shape of WC crystals to flatter triangular prisms decreases the surface area of the intergranular fracture along the carbide–carbide contacts C/C due to the decrease of the contiguity G, but increases both the area of transgranular fracture through the carbide crystals C and the total surface area fraction of the fracture through the carbide phase $(A_A^C + A_A^{C/C})$ for the fixed volume fraction V_V and the *mlicc* $d_{WC} \approx 1$ μm of WC crystals on WC–Ni cemented carbides (Shatov, Ponomarev, & Firstov, 2008). Flatter shape of WC crystals causes the WC crystals to fracture in transgranular mode C at lower *mlicc* $d_{WC} \approx 1$ μm relative to the usually required values of more than $d_{WC} > 2$ μm for the transgranular fracture of the regular bulky shaped WC due to the disproportional increase of the basal edge length in comparison to the prismatic edge of the flatter triangular prism of WC crystals when the basal facets of broken WC crystals are oriented close to perpendicular relative to the crack path direction.

The residual compressive thermal stress[6] imposed on the carbide crystals resists both the transgranular and the intergranular fracture of the carbide crystals (Cutler & Virkar, 1985; Rice, 1983). The residual triaxial tensile thermal stress on the binder phase promotes formation of submicron voids in the binder regions close to the crack path during the crack propagation in addition to the change of the stress level and formation of voids in the binder layers that are crossed by the crack path (McHugh & Connolly, 2003; Schmauder, 2001). The residual tensile thermal stress on the binder phase might also be a reason for the pronounced surface relief of the binder phase regions adjacent to the crack that is observed by Sigl and Exner (1987).

1.10.2.4 Sigl and Exner Correlations of Crack Propagation

Sigl and Exner (1987) found correlations for the fracture surface area fractions A_A^i of the fracture modes ($i =$ C, C/C, B/C, B) versus the volume fraction V_V and the *mlicc* d_{WC} (measured in micrometers) when the shape of WC crystals is not changed on WC–Co alloys.

$$A_A^C + A_A^{C/C} = \exp\left(-1.77\cdot(1-V_V)^{0.78}\right) \tag{2}$$

$$A_A^C = \frac{d_{WC}}{0.4\cdot d_{WC}+3.1}\cdot\exp\left(-1.77\cdot(1-V_V)^{0.78}\right) \tag{3}$$

$$A_A^{C/C} = \frac{-0.6\cdot d_{WC}+3.1}{0.4\cdot d_{WC}+3.1}\cdot\exp\left(-1.77\cdot(1-V_V)^{0.78}\right) \tag{4}$$

$$A_A^{B/C} = \frac{0.5\cdot d_{WC}+1.1}{1.5\cdot d_{WC}+1.1}\cdot\left[1-\exp\left(-1.77\cdot(1-V_V)^{0.78}\right)\right] \tag{5}$$

$$A_A^B = \frac{d_{WC}}{1.5\cdot d_{WC}+1.1}\cdot\left[1-\exp\left(-1.77\cdot(1-V_V)^{0.78}\right)\right] \tag{6}$$

The Sigl and Exner correlations seem to fit well to the experimental data and reflect all the main dependencies of the crack path on the regular WC–Co cemented carbides with *mlicc* d_{WC} between 0.6 and 2.2 μm and the volume fraction of the carbide phase V_V between 75 and 90 vol% (Sigl & Exner, 1987; Sigl & Fischmeister, 1988). The fracture through the carbide phase $(A_A^C + A_A^{C/C})$ from Eqn (2) only depends on the volume fraction V_V and does not depend on the *mlicc* d_{WC}. The value of $(A_A^C + A_A^{C/C})$ is below the volume fraction V_V by about 15–20 vol% in the measured range of V_V. The difference between the volume fraction V_V and $(A_A^C + A_A^{C/C})$ from

---

[6] For more information on residual thermal stress, see Chapter 1.13 Mechanical Properties—Residual/thermal stress in hardmetals.

Eqn (2) increases from 0 for the binderless alloy with $V_V = 100$ vol%, goes through a maximum at about $V_V = 75$ vol% and subsequently decreases. For the nanograined cemented carbides, the Sigl and Exner correlations reasonably predict diminishing values of both the transgranular fracture through the carbide crystals C and fracture through the binder phase B. The crack is expected to propagate by the intergranular fracture along the carbide–carbide contacts C/C and along the carbide–binder interfaces B/C due to very thin binder layers and very high specific surface of the carbide crystals.

Nevertheless, the Sigl and Exner correlations have their limitations. Extrapolation of Eqn (4) to bigger WC grains expects the area of the intergranular fracture of carbide phase C/C to cease and go negative on *mlicc* that are higher than about 5.17 μm (3.1/0.6 ≈ 5.17) that seems to be quite an exaggerated restriction. At the other end, Eqn (2) also expects the fracture through the carbide phase $(A_A^C + A_A^{C/C})$ to be of about 17% even for the pure binder alloy with no carbide phase ($V_V = 0$) as well as the value of the sum $(A_A^C + A_A^{C/C})$ becomes higher than the volume fraction V_V at about 24 vol% of the carbide phase. A caution should be taken when using Eqns (2)–(6) outside the measured range of d_{WC} between 0.6 and 2.2 μm with the measured volume fraction V_V being between 75 and 90 vol% (Sigl & Exner, 1987) where these correlations should be revisited. Furthermore, the fractography correlations (2)–(6) should also be remeasured on other hardmetals and revised for the effect of the flatter shape of WC crystals.

1.10.2.5 Two-Step Crack Propagation

It is possible to control the crack propagation by deforming the specimen at very slow deflection rates of about 0.1 μm min^{-1} (Sigl & Exner, 1987). The controlled stable crack propagation proceeds in small jumps, followed by the critical catastrophic crack propagation through the specimen in just one big jump (Exner, Sigl, Fripan, & Pompe, 2001; Sigl & Exner, 1987). The controlled crack growth and unstable catastrophic crack propagation show no difference as by the crack geometry, so as by the energy release rates on WC–Co cemented carbides that allow studying the crack propagation process in detail (Exner, Sigl, Fripan, & Pompe, 2001; Sigl & Exner, 1987). The crack propagation in cemented carbides proceeds in two consecutive steps that are repeated one after another many times. The first step is the carbide phase precracking, followed by the second step of the multiligament fracture of the binder phase and the fracture along the carbide–binder interfaces.

1.10.2.5.1 Step One—Carbide Phase Precracking

On the first step, the brittle carbide phase undergoes intergranular C/C and transgranular C precracking ahead of the main crack tip with no significant deformation of the binder phase (Evans, Heuer, & Porter, 1977; Fischmeister, 1983; Fischmeister, Schmauder, & Sigl, 1988; Fischmeister, Exner, & Poech, 1989; Gurland, 1988; Sigl & Exner, 1987; Sigl, Exner, & Fischmeister, 1986; Spiegler & Fischmeister, 1992). The carbide phase does not precrack all at once. Therefore, the first step actually consists of substeps when the weakest carbide regions break first, that is followed by the stress redistribution to and fracture of other carbide regions that surround the weakest regions.

In some sense, the identification of the weakest regions is very analogous to the identification of the critical defects for the strength measurement (Section 1.10.4) with the main difference in the stress field. The crack propagation imposes the dynamic stress field that is concentrated ahead of the crack tip and differs from the static evenly and widely spread stress field of the test on strength. In other words, the widely spread stress field allows uncovering bigger variety of the weakest regions of the microstructure that become the critical defects for the strength test, whereas the concentrated stress field with the steep gradient ahead of the crack tip has much smaller choice in selecting the closest weakest regions. Nevertheless, the nature of the material fracture on the initiation and propagation stages of the crack seems to revolve around the same reasons. Moreover, the critical defects identified on the crack initiation stage for the strength test should match the weakest regions during the crack propagation when no difference in the fracture modes and their fracture surface area fractions is observed between the respective fracture stages.

1.10.2.5.1.1 Weakest Carbide Regions for the Carbide Phase Precracking

The weakest carbide regions can be scattered quite aside from the main crack plane because their location depends on both the tensile and shear stress field ahead of the crack that is decreasing with the distance from the crack tip and the spatial scatter and orientation of the weakest carbide regions in the vicinity of the crack tip. There are three types of the weakest regions and one stress precondition that determine the carbide phase precracking.

The residual thermal stresses[7] (RTS) change the stress field of the crack. It is well known that despite the carbide phase is under compressive RTS on average, the actual local stress can vary in a rather wide range and even become tensile on some small fraction of instances of the carbide crystals in cemented carbides (Coats & Krawitz, 2003; Krawitz, Crapenhoft, Reichel, & Warren, 1988; Krawitz, Reichel, & Hitterman, 1989; Weisbrook & Krawitz, 1996). The RTS is added to the tensile and shear stress field of the crack (Cutler & Virkar, 1985; Rice, 1983) that creates a combined stress field of the crack and RTS and, by these means, affects the location of the weakest carbide region.

The first type of the weakest region is the carbide–carbide contacts with varying cohesion strength that depends on the misorientation angle between the contacting carbide crystals and on whether the carbide–carbide contact is a high-coincidence boundary (Deshmukh & Gurland, 1982; Deshmukh & Gurland, 1986; Exner, 1983; Kim & Rohrer, 2004; Ostberg, Farooq, Christensen, et al., 2006; Shatov, Ponomarev, Firstov, & Warren, 2006; Weidow, Norgren, & Andren, 2009; Weidow, Zackrisson, Jansson, & Andren, 2009), as well as on the presence of various chemical elements at the boundary that can either increase or decrease the cohesion strength of the contacts (Christensen & Wahnstrom, 2003; Christensen & Wahnstrom, 2004; Christensen & Wahnstrom, 2006; Elfwing & Norgren, 2005; Henjered, Hellsing, Andren, & Norden, 1986; Ostberg, Buss, Christensen, et al., 2006; Vicens, Benjdir, Nouet, Dubon, & Laval, 1994; Weidow & Andren, 2010; Weidow & Andren, 2011). When the carbide–carbide contacts with the lowest cohesion strength are found in the combined stress field of the crack and RTS, they have to break first.

The second possible type of the weakest region can be the relatively large carbide crystals when the transgranular fracture mode through the carbide crystals C is present and/or prevalent on the fracture surface (Almond, 1983; Almond & Roebuck, 1977; Dusza, Parilak, & Slesar, 1987; Exner & Gurland, 1970; Fischmeister, 1983; Fukatsu, Kobori, & Ueki, 1991; Han & Mecholsky, 1990; Kursawe, Pott, Sockel, Heinrich, & Wolf, 2001; Laptev, Ponomarev, & Ochkas, 2001; Roebuck & Almond, 1988; Roebuck, 1995; Schreiner, Schmitt, Lassner, & Lux, 1984; Suzuki & Hayashi, 1975; Moyle & Kimmel, 1989). Apparently, for the strong carbide crystals to break first, the closest carbide–carbide contacts with lower cohesion strength should be located quite far away from the crack tip that can only be possible on the alloys with rather high *mlicc* $d_{\mathrm{WC}} > 2\ \mu\mathrm{m}$ where the transgranunlar fracture of the carbide crystals C is the prevalent fracture.

Extensive transgranular fracture of the carbide phase C is not always an indication of the weakest carbide region. Changing the shape of WC crystals to flatter triangular prisms allows identification of the carbide–carbide contacts as the effective critical defect (Section 1.10.4.3.6) despite the increase of the fracture surface area fraction of the transgranular mode C on WC–Ni alloys with the *mlicc* $d_{\mathrm{WC}} \approx 1\ \mu\mathrm{m}$ (Shatov, Ponomarev, & Firstov, 2008; Shatov, Ponomarev, & Firstov, 2006). There is no difference in the fracture surfaces between the crack initiation and crack propagation stages on these alloys (Shatov, Ponomarev, & Firstov, 2006). Therefore, only the carbide–carbide contacts are the weakest carbide regions that break first, whereas the increased transgranular fracture of the carbide crystals C happens afterward on the second substep of the carbide phase precracking on these alloys during the crack propagation.

The third possible type of the weakest region is the defects that can also affect the location of the carbide phase precracking on the first step of crack propagation. Despite the defects is an obvious choice for the weakest region, the likelihood of finding the defects on the fracture surface of crack propagation stage is rather close to the likelihood of finding the defects on the planar cross-section for the conventional hardmetals. This is in contrast to the crack initiation stage, where the defects often play a critical role due to the differences in the stress field distribution around the propagating crack and the initial static and widely spread load.

1.10.2.5.1.2 Connecting the Weakest Carbide Regions during the Carbide Phase Precracking

Breaking the weakest carbide regions redistributes the combined stress field of the crack and RTS to other closely located carbide regions that may initially be under the compressive RTS and/or have higher cohesion strength of their carbide–carbide contacts. Eventually, the crack stress redistribution and concentration extends the fracture to all the other surrounding carbide regions on the first step of carbide phase precracking and causes the crack path to deviate from its projected plane. This way, the precracking step of crack propagation is essentially the two-substep process of its own. On the first substep, the weakest carbide regions are broken. On the second substep, the fracture of the rest of the carbide phase connects the broken weakest regions.

---

[7] For more information on residual thermal stress, see Chapter 1.13 Mechanical Properties—Residual/thermal stress in hardmetals.

1.10.2.5.2 Step Two—Multiligament Fracture of the Binder Phase

On the second step, the fracture through the ductile binder phase B and along the carbide–binder interfaces B/C connects the broken carbide areas by formation, growth, and coalescence of voids in the binder layers that are stretched into multiple highly deformed binder ligaments prior to their failure and opening up the crack in a manner that is similar to the tearing of the perforated sheet of paper (**Figure 1**) (Evans, Heuer, & Porter, 1977; Fischmeister, 1983; Fischmeister, Schmauder, & Sigl, 1988; Fischmeister, Exner, & Poech, 1989; Gurland, 1988; Sigl, Exner, & Fischmeister, 1986; Sigl & Exner, 1987; Spiegler & Fischmeister, 1992). Opening the crack up after the multiligament fracture of the ductile binder phase shifts the stress concentration further into the material that causes the repetition of the first step with the brittle precracking of the carbide phase ahead of the crack tip and the continuation of the crack propagation process until the complete failure of the specimen.

1.10.2.6 Preference of Crack Propagation through the Ductile Binder Phase

The preference of the crack to go by more energy expensive path through the ductile binder phase B and along the carbide–binder interfaces B/C, rather than through the brittle carbide phase C and C/C, in comparison to the volume fractions of the respective binder and carbide phases as it is shown in the Sigl & Exner correlation (2) is surprising and still waits for a proper explanation.

1.10.2.6.1 Model of Kotoul for Crack Propagation Preference

Kotoul (1997) suggests that the meandering path of the crack can be a reason for this behavior. To calculate the deviation of the crack modes from the phase proportions on the planar surface, Kotoul (1997) assumes a double sinusoidal profile for the deflection $w(x,y)$ of the fractured surface.

$$w(x,y) = A\cdot\sin(2\cdot\pi\cdot x/L)\cdot\sin(2\cdot\pi\cdot y/L) \tag{7}$$

where A and L are the amplitude and period of the crack tilts and twists, x is the direction of advance of the crack and y is the direction of the crack front. For the selected sinusoidal profile and the amplitude A that is much smaller than the period L, the fracture area on the deflected path is bigger than the planar area by the factor f^{K}.

$$f^{\mathrm{K}} \approx 1 + (\pi\cdot A/L)^2 \tag{8}$$

Kotoul artificially assumes that WC crystals have spherical shape of uniform radius and that the area of the circularly shaped fracture regions through the carbide phase C and along the carbide–carbide circular contacts C/C does not change with the deviation of the fracture surface orientation from the main crack direction. Selectively applying the multiplication factor f^{K} from Eqn (8) only to the planar surface area fraction of the fracture through the binder phase B and the carbide–binder interfaces B/C that is equal to the volume fraction of the binder phase $(1 - V_{\mathrm{V}})$, Kotoul arrives at the relation between the total fracture surface area fraction through the carbide phase $(A_{\mathrm{A}}^{\mathrm{C}} + A_{\mathrm{A}}^{\mathrm{C/C}})$, the volume fraction of the carbide phase V_{V}, and the ratio between the amplitude A and period L of the crack tilts and twists.

$$A_{\mathrm{A}}^{\mathrm{C}} + A_{\mathrm{A}}^{\mathrm{C/C}} = 1 - (1 - V_{\mathrm{V}})\cdot\left(1 + (\pi\cdot A/L)^2\right) \tag{9}$$

Using the Kotoul model (9) does show that the total fracture surface area fraction through the carbide phase is below the volume fraction V_{V}. For an arbitrary chosen $A/L = 0.25$ and $V_{\mathrm{V}} = 85$ vol%, the value $(A_{\mathrm{A}}^{\mathrm{C}} + A_{\mathrm{A}}^{\mathrm{C/C}})$ is very close to about 70% as it is determined by the Sigl and Exner relation (2). Nevertheless, the ratio A/L is not a constant and is expected to depend on the volume fraction V_{V} for Eqn (9) to be close to the relation (2) (Kotoul, 1997).

Despite the promising approach of accounting for the meandering path of the crack, the assumptions in the Kotoul model seem to be rather misleading. Usage of the arbitrary chosen double sinusoidal profile of the deflection $w(x,y)$ and its amplitude A and the period L seem to be relatively rough approximation for the real hardmetals where no regular periodic oscillation of the crack path is usually observed. Therefore, the ratio A/L cannot be really measured on the fracture surface of the alloy. Ignoring the variation in orientation for the fracture mode through the carbide phase C and C/C has no physical explanation and is based on the artificial assumption of the spherical shape of WC crystals that is not valid for the real hardmetals. This assumption of selective application of the increase of the fracture surface area fraction by the factor from Eqn (8) only to the fracture through the binder phase B and the carbide–binder interfaces B/C is the only reason for the effect described by Eqn (9) and therefore, it raises questions on the validity of the main conclusion of the model.

1.10.2.6.2 Geometry-Based Explanation for Crack Path Preference

The geometry of the two-step crack propagation and the spatial scatter of the weakest carbide regions provide a plausible explanation for the crack path preference.

1.10.2.6.2.1 Geometry of the Crack Propagation

According to the stereology principles, the volume fraction of the phase is equal to the area fraction of the phase on any planar cross-section of the specimen (Underwood, 1968). If the planar cross-section is chosen along the average crack direction, then the planar area fraction of the phase can be compared with the fracture surface area fraction for the fracture modes corresponding to the phase (**Figure 1**). For this geometry, the planar area ${}^{P}A_j^i$ of each piece j for the fracture mode i ($i = \mathrm{C}$, C/C, B/C, B) is the projection of the corresponding fracture surface area ${}^{f}A_j^i$ that is oriented at the deviation angle φ_j^i from the crack direction (**Figure 1**).

$$ {}^{P}A_j^i = {}^{f}A_j^i \cdot \cos\left(\varphi_j^i\right) \tag{10} $$

The volume fraction of the carbide phase can now be expressed as the ratio of the sum of each piece of the planar projection of the fracture surface area of the transgranular C and intergranular C/C fracture modes of the carbide phase plus a half of the projected fracture surface area along the carbide–binder interfaces B/C because the B/C surface is statistically evenly divided between the carbide and the binder sides of the interface to the total planar area of the cross-section.

$$ \begin{aligned} V_{\mathrm{V}} &= \left(\sum_{i=\mathrm{C,C/C};j} {}^{P}A_j^i + \frac{1}{2} \sum_j {}^{P}A_j^{\mathrm{B/C}} \right) \Bigg/ \sum_{i=\mathrm{C,C/C,B,B/C};j} {}^{P}A_j^i \\ &= \left(\sum_{i=\mathrm{C,C/C};j} \left({}^{f}A_j^i \cdot \cos\left(\varphi_j^i\right) \right) + \frac{1}{2} \sum_j \left({}^{f}A_j^{\mathrm{B/C}} \cdot \cos\left(\varphi_j^{\mathrm{B/C}}\right) \right) \right) \Bigg/ \sum_{i=\mathrm{C,C/C,B,B/C};j} \left({}^{f}A_j^i \cdot \cos\left(\varphi_j^i\right) \right) \end{aligned} \tag{11} $$

Its counterpart for volume fraction of the binder phase $(1 - V_{\mathrm{V}})$ and the fracture through the binder phase B and the second half of the carbide–binder interfaces B/C has similar dependence.

$$ \begin{aligned} 1 - V_{\mathrm{V}} &= \left(\sum_j {}^{P}A_j^{\mathrm{B}} + \frac{1}{2} \sum_j {}^{P}A_j^{\mathrm{B/C}} \right) \Bigg/ \sum_{i=\mathrm{C,C/C,B,B/C};j} {}^{P}A_j^i \\ &= \left(\sum_j \left({}^{f}A_j^{\mathrm{B}} \cdot \cos\left(\varphi_j^{\mathrm{B}}\right) \right) + \frac{1}{2} \sum_j \left({}^{f}A_j^{\mathrm{B/C}} \cdot \cos\left(\varphi_j^{\mathrm{B/C}}\right) \right) \right) \Bigg/ \sum_{i=\mathrm{C,C/C,B,B/C};j} \left({}^{f}A_j^i \cdot \cos\left(\varphi_j^i\right) \right) \end{aligned} \tag{12} $$

By definition, the fracture surface area of the carbide phase $(A_{\mathrm{A}}^{\mathrm{C}} + A_{\mathrm{A}}^{\mathrm{C/C}})$ is the sum of the fracture surface area fractions of the transgranular C and intergranular C/C fracture modes of the carbide phase.

$$ A_{\mathrm{A}}^{\mathrm{C}} + A_{\mathrm{A}}^{\mathrm{C/C}} = \sum_{i=\mathrm{C,C/C};j} {}^{f}A_j^i \Big/ \sum_{i=\mathrm{C,C/C,B,B/C};j} {}^{f}A_j^i \tag{13} $$

The fracture surface area of the binder phase $(A_{\mathrm{A}}^{\mathrm{B}} + A_{\mathrm{A}}^{\mathrm{B/C}})$ is calculated in the similar way.

$$ A_{\mathrm{A}}^{\mathrm{B}} + A_{\mathrm{A}}^{\mathrm{B/C}} = \sum_{i=\mathrm{B,B/C};j} {}^{f}A_j^i \Big/ \sum_{i=\mathrm{C,C/C,B,B/C};j} {}^{f}A_j^i \tag{14} $$

From comparison of Eqns (11) versus (13) and (12) versus (14), it becomes apparent that there are two reasons for the difference between $(A_A^C + A_A^{C/C})$ and V_V. On one hand, the additional term from the half of the carbide–binder interface B/C in the calculation of the volume fraction V_V (11) shifts the balance toward the excessive value of the volume fraction V_V in comparison to $(A_A^C + A_A^{C/C})$. On the other hand, the volume fraction of the phase and the respective fracture surface area fractions are related through some weighed mean values of the deviation angles φ^i for the respective fracture modes. When the mean deviation angles of the broken carbide regions φ^C and $\varphi^{C/C}$ are smaller than the mean deviation angles of the connections through the binder φ^B and $\varphi^{B/C}$, the resulting fracture surface area fraction through the carbide phase $(A_A^C + A_A^{C/C})$ can become less than the volume fraction of the carbide phase V_V and qualitatively explain the observed crack propagation preference of crossing the energy expensive binder phase and carbide–binder interfaces over the low-energy fracture of the carbide phase expressed by the Sigl and Exner correlation (2).

1.10.2.6.2.2 Crack Path Deviation Due to the Spatial Scatter of the Carbide Phase Precracking

The carbide phase is precracked first and ahead of the crack tip (**Figure 1**) as it is described in Section 1.10.2.5.1. The weakest carbide regions are scattered quite aside from the main crack plane because their location depends on both the tensile and shear combined stress field of the crack and RTS ahead of the crack that is decreasing with the distance from the crack tip and the spatial scatter and orientation of the weakest carbide regions in the vicinity of the crack tip. The orientation of the broken C and C/C surface is expected to be either close to parallel or only slightly vary around the crack direction to produce the biggest energy release per stress field density from the crack. Breaking the carbide regions aside from the crack projected plane results in the crack path deviation.

On the second step, the fracture through the binder phase B and along the carbide–binder interfaces B/C has to connect the broken carbide regions that are located quite aside from the main crack plane. In other words, the path through B and B/C on the second step of crack propagation is predetermined by the location of the precracked C and C/C regions and does not depend on the crack stress field, the orientation of the binder phase regions, and the high energy of the ductile fracture of the binder phase. In this case, the mean deviation angles through the precracked carbide phase φ^C and $\varphi^{C/C}$ can become smaller than the mean deviation angles through the binder phase and along the carbide–binder interfaces φ^B and $\varphi^{B/C}$ that reduces the fracture surface area fraction through the carbide phase $(A_A^C + A_A^{C/C})$ in comparison to the volume fraction of the carbide phase V_V according to the Eqns (11) and (13) and explains the crack propagation preference.

1.10.2.7 Outlook

Advancement in computer simulation of the fracture process promises clearer understanding of nature of the crack propagation including the effect of the RTS of phases and the cohesion strength of the carbide–carbide contacts of hardmetals that might eventually bring a more detailed physical model that explains the Sigl and Exner empirical correlations (2)–(6) to the light of day. In the meantime, it seems that the Sigl and Exner correlations (2)–(6) should be verified on wider range of the stereological parameters, reevaluated for other variations of the microstructure including the shape of WC crystals, and extended to other hardmetals, that all together might offer more complex correlations and perhaps models versus the geometry and chemistry of hardmetals. More research on the effects of RTS of phases and the cohesion strength of the carbide–carbide contacts on the crack propagation versus the geometry parameters of the microstructure seems to be appropriate as well.

1.10.3 Fracture Toughness

1.10.3.1 Fracture Toughness Definition

Fracture toughness is the ability of the material to resist the propagation of the crack. There are two ways that the fracture toughness of hardmetals can be measured by. In fracture mechanics of hardmetals, the fracture toughness stands for the critical stress intensity factor K_{1C} (ASTM B771 and ASTM E399) that is a stress condition required for an existing crack to become critical and cause its uncontrolled catastrophic propagation and failure of the specimen under plane strain load condition. Alternatively, the fracture toughness can be measured from the Exner crack resistance in Palmqvist toughness tests (ISO 28079) that is the stress condition required to stop the growth of the subcritical crack on the surface of the specimen.

1.10.3.1.1 Critical Stress Intensity Factor K_{1C}

The critical stress intensity factor for plane strain K_{1C} is measured by bending the specimen with artificially created single sharp crack of predefined or measurable size and geometry that is intentionally made larger than any other crack that might be present or developed in the specimen during the load to assure that it is this artificial crack that becomes critical under the load. The most common crack introduction techniques vary between electrical discharge machining, mechanical slitting, deep diamond wedge indentation, and "bridge" indentation, whereas the specimen test geometry usually varies between the single-edge notched beam, chevron-notched beam, and double-cantilever beam that undergo either three- or four-point bending (Almond, 1983; Bolton & Keely, 1983; Godse, Gurland, & Suresh, 1988; Han & Mecholsky, 1990; Nakamura & Gurland, 1980; Pickens & Gurland, 1978; Warren & Johannesson, 1984a).

1.10.3.1.2 Exner Crack Resistance W for the Palmqvist Toughness Test

Palmqvist toughness of hardmetals (Exner, 1969; Palmqvist, 1957; Palmqvist, 1962) is measured by determining the total length ΣL_i of the diagonal cracks emanating from the corners of Vickers indent on the surface of the specimen under the applied load P (**Figure 3**). For the crack to occur on the surface of the specimen, the load on the indenter has to exceed some critical value of P_C. Therefore, the loads for the Palmqvist test on hardmetals start from at least 5 kg and usually range between 30 and 100 kg with the highest reported value of up to 250 kg of weight (Almond & Roebuck, 1983; Exner, Pickens, & Gurland, 1978; Han & Mecholsky, 1990; Shetty, Wright, Mincer, & Clauer, 1985; Spiegler, Schmauder, & Sigl, 1990; Warren & Matzke, 1983).

The residual compressive surface stresses (RCSS) after grinding manifest themselves by shortening the surface cracks and possibly introducing the anisotropic length ratio of surface cracks. These RCSS are also one of the reasons for the nonzero value of the critical load P_C (Exner, 1969; Exner, 1979; Shetty, Wright, Mincer, & Clauer, 1985; Viswanadham & Venables, 1977; Warren & Matzke, 1983). Therefore, the residual surface stresses should be reduced or eliminated by polishing to measure the property of the material, rather than the effect of the residual surface stresses on the crack length (Exner, 1969; Exner, 1979; Shetty, Wright, Mincer, & Clauer, 1985; Viswanadham & Venables, 1977).

Exner (1969) found that the total length of cracks ΣL_i in Palmqvist test increases linearly with the load P and suggested characterizing the Palmqvist toughness for the cemented carbides by measuring the crack resistance W that is defined as either the ratio of the excessive load $(P - P_C)$ to the total length ΣL_i of the cracks from the corners of Vickers indent,

$$W = (P - P_C)/\sum L_i \tag{15}$$

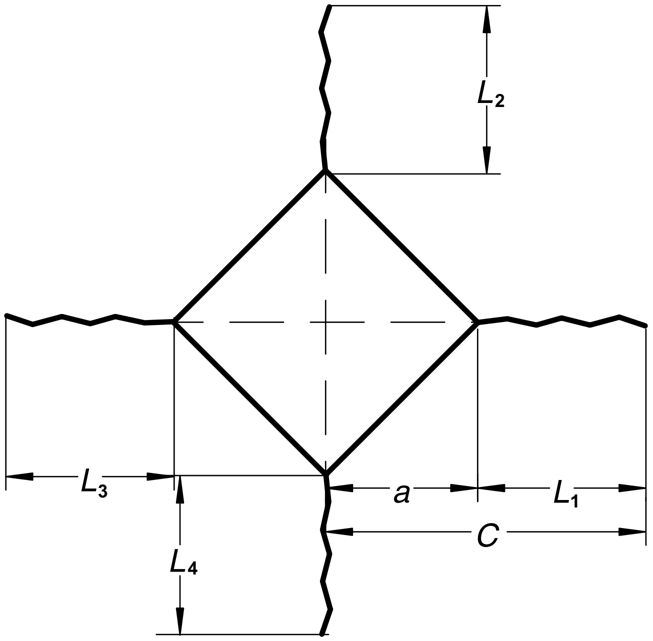

Figure 3 Crack length $\Sigma L_i = L_1 + L_2 + L_3 + L_4$ measurement on the surface of the specimen in Palmqvist test.

or as the inclination of the load versus total length of the crack ΣL_i for incremental loads (Exner, 1969; Fischmeister, 1983; Warren & Matzke, 1983).

$$W = dP/d\left(\sum L_i\right) \tag{16}$$

It is experimentally observed that the Exner crack resistance W remains constant for a wide range of loads and therefore is treated as a property of the material for hardmetals (Exner, 1969; Fischmeister, 1983; Viswanadham & Venables, 1977; Warren & Matzke, 1983).

The total length ΣL_i of the cracks in the Palmqvist toughness test is much lower than the length of the critical crack in bending tests for K_{1C}. In Palmqvist test, the stress condition does not reach the critical value. Therefore, the crack does not become critical and does not propagate through the whole specimen. In other words, the Exner crack resistance W measures the property of the material to stop the propagation of the subcritical crack on the surface of the specimen. Nevertheless, it seems possible to calculate the fracture toughness K_{1C} from Exner crack resistance W as both values are the properties of the material that characterize the resistance to crack propagation.

1.10.3.1.3 Viswanadham and Venables Correlation between the Inverse Exner Crack Resistance W^{-1} and Hardness

Viswanadham and Venables (1977) experimentally found that the inverse value of the Exner crack resistance W^{-1} linearly increases with the Vickers hardness H of WC–Co, (Ti,V)C–Ni, and (Ti,V)C–(Ni,Mo) hardmetals.

$$W^{-1} = A \cdot (H - H_0) \tag{17}$$

where A and H_0 are the constants that depend on the material. H_0 is the minimal hardness at which the material starts to crack in Palmqvist test with WC–Co alloys exhibiting the highest H_0 among the hardmetals.

Further studies (Perrott, 1978; Viswanadham & Precht, 1980; Warren & Matzke, 1983) extended the dependence (17) to wider array of hardmetals. It was also shown that the slope A can increase on cermets with cubic carbides when the fracture mode changes from the excessive fracture through the ductile binder phase to the dominant brittle fracture through the carbide phase on alloys with higher hardness (Viswanadham & Precht, 1980; Warren & Matzke, 1983).

1.10.3.2 Models to Calculate K_{1C} from Exner Crack Resistance W for Palmqvist Test

There are two approaches to calculating the critical stress intensity factor K_{1C} from the Exner crack resistance W that are divided by the choice of the crack geometry (**Figure 4**) (Niihara, Morena, & Hasselman, 1982; Shetty, Wright, Mincer, & Clauer, 1985; Spiegler, Schmauder, & Sigl, 1990; Warren & Matzke, 1983). Four separate cracks of Palmqvist geometry penetrate into the bulk of the material to only some extent, they do not connect to each other under the indent, and their length L is measured from the tip of the corner of the Vickers indent (**Figure 4(a)**). Two semicircular radial-median (half-penny) cracks are connected under the indent and form a single crack that is measured by the total span of the semicircular wings of 2 C from one tip of the crack to the opposite one (**Figure 4(b)**). The half-penny crack usually forms on the brittle materials like ceramics and glasses when the crack easily penetrates under the indenter despite the elastic compression field of the indentation. Introduction of the plasticity to the material that resists the crack growth can reduce the crack penetration depth and prevent the surface cracks from joining under the indenter that leads to the Palmqvist type of cracking. Depending on the plasticity of the material and the crack geometry, different models are appropriate.

1.10.3.2.1 Warren and Matzke (WM) Model for the Palmqvist Crack

The WM model (Warren & Matzke, 1983) is based on the assumption that the cemented carbides exhibit the Palmqvist crack geometry (**Figure 4(a)**). Approximating the Palmqvist crack as a through-crack in an infinite plate, assuming that the tensile stress on the surface is proportional to the indentation load P with x^{-2} spherical expansion of the stress field along the distance from the center of the indentation x, and making an asymptotic approximation that the length L of the Palmqvist crack is much bigger than the half-diagonal a of the indent ($L >> a$) (**Figure 4(a)**) to simplify the calculation, the WM model arrives at the linear proportionality between the fracture toughness K_{1C} and the square root of the product of hardness H by the Exner crack resistance W.

$$K_{1C}^{WM} = \beta \cdot (H \cdot W)^{1/2} \tag{18}$$

where β is a dimensionless proportionality factor.

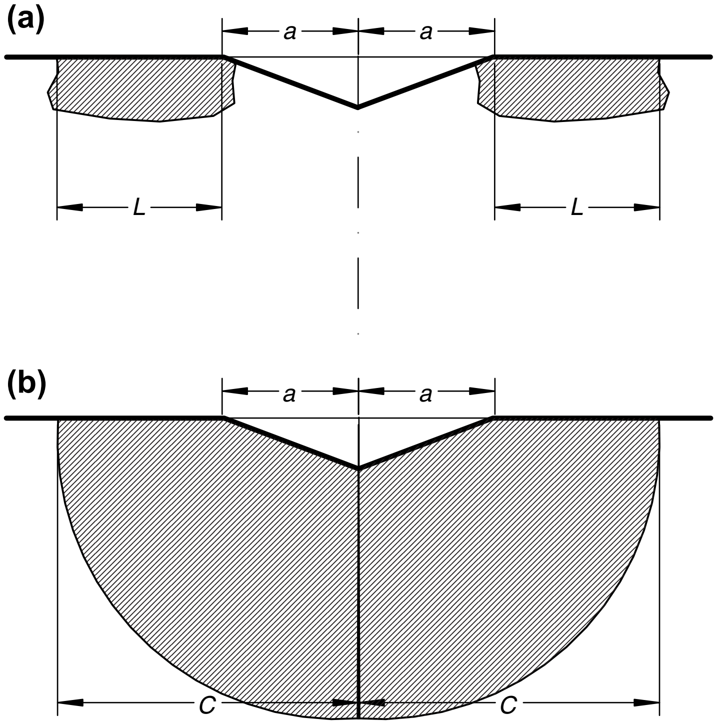

Figure 4 Palmqvist type (a) and semicircular radial-median (half-penny) (b) cracks near and under the indent. Reproduced from Figure 1 in Warren and Matzke (1983) with kind permission from Springer Science+Business Media B.V.

The value of $\beta = 0.087$ is found by fitting the WM model (18) to the experimental data on WC–Co cemented carbides with loads on indenter in the range between 5 and 100 kg of weight (Warren & Matzke, 1983). The asymptotic approximation of very long cracks ($L >> a$) used in the WM model for Palmqvist crack geometry presents an obstacle for the model applicability as such an increase of the relative length should change the geometry to radial-median (half-penny) geometry (**Figure 4(b)**) that is usually observed for $C/a \geq 3$ (Spiegler, Schmauder, & Sigl, 1990). Nevertheless, simplicity of the Eqn (18) and good fit to the experimental data makes the WM model very attractive to use. Moreover, the WM model was experimentally verified on a variety of hardmetals that have the Palmqvist crack geometry (Warren & Matzke, 1983).

1.10.3.2.2 Niihara, Morena and Hasselman (NMH) Model for the Palmqvist Crack

The result of the NMH model for the assumed Palmqvist crack geometry (Niihara, 1983; Niihara, Morena, & Hasselman, 1982) is similar to the WM model (18), but is based on a different approximation of the Palmqvist cracks as four independent elongated semielliptical cracks with relatively low ratio of the length L of the Palmqvist crack to the half-diagonal a of the indent $0.25 \leq L/a \leq 2.5$ (**Figure 4(a)**) that is usually observed on WC–Co cemented carbides.

$$K_{1C}^{\mathrm{NMH}} = 0.0246 \cdot (E/H)^{2/5} \cdot (H \cdot W)^{1/2} \tag{19}$$

where E is the elastic modulus, W is the Exner crack resistance (15), and H is the hardness of the material.

The NMH model predicts slightly more complicated dependence than the WM model (18) and requires knowledge of the elastic modulus E that is not always easily available. In contrast to the WM model that is built on the asymptotic approximation of very long cracks ($L >> a$), the NMH model is developed for the realistic relative length of the Palmqvist crack $0.25 \leq L/a \leq 2.5$ for the hardmetals. Nevertheless, the NMH model still waits for the validation on other than WC–Co hardmetals.

1.10.3.2.3 WM Model Reevaluation by Shetty, Wright, Mincer and Clauer (WM-SWMC) for the Palmqvist Crack

Shetty, Wright, Mincer and Clauer (1985) and Shetty and Wright (1986) experimentally observed and confirmed the Palmqvist-type crack on WC–Co with loads on indenter in the range between 5 and 120 kg of weight by sequential removal of the layers of material by polishing the surface of the specimen. The WM-SWMC model is built on top of the WM model, but avoids the need for the asymptotical calculation and makes minimal number of assumptions based on the experimental observations of the crack geometry. Assuming the two-dimensional geometry of the through-crack along the surface of the specimen as in the WM model, and that the Palmqvist crack is in equilibrium with the post indentation crack opening due to the residual plastic zone that is an analog to the wedge-loaded through crack, using the assumption of the hardness impression volume accommodation by a uniform spherical expansion of the plastic zone from the center of indent, applying the fracture mechanics relations for the wedge-induced surface crack as well as using the geometry parameters of Vickers indenter, the WM-SWMC model arrives at essentially the same formula as the WM model (18), but with no experimental factors.

$$K_{1C}^{\text{WM-SWMC}} = 0.0889 \cdot (H \cdot W)^{1/2} \tag{20}$$

The WM-SWMC model does not require the length L of the Palmqvist crack to be bigger or smaller than the half-diagonal of the indent in contrast to the WM model with loads on indenter in the range between 10 and 80 kg of weight (Shetty, Wright, Mincer, & Clauer, 1985). Furthermore, the dimensionless constant factor of 0.0889 for WC–Co alloys is derived from the geometry of the Vickers indent and Poisson's ratio of the material instead of being determined from the experiments as in case of the WM model. Nevertheless, both the WM and the WM-SWMC models are based on the same main physical ideas of the two-dimensional through-crack along the surface and spherical expansion of the stress field that explains the similarity between Eqns (18) and (20).

1.10.3.2.4 Models for Radial-Median (Half-Penny) Crack

The radial-median (half-penny) crack is usually observed on the brittle materials with very limited plasticity and low fracture toughness like ceramics and glasses as well as at the high-indentation loads when the crack easily propagates along the surface and into the bulk of the specimen (Shetty, Wright, Mincer, & Clauer, 1985; Spiegler, Schmauder, & Sigl, 1990; Warren & Matzke, 1983). This half-penny crack is characterized by relatively high ratio of the crack length C to the half-diagonal of the indent $C/a \geq 3$ (**Figure 4(b)**) (Niihara, 1983; Niihara, Morena, & Hasselman, 1982; Spiegler, Schmauder, & Sigl, 1990). The change of the crack geometry affects the observed correlations for the fracture toughness. A number of models for the radial-median crack geometry are suggested that can be expressed in a general form (Spiegler, Schmauder, & Sigl, 1990).

$$K_{1C}^{\text{half-penny}} = \beta \cdot (E/H)^n \cdot P \cdot C^{-3/2} \tag{21}$$

where β and n are dimensionless experimental factor and power constants, that equal one of the following pairs 0.0309 and 2/5 (Niihara, 1983; Niihara, Morena, & Hasselman, 1982), 0.016 and 1/2 (Anstis, Chantikul, Lawn, & Marshall, 1981; Chantikul, Anstis, Lawn, & Marshall, 1981), or 0.010 and 2/3 (Laugier, 1985), respectively. The dimensionless factor $(E/H)^n$ in Eqn (21) accounts for the effects of the residual stresses beneath the hardness indentation (Spiegler, Schmauder, & Sigl, 1990).

Most of the experimental data for the Palmqvist test of the conventional hardmetals indicates that the half-penny crack is not formed due to relatively high plasticity and toughness of the material under a wide range of loads between 5 and 120 kg of weight (Niihara, 1983; Niihara, Morena, & Hasselman, 1982; Shetty, Wright, Mincer, & Clauer, 1985; Shetty & Wright, 1986; Spiegler, Schmauder, & Sigl, 1990; Warren & Matzke, 1983). Han and Mecholsky (1990) also found that WC–Co develops the Palmqvist crack even at very high loads of about 250 kg of weight during the indentation. It is interesting that the crack geometry can change when the indentation is followed by the fracture tests under which the Palmqvist cracks can grow and join under the indent into the critical half-penny crack (Han & Mecholsky, 1990).

Despite the fact that WC–Co cemented carbides show the Palmqvist cracking, the half-penny models might still be applicable to other hardmetals like TiC–TiN–Ni cermets with lower fracture toughness than WC–Co and further research in this area is expected (Spiegler, Schmauder, & Sigl, 1990). Binderless WC polycrystals exhibit the half-penny cracking under the indenter that indicates that there should be some critical minimal amount of the binder phase in WC–Co at which the crack changes its geometry from Palmqvist to half-penny (Warren & Matzke, 1983). Nanograined hardmetals might also have half-penny cracking as their fracture toughness is at the low boundary of the range (Jia, Fischer, & Gallois, 1998), though no conclusive study is reported in this area and both the WM-SWMC and the half-penny models are often applied to the calculation of the fracture toughness of these materials from Palmqvist test without validation of the models by the direct measurement of the critical stress intensity factor K_{1C} (Fang, Wang, Ryu, Hwang, & Sohn, 2009).

1.10.3.3 Dependencies and Correlations of Fracture Toughness

The values of the fracture toughness K_{1C} of WC–Co cemented carbides lie in the range of 5–26 MPa m$^{1/2}$ when either measured by bending, or calculated from the Exner crack resistance W on the Palmqvist test (Almond, 1983; Bolton & Keely, 1983; Bonache, Salvador, Busquets, et al., 2011; Chermant & Osterstock, 1976; Fang, 2005; Fang, Wang, Ryu, Hwang, & Sohn, 2009; Godse, Gurland, & Suresh, 1988; Godse & Gurland, 1988; Gurland, 1988; Han & Mecholsky, 1990; Jia, Fischer, & Gallois, 1998; Mukhopadhyay & Basu, 2011; Nakamura & Gurland, 1980; Osterstock & Chermant, 1983; Pickens & Gurland, 1978; Prakash, 1993; Richter & Ruthendorf, 1999; Roebuck & Almond, 1988; Warren & Matzke, 1983; http://www.allaboutcementedcarbide.com/). The fracture toughness increases with decreasing volume fraction of the carbide phase V_V and increasing the *mlicc* d_{WC} with maximal values on the high binder alloys and coarse grains of the carbide phase. In other words, the fracture toughness depends on the volume fraction V_V and the *mlicc* d_{WC} in an opposite trend than the hardness (**Figure 5**) (Fang, Wang, Ryu, Hwang, & Sohn, 2009; Jia, Fischer, & Gallois, 1998; Roebuck & Almond, 1988; Warren & Johannesson, 1984b). The nanograined WC–Co hardmetals produced by the new technologies with variety of growth inhibitors promise very high hardness with still reasonable or surprisingly high fracture toughness (**Figure 5**) when it is measured by the Palmqvist test and calculated under unverified assumption of applicability of the WM-SWMC model (20) to the nanoscale (Fang, Wang, Ryu, Hwang, & Sohn, 2009).

1.10.3.3.1 Dependencies on Geometry

Two correlations of the fracture toughness K_{1C} are observed simultaneously when the shape of the WC crystals is kept unchanged on WC-based cemented carbides (**Figure 6**) (Bolton & Keely, 1983; Chermant & Osterstock, 1976; Sigl & Fischmeister, 1988; Slesar, Dusza, & Parilak, 1986) with TiC-based cermets exhibiting similar dependencies (Komak & Novak, 1986). On one hand, the fracture toughness K_{1C} correlates either linearly or close-to-linearly versus the *mlibp* λ either for a variety of the *mlicc* d_{WC} (Gurland, 1988; Sigl & Fischmeister, 1988; Slesar, Dusza, & Parilak, 1986), or for each fixed value of the grain diameters D_{WC} of the carbide crystals (Chermant & Osterstock, 1976) regardless of the volume fraction V_V (**Figure 6(a)**). On the other hand, K_{1C} monotonously decreases with the contiguity of the carbide crystals G for a variety of the volume fractions V_V and *mlicc* d_{WC} (**Figure 6(b)**). The observed difference between the values of the fracture toughness and microstructure parameters from different sources is most likely explained by the possible chemical variations of the alloys, methods of the fracture toughness preparation and measurement, as well as by the tool precision and methods of the microstructure analysis.

Changing the shape of WC crystals to flatter triangular prism for the fixed *mlicc* d_{WC} (Shatov & Firstov, 1995; Shatov, Firstov, & Shatova, 1998) breaks the correlation versus the contiguity G, but preserves the

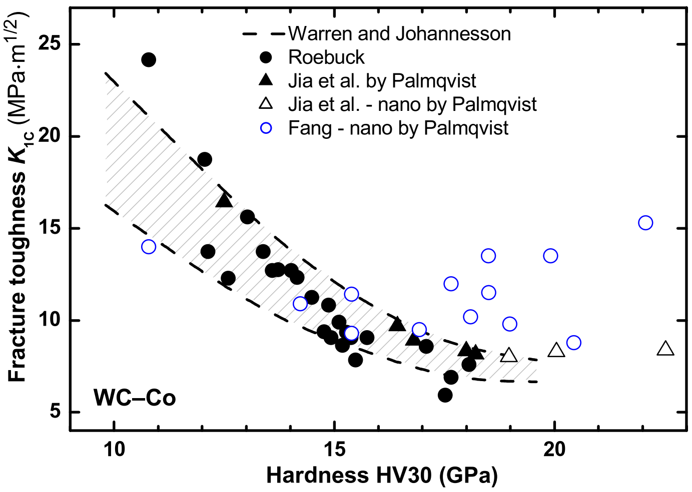

Figure 5 Fracture toughness K_{1C} decreases with the increase of the hardness for conventional WC–Co hardmetals (reproduced from Figure 13 in Roebuck and Almond (1988) with permission from Maney Publishing www.maney.co.uk/journals/imr and www.ingentaconnect.com/content/maney/imr; Figure 8 in Jia, Fischer and Gallois (1998) with permission from Elsevier), but nanograined WC–Co with a variety of growth inhibitors promise higher fracture toughness at very high hardness (reproduced from Figure 8 in Jia, Fischer, and Gallois (1998) with permission from Elsevier; Figure 8 in Fang, Wang, Ryu, Hwang and Sohn (2009) with permission from Elsevier.)

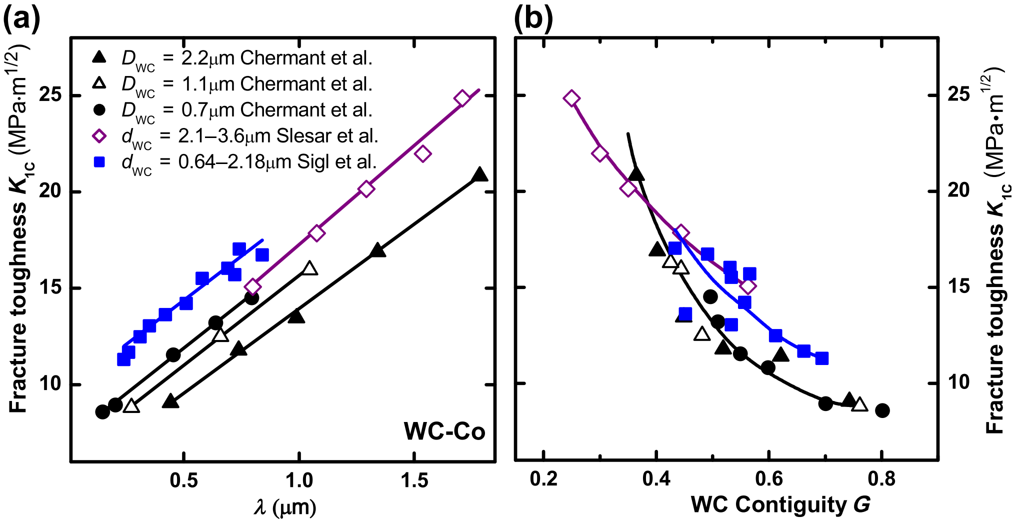

Figure 6 The correlation of the fracture toughness K_{1C} with the mean linear intercept of the binder phase (*mlibp*) λ (a) and with the carbide crystals contiguity G (b) of WC–Co cemented carbides with mean diameters of WC crystals D_{WC} of 0.7, 1.1, and 2.2 μm and volume fraction of the binder phase between 5 and 37 vol% (reproduced from Figures 12 and 14 in Chermant and Osterstock (1976) with kind permission from Springer Science+Business Media B.V.); with the mean linear intercepts of carbide crystals (*mlicc*) from 2.1 to 3.6 μm and volume fraction of the binder phase between 13 and 36 vol% (reproduced from Figure 2 in Slesar, Dusza, and Parilak (1986) with permission from Taylor & Francis Group LLC – Books.), and the *mlicc* d_{WC} from 0.64 to 2.18 μm and volume fraction of the binder phase between 9.8 and 24.7 vol%. (Drawn from Tables 1 and 2 in Sigl and Fischmeister (1988) with permission from Elsevier.)

correlation versus the *mlibp* λ (**Figure 7**) (Shatov, Ponomarev, & Firstov, 2008). The fracture toughness K_{1C} increases with the contiguity G when the volume fraction V_V is fixed while the shape of WC is changing (Shatov, Ponomarev, & Firstov, 2008) that is an opposite change versus the contiguity G when the shape of WC is not changed and the fracture toughness K_{1C} decreases with simultaneous increase of the volume fraction V_V and contiguity G of carbide crystals (**Figure 6(b)**). This experiment indicates that the contiguity G does not affect K_{1C} and should not be used as a parameter in correlations of the fracture toughness. Moreover, the shape of WC crystals also does not affect the fracture toughness directly as the fracture toughness K_{1C} is determined by the *mlibp* λ (**Figure 7(a)**) (Shatov, Ponomarev & Firstov, 2008). Hence, the fracture toughness K_{1C} can only correlate versus the mean linear intercepts of the binder phase and of the

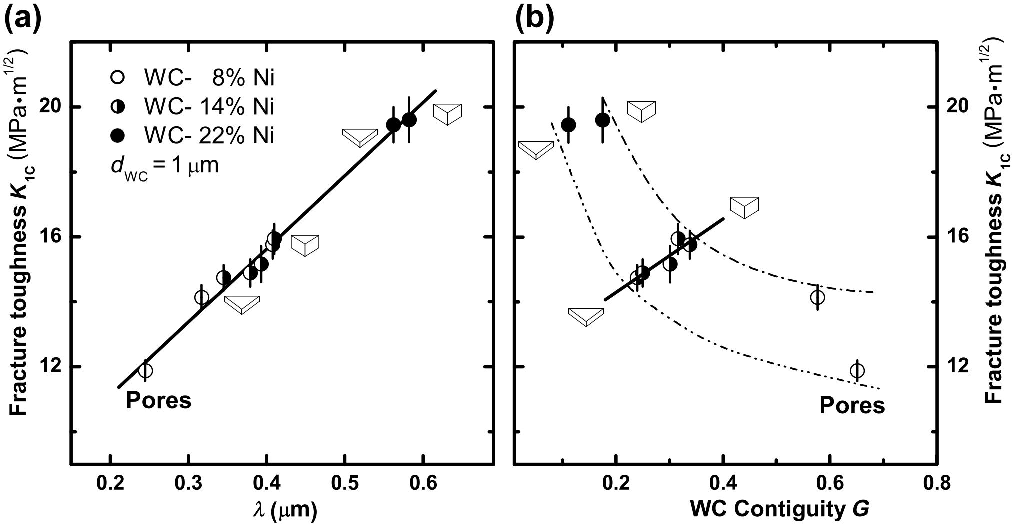

Figure 7 The correlation of the fracture toughness K_{1C} versus the *mlibp* λ (a) and versus the contiguity G of WC crystals (b) on WC–Ni cemented carbides with different shape equiaxiality of WC crystals P_{WC} and different binder content. Reproduced from Figure 4 in Shatov, Ponomarev and Firstov (2008) with permission from Elsevier.

carbide crystals whereas all the other geometrical parameters can affect the fracture toughness only indirectly through the stereological relation between the microstructure parameters (Exner, 1970; Exner, 1979; Exner, 1983; Exner & Fischmeister, 1966; Gurland, 1958; Gurland, 1959; Gurland, 1963a; Gurland, 1963b; Underwood, 1968),

$$\frac{\lambda}{d_{\mathrm{WC}}} = \frac{1 - V_{\mathrm{V}}}{V_{\mathrm{V}} \cdot (1 - G)} \tag{22}$$

coupled with the dependence of the contiguity G on the shape of WC crystals (Shatov, Ponomarev, & Firstov, 2008; Shatov, Ponomarev, Firstov, & Warren, 2006).

1.10.3.3.2 Dependencies on Chemistry, Defects, and Residual Stresses

The value of the fracture toughness exhibits a maximum around the stoichiometric content of the carbon in WC–Co alloys, whereas further deviation from the stoichiometric content and introduction of either η-phase or free-graphite phase causes the fracture toughness to drop rather quickly (Almond & Roebuck, 1988; Bolton & Keely, 1983; Exner, 1983; Roebuck & Almond, 1988). The fracture toughness is usually reduced by coarse pores (Exner, 1983; Laptev, Ponomarev, & Ochkas, 2001). However, presence of fine pores of up to 5% does not break the correlation versus λ on WC–Ni alloys (**Figure 7(a)**) (Shatov, Ponomarev, & Firstov, 2008). The fine pores do not affect directly the fracture toughness, but reduce the mean linear intercepts of the phases that cause the reduction of the fracture toughness. Fracture toughness increases on alloys with abnormally grown grains (AGG) due to the increase of the *mlibp* (Li, T., Li, Q., Fuh, et al., 2007).

Substitution of Co with Co–Ni mixture as the binder phase causes the fracture toughness of WC-based cemented carbides to increase from about 19 MPa $\mathrm{m}^{1/2}$ on WC–10 wt% Co to its maximum of about 31 MPa $\mathrm{m}^{1/2}$ at around 70 wt% Co + 30 wt% Ni on WC–10 wt% (Co,Ni), and further decrease down to about 20 MPa $\mathrm{m}^{1/2}$ on WC–10 wt% Ni, though it is not clear whether the mean linear intercepts of phases were kept unchanged in these experiments (Prakash, 1993; Warren & Matzke, 1983). Similar results with slightly less striking maximum value is reported for WC–15 wt% (Co,Ni) (Sigl & Exner, 1989). As contrast, other similar experiments show no significant change of the fracture toughness on WC–(Co,Ni) (Roebuck & Almond, 1988). Partial or full substitution of Co with Ni binder phase increases the fracture toughness of Ti(C,N)-based cermets (Ettmayer, Kolaska, Lengauer, & Dreyert, 1995). Substitution of the Co-binder phase by the mixtures like Fe–Co–Ni, Ni–Cr–Mo, Ni–Al, Ni–Cr–Mo–Al, or other combination usually decreases or in some cases produce comparable fracture toughness of WC-based cemented carbides (Almond & Roebuck, 1988; Bolton & Keely, 1983; Guilemany, Sanchiz, Mellor, Llorca, & Miguel, 1994; Prakash, 1993; Tracey, 1992). Partial or complete substitution of Co binder with nanograined ceramics $\mathrm{ZrO_2}$ decreases the fracture toughness in comparison to WC–Co (Mukhopadhyay & Basu, 2011; Mukhopadhyay, Chakravarty, & Basu, 2010). Fracture toughness is reduced by the addition or the substitution of WC with/by other carbides like TiC, TaC, NbC, (Ti,V)C with TiC-based cemented carbides showing the lowest fracture toughness (Bolton & Keely, 1983; Doi, 1986; Gurland, 1988; Warren & Matzke, 1983). This makes the WC-based cemented carbides the best choice for the highest fracture toughness and hardness combination among hardmetals.

Solid solution of carbide and other elements in the binder phase are believed to strengthen the binder phase and increase the fracture toughness of hardmetals (Jia, Fischer, & Gallois, 1998; Sigl & Fischmeister, 1988), but no direct conclusive evidence is reported as this state of the microstructure is usually accompanied by other microstructure and chemistry changes like the decrease of the mean linear intercepts and/or occurrence of the third phase of the growth inhibitors. There are also no conclusive results on how the martensitic transformation of Co from fcc to hcp crystalline lattice affects the fracture toughness. Solid solution of Ti in the binder phase of two-phase WC–Ni alloys that causes the change of WC shape to flatter triangular prism does not affect the fracture toughness directly because the correlation of the fracture toughness versus the *mlibp* λ is preserved (**Figure 7**) (Shatov, Ponomarev, & Firstov, 2008). Further research is also appropriate for the effects of the carbide–carbide contacts and carbide–binder interfaces especially with a variety of additional elements segregating at the carbide–binder interface.

The residual compressive thermal stress on the carbide crystals is found to be responsible for the increase of the fracture toughness of WC–Co alloys by up to about 1 MPa $\mathrm{m}^{1/2}$ when the transgranular fracture of the carbide phase C is prevailing over the intergranular fracture of the carbide phase C/C at larger *mlicc* d_{WC} of about 5 μm, but it has no significant effect at lower values of d_{WC} where the carbide phase is predominantly fractured by the intergranular mode C/C (Cutler & Virkar, 1985). On the other hand, the large residual tensile thermal stress on the binder phase causes the binder regions to deform plastically even at very low external compressive stresses that contributes to the elastic strain energy absorption of the alloy and might constitute yet another reason for the high toughness of cemented carbides[8] (Paggett, Krawitz, Drake, et al., 2006; Paggett, Krawitz, Drake, et al., 2007).

1.10.3.4 Models of Fracture Toughness

Modeling of the fracture toughness faces the challenge of estimating the fracture conditions and energies on top of modeling the fracture surface area fractions. It needs to account for the two fracture steps separated in space and time when the brittle carbide phase is broken ahead of the crack tip, followed by the ductile fracture of the multiple ligaments of the binder phase right behind the crack tip and apparently under different stress conditions. Many aspects of the crack propagation have to be taken into account that include the estimation of the size of the plastic zone ahead of the crack, energy for the brittle fracture of the carbide phase, yield stress conditions for the binder layers that are surrounded by the rigid carbide phase, strengthening of the binder phase by tungsten and carbon dissolved in the binder, RTS of the phases, strain hardening of the binder during the plastic deformation, void formation and growth, followed by the condition for the final rupture of the binder ligaments (Gurland, 1988; Roebuck & Almond, 1988; Sigl, Exner, & Fischmeister, 1986; Sigl & Fischmeister, 1988).

The critical strain energy release rate G_{1C} is usually used in the models of fracture toughness instead of the critical stress intensity factor K_{1C} to calculate the energy release contribution from the sequence of the fracture events on the microlevel. The values of K_{1C} and G_{1C} are related through the following equation of the fracture mechanics for the plane strain condition.

$$(K_{1C})^2 = G_{1C}\cdot E/\left(1-\nu^2\right) \tag{23}$$

Alternatively, for the plane stress condition, this relation is described by the following equation.

$$(K_{1C})^2 = G_{1C}\cdot E \tag{24}$$

where E is the elastic modulus and ν is the Poisson's ratio of the alloy (Irwin, 1957; Orowan, 1948).

The critical strain energy release rate G_{1C} is the energy that is dissipated during formation of the area unit of the fracture surface. Assuming that each fracture mode contributes independently, the critical strain energy release rate G_{1C} can be expressed as the sum of the energy for creation of two free surfaces and the energy dissipation of each fracture mode (Gurland, 1988; Roebuck & Almond, 1988; Sigl, Exner, & Fischmeister, 1986; Sigl & Fischmeister, 1988).

$$G_{1C} = \sum_{i=\mathrm{C,C/C,B/C,B}} (2\cdot\gamma_\mathrm{i} + w_\mathrm{i})\cdot A_\mathrm{A}^\mathrm{i} \tag{25}$$

where γ_i is the free surface energy, w_i is the effective surface fracture energy, and $\mathrm{A}_\mathrm{A}^\mathrm{i}$ is the fracture surface area fraction for each of the fracture modes in cemented carbides ($i=$ C, C/C, B/C, B).

The energy contribution $2\cdot\gamma_\mathrm{i}$ from formation of the free surface of the binder and the carbide phases is usually neglected due to their very low value of about 1 J m^{-2} in comparison to the fracture energy of WC–Co cemented carbides that is much higher at 10^2–10^3 J m^{-2} (Sigl, Exner, & Fischmeister, 1986; Sigl & Fischmeister, 1988). The effective surface fracture energy w_i is the energy of plastic deformation and rupture of the phase for the respective fracture mode. The energy of the plastic deformation and trans- and intergranular fractures of the WC carbide phase w_C and $w_\mathrm{C/C}$ is estimated at about

$$w_\mathrm{C} \approx w_\mathrm{C/C} \approx 50\ \mathrm{J\cdot m^{-2}} \tag{26}$$

---

[8] For more information on the effect of the residual thermal stress on toughness of cemented carbides, see Chapter 1.13 Mechanical Properties—Residual/thermal stress in hardmetals.

that is also significantly lower than the measured G_{1C} of WC–Co (Sigl, Exner, & Fischmeister, 1986; Sigl & Fischmeister, 1988). Therefore, the main contributor to the fracture toughness of the cemented carbides is the fracture of the binder phase and carbide–binder interfaces.

In general, the average surface energy of the plastic deformation and rupture of the binder phase $w_{B,B/C}$ can be calculated from the stress–strain dependence as an average integral of the stress σ_B by the displacement u of the binder until it fractures at the critical displacement u_f that is equal to the product of the volume of deformed binder per unit area of the fracture surface V_A and the average integral of the stress σ_B by the strain ε from 0 to its critical value ε_f at fracture of the binder layers (Gurland, 1988; Viswanadham, Sun, Drake, & Peck, 1981).

$$w_{B,B/C} = \int_0^{u_f} \sigma_B(u)\mathrm{d}u = V_A \cdot \int_0^{\varepsilon_f} \sigma_B(\varepsilon)\mathrm{d}\varepsilon \tag{27}$$

Neither the stress–strain dependence $\sigma_B(\varepsilon)$, nor the critical fracture strain ε_f can be easily calculated for the binder layers and binder ligaments at the carbide–binder interfaces from the microstructure of the cemented carbides. The volume per unit area of the fracture surface V_A of the deformed binder is equivalent to the average plastic zone size r_y and its value is also under discussion for the cemented carbides, but it is usually considered as being proportional and close to the *mlibp* λ.

Taking into account the complexity of the fracture process and rich variety of hard to measure parameters in the energy balance Eqns (25) and (27), many models make simplifying assumptions in attempt to identify the main contributor to the fracture toughness. The first simplifying decision is whether to consider the contribution of the fracture through the brittle carbide phase and along the carbide–binder interfaces in addition to the ductile fracture through the binder phase. The second decision is whether to take into account the difference between the fracture surface area fractions versus the volume fractions of the phases.

1.10.3.4.1 Models Based on the Fracture through the Binder Phase Only

1.10.3.4.1.1 Pickens and Gurland (PG) Simple Model of Fracture through the Binder Phase

The PG model (Pickens & Gurland, 1978) assumes that the crack extension proceeds when the size of the heavily deformed region ahead of the crack tip is comparable to the size of the unbroken binder ligaments that is equal to the *mlibp* λ. Not even considering the fracture surface area fractions and assuming the Hall–Petch type relation (Hall, 1952; Petch, 1953) for the yield stress of the binder phase σ_y^B, ignoring the contribution from other fracture modes, the PG model arrives at a very simple relation of the critical strain energy release rate G_{1C} versus the *mlibp* λ.

$$G_{1C}^{PG} = \alpha \cdot \sigma_y^B \cdot \lambda \tag{28}$$

where α is an experimentally determined constant factor.

1.10.3.4.1.2 Godse and Gurland (GG) Model of Contiguous Volume Fraction of the Fracture through the Binder

The GG model (Godse & Gurland, 1988) enhances the PG model by assuming that the carbide phase is broken before the crack propagation and therefore the carbide phase does not carry any load in the process zone around the crack tip. The GG model suggests that the yield stress of the binder phase σ_y^B in Eqn (28) should be reduced proportionally to the contiguous volume fraction of the carbide phase $V_V\,G$.

$$G_{1C}^{GG} = \alpha \cdot \sigma_y^B \cdot (1 - V_V \cdot G) \cdot \lambda \tag{29}$$

where α is an experimentally determined constant factor, G is the contiguity of the carbide crystals in cemented carbides, and the binder yield stress σ_y^B is determined by Hall–Petch-type relation (Hall, 1952; Petch, 1953) versus the *mlibp* λ.

1.10.3.4.1.3 Viswanadham, Sun, Drake and Peck (VSDP) Model of Fracture Surface Area through the Binder

The VSDP model (Viswanadham, Sun, Drake, & Peck, 1981) measures the fracture surface area fraction through the binder phase A_A^B by means of Auger-electron spectroscopy, but ignores the contribution from other fracture modes. Assuming that the plastic zone size r_y is proportional to the *mlibp* λ, whereas the integral in Eqn (27) being proportional to the yield stress σ_y^B multiplied by the fracture strain ε_f of the binder phase, the VSDP model arrives at the simple relation.

$$G_{1C}^{VSDP} = \alpha \cdot \lambda \cdot A_A^B \cdot \int_0^{\varepsilon_f} \sigma_B(\varepsilon) d\varepsilon = \alpha \cdot \sigma_y^B \cdot \varepsilon_f \cdot A_A^B \cdot \lambda \tag{30}$$

where α is an experimental constant. The binder yield stress σ_y^B is determined by Hall–Petch-type relation (Hall, 1952; Petch, 1953) versus the *mlibp* λ.

Apparently, the PG, GG, and VSDP models based on the fracture of only the binder phase predict zero fracture toughness for the binderless cemented carbides that contradicts to the experiment, where the extrapolation of the straight lines toward $\lambda = 0$ gives nonzero values for K_{1C} of polycrystalline WC (**Figure 6(a)**). Therefore, these models can only be considered as a rough initial approximation for the fracture toughness.

1.10.3.4.2 Models Based on the Fracture through the Carbide and Binder Phases

1.10.3.4.2.1 Nakamura and Gurland (NG) Model of Fracture through the Carbide and Binder Phases

The NG model (Nakamura & Gurland, 1980) attempts to take into account the contribution from the fracture of the carbide phase in addition to the fracture through the binder phase. The NG model assumes that the fracture surface areas correspond to the cross-section surface areas of the phases and that the structure of the cemented carbide can be simplistically viewed after Paul (1960) as the cubically shaped isolated noncontiguous carbide crystals imbedded at the constant distance between each other to calculate the volume of deformation from the stereological parameters of microstructure.

The NG model makes an extra effort to account for the contiguity G of the carbide crystals in the real microstructure and to convert the *mlibp* from the noncontiguous value in the model microstructure λ' to the actual value of λ. Further assuming that the plastic zone size r_y is determined by the *mlibp* λ and that the total energy of the fracture through the carbide phase and along the carbide–binder interfaces can be expressed by an effective fracture surface energy γ_{eff}, the NG model arrives at the equation.

$$G_{1C}^{NG} = 2 \cdot \gamma_{eff} \cdot V_V^{2/3} + \alpha \cdot \lambda \cdot V_V^{2/3} \cdot \left(1 - V_V^{2/3}\right) \cdot (1 - V_V)^{-1} \cdot \int_0^{\varepsilon_f} \sigma_B(\varepsilon) d\varepsilon \tag{31}$$

where α is a constant factor.

Both γ_{eff} and the integral in the second term remain undefined in Eqn (31). Moreover, the simplistic modeling of the microstructure by noncontiguous totally isolated carbide crystals seems to be too rough for the conventional cemented carbides with rather high contiguity G. Therefore, the NG model only allows doing rough analysis of the dependencies of the fracture toughness on the microstructure parameters. The comparison with the experiment shows that the total effective fracture surface energy γ_{eff} in the NG model linearly decreases with the volume fraction of the carbide phase V_V from about 200 J m^{-2} at 60 vol% of the carbide phase down to about 50 J m^{-2} at 90 vol% of the carbide phase and the minimal extrapolated value for the binderless WC around 10 J m^{-2}. The integral inside the second term multiplied by the constant α in Eqn (31) decreases from 12×10^8 J m^{-3} at 60 vol% of the carbide phase down to about 2×10^8 J m^{-3} at 90 vol% of the carbide phase for WC–Co (Nakamura & Gurland, 1980).

1.10.3.4.2.2 Modification of NG Model by Ravichandran by Using the PG Model

The Ravichandran model (Ravichandran, 1994) modifies the NG model (Nakamura & Gurland, 1980) by taking into account both the contribution of the fracture through the carbide phase introduced by the NG model and estimated by Eqn (26) (Sigl, Exner, & Fischmeister, 1986; Sigl & Fischmeister, 1988) and the simplified contribution of the fracture through the binder phase developed by the PG model in Eqn (28).

The Ravichandran model reuses the simplistic model for the microstructure with fully isolated noncontiguous carbide crystals of cubic shape imbedded at the constant distance from each other developed in the NG model. No effort is made to introduce the contiguity G of the carbide crystals into consideration in contrast to the NG model. Therefore, the Ravichandran model uses the noncontiguous mean linear intercept of the binder phase λ' instead of the actual *mlibp* λ used by the NG model. These mean linear intercepts of the binder phase are related through the following stereological equation.

$$\lambda' = \lambda \cdot (1 - G) = d_{\mathrm{WC}} \cdot \frac{1 - V_{\mathrm{V}}}{V_{\mathrm{V}}} \tag{32}$$

Arbitrary assuming that the relative contributions of the fracture through the carbide and binder phases are equal to their respective volume fractions by essentially neglecting both the contribution of the fracture along the carbide–binder interfaces and the difference between the fracture surface area fractions and the volume fraction of the phases, the Ravichandran model arrives at the following relation for the critical strain energy release rate of the cemented carbide.

$$G_{1\mathrm{C}}^{\mathrm{R}} = V_{\mathrm{V}} \cdot G_{1\mathrm{C}}^{\mathrm{C}} + \alpha \cdot (1 - V_{\mathrm{V}}) \cdot \sigma_{\mathrm{y}}^{\mathrm{B}} \cdot \lambda' \tag{33}$$

where α is an experimental constant, $\sigma_{\mathrm{y}}^{\mathrm{B}}$ is the flow stress of the binder phase, and $G_{1\mathrm{C}}^{\mathrm{C}}$ is the critical strain energy release rate of the carbide phase taken from Eqn (26).

The Ravichandran model (33) does look simpler than the NG model (31), but essentially still depends on the same yield stress $\sigma_{\mathrm{y}}^{\mathrm{B}}$ of the binder. The Ravichandran model calculates $\sigma_{\mathrm{y}}^{\mathrm{B}}$ by using a non-Hall–Petch relation with dependence on both the *mlicc* d_{WC} and on the noncontiguous *mlibp* λ'.

$$\sigma_{\mathrm{y}}^{\mathrm{B}} = \sigma_0^{\mathrm{B}} \cdot \left[1 + \frac{0.577 \cdot d_{\mathrm{WC}}}{3 \cdot \lambda'}\right] \tag{34}$$

where σ_0^{B} is the bulk yield stress of the binder phase.

Applicability of the non-Hall–Petch relation (34) instead of the conventional Hall–Petch relation (Hall, 1952; Petch, 1953) to the hardmetals seems to be rather questionable and does not have adequate experimental confirmation for hardmetals. According to the stereological relation (32), the ratio of d_{WC}/λ' is a function of the volume fraction V_{V} that makes the $\sigma_{\mathrm{y}}^{\mathrm{B}}$ calculated by Eqn (34) to be purely dependent on the volume fraction V_{V} and not on the size of the binder phase regions that also contradicts to many experimental observations and conventional view on the yield stress of the binder phase. Furthermore, ignoring the contiguity and usage of the noncontiguous *mlibp* λ' instead of λ lacks reasoning for the conventional hardmetals that exhibit high contiguity values.

Nevertheless, the Ravichandran model of Eqn (33) gives roughly valid direction for the dependence of the fracture toughness of the alloy. Therefore, it seems that the Ravichandran model can also be used in the manner similar to the NG model for the rough analysis of the dependencies of the fracture toughness on the microstructure parameters and fracture toughness of the phases.

1.10.3.4.2.3 Mari, Bolognini, Feusier, Cutard, Viatte and Benoit (MBFCVB) Adaptation of Ravichandran Model for Analysis of Phase Properties

Mari, Bolognini, Feusier, et al. (2003) improve the Ravichandran model (Ravichandran, 1994) by using the *mlibp* λ in place of the noncontiguous *mlibp* λ' in Eqn (33).

$$G_{1\mathrm{C}}^{\mathrm{MBFCVB}} = V_{\mathrm{V}} \cdot G_{1\mathrm{C}}^{\mathrm{C}} + \alpha \cdot (1 - V_{\mathrm{V}}) \cdot \sigma_{\mathrm{y}}^{\mathrm{B}} \cdot \lambda \tag{35}$$

Assuming the plane stress condition (24) for the fracture toughness of the alloy and phases, the MBFCVB model arrives at the dependence of the fracture toughness of the alloy on the fracture toughness of the carbide phase $K_{1\mathrm{C}}^{\mathrm{C}}$ and the effective flow stress of the binder phase $\sigma_{\mathrm{y}}^{\mathrm{B}}$.

$$K_{1\mathrm{C}}^{\mathrm{MBFCVB}} = \left[V_{\mathrm{V}} \cdot E \cdot \left(K_{1\mathrm{C}}^{\mathrm{C}}\right)^2 / E_{\mathrm{C}} + \alpha \cdot (1 - V_{\mathrm{V}}) \cdot E \cdot \sigma_{\mathrm{y}}^{\mathrm{B}} \cdot \lambda\right]^{1/2} \tag{36}$$

where E and E_C are the Young's elastic moduli of the alloy and the carbide phase, respectively. The Young's modulus of the alloy E is calculated by the Paul's relation (Paul, 1960) from the Young's elastic moduli of the carbide E_C and binder E_B phases, respectively.

$$E = E_B\cdot\left(E_B + (E_C - E_B)\cdot V_V^{2/3}\right)\Big/\left(E_B + (E_C - E_B)\cdot V_V^{2/3}\cdot\left(1 - V_V^{1/3}\right)\right) \tag{37}$$

Application of the MBFCVB model (36) offers rough qualitative analysis of the dependencies of the fracture toughness of the carbide phase and the effective flow stress of the binder phase σ_y^B on the microstructure parameters by finding the best fit of the model calculation to the measured fracture toughness of the alloy and picking the value for $\alpha = 2$. The reported dependences of the MBFCVB model applied to TiMoCN-based cermets are similar to the observations of the NG model on WC–Co. Both the fracture toughness of the carbide phase and the effective flow stress of the binder phase σ_y^B decrease with the decrease of the volume fraction of the carbide phase V_V, whereas the overall increase of the total fracture toughness of the alloy is mainly due to the volume effect of the binder phase (Mari, Bolognini, Feusier et al., 2003).

Nevertheless, despite the effort to take the fracture of the carbide phase into account, the NG, the Ravichandran and the MBFCVB models still make numerous simplifications about the fracture path and process and are essentially based on the oversimplified noncontiguous model for the microstructure of hardmetals that limits their applicability to only qualitative analysis of the fracture toughness.

1.10.3.4.3 Sigl, Exner and Fischmeister (SEF) Comprehensive Model of Energy Balance of All the Fracture Modes

The SEF semiempirical model (Sigl, Exner, & Fischmeister, 1986; Sigl & Exner, 1987; Sigl & Fischmeister, 1988) is the most comprehensive energy balance calculation of all the fracture modes for WC–Co cemented carbides. The SEF model is based on the Sigl and Exner empirical correlations of the fracture surface area fractions A_A^i for the fracture modes (2)–(6) and it does take into account the fracture energy of the WC phase w_C and $w_{C/C}$ estimated at about 50 J m^{-2} by Eqn (26) into the energy balance (25).

$$G_{1C}^{SEF} = \left(\bar{r}_B\cdot A_A^B + \bar{r}_{B/C}\cdot A_A^{B/C}\right)\cdot\bar{\sigma}_f^B + \left(A_A^{C/C} + A_A^C\right)\cdot w_C \tag{38}$$

where $\bar{r}_B$ and $\bar{r}_{B/C}$ are the mean half-size of the plastic zone of the fractured binder ligaments at the transgranular fracture of the binder phase B and along the carbide–binder interfaces B/C, respectively, whereas $\bar{\sigma}_f^B$ is the mean flow stress of the binder ligaments from plastic deformation and up to the formation and fracture of dimples.

The SEF model calculates the mean flow stress of the binder ligaments $\bar{\sigma}_f^B$ as a sum of the yield σ_y^B and the strain hardening σ_{sh}^B stresses of the binder ligaments.

$$\bar{\sigma}_f^B = \sigma_y^B + \sigma_{sh}^B \tag{39}$$

The yield stress is assumed to follow the Hall–Petch dependence (Hall, 1952; Petch, 1953) with the friction stress σ_0^B and the Hall–Petch strengthening factor K_B^{HP} for the binder phase.

$$\sigma_y^B = \sigma_0^B + K_B^{HP}\cdot\lambda^{-1/2} \tag{40}$$

The SEF model estimates the value of the friction stress at about $\sigma_0^B = 480$ MPa from the yield stress of Co–W–C alloy with the solid solution of W and C matching the solution in the binder phase that is determined by the magnetic saturation of WC–Co alloys (Roebuck, Almond, & Cottenden, 1984). The strengthening factor of the binder phase $K_B^{HP} = 1.35\ \text{MPa}\cdot\text{m}^{1/2}$ is calculated from the value of the Hall–Petch hardening factor of the binder phase $H_{Binder}^{HP} = 3.94\text{MPa}\cdot\text{m}^{1/2}$ in the LG model for hardness (Gurland, 1979; Lee & Gurland, 1978) by using the conventional relation between the yield stress and the hardness H.

$$\sigma_y \approx H/3 \tag{41}$$

Substitution of σ_0^B and K_B^{HP} into Eqn (40) gives the yield stress σ_y^B values between 2.2 and 3.7 GPa depending on the *mlibp* λ that decreases from 0.74 to 0.24 μm (Sigl, Exner, & Fischmeister, 1986; Sigl & Fischmeister, 1988).

The SEF model estimates the strain hardening of the Co-binder ligaments $\sigma_{\mathrm{sh}}^{\mathrm{B}}$ from assumption that the dimples have parabolic depth profile and that the fracture occurs when the stress reaches the saturation level, at which the dislocation has to slip through the saturated number of stacking faults in the binder ligament.

$$\sigma_{\mathrm{sh}}^{\mathrm{B}} \approx 4.7\ \mathrm{GPa} \tag{42}$$

Substitution of all the estimated values into Eqn (39) gives the mean flow stress of the binder ligaments $\overline{\sigma}_{\mathrm{f}}^{\mathrm{B}}$ in the range from 7.0 to 8.4 GPa for the *mlibp* λ that decreases from 0.74 to 0.24 μm (Sigl, Exner, & Fischmeister, 1986; Sigl & Fischmeister, 1988).

The value of the mean plastic zone half-size for B/C fracture $\overline{\mathrm{r}}_{\mathrm{B/C}}$ is empirically measured as a half depth of the shallow binder ligament dimple along the carbide–binder interface at about 0.05 μm. Calculation of the mean plastic zone half-size for the fracture through the binder phase $\overline{\mathrm{r}}_{\mathrm{B}}$ requires solving integral equations and detailed measurement of the distribution of the linear intercepts of the binder ligaments. The mean plastic zone size $2\cdot\overline{\mathrm{r}}_{\mathrm{B}}$ calculated by the SEF model never exceeds the *mlibp* λ and ranges between 0.236 and 0.593 μm for the *mlibp* λ between 0.24 and 0.74 μm. The value of $2\cdot\overline{\mathrm{r}}_{\mathrm{B}}$ is practically equal to λ at lower $\lambda < 0.3$ μm, but $2\cdot\overline{\mathrm{r}}_{\mathrm{B}}$ becomes visibly below λ with further increase of λ. Unfortunately, no empirical approximation for the dependence of $2\cdot\overline{\mathrm{r}}_{\mathrm{B}}$ on λ is provided by the SEF model.

The SEF model covers most of the processes of the fracture and provides viable explanation of the fracture toughness of WC–Co cemented carbides. Nevertheless, despite its comprehensiveness and thorough analysis of the deformation and crack propagation, the SEF model does not allow calculating the fracture toughness from the stereological parameters of the microstructure, but requires tedious empirical measurements of the mean half-sizes $\overline{\mathrm{r}}_{\mathrm{B}}$ and $\overline{\mathrm{r}}_{\mathrm{B/C}}$ of plastic zones for B and B/C fracture modes, respectively, in addition to the empirical measurement of the fracture surface area fractions $A_{\mathrm{A}}^{\mathrm{i}}$ by Eqns (2)–(6). Calculation of the approximated dependences of the plastic zone sizes could facilitate further analysis and extension of the SEF model to other materials.

1.10.3.4.4 Armstrong and Cazacu (AC) Model Based on Strength to Yield Stress Ratio

The AC model (Armstrong, 2011; Armstrong & Cazacu, 2006) approaches the problem of the fracture toughness modeling from an alternative side of the continuum fracture mechanics, where the plastic deformation ahead of the crack tip constitutes the main reason for the crack propagation. Instead of estimating the energies of the fracture modes, the AC model calculates the fracture toughness $K_{1\mathrm{C}}$ from the fracture mechanics relation for the precrack fracture stress σ_{f} and the critical crack size a_{C} by setting the geometry constant $Q = \pi$ in Eqn (49).

$$K_{1\mathrm{C}} = \sigma_{\mathrm{f}}\cdot(\pi\cdot a_{\mathrm{C}})^{1/2} \tag{43}$$

The AC model applies Bilby–Cottrell–Swinden model (Bilby, Cottrell, & Swinden, 1963) of the critical crack growth with an associated plastic zone ahead of the crack tip developed for the single-phase polycrystalline materials like aluminum and steels to the cemented carbides. The material failure is assumed to happen when the stress in the plastic zone ahead of the critical crack reaches the fracture stress σ_{f} of the material. In this case, the ratio of the fracture stress σ_{f} to the yield stress σ_{y} of the alloy linearly depends on the square root of the ratio of crack tip plastic zone size r_{y} to the crack size a_{C} for the plane strain condition.

$$\sigma_{\mathrm{f}} = \sigma_{\mathrm{y}}\cdot\left(8^{1/2}/\pi\right)\cdot\left(r_{\mathrm{y}}/a_{\mathrm{C}}\right)^{1/2} \tag{44}$$

Combining Eqns (43) and (44), the AC model arrives at the relation for the fracture toughness of cemented carbides versus the plastic zone size r_{y} and the yield stress of the alloy σ_{y}.

$$K_{1\mathrm{C}}^{\mathrm{AC}} = (8/\pi)^{1/2}\cdot r_{\mathrm{y}}^{1/2}\cdot\sigma_{\mathrm{y}} \tag{45}$$

The AC model estimates that the plastic zone size r_{y} is proportional to the *mlibp* λ. The yield stress σ_{y} of the alloy is calculated by using the relation (41) between the yield stress and hardness and using the LG model of hardness for the unchanged shape of WC crystals in WC–Co alloys (Gurland, 1979; Lee & Gurland, 1978).

$$H^{\mathrm{LG}} = \left(H_{\mathrm{WC}}^{0} + \frac{H_{\mathrm{WC}}^{\mathrm{HP}}}{\sqrt{d_{\mathrm{WC}}}}\right)\cdot V_{\mathrm{V}}\cdot G + \left(H_{\mathrm{Binder}}^{0} + \frac{H_{\mathrm{Binder}}^{\mathrm{HP}}}{\sqrt{\lambda}}\right)\cdot(1 - V_{\mathrm{V}}\cdot G) \tag{46}$$

where H^0_{WC} and H^0_{Binder} are the bulk hardness, whereas $H^{\mathrm{HP}}_{\mathrm{WC}}$ and $H^{\mathrm{HP}}_{\mathrm{Binder}}$ are the Hall–Petch factors for the carbide phase of WC and Co-binder phase, respectively.

The AC model assumes that the LG model can be simplified by using the stereological relation (22) and that the yield stress σ_{y} of the whole alloy has the Hall–Petch like dependence (Hall, 1952; Petch, 1953) versus the *mlibp* λ only with bulk yield stress of σ_0 and the Hall–Petch strengthening factor K^{HP}. This assumption allows the AC model to finally arrive at the relation for the fracture toughness of cemented carbides versus λ (Armstrong, 2011; Armstrong & Cazacu, 2006).

$$K^{\mathrm{AC}}_{\mathrm{1C}} = \alpha \cdot \lambda^{1/2} \cdot \left(\sigma_0 + K^{\mathrm{HP}} \cdot \lambda^{-1/2}\right) \tag{47}$$

Equation (47) has a limited applicability because the Hall–Petch relation versus λ for the yield stress σ_{y} of the alloy is only valid for a fixed volume fraction V_{V} of the carbide phase and the unchanged shape of WC crystals. Under these conditions, the contiguity G is kept unchanged due to the well-known experimental fact for the conventional hardmetals (Deshmukh & Gurland, 1986; Exner, 1979; Exner & Fischmeister, 1966; Lee & Gurland, 1978; Shatov, Ponomarev, Firstov, & Warren, 2006; Warren & Waldron, 1972).

$$G|_{\mathrm{WC\ Shape=const}} = f(V_{\mathrm{V}}) \tag{48}$$

Therefore, only in this case, the *mlicc* d_{WC} is proportional to λ according to the stereological relation (22) and the LG model (46) can be reduced to the single dependence on the *mlibp* λ similar to the hardness dependence on d_{WC} in the LG model for the fixed volume fraction V_{V} (Cha, Hong, Ha, & Kim, 2001; Jeong, Kim, Doh, et al., 2007; Kim, Massa, & Rohrer, 2007; Lee, Cha, Kim, & Hong, 2006; Milman, Chugunova, Goncharuck, Luyckx, & Northrop, 1997; Milman, Luyckx, & Northrop, 1999; Roebuck, 1995; Roebuck & Almond, 1988). As soon as the volume fraction V_{V} changes, a more complex dependence of the yield stress σ_{y} on all the microstructure parameters should be used instead as it is shown in the LG model for the hardness (46) (Gurland, 1979; Lee & Gurland, 1978). In this light, the more generic Eqn (45) together with the LG model (46) might be a better choice for the cemented carbides.

Furthermore, applicability of Eqn (44) and the fracture criteria of AC model to the cemented carbides lack both the experimental verification and physical interpretation in regard to the stress distribution, fracture modes and stages, as well as the multiligament fracture process discussed in Section 1.10.2, where the brittle fracture of the carbide phase ahead of the crack tip precedes the plastic deformation and fracture of the ductile binder ligaments behind the crack tip, rather than crack growth ahead of the crack tip by the plastic deformation of the binder phase only as it is postulated by the AC model based on the observations for the single-phase polycrystalline materials. Nevertheless, further exploration in this direction promises to reveal possible commonality between the hardmetals and other materials.

1.10.3.5 Outlook

Despite the progress in the development of the models, there still exists a challenge of calculating the fracture toughness from the microstructure parameters and properties of the constituent materials. The measurement of the fracture surface area fractions $A^{\mathrm{i}}_{\mathrm{A}}$ in Eqn (25) presents a challenge of its own and can only be calculated from the microstructure parameters for a limited set of WC–Co alloys through the Sigl and Exner empirical Eqns (2)–(6). There is no model that could explain the value of the fracture toughness of other hardmetals, its change for different binder phase, for multiphase hardmetals, for the changed shape of WC crystals, and for the presence of the microstructure defects like pores and AGG carbide crystals. In other words, the models are still far from being easily transferrable to other hardmetals, require a lot of phenomenological estimations and rely on the empirical data. The effect of the RTS of phases seems to be not fully understood.[9] It is not clear whether and how other elements dissolved in the binder phase and possibly present at the carbide–carbide boundaries and the carbide–binder interfaces can affect the fracture toughness. It is also interesting to see whether the models withstand the change of the microstructure to the nanosized carbide crystals or

---

[9] For more information on the effect of the residual thermal stress on toughness of cemented carbides, see Chapter 1.13 Mechanical Properties—Residual/thermal stress in hardmetals.

introduction of other mechanisms for the grain boundary slippage and cracking would be required as it is the case for the hardness.

1.10.4 Strength and Critical Defects

1.10.4.1 Strength and Critical Defects Definition

Strength is the stress on the surface of the specimen when the stress condition at the critical crack tip in the bulk or on the surface of the specimen causes the uncontrolled catastrophic propagation of the crack and failure of the specimen. Crack can be formed under the load either from the broken defect or from the broken weakest microstructure element(s). When the crack becomes critical, the defect or microstructure element(s) that caused the creation of the critical crack is referred to as *critical defect*.

Two types of strength are usually measured for hardmetals, namely the transverse rupture strength (TRS) that is measured by bending of the specimen (ISO 3327, ASTM B406) and the compressive strength that can be measured either under uniaxial (ISO 4506), or under hydrostatic load. The TRS of WC–Co cemented carbides usually lies in the range between 1 and 4.2 GPa, but in some cases can reach up to 4.5–5.0 GPa (Ettmayer, 1989; Fang, 2005; Fukatsu, Kobori, & Ueki, 1991; Gille, Szesny, Dreyer, et al., 2002; Gurland, 1988; Osterstock & Chermant, 1983; Prakash, 1993; Roebuck, 1979; Roebuck, 1995; Roebuck & Almond, 1988; http://www.allaboutcementedcarbide.com/), whereas the compressive strength lies in the range between 2.5 and 6 GPa, but can reach up to 7.1 GPa on low binder WC–Co with submicron grains (Aleksandrova, Bondarenko, & Loshak, 2005; Ettmayer, 1989; Prakash, 1995; http://www.allaboutcementedcarbide.com/).

1.10.4.2 Dependencies of Strength

1.10.4.2.1 Dependencies of Transverse Rupture Strength

1.10.4.2.1.1 Sensitivity to Defects and Residual Compressive Surface Stresses

The TRS is very sensitive to and decreases with the presence of defects like pores, impurity inclusions, free carbon and η-phase, carbide clusters, lakes of binder, AGG, and even excessively large carbide crystals that are located close to the outer surface of the specimen (Almond, 1983; Almond & Roebuck, 1977; Dusza, Parilak, & Slesar, 1987; Exner & Gurland, 1970; Fischmeister, 1983; Fukatsu, Kobori, & Ueki, 1991; Han & Mecholsky, 1990; Kursawe, Pott, Sockel, Heinrich, & Wolf, 2001; Laptev, Ponomarev, & Ochkas, 2001; Roebuck, 1995; Roebuck & Almond, 1988; Schreiner, Schmitt, Lassner, & Lux, 1984; Suzuki & Hayashi, 1975; Moyle & Kimmel, 1989). All these defects of microstructure are the cause for the wide scatter of the measured values of TRS. Weibull distribution and modulus (Weibull, 1951) are often used to characterize the width of the TRS scatter and can often reveal multimodal distribution associated with various types and sizes of the critical defects (Dusza, Parilak, & Slesar, 1987; Kursawe, Pott, Sockel, Heinrich, & Wolf, 2001).

The TRS is also sensitive to the surface preparation like grinding that can produce the RCSS and even introduce unwanted scratches on the surface. Presence of the scratches plays the role of externally introduced cracks that reduce the strength, whereas RCSS are believed to be a reason for the increase of the measured TRS of hardmetals (Exner, 1969; Exner, 1979; Roebuck, 1979; Roebuck, 1988; Roebuck & Almond, 1988; Exner & Gurland, 1970; Moyle & Kimmel, 1989). Therefore, polishing of the outer surface that undergoes the tensile stress in bending of the specimen or annealing is usually recommended to eliminate the scratches and RCSS for measuring TRS as the property of the material (Almond, 1983; Almond & Roebuck, 1977; Exner, 1979; Roebuck, 1979; Roebuck, 1988; Roebuck, 1995; Roebuck & Almond, 1988). Alternatively, it is also recommended to apply grinding in the longitudinal direction of the specimen so that the created scratches would be oriented perpendicular to the middle line of the highest stress on the outer surface during bending.

1.10.4.2.1.2 Gurland's Experiments for Dependencies on Geometry

It is well known after Gurland's experiments that the TRS initially increases with the *mlibp* λ, reaches the maximal value at around $\lambda^{\mathrm{maxTRS}} = 0.4–0.7\ \mu\mathrm{m}$, and subsequently decreases with further increase of λ on WC–Co with binder content of up to 25 wt% (**Figure 8**) (Exner & Gurland, 1970; Gurland, 1963a; Gurland, 1963b; Gurland, 1988; Gurland & Bardzil, 1955). The curve with maximum is already observed at relatively low binder content of about 12 wt% Co, whereas alloys with even lower binder contents that would have the *mlibp* close to the critical value of $\lambda^{\mathrm{maxTRS}}$ are not available for the study as these alloys would be required to have rather big carbide grains according to Eqn (22). Therefore, WC–Co alloys with binder content below 12 wt% Co only have the increasing

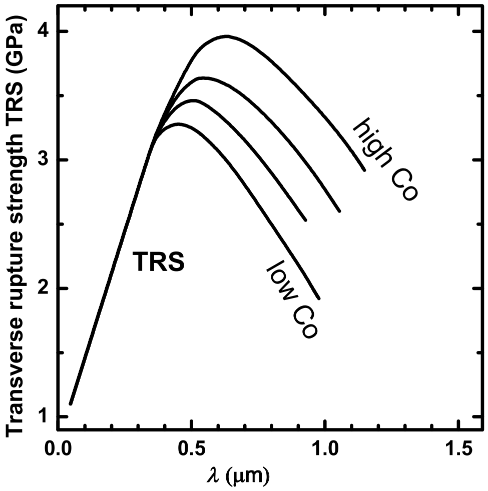

Figure 8 The correlation of the transverse rupture strength (TRS) versus the *mlibp* λ for a variety of the binder contents in WC–Co cemented carbides with low Co binder content corresponding to about 12 wt% Co, whereas the high Co binder content reaching 25 wt% Co. Reproduced from Figure 5(b) in Gurland (1988) with permission from Maney Publishing www.maney.co.uk/journals/imr and www.ingentaconnect.com/content/maney/imr.

part of the curve in **Figure 8** and do not reach the maximum TRS (Exner & Gurland, 1970; Gurland, 1963a; Gurland, 1963b; Gurland & Bardzil, 1955). Both the maximal value of TRS and the corresponding *mlibp* $\lambda^{\mathrm{maxTRS}}$, at which this maximal value is reached, increase with the binder content. The value of TRS is higher for the alloys with higher binder content that is equivalent to the lower volume fraction of the carbide phase V_V on the decreasing side of the dependence, but the volume fraction V_V makes almost no difference on the increasing side of the dependence (**Figure 8**). Alternatively, TRS also shows dependence with maximum against the binder content for the fixed size of the carbide grains that essentially reflects the same dependence due to the stereological relation (22) and the experimental correlation (48) (Osterstock & Chermant, 1983; Sailer, Herr, Sockel, et al., 2001).

1.10.4.2.1.3 Dependencies on Chemistry, Shape of WC, and Correlation versus Hardness

The value of TRS exhibits a maximum around the stoichiometric content of the carbon in WC–Co alloys (Exner, 1979; Exner, 1983; Exner & Gurland, 1970; Fischmeister, 1983; Gurland, 1988; Roebuck & Almond, 1988). Partial substitution of Co with Co–Ni mixture as the binder phase slightly increases TRS at first with further decrease on WC–Ni alloys (Exner, 1983). Substitution of the Co-binder phase by the mixtures like Fe–Co–Ni, Ni–Cr–Mo, Ni–Al, Ni–Cr–Mo–Al, or other combination usually decreases, but in some cases increases TRS in comparison to WC–Co (Almond, 1983; Prakash, 1993; Sailer, Herr, Sockel, et al., 2001). TRS of WC-based cemented carbides can increase as a result of the binder hardening and reinforcement by nanoparticle precipitation in the binder phase (Konyashin, Schafer, Cooper, et al., 2005). Partial or complete substitution of Co binder with nanograined ceramics ZrO_2 produces TRS comparable to WC–Co (Mukhopadhyay, Chakravarty, & Basu, 2010; Mukhopadhyay & Basu, 2011). TRS is reduced by addition or substitution of WC with/by other carbides like TiC, TaC, NbC, and (Ti,V)C (Almond, 1983). Change of the shape of WC crystals to flatter triangular prism increases TRS on WC–Ni cemented carbides (Shatov, Ponomarev, & Firstov, 2006). In general, the TRS tends to either decrease or exhibit a maximum versus the hardness on a variety of hardmetals (**Figure 9**) (Almond, 1983; Fang, 2005).

1.10.4.2.1.4 Dependencies of Compressive Strength

The compressive strength reflects the ability of the material to sustain the compressive deformation in the bulk of the material and in many respects, its dependence on the microstructure parameters follows the dependence of the hardness (Aleksandrova, Bondarenko, & Loshak, 2005; Almond, 1983; Dusza, Parilak, Diblk, & Slesar, 1983; Ettmayer, 1989; Exner & Gurland, 1970; German, Smid, Campbell, Keane, & Toth, 2005; Gurland, 1979; Lee & Gurland, 1978; Roebuck & Almond, 1988). The compressive strength is not as sensitive to the small microstructure defects as TRS. The compressive strength increases with the increase of the volume fraction V_V and with the decrease of the mean linear intercepts of the phases d_{WC} and λ. Both carbide and

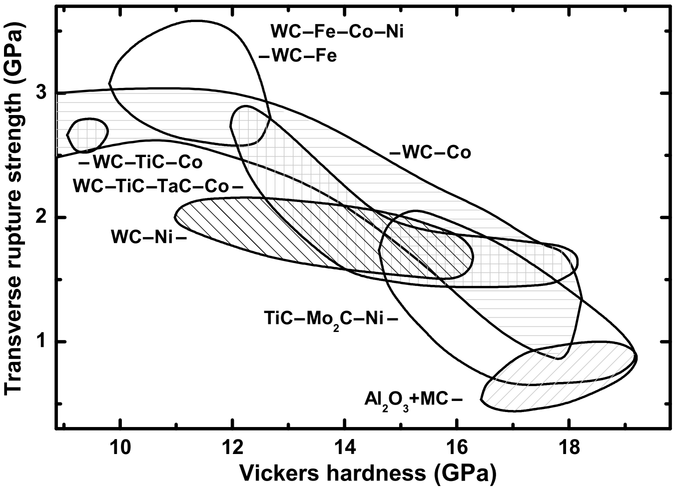

Figure 9 The correlation of the transverse rupture strength (TRS) versus Vickers hardness on a variety of hardmetals. Reproduced from Figure 3 in Almond (1983) with kind permission from Springer Science+Business Media B.V.

binder phases undergo a significant plastic deformation by dislocations slip and pile ups, possible Co-binder lattice martensitic transformation from fcc to hcp, followed by the microcracking along the carbide–carbide boundaries and through the carbide grains that eventually causes the failure of the material (Aleksandrova, Bondarenko, & Loshak, 2005; Dusza, Parilak, Diblk, & Slesar, 1983; Lee & Gurland, 1978; Roebuck & Almond, 1988; Rowcliffe, Jayaram, Hibbs, & Sinclair, 1988; Vasel, Krawitz, Drake, & Kenik, 1985).

1.10.4.3 Models of TRS Based on the Critical Defects and Fracture Mechanics

Most of the research and modeling is devoted to the explanation of the TRS partially because TRS is easier to measure than the compressive strength, but mainly because it offers closer resemblance to the application properties of the hardmetals and has more complex dependence on the microstructure parameters and defects of the hardmetals. Understanding of the strength evolved from the non-fracture mechanics considerations of the brittle–ductile transition with the increase of the binder content to the studies of the fracture mechanics applicability, effects of the externally introduced defects and microstructure-initiated fracture.

1.10.4.3.1 Gurland's Early Idea of Brittle–Ductile Transition

Gurland et al. (Exner & Gurland, 1970; Gurland, 1963a; Gurland, 1963b; Gurland & Bardzil, 1955; Nishimatsu & Gurland, 1960) initially suggested an intuitive idea for the dependence of TRS based on two competing factors that determine the curve with the maximum (**Figure 8**). Co–W–C alloys with very high value of the *mlibp* $\lambda \gg \lambda^{\mathrm{maxTRS}}$ and very low volume fraction of the carbide phase V_V exhibit pronounced plastic deformation because Co is ductile. Addition of WC to ductile Co–W–C alloy decreases the *mlibp* λ and increases the strength of the alloy due to the dispersion strengthening of the ductile Co–W–C by sparse WC grains. The ductile type of fracture was suggested to remain applicable with the decrease of *mlibp* λ and the increase of the volume fraction of the carbide phase V_V up to the maximal TRS at *mlibp* $\lambda > \lambda^{\mathrm{maxTRS}}$, even though the mechanism of the fracture initiation seem to change to the accumulation of the damage in the structure, for instance by multiple microcracking of carbide phase, until the critical number of the broken carbide regions and the remaining material can no longer support the load (Gurland, 1959). On the opposite side of the curve at low-*mlibp* $\lambda < \lambda^{\mathrm{maxTRS}}$ and high volume fraction of the carbide phase V_V, the mechanism of deformation and fracture changes from ductile to brittle because ultimately WC is brittle. The brittle continuous carbide phase in WC–Co presents a longer uninterrupted fracture path and therefore a lower resistance to fracture. Hence, the increasing contiguity of the carbide crystals G was believed to be the main factor for the decreasing TRS with the decrease of the *mlibp* $\lambda < \lambda^{\mathrm{maxTRS}}$ at higher volume fraction of the carbide phase V_V (**Figure 10**) (Exner & Gurland, 1970; Gurland, 1963a; Gurland, 1963b; Gurland & Bardzil, 1955; Nishimatsu & Gurland, 1960).

Even though the Gurland's idea provides two main competing reasons for the dependence with maximum, it does not explain why TRS is higher at higher binder content for the same *mlibp* $\lambda > \lambda^{\mathrm{maxTRS}}$

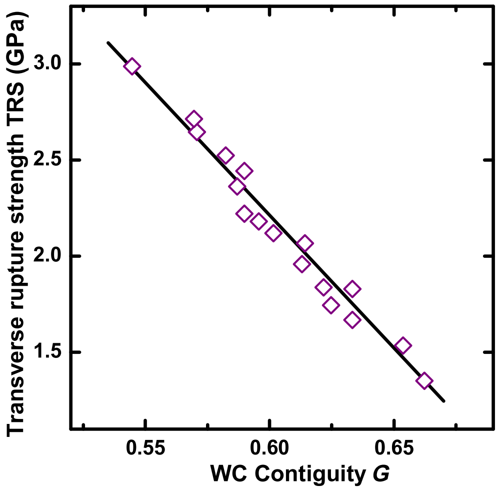

Figure 10 The correlation of the transverse rupture strength (TRS) versus the contiguity *G* in WC–Co. Reproduced from Figure 11 in Exner and Gurland (1970) with permission from Maney Publishing www.maney.co.uk/journals/pom and www.ingentaconnect.com/content/maney/pm.

(**Figure 8**). The conventional cemented carbides with the regular amount of the binder phase of up to 25 wt% exhibit no plastic deformation or subcritical crack growth and fracture as brittle materials on the macrolevel (Exner, Sigl, Fripan, & Pompe, 2001; Exner & Gurland, 1970; Gurland, 1963a; Gurland, 1963b; Gurland & Bardzil, 1955; Johannesson & Warren, 1988; Mari, Bolognini, Feusier, Viatte, & Benoit, 1999; Osterstock & Chermant, 1983; Roebuck & Almond, 1988; Sigl & Exner, 1987). Therefore, it is not clear why the maximum of TRS that is supposedly caused by the brittle–ductile transition is observed entirely in the region of brittle fracture at rather high volume fraction of the carbide phase V_V corresponding to 12–25 wt% Co. In other words, it is not clear why TRS already decreases with the increase of the *mlibp* $\lambda > \lambda^{\mathrm{maxTRS}}$, but the fracture mechanism does not seemingly change from brittle to ductile.

The Gurland's idea of the contiguity *G* being the main determining factor for TRS at low values of the *mlibp* λ is based on the experimental correlation of TRS that linearly decreases with the contiguity *G* (**Figure 10**) (Exner & Gurland, 1970; Gurland, 1963b). Nevertheless, this correlation cannot be considered as a conclusive evidence due to the dependence of the contiguity *G* on the volume fraction V_V (48) and the further dependence of the *mlibp* λ on both the contiguity *G* and the volume fraction of the carbide phase V_V (22) that makes the correlation of TRS versus contiguity *G* interdependent with the dependence of TRS versus λ shown in **Figure 8** (Gurland, 1988). Besides, this early idea is not based on the fracture mechanics approach that requires analysis of the critical defect, crack initiation, and crack propagation through the material with defined fracture toughness.

1.10.4.3.2 Fracture Mechanics of Transverse Rupture Strength

Application of the fracture mechanics to the TRS on hardmetals breaks the problem of fracture of the specimen into consideration of the several sequential fracture stages, namely into crack initiation from the critical defects, potential subcritical growth of the crack, followed by the catastrophic crack propagation that are discussed in Section 1.10.2.2 (Fischmeister, 1983; Gurland, 1988; Osterstock & Chermant, 1983; Roebuck & Almond, 1988). The conventional cemented carbides at room temperature under regular loading rates exhibit brittle fracture with no subcritical crack growth (Exner, Sigl, Fripan, & Pompe, 2001; Johannesson & Warren, 1988; Mari, Bolognini, Feusier, Viatte, & Benoit, 1999; Osterstock & Chermant, 1983; Roebuck & Almond, 1988; Sigl & Exner, 1987). Therefore, the hardmetals have the brittle fracture behavior with only two fracture stages, where the catastrophic crack propagation originates from the cracks initiated on the fractured defects or microstructure elements under normal test conditions. The crack propagation is determined by the fracture toughness K_{1C} that is discussed in Section 1.10.3.

Since Griffith–Orowan–Irwin fracture mechanics (Griffith, 1921; Irwin, 1957; Orowan, 1948) of brittle fracture is applicable to the cemented carbides that show brittle fracture on the macrolevel at room temperature, the critical fracture stress σ_f at the tip of the critical defect with half-diameter a_C can be calculated from the fracture toughness of the material K_{1C} under assumption of the plane strain condition around the crack (Almond & Roebuck, 1977; Fischmeister, 1983; Gurland, 1988; Osterstock & Chermant, 1983; Roebuck, 1995).

$$\sigma_f = K_{1C} \cdot (Q \cdot a_C)^{-1/2} \tag{49}$$

where Q is a constant factor determined by the geometry of the critical defect.

Assuming linear distribution of the stress in the specimen during bending, the fracture stress σ_f at the critical defect is calculated from the measured TRS σ_{TRS} that corresponds to the tensile stress in the middle of the outer surface of the specimen.

$$\sigma_f = \sigma_{TRS} \cdot (2 \cdot x/L) \cdot (2 \cdot y/W) \tag{50}$$

where x is the distance from the critical defect and $L/2$ is the distance from the middle of the specimen on the outer surface to the outer roller, whereas y is the distance from the critical defect to the neutral axis that is located at half-height of the specimen $W/2$ during bending. When the critical defect is located at or very close to and in the middle of the outer surface of the specimen $x = L/2$ and $y = W/2$, the critical tensile stress σ_f becomes equal to the measured TRS σ_{TRS}, otherwise σ_f is somewhat lower than the measured σ_{TRS}.

Hence, the TRS σ_{TRS} can be calculated from the fracture toughness K_{1C}, the size and the location of the critical defect on hardmetals. That reduces the problem of explaining the TRS to identification and measuring of the critical defects on the fracture surface.

Alternatively, when the critical defect cannot be identified on the fracture surface, its size can still be estimated to the extent of unknown constant factor Q from the reversed Eqns (49) and (50) under assumption that the critical defect is located at or very close to and in the middle of the outer surface of the specimen $x = L/2$ and $y = W/2$ and that the plane strain condition is still valid at the critical defect (Fischmeister, 1983; Osterstock & Chermant, 1983; Shatov, Ponomarev, & Firstov, 2006).

$$Q \cdot a_C \approx (K_{1C}/\sigma_{TRS})^2 \tag{51}$$

Since the fracture toughness K_{1C} linearly increases with the *mlibp* λ (**Figure 6(a)**), the critical defect size a_C has to go through a minimum versus λ for the TRS σ_{TRS} to exhibit the maximum according to Eqns (49) or (51) (**Figure 8**). In other words, the critical defect size a_C decreases at first and then increases with the *mlibp* λ on cemented carbides (**Figure 11**) (Osterstock & Chermant, 1983).

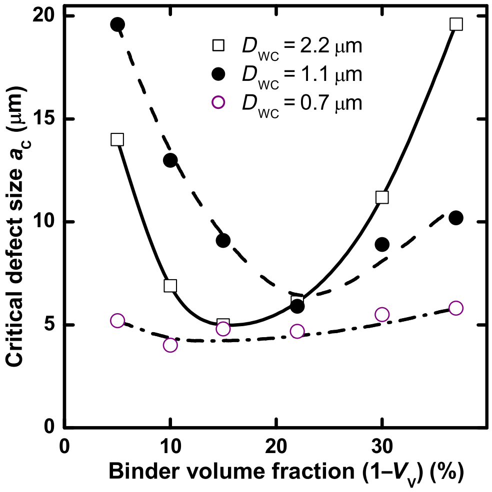

Figure 11 The dependence of the critical defect size a_C on the volume fraction of the binder phase $(1 - V_V)$ for mean diameters of WC crystals D_{WC} of 0.7, 1.1, and 2.2 μm. Reproduced from Figure 4 in Osterstock and Chermant (1983) with kind permission from Springer Science+Business Media B.V.

1.10.4.3.3 Almond and Roebuck (AR) Model of Limiting Strength

Almond and Roebuck (1977) measured the size a_C and location (x,y) of the critical defects and found that the nominal fracture stress σ_f at the site of the critical defect that is calculated from the TRS σ_{TRS} by Eqn (50) has a two-modal distribution versus the size of the critical defects and classified the fracture origins as being defect- and microstructure-initiated on WC–Co with binder contents of 6, 9, and 11 wt% Co with *mlicc* $d_{WC} = 1.4$ μm (**Figure 12**). When the relatively large pores or inclusions with diameters $2 \cdot a_C$ greater than some characteristic length L_C of about 20 μm are present in the alloy, these pores and inclusions play the role of the critical defects and are related to the nominal fracture stress σ_f through the fracture toughness in accordance to Eqn (49).

When the pore and inclusion sizes decrease below the characteristic length $L_C = 20$ μm, the fracture stress reaches a plateau and does not depend on the size of the defects and large carbide crystals found at the fracture initiation site. This high limit of the fracture stress σ_f is referred to as the limiting strength and reflects the strength of the material without externally introduced defects. Fracture initiation for the limiting strength occurs from the microstructure and is inherently related to the fracture of the brittle carbide phase, even though no obvious defect or fracture source of that size can be found or identified at the fracture initiation site (Almond & Roebuck, 1977; Roebuck, 1979; Roebuck, 1988; Roebuck, 1995; Roebuck & Almond, 1988). Statistical analysis of the fracture origins shows that the fraction of the specimens with microstructure-initiated fracture at the limiting strength can be of up to 75% for the regular TRS test and up to 90–100% for the notched bend test on the conventional WC-Co cemented carbides (Almond & Roebuck, 1977; Roebuck, 1979; Roebuck, 1988; Roebuck, 1995; Roebuck & Almond, 1988). Nevertheless, the AR model does not identify the actual microstructure element that plays the role of the critical defect when the fracture is initiated in the microstructure.

The AR model explains the wide scatter of the TRS measurements by the presence and size of the defects. The AR model also suggests modifying Gurland's early idea for the maximum of TRS by stating that TRS can be controlled by the predominance of the defect-initiated fractures at the low-*mlibp* $\lambda < \lambda^{\mathrm{maxTRS}}$, whereas TRS decrease due to the changes in the microstructure at high $\lambda > \lambda^{\mathrm{maxTRS}}$ (**Figure 8**).

Roebuck (1995) further enhanced the AR model by recognizing the presence of microstructure microcracking for the limiting strength and estimated the size of the critical defect a_C for the microstructure initiated fracture from the notch bend strength and the plane strain fracture toughness K_{1C} by using Eqn (51) with $Q = 1.17^{-2}$. Roebuck found that the size of the critical defect a_C for the microstructure initiated fracture depends on and is roughly proportional with the multiplication factor α of between 10 and 30 to the *mlicc* d_{WC} that varies between 0.28 and 2.94 μm for WC-6wt%Co with unchanged shape of WC crystals

$$a_C\Big|_{V_V,\ \mathrm{WC\ Shape} = \mathrm{const}} \approx \alpha \cdot d_{WC} \tag{52}$$

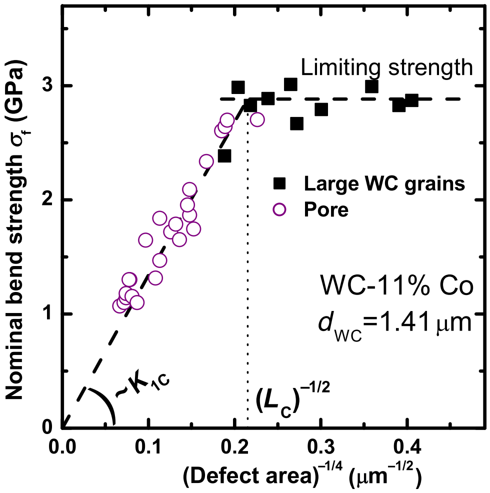

Figure 12 The dependence of the nominal fracture stress σ_f on the critical defect area for WC–11 wt% Co cemented carbides. Reproduced from Figure 11 in Roebuck and Almond (1988) with permission from Maney Publishing www.maney.co.uk/journals/imr and www.ingentaconnect.com/content/maney/imr.

The area of the fracture origin for such a big 'defect' covers several hundreds of WC grains and is several times bigger than the largest WC grain found in the material (Roebuck, 1995). Unfortunately, no specific explanation for the dependence (52) is provided by the AR model. Furthermore, the dependencies of the limiting strength and the size of the critical 'defect' on the volume fraction of the carbide phase V_V and other microstructure parameters remain to be studied.

Later on, the list of the critical defects for materials with TRS below the limiting strength grew up and now includes pores, impurity inclusions, free carbon and η-phase, carbide clusters, lakes of binder, and even abnormally large carbide crystals that are located close to the outer surface of the specimen (Almond, 1983; Almond & Roebuck, 1977; Dusza, Parilak, & Slesar, 1987; Fischmeister, 1983; Fukatsu, Kobori, & Ueki, 1991; Han & Mecholsky, 1990; Laptev, Ponomarev, & Ochkas, 2001; Roebuck, 1995; Roebuck & Almond, 1988).

1.10.4.3.4 Osterstock and Chermant (OC) Model of Microcracking for Maximum of TRS

The OC model (Osterstock & Chermant, 1983) applies the fracture mechanics approach and estimates the average critical defect size a_C from Eqn (51) by measuring the TRS σ_{TRS} and the fracture toughness K_{1C} and assuming that the multiplication factor for the critical defect size is $Q = 1.21 \cdot \pi$ for the volume fractions of the binder phase $(1 - V_V)$ in the range between 5 and 37 vol% on WC–Co cemented carbides (**Figure 11**). The critical defect size a_C decreases at first, reaches the minimum, and subsequently increases with the volume fraction of the binder phase $(1 - V_V)$ (**Figure 11**) (Osterstock & Chermant, 1983). The OC model follows the explanation from the AR model and attributes the decrease of the critical defect size a_C at low binder contents to the presence and elimination of such defects like pores with the increase of the binder content in the alloy.

In an attempt to explain the surprising subsequent increase of the critical defect size a_C at higher binder contents (**Figure 11**), Osterstock and Chermant (1983) first tried to find the subcritical growth of the cracks. Despite all the rigorous analysis and various experiments, no subcritical growth of the cracks was found for WC–Co even at the highest binder contents at room temperature that is consistent with the brittle two-stage fracture of the cemented carbides discussed above (Exner, Sigl, Fripan, & Pompe, 2001; Johannesson & Warren, 1988; Mari, Bolognini, Feusier, Viatte, & Benoit, 1999; Osterstock & Chermant, 1983; Roebuck & Almond, 1988; Sigl & Exner, 1987) and contradicts to the early Gurland's idea of the ductile fracture for hardmetals with high binder content.

Osterstock and Chermant (1983) found a series of microcracks through the carbide crystals and carbide chains on the tensile surface of the specimen after the fracture. The size of the smallest microcrack is found to be comparable to the size of carbide crystals. This observation allowed the OC model to conclude that the fracture of the carbide crystals C and carbide chains C/C constitutes the microstructure-initiated critical 'defect' at higher binder contents. In other words, multiple microcracks are initiated by breaking the carbide phase at the first stage of fracture under stresses that are apparently below the fracture stress that is eventually followed by the second fracture stage of catastrophic crack propagation after the critical stress condition for the crack propagation (49) is met.

Unfortunately, the OC model provides no final explanation on how the critical defect size can actually increase at higher binder contents (**Figure 11**), where there is no subcritical growth of the crack and the fracture surface area fractions through the carbide phase $(A_A^C + A_A^{C/C})$ decreases with the increase of the volume fraction of the binder phase $(1 - V_V)$ according to the Sigl and Exner correlation (2).

1.10.4.3.5 Reformulation of Gurland's Idea for Maximum of TRS by Fracture Mechanics Approach

Application of the fracture mechanics allowed reformulation of the Gurland's early idea and made it possible to suggest models that are based on consideration of the critical defects and dependencies of the fracture toughness and hardness on the *mlibp* λ (**Figure 13**) (Almond & Roebuck, 1977; Fischmeister, 1983; Gurland, 1988; Osterstock & Chermant, 1983; Roebuck & Almond, 1988). The main common agreement is that the increase of TRS at low-*mlibp* $\lambda < \lambda^{\max TRS}$ is determined by the increasing fracture toughness K_{1C} (**Figure 13**) and a variety of the external defects that are often present and are hard to eliminate at lower binder contents, but are readily reduced and disappear with the increase of the binder phase content in the alloy (Fischmeister, 1983; Gurland, 1988; Osterstock & Chermant, 1983; Roebuck & Almond, 1988).

The decreasing side of the TRS-λ dependence with $\lambda > \lambda^{\max TRS}$ (**Figure 8**) is still usually related to the Gurland's early idea of the transition to the ductile fracture that associates TRS with the decreasing hardness and yield stress with the increased plasticity (**Figure 13**) despite the established fact that the alloys do not show any

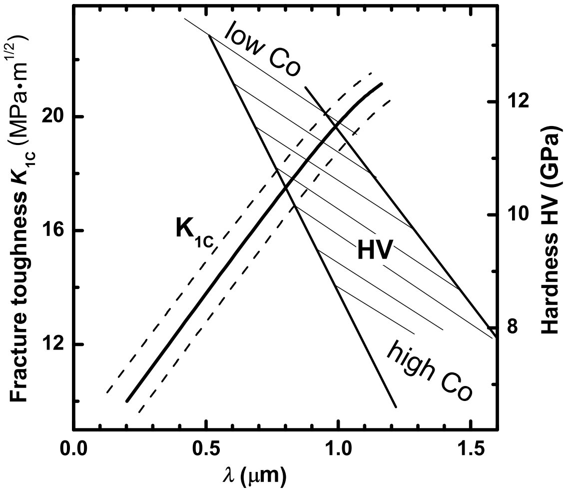

Figure 13 The correlation of the fracture toughness K_{1C} and the Vickers hardness *HV* versus the *mlibp* λ for a variety of the binder contents in WC–Co cemented carbides with low Co binder content corresponding to about 12 wt% Co, whereas the high Co binder content reaches 25 wt% Co. Reproduced from Figure 5(a) in Gurland (1988) with permission from Maney Publishing www.maney.co.uk/journals/imr and www.ingentaconnect.com/content/maney/imr.

plastic behavior on the macrolevel in this range of the *mlibp* λ (Fang, 2005; Fischmeister, 1983; Gurland, 1988; Osterstock & Chermant, 1983; Roebuck & Almond, 1988).

The idea of TRS following the hardness dependence at higher λ also contradicts the Gurland's experimental observations of **Figure 8** that shows that TRS becomes higher for the higher binder content, but the hardness becomes lower for the same higher binder content, when the *mlibp* λ is kept unchanged (**Figure 13**). If TRS would follow the hardness dependence, the value of TRS would become lower, rather than higher, for the higher binder content with unchanged λ. Hence, there should be another reason for the increase of TRS on higher binder content that counteracts the decrease associated with the decrease of the hardness at higher *mlibp* $\lambda > \lambda^{\mathrm{maxTRS}}$. Moreover, the fracture of the cemented carbides on the decreasing side of TRS dependence with $\lambda > \lambda^{\mathrm{maxTRS}}$ is still brittle on the macrolevel as it is discussed in Section 1.10.2. The brittle fracture is also indirectly confirmed by the dependence of the fracture toughness K_{1C} versus λ that does not deviate from the linearity when TRS starts to decrease that indicates that the mechanism of the crack propagation does not change from brittle to ductile on the conventional hardmetals in a wide range of the binder content (Figures 6(a) and 13).

1.10.4.3.6 Shatov, Ponomarev and Firstov (SPF) Model of Carbide–Carbide Contact Microcracking

1.10.4.3.6.1 Effect of the Shape of WC Crystals on TRS at Fixed-Volume Fraction V_V

Shatov, Ponomarev, and Firstov (2006) found that the TRS increases when the shape of WC crystals becomes flatter triangular prism on two-phase WC–Ni cemented carbides doped with TiC at the constant *mlicc* $d_{\mathrm{WC}} = 1$ μm (**Figure 14(a)**). No pores, no third-phase inclusions, no impurities, no abnormally big WC crystals, and no other defects were found in the area of the fracture origin in all the alloys except the porous WC–8wt%Ni alloy with the excessive amount of TiC. Therefore, the measured TRS on these nondefective alloys corresponds to the limiting strength with the microstructure-initiated fracture according to the AR model of limiting strength.

The degree of the flatterness of the WC crystals is quantified through the shape equiaxiality P_{WC} that is defined and measured as the mean ratio of the minimal $D_{\min}$ to maximal $D_{\max}$ chords through the center of mass of cross-section of WC crystals (Shatov, Firstov & Shatova, 1998).

$$P_{\mathrm{WC}} = \langle D_{\min}/D_{\max} \rangle|_{\mathrm{WC\ sections}} \tag{53}$$

The flatter shape of WC crystals corresponds to a lower value of the shape equiaxiality P_{WC}, whereas the ideal sphere has the highest value of $P_{\mathrm{WC}} = 1$ (Shatov, Firstov & Shatova, 1998).

The shape of WC crystals affects the limiting TRS indirectly. The decrease of the shape equiaxiality P_{WC} decreases the contiguity *G* of WC crystals at the fixed-volume fraction of the carbide phase V_V (Shatov, Ponomarev, Firstov, & Warren, 2006). Decrease of the contiguity *G* in its turn linearly decreases the size of the critical 'defect'

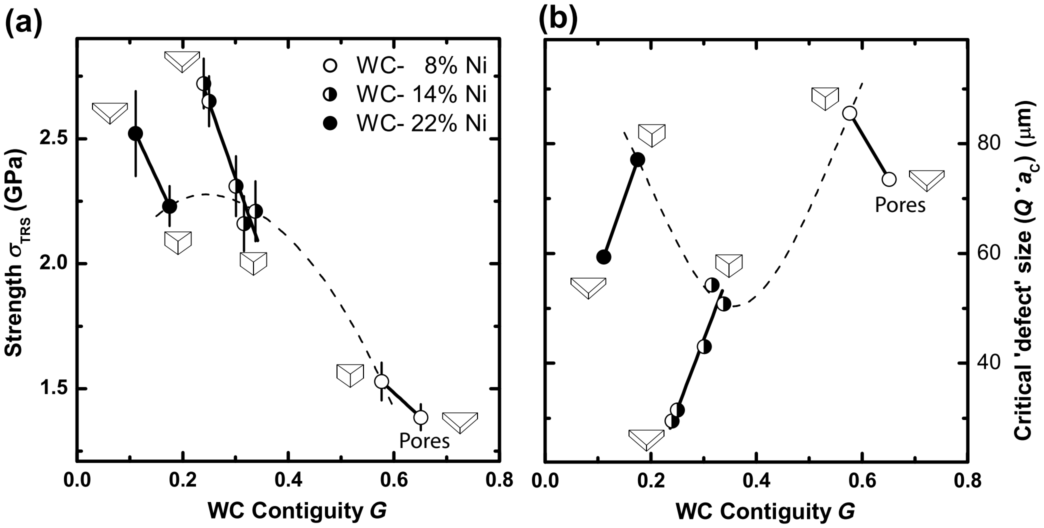

Figure 14 The dependence of (a) the transverse rupture strength and (b) the critical 'defect' size $Q \cdot a_C$ calculated by Eqn (51) on the contiguity G of carbide crystals in WC–8w%Ni, WC–14w%Ni, and WC–22wt%Ni hardmetals for the *mlicc* $d_{WC} \approx 1$ μm and changing shape of WC crystals from bulky to flatter triangular prism. Reproduced from Figure 2 in Shatov, Ponomarev and Firstov (2006).

$Q \cdot a_C$ of nonporous alloys that is estimated from the measured TRS and fracture toughness K_{1C} by Eqn (51) (**Figure 14(b)**). The reduced size of the critical 'defect' $Q \cdot a_C$ explains the increase of TRS at each fixed-volume fraction of the carbide phase V_V.

Observation of the linear correlation between the critical 'defect' size $Q \cdot a_C$ and the contiguity G at the fixed-volume fraction of the carbide phase V_V allows the SPF model to arrive at the conclusion that it is the multiple microcracks initiated from multiple broken carbide–carbide contacts C/C that constitutes the effective critical 'defect' in the alloy. The SPF observation provides the experimental confirmation to the Gurland's early idea that the contiguity is the main factor that determines TRS (**Figure 10**) (Exner & Gurland, 1970; Gurland, 1963b). Moreover, the SPF model expands this idea to the higher *mlibp* $\lambda > \lambda^{\mathrm{maxTRS}}$ and lower volume fraction of the carbide phase V_V. The SPF observation is also closely related to the observation of the series of microcracks through the carbide chains in the OC model (Osterstock & Chermant, 1983) discussed above with the main difference that in the SPF observation only the broken carbide–carbide contacts C/C, rather than both C and C/C fractures, are found to be the initiators of the critical microcracks.

Another interesting consequence of the SPF observation is that the transgranular fracture of the carbide crystals C has to happen only on the second fracture stage of the catastrophic crack propagation, rather than on the first stage of the crack initiation, because the final relative amount of the C/C fracture decreases, while both the relative area of the transgranular fracture C and the total fracture surface area fraction through the carbide phase $(A_A^C + A_A^{C/C})$ increases when the shape of WC becomes flatter (Shatov, Ponomarev, & Firstov, 2008).

1.10.4.3.6.2 SPF Model Explanation for the Maximum of TRS versus the Volume Fraction V_V

The SPF model (Shatov, Ponomarev, & Firstov, 2006; Shatov, Ponomarev, & Firstov, 2014) observed that the critical 'defect' size $Q \cdot a_C$ estimated by Eqn (51) goes through minimum and further increases with the decrease of the volume fraction of the carbide phase V_V (**Figure 14(b)**) similar to the observation of the OC model (**Figure 11**) (Osterstock & Chermant, 1983). To explain the increase of $Q \cdot a_C$, the SPF model suggests taking into account the dependence of the depth of the microcracking d_{mc} on the volume fraction V_V. Under first approximation, the effective size a_C^{eff} of the multiple microcracks can be calculated as the integral of the likelihood $p(x)$ to find a broken carbide–carbide contact at the distance x from the surface that is turned by the angle φ from the main stress plane (**Figure 1**) with x ranging from zero and up to the depth of the microcracking d_{mc}.

$$a_C^{\mathrm{eff}} = \int_0^{d_{mc}} p(x) \cdot \cos(\varphi) \mathrm{d}x \tag{54}$$

The SPF model (Shatov, Ponomarev, & Firstov, 2006; Shatov, Ponomarev, & Firstov, 2014) assumes that the microcracking happens at relatively low stresses that exceed some critical microcracking stress σ_{mc}. Decrease of the microcracking stress σ_{mc} increases both the depth d_{mc} and the likelihood $p(x)$ of microcracking in Eqn (54) that should increase the effective size of the critical 'defect' $a_{\mathrm{C}}^{\mathrm{eff}}$. On the other hand, decrease of the contiguity G has an opposite effect on $a_{\mathrm{C}}^{\mathrm{eff}}$ by reducing the density of the carbide–carbide contacts and, by these means, reducing the likelihood $p(x)$ of C/C microcracking in the alloy. Apparently, the contiguity G cannot affect the depth of the microcracking d_{mc} directly.

The SPF model (Shatov, Ponomarev, & Firstov, 2006; Shatov, Ponomarev, & Firstov, 2014) further assumes that the critical microcracking stress σ_{mc} is proportional to, but is below, the yield stress σ_{y} of the alloy that is related to the hardness H of the alloy by Eqn (41).

$$\sigma_{\mathrm{mc}} = \alpha_{\mathrm{mc}} \cdot \sigma_{\mathrm{y}} \approx \alpha_{\mathrm{mc}} \cdot H/3 \tag{55}$$

where $\alpha_{\mathrm{mc}} < 1$ is a constant microcracking factor.

The hardness H can be calculated from the microstructure parameters by the LG-SPF model for hardness that takes into account the change of the shape equiaxiality P_{WC} of WC crystals (Shatov, Ponomarev, & Firstov, 2009).

$$H^{\mathrm{LG-SPF}} = \left(H_{\mathrm{WC}}^{0} + \frac{H_{\mathrm{WC}}^{\mathrm{HP}}}{\sqrt{\frac{P_{\mathrm{WC}}}{P_{\mathrm{WC}}^{0}} \cdot d_{\mathrm{WC}}}} \right) \cdot V_{\mathrm{V}} \cdot G + \left(H_{\mathrm{Binder}}^{0} + \frac{H_{\mathrm{Binder}}^{\mathrm{HP}}}{\sqrt{\frac{P_{\mathrm{WC}}}{P_{\mathrm{WC}}^{0}} \cdot \lambda}} \right) \cdot (1 - V_{\mathrm{V}} \cdot G) \tag{56}$$

The microcracking stress σ_{mc} is believed to be proportional to the yield stress σ_{y} of the alloy because the microcracking occurs when the deformation of the carbide and binder phases cannot tolerate the difference between them any longer and the more rigid carbide phase has to break to keep up with the elastic deformation of the softer binder phase under the load. Therefore, the microcracking of the carbide phase can occur at somewhat lower stresses than the yield stress σ_{y}, but it happens easier on the alloys that have lower yield stress.

As a result, the SPF model suggests that two counteracting reasons determine the dependence with minimum of the effective size of the critical 'defect' $a_{\mathrm{C}}^{\mathrm{eff}}$ (**Figure 11**) and the related dependence with maximum of TRS (**Figure 8**) against the decreasing volume fraction of the carbide phase V_{V}. Both the contiguity G and the microcracking stress σ_{mc} decrease with the decrease of the volume fraction V_{V} according to Eqns (48) and (55). On one hand, the effective size $a_{\mathrm{C}}^{\mathrm{eff}}$ is expected to decrease due to the decrease of the microcracking likelihood $p(x)$ at lower contiguity G of carbide crystals. On the other hand, both the depth d_{mc} and the likelihood $p(x)$ of the microcracking of carbide–carbide contacts increase due to the decrease of the hardness H in Eqn (55). Apparently, the steep decrease of the contiguity G prevails over the increase of microcracking depth d_{mc} and the likelihood $p(x)$ at higher volume fraction V_{V} that causes the effective size of the critical 'defect' $a_{\mathrm{C}}^{\mathrm{eff}}$ to decrease at first and explains the increase of the limiting TRS. Further reduction of the volume fraction of the carbide phase V_{V} changes the contiguity more gradually, but the hardness of the alloy and the microcracking stress σ_{mc} still decrease significantly, that increases both the depth and the likelihood of the microcracking and causes the effective size $a_{\mathrm{C}}^{\mathrm{eff}}$ of the critical 'defect' to increase that reduces the limiting TRS.

1.10.4.3.6.3 Application of SPF Model to Other TRS Dependencies

The SPF model can qualitatively explain the increase of the effective size of the critical 'defect' of multicracking through the carbide phase versus the *mlicc* d_{WC} in the AR model (52) (Roebuck, 1995). The contiguity G of WC–6 wt% Co alloys is obviously not changed because of the constant volume fraction of the carbide phase V_{V} and the unchanged shape of WC crystals. Increase of the *mlicc* d_{WC} reduces the hardness H of the cemented carbides according to the LG model (46) that causes the microcracking stress σ_{mc} to decrease through Eqn (55) and to increase both the depth d_{mc} and the likelihood $p(x)$ of microcracking in Eqn (54). In their turn, increase of the depth d_{mc} and the likelihood $p(x)$ of the microcracking increases the effective size of the critical 'defect' $a_{\mathrm{C}}^{\mathrm{eff}}$ calculated by Eqn (54) when the *mlicc* d_{WC} increases at the constant contiguity G as it is found in Eqn (52).

The SPF model also explains why TRS is higher on alloys with higher binder content for the same *mlibp* λ in Gurland's experiments (**Figure 8**). Increase of the binder content that is equivalent to the decrease of the volume fraction of the carbide phase V_{V} causes the decrease of the contiguity G. The *mlicc* d_{WC} should be reduced to keep the *mlibp* λ unchanged on the alloys with more binder. Therefore, the reduction of the hardness due to the decrease of the volume fraction V_V and the contiguity G is somewhat compensated by the increase of the Hall–Petch terms with the decrease of d_{WC} that makes the microcracking stress σ_{mc} only slightly reduced in comparison to the relative decrease of the contiguity G. Hence, the decreasing contiguity G plays the major role in decreasing the likelihood of microcracking $p(x)$ in Eqn (54) and reduction of the effective size of the critical 'defect' a_C^{eff} that increases TRS. For the same reason, the maximal TRS value shifts toward the higher *mlibp* λ^{maxTRS} with the increase of the binder content. Since TRS is higher due to the lower value of the contiguity G for the higher binder content at the same *mlibp* λ, a bigger *mlibp* λ is required to reduce the microcracking stress σ_{mc} sufficiently enough to counteract the dominating effect of the contiguity G and achieve the maximal TRS.

1.10.4.3.6.4 Open Issues of SPF Model

Despite the SPF model provides reasonable explanation for the observed dependencies of TRS, it lacks experimental verification of its assumptions about the microcracking stress σ_{mc} value and its relation to the yield stress of the alloy and related dependence on the microstructure parameters expressed in Eqn (55). Perhaps, experiments measuring acoustic emission in 3D during the load can provide adequate measurement of the microcracking location and allow calculating the microcracking stress σ_{mc} and depth d_{mc}. Alternatively, the microcrack sizes can also be measured on the surface of the specimen similar to the OC model but under controlled stress condition to identify the microcracking stress σ_{mc}. On the other hand, the microcracking stress σ_{mc} might also be measured as the lowest stress at which the stress–strain hysteresis occurs (Jaensson, 1971, 1972) if the microcracking is the main reason for the deviation from the linear stress–strain dependence. It is also interesting to measure the effective size of the critical 'defect' perhaps by the measurement of the characteristic length L_C from the AR model and experimentally determine its dependence on the *mlibp* λ for a variety of the volume fractions of the carbide phase V_V. Fracture of the alloys with bigger *mlicc* d_{WC} with the dominating transgranular fracture mode of the carbide crystals might also change the nature of the microcracking and affect the SPF interpretations.

It is still not fully clear how the RCSS after grinding can affect the effective size of the critical 'defect' in Eqn (54). It seems that the RCSS can counteract and suppress opening of the broken carbide–carbide contacts located close to the surface of the specimen that shifts the position of the critical defect deeper into the bulk of the specimen and most likely can only reduce the size of the critical defect calculated by Eqn (54).

1.10.4.4 Alternative and Non-Fracture Mechanics Models of TRS

Despite wide acceptance of the fracture mechanics approach to the explanation of the strength combined with rather detailed understanding of the fracture process and fracture toughness of hardmetals, there are still present several attempts to explain the strength by making various assumptions on the fracture criteria without the consideration of the critical defects, by assuming nonconventional fracture behavior for hardmetals, or by using mechanistic and fractals modeling.

1.10.4.4.1 Model of Fang for Maximum of TRS Due to Yield and Flow

Fang (2005) suggests calculating the TRS σ_{TRS} from the yield stress σ_y of the alloy and the effective flow stress of the binder $\sigma_{eff.b}$ at fracture that exceeds the yield stress of the binder σ_y^B by the work hardening value of $(\sigma_{eff.b} - \sigma_y^B)$ when the TRS is at its limiting value and is therefore determined by the microstructure-initiated fracture, rather than by the defects. Assuming that both the yield stress σ_y and the TRS follow the LG model (Gurland, 1979; Lee & Gurland, 1978) type of relation that depends on the contiguous volume fractions $V_V \cdot G$ (46), Fang arrives at the dependence of TRS versus the yield stress of the alloy σ_y and the work hardening of the binder phase.

$$\sigma_{TRS} = \sigma_y + \left(\sigma_{eff.b} - \sigma_y^B\right) \cdot (1 - V_V \cdot G) \tag{57}$$

Taking into account that the yield stress is proportional to the hardness by Eqn (41), the first term in Eqn (57) σ_y is expected to increase with the volume fraction V_V and contiguity G of the carbide crystals and the related increase of the hardness (46). Assuming that the work hardening $(\sigma_{eff.b} - \sigma_y^B)$ is almost not changing for the cemented carbides and therefore the second term in Eqn (57) decreases with the volume fraction V_V of the carbide phase from its maximal value of $(\sigma_{eff.b} - \sigma_y^B)$ on pure binder down to 0 on the binderless alloy, Fang concludes that the sum of the increasing yield stress σ_y and the decreasing but limited work-hardening term in Eqn (57) should pass through some maximum value and explain the Gurland's experiment for TRS (**Figure 8**).

Assumption that the cemented carbides always fracture at the stress that exceeds the yield stress σ_y of the alloy and therefore should show signs of plastic deformation on the macrolevel is rather controversial for TRS. For the hardness and TRS data provided by Fang (2005), the value of the yield stress $\sigma_y = H/3$ calculated from Eqn (41) rather significantly exceeds the TRS σ_{TRS} with the only exception of the alloy with very high *mlibp* of about $\lambda = 2.07$ μm that essentially invalidates the model (57).

The yield stress estimated from the hardness by Eqn (41) lies in the range between 2.3 and 7 GPa when the hardness ranges between 7 and 22 GPa (Almond, 1983; Ettmayer, 1989; Gille, Szesny, Dreyer, et al., 2002; Gurland, 1988; Jia, Fischer, & Gallois, 1998; Roebuck & Almond, 1988; Sailer, Herr, Sockel, et al., 2001; Schubert, Neumeister, Kinger, & Lux, 1998; http://www.allaboutcementedcarbide.com/). The typical values of σ_{TRS} range between 1 and 4 GPa for WC–Co cemented carbides as it is shown above. The maximal TRS is achieved for the medium *mlibp* $\lambda^{\max TRS}$ between 0.4 and 0.7 μm (**Figure 8**), where the yield stress is expected to be somewhere in the middle of its range at the level of at least $\sigma_y = 4.5$ GPa (**Figure 13**).

It becomes apparent that even at its maximum, the fracture stress σ_{TRS} does not reach the yield stress σ_y of the alloy and therefore the alloy exhibits the brittle fracture as it is discussed in Section 1.10.2. The yield stress σ_y becomes even higher at the lower binder contents with $\lambda < \lambda^{\max TRS}$ where TRS decreases that leaves no chance for the applicability of the Eqn (57) in this range. On the opposite side from the maximal TRS with $\lambda > \lambda^{\max TRS}$, the decreasing yield stress σ_y has a chance to cross with the decreasing TRS, but apparently this can only happen way beyond the regular binder contents of the cemented carbides with very high-*mlibp* $\lambda >> \lambda^{\max TRS}$ where the ductile nature of the Co–W–C will manifest itself with the plastic deformation on the macrolevel. Therefore, despite the promising prediction of the maximum for TRS, the Fang model might benefit by the re-adjustment from the ductile to the brittle fracture to become applicable to the cemented carbides.

1.10.4.4.2 Models not Predicting the Maximum of TRS

There are several alternative models that neither predict, nor explain the maximum of TRS versus the *mlibp* λ or even versus the volume fraction of the carbide phase V_V (**Figure 8**) due to various simplistic or controversial assumptions. Nevertheless, despite the failure to explain the maximum of TRS, the approaches developed in these models offer potentially promising directions and might bring further advancement in understanding of the strength of hardmetals as soon as more realistic assumptions are exercised.

The mechanistic model of Golovchan and Litoshenko (2003), Golovchan (2006, 2009, 2010), and Golovchan and Litoshenko (2010) calculates the ultimate TRS and compressive strength of WC–Co hardmetals from the elastic and plastic stress conditions in the carbide and binder phases that occur during the load by taking into account the RTS and using Balandin fracture criterion (Balandin, 1937) for the WC phase that relates the compression and tensile strengths, but ignores the fracture toughness of the material. This model does predict the maximum of TRS versus the volume fraction of the carbide phase V_V, but fails to predict the maximum of TRS versus the *mlibp* λ at the fixed V_V that contradicts to the experiment (**Figure 8**).

Two-dimensional computer simulation by Kim, Massa, and Rohrer (2006) and Kim, Massa, and Rohrer, (2007) uses rather simplistic fracture criteria with arbitrary introduced constant effective surface fracture energy that conceals all the complexity and dependencies of the fracture process, but does not introduce the mechanism that would explain the maximum of TRS.

Unosson, Olovsson, and Simonsson (2007) determined that the density distribution of imperfections that decreases exponentially with the imperfection size gives the best fit to the TRS statistical distribution of hardmetals, but they provide no actual calculation or prediction for TRS dependence on the microstructure parameters.

Cha, Lee, Ryu, and Hong (2008) found that the fracture during TRS test of WC–10 wt% Co cemented carbides containing large pores is usually initiated from the closed pores located under the surface of the specimen at some critical depth, rather than from the open pores at the surface of the specimen. The fracture mechanics calculations suggest that the lower stress is required for the crack propagation from the closed pore under the surface in comparison to the stress around the open pore located at the surface (Cha, Lee, Ryu, & Hong, 2008). Unfortunately, these calculations cannot be considered as being conclusive due to the possible presence of the RCSS that can also explain the observed effect by counteracting the tensile stress from the load during bending at and close to the surface that should shift the maximal tensile stress from the outer surface deeper under the surface of the specimen (Exner, 1969; Exner, 1979; Roebuck, 1979; Roebuck, 1988; Roebuck & Almond, 1988).

Carpinteri, Pugno and Puzzi (2009) apply the fractals theory and controversially assume that both the strength and fracture toughness of carbide and binder phases have the Hall–Petch relation versus their respective sizes, and that each of these mechanical properties can be superpositioned with the contiguous volume fraction factors to calculate the strength and fracture toughness of the whole alloy similar to the calculation of the hardness in the LG model (46) (Gurland, 1979; Lee & Gurland, 1978). This approach does not exhibit any of the experimentally observed maxima for TRS and therefore has an area for improvement.

1.10.4.5 Outlook

Progress in understanding of the strength of the hardmetals is heavily based on the progress of understanding the fracture toughness and additionally requires research on the dependencies of the population and distribution of both the externally introduced defects and microstructure-initiated fracture. Calculation of the geometry factors and finding the relation between the fracture toughness from the multiple microcracks versus the single defect-initiated fracture would be beneficiary. Determination of the stress condition and the depth of the microcracking and their dependence on the microstructure parameters of the alloy also promises further advancement in understanding the strength. The effect of the RCSS on the effective size of the critical 'defect' should be further investigated for a variety of alloys and microstructures. Application of the computer simulation to the crack initiation and propagation can advance the strength modeling. All the models require verification on a wider range of composition and microstructure of the hardmetals.

Cross-references

1.1 Introduction to Hardmetals—Definitions, Classification and History of Hardmetals
1.2 Introduction to Hardmetals—Fundamentals and General Applications of Hardmetals
1.3 Introduction to Hardmetals—Microstructure and Morphology of Hardmetals
1.4 Class of Materials—Cemented Carbides
1.5 Class of Materials—Cermets
1.6 Powder Synthesis
1.7 Synthesis and Processing—Powder Processing and Green Shaping
1.8 Synthesis and Processing—Consolidation Techniques
1.9 Hardness and Deformation of Hardmetals at Room Temperature
1.11 Mechanical Properties—Fatigue
1.12 Mechanical Properties—Wear of Hardmetals
1.13 Mechanical Properties—Residual/Thermal Stress in Hardmetals
1.14 Mechanical Properties—Plastic, High Temperature

References

All about cemented carbide. http://www.allaboutcementedcarbide.com/.

Aleksandrova, L. I., Bondarenko, V. P., & Loshak, M. G. (2005). Metallographic aspects of deformation and fracture of hard alloys under compression. *Powder Metallurgy and Metal Ceramics, 44*, 489–498.

Almond, E. A. (1983). Deformation characteristics and mechanical properties of hardmetals. In R. K. Viswanadham, D. Rowcliffe, & J. Gurland (Eds.), *Proceedings of the 1st international conference on the science of hard materials* (pp. 517–561). New York: Plenum Press.

Almond, E. A., & Roebuck, B. (1977). Defect-initiated fracture and the bend strength of WC-Co hardmetals. *Metal Science, 11*, 458–461.

Almond, E. A., & Roebuck, B. (1983). Extending the use of indentation tests. In R. K. Viswanadham, D. Rowcliffe, & J. Gurland (Eds.), *Proceedings of the 1st international conference on the science of hard materials* (pp. 597–614). New York: Plenum Press.

Almond, E. A., & Roebuck, B. (1988). Identification of optimum binder phase compositions for improved WC hard metals. *Materials Science and Engineering: A, 105–106*, 237–248.

Anstis, G. R., Chantikul, P., Lawn, B. R., & Marshall, D. B. (1981). A critical evaluation of indentation techniques for measuring fracture toughness: I, direct crack measurements. *Journal of the American Ceramic Society, 64*, 533–538.

Armstrong, R. W. (2011). The hardness and strength properties of WC-Co composites. *Materials, 4*, 1287–1308.

Armstrong, R. W., & Cazacu, O. (2006). Indentation fracture mechanics toughness dependence on grain size and crack size: application to alumina and WC-Co. *International Journal of Refractory Metals and Hard Materials, 24*, 129–134.

Balandin, P. P. (1937). On strength hypotheses. *Vestnik Inzhenera I Tekhnika, 1*, 19–24 (in Russian).

Bilby, B. A., Cottrell, A. H., & Swinden, K. H. (1963). The spread of plastic yielding from a notch. *Proceedings of the Royal Society of London, A272*, 304–314.

Bolton, J. D., & Keely, R. J. (1983). Fracture toughness (K_{IC}) of cemented carbides. *Fibre Science and Technology, 19*, 37–58.

Bonache, V., Salvador, M. D., Busquets, D., et al. (2011). Synthesis and processing of nanocrystalline tungsten carbide: towards cemented carbides with optimal mechanical properties. *International Journal of Refractory Metals and Hard Materials, 29*, 78–84.

Carpinteri, A., Pugno, N., & Puzzi, S. (2009). Strength vs. toughness optimization of microstructured composites. *Chaos, Solitons and Fractals, 39*, 1210–1223.

Cha, S. I., Hong, S. H., Ha, G. H., & Kim, B. K. (2001). Mechanical properties of WC-10Co cemented carbides sintered from nanocrystalline spray conversion processed powders. *International Journal of Refractory Metals and Hard Materials, 19*, 397–403.

Cha, S. I., Lee, K. H., Ryu, H. J., & Hong, S. H. (2008). Effect of size and location of spherical pores on transverse rupture strength of WC-Co cemented carbides. *Materials Science and Engineering: A, 486*, 404–408.

Chantikul, P., Anstis, G. R., Lawn, B. R., & Marshall, D. B. (1981). A critical evaluation of indentation techniques for measuring fracture toughness: II, strength method. *Journal of the American Ceramic Society, 64*, 539–543.

Chermant, J. L., & Osterstock, F. (1976). Fracture toughness and fracture of WC-Co composites. *Journal of Materials Science, 11*, 1939–1951.

Christensen, M., & Wahnstrom, G. (2003). Co-phase penetration of WC(1010)/WC(1010) grain boundaries from first principles. *Physical Review B, 67*, 115415.

Christensen, M., & Wahnstrom, G. (2004). Effects of cobalt intergranular segregation on interface energetics in WC–Co. *Acta Materialia, 52*, 2199–2207.

Christensen, M., & Wahnstrom, G. (2006). Strength and reinforcement of interfaces in cemented carbides. *International Journal of Refractory Metals and Hard Materials, 24*, 80–88.

Coats, D. L., & Krawitz, A. D. (2003). Effect of particle size on thermal residual stress in WC-Co composites. *Materials Science and Engineering: A, 359*, 338–342.

Cutler, R. A., & Virkar, A. V. (1985). The effect of binder thickness and residual stresses on the fracture toughness of cemented carbides. *Journal of Materials Science, 20*, 3557–3573.

Deshmukh, R., & Gurland, J. (1982). Orientation of contiguous tungsten carbide crystals in sintered WC-Co as determined from slip line traces. *Metallography, 15*, 383–390.

Deshmukh, R., & Gurland, J. (1986). A study of microstructural development during the liquid-phase sintering of WC-Co alloys. In E. A. Almond, C. A. Brookes, & R. Warren (Eds.), *Proceedings of 2nd international conference on the science of hard materials* (pp. 347–358). Bristol and Boston: Adam Hilger.

Doi, H. (1986). Advanced TiC and TiC–TiN base cermets. In E. A. Almond, C. A. Brookes, & R. Warren (Eds.), *Proceedings of 2nd international conference on the science of hard materials* (pp. 489–523). Bristol and Boston: Adam Hilger.

Dusza, J., Parilak, L., Diblk, J., & Slesar, M. (1983). Elastic and plastic behaviour of WC-Co composites. *Ceramics International, 9*, 144–146.

Dusza, J., Parilak, L., & Slesar, M. (1987). Fracture characteristics of ceramic and cermet cutting tools. *Ceramics International, 13*, 133–137.

Elfwing, M., & Norgren, S. (2005). Study of solid-state sintered fine-grained cemented carbides. *International Journal of Refractory Metals and Hard Materials, 23*, 242–248.

Ettmayer, P. (1989). Hardmetals and cermets. *Annual Review of Materials Science, 19*, 145–164.

Ettmayer, P., Kolaska, H., Lengauer, W., & Dreyert, K. (1995). Ti(C, N) cermets – metallurgy and properties. *International Journal of Refractory Metals and Hard Materials, 13*, 343–351.

Evans, A. G., Heuer, A. H., & Porter, D. L. (1977). The fracture toughness of ceramics. In D. M. R. Taplin (Ed.), *Proceedings of 4th international conference on fracture* (pp. 529–556). New York: Plenum Press.

Exner, H. E. (1969). The influence of sample preparation on Palmqvist's method for toughness testing of cemented carbides. *Transactions of the Metallurgical Society of AIME, 245*, 677–683.

Exner, H. E. (1970). Method and significance of particle and grain size control in cemented carbide technology. *Powder Metallurgy, 13*, 429–448.

Exner, H. E. (1979). Physical and chemical nature of cemented carbides. *International Metals Reviews*, 149–173.

Exner, H. E. (1983). Qualitative and quantitative interpretation of microstructures in cemented carbides. In R. K. Viswanadham, D. Rowcliffe, & J. Gurland (Eds.), *Proceedings of the 1st international conference on the science of hard materials* (pp. 233–262). New York: Plenum Press.

Exner, H. E., & Fischmeister, H. F. (1966). Structure of sintered tungsten carbide-cobalt alloys. *Archiv fur das Eisenhuttenwesen, 37*, 417–426.

Exner, H. E., & Gurland, J. (1970). A review of parameters influencing some mechanical properties of tungsten carbide-cobalt alloys. *Powder Metallurgy, 13*, 13–31.

Exner, H. E., Sigl, L., Fripan, M., & Pompe, O. (2001). Fractography of critical and subcritical cracks in hard materials. *International Journal of Refractory Metals and Hard Materials, 19*, 329–334.

Exner, E. L., Pickens, J. R., & Gurland, J. (1978). A comparison of indentation crack resistance and fracture toughness of five WC-Co alloys. *Metallurgical and Materials Transactions A, 9*, 736–738.

Fang, Z. Z. (2005). Correlation of transverse rupture strength of WC-Co with hardness. *International Journal of Refractory Metals and Hard Materials, 23*, 119–127.

Fang, Z. Z., Wang, X., Ryu, T., Hwang, K. S., & Sohn, H. Y. (2009). Synthesis, sintering, and mechanical properties of nanocrystalline cemented tungsten carbide – a review. *International Journal of Refractory Metals and Hard Materials, 27*, 288–299.

Fischmeister, H. F. (1983). Development and present status of the science and technology of hard materials. In R. K. Viswanadham, D. Rowcliffe, & J. Gurland (Eds.), *Proceedings of the 1st international conference on the science of hard materials* (pp. 1–46). New York: Plenum Press.

Fischmeister, H. F., Exner, H. E., Poech, M.-H., et al. (1989). Modelling fracture processes in metals and composite materials. *Zeitschrift fur Metallkunde, 80*, 839–846.

Fischmeister, H. F., Schmauder, S., & Sigl, L. S. (1988). Finite element modelling of crack propagation in WC-Co hard metals. *Materials Science and Engineering: A, 105–106*, 305–311.

Fukatsu, T., Kobori, K., & Ueki, M. (1991). Micro-grained cemented carbide with high strength. *International Journal of Refractory Metals and Hard Materials, 10*, 57–60.

German, R. M., Smid, I., Campbell, L. G., Keane, J., & Toth, R. (2005). Liquid phase sintering of tough coated hard particles. *International Journal of Refractory Metals and Hard Materials, 23*, 267–272.

Gille, G., Szesny, B., Dreyer, K., et al. (2002). Submicron and ultrafine grained hardmetals for microdrills and metal cutting inserts. *International Journal of Refractory Metals and Hard Materials, 20*, 3–22.

Godse, R., & Gurland, J. (1988). Applicability of the critical strain fracture criterion to WC-Co hard metals. *Materials Science and Engineering: A, 105–106*, 331–336.

Godse, R., Gurland, J., & Suresh, S. (1988). Effects of residual stresses in fracture toughness testing of hard metals. *Materials Science and Engineering: A, 105–106*, 383–387.

Golovchan, V. T. (2006). On the calculation of deformation curves for two-phase cermets. *Strength of Materials, 38*, 289–298.

Golovchan, V. T. (2009). On bending strength of superhard composite materials based on WC–Co hardmetals. *Strength of Materials, 41*, 603–612.

Golovchan, V. T. (2010). On the strength of polycrystalline tungsten monocarbide. *International Journal of Refractory Metals and Hard Materials, 28*, 250–253.

Golovchan, V. T., & Litoshenko, N. V. (2003). On the contiguity of carbide phase in WC–Co hardmetals. *International Journal of Refractory Metals and Hard Materials, 21*, 241–244.

Golovchan, V. T., & Litoshenko, N. V. (2010). The stress–strain behavior of WC-Co hardmetals. *Computational Materials Science, 49*, 593–597.

Griffith, A. A. (1921). The phenomenon of rupture and flow in solids. *Philosophical Transactions of the Royal Society of London, Series A, 221*, 163–198.

Guilemany, J. M., Sanchiz, I., Mellor, B. G., Llorca, N., & Miguel, J. R. (1994). Mechanical-property relationships of Co/WC and Co-Ni-Fe/WC hard metal alloys. *International Journal of Refractory Metals and Hard Materials, 12*, 199–206.

Gurland, J. (1958). The measurement of grain contiguity in two-phase alloys. *Transactions of the Metallurgical Society of AIME, 212*, 452–455.

Gurland, J. (1959). Observation of the structure and sintering mechanism of cemented carbides. *Transactions of the Metallurgical Society of AIME, 215*, 601–608.

Gurland, J. (1963a). Current views on the structure and properties of cemented carbides. *Jernkontorets Annaler, 147*, 1–18.

Gurland, J. (1963b). The fracture strength of sintered tungsten carbide – cobalt alloys in relation to composition and particle spacing. *Transactions of the Metallurgical Society of AIME, 227*, 1146–1150.

Gurland, J. (1979). A structural approach to the yield strength of two-phase alloys with coarse microstructures. *Materials Science and Engineering, 40*, 59–71.

Gurland, J. (1988). New scientific approaches to development of tool materials. *International Materials Reviews, 33*, 151–166.

Gurland, J., & Bardzil, P. (1955). Relation of strength, composition and grain size of sintered WC-Co alloys. *Transactions of the Metallurgical Society of AIME, 203*, 311–315.

Hall, E. O. (1952). The deformation and ageing of mild steel: III discussion of results. *Proceedings of the Physical Society B, 64*, 747–753.

Han, D., & Mecholsky, J. J. (1990). Fracture analysis of cobalt-bonded tungsten carbide composites. *Journal of Materials Science, 25*, 4949–4956.

Henjered, A., Hellsing, M., Andren, H.-O., & Norden, H. (1986). The presence of cobalt at WC/WC interfaces. In E. A. Almond, C. A. Brookes, & R. Warren (Eds.), *Proceedings of 2nd international conference on the science of hard materials* (pp. 303–309). Bristol and Boston: Adam Hilger.

Hong, J., & Gurland, J. (1983). A study of the fracture process of WC-Co alloys. In R. K. Viswanadham, D. Rowcliffe, & J. Gurland (Eds.), *Proceedings of the 1st international conference on the science of hard materials* (pp. 649–669). New York: Plenum Press.

Irwin, G. (1957). Analysis of stresses and strains near the end of a crack traversing a plate. *Journal of Applied Mechanics, 24*, 361–364.

Jaensson, B. O. (1971). Residual stresses and stress-strain behaviour of the WC-Co composite material. *Materials Science and Engineering, 8*, 41–53.

Jaensson, B. O. (1972). Microstructural interpretation of the stress-strain behaviour of the WC-Co composite material. *Materials Science and Engineering, 9*, 339–346.

Jeong, I. K., Kim, H. C., Doh, J. M., et al. (2007). Mechanical properties and consolidation of WC-8wt%Ni hard materials by HFIHS and PCAS. *Solid State Phenomena, 124–126*, 1153–1156.

Jia, K., Fischer, T. E., & Gallois, B. (1998). Microstructure, hardness and toughness of nanostructured and conventional WC-Co composites. *NanoStructured Materials, 10*, 875–891.

Johannesson, B., & Warren, R. (1988). Subcritical crack growth and plastic deformation in the fracture of hard metals. *Materials Science and Engineering: A, 105–106*, 353–361.

Kim, C. S., Massa, T. R., & Rohrer, G. S. (2007). Modeling the influence of orientation texture on the strength of WC-Co composites. *Journal of the American Ceramic Society, 90*, 199–204.

Kim, C.-S., Massa, T. R., & Rohrer, G. S. (2006). Modeling the relationship between microstructural features and the strength of WC-Co composites. *International Journal of Refractory Metals and Hard Materials, 24*, 89–100.

Kim, C. S., & Rohrer, G. S. (2004). Geometric and crystallographic characterization of WC surfaces and grain boundaries in WC-Co composites. *Interface Science, 12*, 19–27.

Komak, M., & Novak, S (1986). The influence of microstructure and composition on the mechanical behaviour of TiC based hardmetals. In E. A. Almond, C. A. Brookes, & R. Warren (Eds.), *Proc. 2nd Int. Conf. on the Science of Hard Materials.* (pp. 565–575). Bristol and Boston: Adam Hilger.

Konyashin, I., Schafer, F., Cooper, R., et al. (2005). Novel ultra-coarse hardmetal grades with reinforced binder for mining and construction. *International Journal of Refractory Metals and Hard Materials, 23*, 225–232.

Kotoul, M. (1997). On the shielding effect of a multiligament zone of a crack in WC-Co. *Acta Materialia, 45*, 3363–3376.

Krawitz, A. D., Crapenhoft, M. L., Reichel, D. G., & Warren, R. (1988). Residual stress distribution in cermets. *Materials Science and Engineering: A, 105–106*, 275–281.

Krawitz, A. D., Reichel, D. G., & Hitterman, R. I. (1989). Residual stress and stress distribution in a WC-Ni composite. *Materials Science and Engineering: A, 119*, 127–134.

Kursawe, S., Pott, Ph., Sockel, H. G., Heinrich, W., & Wolf, M. (2001). On the influence of binder content and binder composition on the mechanical properties of hardmetals. *International Journal of Refractory Metals and Hard Materials, 19*, 335–340.

Laptev, A. V., Ponomarev, S. S., & Ochkas, L. F. (2001). Structural features and properties of alloy 84%WC-16% Co obtained by hot pressing in the solid and liquid phases. Part 2. Influence of the temperature at which the specimens are made on their physicomechanical properties. *Powder Metallurgy and Metal Ceramics, 40*, 77–83.

Laugier, M. T. (1985). The elastic/plastic indentation of ceramics. *Journal of Materials Science Letters, 4*, 1539–1541.

Lea, C., & Roebuck, B. (1981). Fracture topology of WC-Co hardmetals. *Metal Science, 15*, 262–266.

Lee, K. H., Cha, S. I., Kim, B. K., & Hong, S. H. (2006). Effect of WC/TiC grain size ratio on microstructure and mechanical properties of WC–TiC–Co cemented carbides. *International Journal of Refractory Metals and Hard Materials, 24*, 109–114.

Lee, H. C., & Gurland, J. (1978). Hardness and deformation of cemented tungsten carbide. *Materials Science and Engineering, 33*, 125–133.

Li, T., Li, Q., Fuh, J. Y. H., et al. (2007). Effects of AGG on fracture toughness of tungsten carbide. *Materials Science and Engineering: A, 445–446*, 587–592.

Luyckx, S. B. (1977). Precision matching of mating fracture surfaces of WC-Co alloys. In D. M. R. Taplin (Ed.), *Proceedings of 4th international conference on fracture* (pp. 223–227). New York: Pergamon Press.

Mari, D., Bolognini, S., Feusier, G., et al. (2003). TiMoCN based cermets part II. Microstructure and room temperature mechanical properties. *International Journal of Refractory Metals and Hard Materials, 21*, 47–53.

Mari, D., Bolognini, S., Feusier, G., Viatte, T., & Benoit, W. (1999). Experimental strategy to study the mechanical behaviour of hardmetals for cutting tools. *International Journal of Refractory Metals and Hard Materials, 17*, 209–225.

Mason, A., & Kenny, P. (1970). The structure and fractography of cemented tungsten carbide. *Metallurgia, 82*, 205–212.

McHugh, P. E., & Connolly, P. J. (2003). Micromechanical modelling of ductile crack growth in the binder phase of WC-Co. *Computational Materials Science, 27*, 423–436.

Milman, Yu. V., Chugunova, S., Goncharuck, V., Luyckx, S., & Northrop, I. T. (1997). Low and high temperature hardness of WC-6wt%Co alloys. *International Journal of Refractory Metals and Hard Materials, 15*, 97–101.

Milman, Yu. V., Luyckx, S., & Northrop, I. T. (1999). Influence of temperature, grain size and cobalt content on the hardness of WC-Co alloys. *International Journal of Refractory Metals and Hard Materials, 17*, 39–44.

Mukhopadhyay, A., & Basu, B. (2011). Recent developments on WC-based bulk composites. *Journal of Materials Science, 46*, 571–589.

Moyle, D. R, & Kimmel, E. R. (1989). Effect of coarse WC grains on transverse rupture strength of fine grain hardmetals. In H. Bildstein, & H. M Orthner (Eds.), *Proceedings of 12th International Plansee Seminar* (pp. 311–320). Reutte/Tirol: Metallwerk Plansee.

Mukhopadhyay, A., Chakravarty, D., & Basu, B. (2010). Spark plasma-sintered WC-ZrO2-Co nanocomposites with high fracture toughness and strength. *Journal of the American Ceramic Society, 93*, 1754–1763.

Nabarro, F. R. N., & Bartolucci Luyckx, S. (1968). The theory of the strength of tungsten carbide-cobalt compacts. *Transactions of the Japan Institute of Metals Supplement, 9*, 610–615.

Nakamura, M., & Gurland, J. (1980). The fracture toughness of WC-Co two-phase alloys. A preliminary model. *Metallurgical Transactions A, 11*, 141–146.

Niihara, K. (1983). A fracture mechanics analysis of indentation-induced Palmqvist crack in ceramics. *Journal of Materials Science Letters, 2*, 221–223.

Niihara, K., Morena, R., & Hasselman, D. P. H. (1982). Evaluation of K1c of brittle solids by the indentation method with low crack-to-indent ratios. *Journal of Materials Science Letters, 1*, 13–16.

Nishimatsu, C., & Gurland, J. (1960). Experimental survey of the deformation of the hard-ductile two-phase alloy system WC-Co. *Transactions of ASM, 52*, 469–484.

Orowan, E. (1948). Fracture and strength of solids. *Reports on Progress in Physics, XII*, 185–232.

Ostberg, G., Buss, K., Christensen, M., et al. (2006). Mechanisms of plastic deformation of WC-Co and Ti(C, N)-WC-Co. *International Journal of Refractory Metals and Hard Materials, 24*, 135–144.

Ostberg, G., Farooq, M. U., Christensen, M., et al. (2006). Effect of $\Sigma 2$ grain boundaries on plastic deformation of WC-Co cemented carbides. *Materials Science and Engineering: A, 416*, 119–125.

Osterstock, F., & Chermant, J.-L. (1983). Some aspects of the fracture of WC-Co-composites. In R. K. Viswanadham, D. Rowcliffe, & J. Gurland (Eds.), *Proceedings of the 1st international conference on the science of hard materials* (pp. 615–629). New York: Plenum Press.

Paggett, J. W., Krawitz, A. D., Drake, E. F., et al. (2006). In situ loading response of WC-Ni: origins of toughness. *International Journal of Refractory Metals and Hard Materials, 24*, 122–128.

Paggett, J. W., Krawitz, A. D., Drake, E. F., et al. (2007). In-situ response of WC-Ni composites under compressive load. *Metallurgical and Materials Transactions A, 38*, 1638–1648.

Palmqvist, S. (1957). A method to determine the toughness of brittle materials, especially hard metals. *Jernkontorets Annaler, 141*, 303–307.

Palmqvist, S. (1962). The work for the formation of a crack during Vickers indentation as a measure of the toughness of hard metals. *Archiv fur das Eisenhuttenwesen, 33*, 629–633.

Paul, B. (1960). Prediction of elastic constants of multiphase materials. *Transactions of the Metallurgical Society of AIME, 218*, 36–41.

Perrott, C. M. (1978). On the indentation fracture of cemented carbide II — the nature of surface fracture toughness. *Wear, 47*, 81–91.

Petch, N. J. (1953). The cleavage strength of polycrystals. *The Journal of the Iron and Steel Institute, 174*, 25–28.

Pickens, J. R., & Gurland, J. (1978). The fracture toughness of WC-Co alloys measured on single-edge notched beam specimens precracked by electron discharge machining. *Materials Science and Engineering, 33*, 135–142.

Prakash, L. (1993). A review of the properties of tungsten carbide hardmetals with alternative binder systems. In H. Bildstein, & R. Eck (Eds.), *Proceedings of 13th international plansee seminar* (pp. 80–109). Reutte/Tirol: Metallwerk Plansee.

Prakash, L. J. (1995). Application of fine grained tungsten carbide based cemented carbides. *International Journal of Refractory Metals and Hard Materials, 13*, 257–264.

Ravichandran, K. S. (1994). Fracture toughness of two phase WC-Co cermets. *Acta Metallurgica et Materialia, 42*, 143–150.

Rice, R. W. (1983). Mismatch stress effects on microstructure-flaw size dependence of K_{1C} and strength of metal bonded carbides. In R. K. Viswanadham, D. Rowcliffe, & J. Gurland (Eds.), *Proceedings of the 1st international conference on the science of hard materials* (pp. 631–648). New York: Plenum Press.

Richter, V., & Ruthendorf, M. V. (1999). On hardness and toughness of ultrafine and nanocrystalline hard materials. *International Journal of Refractory Metals and Hard Materials, 17*, 141–152.

Roebuck, B. (1979). The tensile strength of hardmetals. *Journal of Materials Science, 14*, 2837–2844.

Roebuck, B. (1988). Notched bend tests on WC-Co hardmetals. *Journal of Materials Science, 23*, 281–287.

Roebuck, B. (1995). A model for the limiting strength of hardmetals. *Journal of Hard Materials, 6*, 1–15.

Roebuck, B., & Almond, E. A. (1988). Deformation and fracture processes and the physical metallurgy of WC-Co hardmetals. *International Materials Reviews, 33*, 90–110.

Roebuck, B., Almond, E. A., & Cottenden, A. M. (1984). The influence of composition, phase transformation and varying the relative FCC and HCP phase contents on the properties of dilute Co-W-C alloys. *Materials Science and Engineering, 66*, 179–194.

Rowcliffe, D. J., Jayaram, V., Hibbs, M. K., & Sinclair, R. (1988). Compressive deformation and fracture in WC materials. *Materials Science and Engineering: A, 105–106*, 299–303.

Sailer, T., Herr, M., Sockel, H.-G., et al. (2001). Microstructure and mechanical properties of ultrafine-grained hardmetals. *International Journal of Refractory Metals and Hard Materials, 19*, 553–559.

Schmauder, S. (2001). Crack growth in multiphase materials. In K. H. J. Buschow, R. W. Cahn, M. C. Flemings, B. Ilschner, E. J. Kramer, S. Mahajan, et al. (Eds.), *Encyclopedia of materials: science and technology* (pp. 1735–1741). Elsevier.

Schmid, H. G., Mari, D., Benoit, W., & Bonjour, C. (1988). The mechanical behaviour of cemented carbides at high temperatures. *Materials Science and Engineering: A, 105–106*, 343–351.

Schreiner, M., Schmitt, Th., Lassner, E., & Lux, B. (1984). On the origins of discontinuous grain growth during liquid phase sintering on WC-Co cemented carbides. *Powder Metallurgy International, 16*, 180–183.

Schubert, W. D., Neumeister, H., Kinger, G., & Lux, B. (1998). Hardness to toughness relationship of fine-grained hardmetals. *International Journal of Refractory Metals and Hard Materials, 16*, 133–142.

Shatov, A. V., & Firstov, S. A. (1995). Variation of WC crystal shape due to Ti segregation onto interphase boundaries in WC-Ni hardmetals. *Physics of Metals, 14*, 789–797.

Shatov, A. V., Firstov, S. A., & Shatova, I. V. (1998). The shape of WC crystals in cemented carbides. *Materials Science and Engineering: A, 242*, 7–14.

Shatov, A. V., Ponomarev, S. S., & Firstov, S. A. (2006). Strength of WC-Ni cemented carbides with different shape of WC crystals. In , *Hard materials: Vol. 1. Proceedings of the powder metallurgy congress & exhibition Euro PM2006* (pp. 77–82). Ghent: EPMA.

Shatov, A. V., Ponomarev, S. S., & Firstov, S. A. (2008). Fracture of WC-Ni cemented carbides with different shape of WC crystals. *International Journal of Refractory Metals and Hard Materials, 26*, 68–76.

Shatov, A. V., Ponomarev, S. S., & Firstov, S. A. (2009). Modeling the effect of flatter shape of WC crystals on the hardness of WC-Ni cemented carbides. *International Journal of Refractory Metals and Hard Materials, 27*, 198–212.

Shatov, A. V., Ponomarev, S. S., Firstov, S. A., & Warren, R. (2006). The contiguity of carbide crystals of different shapes in cemented carbides. *International Journal of Refractory Metals and Hard Materials, 24*, 61–74.

Shatov, A. V., Ponomarev, S. S., & Firstov, S. A. (2014). *Model for transverse rupture strength of cemented carbides*.

Shetty, D. K., & Wright, I. G. (1986). On estimating fracture toughness of cemented carbides from Palmqvist crack sizes. *Journal of Materials Science Letters, 5*, 365–368.

Shetty, D. K., Wright, I. G., Mincer, P. N., & Clauer, A. H. (1985). Indentation fracture of WC-Co cermets. *Journal of Materials Science, 20*, 1873–1882.

Sigl, L. S., & Exner, H. E. (1987). Experimental study of the mechanics of fracture in WC-Co alloys. *Metallurgical Transactions A, 18*, 1299–1308.

Sigl, L. S., & Exner, H. E. (1989). The flow stress and hardness of metal-reinforced brittle composites. *Materials Science and Engineering: A, 108*, 121–129.

Sigl, L. S., Exner, H. E., & Fischmeister, H. F. (1986). Characterization of fracture processes and fracture relevant parameters in WC-Co hard metals. In E. A. Almond, C. A. Brookes, & R. Warren (Eds.), *Proceedings of 2nd international conference on the science of hard materials* (pp. 631–644). Bristol and Boston: Adam Hilger.

Sigl, L. S., & Fischmeister, H. F. (1988). On the fracture toughness of cemented carbides. *Acta Metallurgica, 36*, 887–897.

Slesar, M., Dusza, J., & Parilak, L. (1986). Micromechanics of fracture in WC-Co hardmetals. In E. A. Almond, C. A. Brookes, & R. Warren (Eds.), *Proceedings of 2nd international conference on the science of hard materials* (pp. 657–668). Bristol and Boston: Adam Hilger.

Spiegler, R., & Fischmeister, H. F. (1992). Prediction of crack paths in WC-Co alloys. *Acta Metallurgica et Materialia, 40*, 1653–1661.

Spiegler, R., Schmauder, S., & Sigl, L. S. (1990). Fracture toughness evaluation of WC-Co alloys by indentation testing. *Journal of Hard Materials, 1*, 147–158.

Suzuki, H, & Hayashi, K. (1975). Strength of WC-Co cemented carbides in relation to their fracture sources. *Planseeberichte fur Pulvermetallurgie, 23*, 24–36.

Tracey, V. A. (1992). Nickel in hardmetals. *International Journal of Refractory Metals and Hard Materials, 11*, 137–149.

Underwood, E. E. (1968). *Quantitative stereology*. London: Addison-Wesley.

Unosson, M., Olovsson, L., & Simonsson, K. (2007). Weakest link model with imperfection density function: application to three point bend of a tungsten carbide. *International Journal of Refractory Metals and Hard Materials, 25*, 6–10.

Vasel, C. H., Krawitz, A. D., Drake, E. F., & Kenik, E. A. (1985). Binder deformation in WC-(Co, Ni) cemented carbide composites. *Metallurgical Transactions A, 16*, 2309–2317.

Vicens, J., Benjdir, M., Nouet, G., Dubon, A., & Laval, J. Y. (1994). Cobalt intergranular segregation in WC-Co composites. *Journal of Materials Science, 29*, 987–994.

Viswanadham, R. K., & Precht, W. (1980). Preparation and properties of VC + Ni cermets with controlled carbon-to-metal ratio. *Metallurgical and Materials Transactions A, 11*, 1475–1485.

Viswanadham, R. K., Sun, T. S., Drake, E. F., & Peck, J. A. (1981). Quantitative fractography of WC-Co cermets by Auger spectroscopy. *Journal of Materials Science, 16*, 1029–1038.

Viswanadham, R. K., & Venables, J. D. (1977). A simple method for evaluating cemented carbides. *Metallurgical and Materials Transactions A, 8*, 187–191.

Warren, R., & Johannesson, B. (1984a). Creation of stable cracks in hardmetals using 'bridge' indentation. *Powder Metallurgy International, 27*, 25–29.

Warren, R., & Johannesson, B. (1984b). Fracture toughness of hardmetals. *International Journal of Refractory Metals and Hard Materials, 3*, 187–191.

Warren, R., & Matzke, H. (1983). Indentation testing of a broad range of cemented carbides. In R. K. Viswanadham, D. Rowcliffe, & J. Gurland (Eds.), *Proceedings of the 1st international conference on the science of hard materials* (pp. 563–582). New York: Plenum Press.

Warren, R., & Waldron, M. B. (1972). Microstructural development during the liquid-phase sintering of cemented carbides. *Powder Metallurgy, 15*, 166–201.

Weibull, W. (1951). A statistical distribution function of wide applicability. *Journal of Applied Mechanics, Transactions of ASME, 18*, 293–297.

Weidow, J., & Andren, H.-O. (2010). Grain and phase boundary segregation in WC-Co with small V, Cr or Mn additions. *Acta Materialia, 58*, 3888–3894.

Weidow, J., & Andren, H.-O. (2011). Grain and phase boundary segregation in WC-Co with TiC, ZrC, NbC or TaC additions. *International Journal of Refractory Metals and Hard Materials, 29*, 38–43.

Weidow, J., Norgren, S., & Andren, H.-O. (2009). Effect of V, Cr and Mn additions on the microstructure of WC-Co. *International Journal of Refractory Metals and Hard Materials, 27*, 817–822.

Weidow, J., Zackrisson, J., Jansson, B., & Andren, H.-O. (2009). Characterisation of WC-Co with cubic carbide additions. *International Journal of Refractory Metals and Hard Materials, 27*, 244–248.

Weisbrook, C. M., & Krawitz, A. D. (1996). Thermal residual stress distribution in WC-Ni composites. *Materials Science and Engineering: A, 209*, 318–328.

1.11 Fatigue of Cemented Carbides

Luis Llanes and Marc Anglada, Departament de Ciència dels Materials i Enginyeria Metal·lúrgica, Universitat Politècnica de Catalunya · Barcelona Tech, Barcelona, Spain
Yadir Torres, Universidad de Sevilla, Department of Mechanical and Materials Engineering—ETSI, Sevilla, Spain

1.11.1 Introduction

Manufacturers and end users of critical engineering parts and components are under increasing pressure to improve operating performance at reduced costs. With a range of applications, from tools used for machining, drilling and mining operations, through dies employed in the forging and stamping industries, to precision parts used in the medical, electronic, aerospace and automobile industries, competitive challenges are making industrial managers more acutely aware of the need to enhance material performance and component lifetime. Within this context, fatigue represents, together with wear and corrosion, one of the most important service degradation phenomena. Fatigue failures of single structural elements are premature and unexpected and then result in downtime for the entire engineering system that is far more costly than the individual components themselves. A clear example of such performance–economy interaction is given by considering the relevance of the quality of tool systems as a substantial economic factor in individual operations, which reaches staggering proportions when accounted in terms of final cost of manufactured products, loss of energy through the diminishing efficiency of deteriorating equipment and waste of resources through the discarding of dull tools and defective products. Under cyclic loads, improving the performance of engineering components and predicting their life requires knowledge, accurate description and understanding of the associated fatigue response and mechanisms. The main goal of this chapter is to present a critical review of the existing information on the fatigue behavior of cemented carbides, materials also referred to as hardmetals. In doing so, special attention is paid to the experimental and analytical approaches used by different research groups as well as to microstructural effects on the strength degradation and subcritical crack propagation assessed for these materials when subjected to cyclic loads. However, in contrast to parameters such as hardness, strength, toughness and wear resistance, for which there exist comprehensive literature surveys about the influence of microstructure (e.g. Exner, 1979; Fischmeister, 1983; Gee, Gant, Roebuck, & K.P. Mingard, 2014; Gurland, 1988; Roebuck & Almond, 1988; Shatov, 2014), information on fatigue behavior is not as extensive.

At this stage, from the information given in companion review papers, the definition and description of cemented carbides as composite materials is well established. However, from a fatigue perspective, the interpenetrating microstructural scenario of these materials should be highlighted. Depending on the metallic phase content (and processing history), the state of aggregation of the ceramic hard phase ranges from more or less isolated ceramic particles dispersed in the binder phase of alloys (high metal content) to a highly connected skeleton of contiguous carbide grains for grades with low binder content (Gurland, 1988). Hence, considering that compositions of commercial grades range from 3 to 30 wt% of metallic binder, cemented carbides may be micromechanically described as composites of ceramic nature (rather than metal-based) reinforced by ductile metallic ligaments, strengthened through the constraint imposed by the very rigid carbide crystals and

http://dx.doi.org/10.1016/B978-0-08-096527-7.00011-8

exhibiting internal residual stresses due to the different thermal contraction of both phases during cooling of the liquid phase sintered components. All these particularities are important for analyzing and discussing the fatigue behavior of these materials.

1.11.2 Strength Degradation under Cyclic Loads

The most widely used approach to study the fatigue behavior of structural materials is determining the stress–number of cycles (*S*–*N*) curves, also referred to as Wöhler plots, and this also applies to cemented carbides. Here, the fatigue life is measured as the number of cycles to fracture for smooth specimens that are subjected to a constant-amplitude stress. An interesting parameter defined from this test methodology is the endurance limit for a specified number of cycles, frequently reported as fatigue limit for the correspondingly defined "infinite fatigue life", usually in the range of 10^6–10^8 cycles.

Strength degradation under cyclic loads for hardmetals is a phenomenon known since the early 1940s (Dawihl, 1941). Surprisingly, additional works on fatigue deformation and fracture (on smooth specimens[1]) during the following half century were just a few, although most of them yielded concordant data as long as they were conducted under similar loading mode (Brookes, 1982; Davies & Barhana, 1972; Drake & Krawitz, 1981; Fujiwara, Ueda, Masatomi, & Suzuki, 1980; Johansson, Persson, & Hiltscher, 1970; Krawitz, Roberts, & Faber, 1986; Miyake, Fujiwara, & Nishigaki, 1968; Otsuka, Tohgo, Sugawara, & Ueda, 1987; Schedler, 1988; Stephenson, Chung, & Coleman, 1985; Vasel, Krawitz, Drake, & Kenik, 1985). Hence, from the information provided by Fujiwara et al. (Fujiwara et al., 1980), Brookes (Brookes, 1982) and Schedler (Schedler, 1988), it could be stated that fatigue limits for similar cemented carbides were in the range of 30–40% of their bending strengths. Fatigue behavior in bending was also studied by Miyake et al. (Miyake et al., 1968) as well as by Davies and Barhana (Davies & Barhana, 1972) on WC–Co alloys with different binder contents, but in both studies, ultimate tensile strength (UTS) was used as reference baseline; accordingly, endurance limit defined at fatigue lives of about 10^7 cycles were assessed at higher relative values (i.e. in the range of about 60–75% of the corresponding UTS). Similarly, only a slight strength lessening (15–30%) under cyclic mechanical loads was discerned under compressive loading for plain WC–Co alloys by Johansson et al. (Johansson et al., 1970). On the other hand, pronounced fatigue effects were assessed by Stephenson et al. (Stephenson et al., 1985) and Otsuka et al. (Otsuka et al., 1987) when studying the influence of surface condition/microstructure and load ratio, respectively, with particular emphasis on failure initiation sites. However, in general, clear trends on microstructural effects described in individual studies were difficult to generalize on the basis of experimental data reported by different authors.

Compressive cyclic loading was also used by Krawitz's group at the University of Missouri (Drake & Krawitz, 1981; Krawitz et al., 1986; Vasel et al., 1985), but in this research program, efforts were concentrated on studying fatigue-induced substructural changes in cemented carbides, particularly binder deformation and residual stress relaxation, instead of fatigue strength. In doing so, the deformation mechanisms operating within the binder in WC–Co and WC-(Co,Ni) were investigated and established through analysis involving two compatible and mutually supportive techniques: neutron diffraction and high-voltage transmission electron microscopy (TEM). One of their main goals was to document and analyze the effective role under monotonic and cyclic compressive loading of the strain-induced transformation experimented by the cobalt binder from metastable face-centered cubic (fcc) to hexagonal closely packed (hcp) phase under load (e.g. Sarin & Johannesson, 1975), relative to other deformation mechanisms, as a function of binder composition.

The research conducted by Krawitz's group yielded several key and interesting conclusions. First, fatigue loading was shown to clearly induce progressive accumulation of deformation in cemented carbides, as evidenced from the significant enhancement of the amount of hcp transformation product for cyclic relative to monotonic mechanical treatment at the same level of plastic strain (Table 1). Furthermore, a large amount of this transformation was found to take place in the first cycle, a behavior correlated with relaxation of the differential thermal residual stress state present in these materials (Krawitz et al., 1986). Second, fatigue damage was shown to be binder intensive and predominantly local in character, the latter resulting in a source of incipient defects and a means of stable propagation of flaws. Additionally, this local scale (WC grain size-like) of fatigue-induced changes implied only modest changes in macroscale properties, i.e. hardness, fracture

---

[1] The referred literature here does not include intentionally some additional studies conducted in the 1980s on the fatigue crack growth behavior of cemented carbides. They will be recalled and discussed in the next section, particularly devoted to fatigue testing of precracked specimens.

Table 1 Volume percent of binder fcc phase (percent of binder transformed to hcp) after mechanical treatment (fatigue or monotonic) as a function of binder composition

		Cermet composition		
Mechanical treatment	*Plastic strain (%)*	*WC-(100Co)*	*WC-(85Co-15Ni)*	*WC-(70Co-30Ni)*
As-sintered	0	23.7 ± 2.2	25.8 ± 1.0	25.0 ± 0.7
Low-fatigue (1.0 GPa/5 × 10^5 cycles)	0.04–0.10	23.0 ± 2.3 (3.0)	25.0 ± 1.0 (3.1)	24.9 ± 1.5 (0.5)
High-fatigue (2.1 GPa/5 × 10^5 cycles)	0.12–0.61	14.6 ± 0.9 (38.2)	18.8 ± 0.8 (27.2)	23.9 ± 2.0 (4.2)
Low monotonic (0.75%/1 cycle)	0.25–0.30	20.4 ± 1.1 (13.9)	23.9 ± 0.5 (7.2)	24.7 ± 1.3 (1.1)
High-monotonic (5.00%/1 cycle)	4.33–4.50	13.1 ± 1.5 (44.5)	17.4 ± 1.5 (32.5)	22.1 ± 1.6 (11.4)

Vasel et al. (1985), Krawitz et al. (1986).

toughness and residual stresses in individual phases. Third, predominant binder-deformation mechanisms were observed to shift with increasing Ni content from the fcc–hcp martensitic transformation to slip plus twinning over the composition range of binder metastability studied, i.e. from 100Co to 70Co-30Ni. However, there was a marked region-to region variation in the deformation structure observed as well as a wide range of distribution of local residual stresses. It pointed out a likely complex interaction between carbide and binder deformation, possibly involving residual stress state, microcracks and geometrically induced local variations, that was not fully understood.

Aware of the need for a more comprehensive description of the behavior of cemented carbides under cyclic loads as well as a more profound scientific understanding of the fatigue process, a systematic and extensive investigation was launched by the research group led by Sockel at the University of Erlangen-Nürnberg in the early 1990s. To date, it is the most complete work following the *S*–*N* approach and it was complemented by detailed electron microscopic analysis, both TEM and scanning electron microscopy (SEM), of microscopic features on fracture surfaces and of the microstructure in the volume in the wake and in the front of growing cracks (Erling, Kursawe, Luyckx, & Sockel, 2000; Kindermann et al., 1999; Kursawe, Pott, Sockel, Heinrich, & Wolf, 2001; Sailer et al., 2001; Schleinkofer, Sockel, Görting, & Heinrich, 1996a; Schleinkofer, Sockel, Görting, & Heinrich, 1996b; Schleinkofer, Sockel, Görting, & Heinrich, 1997; Schleinkofer, Sockel, Schlund, Görting, & Heinrich, 1995; Schlund et al., 1999).

Considering the ceramic/metal (cermet) composite nature of the investigated materials, one of the main goals of this research team was to identify and separate (if possible) the influence of the brittle ceramic phase and the ductile binder on the mechanical behavior of hardmetals (plain WC–Co alloys) and cermets (other combinations) under monotonously increasing, static and cyclic alternating loads. Within this context, testing throughout the program was conducted, for the three different loading conditions, in a modified version of the reversed cantilever bending stress apparatus originally developed by Fett et al. (Fett, Martin, Munz, & Thun, 1991). The static mode option was introduced for assessing possible environmental-assisted (even in air) failure, as it had been reported in glass, porcelain and alumina. On the other hand, there were strong interests in evaluating and analyzing the fatigue behavior of cemented carbides on the basis that microstructural developments leading to an increase of toughness for new ceramic materials and ceramic-containing composites were also found to induce a decreased resistance against cyclic loads (Dauskardt, James, Porter, & Ritchie, 1992; Grathwohl, 1988; Liu & Chen, 1991a; Liu & Chen, 1991b; Ritchie, 1988; Steffen, Dauskardt, & Ritchie, 1991; Suresh, 1991).

Within the above framework, research carried out by Sockel's group was very useful for elucidating several aspects of the fatigue behavior of cemented carbides. It extensively documented the strong strength degradation fatigue under cyclic loads that hardmetals and cermets exhibit (e.g. Figure 1) (Kindermann et al., 1999; Kursawe et al., 2001; Sailer et al., 2001; Schleinkofer et al., 1996a, 1996b; Schleinkofer et al., 1997; Schleinkofer et al., 1995; Schlund et al., 1999). Corresponding fractographic examination permitted to associate such degradation with fatigue mechanisms occurring predominantly in the metallic binder phase (Erling et al., 2000; Schleinkofer et al., 1996a; Schleinkofer et al., 1995) in complete agreement with the findings reported by Drake and Krawitz (Drake & Krawitz, 1981). Consequently, neither mechanical degradation under applied constant load (up to 95% of inert strength) (Schleinkofer et al., 1996b; Schleinkofer et al., 1997; Schleinkofer et al., 1995) nor fatigue life dependence on testing frequency (Schleinkofer et al., 1996b) were assessed; thus, it was concluded that static fatigue effects may be disregarded in those materials.

As it was indicated above, highlighting the relevance of microstructure on the fatigue behavior of cemented carbides was always within the scope of research conducted by Sockel's team. From this viewpoint, studies were

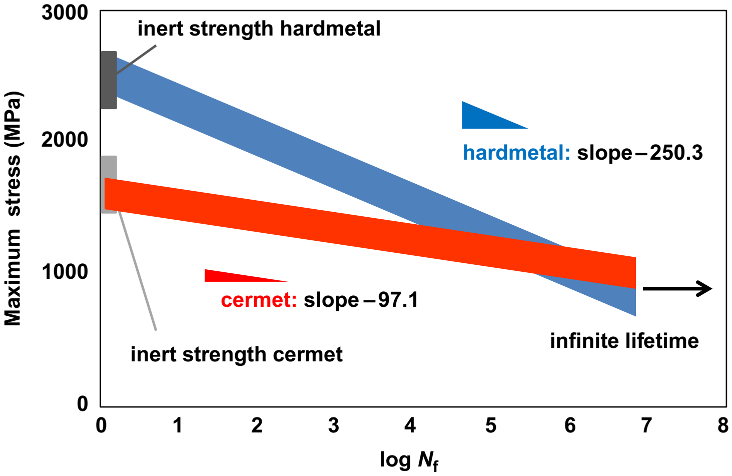

Figure 1 Wöhler plots of the cycles until failure (N_f) for representative hardmetal and cermet grades. Adapted from Schleinkofer et al. (1996a).

focused on the fatigue deformation and damage micromechanisms within ductile ligaments at the wake and around the tip of subcritical propagating cracks. The prevalence of subcritical crack growth over crack nucleation was confirmed, besides evidences from fractographic analysis, on the basis of compliance measurements (Schleinkofer et al., 1997). Within this context, distinct microstructural parameters were investigated, although main efforts concentrated on evaluating the influence of different amount and composition of the ductile binder phase (Kursawe et al., 2001; Sailer et al., 2001; Schleinkofer et al., 1996a, 1996b; Schleinkofer et al., 1997; Schleinkofer et al., 1995).

The relative comparison of susceptibility to strength degradation under cyclic loads was analyzed by Sockel's group by means of normalized Wöhler plots (using the ratio between cyclic experimental and the corresponding monotonic determined strength as plotting parameter), such that steeper slopes in the curves yielded an indication of higher accumulation of damage during the cyclic loading (e.g. Figure 2) (Sailer et al., 2001; Schleinkofer et al., 1997). From the gathered data, it was concluded that plain cobalt (hardmetals) was more fatigue sensitive than CoNi or CoNiFe alloys (cermets), at least in the range of medium- to ultrafine-grained grades (Kursawe et al., 2001; Sailer et al., 2001; Schleinkofer et al., 1997). Similarly, fatigue sensitivity was also shown to increase as the mean free path of metallic binder rose, although this dependence was found to be variable for distinct binder types (Kursawe et al., 2001; Sailer et al., 2001) (Figure 3). The higher susceptibility to strength degradation under cyclic loads for hardmetals, as compared to that of cermets, was correlated to localized damage in shear bands as well as in areas of transformed binder phase. In agreement with the findings

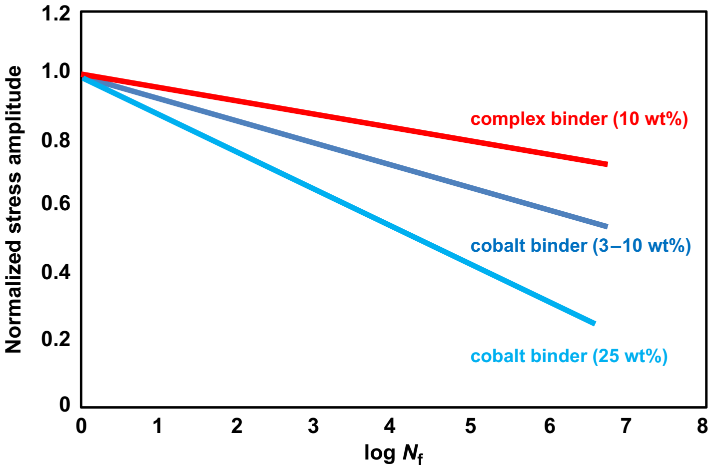

Figure 2 Normalized Wöhler plot of the cycles until failure (N_f) for the evaluation of the fatigue sensitivity of ultrafine-grained hardmetals. Adapted from Sailer et al. (2001).

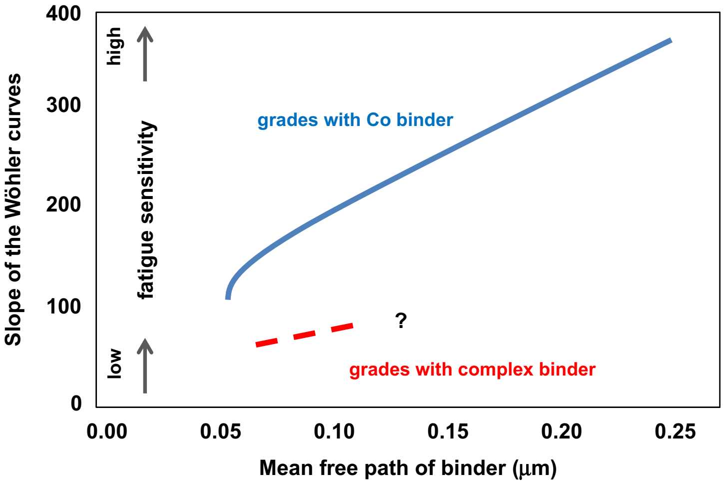

Figure 3 Correlation of the slope of the Wöhler plots, as a measurement of fatigue sensitivity, with the mean free path of binder. Question mark (?) indicates expected but unknown trend for CoNi- and CoNiFe-base cermets. Adapted from Sailer et al. (2001).

by Krawitz and coworkers (Drake & Krawitz, 1981; Vasel et al., 1985), fatigue-induced accumulation of fcc to hcp transformation within the binder, discerned by stacking faults under TEM, was found to diminish and/or become absent for CoNi and CoNiFe binders. As a consequence, the harmful ductility reduction on the reinforced ligaments at the crack wake—main toughening mechanism for cemented carbides (Krstic, 1983; Sigl & Exner, 1987; Sigl & Fischmeister, 1988; Torres, Bermejo, Llanes, & Anglada, 2008; Torres et al., 2012; Viswanadham, Sun, Drake, & Peck, 1981)—recalled by the authors as the dominant fatigue mechanism for hardmetals, was inhibited for the cermets (Erling et al., 2000; Kursawe et al., 2001; Sailer et al., 2001; Schleinkofer et al., 1996a). Nevertheless, special care should be taken in extrapolating these ideas when considering absolute strength (monotonic and cyclic) values, where hardmetals usually outperform cermets with similar microstructural parameters (binder content and carbide grain size). Such better mechanical response goes beyond fatigue; thus, the especially favorable chemical bonding between WC and Co (Exner, 1979) should also be recalled here as the main reason for this behavior. Additionally, as it was already exposed by the authors (Kursawe et al., 2001; Schleinkofer et al., 1997), the fact that the above-mentioned trends were not completely followed in all the cases indicates how difficult it is to make general predictions about the changes of the fatigue resistance with composition and microstructure for materials with interpenetrating networks of two completely different phases. Within this microstructural scenario, subcritical cracks have to travel through both ceramic- and binder-contiguous skeletons; thus, their effective lower energy growth paths and the corresponding interaction with microstructure during fatigue-induced propagation will be controlled not only by the constrained ductility, work hardening and fatigue susceptibility of ductile binder ligaments but also by the intrinsic mechanical properties of the carbides, interface-related aspects and relative microstructural scales (e.g. between carbide grain size and mean free path binder). It is then evident that further research is required in this field if the fatigue performance of cemented carbides, in terms of microstructural design, lifetime and reliability, needs to be improved.

As it was the case before the research program set out by Sockel's group, recent reports on fatigue strength of cemented carbides are also scarce. In general, they correspond to actions much more limited in scope, from a fatigue perspective, than the referred program. All these studies have somehow confirmed already established cyclic stress effects on hardmetals (Ferreira, Pina Amaral, Antunes, & Costa, 2009; Gee, Mingard, & Roebuck, 2009; Ishihara, Goshima, Yoshimoto, & Sabu, 1999; Klaasen, Kübarsepp, Tsinjan, & Sergejev, 2011; Kluensner et al., 2009; Klünser et al., 2010; Li, Zhao, Wang, Gao, & Tang, 2013; Roebuck, 2002; Roebuck, Maderud, & Morrell, 2008; Roebuck, Mingard, Nordenstrom, & Halling, 2009; Sakagami, Kouno, & Yamamoto, 2007; Sakagami & Yamamoto, 2006; Sergejev, Preis, Hussainova, & Kübarsepp, 2008; Sergejev, Preis, Kübarsepp, & Antonov, 2008), but some of them include interesting new findings and approaches. For instance, Klünser et al. (Kluensner et al., 2009; Klünser et al., 2010) reported for different WC–Co alloys the existence of ratcheting behavior in their cyclic stress–strain curve, determined under uniaxial compression loading for stress ratios of -1 and -3, and applied compressive stresses above the elastic limit. In this work, mean stress effects on fatigue strength were also observed to follow similar trends as reported before, i.e. increasing fatigue strength with decreasing stress ratio from 0.1 to −3. Regarding fractographic analysis, as it is also implemented by Sergejev et al. (Sergejev, Preis, Kübarsepp, et al., 2008), Klünsner et al. (Klünser et al., 2010) invoke correlations between fatigue life and size of microstructural defects on the basis of Murakami's geometrical parameter of maximum flaw area. From a testing perspective, Roebuck and coworkers have introduced the use of notched test pieces (Gee et al., 2009; Roebuck, 2002; Roebuck et al., 2008; Roebuck et al., 2009) as baseline for new testing protocols. The main reason for this is that interpretation of results from fatigue bend tests on smooth specimens suffers from the same (or even more) difficulties associated with conventional bend tests in that failures initiate at pores or other internal defects (Roebuck & Almond, 1988). Thus, intrinsic microstructural effects may be hindered by the influence of distribution and size of processing defects and/or the method of surface preparation on strength data. Within this context, the use of V-notched (and annealed) specimens have been successfully implemented for discriminating precompression fatigue effects and fatigue sensitivity among microstructurally different hardmetals: steeper *S*–*N* curves were found with decreasing hardness (and increasing toughness) (Roebuck, 2002; Roebuck et al., 2009). However, results still showed considerable scatter, and further analysis involving fracture mechanics concepts was needed for final rationalization of the experimental *S*–*N* behavior. Although the use of notched specimens by the National Physics Laboratory's (NPL's) group is rather focused on the evaluation of the thermomechanical fatigue response of cemented carbides—as originally aimed (Roebuck & Gee, 1996; Dary, Roebuck, & Gee, 1999), and corresponding results to be commented in a later section—it clearly represents an interesting complementary testing methodology for evaluating and understanding microstructural effects on these materials. Notched specimens have also been employed in several studies recently, although following different objectives: assessment of fatigue notch sensitivity of cermets (Sergejev, Preis, Hussainova, et al., 2008), evaluation of high-temperature fatigue strength (Ferreira et al., 2009), and analysis of microstructural effects on fatigue behavior (Li et al., 2013). The results presented in these studies are promising regarding suitability of using notched specimens for assessing microstructural effects on fatigue response under service-like conditions, i.e. presence of stress concentrators in component geometry and exposure to high temperature. However, special care should be taken when comparing data attained using notched and unnotched specimens because of the uncertainty in the intrinsic influence of microstructure on fatigue notch sensitivity for cemented carbides, a subject for which information in the open literature is extremely limited. Finally, from an in-service viewpoint, it is interesting to highlight the study conducted by Klaasen et al. (Klaasen et al., 2011) where the higher blanking performance of a TiC-based cermet, as compared to the one assessed for a conventional WC-based hardmetal, is rationalized on the basis of the lower fatigue sensitivity (together with a higher adhesive wear resistance) exhibited by the former with respect to the latter.

1.11.3 Fatigue Crack Growth

In many fields of engineering, the traditional stress–life approach described in the previous section competes with a damage-tolerant or fracture mechanics one for assessing probability of fatigue failure on the basis of testing to failure. The latter, although experimentally and analytically more complex and less extensively used than the former, offers many distinct advantages: (1) it is invariably more conservative; (2) it enables a quantitative evaluation of the damaging effect of preexisting flaws or defects in the material; and (3) it provides a rational basis for quality control of the product (Marrey, Burgermeister, Grishaber, & Ritchie, 2006). Within this framework, fatigue life is computed in terms of the time or number of cycles required to propagate the largest preexisting flaw to failure. Hence, description of fatigue crack growth (FCG) kinetics as related to dependence of crack extension rate on the alternating and mean stress intensities, specifically ΔK and K_{max}, and physical understanding of the FCG threshold concept become critical. This is particularly relevant for the case of cemented carbides, materials where it is now well established that crack initiation is invariably associated with some preexisting defect (e.g. Schleinkofer et al., 1997); thus, the subcritical growth of these flaws is indeed the controlling stage in their fatigue failure (Erling et al., 2000; Kindermann et al., 1999; Kursawe et al., 2001; Sailer et al., 2001; Schleinkofer et al., 1996a, 1996b; Schleinkofer et al., 1997; Schlund et al., 1999).

Along the 1970s, the advent of fracture mechanics application to cemented carbides (Chermant, Deschanvres, & Iost, 1973; Exner, Walter, & Pabst, 1974; Ingelström & Nordberg, 1974; Kenny, 1971; Lueth, 1974) brought along the challenge of developing methodologies for introducing sharp stress-free cracks into these materials. Once this was achieved, several studies on the FCG behavior of these materials were conducted in the following three decades (Almond & Roebuck, 1980; Boo & Park, 2005; Evans & Linzer, 1976; Fry & Garret, 1983; Fry & Garret, 1988; Hirose, Boo, Matsuoka, & Park, 1997; Ishihara, Goshima, Yoshimoto, et al., 1999; Ishihara, Goshima, Yoshimoto, Sabu, & McEvily, 2000; James, Human, & Luyckx, 1990; Knee & Plumbridge, 1984; Suresh & Sylva, 1986). Although the scope of most of these studies was distinct among each other, all of them were somehow dealing with a similar goal: to document and analyze the occurrence of a true fatigue process in these materials. In this regard, the reports by Evans and Linzer (Evans & Linzer, 1976), Almond and Roebuck (Almond & Roebuck, 1980), and Fry and Garrett (Fry & Garret, 1983, 1988) should be highlighted.

Evans and Linzer (Evans & Linzer, 1976) were the first to report a strong cyclic effect on hardmetals. However, the primary purpose of their work was to describe techniques and the instrumentation that could be utilized for precise studies of high-frequency cyclic crack propagation effects in ceramic materials; thus, structure–property relationships in these materials were not investigated. Nevertheless, from this early work conducted on a WC-6 wt% Co grade, a significant dependence of FCG on the mean (and peak) values of the stress intensity factor was already pointed out.

Different from the previous work, Almond and Roebuck (Almond & Roebuck, 1980) focused on documenting and understanding the particularities of fatigue degradation and failure in hardmetals. In agreement with the results of Evans and Linzer (Evans & Linzer, 1976) and those of Peck, referred to as unpublished research by Drake and Kratwitz (Drake & Kratwitz, 1981), for the WC-11 wt% Co grade studied, the authors evidenced a dependence of FCG data on applied ΔK stronger than usually observed in metal alloys, i.e. values about 10 instead of 2–4 (Ritchie, 1999), for the exponent m in the semiempirical Paris–Erdogan equation $\mathrm{d}a/\mathrm{d}N = C\Delta K^n$. However, more interesting was their report of relevant differences between fracture surfaces corresponding to stable FCG and unstable fracture. Thus, a transition within binder-phase regions from a ductile rupture during unstable crack propagation to a more brittle mode—cleavage-like with little plastic deformation and characterized by surface markings of crystallographic nature (Roebuck et al., 2009)—for subcritical crack extension was discerned through SEM examination. Hence, this work also yielded support for the existence of true cyclic effects on the crack growth behavior of hardmetals on the basis of different operating mechanisms at the microscale (same order as the carbide grain size) level.

Fry and Garrett (Fry & Garret, 1983, 1988) conducted a large and systematic investigation covering an extensive range of WC–Co hardmetals. FCG behavior of grades with different cobalt content (from 6 to 25 wt% Co) and grain sizes (from fine to coarse) was studied using constant-stress intensity factor double-torsion test specimen geometry. Experimental variables also include load ratio (R) and testing frequency, attempting to evaluate mean stress effects on the FCG behavior and compare monotonic and cyclic crack growth data, respectively. Additionally, as it had been usual for rationalizing microstructural effects on other mechanical parameters (e.g. Viswanadham et al., 1981), these authors include binder mean free path, a normalizing parameter able to uniquely identify any combination of grain size and composition, for discussing the influence of microstructure on FCG response.

In concordance with other authors, the data attained by Fry and Garrett was found (1) to obey a conventional Paris growth law with m values lying in the range of 10–20 and (2) to exhibit substantial influence of mean stress (load ratio) on crack growth rate. The latter was interpreted by the authors, through the influence of $K_{\max}$, in terms of the effect of "static modes" occurring in conjunction with the fatigue process. Regarding microstructural effects, as it may be observed in **Figure 4**, they found an enhancement in FCG resistance with increasing binder mean free path (via rising cobalt content and/or grain size), the changes corresponding relatively well with related variations in fracture toughness. Comparison of monotonic and cyclic crack growth rates, the latter under different test frequency, resulted in quite different slopes in the Paris law plots for monotonic and cyclic data as well as negligible frequency effects. These experimental facts may be taken as definitive for confirming the occurrence of a true fatigue process in these materials. However, in contrast to the findings of Almond and Roebuck (Almond & Roebuck, 1980), fatigue fracture surfaces examined by Fry and Garrett were described by them as being fractographically indistinguishable from those obtained during fast fracture. The whole set of experimental findings was finally interpreted in terms of a model of subcritical crack growth combining debonded grain boundaries, fractured carbide grains and ruptured (small layer thickness, and thus highly constrained) binder, with ligaments of intact, but strained (large layer thickness), cobalt binder interspersed among the already (static-like) broken areas.

Similar trends in load ratio and microstructural effects were also observed by other authors (Boo & Park, 2005; Hirose et al., 1997; Ishihara, Goshima, Yoshimoto, et al., 1999; Knee & Plumbridge, 1984), although specific annotations may be indicated in each case. Knee and Plumbridge (Knee & Plumbridge, 1984) noticed microstructural influence to lessen with decreasing crack growth rates, to the limit of measuring crack propagation thresholds independent of both microstructure and toughness. Hirose et al. (Hirose et al., 1997) and Boo

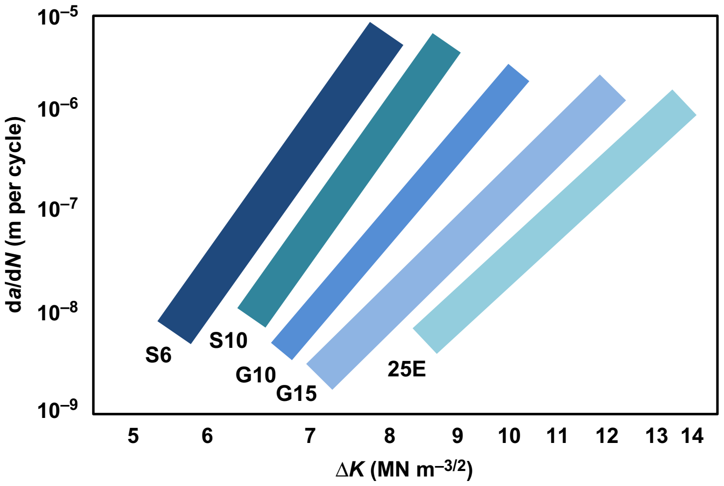

Figure 4 Influence of composition and carbide grain size on FCG behavior in WC–Co hardmetals. Load ratio ranging from 0.04 to 0.08, testing frequency about 5 Hz. S6, WC-6 wt% Co fine grained; S10, WC-10 wt% Co fine grained; G6, WC-6 wt% Co coarse grained; G10, WC-10 wt% Co coarse grained; G15, WC-15 wt% Co coarse grained; 25E, WC-25 wt% Co coarse grained. Adapted from Fry and Garret (1988).

and Park (Boo & Park, 2005) found significant effects of microstructure even when plotting crack growth data in terms of the effective stress intensity factor range, ΔK_{eff} (i.e. after allowing for crack closure). In the latter investigation, a direct relationship was found among cobalt content, amount of fcc to hcp phase transformation and ΔK stress level (high/low). Finally, Ishihara et al. (Ishihara, Goshima, Yoshimoto, et al., 1999) reported a transition in the dominant fracture mechanism parameter for describing FCG kinetics, from K_{max} to ΔK, with decreasing crack growth rates.

The FCG studies reviewed had clearly established the existence of true cyclic fatigue effects as well as the strong dependence of FCG rates on a particularly chosen fracture mechanics parameter (mainly ΔK). However, none of the approaches applied for describing FCG kinetics in these materials had allowed a complete rationalization of the concomitant microstructural and testing effects observed. Within this framework, similar to the investigation conducted by Sockel's team following the *S*–*N* approach, a large research program attempting to gain further knowledge on the referred FCG issues was launched by Llanes and coworkers at the Universitat Politècnica de Catalunya in the late 1990s. In doing so, special attention was paid to analyze relative dominance of static and cyclic failure modes during stable crack propagation as well as fatigue sensitivity, this parameter being defined for precracked samples as the ratio between applied stress intensity factors corresponding to FCG threshold and fracture toughness.

In agreement with previous literature reports, FCG rates for WC–Co cemented carbides were found to exhibit a higher dependence on K_{max} than on ΔK (Llanes, Torres, & Anglada, 2002; Torres, Anglada, & Llanes, 2001). However, the description of FCG kinetics in terms of a modified Paris–Erdogan growth relationship of type $\mathrm{d}a/\mathrm{d}N = CK_{\text{max}}^{m}\Delta K^{n}$, as it had been shown to apply for other brittle-like materials such as structural ceramics (Liu & Chen, 1991b; Steffen et al., 1991) or intermetallics (Badrinarayanan, McKelvey, Venkateswara Rao, & Ritchie, 1996), allowed them to discern a decreasing prevalence of K_{max} over ΔK (m/n ratio) as the controlling fracture mechanics parameter with rising mean binder free path (Figure 5). Such a behavior was associated with the changes in relative predominance of static over cyclic modes of fracture during stable FCG. Moreover, it was established that in contrast to fracture toughness, threshold FCG values do not exhibit a monotonic correlation with microstructural changes; hence, hardmetals with higher binder thickness (or lower carbide contiguity) were found to be more fatigue sensitive in terms of crack growth resistance. These results are in complete concordance with previous findings for plain cobalt hardmetals on the basis of *S*–*N* data by Sailer et al. (Sailer et al., 2001). Attempting to rationalize their findings, Llanes and coworkers recalled the double role, as both toughening and fatigue-susceptible agent, played by the ductile binder in hardmetals under cyclic loading. Hence, they postulated the effective ductility of the constrained binder as the revealing key for understanding microstructural (and load ratio) effects on FCG sensitivity: as it is enhanced (as binder thickness increases), hardmetals exhibit a transition from ceramic-like to metallic-like FCG behavior and the tradeoff between fracture toughness and FCG resistance becomes more prominent.

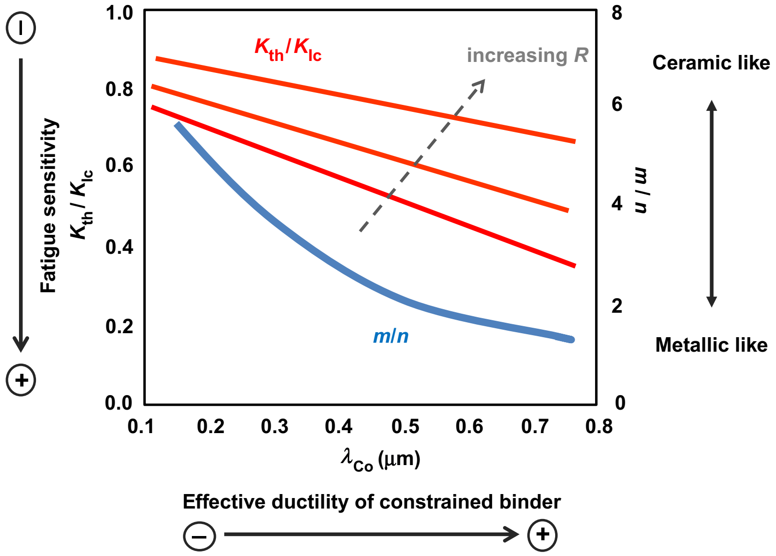

Figure 5 Fatigue sensitivity–(m/n)–microstructure relationships for WC–Co cemented carbides. m and n refer to coefficients in the modified Paris–Erdogan growth relationship of type $da/dN = CK^{m}_{max}\Delta K^{n}$. Adapted from Llanes et al. (2002).

The experimental fact that failure under cyclic loading of hardmetals is controlled by subcritical growth of preexisting flaws (Schleinkofer et al., 1996a, 1996b; Schleinkofer et al., 1997), together with the extremely strong dependence of the FCG rates on the applied stress intensity (Almond & Roebuck, 1980; Fry & Garret, 1983, 1988; Llanes et al., 2002; Torres et al., 2001), point out that a strict damage tolerance analysis for structural design involving these materials is difficult to utilize in practice. Under these considerations, Torres et al. (Torres, Anglada, & Llanes, 2001; Torres, Anglada, & Llanes, 2002) have proposed and validated, under different nonzero mean cyclic stresses, a fatigue mechanics approach based on the assumption of FCG threshold as the effective toughness under cyclic loading as a reliable methodology for correlating FCG and fatigue life, within an infinite fatigue life framework, for these materials. Regarding mean stress effects on the fatigue limit of hardmetals, these authors have also shown that they may be accounted by a Goodman-like relationship whose slope corresponds to the fatigue sensitivity under zero mean cyclic stress conditions for the grade under consideration (Figure 6). Such basic knowledge has proved to be extremely useful for analyzing and assessing

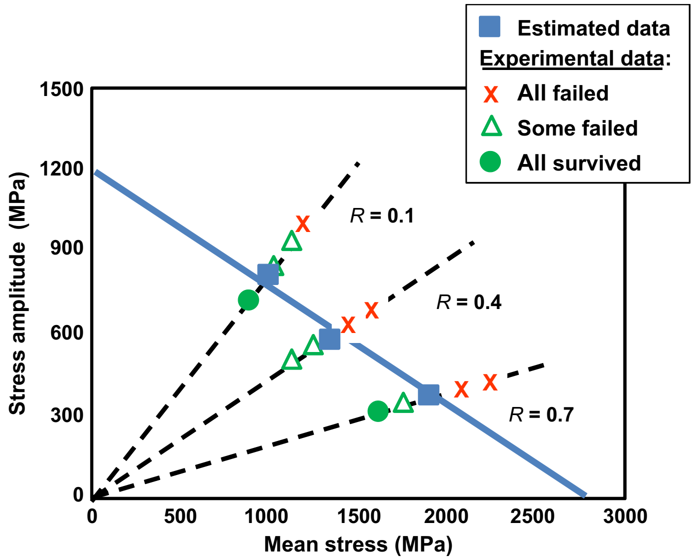

Figure 6 Description through a Goodman-like diagram of mean stress effects on the fatigue limit of a WC-10 wt% Co hardmetal. Adapted from Torres et al. (2001).

the influence of extrinsic residual stresses, as those induced by electrical discharge machining (EDM), as well as the effectiveness of different thermomechanical treatments and surface modification technologies for improving the fracture and fatigue strength of EDMed hardmetals (Casas et al., 2003; Casas, Torres, & Llanes, 2006; Llanes, Casas, Idañez, Marsal, & Anglada, 2004; Llanes, Casas, Torres, Salán, & Mestra, 2013). Finally, the interesting results reported by this research group on loading mode effects on the FCG resistance of hardmetals is worth mentioning. In this regard, Torres et al. (Torres, Sarin, Anglada, & Llanes, 2005) have clearly proved that FCG rates are increased as the loading mode varies from pure shear (mode II) to pure tensile (mode I), rendering then FCG threshold in mode I as a "conservative" parameter for defining the critical condition for FCG initiation, under either pure or mixed loading, in these materials. Such mixed mode FCG experimental data are quite relevant for microstructural design of nude and coated WC–Co cutting tools for improved performance (Park, Kapoor, & DeVor, 2006; Park, Kapoor, & DeVor, 2007).

1.11.4 Fatigue Behavior of Hardmetals under Service-like Conditions

The aim of materials research is to develop materials for practical purposes and services. Consequently, it does not need to distinguish properties and performance in engineering applications. Indeed, fatigue behavior itself is an excellent example of such conceptual approach. However, service-like conditions for hardmetals tools and components usually go beyond variable loading, particularly by including temperature and environmental effects. In this regard, information on thermal and environmental fatigue is extremely scarce, contrasting with the relatively larger amount of literature existing on creep, high temperature strength, corrosion and oxidation of these materials—see, e.g. a companion paper in this volume where some of these fields are reviewed (Mari, 2014). In this section, knowledge acquired from the few existing studies combining temperature fatigue and environment fatigue of hardmetals is summarized.

1.11.4.1 High-Temperature Fatigue

Work conducted on fatigue of hardmetals at high temperature has mainly been done following the *S–N* approach described in Section 1.11.2 (Dary et al., 1999; Ferreira et al., 2009; Kindermann et al., 1999; Roebuck & Gee, 1996; Roebuck et al., 2008), although including particular testing and specimen geometry characteristics in each case. Sockel's research group extended the systematic investigation carried out at room temperature to a quite wide range of temperatures, up to 1000 °C, in air (Kindermann et al., 1999). Results from this study indicated strong and complex temperature effects on fatigue strength, depending on the binder and carbide chemical nature of the grades under consideration: Ti(C,N)/Co and WC/Co–Ni. Hence, minimum fatigue sensitivity values were found at different temperatures, 300 °C for the former and at 700 °C for the latter (Figure 7), as related to controlling temperature-dependent fatigue mechanisms. In the lower temperature range (up to 300 °C), cyclic degradation mechanisms are similar to those identified at room temperature; thus, increasing the temperature results in higher ductility of binder and crack shielding effects. On the other hand, in the higher temperature range (above 500 °C), phase transformation within the binder becomes less important, and rather oxidation resistance of the phases together with brittle–ductile transition of mixed carbides emerge as key factors for fatigue performance. According to their results, the authors propose binder systems with high stacking fault energy and oxidation resistance as microstructural guidelines for improving the fatigue lifetimes of cemented carbides in technical application.

Interesting high-temperature fatigue features have also been reported by NPL's research group (Dary et al., 1999; Roebuck & Gee, 1996; Roebuck et al., 2008). In this case, investigations have been aimed to evaluate both isothermal and thermomechanical fatigue behavior, including development of specific test rigs as well as use of notched specimens. Besides validating the effectiveness of testing variables introduced by the authors, several observations deserve to be highlighted. First, in agreement with the results of Kindermann et al. (Kindermann et al., 1999), fatigue endurance increases at 300 °C and decreases at temperatures above 700 °C. In this regard, a recent study by Ferreira et al. (Ferreira et al., 2009) allows to speculate that fatigue strength enhancement could still be present at temperatures up to 500 °C, although reported results are limited and scatter is relatively high. Second, high-temperature influence depends on applied load ratio: temperature effect is much more pronounced under zero/tension cyclic loads than under symmetrical tension/compression conditions. Such result is suggested to come from the severe fatigue degradation induced under $R = -1$, lessening then any

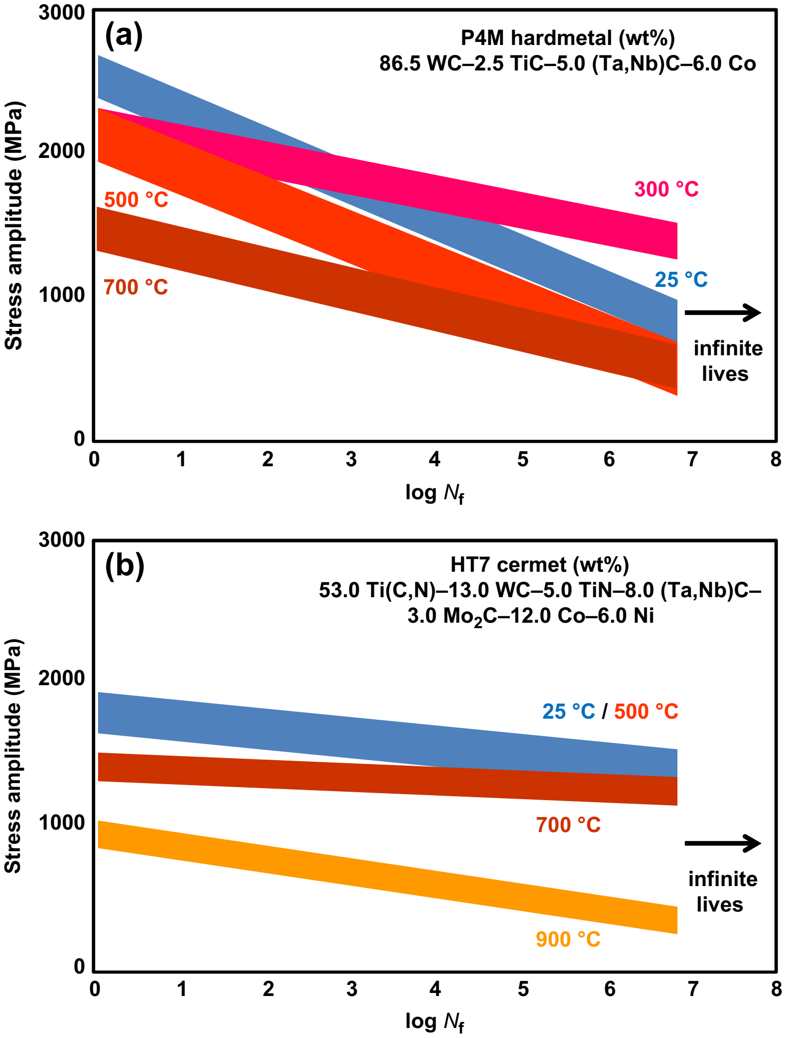

Figure 7 Temperature dependence of the mechanical behavior under cyclic loads for a hardmetal (a) and a cermet (b) between 25 and 900 °C in air. Adapted from Kindermann et al. (1999).

temperature effect. Third, thermomechanical fatigue response was found to improve with decreasing WC grain size, Co and carbon content, and increasing solid solution cubic content.

As it is the case for fatigue assessment at room temperature, research efforts at high temperature have also attempted following the FCG approach. In this regard, a comprehensive study has been recently published by Ishihara et al. (Ishihara, Shibata, Goshima, & Shimizu, 2008), including testing under different load ratios and temperatures ranging from room temperature to 500 °C. In agreement with FCG data analysis presented by other authors, at the medium and low temperature region crack propagation rates are functions of both K_{max} and ΔK. However, as temperatures get higher (up to 500 °C), FCG behavior becomes solely dependent on K_{max} (Figure 8). This finding is interesting because it points out a lessening cyclic stress effect as the temperature gets higher. Regarding crack growth rates, they are found to increase with rising temperature and load ratio. The authors rationalize such behavior on the basis of less-effective toughening effect (ductile ligament bridging) at the crack wake together with weakening at WC–Co interfaces ahead the crack tip as temperature rises, although experimental evidence for such ideas are not clearly presented.

1.11.4.2 Thermal Fatigue

Relevance of thermal fatigue as the failure mechanism in hardmetal application (Bathia, Pandey, & Shan, 1978; Beste, Hartzell, Engqvist, & Axén, 2001; Chandrasekaran & Venkatesh, 1985; Engqvist et al., 2000;

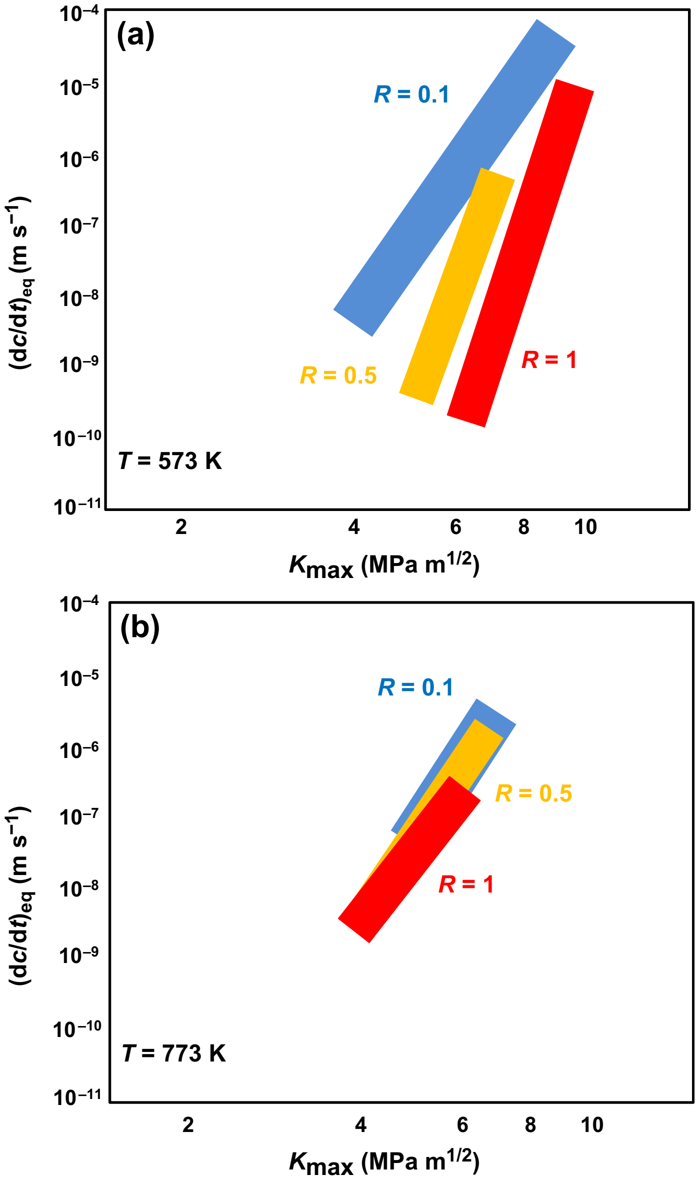

Figure 8 Effect of the R ratio on the relationships between the equivalent crack propagation rate, $(dc/dt)_{eq}$ and the maximum stress intensity factor, K_{max}. Experimental data for three different load ratios, $R = 0.1$, 0.5 and 1 are plotted. (a) $T = 573$ K, (b) $T = 773$ K. Adapted from Ishihara et al. (2008).

Lagerquist, 1975; Perrott, 1979; Stjernberg, Fisher, & Hugoson, 1975) is as large as the complexity associated with its quantification (testing) and analysis, the latter on the basis of correlation among thermal fatigue resistance, conventional parameters (flow stress in tension, Young's modulus, thermal expansion and thermal conductivity coefficients) and microstructure (Roebuck & Almond, 1988). In general, thermal fatigue findings are evaluated as the result of wear/contact service (testing) conditions; thus, it is extremely difficult to separate thermal cyclic effects from those associated with operative wear mechanisms. This is discerned from surface damage observation in rock drill buttons by Beste et al., where they concluded that formation of initial surface cracks and the reptile skin pattern were separate mechanisms, which presumably interact with each other (Beste et al., 2001). This may also be the reason for the opposite effect found by Lagerquist when increasing binder content and carbide grain size on nucleation (higher number) or propagation (lower growth rates) of thermal fatigue cracks (Lagerquist, 1975). In this regard, it is noteworthy that microstructural effects on propagation behavior are similar to those previously reported by Tumanov et al. (Tumanov, Gol'dberg, Chernyshev, & Pavlova, 1966) on the basis of residual strength drop or observation of the first macrocrack after repeated quenching from a high temperature, i.e. increasing thermal shock resistance with increasing cobalt content or carbide grain size.

From a quantitative viewpoint, the work by Ishihara and collaborators on crack propagation behavior under repeated thermal shocks by an improved quench test should be highlighted (Ishihara, Goshima, Nomura, & Yoshimoto, 1999). In doing so, they used both smooth (unnotched) and precracked specimens (cracks here introduced by means of the bridge indentation method), allowing then an evaluation of crack nucleation and propagation (growth kinetics) phenomena under repeated thermal shocks. In this investigation, thermal stresses were determined taking into account the temperature gradient in the direction of the specimen height exclusively, and not in the longitudinal and transverse directions and using average values in the temperature range for the thermal and mechanical properties. As the study was conducted in both hardmetals (WC–Co) and cermets (TiCN–Ni/Co), several interesting conclusions were drawn. First, at low thermal stresses, or in the long life region, thermal fatigue strength for cermets exceeded those of hardmetals (Figure 9(a)). Second, at low stress intensity factor, crack growth rate for cemented carbides are faster than those for cermets, although these differences vanish as the stress intensity factor increases (Figure 9(b)). They rationalized the observed responses on the basis of differences in the linear expansion coefficient of the constitutive phases as well as relative

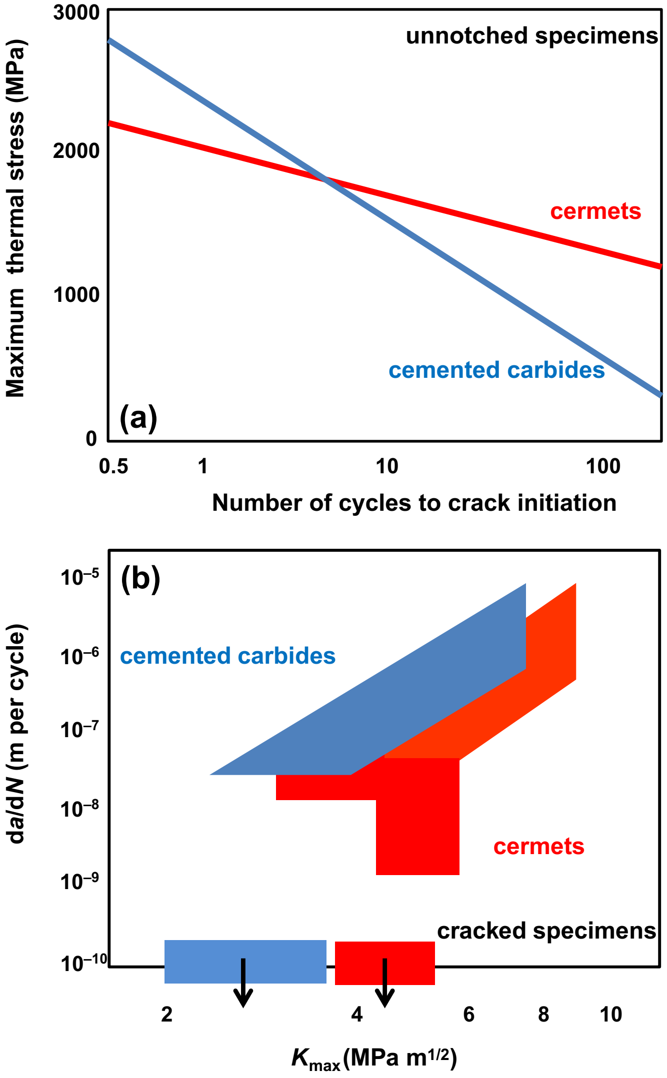

Figure 9 Fatigue-related response for cermets and cemented carbides subjected to repeated thermal shock tests. (a) Relationship between maximum thermal stress and number of cycles to crack initiation observed with unnotched smooth specimen; (b) relationship between d*a*/d*N* and stress intensity factor determined in cracked specimens. Adapted from Ishihara et al. (1999).

Young's modulus for both studied materials. However, the study did not include grades of similar chemical nature with different microstructural assemblages.

Considering the importance of thermal fatigue damage on the performance of hardmetals in many applications, it is clear that design and implementation of a (simple but valuable) testing procedure for investigating microstructure effects on thermal fatigue strength is highly required in this research field.

1.11.4.3 Corrosion Fatigue

Information on servicelike fatigue behavior for hardmetals gets even scarce when considering corrosion effects. To the best knowledge of the authors, it is limited to a unique but very illustrative study by Pugsley and Sockel (Pugsley & Sockel, 2004), complemented by some stress corrosion cracking data published by the same group previously (Pugsley et al., 2001). This investigation was conducted on two cemented carbides (one hardmetal and one cermet) exposed to tannic acid and deionized water, attempting to simulate environments encountered during wood and metal cutting, respectively. It was found that fatigue behavior of the materials studied is strongly influenced by exposure to corrosive environment, reaching fatigue endurance levels half (25% strength) of those measured in air (50% strength) under similar cyclic conditions. As it could be expected from classical corrosion fatigue degradation, the influence of the corrosive environment on fatigue performance was found to increase with decreasing stress amplitude and frequency (Figure 10). It is interesting to highlight that environmental effects under cyclic loading were found for both media to which materials were exposed, independent of whether interaction between static loading and corrosive attack (stress corrosion cracking) was or was not evidenced, i.e. cases of tannic acid and deionized water, respectively. Hence, besides conventional stress corrosion cracking, other corrosion-related mechanisms such as combined action of mechanical damage (plastic strain localization) and corrosive attack are recalled. Finally, it should be pointed out that relative effect of corrosion on mechanical performance of cemented carbides was not found to be directly related to their composite nature but rather to the particular composition of their constitutive phases (Pugsley et al., 2001).

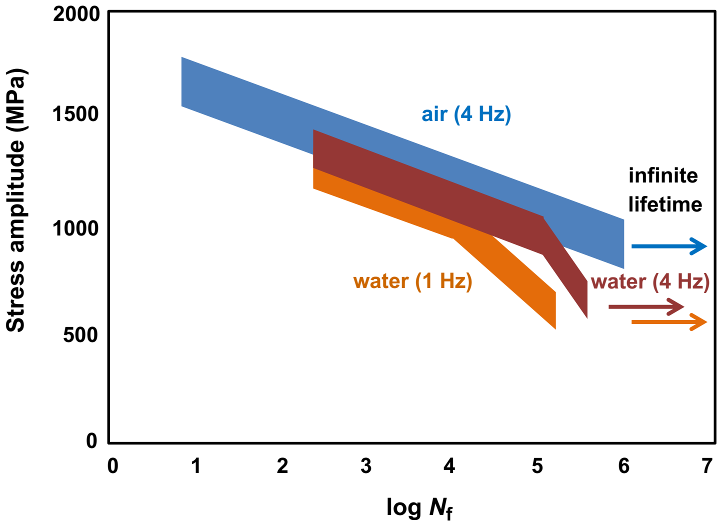

Figure 10 *S–N* diagram for a cermet material tested in a deionized water environment. Separate data are given for specimens tested at 1 and 4 Hz. The results obtained in air at 4 Hz are included for comparison. Adapted from Pugsley and Sockel (2004).

1.11.5 Final Remarks

Cemented carbides are established forefront materials for tools, structural components and wear parts with stringent requirements. They exhibit an exceptional combination of strength, toughness and wear resistance as a result of the extremely different properties of their two interpenetrating constitutive phases: hard, brittle carbides and a soft, ductile metallic binder. Historically, the ever increasing implementation of hardmetal has mainly taken place on the basis of replacement of steels in machining tools because of their higher hardness and improved wear resistance at tool tip temperatures, generally at some expense of fracture toughness. However, the range of applications for cemented carbides is (and attempts to be) much wider: from tools used for drilling and mining operations, through dies employed in the forging and stamping industries, to precision parts used in the medical, electronic, aerospace and automobile industries. Within this evolution trend, although the intrinsic "hard" nature of cemented carbides is always an attribute, most of their "emerging" and/or "to-be-consolidated" applications require a higher relevance of toughness and fatigue resistance (with respect to that of hardness) for enhancing material performance. Two clear examples are their implementation as either forming tools or structural components. In both cases, improved toughness and fatigue strength means increased reliability (i.e. lower probability of premature and unexpected failures), longer component lifetime, and less downtime to either replace broken tools or set out the entire engineering system for which the failed component was a single structural element.

This chapter has concentrated on reviewing the fatigue behavior of cemented carbides. The information has been critically presented following the experimental and analytical approaches used by different research groups, and emphasis has been placed on highlighting microstructural effects on strength degradation and subcritical crack propagation for these materials when subjected to cyclic loads. In most of the cases, a tradeoff between monotonic (fracture strength and toughness) and cyclic (fatigue strength and crack growth resistance) properties is discerned with increasing binder content and carbide grain size, pointing out the compromising role of the ductile binder as the toughening and fatigue-susceptible agent in hardmetals. This by itself points out the importance of a clear and effective microstructural description as well as a deeper understanding of fracture and fatigue micromechanisms at the metallic binder level, if fatigue performance of cemented carbides needs to be improved. In this regard, deformation, fracture and fatigue of grades with metallic binders different from cobalt-base solid solutions and/or exhibiting distinct microstructural assemblages (e.g. bimodal or gradient) are proposed as interesting issues for defining microstructural design guidelines for these materials.

The review has also attempted to cover fatigue behavior under service-like conditions, including temperature and environment effects. In these cases, existing information is rather limited and continued research and development is here recalled. Because under these conditions the factors determining effective performance are many and complex, these research efforts should be rather multidisciplinary and intersectorial, on the basis of innovative testing methodology, multiscale modeling, and advanced characterization (microstructure and damage micromechanisms). Furthermore, design issues must be widened to include notch sensitivity (fatigue design of structural components), mechanical integrity of joints/unions involving cemented carbides, surface integrity effects associated with machining and shaping operations, and influence of service-induced changes on the basis of damage tolerance and reliability, among others. This is essential if technology development related to cemented carbides is to make its optimum contribution to reduction of life cycle costs and improved maintenance management (and consequently into environmental and energy consumption effects) in all industrial sectors where these materials are implemented.

Acknowledgments

This work was supported by the Ministerios de Ciencia e Innovación (Grant MAT2009-14461) and de Economía y Competitividad (Grant MAT2012-34602) of Spain. Additional support was received from Direcció General de Recerca del Comissionat per a Universitats i Recerca de la Generalitat de Catalunya through recognition of CIEFMA as Grup de Recerca Consolidat (Grant 2009SGR01285). The authors gratefully acknowledge all the above-mentioned support.

References

Almond, E. A., & Roebuck, B. (1980). Fatigue-crack growth in WC–Co hardmetals. *Metals Technology, 2*, 83–85.

Badrinarayanan, K., McKelvey, A. L., Venkateswara Rao, K. T., & Ritchie, R. O. (1996). Fracture and fatigue-crack growth behavior in ductile-phase toughened molybdenum disilicide: effects of niobium wire vs particulate reinforcements. *Metallurgical and Materials Transactions A, 27*, 3781–3792.

Bathia, S. M., Pandey, P. C., & Shan, H. S. (1978). Thermal cracking of carbide tools during intermittent cutting. *Wear, 51*, 201–211.

Beste, U., Hartzell, T., Engqvist, H., & Axén, N. (2001). Surface damage on cemented carbide rock-drill buttons. *Wear, 249*, 324–329.

Boo, M.-H., & Park, Y.-C. (2005). Mechanisms of fatigue crack growth in WC–Co cemented carbides. *Key Engineering Materials, 297–300*, 1120–1125.

Brookes, K. J. A. (1982). *World directory and handbook of hard metals*. East Barnet, Herts EN4 8DN, UK: Int. Carb. Data.

Casas, B., Lousa, A., Calderón, J., Anglada, M., Esteve, J., & Llanes, L. (2003). Mechanical strength improvement of electrical discharge machined cemented carbides through PVD (TiN, TiAlN) coatings. *Thin Solid Films, 447–448*, 258–263.

Casas, B., Torres, Y., & Llanes, L. (2006). Fracture and fatigue behavior of electrical-discharge-machined cemented carbides. In: *ICSHM8-8th Int. Conf. on Science of Hard Materials, San Juan, Puerto Rico (2004)*, and *International Journal of Refractory Metals and Hard Materials*, *24*, 162–167.

Chandrasekaran, H., & Venkatesh, V. C. (1985). Thermal fatigue studies on tool carbides and its relevance of milling cutters. *CIRP Annals, 34*, 125–128.

Chermant, J. L., Deschanvres, A., & Iost, A. (1973). Tenacité de WC–Co 15%. *Materials Research Bulletin, 8*, 925–934.

Dary, F.-C., Roebuck, B., & Gee, M. G. (1999). Effects of microstructure on the thermo-mechanical fatigue response of hardmetals using a new miniaturized testing ring. In: *ICSHM6-6th Int. Conf. on Science of Hard Materials, Lanzarote, Spain (1999)*, and *International Journal of Refractory Metals and Hard Materials*, *17*, 45–53.

Dauskardt, R. H., James, M. R., Porter, J. R., & Ritchie, R. O. (1992). Cyclic fatigue–crack growth in a SIC–whisker–reinforced alumina ceramic composite: long and small–crack growth. *Journal of American Ceramic Society, 75*, 759–771.

Davies, T. J., & Barhana, S. (1972). Fatigue of a WC-25% Co alloy. *Plansee Berichte für Pulvermetallurgie, 20*, 30–38.

Dawihl, W. (1941). Die wissenschaftlichen und technischen grundlagen der pulvermetallurgie. *Stahl und Eisen, 61*, 909–919.

Drake, E. F., & Krawitz, A. D. (1981). Fatigue damage in a WC-nickel cemented carbide composite. *Metallurgical Transactions A, 12A*, 505–513.

Engqvist, H., Botton, G. A., Ederyd, S., Pfaneuf, M., Fondelius, J., & Axén, N. (2000). Wear phenomena on WC-based face seals. *International Journal of Refractory Metals and Hard Materials, 18*, 39–46.

Erling, G., Kursawe, S., Luyckx, S., & Sockel, H. G. (2000). Stable and unstable fracture surface features in WC–Co. *Journal of Materials Science Letters, 19*, 437–438.

Evans, A. G., & Linzer, M. (1976). High frequency cyclic crack propagation in ceramic materials. *International Journal of Fracture, 12*, 217–222.

Exner, H. E. (1979). Physical and chemical nature of cemented carbides. *International Metals Review, 4*, 149–173.

Exner, H. E., Walter, A., & Pabst, R. (1974). Zur ermittlung und darstellung der fehlerverteilungen von spröden werkstoffen. *Materials Science and Engineering, 16A*, 231–238.

Ferreira, J. A. M., Pina Amaral, M. A., Antunes, F. V., & Costa, J. D. M. (2009). A study on the mechanical behaviour of WC/Co hardmetals. *International Journal of Refractory Metals and Hard Materials, 27*, 1–8.

Fett, T., Martin, G., Munz, D., & Thun, G. (1991). Determination of $da/dN - \Delta K_I$ curves for small cracks in alumina in alternating bending tests. *Journal of Materials Science, 26*, 3320–3328.

Fischmeister, H. F. (1983). Development and present status of the science and technology of hard materials. In R. K. Viswanadham, D. J. Rowcliffe & J. Gurland (Eds.), *Proc. of ICSHM1 – Int. Conf. on Science of Hard Materials, Jackson, USA (1981)* (pp. 1–45). New York: Plenum Press.

Fry, P. R., & Garret, G. G. (1983). The inter-relation of microstructure, toughness and fatigue crack growth behaviour in WC–Co hardmetals. In N. P. Comins & J. B. Clark (Eds.), *Proc. Int. Conf. on speciality steels and hard materials* (pp. 375–381). London: Pergamon.

Fry, P. R., & Garret, G. G. (1988). Fatigue crack growth behaviour of tungsten carbide–cobalt, hardmetals. *Journal of Materials Science, 23*, 2325–2338.

Fujiwara, Y., Ueda, H., Masatomi, H., & Suzuki, H. (1980). Fatigue of hot isostatic pressed WC-12% Co alloys. *Journal of the Japan Society of Powder Metallurgy, 27*, 181–184.

Gee, Gant, Roebuck, & Mingard, K. P. (2014). Mechanical Properties: Wear of Hardmetals. In V. K. Sarin, Luis Llanes & Daniele Mari (Eds.), *Comprehensive Hard Materials, Volume 1: Hardmetals*. UK: Elsevier Ltd. Oxford.

Gee, M., Mingard, K., & Roebuck, B. (2009). Application of EBSD to the evaluation of plastic deformation in the mechanical testing of WC/Co hardmetal. *International Journal of Refractory Metals and Hard Materials, 27*, 300–312.

Grathwohl, G. (1988). Ermüdung von keramik unter schwingbeanspruchung. *Materialwissenschaft und Werkstofftechnik, 19*, 113–124.

Gurland, J. (1988). New scientific approaches to development of tool materials. *International Materials Review, 33*, 151–166.

Hirose, Y., Boo, M.-H., Matsuoka, H., & Park, Y.-C. (1997). Influence of stress ratio and WC grain size on fatigue crack growth characteristics of WC–Co cemented carbides. *Journal of Society of Materials Science Japan, 46*, 1402–1409.

Ingelström, N., & Nordberg, H. (1974). The fracture toughness of cemented carbide. *Engineering Fracture Mechanics, 6*, 597–607.

Ishihara, S., Goshima, T., Nomura, K., & Yoshimoto, T. (1999). Crack propagation behavior of cermets and cemented carbides under repeated thermal shocks by the improved quench test. *Journal of Materials Science, 34*, 629–636.

Ishihara, S., Goshima, T., Yoshimoto, T., & Sabu, T. (1999). On fatigue lifetimes and crack growth behavior of cemented carbides. In X. R. Wu & Z. G. Wang (Eds.), *Proc. of Fatigue'99 – 7th Int. fatigue congress* (Vol. 3; pp. 1811–1816). Beijing: Higher Education Press/EMAS.

Ishihara, S., Goshima, T., Yoshimoto, T., Sabu, T., & McEvily, A. J. (2000). The influence of the stress ratio on fatigue crack growth in a cermet. *Journal of Materials Science, 35*, 5661–5665.

Ishihara, S., Shibata, H., Goshima, T., & Shimizu, M. (2008). Effect of environmental temperature on the fatigue crack propagation behavior of cemented carbides. *Journal of Thermal Stresses, 31*, 1025–1038.

James, M. N., Human, A. M., & Luyckx, S. (1990). Fracture toughness testing of hard metals using compression-compression precracking. *Journal of Materials Science, 25*, 4810–4814.

Johansson, I., Persson, G., & Hiltscher, R. (1970). Determination of static and fatigue strength of hard metals. *Powder Metallurgy International, 2*, 119–123.

Kenny, P. (1971). The application of fracture mechanics to cemented carbides. *Powder Metallurgy, 14*, 22–38.

Kindermann, P., Schlund, P., Sockel, H. G., Herr, M., Heinrich, W., Görting, K., et al. (1999). High-temperature fatigue of cemented carbides under cyclic loads. In: *ICSHM6-6th Int. Conf. on Science of Hard Materials, Lanzarote, Spain (1999)*, and *International Journal of Refractory Metals and Hard Materials*, *17*, 55–68.

Klaasen, H., Kübarsepp, J., Tsinjan, A., & Sergejev, F. (2011). Performance of carbide composites in cyclic loading wear conditions. *Wear, 271*, 837–841.

Kluensner, T., Marsoner, S., Ebner, E., Glaetzle, J., Pueschel, A., & Pippan, R. (2009). Influence of microstructure on stress–strain behaviour of WC–Co hard metals in static and cyclic loading. In L. S. Sigl, P. Rödhammer & H. Wildner (Eds.), *Proc. 17th Plansee Seminar* (Vol. 3; pp. 1–10). Reutte: Plansee Group. AT 10.

Klünsner, T., Marsoner, S., Ebner, R., Pippan, R., Glätzle, J., & Püschel, A. (2010). Effect of microstructure on fatigue properties of WC–Co hard metals. In: *Proc. Fatigue 2010-10th Int. Fatigue Congress, Prague, Czech Republic (2010)*, and *Proceedings of Engineering*, *2*, 2001–2010.

Knee, N., & Plumbridge, W. J. (1984). The influence of microstructure and stress ratio on fatigue crack growth in WC–Co hardmetals. In S. R. Valluri, D. M. R. Taplin, P. Ramarao, J. F. Knott & R. Dubey (Eds.), *Proc. 6th Int. Conf. Fracture* (Vol. 4; pp. 2685–2692). New Delhi: Pergamon.

Krawitz, A. D., Roberts, R., & Faber, J. (1986). Residual stress relaxation in cemented carbide composites. In *Proc. of ICSHM2 – 2nd Int. Conf. on the Science of Hard Materials, Rhodes, Greece (1984), institute of physics conference series* (Vol. 75; pp. 577–589). Bristol and Boston: Adam Hilger Ltd.

Krstic, V. D. (1983). On the fracture of brittle–matrix/ductile–particle composites. *Philosophical Magazine, 48*, 695–708.

Kursawe, S., Pott, Ph., Sockel, H. G., Heinrich W., & Wolf, M. (2001). On the influence of binder content and binder composition on the mechanical properties of hardmetals. In: *ICSHM7-7th Int. Conf. on Science of Hard Materials, Ixtapa, Mexico (2001)*, and *International Journal of Refractory Metals and Hard Materials*, *19*, 335–340.

Lagerquist, M. (1975). A study of the thermal fatigue crack propagation in WC–Co cemented carbide. *Powder Metallurgy, 18*, 71–88.

Liu, S.-Y., & Chen, I.-W. (1991a). Fatigue of yttria–stabilized zirconia: I, fatigue damage, fracture origins, and lifetime prediction. *Journal of American Ceramic Society, 74*, 1197–1205.

Liu, S.-Y., & Chen, I.-W. (1991b). Fatigue of yttria–stabilized zirconia: II, crack propagation, fatigue striations, and short–crack behavior. *Journal of American Ceramic Society, 74*, 1206–1216.

Li, A., Zhao, J., Wang, D., Gao, X., & Tang, H. (2013). Three-point bending fatigue behavior of WC–Co cemented carbides. *Materials and Design, 45*, 271–278.

Llanes, L., Casas, B., Idañez, E., Marsal, M., & Anglada, M. (2004). Surface integrity effects on the fracture resistance of electrical-discharge-machined WC–Co cemented carbides. *Journal of American Ceramic Society, 87*, 1687–1693.

Llanes, L., Casas, B., Torres, Y., Salán, N., & Mestra, A. (2013). Fatigue performance improvement of electrical discharge machined hardmetals by means of combined thermal annealing and surface modification routes. *International Journal of Refractory Metals and Hard Materials, 36*, 60–65.

Llanes, L., Torres, A., & Anglada, M. (2002). On the fatigue crack growth behavior of WC–Co cemented carbides: kinetics description, microstructural effects and fatigue sensitivity. *Acta Materialia, 50*, 2381–2393.

Lueth, R. C. (1974). Determination of fracture toughness parameters for tungsten carbide–cobalt, alloys. In D. P. Hasselmann & F. F. Lange (Eds.), *Fracture Mechanics of Ceramics* (pp. 791–806). New York: Plenum Press.

Mari. (2014). Mechanical Behavior of Hardmetals at High Temperature. In V. K. Sarin, Luis Llanes & Daniele Mari (Eds.), *Comprehensive Hard Materials, Volume 1: Hardmetals*. UK: Elsevier Ltd. Oxford.

Marrey, R. V., Burgermeister, R., Grishaber, R. B., & Ritchie, R. O. (2006). Fatigue and life prediction for cobalt–chromium stents: a fracture mechanics analysis. *Biomaterials, 27*, 1988–2000.

Miyake, K., Fujiwara, Y., & Nishigaki, K. (1968). On the fatigue of WC–Co alloys. *Nippon Kinzoku Gakkaishi, 32*, 1128–1131.

Otsuka, A., Tohgo, K., Sugawara, H., & Ueda, F. (1987). Tension-compression fatigue of WC-12% Co hardmetal. *Journal of the Society of Materials Science Japan, 36*, 135–140.

Park, S., Kapoor, S. G., & DeVor, R. E. (2006). Microstructure-level model for the prediction of tool failure in WC–Co cutting tool materials. *ASME Journal of Manufacturing Science and Engineering, 128*, 739–748.

Park, S., Kapoor, S. G., & DeVor, R. E. (2007). Microstructure-level model for the prediction of tool failure in coated WC–Co cutting tool materials during intermittent cutting. *ASME Journal of Manufacturing Science and Engineering, 129*, 893–901.

Perrott, C. M. (1979). Tool materials for drilling and mining. *Annual Review of Materials Science, 9*, 23–50.

Pugsley, V. A., Korn, G., Luyckx, S., Sockel, H.-G., Heinrich, W., Wolf, M., et al. (2001). The influence of corrosive wood-cutting environment on the mechanical properties of hardmetal tools. In: *ICSHM7-7th Int. Conf. on Science of Hard Materials, Ixtapa, Mexico (2001)*, and *International Journal of Refractory Metals and Hard Materials*, *19*, 311–318.

Pugsley, V. A., & Sockel, H.-G. (2004). Corrosion fatigue of cemented carbide cutting tool materials. *Materials Science and Engineering A, 366*, 87–95.

Ritchie, R. O. (1988). Mechanisms of fatigue crack propagation in metals, ceramics and composites: role of crack-tip shielding. *Materials Science and Engineering A, 103*, 15–28.

Ritchie, R. O. (1999). Mechanisms of fatigue-crack propagation in ductile and brittle solids. *International Journal of Fracture, 100*, 55–83.

Roebuck, B. (2002). *S–N* fatigue of V-notched hardmetal test pieces. In *Proc. EuroPM 2002*. Lausanne: EPMA.

Roebuck, B., & Almond, E. A. (1988). Deformation and fracture processes and the physical metallurgy of WC–Co hardmetals. *International Materials Review, 33*, 90–110.

Roebuck, B., & Gee, M. G. (1996). Miniaturised thermomechanical tests on hardmetals and cermets. In: *ICSHM5-5th Int. Conf. on Science of Hard Materials, Maui, USA (1995)*, and *Materials Science and Engineering A*, *209*, 356–365.

Roebuck, B., Maderud, C. J., & Morrell, R. (2008). Elevated temperature fatigue testing of hardmetals using notched testpieces. *International Journal of Refractory Metals and Hard Materials, 26*, 19–27.

Roebuck, B., Mingard, K. P., Nordenstrom, H., & Halling, E. (2009). Compression fatigue damage in hardmetals. In L. S. Sigl, P. Rödhammer & H. Wildner (Eds.), *Proc. 17th Plansee Seminar* (Vol. 3; pp. 1–13). Reutte: Plansee Group. AT 9.

Sailer, Th., Herr, M., Sockel, H. G., Schulte, R., Feld, H., & Prakash, L. J. (2001). Microstructure and mechanical properties of ultrafine-grained hardmetals. In: *ICSHM7-7th Int. Conf. on Science of Hard Materials, Ixtapa, Mexico (2001)*, and *International Journal of Refractory Metals and Hard Materials*, *19*, 553–559.

Sakagami, K., Kouno, S., & Yamamoto, T. (2007). Bending fatigue characteristics of cemented carbides for cold forging tools. *Journal of the Japan Society of Powder Metallurgy, 54*, 260–263.

Sakagami, K., & Yamamoto, T. (2006). Study on bending and compressive fatigue characteristics of cemented carbides. *Journal of the Japan Society of Powder Metallurgy, 53*, 202–207.

Sarin, V. K., & Johannesson, T. (1975). On the deformation of WC–Co cemented carbides. *Metal Science, 9*, 472–476.

Schedler, W. (1988). *Hartmetall für den praktiker*. Plansee Tizit: VDI-Verlag GmbH.

Schleinkofer, U., Sockel, H. G., Görting, K., & Heinrich, W. (1996a). Microstructural processes during subcritical crack growth in hard metals and cermets under cyclic loads. In: *ICSHM5-5th Int. Conf. on Science of Hard Materials, Maui, USA (1995)*, and *Materials Science and Engineering A*, *209*, 103–110.

Schleinkofer, U., Sockel, H. G., Görting, K., & Heinrich, W. (1996b). Fatigue of hard metals and cermets. In: *ICSHM5-5th Int. Conf. on Science of Hard Materials, Maui, USA (1995)*, and *Materials Science and Engineering A*, *209*, 313–317.

Schleinkofer, U., Sockel, H. G., Görting, K., & Heinrich, W. (1997). Fatigue of hard metals and cermets – new results and a better understanding. *International Journal of Refractory Metals and Hard Materials, 15*, 103–112.

Schleinkofer, U., Sockel, H. G., Schlund, P., Görting, K., & Heinrich, W. (1995). Behaviour of hard metals and cermets under cyclic mechanical loads. *Materials Science and Engineering A, 194*, 1–8.

Schlund, P., Kindermann, P., Sockel, H. G., Schleinkofer, U., Heinrich W., & Görting, K. (1999). Mechanical behaviour of PVD- and CVD-coated hard metals under cyclic loads. In: *ICSHM6-6th Int. Conf. on Science of Hard Materials, Lanzarote, Spain (1999)*, and *International Journal of Refractory Metals and Hard Materials*, *17*, 193–199.

Sergejev, F., Preis, I., Hussainova, I., & Kübarsepp, J. (2008). Fatigue mechanics of TiC-based cemented carbides. In: *Proc. of the Institute of Mechanical Engineers*, *Journal of Engineering Tribology*, *222*, 201–209.

Sergejev, F., Preis, I., Kübarsepp, J., & Antonov, M. (2008). Correlation between surface fatigue and microstructural defects of cemented carbides. *Wear, 264*, 770–774.

Shatov. (2014). Fracture and Strength of Hardmetals at room temperature. In V. K. Sarin, Luis Llanes & Daniele Mari (Eds.), *Comprehensive Hard Materials, Volume 1: Hardmetals*. UK: Elsevier Ltd. Oxford.

Sigl, S. L., & Exner, H. E. (1987). Experimental study of the mechanics of fracture in WC–Co alloys. *Metallurgical Transactions, 18A*, 1299–1308.

Sigl, L. S., & Fischmeister, H. F. (1988). On the fracture toughness of cemented carbides. *Acta Metallurgica, 36*, 887–897.

Steffen, A. A., Dauskardt, R. H., & Ritchie, R. O. (1991). Cyclic fatigue life and crack-growth behavior of microstructurally small cracks in magnesia-partially-stabilized zirconia ceramics. *Journal of American Ceramic Society, 74*, 1259–1268.

Stephenson, D., Chung, T. E., & Coleman, D. S. (1985). The effect of surface conditions on the fatigue strength of cemented tungsten carbides containing 6 and 25% cobalt. In H. Bildstein & H. M. Ortner (Eds.), *Proc. 11th Int. Plansee Seminar* (Vol. 2; pp. 619–642). Reutte, Austria: Plansee.

Stjernberg, K. B., Fisher, U., & Hugoson, N. I. (1975). Wear mechanisms due to different rock drilling conditions. *Powder Metallurgy, 18*, 89–106.

Suresh, S. (1991). Crack growth in brittle materials. *Journal of Hard Materials, 2*, 29–54.

Suresh, S., & Sylva, L. A. (1986). Room temperature fatigue crack growth in cemented carbides. *Materials Science and Engineering A, 83*, L7–L10.

Torres, Y., Anglada, M., & Llanes, L. (2001). Fatigue mechanics of WC–Co cemented carbides. In: *ICSHM7 – 7th Int. Conf. on Science of Hard Materials, Ixtapa, Mexico (2001)*, and *International Journal of Refractory Metals and Hard Materials*, *19*, 341–348.

Torres, Y., Anglada, M., & Llanes, L. (2002). Fatigue limit – fatigue crack growth threshold correlation for hardmetals: influence of microstructure. In A. F. Blom (Ed.), *Proc. of Fatigue'02-8th Int. Fatigue Congress*. Stockholm: EMAS.

Torres, Y., Bermejo, R., Llanes, L., & Anglada, M. (2008). Influence of notch radius and R-curve behaviour on the fracture toughness evaluation of WC–Co cemented carbides. *Engineering Fracture Mechanics, 75*, 4422–4430.

Torres, Y., Sarin, V. K., Anglada, M., & Llanes, L. (2005). Loading mode effects on the fracture toughness and fatigue crack growth resistance of WC–Co cemented carbides. *Scripta Materialia, 52*, 1087–1091.

Torres, Y., Tarrés, E., Roebuck, B., Chan, P., James, M., Liang, B., et al. (2012). Fracture toughness of rock bit cemented carbides. In *Proc. Euro PM 2012* (Vol. 2; pp. 45–50). Basel: EPMA.

Tumanov, V. I., Gol'dberg, Z. A., Chernyshev, V. V., & Pavlova, Z. I. (1966). Thermal shock resistance of tungsten carbide–cobalt alloys. *Soviet Powder Metallurgy and Metal Ceramics, 5*, 818–822.

Vasel, C. H., Krawitz, A. D., Drake, E. F., & Kenik, E. A. (1985). Binder deformation in WC-(Co, Ni) cemented carbide composites. *Metallurgical Transactions A, 16A*, 2309–2317.

Viswanadham, R. K., Sun, T. S., Drake, E. F., & Peck, J. A. (1981). Quantitative fractography of WC–Co cermets by Auger spectroscopy. *Journal of Materials Science, 16*, 1029–1038.

1.12 Wear of Hardmetals

Mark G. Gee, A.J. Gant, B. Roebuck, and K.P. Mingard, National Physical Laboratory, Teddington, Middlesex, TW, UK

Glossary

Wear The removal of material from surfaces in contact and in relative movement.
Friction The force generated between two surfaces in contact and in relative motion.
Abrasion The process of material removal from loose particles or asperities on an opposing surface that are moving against the abraded surface.
Erosion The process of material removal from particles that impact against a surface.

1.12.1 Introduction

Hardmetals (cemented carbides) are hard tool materials essential to the modern manufacturing and engineering industry. Their use mostly falls into two main categories.

The first of these is metal cutting applications including cutting, machining, drilling and milling. Hardmetals used in these applications normally have a hard phase grain size between 0.5 and 5 mm and cobalt binder phase composition ranging from 5 to 12 wt%. Often, the hard phase can be a mixture of tungsten carbide (WC) and cubic carbides such as WC, TiC, and TaC. These tools are frequently coated to improve wear resistance and reduce chemical attack at the high temperatures often encountered in these applications. Their use underpins advanced manufacturing technologies that depend on materials such as Ni-base alloys and Ti alloys for aeroengines and steels and Al alloys for engineering, transportation and construction industries.

The second, but equally important category, is nonmetal cutting applications including mining (Osburn, 1969; Yardley, 1981), oil and gas drilling and production (Beste & Jocabson, 2002), fluid handling, metal forming (Klaasen & Kubarsepp, 2004; Klassen & Kubarsepp, 2011), cutting and drilling in the civil engineering and construction industries, and woodworking (Herr et al., 2001). Here, the hardmetals normally have a grain size ranging from 0.2 to 8 μm and Co binder phase composition ranging from 5 to 30%.

In both these application areas, good resistance to wear is fundamental to hardmetal operation. The conditions under which this wear takes place vary from one application to another, but can involve high temperatures, high stresses, impact loading and aggressive chemical environments. It is the unique combination of high hardness combined with respectable levels of toughness and high modulus that lead to the likelihood of good wear resistance for WC–Co hardmetals.

There is a long history of the examination of the wear behavior of WC-based hardmetals. Much of the early work was concerned with the forensic examination of WC–Co components used in mining and mineral extraction applications; this was combined with laboratory-based testing, and attempts to develop some understanding of the mechanisms of wear that occur in abrasion and erosion (Bailey & Perrott, 1974; Blombery, Perrott, & Robinson, 1974a; Blombery, Perrott, & Robinson, 1974b; Conrad, McCabe, & Sargent, 1981; Dahlin, 1962; Dawihl & Frisch, 1968; Jonsson, 1976; Larsen-Basse & Koyanagi, 1979; Larsen-Basse, 1973; Larsen-Basse, 1981a, 1981b; Larsen-Basse, 1983, 1985b; Larsen-Basse, Perrott, & Robinson, 1974; Larsen-Basse, Shishido, & Tanouye, 1974; Latin, 1961; Montgomery, 1968; Montgomery, 1969; Osburn, 1969; Precht, Viswanadham, & Venables, 1981; Stjernberg, Fischer, & Hugoson, 1975; Wright, Shetty, & Clauer, 1983; Yardley, Johnson, & Kenny, 1981). Often these studies were combined with evaluation of the microstructure and mechanical performance of the materials, so that information on how the wear resistance alters with changes in material makeup could be gathered. Attempts have also been made to model the wear so that equations linking the wear to materials properties such as hardness, toughness and grain size could be developed (Ball & Paterson, 1985; Bata, Dallaire, & Champagne, 1985; Hack, 1985; Jonsson, 1976; Peters & Brabyn, 1985; Stjernberg, 1975; Wright et al., 1985).

There have also been a few standards developed for the abrasive wear resistance of hardmetals. ASTM B611 was developed in the 1960s for mining grades of WC/Co and was subsequently developed as a standard. This standard is widely used to determine the abrasion resistance of hardmetals. More recently, an ISO standard for abrasion testing of hardmetals, ISO 28080:2011, that specifies a generic test method to determine the abrasion wear characteristics of hardmetals has been introduced. The procedure complements the ASTM G65 method for dry sand/rubber wheel abrasion, the ASTM B611 method for abrasive wear resistance of cemented carbides, and the ASTM G105 method for conducting wet sand/rubber wheel abrasion tests.

This chapter gives a brief description of the different types of wear that can occur and then reviews the behavior of hardmetals under these types of wear. The majority of the published work is concerned with abrasion and erosion studies and thus this is the topic on which this review concentrates, but some comments are also added on sliding wear papers. Most of the literature that is reviewed covers the period from the 1970s, but there is also reference to earlier work where wear behavior limits performance. It should be noted that papers on cutting, machining and milling behavior of hardmetals and cermets are largely not included.

1.12.2 Main Types of Wear

The main types of wear are shown diagrammatically in Figure 1 (Gee & Neale, 2002). The main categories of concern for hardmetals are abrasion, erosion, and sliding wear; the first two are discussed in more detail in the relevant sections of this chapter. Impact and thermal fatigue are also important in some rock drilling applications. In many cases, several of these different types of wear operate at the same time, making the interpretation of wear damage very complex and difficult and also giving rise to enhanced removal rates compared with the individual types of wear. However, recent advances in preparation and high-resolution imaging techniques promise additional quantitative information on wear mechanisms that should materialize in the next decade or so. Some progress has already been made with the application of orientation imaging studies (electron backscattered diffraction (EBSD)) of deformed material close to tool surfaces that is providing the much needed insight (Gee & Mingard, 2009). Furthermore, single-point abrasion tests are becoming more popular as a model for using these high-resolution characterization techniques to provide detailed understanding of microstructural wear processes that are hard to interpret in complex multibody abrasion systems. Consequently, this chapter also includes critical aspects of this new approach.

It is also true that in many types of wear a synergy can occur between the environment and tool/workpiece system, leading to enhancement of wear rates greater than would be estimated from a knowledge of each mechanism individually. Often, this can occur through formation of tribofilms that are incredibly thin and extremely difficult to characterize, particularly for sliding wear systems. Also, surface layers in wear processes are subjected to elevated temperatures. The magnitude of this elevation and its distribution with depth is arguably

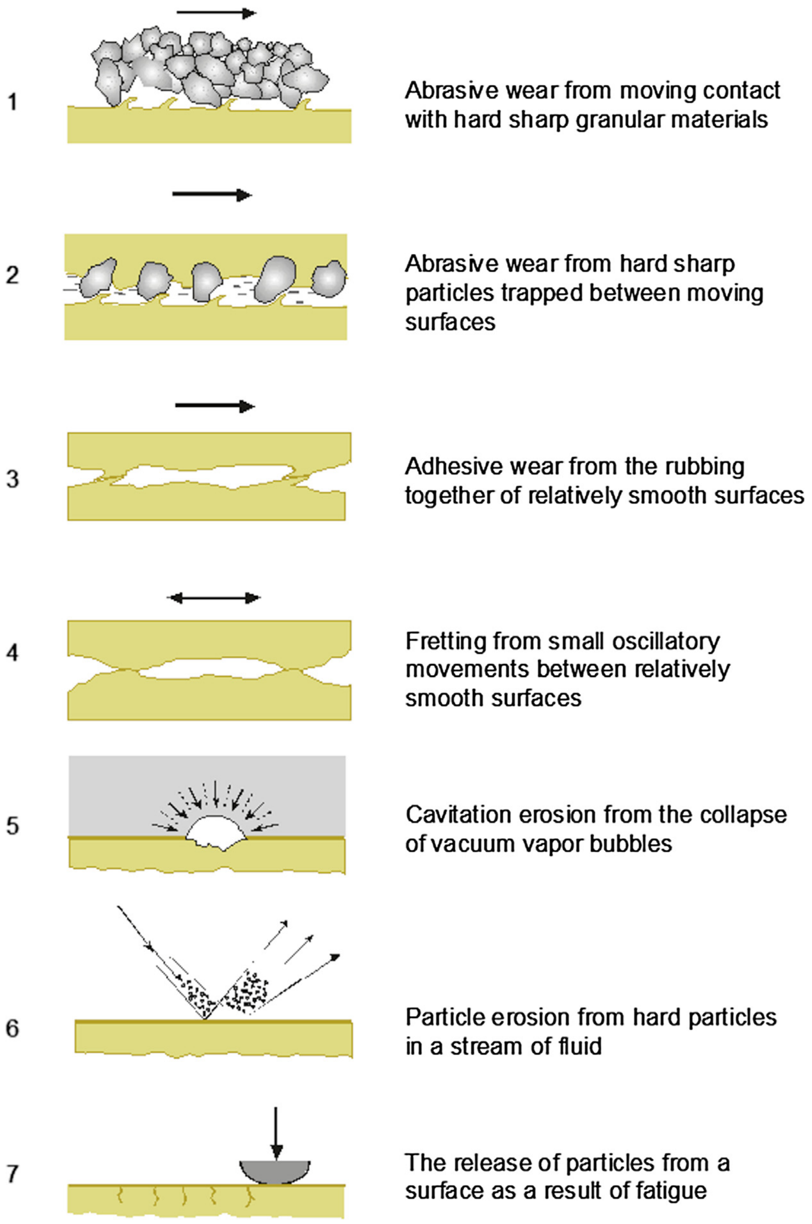

Figure 1 The main types of wear relevant to hardmetal usage.

the least well-understood aspect in understanding wear processes of all kinds. Both these aspects of the wear behavior of tools merit further research.

1.12.3 Abrasion

Abrasion wear occurs when hard particles from, or within, the worked material (rock, metal, ceramic) are dragged across the surface of the tool or wear part. Abraded surfaces are usually very rough, possibly reflecting the anisotropic nature of deformation in individual WC crystals. They characteristically show damage which can range from fine scratching to deep gouges. Abrasion wear inversely depends on hardness but there is still some uncertainty as to the effects of changing WC grain size and binder phase content at constant hardness values.

Depending on the conditions, abrasion of hardmetals normally shows a strong dependence on the hardness of the hardmetal (Gant & Gee, 2001; Gant & Gee, 2006; Herr et al., 2001, Luyckx, Sacks, & Love, 2007; Quigley,

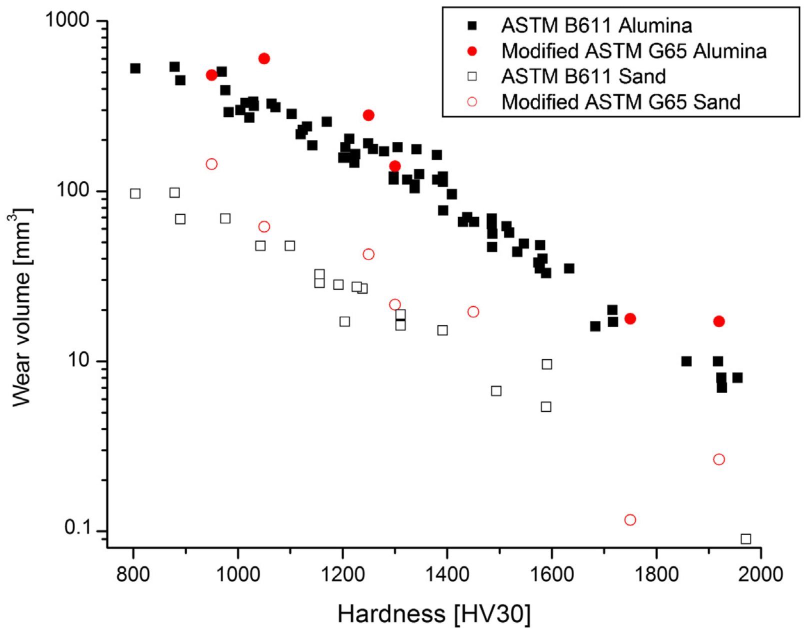

Figure 2 Relationship between abrasion volume loss and hardness for range of WC–Co hardmetals. Gee, Roebuck, et al. (2005).

Luyckz, & James, 1997). For abrasion under high stress conditions such as those experienced in the ASTM B611 test, the behavior follows an approximately log linear relationship at hardness values above about 1200 HV that can be expressed as:

$$V = Ae^{-BH}$$

where V is the volume of material lost, A and B are constants, and H is the hardness (Figure 2). Below this value of hardness (1200 HV), the volume lost is lower than this relationship predicts. This, rather straightforward, equation is perhaps quite surprising, as WC–Co hardmetals can have different microstructures and still have the same hardness by choosing specific, but variable, combinations of Co binder phase content and WC grain size. The relationship, however, suggests that simple microstructural parameters control the magnitude of wear. The reasons for this simple relationship with hardness are not fully understood, particularly with respect to the microstructural parameters of the hardmetal such as the binder phase content and the grain size, but Luyckx et al., 2007 thought that the ratio of binder phase area to the area of WC grain on the surface that was being abraded must control the damage that occurred.

The magnitude of wear that is found depends on the abrasion conditions that occur. Thus, there is a dependence on the type of abrasive that is used, where the harder the abrasive, the more is the wear shown (Feld & Walter, 1975; Gee, Gant, & Roebuck, 2006, pp. 189–194; Larsen-Basse, 1981a, 1981b). Gee et al. (2006), pp. 189–194 showed that when abrasive wear occurred to a range of WC–Co hardmetals under the same test conditions (same test system, applied load and speed), increase in wear by almost an order of magnitude occurred when an alumina abrasive was used instead of silica (Figure 2). These results also show the same functional relationship between wear volume loss and hardness, despite the fact that the hardness of the alumina abrasive is higher (~2300 HV) than that of most of the WC–Co materials tested and that the hardness of the silica sand (~1100 HV) is toward the lower end of the range of WC–Co materials tested. This is in contrast to many theories of abrasion which suggest that there should be a dramatic change in abrasion rate when the hardness of the abrasive reduces below ~1.1 times the hardness of the material being abraded.

The size of the abrasive also has a major effect on the magnitude of wear. Gee, Phatak, and Darling (2005), Gee, Roebuck, and Gant (2005) found that when alumina abrasive of different sizes was used in the abrasion of WC/Co samples, there was a significant increase in abrasion when the size of the abrasive was increased. For silica abrasive, there was little effect of size. This was felt to be due to the difference in the friability of the abrasive, where the silica was reduced to a much smaller average size after the abrasion process, whereas there was little change in size for the alumina abrasive.

Another effect that has been observed is that when the abrasive size is about the same as the WC grain size, the magnitude of wear alters. Thus, Shewmon (1981) and Gant and Gee (2004) carried out independent microscale abrasion tests of WC/Co materials where the SiC abrasive size was about 4 μm. They found that a straightforward decrease in the magnitude of wear with increasing hardness was not found. This was thought to be due to mechanical damage of the material due to pluck-out of carbide grains by the abrasive particles. Similar observations were made by Krakhmalev (2008) and Engqvist and Axen (1999).

The shape of the abrasive is also likely to have an effect on the wear that is seen, with angular abrasive particles giving more wear than rounded particles (Gee, Gant, & Hutchings, 2002).

The magnitude of abrasion depends critically on the microstructure of the WC/Co. This has already been described since the hardness of WC/Co depends on the two fundamental structure parameters of WC grain size and volume fraction Co binder phase; hence the variation in abrasion wear volume over two orders of magnitude through the hardness range for WC/Co materials is due to changing the microstructural makeup of the WC/Co material. In a study carried out on a carefully manufactured set of samples with well-defined microstructures, Luyckx and Sacks (2007) described results that indicated that the abrasion resistance of WC/Co materials could be increased by increasing the grain size while adjusting the cobalt content to keep the hardness constant. They attributed the increase in abrasion resistance with increasing grain size to a decrease in the ratio of the cobalt mean free path to average WC grain size. However, it must be noted that these two parameters are not independent and are related through the volume fraction of Co (Roebuck & Bennett, 1986), not to mention possible effects of hard phase contiguity.

Some authors (Engqvist & Axen, 1999; Jia & Fischer, 1996) suggest that when the WC grain size becomes very small, the abrasion resistance increases more than would be expected from the increase in the hardness and postulate that there is a change in the mechanism with less carbide fracture and more plastic deformation of the structure.

Roebuck and Gee (2002) also showed that the width of the WC grain size distribution could have an effect on the abrasion of hardmetals. They showed that WC/Co grades that had been processed specifically to give wide grain size distributions all gave lower wear than the conventional grades with the same hardness (**Figure 3**).

With this complex dependence of the volume of abrasion on controlling microstructural parameters, Roebuck, Gant, and Gee (2007) demonstrated how mapping properties such as abrasion against microstructural parameters such as grain size and binder phase content could be used as an aid to the selection of grades.

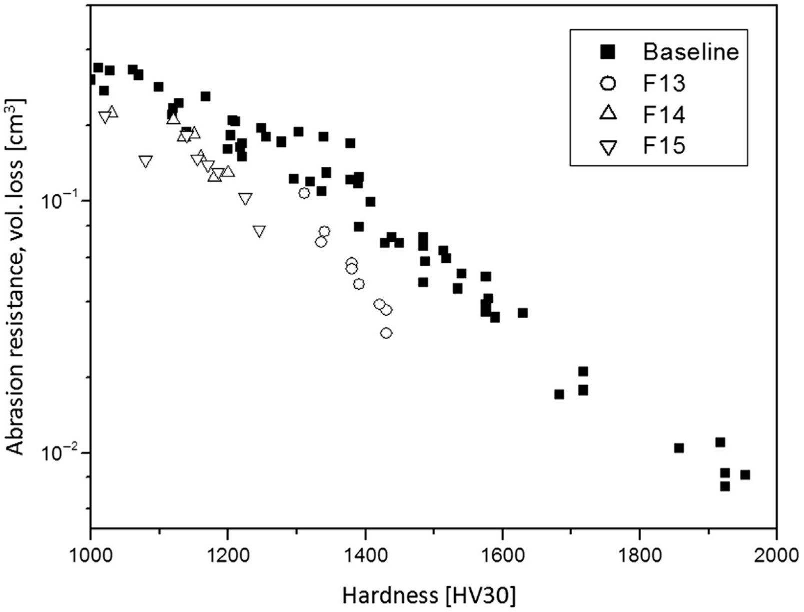

Figure 3 Effect of wide grain size distributions on ASTM B611 wear of hardmetals, Roebuck and Gee (2002). Baseline refers to a range of conventional hardmetals with different percentage of Co binder phase and WC grain sizes. F13, 14 and 15 refer to three sets of hardmetals manufactured to have wide grain size distributions.

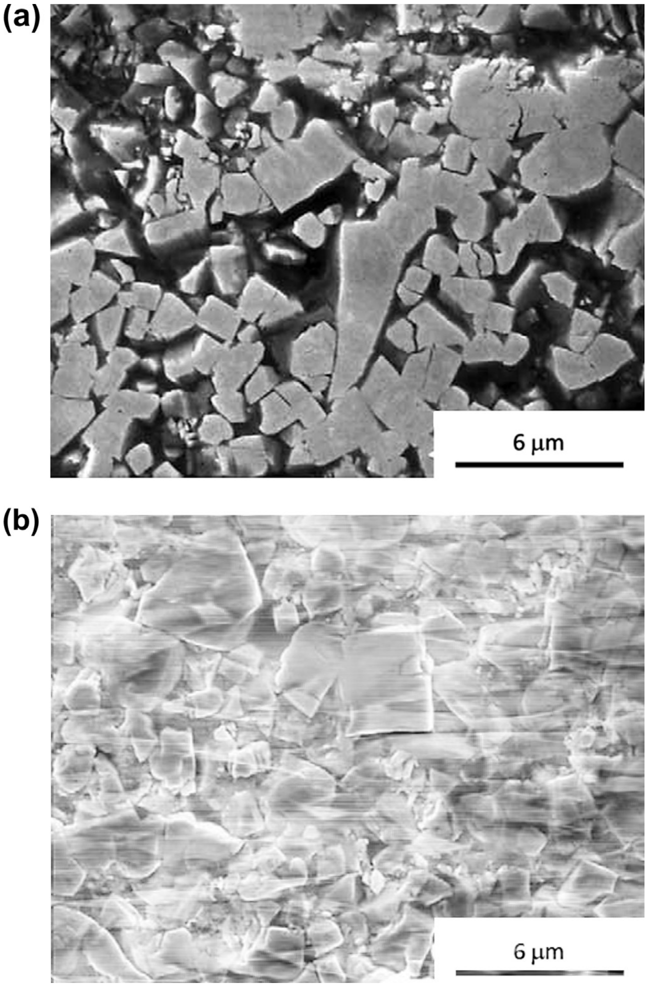

Figure 4 Comparison of wear surface for WC/Co hardmetal abraded in the presence of (a) pH 13 calcium hydroxide solution and (b) pH 1.1 sulfuric acid solution. Gant, Gee, et al. (2004).

The chemical environment of the materials can radically affect the wear that occurs. With aqueous media, the pH affects the wear through a synergistic wear–corrosion effect (Gant & Gee, 2004; Gant, Gee, et al., 2004). This affects the mode of wear with much greater removal of the Co from the wear surface under acid conditions (Figure 4). This resulted in a rate of abrasion that was about an order of magnitude worse under acidic conditions than under alkaline conditions.

Reaction of hardmetals with the material that is being drilled has also been demonstrated in a series of papers by Beste and coworkers that used a range of techniques including advanced sectioning and high-resolution microscopy (Beste & Jocabson, 2002; Beste & Jocabson, 2008a; Beste & Jocabson, 2008b; Beste, Jocabson, & Hogmark, 2008; Beste, Coronel, & Jocabson, 2006; Beste, Hammerstrom, Engqvist, Rimlinger, & Jacobson, 2001; Beste, Hartzell, Engqvist, & Axén, 2001). An interface zone was found between the rock and the WC/Co button material which contained both rock and WC fragments. This was thought to be caused by local melting of the quartz rock which mixed intimately with the WC fragments to form the final interfacial zone.

1.12.4 Sliding Wear

Sliding wear of hardmetals, for example in face seals or in forging tools, occurs when two solid surfaces slide over each other, with or without lubricant. Sliding wear is more of a surface phenomenon than abrasion wear. Although the sliding wear of hardmetals has not been examined as extensively as abrasion or erosion, there has still been enough work published to enable some comments to be made.

Bonny et al. have carried out an extensive series of experiments on the reciprocating sliding wear of WC/Co hardmetals. They found that a major effect on the magnitude of wear was such that it increased as the test load was increased, and the friction coefficient displayed the opposite trend (Bonny et al., 2010a). The oscillating frequency increased both the friction coefficient and the wear. They also found a major effect of surface finishing techniques where Electro Discharge Machining (EDM) was shown to give higher wear and friction than polishing or grinding (Bonny et al., 2009; Bonny et al., 2010b). This was thought to be at least partly due to the residual stress state of the samples which has surface tensile stresses for the EDM samples compared with compressive stresses for the ground and polished samples.

Engqvist, Beste, and Axen (2000) showed that the pH of the environment surrounding the wear couple had a major effect on the friction and wear that was found in lubricated pin-on-disc tests. For conventional carbides, the wear increased as the pH of the lubricant decreased, but for the binderless carbide that was examined, a low wear rate was shown in acidic environments compared to an elevated wear rate in alkali environments.

Engqvist, Högberg, Botton, Ederyd, and Axen (2000) also showed how the friction that was generated in a sliding interface was affected by the ambient atmosphere, with lower friction in air than in nitrogen for conventional carbides and similar friction for both atmospheres for a binderless grade. This was felt to be due to the dynamics of oxide formation.

Jia and Fischer (1997) also examined the sliding wear of various WC/Co grades and found that the wear rate was proportional to the hardness.

1.12.5 Erosion

Erosion involves the removal of material from the surface of a component by the high-speed impact of a liquid or of a stream of hard particles carried in a fluid flow. The two common types of erosion are cavitation erosion and particle erosion. In particle erosion, a stream of hard particles are driven against the surface of the tool or wear part through the medium of a carrier, which can be a gas or a liquid. It occurs in pipelines and associated components carrying slurries or crude oil containing sand. Erosion is fundamentally about the relative ability of an erodent particle to indent plastically or to fracture WC grains (Pugsley, 1999).

It should be noted that cavitation erosion is not considered in this chapter.

1.12.5.1 Wet and Dry Erosion

Little distinction is made in the literature between gas particulate (i.e. dry) erosion and erosion involving a liquid carrier medium (often referred to as "slurry erosion") as hardmetal properties and microstructures do not readily lend themselves to erodent embedment in the surface being worn and damage will depend primarily on the kinetic energy of the particle striking the surface.

The primary distinction between the two erosion regimes occurs when a corrosive carrier medium is used, generally accelerating material removal via enhanced binder removal with possible undermining of carbide grains (Wentzel, 1995).

1.12.5.2 Unique Material Response

In terms of mechanical properties and material response to external conditions, hardmetals are nonclassical, appearing macroscopically brittle but commonly having a mixed ductile–brittle response at the microscopic level. This should be borne in mind when considering their behavior when subjected to erosive environments. Materials that are brittle in the "classical" sense such as glasses and a range of technical ceramics have been the subject of a number of studies looking at the response to single-particle impacts in terms of fracture, which can be lateral, cone and median cracks. Models have been produced which describe such materials' response as quasi-static or dynamic impact (Evans, 1978; Ruff, 1979). By contrast, WC/Co hardmetals do not always behave in a classical brittle manner when subjected to an erosive fluid jet, at least on the microscopic scale. At this scale, they can sometimes behave in a ductile manner or display some attributes of both ductile and brittle behavior. The combination of test conditions and material properties/microstructure determine the response of a particular WC/Co hardmetal to an erodent stream, the severity of erosion and whether erosion is primarily brittle or ductile in nature (Freinkel, 1989). Factors determining the severity of erosion are principally jet velocity (high velocities produce more severe wear) and high impingement angles (90° or approaching normal incidence). Also, the nature of the erodent itself determines as to whether severe erosion (characterized by a ductile response) or a mild erosion regime will prevail (characterized by a brittle response); in short, large particle sizes, high particle hardness and also angularity will promote severe wear.

1.12.5.3 Erosion Dominated by the Brittle Regime

Erosion with ductile response is one in which plasticity takes place on the scale of a typical erosion crater (Gee, 2003; Gee, 2005); this is seen in metals exhibiting macroscopic ductility. This mechanism does not occur in hardmetals when material removal takes place in a nominally brittle fashion, yet it is preceded by obvious local plastic deformation on a very small scale. In practical terms, this means deformation and fracture of individual grains (primarily in larger WC grains) and grain chipping (Figure 5). It should be borne in mind that, in hard materials of this type, large-scale lateral cracking like that observed in technical ceramics is not seen. Where subsurface cracks are seen in hardmetals, they are generally noted to be limited to the size of the grain, i.e. they do not traverse the WC/binder interface, and polished transverse sections through eroded surfaces confirm this. It is proposed that this is at least one explanation why the brittle erosion models developed by Wiederhorn and others (Evans, 1978; Ruff, 1979; Wiederhorn, 1977) have limited applicability in these materials; crack lengths being limited by grain size with a concomitant drop in material removal efficiency for a given fracture toughness; see Figure 6 as an example of the grain-limiting size effect on lateral cracking.

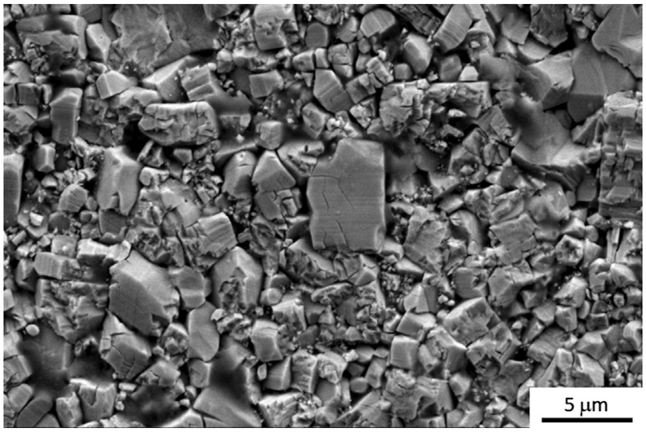

Figure 5 Hardmetal erosion in which a brittle regime predominates; 6% Co hardmetal (mean WC grain size 1.37 μm), subjected to a silica sand slurry at 45° impingement and 19.9 ms^{-1} velocity.

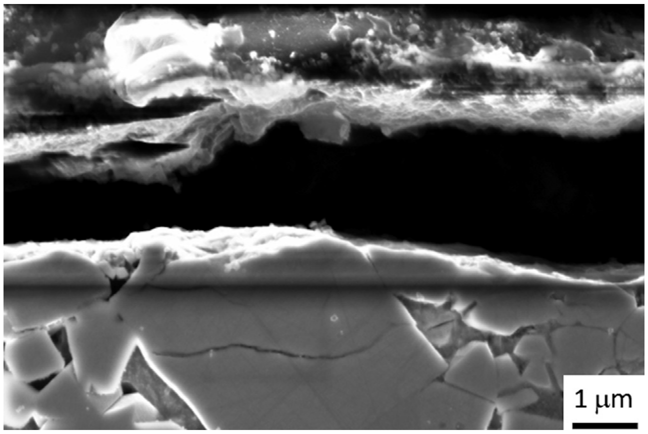

Figure 6 Cross-section through wear scar in a 11% Co hardmetal (mean WC grain size 0.86 μm), subjected to a silica sand slurry at 90° impingement and 19.9 ms^{-1} velocity.

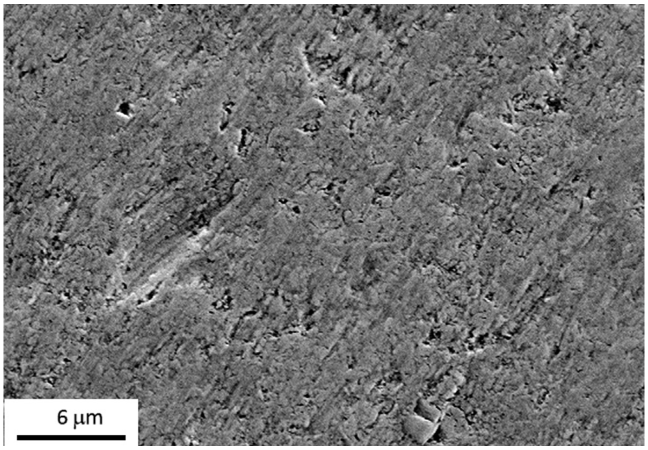

Figure 7 Hardmetal erosion in which a ductile regime predominates; 7% Ni/Co hardmetal (mean WC grain size 0.26 μm), 45° impingement, velocity 19.9 ms^{-1}, using alumina slurry.

Of related interest is the work done on the erosion of binderless WC by Engqvist (Engqvist, 1997), who found that in terms of material response to an erodent stream these materials behaved more in line with technical ceramics than with WC/Co, one explanation possibly being the inherent plasticity in WC due to easier slip than in technical ceramics.

1.12.5.4 Erosion Dominated by the Ductile Regime

Material removal in the ductile regime occurs in a similar manner to softer and more ductile alloys, i.e. material is displaced and subsequently plastically deformed before being detached from the surface (Figure 7).

1.12.5.5 Scaling Effects

Anand and Conrad have undertaken extensive research into the importance of scaling effects in the erosion of WC/Co (Anand, 1988a; Anand, 1988b). They considered the erosion response of WC/Co to be highly dependent on the scale of the impact zone relative to the microstructure; when the impact crater encompasses less than 10 WC grains, material removal occurs principally in a brittle manner via WC grain fracture, while if the impact zone encompasses more than 10 grains, the material response consists mainly of bulk ductile deformation.

In relation to scaling effects, both WC grain size and binder linear intercept are of prime importance: as the grain size is reduced, for a constant volume of binder content, the binder mean free path also decreases which results in enhanced plastic constraint due to the greater interfacial area between the grains and the binder, which has the effect of strengthening the binder phase making dislocation movement and hence shear more difficult. A concomitant increase in the WC/Co bulk hardness of approximately 700 HV is produced as the grain size is reduced from 3 to 0.5 μm. This in turn inhibits cobalt deformation and removal and increases hardmetal wear resistance. Since the deformation resistance of a binder phase has been shown to increase exponentially with a decrease in the binder mean free path, one can expect that the wear resistance of the WC/Co would follow a similar relationship (Unkcel, 1951).

1.12.5.6 Impingement Angle Relationships

Identifying the predominant material removal mechanism is of particular importance for matching an industrial application to a particular hardmetal grade, as the impingement angle at which maximum wear will occur will change with microstructure.

For metallic materials, the maximum material loss occurs at low angles of incidence where ductile mechanisms such as plowing take place. In brittle materials such as ceramics, the maximum wear takes place at a normal angle of incidence where fracture processes dominate.

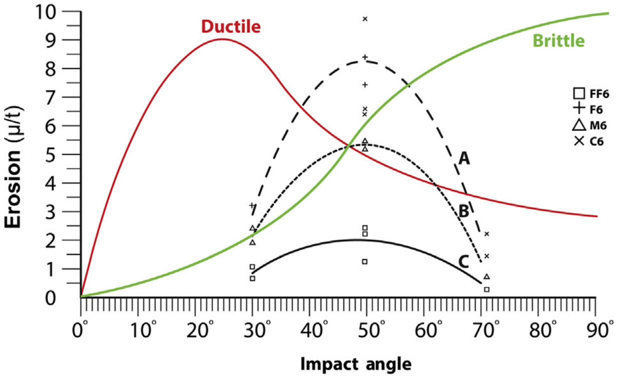

Figure 8 Erosion rate angular dependence in a series of 6% Co hardmetals. Red and green lines are schematic to indicate typical ductile and brittle response to erosion compared to experimental data for hardmetals. A, B, C are different grades of WC/Co hardmetals. From Freinkel (1989).

For hardmetals, because of the two-phase structure of the material, a more complex response occurs, with the maximum erosion occurring at intermediate impact angles (Figure 8). Thus when erosion is dominated by the binder, the material will respond in a brittle manner (as determined from an erosion versus impingement angle plot), as long as the binder is severely constrained by the carbides. This is the case even where there is sufficient binder for ductile erosion mechanisms such as crater lip formation to take place. At high carbide fractions, the carbide phase controls erosion, but since WC is not monolithic, conventional elastic–plastic fracture does not occur and erosion rates do not increase monotonically with impact angle to 90°. Instead, erosion maxima occur at intermediate impact angles. A typical erosion rate–impingement angle relationship is shown in Figure 8 (Freinkel, 1989).

1.12.5.7 Threshold Velocity

As is the case with both ductile metals and monolithic, brittle materials, such as technical ceramics, and hardmetals classically exhibit a threshold velocity to cause material loss by erosion. For technical ceramics and ductile metals, several authors have investigated solid particle erosion through analysis of threshold effects of impact velocity and particle size on the erosion mechanism (Shewmon, 1981; Lawn, 1975). A threshold particle size for erosion of ductile materials was derived (Shewmon, 1981), where it was pointed out that particle sizes below a nominal threshold value were incapable of removing material through plastic work. Lawn and coworkers (Lawn, 1975; Lawn, 1977; Marshall, 1982; Wiederhorn, 1977), and Swain (Swain, 1976) identified particle size to play a key role in the indentation fracture mode of a brittle material. Impacting particles greater than 1 mm in diameter were thought to cause Hertzian cracking, whereas impacts below this size were thought to result in plastic deformation and formation of median cracks. Erosion maps for ceramics have also been generated using threshold velocity criteria and indicated the importance of particle size and velocity on the erosion rate transitions for these materials. However, Jana and Stack (Jana, 2011) have recently attempted to use such threshold velocity criteria for the ductile and ceramic phases of an metal matrix composite (MMC) to model the erosion behavior of a WC/Co hardmetal. Their erosion model was based on the establishment of critical velocity transitions for the onset of plastic deformation of the ductile matrix material and median crack formation of the brittle reinforcement, with the model predictions showing qualitative agreement with some, but not all, of the trends observed for the solid particle erosion of MMCs in the literature.

1.12.6 Impact Wear and Thermal Fatigue

Impact fatigue of surfaces can also lead to the loss of material when fatigue cracks in the surface join together to create loose particles. Surface fatigue can arise from contact or thermal stress (or both in synergy) fatigue mechanism.

Very high intermittent contact stresses are generated in applications such as percussive drilling (Larsen-Basse, 1973; Montgomery, 1968). These stresses aggravate the wear that takes place through mechanisms such as fracture and spallation of individual or small clusters of WC grains. In an attempt to understand this type of process in more detail, Sergejev and Preis (2008) correlated the surface fatigue of WC–Co hardmetals with microstructural defects.

Thermal fatigue cracking arises from the transient heating and cooling of a surface, particularly when combined with surface frictional forces. This can occur in many applications of WC/Co hardmetals such as rock cutting.

1.12.7 Scratch Experiments as Models of Single-Point Abrasion

Abrasion is a wear mode which is a summation of individual single-point abrasion events. For this reason, a number of workers have used scratch testing as a model for abrasion to allow a better understanding to be developed of the mechanisms that take place in abrasion and the relationship of these mechanisms with the microstructure. Gee (2001) carried out low-load scratch tests on a range of WC/Co hardmetals and found that as the number of repeat scratches was increased, the width of the scratch increased. Fracture was the predominant form of damage in both hardmetals and ceramics. As the number of repeat scratches was increased, it was found that a cobalt-rich layer of material was built up on the surface of the hardmetal that also contained fragments of WC (**Figures 9** and **10**) (Gee & Gant, 2007; Gee, 2001). **Figure 10** also shows the surface of a fine-grained hardmetal which appears to have worn in a more ductile manner. However, when examined at high magnification fragmentation of WC grains and buildup of a layer on the surface were also seen.

The effect of grain size was also explored by Sun et al. (2010) who compared nanoscratching of a coarse-grained hardmetal with that of a fine-grained material. They found that scratching damage was dominated

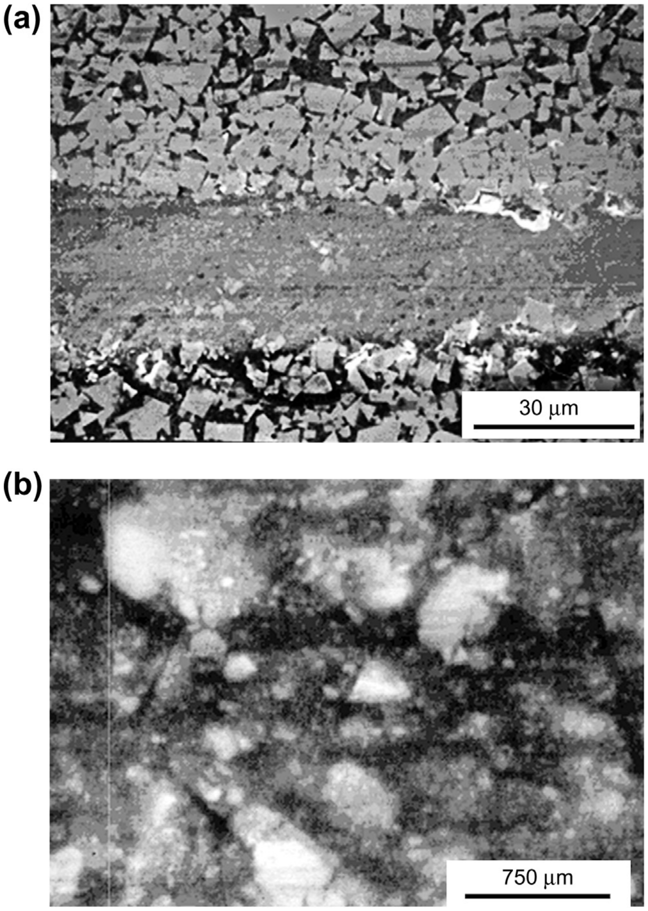

Figure 9 Multiple low-load pass scratching on coarse-grained 20% Co binder phase hardmetal. (a) 100 passes and (b) close-up of (a). Gee (2001).

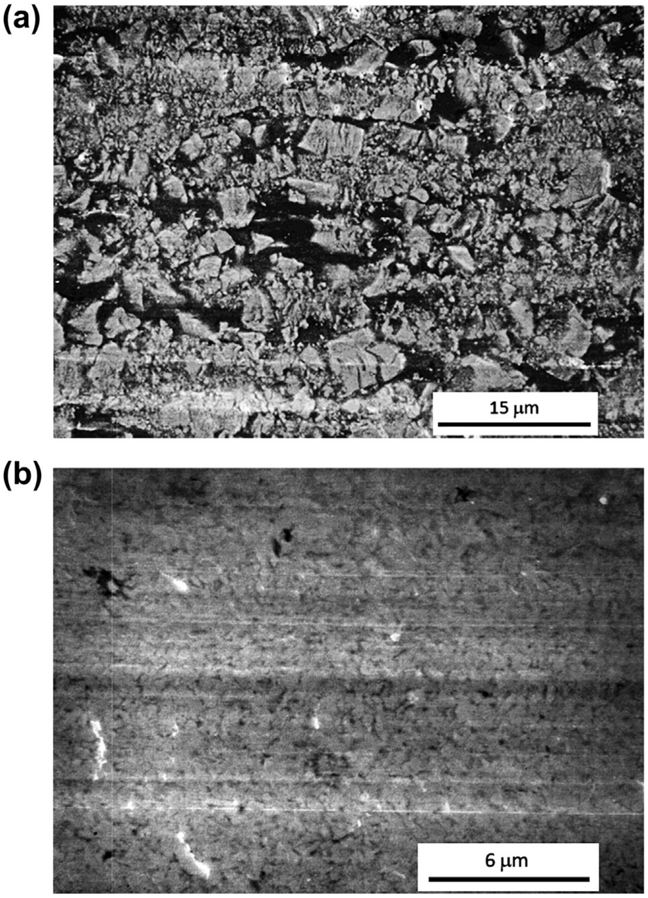

Figure 10 High-load scratch tests on hardmetals. (a) Coarse-grained WC with 20% Co and (b) ultrafine-grained WC/Co hardmetal. Gee and Gant (2007).

by plastic deformation and fracture of grains in the coarse-grained material, but by ductile deformation processes in the fine-grained material.

Further experiments (Gee, 2010; Gee & Nimishakavi, 2011) not only confirmed these earlier results but also showed that when scratches were carried out in the presence of an acidic environment, the cobalt binder phase was removed completely from the surface of the WC/Co sample, leading to severe fracture damage to the WC grains. The area of WC/Co hardmetal to the side of the scratch had suffered little cobalt binder phase removal, despite also being in the acidic environment (Figure 11).

Mingard and Gee (2007), Gee and Mingard (2009) extended this work by applying EBSD analysis to look at scratches made on WC/Co samples (Figure 12). The backscattered electron diffraction yields orientation information on a pixel-by-pixel basis across the area being analyzed. The quality of the electron diffraction can also be analyzed to give information related to the deformation at the pixel analyzed, so that the white areas in the center of the scratch in Figure 12(b) are positions where deformation is so high that the diffraction pattern is not sharp enough to allow the orientation at this point to be indexed. Analysis of the variation in orientation from point to point also gives information on deformation, so Figure 12(b) shows a map of the misorientation from one pixel to another in the same grain. This misorientation is related to plastic deformation. Figure 12(a) shows an electron image formed with detectors orientated so that they contain contrast due to the angular diffraction of backscattered electrons, giving contrast related to deformation (the scratch gives darker contrast than the surrounding area). The EBSD analysis gave clear information on deformation that could be correlated with the degree of cracking and plastic deformation in the worn areas.

Engqvist, Ederyd, Axen, and Hogmark (1999) studied the anisotropic nature of WC single crystal in single-tip scratch testing made with a Vickers diamond indenter. The tests were performed on both the prism and basal planes of the WC crystals. The results showed that there are differences in both the amount of wear and the wear

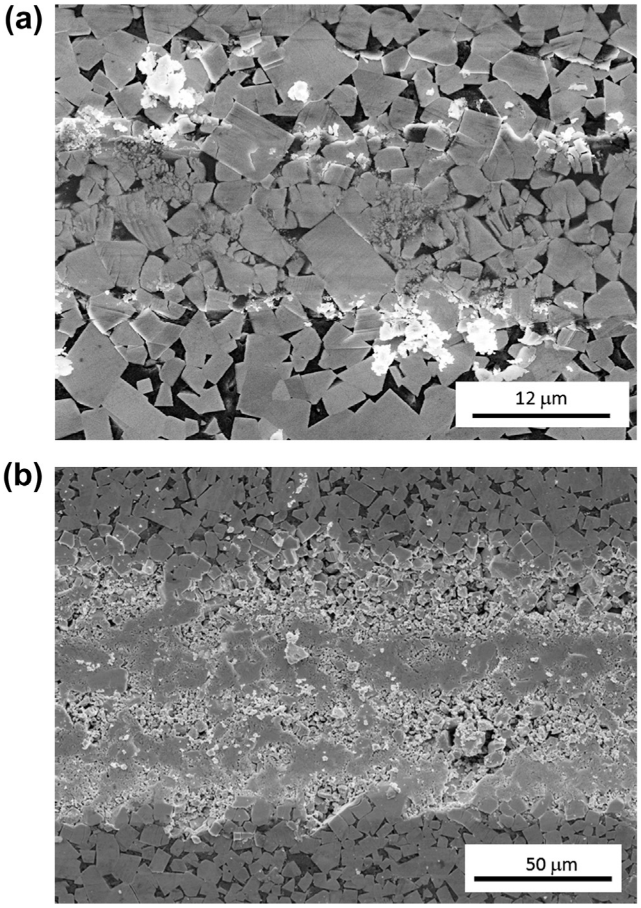

Figure 11 Repeated scratch experiments on 11% Co binder medium grain-sized hardmetal with 30 μm radius indenter and applied load of 400 mN after 100 passes (a) in air and (b) in concentrated HCl. Gee (2010), Gee and Nimishakavi (2011).

mechanisms between different crystallographic directions of WC. Depending on the direction of the slip planes in relation to the groove direction, the wear mechanisms change from ductile grooves parallel to the slip planes to brittle grooves perpendicular to the slip planes. It is also shown that WC tends to wear by the formation of angular rod-shaped wear debris with the slip planes as the preferred surface planes.

Beste and Lundvall (2004) used model scratch testing to study the interaction between WC/Co styli and rock samples. The wear of the tip was found to be correlated to the hardness of the rocks, but was also influenced by the grain size, the quartz content and the grain isotropy.

1.12.8 Wear of Cermets and Surface-Modified WC/CO Carbides

Other types of hard composite materials have also been explored for wear-resistant tool applications. Thus TiC-based cermets have been tested for their abrasion resistance, their erosion resistance and applications in metal forming.

Larsen-Basse (1988) found that the abrasion resistance of a range of TiC–TiN cermets varied with the hardness of the material, with the best wear resistance for the hardest materials.

With respect to erosion, it was found (Hussainova, Antonov, & Voltsihhin, 2001; Hussainova, Kolesnikova, & Hussainov, 2009, Hussainova, Pirso, Antonov, & Juhain, 2009) that the mechanisms for wear were binder removal, grain debonding and pullout. Elevated temperature tests were also carried out, where it was found that the erosion rate decreased with the increase of TiC and Mo contents in the composite. At high temperatures, oxidation became a predominant mechanism.

In the metal forming application (Klassen, Kübarsepp, Roosaara, Viljus, & Traksmaab, 2010; Klassen, Kübarsepp, Tsinjan, & Sergejev, 2011) where high contact adhesive wear predominates, it was found that

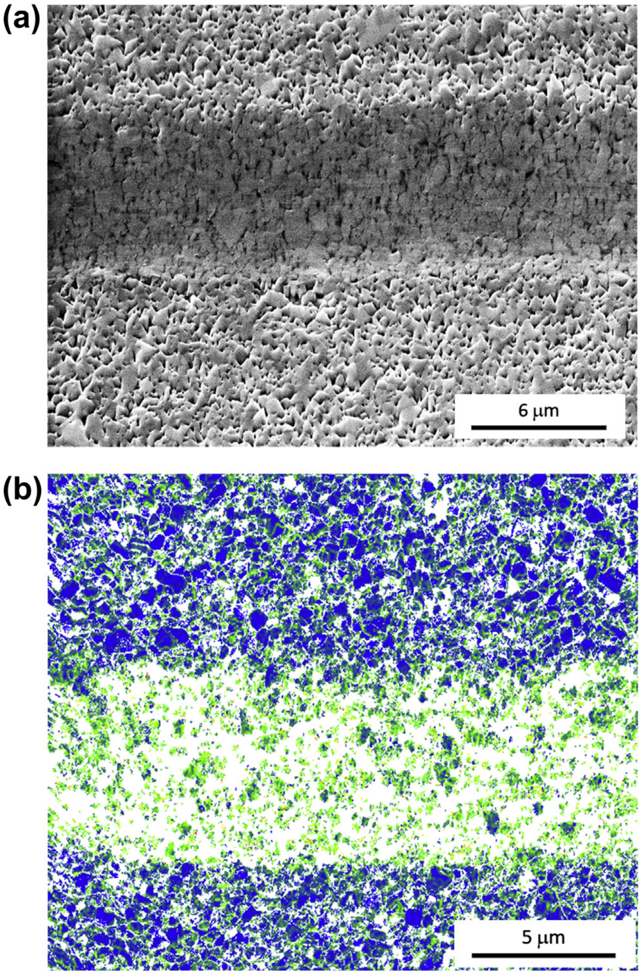

Figure 12 Electron images and EBSD results for single-pass scratch on 7% fine grain size hardmetal under applied load of 450 mN and using a 30 μm radius indenter. (a) Forescatter backscattered image and (b) local misorientation (LM) image, Mingard and Gee (2007); Gee and Mingard, 2009. Note that in **Figure 12(b)**, blue indicates low misorientation, green indicates moderate misorientation and red indicates high misorientation.

TiC-based cermets had better performance than WC/Co hardmetals. The mechanisms of wear were initial removal of the binder phase followed by failure of the hard particle phase. Plastic deformation was found to occur in both the binder phase and the hard phase.

Hussainova et al. (2011) have recently tested WC/Co composites with doping of yttria-stabilized zirconia which they found gave lower wear rates than conventional WC/Co materials, which was thought to be due to the lower susceptibility of zirconia to transgranular crack propagation, smaller mean free path between ceramic grains and the formation of a lubricating glazed silica-rich layer.

1.12.9 Mechanisms of Wear for Hardmetals

1.12.9.1 Abrasion

In abrasion, a number of different mechanisms of damage have been observed. In some early papers Co extrusion, and thus loss of mechanical integrity, was thought to be the primary wear mechanism (Larsen-Basse, 1981a; Larsen-Basse & Devnani, 1986). There was certainly some evidence for extrusion of cobalt from the WC/Co materials, and there is some evidence that the surface layers of WC/Co have lower binder phase content than the bulk of the sample, but mechanical removal with the binder phase pushed to the side of the abrasion event would also seem to be an important mechanism. More papers that investigate sections through

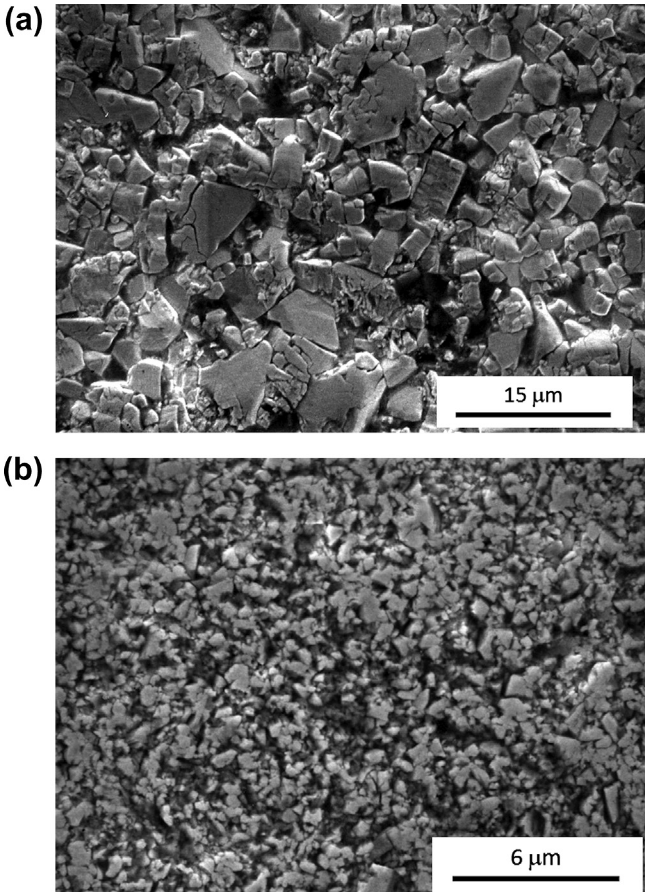

Figure 13 Surface of worn sample tested with modified ASTM G65 test system using medium sand. (a) Coarse-grained hardmetal and (b) fine-grained hardmetal. Gee and Gant (2006).

worn surfaces are needed to bring the much needed quantification to this debate. It is certainly clear that the cobalt binder phase is often removed from the surface of abraded WC/Co samples (Figure 13) (Gee & Gant, 2007; Gee et al., 2006, pp. 189–194), leaving the WC grains elevated above the overall surface and mechanically unsupported. However, in some cases, reembedding of WC fragments to the cobalt binder gives a mechanically formed tribolayer at the surface of the material (Figures 14(c) and 14(e)).

Plastic deformation in WC grains, as evidenced by slip line traces, can also be seen in many cases. Figure 15 shows an excellent example of deformation in a large carbide grain with clear deformation aligned along the crystallographic planes of the crystal.

Fracture of the WC grains is also a major feature of abrasion damage (Figures 14(a–c)). This cracking eventually leads to loss of carbide grains or groups of grains from the surface of the hardmetal (Figure 14(d)). Fragmented grains of WC, with size down to a few tens of nanometers, often reembed into the binder phase on the surface (Figures 14(c) and 14(e)). Subsurface cracking through the bulk of the material has also been observed (Figures 14(f) and 14(g)). Although in some cases the cracks can be quite long (Figure 14(f)), it is more normal to see that cracks extend only a few grains (Figure 14(g)).

1.12.9.2 Stepwise Approach: Understanding Erosion Processes at the Microscopic Scale

In erosion, although the detailed material removal processes are still poorly understood, features similar to those observed in abrasion are evident. Stepwise testing is a recent approach that has been developed by Gee and coworkers (Gee, Gee, & McNaught, 2003; Gee, Phatak, et al., 2005, Gee, Roebuck, et al., 2005) as a way of providing information on damage accumulation in erosion. The technique uses a combination of exposing a test sample to repeated very-low-duration abrasion or erosion followed by accurate relocation in the scanning electron microscopy. This enables the real wear processes within a material to be followed in considerable

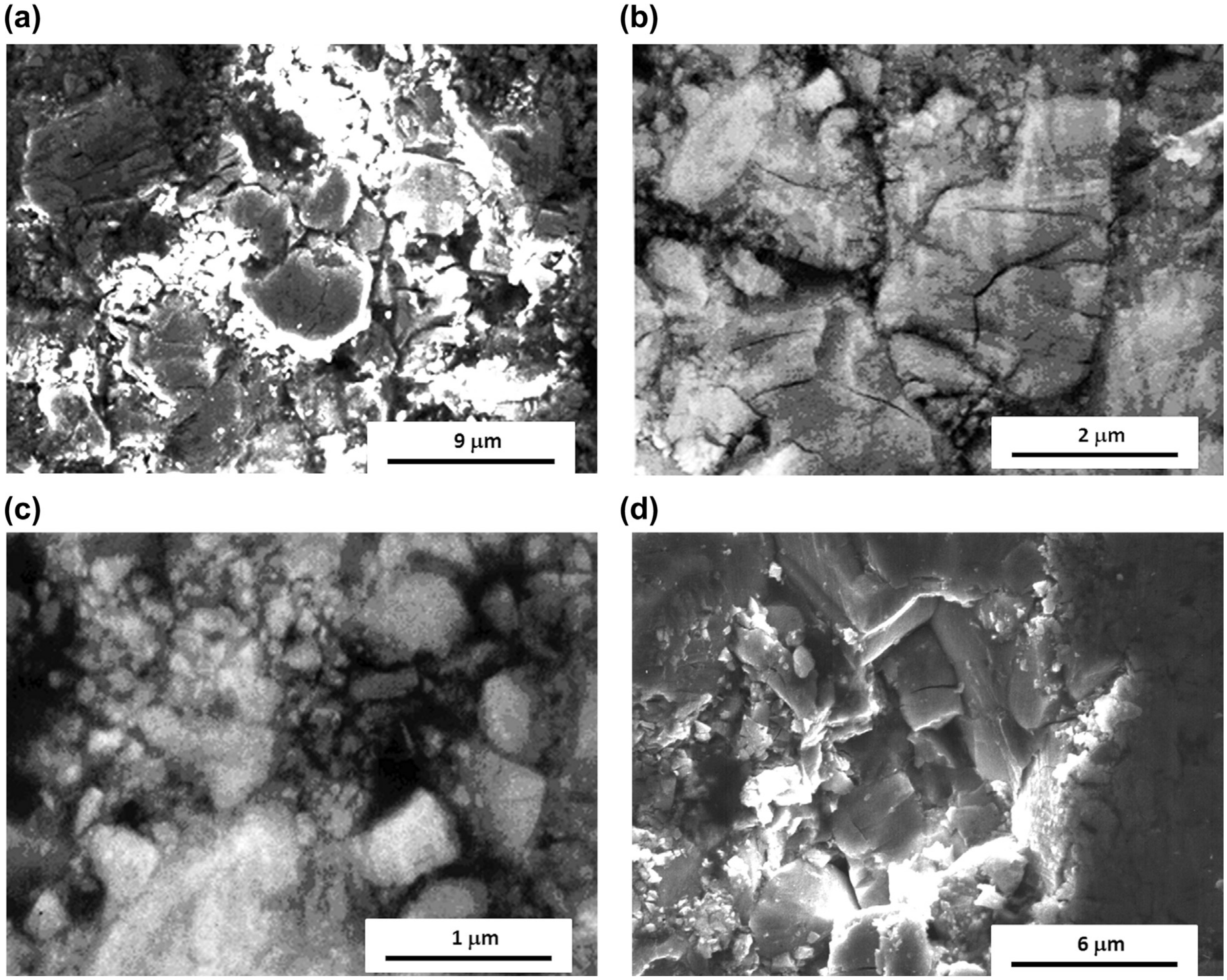

Figure 14 Examination of wear surfaces for hardmetals tested in ASTM B611 with 660 μm alumina abrasive except where specified. (a, b) Fracture damage, (c) reembedding of small fragments of WC particles, (d) breakaway of areas of material, (e) reembedded regions at edge between worn surface and polished cross-section, (f) edge between worn surface and polished cross-section, (g) cross-section. **Figures 14(a–d)** were taken on coarse-grained 6% hardmetal with a hardness of 1221 HV30, **Figure 14(e)** was on a coarse-grained 24% Co hardmetal, **Figure 14(f)** with a coarse-grained 9% Co hardmetal with a hardness of 982 HV30, and **Figure 14(g)** with a coarse-grained 6% hardmetal. Gee and Gant (2007).

detail, giving an excellent basis for developing new and improved models. In the initial study (Gee et al., 2003), the technique was applied to the gas-borne particulate erosion wear of a WC/Co hardmetal. The study showed that wear occurred by the accumulation of damage, fracture and removal of single WC grains.

The buildup of plastic strain in individual WC grains often reached the point at which fracture occurred, weakening and fragmenting the individual WC grain. In addition, the growth of cracks between one WC grain and the next broke down the strong WC intergrain network or skeleton in the material leading to a general weakening of the structure and increasing the likelihood of breakaway of WC grains (Figure 16).

It was also observed that in the initial stage of wear, although gross damage to the structure of the material occurred over the localized area corresponding to the impact area of the particle, some damage occurred over a much wider area. This was thought to be due to the immediate fragmentation of impacting particles followed by scouring of the surface near the impact site by fragments.

Further damage was caused by a combination of additional removal of the binder phase, buildup of plastic deformation in single WC grains followed by fracture and fragmentation and removal, and intergranular fracture of the WC skeleton. Multigrain cracking was not observed, suggesting that models based on indentation cracking are not realistic. There was no evidence at all for long multigrain cracks on the exposed wear surface; this contradicts some theories of the wear of these materials that expect that wear occurs by the lateral crack

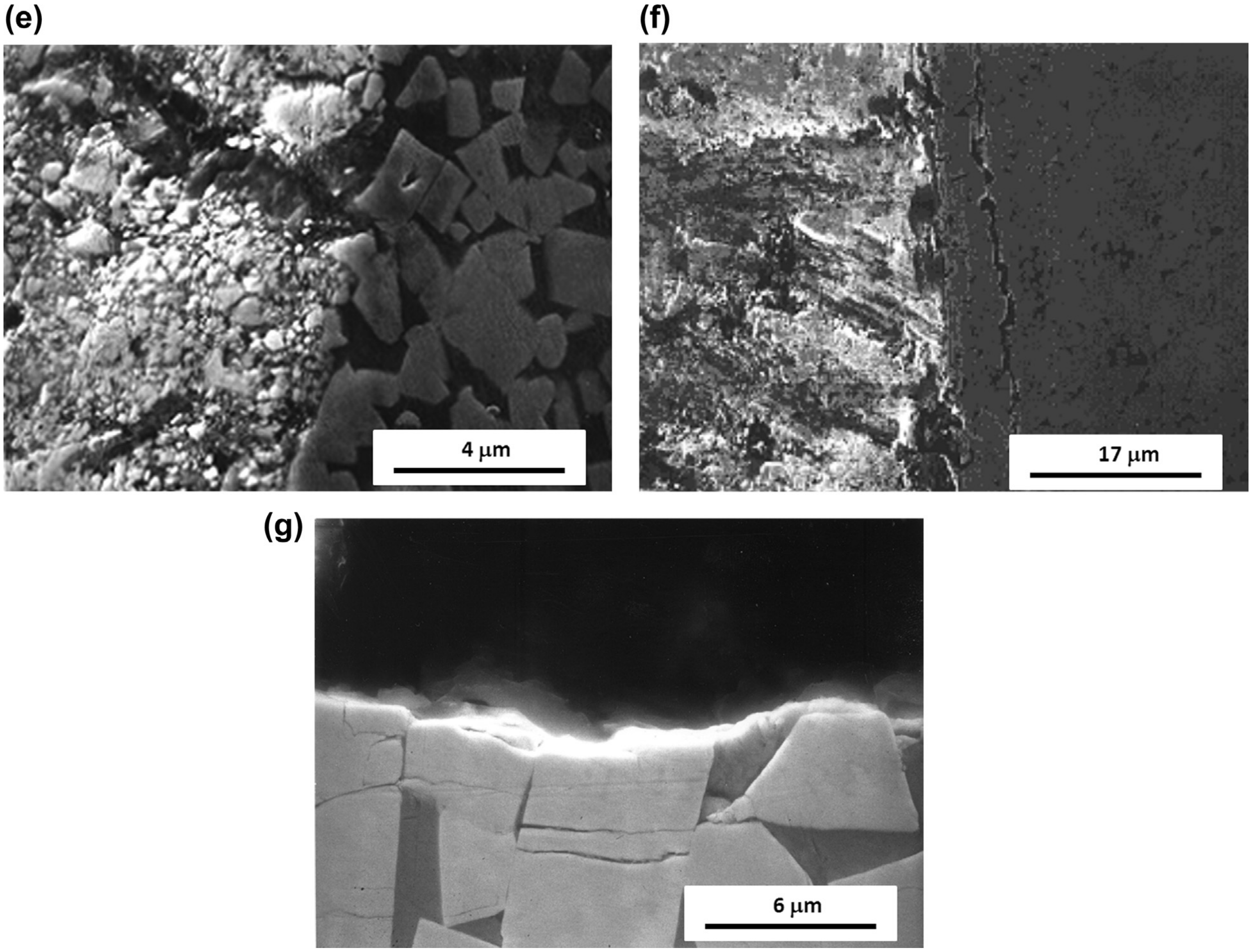

Figure 14 (*continued*).

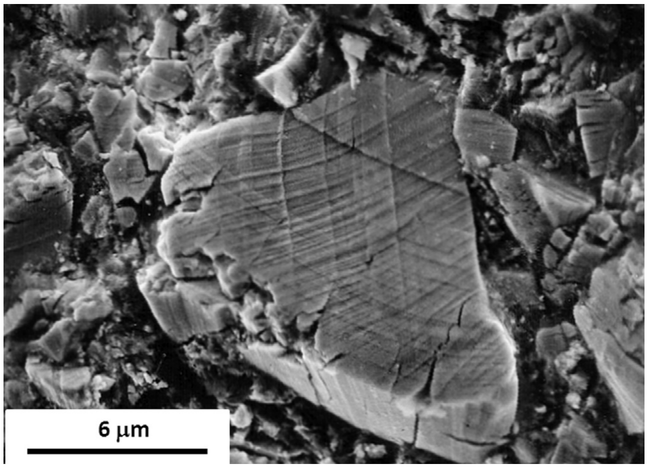

Figure 15 Large-grained WC/Co hardmetal tested in ASTM B611 test with silica abrasive.

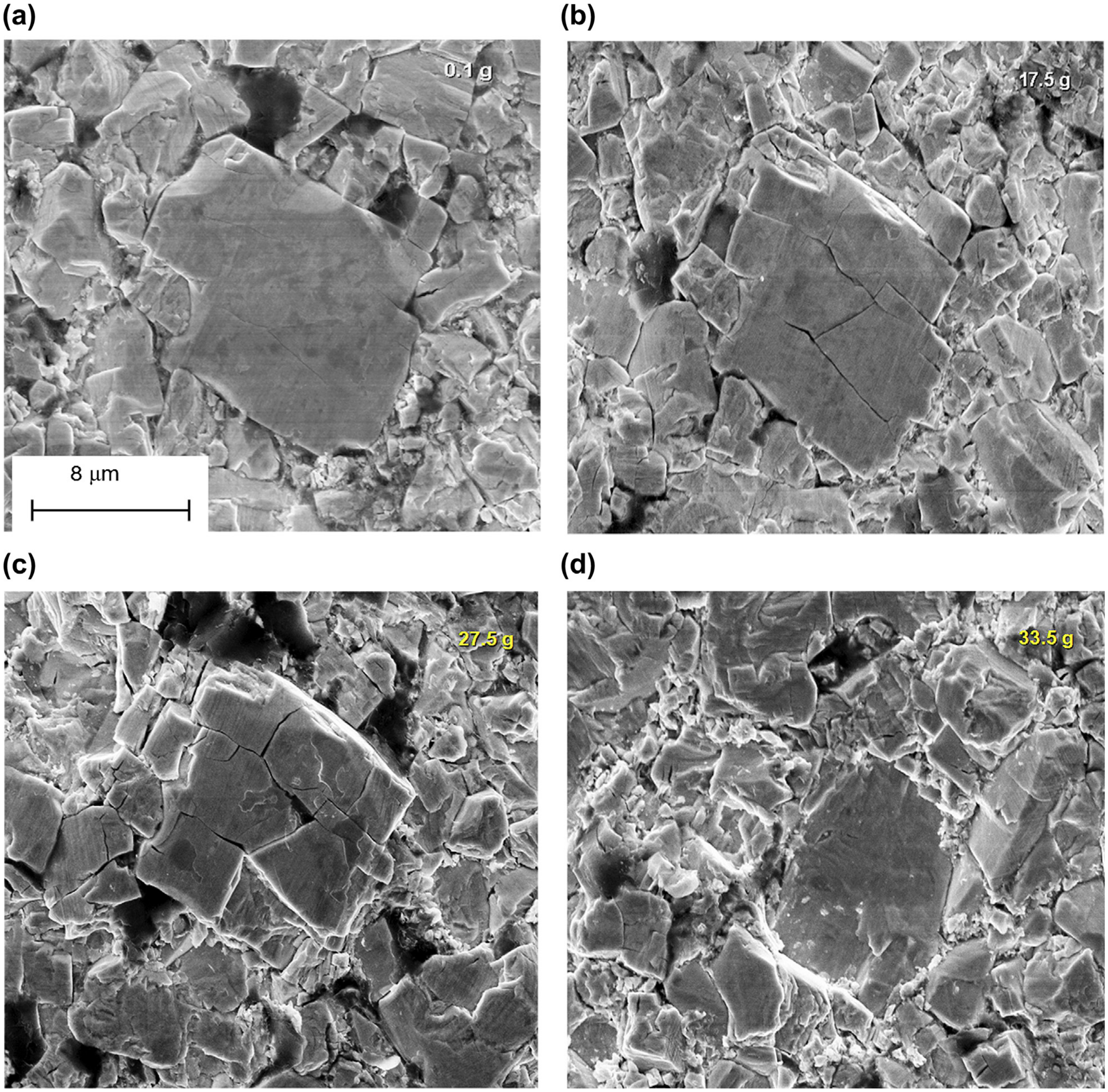

Figure 16 Sequences of images from area on large-grain-size sample after exposure in ASTM G76 test to different quantities of silica erodant. (a) 0.1 g, (b) 17.5 g, (c) 27.5 g, and (d) 33.5 g. Gee, Phatak, et al. (2005).

mechanism that occurs in indentation (Anand, 1986; Almond, 1986; Evans, 1980). If these cracks existed, they would extend across many grains. In fact all the cracks that were observed were only a single grain or less in size. This confirms similar observations by other studies of the erosive wear of coarse-grained hardmetals (Larssen-Basse, 1973; Larssen-Basse, 1985a, 1985b).

Gee (2005) followed up the initial study with a further investigation of coarse and fine-grained WC/Co and found detailed differences between the two, namely, that although considerable evidence was seen for plastic deformation in the large-grained material as evidenced by the slip line traces on the larger grains, there was no sign of these slip lines in the finer grained materials. However, the microcracking of individual grains was very similar, suggesting that similar processes were occurring in the wear of both hardmetal samples. In particular, fracture and removal of grains is still the main mechanism of wear with no evidence for the gross plastic deformation that has been suggested as the key mechanism of wear for fine-grained materials (Allen, 2001; Beste, 2001; Jia & Fischer, 1996).

1.12.9.3 Summary of Wear Mechanisms

In abrasion, erosion, and single-point modeling of abrasion, similar mechanisms were found. Although the detail changes with conditions, the normal contributory events are:

- Bulk movement of binder phase in the surface layer of the sample, including some loss.
- Plastic deformation and damage to the remaining binder phase.
- In corrosive conditions, removal of binder phase by chemical attack.
- Accumulation of plastic strain in WC grains.
- Fracture and fragmentation of individual WC grains.
- Reembedment of WC fragments in a Co-rich surface layer.
- Cracking between WC grains.
- Breakaway of unsupported WC grains and groups of grains, sometimes with Co films attached.

To some extent, these processes can occur in parallel, but it is the damage and then the removal of the binder phase that leaves mechanically unsupported carbide grains, that are progressively removed from the surface, resulting in larger scale damage to the surface.

Reembedment of WC fragments is not observed in all cases, but when it does occur, it acts as a mechanism to protect the rest of the surface.

References

Almond, E. A. (1986). Indentation phenomena and the wear of surfaces and edges. *Materials Science and Technology, 2*, 641–646.

Anand, K., Morrison, C., Scattergood, R. O., Conrad, H., Routbort, J. L., & Warren, R. (1986). Erosion of multiphase materials. *Institute of Physical Conference Series, 75*, 949–961.

Anand, K., & Conrad, H. (1988a). Local impact damage and erosion mechanisms in WC-6wt.%Co alloys. *Materials Science and Engineering A, 105/106*, 411–421.

Anand, K., & Conrad, H. (1988b). Microstructure and scaling effects in the damage of WC–Co alloys by single impacts of hard particles. *Journal of Materials Science, 23*, 2931–2942.

Ball, A., & Paterson, W. (1985). The microstructural design of erosion resistant hard materials. *11th Int. Plansee Seminar 20–24 May 1985, Vienna, Austria. Proceedings* (Vol. 2, pp. 377–391).

Bata, G. L., Dallaire, S., & Champagne, B. (1985). Development and application of hard metals for protection against wear. *11th Int. Plansee Seminar 20–24 May 1985, Vienna* (Vol. 2, pp. 687–708).

Bailey, S. G., & Perrott, C. M. (1974). Wear processes exhibited by WC–Co rotary cutters in mining. *Wear, 29*, 117–128.

Beste, U., Coronel, E., & Jocabson, S. (2006). Wear induced material modifications of cemented carbide rock drill buttons. *International Journal of Refractory Metals and Hard Materials, 24*(1–2), 168–176.

Beste, U., Hammerström, L., Engqvist, H., Rimlinger, S., & Jacobson, S. (2001). Particle erosion of cemented carbides with low Co content. *Wear, 250*, 809–817.

Beste, U., Hartzell, T., Engqvist, H., & Axén, N. (2001). Surface damage on cemented carbide rock-drill buttons. *Wear, 249*(3–4), 324–329.

Beste, U., & Jacobson, S. (2002). Friction between a cemented carbide rock drill button and different rock types. *Wear, 253*(11–12), 1219–1221.

Beste, U., & Jacobson, S. (2008a). A new view of the deterioration and wear of WC/Co cemented carbide rock drill buttons. *Wear, 264*(11–12), 1129–1141.

Beste, U., & Jacobson, S. (2008b). Targeting micro-sectioning: a technique to study subsurface features in worn specimens. *Wear, 264*(11–12), 1152–1156.

Beste, U., Jacobson, S., & Hogmark, S. (2008). Rock penetration into cemented carbide drill buttons during rock drilling. *Wear, 264*(11–12), 1142–1151.

Beste, U., Lundvall, A., & Jocabson, S. (2004). Micro-scratch evaluation of rock types – a means to comprehend rock drill wear. *Tribology International, 37*(2), 203–210.

Blombery, R. I., Perrott, C. M., & Robinson, P. M. (1974a). Similarities in the mechanisms of wear of tungsten carbide–cobalt tools in rock and metal cutting. *Wear, 27*, 383–390.

Blomberry, R. I., Perrot, C. M., & Robinson, P. M. (1974b). Abrasive wear of tungsten carbide–cobalt composites II wear mechanisms. *Materials Science and Engineering, 13*, 93–100.

Bonny, K., De Baets, P., Ost, W., Vleugels, J., Huang, S., Lauwers, B., et al. (2009). Influence of electrical discharge machining on the reciprocating sliding wear response of WC–Co cemented carbides. *Wear, 266*(1–2), 84–95.

Bonny, K., De Baets, P., Perez, Y., Vleugels, J., & Lauwers, B. (2010a). Friction and wear characteristics of WC–Co cemented carbides in dry reciprocating sliding contact. *Wear, 268*(11–12), 1504–1517.

Bonny, K., De Baets, P., Quintelier, J., Vleugels, J., Jiang, D., Van der Biest, O., et al. (2010b). Surface finishing: impact on tribological characteristics of WC–Co hardmetals. *Tribology International, 43*(1–2), 40–54.

Conrad, H., McCabe, D., & Sargent, G. A. (1981). Effects of microstructure on the erosion of WC–Co alloys. In: *Proc. 1st Int. Conf. on the science of hard materials* (pp. 775–796). Plenum Press.

Dahlin, C. (1962). Factors influencing the life of drill steel equipment. *International Symposium on Mining Research, 1*, 351–369.

Dawihl, W., & Frisch, B. (1968). Wear properties of tungsten carbide and aluminium oxide sintered materials. *Wear, 12*, 17–25.

Engqvist, H., & Axén, N. (1999). Abrasion of cemented carbides by small grits. *Tribology International, 32*(9), 527–534.

Engqvist, H., Axen, N., & Hogmark, S. (1997). Resistance of a binderless cemented carbide to abrasion and particle erosion. *Tribology Letters, 4*, 251–258.

Engqvist, H., Beste, U., & Axen, N. (2000). Influence of pH on sliding wear of WC-based materials. *International Journal of Refractory Metals and Hard Materials, 18*(2), 103–109.

Engqvist, H., Ederyd, S., Axen, N., & Hogmark, S. (1999). Grooving wear of single-crystal tungsten carbide. *Wear, 230*, 165–174.

Engqvist, H., Högberg, H., Botton, G. A., Ederyd, S., & Axen, N. (2000). Tribofilm formation on cemented carbides in dry sliding conformal contact. *Wear, 239*(2), 219–228.

Evans, A. G., Gulden, M. E., & Rosenblatt, M. (1978). Impact damage in brittle materials in the elastic-plastic response regime. *Proceedings of the Royal Society A, 361*, 343.

Evans, A. G., & Marshall, D. B. (1980). Wear mechanisms in ceramics. In D. A. Rigney (Ed.), *Fundamentals of friction and wear of materials* (pp. 439–452). Cleveland, OH: ASM.

Feld, H., & Walter, P. (1975). Contribution to the understanding of mineral hard metal abrasive wear. *Powder Metallurgy, 7*, 188–190.

Freinkel, D. M., & Luyckx, S. B. (1989). Energy loss mechanisms in the erosion of cemented tungsten carbide. *Scripta Metallurgica, 23*, 659–664.

Gant, A. J., & Gee, M. G. (2001). Wear of tungsten carbide–cobalt hardmetals and hot isostatically pressed high speed steels under dry abrasive conditions. *Wear, 250–251*, 908–915.

Gant, A. J., Gee, M. G., & May, A. T. (2004). The evaluation of tribo-corrosion synergy for WC–Co hardmetals in low stress abrasion. *Wear, 256*(5), 500–516.

Gant, A. J., & Gee, M. G. (2004). Microabrasion of WC–Co hardmetals in corrosive media. *Wear, 256*, 954–962.

Gant, A. J., & Gee, M. G. (2006). Abrasion of tungsten carbide hardmetals using hard counterfaces. *International Journal of Refractory Metals and Hard Materials, 24*, 189–198.

Gee, M. G. (2001). Low load multiple scratch tests of ceramics and hard metals. *Wear, 250–251*(1), 264–281.

Gee, M. G. (2010). Model scratch corrosion studies for WC/Co hardmetals. *Wear, 268*(9–10), 1170–1177.

Gee, M. G., Gant, A. J., & Hutchings, I. M. (2002). *Rotating wheel abrasive wear testing*. NPL Good Practice Guide No 55.

Gee, M. G., Gant, A. J., & Roebuck, B. (October 2006). *Wear mechanism in abrasion of WC/Co and related hardmetals*. Ghent, Belgium: EuroPM2006 – Hard Materials and Diamond Tools.

Gee, M. G., Gant, A., & Roebuck, B. (2007). Wear mechanisms in abrasion and erosion of WC/Co and related hardmetals. *Wear, 263*(1–6), 137–148.

Gee, M. G., Gee, R. H., & McNaught, I. (2003). Stepwise erosion as a method for determining the mechanisms of wear in gas borne particulate erosion. *Wear, 255*, 44–54.

Gee, M., Mingard, K. P., & Roebuck, B. (2009). Application of EBSD to the evaluation of plastic deformation in the mechanical testing of WC/Co hardmetal. *International Journal of Refractory Metals and Hard Materials, 27*(2), 300–312.

Gee, M. G., & Neale, M. J. (2002). *General approach and procedures for unlubricated sliding wear tests*. NPL Good Practice Guide No 51.

Gee, M. G., & Nimishakavi, L. (2011). Model single point abrasion experiments on WC/Co hardmetals. *International Journal of Refractory Metals and Hard Materials, 29*(1), 1–9.

Gee, M. G., Phatak, C., & Darling, R. (2005). Determination of wear mechanisms by stepwise erosion and stereological analysis. *Wear, 258*, 412–425.

Gee, M. G., Roebuck, B., & Gant, A. J. (2005). Abrasive wear testing with the ASTM B611 and modified ASTM G65 rotating wheel test systems. *16th Int. Plansee Seminar high performance PM materials, Reutte, Austria, 30 May–3 June 2005* (Vol. 2, pp. 1235–1249).

Hack, T. A., & Peters, C. T. (1985). A model for the wear behaviour of hardmetal rock-bit inserts in percussive drilling. *11th Int. Plansee Seminar 20–24 May 1985, Vienna, Austria. Proceedings* (Vol. 1, pp. 799–813).

Herr, M., Sailer, T., Sockel, H. G., Schulte, R., Feld, H., & Prakash, L. J. (2001). Characterisation of wear properties of ultra fine-grained hardmetals using a special abrasive wheel test. *International Journal of Refractory Metals and Hard Materials, 19*, 371–379.

Hussainova, I., Antonov, M., & Voltsihhin, N. (2011). Assessment of zirconia doped hardmetals as tribomaterials. *Wear, 271*, 1909–1915.

Hussainova, I., Kolesnikova, A., & Hussainov, M. (2009). Effect of thermo-elastic residual stresses on erosive performance of cermets with core-rim structured ceramic grains. *Wear, 267*(1–4), 177–185.

Hussainova, I., Kubarsepp, J., & Pirso, J. (2001). Mechanical properties and features of erosion of cermets. *Wear, 250*(1–12), 818–825.

Hussainova, I., Pirso, J., Antonov, M., & Juhani, K. (2009). High temperature erosion of Ti(Mo)C-Ni cermets. *Wear, 267*(11), 1894–1899.

Jana, B. D., & Stack, M. M. (2011). A note on threshold velocity criteria for modelling the solid particle erosion of WC/Co MMCs. *Wear, 270*, 439–445.

Jia, K., & Fischer, T. E. (1996). Abrasion resistance of nanostructured and conventional cemented carbides. *Wear, 200*, 206–214.

Jia, K., & Fischer, T. E. (1997). Sliding wear of conventional and nanostructured cemented carbides. *Wear, 203–204*, 310–318.

Jonsson, H. (1976). Wear of cemented carbide bits during percussive drilling in magnetite-rich ore. *Planseeberichte für Pulvermetallurgie, 24*, 108–135.

Klaasen, H., Kübarsepp, J., Roosaara, T., Viljus, V., & Traksmaab, R. (2010). Adhesive wear performance of hardmetals and cermets. *Wear, 268*(9–10), 1122–1128.

Klaasen, H., Kübarsepp, J., Tsinjan, A., & Sergejev, F. (2011). Performance of carbide composites in cyclic loading wear conditions. *Wear, 271*(5–6), 837–841.

Krakhmalev, P. V. (2008). On the abrasion of ultrafine WC–Co hardmetals by small SiC abrasive. *Tribology Letters, 30*(1), 35–39.

Larsen-Basse, J. (1973). Wear of hard metals in rock drilling: a survey of the literature. *Powder Metallurgy, 16*, 1–32.

Larsen-Basse, J. (1981a). Resistance of cemented carbides to sliding abrasion: Role of binder metal. In: *Proc. 1st Int. Conf. on the science of hard materials* (pp. 797–813). Plenum Press.

Larsen-Basse, J. (1981b). Abrasive wear resistance of tungsten carbide composites with iron-nickel binder. In: *Proc. Int. Conf. on wear of materials* (pp. 534–538). San Francisco: ASME.

Larsen-Basse, J. (1983). Effect of composition, microstructure and service conditions on the wear of cemented carbides. *Journals of Metals, 35*(11), 35–42.

Larsen-Basse, J. (1985a). Binder extrusion of sliding wear of WC–Co alloys. In: *Proceedings of the international conference on wear of materials* (pp. 39–44). New York: ASME.

Larsen-Basse, J. (1985b). Binder extrusion in sliding wear of WC–Co alloys. *Wear, 105*, 247–256.

Larsen-Basse, J. (1988). Abrasive wear of some titanium-carbonitride-based cermets. *Materials Science and Engineering, 105–106*, 395–400.

Larsen-Basse, J., & Devnani, N. (1986). *Binder extrusion as a controlling mechanism in abrasion of WC–Co cemented carbides*. Rhodes, Gr.

Larsen-Basse, J., & Koyanagi, E. T. (1979). Abrasion of WC–Co alloys by quartz. *Journal of Lubrication Technology, 101*, 208–211.

Larsen-Basse, J., Perrott, C. M., & Robinson, P. M. (1974). Abrasive wear of WC–Co composites in rotary drilling tests. *Materials Science and Engineering, 13*, 83–91.

Larsen-Basse, J., Shishido, C. M., & Tanouye. (1974). Some features of abraded WC–Co surfaces. *Journal of Australian Institute of Metals, 19*, 271–275.

Latin, A. (1961). The properties of tungsten carbide–cobalt alloys used for mineral cutting tools. *Metallurgia, 64*, 211–216.

Lawn, B. R., & Evans, A. G. (1977). A model for crack initiation in elastic/plastic indentation fields. *Journal of Materials Science, 12*, 2195–2199.

Lawn, B. R., & Wilshaw, R. (1975). Indentation fracture: principles and applications. *Journal of Materials Science, 19*, 1049–1081.

Luyckx, S., Sacks, N., & Love, A. (2007). Increasing the abrasion resistance without decreasing the toughness of WC–Co of a wide range of compositions and grain sizes. *International Journal of Refractory Metals and Hard Materials, 25*(1), 57–61.

Marshall, D. B., Lawn, B. R., & Evans, A. G. (1982). Elastic/Plastic indentation damage in ceramics: the lateral crack system. *Journal of the American Ceramic Society, 65*, 561–566.

Mingard, K. P., & Gee, M. G. (2007). EBSD examination of worn WC/Co hardmetal surfaces. *Wear, 263*(1–6), 643–652.

Montgomery, R. S. (1968). The mechanism of percussive wear of tungsten carbide composites. *Wear, 12*, 309–329.

Montgomery, R. S. (1969). Percussive wear properties of cemented carbides. *Transactiona of the American Institute of Mining Metallurgical and Petroleum Engineering, 244*, 153–157.

Osburn, H. J. (1969). Wear of rock-cutting tools. *Powder Metallurgy, 12*(24), 471–502.

Peters, C. T., & Brabyn, S. M. (1985). Properties of nickel-substituted hardmetals and their performance in hard rock drill bits. In *11th Int. Plansee Seminar 20–24 May 1985, Vienna, Austria. Proceedings* (Vol. 1, pp. 877–886).

Precht, W., Viswanadham, R. K., & Venables, J. D. (1981). Abrasion resistance of cermets containing Co/Ni binders. In: *Proc. 1st Int. Conf. on the science of hard materials* (pp. 815–828). Plenum Press.

Pugsley, V. A., & Allen, C. (1999). Microstructure/property relationships in the slurry erosion of tungsten carbide–cobalt. *Wear, 233–235*, 93–103.

Quigley, D. G. F., Luyckz, S., & James, M. N. (1997). An empirical ranking of a wide range of WC–Co grades in terms of their abrasion resistance measured by the ASTM standard B611-85 test. *Insternational Journal of Refractory and Hard Materials, 15*, 73–79.

Roebuck, B., & Bennett, E. G. (1986). Phase size distribution in WC/Co hardmetals. *Metallography, 19*(1), 27–47.

Roebuck, B., Gant, A. J., & Gee, M. G. (2007). Abrasion and toughness property maps for WC/Co hardmetals. *Powder Metallurgy, 50*(2), 111–114.

Roebuck, & Gee, M. G. (2002 October). *Abrasion resistance of wide grained WC/Co hardmetals*. Lausanne: EUROMET.

Ruff, A. W., & Wiederhorn, S. M. (1979). Erosion by solid particle impact. *Treatise on Materials Science and Technology, 16*, 69.

Sergejev, F., Preis, I., Kubarsepp, J., & Antonov, M. (2008). Correlation between surface fatigue and microstructural defects of cemented carbides. *Wear, 264*(9–10), 770–774.

Shewmon, P. G. (1981). Particle size threshold in the erosion of metals. *Wear, 68*, 253–258.

Shipway, P. H., & Hogg, J. J. (2005). Dependence of microscale abrasion mechanisms of WC–Co hardmetals on abrasive type. *Wear, 259*, 44–51.

Stjernberg, K. G., Fischer, U., & Hugoson, N. I. (1975). Wear mechanisms due to different rock drilling conditions. *Powder Metallurgy, 18*(35), 89–106.

Sun, H. Q., Irwan, R., Huang, H., & Stachowiak, G. W. (2010). Surface characteristics and removal mechanism of cemented tungsten carbides in nano-scratching. *Wear, 268*, 1400–1408.

Swain, V., & Hagan, J. T. (1976). Indentation plasticity and the ensuing fracture of glass. *Journal of Physics D: Applied Physics, 9*, 2201–2214.

Unckel, H. (1951). Zur Abhängigkeit der Mechanischen Eigenshaften von der Structur bei Zwei-Phasen-Legierungen. *Metallurgy, 5*, 146–150.

Wentzel, E. J., & Allen, C. (1995). Erosion–corrosion resistance of tungsten carbide hard metals with different binder compositions. *Wear, 181–183*, 63–69.

Wiederhorn, S. M., & Lawn, B. R. (1977). Strength degradation of glass resulting from impact with spheres. *Journal of the American Ceramic Society, 60*, 451–458.

Wright, I. G., Shetty, D. K., & Clauer, A. H. (1983). Slurry erosion of WC–Co cermets and its relationship to material properties. In: *Proc. 6th Int. Conf. on erosion by liquid and solid impact* (pp. 1–8).

Wright, I. G., Shetty, D. K., & Clauer, A. H. (1985). A comparison of the slurry erosion behaviour of WC–Co cermets and ceramics. In *11th Int. Plansee Seminar 20–24 May 1985, Vienna* (Vol. 2, pp. 643–658).

Yardley, E. D., Johnson, S. N., & Kenny, P. (1981). The wear of tools used for cutting coal and rock. In: *Proc. Int. Conf. on wear of materials, San Francisco, March 30-April 1, 1981*.

1.13 Residual Stresses

Aaron D. Krawitz, University of Missouri, Columbia, Missouri, USA
Eric F. Drake, Rice University, Houston, Texas, USA

1.13.1 Introduction

The subject of residual stresses in cemented carbides is an interesting one. The thermal residual stresses that are established between the binder and hard phases upon cooling from liquid- or solid-phase sintering temperatures are large and complex. They arise due to the difference in thermal expansion between the metal binder and the refractory carbide. Such stresses are classified as thermal residual *microstresses* or Type II residual stresses. Type I residual stresses are *macrostresses* that equilibrate over the length scale of a part. They arise from thermal and/or deformation treatments that subject the part to differences in thermal or mechanical treatment, such as welding or shot-peening. Type III stresses are very short range and result from plastic deformation, usually the strain fields associated with dislocations and are generally not treated as residual stresses.

Though Type II stresses in cemented carbide composites are created during cooling after liquid-phase or solid-state sintering and are ubiquitous in these materials, their presence has not been characterized and their role in material performance has not been understood. Interest in these stresses largely derives from their huge levels. The values are high in the metal binder phase due to the small volume fraction present and the constraint provided by the surrounding carbide particles. An estimate may be obtained from the misfit strain in a spherical WC particle in an infinite matrix whose properties are composed of the average composite values of thermal expansion and elastic constants. Using the values in **Table 1**, results are shown in **Table 2** for WC–Co composites using Gurland's approach (Liu & Gurland, 1965). The thermal stress in a sphere of WC surrounded by a sphere of material representing the average properties of the composite for a specified composition is given by

$$\sigma_{\mathrm{WC}} = \frac{2E_{\mathrm{WC}}E_{\mathrm{comp}}\left(\alpha_{\mathrm{comp}} - \alpha_{\mathrm{WC}}\right)\Delta T}{\left(1+\nu_{\mathrm{comp}}\right)E_{\mathrm{WC}} + 2(1-2\nu_{\mathrm{WC}})E_{\mathrm{comp}}} \tag{1}$$

Table 1 Some room-temperature properties of WC, Co and Ni

Properties	*WC*	*Co*	*Ni*
E (GPa)	672	200	207
K (GPa)	397	185	192
G (GPa)	292	76	79
ν	0.25	0.32	0.31
α (°C^{-1}) × 10^6	6.2	13.8	13.3
ρ (Mg m^{-3})	15.7	8.8	8.9

where σ is the stress, E is the Young's modulus, α is the linear coefficient of thermal expansion, ν is the Poisson's ratio, and the comp values for the composite are given by

$$E_{\text{comp}} = \left(\frac{f_{\text{WC}}}{E_{\text{WC}}} + \frac{f_{\text{Co}}}{E_{\text{Co}}}\right)^{-1}$$

$$\alpha_{\text{comp}} = f_{\text{WC}}\alpha_{\text{WC}} + f_{\text{Co}}\alpha_{\text{Co}} \tag{2}$$

$$\nu_{\text{comp}} = E_{\text{comp}}\left(\frac{f_{\text{WC}}\nu_{\text{WC}}}{E_{\text{WC}}} + \frac{f_{\text{Co}}\nu_{\text{Co}}}{E_{\text{Co}}}\right)$$

where f is the volume fraction. Stresses for Co may be obtained by exchanging the WC subscripts for Co subscripts in Eqn (1). The values shown in **Table 2** have been shown to be reasonable compared to those measured in typical materials. Thus, for a WC–10 wt% Co sample, values of +2061 MPa for Co and −407 MPa for WC were obtained using neutrons (Livescu et al., 2005). The Co values cannot be directly measured because Co gains W and C in solid solution during liquid-phase sintering so that the reference (zero stress) cell parameter is not known. Rather, the Co stress values are obtained from the force–balance relation that applies for microstresses, namely that the force exerted by each phase must balance for equilibrium:

$$f_{\text{Co}}\bar{\sigma}_{\text{Co}} + f_{\text{WC}}\bar{\sigma}_{\text{WC}} = 0 \tag{3}$$

where f_{i} and $\bar{\sigma}_{\text{i}}$ are the volume fraction and average stress, respectively, of the ith phase (Hutchings, Withers, Holden, & Lorentzen, 2005; Noyan & Cohen, 1987). Though Gurland's formulation is for an elastic system, the values in **Table 2** are lower than those measured, though actually quite close.

The actual values depend on more than just the relative amounts of the two phases and an effective set-up temperature. Factors such as cooling rate, carbide size, carbide shape, in situ binder yield strength, and the point-to-point distribution of local stress in both the particles and binder are not addressed by such analytical relations. As will be seen, carbide particle size can have a large effect on the thermal stress magnitude and distribution. The stress magnitude increases as the particle size decreases due to the greater constraint of the binder phase through reduced binder mean free path. Also, the distribution of stress within the carbide particles and matrix is substantial and important. It is due to the angular shape of the particles, the crystallography of the hexagonal WC, and the variable binder distances of the complex microstructure. The range of stress around the mean values in the binder and carbide is, we now know, significant. This has been investigated in a preliminary

Table 2 Thermal residual stresses using Gurland's formulation (Liu & Gurland, 1965)

wt% Co	*vol% Co*	*σ_{Co} (MPa)*	*σ_{WC} (MPa)*
5	8.6	+2222	−209
10	16.5	+1840	−364
20	30.8	+1305	−581

way using finite-element analysis and "real," two-dimensional microstructure meshes, and documented through diffraction peak shape effects.

Finally, the interaction of the residual stresses with applied load has been explored. The response to uniaxial tension and compression has been studied in detail, as well as effects due to cyclic loading. The results suggest that this interaction provides an important contribution to the unusual toughness of cemented carbide composites.

The method of choice for these studies is neutron diffraction. *Diffraction* provides independent views of the binder and carbide phases, and their response to in situ loading. *Neutrons* are not subject to the extremely high absorption of X-rays in the presence of the heavy metal tungsten because they are uncharged particles, so that meaningful averages over many particles and freedom from surface effects may be obtained.

1.13.2 Method of Measurement

1.13.2.1 The Diffraction Method

The utility of diffraction to measure *elastic* strain can be seen using Bragg's law:

$$\lambda = 2d_{\mathrm{hkl}} \sin \theta_{\mathrm{hkl}} \tag{4}$$

where λ is the *wavelength* of the incident radiation, d_{hkl} is the *interplanar* or *d-spacing* of the hkl planes, and $2\theta_{\mathrm{hkl}}$ is the *diffraction angle* for the hkl planes (Krawitz, 2001). The atomic plane spacings are used as "strain gauges" to measure changes due to elastic load. The idea is that (1) stress creates strain; (2) strain alters *d*-spacings; and (3) changes in *d*-spacings cause changes in diffraction peak positions. Cemented carbides are polycrystalline so that measurements can be made in arbitrary sample orientations, and individual diffraction peaks can be used to yield strain information in specific crystallographic orientations. Strain is given by

$$\varepsilon = \frac{d - d_{\mathrm{o}}}{d_{\mathrm{o}}} \tag{5}$$

where d is the interplanar spacing and d_{o} is the stress-free interplanar spacing. Strains as low as 1×10^{-4} can be reproducibly measured.

Obtaining stress-free interplanar spacings can be problematic. In cemented carbides with WC as the carbide, the WC is a reliable reference phase because it remains stoichiometric and does not take solute in solution. However, the metal binder does take W and C into solution during sintering, so that the starting binder powder cannot be used as a stress-free reference. In this case, as stated, Eqn (3) is used to obtain the mean binder stress. For applied stress (in situ) measurements, *changes* in binder stress can be readily measured relative to the starting—unstressed—value regardless of any uptake of W or C.

In addition to the determination of existing residual stresses, in situ response of a material or component to mechanical and/or temperature loading can be observed. In situ capability can also be used for validation of finite-element modeling (FEM), analytical calculations, or vetting of other measurement methods (Krawitz, 2001). Recently, a multiaxial loading capability has been introduced, as well as a more sophisticated capability for making temporal measurements as a function of temperature or load (Liaw, Choo, Buchanan, Hubbard, & Wang, 2006). In principle, as mentioned above, in situ measurements are simpler with respect to stress-free reference values because the strains are reckoned relative to the initial values of interplanar spacing, regardless of the residual stress state:

$$\varepsilon = \frac{d - d_{\mathrm{i}}}{d_{\mathrm{i}}} \tag{6}$$

where d_{i} is the initial *d*-spacing before load/temperature is applied, which may include microstresses and/or macrostresses. However, the situation becomes complicated if the preexisting stresses change during mechanical or thermal treatment (Paggett et al., 2007). High-temperature measurements may be particularly problematic as compositional changes can occur, in which case the initial values of the *d*-spacings are no longer meaningful. Thus, creep or other time-dependent changes with temperature (e.g. phase change, precipitation, and composition) are problematic with respect to the direct measurement of change in the binder phase (Mari, Clausen, Bourke, & Buss, 2009).

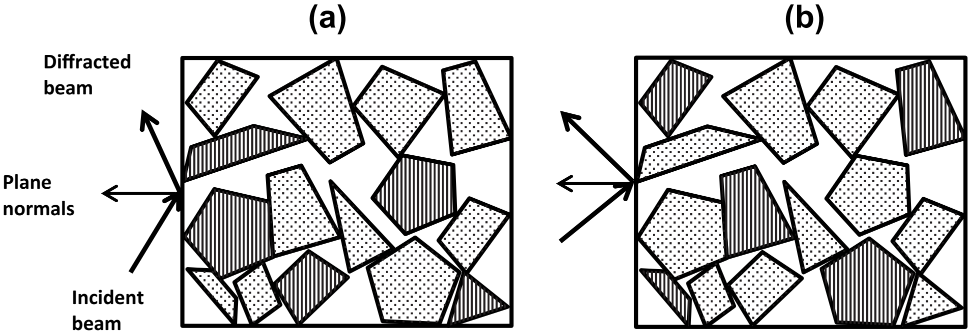

Figure 1 Schematic showing that different particles are selected to diffract at (a) low and (b) high diffraction angles.

The diffraction process involves a great deal of averaging, especially for powder diffraction. Figure 1 shows the schematic of a small portion of microstructure. Sketches 1(a) and 1(b) show that different grains are oriented to diffract for each hkl peak. This depicts a fixed wavelength, angular scan mode of data collection. There is also a fixed angle, variable wavelength (energy) mode in which case the grains satisfying the diffraction conditions vary with the wavelength and Bragg's law becomes

$$\lambda_{\rm hkl} = 2d_{\rm hkl}\sin\theta \tag{7}$$

Due to the angularity of the WC particles, there is a considerable range of stress values, as discussed below. However, this range of values is averaged over the volume of each diffracting grain for the Bragg angle (or incident beam energy) being measured. Thus, grains in many different local environments contribute to a given diffraction peak, and another set contributes to the next diffraction peak, creating another layer of averaging. Finally, the information in each peak is averaged to create an average cell parameter for the structure. This is usually done by fitting the overall pattern using the Rietveld profile refinement method (Rietveld, 1969). Since there is no preferred orientation of the carbide grains, the same averaged diffraction pattern will be seen no matter how the sample is oriented in the beam because the statistical sample is so large (some 10^9 WC grains would be irradiated in a $3 \times 3 \times 3$ mm^3 volume). Thus, the average values of the cell parameters (peak position) and the range of those values (peak shape) do not change as a function of sample orientation in the beam even though there are significant variations from point to point within a grain, and from grain to grain. The stress state appears, after all the averaging is done, to be hydrostatic—the same in all directions. The distinction between a mechanically hydrostatic and a diffraction hydrostatic stress state is in the shape of the diffraction peak. A particle under a true hydrostatic stress state, for example, a sphere surrounded by a matrix that has been thermally shrunk around it, would exhibit an instrumentally sharp peak, i.e. the peak breadth would represent the minimum breadth achievable due to beam size, beam divergence, monochromator mosaic, sample size, etc., because the stress in the sphere would be the same everywhere. In the diffraction hydrostatic case, the averaging process would result in a broadened peak due to the *range* of interplanar spacings diffracting. The situation is schematically illustrated in Figure 2. It shows (1) the sharpest peak obtainable for a given instrumental configuration, from an unstressed assemblage of annealed particles; (2) the peak obtained from a spherical particle under a uniform hydrostatic compression that is still instrumentally sharp but has shifted to higher angle due to a uniform hydrostatic compression; and, (3) the same peak but diffracting from angular particles that are under the same average particle compression as in (2). Since there are a range of stresses in the particles due to their angularity, the result is a peak whose mean position is the same but whose shape is broader.

1.13.2.2 Use of Neutrons

Neutrons enable study of the volumetric residual thermal microstresses in cemented carbides due to their much greater penetration power in most engineering materials because they are uncharged particles. Two types of neutron sources are now utilized. *Reactor sources* produce beams via nuclear fission from which fixed wavelengths are extracted with monochromators. The use of position-sensitive linear or area detectors enables whole

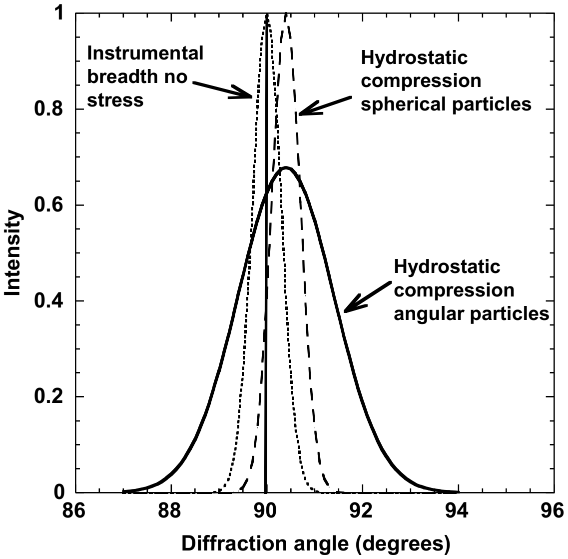

Figure 2 Schematic showing the relative peak position and peak shape for (1) an instrumentally sharp peak from annealed powder particles of a carbide phase, for which the peak position is taken as 90°; (2) spherical carbide particles under uniform hydrostatic compression; and (3) angular carbide particles under the same mean hydrostatic compression.

peaks to be collected without scanning, increasing throughput. Reactor spectrometers are similar in concept to X-ray instruments. *Pulsed neutron sources*, also called *spallation sources*, produce neutrons by the impact of accelerated particles on a heavy-metal target, rather than by fission. The resultant neutron beam has a range of velocity (energy) and, hence, wavelength. In this case, the diffraction angle is fixed and there is a range of wavelengths in the incident beam, typically from 0.05 to 0.50 nm. The energies are resolved using time-of-flight methods. This enables whole diffraction patterns to be recorded simultaneously, without the requirement of sample motion. The neutron energy, velocity and wavelength are related by

$$E = \frac{1}{2}mv^2 = \frac{1}{2m}\left(\frac{h}{\lambda}\right)^2 \tag{8}$$

where E is the kinetic energy of the neutron, v is the neutron velocity, m is the neutron mass, h is the Planck's constant and λ is the wavelength (Bacon, 1975). The relation between time-of-flight t, distance traveled L, and wavelength λ is given by

$$t = \frac{mL\lambda}{h} \tag{9}$$

More and more neutron measurements are being done at pulsed sources. Advantages include (1) the ability to record whole patterns from all phases simultaneously with no sample or detector movement; (2) the ability to measure in two orthogonal directions simultaneously, as shown in Figure 3; (3) superior data for low-symmetry structures; and (4) greater ease of use for mechanical/temperature stages. A listing of both types of neutron facilities is given by Krawitz (2011).

A few words about the flux (number of neutrons per unit area per unit time at a specified distance) of sources are in order, as the low flux in neutron beams relative even to laboratory X-rays is often cited as a limitation of the method. While it is true that incident beam flux is low relative to laboratory and, especially, synchrotron X-rays, this argument does not account for the "effective flux" represented by the measurement of whole diffraction patterns of all crystalline phases, and in two orthogonal directions simultaneously. These features represent a significant gain in effective flux over the traditional peak-scanning mode of recording used for many years on neutron powder instruments. Also, detector efficiency has improved. The performance of hundreds of measurements on engineering materials is testament to the practical utility of the method. Thus, the answer to the question "Can useful measurements be made in reasonable times?" is yes, within limits that allow many aspects to be studied—aspects that cannot be addressed as effectively in other ways.

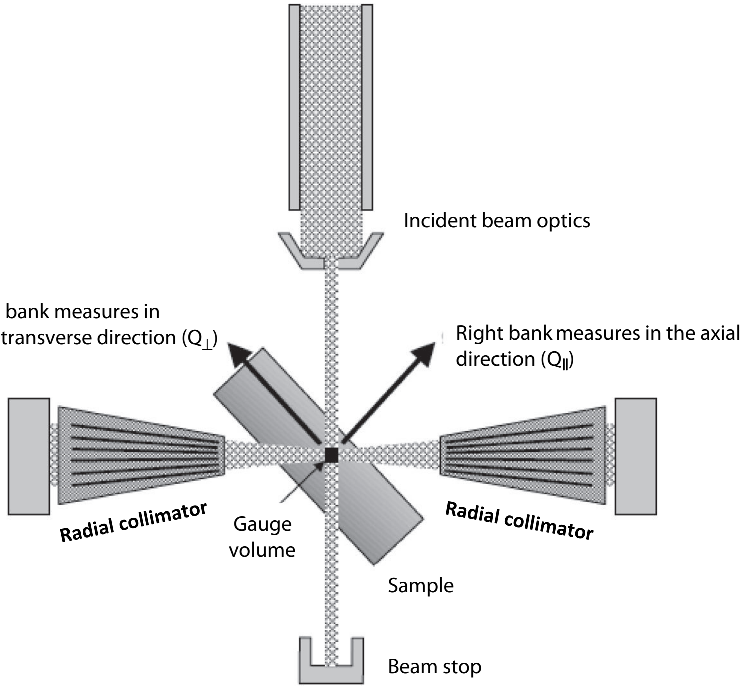

Figure 3 The geometry often used for strain measurements at pulsed neutron sources, from Tanaka et al., 2002. The sample is at a 45° angle to the incident beam. There are two detector banks: the right bank measures in the axial direction ($Q_\parallel$) and the left bank measures in the transverse direction ($Q_\perp$).

Neutrons measure in three dimensions, and therefore fundamentally differ from traditional X-ray stress measurements. A major implication of the three-dimensional character of neutron strain measurements is that stress-free interplanar spacings are required to convert measured *d*-spacings to strains. Useful discussions of stress-free reference values in neutron strain measurements can be found in the literature (Tanaka, Akinawa, & Hayashi, 2002; Withers, Preuss, Steuwer, & Pang, 2007). For WC-based cemented carbides, the procedure is to use loose WC powder as the stress-free reference material and to directly determine strain in WC. The powder should be contained in a can having a shape as close as possible to that of the samples. WC is an ideal standard material because it is stoichiometric and does not take binder elements into solution during sintering. To obtain thermal residual stress values, strain is converted to stress using

$$p_{\mathrm{WC}} = K_{\mathrm{WC}}\Delta_{\mathrm{WC}} = 3K_{\mathrm{WC}}\varepsilon_{\mathrm{WC}} \tag{10}$$

where p_{WC} is the average *diffraction hydrostatic* thermal stress of WC, K_{WC} is the bulk modulus, and $\varepsilon_{\mathrm{WC}}$ is the strain measured in one direction by use of Eqn (10). The stress in the binder phase is obtained using Eqn (3). If the strain is not the same in all directions, then a stress state must be assigned that matches the observed data. Examples can be found in Krawitz (2001).

A general diffraction text that discusses diffraction stress measurements (Krawitz, 2001) and more specialized neutron (Hutchings et al., 2005; Kisl & Howard, 2008), and neutron and synchrotron stress measurements (Reimers, Pyzalla, Schreyer, & Clemens, 2008) is also available. A standard source book on residual stresses and their measurement by diffraction is by Noyan and Cohen (1987).

1.13.2.3 Limitations of X-rays

The problem with using X-rays to study thermal residual stresses in cemented carbide composites is the high absorption of W, as indicated in Table 3. It leads to shallow beam penetration and the inability to properly measure the bulk, volumetric stress state. The absorption of a beam of intensity I_{o} is given by

$$I = I_{\mathrm{o}}e^{-\mu_{\mathrm{l}}t} \tag{11}$$

Table 3 Comparison of neutron and X-ray scattering and absorption. The scattering powers of neutrons (*b*) and X-rays (*f*) are given in scattering length units for direct comparison. μ_l is the linear absorption coefficient and $t_{50\%}$ is the thickness to absorb 50% of the incident beam intensity at normal incidence

	Neutrons[a]			*X-rays*[b]		
Z	b *(10^{-12} cm)*	μ_l *(cm^{-1})*	$t_{50\%}$ *(cm)*	f *(10^{-12} cm)*	μ_l *(cm^{-1})*	$t_{50\%}$ *(μm)*
C	0.6646	0.98	0.71	1.00	15.8	439
Al	0.3449	0.10	6.93	2.58	133.9	51.8
Co	0.250	3.89	0.18	5.94	2857	2.43
Ni	1.03	2.10	0.33	6.24	434	16.0
W	0.477	1.45	0.48	17.62	3251	2.13

[a] *Thermal neutrons with a wavelength of 0.1798 nm.*

[b] *Copper Kα X-rays with a wavelength of 0.154178 nm (average of Kα_1 and Kα_2).*

where I is the intensity of the absorbed beam, μ_l is the linear absorption coefficient, and t is the thickness of the plate of material (or the path length). The scattering powers for the elements are shown in **Table 3** as b for neutrons and f for X-rays. They have been represented as scattering cross-sections so they can be directly compared. It is seen that the absorption values for X-rays are, in general, much greater than for neutrons, typically three orders of magnitude greater. This is especially true for heavy elements. This is reflected in the $t_{50\%}$ values in **Table 3**. These are the plate thicknesses required to reduce the intensity of a normally incident beam by 50%. In general, the values are in millimeters for neutrons and in micrometers for X-rays. The contrast is greatest for high-Z elements. Thus, it takes 4.8 mm of W to absorb half the intensity of a thermal neutron beam and 2.1 μm for Cu X-rays. This illustrates the difficulty of using X-rays to study heavy elements, a problem even with synchrotron radiation. The greater penetration of neutrons offers several advantages: (1) surface effects such as deformation due to grinding or polishing, or oxidation are avoided; (2) X-rays are largely confined to the relaxation region near the surface for microstresses whereas this is not an issue for neutrons, i.e. neutrons enable proper measurement of such stresses; (3) good volume sampling is achieved; and (4) the use of mechanical and/or thermal stages is greatly facilitated because neutrons can pass through enclosure materials and strain gauges.

To emphasize potential problems with X-ray stress measurements in heavy-metal systems, the standard X-ray approach to the measurement of residual stresses is briefly considered. It assumes that the residual stress state is two-dimensional and lies in the plane of the surface of the sample. This is because of the shallow penetration of X-rays and the fact that stress components normal to the surface go to zero as the surface is approached. In addition, near-surface stress states are far greater in the plane parallel to the surface than normal to it. The assumption greatly simplifies the measurement and analysis. The surface is systematically tilted by the angle ψ in a surface direction given by φ (**Figure 4(a)**). A view looking normal to the plane containing directions X_3 and L_3 is shown in **Figure 4(b)**. The interplanar spacing $d_{\varphi\psi}$ in the direction φ at tilt ψ, which lies in the surface, is given by

$$d_{\phi\psi} = d_o\frac{1+\nu}{E}\sigma_\phi \sin^2\psi - d_o\frac{\nu}{E}(\sigma_{11}+\sigma_{22}) + d_o \qquad (12)$$

where ν is the Poisson's ratio, E is the Young's modulus, and σ_{11} and σ_{22} are the principal plane stresses (Krawitz, 2001). A plot of $d_{\phi\psi}$ versus $\sin^2\psi$ is linear and the slope gives the desired stress σ_φ. The slope contains the term d_o, which is the stress-free interplanar spacing. The approximation $d_o \approx d_{\psi=0°}$ is made, which introduces a very small error (equal to the elastic strain, i.e. a few tenths of a percent or less). It also alleviates the need for knowing d_o.

For WC–10 wt% Co, depths from which 50 and 90% of the diffracted beam arises are given in **Table 4** for laboratory X-rays and thermal neutrons (Krawitz, 1985). Let us view the situation through the classical d versus $\sin^2\psi$ plot. Suppose the WC is subject to an average thermal microstress of −400 MPa at room temperature. If the WC 201 peak is measured as a function of ψ-tilt and plotted as d versus $\sin^2\psi$, the possibilities are shown in **Figure 4(c)**. The d-spacing for the (201) planes is 0.11520 nm. If the WC phase is free of stress, the d versus $\sin^2\psi$ plot would be the horizontal line marked "stress free". If it is under an average stress of −400 MPa, the result would be the horizontal line marked "hydrostatic". If the beam penetration is so low that only the surface is

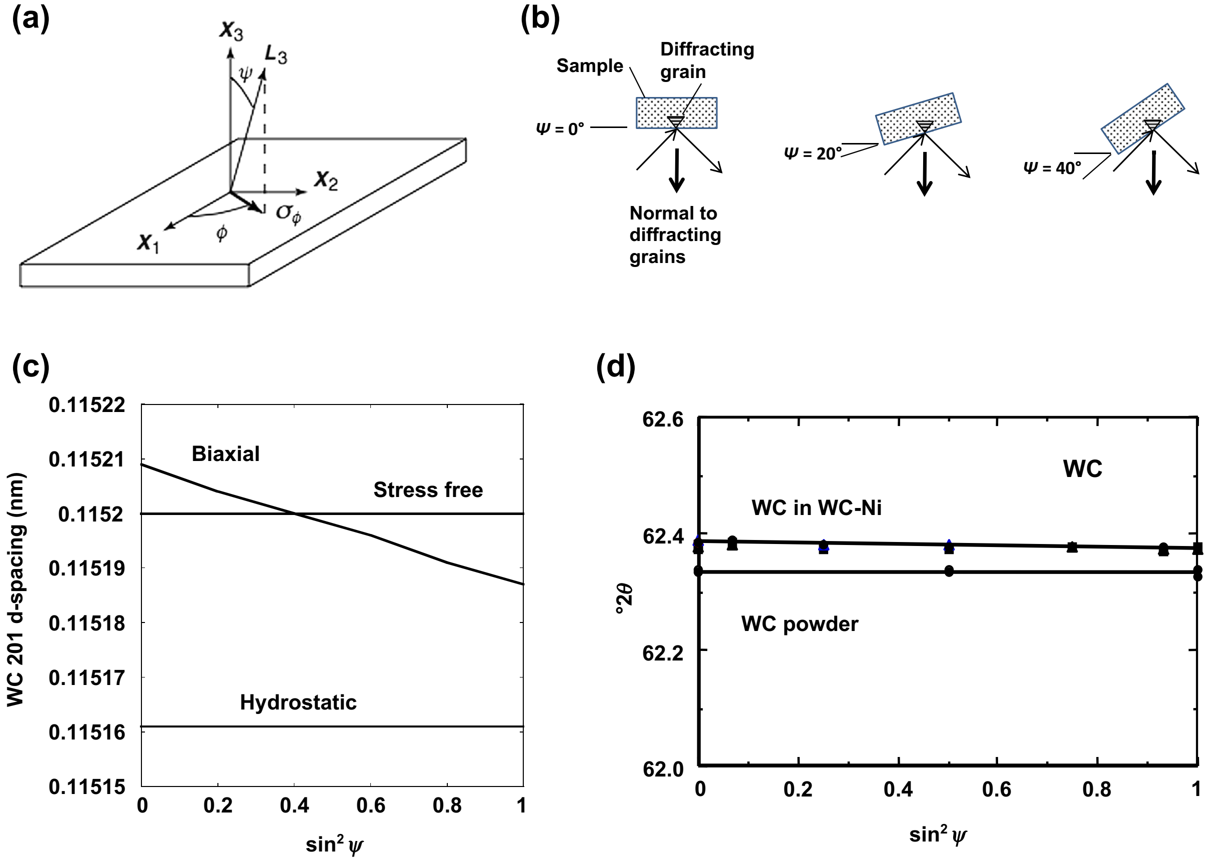

Figure 4 (a) Geometry of the $\sin^2\psi$ method of diffraction stress measurement. The angle φ determines the direction in the surface plane that the stress is measured. Values of interplanar spacing are measured as a function of sample tilts given by ψ. (b) View of ψ tilts normal to the X_3–L_3 plane. Three ψ tilts are shown. The stress component that is horizontal and in the plane of the surface is being measured. (c) Schematic showing the variation in diffraction peak position with sample tilt ψ for a material that is in three different stress states: (i) stress free; (ii) hydrostatic; and (iii) a biaxial stress state in the plane of the sample surface. (d) Actual results for the WC phase in a WC–Ni cemented carbide with angular particles. The WC is under compression that is diffraction hydrostatic.

measured, a two-dimensional stress state results for which the limiting case is the line marked "biaxial". If the penetration depth contains the beam within the relaxation region of the volumetric thermal residual stress, a sloped line would result somewhere between the "biaxial" and "hydrostatic" lines. If the partially relaxed line is processed using Eqn (12), a compressive stress of a significantly lower value than the true −400 MPa would result. Another way to say this is if a sloped line is obtained, the true thermal microstress is not being measured, provided no other sources of residual stress are present. An example of a d versus $\sin^2\psi$ measurement with neutrons is shown in Figure 4(d) (Krawitz, Reichel, & Hitterman, 1989). It was made at a reactor neutron source and is plotted as ψ-tilt versus diffraction angle. It shows the *diffraction hydrostatic* nature of the thermal residual

Table 4 Depths of penetration in WC–10 wt% Co from which 50 and 90% of the diffracted intensity arises for four X-ray wavelengths and thermal neutrons

Radiation	μ_l *(cm^{-1})*	*50%*	*90%*
Mo	1239	2.7	9.1
Cu	2594	1.3	4.3
Co	3691	0.9	3.0
Cr	5981	0.6	1.9
1.8 Å neutrons	1.28	2.6×10^3[a]	8.8×10^3[a]

[a] *0.26 cm and 0.88 cm, respectively.*

stress state in cemented carbide composites: the d versus $\sin^2 \psi$ line has no slope. The compressive stress in WC reduces the d-spacing, thereby increasing the Bragg angle relative to the unstressed state. An illustrative work on steel matrix–NbC particulate composites used both X-rays and neutrons (Pyzalla, Genzel, & Reimers, 1996). It grapples with the complexities of using X-rays to attempt measurements of bulk thermal microstresses.

From about 1960 to 1980, a number of X-ray studies were conducted and have been reviewed by Krawitz (1985). Some dealt with surface grinding/polishing issues and not just thermal stresses. Near-surface stresses due to grinding, thermal spray coatings, or even diamond coatings can, in principle, be measured with X-rays. However, it is possible that, for the case of surface ground/polished cemented carbides, relaxation of the thermal stress state affects the results. If it is known that the surface treatment relieves the thermal stress, leaving a macrostress due to plastic deformation of the binder, then useful data can be collected. Coatings may be very appropriate for laboratory and/or synchrotron X-ray study, and indeed many such studies are being made because of the importance of coated products. It is not the purpose of this chapter to evaluate such studies.

1.13.3 Bulk Thermal Residual Microstresses

A number of neutron diffraction measurements have been made using model WC–Ni-cemented carbides. This is because Ni is a very good neutron scatterer (**Table 3**) and has a stable *fcc* structure over a wide range of temperature. Co, on the other hand, scatters neutrons poorly and tends to stay in the high-temperature *fcc* structure upon cooling rather than transforming to the room-temperature *hcp* phase due to the sluggish *fcc*-to-*hcp* transformation. The reasoning was that WC–Ni would more clearly reveal the fundamental responses of the composites with respect to binder content, carbide particle size, temperature, stress distribution, and interaction with external loads. Studies have also been performed on WC–Co materials and are included here.

1.13.3.1 Magnitude

1.13.3.1.1 Binder Volume Fraction

The role of binder fraction is shown in **Figure 5**, for both WC–Co (Coats & Krawitz, 2003; O'Quigley, Luyckx, & James, 1997) and WC–Ni (Paggett, 2005; Paggett et al., 2007). The square symbols are from samples of a different source than the triangle symbols. However, only WC particle sizes of about 1 μm were used. The "*x*" symbols are calculated values using Eqn (1) for WC and Eqn (3) for Ni and Co. A temperature drop of 800 K from the sintering temperature was used. This ΔT was chosen to best fit the data and is rather high even though Eqn (1) is an elastic formulation. The constraint imposed by the fine-scale three-dimensional microstructure is not part of analytical calculations and is complicated for finite-element formulations, where a realistic three-dimensional microstructure is required for an optimal result. As a result, an artificially high set-up temperature is needed to account for the constraint of surrounding WC particles. However, the calculated values show the proper functional form for variation of binder content over a wide range (about 5–50%). Processing and binder (Co and Ni) do not make much difference.

1.13.3.1.2 Temperature

Samples of WC–9.2 vol% Ni and WC–29 vol% Ni were measured in the temperature range 100–900 K (Seol, Krawitz, Richardson, & Weisbrook, 2005). The resultant thermal stresses are shown in **Figure 6**. The set-up temperature is about 900 K. The stresses are elastic so the curves are reversible with thermal cycling, though low-level damage likely accrues. This damage would eventually appear as a change in peak shape and position, particularly for the binder, and would indicate accumulating plastic damage in the binder and a concomitant relaxation in the elastic thermal stress state, which would shift the peaks of both phases. Presumably this would lead to binder embrittlement after which crack initiation and growth would proceed. These data also show the effect of composition discussed above. The residual stresses for these materials are very high because the WC particle size is 0.5 μm (Section 1.13.3.1.3).

Mari et al. measured stress as a function of temperature in WC–11 wt% (17.8 vol%) Co, and followed two heating–cooling cycles from room temperature to 1273 K (Mari et al., 2009; Mari, Krawitz, Richardson, & Benoit, 1996). Above about 1000 K, the cell parameter of Co increases due to solubility of W and C, not to residual stress. The observed hysteresis between heating and cooling is attributed to a "difference in heating and cooling kinetics of solution-precipitation". These important studies indicate the complexity of the systems at temperatures where diffusional changes can occur.

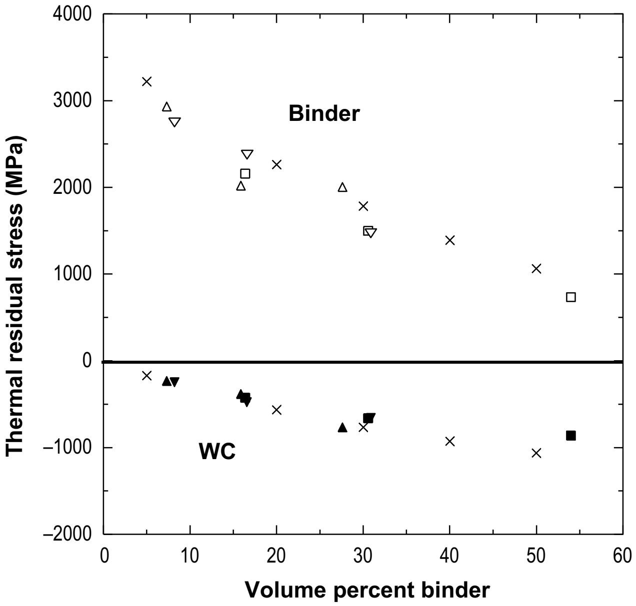

Figure 5 Compilation of many WC-based cemented carbides, all with approximately 1 μm WC particles. The experimental values are for WC–Ni (upward triangles) (Paggett et al., 2007) and WC–Co (squares (Coats & Krawitz, 2003; O'Quigley et al., 1997) and downward triangles (Paggett, 2005)). The "*x*" symbols are calculated values using Eqn (1). Experimental binder stress values are calculated using Eqn (3).

1.13.3.1.3 Particle Size

The variation of the thermal residual stress with binder content and carbide particle size for a series of WC–Co composites is shown in **Figure 7** (Coats & Krawitz, 2003; O'Quigley, Luyckx, & James, 1997). Composites with 10, 20 and 40 wt% Co (16.4, 30.6 and 54.0 vol% Co, respectively) and four particle sizes were measured for thermal stress. The particle sizes are ultrafine (0.6 μm), fine (1.0 μm), medium (3 μm) and coarse (5 μm). Two effects are represented. First, as the amount of a phase increases, its average residual stress decreases to satisfy the force balance. This composition effect has been discussed above. Second, for a given composition, as the WC particle size decreases, the stress magnitude in both phases increases. For example, as the WC particle size is

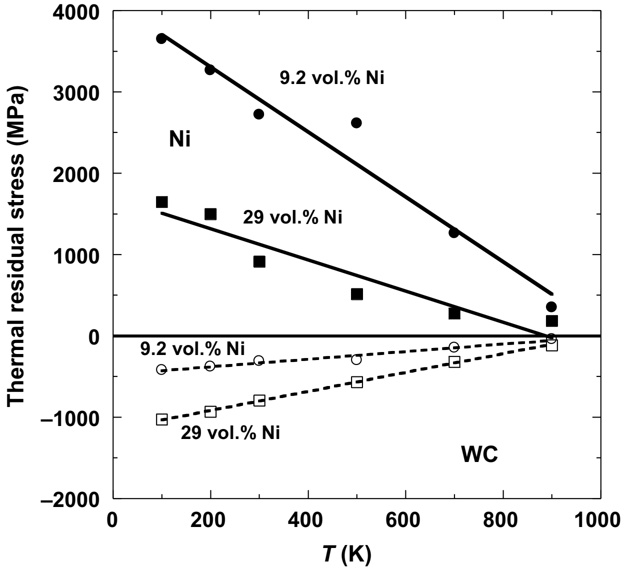

Figure 6 Thermal residual stress from 100 to 900 K for samples of WC–9.2 vol% Ni and WC–29 vol% Ni (Seol et al., 2005). The stresses are elastic and reversible with heating and cooling.

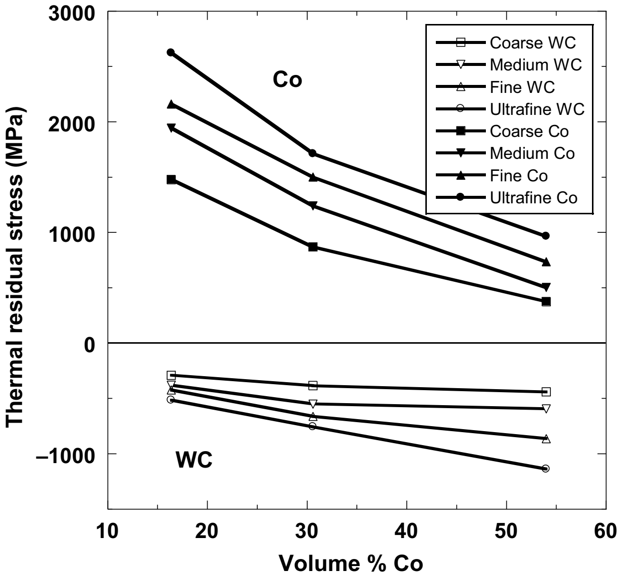

Figure 7 The strong effect of carbide particle size on the thermal residual stress for a matrix of WC–Co samples (Coats & Krawitz, 2003; O'Quigley et al., 1997).

reduced from 5 to 0.6 μm for WC–10 wt% Co, the thermal stress in the Co increases from +1500 to +2600 MPa, and, for WC–40 wt% Co, the change is from +400 to +1000 MPa. The mean free paths in the Co binder range from 6.3 μm for coarse WC (5 μm) and 54.0 vol% Co to 0.2 μm for ultrafine WC (0.6 μm) and 16.4 vol% WC (Coats & Krawitz, 2003; O'Quigley et al., 1997). This very strong particle size effect has not, to our knowledge, been analytically modeled.

1.13.3.2 Distribution

The residual thermal stress values are averages over the volume of the sample, as discussed in Section 1.13.2.1. **Figure 8** shows how the breadths of diffraction peaks from each phase, the WC 201 peak and the Ni 311 peak, vary with *T* for the samples shown in **Figure 6** (Seol et al., 2005). These values are the Gaussian component of the peak breadths and are a measure of the range of elastic stresses in the sample. They are directly compared with breadths of the same peaks from annealed, stress-free WC and Ni powders, which do not change with *T* and represent the instrumental breadth plus any (minor) broadening sources in the annealed powder material. The breadth values are in microseconds as the data was taken at a pulsed source; see Eqns (7) and (9). This breadth versus *T* response is elastic, that is, the broadening is due to the distribution of elastic strain that exists in the irradiated volume. As the mean stress increases, the distribution broadens, and this effect is essentially reversible over a small number of cycles. However, as discussed in Section 1.13.3.1.2, many thermal cycles would lead to irreversible changes, though such an experiment has yet to be done. Finally, it is noted that if the Ni content increases, the stress in WC decreases and vice versa.

The elastic strain distribution cannot be directly converted to a stress distribution (Krawitz, Winholtz, & Weisbrook, 1996). However, bounds can be set between pure deviatoric and pure hydrostatic limits. It has been shown that the stress state is close to the deviatoric (lower) bound in similar WC–Ni material (Krawitz et al., 1996). For the cemented carbides shown in **Figures 6** and **8**, the room-temperature thermal stresses in the WC phase are about −300 and −800 MPa for the 9.2 vol% Ni and 29 vol% Ni composites, respectively. The deviatoric standard deviations are about 400 and 800 MPa, respectively. It seems clear that the range of stress in WC ranges from very high compression to significant tension. Conversely, the binder stress ranges from compression to very high tension.

It is apparent from the foregoing that diffraction and the sampling capability of neutrons offer an unprecedented view of the micro- and macrobehavior of cemented carbides. However, the quantification and roles of microscale plasticity behavior in these composites have awaited the application of microstructural FEM. Such work allows independent assessment of both elastic and plastic strain components developing during thermal

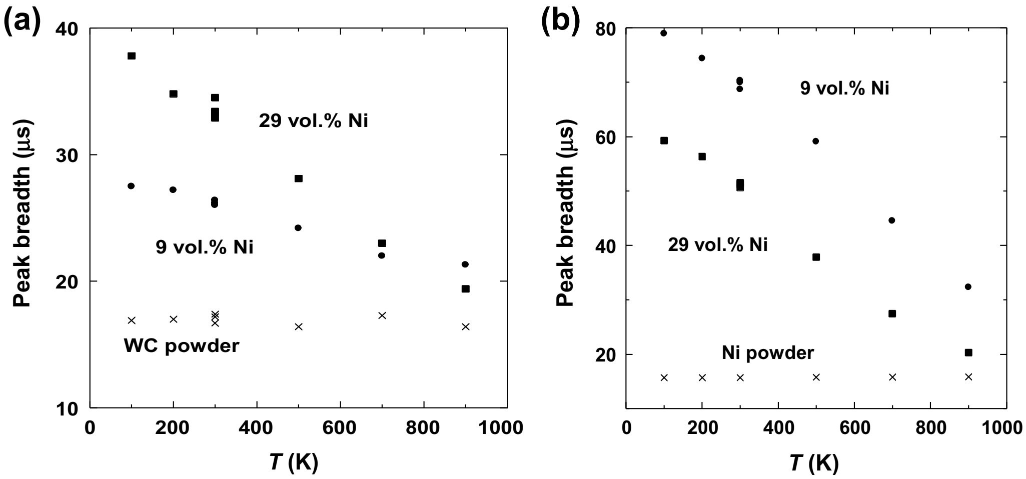

Figure 8 Variation of peak breadth for WC–9.2 vol% Ni and WC–32 vol% Ni sample as a function of *T*. These are the same samples as shown in **Figure 6**. (a) WC 201 peak; (b) Ni 311 peak.

and mechanical loadings. Such modeling would enable both prediction of macroscopic response and interpretation/validation of diffraction results.

Finite-element studies have been conducted to gain insight into diffraction results, using a series of WC–Ni cemented carbides that were both modeled and physically produced and measured (Weisbrook, Gopalaratnam, & Krawitz, 1995; Weisbrook & Krawitz, 1996). The meshes employed were two-dimensional plane stress elastic models based on real microstructures and looked schematically like that shown in **Figure 1**. These model results corroborated both the diffraction mean stresses in WC and Ni and the observed broad distributions, including regions of tension and extreme compression in WC and regions of compression and extreme tension in Ni. They also provided insights into how these distributions develop and resolve on the scale of the microstructures, for example, showing the highest tensile stresses in WC at corners and near WC/Ni interfaces. Compressive areas in Ni were less widespread as the WC content increases, occurring in narrow Ni bands between WC grains. This is because the mean binder stress becomes increasingly tensile for high carbide-fraction material, which is the usual case.

1.13.4 Interaction with External Loads

1.13.4.1 Monotonic Loading

1.13.4.1.1 Compression

Applied stress interacts with the preexisting thermal residual stress in cemented carbide composites. **Figure 9** shows the axial response of the Ni phase in WC–20 wt% Ni as well as the macroscopic stress–strain curve for uniaxial compression to −2000 MPa (Paggett et al., 2007). The Ni curve shows only the elastic strain measured by diffraction while the composite curve shows the sum of the elastic and plastic strain response. Both curves show nonlinearity that begins below 0.2% strain. The rate of strain accumulation increases for *total macroscopic strain* in the composite but decreases for *elastic strain* in the Ni. Upon unloading, the composite sample is shorter by more than 0.3% while the elastic tensile strain in the Ni has actually *increased* by almost 0.1%.

Elastic strain changes in both the axial and transverse directions are shown in **Figure 10** for the Ni phase. These are the responses of the Ni phase during uniaxial compression to −2000 MPa for (1) WC–5 wt% Ni, (2) WC–10 wt% Ni, and (3) WC–20 wt% Ni. The transverse response for WC–5 wt% Ni (**Figure 10(a)**) shows that accumulation of positive Poisson strain slows down and actually begins to reverse at the end of the load cycle. After unloading, there is a net reduction in transverse strain and a net increase in axial strain. The increase in axial strain is due to the Poisson effect that results from the (greater) decrease in transverse strain. This trend increases in the 10% Ni and 20% Ni composites, where plasticity in the Ni is greatly increased. As for the 5% Ni material, the transverse strain magnitude in the 10% Ni and 20% Ni composites initially increases due to the axial compression, then decreases. The decrease is so great that the strain goes below the initial value for both

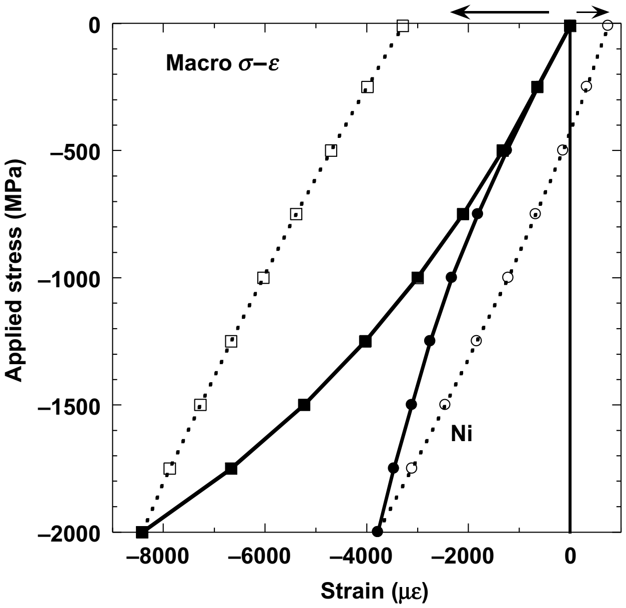

Figure 9 The macroscopic (elastic–plastic) load–unload stress–strain curves and the Ni phase load–unload (elastic-only) stress–strain curves for WC–20 wt% Ni in the axial direction (Paggett et al., 2007).

compositions. It is emphasized that these changes are relative to the starting values of thermal residual strain, and are the same in all directions when averaged over all diffracting grains. The Poisson reaction in the axial direction leads to an increase in the mean Ni strain in that direction even though there is an overall reduction in the thermal residual stress. The mechanics of the thermal stress relaxation is shown schematically in Figure 11. The applied uniaxial compressive strain *opposes* the mean tensile residual stress in the axial direction (Figure 11(a)). However, in the transverse direction, the applied Poisson strain is tensile and *adds* to the thermal residual strain in the Ni. This leads to preferential flow of the Ni in the transverse direction and asymmetric relaxation of the thermal residual stress. The transverse relaxation, in turn, induces a Poisson expansion in the axial direction, as indicated in Figure 11(b). For the WC–20 wt% Ni composite, the result is reduction in the transverse and axial thermal residual stresses by −523 and −227 MPa, respectively. Thus, the relaxed residual stress state becomes cylindrical and, for the WC–20 wt% Ni sample, is +1778 MPa in the axial direction and +1482 MPa in the transverse direction.

To summarize, upon uniaxial compressive loading/unloading, the thermal residual *stress* in the Ni phase *decreases* in both the axial and transverse directions, but does so asymmetrically; the decrease is greater in the transverse direction. The elastic *strain* in the Ni phase, however, *decreases* in the *transverse* direction but *increases* in the *axial* direction, due to the Poisson effect.

Macroscopic load–unload stress–strain curves of WC–10 wt% Ni for −500 and −2000 MPa are shown in Figure 12(a). An enlarged plot of the −500 MPa load–unload sequence is shown in Figure 12(b). This is shown to emphasize that nonlinearity begins very early in the loading cycle. By −500 MPa, a clear hysteresis is present. This is due to the interaction between the applied stress and the thermal residual stress.

It can be shown that composite density is not conserved when the thermal residual stress levels decrease in the WC and Ni phases. The forces remain balanced but the density actually increases upon relaxation of the initial thermal stress. This is because, upon relaxation of the thermal residual stresses in the Ni and WC, the decrease of the Ni phase volume is greater than the increase of the WC-phase volume so that the density of the composite increases.

1.13.4.1.2 Tension

The application of uniaxial tension also creates an asymmetric relaxation of the thermal residual stress, but in the opposite sense of that for compression. This is shown schematically in Figure 13. In this case, the applied axial tension leads to preferential flow of the Ni in the axial direction because the applied strain adds to the positive residual strain in this direction. In the transverse direction, the applied Poisson compressive strain is now negative and opposes the mean Ni thermal residual strain, which is tensile (positive). The result is greater

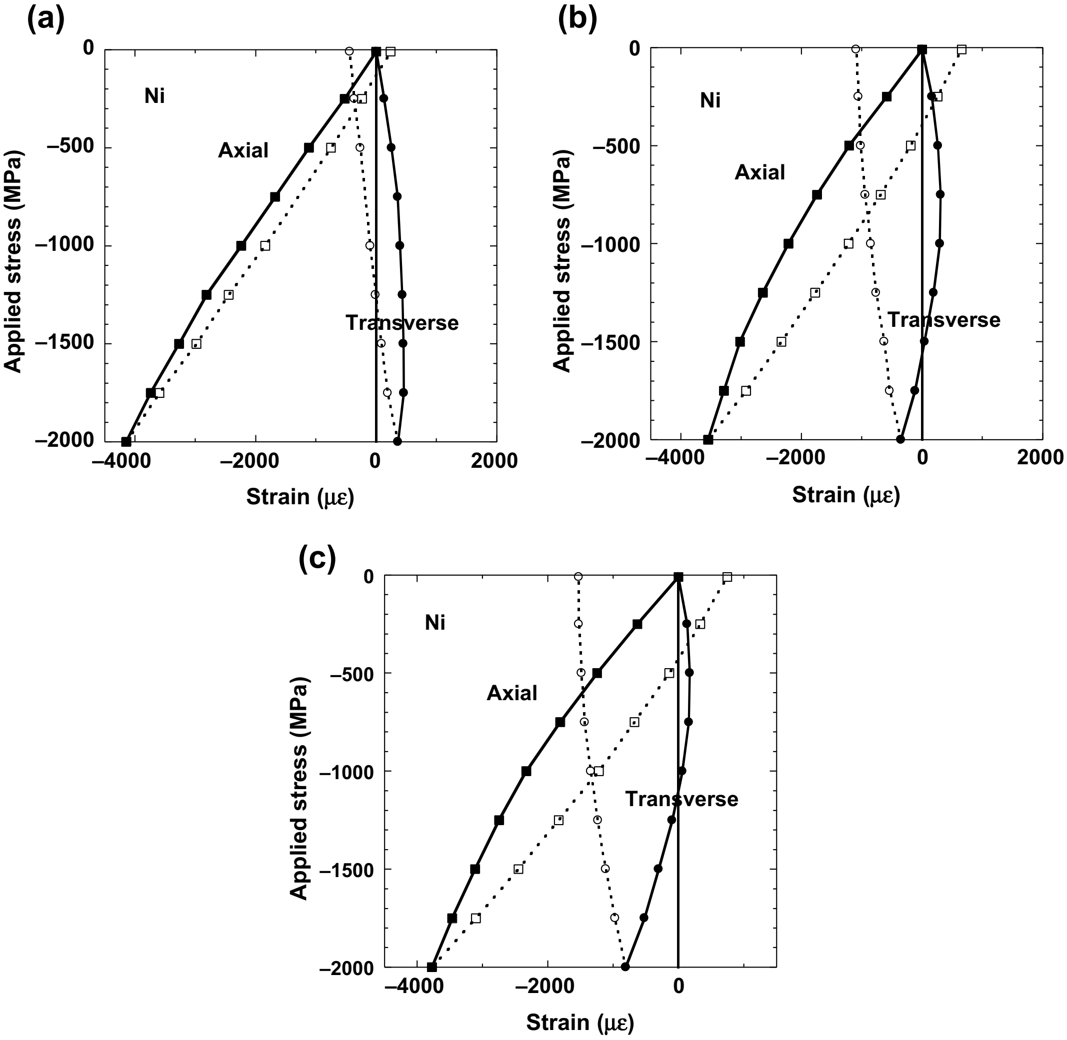

Figure 10 The Ni phase load–unload stress–strain curves in the axial and transverse directions due to uniaxial compression in (a) WC–5 wt% Ni, (b) WC–10 wt% Ni, and (c) WC–20 wt% Ni.

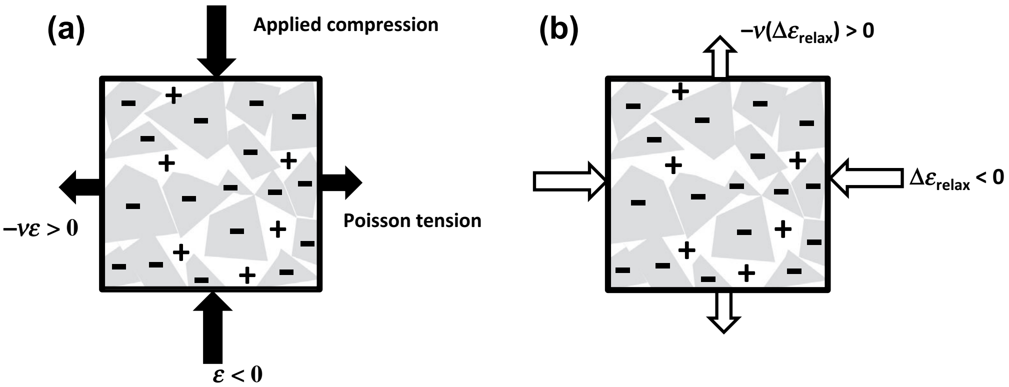

Figure 11 Schematic response of WC–Ni to uniaxial compression. (a) Applied strain to composite in the axial and transverse directions. (b) Anisotropic relaxation response of the thermal residual stress for the Ni phase.

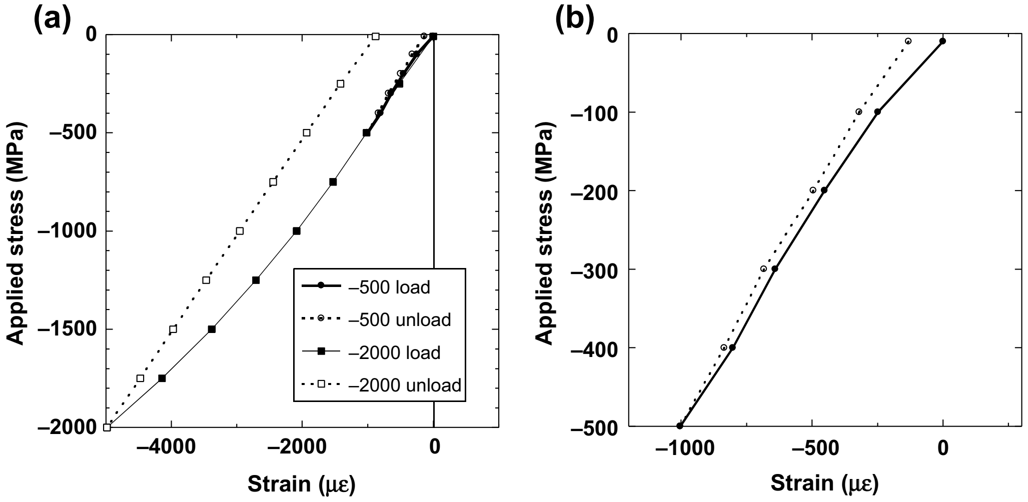

Figure 12 The WC–10 wt% Ni macroscopic load–unload stress–strain curves of (a) −500 and −2000 MPa loadings and (b) enlargement of −500 MPa load–unload. Note that the 0 load level is actually −10 MPa in order to keep tension on the sample. This is true in all plots but is visible here due to the expanded scale.

relaxation of the thermal residual *stress* in the axial direction than in the transverse direction. In this case, the change in elastic strain in the Ni is negative in the axial direction and positive in the transverse direction.

The situation is illustrated for a WC–10 wt% Ni composite that was subjected to a +1500 MPa tensile stress, the highest value that could be obtained without fracture (Figure 14) (Krawitz, Drake, & Clausen, 2010). The response of the Ni phase is shown in Figure 14(a). For comparison, Ni-phase curves are shown for loading to −1000 MPa (Figure 14(b)). The relaxation asymmetry is reversed for tensile versus compressive loading. The macroscopic load–unload stress–strain curves for WC–10 wt% Ni to +1500 MPa are shown in Figure 15(a). The corresponding curve for WC–10 wt% Ni loaded to −1000 MPa is shown in Figure 15(b). (The macroscopic load–unload stress–strain curves to −500 and −2000 MPa are shown in Figure 12.) The reverse nature of the relaxation asymmetry is clearly shown. For the −1000 MPa case, the composite has already been subjected to three load–unload cycles to −500 MPa, which induced some plasticity. Thus, the effect should be somewhat stronger than it appears.

To summarize, upon uniaxial tensile loading/unloading, the thermal residual stress in the Ni phase decreases in both the axial and transverse directions, but does so asymmetrically: the decrease is greater in the axial direction. The elastic strain in the Ni phase, however, decreases in the axial direction but increases in the transverse direction, due to the Poisson effect.

In both the compressive and tensile cases, the applied plastic strain is opposed by the change in Ni strain due to relaxation of some of the thermal residual stress. However, for applied uniaxial compression, it is the tensile

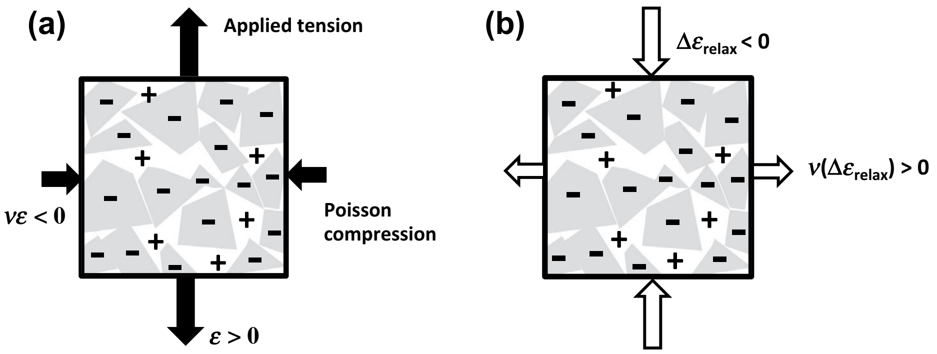

Figure 13 Schematic response of WC–Ni to uniaxial tension. (a) Applied strain to the composite in the axial and transverse directions. (b) Anisotropic relaxation response of the thermal residual strain for the Ni phase.

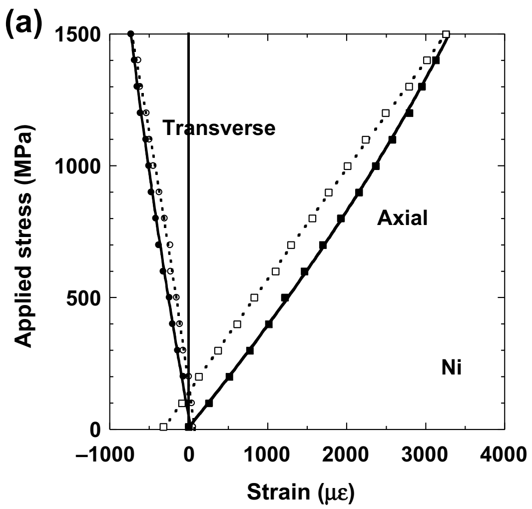

Figure 14 The Ni phase load–unload stress–strain curves for WC–10 wt% Ni under (a) 1500 MPa tension and (b) −1000 MPa compression.

Poisson reaction of the Ni elastic strain that opposes the applied compression while, for applied uniaxial tension, it is the direct reduction of the Ni elastic strain that opposes the applied uniaxial tension. This suggests, as is observed, that the overall macroscopic length change will be greater for applied compression.

1.13.4.2 Cyclic Loading

1.13.4.2.1 Repeated Loading

The effect of repeatedly loading a cemented carbide was studied using a WC–10 wt% Ni sample subjected to 100 cycles of uniaxial compression from −10 to −2500 MPa (Krawitz, Venter, Drake, Luyckx, & Clausen, 2009). Diffraction data were taken during load–unload cycles 1, 2, 3, 10, 25, 50 and 100. The macroscopic response of the Ni phase for cycles 1 and 100 is shown in Figure 16. The changes occurring in the Ni phase are shown in Figure 17. The relaxation process is best seen as a function of the number of cycles (Figure 18). Most of the change occurs during the first three cycles, with a stable state reached after about 10 cycles. Although the

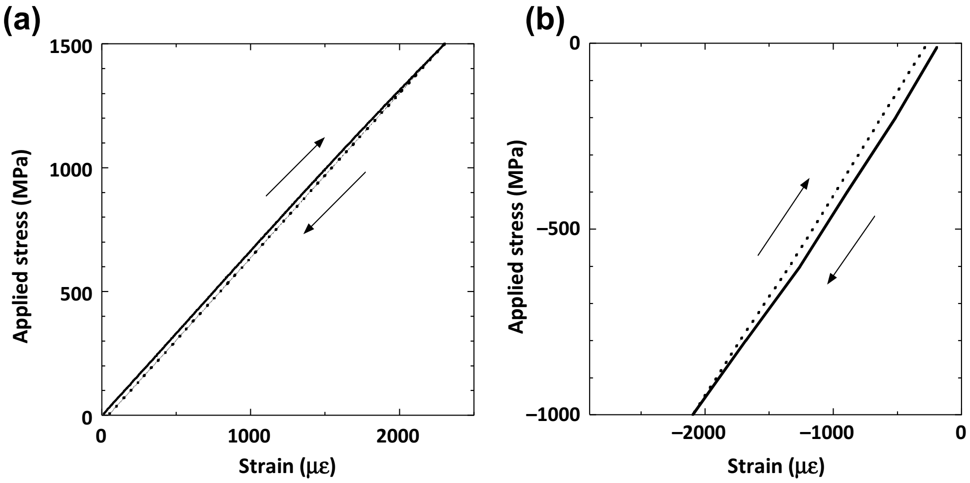

Figure 15 The macroscopic load–unload stress–strain curves for WC–10 wt% Ni for (a) +1500 MPa tension and (b) −1000 MPa compression.

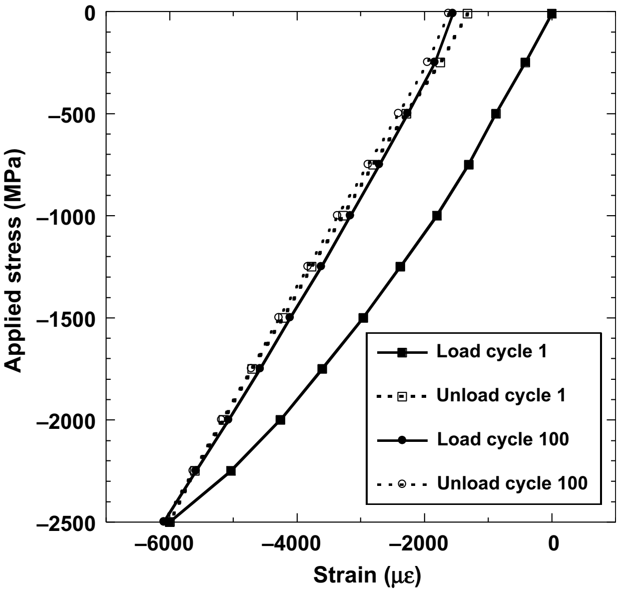

Figure 16 Macroscopic load–unload stress–strain curves for WC–10 wt% Ni loaded to −2500 MPa for 100 cycles.

relaxation stabilizes rather early in the process, there is still a hysteresis present in both the axial and transverse directions. Most of the composite volume does not yield but rather is elastically strained under load. This creates a range of strain in the sample that contributes to a strain variance (peak broadening) that is reversed upon unloading. The peak breadth responses follow a similar pattern and, after 10 cycles, are about 75% of the starting values, that is, they narrow because the mean thermal residual stress decreases (Krawitz et al., 2009).

1.13.4.2.2 Stepped Loading

The stepped loading response of WC–Ni helps explain the response of the composite in service, and in accounting for the unusual toughness of cemented carbides (**Figure 19**). The hysteresis closes significantly after three cycles but, if the load is subsequently increased, the process begins again, as shown by the first cycles to −1000 and −2000 MPa following the initial loading to −500 MPa. A component in service would be able to absorb additional energy through the plastic deformation/relaxation process in regions where it experienced an increase in load as well as through the ongoing hysteresis process.

1.13.5 Role of Residual Stresses in Mechanical Behavior

Long-recognized but unexplained mechanical behavior anomalies of cemented carbides are now attributable to the influences of residual stresses, including small-strain yielding and plasticity-induced relaxation. The absence of linear elastic load response of commercial WC–Co grades is perhaps the principal observation. Felgar and Lubahn (1957) measured samples in both tension and compression. Nonlinearity in tension was observed at strains as low as 0.1%, as well as nonlinear responses, that were termed "anelastic", in both tension and compression. These behaviors, identical to those seen herein, are due to thermal stress relaxation and the volumetric, asymmetric nature of the response of the system to applied stress. Another example is that preloading in compression has been observed to increase density and cause asymmetric Palmquist crack lengths (Exner & Gurland, 1970). Both are due to the asymmetric stress relaxation that results from the interaction of nonuniform applied strains with the preexisting thermal residual stresses. In general, the longer Palmquist cracks are in the direction of higher residual stress while the shorter ones are in the direction that has experienced greater relaxation. Finally, variation in Poisson's ratio was observed during uniaxial compressive loading (Drake, 1980). Specifically, the initial value of Poisson's ratio in a WC–15.6 wt% Ni sample began decreasing with the onset of load for the two load cycles measured. This is due to the greater stress relaxation in the

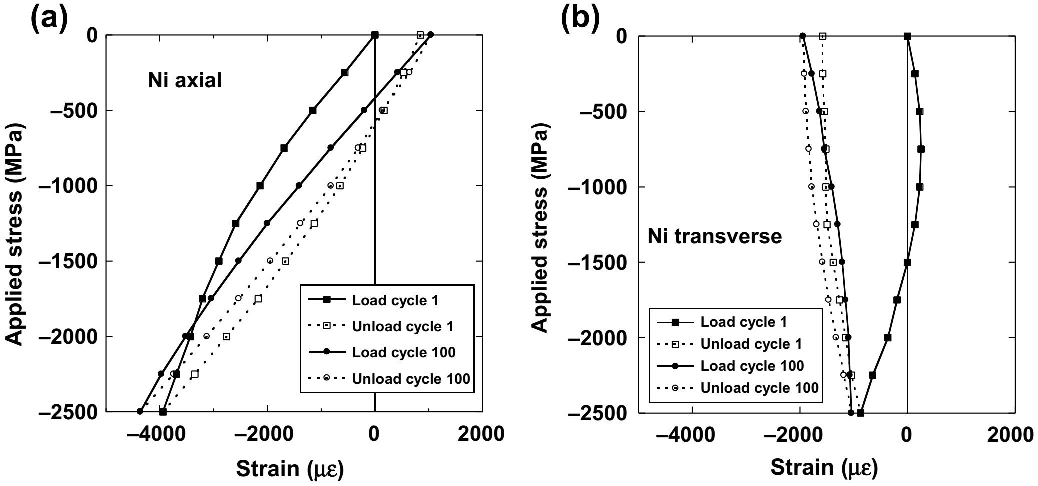

Figure 17 The Ni phase response in WC–10 wt% Ni after 1 and 100 cycles of repeated compression loading to −2500 MPa: (a) axial direction; (b) transverse direction.

directions normal to the compression axis. Poisson's ratio $\nu = -\varepsilon_x/\varepsilon_z$ and the transverse direction x experiences a higher degree of strain relaxation than the direction of compressive loading, z.

The plasticity behavior appears to comprise a primary source of toughening characteristic of cemented carbides. This suggests the feasibility of sufficiently realistic and scaled-up microstructural modeling, which would provide predictive capability for mechanical response of cemented carbide composites in terms of composition, microstructure, and thermal and load history.

Toughness, perhaps the most important attribute of cemented carbides, and the one that distinguishes them from other engineering materials at equivalent hardness levels, has been quantified by fracture toughness testing based on linear elastic fracture mechanics (Chermant & Osterstock, 1976; Igelstrom & Nordberg, 1974; Lueth, 1972; Murray, 1977). Much effort has been given to explaining and predicting observed toughness in terms of microstructural parameters and in situ elastic/plastic behavior of the binder and carbide phases (Chermant & Osterstock, 1976; Igelstrom & Nordberg, 1974; Murray, 1977; Pickens & Gurland, 1978). However, assumptions implicit in this approach including far-field linear elasticity and isotropy are not valid for cemented carbides. The emergent view of cemented carbide mechanics seems to require a new, nonlinear-elastic model of

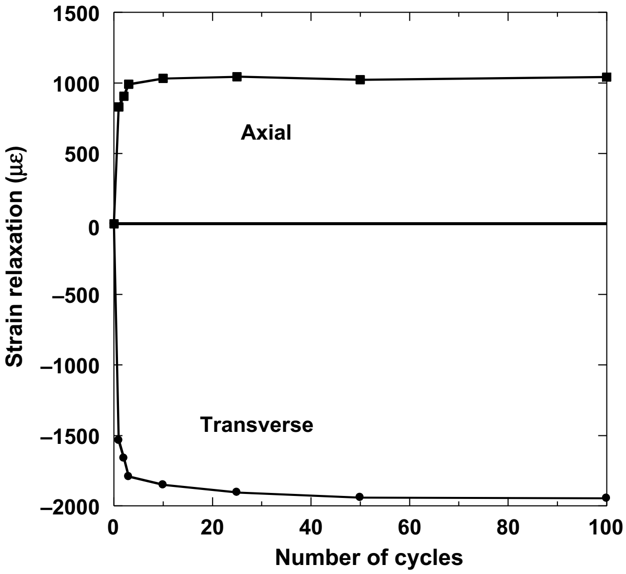

Figure 18 Strain relaxation versus number of cycles for WC–10 wt% Ni under repeated uniaxial compression to −2500 MPa.

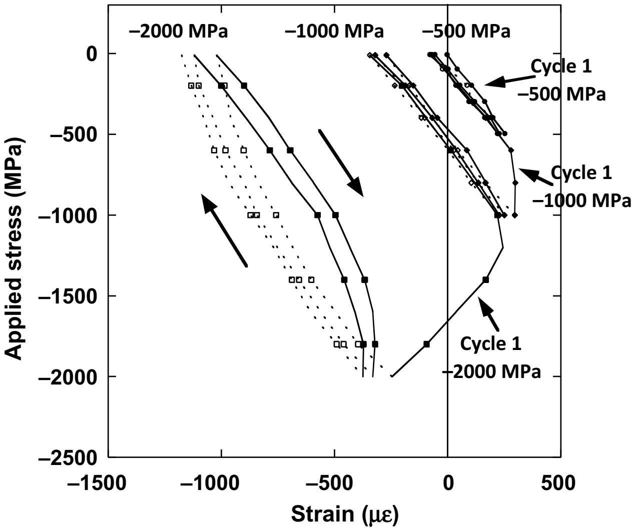

Figure 19 Stepped loading of WC–10 wt% Ni: three cycles to −500 MPa, three cycles to −1000 MPa and then three cycles to −2000 MPa. The loading cycles are solid lines; the unloading are dashed.

toughness behavior in these materials, both in terms of bulk "continuum" response and response in the presence of defects. Moreover, such models, if they are to provide accuracy, must also take into account the documented anisotropic relaxation and plasticity effects and their sensitivity to load directionality and history.

In conclusion, it is apparent from the foregoing that diffraction techniques in combination with the sampling capability of neutrons provide an unprecedented view of the micro- and macroelastic behaviors in cemented carbides, and also allow by deduction an emergent understanding of macroplasticity response. However, the quantification and roles of microscale *plasticity* behavior in these composites has awaited the application of microstructural FEM. Recent 3-D elastic–plastic FEM efforts in this vein utilizing idealized cemented carbide microstructures with increasing levels of similitude have semiquantitatively corroborated the measured micro and macro components of residual stresses and their interaction with applied loads (Livescu et al., 2005), demonstrating the development of elastic and plastic strains on a microstructural scale arising from both thermal and applied loadings.

References

Bacon, G. E. (1975). *Neutron diffraction*. Oxford: Clarendon Press.

Chermant, J. L., & Osterstock, F. (1976). Fracture toughness and fracture of WC-Co composites. *Journal of Materials Science, 11*, 1939–1951.

Coats, D. L., & Krawitz, A. D. (2003). Effect of particle size on thermal residual stress in WC-Co composites. *Materials Science and Engineering, A, 359*, 338–342.

Drake, E. F. (1980). *Fatigue damage in a WC-nickel cemented carbide composite* (Ph.D. dissertation). Rice University.

Exner, H. E., & Gurland, J. (1970). The effect of small plastic deformations on the strength and hardness of a tungsten carbide-cobalt alloy. *Journal of Materials, 5*, 75–85.

Felgar, R. P., & Lubahn, J. D. (1957). Mechanical behavior of cemented carbides. *Proceedings, American Society for Testing and Materials, 57*, 770–790.

Hutchings, M. T., Withers, P. J., Holden, T. M., & Lorentzen, T. (2005). *Introduction to the characterization of residual stress by neutron diffraction*. Boca Raton: CRC Taylor & Francis.

Igelstrom, N., & Nordberg, H. (1974). The fracture toughness of cemented tungsten carbides. *Engineering Fracture Mechanics, 6*, 597–607.

Kisl, E. H., & Howard, C. J. (2008). *Applications of neutron powder diffraction*. Oxford: Oxford University Press.

Krawitz, A. D. (1985). The use of X-ray stress analysis for WC-base cermets. *Materials Science and Engineering, 75*, 29–36.

Krawitz, A. D. (2001). *Introduction to diffraction in materials science and engineering*. New York: John Wiley.

Krawitz, A. D. (2011). 25 year perspective: neutron strain measurement. *Materials Science and Technology, 27*, 589–603.

Krawitz, A. D., Drake, E. F., & Clausen, B. (2010). The role of residual stress in the tension and compression response of WC-Ni. *Materials Science and Engineering, A, 527*, 3595–3601.

Krawitz, A. D., Reichel, D. G., & Hitterman, R. (1989). Residual stress and stress distribution in a WC-Ni composite. *Materials Science and Engineering, A, 119*, 127–134.

Krawitz, A. D., Venter, A. M., Drake, E. F., Luyckx, S. B., & Clausen, B. (2009). Phase response of WC–Ni to cyclic compressive loading and its relation to toughness. *International Journal of Refractory Metals and Hard Materials, 27*, 313–316.

Krawitz, A. D., Winholtz, R. A., & Weisbrook, C. M. (1996). Relation of elastic strain distributions determined by diffraction to corresponding stress distributions. *Materials Science and Engineering, A, 206*, 176–182.

Liaw, P. K., Choo, H., Buchanan, R. A., Hubbard, C. R., & Wang, X. L. (2006). Development of an in situ neutron-scattering facility for research and education in the mechanical behavior of materials. *Materials Science and Engineering, A, 437*, 126–133.

Liu, C. T., & Gurland, J. (1965). Thermally induced residual stresses in silicon phase of Al-Si alloys. *Transactions of the American Society of Metals, 58*, 66–73.

Livescu, V., Clausen, B., Paggett, J. W., Krawitz, A. D., Drake, E. F., & Bourke, M. A. M. (2005). Measurement and modeling of room temperature Co-deformation in WC-10 wt.% Co. *Materials Science and Engineering, A, 399*, 134–140.

Lueth, R. C. (1972). *A study of the strength of tungsten carbide cobalt from a fracture mechanics viewpoint* (Ph.D. dissertation). Michigan State University.

Mari, D., Clausen, B., Bourke, M. A. M., & Buss, K. (2009). Measurement of residual thermal stress in WC-Co by neutron diffraction. *International Journal of Refractory Metals and Hard Materials, 27*, 282–287.

Mari, D., Krawitz, A. D., Richardson, J. W., & Benoit, W. (1996). Residual stress in WC-Co measured by neutron diffraction. *Materials Science and Engineering, A, 209*, 197–205.

Murray, M. J. (1977). Fracture of WC-Co alloys: an example of spatially constrained crack tip opening displacement. *Proceedings of the Royal Society of London, A, 356*, 483–508.

Noyan, I. C., & Cohen, J. B. (1987). *Residual stress: measurement by diffraction and interpretation*. New York: Springer-Verlag.

O'Quigley, D. G. F., Luyckx, S., & James, M. N. (1997). An empirical ranking of a wide range of WC-Co grades in terms of their abrasion resistance measured by the ASTM standard B 611-85 test. *International Journal of Refractory Metals and Hard Materials, 17*, 117–122.

Paggett, J. W. (2005). *Neutron diffraction study of load response and residual stresses in WC-(Ni/Co) composites* (Ph.D. dissertation). Univ. of Missouri.

Paggett, J. W., Krawitz, A. D., Drake, E. F., Bourke, M. A. M., Clausen, B., & Brown, D. W. (2007). In situ response of WC-Ni composites under compressive load. *Metallurgical and Materials Transactions, A, 38*, 1638–1648.

Pickens, J. R., & Gurland, J. (1978). Fracture toughness of WC-Co alloys measured on single-edge notched beam specimens precracked by electron discharge machining. *Materials Science and Engineering, 33*, 135–142.

Pyzalla, A., Genzel, C., & Reimers, W. (1996). Thermal residual microstresses in steel-NbC particulate composites studied by X-ray and neutron diffraction. *Materials Science and Engineering, A, 212*, 130–138.

Reimers, W., Pyzalla, A., Schreyer, A., & Clemens, H. (Eds.). (2008). *Neutrons and synchrotron radiation in engineering materials science: From fundamentals to material and component characterization*. Weinheim: Wiley-VCH Verlag.

Rietveld, H. M. (1969). A profile refinement method for nuclear and magnetic structures. *Journal of Applied Crystallography, 2*, 65–71.

Seol, K., Krawitz, A. D., Richardson, J. W., & Weisbrook, C. M. (2005). Effects of WC size and amount on the thermal residual stress in WC-Ni composites. *Materials Science and Engineering, A, 398*, 15–21.

Tanaka, H., Akinawa, Y., & Hayashi, M. (2002). Neutron diffraction measurements of residual stresses in engineering materials and components. *Materials Science Research International, 8*, 165–174.

Weisbrook, C. M., Gopalaratnam, V. S., & Krawitz, A. D. (1995). Use of finite element modeling to interpret diffraction peak broadening from elastic strain distributions. *Materials Science and Engineering, A, 201*, 134–142.

Weisbrook, C. M., & Krawitz, A. D. (1996). Thermal residual stress distribution in WC-Ni composites. *Materials Science and Engineering, A, 209*, 318–328.

Withers, P. J., Preuss, M., Steuwer, A., & Pang, J. W. L. (2007). Methods for obtaining the strain-free lattice parameter when using diffraction to determine residual stress. *Journal of Applied Crystallography, 34*, 891–904.

1.14 Mechanical Behavior of Hardmetals at High Temperature

Daniele Mari, Laboratoire de Physique de la Matière Complexe, Ecole Polytechnique Fédérale Lausanne, Lausanne, Switzerland

1.14.1 Introduction

Since the introduction of WC–Co in the 1920s, a wide variety of hardmetals has been developed for the manufacture of cutting tools. Two main families of hardmetals can be defined according to the type of the carbide phase that is used: cemented carbides based on a tungsten carbide (WC) ceramic matrix and cermets based on titanium carbide (TiC) and titanium nitride matrix (Mari, 2001). The binder can be an alloy of cobalt or nickel in both cases. The cemented carbides based on WC are characterized by values of hardness and elastic modulus higher than that of carbide-based cermets containing TiC (carbonitride, TiCN). During machining, the temperatures that develop at the cutting edge of the tools can be very high, on the order of 1000 °C or even above. The observation of a tool edge after machining often shows evident signs of plastic deformation (**Figure 1**). Consequently, it is essential to know and understand the mechanical properties of hardmetals at high temperature where plastic deformation may be the principal reason for wear (Mari & Gonseth, 1993). In this chapter, the evolution of high-temperature mechanical behavior of hardmetals is presented. From the

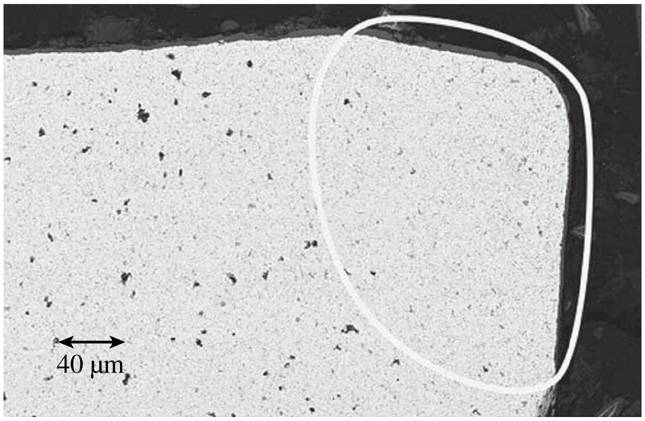

Figure 1 SEM micrograph of the tip of a WC–TaC–Co cutting tool after turning at 450 m min^{-1}. The image shows a view of the cross-section of the cutting edge. Clearly, plastic flow of the material is observed. Östberg et al. (2006a).

behavior of the base materials, WC–Co or TiCN–Co/Ni, the behavior of the cutting tool can be modeled as a function of the cutting parameters.

1.14.2 Materials

Hardmetals are obtained by sintering of metal powders and ceramics. The ceramic phase is composed of carbides and/or nitrides, which partially dissolve in the liquid metal and precipitate again producing the shape and the final structure of the ceramic grains. The morphology of the carbide phase can be described by a structure consisting of two interpenetrating skeletons: a ceramic one and a metal one (Cutard, Viatte, Feusier, & Benoit, 1996). A chain of single crystals of carbide/carbonitride gives the ceramic skeleton. In WC–Co, the grains are faceted with a triangular or rectangular shape that reveals the hexagonal crystal structure of WC. The solubility of the other metallic elements in the WC is very low. For this reason, the WC phase is almost pure. However, additional elements such as vanadium or chromium may precipitate at the surface of WC in the form of carbides. The carbides and nitrides of transition metals with cubic crystal structure have a high mutual solubility and can exchange cations with nitrogen or carbon. In composites based on TiC, TiN or TiCN, the crystals have a structure called "core–rim". The core is the remainder of undissolved TiCN powder grains during sintering. The rim (Ti,Me)CN precipitates in the liquid phase during sintering and is made of cubic titanium carbonitride, in which other transition metals (Me) are found in the solution (Chun & Kim, 1993; Lindau & Stjernberg, 1976). Figure 2(b) shows, for example, a cermet sintered from powders of TiCN, WC and Co. The ceramic grains show typical core–rim morphology. The core corresponds to the undissolved particles, while the rim is made up of cubic TiWCN (Lindahl, Mainert, Jonsson, & Andrén, 1993). The rim and the core have the same crystal orientation. The presence of a skeleton is also supported by the fact that one can completely remove the metal binder without affecting the integrity of the material. A chemical etching (by HCl for example) allows the removal of cobalt or nickel. Later on in this paper, we will relate the mechanical behavior of the skeletons constituted of TiCN or WC.

Hardmetals are characterized by an optimum combination of the ceramic phase (carbide) and of the metallic one to meet three main criteria: good liquid-phase sintering, high hardness and high toughness. At first glance, the mechanical properties of these composites could be analyzed on the basis of the combination of the properties of the constituents. In fact, good predictions are obtained when the mechanical properties at room temperature are evaluated (see Chapters 1.09 and 1.10, this volume). However, the physical properties, the chemistry and the microstructure change due to the interaction of the constituents evolve rapidly at high temperatures, making it difficult to predict the mechanical behavior of hardmetals based on the properties of pure constituents. For example, it is well known that pure cobalt has a hexagonal compact structure at room temperature and undergoes a transition to the face-centered cubic structure (FCC) at about 700 K. However, most of the observations (Lui et al., 1983; Sarin & Johannesson, 1975; Schaller, Mari, Maamouri, & Ammann, 1992) indicate that the cobalt in WC–Co has an FCC structure even at room temperature due to internal stress and to the presence of tungsten in solid solution. The dense network of interwoven stacking faults (Schaller et al., 1992) is a characteristic of the particular state of cobalt in the hardmetals, which justifies yield stresses unattainable in pure metal (Sigl & Fischmeister, 1988). Consequently, only in situ observations may give an

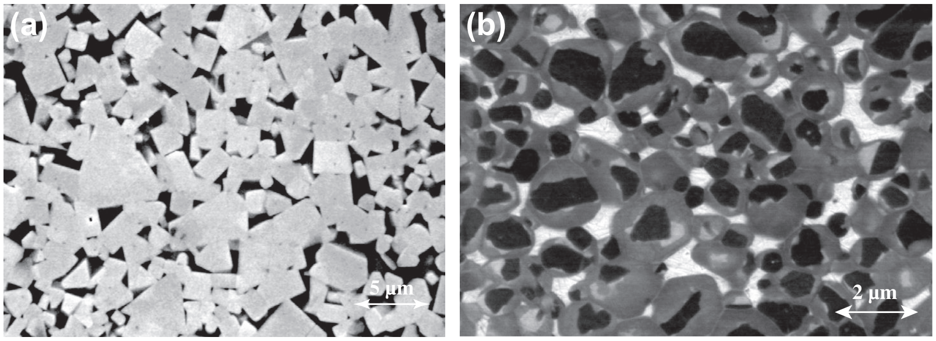

Figure 2 Morphology of (a) WC–Co and (b) Co–TiWCN. In scanning microscopy images, the cobalt appears in dark in WC–Co and in white in Co–TiWCN.

appropriate description of the behavior of metallic binder within the carbide skeleton (Schaller et al., 1992). It should be noticed that as pointed out by some authors (Heuer, Sears, & Zaluzec, 1986; Suzuki, Hayashi, & Taniguchi, 1979) and recently examined in detail by electron backscattered diffraction (Mingard, Roebuck, Marshall, & Sweetman, 2011), the cobalt or the nickel binder always show a crystal size much larger than that of the ceramic particles. The cobalt can be viewed as a single-crystal sponge that envelops the ceramic grains. The size of cobalt domains can reach 50–100 μm.

1.14.3 Mechanical Properties at Room Temperature

Hardmetals are generally brittle and show an elastic behavior at room temperature. Hardness, toughness and transverse rupture strength (TRS) are the mechanical properties that best characterize this behavior (see Chapters 1.10 and 1.17, this volume). In general, the mechanical properties at room temperature of WC–Co cemented carbides and of cermets depend essentially on the properties of the constituents when taken in appropriate conditions i.e. the conditions in which they are located inside the composite material. For example, the cobalt is in an alloyed state and contains significant amounts of tungsten in solid solution. Moreover, it is in a state of extreme hydrostatic tensile stress (see Chapter 1.13, in this volume) so that in WC–Co such tensile internal stress can exceed 2–3 GPa. Models based on these properties allow us to predict and estimate the hardness of different types of hardmetals (see Chapter 1.09, in this volume).

1.14.4 Evolution of Mechanical Properties with Temperature

1.14.4.1 Hot Hardness and Toughness

There are few studies about the measurement of hardness as a function of temperature in cemented carbide (Armstrong, 2011; Laugier, 1986; Lee, 1983; Milman, Luyckx, & Northrop, 1999). They all show a similar trend with a continuously decreasing hardness as temperature increases (Figure 3). However, in most experiments, an abrupt change of slope between 600 and 800 °C as evidenced by Milman et al. (1999) and Lee (1983). The reason evoked is a change in the mechanism controlling hot hardness. Up to about 600 °C, the decrease in hardness with increasing temperature is related to the decrease in the intrinsic hardness of the individual phases. Above 600 °C, the decrease in hardness appears to be mostly due to grain boundary sliding. The hardness of binderless WC strongly decreases up to 500 °C (Lee, 1983) in particular in single crystals oriented along the (100) direction. Above 600 °C instead, the presence of cobalt appears to be critical for hardness decrease. It has been always observed that the hardness decreases with increasing the carbide grain size at room temperature but such a trend reverses at high temperature (Lee, 1983).

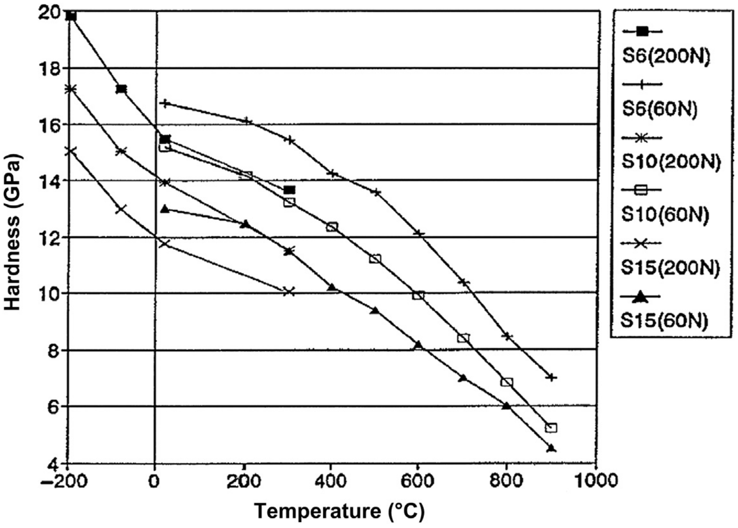

Figure 3 Plots of hardness versus temperature of three sets of WC–Co grades. Milman et al. (1999).

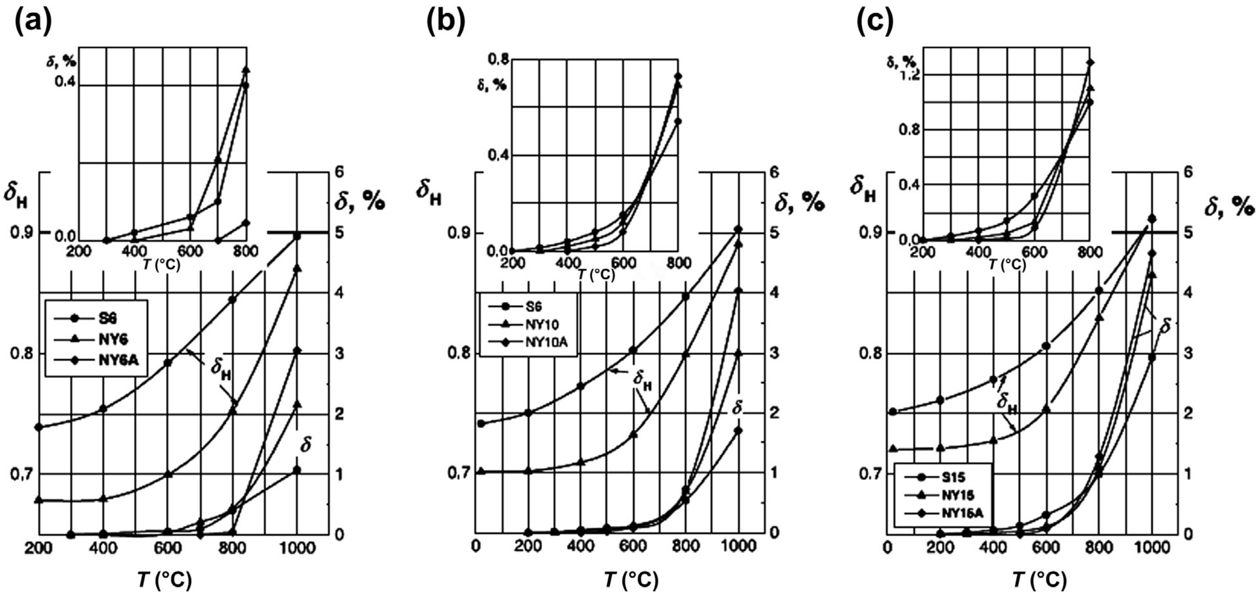

Figure 4 Deformation and indentation plasticity δ_H: (a) WC–6 wt% Co; (b) 10 wt% Co; (c) 15 wt% Co (Milman et al., 2002). Grades S have a WC grain size of 1.3 μm while grades NY have a WC grain size of 0.3 μm except NY10 (0.4 μm) and NY15 (0.35 μm).

A detailed study of the reasons for hardness change with temperature was made by Milman, Luyckx, Goncharuck, and Northrop (2002) over a large number of WC–Co grades varying the cobalt content and the WC grain size.

From the data obtained, the authors extract a parameter δ_H (indentation plasticity), which normalizes the hardness with respect to the elastic constants:

$$\delta_H = 1 - 14.3 \cdot \left(1 - \nu - 2\nu^2\right) \frac{H_V}{E} \tag{1}$$

Figure 4 shows the different curves for the WC–Co with different levels of cobalt. It can be seen that a brittle–ductile transition marked by a sudden increase of strain at rupture is found at about 800 °C. The parameter δ_H shows that the material can undergo substantial plastic deformation even at temperatures lower than 800 °C. We also note that the transition temperature little depends on the amount of cobalt. Instead an inversion of the dependence of δ_H as a function of grain size is observed at 800 °C (insets in Figure 4). The plastic deformation dramatically increases in small grain size samples at high temperature. The authors have attributed such transition to a change of the deformation mechanism passing from the deformation of the binder at low temperature to the deformation of the carbide skeleton by grain boundary sliding.

Both cermets and cemented carbides show, above a certain temperature, a strong increase in toughness (Figure 5) accompanied by a decrease, even stronger, of the yield stress (Fantozzi, Mohand, & Orange, 1986): the material deforms plastically.

If plastic deformation occurs around the crack tip, the toughness K_{IC} is no longer a significant parameter for determining the performance of the material. We must therefore examine more thoroughly the plastic deformation of the carbide to understand and predict the mechanical behavior of the cutting tool.

1.14.4.2 Plastic Deformation at High Temperature

Given the importance of the high-temperature behavior of hardmetals for metal cutting performance, a number of investigations, since the 1980s, about high-temperature creep are found in the literature (Fährmann, 1989; Smith & Wood, 1968; Suzuki, Hayashi, Taniguchi, & Matsubara, 1982). However, due to the experimental difficulties, the studies of this kind are much less numerous than tests performed at ambient temperature. The creep rate is tested as a function of different morphological parameters such as the ceramic grain size, the binder content or the stoichiometry as well as the test temperature and stress. The general idea that comes from these initial articles is that the plastic deformation is controlled by the cobalt phase. However, the interpretations of

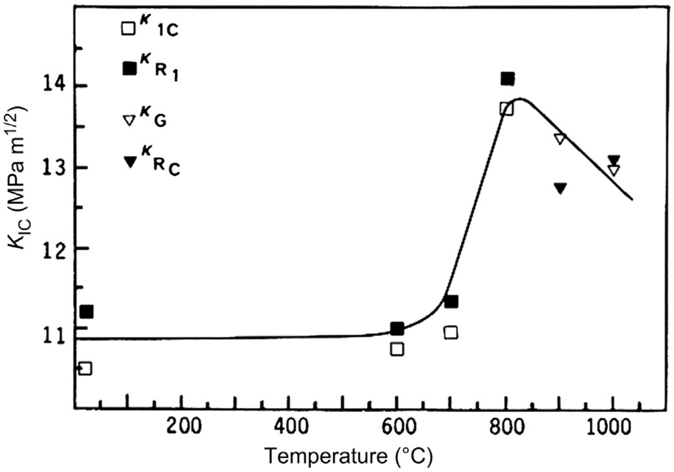

Figure 5 Measurement of hot toughness K_{IC} in samples of WC–6 wt% Co. Fantozzi et al. (1986).

the fundamental mechanism can be quite different. Smith and Wood (1968) investigated different WC–Co materials between 800 and 1000 °C and notice that at low stress the deformation rate is inversely proportional to the size of the WC grains while the trend is reversed at high stress. The creep activation energy was 2.5 eV per atom close to that of the cobalt self-diffusion which is 2.9 eV per atom. They propose that at low-stress creep is controlled by cobalt diffusion. At high stress instead dislocation climb is evoked. Suzuki et al. (1982) studied the bending deformation of WC–Co in the 600–1000 °C temperature range and notice for the first time a change of the flow stress as a function of grain size between high and low temperatures. In fact, examining two grades with 1.3 and 3.8 μm average WC grain size, they observe that fine grain samples show the highest flow stress below 900 °C while the samples with coarse grains have a higher resistance to deformation above such a temperature. They also attribute such a change to different modes of deformation of the cobalt. They suppose that at low temperature the cobalt is dispersion strengthened. At high temperature, large grains are supposed to reduce dynamic recovery of dislocations in Co, which produces a strengthening of the binder. They also evidence that the large cobalt single crystalline domains deform homogeneously but strain incompatibilities between these domains may lead to crack formation. Then, not only the WC grain size but also the cobalt grain size can have an influence on the deformation rate. However, the authors notice that high-temperature deformation of WC–Co not only implies bulk deformation but also stable microcrack growth. The strain incompatibilities between the cobalt single-crystal domains play a role in generating microcracks. In another study, the same authors (Suzuki et al., 1979) show that TRS increases when WC–Co materials are sintered in order to obtain large cobalt domains. They believe that such an increase is due to retardation of stable crack growth, which plays an important role into the macroscopic deformation of the material. The role of WC grain size was investigated by Ueda, Doi, Fujiwara, and Masatomi (1977). They envisage a brittle–ductile transition between 600 and 800 °C. This transition is characterized by a reversal of the TRS. The fine-grained materials have a TRS lower than coarse-grained ones at high temperature. The opposite behavior is found at low temperature. The transition temperature depends on cobalt content: it is 900 °C for 6 wt% Co and as low as 600 °C for 20 wt% Co. Ueda et al. introduced for the first time a classification of the mechanical behavior of WC–Co into different domains: brittle, below 600 °C; transition domain, between 600 and 800 °C; and plastic domain, above 800 °C. This domain is characterized by pore formation in the cobalt and intragranular crack propagation between WC grains.

Studies on cermets are less numerous but they evidence the same type of behavior as WC–Co with different temperature domains. The bend deformation (Suzuki, Hayashi, & Kubo, 1980) and the TRS (Suzuki, Hayashi, & Yamamoto, 1978) were investigated by Suzuki et al. in the 1980s. These authors use similar models as those already proposed for WC–Co to explain the high-temperature behavior and attribute the deformation to the binder. They notice that a cobalt binder produces a better strength than Ni. They also notice that the introduction of TiN together with TiC, and therefore the formation of TiCN, produces a higher high-temperature hardness and lower TRS. Generally, the addition of TiN produces an increase of the flow stress at 1000 °C. The authors attribute still this refractory behavior to strain hardening of the binder. A further increase of the creep resistance was obtained by the addition of Mo_2C (Suzuki, Hayashi, Matsubara, & Tokumoto, 1983).

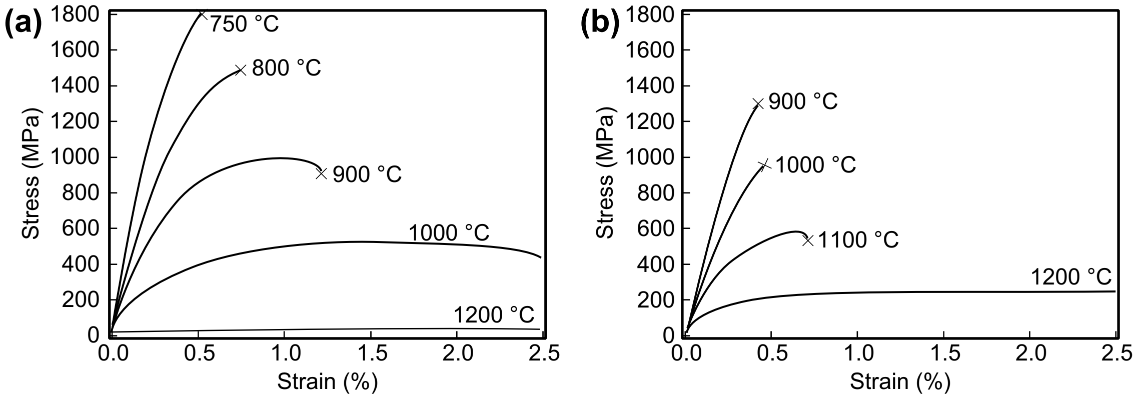

Figure 6 Three-point bending measurements at different temperatures showing a transition from brittle to ductile and to highly plastic behavior for (a) the WC–Co and (b) the cermet.

The plastic deformation of TiC at 1000 °C cannot be neglected as shown by Williams (1964) and Hollox and Smallman (1966). However, as shown by Wolfe and Williams (1986), the comparison of the deformation of a TiC–Mo–Ni with a TiC cannot justify the deformation rate above 1200 °C. These authors conclude that the high-temperature deformation must be attributed to TiC grain boundary sliding. Instead, below 1200 °C, Hall–Petch (Hall, 1951; Petch, 1953) strengthening of dislocations in the TiC grains is envisaged as the main mechanism of deformation. Fährmann (1989) investigated the compressive creep behavior of TiCN–Mo–Ni cermets between 1000 and 1200 °C. They measured creep activation energy of 4 eV per atom and a stress exponent around 1. They conclude from the activation parameters that the deformation occurs by grain boundary sliding promoted by a thin binder film between them.

The stress–strain curves of two hardmetals, a cemented carbide WC–10% Co and a cermet TiWCN–10% CO, fabricated in order to obtain a cobalt metal matrix with same composition and content, are presented in Figure 6 (Östberg et al., 2006b).

The WC–Co exhibited some plastic deformation already at 750 °C when the TiWCN–Co was still very brittle. At a temperature of 1200 °C, both materials are highly plastic, but the TiWCN–Co shows a flow stress much higher than the WC–Co. In order to investigate the deformation rate controlling mechanism, several authors have performed creep tests at high temperature. The activation energy measured for creep in WC–10 wt% Co shows a transition passing from a value of about 2.5 eV per atom below 750 °C to a value of 4.5 eV per atom (Mari, Bolognini, Feusier, Viatte, & Benoit, 1999). Cermets of TiCN–Co type also show a similar transition at 900 °C passing from an activation energy of 1.7 eV per atom to 5.2 eV and even 7.5 eV at 1150 °C (Bolognini, Feusier, Mari, Viatte, & Benoit, 2003). In effect, by choosing a WC–Co and a TiCN–Co with identical Co volume content (10%), Buss and Mari (2002), pp. 72–77 have shown that the transition temperature is the same, which is 950 °C (Figure 7).

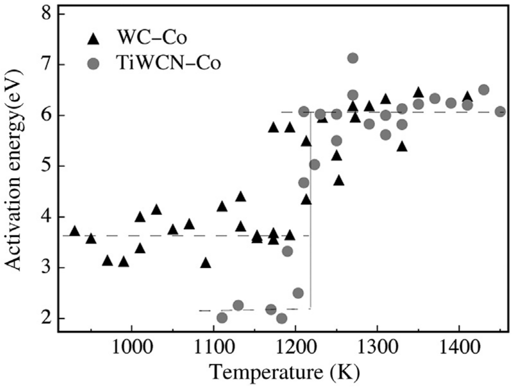

Figure 7 Activation energies obtained from temperature jump experiments at different temperatures and creep stresses. A transition from the high-temperature creep regime to the low-temperature one (lower activation energies) is seen in both WC–Co and TiWCN–Co.

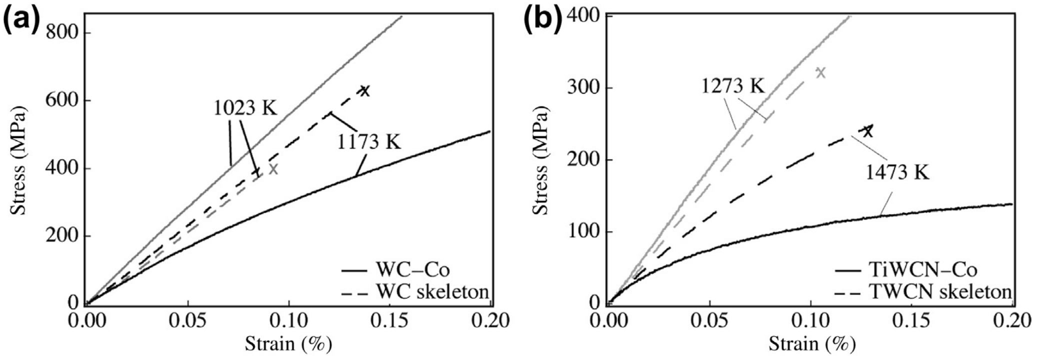

Figure 8 Direct comparison of the stress–strain curves for the materials and their complete skeletons: (a) WC–Co and WC skeleton and (b) Co–TiWCN and TiWCN skeleton. At the highest temperatures, the ceramic skeleton deformations are clearly enhanced by the presence of cobalt (i.e. in the complete hardmetals). Buss and Mari (2002), pp. 72–77.

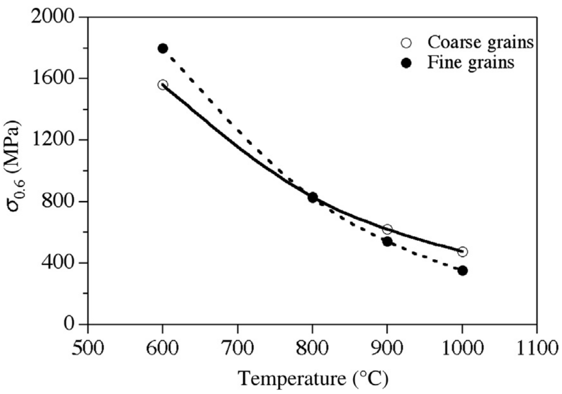

Figure 9 Flow stress measured at 0.6% strain in three-point bending in a WC–11 wt% Co (Mari & Gonseth, 1993). The fine-grained samples (1 μm) have a better resistance to deformation at a temperature below 800 °C. In contrast, coarse-grained samples (3.1 μm) show a better resistance to deformation at high temperatures.

A surprising behavior is obtained by the comparison of the deformation at high temperature of as-sintered hardmetals with their respective skeletons obtained by etching the cobalt (Figure 8). At low temperature, skeletons show a flow stress below that of the complete materials, which can be explained by a reduced effective cross-section due to the removal of the metallic phase. Surprisingly, at high temperature, the stress needed to deform samples consisting only of the skeleton is higher than that of the complete ceramic materials (Figure 8).

The transition between these two regimes occurs at different temperatures in the two materials, around 1100 K for the WC–Co and around 1300 K for the TiWCN–Co. The total plastic deformation of the complete material exceeds the rupture strain of the skeletons in all temperature ranges. Another sign of this transition is a change in behavior as a function of grain size of ceramics. As can be seen in Figure 9, which refers to the WC–Co, the yield stress is lower for materials with fine grain size at low temperature. At high temperature this behavior is reversed.

A behavior similar to that observed in WC–Co cermets was found in cermets (Mari et al., 1999). In Figure 10, stress and strain at fracture for two cermets with Ni and Co matrix are shown. The brittle–ductile transition occurs at about 950 °C, a temperature higher than that mentioned above for WC–Co.

1.14.4.3 Cemented Carbide and Cermet Deformation at Extreme Temperatures

Since extensive plastic deformation already occurs below 1000 °C, there are very few studies at very high temperatures. It is however worth mentioning the work performed by Lay, Vicens, and Osterstock (1987) who studied the compression deformation of WC–Co at very high temperature, between 1050 and 1350 °C. They always find a characteristic sigmoidal shape of log $\sigma - \log \dot{\varepsilon}$ curves (σ being the compression stress and $\dot{\varepsilon}$ being

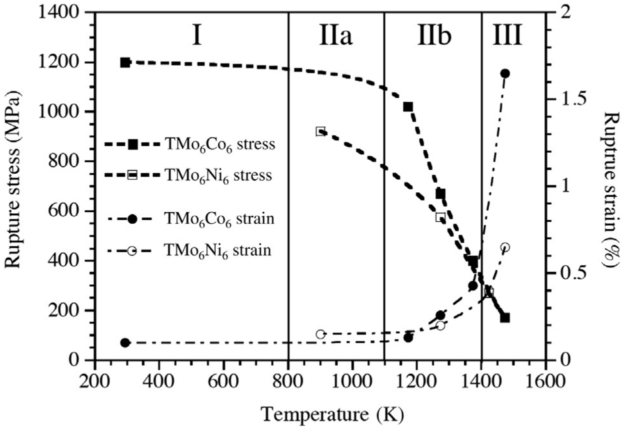

Figure 10 Strain and stress at fracture in two TiCN-based cermets: TiCN–6% Co and TiCN–6% Ni. Cermets with cobalt-based metal matrix show a higher toughness.

the strain). They explain such a behavior by a transition from grain boundary sliding accommodating bulk deformation at low stress to intragranular deformation of WC at high stress. They also notice that the deformation of the WC depends on the relative orientation of the grains, which implies that some grain boundaries can glide and others cannot, e.g. those that have a coincidence relation of type $\Sigma = 2$. The WC therefore is considered as composed of chains of grains that withstand any relative sliding and can only deform by bulk deformation. Other grains instead can glide and accommodate more easily the bulk deformation. The activation energy for creep was about 5–5.5 eV per atom. These values were confirmed by Sakuma and Hondo (1992) who, however, attribute the creep to grain boundary sliding.

Okuyama and Sakuma (1995) have analyzed the creep of $TiC–Mo_2C–20wt\%Ni$ between 1100 and 1225 °C. They also obtain a sigmoidal curve in $\log\sigma - \log\dot{\varepsilon}$ curves showing three regions of behavior. The creep exponents were ranging between 1.6 and 2.5 with the lowest exponent found in the intermediate stress region. The activation energy for creep was between 6.5 and 9 eV per atom, the lowest value being obtained in the intermediate region. The authors propose that TiC grain boundary sliding is the mechanism active for such intermediate region, while at high stress (200 MPa) the rate controlling mechanism would be dislocation climb in the TiC.

1.14.5 Deformation of Cemented Carbides: General Discussion

The data presented above show that there is a general consensus on the fact that the mechanical behavior of the cermets can be divided into three temperature zones: a fragile zone (zone I), a tough and limited deformation zone (zone II) and a strong deformation zone (zone III) that affects the strain at fracture (Han, Sacks, Milman, & Luyckx, 2009; Mari et al., 1999; Milman et al., 2002).

1.14.5.1 Mechanisms of Deformation: Microstructure Observation

These zones are found in all hardmetals. The temperature range of each zone depends however on grain size and composition. At low temperature (I) hardmetals are brittle and macroscopic deformation is elastic. In a range between 600 and 800 °C the deformation predominantly occurs in the binder (IIa). It can be said that the behavior is essentially anelastic, which means that plastic deformation is concentrated in the metallic phase, while the deformation of the ceramic remains elastic: if the applied stress is released, the elastic stress in the carbide restores progressively the original shape. Moreover, as noted earlier, the metal has an atypical behavior under stress and its yield stress can be much higher than that of the free metal. For example, cobalt is characterized by a dense network of stacking faults caused by the dissociation of Shockley partial dislocations (Schaller et al., 1992) (Figure 11). This network is reduced at 600 °C due to the recombination of partial dislocations. Cobalt becomes more ductile and deformation begins. However, to have a larger deformation the ceramic phase must also be deformable. This deformation can be observed for example in the carbide/carbonitride phase of

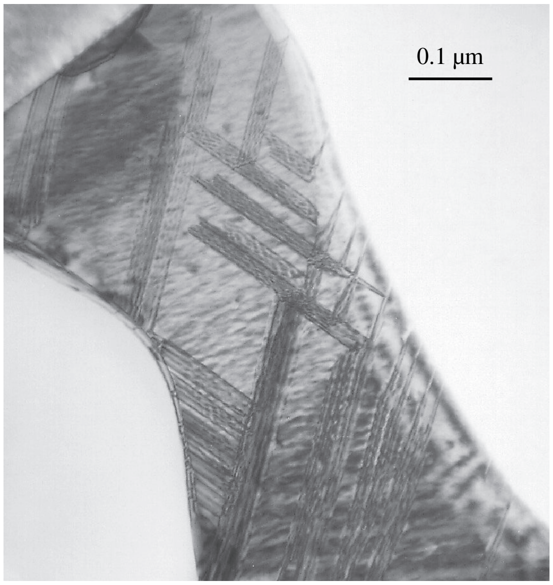

Figure 11 Stacking faults in the cobalt phase of a TiCN–18 vol% Co observed by TEM.

cermets from 900 °C (zone IIb). The microstructure of a cermet deformed at 1000 °C is presented in Figure 12. An increasing density of dislocations characterizes it. However, the contribution of the carbonitride phase to the total deformation is still limited.

The WC phase requires higher temperatures and stress before undergoing deformation at least under tensile stress. However, a dislocation density increase has been observed in WC after indentation even at room temperature (Sarin & Johannesson, 1975). The dependence of the deformation on grain size clearly shows a Hall–Petch behavior (Hall, 1951; Petch, 1953) as evidenced by Lee (1983). However, in all these studies, in order to observe the deformation of the specimens before failure, tests were made under compression. That is why, before obtaining an extended deformation of the WC, another phenomenon appears upon deformation at high temperature: grain boundary sliding. This phenomenon can be observed in Figure 13, where the WC grains were marked with a microgrid. In a previous work, Wirmark, Dunlop, and Chatfield (1986) had already

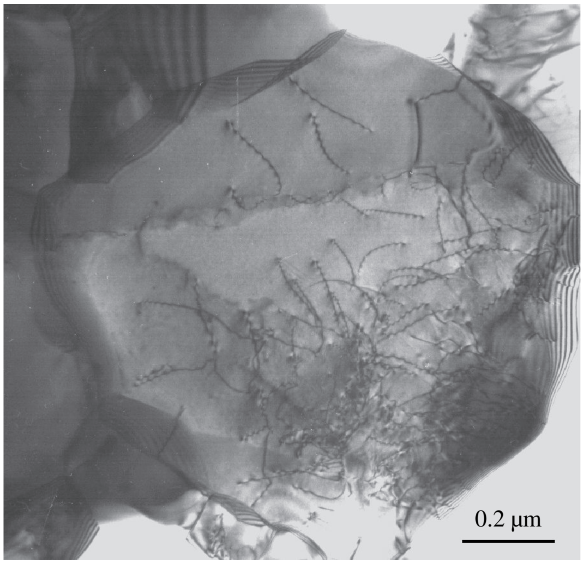

Figure 12 Formation of dislocations in the grain of a TiCN cermet of a TiCN–6 wt% Co cermet after deformation at 1000 °C. The presence of dislocations indicates the deformation of TiCN grains.

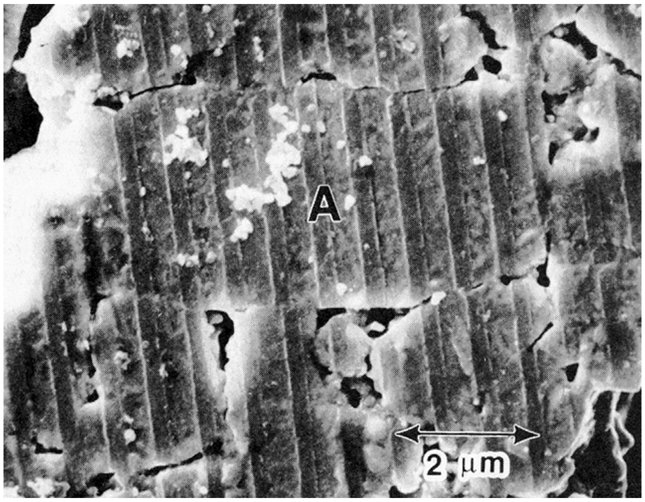

Figure 13 In this sample of WC–11 wt% Co, sliding of WC grains after deformation at 900 °C is observed. The movement of the grain A with respect to the upper and lower ones is shown by the reference grid. Mari, Marti, and Silva (1992).

observed marker line shift upon deformation at 900 °C and concluded that grain boundary sliding was the controlling mechanism of deformation. Another phenomenon observed after deformation at high temperature is the infiltration of ceramic grain boundaries of the metal as shown for a TiCN-Co cermet in Figure 14. This is a sign that the metallic phase plays a crucial role in the deformation of hardmetals not only at relatively low temperature but also at high temperature. Therefore, the interaction between the metal and the carbide can be the key mechanism for the deformation observed in cutting tools in critical conditions implying high working temperatures. Such conditions are encountered more and more frequently due to the increase in cutting speed and mass processes. Östberg and Andrén (2006) studied extensively the microstructure of WC–Co and TiCN–WC–Co cutting inserts after that plastic deformation had occurred upon high-speed turning. They found that after deformation, the binder phase had infiltrated some of the grain boundaries and formed lamellae between the hard phase grains (Figure 15). The infiltration of grain boundaries was assumed to occur by a stress-induced dissolution along the grain boundaries of the hard phase grains. Some localized dissolution of the hard phase could also be seen as faceting of grains in WC–Co and at triple points in cermets. It was concluded that the plastic deformation occurs by grain boundary infiltration by the cobalt with simultaneous grain boundary sliding. The rate of deformation is controlled by the dissolution of the hard phase grains.

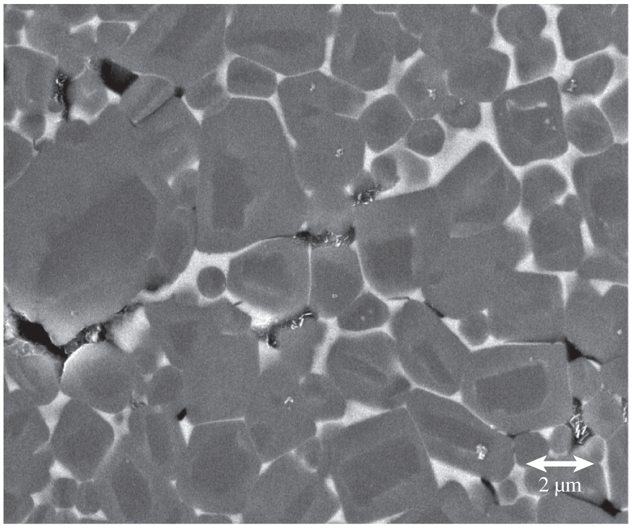

Figure 14 In this sample, TiMoCN–6 wt% Co deformed at 1200 °C, the decohesion of the TiMoCN grains and the infiltration of some grain boundaries by cobalt (in white) are observed. Bolognini et al. (2003).

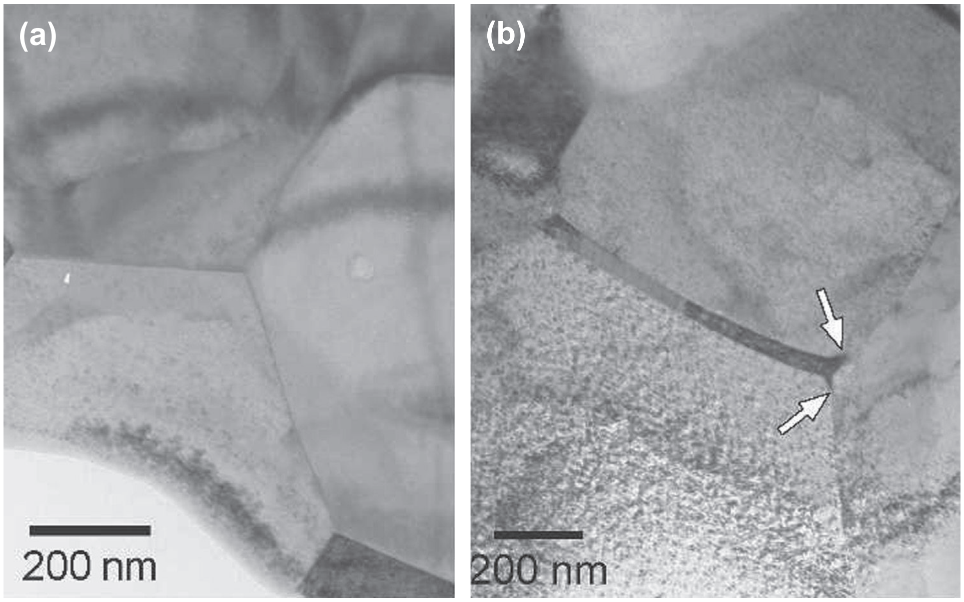

Figure 15 Comparison of triple points between TiCN grains (a) before deformation and (b) after deformation (Östberg & Andrén, 2006) in a TiCN–Co hardmetal.

1.14.5.2 Role of Mechanical Spectroscopy in the Analysis of High-Temperature Deformation

An original contribution to the classification of the physical mechanisms responsible for the evolution of the mechanical behavior of hardmetals was given by mechanical spectroscopy (Mari et al., 1999). In fact, all phenomena that dissipate mechanical energy, such as plastic deformation, give rise to internal friction (IF) (mechanical loss) even if the mechanical stresses are very weak. Mechanical spectroscopy consists in applying a periodic stress to the samples and measuring the related strain response. The phase lag tan(δ) between the applied stress and the strain accounts for the internal energy dissipation. When plotting tan(δ) as a function of the temperature or frequency, a so-called IF spectrum is obtained. Figure 16 shows an IF spectrum as a function

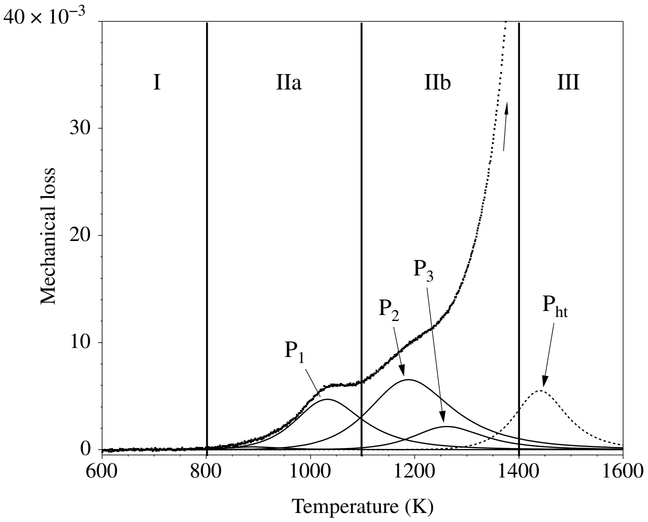

Figure 16 Internal friction spectrum of TiMoCN–6 wt% Co measured at 1 Hz as a function of the temperature. The spectrum deconvolution is constituted of four peaks P_1, P_2, P_3 and P_{ht} and of an exponential background (not shown). The temperature domains defined by the deformation behavior are also reported.

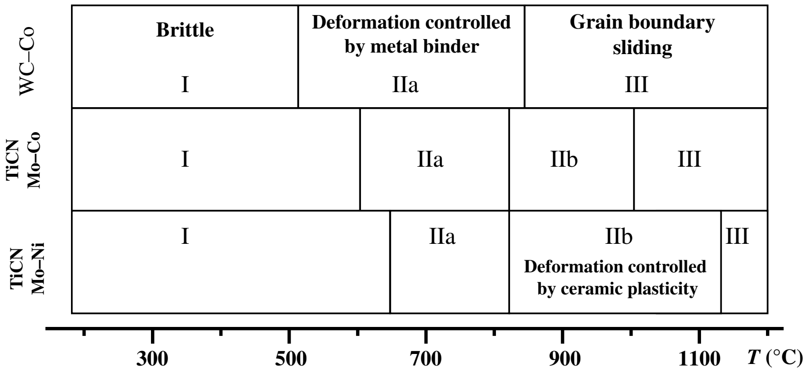

Figure 17 Schematic description of the mechanisms of deformation that appear in some hardmetals. The transition temperatures can vary depending on the composition.

of temperature measured in a TiCN–Co cermet. It is constituted of a series of peaks each one linked to a specific physical phenomenon. From the combination of the two phases of a cermet, the ceramic and the metal, one could expect to find, depending on the temperature, first the deformation of the ductile phase and then the deformation of the hard phase and eventually the decohesion of the material due to the slip and decohesion of grain boundaries of the ceramic phase. It is actually what one may observe on the spectrum of IF of TiCN–Co cermets (Figure 16). We can indeed observe a first peak P_1 located at 800 °C, which is attributed to the deformation of cobalt. A pair of peaks P_2–P_3 can be attributed to the deformation of the ceramic phase: the TiCN. The peak P_{ht} is not visible in the temperature scan but it can be observed in isothermal scans as a function of the frequency. It was attributed to grain boundary sliding. The temperature zones in which these peaks are observed justify the subdivision of deformation described above. The activation energy of the peak P_1 (similarly found in WC–Co) is about 2.9 eV per atom, which corresponds well with that of the cobalt self-diffusion. The activation energy of P_2–P_3 (2.1 and 2.7 eV per atom, respectively) is close to that of the Ti diffusion in TiC. Finally, a proper analysis of the behavior of P_{ht} considering microstructure changes leads to an activation energy of 4 eV (Mari, 2009). There is a fair correspondence with the activation energies measured in creep experiments. If we consider that mechanical spectroscopy produces activation energy values that are directly related to a single physical mechanism one could infer that at very high temperature, the creep tests tend to overestimate the activation energy. This is due to the continuous change of the microstructure.

To summarize, the mechanical behavior of the cermets can be classified into three temperature zones, each characterized by a specific mechanism that controls the deformation (Figure 17) (Mari et al., 1999). The activation of each of these mechanisms is characterized and evidenced by an IF peak.

At low temperatures, the overall mechanical behavior of cermets is elastic up to failure (zone I).

1.14.5.2.1 Plastic Deformation Zone II

In this area, fine-grained samples have a better resistance to deformation. In a region located between 550 and 950 °C, the metal begins to deform (IIa). The plastic deformation is still limited because the ceramic skeleton does not deform: the solid is anelastic. Cobalt deformation is accompanied by the shrinkage of stacking faults limited by partial dislocations. In nickel instead, the slip of perfect dislocations is likely to be responsible for the plastic deformation. Impurities in solid solution in the metal control the deformation rate. The deformation tests and TEM images show that the hardening is due to the multiplication of dislocations, which justifies the higher resistance to deformation of fine-grained specimens. In WC–Co, only the IIa is detected that corresponds to the deformation of metal while that of the carbide TiCN (IIb) is found in cermets.

1.14.5.2.2 Plastic Deformation Zone III

At a temperature starting from 900 °C for the WC–Co at 1100 °C for cermets, there is a transition to a behavior where larger particle size of the ceramic phase improves the resistance to deformation, contrary to what is observed in the region II (Figure 9). Experimental evidences suggest that the phenomenon responsible for this change of behavior is the sliding of grain boundaries that at this point controls the deformation. This process deforms the ceramic skeleton but the presence of cobalt increases the flow speed progressively infiltrating the ceramic grain boundaries.

1.14.6 Model of the Life of Carbide Tools

Many theories have attempted to explain the rate of wear of cutting tools (Colding & König, 1971; Taylor, 1907) but none of them provides a completely satisfactory model for the prediction of tool life. The two main reasons are

- the presence of multiple processes of wear in any machining operation;
- the limited use of the mechanical properties of the materials constituting the tool to predict the life duration, due in part to limited knowledge of these properties.

Among the processes of wear that have been described or studied, we can list the adhesion of the material worked on the cutting edge (built-up edge) (Hauser, 1980), diffusion (Kramer & Suh, 1980), abrasion (Suh, 1986), and oxidation (Colding & König, 1971). We note, however, that the almost systematic use of a coating eliminates most of the phenomena that involve a chemical reaction or diffusion. A good mechanical deformation resistance of the tool is therefore of utmost importance. The tool wear depends on the type of work. Two main types of machining can be considered: continuous cutting, carried out mainly in turning, and interrupted cuts made in milling.

Below, a semiquantitative model of tool wear is presented. Such model relates particularly to cemented carbides for which experimental data are more abundant. Given the similarities in the evolution of mechanical behavior, these models could well be extended to the cermet.

1.14.6.1 Continuous Cut

If we trace the life of cutting tool T (VB for a given wear rate—usually 0.3 mm flank wear) versus the cutting speed V on a logarithmic plot, we obtain the curve shown in **Figure 18** (Verein Deutscher Ingenieure, 1976) where we can relate the various segments to different wear processes. A process may dominate others in a specific range of cutting speeds. In fact, the main parameter that varies with the cutting speed is temperature. As the temperature increases with speed, thermally activated processes can begin to control the wear.

The curve presented in **Figure 18** shows a peak in the wear life of the tool, and then, in the domain of high-speed cutting known as Taylor's domain, the tool life decreases rapidly. At high speed, the tool life (in log scale) compared to the logarithm of the cutting speed is often approximated by a linear dependence. In practice, the ancient Taylor's equation (Taylor, 1907) is often used to evaluate the tool life:

$$V \cdot T^n = C \qquad (2)$$

where n is the Taylor exponent, V is the cutting speed, T is the tool life and C is the constant. The exponent n is strongly influenced by the presence of a liquid lubricant and depends on temperature. Colding and König

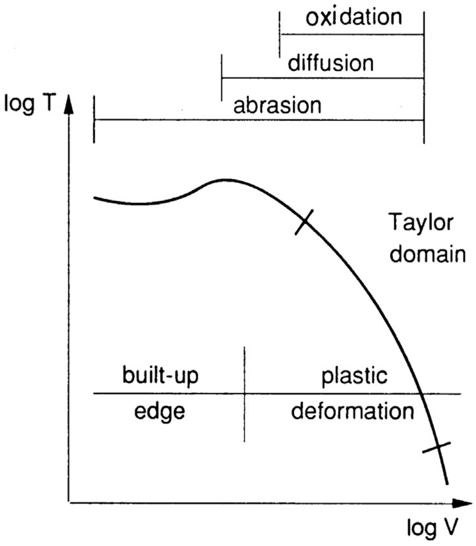

Figure 18 Life of the tool as a function of cutting speed (Verein Deutscher Ingenieure, 1976) and mechanisms of wear.

(1971) have shown that if a sufficient range of cutting speeds is considered, the curve log T–log V in the Taylor domain is not a straight line. This indicates that even in the Taylor region, different mechanisms may be active and therefore can dominate a side or the other of the Taylor curve, according to the range of temperature.

Mari and Gonseth (1993) proposed a model of wear that associates the temperature zones, which mark the changes of mechanical properties of WC–Co (**Figure 17**), with the domains observed in the tool life depending on cutting speed. The fundamental hypothesis of the model was that the tool wear depends largely on the energy dissipated E_{diss} in the tool itself. This energy is in part causing a surface temperature increase (related to traditional friction) and in part is related to the dissipative phenomena such as thermally activated plastic deformation of the tool. E_{diss} can be decomposed into

$$E_{\mathrm{diss}} = E_{\mathrm{fr}} + E_{\mathrm{ta}} \tag{3}$$

It is noteworthy that the main source of the temperature increase of the tool is the heat that comes from chipping. It can be assumed that achieving a level of wear given by VB = constant is associated with a tool life T corresponding to a total dissipated energy threshold E_{C}. Using a model of the relationship between temperature and cutting speed and assuming that at a certain temperature, the wear is dominated by thermally activated phenomena, it was shown (Mari & Gonseth, 1993) that

$$T = \frac{E_{\mathrm{C}}}{\alpha V + \beta \cdot e^{\frac{-Q}{k\theta}}} \tag{4}$$

where V is the cutting speed and θ is the temperature. This equation is similar to that obtained by Koren (1977) on the basis of an empirical model. In the model by Mari and Gonseth however, the adjustable parameters of Eqn (4) have a physical meaning and can be connected to the parameters that characterize the mechanical properties of WC–Co as, for example, the activation energy for creep. Colding and König (1971) made extensive measurements of wear in cemented carbide tools. In the example shown in **Figure 19**, some data referring to cutting tools ISO-P10 (often similar in terms of composition to the WC–11 wt% Co) are fitted by the model described by Eqn (4). The activation energies obtained from the fits range between 1 and 3.5 eV. They correspond rather well, given the equivalent tool temperature with those measured by creep tests or by mechanical spectroscopy.

The values of activation energy of 2.5 and 3.5 eV correspond to the ranges of temperature II and III. The mechanisms of plastic deformation identified in Section 1.14.4.2 (**Figure 17**) can therefore be associated with the tool wear: deformation of cobalt in zone II and deformation of the WC in zone III. The energy of 1 eV (zone I) can be attributed to an oxidation process. Colding and König (1971) were able to correlate the extent of wear of WC–Co with the penetration of oxygen measured in the diffusion of radioactive isotopes. In effect, the oxidation of WC has an energy of activation between 1 (Gumnitskii, Pelekh, & Givlyud, 1989) and 1.6 eV (Larikov, Tishkova, Tyshkevich, & Shmatko, 1990).

A model similar to that adopted for continuous cutting was developed in order to justify the typical wear obtained in cutting tools during milling called *comb cracking* (Mari & Gonseth, 1993). Comb cracking usually appears on the rake face of the cutting tool, perpendicular to the cutting edge. It is the most important source of wear in interrupted cutting. There are several arguments that permit us to say that comb cracks are due to thermal fatigue.

1. They appear only in interrupted cutting, where there is a cycle of heating and cooling during cutting and idling, respectively. Moreover, they appear while exiting from the workpiece and not during the cutting period.
2. The predominant mechanical forces acting on the cutting edge during cutting are perpendicular to it, so that the cracks, due to the mechanical stress, should be parallel to the cutting edge. Instead, comb cracks (**Figure 20**) are perpendicular to the cutting edge, so they can hardly be attributed to mechanical stress during cutting.

However, plastic deformation plays a fundamental role in the wear mechanism. Two subsequent processes participate to comb cracking (**Figure 21**). First, the surface of the tool reaches a temperature higher than the substrate during cutting. The surface is compressed by the substrate, which is cooler, and deforms shrinking. This deformation enhances the effect produced during idling: the surface, which cools more rapidly than the substrate is under tension and creep cracks are generated below the surface of the tool. The pull-out of the carbide grains around these cracks gives rise to the formation of the grooves that are characteristic of comb cracking.

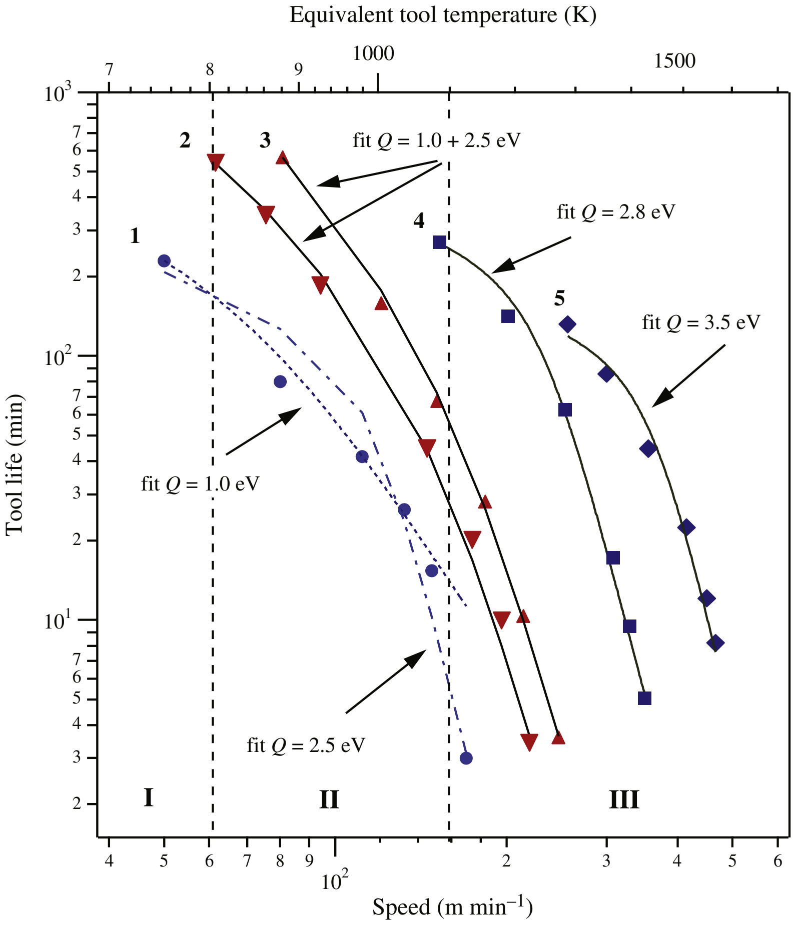

Figure 19 Measurement of tool life as a function of speed of a P10-type tools according to the criterion VB = 0.3 mm (Colding & König, 1971). The temperature equivalent to the speed is shown on the abscissa. The model given by Eqn (4) is valid in a limited range of temperature because the activation energies increase with the temperature. Therefore, curves 2 and 3 are obtained by the superimposition of two characteristic activation energies.

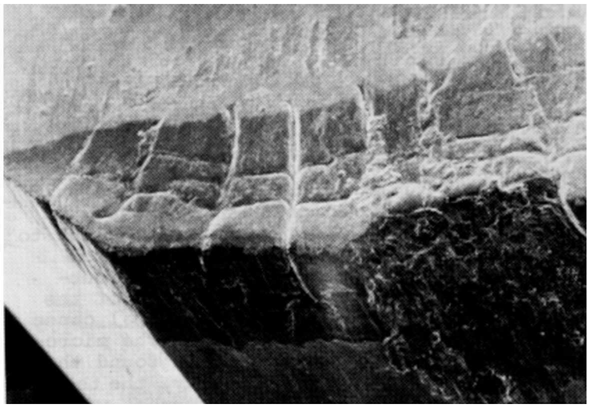

Figure 20 Edge of TiC–WC–Mo–Ni cermet after milling cast iron at 420 m min^{-1}. Uehara (1981).

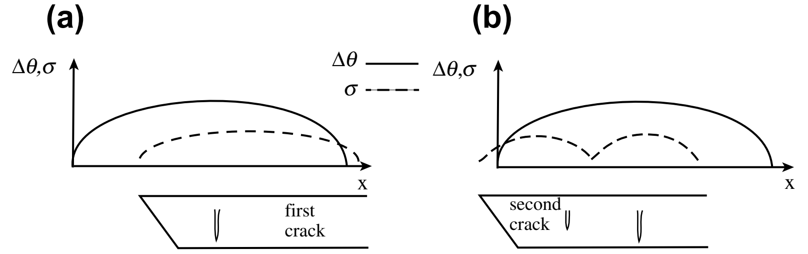

Figure 21 Schematic view of the process of comb cracking. The temperature profile $\Delta\theta$ corresponds with the thermal stress gradient. (a) The plastic deformation occurs at the maximum of the stress profile and initiates the crack formation. (b) When the crack is formed stress is relaxed and the new cracks will form on secondary stress maxima.

1.14.7 Conclusions

The high-temperature mechanical properties of cemented carbides and cermets are characterized by a substantial plastic deformation. Different domains of behavior can be envisaged as a function of temperature, each one characterized by a specific mechanism.

1. In a range between 500 and 800 °C, the deformation is controlled by the metal binder. The deformation is limited by the presence of a stiff ceramic skeleton.
2. In a range between 800 and 1000 °C, the plastic deformation of the bulk ceramic grains may be observed in particular in the hardmetals that contain cubic carbides.
3. At high temperature, above 900 °C, extended plastic deformation is observed mainly due to the opening or slide of the grain boundaries of the ceramic skeleton. Such phenomenon is generally enhanced by the binder infiltration into the grain boundaries.

The plastic deformation of hardmetals is the main source of wear in high-speed cutting. A model taking into account the different mechanisms of deformation and their activation energies can be elaborated in order to account for the wear rate of the cutting tool. In interrupted cutting, such as milling, the interplay between thermal stress and plastic deformation leads to a characteristic wear pattern formed by comb cracks.

References

Armstrong, R. W. (2011). The hardness and strength properties of WC–Co composites. *Materials, 4*, 1287–1308.

Bolognini, S., Feusier, G., Mari, D., Viatte, T., & Benoit, W. (2003). TiMoCN based cermets: high temperature deformation. *International Journal of Refractory Metals and Hard Materials, 21*, 19–29.

Buss, K., & Mari, D. (2002). Published. *High temperature deformation of cermets and cemented carbides with same amount of binder phase*. EPMA Euro PM 2002, Lausanne.

Chun, D. I., & Kim, D. Y. (1993). Microstructural evolution during the sintering of TiC–Mo–Ni cermets. *Journal of the American Ceramic Society, 76*, 2049–2052.

Colding, B., & König, W. (1971). Validity of the Taylor equation in metal cutting. *Annals of the C.I.R.P., 19*, 303–309.

Cutard, T., Viatte, T., Feusier, G., & Benoit, W. (1996). Microstructure and high temperature mechanical properties of TiC$_{0.7}$N$_{0.3}$–Mo$_2$C–Ni cermets. *Materials Science and Engineering: A, 209*, 218–227.

Fährmann, M. (1989). High temperature creep of Ti(C, N) based cermets. *International Journal of Refractory Metals and Hard Materials, 8*, 219–223.

Published Fantozzi, G., Mohand, H. S., & Orange, G. (1986). High temperature mechanical behaviour of WC–6 wt% Co cemented carbide. In E. A. Almond, C. A. Brookes, & R. Warren (Eds.), *2nd Int. Conf. Science Hard Mater., 1984 Rhodes. Inst. Phys. Conf. Ser. N.75* (pp. 699–712). Adam Hilger Ltd.

Gumnitskii, Y. M., Pelekh, M. P., & Givlyud, N. N. (1989). Special features of kinetics of high-temperature oxidation of VK8VK alloy. *Soviet Materials Science, 24*, 458–463.

Hall, E. O. (1951). The deformation and aging of mild steel: III discussion of results. *Proceedings of the Physical Society B, 64*, 747–753.

Han, X., Sacks, N., Milman, Y. V., & Luyckx, S. (2009). On plastic deformation mechanisms of WC–15 wt% Co alloys at 1000 °C. *International Journal of Refractory Metals and Hard Materials, 27*, 274–281.

Hauser, C. (1980). Technologie et quelques problemes lies au revetement. *Wear, 62*, 59–82.

Published Heuer, A. H., Sears, J. S., & Zaluzec, N. J. (1986). Analytical electron microscopy of phase separated Ti/Mo cemented carbides and carbonitrides. In E. A. Almond, C. A. Brookes, & R. Warren (Eds.), *2nd Int. Conf. Science Hard Mater., 1984 Rhodes* (pp. 321–334). Bristol: Adam Hilger.

Hollox, G. E., & Smallman, R. E. (1966). Plastic behavior of titanium carbide. *Journal of Applied Physics, 37*, 817–823.

Koren, Y. (1977). *Flank wear model of cutting tools using control theory*. ASME.

Kramer, B. M., & Suh, N. P. (1980). Tool wear by solution – a quantitative understanding. *Journal of Engineering for the Industry Transactions of the ASME, 102*, 303–309.

Larikov, L. N., Tishkova, T. T., Tyshkevich, V. M., & Shmatko, O. A. (1990). Study of the kinetics of oxidation of W–Co and WC–Co alloys. *Protection of Metals, 25*, 524–526.

Laugier, M. T. (1986). A microstructural model relating fracture toughness and hardness in WC–Co composites. *Powder Metallurgy International, 18*, 330–332.

Lay, S., Vicens, J., & Osterstock, F. (1987). High temperature creep of WC–Co alloys. *Journal of Materials Science, 22*, 1310–1322.

Lee, M. (1983). High temperature hardness of tungsten carbide. *Metallurgical Transactions A, 14*, 1625–1629.

Lindahl, P., Mainert, T., Jonsson, H., & Andrén, H.-O. (1993). Microstructure and mechanical properties of a (Ti, W, Ta, Mo)(C, N)-(Co, Ni)-type cermet. *Journal of Hard Materials, 4*, 187–204.

Lindau, L., & Stjernberg, K. G. (1976). Grain growth in TiC–Ni–Mo and TiC–Ni–W cemented carbides. *Powder Metallurgy, 4*, 210–213.

Lui, M., Huang, X., Duan, S., Shao, D., Cui, Y., & Yao, Z. (1983). Diffraction-contrast study of microstructure and deformation process of WC–Co cemented carbide. *International Journal of Refractory Metals and Hard Materials, 2*, 129–132.

Mari, D. (2001). *Cermets and hardmetals. Encyclopedia of materials*. Amsterdam: Elsevier Science Publisher Pergamon Press.

Mari, D. (2009). Understanding the mechanical properties of hardmetals through mechanical spectroscopy. *Materials Science and Engineering: A, 521–522*, 322–328.

Mari, D., Bolognini, S., Feusier, G., Viatte, T., & Benoit, W. (1999). Experimental strategy to study the mechanical behaviour of hardmetals for cutting tools. *International Journal of Refractory Metals and Hard Materials, 17*, 209–225.

Mari, D., & Gonseth, D. R. (1993). A new look at carbide tool life. *Wear, 165*, 9–17.

Mari, D., Marti, U., & Silva, P. C. (1992). A new photolithographic technique to detect the local deformation of materials: application to WC–Co composites. *Materials Science and Engineering: A, 158*, 203–206.

Milman, Y. V., Luyckx, S., Goncharuck, V. A., & Northrop, J. T. (2002). Results from bending tests on submicron and micron WC–Co grades at elevated temperatures. *International Journal of Refractory Metals and Hard Materials, 20*, 71–79.

Milman, Y. V., Luyckx, S., & Northrop, I. (1999). Influence of temperature, grain size and cobalt content on the hardness of WC–Co alloys. *International Journal of Refractory Metals and Hard Materials, 17*, 39–44.

Mingard, K. P., Roebuck, B., Marshall, J., & Sweetman, G. (2011). Some aspects of the structure of cobalt and nickel binder phases in hardmetals. *Acta Materialia, 59*, 2277–2290.

Okuyama, K., & Sakuma, T. (1995). High temperature plastic flow in TiC–20 wt% Mo_2C–20 wt% Ni cermet. *Material Sciences and Engineering: A, 194*, 63–68.

Östberg, G., & Andrén, H.-O. (2006). Microstructural changes during wear by plastic deformation of cemented carbide and cermet cutting inserts. *Metallurgical and Materials Transactions A, 37*, 1495–1506.

Östberg, G., Buss, K., Christensen, M., Norgren, S., Andrén, H.-O., Mari, D., et al. (2006a). Effect of TaC on plastic deformation of WC–Co and Ti(C, N)–WC–Co. *International Journal of Refractory Metals and Hard Materials, 24*, 145–154.

Östberg, G., Buss, K., Christensen, M., Norgren, S., Andrén, H.-O., Mari, D., et al. (2006b). Mechanisms of plastic deformation of WC–Co and Ti(C, N)–WC–Co. *International Journal of Refractory Metals and Hard Materials, 24*, 135–144.

Petch, N. J. (1953). The cleavage strength of polycrystals. *Journal of the Iron and Steel Institute, 174*, 25–28.

Sakuma, T., & Hondo, H. (1992). Plastic flow in WC–13 wt% Co at high temperature. *Materials Science and Engineering: A, 156*, 125–130.

Sarin, V. K., & Johannesson, T. (1975). On the deformation of WC–Co cemented carbides. *Metal Science Journal, 9*, 472–476.

Schaller, R., Mari, D., Maamouri, M., & Ammann, J. J. (1992). Mechanical behaviour of WC–11 wt% Co studied by bending tests, internal friction and electron microscopy. *Journal of Hard Materials, 3*, 351–362.

Sigl, L. S., & Fischmeister, H. F. (1988). On the fracture toughness of cemented carbides. *Acta Metallurgica, 36*, 887–897.

Smith, J. T., & Wood, J. D. (1968). Elevated temperature compressive creep behavior of tungsten carbide–cobalt alloys. *Acta Metallurgica, 16*, 1219.

Suh, N. P. (1986). *Tribophysics*. Englewood Cliffs, NJ: Prentice Hall.

Suzuki, H., Hayashi, K., & Kubo, Y. (1980). Bend-deformation characteristics of TiC-base cermet at elevated temperatures. *Journal of the Japan Society of Powder and Powder Metallurgy, 27*, 266–270.

Suzuki, H., Hayashi, K., Matsubara, H., & Tokumoto, K. (1983). High temperature strength of TiC–Mo_2C–Ni alloys containing nitrogen. *Journal of the Japan Society of Powder and Powder Metallurgy, 30*, 106–111.

Suzuki, H., Hayashi, K., & Taniguchi, Y. (1979). Effects of domain size of binder phase on high temperature strength of WC–Co cemented carbides. *Planseeberichte für Pulvermetallurgie, 27*, 215–222.

Suzuki, H., Hayashi, K., Taniguchi, Y., & Matsubara, H. (1982). The bend deformation of WC–Co cemented carbides at temperatures up to 1273 K. *Transactions of the Japan Institute of Metals, 23*, 77–84.

Suzuki, H., Hayashi, K., & Yamamoto, T. (1978). High temperature transverse-rupture strength of TiC-base cermets. *Journal of the Japan Society of Powder and Powder Metallurgy, 25*, 136–140.

Taylor, F. W. (1907). On the art of cutting metal. *Transactions of the American Society of Mechanical Engineers, 28*, 31–279.

Ueda, F., Doi, H., Fujiwara, F., & Masatomi, H. (1977). Bend deformation and fracture of WC–Co alloys at elevated temperatures. *Transactions of the Japan Institute of Metals, 18*, 247–256.

Uehara, K. (1981). Fundamental approach to the thermal crack of cermet cutting tools. *Annals of the C.I.R.P., 30*, 47–51.

Verein Deutscher Ingenieure Richtlinie 3321, Blattl, VDI-Verlag, Diisseldorf, (1976).

Williams, W. S. (1964). Influence of temperature, strain rate, surface condition, and composition on the plasticity of transition-metal carbide crystals. *Journal of Applied Physics, 35*, 1329–1338.

Wirmark, G., Dunlop, G. L., & Chatfield, C. (1986). Tensile creep of WC–Co cemented carbides at 800–900 °C. *International Journal of Refractory Metals and Hard Materials, 5*, 153–157.

Wolfe, C. F., & Williams, W. S. (1986). Plastic deformation of TiC/Ni–Mo composites at high temperature. In E. A. Almond, C. A. Brookes, & R. Warren (Eds.), *2nd Int. Conf. Science Hard Mater., 1984 Rhodes* (pp. 691–697). Bristol: Adam Hilger.

SECTION V

APPLICATIONS

1.15 Cemented Carbides for Mining, Construction and Wear Parts

Igor Konyashin, Element Six Hard Materials, Element Six GmbH, Städeweg, Burghaun, Germany

Glossary Terms and Definitions

TRS Transverse rupture strength

HV Vickers hardness

K_{1C} Palmquist fracture toughness

E6HM Element Six Hard Materials

1.15.1 Introduction

The invention of tungsten carbide–cobalt (WC–Co) cemented carbides by K. Schröter in Germany in 1922 was one of the most important technological revolutions of the twentieth century. In the late 1920s and early 1930s, cemented carbides were produced by Friedrich Krupp AG (Germany) and employed mainly in metal cutting and wire drawing. One of the major reasons for a limited application of cemented carbides at that time was presumably their very high price, which was nearly US \$1 g^{-1} WC–Co, so that they were more expensive than gold. Nevertheless, even in the 1930s, there were first attempts by Friedrich Krupp AG to employ cemented carbides for mining and construction tools (Kolaska, 1992a, 1992b), which were coal borers, rotary drills, bits for salt and coal mines, chain trenchers, etc.

The intensive research and development (R&D), and continuous progress in improvement of the cemented carbide technology significantly lowered the price of cemented carbides in the late 1930s and early 1940s. In the early 1930s, the production of WC–Co cemented carbides was started in Sweden on a large scale, presumably because the Schröter's patents were applied only in Germany, Great Britain and the USA and the priority date in other countries was missed. The importance of mining industry in Sweden obviously caused intensive research on the possibility of employing WC–Co cemented carbides in mining tools for rock drilling, so that the first experimental production of cemented carbide rock drilling tools was started at Seco in Sweden in 1940 (see the

http://dx.doi.org/10.1016/B978-0-08-096527-7.00015-5

Internet site of Seco Tools). Cemented carbide-coated rock drills were developed by Sandvik, another Swedish company, in 1942 and cemented carbide-tipped rock drills were used by this company for the first time in 1944 (see the Internet site of Sandvik). Kennametal Inc. (USA) began to develop tools for the mining industry in the middle of the 1940s and a new plant was built in Bedford, Pennsylvania for the production of these mining tools (see the Internet site of Funding Universe, Kennametal Inc., Company History). In the early postwar years, cemented carbide-tipped drill steels for mining were imported mainly from Sweden to various countries and even became known as “Swedish steel” (Howard, 1996). Cemented carbides for mining started spreading all over the world at this time and a factory for production of cemented carbides and mining tools was built by Boart in South Africa in 1949. This factory is now a part of the Element Six Hard Materials (E6HM).

The use of cemented carbides by the construction industry for drilling stone and concrete as well as for tunneling and similar operations were presumably started also in the postwar period, as these applications are similar to rock drilling. The dramatic increase in the demand on cemented carbide tools for construction was related to the development of technology of road repairing based on cold milling instead of hot milling in the 1970s (see the Internet site of the Wirtgen Group). As a result of this, road-planing picks with carbide tips were developed, which are now produced on a scale of nearly 55 million picks annually.

There is no information in the literature on the first employment of cemented carbides as wear parts. Nevertheless, it can be expected that this was related to a significant decrease of the cemented carbide price and dramatic growth of the total carbide production in the 1940s.

By 2013, the estimated proportion of cemented carbides for mining, oil drilling and tunneling is 13% and for construction is 9% in the whole cemented carbide production according to Upadhyaya (1998). According to Schubert, Lassner and Böhlke, the estimated portions of the worldwide consumption of cemented carbides are as follows: wear applications—17%, stone working—26%, and the rest is wood and plastic working, chipless forming and metal cutting (see the Internet site of International Tungsten Industry Association, ITIA).

1.15.2 Special Features of Applications of WC–Co Cemented Carbides in Mining, Construction and as Wear Parts

Cemented carbides are widely employed for exploitation drilling on oil and gas, geotechnical works, coal and ore mining and different construction works, such as tunneling, road planing, trenching, soil stabilization, and so on. Two following major fields of application of cemented carbides in mining and construction can be distinguished: (1) drilling holes and wells by use of drilling bits and (2) cutting rock, asphalt and concrete by use of picks. The application conditions of cemented carbides for mining and construction are described in detail in the two following books on cemented carbides (Kolaska, 1992a, 1992b; Panov, Chuvilin, & Falkovsky, 2004).

1.15.2.1 Rock Drilling

Drilling of holes and wells can be divided into the four following application ranges: (1) rotary drilling and overburden drilling by use of cutters or bits; (2) percussive drilling; (3) rotary percussive drilling; and (4) rotary drilling by use of roller-cone bits.

Rotary drilling of the first type is typically used for making holes in rocks before blasting. Rocks of low to medium hardness and toughness, such as mineral salts, ores, coal, and so on, are usually subjected to rotary drilling by use of cutters or bits. Typical drilling bits and cutters for rotary drilling and overburden drilling are shown in Figure 1(a). The bits comprise carbide plates or inserts brazed to steel bodies, which rotate without percussion and cut the rock or coal. In this case, rock or coal is destroyed by mainly compression, crushing and cutting. The rotation speed usually varies from nearly 100 revolutions min^{-1} in rock up to 1500 revolutions min^{-1} in coal. There is a certain value of force applied to the bit needed to overcome the rock toughness and get a certain rate of penetration into the rock. After obtaining certain wear of carbide plates, they have to be reground to maintain the penetration rate. Bits for overburden drilling, which are mainly employed for geotechnical drilling, work similarly. In rotary drilling, cemented carbides are subjected to compression and bending stresses, as well as to abrasive wear and thermal shock. In some cases, e.g. in cutting mineral salts, water cooling is unacceptable, so that air cooling is used, which can lead to high contact temperatures on cutting edges.

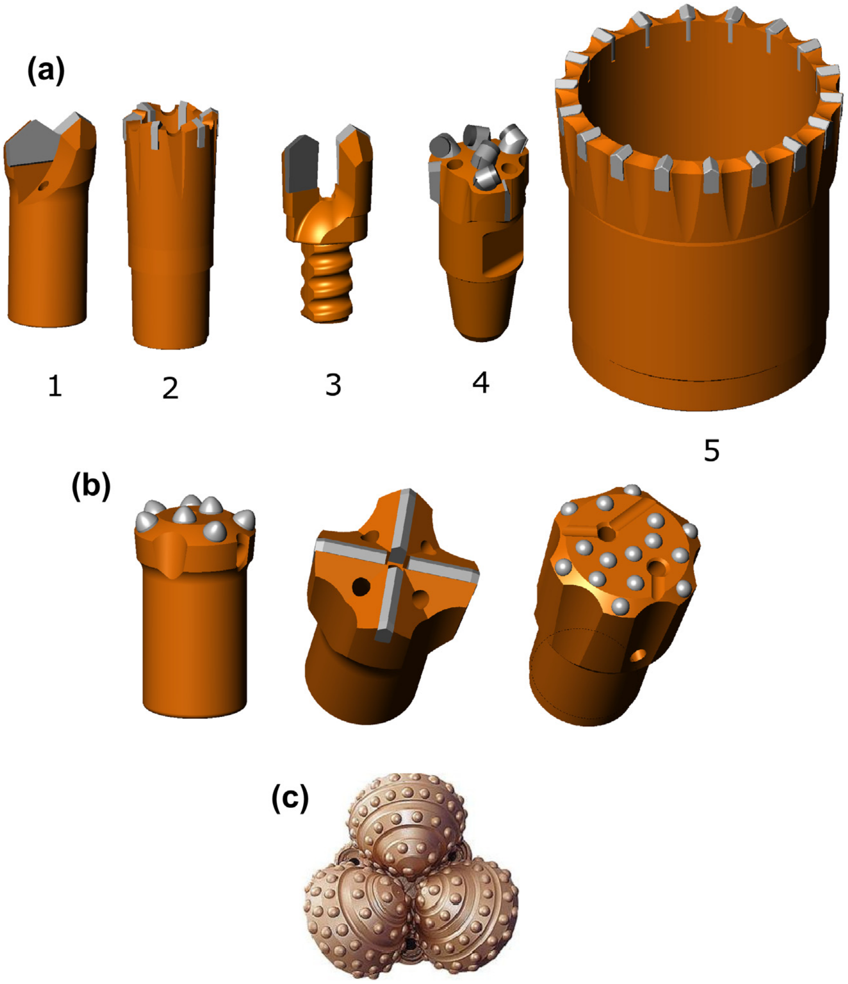

Figure 1 Typical bits for rock drilling: (a) 1–3—bits for rotary drilling with carbide plates, 4—bit for rotary drilling with carbide/PCD (polycrystalline diamond) cutters, and 5—a bit for overburden drilling; (b) typical bits for percussive drilling; and (c) a typical roller-cone bit for rotary drilling. (a and b) Redrawn from the brochure and with permission of Element Six Hard Materials.

Percussive drilling is employed for degradation of rocks with medium to very high hardness and performed by creating high-impact loads on the rock surface as a result of percussion. The bit strikes the rock and rotates at a certain speed to move the position of carbide insert or plate to another part of rock; the typical bit blow frequency is 2000–3000 blows/min and the rotation speed is 50–150 revolutions/min. Typical percussive drilling bits with carbide plates or inserts are shown in Figure 1(b). Carbide plates are usually brazed (Chapter 1.12 "Joining"); inserts are pressed into steel bodies at elevated temperatures, which allows formation of residual compression stresses between the steel body and insert after cooling down to room temperature. The major mechanism of rock degradation in percussion drilling is the formation of micro- and macrocracks in the rock under high-energy stroke and high compressive stress leading to rock crushing and chip formation. In some cases, e.g. in drilling iron ores, high contact temperatures on the carbide surface can occur leading to severe thermal shock and thermal fatigue.

Percussive rotary drilling is a combination of rotary and percussive methods. A chisel bit is used, as in percussive drilling, but the bit is held against the rock surface under considerable load and tuned between the impacts. The tool wedge angle is often nearly 90° and its axis forms an oblique angle with the rock face to give an acceptable rake angle for the cutting action. The impact removes some material directly and also forms cracks that facilitate chip formation in the cutting part of the cycle. The wear rate lies between the rates for rotary and percussive drilling, and percussive rotary drilling is therefore useful for application to rocks that are too abrasive for rotary drilling. The bit remains for most of the time under compression and higher impact energies can be employed than in strait percussive drilling. Another type of percussive rotary drilling is down the hole drilling, which is characterized by the presence of pneumatic or hydraulic shock workers directly near the drilling bit.

Rotary drilling performed by roller-cone bits is employed for drilling holes of large diameters, which are needed for oil and gas drilling or surface drilling of large holes, e.g. in iron-ore quarries. An example of roller-cone bits is shown in Figure 1(c). The roller cones rotate together with the drill rod and cut the rock without percussion under pressure provided by the drill rod from the surface. Carbide inserts situated on the surface of the roller cones penetrate into the rock under pressure and crush it. In this case, carbide inserts having a relatively long conical part are used, so that bending loads on them are high.

The mechanism of wear of cemented carbides in rock drilling was examined in detail and is presently well understood. The results on the carbide wear in rock drilling are summarized by Larsen-Basse (1973). Important new results on the deterioration and wear of cemented carbides in rock drill bits were obtained by Beste et al. (2008). The most important macromechanisms of wear behavior of WC–Co in rock drilling are the following:

- Impact spalling
- Impact fatigue spalling
- Sliding abrasion
- Thermal fatigue.

Impact and impact fatigue wear are most important when hard rocks are drilled by percussive methods; abrasive wear is most important for drilling in softer, abrasive rocks; and thermal fatigue in most important for high-temperature-generating rocks, e.g. iron ores. Beste and Jacobson (2008a, 2008b) found that temperatures in a very thin near-surface layer of carbide inserts can reach or even exceed the melting point of quartz leading to the penetration of fine quartz particle into WC–Co and their intermixing with the Co binder of cemented carbides. According to Beste et al., the major micromechanisms of wear and degradation of cemented carbides in rock drilling, which are schematically shown in Figures 2(a)–2(e), are the following:

- Crushing of WC grains and release of fragments;
- Detachment of whole WC grains and their removal from the worn surface;
- Crushing of binder/rock mixture formed as a result of rock penetration into the binder and release of fragments;
- Tribochemical wear, scraping and pounding off of corroded or oxidized superficial layers on WC;
- Detachment of WC–Co chips comprising a number of WC grains.

Besides these mechanisms, the two following wear mechanisms can also play an important role during rock drilling:

- Extrusion and removal of the binder phase;
- Abrasion of individual WC grains.

Figure 2(f) clearly shows the binder removal, abrasion of individual WC grains, traces of detachment of whole WC grains or their agglomerates, and crushing and microchipping of WC grains as a result of percussive drilling of quartzite. It is also clearly seen in Figure 2(f) that the binder is selectively worn out leaving unsupported WC grains on the carbide surface during percussive drilling.

It should be noted that in spite of numerous studies of wear mechanisms of cemented carbides in rock drilling and cutting, the wear mechanism for one tool and one rock type is still unique, to that the particular situation cannot be usually applied to other rock tools and rock types.

1.15.2.2 Rock-, Coal-, Asphalt- and Concrete Cuttings

Rock-, coal-, asphalt- and concrete cuttings are performed by picks with cemented carbide inserts or tips. The picks are inserted in large drums or heads which rotate with a rotation speed of nearly 2–6 m/s and press on the workpiece material to obtain the cutting feed of roughly 0.2–2 m/min. Picks for cutting coal and rock as well as for trenching and soil stabilization, which are shown in Figure 3(a), are designed in such a way that they rotate either during or after each cut leading to continuous wear propagation in the whole volume of the carbide insert. The picks for road planing (asphalt cutting) shown in Figure 3(b) generally are similar to those shown in Figure 3(a) except for that they comprise a carbide tip or “cap” brazed to a steel pick body instead of a carbide insert. Road planing picks for concrete cutting comprise a carbide insert brazed into the steel pick body.

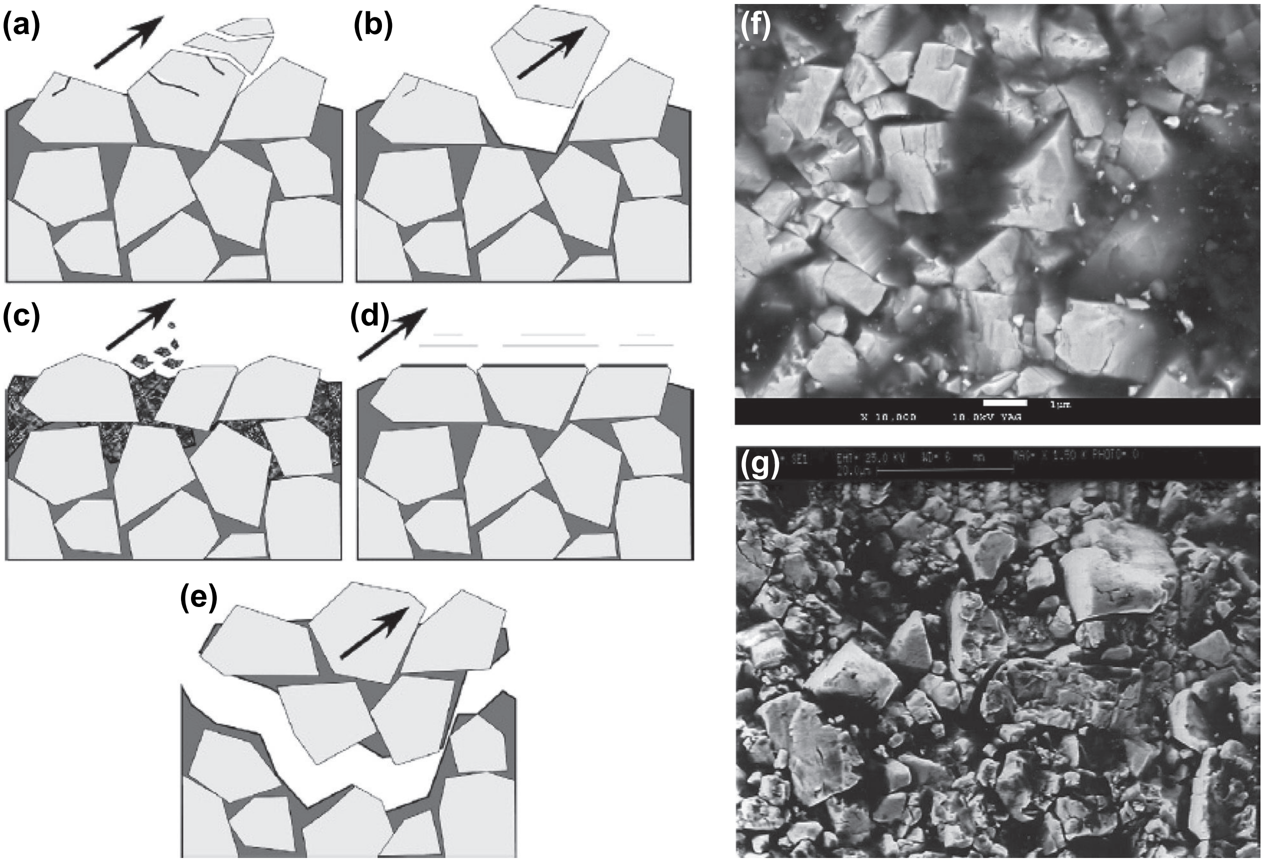

Figure 2 Schematic illustration of the five most important mechanisms of material removal in cemented carbide for rock drilling: (a) crushing of WC grains and release of fragments; (b) detachment of whole or parts of WC grains losing their hold in the microstructure; (c) crushing of binder/rock mixture after the rock penetration and release of fragments; (d) tribological wear, scraping and pounding of corroded or oxidized superficial layers on WC, and (e) detachment of composite-scale fragments. (Redrawn from Beste and Jacobson (2008a, 2008b).) (f) Typical wear pattern of coarse-grain carbide grade with 6% Co after percussive drilling of quartzite. (With the permission of Element Six Hard Materials.) (g) Dominant wear of binder interlayers in the ultra-coarse cemented carbide after road planing. Redrawn from Konyashin et al. (2005).

Cutting of rocks and asphalt leads to formation of high-impact loads, intensive abrasion and high cutting temperatures resulting in strong thermal shock and extremely severe thermal fatigue. In coal-cutting itself, the abrasion wear and thermal shock are relatively insignificant; however, in many cases, layers of coal are situated between layers of sandstone, which is an extremely heat-generating rock. Sandstone cutting leads to formation of very high cutting temperatures visible by intensive sparking, which results in severe thermal fatigue. In many cases, e.g. in tunneling, water cooling cannot be employed and only water spraying for suppression of dust formation is used, so that cutting temperatures on the carbide surface can be extremely high. As a result of this, the formation of network of thermal fatigue cracks, which are designated in the literature as "snake skin" or "reptile skin", is in many cases the major mechanism of failure of WC–Co cemented carbides. Typical thermal cracks or "snake skin" on the surface of cemented carbides after sandstone cutting and asphalt cutting are shown in Figure 4 (Konyshin et al., 2005). As it can be seen in Figure 4, the thermal cracks can easily propagate into the cemented carbide insert under the influence of high mechanical impact loads and thermal shock leading to chipping the insert and finally resulting in premature failures. It is well known that cemented carbides work also in the conditions of very severe thermal fatigue in concrete cutting.

According to Konyshin et al. (2005), another very important mechanism of wear of ultra-coarse carbide grades in rock- and asphalt cuttings is related to the presence of thick binder interlayer in their microstructure. In this case, the size of such interlayers becomes comparable with the size of fine abrasive particles present in rock- and asphalt cuttings. As a result, the binder is rapidly worn out leaving naked and unsupported WC grains on the carbide

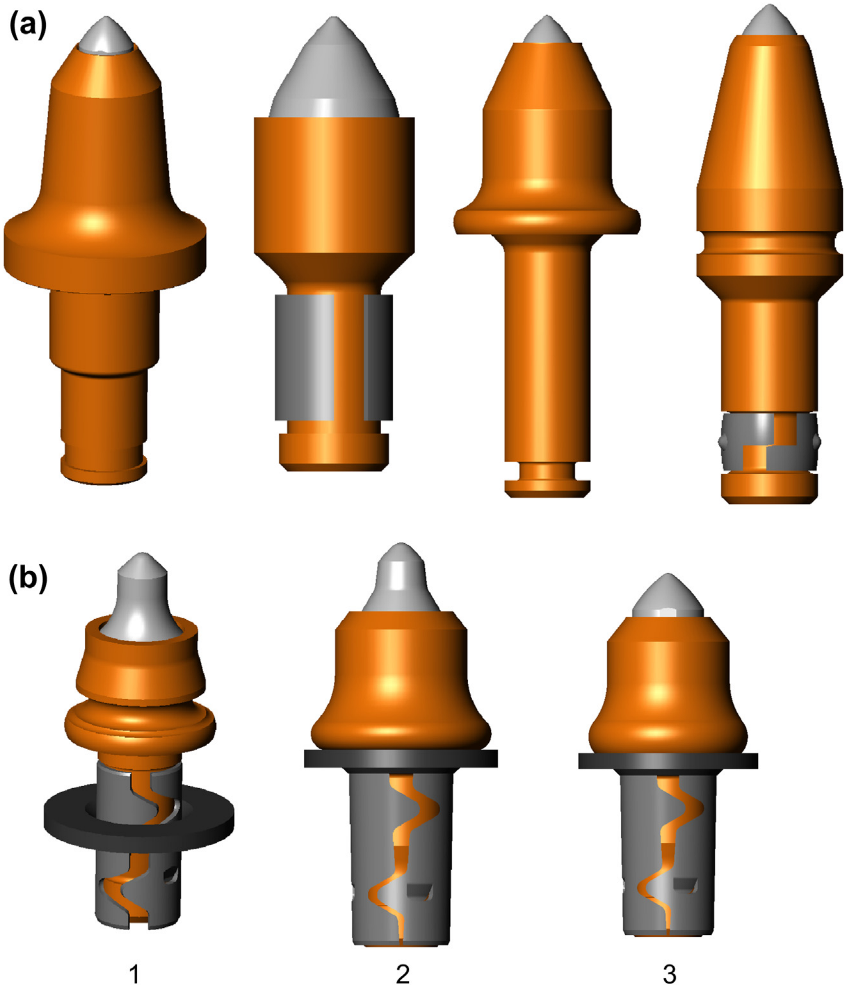

Figure 3 Typical picks for mining and construction: (a) round shank picks for tunneling, coal mining, trenching, etc. (b) picks for road planing: 1 and 2—picks for asphalt planing and 3—pick for concrete planing. Redrawn from the brochure and with permission of Element Six Hard Materials.

surface, which is shown in Figure 2(g). Such unsupported WC grains can be easily cracked, destroyed and pulled out during rock or asphalt degradation resulting in rapid wear of the whole cemented carbide insert.

1.15.2.3 Wear Parts

Figure 5 shows schematically some wear parts made of cemented carbides. The cemented carbide wear parts are employed in machines, equipment or tools, where some components are subjected to intensive abrasion and/or erosion. Numerous carbide wear parts include, for example, valves of pumps operating in abrasive media, nozzles and blades of sand-blasting equipment, nozzles of paint-spraying equipment, molds for pressing plastics, ceramics, bricks and tiles, etc. In many cases, e.g. in molds for pressing, the fracture toughness of cemented carbides does not play an important role, so that carbide grades with high hardness and relatively low fracture toughness can be employed. In some applications, where wear parts are subjected to impact loads, medium-grained grades with relatively low hardness but high fracture toughness are used. Wear parts made of cemented carbides vary from very small articles, such as balls for ball-point pens, to large and heavy parts, such as punches, dies or large valves for pumps for the oil and gas industry with weights of up to 100 kg. The shape and geometry of wear parts are generally limited by the necessity of producing them from WC–Co powders. Nevertheless, the limitations can be overcome by use of fine diamond grinding, polishing, wire erosion, as well as by diffusion bonding of sintered and ground carbides articles to produce large hollow parts with complicated channels.

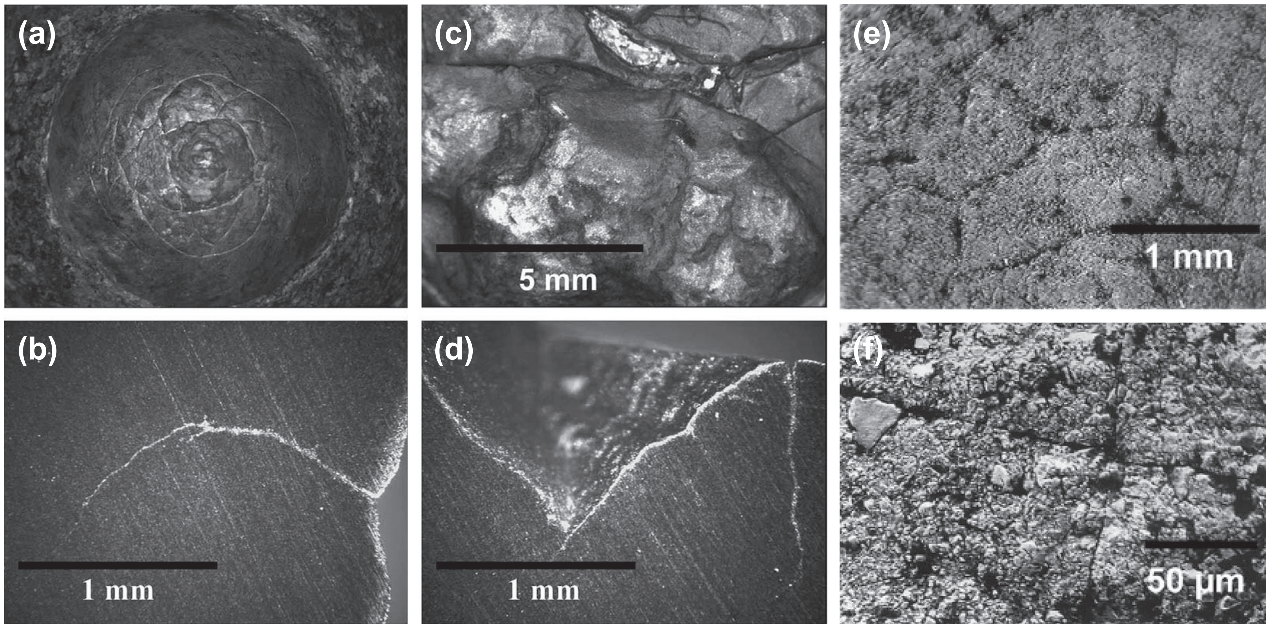

Figure 4 (a and c) Thermal cracks on the surface of a coal-cutting pick ("snake skin"). (b and d) Failures formed as a result of the propagation of thermal cracks into cemented carbides. (e and f) Thermal cracks on the surface of road-planing picks. Redrawn from Konyshin et al. (2005).

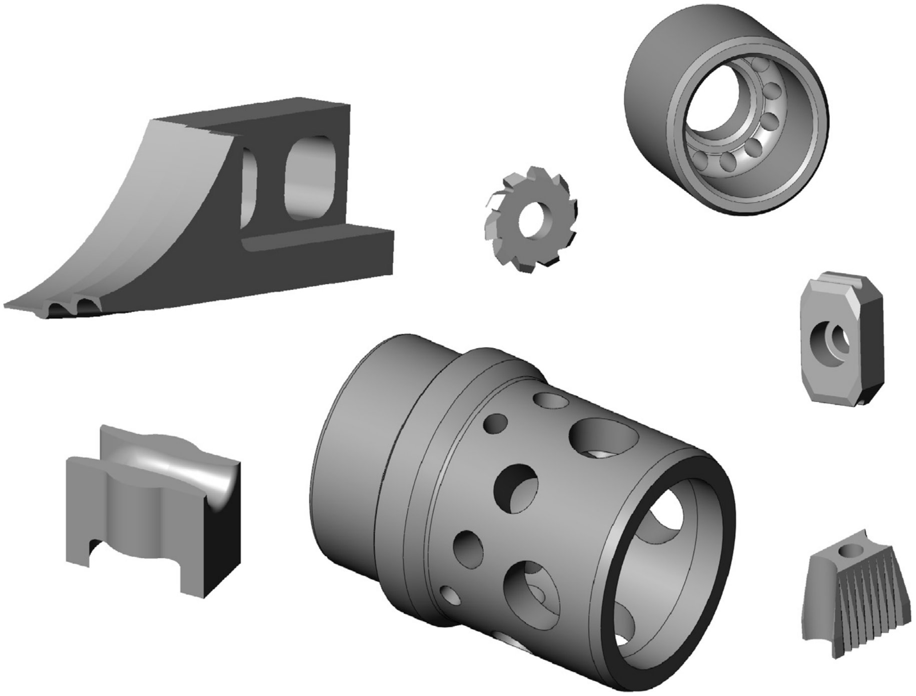

Figure 5 Typical cemented carbide wear parts. Redrawn from the brochure and with the permission of Element Six Hard Materials.

1.15.3 Basic Industrial Cemented Carbides for Mining and Construction

It is well known that the major parameters of WC–Co cemented carbides influencing their hardness, fracture toughness, compressive strength, transverse rupture strength (TRS) and other properties are the Co content and WC mean grain size. Besides the Co content and WC mean grain size, some other characteristics of WC–Co materials, which will be described below, play also an important role with respect to obtaining the best combination of physical, mechanical and performance properties of cemented carbides for each concrete application of mining and construction.

1.15.3.1 Co Content and WC Mean Grain Size

The majority of industrial WC–Co carbide grades for mining and construction with different combinations of properties are fabricated by varying the Co content and WC mean grain size. The influence of Co content and WC mean grain size on mechanical and performance properties of WC–Co cemented carbides was examined in numerous publications, and these results were summarized in the book of Kreimer (1968) and the review article of Exner and Gurland (1970).

The fracture toughness and hardness, which are the major parameters determining the performance of cemented carbides, are known to monotonically change when varying the Co content and WC mean grain size. The fracture toughness increases and hardness decreases with increasing both the Co content and WC mean grain size and, except for some special cases, the fracture toughness can be improved only at the expense of hardness and consequently wear-resistance.

According to Kreimer (1968), the dependence of compressive strength upon Co contents of WC–Co cemented carbides with WC mean grain sizes from 1.4 to 5.3 μm is characterized by the maximum at 4.5–6 wt.% Co. In spite of the fact that the maximum compressive strength is obtained with the WC mean grain size of 1.4–1.7 μm, it was not found that the compressive strength significantly decreased when further decreasing the WC mean grain size. WC–Co cemented carbides for percussive drilling should have the optimum combination of just the compressive strength, fracture toughness and hardness, which is achievable at the Co content of 6 wt.% and WC mean grain size of nearly 1.4–1.9 μm. **Table 1** shows the typical carbide grades for percussive drilling and **Figure 6** shows the typical microstructures of cemented carbides for percussive drilling. The conventional WC–Co grade for percussive drilling button bits is, for example, T6 (E6HM), in which the Co content and WC mean grain size are compromised with respect to the optimal combination of compressive strength, fracture toughness and hardness. Typical properties of the grade are the hardness of roughly 1450 Vickers units, TRS of at least 2400 MPa, fracture toughness of above 12.7 MPa m$^{1/2}$ and compressive strength of more than 4500 MPa. Carbides grades for percussive drilling bits with brazed inserts and plates typically comprise 8–10% Co, e.g. the B20 and B25 grades (E6HM), due to the need to have a higher fracture toughness of carbide articles subjected to brazing.

According to Gurland and Bardzil (1995), the TRS of cemented carbides with 12% Co has a maximum at WC mean grain size of nearly 2.5 μm. According to Exner and Gurland (1970), the dependence of TRS on the Co mean free path is characterized by the maximum at the Co mean free path of roughly 0.3–0.6 μm. Cemented carbides for rotary drilling have to possess the optimum combination of TRS, fracture toughness and hardness, which is achievable at the Co content of more than 8% and WC mean grain size of between roughly 2 and 4 μm. **Table 1** and **Figure 6(b)** show typical grades for rotary drilling, two of which are, for example, B25 and B30 (E6HM) with 10% Co and 11% Co having a WC mean grain size of about 2.5 μm. The Co mean free path of these grades calculated by using the equation given by Schatt, Wieters, and Kiebach (2007) is equal to roughly 0.5 μm, which corresponds to the maximal TRS of WC–Co materials. Typical grades for rotary drilling are

Table 1 Industrial cemented carbide grades for mining and construction of Element Six Hard Materials

	Composition			*Hardness*				
Grade	*Co (%)*	*WC (%)*	*Grain size*	*Vickers (HV_{10})*	*Rockwell (HRA)*	*TRS (MPa^{-2})*	*Compressive strength (MPa^{-2})*	*Fracture toughness K_{1c} (MPa $m^{1/2}$)*
T6	6.0	94.0	Coarse	1450	90.6	2400	4500	12.7
B20/H8	8.0	92.0	Coarse	1250	88.7	2700	4000	14.6
BH9/H9	9.0	91.0	Coarse	1250	88.7	2600	4000	14.6
B25/G10	10.0	90.0	Coarse	1200	88.2	2800	4000	14.6
B30/J11	11.0	89.0	Coarse	1150	87.7	2700	3900	15.2
B40/G15	15.0	85.0	Coarse	1050	86.5	2800	3600	16.3
B15N	6.5	93.5	Ultra-coarse	1100	87.2	2200	3600	16.3
B20N	8.6	91.4	Ultra-coarse	1050	86.5	2300	3500	16.9
B25SN	9.5	90.5	Ultra-coarse	1050	86.5	2300	3500	16.9

With the permission of Element Six Hard Materials.

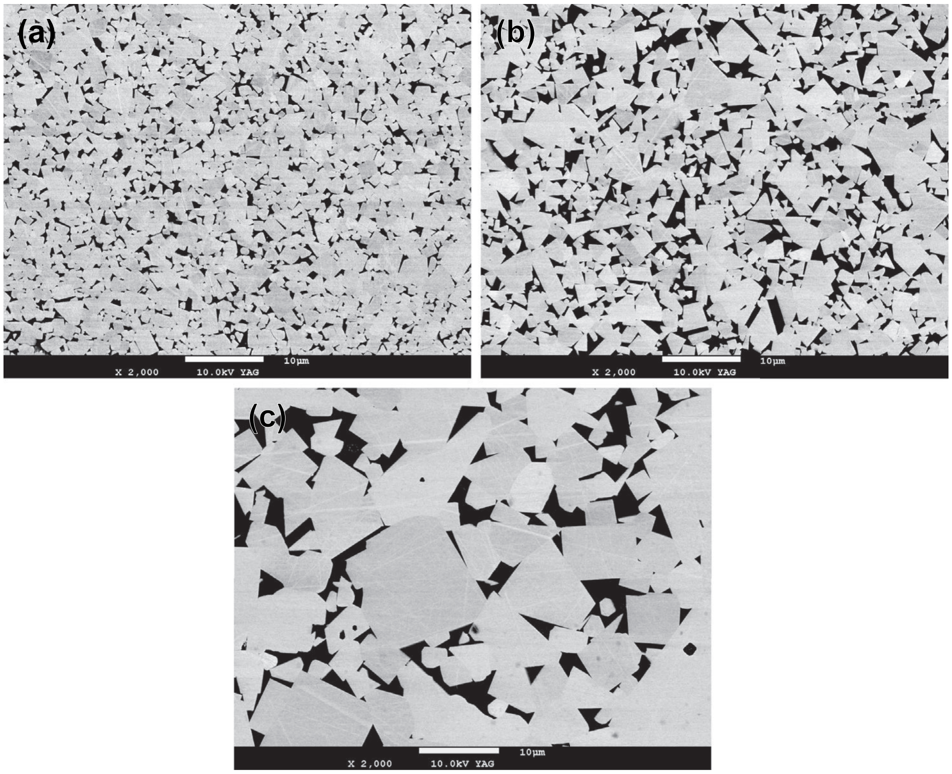

Figure 6 Typical microstructures of cemented carbides for mining and construction (2000×): (a) T6 (6% Co, coarse-grain) for percussive drilling; (b) B25 (10% Co, coarse-grain) for rotary and percussive drilling; and (c) B15N (6.5% Co, ultra-coarse-grain) for road planing. With the permission of Element Six Hard Materials.

characterized by the following properties: hardness of 1200 ± 100 Vickers units, fracture toughness of above 14.6 MPa $m^{1/2}$ and TRS of at least 3900 MPa. For some special applications, carbide grades with a higher Co content of up to 15% can be employed. Such grades are, however, characterized by a slightly decreased TRS compared to the grades with 8–12% Co, as they have a Co mean free path higher than the optimal value with respect to TRS.

Carbide grades for rock-, asphalt- and concrete cuttings have to possess a very high level of fracture toughness because of the presence of severe thermal shock and consequently thermal fatigue in these applications. Usually, ultra-coarse carbide grades with WC mean grain size of nearly 5 μm or higher and Co contents of between 6 and 11% are employed in these applications. Such grades are characterized by the extremely high fracture toughness of at least 15 MPa $m^{1/2}$ and moderate hardness of 1100 ± 100 Vickers units. Properties and microstructure of the ultra-coarse grade for road planing with 6.5% Co B15N (E6HM) are shown in Table 1 and Figure 6(c). It can be seen in Figure 6(c) that its microstructure comprises very thick Co interlayer among the ultra-coarse WC grains. This allows the nucleation and propagation of cracks to be effectively suppressed during operation resulting in the high-performance toughness. The high fracture toughness, however, is achieved at the expense of compressive strength and TRS, as the ultra-coarse grades lie on the downturn part of the curves: TRS—Co mean free path, and compressive strength—Co content. The typical TRS value for the ultra-coarse grades with 6–10% Co is nearly 2300 MPa and compressive strength value is roughly 3500 MPa.

It should be noted that the ultra-coarse grades are relatively "young" in comparison with the other grades for mining and construction, which were developed in the 1950s and 1960s. The origin of ultra-coarse grades goes back to the 1980s when the so-called "macrocrystalline thermit process" or "Menstruum process" was developed and patented by Kennametal Inc. (Terry, 1989). According to the process, ore concentrates or other sources of tungsten (WO_3) are reduced or carburized, simultaneously, in a thermit reaction with aluminum as the reducing agent or fuel, and CaC_2 as a source of carbon for the carburization of the tungsten metal. As a result, a very coarse WC powder with grain size of up to 100 μm is produced. Such a powder can be milled to various sizes for production of cemented carbides for mining bits, coal mining, road construction, and so on

(Terry & Morris, 1999). Cemented carbides with ultra-coarse microstructure having low values of hardness at a given Co content compared to conventional coarse-grain WC–Co materials were developed and patented by Kennametal Inc. at nearly the same time (Greenfield & Edward, 1989). Later on, cemented carbides with WC grains of 8–30 μm having a round shape were patented by Sandvik (Akerman & Ericson, 1997).

The employment of coarse-grain and especially ultra-coarse-grain carbide grades for mining and construction applications operating in conditions of intensive abrasive wear needs a special consideration. It is well known that the abrasive wear-resistance is directly dependent on mainly the cemented carbide hardness (Gee, Gant, & Roebuck, 2007). However, results obtained by Luyckx, Sacks, and Love (2007) and O'Quigley, Luyckx, and James (1997) provided evidence that the abrasion resistance of WC–Co cemented carbides having the same hardness decreases with decreasing the WC mean grain size and consequently increasing the Co content. The issue of the influence of WC mean grain size on the wear-resistance of WC–Co materials was examined in detail by Konyashin et al. (2010a). The wear of cemented carbides with almost the same hardness of 13 ± 0.2 GPa, WC mean grain size varying from 0.2 to 4.8 μm and Co contents varying from 3% to 25% in the ASTM B611 wear test steadily decreases with increasing the WC mean grain sizes and decreasing the Co content. The wear of the grade with WC mean grain size of 0.2 μm and 25% Co is higher compared to the grade with WC mean grain size of about 5 μm and 3% Co by more than three times. The difference between the extremely fine and ultra-coarse carbide grades with the similar hardness but different combinations of WC grain sizes and Co contents is found to be even more significant (up to 10 times) in laboratory performance tests on percussive drilling of quartzite and cutting of abrasive concrete and granite. In this case, the proportion of the soft binder phase on the surface subjected to abrasive particles during performing the tests is significantly higher for the fine-grain cemented carbide with higher Co contents compared to the coarse- and ultra-coarse-grain carbides with lower Co contents. Therefore, just coarse- and ultra-coarse-grain carbide grades are usually employed for mining and construction, but not medium- and fine-grain cemented carbides.

1.15.3.2 WC Grain Size Distribution

There is no general viewpoint on the optimal microstructure with respect to the WC grain size distribution of cemented carbides for mining and construction. The majority of carbide grades for mining and construction are characterized by a certain amount of bimodality, which is shown in Figure 6, so that there are both fine-grain and coarse-grain fractions in the microstructure. In many cases, such microstructures allow one to achieve the optimal combination of hardness and fracture toughness.

The only commonly accepted viewpoint is that the microstructure has to be free of abnormally large WC grains, the size of which exceeds the WC mean grain size by nearly three times. Such abnormally large WC grains can initiate the crack propagation during the performance of carbide inserts in mining and construction tools, so that they may act as "voids" in the carbide microstructure. The reason for the formation of such grains is believed to be related to local deviations in the carbide composition, mainly carbon content, and the presence of abnormally large WC grains in the original WC powder (Schreiner, Schmitt, Lassner, & Lux, 1984). However, the phenomenon of formation of abnormally large WC grains in the carbide microstructure is still not fully understood as they can unexpectedly appear in the microstructure of cemented carbides produced from very uniform and defect-free WC–Co powders. In many cases, the growth of abnormally large WC grains can be suppressed or eliminated by introducing grain growth inhibitors; however, as it will be shown below, this is usually unacceptable for mining and construction grades. Different approaches to the elimination of growth of abnormally large WC grains in the carbide microstructure are described in the literature. Yang and Kang (2009) suggested carrying out high-temperature presintering in the solid state, which is said to prohibit the abnormal grain growth by use of very fine WC powder of 0.4 μm. Konyashin, Anikeev, Senchihin, and Glushkov (1996), and Konyashin, Eschner, Aldinger, and Senchihin (1999) developed a new technology for fabrication of W and WC powders, which can completely prevent the formation of abnormally large WC particles in the WC powder, thus eliminating the presence of abnormally large WC grains in the carbide microstructure. Gusafson, Wandenstroem, and Norgren (2004) suggested to pre-sinter carbide green bodies in nitrogen to prevent the formation of irregular and large WC grains in the carbide microstructure.

Another philosophy with respect to the microstructure of carbide grades for mining and construction is represented by the Sandvik XT48 grade (see the Internet site of Sandvik). The microstructure of this grade is said to be characterized by very homogeneous structure, so that only WC grains of similar sizes without fine grain fraction are present in it. The XT48 grade is reckoned to have a higher density and more homogeneous structure as a result of new manufacturing techniques, which are not disclosed. One can presume that the XT48 grade contains less Co than conventional grades of similar hardness and fracture toughness, as it is characterized by a higher density, which means a higher WC content. It is said that the average increase in life by use of the XT48 grade is 10–30% depending on the rock conditions.

1.15.3.3 Carbon Content

There are numerous publications on the influence of carbon content in WC–Co cemented carbides on their mechanical properties, the most important of which is the paper of Suzuki and Kubota (1966). The published works on this issue were reviewed in the book of Tretyakov (1975) and by Exner and Gurland (1970). It is well established that both the TRS and fracture toughness decrease outside the two-phase region, i.e. after the appearance of either the η-phase or free carbon in the carbide microstructure, so that the presence of η-phase or free carbon in industrial cemented carbides is unacceptable. The carbon content is found to have an influence on both TRS and hardness being varied within the two-phase region. The hardness increases when decreasing the carbon content. The TRS increases with increasing the carbon content for fine-grain alloys but decreases in coarse-grain alloys. The microhardness of the Co-based binder phase was found to decrease from roughly 4.5 GPa for low-carbon alloys with 25% Co to below 2.5 GPa for high-carbon alloys (Suzuki and Kubota, 1966). The results of Konyashin et al. (2008) indicate a less significant difference between the microhardness values of high-carbon and low-carbon model WC–Co alloys comprising 50% Co. The binder microhardness is equal to 4.7 GPa for the alloy comprising some η-phase and 3.6 GPa for the alloy comprising free carbon.

The results mentioned above should be considered more carefully when taking into account recent results of Konyashin et al. (2009) on the dependence of the WC recrystallization rate during liquid-phase sintering of cemented carbides on the carbon content. It was found that even within the two-phase region, the recrystallization rate of fine WC fraction in the alloy with low carbon content is about six times lower than that in the alloy with high carbon content. On this ground, coarse-grain cemented carbides with low carbon contents produced and examined by Suzuki and Kubota should be noticeably finer and consequently harder due to the presence of the non-recrystallized fine WC fraction than those with high carbon contents.

Nevertheless, as it was mentioned by Exner and Gurland (1970), commercial cemented carbides for mining and construction are usually produced with high carbon contents close to the region of the free-carbon formation according to the ternary W–Co–C phase diagram. There are two following reasons for this. (1) According to Branard (1957), cemented carbides with the presence of an insignificant amount of free carbon are characterized by no or only a very insignificant decrease of TRS, while the presence of η-phase in the microstructure leads to a sharp decrease of TRS and fracture toughness. Therefore, cemented carbides for mining and construction should be produced with high carbon contents to minimize the risk of the η-phase formation. (2) According to Cho, Chung, and Lee (1999), Konyashin et al. (2009), Konyashin et al. (2010), when producing coarse- or ultra-coarse-grain cemented carbides with low carbon contents, the fine-grain WC fraction formed as a result of milling does not recrystallize on coarse WC grains leading to a noticeably reduced WC mean grain size. This results in a lower fracture toughness of the cemented carbides with the low carbon content, so that the carbon content in cemented carbides for mining and construction should be high to allow the fine-grain fraction to fully recrystallize on large WC grains.

The carbon content in cemented carbides can be controlled both/either by adjusting the WC–Co-graded powders and/or by carburization or decarburization of green bodies during presintering. The carburization is usually carried out by use of hydrogen–hydrocarbon mixtures comprising mainly methane (Lueth, 1986). The decarburization is typically performed in hydrogen or CO_2 (Taniguchi et al. 1986; Konyashin et al., 2010).

Almost exceptionally, WC–Co cemented carbides are fabricated without the presence of η-phase due to its very detrimental influence on the TRS and fracture toughness. The only exception is the Sandvik DP60 grade, which is functionally graded cemented carbide, or so-called "dual properties" cemented carbide. This grade is employed for rock drilling and mineral cutting and comprises a core with the η-phase (Aronsson, Hartzell, & Aakerman, 1988, pp. 19/1–19/6; Fischer, Hartzell, & Akerman, 1988). Functionally graded cemented carbides similar to the Sadnvik DP60 grade were produced and examined in detail by Zhang, Wang, et al. (2008), Zhang, Zhan, et al. (2008), Liu, Wang, Yang, Huang, and Long (2004), and Liu et al (2006); the results of these publications are shown in **Figure 7**. The functionally graded cemented carbides are produced in a two-stage process comprising (1) fabrication of fully sintered carbide articles deficient with respect to carbon and therefore containing the η-phase and (2) carburization of the articles in a carburizing atmosphere at temperatures above 1300 °C in the presence of liquid phase. As a result of this fabrication process, carbon diffuses from the surface toward the core leading to carburization of the η-phase and its disappearance in the near-surface

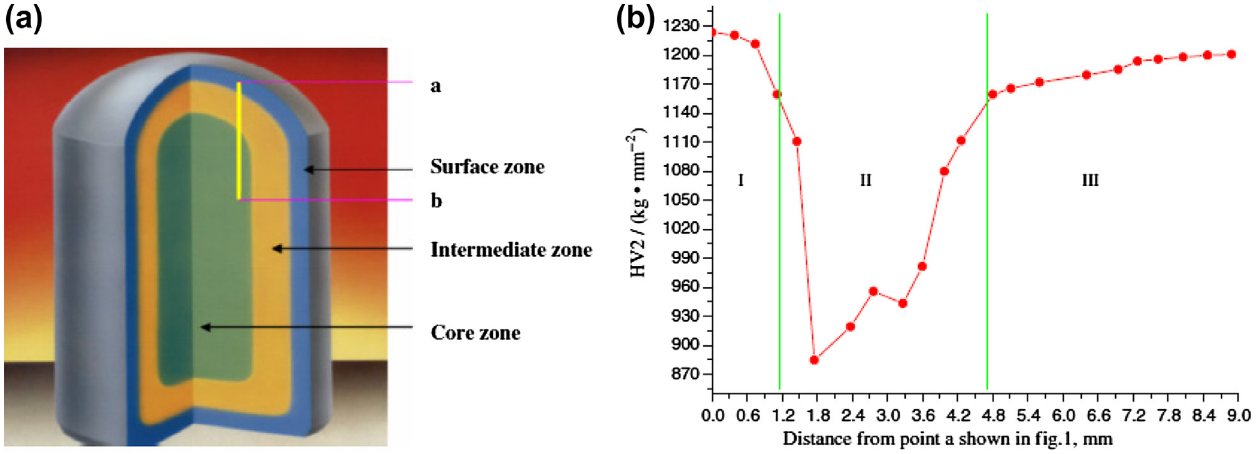

Figure 7 (a) Sketch diagram of the cross-section of WC–Co DP cemented carbide button insert. (b) Vickers hardness (HV2) profile on the cross-section of WC–Co DP cemented carbide button insert. Redrawn from Zhang, Wang, et al. (2008) and Zhang, Zhan, et al. (2008).

layer, which causes a Co drift from the surface toward the interface with the core comprising the η-phase. As a result, a graded structure generally comprising the three following constituent parts forms (1) a near-surface layer of nearly 1–2 mm characterized by a significantly lower Co content and higher hardness than on average; (2) a layer adjacent to the near-surface layer comprising no η-phase and having a noticeably higher Co content and lower hardness than on average; and (3) a core comprising η-phase. In spite of the presence of the brittle core containing the η-phase, the functionally graded cemented carbides can be employed in mining and construction due to the presence of the near-surface layer with high hardness.

1.15.3.4 Composition and State of the Binder Phase

The composition and state of the binder play an important role in the performance of coarse- and especially ultra-coarse-grain cemented carbides. As it was mentioned above, the size of binder interlayers in such cemented carbides is comparable with the size of abrasive particles present during rock cutting and drilling, so that the properties of the binder phase, especially its hardness, play the decisive role. The conventional Co-based binders in WC–Co cemented carbides are characterized by relatively low hardness, which leads to its dominant wear during performance resulting in intensive wear of the whole carbide insert.

In order to solve the problem of low hardness and wear-resistance of the binder in ultra-coarse cemented carbides, novel grades with nanograin-reinforced binder with the brand name Master Grades® were developed and patented by E6HM (Konyashin et al., 2004, 2005, 2006, 2008, 2011). The structure of the Master Grade for road planing and its binder on the micro, nano and atomic levels is shown in Figure 8. It consists of rounded WC grains with thick and uniform interlayers of the Co-based binder among them, which allows lower internal stresses and high fracture toughness to be obtained. The Co-based binder of the Master Grades is reinforced and hardened by nanoparticles of the θ-phase (Co_2W_4C), the mean grain size of which is significantly below 10 nm. As a result, the binder nanohardness of the Master Grades is equal to 10.2 GPa, whereas that of conventional grades without nanograin reinforcement is equal to 7.5 GPa. This leads to a significant increase in wear-resistance and some increase in TRS of the Master Grades in comparison with conventional grades with the same Co content and similar WC mean grains without losing the fracture toughness of the Master Grades. The tool lifetime of road planing picks and mining picks with inserts of the Master Grades is prolonged by a factor of roughly 1.5–2.5, which is accomplished by a noticeable decrease in a number of premature failures during operation. Typical road planing picks with tips of the Master Grade and standard grade with the same Co content and similar WC mean grain size before and after a field test on asphalt cutting are shown in Figure 8(d).

It is well known that the Co-based binder is subjected to the transformation from the face centered cubic (fcc) to the hexagonal close packed (hcp) crystal lattice under condition of cyclic loads or fatigue (Schleinkofer, Sockel, Görting, & Heinrich, 1996). Cracks are found to propagate through the hcp Co phase, which is more

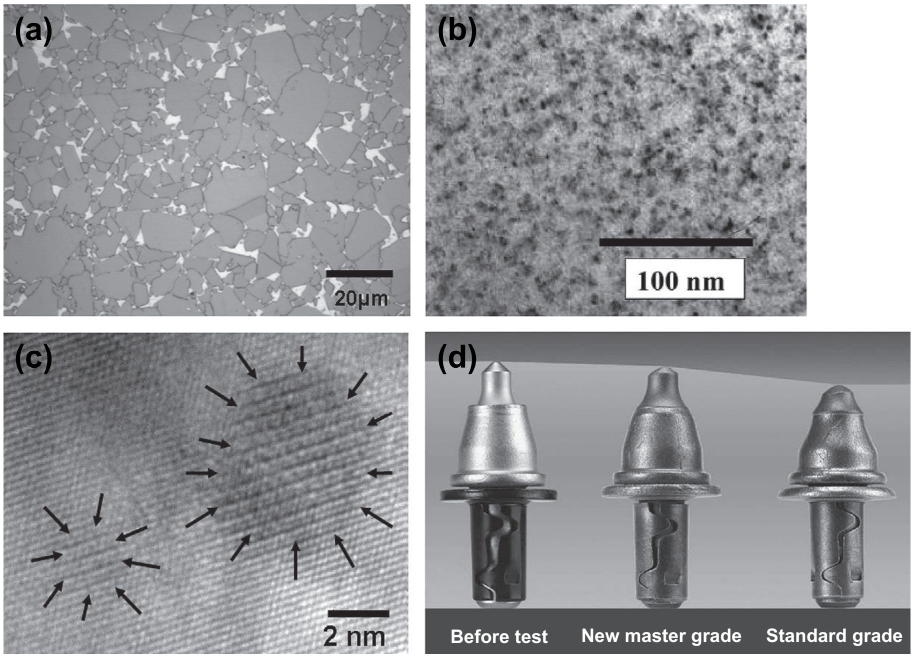

Figure 8 Structure of the Master Grade for road planing on the (a) microlevel, (b) binder nanostructure of the nanolevel (dark field TEM image of the binder taken using the (111) reflection of the θ-phase) and (c) binder atomic structure on the atomic level (HRTEM image, nanoparticles of the θ-phase embedded in the fcc Co matrix are indicated by arrows). (d) Typical worn road-planing picks with the Master Grade in comparison with the standard ultra-coarse grade of the same Co content and similar WC mean grain size before and after a field test on asphalt cutting. (b and d) Redrawn from Konyashin et al. (2005). (a and c) With the permission of Element Six Hard Materials.

brittle than fcc Co, during failure under fatigue conditions. In order to solve this problem, it was suggested to substitute the Co binder by the Co–Ni or Fe–Co–Ni binders in cemented carbides for mining and construction (Prakash & Gries, 2009, pp. 5/1–5/14; Heinrich, Wolf, Schmidt, & Schleinkoffer, 1999). Also, the Fe–Co–Ni powders are believed to have advantages over Co powders with respect to the health issues. Nevertheless, there are some difficulties with respect to fabrication of cemented carbides with the Fe–Ni–Co binders, such as the narrower two-phase field regarding the carbon content compared to the Co-based binders, the necessity of more precise adjustment of the binder system depending on the production conditions, and so on. Also, in the literature, there are no results of large-scale performance tests of cemented carbides with the Fe–Ni–Co binders clearly indicating their significant advantage over WC–Co cemented carbides in mining and construction. One of the examples of the employment of the Fe–Co–Ni binder is the Ceratizit CTU30/SNK30 grade for wear applications (see the Internet site of Ceratizit).

Another approach to altering the composition of the binder phase and carbide microstructure as a whole is realized in the Dyanite® grade containing boron, which was developed by Multi-Metals (see the Internet site of Multi-Metals). It is said that "… Dyanite® allows for the use of higher hardness inserts without sacrificing the fracture toughness needed in many applications". It appears that boron is added to cemented carbides in this case by use of a special technology, when taking into account the known detrimental role of even insignificant amounts of boron on the microstructure uniformity of WC–Co (Lassner et al., 1972).

1.15.3.5 Origin of WC Powders

The origin of WC powders produced by the conventional technology of hydrogen reduction of tungsten oxides with consequent carburization of tungsten metal plays an important role with respect to the WC mean grain size, grain size distribution and level of inevitable impurities in WC–Co cemented carbides. Furthermore, the use of alternative technologies, e.g. the Menstruum process mentioned above and direct carburization of WC from WO_3, described in detail in the book of Lassner and Schubert (1999) can significantly affect the microstructure and properties of WC–Co cemented carbides.

The WC grain size and uniformity are strongly dependent on the hydrogen reduction and carburization parameters, which is a topic in the chapter 1.7 "Synthesis and Processing", this volume. Therefore, this issue is not taken into consideration in this chapter because of its limited volume. Nevertheless, one parameter of the production technology, namely the influence of temperature of WC carburization on mechanical properties of mining grades, will be briefly described below.

The temperature of WC carburization was found to have the major influence on plastic properties of coarse-grain WC–Co cemented carbides for mining applications. A technology for fabrication of WC powders by the high-temperature hydrogen reduction of WO_3 at 900–1200 °C and high-temperature carburization of the W powder at 2000–2200 °C was developed in the Soviet Union in the 1960s and afterward patented worldwide (Ivensen et al., 1977). The fact of significantly higher plastic deformation of WC–Co cemented carbides obtained from the high-temperature carburized WC powders is well established and described in detail by Tretyakov (1975). For example, two grades having 20% Co and nearly the same WC grain size of 2.1 μm but produced from WC powders carburized at 1450 and 2200 °C are characterized by similar compressive strength and TRS values. However, the carbide samples obtained from the high-temperature carburized WC have a plastic deformation before failure in compression of 5.5–6.8%, whereas those obtained from the low-temperature carburized WC have a deformation of 2.9–3.1%. The carbide samples having the similar WC mean grain size and 6% Co produced from the high-temperature and low-temperature carburized WC powders are also characterized by similar values of compression strength and TRS; however, the deformation before failure of the samples obtained from the high-temperature carburized WC is nearly 2.3 times higher than that of the samples obtained from the low-temperature carburized WC. This was found to lead to a significant increase in the crack resistance parameter of the cemented carbides produced from the high-temperature WC powder. Falkovsky (1997) established that the cemented carbides obtained from the high-temperature WC powders are characterized by noticeably higher fracture toughness.

The reason for the higher plasticity of cemented carbides produced from high-temperature carburized WC powders is still a matter of discussion. Some authors believe that it is related to a higher rate of perfection and special structure of the crystal lattice of WC obtained at higher carburization temperatures (Ivensen, Eiduk, & Artemev, 1970). Other authors believe that this is a result of the purification of WC carburized at higher temperatures, as the content of inevitable impurities, particularly Mg, Na, As, Ca and Si, is significantly lower in the WC powders carburized at high temperatures (Tretyakov, 1975). Kreimer (1968) believes that the higher plasticity of cemented carbides obtained from high-temperature WC powders is a result of coarse WC grain size and special WC grain size distribution. The high-temperature carburized WC powders are widely employed in the manufacture of cemented carbides for mining and construction, e.g. the VK-KS grades produced in Russia (Panov et al., 2004). It should be mentioned that the high-temperature carburized WC powders are more expensive than those produced at medium temperatures, so that the use of either "medium-temperature" or "high-temperature" WC powders for each concrete carbide grade and application is a matter of special consideration.

1.15.3.6 Grain Growth Inhibitors

As it will be mentioned below, grain growth inhibitors (VC, Cr_3C_2, TaC, NbC, TiC, ZrC, HfC and Mo_2C) are widely employed in the production of fine- and medium-grain cemented carbides for wear parts. The use of grain growth inhibitors in carbide grades for mining and construction is relatively unconventional.

There are very few results in the literature on the influence of grain growth inhibitors on the properties of coarse-grain cemented carbides. Kiefer and Benesovsky (1965) in their book described the influence of different amounts of TaC and TaC/NbC as well as NbC, VC and Cr_3C_2 on the TRS of middle-grained WC–Co cemented carbides containing 5–6.5% Co. A mixture of TaC/NbC being added in amount of up to 3% and TaC in amount of up to 10% was found to have almost no influence on the TRS. Kreimer (1968) indicated that an insignificant amount of TaC being added to coarse-grain cemented carbides did not decrease their TRS. Tretyakov (1975) mentioned that additions of TaC in amount of 2–8% to coarse-grain mining grades did not lead to a noticeable decrease of their properties, whereas according to Exner and Gurland (1970), even an insignificant amount of other grain growth inhibitors (e.g. Cr_3C_2) reduces the TRS. The evidence mentioned above can be understood when taking into account the recent results on high-resolution transmission electron microscopy of WC–Co interfaces in cemented carbides containing grain growth inhibitors (Lay, Hamar-Thibault, & Lackner, 2002; Warbichel, Hoferm, Grogger, & Lackner, 2001, pp. 65–74). Almost all the grain growth inhibitors, except for Ta, tend to segregate at WC/WC grain boundaries; the grain growth inhibitors also

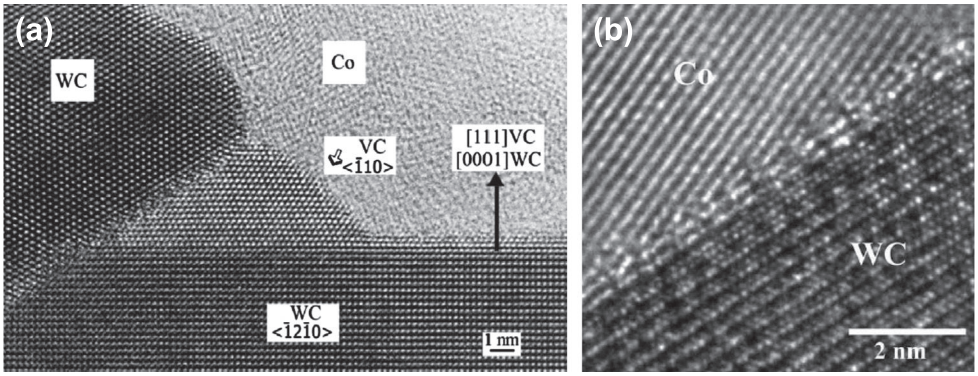

Figure 9 HRTEM images of WC–Co interfaces of (a) WC–Co cemented carbide containing VC. (Redrawn from Lay et al. (2002).) (b) WC–Co cemented carbide with low carbon content corresponding to the η-phase formation. Redrawn from Konyashin et al. (2010).

segregate at WC-Co interfaces leading in some cases to formation of thin layers of mixed carbides, an example of which is shown in Figure 9(a). This is believed to lead to the suppression of WC grain growth. However, the segregation of the grain growth inhibitors at WC–Co interfaces is detrimental with respect to the TRS and fracture toughness of WC–Co materials containing all the grain growth inhibitors except for tantalum. It is interesting to note that according to Konyashin et al. (2010), straight WC–Co cemented carbides with low carbon contents not containing grain growth inhibitors do not comprise any additional phases at WC–Co interfaces, which is shown in Figure 9(b); in this case only an extremely thin interface layer, which is designated in literature as "complexion", forms. In this case, the dissolution of fine-grain WC fraction in the liquid Co phase and its recrystallization is strongly suppressed during sintering similarly to WC–Co materials containing grain growth inhibitors.

Due to the reasons mentioned above, usually, no grain growth inhibitors are employed in carbide grades for mining and construction. The only exception appears to be the BS grades containing TaC produced in Russia according to Panov et al. (2004).

1.15.3.7 Shape and Contiguity of WC Grains

Typically, conventional WC–Co cemented carbides consist of WC single crystals having a form of truncated trigonal prisms with sharp edges. Sharp edges of adjacent WC grains are believed to lead to stress concentrations during loading, thus promoting the crack initiation and propagation. According to Herber, Schubert, and Lux (2006), cemented carbides with WC grains containing no sharp edges obtained by substituting the prismatic WC grains by rounded ones have an improved toughness and reduced sensitivity to cracking. As it was shown above, the presence of rounded WC grains in the microstructure of the Master Grades allows their TRS to be improved, so that the employment of rounded WC grains instead of facetted appears to be advantageous. According to Akerman and Ericson (2000), cemented carbides with rounded WC grains have a high thermal conductivity, which is very positive for carbide inserts operating in condition of severe thermal fatigue in mining and construction. Such WC–Co cemented carbides can be produced by coating WC powders with Co instead of mixing/milling with Co, which allows the suppression of WC recrystallization during sintering (Akerman & Ericson, 1997). They can also be produced by very gentle milling of WC powders having originally a rounded shape and by adding grain growth inhibitors, thus suppressing the WC grain growth during sintering (Herber et al., 2006).

The approach of "rounding" WC grains in WC–Co cemented carbide can also influence the contiguity of WC grains in the microstructure, thus affecting the WC skeleton formation. According to Exner and Gurland (1970), the hardness of WC–Co increases and TRS decreases with increasing the contiguity. It should be noted that according to the recent results on the structure and composition of WC–WC interfaces in cemented carbides, almost all the WC grains are separated from each other by a thin Co film of a single atomic monolayer or a few Co atomic monolayers (Sharma, Wards, Fraser, & Williams, 1980; Henjered, Hellsing, Nouet, Dubon, & Laval, 1994). Although such thin Co interlayers are presumably characterized by very special physical and mechanical properties, the WC skeleton in form, in which it was considered before, is thought to be absent in WC–Co, so that the WC contiguity should not play an important role.

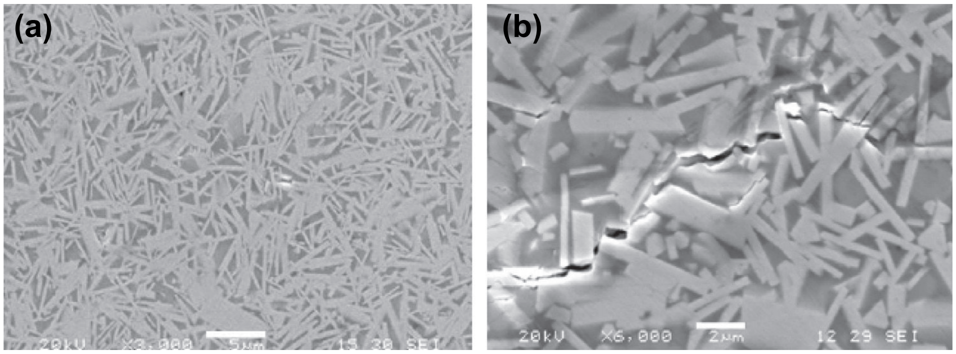

Figure 10 SEM microstructures and cracks path in the WC platelet containing cemented carbide. Redrawn from Nam et al. (2010).

Another approach to the fabrication of cemented carbides with unusual WC grain shape was developed and patented by Toshiba Tungaloy Co. Ltd in Japan in 1996 (Kobyashi and Kinoshita, 1995). In this case, WC–Co cemented carbides are produced with WC grains in the form of thin platelets or discs. The so-called "Disc Reinforced Technology" (see the Internet site of Toshiba Tungaloy) is said to allow obtaining a better combination of hardness and fracture toughness. This is believed to be achieved because the WC platelets have a higher percentage of the harder WC crystal planes and the crack nucleation and propagation can be suppressed in such cemented carbides (Figure 10). The technology for fabrication of such cemented carbides includes the production of tungsten powders in the form of flat platelet-like particles and their carburization by adding a carbon-source material, preferably graphite, during liquid-phase sintering (Kobyashi and Kinoshita, 1995). Konyashin (Konyashin, 2002) developed coarse-grain cemented carbides with WC grains in the form of platelets for mining and construction applications. Nam, Lim, and Kang (2010) suggested to produce platelet-reinforced cemented carbides by decomposition of (Ti, W)C oversaturated with tungsten during liquid-phase sintering. This is said to result in the formation of WC platelets with high aspect ratios shown in Figure 10 leading to an improved combination of hardness and fracture toughness.

1.15.4 Basic Industrial Cemented Carbides for Wear Parts

Cemented carbides for wear parts are mainly medium-grain or submicron cemented carbides as well as near-nano cemented carbides. Almost all the grades for wear parts are produced by the use of various amounts of grain growth inhibitors. Figure 11 and Table 2 show typical carbide grades for wear parts and their microstructure.

When wear parts are subjected to impact loads or thermal shock, medium-grain cemented carbides are employed. Such grades can also be used for metal cutting, so that many companies do not distinguish grades of these two types. As it can be seen in Table 2, the medium-grain grades contain 6–26% Co and comprise insignificant amounts of grain growth inhibitors to prevent the formation of abnormally large WC grains. The hardness of such grades varies from nearly 900 to 1600 Vickers units and their fracture toughness varies from roughly 9 to 19 MPa $m^{1/2}$. The grades with high Co contents, such as G40 and G55, produced by E6HM are employed in applications where extremely high fracture toughness is needed, such as tools for chipless forming. Table 2 indicates only the basic grades for wear parts produced by E6HM, which are supplemented by other special grades tailored for particular applications.

In many applications of wear parts, there is no need of high fracture toughness. In these cases, submicron cemented carbides can be employed, which are shown in Table 2 and Figure 11. They contain usually roughly 5–15% binder and relatively large amounts of grain growth inhibitors needed to maintain the original fine grain size of WC powders during sintering. The hardness of such grades varies from nearly 1200 to 1900 Vickers units and fracture toughness varies from about 9 to 13 MPa $m^{1/2}$. In each concrete case of each wear part, the WC mean grain size, Co content and grain growth inhibitors have to be optimized to obtain the best combination of hardness and fracture toughness. Usually, the fracture toughness of the submicron cemented carbides can be improved at the expense of hardness by varying the WC mean grain size, Co content and amount of grain growth inhibitors. The choice of the optimal composition and amount of grain growth inhibitors is a relatively

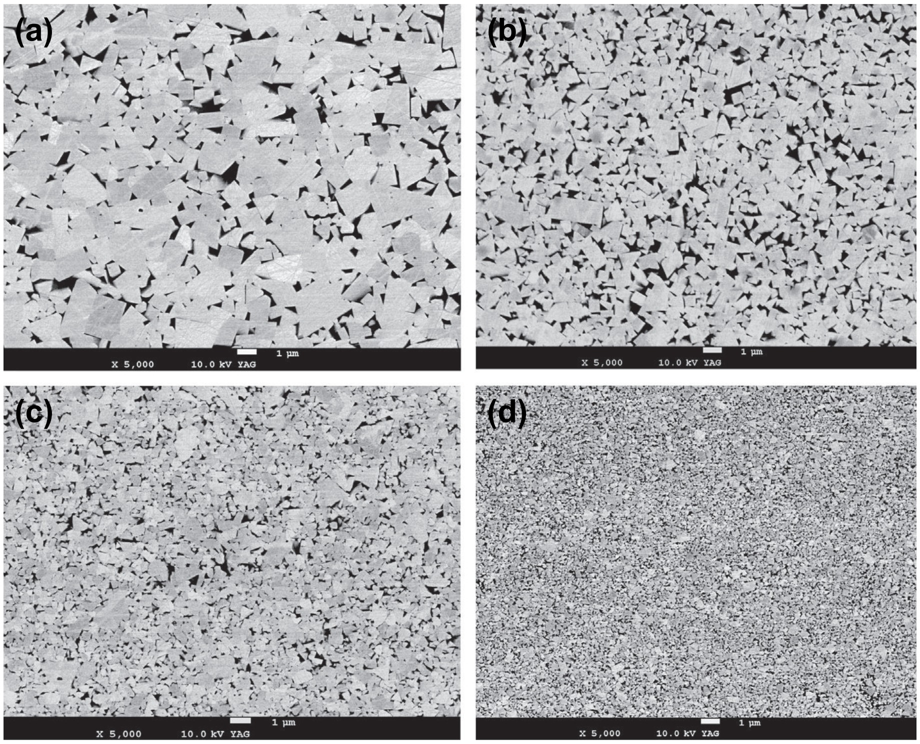

Figure 11 Typical microstructures of cemented carbides for wear parts (5000×): (a) G10 (medium-grain, 6% Co); (b) K010 (10%Co, submicron); (c) NK07 (7% Co + Ni, submicron); and (d) near-nano grade with 10% Co. With the permission of Element Six Hard Materials.

complicated task, as the nature and amount of different grain growth inhibitors have a pronounced impact on both hardness and fracture toughness of submicron cemented carbides.

The influence of different grain growth inhibitors on the WC grain growth, hardness, TRS and fracture toughness in fine-grain cemented carbides was examined in numerous publications (Egami, Kusava, Machida, & Kobayashi,

Table 2 Industrial cemented carbide grades for wear parts of Element Six Hard Materials

	Composition (%)						*Hardness*				
Grade	*Co*	*Ni*	*VC*	*Cr_3C_2*	*WC*	*Grain size*	*Vickers (HV_{10})*	*Rockwell (HRA)*	*TRS (MPa^{-2})*	*Compressive strength (MPa^{-2})*	*Fracture toughness (MPa m$^{1/2}$)*
G10	6.0		0.15		93.9	Medium	1600	91.9	2800	5000	10.7
G15	8.0		0.15		91.9	Medium	1480	90.9	3000	4700	11.8
G20	11.0		0.15		88.9	Medium	1320	89.4	3200	4300	13.1
G30	15.0		0.15		84.9	Medium	1200	88.2	3000	3900	15.2
G40	20.0		0.15		79.9	Medium	1050	86.5	2900	3500	16.9
G55	26.0		0.15		73.9	Medium	870	84.4	2800	3000	18.9
K05	5.0		0.2		94.8	Submicron	1800	93.0	2800	5200	9.6
K06/Z6	6.0		0.2		93.8	Submicron	1750	92.7	3100	5200	9.9
K07	7.0		0.3	0.2	92.5	Submicron	1700	92.5	3100	5400	9.0
K08/Z8	8.0		0.3	0.2	91.5	Submicron	1650	92.2	3200	5400	9.0
K010/Z10	10.0		0.3	0.2	89.5	Submicron	1620	92.0	3600	5000	10.7
K015	15.0		0.4	0.5	84.1	Submicron	1400	90.2	3600	4500	12.7
N6		6.0		0.5	93.5	Submicron	1600	91.9	2400	4800	12.1
N12		12.0		0.5	87.5	Submicron	1200	88.2	2800	3900	15.2
NK07	4.8	2.0	0.3	0.3	92.6	Submicron	1850	93.4	3000	5400	8.8

With the permission of Element Six Hard Materials.

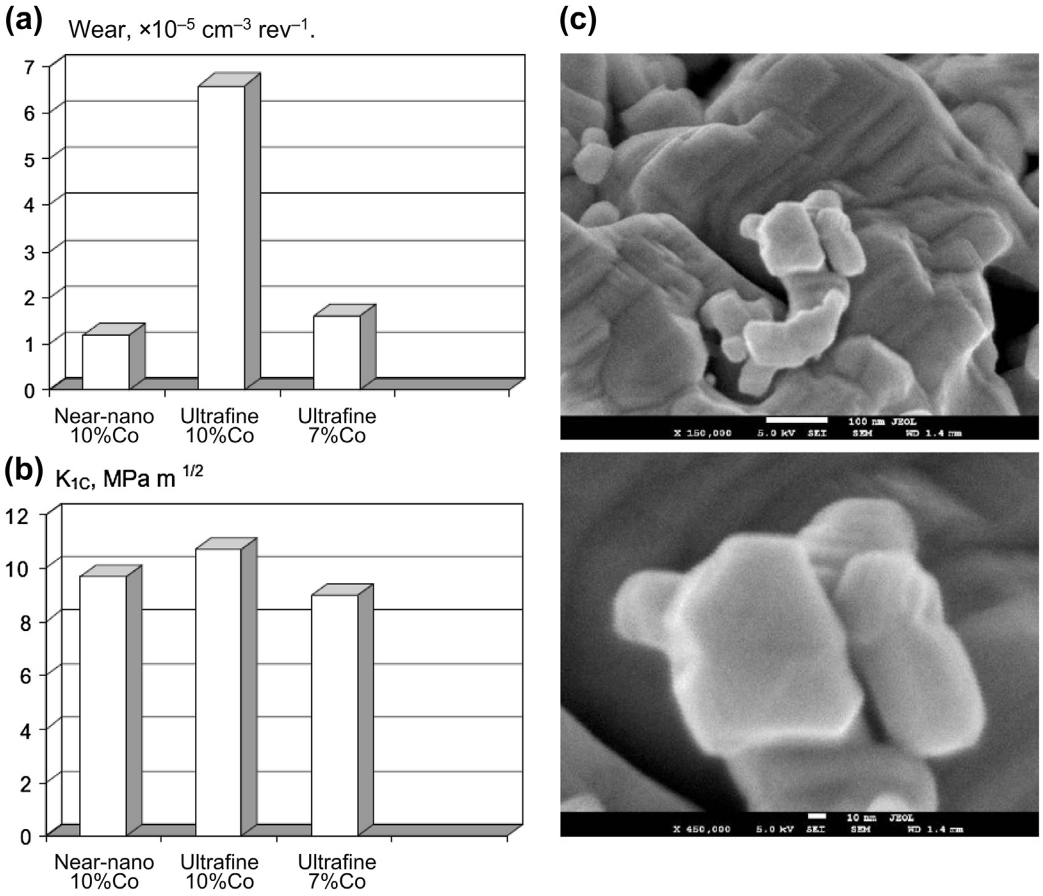

Figure 12 (a) Wear-resistance and (b) fracture toughness of the near-nano cemented carbide with 10% Co and WC mean grain size of 0.2 μm. (c) Morphology of the WC powder DN 4.0 (4NP0) (H.C. Starck) employed for fabrication of the near-nano cemented carbide. Redrawn from Konyashin et al. (2010a).

1989, pp. 53–70; Caroll, 1997, pp. 168–182; Porat and Berger, 1997; Gille, Szesny, Leitner, & Caroll, 1997, pp. 139–167). VC is found to have the strongest effect on the WC mean grain size followed by Cr_3C_2, NbC, TaC and Mo_2C. VC has also the most detrimental effect on the fracture toughness followed by Cr_3C_2 and other carbides. The most widely employed grain growth inhibitors are VC and Cr_3C_2. For some cemented carbides, Mo_2C is used (Carpenter, 2003; Almond & Roebuck, 1987), which is the only carbide that has a mutual solubility with WC. It should be noted that the TRS of the submicron cemented carbides even containing relatively large amounts of grain growth inhibitors can be very high (up to 4000 MPa), which is still combined with their relatively poor fracture toughness compared to coarse- and medium-grained carbide grades.

Cemented carbides for wear parts are usually produced with lower carbon content than those for mining and construction, which is needed to suppress the WC recrystallization and growth. As it was mentioned by Lassner and Schubert (1999), the submicron WC powders employed for the production of fine and submicron WC–Co grades frequently contain grain growth inhibitors (mainly V and Cr).

For wear parts operating in corrosive media (acidic), Co-based binders are usually partially or fully substituted by Ni and Cr having a significantly improved corrosion resistance. In this case, a large amount of chromium carbide is usually employed up to its solubility limit in the Co, Co–Ni or Ni binders, which dramatically increases the binder corrosion resistance. Typical grades with such binder systems are the N6, N12 and NK07 grades, the properties of which are shown in Table 2, produced by E6HM.

The trend of decreasing the WC mean grain size in WC–Co cemented carbides resulted in the development of cemented carbides with WC grain size close to the nanoregion (100 nm or less). Such cemented carbides with WC mean grain size of nearly 0.2 μm (200 nm) are designated in the literature as "near-nano cemented carbides" (Brieseck, et al., 2009, pp. 239–246). Very fine, uniform and inactive WC powders are needed for fabrication of such cemented carbides. Only recently, very fine-grain WC powders characterized by the low activity with respect to recrystallization during liquid-phase sintering were developed and implemented (Caspers, Säuberlich, & Reiss, 2008, pp. 50–58; Eiling, Caspers, Gille, & Gries, 2008, pp. 91–106). The morphology of such powders redrawn from (Konyashin et al., 2010a) is shown in Figure 12. Figure 11 shows the microstructure of the near-nano cemented carbide with 10% Co providing evidence for its extremely fine and homogeneous microstructure. Figure 12 shows the wear of the near-nano cemented carbide with 10% Co and hardness of 20 GPa in comparison with that of the standard ultra-fine grades with 10% Co and 7% Co (Konyashin et al., 2010a). It can be seen that the wear-resistance of the near-nano grade is roughly six times higher than that of the ultrafine grade with 10% Co and nearly 50% higher than that of the ultrafine grade with 7% Co. This is accomplished by only a marginally decreased fracture toughness of the near-nano grade. Thus, the near-nano cemented carbides are believed to have a significantly improved wear-resistance compared to the conventional submicron grades at hardness of above 19 GPa.

1.15.5 Modern Trends in Research and Development of Novel Cemented Carbides for Mining, Construction and Wear Parts

Because of the limited volume of this chapter, it is impossible to cover all the modern trends of R&D in the field of cemented carbides for mining, construction and wear parts. Below there are some general trends of research on novel cemented carbides, which can potentially lead to breakthroughs with respect to the performance of WC–Co cemented carbides.

As it was mentioned above, in the most cases, the hardness and consequently wear-resistance of WC–Co cemented carbides can be improved only at the expense of fracture toughness. As it can be seen in Figure 13(e), conventional cemented carbides obtained by varying the WC mean grain size and Co content lie within a

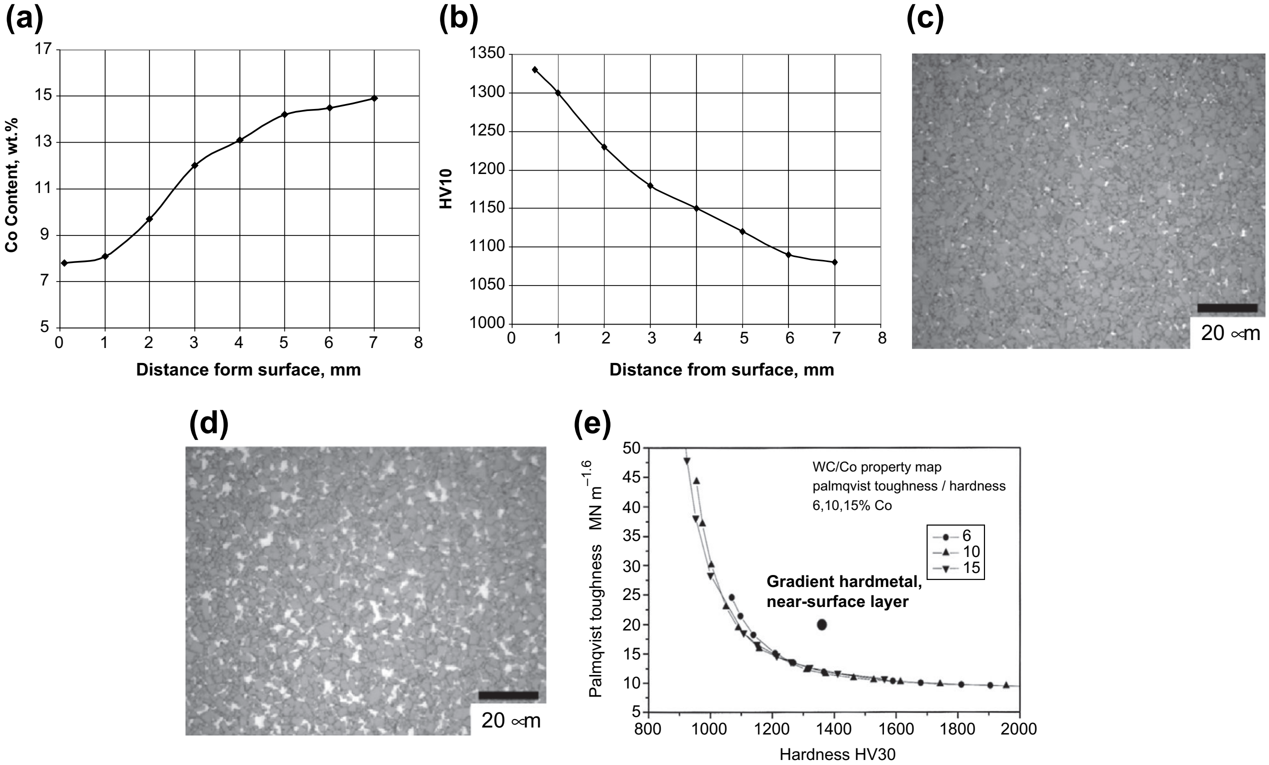

Figure 13 Curves characterizing the functionally gradient WC-10% Co cemented carbide: (a) Co distribution and (b) hardness distribution. Microstructure of (c) the near-surface layer and (d) the core of the functionally gradient WC-10% Co cemented carbide. (e) WC–Co property map according to Roebuck et al. (2001) showing the point corresponding to the combination of the fracture toughness/Vickers hardness of the near-surface layer of the functionally gradient WC-10% Co cemented carbide. Redrawn from Konyashin et al. (2013).

narrow band on the curve: Palmquist toughness–hardness (Roebuck, Gee, & Morrell, 2001). The major challenge of R&D in the cemented carbide field is to "escape" from this band, in other words, to simultaneously improve both hardness/wear-resistance and fracture toughness of WC–Co cemented carbides.

1.15.5.1 Functionally Graded WC–Co Cemented Carbides

As it was shown above, functionally graded cemented carbides with a hard near-surface layer can potentially be widely employed in mining and construction. The major disadvantage of the presently produced functionally graded cemented carbides is the presence of the brittle core comprising the η-phase and the intermediate layer with low hardness between the hard near-surface layer and the core. It would be ideal to be able to produce functionally graded cemented carbides with a surface layer with a low Co content and a smooth Co gradient from the surface toward the core not comprising the η-phase. The fabrication of WC–Co cemented carbides with gradient composition, microstructure and properties has been the issue of great interest in the carbide industry for a long time. If one can produce cemented carbides with a near-surface region with a significantly lower Co content than the average Co content, this region would have a high hardness leading to its better wear-resistance. It is also expected that this near-surface region would be characterized by high residual compression stresses resulting in its higher fracture toughness. This occurs as a result of very different shrinkage rates in two parts of a carbide article with various Co contents during liquid-phase sintering, as the shrinkage factor of the part with a higher Co content is significantly greater than that of the part with a lower Co content.

First attempts to produce cemented carbides with various WC mean grain sizes and Co contents were based on pressing articles from two different graded WC–Co powders (Colin, Durant, & Favrot, 1993–1994). However, this approach has a limited practical applicability as Co drifts very fast from a part with a higher Co content into a part with a lower Co content during liquid phase sintering. Also, it is very difficult or impossible to produce carbide articles of complicated shape by use of this approach, so that it would be ideal to produce functionally graded cemented carbides from one WC–Co powder by use of controlled Co drift during sintering. Nevertheless, according to Rassbach, Moseley, and Böhlke (2009), two-layer cemented carbides produced by pressing two different graded WC–Co powders were successfully implemented and introduced onto the market.

In the literature, the two following major approaches to the fabrication of functionally graded cemented carbides from a single WC–Co powder are described.

First approach is based on selective introduction of WC grain growth inhibitors (mainly Cr and V) into the cemented carbide near-surface layer as a result of applying the grain growth inhibitors or their precursors to the surface of green articles (Collin & Norgren, 2008; Glatzle, Kosters, & Glatzle, 2004; Greenfield, 1997). As a result of this technology, the near-surface region comprising much Cr or V becomes significantly finer than the core after liquid-phase sintering resulting in its high hardness and wear-resistance. Nevertheless, there might be significant difficulties related to applying the grain growth inhibitors or their precursors to the surface of carbide articles of complicated shape in the green state, as they are very fragile. Also, the presence of high concentrations of V and Cr in the near-surface layer can lead to its decreased fracture toughness.

Second approach is based on obtaining a Co drift in carbide articles, which are inhomogeneous with respect to their WC mean grain size and/or carbon content in the green state. In general, the following two major phenomena can be used for fabrication of gradient WC–Co materials in this case: (1) If there are two adjacent layers of WC–Co with various carbon contents in the green state, cobalt drifts from the layer with the higher carbon content into the layer with the lower carbon content during liquid-phase sintering. (2) If there are two adjacent layers of WC–Co with various WC mean grain sizes in the green state, cobalt drifts from the layer with coarser microstructure into the layer with finer microstructure during liquid-phase sintering as a result of different capillary forces. These phenomena were described in detail in numerous publications with respect to bilayer cemented carbides pressed and sintered from various graded powders (Liu et al., 2004; Eso, Fang, & Griffo, 2005; Eso, Fang, & Fang, 2007).

It can be expected that if one can selectively regulate the WC mean grain size and/or carbon content in the carbide near-surface layer and core in the green state, it would be possible to create and control the Co drift during the final liquid-phase sintering thus obtaining functionally graded cemented carbides.

A new technology for fabrication of WC–Co articles with a low cobalt content and consequently high hardness of the near-surface layer and not comprising the η-phase was described by Guo, Fan, and Fang (2009), and Fang, Fan, and Guo (2010). According to this technology, WC–Co articles with original low carbon contents are subjected to carburization at a temperature at which solid WC, liquid cobalt and solid Co coexist.

In spite of the fact that there is neither η-phase nor free carbon in the functionally graded carbides obtained in such a way, the technology mentioned above allows formation of only very thin hard near-surface layers with thickness of below 0.5 mm. It appears that such thin hard layers might have a limited application in mining and construction, as the wear of carbide inserts in these applications is typically of the order of 1 mm or more.

Konyashin et al. elaborated another new technology for fabrication of functionally graded cemented carbides, or so-called "gradient cemented carbides", comprising neither η-phase nor free carbon (Konyashin et al., 2010; Konyashin, Hlawatschek, et al., 2010a, 2010b; Konyashin et al., 2012; Konyashin et al., 2013). It is based on the following steps: (1) making WC–Co grade powders with a low carbon content but not corresponding to the η-phase formation and pressing green articles; (2) controlled presintering of the green articles to obtain a certain gas permeability of their near-surface layer in the green state; (3) selective carburization of this near-surface layer to a certain depth and carbon content in the solid state; and (4) final liquid-phase sintering of the articles to obtain a Co drift in the liquid phase from the surface toward the core and their full densification. The major advantage of this technology is the possibility of regulating the Co drift from the surface toward the core. As a result of this, it is possible to vary the thickness of the layer with the low Co content and consequently high hardness in a range of nearly 1 mm to several millimeters. This allows one to produce carbide articles for various applications with tailored near-surface layers characterized by high combinations of hardness and fracture toughness. **Figures 13(a) and 13(b)** show curves indicating the typical Co and hardness distribution in the gradient cemented carbide for mining applications with 10% Co (Konyashin et al., 2013). The Co content in the near-surface layer is about 50% lower than in the core, which leads to the fact that its hardness is higher than that of the core by roughly 250 Vickers units. The near-surface layer is found to be characterized by high residual compression stresses of more than −400 MPa in both the WC and Co phases, resulting in the high fracture toughness of the near-surface layer. This leads to a very high combination of hardness and fracture toughness of the near-surface layer shown in **Figure 13(e)**, providing evidence that it is possible to "escape" from the curve: Palmquist toughness–hardness for conventional WC–Co materials. Wear resistance of the gradient cemented carbides with 6–10% Co in percussive drilling of quartzite and cutting of abrasive concrete was found to be higher compared to conventional cemented carbides by a factor of up to four (Konyashin et al., 2013).

1.15.5.2 Nanostructured Cemented Carbides

There is a general trend in the modern carbide industry to produce WC–Co materials with WC mean grain sizes as small as possible with the target of achieving the range of nanomaterials. According to the general principles of nanomaterials (Hornbogen, 2001), nanostructured WC–Co cemented carbides with WC mean grain size of significantly below 100 nm should possess a combination of both higher hardness and fracture toughness. On this ground, in recent time, there was a significant research effort with respect to the development of nanostructured cemented carbides with WC mean grain size finer than 100 nm from WC nanopowders. Numerous publications in this field are summarized in the review paper of Fang, Wang, Ryu, Hwang, and Sohn (2009) (see also Arato, Bartha, Porat, Berger, & Rosen, 1998; Berger, Porat, & Rosen, 1997; Fang et al., 2005; Goren-Muginstein, Berger, & Rosen, 1998; Shao et al., 2003).

In spite of the substantial research effort in the field of nanostructured WC–Co materials, it did not result in obtaining cemented carbides with WC mean grain size noticeably lower than 100 nm because of the very intensive growth of WC nanopowders during sintering. It should be noted that according to Konyashin et al. (2010a), even if the nanostructured cemented carbides can be produced from nanopowders with the aid of much grain growth inhibitors, they will unlikely substitute conventional coarse-grain carbide grades for mining and construction. The reason for this is that such nanostructured cemented carbides have to contain much Co to achieve a required level of fracture toughness typical for mining and construction grades. As a result, their wear-resistance is expected to be noticeably lower than that of coarse- and ultra-coarse grades with a similar combination of hardness and fracture toughness. The only application range, where nanostructured cemented carbides are believed to potentially substitute conventional ultrafine grades, is the hardness of above 19 GPa.

It appears, however, that the conventional powder metallurgy route cannot be employed for fabrication of nanostructured cemented carbides with carbide grain size of the order of 10 nm or less, which are expected to possess an improved combination of hardness and fracture toughness. Therefore, only fundamentally novel techniques for fabrication of nanostructured hard materials, e.g. Physical Vapour Deposition (PVD) (Greer & Wilde, 2001) or Chemical Vapour Deposition (CVD) (Zhuk, 2007), allowing one to produce nanomaterials with a mean grain size of carbide phases of below 10 nm without using grain growth inhibitors might potentially be of practical importance. In particular, nanostructured hard materials consisting of W_2C nanoparticles of <10 nm in size embedded in the W binder obtained by CVD were developed and patented by Hardide Plc (see the Internet site of Hardide Plc). These materials are reckoned to have an exceptionally high combination of hardness, wear-resistance and toughness and have been employed in the oil drilling, aircraft and pump production on a large scale for several years. The possibility of fabrication of WC–Co cemented carbides by CVD was established by Fitzsimmons and Sarin (2001) and by electron cladding was evaluated by Abe, Morimoto, Tomie, and Doi (2000).

Another unconventional approach to fabrication of nanostructured WC–Co cemented carbides for mining applications was developed and patented by Smith Int. (Zhang, Wang, et al., 2008; Zhang, Zhan, et al., 2008). It is based on the employment of carbon or inorganic nanotubes added to WC–Co powder mixtures. The authors suggested depositing a protective coating on the nanotubes consisting of metal or ceramic materials of 1–10 nm. In spite of the potentially high importance of carbon nanotubes, it is not clear from (Zhang, Wang, et al., 2008; Zhang, Zhan, et al., 2008) how the problem of very fast dissolution of carbon in Co by use of either solid-state or liquid-phase sintering was addressed.

1.15.5.3 Diamond-Enhanced Cemented Carbides

By 2013, tools for mining and construction with inserts comprising cemented carbide substrates and a layer of polycrystalline diamond (PCD) produced at ultrahigh pressures have become very popular and partially substitute conventional WC–Co cemented carbides (see the Internet site of Element Six). In spite of relatively high production costs and consequently high prices of the PCD inserts produced at ultrahigh pressures, their employment in many applications of mining and construction is economically reasonable due to their dramatically prolonged tool life. According to the forecast of Bellin, Dourface, and King (2010), drilling bits with PCD inserts will substitute conventional roller-cone bits with cemented carbide inserts with respect to the "footage drilled" by at least 80% in the next 5–10 years.

Between 2001 and 2010, diamond-containing cemented carbides or diamond-enhanced carbides produced at ultrahigh pressure were a topic of intensive research work. One of the examples of such materials is so-called "cellular diamond grade" developed by Smith Int. (Griffo, Brown, & Keshvan, 2003). This material is composed of "…repeating units of honeycomb composite material of polycrystalline diamond/PCD and WC–Co material…" and said to combine the high wear-resistance of PCD with high fracture toughness of WC–Co. This material can be fabricated only at ultrahigh pressures, at which diamond is thermodynamically stable in contact with WC–Co, which would presumably lead to its high production costs.

In the past years, much attention was paid to the possibility of producing diamond-enhanced carbides not employing ultrahigh pressures (at pressures below 1 GPa), at which diamond is thermodynamically unstable. The production of diamond-enhanced carbides is a great challenge; however, if such materials can be produced on a large scale, this is expected to dramatically increase hardness and improve the wear-resistance of WC–Co by at least one order of magnitude without sacrificing the fracture toughness. There are two major approaches to the development of diamond-enhanced carbides: (1) the use of binders not containing Fe-group metals in combination with uncoated diamond and (2) the employment of Co or other Fe-group metals as a binder in combination with diamond grains coated by barrier layers to prevent the diamond graphitization.

The first approach is based on sintering of diamond and carbides with binders based on either non-carbide-forming chemical elements, such as Cu, Ag, etc., or Al (Kösters & Lüdtke, 2005). Carbide-forming chemical elements, such as Ti (Pereyaslov, Primak, Voloshin, Gordienko, & Kolomiez, 1987) or Ti with additions of Cu and Ag to reduce its melting point (Ikawa & Miyashi, 1972), can also potentially be used. For the diamond-containing cemented carbides of the first type, the major problem is the very poor wettability of diamond and other carbides by non-carbide-forming metals, which can presumably be improved by adding some carbide-forming elements such as Zr, B, Si, and so on. The major problem of the diamond-containing cemented carbides of the second type is the very intensive and fast interaction of diamond with any carbide-forming element during sintering leading to the formation of high-melting-point carbides, which supresses the shrinkage during sintering. Wittmer and Filip (2006) suggested producing diamond-containing composites with a binder consisting mainly of Ni_3Al processed at temperatures of above 1200 °C. Such composites are reckoned to comprise diamond particles not converted to graphite.

The second approach was developed and patented by Sandvik (Brandrup-Wognsen & Ederyb, 1996) and Sumitomo (Miyamoto, Moriguchi, & Ikegaya, 1997). According to Brandrup-Wognsen and Ederyb (1996), a wear-resistance material consisting of 3–60% diamond grains having a coating of at least 1 μm of carbide, nitride or carbonitride of refractory metals can be sintered with Co, Ni and/or Fe in the solid state under pressure of nearly 33 MPa without diamond graphitization. According to Miyamoto et al. (1997) and Moriguchi, Tsuduki, Ikegaya, Miyamoto, and Morisada (2007), a material consisting of cemented carbide plus diamond coated with SiC can be sintered at 1300 °C at 41 MPa for 3 min by use of pulsed-electric current sintering. No graphitization of diamond in such a material was found and it has a 50% larger fracture toughness and 10 times better wear-resistance compared to conventional cemented carbides. Kuribayashi et al. (2006) suggested sintering diamond-containing cemented carbides containing phosphorus to reduce the binder melting point. Konyashin et al. (2010c) developed a new low-melting-point binder of the system: Fe-group metal–chromium–silicon–carbon with a melting point of nearly 1140 °C for fabrication of diamond-enhanced carbides. The diamond-enhanced carbides produced from diamond grains having a TiC coating of 0.5 μm, WC, Co, Cr_3C_2 and Si were sintered at 1160 °C with the presence of liquid phase, which allowed obtaining its full density. No diamond graphitization was found at the diamond–carbide–binder interface visible by the absence of signals from sp^2-hybridized carbon in the Raman spectra, as shown in Figure 14. The wear-resistance of this material in a grinding test against a diamond-grinding wheel was found to be nearly 100 times higher than that of the conventional WC–Co cemented carbides. Diamond-enhanced carbides by use of coated diamond grits can also be produced in the form of hard-facing on steel (Konyashin et al., 2010b).

It should be noted that in spite of the intensive research and numerous patents in the field of diamond-enhanced carbides with a metal binder obtained at pressures lower than 1 GPa, there are still no such materials on the market. This is presumably associated to difficulties related to producing dense diamond-containing cemented carbides with binders based on non-carbide-forming metals. In case of diamond-enhanced cemented carbides with binders on the basis of Fe-group metals, the major difficulty appears to be the fabrication of thick,

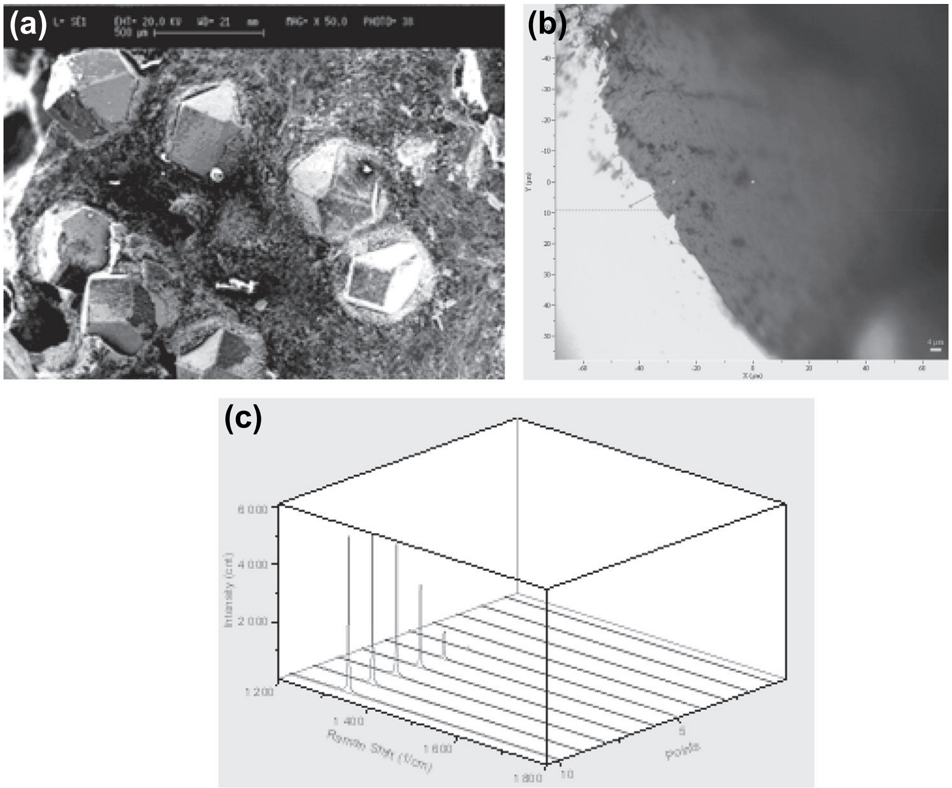

Figure 14 Diamond-enhanced carbide produced by use of a binder with a low melting point: (a) fracture surface; (b) cross-section of the diamond–carbide interface with the line indicating at which positions Raman spectra were taken; and (c) Raman spectra obtained on the cross-section shown in (b) at different distances from the diamond–carbide interface. Redrawn from Konyashin et al. (2010c). Reproduced with the permission of the World Intellectual Property Organization (WIPO); WIPO is not responsible for any transformation of the material.

continuous and defect-free barrier coatings on diamond, which have to completely prevent diamond graphitization during sintering.

Acknowledgments

The author gratefully acknowledges the assistance of Mr B. Ries and Dr M. Fish in the chapter preparation and fruitful discussions as well as Mr. K.-G. Hildebrand and the management of Element Six Hard Materials for the permission to publish illustrative materials.

References

Abe, N., Morimoto, J., Tomie, M., & Doi, C. (2000). Formation of WC-Co layers by an electron beam cladding method and evaluation of the layer properties. *Vacuum, 59*, 373–380.

Akerman, J., Ericson, T. (1997). Cemented carbide body with improved high temperatures and thermomechanical properties. US Patent 6,126,709.

Almond, E., & Roebuck, B. (1987). Identification of optimum binder phase composition for improved WC hard metals. *Materials Science and Engineering: A, 105/106*, 237–248.

Arato, P., Bartha, L., Porat, R., Berger, S., & Rosen, A. (1998). Solid or liquid phase sintering of nanocrystalline WC/Co hard metals. *Nanostructured Materials, 10*, 245–255.

Aronsson, B., Hartzell, T., & Aakerman, J. (1988). Structure and properties of dual carbide for rock drilling. In *Proceedings of advance hard material product conference*. Shrewsbury, UK: MPR Publ. Serv. Ltd.

Bellin, F., Dourface, A., King, W., & Thigpen, M. (November 2010). The current state of PDC technology. *World Oil*, 67–71.

Berger, S., Porat, R., & Rosen, R. (1997). Nanocrystalline materials: a study of WC-based hard metals. *Progress in Materials Science, 42*, 311–320.

Brandrup-Wognsen, H., Ederyb, S. (1996). Diamond-impregnated hard material. US Patent 5,723,177.

Brieseck, M., Hünsche, I., Caspers, B., Szesny, B., Gille, G., & Lengauer, W. (2009). *Optimised sintering and grain-growth inhibition of ultrafine and near-nano hard metals*. In *Proceedings of international conference PM* (Vol. 1). Copenhagen, Denmark: EPMA.

Brooks, K. J. A. (1996). *World directory and handbook of hard metals and hard materials* (6th ed.). United Kingdom: International Carbide Data.

Colin, C., Durant, L., & Favrot, N. (1993–1994). Processing of functional-gradient WC-Co cermets by powder metallurgy. *International Journal of Refractory Metals and Hard Materials, 12*, 145–152.

Collin, M., Norgren, S. (2008). Cemented carbide insert and method of making the same. European Patent EP1548136B1.

Beste, U., & Jacobson, S. (2008a). A new view of the deterioration and wear of WC/Co rock drill carbide buttons. *Wear, 264*, 1129–1141.

Beste, U., & Jacobson, S. (2008b). Rock penetration into cemented carbide drill buttons during rock drilling. *Wear, 264*, 1142–1151.

Branard, R. (1957). Physikalische Eigenschaften der Hartmetalle in Abhängigkeit vom Kohlestoffgehalt. *Neue Hütte, 12*, 757–761.

Caroll, D. F. (1997). Processing and properties of ultrafine WC/Co hard materials. In G. Kneringer, P. Rödhammer & P. Wilhartitz (Eds.), *Proceedings of the 14th international plansee seminar 1997* (Vol. 2). Reutte, Austria: Plansee Group.

Carpenter, M. (2003). Sintered carbide alloys with fine-grain WC for toughness and erosion resistance. European Patent EP1413637.

Caspers, B., Säuberlich, T., & Reiss, M. (2008). *Influence of manufacturing parameters on properties of nano tungsten carbide*. In *Proceedings of intrenational conference on tungsten, refractory and hard metals VII*. Washington, USA: Metal Powder Industries Federation.

Cho, K. H., Chung, I. S., & Lee. (1999). The influence of carbon content of the properties of binder and carbide phase of cemented carbide. *Interceram, 48*, 30–34.

Eiling, A., Caspers, B., Gille, G., & Gries, B. (2008). Nanoskalige Hartmetalle mit Fe-basierten Bindern. In H. Kolaska (Ed.), *Pulvermetallurgie: Neue Anforderungen – Neue Produkte – Neue Verfahren*. Hagen, Germany: Fachverband Pulvermetallurgie.

Fang, Z., Mahesdhwari, P., Wang, X., Sohn, H., Griffo, A., & Riley, R. (2005). An experimental study of the sintering of nanocrystalline WC-Co powders. *International Journal of Refractory Metals and Hard Materials, 23*, 249–257.

Fischer, U., Hartzell, E., Akerman, J. (1988). Cemented carbide body used preferably for rock drilling and mineral cutting. US Patent 4,743,515.

Fitzsimmons, M., & Sarin, V. K. (2001). Development of CVD WC-Co coatings. *Surface and Coatings Technology, 137*, 158–163.

Gee, M. G., Gant, A., & Roebuck, B. (2007). Wear mechanisms in abrasion and erosion of WC/Co and related hard metals. *Wear, 263*, 137–148.

Gille, G., Szesny, B., Leitner, G., & Caroll, D. F. (1997). A new 0.3 μm WC powder as well as powder-related properties and sintering behaviour of 0.6 to 30 μm WC-Co hard metals. In G. Kneringer, P. Rödhammer & P. Wilhartitz (Eds.), *Proceedings of the 14th international plansee seminar 1997* (Vol. 2). Reutte, Austria: Plansee Group.

Glatzle, J., Kosters, R., Glatzle, W. (2004). Hard metal component with a graduated structure and methods of producing the component. US Patent Application US2004/0009088.

Greenfield, M. (1997). Sintered hard-alloy composites and tools manufactured with microstructural zones by grain refining. US Patent 5,623,723.

Greer, A. L., & Wilde, J. R. (2001). Novel Ni-TaC nanocrystalline cermets. *Materials Science Forum, 360–362*, 261–266.

Griffo, A., Brown, R., & Keshvan, K. (June 2003). Oil and gas drilling materials. *Advanced Materials and Processes*, 59–60.

Gurland, J., & Bardzil, P. (1955). Relation of strength, composition, and grain size of sintered tungsten-carbide-cobalt alloys. *Journal of Metals, 7*, 311–315.

Gusafson, P., Wandenstroem, M., Norgren, S. (2004). Manufacture of fine-grain WC-Co alloy by sintering under nitrogen before pore closure. European Patent application EP1500713.

Egami, A., Kusava, T., Machida, M., & Kobayashi, K. (1989). Ultra sub micron hard metals for miniature drills. In H. Bildstein & H. Ortner (Eds.), *Proceedings of the 12th international plansee seminar 1989* (Vol. 2). Reutte, Austria: Plansee Group.

Eso, O., Fang, Z., & Griffo, A. (2005). Liquid phase sintering of functionally graded WC-Co composites. *International Journal of Refractory Metals and Hard Materials, 23*, 233–241.

Eso, O., Fang, P., & Fang, Z. (2007). A kinetic model for cobalt gradient formation during liquid phase sintering of functionally graded WC-Co. *International Journal of Refractory Metals and Hard Materials, 25*, 286–293.

Exner, H., & Gurland, J. (1970). A review of parameters influencing some mechanical properties of tungsten carbide-cobalt alloy. *Powder metallurgy, 13*, 13–31.

Falkovsky, V. A. (1997). *Theoretic bases of development and examination of cemented carbides for stamping*. Author's abstract of D.Sc. dissertation. Moscow, Russia: MISIS.

Fang, Z., Fan, P., Guo, J. (2010). Functionally graded cemented carbide with engineered hard surface and the methods for making the same. US Patent Application US2010/0101368A1.

Guo, J., & Wang, F. (2010). *A novel approach for manufacturing functionally graded cemented tungsten carbide composites*. Advanced in powder metallurgy & particulate materials. Washington, USA: Metal Powder Industries Federation.

Guo, J., Fan, P., & Fang, Z. (2009). A new method for making graded WC-Co by carburizing heat treatment of fully densified WC-Co. In L. Sigl, P. Rödhammer & H. Wildner (Eds.), *Proceedings of the 17th international plansee seminar* (Vol. 2). Reutte: Plansee Group.

Henjered, A., Hellsing, M., Nouet, G., Dubon, A., & Laval, J. (1994). Quantitative microanalysis of carbide/carbide interfaces in WC-Co base cemented carbides. *Materials Science and Technology, 2*, 847–855.

Heinrich, H.-W., Wolf, M., Schmidt, D., Schleinkoffer, U. (1999). A cermet having a binder with improved plasticity, a method for manufacture and use thereof. PCT Patent Application WO 99/10549.

Ikawa, T., Miyashi, K. (1972). Fitting diamond in metal. Japan Patent JP47044134.

Ivensen, V. A., Eiduk, O. N., Fal'kovskii, V. A., Lukashova, N. M., Chumakova, L. A., Gol'dberg, Z. A. (1977). Process for preparing cemented tungsten carbides. Great Britain Patent 1483527.

Ivensen, V. A., Eiduk, O. N., & Artemev, S. I. (1970). The dependence of plasticity of WC-Co cemented carbide on the carburisation temperature of tungsten and tungsten carbide. In *Hardmetals*. Moscow, Russia: Metallurgiya.

Fang, Z., Wang, X., Ryu, T., Hwang, K. S., & Sohn, H. Y. (2009). Synthesis, sintering and mechanical properties of nanocrystalline cemented tungsten carbide – a review. *International Journal of Refractory Metals and Hard Materials, 27*, 288–299.

Goren-Muginstein, G., Berger, S., & Rosen, A. (1998). Sintering study of nanocrystalline tungsten carbide powder. *Nanostring Materials, 10*, 795–804.

Greenfield, M. S., Edward, V. C. (1989). Earth working tool having a working element fabricated from cemented tungsten carbide compositions with enhanced properties. US Patent 4,859,543.

Herber, R.-P., Schubert, W.-D., & Lux, B. (2006). Hardmetals with "rounded" WC grains. *International Journal of Refractory Metals and Hard Materials, 24*, 360–364.

Hornbogen, E. (2001). Dispersion hardening—the oldest nanotechnology. *Metall, 55*, 522–526.

Howard, T. (1996). *Diamond year*. Sandton, South Africa: Boart Longyear Limited.

Kiefer, R., & Benesovsky, F. (1965). *Hrtmetalle*. Wien, Austria: Springer-Verlag.

Kolaska, H. (1992a). The dawn of the hard metal age. *Powder Metallurgy International, 24*(5), 311–314.

Kolaska, H. (1992b). *Pulvermetallurgie der Hartmetalle*. Hagen, Germany: Fachverband Pulvermetallurgie.

Kobayashi, M., Kinoshita, S. (1995). Grain-oriented WC-base hard alloy having high fracture toughness and wear-resistance and its manufacture. Japan Patent JP08199285.

Konyashin, I. (2002). Hard metal body with tungsten carbide in form of platelets for mining tools. German Patent DE10109634.

Konyashin, I., Schaefer, F., Cooper, R., Ries, B., Mayer, J., & Weirich, T. (2005). Novel ultra-coarse hard metal grades with reinforced binder for mining and construction. *International Journal of Refractory Metals and Hard Materials, 23*, 225–232.

Konyashin, I., Anikeev, A., Senchihin, V., & Glushkov, V. (1996). Development, production and application of novel grades of coated hard metals in Russia. *International Journal of Refractory Metals and Hard Materials, 14*, 41–48.

Konyashin, I., Ries, B., & Lachmann, F. (2010a). Near-nano WC-Co hard metals: will they substitute conventional coarse-grain mining grades. *International Journal of Refractory Metals and Hard Materials, 28*, 489–497.

Konyashin, I., Hlawatschek, S., Ries, B., Lachmann, F., Weirich, T., Dorn, F., et al. (2009). On the mechanism of WC coarsening in WC-Co hard metals with various carbon contents. *International Journal of Refractory Metals and Hard Materials, 27*, 234–243.

Konyashin, I., Hlawatschek, S., Ries, B., Lachmann, F., Sologubenko, A., & Weirich, T. (2010). A new approach to fabrication of gradient WC-Co hard metals. *International Journal of Refractory Metals and Hard Materials, 28*, 228–237.

Konyashin, I., Eschner, T., Aldinger, F., & Senchihin, V. (1999). Cemented carbides with uniform microstructure. *Zeitschrift für Metallkund, 90*, 403–406.

Konyashin, I., Ries, B., Lachmann, F., Cooper, R., Mazilkin, A., Straumal, B., et al. (2008). Hardmetals with nano-grain reinforced binder: binder fine structure and hardness. *International Journal of Refractory Metals and Hard Materials, 26*, 583–588.

Konyashin, I., Ries, B., Lachmann, F., Mazilkin, A., & Straumal, B. (2011). Novel hard metal with nano-strengthened binder. *Inorganic Materials: Applied Research, 2*(1), 19–21.

Konyashin, I., Cooper, R., Ries, B. (2004). Cemented carbide in particular for cutting stone, concrete and asphalt. European Patent 1520056.

Konyashin, I., Cooper, R., Ries, B. (2006). Cemented carbide in particular for cutting stone, concrete and asphalt. German Patent 10258537.

Konyashin, I. (2002). Hard metal with tungsten carbide in form of platelets for mining tools. German Patent 10109634.

Konyashin, I., Hlawatschek, S., Ries, B., Lachmann, F. (2010a). A hard-metal body. PCT Patent Application WO2010/097784A1.

Konyashin, I., Hlawatschek, S., Ries, B., Lachmann, F. (2010b). A superhard element, a tool comprising same and methods for make such superhard element. PCT Patent Application WO2010/103418A1.

Konyashin, I., Ries, B., Lachmann, F., & Fry, A. T. (2012). A novel sintering technique for fabrication of functionally gradient WC–Co cemented carbides. *Journal of Materials Science, 47*, 7072–7084.

Konyashin, I., Ries, B., Lachmann, F., & Fry, A. T. (2013). Gradient hardmetals: theory and practice. *International Journal of Refractory Metals and Hard Materials, 36*, 10–21.

Konyashin, I., Ries, B., Lachmann, F. (2010b). Wear part with hard facing. PCD Patent Application WO2010/029552A2.

Konyashin, I., Ries, B., Lachmann, F. (2010c). A hard-metal. PCD Patent Application WO2010/029518A1.

Kösters, R., Lüdtke, A. (2005). Wearing part consisting of a diamante ferrous composite. PCD Patent Application WO2005/118901A1.

Kreimer, G. S. (1968). *Strength of hard alloys*. New York, USA: Consultants Bureau.

Kuribayashi, N., Ishizaki, K. and Matsumari K. (2006) Composite wear-resistant memebr adn method for manufacture thereof. PCT Patent Application WO2006/080302A1.

Lassner, E., & Schubert, W.-D. (1999). *Tungsten*. New York, USA: Kluwer Academic/Plenum Publishers.

Lassner, E., Schreiner, M., & Lux, B. (1982). Influence of trace elements in cemented carbide production. Part 2. *International Journal of Refractory Metals and Hard Materials, 1*(3), 97–102.

Larsen-Basse, J. (1973). Wear of hard-metals in rock drilling: a survey of the literature. *Powder Metallurgy, 16*, 1–31.

Lay, S., Hamar-Thibault, S., & Lackner, A. (2002). Location of VC in VC, Cr3C2 codoped WC-Co cermets by HRTEM and EELS. *International Journal of Refractory Metals and Hard Materials, 20*, 61–69.

Liu, Y., Wang, H., Long, Z., Liaw, P., Yamg, J., & Baiyun, H. (2006). Microsctructural evolution and mechanical behaviours of graded cemented carbides. *Materials Science and Engineering: A, 426*, 346–354.

Liu, Y., Wang, H., Yang, J., Huang, B., & Long, Z. (2004). Formation mechanism of cobalt-gradient structure in WC-Co hard alloy. *Journal of Materials Science, 39*, 4397–4399.

Lueth, R. (1986). Method for carbon control of carbide performs. US Patent 4,579,713.

Luyckx, S., Sacks, N., & Love, A. (2007). Increasing the abrasion resistance without decreasing the toughness of WC-Co of a wide range of compositions and grain sizes. *International Journal of Refractory Metals and Hard Materials, 25*(1), 57–61.

Mischalsky, A., & Rosinsky, M. (2008). *Journal of the American Ceramic Society, 91*(11), 3650–3565.

Miyamoto, Y., Moriguchi, H., Ikegaya, A. (1997). Ultrahard composite members comprising diamond particles dispersed in cemented carbide or cermets matrix having high hardness and wear-resistance and their preparation. Japan Patent JP10310838.

Moriguchi, H., Tsuduki, K., Ikegaya, A., Miyamoto, Y., & Morisada, Y. (2007). *International Journal of Refractory Metals and Hard Materials, 25*(3), 237–243.

Langford, J. W., Delwiche, R. (1998). Hardfacing with coated diamond particles. US Patent 5,755,299.

Nam, H., Lim, J., & Kang, S. (2010). Microstructure of (W, Ti)C-Co system containing platelet WC. *Materials Science and Engineering: A, 527*, 7163–7167.

O'Quigley, D. G. F., Luyckx, S., & James, M. N. (1997). An empirical ranking of a wide range of WC-Co grades in terms of their abrasion resistance measured by the ASTM standard B611-85 test. *International Journal of Refractory Metals and Hard Materials, 15*, 73–79.

Panov, V. S., Chuvilin, A. M., & Falkovsky, V. A. (2004). *Technology and properties of sintered cemented carbides and articles thereof*. Moscow, Russian Federation: MISIS.

Pereyaslov, V., Primak, L., Voloshin, M., Gordienko, V., & Kolomiez, B. (1987). *Superhard Materials, 2*, 27–29.

Prakash, L., & Gries, B. (2009). WC hardmetals with iron based binders. In L. Sigl, P. Rödhammer & H. Wildner (Eds.), *Proceedings of the 17th international plansee seminar* (Vol. 2). Reutte, Austria: Plansee Group.

Rassbach, S., Moseley, S., & Böhlke, W. (2009). Metallurgical fundamentals of macroscopic gradient hardmetals. In L. Sigl, P. Rödhammer & H. Wildner (Eds.), *Proceedings of the 17th international plansee seminar* (Vol. 2). Reutte, Austria: Plansee Group.

Roebuck, B., Gee, M. G., & Morrell, R. (2001). Hardmetals – microstructural design, testing and property maps. In G. Kneringer, P. Rödhammer & H. Wildner (Eds.), *Proceedings of the 15th international plansee seminar* (Vol. 4). Reutte, Austria: Plansee Group.

Schreiner, M., Schmitt, Th, Lassner, E., & Lux., B. (1984). On the origin of discontinuous grain growth during liquid phase sintering of WC-Co cemented carbides. *Powder Metallurgy International, 16*, 180–183.

Shao, G., Duan, X.-L., Xie, J., Yu, X., Zhang, W., & Yuan, R. (2003). Sintering of nanocrystalline WC-Co composite powder. *Reviews on Advanced Materials Science, 5*, 281–286.

Terry, C. J. (1989). Macrocrystalline tungsten monocarbide powder and process for production. US Patent 4,834,963.

Terry, C., & Morris, J. (December 1999). Macrocrystalline thermit process revealed. *Metal Powder Report*, 22–26.

Tretyakov, V. I. (1975). *Basics of materials science and production technology of sintered cemented carbides*. Moscow, Russia: Metallurgiya.

Schatt, W., Wieters, K. P., & Kiebach, B. (2007). *Pulvermetallugie*. Würzburg, Germany: Springer.

Schleinkofer, U., Sockel, H.-G., Görting, K., & Heinrich, W. (1996). Microstructural processes during subcritical crack growth in hard metals and cermets under cyclic loads. *Materials Science and Engineering: A, 209*, 103–110.

Sharma, N. K., Wards, I. D., Fraser, H. L., & Williams, W. S. (1980). SREM analysis of grain boundaries in cemented carbides. *Journal of the American Ceramic Society, 63*, 194–196.

Suzuki, H., & Kubota, H. (1966). The influence of binder phase composition on the properties of tungsten carbide-cobalt cemented carbides. *Planseeberichte Fuer Pulvermetallurgie, 14*(2), 96–109.

Taniguchi, Y., Sasaki, H., Ueki, M., Kobopri, K. (1986). Manufacture of surface-refined sintered alloy. Japan Patent Application 1986-314817.

Upadhyaya, S. (1998). *Cemented tungsten carbides: Production, properties and testing*. New Jersey, USA: Noyes Publications.

Warbichel, P., Hoferm, F., Grogger, W., & Lackner, A. (2001). EFTEM-EELS characterization of VC and Cr_3C_2 doped cemented carbides. In G. Kneringer, P. Rödhammer & H. Wildner (Eds.), *Proceedings of the 15th international plansee seminar* (Vol. 2). Reutte, Austria: Plansee Group.

Wittmer, D. E., Filip, P. (2006). Manufacture of composite containing nickel aluminide (Ni_3Al) intermetallic binder and reinforced with diamond particles in amount of 20–70%. International Patent Application WO2006107628.

Yang, D.-Y., & Kang, S.-J. (2009). Suppression of abnormal grain growth in WC-Co via presintering treatment. *International Journal of Refractory Metals and Hard Materials, 27*, 90–94.

Zhang, L., Wang, Y., Yu, X., Chen, S., & Xiong, X. (2008). Crack propagation characteristics and toughness of functionally graded WC-Co demented carbides. *International Journal of Refractory Metals and Hard Materials, 26*, 295–300.

Zhang, Y., Zhan, G., Sheng, X., Locksetdt, A., Griffo, A., Shen, Y., Deng, H., Keshavan, M. (2008). Nano-reinforced WC-Co for improved properties. US Patent Application US2008179104A.

Zhuk, Y. (2007). Hardide™: advanced nanostructured CVD coating. *International Journal of Microstructure and Materials Property, 2*(1), 90–98.

List of Relevant Websites

1. http://legacy.secotools.com
2. http://sandvik.net
3. http://www.fundinguniverse.com/company-histories/Kennametal-Inc-Company-History.html
4. http://www.wirtgen-group.de
5. http://www.ceratizit.com
6. http://www.tungaloy.com
7. http://www.multi-metals.com
8. http://www.itia.info
9. http://hardide.com/
10. www.e6.com

1.16 Coating Applications for Cutting Tools

Uwe Schleinkofer and Christoph Czettl, CERATIZIT Austria GmbH, Reutte, Austria
Claude Michotte, CERATIZIT Luxembourg S. à. r. l., Route de Holzem, Mamer, Luxembourg

1.16.1 Introduction

Typically, hard coatings are produced via condensation from the vapor phase. In chemical vapor deposition (CVD) gaseous precursor vapors at elevated temperatures react and form the desired chemical compound of the coating. Since high temperatures are necessary to deposit most of these hard coatings, substrate materials are mainly limited to cemented carbides. CVD processes are suitable for coating parts with complex geometries, can produce relatively thick coatings, and characteristically yield crystalline oxide coatings. Physical vapor deposition (PVD) processes generate the vapor from a solid source by physical methods and are generally conducted at lower temperatures, enabling the use of metallic substrate materials. Ionization of the reactant species and low deposition temperatures permit the deposition of metastable coatings, far from the thermodynamic equilibrium, a major reason why PVD is a flexible process that can produce a broad variety of coatings.

This chapter addresses the history of CVD and PVD coatings, their technological aspects, coating architectures, and finally their range of application and why in some regions one technology dominates and in others both are competitive.

1.16.2 CVD Hard Coatings

Hard coatings deposited via CVD are still dominant, with coating thickness up to 30 μm being used for wear protection and thick Al_2O_3 layers as thermal barrier coatings. Important applications include turning cast

http://dx.doi.org/10.1016/B978-0-08-096527-7.00016-7

irons and steel, in both continuous and interrupted, where thicker coating and good adherence are beneficial (Ruppi, 2001).

1.16.2.1 Development of CVD Hard Coatings

The introduction of TiC-coated cemented carbide cutting tools in 1969 led to a significant increase in tool life. The next step of development (1973) was the introduction of multilayer coatings using combinations of TiC, TiCN and TiN (**Figure 1**). In 1975, the first Al_2O_3-coated cutting tools were marketed. Very early in their development it became evident that the nucleation step was crucial to the quality of the coatings (Kornmann, Schachner, Funk, & Lux, 1975). While most of the Al_2O_3 coatings in the initial stages of their development were mixtures of the stable α-Al_2O_3 phase and the metastable κ-Al_2O_3 phase, some single-phased coatings were also reported. Funk, Schachner, Triquet, Kornmann, and Lux (1976) presented the possibility of depositing α-Al_2O_3 coatings at temperatures as low as 850 °C and reported their beneficial effect on turning low-carbon steel. In the beginning of the 1980s, Altena (Altena, 1982) investigated the rate of growth of α-Al_2O_3 on single crystalline sapphire; impurities like Cr, Si, Au, Fe, Ni and Co; and cemented carbide substrates. The coatings were reported to be single phased with homogenous-sized crystallite. Colombier (Colombier, 1984) investigated the influence of gas phase and substrate material and found that thin layers were not strongly textured, while thicker coatings showed (104), (116) and (124) texture. The use of H_2S as a catalyst during Al_2O_3 deposition was one of the most important steps in the development of CVD Al_2O_3 coating. It suppressed the dog bone effect, i.e. higher coating thickness in the cutting edge, and significantly increased deposition rates (Ruppi & Larsson, 2000; Smith & Lindström, 1986). Consequently, this development led to optimization of deposition conditions (Ruppi, 1994) and helped generate highly textured coatings. Further documents where the Patents from Ljungberg (Ljungberg, 1998; Ljungberg, 2007; Ljungberg & Lenander, 1993) who claimed also the preferred orientation in (012), (104) and (110) orientation, but considered only fewer peaks for the calculation, which led to higher coefficients. As discussed by Spieß et al., one has to be careful because the texture coefficient is only a rough estimation of preferred orientation. For thin films, the pole figures are more adequate to describe the crystal orientation (Birkholz, 2006; Spieß, Schwarzer, Behnken, & Teichert, 2005). One example is the 006 texture, which has a very low standard intensity of 2% and shows high textures with low peak intensities. This orientation was neglected in the earlier patents, although its existence was discussed in earlier works (Altena, 1982; Colombier, 1984). The Walter WAK20 shown in **Figure 2** was one of the first coatings which showed this strong orientation.

During the past decade, the mechanical properties and also wear behavior of the different textures were investigated in detail (M'saoubi & Ruppi, 2009; Ruppi, 2008; Ruppi, Larsson, & Flink, 2008). The gas systems mainly used for the deposition of Al_2O_3 coatings are mixtures of H_2 as so-called "carrier gas", $AlCl_3$ which is formed due to in situ chlorination of Al with HCl and CO_2 and/or CO as oxygen feed and H_2S as catalytic agent. Beside the main component Ar, N_2 as well as numerous dopants can be introduced.

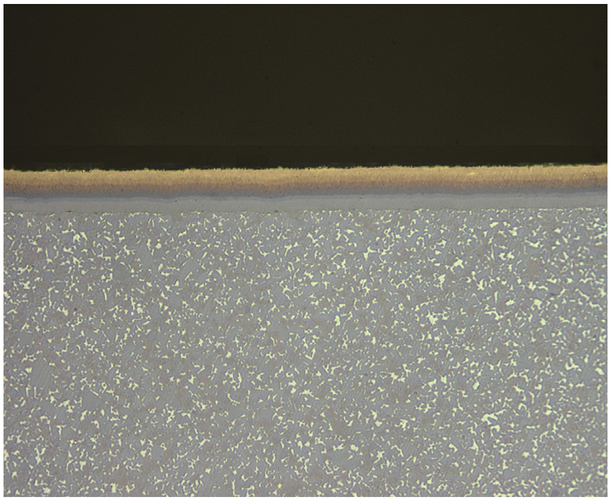

Figure 1 Light optical microscope cross section of a Goldmaster GM35 Multilayer coating architecture with TiC and TiCN, with increasing nitrogen content and a total thickness of 12 μm.

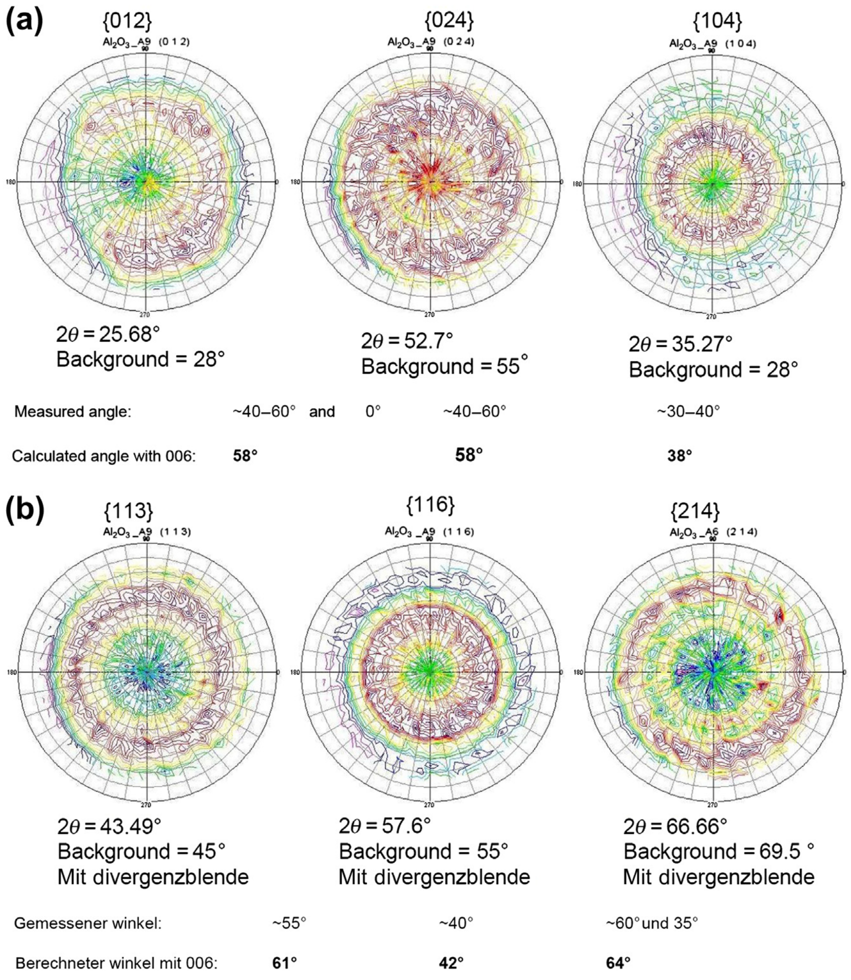

Figure 2 Pole figures of a Walter WAK20 grade from 2001 with preferred 001 orientation of α-Al_2O_3, showing the pole figures of (012), (104), (113), (024), (116) and (214) orientation and the tilt angle to 006.

Beside the developments on the Al_2O_3 coatings, the TiCN base layer was also revolutionized. At the end of the 1980s, the medium-temperature titanium carbonitride (MT-TiCN) coatings deposited from $TiCl_4$–CH_3CN–H_2–N_2 gas mixture were introduced to the market and substituted the conventional TiC or TiCN base layer, deposited using $TiCl_4$–CH_4–H_2–N_2 gas mixture (Bonetti-Lang, Bonetti, Hintermann, & Lohmann, 1982; Bonetti & Wahl, 1983; Kübel, 1991; Ruppi, 2001). The main advantage is the increased toughness by avoiding the brittle eta phase formation, because of the lower deposition temperatures which were possible due to the lower bonding strength of CH_3CN compared to CH_4. The typical columnar structure in combination with the optimized deposition conditions led to an increased reliability in the application (Larsson & Ruppi, 2002).

For some special applications like milling of titanium or when higher toughness is needed, coating systems deviate from the common TiN–MT-TiCN–Al_2O_3 architecture. Where very hard and wear-resistant coatings are needed, coatings containing boron like TiBN, TiCNB or TiB_2 deposited via CVD can be applied. Especially the TiB_2 coatings (cf. **Figure 3**) are very interesting due to their high hardness of around 40 GPa and their residual compressive stresses, which are uncommon for CVD coatings on cemented carbide cutting tools. They also show a very fine structure and smooth surface that are properties usually found in PVD coatings (Holzschuh, 2004, Holzschuh, 2005; Mitterer et al., 1999; Wallgram & Schleinkofer, 2009).

1.16.2.2 Processes

Nowadays, for the industrial application of CVD hard coatings on cemented carbide cutting tools, the classical process is used without activation or assistance by plasma, laser or microwaves. The main components of an industrial-scale CVD unit are shown in **Figure 4**.

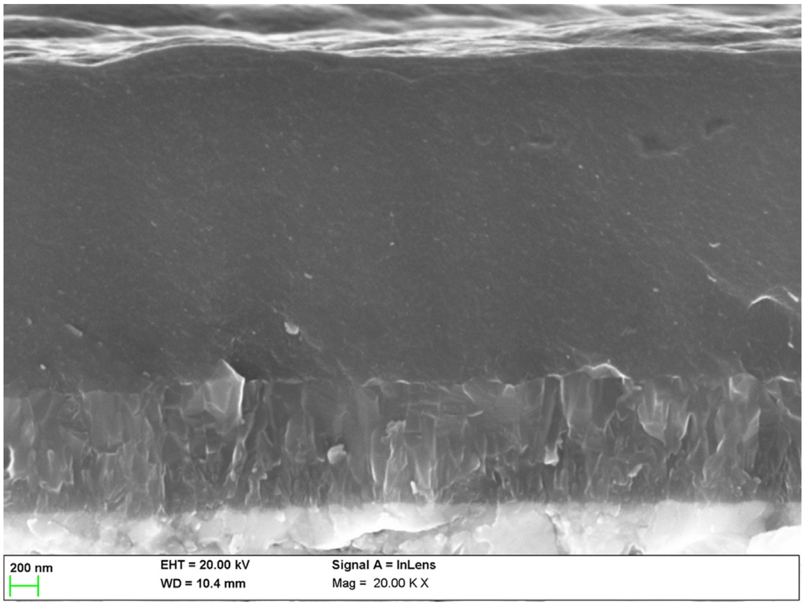

Figure 3 Scanning electron microscopic image of fracture cross-section of CVD TiN–TiB_2 coating of CERATIZIT grade CTC5240.

Plasma-activated CVD (PACVD) which was intermediate between CVD and PVD was rapidly dropped because of the improvements of CVD and the possibility of depositing thicker coatings including Al_2O_3 with PVD technology (EMUGE-Franken, 2004; Prengel, Pfouts, & Santhanam, 1998).

In particular, the gas distribution is crucial in large-scale CVD production where up to 15,000 half-inch inserts have to be coated as homogeneously as possible. The former used gas flow from bottom to top or

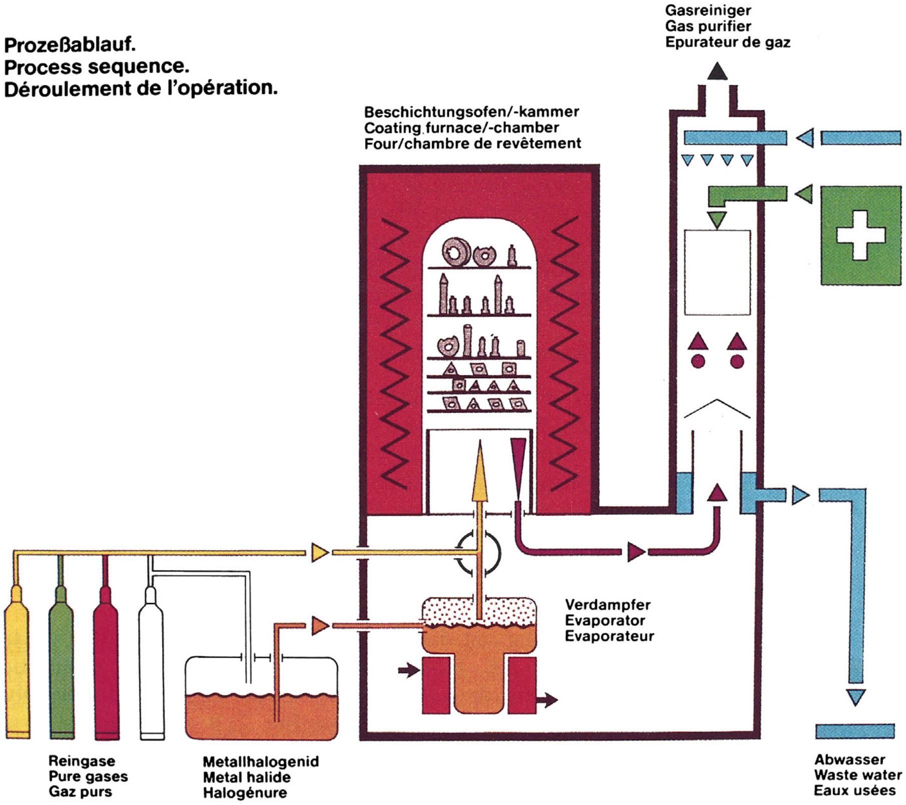

Figure 4 Main components of an industrial-scale CVD unit (Schedler, 1988).

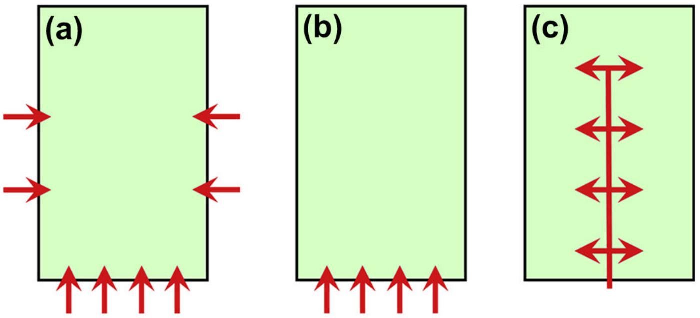

Figure 5 Gas flow principles for CVD coating of cemented carbide inserts with gas flow from bottom to top (b), with additional gas inlet (a) and centric feed gas tube (c) (Czettl et al., 2009).

top down (cf. **Figure 5(a)**) and additional gas inlets (cf. **Figure 5(b)**) are widely substituted by the centric feed gas tube (cf. **Figure 5(c)**) with rotation, which is the key for homogenous MT-TiCN coatings (Czettl, Mitterer, Michotte, Penoy, & Kathrein, 2009).

The gas distribution and also the preheating of the reactive gases are the most important steps when dealing with highly reactive precursors like NH_3 or B, which are in focus for new developments (Endler et al., 2008; Endler et al., 2010; Wagner et al., 2008).

1.16.2.3 Additional Elements

The effect of impurities (originally unwanted) has been investigated in detail since the beginning of CVD. Their effect on the microstructure and mechanical properties led to the systematic doping or alloying of elements to increase the tool lifetime (Altena, 1982; Barna, 1981; Wilhartitz, Grasserbauer, Altena, & Lux, 1986).

The influence of numerous additional elements like B, Zr, Hf, C_2H_6 and CO has been reported for TiN, TiCN and MT-TiCN coatings. This led to a wide range of modifications of structure, tribological, and mechanical properties of the coatings (Czettl et al., 2011; Hiroyuki, 2001; Holzschuh, 2000b; Holzschuh, 2004; Holzschuh, 2005; Ruppi & Larsson, 2003; Wagner et al., 2006). The modification of the Al_2O_3 phase due to additional elements was extensively investigated. In case of κ-Al_2O_3 coatings, stabilization of the thermal transformation was one goal besides the improvement of mechanical properties (Hochauer et al., 2010; Kathrein, 2001; Kathrein, Schintlmeister, Wallgram, & Schleinkofer, 2003; Okude, Tomita, Nakamura, & Osada, 2011). The doping of α-Al_2O_3 was investigated to enhance the tribological properties as well as the cutting performance (Hochauer et al., 2008; Kathrein, 2001).

1.16.3 PVD Hard Coatings

Hard coatings deposited via PVD are dominant when sharp cutting edges are used and are high demands relating to toughness are needed. Beside coating of drills and end mills, PVD-coated indexable inserts are commonly used for milling applications as well as interrupted turning operations, when difficult-to-cut materials have to be machined.

1.16.3.1 Development of PVD Hard Coatings

During the early 1980s, the first industrially developed hard coatings were based on binary carbides and nitrides of transition metals, namely, TiC, TiN and CrN. TiN has been one of the most used hard coatings. The main reasons for this were its good thermal stability and better resistance to crater wear compared to TiC at least until 550 °C where it starts to oxidize in ambient air. The introduction of TiN-coated high speed steel (HSS) drills and turning tools increased the tool lifetime up to five times and three times, respectively. Moreover, its fairly good mechanical, thermal and wear properties as well as the shiny golden color made TiN very attractive. Although these coatings are still applied successfully in certain fields, they have been replaced in most applications due to the demand of industry to higher machining speeds and higher feed rates in combination with longer service times of the tools. The desire of reducing the used polluting and expensive lubricant coolants are leading to elevated tool tip temperatures up to more than 900 °C, which is beyond the possibilities of these coating systems because of their low resistance to oxidation. In fact, TiN starts to oxidize rapidly at about 500 °C and forms the rutile structure TiO_2, which leads to deterioration of mechanical properties. Therefore, huge efforts have been made to develop a new generation of coating materials that possess adapted properties. One approach was to expand the already existing and well-established binary coating systems by adding other elements. This has led to the development of Ti–Al–N and Cr–Al–N coatings. The incorporation of Al in the TiN system to form Ti–Al–N (Münz, 1986) was the first step to launch a new generation on hard coatings. Al incorporated into the face-centered cubic structure (fcc) of TiN results in the formation of a metastable ternary solid solution Ti–Al–N, which is well known to improve the cutting performance (Knotek, Munz, & Leyendecker, 1987) because of its high hot hardness due to age hardening (Mayrhofer et al., 2003) and excellent oxidation behavior up to temperatures of 800 °C (Kim & Kim, 1997) due to the formation of a self-renewing protective Al-rich oxide layer (Al_2O_3) at the film surface (Mcintyre, Greene, Hakansson, Sundgren, & Munz, 1990).

Ti–Al–N coatings have become the standard choice for many applications, e.g. dry cutting with high operating temperatures and the superior performance, compared to TiN and Ti–C–N-coated tools, has been demonstrated in diverse cutting tests.

However, the developments in machining technology have led to an enormous variety of different requirements for cutting tools. This makes it impossible to provide one single solution or the "ultimate hard coating" for all purposes. The current trend in thin film technology is the development of hard coatings with tailored properties for the respective application. Obviously, the choice of the appropriate alloying element and alloying content as well as the incorporation of several alloying elements forming multicomponent single- or multilayered coatings combining different mechanisms are the key functions of coating development. Therefore, a basic understanding of the relation between the deposition process, the structure and morphology of the coating and the resulting mechanical, tribological, physical and chemical properties is needed. This is far from being a simple task since process parameters like gas flow, electrical current and voltage, alloying elements and alternating layer architectures can have a dramatic influence on the nucleation and growth conditions and thus on the coating structure, properties and the cutting performance. In addition, findings and relations developed on laboratory-scale facilities are not necessarily directly applicable to industrial production plants, which adds the issue of upscaling to industrial conditions to the challenges mentioned before. In total, all these effects make it scientifically and technically demanding to elucidate principle relations in hard coating deposition.

1.16.3.2 Processes

The general principles of PVD processes are simple. In a reduced pressure environment, a vapor of the so-called target, acting as the material source for the coating, is produced by physical mechanisms (evaporation or collision impact). This is followed by transportation of the vapor to the substrate, where it condenses and forms a solid film. This simple setup provides one of the major benefits of the PVD processes, which is the high flexibility. The application of reactive gases in the working chamber fosters reactions between the vapor and the reactive gas and enables the deposition of compounds like nitrides, carbides and oxides. Also the methods to generate the vapor and to transport it to the substrate and the conditions of condensation can be varied and modified in a broad range, giving rise to the possibility of tailoring the coatings to the respective application and desired properties. This led to an extremely wide field of process modifications in the field of PVD.

1.16.3.2.1 Thermal Evaporation

In the thermal evaporation process, the deposition material is vaporized in high vacuum by heating with different methods, i.e. resistance heating, induction heating, electron beam or laser beam. The produced particles are nonionized or insignificantly ionized and have low energy. Due to the vacuum in the deposition chamber, the particle flux condenses on the "cold" substrates, which are normally also heated in order to reach good coating properties, and chamber walls.

1.16.3.2.2 Ion Plating

The characteristic of an ion plating process is the additional bombardment of the already deposited coating, most often with argon ions. The substrate is charged with a high negative voltage (0.3–5 kV) in order to generate a glow discharge that enables a constant sputtering of the coating. However, the condensation rate on the substrate has to be higher than the rate of backsputtering. The evaporation itself can be either a thermal evaporation or a sputter process. Consequences of the ion plating method are a high defect density and therefore a high nucleation rate which produces dense coating and grain refinement.

1.16.3.2.3 Cathodic Arc Evaporation

Since its introduction into large-scale industrial coating processes in the early 1980s, cathodic arc evaporation (CAE) has become one of the most important production techniques for wear-protective coatings on tools. CAE is generally used for the evaporation of Ti, Al or Cr and their alloys. The introduction of reactive gases permits the deposition of hard coatings like nitrides such as Ti–Al–N and Cr–Al–N, carbides, oxides and mixtures of them. Arc technology provides the possibility of producing dense and well-adherent coatings at rather high deposition rates compared to the other PVD methods. Moreover, the formation of compressive residual stress can also be mentioned as an advantage of cathodic arc deposition.

In this process, ignition plasma between the anode, constituted by the grounded chamber wall, and the negatively charged cathode, the so-called target, is used to evaporate the deposition material. The targets could be circular, rectangular or cylindrical and the ignition plasma can be generated using various methods.

The evaporation takes place in inert working gas (e.g. Ar) or a reactive atmosphere (e.g. N_2) with a residual gas pressure smaller than a few pascals. A stream of electrons of a few 10–100 A is generated and flows through the cathode. Compared to the sputter process, this leads to very high currents and power densities on the target (about 1013 W/m^2) and causes a localized evaporation of the target material. Hence, positive and highly ionized high energetic plasma is formed.

The initiation of the arc can be realized via a trigger wire, which is brought into short contact with the cathode leading to high ionization of the cathode surface. After initiating, the arc is moving randomly over the target or can be steered by a dynamic magnetic field, evaporating the target surface. The arc can be run in continuous direct current (DC) mode, although pulsed power supplies—based on discontinuous arc burning—are used in some cases. Pulsed operation systems have the advantage of reduced cathode heating at the spot due to the relatively low average power compared to the DC mode.

After evaporation, the ejected ions are accelerated toward the substrate by applying a negative potential (bias voltage) on the substrate material. With the bias voltage, the impact energy of a large fraction of the ionized particles can be controlled, which enables the modification of film growth conditions and therefore also coating properties.

The existence of “droplets”, tiny globules of metal ranging in size from a few 100 nm up to a few 10 μm, is the main disadvantage of cathodic arc deposition since some of them reach the substrate leading to the formation of undesired macroparticles. These particles end up as defects in the coating and are responsible for high roughness, inhomogeneous microstructures or the formation of voids.

There are some methods to filter such macroparticles from the plasma stream such as the filtered arc deposition where the electrons and ions are guided through a curved trajectory where droplets cannot follow, slamming into the walls. Another way to reduce the number of droplets is to speed up the arc spot movement, but all these techniques decrease the deposition rate. Summarizing, the possibility to steer the arc spot, the high ionization rate and the high deposition rate are the main advantages of the CAE process.

1.16.3.2.4 Sputtering

Sputtering designates the effect of direct ejection of a target surface by momentum transfer from incident particles, usually Ar^+ ions provided by argon gas generated in a glow discharge.

The Ar^+ ions are generated by collision of accelerated free electrons with neutral particles, such as argon atoms. The ejected and decelerated electrons may be accelerated again within the electric field and collide once more. Consequently, the number of charge carriers multiplies. The Ar^+ ions move toward the negative cathode, whereas the electrons are accelerated toward the substrate. Hence, the Ar^+ ions are the charge carriers responsible for sputtering of the target surface atoms. Subsequently, the ejected atoms are transported toward the substrate and condense onto its surface. The number of atoms ejected by an incident particle depends on mass ratio, angle of incidence, surface energy and the target material’s sublimation heat. Furthermore, the condition of the target, such as its roughness, crystalline structure and temperature, are of importance.

1.16.3.2.4.1 DC-Sputtering

DC mode is usually used for conductive targets. After the ignition of the glow discharge, the ions move toward the cathode and eject the target atoms, which consequently form the vapor phase that is supposed to coat the substrate. Due to collisions with the plasma particles, the sputtered atoms move with a certain angle and energy distribution toward the substrate in an unordered way and condense at the substrate as well as the chamber walls.

1.16.3.2.4.2 Radio-Frequency Sputtering

In radio-frequency (RF) mode, a high-frequency alternating electrical field is applied between the anode and the target. This alternating field causes the ions and the electrons to be accelerated in both directions in alternation. Furthermore, electrons reach the target surface during the positive half-wave on the target, generating a negative charge. Consequently, the positive argon ions are accelerated toward the target surface. RF sputtering imposes no restrictions on the layers which can be deposited, since nonconductive or semiconductive materials such as Si_3N_4, Al_2O_3, BN or TiB_2 can also be sputtered.

1.16.3.2.4.3 Magnetron Sputtering

One of the major disadvantages of conventional sputtering systems is their rather low coating yield. Typically required coating thickness of 3–5 μm in case of hard coatings is only obtained after several hours of deposition. By using a magnetron sputtering array, the deposition rate could be increased by a factor of 5.

The term "magnetron sputtering" is used when a magnetic field is inserted behind the target in order to intensify the sputtering process. Due to the superimposition of the electric fields and the magnetic field by the Lorentz force, the electrons from the glow discharge no longer move parallel to the electric field lines, but instead along a cycloid motion that leads to a higher ionization yield, minimizes the loss of electrons by wall reactions and, finally, leads to a higher deposition rate. Electron density, and therefore also ion density, is highest in the zone in which the magnetic field is parallel to the target surface. Due to their high mass, the ions are hardly deflected by the magnetic field, and the greatest erosion of the target occurs below this zone leading to typical "racetrack" erosion on the target.

In general, magnetron devices can be divided into two types:

- Conventional balanced magnetrons
- Unbalanced magnetrons

In reactive magnetron sputtering, reactive gaseous components, such as N_2, CH_4, or O_2, are added to the working gas (usually argon), become part of the plasma, and contribute actively to the process of film formation on the substrate by reacting with the atoms eroded from the target.

1.16.3.2.4.4 Pulsed High-Current Sputtering

In the different sputtering modes, plasma ionization is significantly below the values achieved in CAE, which leads to negative effects for layer properties. In comparison to CAE, the power density at the target should be increased by a factor of 10–100 to achieve similar material-vapor plasma ionization. Power densities in the range of a few 100 W/cm^2 to several 1000 W/cm^2 are used in pulsed high-current sputtering (high power impulse magnetron sputtering, HPPMS, HIPIMS,…). Continuous operation of such a process is not possible since the target would overheat. Therefore, pulses with different durations and frequencies are used, with intervals between pulses of a few milliseconds. By the way, ionization of the sputtered material in the plasmas may reach approximately the same values as in CAE and, as a consequence, morphologically dense layers can be also deposited. With an optimized deposition process, the layers are free of droplets and less rough than layers produced by CAE.

Pulsed high-current sputtering is a complementary technology to CAE, particularly as a hybrid process used in one and the same PVD device, parallel or alternating to evaporate the target material (cf. Section 1.16.3.2.5).

1.16.3.2.5 Hybrid Processes

By hybrid processes, we mean that different processes are used in the same coating system to create a coating. Different systems already exist in the market and are used to create some dedicated coatings as described below.

The deposition of low-friction diamondlike carbon (DLC) layers requires an intermediary sublayer to attain adhesion. The sublayer is generally created by a PVD process followed by the functional and high-quality tribological DLC top layer created by a plasma-assisted CVD process (PACVD).

CAE can also be combined with a sputtering process when a high-performance layer has to combine nonconductive or semiconductive materials which cannot be evaporated by CAE.

Till now, combination of CAE and standard sputtering processes did not lead to significant benefits due to the different characteristics of each process. Nevertheless, the improvement in sputtering due to the development of the "pulsed high-current" process (cf. Section 1.16.3.2.4.4) should be the key to combine the advantages of arc and sputtering technologies: high ionization with virtually no droplets to create smooth and dense coatings with optimized coatings structure and properties.

1.16.3.3 Coating Architecture

1.16.3.3.1 Monolayer

Classical PVD layers like TiN, Ti–C–N, CrN, Ti–Al–N are based on a monolayer architecture where different features like structure, morphology, composition gradient, grain size and defects are influenced by the process parameters with an impact on the layer properties (e.g. hardness, phase stability, tribological properties). The incorporation of further additional elements opens new abilities to improve machining performance (cf. Section 1.16.3.4).

1.16.3.3.2 Multilayer

Multilayered coatings are composed of a periodically repeated structure of lamellae of two or more materials. The use of multilayer coatings exhibits benefits in modifying stresses, enhancing substrate adhesion and improving the resistance for crack propagation. Moreover, a multifunctional coating design depending on the alternating coating systems is realizable. In order to meet the requirements for a given cutting application, adjustment of the layer composition and thickness is needed. When different alloyed systems are combined, each layer with optimized chemical and structural composition fulfills separate tasks to contribute to strengthening, controlled lubrication and increase of oxidation resistance; it is assumed that adjustment of the different compositions and the control of the layer thicknesses will meet the requirements for given cutting applications (cf. **Figure 6**).

1.16.3.3.3 Superlattice

The so-called superlattices, which are nanoscale multilayer coatings, have been developed in order to increase the hardness and toughness of the system. Key elements of the concept are that very thin layers (about 10 nm) inhibit dislocation formation, while differences in elastic modulus between layers inhibit dislocation mobility. Hardness and periodicity are related by a Hall–Petch relationship where periodicity is the minimum periodic length between layers in the multilayer coating. It is possible to produce coatings significantly harder than the individual layers when these layers have sharp interfaces and periodicity of about 10 nm. Nevertheless, the superlattice effect could disappear if the layers are not of correct periodicity. Another technology is able to overcome this shortcoming by creating three-dimensional nanoscale coatings (cf. Section 1.16.3.3.4).

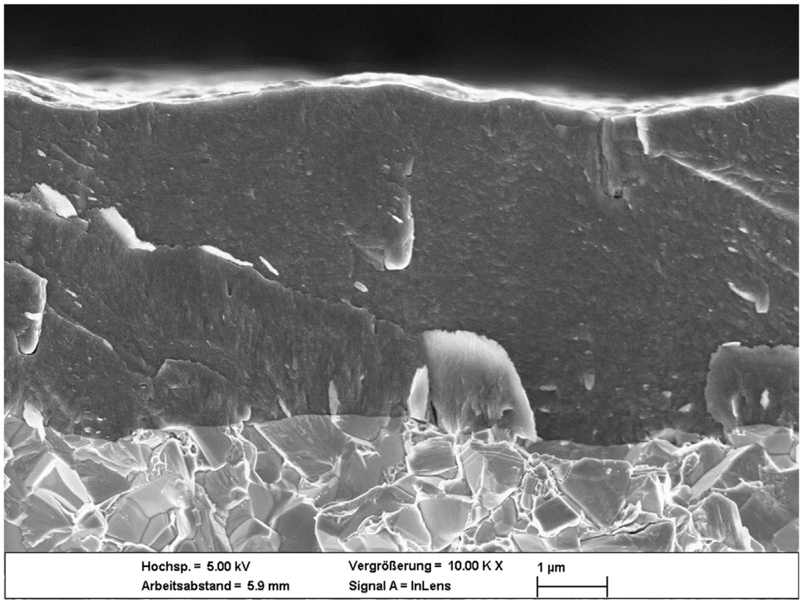

Figure 6 Scanning electron microscopic image of fracture cross-section of TiAlN-based multilayer coating of CERATIZIT milling grade 1112.

1.16.3.3.4 Nanocomposite

Nanocomposite coatings are composed of at least two immiscible phases: two nanocrystalline ones (nc/nc) or, more commonly, one nanocrystalline and one amorphous phase (nc/a). A variety of hard compounds can be used as the nanocrystalline phase, including nitrides, carbides, borides, oxides and silicides. Different possibilities exist for the amorphous phase, like Si_3N_4, BN, and C.

High hardness can be obtained if two or more nanocrystalline phases (nc/nc) are combined which provide complex boundaries to accommodate the coherent strain (TiN–TiB_2, Ti–B–N, Ti–Si–N), or the second nanocrystalline phase segregates to grain boundaries of the matrix phase. Thus grain boundary hinders grain growth. Nanocrystalline grains embedded in an amorphous phase (nc/a) can slide in the amorphous structure to release strain and give high toughness. The size, volume percentage and distribution of the nanocrystals need to be optimized to obtain a compromise between hardness and toughness. According to Veprek, the optimum should be obtained with nanocrystalline grains in the range of 3–10 nm separated by 1–2 nm within the amorphous phase. Ternary systems like nc-TiN/a-Si_3N_4 nanocomposites showed high hardness and excellent thermal stability up to 1000 °C due to the incorporation of Si.

1.16.3.4 Additional Elements

Tools for cutting applications, e.g. cemented carbide inserts, are most commonly used after coating them via CVD or PVD techniques. In contrast to the CVD coatings, PVD-deposited films offer the advantage of showing compressive stresses which are useful in interrupted cutting applications; moreover they offer the possibility to deposit metastable coating systems.

Over years, TiN has been the most widely used hard coating material for such applications. Next to TiN, CrN and TiC hard coatings also showed success in increasing lifetime and enhancing working conditions like high cutting speeds and feed rates compared to the uncoated tool. However, TiN starts to oxidize rapidly at 500 °C and forms the rutile structure TiO_2, which leads to deteriorating mechanical properties. These hard coatings have been improved by alloying a third component to increase their hardness and wear and oxidation resistance. The incorporation of Al in the TiN system to form Ti–Al–N was to launch a new generation of hard coatings. Al incorporated into the fcc structure of TiN results in the formation of a metastable ternary solid solution Ti–Al–N, which is well known to improve the cutting performance because of its high hot hardness due to age hardening and excellent oxidation behavior up to temperatures of 700 °C due to the formation of a protective Al-rich oxide layer at the film surface. Ti–Al–N coatings have become the standard choice for many applications e.g. dry cutting with high operating temperatures.

The incorporation of further elements like Zr, Cr, Y, Ta, Nb, Hf, and Si opens new possibilities to improve machining performance by solid solution hardening or grain refinement, or by the incorporation of an element which stabilizes the cubic phase at even higher Al contents (Knotek, Löffler, & Krämer, 1996; Kutschej et al., 2005a, Kutschej et al., 2005b; Smith, Münz, Donohue, Petrov, & Greene, 1998). A complex microstructural design aims at increasing bulk and grain boundary strength, which contributes to an increase of hardness and toughness; it may also reduce diffusion effects by increasing the oxidation resistance. The implementation of multicomponent nanocomposite and multilayer coatings is often cited as the step forward in coating development (Kathrein, Michotte, Penoy, Polcik, & Mitterer, 2005). In particular, Ta is known to produce the fcc structure in TiAlN systems at the expense of hexagonal close packed (hcp) phases. A pure fcc structure can be reached, even at high Al contents, by applying an enhanced bias voltage to the substrate during the deposition process, which should result in increased hardness and Young's modulus. Beneficial effects on the oxidation resistance and on the wear behavior at high temperatures due to Ta alloying of TiAlN coatings are reported (Pfeiler et al., 2008; Pfeiler, Scheu, et al., 2009). Alloying with high content of Si and B can lead to the formation of a completely different structure. This structure consists of an amorphous Si_3N_4 or BN tissue phase surrounding small nanocrystalline TiAlN grains and forming nanocomposites (Veprek & Veprek-Heijman, 2008) with enhanced mechanical properties. The hardness enhancement of these structures exceeds the Hall–Petch effect. The improved hardness of nanocomposites could be connected with coherency stresses, i.e. intrinsic stresses at the crystallite boundaries. However, if a certain thickness of the amorphous tissue phase (i.e. a certain content of B or Si) is exceeded, the crystallites become noncoherent and the hardness is increased (Rafaja et al., 2007). Even with low contents of B and Si, Ti–Al–Si–N and Ti–Al–B–N coatings show excellent resistance to high-temperature oxidation (Pfeiler, Zechner, et al., 2009). If the contents of Si and B are low, the Ti–Al–N structure is maintained and the amorphous tissue phases and thus nanocomposites are not observed. Although Si and B promote the formation of the generally undesired hcp

Ti–Al–N phase, the mechanical properties do not deteriorate to the extent expected. The reason might be the low content of B and Si, making it more appropriate to speak about Si- and B-doped coatings, instead of alloyed ones. Moreover, Si and B improve the high-temperature oxidation resistance. The same mechanisms act for both elements; however Si doping is superior over B doping because of a better stability of the doping effect. Si doping leads to results that are comparable to those of Ta-doped coatings. Consequently, Ta- and Si-alloyed Ti–Al–N coatings are promising candidates for cutting under severe conditions, where high-temperature oxidation governs the wear behavior. Since both elements improve the oxidation resistance but seem to act via different mechanisms, there is the potential for even higher oxidation resistance by combining both effects in a Ti–Al–Ta–Si–N coating. Interesting impact of small amounts of Ru as doping element on structure, thermal stability, tribological and mechanical properties of Ti–Al–N hard coating has also been investigated in order to achieve beneficial properties for applications in severe conditions (Pohler, Michotte, Penoy, Mitterer, & Kathrein, 2009). The friction coefficient of most hard coatings is fairly high and the tribological effectiveness especially at elevated temperatures is insufficient. Therefore, a lot of effort was made in the past years to lower the friction coefficient at room as well as at high temperatures. An improvement has been made by adding lubricating phases like DLC or MoS_2 to hard coatings to decrease their friction coefficient. Nevertheless, these lubricating phases, which are responsible for excellent friction performance at low temperatures, lose their effectiveness due to degradation at elevated temperatures (e.g. $>500\,^{\circ}C$) (Gilmore et al., 1998). Thus, a new high-temperature low-friction concept based on Magnéli phase oxides has been studied (Lugscheider, Knotek, Bobzin, & Bärwulf, 2000; Mayrhofer, Hovsepian, Mitterer, & Münz, 2004). These Magnéli phase oxides (e.g. W–O, Mo–O, V–O (Gassner, Mayrhofer, Kutschej, Mitterer, & Kathrein, 2006)) exhibit crystallographic planes that shear easily and are thermally stable up to relatively high temperatures (Hovsepian & Münz, 2002; Lugscheider et al., 2000). It has been observed that Ti–Al–N/VN superlattice coatings (Mayrhofer et al., 2004) as well as Ti–Al–V–N solid solutions (Kutschej, Mayrhofer, Kathrein, Polcik, & Mitterer, 2004; Pfeiler, Kutschej, et al., 2009) show a combination of high hardness, good wear behavior and low friction coefficients; the last of these three features is attributed to the formation of V_2O_5 and other Magnéli oxides showing lubricious effects. Nevertheless, the relatively fast diffusion of the V out of the coating to the surface leads to a quick loss of the lubricating effect; moreover, the remaining porous Ti–Al–N network offers fast oxidation paths through the coating, enhancing coating failure (Kutschej et al., 2004). A way to hinder the diffusion of V out of the coating is to use multilayering architecture generating diffusion barriers which are of major importance to provide higher oxidation resistance (Kathrein, Michotte, & Polcik, 2005). This results in a remarkable improvement of the tribological performance of Ti–Al–V–N and widens the temperature range, where V-containing coatings can be applied.

Summarizing, the trend to multifunctional tools demands new solutions in the design of tools. Several tribological systems may appear during the lifetime of a tool or occur simultaneously at different locations on the tool surface.

The choice of the different combinations allows tailoring of coating properties in the triangle between low friction, high wear resistance, and high oxidation resistance, in combination with high toughness.

On the other hand, the combination of different materials and their beneficial properties in alternating layered structures is a current trend in the industrial applications of hard coatings. Multilayers exhibit higher density and finer grains, compared to single-layer coatings because columnar growth is interrupted by the nucleation of the second phase. The higher amount of phase boundaries and interfacial area may increase hardness and wear resistance. Furthermore, the so-called superlattice effect can lead to a significant hardness enhancement. The growth of multilayered structures can also be used to deposit material with epitaxial stabilized phases. As a consequence, the utilization of the template effect for Ti–Al–N-based coatings offers another possibility to decrease the fraction of hcp phases by epitaxial stabilization of fcc Ti–Al–N phases. Ti–Al–N with a sufficiently low Al content crystallizes as a single-phase fcc structure and has necessarily a high similarity to other Ti–Al–N-based layer materials. Thus, it can act as the perfect fcc-stabilizing template layer for initially dual phase structured layer. Initially dual phase Ti–Al–V–N has been stabilized by template effect by a Ti–Al–N template up to multilayer wavelengths of 20 nm (Pfeiler, Mitterer, Penoy, Michotte, & Kathrein, to be published). However, in this case the second layer has a high Al content or a high content of hcp-promoting alloying elements (e.g. Si, B or Ru); the template effect and increased bias voltage can act additively; The fcc structure can be reached at lower bias voltages and consequently lower residual stresses. Both template effect and bias voltage for Ti–Al–N/Ti–Al–Ta–N multilayers have been investigated (Radanitsch, 2009). The reduction of hcp phases by the template/multilayer approach was found to be highly beneficial for the mechanical and tribological properties as well as for the resistance to oxidation.

1.16.4 Posttreatment

For modern cutting tools the posttreatment process has to be coupled and adapted to the coating process. Wet or dry abrasive blasting, also called shot peening processes are used to reduce the surface roughness and residual tensile stresses in case of CVD coatings, or to remove the droplets in case of PVD arc processes. Modification of the stress state of the coating and substrate material leads to higher reliability in the cutting operation and expands the field of application (Barbatti et al., 2009; Bouzakis et al., 2011; Bouzakis, Skordaris, Michailidis, Asimakopoulos, & Erkens, 2005; Holzschuh, Klaus, & Genzel, 2008; Klaus, Genzel, & Holzschuh, 2008; Westphal, 2005; Westphal & Sottke, 2002). Also the application of a metallic layer by using metal blasting media is a proper way to influence the tribological behavior of the cutting tool (Riedl, Schalk, Czettl, Satory, & Mitterer, 2012; Wallgram, Schleinkofer, Gigl, Thurner, & Schintlmeister, 2006).

1.16.5 Application Example

1.16.5.1 Steel Turning Operation

Turning low-alloyed steels encompassing a huge variety of workpiece materials in a variety of heat-treated states is one of the most predominant areas of machining. The scope ranges from heavy roughing operations with high feed rates to finishing operations with cutting speeds around 500 m min^{-1}. Cemented carbide cutting tools have to survive highly interrupted cutting conditions as well as high temperatures due to continuous operations. For such steel turning (ISO-P) applications, the use of CVD-coated cutting inserts with TiN–TiCN–Al_2O_3 layered architecture from 10 to 25 μm is common. Typical substrate materials are WC–Co cemented carbides with Co contents between 5 and 12 wt%, cubic carbides up to 8 wt% and a Co-enriched surface zone, essentially free of cubic carbides up to 50 μm, to increase the toughness of the tool (Lengauer & Dreyer, 2002; Söderberg, Sjöstrand, & Ljungberg, 2001).

For further enhancement of toughness of the cutting inserts the structure of the coatings has to be optimized. One possible route is grain refinement of the columnar structure of MT-TiCN. This can be achieved, for example, by the addition of low percentage of CO to the feed gases. The typical equiaxed grains of the MT-TiCN transform to fine-grained platelike morphology (**Figure 7**) (Czettl et al., 2011). These effects make the cutting tools more reliable and extend their desired application range. These MT-TiCN base layers are typically combined with an Al_2O_3 top layer, which commonly exhibits the α-Al_2O_3 structure in (001), (012) (104) or (100) orientation, sometimes κ-Al_2O_3, ranging from 3 to 15 μm in thickness. The resulting architecture has excellent hardness and

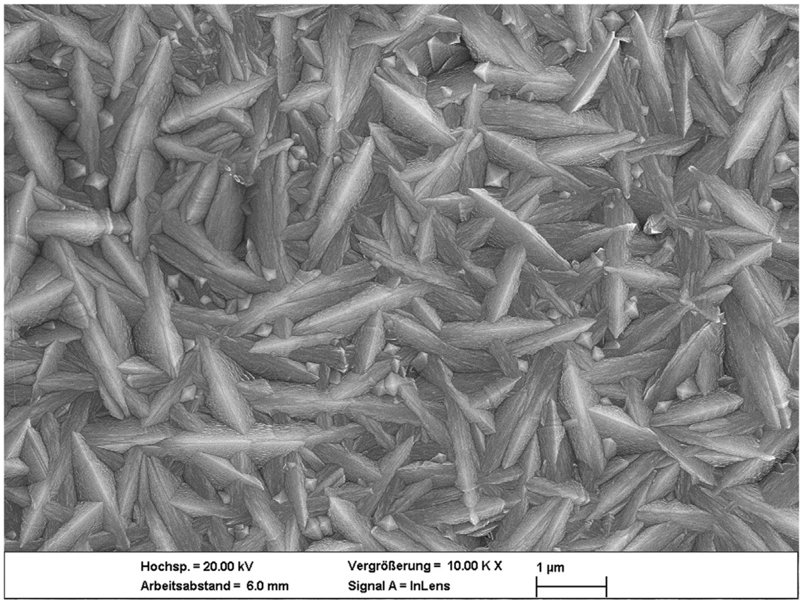

Figure 7 Scanning electron microscopic top-view image of fine-grained MT-TiCN coating with CO addition (Czettl et al., 2011).

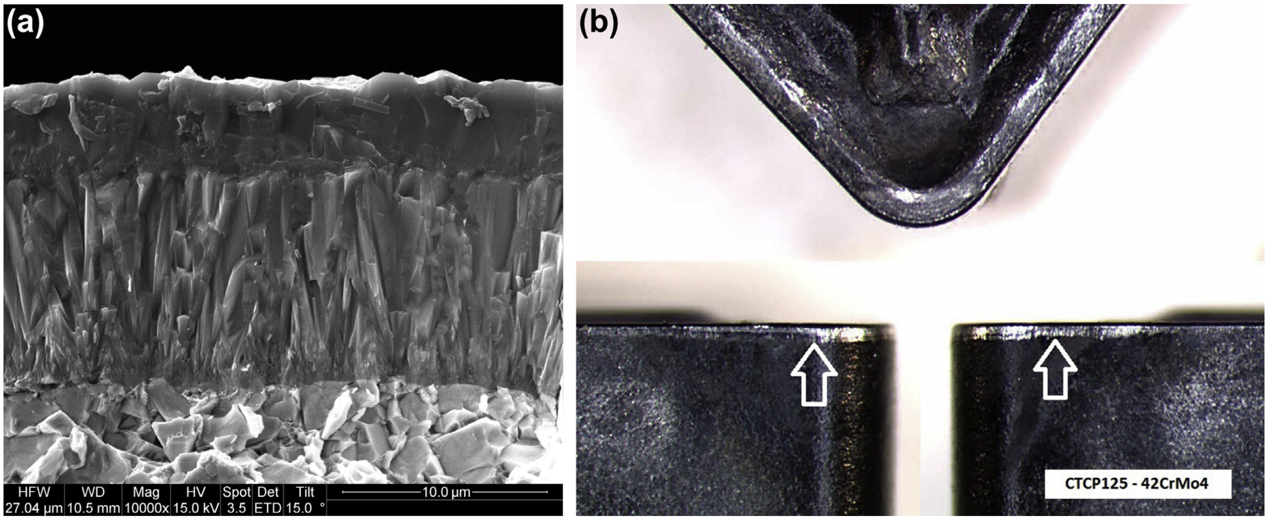

Figure 8 (a) Scanning electron microscopic image of fracture cross-section of the TiN–MT-TiCN–κ-Al_2O_3 architecture of CERATIZIT grade CTCP125 and (b) light optical microscopic images of flank wear after combined turning operation using 42CrMo4 workpiece material.

oxidation and wear resistance at elevated temperatures. The adherence between the Al_2O_3 and the MT-TiCN base layer is crucial to the performance, and is usually achieved by Ti–Al–C–N–O bonding layers (Halvarsson, Norden, & Vuorinen, 1994; Holzschuh, 2000a; Ruppi, 1997). This leads to an all-round cutting tool with excellent chipping resistance, as shown in **Figure 8** (Funk et al., 1976; Mehrotra & Quinto, 1986; M′saoubi & Ruppi, 2009).

1.16.5.2 Difficult-to-Cut Material

Advantages in performance can be achieved by using new coating architecture like TiB_2 deposited by the CVD process as already mentioned above (cf. Section 1.16.2.1). A comparison of lifetime performance tests between PVD and CVD TiB_2 and state-of-the-art commercial coatings architecture to machine TiAl6V4 is shown in **Figure 9**. More than a 50% improvement in lifetime for the newly developed CVD TiB_2 was observed (Wallgram & Schleinkofer, 2009 for CTC5240).

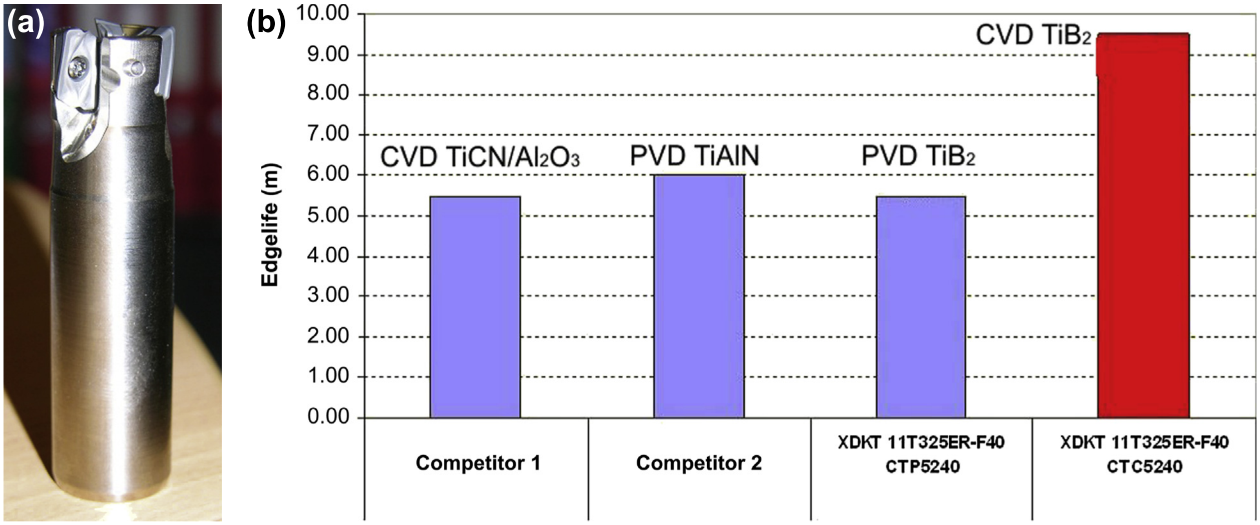

Figure 9 (a,b) Cutting results with edge milling system C211.

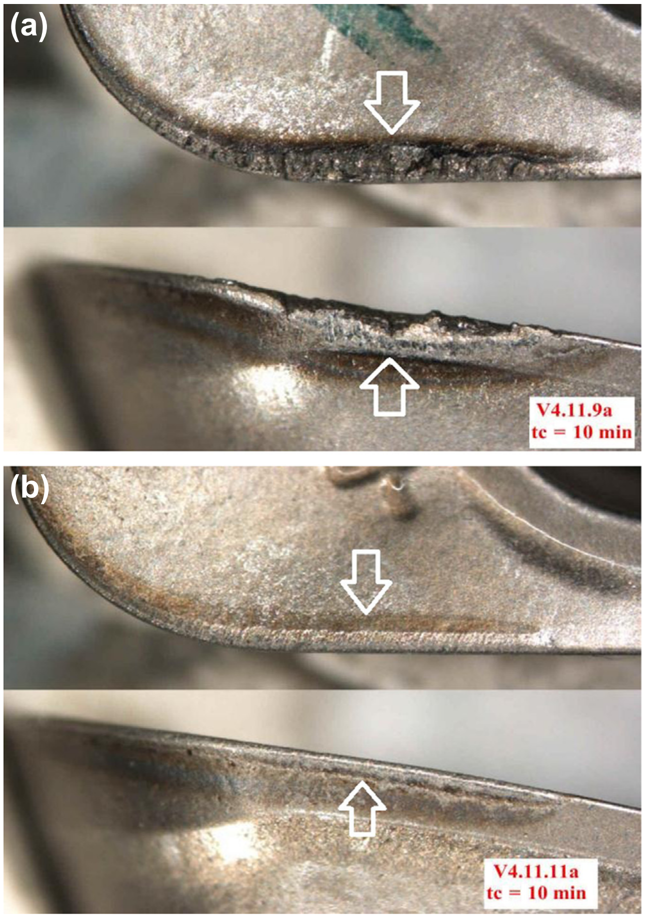

Figure 10 Flank wear pattern of the PVD TiB_2-coated version (a) and the CVD TiB_2 version (b) are shown after 10 min of application.

For cutting tests, a variety of different milling inserts were produced and tested in different cutting conditions. In this chapter, one representative example is described.

1.16.5.3 Test with Edge Milling System C211/XDKT11T325ER-F40 on TiAl6V4

For this experiment, the edge milling system C211 was used as shown in Figure 8 for the machining of TiAl6V4 on an EXCELLO milling machine with a cutting speed of 50 m/min and a feed rate per teeth of 0.12 mm at the entrance of the cut and 0.08 mm at the exit of the cut with a depth of cut a_p of 5 mm. Especially the comparison between the PVD TiB_2 coating and the newly developed CVD TiB_2 coating was the focus of this experiment. Some lifetime results of competitor systems are shown also in Figure 9 for completion of this overview. The lifetime criterion for this experiment was a flank wear of 0.3 mm.

As shown in Figure 9, the CVD TiB_2-coated version designated as CTC5240 exhibits more than 50% more lifetime compared to competitors, which are state-of-the-art CVD and PVD coatings without TiB_2 content, and the PVD TiB_2 version CTP5240.

The increase in lifetime was found to be controlled by the higher edge stability and reduced wear. The combination of the fine-grained morphology, a smooth surface, and residual compressive stresses in the coating are considered to be the cause of the improved wear behavior (Figure 10) (Wallgram & Schleinkofer, 2009). This effect is further enhanced by the improved coating adhesion due to the CVD process.

1.16.6 Summary and Outlook

In this chapter, the historical development of CVD and PVD coatings was illustrated. It was shown that the coating process and coating design, with respect to coating architecture and microstructure, gives still enough space for further improvement in wear-active applications. Newer developments like CVD TiB_2, textures of Al_2O_3 structures, PVD oxides, as well as TiAlN CVD coatings have led to an increasing overlap between the various deposition technologies. The requirements of high-performance cutting processes by increasing cutting speed and feed rates, as well as difficult-to-machine materials like titanium and superalloys, has led to higher demands for coatings and posttreatment methods. The coatings in combination with tailored substrate materials and cutting-edge geometries have to be adjusted for specific applications to obtain highest performance in technically challenging applications.

References

Altena, H. (1982). *Untersuchungen an Al_2O_3-CVD-Schichten; Einfluss von Substrat und Spurenverunreinigungen* (Ph.D.). TU-Wien.

Barbatti, C., Garcia, J., Pitonak, R., Pinto, H., Kostka, A., Di Prinzio, A., et al. (2009). Influence of micro-blasting on the microstructure and residual stresses of CVD kappa-Al_2O_3 coatings. *Surface and Coatings Technology, 203*, 3708–3717.

Barna, P. B. (1981). Surface chemical phenomena and growth of films. *Thin Solid Films, 85*, 263–264.

Birkholz, M. (2006). *Thin film analysis by X-ray scattering*. Weinheim: Wiley-VCH Verlag.

Bonetti-Lang, M., Bonetti, R., Hintermann, H. E., & Lohmann, D. (1982). Carbonitride coatings at moderate temperature obtained from organic C/N-compounds. *International Journal of Refractory Metals & Hard Materials, 1*, 161–165.

Bonetti, R., & Wahl, H. (1983). Industrialisation of titanium carbonitride deposition process at moderated temperatures. In J. Bloem, G. Verspui, & L. R. Wolff (Eds.), *Euro CVD IV* (pp. 510–516). Netherlands: Eindhoven.

Bouzakis, K. D., Klocke, F., Skordaris, G., Bouzakis, E., Gerardis, S., Katirtzoglou, G., et al. (2011). Influence of dry micro-blasting grain quality on wear behaviour of TiAlN coated tools. *Wear, 271*, 783–791.

Bouzakis, K. D., Skordaris, G., Michailidis, N., Asimakopoulos, A., & Erkens, G. (2005). Effect on PVD coated cemented carbide inserts cutting performance of micro-blasting and lapping of their substrates. *Surface and Coatings Technology, 200*, 128–132.

Colombier, C. (1984). *Untersuchung an Al_2O_3-CVD-Schichten; Einfluss von Substrat und Gasphase* (Ph.D.). TU-Wien.

Czettl, C., Mitterer, C., Michotte, C., Penoy, M., & Kathrein, M. (2009). Homogeneity of industrial scale thermal CVD processes for TiCN hard coatings. In L. S. Sigl, P. Rödhammer, & H. Wildner (Eds.), *Plansee seminar*. Reutte, Austria: Plansee Group. HM71.1-HM71.8.

Czettl, C., Mitterer, C., Mühle, U., Rafaja, D., Puchner, S., Hutter, H., et al. (2011). CO addition in low-pressure chemical vapour deposition of medium-temperature TiC_xN_{1-x} based hard coatings. *Surface and Coatings Technology*.

EMUGE-Franken. (2004). *Handbuch der Gewindetechnik und Frästechnik*. Erlangen: Emuge-Franken.

Endler, I., Höhn, M., Herrmann, M., Holzschuh, H., Pitonak, R., Ruppi, S., et al. (2010). Aluminum-rich TiAlCN coatings by low pressure CVD. *Surface and Coatings Technology, 205*, 1307–1312.

Endler, I., Hohn, M., Herrmann, M., Pitonak, R., Ruppi, S., Schneider, M., et al. (2008). Novel aluminum-rich $Ti_{1-x}Al_xN$ coatings by LPCVD. *Surface and Coatings Technology, 203*, 530–533.

Funk, R., Schachner, H., Triquet, C., Kornmann, M., & Lux, B. (1976). Coating of cemented carbide cutting tools with alumina by chemical vapor-deposition. *Journal of the Electrochemical Society, 123*, 285–289.

Gassner, G., Mayrhofer, P. H., Kutschej, K., Mitterer, C., & Kathrein, M. (2006). Magnéli phase formation of PVD Mo–N and W–N coatings. *Surface and Coatings Technology, 201*, 3335–3341.

Gilmore, R., Baker, M. A., Gibson, P. N., Gissler, W., Stoiber, M., Losbichler, P., et al. (1998). Low-friction TiN–MoS_2 coatings produced by dc magnetron co-deposition. *Surface and Coatings Technology, 108–109*, 345–351.

Halvarsson, M., Norden, H., & Vuorinen, S. (1994). The microstructure of bonding layers for CVD alumina coatings. *Surface and Coatings Technology, 68*, 266–273.

Hiroyuki, K. (2001). EP1138800A1: Coated cutting tool and method for producing the same.

Hochauer, D., Mitterer, C., Penoy, M., Michotte, C., Martinz, H. P., & Kathrein, M. (2008). Titanium doped CVD alumina coatings. *Surface and Coatings Technology, 203*, 350–356.

Hochauer, D., Mitterer, C., Penoy, M., Michotte, C., Martinz, H. P., & Kathrein, M. (2010). Thermal stability of doped CVD κ-Al_2O_3 coatings. *Surface and Coatings Technology, 204*, 3713–3722.

Holzschuh, H. (2000a). EP1113092B1: Schneidwerkzeug mit mehrlagiger, verschleißfester Beschichtung.

Holzschuh, H. (2000b). Moderate temperature CVD of Ti-B-C-N on cemented carbide tools: properties and metal-cutting tests. *Journal De Physique IV, 10*, 49–54.

Holzschuh, H. (2004). Deposition of Ti-B-N (single and multilayer) and Zr-B-N coatings by chemical vapor deposition techniques on cutting tools. *Thin Solid Films, 469–70*, 92–98.

Holzschuh, H. (2005). Moderate temperature CVD coatings in the Ti-B-N system. In G. Kneringer, P. Rödhammer, & H. Wildner (Eds.), *Plansee seminar*. Reutte: Plansee Holding AG. HM59.

Holzschuh, H., Klaus, M., & Genzel, C. (2008). Influence of the residual stress state on the toughness of CVD coated cemented carbide cutting tools. In *Advances in powder metallurgy & particulate materials* (pp. 100–106). Washington D.C.

Hovsepian, P. E., & Münz, W. D. (2002). Recent progress in large-scale production of nanoscale multilayer/superlattice hard coatings. *Vacuum, 69*, 27–36.

Kathrein, M. (2001). Verschleißfeste CVD-Aluminiumoxidschichten auf Hartmetall für die Zerspanung (Ph.D.). Montanuniversität.

Kathrein, M., Michotte, C., Penoy, M., Polcik, P., & Mitterer, C. (2005). Multifunctional multi-component PVD coatings for cutting tools. *Surface and Coatings Technology, 200*, 1867–1871.

Kathrein, M., Michotte, C., & Polcik, P. (2005). Multi-functional multi-component PVD coatings. In G. Kneringer, P. Rödhammer, & H. Wildner (Eds.), *Plansee seminar* (pp. 906–916). Reutte: Plansee Holding AG.

Kathrein, M., Schintlmeister, W., Wallgram, W., & Schleinkofer, U. (2003). Doped CVD Al_2O_3 coatings for high performance cutting tools. *Surface and Coatings Technology, 163*, 181–188.

Kim, C. W., & Kim, K. H. (1997). Anti-oxidation properties of TiAlN film prepared by plasma-assisted chemical vapor deposition and roles of Al. *Thin Solid Films, 307*, 113–119.

Klaus, M., Genzel, C., & Holzschuh, H. (2008). Residual stress depth profiling in complex hard coating systems by X-ray diffraction. *Thin Solid Films, 517*, 1172–1176.

Knotek, O., Löffler, F., & Krämer, G. (1996). Cutting performance of multicomponent and multilayer coatings on cemented carbides and cermets for interrupted cut machining. *International Journal of Refractory Metals & Hard Materials, 14*, 195–202.

Knotek, O., Munz, W. D., & Leyendecker, T. (1987). Industrial deposition of binary, ternary, and quaternary nitrides of titanium, zirconium, and aluminum. *Journal of Vacuum Science & Technology, A: Vacuum, Surfaces, and Films, 5*, 2173–2179.

Kornmann, M., Schachner, H., Funk, R., & Lux, B. (1975). Nucleation of alumina layers on TiC and cemented carbides by chemical vapor-deposition. *Journal of Crystal Growth, 28*, 259–262.

Kübel, E. (1991). New developments in chemically vapour-deposited coatings from an industrial point of view. *Surface and Coatings Technology, 49*, 268–274.

Kutschej, K., Fateh, N., Mayrhofer, P. H., Kathrein, M., Polcik, P., & Mitterer, C. (2005). Comparative study of $Ti_{1-x}Al_xN$ coatings alloyed with Hf, Nb, and B. *Surface and Coatings Technology, 200*, 113–117.

Kutschej, K., Mayrhofer, P. H., Kathrein, M., Michotte, C., Polcik, P., & Mitterer, C. (2005). Multi-functional multi-component $Ti_{1-x}Al_xN$ based coatings. In G. Kneringer, P. Rödhammer, & H. Wildner (Eds.), *Plansee seminar* (pp. 774–788). Reutte: Plansee Holding AG.

Kutschej, K., Mayrhofer, P. H., Kathrein, M., Polcik, P., & Mitterer, C. (2004). A new low-friction concept for $Ti_{1-x}Al_xN$ based coatings in high-temperature applications. *Surface and Coatings Technology, 188–189*, 358–363.

Larsson, A., & Ruppi, S. (2002). Microstructure and properties of Ti(C, N) coatings produced by moderate temperature chemical vapour deposition. *Thin Solid Films, 402*, 203–210.

Lengauer, W., & Dreyer, K. (2002). Functionally graded hardmetals. *Journal of Alloys and Compounds, 338*, 194–212.

Ljungberg, B. (1998). EP0659903B1: Alumina coated cutting tool.

Ljungberg, B. (2007). EP0738336B2: Oxide coated cutting tool.

Ljungberg, B. & Lenander, A. (1993). EP0603144B1: Oxide coated cutting tool.

Lugscheider, E., Knotek, O., Bobzin, K., & Bärwulf, S. (2000). Tribological properties, phase generation and high temperature phase stability of tungsten- and vanadium-oxides deposited by reactive MSIP-PVD process for innovative lubrication applications. *Surface and Coatings Technology, 133–134*, 362–368.

M'saoubi, R., & Ruppi, S. (2009). Wear and thermal behaviour of CVD alpha-Al_2O_3 and MTCVD Ti(C, N) coatings during machining. *CIRP Annals-Manufacturing Technology, 58*, 57–60.

Mayrhofer, P. H., Hörling, A., Karlsson, L., Sjölén, J., Larsson, T., Mitterer, C., et al. (2003). Self-organized nanostructures in the Ti-Al-N system. *Applied Physics Letters, 83*, 2049–2051.

Mayrhofer, P. H., Hovsepian, P. E., Mitterer, C., & Münz, W. D. (2004). Calorimetric evidence for frictional self-adaptation of TiAlN/VN superlattice coatings. *Surface and Coatings Technology, 177–178*, 341–347.

Mcintyre, D., Greene, J. E., Hakansson, G., Sundgren, J. E., & Munz, W. D. (1990). Oxidation of metastable single-phase polycrystalline $Ti_{0.5}Al_{0.5}N$ films: kinetics and mechanisms. *Journal of Applied Physics, 67*, 1542–1553.

Mehrotra, P., & Quinto, D. T. (1986). High-Temperatures microhardness profiles of hard CVD coatings. *High Temperatures – High Pressures, 18*, 199–210.

Mitterer, C., Mayrhofer, P. H., Beschliesser, M., Losbichler, P., Warbichler, P., Hofer, F., et al. (1999). Microstructure and properties of nanocomposite Ti–B–N and Ti–B–C coatings. *Surface and Coatings Technology, 120–121*, 405–411.

Münz, W. D. (1986). Titanium aluminium nitride films: a new alternative to TiN coatings. *Journal of Vacuum Science & Technology, A, 4*, 2717–2725.

Okude, M., Tomita, K., Nakamura, E., & Osada, A. (2011). Thermal stability and cutting performance of Ti or Zr-doped kappa-Al_2O_3 coatings by CVD. In *ICMCTF 2011. San Diego, CA*.

Pfeiler, M., Fontalvo, G. A., Wagner, J., Kutschej, K., Penoy, M., Michotte, C., et al. (2008). Arc evaporation of Ti-Al-Ta-N coatings: the effect of bias voltage and Ta on high-temperature tribological properties. *Tribology Letters, 30*, 91–97.

Pfeiler, M., Kutschej, K., Penoy, M., Michotte, C., Mitterer, C., & Kathrein, M. (2009). The effect of increasing V content on structure, mechanical and tribological properties of arc evaporated Ti–Al–V–N coatings. *International Journal of Refractory Metals & Hard Materials, 27*, 502–506.

Pfeiler, M., Mitterer, C., Penoy, M., Michotte, C., & Kathrein, M. (to be published).

Pfeiler, M., Scheu, C., Hutter, H., Schnoller, J., Michotte, C., Mitterer, C., et al. (2009). On the effect of Ta on improved oxidation resistance of Ti–Al–Ta–N coatings. *Journal of Vacuum Science & Technology, A: Vacuum, Surfaces, and Films, 27*, 554–560.

Pfeiler, M., Zechner, J., Penoy, M., Michotte, C., Mitterer, C., & Kathrein, M. (2009). Improved oxidation resistance of TiAlN coatings by doping with Si or B. *Surface and Coatings Technology, 203*, 3104–3110.

Pohler, M., Michotte, C., Penoy, M., Mitterer, C., & Kathrein, M. (2009). Ruthenium containing Ti-Al-N hard coatings. In L. S. Sigl, P. Rödhammer, & H. Wildner (Eds.), *Plansee seminar*. Reutte, Austria: Plansee Group. HM72.1-HM72.10.

Prengel, H. G., Pfouts, W. R., & Santhanam, A. T. (1998). State of the art in hard coatings for carbide cutting tools. *Surface and Coatings Technology, 102*, 183–190.

Radanitsch, J. (2009). Alloying of TiAlN single- and multilayer thin films (Master). Montanuniversität.

Rafaja, D., Poklad, A., Klemm, V., Schreiber, G., Heger, D., & Šíma, M. (2007). Microstructure and hardness of nanocrystalline $Ti_{1-x-y}Al_xSi_yN$ thin films. *Materials Science and Engineering, A, 462*, 279–282.

Riedl, A., Schalk, N., Czettl, C., Satory, B., & Mitterer, C. (2012). Tribological properties of Al_2O_3 hard coatings modified by mechanical blasting and polishing post-treatment. *Wear, 289*.

Ruppi, S. (1994). EP0408535B1.

Ruppi, S. (1997). US5700569: Multilayered alumina coated cemented carbide body.

Ruppi, S. (2001). Advances in chemically vapour deposited wear resistant coatings. *Journal De Physique IV, 11*, 847–859.

Ruppi, S. (2008). Enhanced performance of alpha-Al_2O_3 coatings by control of crystal orientation. *Surface and Coatings Technology, 202*, 4257–4269.

Ruppi, S., & Larsson, A. (2000). Effect of H_2S on the microstructure and deposition characteristic of CVD Al_2O_3. In *Fifteenth international symposium on chemical vapor deposition* (pp. 372–378). The Electrochemical Society Inc.

Ruppi, S., & Larsson, A. (2003). Deposition, microstructure, and properties of nanocrystalline Ti(C, O, N) coatings. *Journal of Vacuum Science & Technology, A, 21*, 66–75.

Ruppi, S., Larsson, A., & Flink, A. (2008). Nanoindentation hardness, texture and microstructure of alpha-Al_2O_3 and kappa-Al_2O_3 coatings. *Thin Solid Films, 516*, 5959–5966.

Schedler, W. (1988). *Hartmetall für den Praktiker*. Düsseldorf: Plansee TIZIT.

Smith, U. K. H. & Lindström, J. (1986). US4619866: Method of making a coated cemented carbide body and resulting body.

Smith, I. J., Münz, W. D., Donohue, L. A., Petrov, I., & Greene, J. (1998). *Surface Engineering, 14*, 37.

Söderberg, S., Sjöstrand, M., & Ljungberg, B. (2001). Advances in coating technology for metal cutting tools. *Metal Powder Report, 56*, 24–30.

Spieß, L., Schwarzer, R., Behnken, H., & Teichert, G. (2005). *Moderne Röntgenbeugung*. Wiesbaden, B. G.: Teubner Verlag/GWV Fachverlage GmbH.

Veprek, S., & Veprek-Heijman, M. J. G. (2008). Industrial applications of superhard nanocomposite coatings. *Surface and Coatings Technology, 202*, 5063–5073.

Wagner, J., Edlmayr, V., Penoy, M., Michotte, C., Mitterer, C., & Kathrein, M. (2008). Deposition of Ti-Al-N coatings by thermal CVD. *International Journal of Refractory Metals & Hard Materials, 26*, 563–568.

Wagner, J., Hochauer, D., Mitterer, C., Penoy, M., Michotte, C., Wallgram, W., et al. (2006). The influence of boron content on the tribological performance of Ti-N-B coatings prepared by thermal CVD. *Surface and Coatings Technology, 201*, 4247–4252.

Wallgram, W., & Schleinkofer, U. (2009). Synthesis, structure, and behaviour of a new CVD TiB_2 coating with extraordinary properties for high performance applications. In L. S. Sigl, P. Rödhammer, & H. Wildner (Eds.), *Plansee seminar*. Reutte, Austria: Plansee Group. HM32-1/HM32-7.

Wallgram, W., Schleinkofer, U., Gigl, K., Thurner, J., & Schintlmeister, W. (2006). WO2006058353A1: Machining tool.

Westphal, H. (2005). Einfluss von Eigenspannungen in CVD-Hartstoffschichten auf die Spanungsleistung von Hartmetallen. In K. Weinert (Ed.), *Spanende Fertigung* (4th ed).

Westphal, H. & Sottke, V. (2002). DE10123554: Verfahren zur Erhöhung der Druckspannung oder zur Erniedrigung der Zugeigenspannung einer CVD-, PCVDoder PVD-Schicht und Schneideinsatz zum Zerspanen.

Wilhartitz, P., Grasserbauer, M., Altena, H., & Lux, B. (1986). Distribution analysis of carbon and sulfur in CVD-Al_2O_3-layers by SIMS using Cs^+ primary ions. *Surface and Interface Analysis, 8*, 159–165.

This page intentionally left blank

1.17 Coatings by Thermal Spray

Lutz-Michael Berger, Fraunhofer Institute IWS, Dresden, Germany

http://dx.doi.org/10.1016/B978-0-08-096527-7.00017-9

Glossary

Agglomeration and plasma densification (a&pd) Technology for feedstock powder preparation, including spray drying of mixtures of hard phase and binder metal powders, and subsequent densification by a plasma for consolidation of the spherical granules.

Agglomeration and sintering (a&s) Technology for feedstock powder preparation, including spray drying of mixtures of hard phase and binder metal powders, and subsequent mild sintering for consolidation of the spherical granules.

Atmospheric plasma spraying (APS) Thermal spray process using plasma in atmospheric conditions as the enthalpy source for heating and accelerating the feedstock powder particles.

Deposition efficiency Ratio of the material deposited on the substrate to the feeded material.

Detonation gun spraying (DGS) Thermal spray process using discontinuous burning (controlled explosions) of gaseous fuel and oxygen in the spray gun for heating and accelerating the feedstock powder particles.

Fusing and crushing (f&c) Technology for feedstock powder preparation, including liquid-phase sintering at high temperatures of hard phase and binder metal powders, subsequent milling and classification.

High-velocity air fuel (HVAF) spraying Thermal spray process using continuous burning of gaseous fuel and air under high pressure for heating and accelerating the feedstock powder particles.

High-velocity oxy-fuel (HVOF) spraying Thermal spray process using continuous burning of gaseous or liquid fuel and oxygen under high pressure for heating and accelerating the feedstock powder particles.

Sintering and crushing (s&c) Technology for feedstock powder preparation, including dense sintering of mixed hard phase and binder metal powders, subsequent milling and classification.

Nomenclature

CTE Coefficient of thermal expansion
DE Deposition efficiency
DLC Diamond-like carbon
IDT Indentation fracture toughness
NDT Nondestructive testing

1.17.1 General

Thermal spray processes represent an important and rapidly growing group of surface modification technologies using a very wide range of solid feedstock materials (including metals and alloys, hardmetals, ceramics and polymers) mostly in the form of particles, wires, and suspensions. For coating formation, plastic deformation of the feedstock particles at the moment of impact is a precondition after acceleration inside or outside of the spray gun. In most of the thermal spray processes, this is achieved by full or partial melting of the feedstock material, while the substrate remains unmelted, i.e. the coating is primarily mechanically bonded to the substrate. Hardmetals are one of the most important group of materials processed by thermal spray processes into coatings. Thermal spray is a technology that allows the development of large parts, which cannot be produced by powder metallurgy for technical and economical reasons, with hardmetal characteristics via the application of hardmetal coatings (Berger, 2007). Coating properties depend both on the feedstock material and the spray process.

Different thermal spray processes can be basically characterized in terms of particle velocity and process temperature, as shown in **Figure 1**. Economic factors such as deposition efficiency (DE) and powder feedrates are additional factors for the realization of efficient coating solutions. With respect to hardmetal coatings, the whole development is basically characterized by the search of optimum combination of particle velocity and process temperature with simultaneously high DE and feedrates.

A general overview of thermal spray technologies can be found in several books (Davis, 2004; Mathesius & Krömmer, 2009; Pawlowski, 2008). A more specialized book deals with coating preparation by high-velocity oxy-fuel (HVOF) spraying (Sobolev, Guilemany, & Nutting, 2004).

The state-of-the-art process of hardmetal coating preparation by thermal spraying is illustrated in **Figure 2**, showing the deposition by HVOF spraying. Coatings are usually prepared from feedstock powders consisting of small hardmetal particles, commonly in the size range 10–45 μm. Thus, preparation of thermal spray coatings can also be considered as the preparation of a shaped hardmetal using a two-step technology: first, feedstock powder preparation and second, the spray process. WC–12Co, WC–17Co, WC–10Co–4Cr, WC–20"CrC"–7Ni and Cr_3C_2–(20–25)NiCr (all compositions are in weight percent unless otherwise indicated) are the main commercially available compositions. In the past, progress in coating performance was mainly obtained by improving the spray processes, while the main commercial feedstock compositions remained unchanged. The coatings have a typical thickness within the range of 100–500 μm. The resulting coating properties are always a combination of the thermal spray process conditions and the composition and properties of the feedstock material. During spraying a number of metallurgical processes like carbide dissolution in the binder and changes in chemical and phase composition of the material occur in an extremely short time, resulting in high stresses. As for bulk hardmetal production, control of carbon content is a critical issue in coating preparation. The process of coating formation is characterized by high cooling rates, leading to the existence of high-temperature and nonequilibrium phases and nanocrystalline structures, in particular in the binder phase.

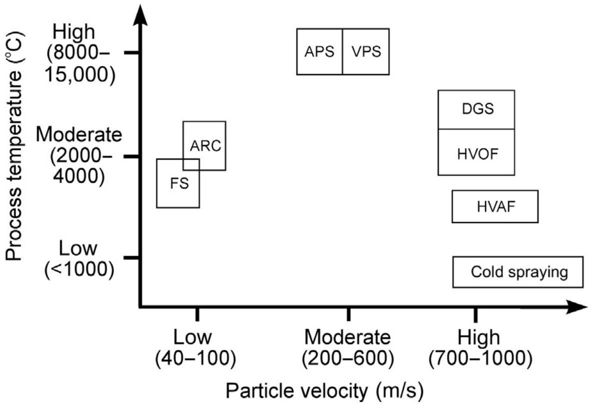

Figure 1 Schematic presentation of the combination of process temperature and velocity for the different spray processes. (FS, flame spraying; ARC, arc spraying; APS/VPS, atmospheric/vacuum plasma spraying; DGS, detonation gun spraying; HVOF, high-velocity oxy-fuel spraying; HVAF, high-velocity air fuel spraying) (Berger, 2011). Modification of an older version (Berger, Hermel, Vuoristo, Mäntylä, Lengauer, & Ettmayer, 1996).

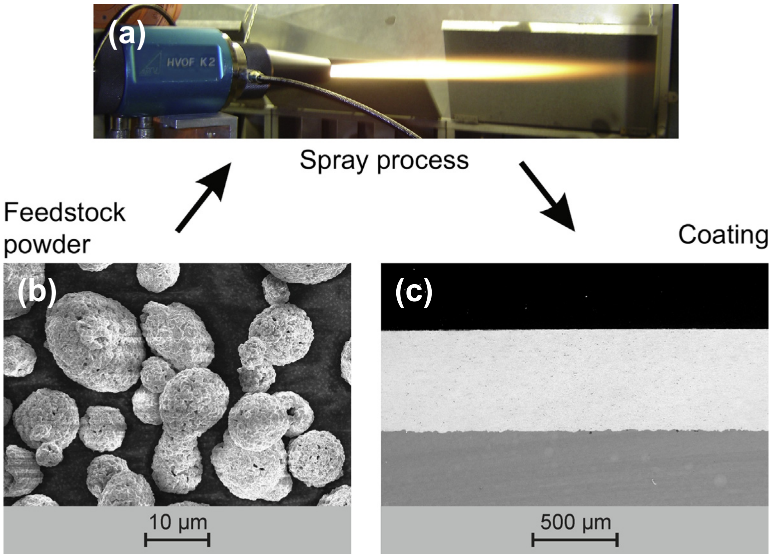

Figure 2 Illustration of hardmetal coating preparation by the high-velocity oxy-fuel (HVOF) spray process. (b) SEM of the feedstock powder. Here an agglomerated and sintered WC–17Co powder is shown. (a) HVOF spray process. Here a liquid-fueled process is shown. (c) Dense WC–Co coating. Modification of an older version (Berger, 2005).

The basic coating formation process is illustrated in **Figure 3(a)** showing a deformed hardmetal powder particle ("splat") after impact at the substrate surface (Berger, 2007). The coating is formed from a concentrated particle stream to give a pass; a number of parallel passes are necessary to cover a surface. To obtain the desired coating thickness, this procedure is normally repeated several times. The top view of an as-sprayed hardmetal coating is shown in **Figure 3(b)**.

Although typically the same hard phase–binder metal composite materials are used, the technical development in powder metallurgy and thermal spray were practically independent of each other. Also, the traditional terminology for these composites in these areas is different and leads often to misunderstandings (Berger, 2007). Bulk parts prepared by powder metallurgy are termed "hardmetals" or "cemented carbides", whereas the term "cermet" is used for TiC–Ni-based materials only. In thermal spraying, all hard phase-based coatings are usually designated as "carbide coatings", but sometimes also as "cermets". It appears that the designation "hardmetal coatings" best describes the state-of-the-art thermal spray coatings of this class of material.

An important difference between bulk hardmetals and thermally sprayed hardmetal coatings is that the properties of the coatings are not as exactly defined as for the same nominal composition of a sintered body, e.g. WC–12Co. The range of values for one specific property is significantly larger, as schematically illustrated in **Figure 4**. This results from feedstock powders prepared by different technologies, which are used with different spray processes (including HVOF devices of different construction) and different spray conditions and parameters. Also, different test procedures and conditions contribute to a scattering of values for coating properties.

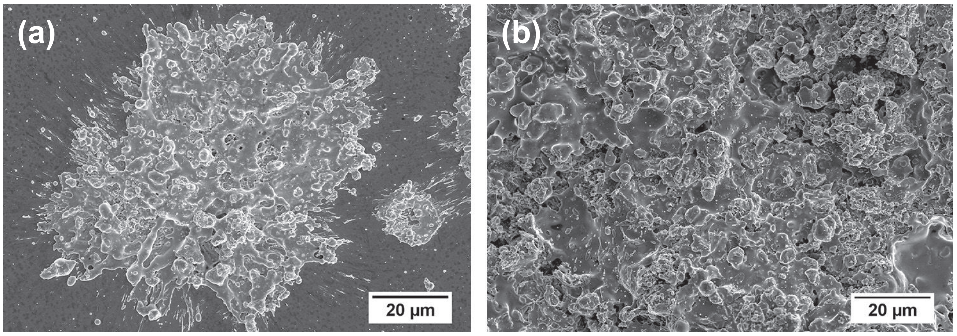

Figure 3 (a) A WC–(W,Cr)$_2$C–Ni feedstock powder particle after impact on substrate surface in an HVOF process (Berger, 2007). (b) Top view of the surface of an as-sprayed Cr_3C_2–NiCr HVOF coating.

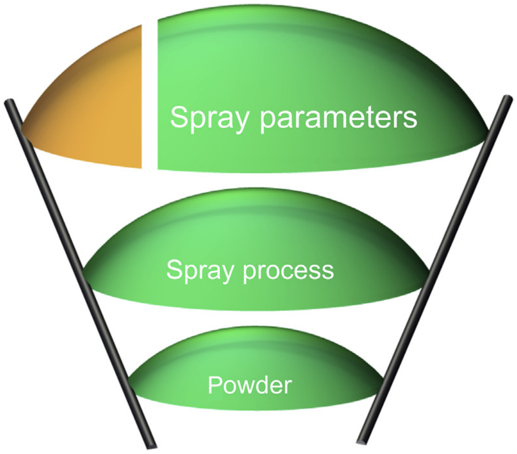

Figure 4 Factors influencing the property range of a thermal spray coating for a certain nominal composition (Berger, 2011). Modification of an older version (Berger, Woydt, & Saaro, 2007).

The yellow section in the highest area in **Figure 4** demonstrates that some of the coatings of this composition will fulfill the requirements of service in a certain application, while the remaining nominally identical coatings are not suitable. Developments in thermal spray technology and feedstock materials have already narrowed the coating property ranges of individual compositions and this tendency is expected to progress further.

1.17.2 Historical Development of the Spray Processes for Hardmetal Coatings

The first preparation of a hardmetal coating using an arc spray process was reported by Schoop, the Swiss inventor of thermal spray, in 1942 (Schoop, 1942).

The development of detonation gun spraying (DGS) (Perry, 1952; Poorman, Sargent, & Lamprey, 1952) gave for the first time a suitable combination of moderate process temperature and high particle velocity (see **Figure 1**). Spraying of WC–9Co is mentioned as a coating example in the patent of the DGS process (Poorman et al., 1952). At the same time, this stimulated the development of proprietary hardmetal powder and coating compositions by the same company, e.g. WC–(W,Cr)$_2$C–Ni (Pelton & Koffskey, 1958) and Cr$_3$C$_2$–NiCr (Pelton & Koffskey, 1960). As a result of the policy of the company owning the patent rights, only the coatings but not the equipment were commercialized. For the description of coating processes in the earlier literature, there is often no clear differentiation between welded (clad) and thermal spray coatings (e.g. Kieffer & Benesovsky, 1965; Schedler, 1988). The use of the historic term "flame plating" in these books corresponds to DGS in the current terminology.

According to Krainer and Robitsch (Krainer & Robitsch, 1967a), DGS (Kirner, 1989; Kieffer & Benesovsky, 1963) was one of the technical processes where in the 1950s in corresponding WC-based samples (in the case of DGS WC–Co coatings) the high-temperature cubic phase WC$_{1-x}$ was discovered, which led later to a correction of the W–C phase diagram (see Section 1.17.3).

Since DGS was not serving the mass market atmospheric plasma spraying (APS) was mentioned as an economic and flexible process for hardmetal coatings production since the 1960s (Kieffer & Benesovsky, 1965; Schedler, 1988). However, the high temperatures and atmospheric conditions of the APS process generated significant problems of decomposition and oxidation of the material, with the resultant coating properties not being competitive with those of coatings prepared by DGS. Thus, protection against oxidation became an aim in the technical development of plasma spray processes, e.g. by use of vacuum plasma spraying (VPS) (Mäntylä, Niemi, Vuoristo, Barbezat, & Nicoll, 1991; Tu, Chang, Chao, & Lin, 1985). Not taking into account the high costs of the VPS process, the negative effect of high temperature remained and the quality of DGS hardmetal coatings was never attained with any of the plasma spray processes.

The invention of HVOF spraying in the 1980s (Browning, 1981), and its broad introduction into industrial practice in the 1990s, created a process that finally gave competitive coating quality to DGS coatings. However, continuous HVOF and pulsed DGS are not equivalent spray processes. In DGS devices, longer contact times of

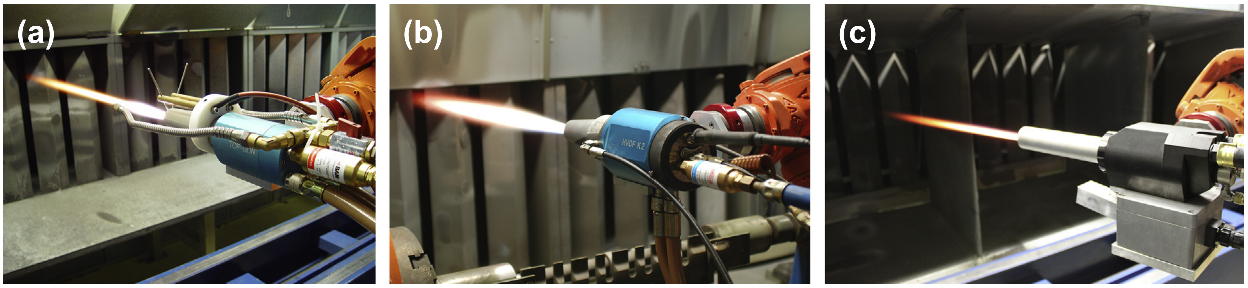

Figure 5 Different types of high-velocity flame processes, operated at Fraunhofer IWS, Dresden, Germany. (a) Second-generation gas-fueled HVOF gun (TopGun, GTV, Germany). (b) Third-generation paraffin-fueled HVOF gun (K2, GTV, Germany). (c) Gas-fueled HVAF-process (M2, Uniquecoat, USA).

the feedstock particles in the combustion gases and higher temperatures (also due to operation with acetylene) are realized (Kirner, 1989). Nowadays HVOF has become the industrial standard technology for preparation of hardmetal coatings. Recent summaries on the development of HVOF spray technology are given in the literature (Gärtner, Kreye, & Richter, 2006; Krömmer, Heinrich, & Kreye, 2009). Three generations of HVOF spray gun devices can be distinguished, which differ in many design parameters but have a pressurized combustion chamber as the common feature. Different types of fuel are used: not only gases such as propane, ethene and hydrogen but also liquid fuel (paraffin). Most of the gas-fueled HVOF systems provide higher particle temperatures then liquid-fueled systems, while the latter are characterized by higher particle velocities (Zimmermann & Keller, 2009). The selection of the fuel is driven both by technical and economic parameters, such as price, availability, and purity in order to increase stability of coating properties, etc. (Mathesius & Krömmer, 2009). Examples of operating HVOF spray guns are shown in **Figures 5(a) and 5(b)**.

The effect of the spray process on the coating microstructures of APS and HVOF is shown for the WC–(W,Cr)$_2$C–Ni composition in **Figure 6**. While for the APS coating the hardmetal structure of the feedstock powder particle is destroyed, it is evident in the HVOF coating (Berger, Saaro, Naumann, Kašparova, & Zahálka, 2010). HVOF-sprayed hardmetal coatings are characterized by high reliability and repeatability of the coating properties since the process is not influenced by strongly wearing parts of the spray guns.

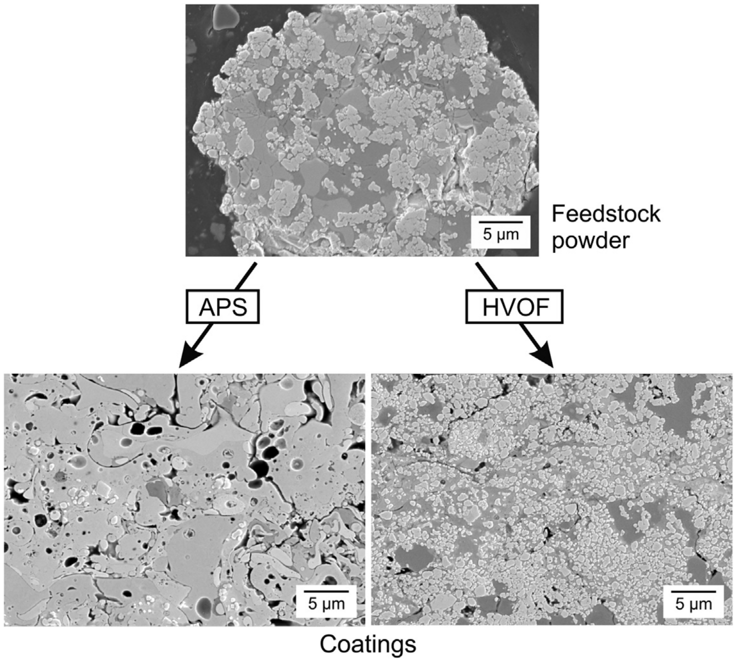

Figure 6 Comparison of microstructures of HVOF- and APS-sprayed WC–(W,Cr)$_2$C–Ni coatings prepared from one feedstock powder (Berger et al., 2010).

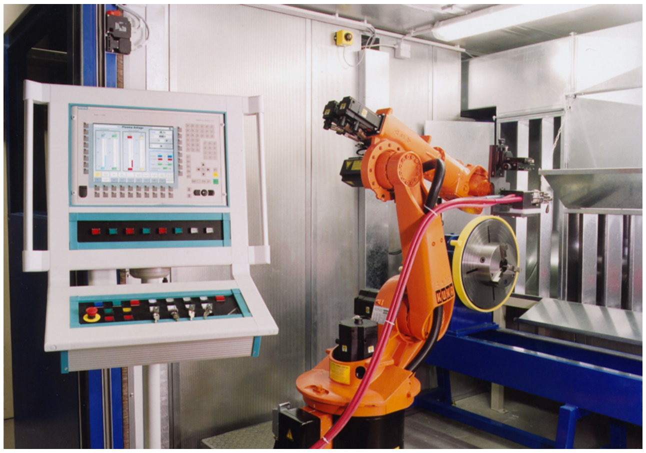

Figure 7 Spray cabin for operating HVOF processes at Fraunhofer IWS, Dresden, Germany.

The current development is characterized by the search for still better combinations of particle velocity and process temperature than in HVOF processes taking into account the economics of the spray process. Such a process variation is the high-velocity air fuel (HVAF) spraying, which uses air instead of oxygen for combustion (Berger, Puschmann, Spatzier, & Matthews, 2013). **Figure 5(c)** shows an HVAF spray system in operation. Also, a modified HVOF spray process with an additional mixing chamber in order to introduce inert gas designated as "warm spray" has been recently developed (Chivavibul, Watanabe, Kuroda, et al., 2011; Kuroda, Watanabe, Kim, & Katanoda, 2011).

Following the intensive development of cold spray since the 1990s hardmetal coating preparation by this technology (e.g. Kim, Lee, & Hwang, 2005; Li, Yang, Gao, Ma, Wang, & Li, 2007) and related processes, e.g. kinetic metallization (Gabel, 2004) were studied.

The DGS process is still in use and has found some distribution, in particular in Asia. There are also some new developments, like a computer-controlled process (Ulianitsky, Shtertser, Zlobin, & Smurov, 2011). Also, improved plasma spray processes may become increasingly competitive for hardmetal coating preparation in broad industrial practice (Barth, Chen, & Dambra, 2011).

In addition to the spray process itself, the technical surrounding has contributed significantly to the improvement of coating quality and reliability in the past 20 years. Simple manipulating systems, or robots, are the technical standard for spray gun handling, ensuring constant surface speeds and spray distances. The introduction of computer control systems and mass flow controllers has also played a significant role. Typically, all modern spray guns are operated in sound isolation chambers, often named spray booth or spray cabin (Berger, 2007), as shown in **Figure 7**.

1.17.3 Hard-Phase Properties

Carbides, and in particular WC and Cr_3C_2, are the dominating hard-phase materials used in compositions for thermally sprayed coatings. TiC can be regarded as the most promising alternative hard-phase material (Berger et al., 1996). The properties of WC, Cr_3C_2 and TiC (Ettmayer & Lengauer, 1994) which are compiled in **Table 1**, are differing significantly. The solubility of these hard phases in liquid binder metals is a highly important property for processing. High-temperature properties, such as thermal decomposition and oxidation, are of greater importance for processing by thermal spraying than for bulk parts production by sintering.

In the W–C and Cr–C systems, carbides other than WC and Cr_3C_2 exist. Since they appear sometimes in the feedstock powders and often in the coatings, they have to be discussed as well.

As in bulk hardmetals, of the three reported carbide phases in the W–C system, namely, WC, W_2C and WC_{1-x} (Massalski, 1990), WC is the target phase that should be present in the coatings for optimum properties. WC is the only stable carbide at room temperature. According to the earlier phase diagram, it undergoes a peritectic decomposition into carbon and the melt at 2785 °C (Massalski, 1990). According to the latest published phase diagram, phase relationships in the high-temperature area of the phase diagram, close to stoichiometric WC, are

Table 1 Physical properties of WC, Cr_3C_2 and TiC (Ettmayer & Lengauer, 1994)

	WC	*Cr_3C_2*	*TiC*
Crystal structure	Hexagonal	Orthorhombic	Cubic (fcc)
Lattice parameters (at RT), nm	0.251 0.284	1.147 0.554 0.283	0.4328
Melting/peritectic temperature, °C	2785 Peritectic	1811 Peritectic	3067 Congruent
Density, g/cm^3	15.7	6.68	4.93
Young's modulus, GPa	700	370	450
Microhardness (100 g load), GPa	19	14	28.9[a]
Heat conductivity (at RT), W/m∗K	121	19	21
Coefficient of thermal expansion, $*10^{-6}$, K^{-1}	5.9	10.3	7.7
Electrical resistivity (at RT), $\mu\Omega*$cm	22	75	55

[a] *Knoop hardness for single crystals in the [100] direction.*

complex and include the transformation of hexagonal WC into stoichiometric cubic WC already at 2720 °C, basically before the appearance of the liquid phase in the W–C system (Kurlov & Gusev, 2006).

WC is a unique chemical compound with very special properties. Its extremely high Young's modulus, excellent heat conductivity, plasticity and high toughness as a hard phase are of importance for the properties of hardmetals on its base (Lassner & Schubert, 1999). Other outstanding properties of WC for sintering of hardmetals are its good wettability by and solubility in binder metals at elevated temperatures. The disadvantages of WC are its low alloyability with other metallic or nonmetallic elements and the very low oxidation resistance.

Cubic WC, which had been found already in the 1950s in DGS-sprayed WC–Co coatings (Kirner, 1989), is often described to exist as substoichiometric WC_{1-x} (Massalski, 1990), but its homogeneity range has been proposed to extend up to stoichiometry (Krainer & Robitsch, 1967a; Kurlov & Gusev, 2006). Thus cubic WC can be formed as stoichiometric composition at 2720 °C (Kurlov & Gusev, 2006). For cast specimen, the solution of chromium in the cubic WC is described (Gladyshevskii, Telegus, Fedorov, & Kuz'ma, 1967). It is described as unstable in the case of mechanical loads, such as polishing of samples (Krainer & Robitsch, 1967a, 1967b). No information on other properties, such as hardness, are given (Lassner & Schubert, 1999). However, cubic WC can appear in feedstock powders prepared at high temperatures and in APS-sprayed coatings (e.g. Berger et al., 2010; Ramnath & Jayaraman, 1989) (see **Figure 6**). It can be assumed that its existence in feedstock powders and coatings where processing temperatures (at least locally) exceeded 2720 °C was also often not recognized.

W_2C melts congruently at 2785 °C and shows three modifications. However, at 1250 °C it decomposes into WC and metallic tungsten (Kurlov & Gusev, 2006; Massalski, 1990). The W_2C is a rather unwanted hard phase both in the feedstock powder and in the coatings. The phase was often present in feedstock powders prepared by some older feedstock preparation technologies and in large amounts in coatings prepared by plasma spray processes. Possible mechanisms of W_2C formation are largely discussed, but the conditions of the different spray processes (see Section 1.17.6.3.1) as well as the character of an unstable phase are not always taken accurately into account.

Due to the extended use of chromium-alloyed hardmetal compositions in thermal spraying, the ternary W–Cr–C phase diagram (Gladyshevskii et al., 1967) is of special interest. The W_2C shows the ability to replace large amounts of tungsten by chromium (Eremenko, Velikanova, & Bondar, 1986; Gladyshevskii et al., 1967; Hinnüber & Rüdiger, 1953; Stecher, Benesovsky, & Nowotny, 1964). The formation of $(W,Cr)_2C$ has been observed in hot-pressed WC–Cr_3C_2 specimen (Hinnüber & Rüdiger, 1953) and as a result of annealing of Cr_3C_2–WC diffusion couples (Brieseck, Bohn, & Lengauer, 2010). However, there is insufficient knowledge about the influence of chromium on the homogeneity range of W_2C and its properties with changing chromium content.

An important role is played by the η-phases M_6C and $M_{12}C$, which are formed as equilibrium phases in particular in the plain W–C–Co and alloyed W–Cr–C–Co systems in the case of carbon deficiency. When appearing in the feedstock powder, they negatively influence the processability but can increase the corrosion resistance. In the early history of hardmetals, sintered corrosion-resistant wear parts consisting mostly of η-phase were produced under the trade name Elmarid (Schedler, 1988).

There exist three stable carbides in the Cr–C system: Cr_3C_2, Cr_7C_3 and $Cr_{23}C_6$ (Eremenko, Velikanova, & Bondar, 1987; Venkatraman & Neumann, 1990). Cr_3C_2 and $Cr_{23}C_6$ show peritectic decomposition at 1811 °C (1829 °C) and 1576 °C (1612 °C), respectively, while Cr_7C_3 is congruently melting at 1766 °C (1781 °C) (Venkatraman & Neumann, 1990) (values in parenthesis by Eremenko et al. (1987)). This means that in contrast to WC and TiC, the formation of a liquid phase directly from the carbides is also possible in HVOF spray processes. According to Kieffer and Benesovsky (1963), the physical properties of Cr_3C_2 compared to those of the lower carbides Cr_7C_3 and $Cr_{23}C_6$ show rather small differences, but in general, the fundamental knowledge on the properties of the chromium carbides is insufficient. For example, contradictory hardness values for these three carbides are reported in the literature; however, a decrease with decreasing carbon content was confirmed (Mayr, Lengauer, Ettmayer, Rafaja, Bauer, & Bohn, 1999). Usually Cr_3C_2 is the target phase in the coatings. The alloyability of Cr_3C_2 with other metallic and nonmetallic elements is low. The structures of Cr_7C_3 and $Cr_{23}C_6$ are known to exist in hardened steels (Berns, 1998). Cr_3C_2 has the highest oxidation resistance of all group IVa–VIb transition metal carbides (Voitovich, 1981). It shows also a very high corrosion resistance (Hinnüber & Rüdiger, 1953).

As a low-cost alternative, the use of a FeCrC hard phase has been recently tested (Zimmermann, Gries, & Brüning, 2011).

Due to its physical properties and availability, TiC has been most often considered as an alternative hard-phase material to WC and Cr_3C_2 (Berger et al., 1996). Most important properties addressed are the high hardness and low density. In contrast to WC and Cr_3C_2, TiC is congruently melting. The face-centered cubic (fcc) cubic crystal lattice is characterized by the possibility of being nonstoichiometric. The carbon can be fully replaced by nitrogen and/or oxygen; a full solubility in the pseudoternary TiC–TiN–TiO system exists (Neumann, Kieffer, & Ettmayer, 1972). Titanium can be replaced by other metals, e.g. a wide solubility of tungsten in TiC exists. (W,Ti)C was earlier used as a hard phase (Eschnauer, 1980). The main concern regarding application of TiC for thermally sprayed coatings is an inclination to oxidation (Beczkowiak, Keller, & Schwier, 1996; Kirsten, Oechsle, & Moll, 2005). However, after Cr_3C_2, it has the highest oxidation resistance of all group IVa–VIb transition metal carbides (Voitovich, 1981). For powders, an oxidation resistance $Cr_3C_2 > TiC_{0.7}N_{0.3} > TiC > WC$ has been determined by thermoanalytic measurements (Berger, Vuoristo, Mäntylä, & Gruner, 1998). Significant interest in TiC-based materials has also been generated since a beneficial action as solid lubricants ("lubricious oxides") of titanium suboxides having Magnéli-phase structures, which are formed as a result of tribo-oxidation and atmospheric oxidation, was proposed (Gardos, 1988; Woydt, Kadoori, Hausner, & Habig, 1990).

In the past, both borides and nitrides have been explored (Eschnauer, 1980). Borides have been studied repeatedly, e.g. TiB_2 (Jones, Horlock, Shipway, McCartney, & Wood, 2001) and MoB, (Mizuno & Kitamura, 2007) and are used for special applications.

1.17.4 Hardmetal Compositions for Thermal Spray Coatings

In this section, the most common hardmetal compositions are discussed, independent of the feedstock powder preparation technology and the spray process. Despite the changes of chemical and phase compositions induced by the spray process, different cooling rates, etc., commercial feedstock powders (see Section 1.17.6) and coating compositions are designated in the same manner.

Cobalt and nickel are most widely used as binder metals. In the majority of commercially available materials, the amount of metallic binder phase lies in the range 20–30 vol%. There are many coating solutions with higher binder concentrations, e.g. mechanical blends with additional binders such as self-fluxing alloys. These are out of the scope of this contribution. Carbides with very different grain sizes have been used for feedstock powder and coating preparation (see Sections 1.17.5.1, 1.17.5.2.3 and 1.17.8.1), while the available commercial compositions remained largely unchanged.

For WC, compositions with plain, but varying amount of cobalt and nickel binder were applied from the beginning of the development. Cobalt is predominantly used as binder metal (WC–12Co, WC–17Co), but compositions with nickel (WC–12Ni; also WC–10Ni and WC–17Ni) are also commercially available.

While for cutting operations hardmetal compositions are modified by the introduction of a second hard phase with cubic crystal lattice (Lassner & Schubert, 1999), for thermal spray, large additions of chromium carbides (or chromium) are applied. These additions significantly exceed the amounts of chromium carbide added for grain growth inhibition in bulk hardmetals. The high chromium content reflects differences in service conditions compared to sintered hardmetals, e.g. high requirements for corrosion and oxidation resistance (Berger, Woydt, et al., 2007; Berger, Zieris, & Saaro, 2005). It is mainly proposed that the chromium additions alloy the metallic binder for improving its corrosion resistance.

For both binder metals, three compositions with high chromium content are commercially available: WC–10-Co–4Cr, WC–6Co–8Cr and 73WC–20"CrC"–7Ni. Compared to WC–10Co–4Cr and 73WC–20"CrC"–7Ni, WC–6Co–8Cr is only rarely used. Large amounts of chromium lead to the formation of $(W,Cr)_2C$ or easier formation of η-phases in the case of carbon deficiency, for nickel and cobalt binders, respectively.

Nowadays, the composition WC–10Co–4Cr is widely used for the preparation of coatings having simultaneously high wear and corrosion resistance. The ratio of cobalt to chromium in this composition is 2:1 by volume (Berger, Ettmayer, Vuoristo, Mäntylä, & Kunert, 2001). Intensive studies on this composition have started since the end of 1990s and were closely connected with the increasing use of HVOF-sprayed coatings. WC, the η-phase $(Co,Cr)_3W_3C$, and a (Co,Cr,W) alloy binder are expected to be in thermodynamic equilibrium. Thus, chromium is contained both in metallic binder and the hard phase (Berger et al., 2001; Gries & Zimmermann, 2012). Basically the chromium addition intensifies the effect of η-phase formation compared to plain WC–Co. In general, it seems that WC–10Co–4Cr is a good empirically derived and balanced formulation for the preparation of simultaneous wear- and corrosion-resistant coatings (Berger et al., 2001).

Feedstock powders of the composition WC–$(W,Cr)_2C$–Ni, which was invented in 1958 for coatings sprayed by DGS, can be preferably prepared from 70% WC, 24% Cr_3C_2 and 6% Ni (Pelton & Koffskey, 1958). There are variations in contents of the components in the range of 1–4% from different manufacturers, but feedstock powders of this composition are currently traded with designations such as WC–"CrC"–Ni, WC–"Cr_3C_2"–Ni or WC–NiCr (Berger, Saaro, Naumann, Kašparova, & Zahálka, 2008). This composition excels by an unusual low metallic binder content (about 10 vol%) but can be sprayed with a high DE (Berger, Saaro, Naumann, Kašparova, et al., 2008; Berger et al., 2010). The phase composition depends on the progress of the metallurgical reactions between WC and Cr_3C_2, which occurs in most cases during feedstock powder preparation and also during the spray process. When the reaction is complete, WC–$(W,Cr)_2C$–Ni (unlike WC–Co and Cr_3C_2–NiCr), is not a simple binary hard phase–binder metal composite; besides WC, the second hard phase $(W,Cr)_2C$ with varying chromium content appears in larger amounts (Berger, Saaro, Naumann, Kašparova, et al., 2008). Therefore, there is no clear definition of a "carbide grain size" for this composition. Coatings can be applied at high temperatures in atmospheric conditions due to a high oxidation resistance; this is another major difference from plain WC–Co and WC–10Co–4Cr (Berger, Saaro, Naumann, Kašparova, et al., 2008; Berger et al., 2010). This composition is widely used in Asia, hence studies were mostly performed in this region (e.g. Ishikawa, Kawakita, Osawa, Itsukaichi, Sakamoto, & Takaya, 2005; Ishikawa, Kuroda, Kawakita, Sakamoto, & Takaya, 2007). However, as opposed to studies on WC–Co and WC–CoCr coatings, investigations of this composition have been comparatively rare.

The corrosion resistance of WC-based coatings with cobalt or nickel binder is often not satisfactory. The use of mechanical blends of standard hardmetal with atomized corrosion-resistant metal feedstock powders leads to inhomogeneous, also not satisfactory coating structures (Zimmermann et al., 2011). The preparation of feedstock powders with complex corrosion-resistant binder alloys by agglomeration and sintering requires that binder particles are available in the same size range as the carbides. With their availability, a WC-based grade with a Hastelloy C-type (NiMoCrFeCo) binder matrix entered the market (Zimmermann, Keller, & Schwier, 2003), and later a WC–FeCrAl composition ("green carbide") (Zimmermann et al., 2011). However, the WC is not in equilibrium with these complex binder alloys, leading to metallurgical reactions during feedstock powder preparation. Investigations for these compositions are still rare (e.g. Bolelli, Börner, Bozza, Cannillo, Cirillo, & Lusvarghi, 2012; Houdková, Zahálka, Kašparová, & Berger, 2011).

The Cr_3C_2 is predominantly used with 20–25% NiCr binder. This composition was invented in 1960 (Pelton et al., 1960) also in connection with the development of DGS. Under equilibrium conditions, the compositions of the hard phase and the binders are governed by the Cr–Ni–C phase diagram. Thus, the NiCr alloy binder composition is in thermodynamic equilibrium with Cr_3C_2 while it will react with pure nickel binder (Holleck, 1984; Velikanova, Bondar, & Grytsiv, 1999). Simultaneously, the use of NiCr binder increases the corrosion resistance of the composite. Also, Cr_3C_2-based feedstock powders with complex binder alloys (Cr_3C_2–50-NiCrMoNb) became recently commercially available (Zimmermann et al., 2011).

Starting with plain TiC (Brunet & Dallaire, 1987) and cladded TiC–Ni (Stenberg, Niemi, Vuoristo, Vuorinen, Mäntylä, & Tiainen, 1995), numerous compositions and concepts to use TiC as the main hard phase for hardmetal coatings have been developed. Compositions with cubic (Ti,W)C were earlier commercially available (Eschnauer, 1980). The choice of the composition and the metallic binder for TiC-based powders are often connected with the possibilities of the different feedstock powder preparation technologies, e.g. "agglomerating and sintering" and self-propagating high-temperature synthesis (SHS) (see Section 1.17.5.2). Most often nickel and cobalt were selected as binder metals (typically 20–27 vol%), but iron is also often considered. Since hardmetal research has shown the advantage of modification of plain TiC for improved performance of the composite (Ettmayer & Lengauer, 1989), different compositions of (Ti,Mo)(C,N)–Ni(Co) powders with a core–rim structured cubic hard phase have been developed (Berger, Thiele, Vuoristo, Mäntylä, Keller, et al., 2002). The main function of Mo as an alloying element is to improve wetting between the hard phase and binder, while the function of N is grain growth inhibition of the core–rim structured hard phase grains.

1.17.5 Feedstock Materials

1.17.5.1 General

Since in thermal spraying the coating is formed from solid feedstock, its quality is essential to the coating properties. The dominating feedstock for hardmetal coatings are powders consisting of granules; their particle size has to be adapted to the needs of each spray process (see Section 1.17.1). There are a number of commercial production methods and some laboratory preparation routes (Berger et al., 1996). Historically, feedstock powder development was predominantly carried out in industrial research hence documentation in the literature is rather poor. There are some earlier overviews on feedstock powder preparation technologies (e.g. Eschnauer, 1980; Eschnauer & Knotek, 1977; Eschnauer & Lugscheider, 1991). Depending on the preparation technology and the resulting characteristics, they behave differently in the spray processes. The influence of the feedstock powder preparation technologies on coating properties for different spray processes were discussed for commercial compositions, such as WC–Co (de Villiers Lovelock, 1998; Ramnath & Jayaraman, 1989), WC–10Co–4Cr (Berger et al., 2001), WC–(W,Cr)$_2$C–Ni (Berger, Saaro, Naumann, Kašparova, et al., 2008; Berger et al., 2010), and Cr$_3$C$_2$–NiCr (Keller, Pross, & Schwier, 2000).

Feedstock powder preparation technologies are characterized by very different process conditions and temperatures, including different cooling rates. They result in different particle morphologies and are characterized by different hard-phase grain sizes, too. In the early period (1960s–1980s), feedstock powders with coarse carbide grains and irregular particle shape (plain cast carbides blended with large metal powder particles, fused or sintered and crushed (s&c), cladded powders) were used. This is connected not only with the dominating role of APS at that time but also with limited availability of fine hard phases.

The flowability, and consequently processability, of the feedstock powders can be significantly improved by a spherical particle shape which can be obtained in the required size by agglomeration (spray drying). At the beginning, such powders were reported as "micropellets" (Eschnauer & Knotek, 1977). For improved processability by APS, mechanically stable feedstock powders were required and plasma densification of spray-dried granules was applied (Houck & Cheney, 1984). However, due to possible decomposition of the hard phase by the plasma process, a decrease of the consolidation temperature by sintering is highly advantageous, in particular for powders applied in low-temperature spray processes such as HVOF. The quality of the feedstock powders manufactured by "agglomeration and sintering" has been permanently improved and their market share has been continuously increased in the past few years. Currently, the majority of the feedstock powders in the market is produced by this technology (Zimmermann & Keller, 2009).

Although there is often some porosity, feedstock powders produced with advanced technologies show microstructures similar to those of bulk hardmetals of corresponding compositions and carbon content close to stoichiometry. Following also the tendencies in bulk hardmetal production, where the advantages of small carbide grain sizes have been shown, there have been many developments in order to introduce nanosized carbides into feedstocks and coatings sprayed thereof (e.g. He & Schoenung, 2002). However, influencing factors on carbide grain size, e.g. the dependence on alloying carbides and on the carbon content, were studied only for WC–Co (Chivavibul, Watanabe, Kuroda, & Kentaro, 2007) and much less systematically than for sintered hardmetals.

A complete feedstock powder characterization is very laborious but necessary at least for research purposes. One example is described for WC–10Co–4Cr (Berger et al., 2001). Such a complete characterization can be divided into the characterization of the physical properties (morphology, particle size distribution, density and porosity) and the determination of the chemical and phase compositions. In the industrial environment, the feedstock powder characterization is limited to relatively few parameters. Depending on the spray gun characteristics, the particle size range of the powder is selected; this so called "cut" characterizes the nominal lower and upper particle sizes, but is not a measure of the particle size distribution. A narrow particle size distribution can be assumed as advantageous for a steady and homogeneous heat-up in the spray process. Depending on the characteristics of the HVOF process, the increase of the apparent density (as determined by ASTM B212) can lead to significantly higher DE (Zimmermann & Keller, 2009).

For low-cost applications, the use of flexible cored wires (Pawlowski, 2008) is common. One other alternative for low-cost applications is the feedstock powder preparation from hardmetal scrap (Kanerva, Lagerbom, & Vuoristo, 2007).

1.17.5.2 Main Powder Feedstock Preparation Technologies

1.17.5.2.1 Powders Based on Fusing or Sintering

Fusing or sintering with subsequent crushing leads to relatively dense spray powders with an angular and blocky morphology. A typical example is shown for an s&c WC–10Co–4Cr powder in **Figure 8(a)**. The microstructure and the phase composition of the feedstock powder particles depends on the total carbon content, leading to the appearance of W_2C and η-phases in WC–Co and WC–CoCr feedstock powders. Since the formation of η-phases is a "binder-consuming" process (Berger et al., 1996), at some degree of carbon deficiency the composite will consist of hard and brittle phases only. The carbon content of fused powders was particularly lower than those of sintered powders. A lower DE is reported for η-phase-containing powders (Schwetzke & Kreye, 1999). Thus, when HVOF became the dominating spray process, the powders had to be improved by increasing the total carbon content. The cross-sections of powders with low and high total carbon content are shown in **Figures 8(b) and 8(c)**, respectively. Individual powder particles of the former figure show strongly different microstructures resulting from an inhomogeneous distribution of the elements.

For an s&c WC–$(W,Cr)_2C$–Ni powder, due to the high sintering temperature the starting carbides have already reacted. An EDX (energy dispersive x-ray spectroscopy) analysis of the powder shown in **Figure 8(d)** revealed that areas of WC distributed in an alloyed Ni matrix coexist together with large areas consisting of $(W,Cr)_2C$ (Berger, Saaro, Naumann, Kašparova, et al., 2008).

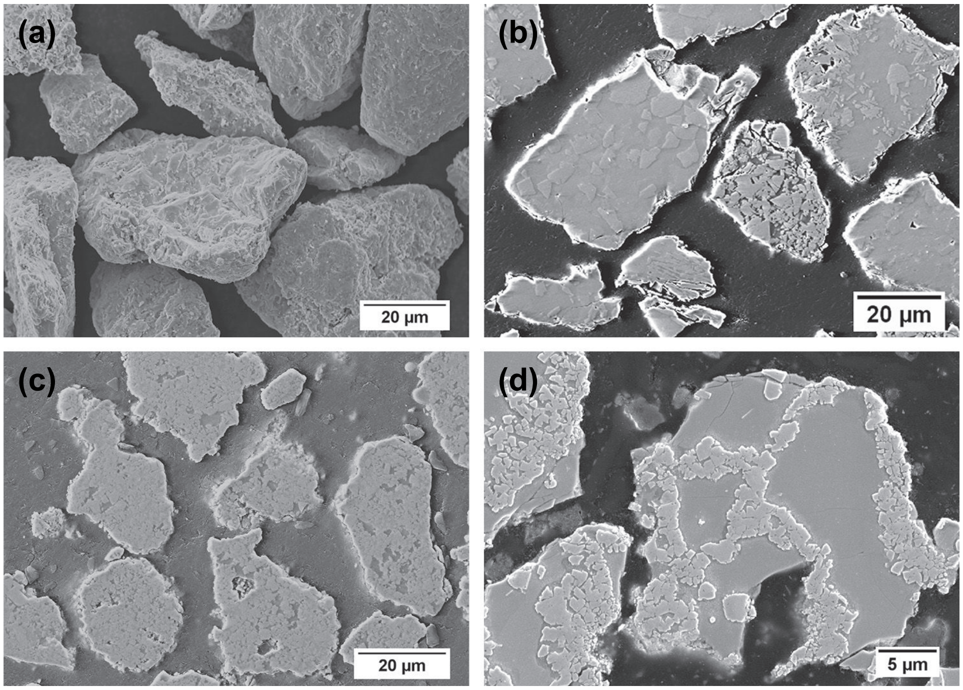

Figure 8 Scanning electron micrographs of feedstock powders: (a) morphology of an s&c WC–10Co–4Cr powder, (b) cross-section of a "fused and crushed" WC–10Co–4Cr powder with low carbon content (C_{total}: 3.65%), (c) cross-section of an s&c WC–10Co–4Cr powder with high carbon content (C_{total}: 5.23%), and (d) cross-section of an s&c WC–$(W,Cr)_2C$–Ni feedstock powder (Berger et al., 2010).

Despite the increasing importance of s&c powders, for particular applications s&c feedstock powders are still in use (Zimmermann & Keller, 2009). This also relates to WC-based powders with low carbon content due to the good corrosion resistance of the corresponding coatings.

1.17.5.2.2 Cladded Powders

Cladded (dense coated) powders are prepared by coating large fused or sintered carbide particles with a chemical process. These coatings are relatively thin, representing an unfavorable distribution of the binder and hard phase, leading to very low DE, e.g. for Cr_3C_2–NiCr (Keller et al., 2000). For WC–Co (Li, Ohmori, & Harada, 1996a) and for TiC–Ni (Stenberg et al., 1995) powders, this is explained with rebounding of carbide particles from the substrate during spraying.

1.17.5.2.3 Powders Based on Agglomeration

Spray drying is the preferred technology to prepare spherical feedstock powder particles. There are two methods of consolidation, which are plasma densification and sintering. Improved processability by enhanced flowability is the main advantage of these powders which is a critical issue, particularly for materials with low density.

The morphology and the cross-section of an agglomerated and plasma-densified (a&pd) WC–10Co–4Cr feedstock powder are shown in **Figure 9** (Berger et al., 2001). Defects originating from the spray drying process like large pores could not be fully eliminated (see **Figure 9(b)**). High process temperatures and cooling rates cause effects similar to plasma spray process. Thus, in these powders, high temperature and nonequilibrium phases are commonly observed. The appearance of free carbon due to the peritectic decomposition of WC and the formation of $(W,Cr)_2C$ rims around the WC grains have been observed for a WC–10Co–4Cr powder (Berger, 2007; Berger et al., 2001). A positive effect is the decrease or elimination of impurities by the action of the plasma. As a result, the microstructures and process properties of the plasma-densified powders strongly deviate from others. Thus, plasma treatments of feedstock powders appear as a solution when the processability has to be improved, e.g. if very fine feedstock powders have to be used (Matthäus & Stevens, 2003). However, a high-temperature treatment in feedstock powder preparation is contradictory to the use of low-temperature spray processes, such as HVOF.

The typical morphology and the cross-section of the particles of an a&s feedstock powder is shown in **Figures 10(a) and 10(b)**, respectively. Special advantages of a&s powders are comparatively few changes in chemical composition, the formation of a homogeneous microstructure in all powder particles close to bulk hardmetals with predominance of equilibrium phases, and a controlled hard-phase grain size. Along with the use in APS and different HVOF processes, the carbide grain size in a&s WC–Co powders was decreasing (Zimmermann, Keller, & Schwier, 2006). Currently micron-sized carbides are the industrial standard. As was demonstrated for the WC–$(W,Cr)_2C$–Ni composition, the a&s powders are superior to s&c and a&pd powders in terms of processability by HVOF, coating microstructures and abrasion wear resistance (Berger et al., 2010).

Porosity of a&s powders can be reduced and controlled by appropriate selection of the raw materials and by optimization of the spray drying process. High green densities of the spray-dried granules might be required for the formation of typical microstructures in the sintering step, e.g. the formation of the core–rim structure of hard phases of TiC-based powders (Berger et al., 2002). Also, the phase composition of a&s WC–$(W,Cr)_2C$–Ni powders can be strongly different (Berger et al., 2010), probably depending both on the green density and the

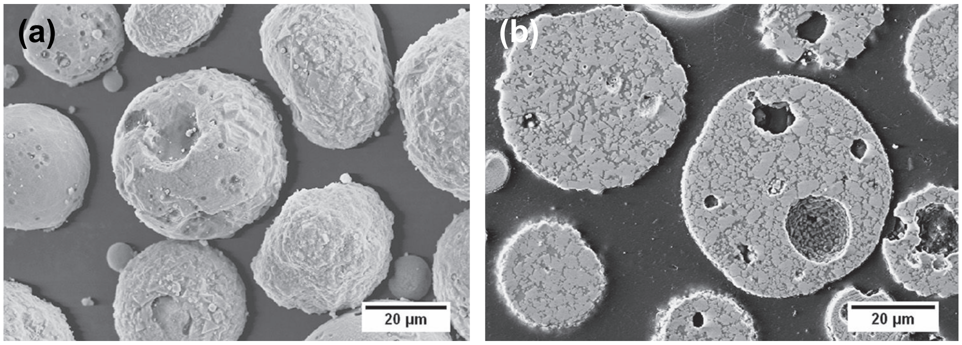

Figure 9 Scanning electron micrographs of an agglomerated and plasma densified WC–10Co–4Cr spray powder (Berger et al., 2001): (a) morphology and (b) cross-section.

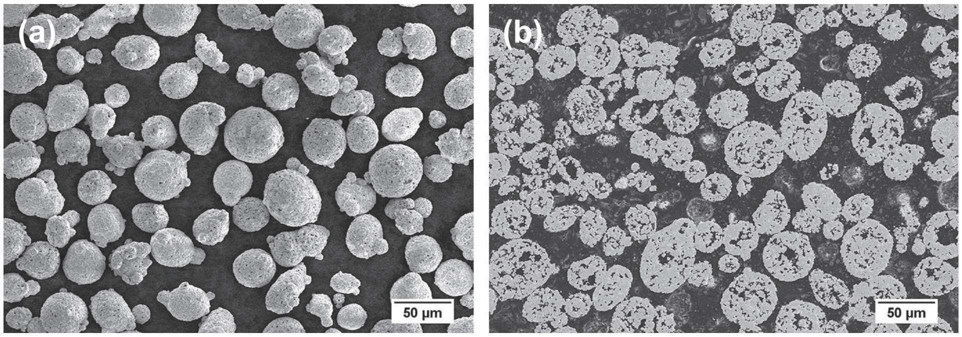

Figure 10 Scanning electron micrographs of a commercial a&s powder (WC–12Co): (a) morphology and (b) cross-section.

sintering temperature. In particular, there is a maximum of the DE depending on the apparent density and the spray process. The open porosity leads not only to improved melting but also to stronger reactions with the flame (Zimmermann and Keller, 2009).

1.17.5.2.4 Powder Blends

Although their importance is continuously decreasing with time, different types of mechanical powder blends of powder particles of comparative size are still often applied. The advantage is a fast preparation of different compositions. Typical examples of blends are coarse-grained Cr_3C_2 with NiCr (Keller et al., 2000; Matthews, James, & Hyland, 2010), standard hardmetal with atomized powders in order to increase corrosion resistance of the coatings (Zimmermann et al., 2011), and blends of different hardmetal powders (Matz & Kennedy, 2011). For mechanical blends, the spray parameters can be optimized only for one component, the other is always sprayed under less-favorable conditions (Zimmermann et al., 2011). For blended Cr_3C_2-NiCr, a very low DE is reported (Keller et al., 2000).

1.17.5.2.5 Other Methods

In contrast to compositions based on WC and TiC, powders based on chromium carbides can also be prepared by atomization (Jarosinski, Temples, & Londry, 1996; Laul, Dorfman, & Somoskey, 1998).

SHS is making use of the high exothermal heat of the reaction of metallic titanium with carbon for the preparation of TiC-based feedstock powders (e.g. Jones et al., 2001; Sobolev et al., 2004). However, they are often characterized by an irregular morphology and large and inhomogeneous carbide grain size.

Another method is high-energy milling, also applied for TiC-based powders (Eigen, Gärtner, Klassen, Aust, Bormann, & Kreye, 2005; Stenberg et al., 1995). Spray drying and sintering can improve the processability of these powders (Eigen et al., 2005).

1.17.6 Processes during Spraying and Coating Formation

1.17.6.1 Coating Formation

Coating formation is the second step of hardmetal coating preparation following feedstock powder manufacturing (see Section 1.17.1). Feedstock powder properties represent the initial conditions for the spray process. The combination of feedstock powder properties with the spray process results in the coating properties. All processes occurring in-flight have to be discussed for all feedstock powders and spray processes individually. Sometimes other concepts, like *in-situ* carbide formation during the spray process, have also been studied (e.g. Smith & Mutasim, 1992). However, such processes are extremely difficult to control.

In order to realize a hardmetal structure in the coatings, in an idealized case the composition and the microstructure preformed in the feedstock powder should be transferred to the coating without chemical or phase changes (Berger et al., 1996). However, fast heating and cooling rates and the very harsh environment of a real thermal spray process result in extremely complex and overlapping chemical and metallurgical processes in the hardmetal composition. The intensity of these changes depends on the spray process, and all technical development was directed to their minimization. However, in state-of-the-art HVOF and HVAF spray processes also changes in the chemical and the phase compositions are unavoidable (see Section 1.17.6.2). It should also to be taken into account that the coating is formed from a large number of powder particles where each of these particles had its individual history in the spray process.

The questions of momentum and heat transfer in-flight from the flame to the powder, deformation and heat transfer at the substrate surface are extremely complex processes and they are summarized in detail elsewhere (Pawlowski, 2008; Sobolev et al., 2004). In order to have the ability of plastic deformation at the moment of impact leading to good microstructure formation, the feedstock powder particles have to be brought to such a state by melting of the binder and the proper solution of the hard-phase particles in the binder (often only described as particle melting degree (e.g. Chivavibul et al., 2007)). Particle size and shape as well as density and the heat capacity are the most important parameters for this process (Chivavibul et al., 2007; Zimmermann & Keller, 2009). Porosity in the feedstock powder particles leads to a more effective particle heating but at the same time to a more intensive oxidation. Carbides that have been dissolved in the binder often remain in significant amounts in the binder phase of the coatings which is in an amorphous or nanocrystalline state due to fast cooling, giving rise to broad, diffuse peaks in the corresponding X-ray diffraction (XRD) patterns. Thus, each hardmetal coating is practically nanostructured.

Thermal spraying has the character of a line-of-sight process. A particle impact angle of 90° is optimum for coating formation (Davis, 2004; Mathesius & Krömmer, 2009). When coating properties are discussed, it is normally understood that the spray angle corresponds to 90°. Due to the changes in properties, a spray angle of at least 60° for WC–Co and at least 75° for Cr_3C_2–NiCr coatings is recommended (Houdková, Kašparová, & Zahálka, 2010). For parts of complex geometry, local different thicknesses resulting from different DE in result of different spray angles can occur.

For different WC–Co compositions sprayed with a liquid-fueled HVOF process, a temperature range 1580–1680 °C and particle velocities mostly around 800 m/s are reported (Chivavibul et al., 2007). For a commercial a&s WC–10Co–4Cr powder sprayed with a hydrogen-fueled HVOF process for the coating with the lowest porosity (0.2%) and lowest oxygen content (0.32%), a temperature of 2116 °C and a particle velocity of 497 m/s was measured (Zhao, Maurer, Fischer, & Lugscheider, 2004). It has to be taken into account that these temperatures measured with on-line particle monitoring systems relate to the particle surface in-flight. For spray processes exceeding particle velocities of 400 m/s, the transformation of kinetic energy into heat upon impact has to be considered (Pawlowski, 2008). In a certain range, for each HVOF and HVAF process, particle temperature and velocity can be influenced not only by the oxygen-to-fuel ratio but also by the pressure in the burning chamber and other parameters.

There have been several attempts to simulate the coating deposition process (e.g. Sobolev et al., 2004). However, simulation is lacking detailed knowledge of the in-flight processes and reliable thermophysical data of the materials (in particular at high temperatures) and is further complicated by the large variety of processes, equipment and feedstock powders. Due to these difficulties, such simulation models are not able yet to predict coating properties in a satisfactory way.

Thus, improvements in coating properties can be reached both by technological measures and improvements in the feedstock materials, but best by coordinating both factors together.

1.17.6.2 Changes in Chemical and Phase Composition

Processes for changes in chemical and phase composition are numerous, including carbon loss, oxidation, vaporization of components, rebounding of particles at impact, and rapid cooling. The phase composition of the coating results from the change of both the chemical composition and cooling rate. Nonequilibrium phases can be observed for many coatings.

Figure 11 shows three distinguishable regions of the HVOF spray process (Hackett & Settles, 1995) where hardmetal powder particles interact with the combustion products and air. Region I covers the distance from the point of injection up to the end of the visible flame. In this region, the particles are heating up and are subjected to oxidation by remaining oxygen from incomplete combustion and the combustion products (Hackett & Settles, 1995; Zimmermann & Keller, 2009). Water as combustion product has a highly oxidative action to the material (Korpiola, 2004). Region II is described as the mixing region from the end of the visible flame up to the substrate surface with full entrainment of the atmosphere into the jet. Temperature of the particles is decreasing in this region but they are subject to in-flight oxidation. Region III represents predominantly the surface of the last spray pass in contact with the boundary gas flow. While in regions I and II oxidation occurs in milliseconds, the time in region III is significantly longer.

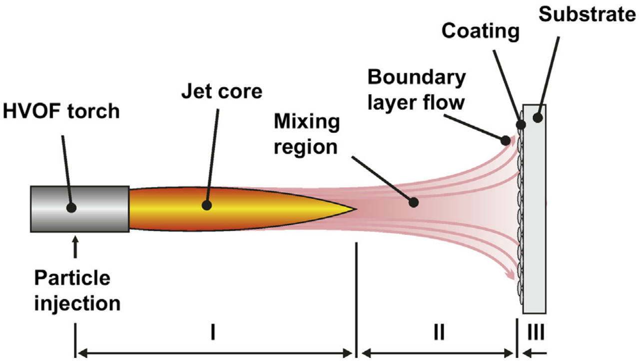

Figure 11 Regions of oxidation for the HVOF spray process according to Hackett and Settles (1995).

The term oxidation is mostly used together for both carbon loss and oxygen uptake. These are the most frequently studied changes of the chemical composition (e.g. Berger et al., 1998; Zimmermann et al., 2003; Zimmermann et al., 2006), while a complete analysis including the metallic components is only seldom reported, e.g. for WC–Co (Chivavibul et al., 2007). Carbon loss and oxygen uptake mainly depend on the chemical properties both of the hard phase and the metallic binder. Mechanisms of carbon loss and oxygen uptake during spraying and as a coating can be different, as observed for plain WC–Co (Berger et al., 1998). On the contrary, the mechanisms for Cr_3C_2–NiCr during spraying and as a coating in air are similar (Berger et al., 1998).

There are different types of rebounding of particles. Rebounding is a general phenomenon in the case of insufficiently heated particles unable to deform plastically at the moment of impact. Another phenomenon is selective rebounding of particles deviating from the average composition, e.g. leading to a strong of carbon loss (Li, Ji, Wang, & Sonoya, 2002). Rebounding is in particular often reported for cladded powders (see Section 1.17.5.2.2).

The content of the binder metals can be decreased by evaporation. Also, volatility of oxides or low adhesion of oxide scales formed during spraying, such as WO_3, will influence the chemical composition (Berger et al., 1998; Kreye, Gärtner, & Richter, 2003).

1.17.6.3 Particularities of the Most Common Compositions

1.17.6.3.1 WC–Co and WC–CoCr

There is a previous extended review on the state of the art on preparation and properties of WC–Co coatings (de Villiers Lovelock, 1998). WC is the target phase which has to be transferred from the feedstock powder to the coating with minimum losses. For avoiding the decomposition of WC during spraying, process temperatures below the decomposition temperature of 2720 °C (Kurlov & Gusev, 2006) or short dwell times should be selected (Kirner, 1989). The maximum flame temperatures of most common gases (ethene, propane, hydrogen, etc.) and paraffin in HVOF processes are up to about 200 K higher (Mathesius & Krömmer, 2009) than the temperature of decomposition of WC. The process temperature of DGS is mostly higher, since acetylene with a maximum flame temperature of 3160 °C is widely used.

The decomposition and oxidation of WC–Co during spraying is usually analyzed in terms of the three-step mechanism originally proposed for APS (Vinayo, Kassabji, Guyonnet, & Fauchais, 1985):

$$2WC \rightarrow W_2C + C \quad (1)$$

$$W_2C + 1/2O_2 \rightarrow W_2(C,O) \quad (2)$$

$$W_2(C,O) \rightarrow 2W + CO \quad (3)$$

Although formulated as a hypothesis (Vinayo et al., 1985), in numerous later citations these reactions have tended to be treated as experimentally verified fact (Berger, 2007) and were also used to describe the reactions in HVOF processes, e.g. by Guilemany, de Paco, Nutting, and Miguel (1999). W_2C is very often described as a phase present in HVOF-sprayed coatings (e.g. Guilemany et al., 1999; Li et al., 1996a; Li, Ohmori, & Harada, 1996b; Schwetzke & Kreye 1999; Stewart, Shipway, & McCartney, 1998; Stewart, Shipway, & McCartney, 2000;

Verdon, Karimi, & Martin, 1998). It is described to be located in rims around WC grains by several authors (Guilemany et al., 1999; Schwetzke & Kreye, 1999; Stewart et al., 2000; Verdon et al., 1998). Other than in the work of Vinayo et al. (1985), only Li et al. (1996a) mention the existence of $W_2(C,O)$ (JCPDS card 22–959) in plasma-sprayed coatings. However, this phase has an fcc lattice and was described as resulting from a reaction of tungsten oxide vapors on graphite surfaces (Babad-Zakhryapin, Gert, & Valyavko, 1968). Such conditions are rather unlikely in thermal spray processes. Metallic tungsten is also often observed in WC–Co coatings sprayed by APS, DGS and HVOF, when intensive degradation occurs (Schwetzke & Kreye, 1999; Verdon et al., 1998; Vinayo et al., 1985; Vuoristo, Niemi, Mäntylä, Berger, & Nebelung, 1995).

As a result of the spray process (liquid-fueled HVOF process) the cobalt content increased by 10–30%, while the carbon decreased more than the tungsten content (Chivavibul et al., 2007). The oxygen content in HVOF-sprayed WC–Co coatings is very small. Mostly values of <0.2 wt% (Chivavibul et al., 2007; Schwetzke & Kreye, 1999; Zimmermann et al., 2003; Zimmermann et al., 2011) have been reported. Low-oxide-scale adhesion strengths (Berger et al., 1998) and, possibly, the high volatility of WO_3 (Kreye et al., 2003) seem to be responsible for this.

Recently, it was shown that the phase composition and the microstructure of the coating obviously depend on the cooling rate (Thiele, Sempf, Jaenicke-Roessler, Berger, & Spatzier, 2011). Both W_2C and metallic tungsten are characteristic phases for the nonequilibrium state of as-sprayed hardmetal coatings. Sometimes, the existence of η-phases in as-sprayed coatings is also reported (e.g. Li et al., 1996a, 1996b). The effect that η-phases have on coating lifetime depends on the service conditions.

For WC–10Co–4Cr no special studies on the reactions during the spray process were performed. It can be assumed that they are similar as for plain WC–Co. However, due to the presence of chromium, the oxygen content in the coatings is higher and mostly reported in the range 0.3–0.5% (Zhao et al., 2004; Zimmermann et al., 2006; Zimmermann et al., 2003; Zimmermann et al., 2011). The η-phase formation is also characteristic for WC–10Co–4Cr.

1.17.6.3.2 WC–(W,Cr)$_2$C–Ni

The metallurgical processes during spraying for this composition have been studied in detail only recently and depend on the phase composition of the feedstock powder (Berger, Saaro, Naumann, Kašparova, et al., 2008; Berger et al., 2010). If not present in the feedstock powder, the $(W,Cr)_2C$ phase can be formed in the HVOF process. When already existing in the feedstock powder, during spraying, the Cr/W ratio of this phase can change over a wide range (Berger et al., 2010). Currently, information about changes of the chemical composition is limited to the oxygen content of the coatings, which is reported to be about 1.7% (Zimmermann et al., 2003; Zimmermann et al., 2006). Due to the possibility of applying coatings of this composition at significantly higher temperatures than plain WC–Co and WC–10Co–4Cr, an increasing interest for understanding the complex metallurgical processes exists (e.g. Hou, Zhou, An, Liu, Chen, & Chen, 2011).

1.17.6.3.3 Cr$_3$C$_2$–NiCr

According to the original patent (Pelton & Koffskey, 1960), first coatings of this composition have been prepared from mechanical blends of Cr_3C_2 and NiCr particles. These coatings remained the most important for a long time (Matthews et al., 2010). Detailed investigations on the metallurgical processes of this composition have started with the broad introduction of HVOF into industrial practice (e.g. Vuoristo, Niemi, Mäkela, & Mäntylä, 1994; Zimmermann & Kreye, 1996). The broad variety of feedstock powders prepared by different technologies (Keller et al., 2000) is influencing strongly the changes in chemical and phase composition. Since Cr_3C_2 is able to form a liquid phase during the spray process, a higher amount of the amorphous phase is usually present in the coatings. Carbon loss depends on the HVOF system and can be significant (Zimmermann & Kreye, 1996). However, due to their low intensities and coincidence of lines in the XRD pattern, the existence of the lower carbides Cr_7C_3 and $Cr_{23}C_6$ in the coatings is difficult to confirm. When sprayed from a&s powders with a liquid-fueled HVOF system, Cr_3C_2 was the only carbide clearly detected (Thiele, Sempf, Berger, & Spatzier, 2011). For hotter processes, most probably, strongly adhering oxide scales are formed on the surfaces of the feedstock particles and are incorporated into the coating, as XRD studies show the presence of Cr_2O_3 in these coatings. An oxygen content of the coatings of up to 2.3% is reported (Zimmermann et al., 2003; Zimmermann et al., 2006).

1.17.6.3.4 TiC-Based Materials

The high phase stability of TiC-based compositions during spraying has been demonstrated several times (e.g. Berger et al., 2002; Vuoristo, Mäntylä, Berger, & Nebelung, 1998). The oxygen content in the coatings sprayed with a liquid-fueled HVOF process from a&s powders reached up to 7 wt% depending strongly on the spray parameter set, but only with traces of oxides appearing in the XRD patterns. At the same time, decrease of nitrogen and total carbon content was independent of the spray parameter set and amounted to about 1.5–2 wt% each (Berger, Zimmermann, Keller, Schwier, Scholl et al., 2003).

1.17.6.4 Substrate Materials and Preparation

Since the heat input into the substrate and its temperature during the spray process are low (in the range 100–200 °C, and in exceptional cases 500 °C and more (Mathesius & Krömmer, 2009)), nearly any type of material can be coated. The thermophysical properties of the substrate, in particular the heat conductivity, play a significant role for the coating formation and adhesion; the substrate size and the coefficient of thermal expansion (CTE) are also of importance. Metallic substrates, such as low-carbon steel, stainless steel, aluminum and copper, are dominating by far. The substrate temperature can be controlled by cooling (not only air jets but also CO_2 cooling) or additional heating.

There are a number of measures and procedures for substrate preparation (Mathesius & Krömmer, 2009), and most important are degreasing, masking (if necessary) and surface roughening. Degreasing by suitable liquids (alcohol, acetone) is the first step of substrate preparation. Due to mechanical anchoring as the main mechanism of bonding of the coatings to the substrate, surface roughness is a key issue. Recommended surface roughness for conventional processes is R_z of 30 μm or R_a of 4 μm (Mathesius & Krömmer, 2009) and is realized mainly by abrasive grit blasting. Choice of the materials for the grit depends on its costs and substrate characteristics and includes alumina, silicon carbide and others (Davis, 2004; Mathesius & Krömmer, 2009). Substrate hardness (e.g. hardened steels) can significantly influence the quality of surface preparation by grit blasting.

1.17.6.5 Engineering and Economic Parameters of the Spray Processes

1.17.6.5.1 Engineering Parameters

Coatings consist of a number of individual layers. One cycle across the substrate surface yields one complete layer (Davis, 2004); partially overlapping passes should result in the required thickness per layer. The thickness per layer is a compromise between technical and economical parameters, such as the required coating properties may result in limitations for the thickness per layer, while from the economic side a maximum thickness per layer with highest possible DE is advantageous. Thus spray parameters such as powder feedrate and the relative surface speed of the spray gun over the substrate have to be correctly adjusted for optimum result.

From the practical point of view, the long-term stability of the spray process is decisive for parameter selection. Coating properties, which can be reached using extreme spray parameters are sometimes applicable only for research purposes but might be not appropriate under industrial conditions (e.g. danger of the interruption of the spray process, e.g. by clogging).

1.17.6.5.2 Feedrates and DE

The feedrate and the DE are the most important economic parameters of the spray process and are selected with respect to the lowest possible coating time for the workpiece.

The density of the material strongly influences the feedrate. Typical feedrates for HVOF processes also depend on the fuel; with liquid-fueled guns higher powder feedrates can be realized. Thus for an industrial environment for WC–10Co–4Cr feedrates of 105 and 70 g/min and for Cr_3C_2–NiCr feedrates of 60 and 40 g/min are given for liquid- and gas-fueled processes, respectively (Schwetzke, Krömmer, & Heinrich, 2006).

Very often coatings are described to be deposited by optimized spray parameter sets. In a commercial environment this means often a maximum DE. The DE can be determined by EN ISO 17836. A desired combination of the maximum DE and optimum properties can often not be realized (Zimmermann & Keller, 2009). In scientific and research environment the optimum of a certain coating property is more often in the focus than the DE.

The DE not only is a function of the hardmetal composition, the feedstock powder characteristics including carbide grain size and feedrates, the spray process including the spray angle and the fuel but also is strongly influenced by the geometry and the size of the parts to be coated. Maximum DE is found at the spraying angle of 90° (Houdková et al., 2010). The DE for gas-fueled spray guns is higher (50–70%) than for liquid-fueled guns (35–50%) (Davis, 2004). The DE for gas-fueled systems was in the range of 54–61% for WC–10Co–4Cr

(Schwetzke et al., 2006) and 46–52% for Cr_3C_2–NiCr (Schwetzke et al., 2006). The DE for liquid-fueled processes for WC-based coatings is only slightly above 40% and for Cr_3C_2–NiCr, below 40% (Houdková et al., 2010; Schwetzke et al., 2006).

1.17.6.6 Posttreatments

Only a smaller part of the coatings is directly used as-sprayed. There are a number of posttreatment operations, such as mechanical, thermal and chemical/physical treatments (Davis, 2004; Mathesius & Krömmer, 2009). Posttreatments are compiled in the standard EN ISO 14924. The most important mechanical treatment is finishing like grinding and polishing in order to produce the required surface roughness. For this purpose an excess of coating thickness has to sprayed. There are attempts to minimize grinding and polishing operations, e.g. near-net shaping by using fine carbides in the feedstock powders. In order to prevent from pitting, crevice and interface corrosion also hardmetal coatings are often sealed (Gries & Zimmermann, 2012).

1.17.7 Coating Characterization Methods

1.17.7.1 General

The methods which are applied for thermal spray coating characterization are numerous (Davis, 2004; Pawlowski, 2008). These methods include standardized procedures, customized tests developed and applied in single companies or research laboratories, or highly sophisticated research methods, accessible only with special equipment. A general guidance for test and characterization methods is given in the standard EN ISO 14923. In some areas of industry, e.g. in the aircraft industry, there are additional special coating characterization methods (Davis, 2004). Most important methods related to hardmetal coatings are compiled below. The development of nondestructive test (NDT) methods is in progress but is complicated by the complex structure of thermal spray coatings (Davis, 2004).

Many coating properties are determined in the as-sprayed state only. Changes of properties occurring during service are most often unknown but can be significant in particular at elevated service temperatures. Investigation methods typical for bulk hardmetals, such as magnetic saturation and mean free path of the binder, are currently not or very seldom (e.g. Chivavibul et al., 2007), used for hardmetal coating characterization.

1.17.7.2 Thickness

A guidance of methods for measuring coating thickness is given in the standard EN ISO 2064. In the case of hardmetal coatings methods based on magnetic properties can cause discrepancies, due to the state of Co or Ni in the coating (metallic, alloyed, bonded in η-phases).

1.17.7.3 Adhesion

Adhesion is a property of major concern for thermal spray coatings (Davis, 2004). Coating adhesion is predominantly determined by tensile adhesion testing according to standards DIN EN 582 and ASTM C633-01. The basic steps of the testing procedure are applying an epoxy glue to the coating and to grippable bars, curing the resin at elevated temperature, pulling apart the assembly with a certain load to determine the adhesion strength, and investigating the location of failure (Davis, 2004). For coatings produced by HVOF the adhesion strength often exceeds the strength of the epoxy glues. Due to the large variance of test results, the method is controversially discussed, and was recently evaluated (Bobzin, Schläfer, & Aumund-Kopp, 2010).

Alternatively, coating adhesion can be determined by shear testing according EN 15340. Another alternative method is the interface fracture toughness using prenotched four-point bending tests (Watanabe, Owada, Kuroda, & Gotoh, 2006).

1.17.7.4 Internal Stresses

Although the exact knowledge of the internal stresses would be highly important, they are very difficult to measure. There is a detailed analysis (Clyne & Gill, 1996) and several short reviews (Bolelli, Lusvarghi, Varis, Turunen, Leoni, et al., 2008; Davis, 2004; Pawlowski, 2008) of the methods including modified layer removal, the XRD stress measurement method, substrate curvature (strip deflection) measurement, the hole drilling method. Hole drilling method is described by a standard (ASTM E837) and in the literature (e.g. Wenzelburger, López, & Gadow, 2006). The simplest method applied is substrate curvature measurements (e.g. Almen strip tests), but continuous measurement during deposition would be preferable (Clyne & Gill, 1996).

1.17.7.5 Metallographic Preparation

Metallographically prepared cross-sections have a high importance for investigation of the coating microstructure including the determination of porosity by optical microscopy, scanning electron microscopy (SEM) and, occasionally, transmission electron microscopy (TEM) (see also Pawlowski, 2008). They have an additional high importance because many investigation methods, such as hardness measurements, Young's modulus by indentation methods and indentation fracture toughness (IFT) determinations are also using the cross-sections.

There are recommended metallographic preparation procedures by ASTM E1920 and in the literature (e.g. Davis, 2004).

1.17.7.6 Coating Porosity and Density

Porosity is measured according to ASTM E2109 on metallographic cross-sections by direct comparison to standard images and image analysis methods. Thus the quality of the metallographic preparation directly influences the result. Both optical and scanning electron micrographs can be used. For methodical reasons, porosity measurements by nitrogen adsorption or mercury intrusion are not applicable to dense coatings.

Coating density is often determined by the Archimedean method; for this purpose the coating has to be separated from the substrate. It has to be taken into account that coating density is influenced not only by the porosity but also by the possible phase changes induced by the spray process, e.g. formation of W_2C.

1.17.7.7 Chemical and Phase Composition

XRD is the main tool for investigation of the phase composition of the coatings; changes in phase composition during spraying can be established as well when the diffraction pattern is compared with those of the feedstock powder. The interpretation of the diffraction pattern might be difficult, e.g. by existence of solid solutions, small differences in the pattern like η phases Co_3W_3C and Co_6W_6C, different chromium carbides, poor crystallization, and appearance of a high nanocrystalline or amorphous content, and is thus sometimes subjective. The existence of a phase cannot be confirmed from the existence of one peak, as often practiced in the literature. For determination of the real phase composition, a combination with independent methods may be necessary. Peak shifts can appear as result of internal stresses (e.g. Chivavibul et al., 2007).

The change in the nonmetal content in the spray process is often studied by chemical analysis of the total carbon content by the combustion, oxygen and, occasionally, nitrogen by the carrier gas hot extraction, using commercial analytic equipment (e.g. Berger et al., 1998; Zimmermann & Kreye, 1996; Zimmermann et al., 2003).

Other methods of chemical analysis often applied include the electron microprobe analysis and related methods as well as selected area diffraction, all connected with SEM or TEM. There are still other spectroscopic methods, such as infrared absorption spectroscopy, Raman spectroscopy, X-ray photoelectron spectroscopy and X-ray fluorescence spectroscopy (Pawlowski, 2008).

1.17.7.8 Mechanical Properties

From the early stage of hardmetal coating development (e.g. Poorman et al., 1952), hardness represents the most often used reference value to characterize a sprayed coating. The Young's modulus and the fracture toughness find increasing interest since the early 1990s (e.g. Brandt, 1995; Sahoo, 1993; Wayne & Sampath, 1992). There is an increasing tendency to link these mechanical properties with wear resistance of the coatings.

1.17.7.8.1 Hardness

Hardness is most often measured in the metallographically prepared coating cross-section according to the standards EN ISO 14923 and ASTM E384. Most often, Vickers hardness test is applied, the most common load being 2.94 N (300 g) (Davis, 2004). Sometimes Knoop and Berkovich indentations are given preference. Typical loads of <10 N describe the microhardness (Pawlowski, 2008). There is some controversial discussion on how much the microhardness value depends on the load (Davis, 2004; Pawlowski, 2008). In the case of hardmetal coatings, this depends in particular on the grain size of the hard phase (see Section 1.17.8.4.1).

Rockwell superficial hardness (HR15N) measured in accordance with EN ISO 6508-1 or ASTM E18 is sometimes also used (e.g. Houdková et al., 2011; Tillmann, Hussong, Erne, Möhwald, & Maier, 2013).

1.17.7.8.2 Young's Modulus

Methods for measurement of the Young's modulus include destructive tests (depth-sensing indentation, three- and four-point bending, tensile test, and cantilever beam method) and nondestructive (laser acoustic surface waves, nanoindentation and ultrasonic) tests (Buchmann, Escribano, Gadow, Bürkle, Mahlich & Fecht, 2002; Pawlowski, 2008). The test methods evaluate very different volumes of the coatings, thus the results might be differently influenced by coating defects, such as cracks and pores. For some of these test methods, e.g. tensile tests, the coatings have to be separated from the substrate and sample preparation is very laborious. WC–12Co coatings showed an anisotropic behavior for Young's modulus measurement by different methods (Lima, Kruger, Lamouche, & Marple, 2005).

The cantilever beam method was one of the first explored for Young's modulus and Poisson ratio evaluation (Rybicki, Shadley, Xiong, & Greving, 1995). In the past years, the depth-sensing indentation and laser acoustic surface waves were most widely used (Berger, Schneider, & Großer, 2007; Berger, Schneider, Barbosa, & Puschmann, 2012; Bescond, Kruger, Lévesque, Lima, & Marple, 2007; Buchmann et al., 2002). While depth-sensing indentation requires the preparation of coating cross-section, laser acoustic surface wave method relates to the nondestructive test methods.

1.17.7.8.3 Indentation Fracture Toughness

IFT is a standard characterization method for bulk hardmetals, where the crack propagation is measured for Vickers indents. Fracture toughness is proposed as an important parameter for the description of coating behavior in different types of wear attack such as erosion, cavitation and abrasion, but especially for new applications, e.g. contact loading (Ahmed & Hadfield, 2002; Lima, Godoy, Avelar-Batista, & Modenesi, 2003; Sahoo, 1993). Although the fracture toughness is increasingly determined, there is no standardized procedure. The application of high loads (HV5 or HV10) needed for crack formation requires a sufficient coating thickness. Many equations for calculation of IFT, based on the two basic types of crack propagation (Palmqvist and half-penny cracks) are given in the literature (Ponton & Rawlings, 1989).

1.17.7.9 Thermophysical and High-Temperature Properties

Methods of thermal analysis (thermogravimetry (TG), differential thermal analysis (DTA), differential scanning calorimetry (DSC), and dilatometry) are often applied, but special coating samples have to be prepared and have to be separated from the substrate (Thiele, Sempf, Jaenicke-Roessler, et al., 2011). Structural changes can also be investigated by methods such as mechanical spectroscopy (Mari, Berger, & Stahr, 2012). All these measurements have to performed in a nonreactive atmosphere.

Among thermophysical coating properties, the temperature-dependent heat conductivity λ is of special importance. This property cannot be measured directly; it has to be calculated according to Eqn (4)

$$\lambda(T) = a(T) * C_{\mathrm{p}}(T) * \rho(T) \tag{4}$$

where a is the thermal diffusivity, C_{p} is the specific heat capacity and ρ is the density, calculated from the CTE $\alpha(T)$ and the room temperature density $\rho_0(RT)$ (Thiele, Sempf, Jaenicke-Roessler, et al., 2011).

For determination of the temperature-dependent heat conductivity λ, three different thermophysical measurements are necessary: the CTE obtained by dilatometry, the specific heat capacity obtained by DSC and thermal diffusivity obtained by laser flash method (Thiele, Sempf, Jaenicke-Roessler, et al., 2011). For correct results, all measurements have to be performed twice (as-sprayed and after the first thermal cycle) in order to take into account the significant structural and compositional changes occurring during first heat treatment of the as-sprayed coating.

1.17.7.10 Oxidation

Oxidation can be studied by thermoanalytical methods, as described in Section 1.17.7.9, in streaming oxygen-containing atmospheres. When studying oxidation by TG it should be taken into account that the measurement of mass gain is not an equivalent for oxidation. This is due to overlapping effects of mass loss (carbon) and mass gain (oxygen). Both processes are overlapping; as long as carbon is lost, the total mass gain is low.

Coated specimen can be oxidized by exposure testing in furnaces. The early stages of oxide scale formation at the coating surface can easily be studied by XRD. It depends on the penetration depth of the X-rays and oxide scale growth, if information on oxide scale and coating microstructure are collected together. In addition to any special exposure test, specimen from other investigation methods, such as high-temperature tribology experiments, can be used to obtain information on coating oxidation. Thick oxide scales can be studied by microscopic method using coating cross-sections.

1.17.7.11 Corrosion

As coating service is very often connected with corrosive attack (also in combination with mechanical wear, e.g. ASTM G119), determination of the corrosion resistance is also a property of major concern. Corrosion resistance depends on the service conditions and is a system property. Corrosion of hardmetal coatings mostly occurs by contact with liquid or gaseous media at room or elevated temperature, but there are also special cases like corrosion against liquid metals or molten ashes.

Correspondingly, there is wide spectrum of corrosion test methods, which include several standard methods (Davis, 2004). The list of test methods given here is not complete. Common ones are electrochemical test methods in aqueous media, like polarization test according to ASTM G5 (e.g. Kirsten et al., 2005; Zimmermann et al., 2011). Salt spray tests according to DIN 50021 or ASTM B117 are also widely used (e.g. Schwetzke & Kreye, 1999; Zimmermann et al., 2011). Resistance in SO_2 atmosphere (Kesternich test) can be studied according to DIN 50018 (e.g. Schwetzke & Kreye, 1999).

Exposure testing is mostly customized to the different corrosive media, such as corrosive liquids (e.g. Gries & Zimmermann, 2012; Zimmermann et al., 2011).

1.17.7.12 Tribological Testing

Tribological properties are always system properties, i.e. the tribological behavior depends strongly on the counterparts and the environment. Since wear protection is the main application of hardmetal coatings there are numerous methods for investigation. They include both standardized and customized methods. The different test methods address the different wear mechanisms and failure modes (Holmberg & Matthews, 2009). However, real service conditions are often difficult to simulate in these tests. At the same time, some of these tribological test methods (dry abrasion wear tests and cavitation test) are often used for coating development and comparative purposes (e.g. Houdková et al., 2011; Kirsten et al., 2005; Schwetzke & Kreye, 1999; Vuoristo et al., 1998; Zimmermann et al., 2011).

1.17.7.12.1 Abrasion

Abrasion is most intensively studied, in particular by the dry sand rubber wheel test according to ASTM G65 (e.g. Houdková et al., 2011; Kirsten et al., 2005; Oechsle, 2006; Vuoristo et al., 1998; Zimmermann et al., 2011). Modifications from the standard relate most often to the abrasive material used in this test. Alternatively, ASTM D6037 or JIS H8615 (Suga abrasion test) is widely applied (Sato, Mizuno, Tawada, & Kitamura, 2008; Schwetzke & Kreye, 1999). The ASTM G75 wet slurry abrasion test reflects the simultaneous action of a liquid to the coating, including a corrosive attack (e.g. Houdková et al., 2011).

1.17.7.12.2 Erosion by Solids and Fluids

Procedure for air jet erosion testing is described in ASTM G76. Accordingly, erosion wear of the hardmetal coatings is studied with the help of centrifugal accelerator devices (e.g. Berger, Saaro, Naumann, Wiener, Weihnacht, Thiele, et al., 2008; Kleis & Kulu, 2008). Sand is most often applied as erodent, and impact angles between 15° and 90° are studied. However, the tests are often limited to one to two different angles. Most important parameters are the hardness, size and morphology of the erodent, its velocity and the temperature. For slurries pot-type erosion tests are applied (e.g. Hawthorne, Arsenault, Immarigeon, Legoux, & Parameswaran, 1999; Thakur, Arora, Jayaganthan, & Sood, 2011).

Erosion by fluid impact is normally classified into liquid droplet erosion and cavitation erosion (Shipway & Gupta, 2011). Water droplet erosion is only rarely studied (e.g. Shipway & Gupta, 2011).

A procedure modified from ASTM G32 can be used for coating characterization by cavitation erosion (e.g. Schwetzke & Kreye, 1996; Zimmermann et al., 2011).

1.17.7.12.3 Sliding

Since hardmetal coatings are often serving under these conditions, the coating is tested in a broad variety of tests for dry (including high temperature) and lubricated sliding. Sliding motion can be unidirectional, oscillating or reciprocating. There are several standards like ASTM G99 for pin-on-disk or ASTM G77 for block-on-ring testing. Testing can be performed against different counterpart materials, such as alumina or hardmetals, different sliding speeds or frequencies and loads. Self-mated testing of coatings can also be performed. Results of high-temperature sliding are strongly influenced by the formation of oxide scales, as well as by the lubricants in lubricated sliding. A systematic and comparative study of state-of-the-art hardmetal coatings in sliding wear conditions was recently performed (Berger, Woydt, et al., 2007; Berger, Woydt, & Saaro, 2009).

1.17.7.12.4 Constant Amplitude and Rolling Contact Fatigue

Axial force fatigue can be studied according to ASTM E466, other types of loads, e.g. rotary and plane bending, exist as well. Rolling contact fatigue (RCF) can be studied under dry conditions in a twin-disk tribometer (Martens, 2008) or in lubricated conditions. For the latter, a four-ball machine (Ahmed & Hadfield, 2002) or customized test benches, such as that developed by the company Zahnradfabrik Friedrichshafen (e.g. Berger, Lipp, Spatzier, & Bretschneider, 2011; Berger, Spatzier, Bretschneider, Lipp, & Thiele, 2009), can be used.

1.17.7.12.5 Impingement Resistance

The impingement resistance can be determined by free-fall experiments of steel balls (Deng, Liu, Zhou, & Song, 2007). Another method is cyclic steel ball drop impact (Bolelli et al., 2012).

1.17.8 Coating Microstructures and Properties

1.17.8.1 General

Thermal spray coatings are characterized by wide ranges of microstructures and properties for a particular nominal composition, e.g. WC–12%Co (see also Section 1.17.1). Thus, many studies reflect only a part of these property ranges, since a limited number of coatings with limited variations (feedstock powder spray process, spray parameters, and test conditions) are considered. Therefore data published in one particular reference can be significantly different from another.

In the scope of this contribution, only microstructures and properties of HVOF-sprayed coatings is discussed. Some differences with coatings sprayed by DGS (e.g. Murthy & Venkataraman, 2006; Vuoristo et al., 1994), and HVAF (Berger et al., 2013) exist; these differences were mostly studied with respect to tribological properties, e.g. wear resistance.

There are only relatively few studies comparing the microstructure and properties of bulk hardmetals and hardmetal coatings (e.g. Luyckx & Machio, 2006; Sato et al., 2008; Wayne & Sampath, 1992). Regarding the microstructure, there is a lower contiguity of the WC and wider grain size distribution in coatings than in bulk hardmetal, leading to lower hardness (Luyckx & Machio, 2006; Sato et al., 2008).

Due to the principle of formation coatings have anisotropic properties, although state-of-the-art spray processes have led to a reduction of anisotropy. The most known and visual impression is the lamellar microstructure appearing in micrographs of the cross-sections. Anisotropy is reflected by several coating properties, and is, e.g. discussed for coating hardness (e.g. Houdková et al., 2011); Young's modulus (e.g. Lima et al., 2005); and IFT (e.g. Chivavibul et al., 2007; Houdkova, Enzl, Zahalka, & Blahova, 2005).

In general, WC-based and Cr_3C_2–NiCr hardmetal coatings provide properties suitable for extreme requirements: WC-based coatings show the highest wear resistance, whereas Cr_3C_2–NiCr has advantages in high temperature and highly corrosive environments. In many stress profiles, TiC-based coatings are characterized by an intermediate position in properties (e.g. Houdková et al., 2011). They do not reach the wear performance of WC-based coatings, while under oxidative and corrosive stress, Cr_3C_2–NiCr coatings show better results.

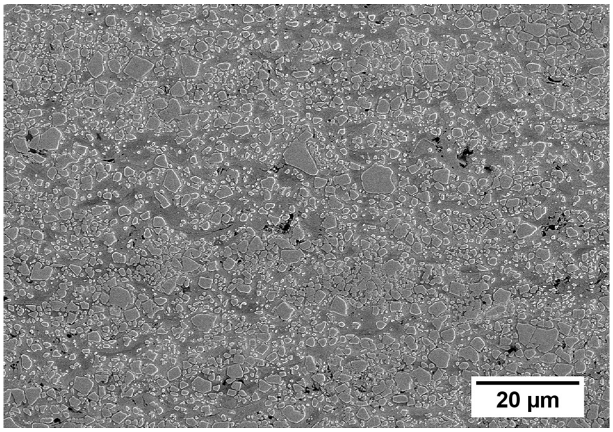

Figure 12 Microstructure of an HVOF-sprayed WC–17Co coating.

Coatings from nanostructured powders show a much less real gain in coating properties than expected, e.g. WC–Co coatings usually showed higher hardness but lower wear resistance than conventional coatings and thus a disappointing performance (Chivavibul et al., 2007). This can be appointed with the more intensive metallurgical reaction, associated with the finer WC grain size. Often coatings prepared from nanostructured powders are also not benchmarked against the most advanced conventional coatings, e.g. nanostructured Cr_3C_2–NiCr coatings against coatings prepared from blended powder and not from a&s powder (e.g. He & Schoenung, 2002).

1.17.8.2 Microstructures of As-sprayed Coatings

1.17.8.2.1 General

Here typical microstructures of the coatings sprayed by HVOF and of main commercial compositions are shortly presented by scanning electron micrographs of coating cross-sections. In the industrial environment the microstructure is still mainly studied by optical microscopy; however, phases appearing dark in these micrographs can be easily misinterpreted as porosity. The microstructures strongly depend on the properties of the feedstock and the spray conditions.

1.17.8.2.2 WC–Co and WC–CoCr

A low-magnification scanning electron micrograph of a high-quality WC–17Co coating (Berger et al., 2011) is shown in Figure 2. Figures 12 and 13 show high-magnification scanning electron micrographs of typical microstructures of WC–Co and WC–CoCr coatings.

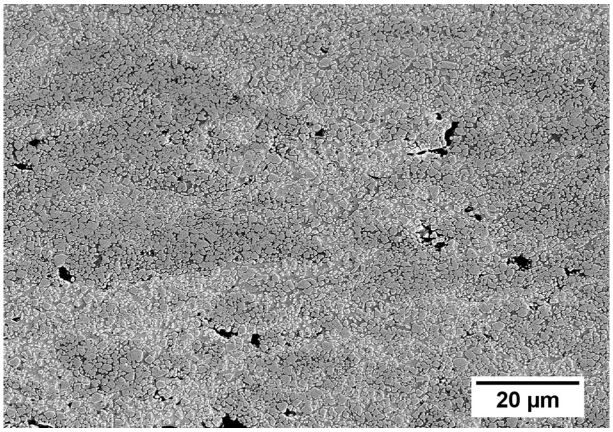

Figure 13 Microstructure of an HVOF-sprayed WC–10Co–4Cr coating.

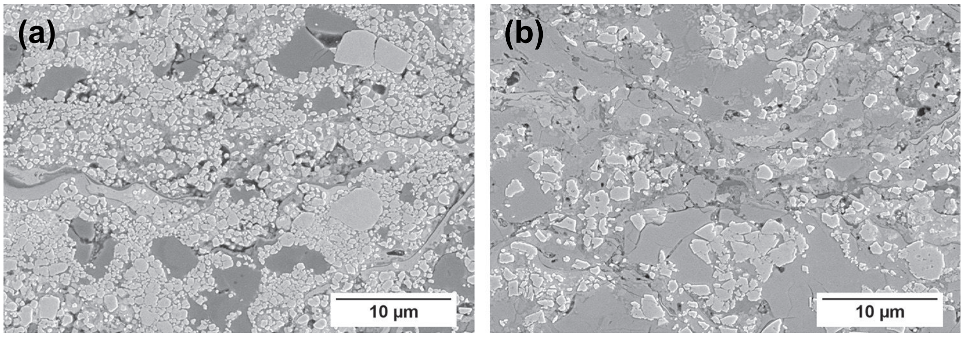

Figure 14 Large magnification SEM images of the cross-sections of WC–(W,Cr)$_2$C–Ni coatings sprayed by JP-5000 from (a) a&s powder (b) s&c powder (Berger, Saaro, Naumann, Kašparova, et al., 2008).

1.17.8.2.3 WC–(W,Cr)$_2$C–Ni

As demonstrated by the scanning electron micrographs presented in **Figure 14**, coatings of this composition show a more or less inhomogeneous distribution of the hard phases (Berger et al., 2010). Microstructural features of the coatings, such as WC and (W,Cr)$_2$C content and WC grain size distribution, depend strongly on the feedstock powder properties, mostly resulting from different sintering temperatures (Berger et al., 2010).

1.17.8.2.4 Cr$_3$C$_2$–NiCr

The microstructures of Cr$_3$C$_2$–NiCr coatings are influenced by the very broad variety of feedstock powder preparation technologies (e.g. Keller et al., 2000). For illustration, **Figure 15(a)** shows an optical micrograph of a Cr$_3$C$_2$–NiCr coating. **Figure 15(b)** shows typical microstructural feature of Cr$_3$C$_2$–NiCr coatings sprayed from an a&s powder (Berger, 2007). Many Cr$_3$C$_2$ grains have a poor bonding to the surrounding matrix; microcracks appear along the carbide grain boundaries and also in some carbide grains.

1.17.8.2.5 TiC-Based Materials

Unlike WC-based compositions and Cr$_3$C$_2$–NiCr, TiC-based compositions made from a&s feedstock powders with core-rim structured hard phases can be processed to coatings of acceptable quality also by APS (Berger, Nebelung, Vuoristo, Heinonen, Mäntylä, et al., 1999; Berger et al., 2002). For illustration, an APS-sprayed (Ti,Mo)(C,N)–35.6Ni coating is shown in **Figure 16(a)**. **Figure 16(b)** shows details of an HVOF-sprayed (Ti,Mo)(C,N)–29Co coating, prepared with a liquid-fueled spray system.

1.17.8.3 Internal Stresses

Still with the early gas-fueled HVOF processes (see Section 1.17.2) coatings with tensile stresses were produced (e.g. Stewart et al., 1998). Later, liquid-fueled HVOF processes allowed the deposition of hardmetal coatings with compressive stresses (Davis, 2004). Also in coatings sprayed with improved gas-fueled HVOF and plasma

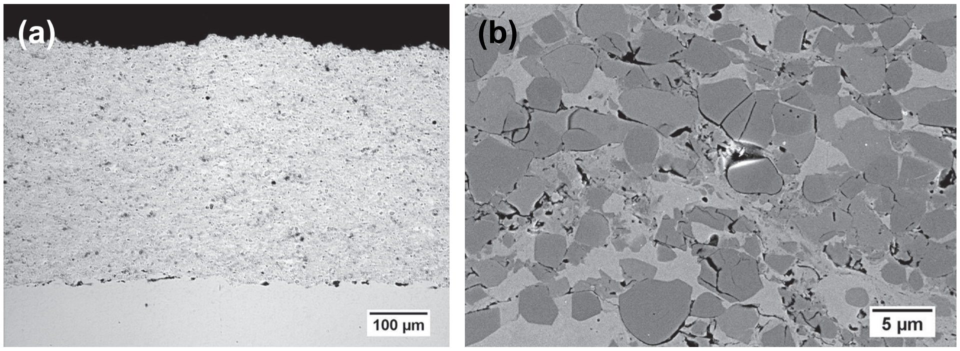

Figure 15 (a) Optical micrograph of a Cr$_3$C$_2$–NiCr coating sprayed with a liquid-fueled HVOF system from an a&s powder. (b) High-resolution scanning electron micrograph showing a typical microstructure of a Cr$_3$C$_2$–NiCr coating.

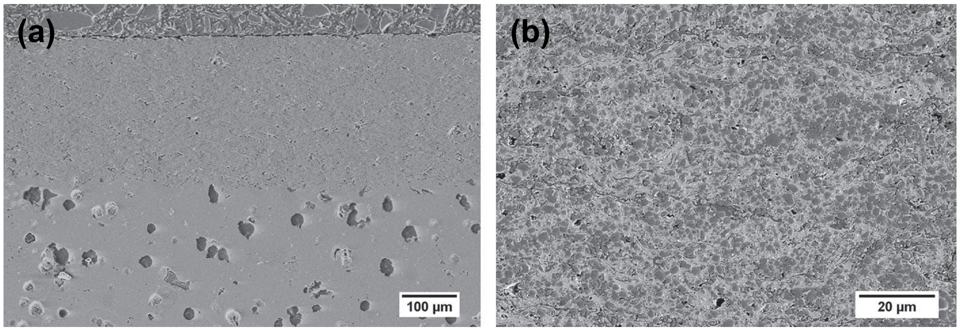

Figure 16 Scanning electron micrographs of (a) TiC-based coatings sprayed from a&s powders by APS (Ti,Mo)(C,N)–35.6Ni coating deposited on cast iron piston ring (Berger et al., 1999) and (b) detail of HVOF-sprayed (Ti,Mo)(C,N)–29Co coating.

spray processes, compressive stresses are found (Barth et al., 2011). Different residual stress conditions exist through the coating thickness (e.g. Brandt, 1995; McGrann, Shadley, Rybicki, Bodger, Emery, et al., 1998). A heat treatment in inert atmosphere changes the stresses in the coating, but is influenced by the mismatch of the CTE of the coating and the substrate (Stewart et al., 1998).

1.17.8.4 Mechanical Properties

1.17.8.4.1 Hardness

While for sintered bulk hardmetals their hardness can be described as a function of binder content and carbide grain size, the hardness of coatings results from significantly more parameters (Chivavibul et al., 2007). In addition to binder content and carbide grain size, it can be described as the balance of coating microstructure, phase composition, porosity, peening effect, hardening of the binder phase, etc. In general, coating hardness depends much more on the properties of the binder (Chivavibul et al., 2007).

Figures 17(a) and 17(b) show scanning electron micrographs of indents made with loads of 2.94 and 0.5 N, respectively, for a WC–12.5Co–1.5Cr coating (experimental composition). They demonstrate that for a coating microstructure with fine carbides values of hardness measurements (963 HV0.3 and 936 HV0.05) are similar (Berger, Schneider, et al., 2007). The standard deviation for the load of 0.5 N was higher.

Typical hardness values for the main commercial compositions given in comparative studies are compiled in **Table 2**.

A study aimed at prevention of experimental errors, including influence of porosity, and statistical analysis of Vickers and Rockwell superficial hardness indents have shown that the latter shows a better reliability and reproducibility (Tillmann et al., 2013).

High hardness is very often associated with a high wear resistance, but it has been shown that such a direct connection does not exist (e.g. Keller et al., 2000; Vuoristo et al., 1994). For hardmetal coatings there is an optimum hardness. Up to a certain degree increasing hardness values are a measure for increasing coating

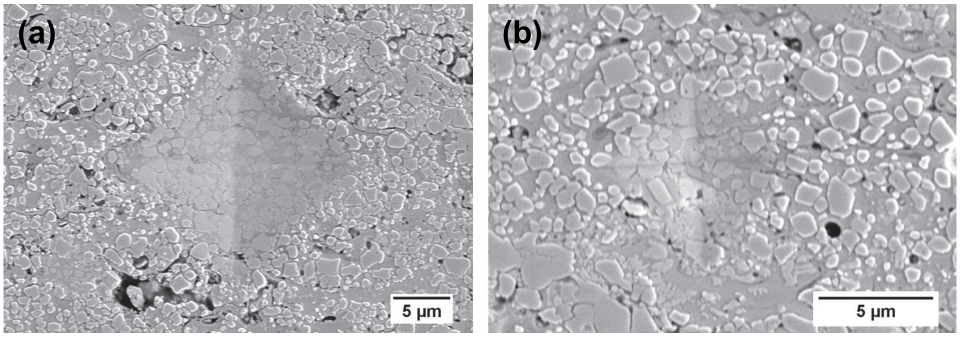

Figure 17 Scanning electron micrographs of Vickers microhardness indents in coating cross-sections of a WC–12.5Co–1.5Cr coating (experimental composition) (Berger, Schneider, et al., 2007) for (a) load 2.94 N and (b) load 0.5 N.

Table 2 Typical hardness values HV0.3 for the main commercial compositions taken from Oechsle (2006) and Zimmermann et al. (2006)

Composition	*Reference (Oechsle, 2006)*	*Reference (Zimmermann et al., 2006)*
WC–12Co	1250	1376
WC–17Co	1200	1358
WC–10Co–4Cr	1350	1274
WC–(W,Cr)$_2$C–7Ni	1300	1242
Cr$_3$C$_2$–25NiCr	1150	1080

integrity; this means absence of defects, such as pores. Hardness values above the optimum can indicate decarburization and formation of other hard phases.

1.17.8.4.2 Young's Modulus

Comparative studies using depth-sensing indentation and laser acoustic surface waves have shown good agreement of the results for different hardmetal coatings (Berger, Schneider, et al., 2007; Berger et al., 2012). However, larger differences can appear in the case of coating defects, such as cracks and pores, which influence the laser acoustic surface wave method due to the higher coating volume used for the acquisition of the value.

As a rule of thumb, it is stated that the Young's modulus of thermally sprayed coatings is about one-third that of the corresponding bulk material (Ahmed, 2002). HVOF-sprayed coatings based on WC show values of more than 200 GPa (Berger et al., 2012). For a WC–12Co coating, a value of 194 ± 39 GPa obtained by Knoop indentation method is reported (Lima et al., 2003). The value for a Cr$_3$C$_2$–25NiCr coating is only 137 GPa, as determined by the laser acoustic surface wave method. WC-based coatings sprayed by HVAF show significantly higher values (>300 GPa) (Berger et al., 2012).

1.17.8.4.3 Indentation Fracture Toughness

Figure 18(a) shows the optical micrograph of a Vickers indent (HV5) in a WC–17Co coating. Due to coating anisotropy, crack propagation occurs in parallel to the coating surface. **Figure 18(b)** shows a typical crack propagation through the binder regions.

The crack regime (Palmqvist or half-penny) was found to depend on the indentation load, while heat treatment can significantly improve the IFT (Lima et al., 2003). When equations independent of the Palmqvist and half-penny model of crack propagation were applied for a number of coatings, it was found that the ranking of the IFT of the coatings was independent of the equation applied (Houdkova et al., 2005). Thus, the absolute values in the literature are very uncertain, since they are given usually without consideration of the applicability of the calculation model (e.g. verification of crack propagation, ratio of the crack length to the size of the indent). For WC–Co coatings, values from 3 to 5 MPa m$^{1/2}$ are reported, while the values of bulk WC–Co are in the range of 9–20 MPa m$^{1/2}$ (Chivavibul et al., 2007).

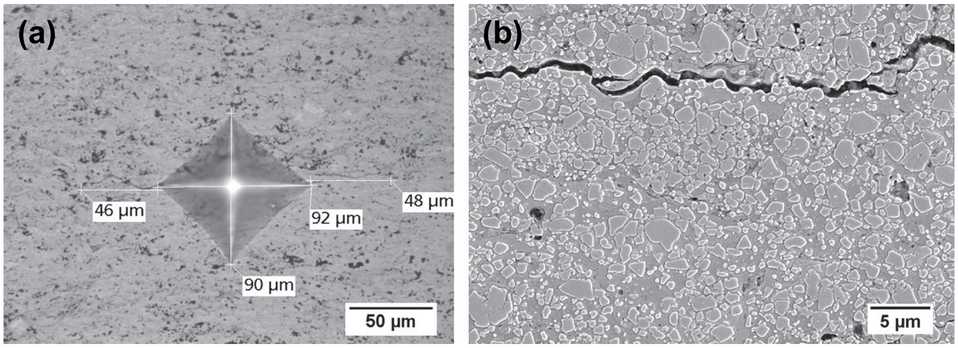

Figure 18 (a) Optical micrograph of a Vickers indent (load 49 N) in a WC–17Co coating with indication of the lengths of the cracks. (b) Propagation of a crack (load 98 N) in a WC–10Co–4Cr coating (scanning electron micrograph).

1.17.8.5 Heat Conductivity

For a WC–17Co coating, prepared by a liquid-fueled HVOF process from an a&s feedstock powder, heat conductivities ranging from 29.2 W/(mK) at 50 °C to 35.4 W/(mK) at 700 °C were determined (Thiele, Sempf, Jaenicke-Roessler, et al., 2011). In comparison, the heat conductivity of a WC–15Co hardmetal is reported to be 60 W/(mK) (Kolaska & Weith, 1995).

The heat conductivities for HVOF-sprayed Cr_3C_2–NiCr coatings prepared from two different a&s feedstock powders are corresponding at 11.2 and 13.4 W/(mK) at 50 °C and at 18.9 and 20.1 W/(mK) at 700 °C. A difference between the two coatings was clearly detectable but decreased with temperature (Thiele, Sempf, Berger & Spatzier, 2011). The heat conductivity of the coatings is comparable to that of a bulk Cr_3C_2–12% NiCr hardmetal (14 W/(mK)) (Kolaska & Weith, 1995).

1.17.8.6 Effect of Thermal Treatments and Oxidation

Thermal treatments are also considered as posttreatment processes (see Section 1.17.6.6). As a rule, as-sprayed coatings are in an extreme nonequilibrium state, therefore any action of heat leads to changes in the microstructure, possibly, phase composition, and properties. In inert atmosphere, these changes lead slowly from the nonequilibrium state toward the equilibrium state; in oxygen-containing atmospheres, these changes overlap with the oxidation processes. Oxidation processes can include diffusion of oxygen into the coating (e.g. Matthews, Hyland, James, & Levi, 2002) but main result is the formation of oxide scales at the coating surface. Some oxide scales, such as Cr_2O_3, can protect the coating from further oxidation; in this case microstructural changes toward the equilibrium state will occur inside the coating simultaneously. In general, the influence of the HVOF spray process on the oxidation resistance of the coatings is relatively small (Berger et al., 2005). First oxides can be detected at the coating surfaces of all commercial compositions at 350 °C for longer exposure times (128 h) (Berger et al., 2005).

Thermal treatments of WC–Co coatings in inert atmosphere or vacuum above 600 °C shift the phase composition toward the equilibrium state. The W_2C, amorphous phase and metallic W are disappearing and the formation of η-phases is observed (e.g. Li et al., 1996b; Lima et al., 2003; Nerz, Kushner, & Rotolico, 1992; Schwetzke & Kreye, 1999; Stewart et al., 1998).

Coatings of standard compositions WC–Co and WC–10Co–4Cr are characterized by a low oxidation resistance and rapid oxide scale growth. In oxygen-containing atmosphere, oxidation occurs much faster then microstructural changes can be observed. As observed for WC–12Co coatings in air, the temperature (350–500 °C) of formation of the first oxide, WO_3, depends on the time of exposure (2–128 h) (Berger et al., 2005). The only other oxide observed ($CoWO_4$) is assumed to be formed as a result of a secondary reaction of WO_3. Thick porous oxide scales (with thicknesses reaching at least 50 μm) are observed for WC–Co coatings in the temperature range 600–700 °C for 2 h; see **Figure 19(a)**. These experiments are in agreement with other oxidation experiments on WC–Co coatings (Nolan, Mercer, & Samandi, 1998), feedstock powders (Berger et al., 1998) and bulk hardmetals (Basu & Sarin, 1996; Voitovich, Sverdel, Voitovich, & Golovko, 1996) and confirm that for WC–Co the oxidation mechanisms in the spray process (see Section 1.17.6.3.1) and in air are totally different.

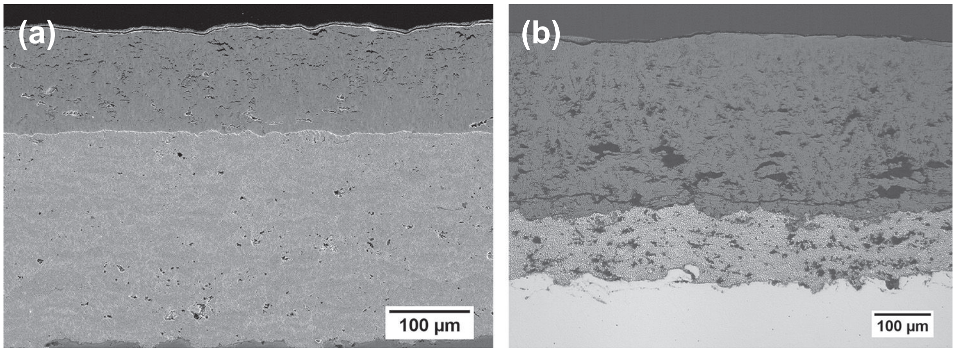

Figure 19 (a) Scanning electron micrograph of a WC–17Co coating after oxidation at 700 °C for 2 h (Berger et al., 2005). (b) Optical micrograph of the WC–10Co–4Cr coating (thickness of the remaining hardmetal coating about 120 μm) with oxide scale, taken from a specimen after tribological testing at 800 °C (total oxidation time about 90 min) in the area of the wear track (Berger, Woydt, et al., 2007).

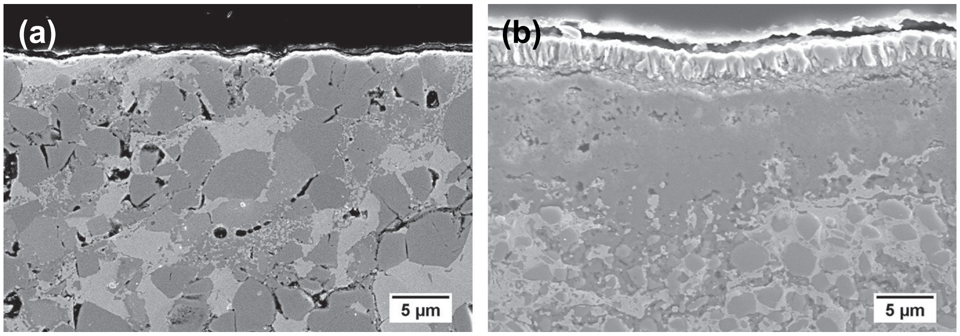

Figure 20 (a) Scanning electron micrograph of the surface region of a Cr_3C_2–NiCr coating after a dry sliding wear test outside the wear track at 800 °C (duration about 90 min) (Berger, Woydt, Zimmermann, Keller, Schwier, et al., 2004). (b) Oxide scale at the surface of a (Ti,Mo)(C,N)–Ni coating outside the wear track after a dry sliding wear test at 800 °C (duration about 16 h) (Berger, Woydt, et al., 2007).

As shown in **Figure 19(b)**, the oxidation resistance of WC–10Co–4Cr coatings differs only insignificantly from those of WC–Co coatings (Berger et al., 2005) and has been shown to be much less than previously assumed (Berger et al., 1998). Due to increase of the volume by oxidation, the total coating thickness (original coating + oxide scale) is higher than the thickness of the as-sprayed coating.

High chromium-containing compositions (WC–$(W,Cr)_2C$–Ni and Cr_3C_2–NiCr) show a high oxidation resistance due to protective oxide scale formation. In particular, the composition WC–$(W,Cr)_2C$–Ni shows an oxidation resistance close to that of Cr_3C_2–NiCr and much higher than that of WC–Co and WC–10Co4–Cr coatings (Berger et al., 2005; Berger, Woydt, et al., 2007).

Even after high-temperature oxidation at 800 °C, the thickness of the Cr_2O_3 oxide scale at the surface of a Cr_3C_2–NiCr coating is very low, to the extent that it is difficult to study in coating cross-sections (**Figure 20(a)**). Inside the coatings, as a result of the high temperature, reprecipitation of fine carbide particles appear in the binder matrix (Berger, Woydt, Zimmermann, Keller, Schwier, et al., 2004; Matthews, Hyland, & James, 2003).

The oxidation resistance of (Ti,Mo)(C,N)-based coatings in air is much higher than that of WC-based coatings (except WC–$(W,Cr)_2$–Ni), but lower than that of Cr_3C_2–NiCr. **Figure 20(b)** shows the oxide scale at the surface of a (Ti,Mo)(C,N)–29Ni coating after oxidation at 800 °C (oxidation time about 16 h) (Berger, Woydt, et al., 2007). This oxide scale, with a thickness of 12–15 µm, consists of three subscales: the outer of NiO, the middle of $NiMoO_4$, and the inner of $NiMoO_4$ and TiO_2 (rutile). When Co is used as the binder, the oxidation resistance is lower than with Ni and the corresponding oxides of Co are formed (Co_3O_4 and $CoMoO_4$) (Berger, Woydt, et al., 2007).

1.17.8.7 Corrosion

Corrosion resistance can be defined as the ability to protect the substrate from corrosion. In this case coating microstructure, in particular the appearance of open porosity and cracks, can be more important than the coating composition.

The corrosion resistance of the hardmetal coatings depends on the binder properties, since carbides are highly resistant to acidic and alkaline solutions. Many factors are influencing the state of the binder, mostly the feedstock powder, spray process and cooling rate. For example, an η-phase-containing coating withstands corrosive attack better than pure WC–Co. Thus higher flame temperatures will lead to denser coatings and metallurgical processes supporting a high corrosion resistance. Due to these facts, it is also not surprising that contradictory results and interpretations exist in the literature for nearly all commercial compositions. Ventilation during testing or in service is also an important influencing factor on the corrosion resistance (Gries & Zimmermann, 2012).

Cr_3C_2–NiCr coatings which are often considered as corrosion resistant show low corrosion resistance in acids (Gries & Zimmermann, 2012).

1.17.8.8 Tribology

In many cases tribological investigations are limited to specific coating properties, e.g. carbide grain size, type of binder metal, or certain system properties (abrasive particle size, impact angle, etc.) and a comparison with a benchmark (e.g. hard chromium coatings). Other studies compare different spray processes or coating compositions, but include only a phenomenological interpretation of tribological test results and the wear mechanisms. Many studies are not dealing with detailed microstructural investigations of the coatings and coating preparation conditions (feedstock powder, spray process and parameters, etc.) are not completely described. Since the scatter of properties of nominally analogous compositions is large (see Section 1.17.1) this can lead to contradictory rankings.

1.17.8.8.1 Abrasion

There are many comparative studies regarding the dry abrasion wear resistance according to ASTM G65 (e.g. Houdková et al., 2011; Kirsten et al., 2005; Oechsle, 2006; Vuoristo et al., 1994, 1998; Zimmermann et al., 2011). The abrasion wear resistance of WC-based hardmetal coatings and bulk hardmetals is comparable (Sato et al., 2008; Stewart et al., 1998). A heat treatment (even at 250 °C) increases the abrasion wear resistance (Stewart et al., 1998).

The properties of coatings prepared from plain TiC–Ni (or TiC–Co) systems can be significantly improved by alloyed, core–rim structured TiC–Ni(Co) feedstock powders. The abrasion wear resistance of DGS-sprayed coatings, was significantly improved compared with simple binary TiC–Ni coatings (Berger et al., 2002; Vuoristo et al., 1998). A (Ti,Mo)(C,N)–NiCo coating showed an intermediate abrasion wear resistance between superior WC-based coatings and the Cr_3C_2–NiCr coating (Houdková et al., 2011).

1.17.8.8.2 Erosion

In many studies of the dry erosion wear resistance the number of impact angles is limited to two or three. A study of HVOF-sprayed with plain and chromium-alloyed WC–Co and WC–Ni coatings with impact angles between 15° and 90° (steps of 15°) showed that a maximum in wear at 45° and a more or less pronounced increase at 90° were observed (Berger, Saaro, Naumann, et al., 2008). While a maximum erosive wear at about 45° is typical for hardmetals, the increase of the erosive wear at 90° is typical for brittle materials. The wear resistance was improved when cobalt was used as binder metal, while a dependence on the chromium content was not found. Besides the microstructure, the coatings were characterized by porosity, hardness and Young’s modulus; however, these properties alone are insufficient to interpret the wear resistance of these compositions (Berger, Saaro, Naumann, et al., 2008). The ratio of wear for impact angles of 45° and 90° were confirmed for WC-based coatings, while Cr_3C_2–NiCr and TiC-based coatings showed a much higher mass loss at 90° (Houdková et al., 2011).

The dry erosion resistance of WC–12Co coatings was significantly lower than those of bulk hardmetals (Sato et al., 2008). At low impact angles many hardmetal coatings showed a better wear resistance than low-carbon steel, while at 45° and higher steel is superior.

1.17.8.8.3 Sliding

For application of hardmetal coatings in sliding conditions it is important to consider that not only the wear resistance of the coating but the total wear rate of the coating and the counterpart together is decisive.

In a systematic study of unidirectional sliding wear of hardmetal coatings against sintered alumina with sliding speeds in the range 0.1–3 m/s, a total volumetric wear coefficient below 10^{-6} mm^3/Nm for a number of test conditions was found (Berger, Woydt, et al., 2007). This value characterizes the borderline between dry friction and mixed/boundary lubrication and characterizes the ability of coatings to serve in dry conditions. While WC–Co and WC–CoCr are limited in service for the temperature range below 600 °C (see Section 1.17.7.10) (Ti,Mo)(C,N)-based coating can serve up to 700 °C. For (Ti,Mo)(C,N)-based coatings coefficients of friction were found at about 0.2 for room temperature. Testing of different hardmetal coatings for dry unidirectional sliding at room temperature in an equipment of different construction resulted in comparable values for the total volumetric wear coefficient and the coefficient of friction (Houdková et al., 2011).

Preoxidation of hardmetal coatings did not result in an improvement in the performance (Berger, Woydt, et al., 2007). For self-mated pairs higher total volumetric wear coefficients were found, but in some cases the values were still below 10^{-6} mm^3 Nm^{-1} (Berger, Woydt, et al., 2007, 2009).

The (Ti,Mo)(C,N)-based coatings show functional benefits in high-temperature dry sliding wear resistance. However, really existing functional benefits of these materials are different from the meaning “lubricious oxide” (Berger, Stahr, Saaro, Thiele, Woydt & Kelling, 2009) as originally emphasized by Gardos, (1988).

Under lubricated conditions a hard chromium coating showed a lower total volumetric wear coefficient than for the hardmetal coatings (Berger, Woydt, et al., 2007).

1.17.8.8.4 Cavitation

Cavitation testing can be considered as a useful tool to characterize the cohesive strength between individual splats in the coating (Schwetzke & Kreye, 1996). A strong influence of the spray process was found due to the differences of particle velocity. Best coatings can reach a cavitation erosion resistance as bulk AISI 321 and 316 L steel (Schwetzke & Kreye, 1996).

1.17.8.8.5 Fatigue

Use of the coatings as functional elements in fatigue applications was formerly precluded due to inadequate coating properties, connected with the experience of sudden coating failure. With the introduction of HVOF spraying a process for preparation of high-quality hardmetal coatings became available, enabling the development of coating solutions for structural components (Berger, 2007; Berger, Spatzier, et al., 2009; Berger et al., 2011).

A cantilever bending test has shown that hardmetal coatings increase the number of cycles to failure compared to the substrate (McGrann et al., 1998).

In a comparative study of RCF, the best results were obtained for HVOF-sprayed WC–17%Co coatings (Nieminen, Vuoristo, Niemi, Mäntylä & Barbezat, 1997). A systematic damage and failure analysis for WC–12% Co and WC–15%Co showed a significantly improved coating performance through the use of a liquid-fueled HVOF spray process (Ahmed, 2002; Ahmed & Hadfield, 2002). There are four distinct modes of damage and failure in RCF: abrasion (micropitting), delamination, bulk failure and spalling (Ahmed & Hadfield, 2002). Delamination forms sheetlike debris with dimensions of a few millimeters and can occur for WC–Co coatings at the coating–substrate interface (adhesive) as well as within the coating material (cohesive). Spalling differs from delamination failure in terms of the area-to-depth ratio and is localized within the wear track (Ahmed, 2002).

The durability of coated specimen was compared with uncoated case-hardened 16MnCr5 specimen, representing an industrial standard solution, in a RCF test with 5×10^7 cycles (Berger, Spatzier, et al., 2009; Berger et al., 2011). When using unhardened 16MnCr5 steel as substrate all specimens with 600 µm coating thickness showed a higher durability than the industrial standard solution (Berger, Spatzier, et al., 2009). For WC–17Co coatings it was demonstrated that the highest durability was reached with a quenched and tempered 16MnCr5 substrate, having a higher hardness (Berger et al., 2011). A minimal amount of micropits were formed at the surface of a WC–17Co coating (**Figure 21(a)**) (Berger, Spatzier, et al., 2009). Large cracks which in a later stage lead to coating delamination (see **Figure 21(b)**) were found.

1.17.9 Applications

Wear protection in a spectrum of applications in different branches of industry is the main use of hardmetal coatings. Examples for current applications are given in textbooks (Davis, 2004; Pawlowski, 2008) and papers (e.g. Vuoristo, 2007). Ongoing progress in technology and materials creates continuously new applications, e.g. under contact fatigue use by general improvement of microstructure and properties (Ahmed & Hadfield, 2002;

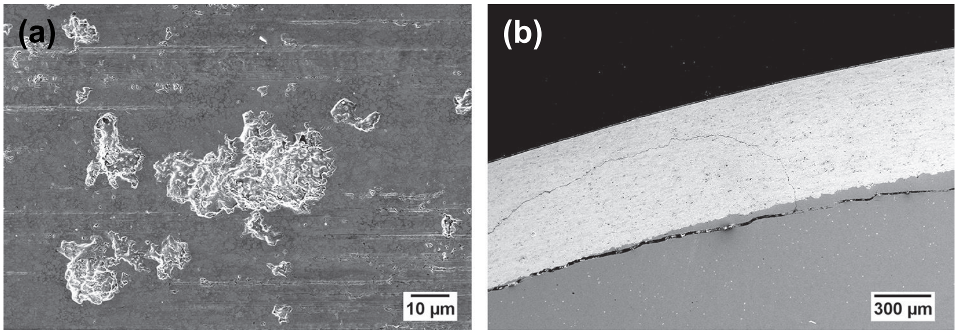

Figure 21 Scanning electron micrographs of (a) micropittings at the surface of a WC–17Co coating (Berger, Spatzier, et al., 2009) and (b) cracks in coating, at the substrate–coating interface of a WC–17Co coating in the contact area after RCF testing (Berger et al., 2011).

Berger, Spatzier, et al., 2009) or combination with thin-film coatings, such as diamond-like carbon (DLC) (Bolelli, Lusvarghi, Montecchi, Pighetti Mantini, Pitacco, et al., 2008). In part, thermally sprayed hardmetal coatings compete with other surface technologies, e.g. coating solutions directed to hard chromium replacement (Bolelli, 2009; Sartwell & Bretz, 1999).

References

Ahmed, R. (2002). Contact fatigue failure modes of HVOF coatings. *Wear, 253*(3–4), 473–487.

Ahmed, R., & Hadfield, M. (2002). Mechanisms of fatigue failure in thermal spray coatings. *Journal of Thermal Spray Technology, 11*(3), 333–349.

Babad-Zakhryapin, A. A., Gert, L. M., & Valyavko, L. R. (1968). Possibility of forming tungsten oxycarbide with a fcc lattice. *Izvestiya Akademii Nauk SSSR, Neorganicheskie Materialy, 4*(8), 1366–1367.

Barth, A., Chen, D., & Dambra, C. (2011). Influences of process and material morphology on the case of carbide coatings. *Thermal Spray Bulletin, 4*(2), 102–105.

Basu, S. N., & Sarin, V. K. (1996). Oxidation behavior of WC–Co. *Materials Science and Engineering, A209*, 206–212.

Beczkowiak, J., Keller, H., & Schwier, G. (1996). Pulverförmige Zusatzwerkstoffe für das thermische Spritzen. *Schweissen Schneiden, 48*, 132–136.

Berger, L.-M. (2005). Hard but slippery – titanium hardmetal coatings have industrial potential. *Metal Powder Report, 60*(5), 28, 29, 31.

Berger, L.-M. (2007). Hardmetals as thermal spray coatings. *Powder Metallurgy, 50*(3), 205–214.

Berger, L.-M. (2011). Thermisch gespritzte Hartmetallschichten – ein Überblick. In F. Franek, & A. Pauschitz (Eds.), *Tribologie in Industrie und Forschung: Werkstoff- und Energieeffizienz – Herausforderung und Lösungsansätze, Symposium 2011 der Österreichischen Tribologischen Gesellschaft, 24 November 2011, Wiener Neustadt, Austria* (pp. 27–38). Wien: Österreichische Tribologische Gesellschaft.

Berger, L.-M., Ettmayer, P., Vuoristo, P., Mäntylä, T., & Kunert, W. (2001). Microstructure and properties of WC–10%Co–4% Cr spray powders and coatings: part 1. Powder characterization. *Journal of Thermal Spray Technology, 10*(2), 311–325.

Berger, L.-M., Hermel, W., Vuoristo, P., Mäntylä, T., Lengauer, W., & Ettmayer, P. (1996). Structure, properties and potentials of WC–Co, Cr_3C_2–NiCr and TiC–Ni-based hardmetal-like coatings. In C. C. Berndt (Ed.), *Thermal spray: Practical solutions for engineering problems, Proc. 9th National Thermal-Spray-Conf., 7–11 October 1996, Cincinnati, Ohio, USA* (pp. 89–96). Materials Park/OH: ASM International.

Berger, L.-M., Lipp, K., Spatzier, J., & Bretschneider, J. (2011). Dependence of the rolling contact fatigue of HVOF-sprayed WC–17%Co hardmetal coatings on substrate hardness. *Wear, 271*(9–10), 2080–2088.

Berger, L.-M., Nebelung, M., Vuoristo, P., Heinonen, M., Mäntylä, T., Reinhardt, T., et al. (1999). Development and application of TiC–Ni based plasma sprayed coatings. In E. Lugscheider, & P. A. Kammer (Eds.), *United Thermal Spray Conf., Conf. Proc., 17–19 March 1999, Düsseldorf, Germany* (pp. 128–133). Düsseldorf: DVS-Verlag.

Berger, L.-M., Puschmann, R., Spatzier, J., & Matthews, S. (2013). Potential of HVAF spray processes. *Thermal Spray Bulletin, 6*(1), 16–20.

Berger, L.-M., Saaro, S., Naumann, T., Kašparova, M., & Zahálka, F. (2008). Microstructure and properties of HVOF-sprayed WC–$(W,Cr)_2C$–Ni coatings. *Journal of Thermal Spray Technology, 17*(3), 395–403.

Berger, L.-M., Saaro, S., Naumann, T., Kašparova, M., & Zahálka, F. (2010). Influence of feedstock powder characteristics and spray processes on microstructure and properties of WC–$(W,Cr)_2C$–Ni hardmetal coatings. *Surface and Coatings Technology, 205*(4), 1080–1087.

Berger, L.-M., Saaro, S., Naumann, T., Wiener, M., Weihnacht, V., Thiele, S., et al. (2008). Microstructure and properties of HVOF-sprayed chromium alloyed WC–Co and WC–Ni coatings. *Surface and Coatings Technology, 202*(18), 4417–4421.

Berger, L.-M., Schneider, D., Barbosa, M., & Puschmann, R. (2012). Laser acoustic surface waves for the non-destructive characterisation of thermally sprayed coatings. *Thermal Spray Bulletin, 5*(1), 56–64.

Berger, L.-M., Schneider, D., & Großer, T. (2007). Non-destructive testing of coatings by surface acoustic waves, Global Coating Solutions. In B. R. Marple, M. M. Hyland, Y.-C. Lau, C.-J. Li, R. S. Lima, & G. Montavon (Eds.), *Proc. 2007 Int. Thermal Spray Conf., May 14–17, 2007, Beijing, People's Republic of China* (pp. 916–921). Materials Park/OH: ASM International.

Berger, L.-M., Spatzier, J., Bretschneider, J., Lipp, K., & Thiele, S. (2009). Rolling contact fatigue of HVOF-sprayed hardmetal coatings on unhardened substrates. *Thermal Spray Bulletin, 2*(2), 133–140.

Berger, L.-M., Stahr, C. C., Saaro, S., Thiele, S., Woydt, M., & Kelling, N. (2009). Dry sliding up to 7.5 m/s and 800 °C of thermally sprayed coatings of the TiO_2–Cr_2O_3 system and (Ti, Mo)(C, N)–Ni(Co). *Wear, 267*(5–8), 954–964.

Berger, L.-M., Thiele, S., Vuoristo, P., Mäntylä, T., Keller, H., Proß, E., et al. (2002). Titanium carbide-based powders and coatings – compositions, processability and properties. In E. Lugscheider (Ed.), *Proc. Int. Thermal Spray Conf., 4–6 March 2002, Essen, Germany* (pp. 727–732). Düsseldorf: DVS-Verlag.

Berger, L.-M., Vuoristo, P., Mäntylä, T., & Gruner, W. (1998). A study of oxidation behaviour of WC–Co, Cr_3C_2–NiCr and TiC–Ni–based materials. In C. Coddet (Ed.), *Thermal spray: Meeting the challenges of the 21st century, Proc. 15th Int. Thermal Spray Conf., 25–29 May 1998, Nice, France* (pp. 75–82). Materials Park/OH: ASM International.

Berger, L.-M., Woydt, M., & Saaro, S. (2007). Reib-/Gleitverschleiß von thermisch gespritzten Hartmetallschichten. In R. Suchentrunk (Ed.), *Jahrbuch Oberflächentechnik* (Vol. 63; pp. 242–267). Bad Saulgau: Eugen G. Leuze Verlag.

Berger, L.-M., Woydt, M., & Saaro, S. (2009). Comparison of self-mated hardmetal coatings under dry sliding conditions up to 600 °C. *Wear, 266*(3–4), 406–416.

Berger, L.-M., Woydt, M., Zimmermann, S., Keller, H., Schwier, G., Enžl, R., et al. (2004). Tribological behavior of HVOF-sprayed Cr_3C_2–NiCr and TiC-based coatings under high-temperature dry sliding conditions. In *Proc. Int. Thermal Spray Conf. ITSC 2004, 10–12 May 2004, Osaka, Japan*. Düsseldorf: DVS-Verlag, 10 p.

Berger, L.-M., Zieris, R., & Saaro, S. (2005). Oxidation of HVOF-sprayed hardmetal coatings. *Proc. Int. Thermal Spray Conf. ITSC 2005, 2–4 May 2005, Basel, Switzerland*. Düsseldorf: DVS-Verlag, 8 p.

Berger, L.-M., Zimmermann, S., Keller, H., Schwier, G., Scholl, R., Thiele, S., et al. (2003). Microstructure and properties of HVOF-sprayed TiC-based coatings. In B. R. Marple, & C. Moreau (Eds.), *Thermal spray 2003: Advancing the science and applying the technology, Proc. 2003 Int. Thermal Spray Conf., 5–8 May 2003, Orlando, Florida, USA* (pp. 793–799). Materials Park/OH: ASM International.

Berns, H. (Ed.), (1998). *Hartlegierungen und Hartverbundwerkstoffe: Gefüge, Eigenschaften, Bearbeitung, Anwendung.* Berlin etc: Springer.

Bescond, C., Kruger, S. E., Lévesque, D., Lima, R. S., & Marple, B. R. (2007). In-situ simultaneous measurement of thickness, elastic moduli and density of thermal sprayed WC–Co coatings by laser-ultrasonics. *Journal of Thermal Spray Technology, 16*(2), 238–244.

Bobzin, K., Schläfer, T., & Aumund-Kopp, C. (2010). Investigation and assessment of the error variables in the adhesive tensile strength test according to DIN EN 582. *Thermal Spray Bulletin, 3*(1), 30–35.

Bolelli, G. (2009). Replacement of hard chromium plating by thermal spraying – problems, solutions and possible future approaches. *Surface Engineering, 25*(4), 263–269.

Bolelli, G., Börner, T., Bozza, F., Cannillo, V., Cirillo, G., & Lusvarghi, L. (2012). Cermet coatings with Fe-based matrix as alternative to WC–CoCr: mechanical and tribological behaviours. *Surface and Coatings Technology, 203*(5–7), 699–703.

Bolelli, G., Lusvarghi, L., Montecchi, M., Pighetti Mantini, F., Pitacco, F., Volz, H., et al. (2008). HVOF-sprayed WC–Co as hard interlayer for DLC films. *Surface and Coatings Technology, 203*(5–7), 699–703.

Bolelli, G., Lusvarghi, L., Varis, T., Turunen, E., Leoni, M., Scardi, P., et al. (2008). Residual stresses in HVOF-sprayed ceramic Coatings. *Surface and Coatings Technology, 202*(19), 4810–4819.

Brandt, O. C. (1995). Mechanical properties of HVOF coatings. *Journal of Thermal Spray Technology, 4*(2), 147–152.

Brieseck, M., Bohn, M., & Lengauer, W. (2010). Diffusion and solubility of Cr in WC. *Journal of Alloys and Compounds, 489*(2), 408–414.

Browning, J. A. (1981). Highly concentrated supersonic liquified material flame spray method and apparatus, US 4,416,421, filed: 28 July 1981, granted 22 November 1983 (also EP 49 915).

Brunet, C., & Dallaire, S. (1987). The importance of particle size distribution on the plasma spraying of TiC. *Surface and Coatings Technology, 31*(1), 1–10.

Buchmann, M., Escribano, M., Gadow, R., Bürkle, G., Mahlich, M., & Fecht, H. J. (2002). On the elastic mechanical properties of thermally sprayed coatings. In E. Lugscheider (Ed.), *Proc. Int. Thermal Spray Conf., 4–6 March 2002, Essen, Germany* (pp. 598–605). Düsseldorf: DVS-Verlag.

Chivavibul, P., Watanabe, M., Kuroda, S., & Shinoda, K. (2007). Effects of carbide size and Co content on the microstructure and mechanical properties of HVOF-sprayed WC–Co coatings. *Surface and Coatings Technology, 202*(3), 509–521.

Chivavibul, P., Watanabe, M., Kuroda, S., Kawakita, J., Komatsu, M., Sato, K., et al. (2011). Effects on particle strength of feedstock powders on properties of warm-sprayed WC–Co coatings. *Journal of Thermal Spray Technology, 20*(5), 1098–1109.

Clyne, T. W., & Gill, S. C. (1996). Residual stress in thermal spray coatings and their effect on interfacial adhesion: a review of recent work. *Journal of Thermal Spray Technology, 5*(4), 401–418.

Davis, J. R. (Ed.), (2004). *Handbook of thermal spray technology.* Materials Park/OH: ASM International.

de Villiers Lovelock, H. L. (1998). Powder/processing/structure relationship in WC–Co thermal spray coatings: a review of the published literature. *Journal of Thermal Spray Technology, 7*(3), 357–373.

Deng, C., Liu, M., Zhou, K., & Song, J. (2007). Impingement resistance of HVAF WC-based coatings. *Journal of Thermal Spray Technology, 16*(5–6), 604–609.

Eigen, N., Gärtner, F., Klassen, T., Aust, E., Bormann, R., & Kreye, H. (2005). Microstructures and properties of nanostructured thermal sprayed coatings using high-energy milled cermet powders. *Surface and Coatings Technology, 195*(2–3), 344–357.

Eremenko, V. N., Velikanova, T. Ya., & Bondar, A. A. (1986). The phase diagram of the Cr–W–C system at high temperatures. *Doklady Akademii Nauk Ukrainskoi SSR, Seriya A, Fiziko-Matematichni ta Tekhnichni Nauki, 11*, 74–78.

Eremenko, V. N., Velikanova, T. Ya., & Bondar, A. A. (1987). The phase diagram of the Cr–Mo–C system. I. Phase equilibria in the area of crystallization of alloys of the Mo–Mo_2C–Cr_7C_3–C partial system. *Poroshkovaya Metallurgiya* (5), 70–76; *Soviet Powder Metallurgy Metal Ceramics*, *26*(5), 409–414.

Eschnauer, H. (1980). Hard material powders and hard alloy powders for plasma surface coating. *Thin Solid Films, 73*(1), 1–17.

Eschnauer, H. R., & Knotek, O. (1977). Complex carbide powders for plasma spraying. *Thin Solid Films, 45*(2), 287–294.

Eschnauer, H., & Lugscheider, E. (1991). Fortschritte beim Thermischen Spritzen. *Metall, 45*(5), 458–466.

Ettmayer, P., & Lengauer, W. (1989). The story of cermets. *Powder Metallurgy International, 21*(2), 37–38.

Ettmayer, P., & Lengauer, W. (1994). *Encyclopedia of inorganic chemistry* (Vol. 2). Chichester, etc.: John Wiley & Sons, 519–531.

Gabel, H. (2004). Kinetic metallization compared with HVOF. *Advanced Materials and Processes, 162*(5), 47–48.

Gardos, M. N. (1988). The effect of anion vacancies on the tribological properties of Rutile (TiO_{2-x}). *Tribology Transactions, 31*(4), 427–436.

Gärtner, F., Kreye, H., & Richter, H. J. (2006). HVOF spraying with powder and wire. In *Proc. 7th Kolloquium Hochgeschwindigkeitsflammspritzen, 9–10.11.2006,* Erding, Germany (pp. 39–56). Unterschleißheim: Gemeinschaft Thermisches Spritzen.

Gladyshevskii, E. I., Telegus, V. S., Fedorov, T. F., & Kuz'ma, Yu. B. (1967). Tungsten–chromium–carbon ternary system. *Izvestiya Akademii Nauk SSSR, Metally, 1*, 190–193.

Gries, B., & Zimmermann, S. (2012). Corrosion behaviour of HVOF sprayed carbide coatings. In *Proc. 9th HVOF Kolloquium, 8–9 November, 2012,* Erding, Germany (pp. 71–78). Unterschleißheim: Gemeinschaft Thermisches Spritzen e.V.

Guilemany, J. M., de Paco, J. M., Nutting, J., & Miguel, J. R. (1999). Characterization of the W_2C phase formed during the high velocity oxygen fuel spraying of a WC + 12%Co. *Metallurgical and Materials Transactions, 30A*, 1913–1921.

Hackett, C. M., & Settles, G. S. (1995). Research on HVOF gas shrouding for coating oxidation control. In C. C. Berndt, & S. Sampath (Eds.), *Advances in thermal spray science and technology, Proc. 8th National Thermal Spray Conf., 11–15 September 1995, Houston, Texas* (pp. 21–29). Materials Park/OH: ASM International.

Hawthorne, H. M., Arsenault, B., Immarigeon, J. P., Legoux, J. G., & Parameswaran, V. R. (1999). Comparison of slurry and dry erosion behaviour of some HVOF thermal sprayed coatings. *Wear, 225–229*, 825–834.

He, J., & Schoenung, J. M. (2002). Nanostructured coatings. *Materials Science and Engineering A, 336*(1–2), 274–319.

Hinnüber, J., & Rüdiger, O. (1953). Hartmetall-Legierungen hoher Korrosions- und Oxydationsbeständigkeit. *Archiv für das Eisenhüttenwesen, 24*(5–6), 267–274.

Holleck, H. (1984). *Binäre und ternäre Carbid- und Nitridsysteme der Übergangsmetalle.* Berlin and Stuttgart: Gebrueder Borntraeger.

Holmberg, K., & Matthews, A. (2009). *Coatings tribology. Properties, mechanisms, techniques and applications in surface engineering* (2nd ed.) Amsterdam, etc.: Elsevier.

Hou, G. L., Zhou, H. D., An, Y.-L., Liu, G., Chen, J.-M., & Chen, J. (2011). Microstructure and high-temperature friction and wear behavior of WC–$(W,Cr)_2C$–Ni coating prepared by high velocity oxy-fuel spraying. *Surface and Coatings Technology, 206*(1), 82–94.

Houck, D. L., & Cheney, R. F. (1984). Comparison of properties of Cr_3C_2–Ni–Cr coatings thermally sprayed from pre-alloyed and mechanically mixed powders. *Thin Solid Films, 118*(4), 507–513.

Houdkova, S., Enzl, R., Zahalka, F., & Blahova, O. (2005). The indentation tests for evaluation of HVOF coatings mechanical properties. In *Proc. Int. Thermal Spray Conf. ITSC 2005, 2–4 May 2005, Basel, Switzerland* (pp. 1521–1525). Düsseldorf: DVS-Verlag.

Houdková, Š., Kašparová, M., & Zahálka, F. (2010). The influence of spraying angle on properties of HVOF-sprayed hardmetal coatings. *Journal of Thermal Spray Technology, 19*(5), 893–901.

Houdková, Š., Zahálka, F., Kašparová, M., & Berger, L.-M. (2011). Comparative study of thermally sprayed coatings under different types of wear conditions for hard chromium replacement. *Tribology Letters, 43*(2), 139–154.

Ishikawa, Y., Kawakita, J., Osawa, S., Itsukaichi, T., Sakamoto, Y., Takaya, M., et al. (2005). Evaluation of corrosion and wear resistance of hard cermet coatings sprayed by using an improved HVOF process. *Journal of Thermal Spray Technology, 14*(3), 384–390.

Ishikawa, Y., Kuroda, S., Kawakita, J., Sakamoto, Y., & Takaya, M. (2007). Sliding wear properties of HVOF sprayed WC–20%Cr_3C_2–7%Ni cermet coatings. *Surface and Coatings Technology, 201*(8), 4718–4727.

Jarosinski, W. J. C., Temples, L. B., & Londry, C. H. (1996). A method for producing a chromium carbide–nickel chromium atomized powder, US 5,863,618, filed: 3 Oct 1996, granted 26 Jan 1999 (also EP 834,585 B1).

Jones, M., Horlock, A. J., Shipway, P. H., McCartney, D. G., & Wood, J. V. (2001). A comparison of the abrasive wear behaviour of HVOF sprayed titanium carbide- and titanium boride-based cermet coatings. *Wear, 251*(1–12), 1009–1016.

Kanerva, U., Lagerbom, J., & Vuoristo, P. (2007). Development of thermal spray powders for improved tribological and corrosive applications and cost-effective solutions. *International Journal of Materials and Product Technology, 18*(3/4), 377–398.

Keller, H., Pross, E., & Schwier, G. (2000). *Influence of the powder type on the structure and the properties of chromium carbide/nickel chromium coatings.* Offprint. H.C.Starck GmbH & Co. KG. p. 8.

Kieffer, R., & Benesovsky, F. (1963). *Hartstoffe*. Wien: Springer-Verlag.

Kieffer, R., & Benesovsky, F. (1965). *Hartmetalle*. Wien, New York: Springer-Verlag.

Kim, H.-J., Lee, C.-H., & Hwang, S.-Y. (2005). Fabrication of WC–Co coatings by cold spray deposition. *Surface and Coatings Technology, 191*(2–3), 335–340.

Kirner, K. (1989). Zur Metallurgie der Wolframcarbide beim thermischen Spritzen. *Schweissen und Schneiden, 41*(11), 583–586.

Kirsten, A., Oechsle, M., & Moll, R. F. (2005). Carbide containing materials for hard chromium replacement by HVOF-spraying. In *Proc. Int. Thermal Spray Conf. ITSC 2005, 2–4 May 2005, Basel, Switzerland.* Düsseldorf: DVS-Verlag, 6 p.

Kleis, I., & Kulu, P. (2008). *Solid particle erosion: Occurrence, prediction und control.* London: Springer.

Kolaska, H., & Weith, W. (1995). Hartmetalle als Werkstoffe für Konstruktionsbauteile. *Metall, 49*(2), 104–111.

Korpiola, K. (2004). High temperature oxidation of metal, alloy and cermet powders in HVOF spraying process, Dissertation, Helsinki University of Technology.

Krainer, E., & Robitsch, J. (1967a). Röntgenografischer Nachweis des kubischen Wolframkarbides in funkenerosiv bearbeiteten Hartmetallen und in reinen Wolframschmelzkarbiden. *Planseeberichte für Pulvermetallurgie, 15*(1), 46–56.

Krainer, E., & Robitsch, J. (1967b). Zur Frage des kubischen Wolframkarbids. *Planseeberichte für Pulvermetallurgie, 15*(1), 179.

Kreye, H., Gärtner, F., & Richter, H. J. (2003). High velocity oxy-fuel flame spraying – state of the art, new developments and alternatives. In *Proc. 6th Kolloquium Hochgeschwindigkeitsflammspritzen, 27–28 November 2003, Erding, Germany* (pp. 5–17). Unterschleißheim: Gemeinschaft Thermisches Spritzen.

Krömmer, W., Heinrich, P., & Kreye, H. (2009). High velocity oxy-fuel flame spraying: past – present – future. In *Proc. 8th Kolloquium Hochgeschwindigkeitsflammspritzen, 5–6 November 2003, Erding, Germany* (pp. 9–16). Unterschleißheim: Gemeinschaft Thermisches Spritzen.

Kurlov, A. S., & Gusev, A. I. (2006). Tungsten carbides and W–C phase diagram. *Neorganicheskie Materialy, 42*(2), 156–163 (also *Inorganic Materials*, *42*(2), 121–127).

Kuroda, S., Watanabe, M., Kim, K. H., & Katanoda, H. (2011). Current status and future prospects of warm spray technology. *Journal of Thermal Spray Technology, 20*(4), 653–676.

Lassner, E., & Schubert, W.-D. (1999). *Tungsten: Properties, chemistry, technology of the element, alloys, and chemical compounds.* New York, etc.: Kluwer Academic/Plenum Publishers.

Laul, K., Dorfman, M. R., & Somoskey, R. E., Jr. (1998). Powder of chromium carbide and nickel chromium, US 6,071,324, filed: 28 May 1998, granted 6 June 2000 (also EP 960,954 B1).

Li, C.-J., Ji, G.-C., Wang, Y.-Y., & Sonoya, K. (2002). Dominant effect of carbide rebounding on the carbon loss during high velocity oxy-fuel spraying of Cr_3C_2–NiCr. *Thin Solid Films, 419*(1–2), 137–143.

Li, C.-J., Ohmori, A., & Harada, Y. (1996a). Effect of powder structure on the structure of thermally sprayed WC–Co coatings. *Journal of Materials Science, 31*(3), 785–794.

Li, C.-J., Ohmori, A., & Harada, Y. (1996b). Formation of an amorphous phase in thermally sprayed WC–Co. *Journal of Thermal Spray Technology, 5*(1), 69–73.

Li, C. J., Yang, G. J., Gao, P. H., Ma, J., Wang, Y. Y., & Li, C. X. (2007). Characterisation of nanostructured WC–Co deposited by cold spraying. *Journal of Thermal Spray Technology, 16*(5–6), 1011–1020.

Lima, M. M., Godoy, C., Avelar-Batista, J. C., & Modenesi, P. J. (2003). Toughness evaluation of HVOF WC–Co coatings using non-linear regression analysis. *Materials Science and Engineering A, 357*(1–2), 337–345.

Lima, R. S., Kruger, S. E., Lamouche, G., & Marple, B. R. (2005). Elastic modulus measurements via laser-ultrasonic and Knoop indentation techniques in thermally sprayed coatings. *Journal of Thermal Spray Technology, 14*(1), 52–60.

Luyckx, S., & Machio, C. N. (2006). WC–VC–Co as bulk hardmetal and coatings. In *Proc. Euro PM2006, 23–25 October, 2006, Ghent, Belgium* (Vol. 1; pp. 311–316). Shrewsbury: EPMA.

Mäntylä, T. A., Niemi, K. J., Vuoristo, P. M. J., Barbezat, G., & Nicoll, A. R. (1991). Abrasion wear resistance of tungsten carbide coatings prepared by various thermal spray techniques. In S. Blum-Sandmeier, H. Eschnauer, P. Huber, & A. R. Nicoll (Eds.), *Proc. 2nd Plasma-Technik Symposium, June 5–7, 1991, Lucerne, Switzerland* (Vol. 1; pp. 287–297). Wohlen: Plasma-Technik AG.

Mari, D., Berger, L.-M., & Stahr, S. (2012). Analysis of microstructural changes with temperature of thermally sprayed WC-Co coatings by mechanical spectroscopy. In R. Schaller, & D. Mari (Eds.), *Internal Friction and Mechanical Spectroscopy, 16th Int. Conf. on Internal Friction and Mechanical Spectroscopy (ICIFMS-16), July 3–8, 2011, Lausanne, Switzerland, Solid State Phenomena* (Vol. 184; pp. 313–318). Switzerland: Lausanne.

Martens, S. (2008). Ölfreie Industriegetriebe: Maßnahmen und Möglichkeiten zur Minimierung bzw. Eliminierung herkömmlicher Schmierstoffe, Dissertation, Technische Universität Dresden.

Massalski, T. B. (Ed.), (1990). *Binary alloy phase diagrams* (2nd ed.) (Vol. 1). ASM International.

Mathesius, S., & Krömmer, W. (2009). *Praxis des thermischen Spritzens: Anleitung für das Fachpersonal*. Düsseldorf: DVS-Media.

Matthäus, G., & Stevens, G. (2003). New HVOF equipment and technology for the use of superfine powders -10 μm and internal coating applications. In *Conf. proc. 6. Kolloquium Hochgeschwindigkeitsflammspritzen, 27–28 November 2003, Erding, Germany* (pp. 167–176). Unterschleißheim: Gemeinschaft Thermisches Spritzen.

Matthews, S., Hyland, M., & James, B. (2003). Microhardness variation in relation to carbide development in heat treated Cr_3C_2–NiCr thermal spray coatings. *Acta Materialia, 51*(14), 4267–4277.

Matthews, S., Hyland, M., James, B., & Levi, T. (2002). Isothermal oxidation of Cr_3C_2–NiCr coatings sprayed by high velocity techniques. In E. Lugscheider (Ed.), *Proc. Int. Thermal Spray Conf., 4–6 March 2002, Essen, Germany* (pp. 698–704). Düsseldorf: DVS-Verlag.

Matthews, S., James, B., & Hyland, M. (2010). The effect of heat treatment of the oxidation mechanism of blended powder Cr_3C_2–NiCr coatings. *Journal of Thermal Spray Technology, 19*(1–2), 119–127.

Matz, M.-M., & Kennedy, M. (2011). New concepts for thermally coated piston rings in modern two-stroke internal combustion engines. *Thermal Spray Bulletin, 4*(1), 20–24.

Mayr, W., Lengauer, W., Ettmayer, D., Rafaja, D., Bauer, J., & Bohn, M. (1999). Phase equilibria and multiphase reaction diffusion in the Cr–C and Cr–N Systems. *Journal of Phase Equilibria, 20*(1), 35–44.

McGrann, R. T. R., Shadley, J. R., Rybicki, E. F., Bodger, B. E., Emery, W. A., Somerville, D. A., et al. (1998). Evaluation of residual stress and fatigue life of tungsten carbide thermal spray coated aircraft landing gear materials. In C. Coddet (Ed.), *Thermal spray: Meeting the challenges of the 21st century, Proc. 15th Int. Thermal Spray Conf., 25–29 May 1998, Nice, France* (pp. 557–562). Materials Park/OH: ASM International.

Mizuno, H., & Kitamura, J. (2007). MoB/CoCr cermet coatings by HVOF spraying against erosion by molten Al–Zn alloy. *Journal of Thermal Spray Technology, 16*(3), 404–413.

Murthy, J. K. N., & Venkataraman, B. (2006). Abrasive wear behaviour of WC–CoCr and Cr_3C_2–20(NiCr) deposited by HVOF and detonation spray processes. *Surface and Coatings Technology, 200*(8), 2642–2652.

Nerz, J., Kushner, B., & Rotolico, A. (1992). Microstructural evaluation of tungsten carbide–cobalt coatings. *Journal of Thermal Spray Technology, 1*(2), 147–152.

Neumann, G., Kieffer, R., & Ettmayer, P. (1972). The TiC–TiN–TiO system. *Monatshefte für Chemie, 103*(4), 1130–1137.

Nieminen, R., Vuoristo, P., Niemi, K., Mäntylä, T., & Barbezat, G. (1997). Rolling contact fatigue failure mechanisms in plasma and HVOF sprayed WC–Co coatings. *Wear, 212*(1), 66–77.

Nolan, D., Mercer, P., & Samandi, M. (1998). Microstructural stability of thermal sprayed WC–Co composite coatings in oxidising atmospheres at 450 °C. *Surface Engineering, 14*(2), 124–128.

Oechsle, M. (2006). Carbide containing spray powders and HVOF-coatings. In *Proc. 7. HVOF-Kolloquium 2006, 9–10 November 2006, Erding, Germany* (pp. 57–62). Unterschleißheim: Gemeinschaft Thermisches Spritzen e.V.

Pawlowski, L. (2008). *The science and engineering of thermal spray coatings* (2nd ed.) Chichester: John Wiley & Sons.

Pelton, J. F., & Koffskey, J. M., Jr. (1958). Process of flame spraying a tungsten carbide–chromium carbide–nickel coating, and article produced thereby, US 3,071,489, filed: 28 May 1958, granted 1 Jan 1963 (also GB 874,463).

Pelton, J. F., & Koffskey, J. M., Jr. (1960). Coating composition, method of application, and product thereof, US 3,150,938, filed: 9 June 1960, granted 29 September 1964 (also GB 929,205).

Perry, H. W. (1952). Flame plating. *Metal Industry, 81*, 421–422.

Ponton, C. B., & Rawlings, R. D. (1989). Vickers indentation fracture toughness test. Part 1. Review of literature and formulation of standardised indentation toughness equations. *Materials Science and Technology, 5*(9), 865–872.

Poorman, R. M., Sargent, H. B., & Lamprey, H. (1952). Method and apparatus utilizing detonation waves for spraying and other purposes, US Patent 2,714,563, filed: 7 March 1952, granted: 2 August 1955.

Ramnath, V., & Jayaraman, N. (1989). Characterisation and wear performance of plasma sprayed WC–Co coatings. *Materials Science and Technology, 5*(4), 382–388.

Rybicki, E. F., Shadley, J. R., Xiong, Y., & Greving, J. (1995). A cantilever beam method for evaluating Young's modulus and Poisson's ratio of thermal spray coatings. *Journal of Thermal Spray Technology, 4*(4), 377–383.

Sahoo, P. (1993). High-performance wear coatings – the quest continues. *Powder Metallurgy International, 25*(2), 73–78.

Sartwell, B. D., & Bretz, P. E. (1999). HVOF thermal spray coatings replace hard chrome. *Advanced Materials and Processes, 156*(2), 25–28.

Sato, K., Mizuno, H., Tawada, S., & Kitamura, J. (2008). Comparative study on the mechanical properties of WC/Co between HVOF coatings and hard Materials. *Tribology Online, 3*(2), 137–142.

Schedler, W. (1988). *Hartmetall für den Praktiker*. Düsseldorf: VDI-Verlag (Plansee TIZIT GmbH).

Schoop, M. U. (1942). Über die Herstellung von Überzügen aus Wolfram, bzw. Wolfram-Karbid mittels der "Schoop-Pistole". *Korrosion and Metallschutz, 18*(7), 243–244.

Schwetzke, R., & Kreye, H. (1996). Cavitation erosion of HVOF coatings. In C. C. Berndt (Ed.), *Thermal spray: Practical solutions for engineering problems, Proc. 9th National Thermal Spray Conf., 7–11 October 1996, Cincinnati, Ohio, USA* (pp. 153–158). Materials Park/OH: ASM International.

Schwetzke, R., & Kreye, H. (1999). Microstructure and properties of tungsten carbide coatings sprayed with various high-velocity oxygen fuel spray systems. *Journal of Thermal Spray Technology, 8*(3), 433–439.

Schwetzke, R., Krömmer, W., & Heinrich, P. (2006). Economic considerations with respect to HVOF spraying. In *Proc. 7th Kolloquium Hochgeschwindigkeitsflammspritzen, 9–10 November 2006, Erding, Germany* (pp. 63–70). Unterschleißheim: Gemeinschaft Thermisches Spritzen.

Shipway, P. H., & Gupta, K. (2011). The potential of WC–Co hardmetals and HVOF sprayed coatings to combat water-droplet erosion. *Wear, 271*(9–10), 1418–1425.

Smith, R. W., & Mutasim, Z. Z. (1992). Reactive plasma spraying of wear-resistant coatings. *Journal of Thermal Spray Technology, 1*(1), 57–63.

Sobolev, V. V., Guilemany, J. M., & Nutting, J. (2004). *High velocity oxy-fuel spraying: Theory, structure-property relationships and applications*. Leeds: Maney.

Stecher, P., Benesovsky, F., & Nowotny, H. (1964). Untersuchungen im System Chrom–Wolfram–Kohlenstoff. *Planseeberichte für Pulvermetallurgie, 12*, 89–95.

Stenberg, T. H., Niemi, K. J., Vuoristo, P. M. J., Vuorinen, J. E., Mäntylä, T. A., & Tiainen, T. J. (1995). Effect of powder manufacturing method, particle size and binder content on the properties of TiC–Ni composite coatings. In A. Ohmori (Ed.), *Thermal spraying current status and future trends, Proc. 14th Int. Thermal Spray Conf., 22–26 May 1995, Kobe, Japan* (Vol. 2; pp. 1145–1150). Osaka: High Temperature Society of Japan.

Stewart, D. A., Shipway, P. H., & McCartney, D. G. (1998). Influence of heat treatment on the abrasive wear behaviour of HVOF sprayed WC–Co coatings. *Surface and Coatings Technology, 105*(1–2), 13–24.

Stewart, D. A., Shipway, P. H., & McCartney, D. G. (2000). Microstructural evolution in thermally sprayed WC–Co coatings: comparison between nanocomposite and conventional starting powders. *Acta Materialia, 48*(7), 1593–1604.

Thakur, L., Arora, N., Jayaganthan, R., & Sood, R. (2011). An investigation on erosion behavior of HVOF sprayed WC–CoCr coatings. *Applied Surface Science, 258*(3), 1225–1234.

Thiele, S., Sempf, K., Berger, L.-M., & Spatzier, J. (2011). *Thermophysical and microstructural studies on thermally sprayed chromium carbide coatings*. In *Proc. Int. Thermal Spray Conf. ITSC 2011, 27–29 September, 2011, Hamburg, Germany; DVS-Berichte* (Vol. 276). Düsseldorf: DVS-Verlag GmbH, 137–142.

Thiele, S., Sempf, K., Jaenicke-Roessler, K., Berger, L.-M., & Spatzier, J. (2011). Thermophysical and microstructural studies on thermally sprayed tungsten carbide–cobalt coatings. *Journal of Thermal Spray Technology, 20*(1–2), 358–365.

Tillmann, W., Hussong, B., Erne, M., Möhwald, K., & Maier, H. J. (2013). Qualification of the pore and indentation hardness measurement on thermally sprayed coatings. *Thermal Spray Bulletin, 6*(1), 30–37.

Tu, D., Chang, S., Chao, C., & Lin, C. (1985). Tungsten carbide phase transformation during the plasma spray process. *Journal of Vacuum Science and Technology A, 3*(6), 2479–2482.

Ulianitsky, V., Shtertser, A., Zlobin, S., & Smurov, I. (2011). Computer-controlled detonation spraying: from process fundamentals toward advanced applications. *Journal of Thermal Spray Technology, 20*(4), 791–801.

Velikanova, T. Ya., Bondar, A. A., & Grytsiv, A. V. (1999). The chromium–nickel–carbon (Cr–Ni–C) phase diagram. *Journal of Phase Equilibria, 20*(2), 125–147.

Venkatraman, M., & Neumann, J. P. (1990). The C–Cr (carbon–chromium) system. *Bulletin of Alloy Phase Diagrams, 11*(2), 152–159.

Verdon, C., Karimi, A., & Martin, J.-L. (1998). A study of high velocity oxy-fuel thermally sprayed tungsten carbide based coatings. Part 1: microstructures. *Materials Science and Engineering A, 246*(1–2), 11–24.

Vinayo, M. E., Kassabji, F., Guyonnet, J., & Fauchais, P. (1985). Plasma sprayed WC–Co coatings: influence of spray conditions (atmospheric and low pressure plasma spraying) on the crystal structure, porosity, and hardness. *Journal of Vacuum Science and Technology A, 3*(6), 2483–2489.

Voitovich, R. F. (1981). *Okislenie karbidov i nitridov*. Kiev: Naukova dumka.

Voitovich, V. B., Sverdel, V. V., Voitovich, R. F., & Golovko, E. I. (1996). Oxidation of WC–Co, WC–Ni and WC–Co–Ni hard metals in the temperature range 500–800 °C. *International Journal of Refractory Metals and Hard Materials, 14*(4), 289–295.

Vuoristo, P., Niemi, K., Mäkela, A., & Mäntylä, T. (1994). Abrasion and erosion wear resistance of Cr_3C_2–NiCr coatings prepared by plasma, detonation and high-velocity oxyfuel spraying. In C. C. Berndt, & S. Sampath (Eds.), *Thermal spray ind. applications: Proc. 7th National Thermal Spray Conf., 20–24 June 1994, Boston, Mass* (pp. 121–126). Materials Park/OH: ASM International.

Vuoristo, P., Niemi, K., Mäntylä, T., Berger, L.-M., & Nebelung, M. (1995). Comparison of different hardmetal-like coatings sprayed by plasma and detonation gun processes. In C. C. Berndt, & S. Sampath (Eds.), *Advances in thermal spray science and technology, Proc. 8th National Thermal Spray Conf., 11–15 September 1995, Houston, TX, USA* (pp. 309–315). Materials Park/OH: ASM International.

Vuoristo, P., Mäntylä, T., Berger, L.-M., & Nebelung, M. (1998). Sprayability and properties of TiC–Ni based powders in the detonation gun and HVOF processes. In C. Coddet (Ed.), *Thermal spray: Meeting the challenges of the 21st century, Proc. 15th Int. Thermal Spray Conf., 25–29 May 1998, Nice, France* (pp. 909–915). Materials Park/OH: ASM International.

Vuoristo, P. M. J. (2007). High velocity sprays boost hardmetal industrial coatings. *Metal Powder Report, 62*(3), 22–29.

Watanabe, M., Owada, A., Kuroda, S., & Gotoh, Y. (2006). Effect of WC size on interface fracture toughness of WC–Co HVOF sprayed coatings. *Surface and Coatings Technology, 201*(3–4), 619–627.

Wayne, S. F., & Sampath, S. (1992). Structure/property relationships in sintered and thermally sprayed WC–Co. *Journal of Thermal Spray Technology, 1*(4), 307–315.

Wenzelburger, M., López, D., & Gadow, R. (2006). Methods and application of residual stress analysis on thermally sprayed coatings and layer composites. *Surface and Coatings Technology, 201*(5), 1995–2001.

Woydt, M., Kadoori, J., Hausner, H., & Habig, K.-H. (1990). Development of engineering ceramics according to tribological considerations. *Ceramic Forum International/Berichte der Deutschen Keramischen Gesellschaft, 67*(4), 123–130.

Zhao, L., Maurer, M., Fischer, F., & Lugscheider, E. (2004). Study of HVOF spraying of WC–CoCr using on-line particle monitoring. *Surface and Coatings Technology, 185*(2–3), 160–165.

Zimmermann, S., Gries, B., & Brüning, B. (2011). New cermet powders for HVOF spraying with improved corrosion and oxidation resistance for offshore, mining and power generation applications. *Thermal Spray Bulletin, 4*(2), 94–100.

Zimmermann, S., & Keller, H. (2009). Powder – just one precondition for the success of the coating. In *8. Kolloquium HVOF spraying 2009, 5–6 November 2009, Erding, Germany, Unterschleißheim* (pp. 167–173). Gemeinschaft Thermisches Spritzen e.V.

Zimmermann, S., Keller, H., & Schwier, G. (2003). New carbide based materials for HVOF spraying. In B. R. Marple, & C. Moreau (Eds.), *Thermal spray 2003: Advancing the science and applying the technology, Proc. 2003 Int. Thermal Spray Conf., 5–8 May 2003, Orlando, Florida, USA* (pp. 227–232). Materials Park/OH: ASM International.

Zimmermann, S., Keller, H., & Schwier, G. (2006). Improved coating properties by optimised carbide powders for modern HVOF systems. In *7. HVOF-Kolloquium 2006, 9–10 November 2006, Erding, Germany* (pp. 31–37). Gemeinschaft Thermisches Spritzen e.V.

Zimmermann, S., & Kreye, H. (1996). Chromium carbide coatings produced with various HVOF spray systems. In C. C. Berndt (Ed.), *Thermal spray: Practical solutions for engineering problems, Proc. 9th National Thermal Spray Conf., 7–11 October 1996, Cincinnati, Ohio, USA* (pp. 147–152). Materials Park/OH: ASM International.

1.18 Coatings by Laser Cladding

Steffen Nowotny, Lutz-Michael Berger, and Jörg Spatzier, Fraunhofer Institut IWS, Dresden, Germany

Glossary

HVOF	High-velocity oxy-fuel spraying, a thermal spray technology widely used for the preparation of hardmetal coatings
Laser	Light amplification by stimulated emission of radiation
Laser cladding	Deposition of feedstock materials with the aim to realize a metallurgical bonding between substrate and coating but simultaneously to minimize the mixing of elements contained in the substrate and feedstock
Laser dispersing	Process which introduces coarse hard-phase materials into the locally molten outer zone of the substrate with the aim of realizing in this area a composite material
Laser alloying	Process with full dissolution of the feedstock material in the locally molten outer zone of the substrate and a maximum of mixing of the elements contained in the substrate and in the feedstock in the melt pool produced by the laser
MMC	Metal matrix composite
PTA	Plasma transferred arc welding, traditional technology for surface protection against wear
TIG	Tungsten inert gas welding, traditional technology for surface protection against wear

1.18.1 Overview of Laser Processes for Surface Modifications Using Feedstock Materials

Lasers are widely used for a large number of technical applications; among them are processes for surface modifications, e.g. coating processes, structuring, hardening, etc. (Beyer & Wissenbach, 1998). There are three processes where solid feedstock materials are used for surface modification processes: laser cladding, laser dispersing and laser alloying. Currently, in industrial practice, laser cladding is by far the most important. In the literature there are alternative terms used for this process (Toyserkani, Khajepour, & Corbin, 2005), like "direct metal deposition" (DMD) (Mazumder, Dutta, Kikuchi, & Ghosh, 2000), "laser engineered net shaping" (LENS) (Griffith, Keicher, & Romero, 1996) and "laser additive manufacturing" (LAM) (Backes, Kelbassa, Weisheit, Wissenbach, & Gasser, 2010). However, there is no standardized international nomenclature (Toyserkani et al., 2005).

http://dx.doi.org/10.1016/B978-0-08-096527-7.00018-0

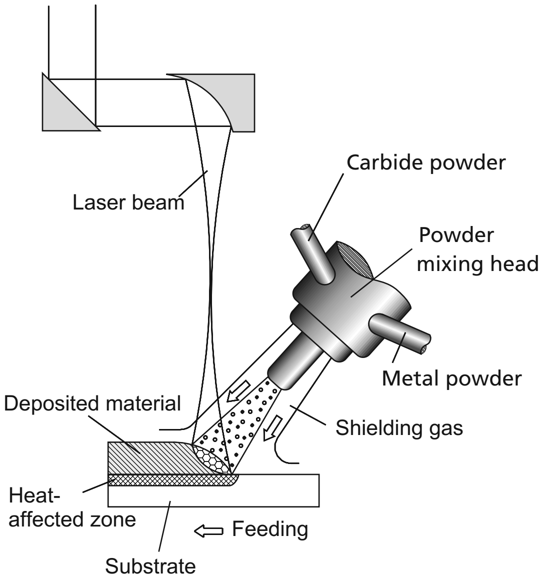

Figure 1 Principle of the one-step laser cladding process.

Laser cladding includes the deposition of feedstock materials with the aim of not only achieving a metallurgical bonding between substrate and coating but also simultaneously minimizing the mixing of elements contained in the substrate and feedstock. This can be accomplished in a one-step process with direct feeding of the feedstock material (**Figure 1**) or as a two-step process with remelting of a previously deposited coating, e.g. a thermal spray coating (**Figure 2**) (e.g. Beyer & Wissenbach, 1998; Liang, Wong, MacAlpine, & Su, 2000; Pawlowski, 1999). With the improvement of thermal spray coating properties by the use of high velocity oxy-fuel (HVOF) spraying (see Chapter 1.17), in particular for hardmetal coatings, the laser remelting technique has been practically abandoned.

Laser alloying includes the full dissolution of the feedstock material in the local molten outer zone of the substrate (workpiece) and the maximum of mixing of the elements contained in the substrate and feedstock in the melt pool (**Figure 3**). As a result of the cooling process, finely precipitated hard-phase particles occur in the outer zone of the substrate (Ariely, Bamberger, Hügel, & Schaaf, 1995). The principle of laser alloying is

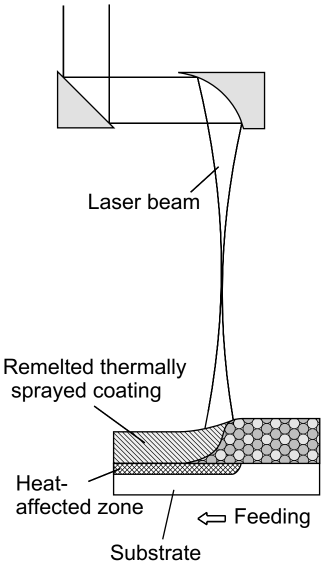

Figure 2 Principle of the two-step laser cladding process with remelting of a previously deposited thermally sprayed coating.

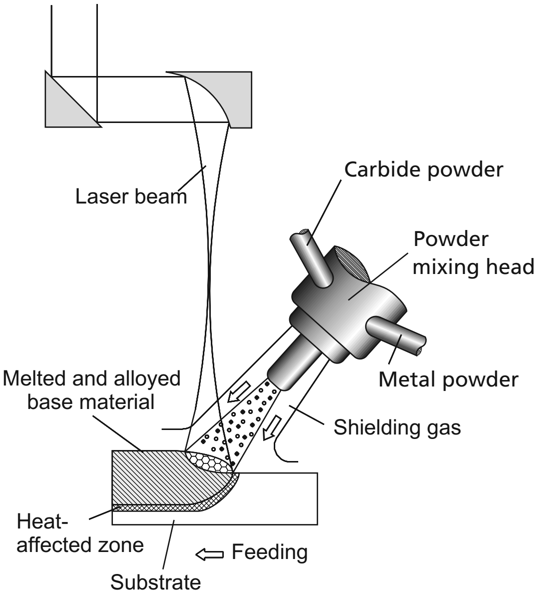

Figure 3 Principle of the one-step laser alloying process.

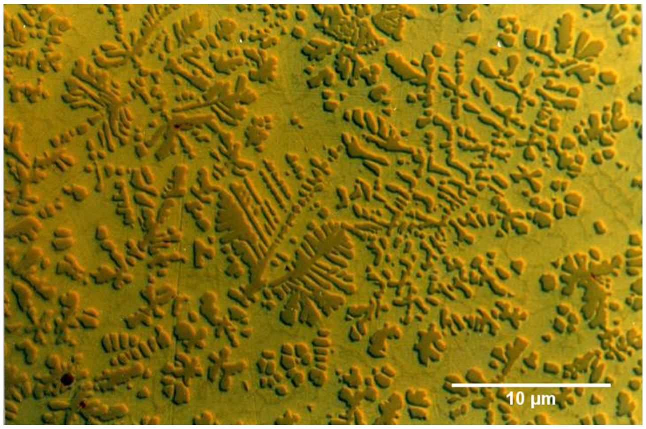

Figure 4 Fine precipitations of TiC obtained by hard-phase alloying of a 16MnCr5 steel.

demonstrated in Figure 4, showing fine precipitations of TiC in a 16MnCr5 steel matrix. Laser alloying can also be achieved as a one-step process with direct feeding of the feedstock material or as a two-step process with remelting of previously deposited coating, e.g. thermal spray coatings (Beyer & Wissenbach, 1998); Nowotny & Kunzmann, 1988).

Laser dispersing includes the introduction of coarse hard-phase materials into the locally molten outer zone of the substrate (workpiece) with the aim of obtaining a composite material (Figure 5) in this localized area. The dissolution of the mostly coarse hard-phase particles should be minimized. Like cladding and alloying, this process can also be achieved as a one-step or two-step process, e.g. by screen-printed hard-phase layers (Löschau, Juch, & Reitzenstein, 1992). As an example, laser-dispersed coarse-grained TiC in an AlSi10Mg matrix is shown in Figure 6.

Summarizing, laser alloying and dispersing include an intensive melting of the substrate material at their surfaces where feedstock material is incorporated and interacts with the melt. In contrast, laser cladding includes the melting of the feedstock material, while melting of the substrate material is minimized.

Laser cladding, dispersing and alloying can be applied for a large number of substrate materials: different grades of steel, cast iron, and nonferrous metals, e.g. alloys of nickel, titanium, and aluminum. An extended summary of applied substrate materials is given by Tuominen (2009).

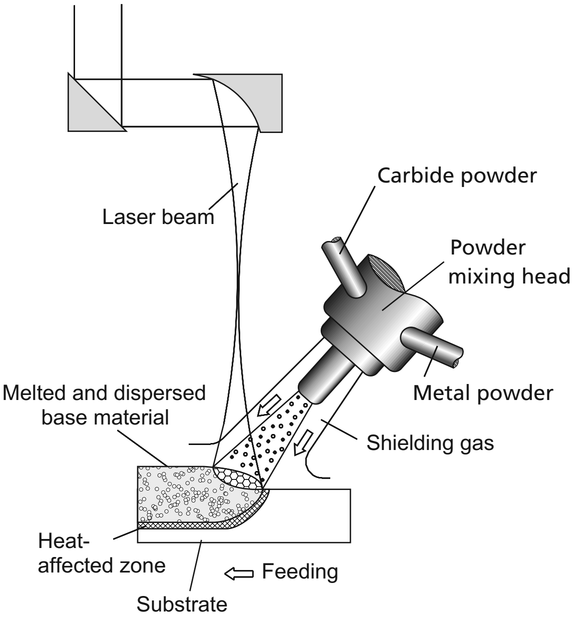

Figure 5 Principle of the one-step laser dispersing process.

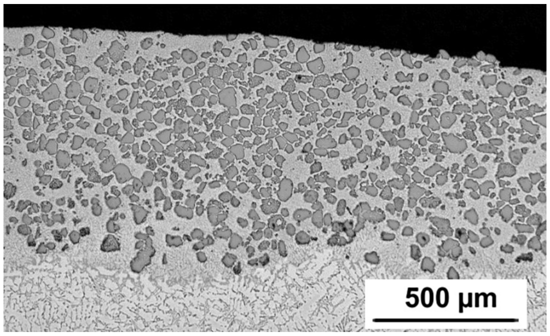

Figure 6 Microstructure of a coating prepared by laser dispersing of coarse-grained TiC particles into an AlSi10Mg matrix.

The feedstock materials include a wide variety of metals and alloys (predominantly hard alloys on the base of Ni, Co and Fe) as well as a large variety of compositions of hard-phase materials and metals or alloys. The latter are often also called metal matrix composite or carbide-reinforced coatings. This chapter is limited to the use of hard-phase materials or hard phase–metallic binder composites in these processes.

Initial publications on laser dispersing of hard-phase materials first appeared around 1980 (e.g. Ayers, 1984; Ayers & Bolster, 1984), while publications on laser cladding started to appear in the 1990s, e.g. WC–Co coatings (Eschnauer & Lugscheider, 1991). No specially designed or developed feedstocks were used initially for all three laser surface modification processes, but materials applied for other surface technologies which already existed were adopted. In particular, common feedstocks from plasma transferred arc welding (PTA) and thermal spray processes were used. Not only coarse-grained tungsten (including cast tungsten carbide) and chromium carbides with different carbon content but also titanium carbide was available at that time (Eschnauer, 1975; Eschnauer, 1980). Also, coarse-grained powders surrounded by an additional metallic layer ("composite powders" or "cladded powders") (Eschnauer, 1975; Eschnauer, 1980) as well as fused and crushed WC–Co powders (with carbon contents much below stoichiometry) were available. These coarse-grained powders were blended with metallic hard alloy feedstock powders. For several service conditions, and also for easier finishing, cladded coatings with fine carbides are required (See Section 1.18.2).

The behavior of the different hard-phase materials, such as cast tungsten carbide, during processing depends on the phase equilibria of these materials with the different metals and alloys. For laser alloying and dispersing, the interaction of the hard-phase materials occurs with the substrate material, while in laser cladding, the interaction occurs predominantly with the second (metallic) feedstock added by blending. If the hard-phase material is not in equilibrium with the composition of the metal or alloy, metallurgical reactions will occur; otherwise only dissolution and reprecipitation will take place during heating and cooling in the process, respectively. The extent of these processes is strongly influenced by the melting temperature of the metal, the higher the melting temperature, the more intensive they are. For this reason, in the case of laser dispersing, this process has gained practical importance only for hard-phase particles imbedded in aluminum alloys.

1.18.2 The Laser Cladding Process

Figure 7 illustrates a typical one-step laser cladding process for coating deposition using a powder blend of coarse hard-phase particles with a metallic alloy. Typical particle size ranges of both feedstock materials are 45–90 μm and 45–125 μm. For special purposes, smaller particle size fractions like 20–45 μm can be used. Both components are mechanically blended in the powder feeder/laser cladding nozzle. The powder or a mechanical blend of several powders are preheated while traveling by gravity through the laser beam, but melting occurs in the melt pool only. This melt pool, formed at the surface of the workpiece by the laser, is strongly localized and consists predominantly of the feedstock material. The limited partial melting of the substrate material for creating the metallurgical bonding is realized predominantly by heat transfer into the cold substrate. As a result of a permanent relative movement of the laser cladding unit and/or of the substrate and the fast solidification of the coating material, a single welded track is formed. The surfaces are coated track by track with a partial overlapping, which includes a partial remelting of the previously deposited adjacent track. The resulting coating is characterized by a typical thickness range of 100–2000 μm and a metallurgical bonding to the substrate material. Coating properties depend not only on the materials but also on the type of laser and the process conditions. According to the historical development of laser technology, different types of laser sources were available for laser cladding processes (see Section 1.18.3).

The deposition of coatings is the predominant purpose of laser cladding, but the process can also be used for repair and refurbishment of parts and for the generation of three-dimensional parts. Metals and alloys are often processed alone for coating deposition, but for the generation of three-dimensional parts they are exclusively used. So far, hard phase–binder alloy compositions are playing a role for coating deposition only. They constitute probably the most studied group of coatings deposited by laser cladding (Tuominen, 2009).

Coating deposition by laser cladding is currently preformed as a one-step process only. The predominant type of feedstock material is powders. Due to relatively smalls amounts compared to other surface modification technologies, such as PTA and thermal spray, no special feedstock material is commercially available. Most often they are applied as mechanical blends. Coarse hard-phase particles like cast tungsten carbide are

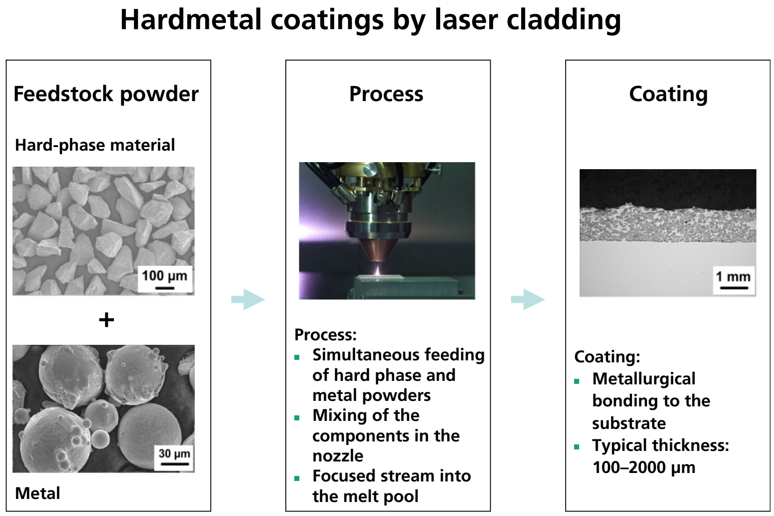

Figure 7 Principle of laser cladding. The schematic shows a one-step process using a mechanical mixture of hard-phase particles and an atomized binder alloy.

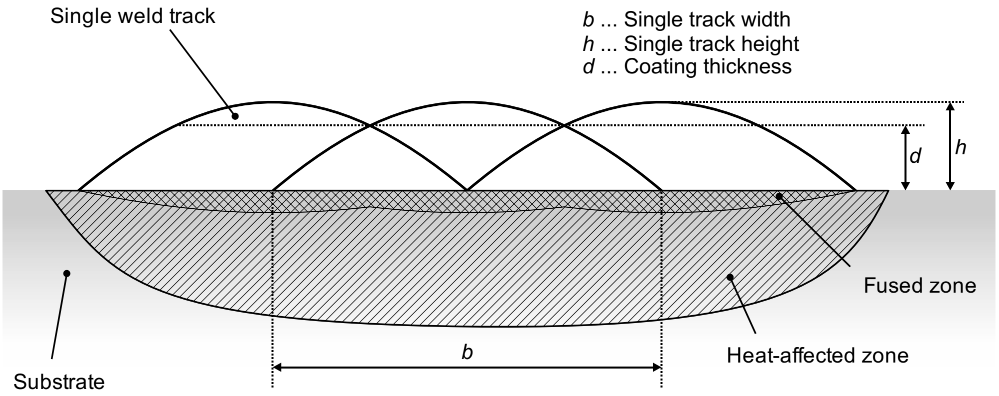

Figure 8 Schematic of the structure of a cladded coating showing the cross-section of three overlapping single welding track.

mechanically blended with different hard alloy powders based on Co or Ni. Due to dissolution and metallurgical reaction, the hard-phase particle size decreases in the cladding process.

Composite (hardmetal) feedstock powders, containing fine-grained hard phases with metallic binder are also mechanically blended with additional metal or alloy powders since the metallic binder content in the former is too low for deposition of crack-free coatings. Such fine-grained structures are currently mostly realized with agglomerated and sintered powders (see Section 1.18.7) on the base of cubic hard phases, such as titanium and vanadium carbides.

The coating process is characterized by complex metallurgical processes between the hard-phase particles and the metallic material. This includes some dissolution of the substrate material, although it is generally attempted to minimize the mixing of substrate elements into the coating. Depending on the selected binder material, the reachable hard phase content differs, but is limited to about 50 vol.%. Well-deposited coatings are characterized by the absence of porosity.

Alternatively, with suitable hardware modifications, wires can be used, but in the case of hard-phase containing composites, this feedstock is limited to flux-cored wires.

Figure 8 shows the cross-section of three single tracks for demonstration of the principle of coating formation. Single tracks are characterized by their width b and their height h. The maximum coating thickness d results from the thickness of two tracks at their overlapping point. Typical values are $b = 0.1–8$ mm, $h = 0.1–2.5$ mm, and $d = 0.1–2$ mm. One of the most important parameters is dilution, which has a metallurgical and geometrical definition (Toyserkani et al., 2005). Metallurgical dilution is determined by measuring the content of a substrate element in the coating, e.g. iron in the case of steel in the area of a Co-based binder alloy. This is most often applied for practical purposes. For state-of-the-art processes, a dilution of the substrate material into the coating material of about 5% can be achieved.

The geometrical dilution is determined by the equation $\zeta = A_2/(A_1 + A_2)$, where A_1 and A_2 are the areas of a single welding track and the fused zone in a coating cross-section, respectively (Figure 9). For a fast estimation, the ratio between the height of A_1 and A_2 can be used.

In the deposition of hard phase-based coatings, wetting is important in two areas: it is an important parameter during processing in relation of the coating to the substrate and of the hard-phase particles to the binder matrix. The former is governed by the behavior of the metallic binder material to the substrate material and is only little influenced by the hard-phase particles.

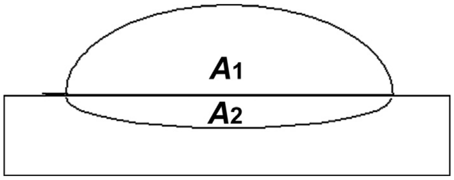

Figure 9 Schematic of a single welding track.

The deposition rate is determined as the product of the powder feed rate and the deposition efficiency. It is mainly influenced by the ratio of size of the melt pool to the cross-sectional area of the powder stream. Most typical deposition efficiencies are in the range of 60–90%; in exceptional cases, up to 98% can be reached.

Under nonoptimum process conditions, several types of defects can occur, such as cracks, pores/voids, excessive dilution and compositional nonhomogeneity (Tuominen, 2009). For all these types of defects, technological countermeasures exist, e.g. cracks can be avoided by additional heating. For several applications, e.g. as wear-resistant coatings without corrosive attack, cracks are sometimes tolerated.

1.18.3 Historical Development of Laser Cladding

The basic patent for the process of laser cladding was filed in the United States in 1974 (Gnanamuthu, 1974). The motivation for the development was the disadvantages of the traditional and established arc welding processes tungsten inert gas welding (TIG) and PTA: high degree of dilution of the substrate material into the coating, high heat input into the workpiece resulting in distortions and very limited precision of the material deposit. The application of the laser as a new tool resulted in significant improvements: for this process, the local precision of material deposition is very high, the dilution and heat input into the substrate are low, the laser beam does not cause unfavorable mechanical impact onto the melt pool, and the cladding process can be controlled online. However, the productivity of the process, as measured by the deposition rate is lower.

In the late 1970s and 1980s, the scientific and engineering fundamentals for industrial applications of the laser cladding process in the 1990s were developed (Gnanamuthu, 1980; Mazumder & Singh, 1986; Weerasinghe & Steen, 1983). Basic connections between material properties, process parameters, coating structure and properties were established in this period (Mordike, 1992). The investigations in this period were performed by CO_2 laser with power in the range of several kilowatts, allowing for the first time material treatment in a macroscopic scale with relevance to practical applications. With the growing number of industrial applications, two main directions of development became visible: on one hand, the development of wear- and corrosion-resistant laser clad coatings and on the other hand, the development of laser technologies for three-dimensional material deposition for production and repair of aeroengines, gas turbines and injection molds. These application developments were accompanied by a highly dynamic development of the related system technology: laser optics, cladding heads and devices for process control (Schubert, 1992; Sievers, 1994; Waidelich, 1993). In particular, the powder supply plays a decisive role. In the beginning, off-axis feedstock supply was mostly realized; see also Toyserkani et al. (2005). Later, coaxial powder nozzles were developed (e.g. Nowotny & Scharek, 2000; Nowotny, Scharek, Kempe, & Beyer, 2003).

In general, coatings prepared with CO_2 lasers showed a high bonding strength, absence of cracks and high wear resistance (Corbin & Wilkinson, 1994; Grünenwald, Shen, Dausinger, & Nowotny, 1992; Nowotny, Techel, Luft, & Reitzenstein, 1993). CO_2 lasers are relatively inexpensive, characterized by good beam quality with sufficient power. However, the relatively long wavelength of 10.6 μm causes technological and economic limits. Laser light energy of this wavelength is absorbed by metals and their melts only by 5% up to maximum 25%. Moreover, it can not be transmitted through glass fibers.

In the 1960s, another type of laser, the Nd:YAG solid-state laser with lower wavelength was developed. Only in the 1990s was this type of laser produced by the industry with a power range up to 3 kW. In this first version, the YAG glass rod was pumped conventionally by flash lamps. This was a relatively inexpensive type of laser, however, characterized by only moderate focusing properties and low efficiency of only 3%. In comparison with CO_2 laser, transmission of laser light by fibers is possible, and the energy absorption by the metallic melts reaches values up to 60%. The disadvantages regarding efficiency and beam quality have been solved by another type of Nd:YAG solid-state laser, using laser diodes for excitation. Such diode-pumped solid-state laser was presented in 1993 (Freitag, Zellmer, Schöne, Golla, & Welling, 1993) and commercialized in the second half of the 1990s. The efficiency of these systems ranges from 10% to 12%, and the beam quality is also improved considerably. At the final stage of this development, the technical parameters of the solid-state laser corresponded to those of the CO_2 laser, but with the advantage of laser light transmission through fibers and absorption values at least doubled. The main disadvantage of the diode-pumped Nd:YAG solid-state laser compared to the CO_2 laser was the significantly higher price.

As a result of this development, the CO_2 laser was nearly fully replaced by the solid-state laser as a beam source for laser cladding. However, high investment costs and still insufficient efficiency were reasons for limited commercial use. Today, diode-pumped YAG lasers are not manufactured anymore, but there are still some systems in use.

The next generation of laser suitable for laser cladding—diode laser—was presented with sufficient power in 1992 (Krause, Treusch, Beyer, & Loosen, 1992). With the commercial availability of high-power diode laser (HPDL) around 2000, a breakthrough of the commercial application of laser cladding was realized, leading to a highly dynamic process of development. With an output power up to 15 kW and the characteristic hat profile of power distribution, modern HPDLs are tailored for laser cladding applications. The cross-section of the laser beam can be varied to round, rectangular and quadratic. If required, focus diameters of about 200 μm are available. The efficiency amounts to >50%, due to the short wavelength of 860 nm; the energy absorption at the melting pool can be also >50% (Bachmann, Loosen, & Poprawe, 2007). Compared to CO_2 laser with the same power output, the deposition rate is increased by a factor of 2.5 (Richter, Nowotny, Naumann, & Beyer, 1999). Since the costs per kilowatt laser power are much lower compared to those of the diode-pumped Nd:YAG solid-state laser and even lower compared to the CO_2 laser, HPDL became the preferred tool for laser cladding and has replaced all other types of lasers. Typical deposition rates are, e.g. about 8 kg h^{-1} WC/NiBSi feedstock, using 6 kW HPDL power. Further increase of the deposition rate, and productivity, was reached by hybrid technologies, using additional energy sources (see Section 1.18.4).

A new dimension of lateral resolution of material deposition is offered by the latest generation of lasers—Yb:YAG fiber laser and disk laser. These are solid-state lasers in the power range up to 30 kW, characterized by a high beam quality and a focus diameter of about 10 μm, irradiation mode easy to pulse, high efficiency and moderate investment costs (Giesen, 2005; Krastel, 2009; Weiler, 2010). Very small single tracks of about 30 μm were realized by using Ni superalloys (Brückner, Nowotny, Riede, Lepski, & Beyer, 2010). This opens up the opportunity for deposition of small tracks also for hard phase–binder composites, but this is not realized so far with these new types of laser. Such opportunities should be accompanied with corresponding feedstock powder developments.

1.18.4 State-of-the-Art Laser Cladding Process

Besides the development of laser sources, the development of different hardware components and corresponding system technology has strongly influenced the quality and reliability of laser clad coatings. According to the state-of-the-art, a coaxial powder supply is predominantly used. The basic principles of a laser cladding process using coaxial powder feedstock supply are shown in Figure 10. The most important advantage of this principle is the omnidirectional powder supply and, thus, the direction-independent welding process. Additionally, the interaction time of the powder particles with the laser beam is longer compared to the off-axis type of nozzle. As a result, the temperature of the particles may be advantageously higher when they reach the melt bath (compare Figure 1). This allows the preparation of any two-dimensional coating, fully or partially covering the workpiece, and also the generation of three-dimensional parts. In the case of powder mixtures, the components are fed separately into the nozzle, and mixed in a fluidized bed. After exiting from the nozzle, the powder is moving to the substrate mostly by gravity. Special constructions of the nozzle allow cladding in overhead conditions, as well as of internal diameters (Nowotny, Spatzier, Kubisch, Scharek, Ortner, & Beyer 2012). However, for areas with limited access, the off-axis powder supply is applied.

Figure 11 shows a typical assembly of a coaxial laser cladding head, which allows a pneumatic homogeneous *in-situ* blending of two to four different powders. This also allows the processing of powder components of different density and change of the mixing ratio during the running coating process. The construction of the coaxial powder nozzles allows the precise adaptation of the powder particle stream to the geometry of the melt pool. Taking into account, in addition, the laser parameters and substrate properties, the height and width of the weld track can be tailored. Figures 12 and 13 show as examples the cladding processes of industrial components.

Predominantly, the laser cladding process is performed in atmospheric conditions without preheating of the substrate. Substrate cooling can be required, in the case of a nonadvantageous ratio of substrate thickness to coating thickness. An inert shielding gas flowing through the powder nozzle can protect the melting pool from the surrounding atmosphere. For higher degrees of protection, the process can be performed in a controlled atmosphere of a chamber (controlled atmosphere laser cladding).

An increased process efficiency can be realized by the use of hybrid processing heads, which include a module for additional inductive heating of the substrate during the laser cladding process. This localized

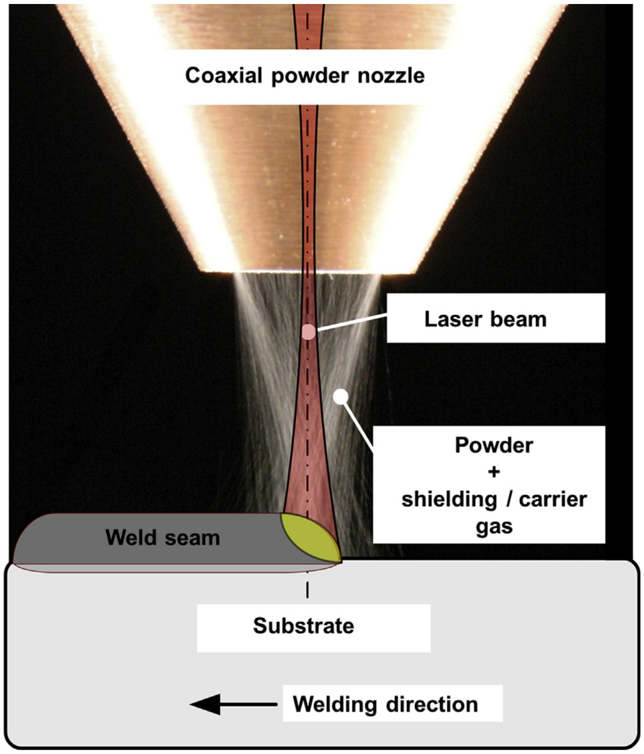

Figure 10 Laser cladding with coaxial powder supply.

Figure 11 Laser cladding head.

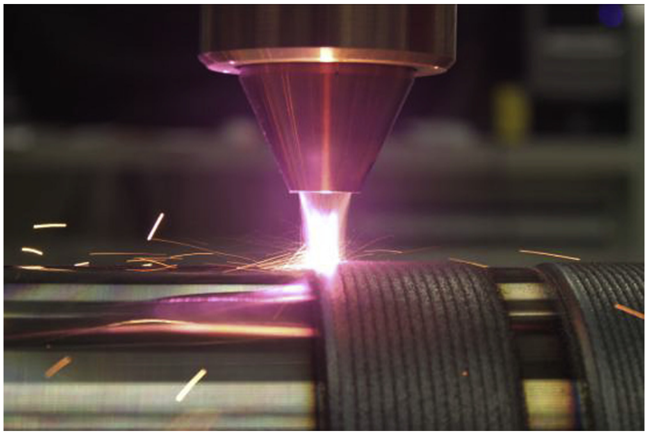

Figure 12 Process of laser cladding using 8 kW diode laser power.

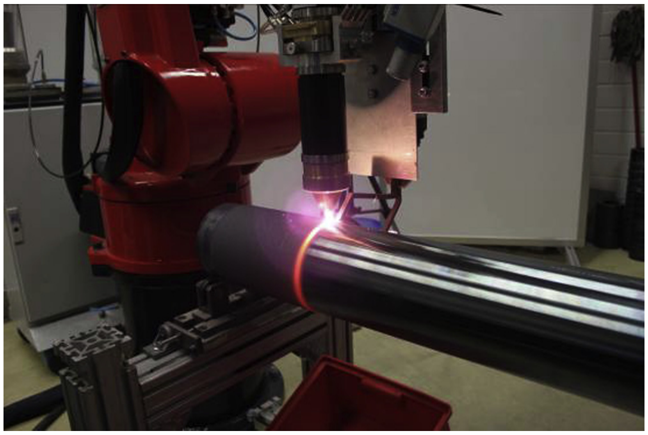

Figure 13 High-performance laser cladding using the laser induction hybrid cladding head.

inductive heating allows higher powder feed rates of, e.g. up to 25 kg h^{-1} WC and an increase of the deposition rates by a factor of 2–2.5 (Nowotny, 2011). This combination of energy sources also allows the development of tailored heat managements for the coatings. The additional heat leads to a significantly increased cooling time $t_{8/5}$, as well as to decreased spatial temperature gradients. In particular, this facilitates the crack-free processing of hard phase-containing coatings (Beyer, Nowotny, Brueckner, Hillig, & Techel, 2011). Local inductive preheating is also applied for combinations of substrate and coating materials sensitive to crack formation. Laser cladding with simultaneous inductive heating of the substrate has already gained high practical importance (Beyer et al., 2011).

For application, finishing of the laser clad coatings is necessary. Commonly, grinding with diamond wheels is applied. There also exist complete technical solutions in laser milling centers, where cladding and finishing by milling are combined (Nowotny, Münster, Scharek, & Beyer, 2010). Use of fine carbides results in lower surface roughness at lower finishing costs.

1.18.5 Materials and Interactions

1.18.5.1 Hard-Phase Materials

The most important hard-phase materials for laser cladding are transition metal carbides of the IVb, Vb and VIb groups of the periodic table: WC, TiC, VC, and Cr_3C_2. Important properties for laser cladding are room- and high-temperature hardness, wetting angle with binder metals and solubility in these binder metals. The change of these properties for carbides of the IVb, Vb and VIb groups of the periodic table is illustrated in Figure 14

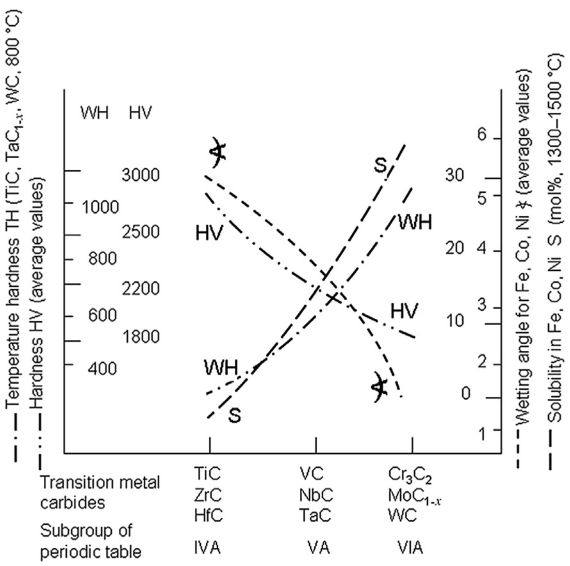

Figure 14 Change of basic properties of transition metal carbides with their position in the periodic table (Holleck, 1981).

(Holleck, 1981). The increase of metallic bonding in the carbides with increasing group number leads to a decrease of hardness and of the wetting angle, while the solubility in metals of the iron group is increasing.

The solubility for some hard phases with nickel and cobalt according to Ettmayer, Kolaska, Langauer, and Dreyer (1995) and Edwards and Raine (1953) is compiled in Table 1. Among the carbides, WC excels by the best solubility.

Due to the technical importance of cast tungsten carbide, representing a eutectic mixture of WC and W_2C, the differences between these two hard phases (Lassner & Schubert, 1999) are of importance. W_2C differs from WC by its relatively wide homogeneity range; it can also replace tungsten by other transition metals like chromium without change of the structure of its crystal lattice (see Chapter 1.17).

There exist three carbides in the Cr–C phase diagram: Cr_3C_2, Cr_7C_3, and $Cr_{23}C_6$. Cr_3C_2 and $Cr_{23}C_6$ are characterized by a peritectic decomposition, and Cr_7C_3 has a congruent melting point. However, all peritectic and melting temperatures are below 2000 °C which is much lower that than for other transition metal carbides. Structures of Cr_7C_3 and $Cr_{23}C_6$ are known to appear in hardened steels and hard alloys (Berns, 1998) where chromium in the crystal lattice can be partially replaced by other metals, e.g. nickel (see Chapter 1.17).

Titanium carbide, TiC, is the only compound in the Ti–C phase diagram which is characterized by a wide range of stoichiometry and a congruent melting point. TiC can incorporate other metals like W and Mo as well as nonmetals like O and N into its cubic lattice without changing the crystal structure. Besides this good alloyability and high thermal stability, its high hardness, low density, and chemical stability makes this hard phase also attractive for the preparation of laser clad coatings. Alloying with Mo and W and formation of

Table 1 Solubility of carbides in metals at 1250 °C (Edwards & Raine, 1953) and at 1400 °C (Ettmayer et al., 1995)

	Solubility of the hard phase				
Hard phase	*in Ni (Mass%)*		*in Co (Mass%)*		*in Fe (Mass%)*
	At 1250 °C	At 1400 °C	At 1250 °C	At 1400 °C	At 1250 °C
TiC	1	11	5	10	<0.5
TiN	<0.1	<0.5	<0.1	<0.5	<0.1
Mo_2C	13	36	8	39	5
WC	22	27	12	39	7
TaC	3	6.3	5	6.3	0.5
NbC	5	7	3	8.5	1
VC	7	14	6	19	3
Cr_3C_2	12	–	12	–	8

core–rim structured hard-phase particles can improve the wetting of TiC with the metallic binders (Techel, Berger, & Nowotny, 2007) (see Chapter 1.17).

The main hard phases in the V–C phase diagram are VC and V_2C. VC has an extremely wide homogeneity range, where ordered substoichiometric VC phases (V_8C_7, V_6C_5, V_4C_3) exist as well. The cubic VC can also incorporate other transition metals into its crystal lattice.

Besides technical performance availability and costs are also of importance for the choice of the carbides. All carbides mentioned above are available in large amounts at reasonable costs.

1.18.5.2 Metallic Binder Materials

There is a large number of possible binder materials, including basically all metals which can be processed. Due to the wide use of mechanical blending, a large amount of possible combinations of hard phase and binder materials exists.

Hard alloys are an important group of materials widely used for wear protection, including hard surfacing by laser cladding (Berns, 1998). These are Co-, Ni- and Fe-based alloys forming hard phases by precipitation. All of them are characterized by a good processability in air. Only blends of hard alloys with hard-phase particles will be considered here; this is often described by the term "reinforcement".

Due to their good processability, nickel-based so-called self-fluxing alloys are often selected as metallic binder. In order to prevent from additional metallurgical reactions with the carbides, compositions free of chromium are selected. The components Si and B are forming a relatively low-temperature eutectic, which is mainly responsible for the good processing properties, but hinders the high-temperature application of the corresponding coatings. Other nickel-based alloys, such as Inconel® (NiCrMo-based alloy), are rather rarely used.

Cobalt-based Co-Cr-Mo-W-C hard alloys (Stellite®) are also widely used as binder alloys. Some of these alloys are characterized by good high-temperature properties up to 700 °C and stability in corrosive environments.

Iron-based hardfacing alloys are used as cheaper alternative to the Co- and Ni-based alloys. They have a special importance in combination with VC as a hard phase. Alloy 316L is often used as a Fe-based binder alloy.

1.18.5.3 Interactions of Hard Phase and Binder Materials during Processing

Analysis of the literature shows that mostly the dissolution of hard-phase particles in the binder is discussed, but there is no differentiation on pure physical dissolution and metallurgical reactions. The solubility of the hard phase in the binder is one of the key parameters of interaction of both components in the cladding process (see Section 1.18.5.1). The importance of the metallurgical reactions is often neglected. When heated up under the influence of the laser beam in the melt pool, hard-phase particles which are not in equilibrium with the metallic binder start to react if the activation energy for this particular reaction is reached. In particular, WC and W_2C, as well as Cr_3C_2, show strong metallurgical reactions with the most common binder materials and form new phases. Metallurgical reactions are also due to the content of hard phase-forming elements such as chromium and vanadium in the hard alloys used as metallic binder.

For incorporation of coarse hard-phase particles in the coating, the kinetics of dissolution and metallurgical reactions play a significant role. They are influenced by the melting pool temperature and interaction time during laser cladding process.

It can be assumed that the technical parameters of the different laser sources such as the different wavelength and profiles of power distribution have only a little influence on the metallurgical processes between the hard phase and the binder during coating formation. For this reason, information independent of the type of laser source can be considered.

1.18.6 Methods of Coating Characterization

Metallographic preparation and investigation of coating cross-sections by optical microscopy and scanning electron microscopy (SEM) are the most common investigation methods. The hard phase content in the coatings is often analyzed by image analysis of optical and scanning electron micrographs. For coarse hard-phase particles this is an easy task, in the case of fine hard-phase grains and reprecipitates, they might be difficult to analyze (Techel et al., 2007). Studies on the distribution of elements in the coating are performed by different methods, such as energy dispersive X-ray spectroscopy (EDX).

Hardness is also most commonly studied and measured in the cross-section. Care should be taken for the selection of the load for coatings containing coarse hard-phase particles.

Phase composition of the coatings is studied by X-ray diffraction. Residual stresses are also the topic of several studies (e.g. Tuominen, 2009).

Most often, the coatings are studied by different methods for their wear resistance. This includes mostly abrasion, sliding, and erosion. Standardized methods are often applied for investigation. However, there are a large number of customized methods, which should reflect the conditions of service as close as possible.

Corrosion properties in different customized media at room and elevated temperature are also often investigated.

1.18.7 Hard Phase Feedstock Materials

1.18.7.1 Tungsten Carbides

In the early developments of laser clad coatings, different types of tungsten carbide-based feedstock materials were used, such as coarse-grained fused and crushed WC–Co, agglomerated WC cladded with Co, and cast tungsten carbide (e.g. Gassmann, 1996; Techel, 2001; Tuominen, 2009). With the evolution of thermal spray technology in the 1990s, the former types of powders disappeared from the market.

Currently, feedstocks based on cast tungsten carbide are dominating by far for laser cladding, but they are also widely used in welding processes, such as PTA (Schreiber, 2002). Cast tungsten carbide is a eutectic mixture of WC and W_2C with a carbon content in the range 3.8–4.2%, corresponding to a phase content of 73–80% W_2C and 20–27% WC (Schreiber, 2002). The typical morphology of cast tungsten carbide particles and a typical cross-section of one particle are shown in Figure 15. The distribution of the phases WC and W_2C in the coarse particle is a quality criterion. Fine "feather" structures can be obtained through special processing with rapid cooling of the melt.

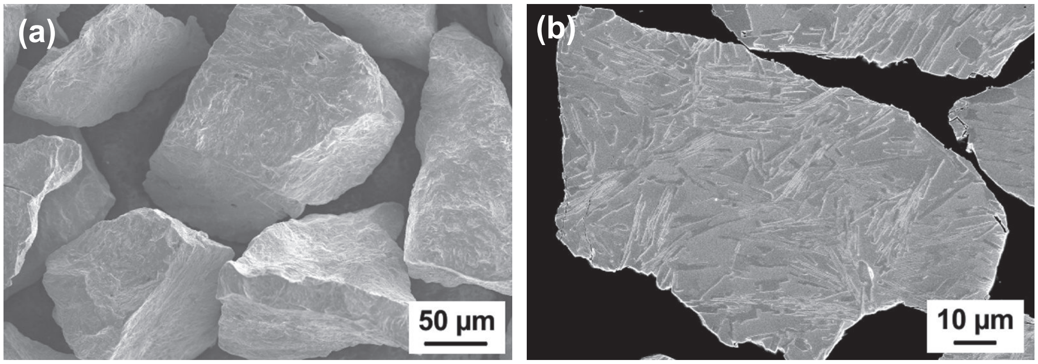

Figure 15 Scanning electron micrographs ((a)morphology and (b) cross-section) of a cast tungsten carbide, particle size: 45–100 μm.

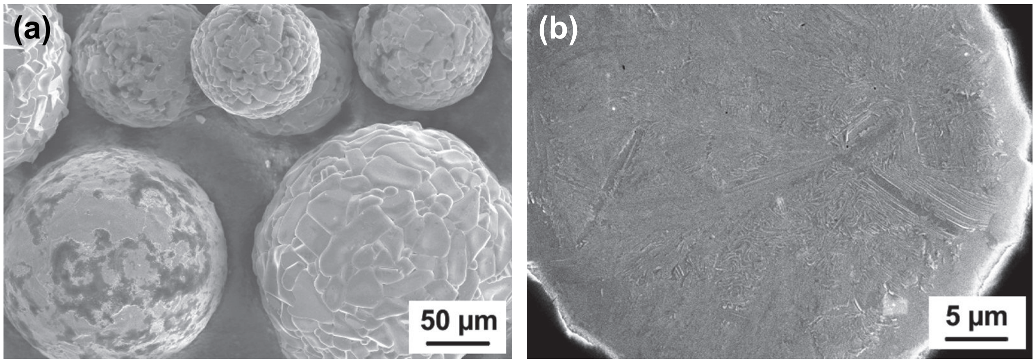

Figure 16 Scanning electron micrographs ((a)morphology and (b) cross-section) of a spheroidized cast tungsten carbide, particle size: 45–100 μm.

For improved processing and wear properties, spheroidized cast tungsten carbides were developed. There are different technologies for spheroidization (Brunet, Esnault, Maybon, & Perrier de la Bathie, 1986; Linke, Weiss, & Nutsch, 2003; Schreiber, 2002). The typical morphology of the particles and the cross-section of one particle are shown in Figure 16. Spheroidized tungsten carbides are characterized by a finer distribution of WC and W_2C.

Typical micrographs of coatings using angular and spheroidized cast tungsten carbides prepared from blends with 50 vol.% NiBSi matrix are shown in Figure 17. The coatings showed no cracks and were almost free of pores. The carbide particles are homogeneously distributed in the coating; only in the area of track overlaps, there are small zones containing less carbide particles. Due to the high density difference between the binder alloy and the hard phase, some sedimentation of the carbide particles was observed. For the cast tungsten carbide, an average content of about 45 vol.% was determined by quantitative image analysis.

According to earlier studies, compositions containing up to 45–50 vol.% cast tungsten carbide could be deposited free of cracks with NiBSi, while the upper limit using Stellite 21 was 35–40 vol.% (Luft, Techel, & Nowotny, 1995; Nowotny et al., 1993; Techel, Luft, Müller, & Nowotny, 1995). The lower melting temperature of self-fluxing Ni-based alloys and the lower solubility of WC in this type of binder compared to Co- and Fe-based alloys contribute to the reduction of dissolution of coarse carbide particles.

For a NiBSi binder alloy, the dissolution rate of W_2C is significantly higher than for WC, while in CoCr28MoNi alloy, it is nearly equal (Techel, 2001). Typical micrographs of higher magnification demonstrating the differences in the dissolution process of angular and spherical WC/W_2C particles in a NiBSi matrix are shown in Figure 18. Both angular and spherical cast tungsten carbide particles exhibit highly rough surfaces with blocked protrusions as a result of the different rates of dissolution of WC (dark gray) and W_2C (light gray). For the spheroidized carbides, the reaction zone appears more uniformly. However, there are contradictory opinions on the dissolution kinetics for cast and spheroidized tungsten carbide in the literature (e.g. Huang, Samandi, & Brandt, 2004; Nurminen, Näkki, & Vuoristo, 2009)

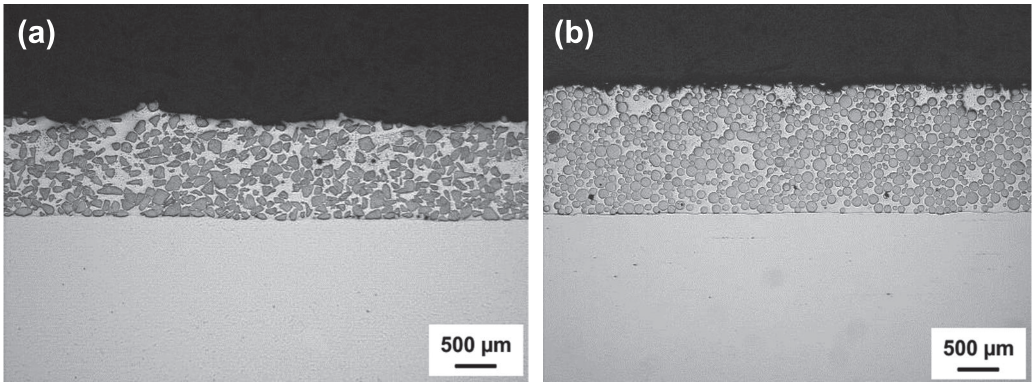

Figure 17 Optical micrographs of laser clad coatings with NiBSi binder matrix: (a) cast tungsten carbide and (b) spheroidized cast tungsten carbide.

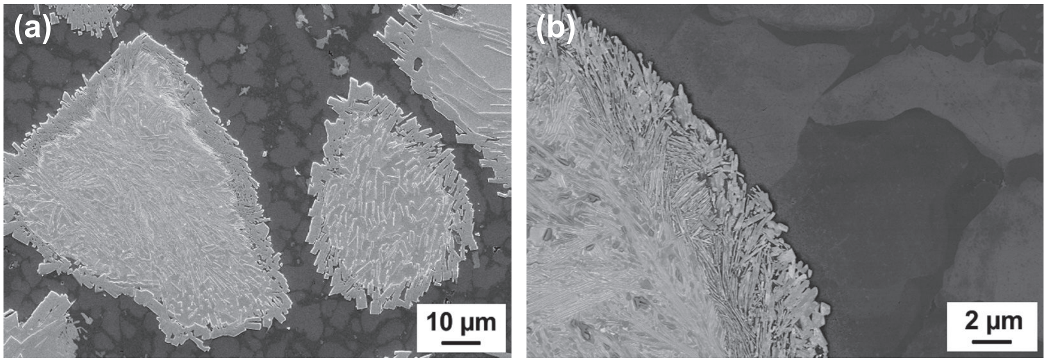

Figure 18 (a) Dissolution of a cast tungsten carbide and (b) a spherodized cast tungsten carbide in a NiBSi binder.

In result of reactions of dissolved WC and W_2C with components of the binder matrix, mixed carbides, such as Co_xW_yC, Fe_xW_yC and Ni_xW_yC are formed (e.g. Huang et al., 2004; Techel, 2001; Tuominen, 2009). Partially dissolved WC precipitates independent of metal matrix in dendritic form (e.g. Huang et al., 2004).

1.18.7.2 Chromium Carbide

Coarse sintered Cr_3C_2 feedstock powders have been commercially available for long time and were already tested in the early stage of laser cladding technology (Kathuria, 2001). Cr_3C_2 is not in equilibrium with many metallic binder phases, leading to metallurgical reactions during the cladding process. It can also be expected that at the process temperatures, Cr_3C_2 is peritectically decomposed. Indeed, coarse Cr_3C_2 particles are described to be dissolved fast in the metal matrix and tend to precipitate as mixed hard phases, which leads to embrittlement of the matrix (Nurminen et al., 2009; Theiler, Seefeld, & Sepold 2001; Tuominen, 2009). The Cr_3C_2 can exist in Cr_3C_2/NiBSi coatings only when the initial carbide content in the blend is high (Theiler et al., 2001). Due to the formation of other hard phases, coatings prepared from coarse Cr_3C_2 with metallic binder alloys show high wear resistance (Kumar & Goswami, 2006; Nurminen et al., 2009; Tuominen, 2009).

1.18.7.3 Titanium Carbide

Coarse sintered TiC feedstock powders have also been commercially available for long time (Eschnauer, 1975) and were used for laser cladding experiments with different binder alloys (e.g. Kathuria, 2001; Nurminen et al., 2009; Tuominen, 2009). Coatings with fine hard-phase grains can be prepared from (Ti,Mo)(C,N)-based agglomerated and sintered feedstock powder. Such powders have core–rim structured hard phases, and were originally developed for thermal spray processes (Berger, Thiele, Vuoristo, Mäntylä, Keller, Proß, & Scholl, 2002) (Figure 19). These powders contain up to 27 vol.% Ni, Co or mixed Ni/Co binder, and can be blended with

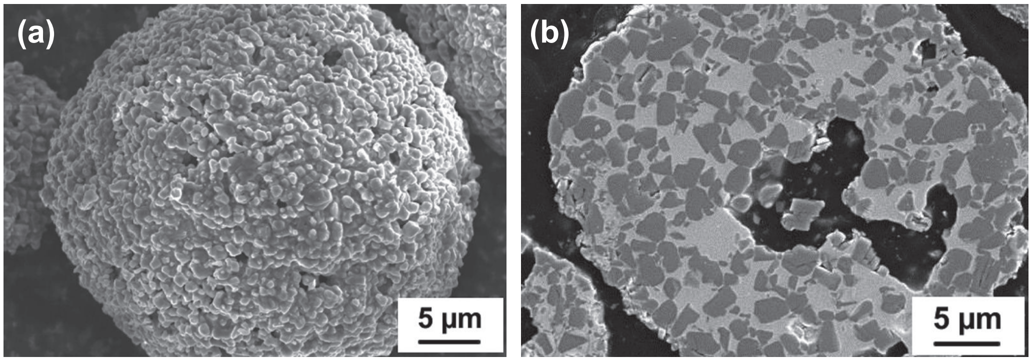

Figure 19 (a) Morphology and (b) cross-section of agglomerated and sintered (Ti,Mo)(C,N)-Ni powder particle with a carbide grain size ranged 1–5 µm (Nowotny et al., 2012).

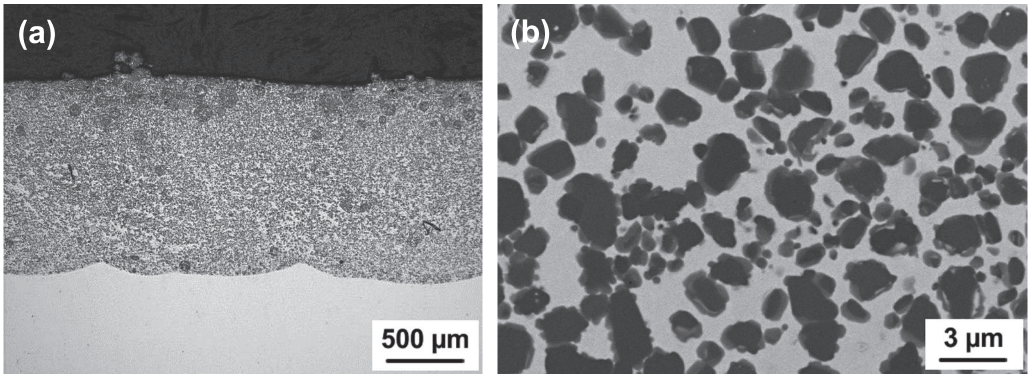

Figure 20 (a) Optical and (b) scanning electron micrographs of coating prepared from the mixture of fine-grained (Ti,Mo)(C,N)-Ni and NiBSi powders.

additional binder alloys (Techel et al., 2007). Similar coating microstructures can be obtained using feedstock powders prepared by self-propagating high-temperature synthesis (SHS) (Tuominen, 2009). Another technology of deposition of TiC-based coatings is the *in-situ* formation of carbide in the melt pool, starting from Ti, graphite and Fe powders, all of particle size up to about 45 μm (Emamian, Corbin, & Khajepour, 2011).

Coarse TiC does not show any metallurgical reactions with binder alloy and precipitates in dendritic structures (Gassmann, Nowotny, Luft, & Reitzenstein, 1992; Sun, Yang, Guo, & Dong, 2001). Crack-free coatings with a volume fraction of up to 80% (TiC/Ni-AlSi) were reported (Gassmann et al., 1992). Such high amount of carbides is often limited to the top layer of functionally graded coatings in order to avoid crack formation. A content of TiC on the top layer of up to 95% was achieved (Liu & DuPont, 2003).

Typical microstructures of coatings using core–rim structured agglomerated and sintered (Ti,Mo)(C,N) feedstock powders blended with NiBSi binder alloy are illustrated in Figure 20. X-ray diffraction demonstrates the high stability of the cubic hard phases during processing (Nowotny et al., 2012; Techel et al., 2007). The hard-phase grains are homogeneously distributed, show a rounded shape and have mainly a grain size of smaller than 5 μm. SEM images with a high magnification and the corresponding elemental EDX mappings showed that the core–rim structure of the hard-phase grains in the feedstock powder is transferred to the coating (Nowotny et al., 2012; Techel et al., 2007). A full mixture of the binder elements in the coating was shown (Techel et al., 2007). Also, Fe coming from the substrate is homogeneously distributed in the binder.

A homogeneous distribution of hard particles can be obtained when the content of hard phases does not exceed 50 vol.%. Coatings containing higher amounts of carbide particles show an inhomogeneous distribution of carbides which is usually detrimental to coating properties, such as a uniform hardness, fracture toughness as well as wear resistance. Depending on the content of hard particles and the metal matrix used, a coating hardness of 700–1130 HV0.3 is achieved.

1.18.7.4 Vanadium Carbide

Iron is the preferred binder material for vanadium carbide. For a carbon content above the amount needed for VC formation, vanadium will be contained both in the hard and in the martensitic binder phases (Hougardy, 1931).

Plain VC, and very different VC-containing and VC-based compositions, have been studied and can be processed. Historically, VC-containing feedstock powders were manufactured from compositions of Fe, Cr, V, and C by gas atomization. However, this technology is limiting the VC content to an amount of 12–18 mass% (20–24 vol.%) VC. Plain VC in a particle range of 1–10 μm (Herrera, 1998) can be applied and is commercially available as sintered coarse porous powder blended with different metal alloy powders (Nurminen et al., 2009; Tuominen, 2009). Experimental agglomerated and sintered VC–Fe feedstock powder blended with a binder alloy was also used (e.g. Nowotny et al., 2012).

Different VC-based composites with martensitic, chromium-martensitic and austenitic steel matrix are particularly often studied for PTA processes (e.g. Bouaifi, Draugelates, & Gebert, 2004; Bouaifi, Gebert, & Heinze, 1993; Gebert, Heinze, & Wesling, 2004).

For illustration, Figure 21 shows the microstructure of a laser-cladded VC–Fe-based coating. The hard-phase grains have a rounded shape and a grain size below 5 μm.

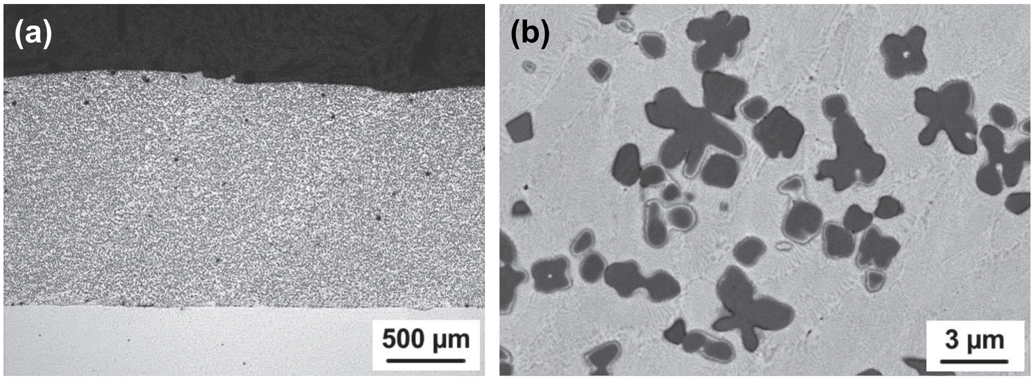

Figure 21 (a) Optical and (b) scanning electron micrographs of laser-cladded coating prepared from the blend of fine-grained agglomerated and sintered VC–Fe powder and Fe-based binder alloy.

The stability of the cubic VC is demonstrated by the comparison of the X-ray diffraction patterns of the powder and the coating (Nowotny et al., 2012). Dissolved VC does not show metallurgical reactions leading to the formation of brittle phases; cubic hard phases were identified as ordered substoichiometric phases V_8C_7 and V_4C_3 (Herrera, 1998).

The combination of VC with a tool steel resulted in coatings with particular high wear resistance (Nurminen et al., 2009).

1.18.8 Wear Resistance and Applications

The main and dominating application are wear-resistant coatings. The hard phase content and particle size in the coating are general issues. The wear resistance is strongly connected with the application conditions, e.g. the size of the wearing particles and possible corrosive action of the environment. The service temperature is determined by the properties of the metallic binder (e.g. self-fluxing alloys are limited to low-temperature applications). The oxidation resistance depends both on the hard and binder phases.

Due to the innumerable different starting materials, process conditions and test conditions, it is not surprising that many contradictory statements on wear resistance are published in the literature. However, it should also be taken into account that many individual industrial problem solutions are developed and not published in the open literature. Thus only some few general trends can be outlined here.

The most important applications are wear-resistant coatings for tools for the mining and oil and gas industries as well as the corrosion protection of large hydraulic cylinders for offshore applications. For these applications, coarse hard particles based on cast and spheroidized tungsten carbide are dominating by far.

However, for several industrial applications, coatings containing fine carbide grains are advantageous, e.g. when a high fracture toughness is required. Such fine-grained coatings are preferably produced based on TiC and VC. One example is application under high impact stresses (e.g. forming tools). With finer carbides, lower surface roughness can also be reached, which are in particular advantageous for decreased sliding wear rates and lower coefficients of friction (e.g. Nurminen et al., 2009).

The abrasion wear resistance can be mainly related to the volume fraction of hard-phase particles. In general, it is established, that a higher content of hard-phase particles results in an increased wear resistance of coatings. The direct relationship between the volume fraction of hard-phase particles and wear resistance is mainly explained by the decrease of the mean free path between the hard particles in the metal matrix, which should be smaller than the abrasive particles, in order to prevent microcutting of metal matrix. In general, when fine-grained hard-phase particles are used, a smaller mean free path between hard particles and a more homogeneous distribution can be achieved. Such coatings show an improved wear resistance against fine-grained abrasive particles. The increase of the hard-phase content is limited due to coating defects appearing with certain concentrations during the cladding process. The influence of the particle size in a range from below 1 μm up to 1 mm was repeatedly studied (e.g. Jiang & Molian, 2001; Techel et al., 1995; Van Acker, Vanhoyweghen, Persoons, & Vangrunderbeek, 2005; Zhu, Zeng, Tao, Yang, & Cui 1993), as well as the influence of hard-phase particle shape (Amado, Tobar, Alvarez, Lamas, & Yáñez, 2009; Huang et al., 2004; Nurminen et al., 2009).

References

Amado, J. M., Tobar, M. J., Alvarez, J. C., Lamas, J., & Yáñez, A. (2009). Laser cladding of tungsten carbides (Spherotene®) hardfacing alloys for the mining and mineral industry. *Applied Surface Science, 255*(10), 5553–5556.

Ariely, S., Bamberger, M., Hügel, H., & Schaaf, P. (1995). Phase investigation in laser surface alloyed steels with TiC. *Journal of Materials Science, 30*(7), 1849–1853.

Ayers, J. D. (1984). Wear behavior of carbide-injected titanium an aluminium alloys. *Wear, 97*(3), 249–266.

Ayers, J. D., & Bolster, R. N. (1984). Abrasive wear with fine diamond particles of carbide-containing aluminium and titanium alloy surfaces. *Wear, 93*(2), 193–205.

Bachmann, F., Loosen, P., & Poprawe, R. (Eds.). (2007). *High power diode lasers – technology and applications*. Springer Verlag.

Backes, G., Kelbassa, I., Weisheit, A., Wissenbach, K., & Gasser, A. (2010). Laser additive manufacturing. *Laser Technik Journal, 7*(2), 58–63.

Berger, L.-M., Thiele, S., Vuoristo, P., Mäntylä, T., Keller, H., Proß, E., & Scholl, R. (2002). Titanium carbide-based powders and coatings-compositions, processability and properties. In E. Lugscheider (Ed.), *Proc. Int. Thermal Spray Conf. March 4–6, 2002, Essen, Germany*, (pp. 727–732). Düsseldorf: DVS-Verlag.

Berns, H. (Ed.). (1998). *Hartlegierungen und Hartverbundwerkstoffe: Gefüge, Eigenschaften, Bearbeitung, Anwendung*. Berlin etc: Springer.

Beyer, E., & Wissenbach, K. (1998). *Oberflächenbehandlung mit Laserstrahlung, Laser in Technik und Forschung*. G. Herziger, & H. Weber (Eds.). Berlin etc: Springer.

Beyer, E., Nowotny, S., Brueckner, F., Hillig, H., & Techel, A. (2011). New industrial systems for high performance laser cladding. *LIA Today, 19*(4), 18–19.

Bouaifi, B., Gebert, A., & Heinze, H. (1993). Plasma-Pulver-Auftragschweißen zum Verschleißschutz abrasiv beanspruchter Bauteile mit Kantenbelastung. *Schweissen and Schneiden, 9*, 506–509.

Bouaifi, B., Draugelates, U., & Gebert, A. (2004). Standzeitverbesserung durch Einsatz vanadinkarbidhaltiger Nickelbasis-Schutzschichten. *HTM - Journal of Heat Treatment and Materials, 59*(5), 329–334.

Brückner, F., Nowotny, S., Riede, M., Lepski, D., & Beyer, E. (2010). Generation of high-precision metallic 3D structures with brilliant lasers. *Proc. of Int. Laser Symposium Fiber & Disc, Dresden, October 5–6, 2010*.

Brunet, P., Esnault, F., Maybon, G., & Perrier de la Bathie, R. (1986). Method and device for producing refractory materials by induction, EP 238 425, filed 13 March, 1986, granted 14 August, 1991; US 4,723,996, granted 9 February, 1988.

Corbin, S. F., & Wilkinson, D. S. (1994). Influence of matrix strength and damage accumulation on the mechanical response of a particulate metal matrix composite. *Acta Metallurgica et Materialia, 42*(4), 1329–1335.

Edwards, R., & Raine, T. (1953). The solid solubilities of some stable carbides in cobalt, nickel, and iron at 1250°. *Plansee Proceedings, 1952*, 232–243.

Emamian, A., Corbin, S. F., & Khajepour, A. (2011). The influence of combined laser parameters in-situ formed TiC morphology during laser cladding. *Surface and Coatings Technology, 206*(1), 124–131.

Eschnauer, H. R. (1975). Pulverförmige Hartstoffe – eine Übersicht für Beschichtungsverfahren. *DVS-Berichte, 37*, 33–38.

Eschnauer, H. (1980). Hard material powders and hard alloy powders for plasma surface coating. *Thin Solid Films, 73*(1), 1–17.

Eschnauer, H., & Lugscheider, E. (1991). Fortschritte beim Thermischen Spritzen. *Metall, 45*(5), 458–466.

Ettmayer, P., Kolaska, H., Langauer, W., & Dreyer, K. (1995). Ti(C, N) cermets – metallurgy and properties. *International Journal of Refractory Metals and Hard Materials, 13*(6), 343–351.

Freitag, I., Zellmer, H., Schöne, W., Golla, D., & Welling, H. (1993). In W. Waidelich (Ed.), *Diode-pumped single frequency high power Nd:YAG system, lasers in engineer* (pp. 17–20). Springer Verlag.

Gassmann, R., Nowotny, S., Luft, A., & Reitzenstein, W. (1992). Laser cladding of hard particles rich alloys. *Proc. ICALEO'92, int. congress on applications of lasers and electro-optics, SPIE, October 1992, Orlando, FLA, USA* (pp. 288–300).

Gassmann, R. C. (1996). Laser cladding with (WC+W_2C)CoCrC and (WC+W_2C)NiBSi composites for enhanced abrasive wear resistance. *Materials Science and Technology, 12*, 691–696.

Gebert, A., Heinze, H., & Wesling, V. (2004). Entwicklung vanadincarbidhaltiger Schweißzusatzwerkstoffe auf Nickelbasis zum Schutz gegen Verschleiß und Korrosion. *Schweissen & Schneiden, 56*, 271–275.

Giesen, A. (2005). Thin disk lasers – power scalability and beam quality. *Laser Technik Journal, 2*(2), 42–45.

Gnanamuthu, D. S. (1974). Cladding, US 3,952,180, filed 4 December, 1974, granted 20 April, 1976.

Gnanamuthu, D. S. (1980). Laser surface treatment. *Optical Engineering, 19*(5), 783–793.

Griffith, M. L., Keicher, D. L., Romero, J. T., Smugeresky, J. E., Atwood, C. L., Harwell, L. D., & Greene, D. L. (1996). Laser engineered net shaping for the fabrication of metallic components. Amer. Soc. Mechan. Engineers ASME, Metals Division. *Advanced Materials: Development, Characterization, Processing, and Mechanical Behaviour, 74*, 175–176.

Grünenwald, B., Shen, J., Dausinger, F., & Nowotny, S. (1992). In B. L. Mordike (Ed.), *Laser cladding with a heterogeneous powder mixture of WC/Co and NiCrBSi, laser treatment of materials* (pp. 411–418). DGM Informationsgesellschaft Verlag.

Herrera, Y. (1998). Microstructural characterization of vanadium carbide laser clad coatings. *Surface and Coatings Technology, 108–109*, 308–311.

Holleck, H. (1981). Ternäre Karbidsysteme der hochschmelzenden Übergangsmetalle – Teil 1. *Metall, 35*(10), 999–1004.

Hougardy, H. (1931). Beitrag zur Erkenntnis des Systems Eisen-Kohlenstoff-Vanadin. *Archiv für das Eisenhüttenwesen, 4*(10), 497–503.

Huang, S. W., Samandi, M., & Brandt, M. (2004). Abrasive wear performance and microstructure of laser clad WC/Ni layers. *Wear, 256*(11–12), 1095–1105.

Jiang, W., & Molian, P. (2001). Nanocrystalline TiC powder alloying and glazing of H13 steel using a CO_2 laser for improved life of die-casting dies. *Surface and Coatings Technology, 135*(2–3), 139–149.

Kathuria, Y. P. (2001). Nd-YAG laser cladding of Cr_3C_2 and TiC cermets. *Surface and Coatings Technology, 140*(3), 195–199.

Krastel, K. (2009). Fiber lasers – a universal tool for industrial applications. *Proc. of 5th International Workshop on Fiber Lasers, Dresden, September 30–October 01, 2009*.

Krause, V., Treusch, H.-G., Beyer, E., & Loosen, P. (1992). In B. L. Mordike (Ed.), *High power laser diodes as a beam source for materials processing, laser treatment of materials* (pp. 27–32). DGM Informationsgesellschaft Verlag.

Kumar, S., & Goswami, G. L. (2006). Wear behaviour of various Ni-based laser clad materials. *Lasers in Engineering, 16*, 305–315.

Lassner, E., & Schubert, W.-D. (1999). *Tungsten: Properties, chemistry, technology of the element, alloys, and chemical compounds*. New York: Kluwer Academic/Plenum Publishers.

Liang, G. Y., Wong, T. T., MacAlpine, J. M. K., & Su, J. Y. (2000). A study of wear resistance of plasma-sprayed and laser-remelted coatings on aluminium alloy. *Surface and Coatings Technology, 127*(2–3), 233–238.

Linke, P., Weiss, K.-H., & Nutsch, G. (2003). Neue Technologie zur Herstellung von Wolframschmelzkarbid. *Materialwissenschaft und Werkstofftechnik, 34*(7), 613–617.

Liu, W., & DuPont, J. N. (2003). Fabrication of functionally graded TiC/Ti composites by laser engineered net shaping. *Scripta Materialia, 48*(7), 1337–1342.

Löschau, W., Juch, K., & Reitzenstein, W. (1992). Alloying and dispersion of TiC base hard particles into tool steel surfaces using a high power laser. *Proc. of ECLAT'92* (pp. 281–285).

Luft, A., Techel, A., & Nowotny, S. (1995). Microstructures and dissolution of carbides occurring during the laser cladding of steel with tungsten carbide reinforced Ni- and Co- hard alloys. *Practical Metallography, 32*(5), 235–247.

Mazumder, J., & Singh, J. (1986). Laser surface alloying and cladding for corrosion and wear. *High Temperature Materials and Processes, 7*, 101–106.

Mazumder, J., Dutta, D., Kikuchi, N., & Ghosh, A. (2000). Closed loop direct metal deposition: art to part. *Optics and Lasers in Engineering, 34*, 397–414.

Mordike, B. L. (Ed.). (1992). *Laser treatment of materials*. DGM Informationsgesellschaft Verlag.

Nowotny, S., & Kunzmann, E. (1988). Improved wear properties of thermally sprayed coatings by post-treatment using CO_2 lasers. *Schmierungstechnik, 19*(6), 166–169.

Nowotny, S., Techel, A., Luft, A., & Reitzenstein, W. (1993). Microstructure and wear properties of laser clad carbide coatings. *Proc. Int. Congr. on Applications of Lasers and Electro-Optics, ICALEO1993, in SPIE 2306* (pp. 985–993).

Nowotny S., & Scharek S. (2000). Machining head and process for the surface machining of workpieces by means of a laser beam, DE 199 09 390, C1, filed March 4, 1999, granted November 9, 2000; US 6,316,744, B1, granted November 13, 2001.

Nowotny, S., Scharek, S., Kempe, F., & Beyer, E. (2003). COAXn modular system of powder nozzles for laser beam build-up welding. In: *Proc. ICALEO'2003, LMP section* (pp. 190–193). LIA.

Nowotny, S., Münster, R., Scharek, S., & Beyer, E. (2010). Integrated laser cell for combined laser cladding and milling. *Emerald's Assembly Automation, 30*(1), 35–39.

Nowotny, S. (2011). Current use of laser technology for build-up welding applications. *Surface Engineering, 27*(4), 231–233.

Nowotny, S., Spatzier, J., Kubisch, F., Scharek, S., Ortner, J., & Beyer, E. (2012). Repair of erosion defects in gun barrels by direct laser deposition. *Journal of Thermal Spray Technology, 21*(6), 1173–1183.

Nurminen, J., Näkki, J., & Vuoristo, P. (2009). Microstructures and properties of hard and wear resistant MMC coatings deposited by laser cladding. *International Journal of Refractory Metals Hard Materials, 27*(2), 472–478.

Pawlowski, L. (1999). Thick laser coatings: a review. *Journal of Thermal Spray Technology, 8*(2), 279–295.

Richter, A., Nowotny, S., Naumann, T., & Beyer, E. (1999). Auftragschweißen mit dem Hochleistungs-Diodenlaser. *LaserOpto, 31*(3), 63–66.

Schreiber, F. (2002). Verschleißschutz durch Einsatz von Wolfram-Schmelzcarbid. *Ziegelindustrie International, 55*(6), 12–17.

Schubert, S. (Ed.). (1992). *Surface treatment using CO_2 lasers*. VDI Technologiezentrum, Physikalische Technologien.

Sievers, E. R. (Ed.). (1994). *Materials processing with high-power CO_2 lasers*. VDI Technologiezentrum Physikalische Technologien.

Sun, R. L., Yang, D. Z., Guo, L. X., & Dong, S. L. (2001). Laser cladding of Ti-6Al-4V alloy with TiC and TiC+NiCrBSi powders. *Surface and Coatings Technology, 135*(2–3), 307–312.

Techel, A., Luft, A., Müller, A., & Nowotny, S. (1995). Production of metal-like wear protection coatings by CO_2 laser cladding. *Optical and Quantum Electronics, 27*, 1313–1318.

Techel, A. (2001). *Gefüge und Eigenschaften von hartstoffverstärkten Laserstrahlbeschichtungen auf Stahl und Titan*. Stuttgart: Fraunhofer IRB Verlag.

Techel, A., Berger, L.-M., & Nowotny, S. (2007). Microstructure of advanced TiC-based coatings prepared by laser cladding. *Journal of Thermal Spray Technology, 16*(3), 374–380.

Theiler, C., Seefeld, T., & Sepold, G. (2001). Microstructure and properties of graded metal-carbide claddings. In: *Ceramic Transactions: Vol. 114. Proc. 6th Int. Symp. Functionally Graded Mater.* (pp. 127–134).

Toyserkani, E., Khajepour, A., & Corbin, S. (2005). *Laser cladding*. CRC Press LLC.

Tuominen, J. (2009). *Engineering coatings by laser cladding-the study of wear and corrosion properties*. Tampere University of Technology. Thesis.

Van Acker, K., Vanhoyweghen, D., Persoons, R., & Vangrunderbeek, J. (2005). Influence of tungsten carbide particle size and distribution on the wear resistance of laser clad WC/Ni coatings. *Wear, 258*(1–4), 194–202.

Waidelich, W. (Ed.). (1993). *Lasers in engineering*. Springer Verlag.

Weerasinghe, V. M., & Steen, W. M. (1983). Laser cladding by powder injection transport phenomena in materials processing. *ASME*, 15–23.

Weiler, S. (2010). Fiber and disk technology for high power picosecond lasers. In: *Proc. Int. Laser Symp. Fiber & Disc, Dresden, October 5–6, 2010*.

Zhu, B., Zeng, X., Tao, Z., Yang, S., & Cui, K. (1993). Coarse cemented WC particle ceramic-metal composite coatings produced by laser cladding. *Wear, 170*(2), 161–166.

1.19 Joining Cemented Carbides

Rosa M. Miranda, UNIDEMI, Departamento de Engenharia Mecânica e Industrial, Faculdade de Ciências e Tecnologia, Universidade Nova de Lisboa, Caparica, Portugal

Glossary

Brazing It is a joining process, in which two materials are joined by heating them with a filler metal with a low melting temperature below 450 °C

Continuous wave (CW) and pulsed wave (PW) These are the two basic laser working modes where the laser radiation can be produced in either continuous or pulsed mode

Diffusion bonding It is a solid state joining process in which the joint is produced by short-distance diffusion at a temperature below the melting temperature of base materials under a static load

Metal inert gas (MIG) This is a fusion welding process using a consumable electrode in an inert gas atmosphere

Metal active gas (MAG) This is a fusion welding process using a consumable electrode in an active gas atmosphere

Soldering is a joining process, in which two materials are joined by heating them with a filler metal with a melting temperature above 450 °C but below the fusion temperature of materials being joined

Shielding gas It is the protective gas used in fusion welding to prevent the molten metal and the heat-affected zone to contact air environment and oxidize

Tungsten inert gas (TIG) It is a fusion welding process using a nonconsumable electrode in tungsten in an inert gas atmosphere

tw This is the horizontal distance between the laser spot center and the weld line measured on the upper surface of the material

1.19.1 Introduction

Welding and joining encompass a large diversity of technological processes that can be considered for component or structure manufacturing, maintenance and repair. In the manufacturing stage, they allow to produce complex components difficult to make in monolithic shapes or with different properties within the same component which is more frequent when cemented carbides are concerned. A situation often required in tool industry involves producing bimetallic components made of a cemented carbide (active part) joined to a ductile material, such as steel, which is able to accommodate mechanical stresses and vibrations.

According to the International Institute of Welding classification, welding and joining processes can be divided into four major groups: mechanical assembly, fusion processes, solid-state processes and brazing and soldering.

http://dx.doi.org/10.1016/B978-0-08-096527-7.00019-2

Mechanical assembly involves the use of fasteners, bolts, nuts, screws and rivets in nonpermanent joints easy to substitute or repair.

Fusion processes are the most common in welding construction. These involve melting of both materials to weld, with or without filler material, followed by solidification. The heat to melt can be supplied by different types of energy: electrical (as in arc welding), chemical or radiation (as in laser beam).

In solid-state processes, none of the parts to weld undergo melting and the joining occurs by interfacial phenomena such as atomic interdiffusion. Unlike the previous fusion welding processes, in solid-state processes, no significant phase transformations are induced and thus, the volume variations and residual stresses can be negligible.

Brazing and soldering use filler materials with a melting temperature lower than that required for the pieces to join and the heat is supplied externally, so that the joint is produced in liquid–solid phase where the filler material melts and the parts to be joined do not go into fusion. Short-distance diffusion ensures metallic continuity between the parts (Welding Handbook).

Cemented carbides have unique properties, which make them suitable for applications requiring high wear resistance, such as in tool manufacturing. WC–Co type finds application in automotive industry parts, in tools and dies for mining and geological exploitation as well as in gas and oil prospecting. High hardness values, especially at high temperature, are due to the presence of tungsten carbide particles of controlled shape and dimensions in a binder matrix usually of cobalt. Alloying elements are added for specific purposes (Brookes, 1996). As an example, tantalum is added to inhibit grain growth of the carbides and increase hardness at high temperature; chromium improves corrosion resistance and titanium forms carbides that prevent chip's adherence to cutting tools (Figure 1) (Stevenson, 1984). Due to their mechanical properties, namely, low ductility, high tensile strength and hardness, they are not the best materials to weld or join by fusion in liquid–solid phase or in solid state like other high-resistance composites.

The high cost of cemented carbide-based components and the limited availability of some elements such as tungsten and cobalt demand for combining these to other materials in order to produce components with different, sometimes incompatible, properties.

When selecting a welding process several criteria have to be considered, the most important being the two material properties, dimensions and joint resistance required. As far as materials properties are concerned, their chemistry, microstructure and mechanical characteristics are fundamental.

It is clear that cemented carbides require specific joining processes, mainly those involving low heat inputs, minimizing phase transformations and excessive residual stresses. So, from the large diversity of existing welding processes, this chapter will focus on mechanical assembly, diffusion bonding, brazing and soldering and finally laser welding, including hybrid laser/arc welding. The selection of joining processes was made on the basis of in-use in industry and state-of-the-art research.

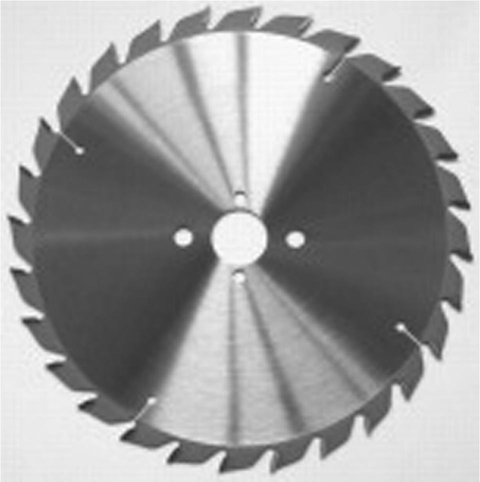

Figure 1 Saw blade.

1.19.2 Joining Processes

1.19.2.1 Mechanical Assembly

Mechanical fastening is the simplest way to put two pieces together and is often preferred to other methods because it is easy to perform, replace, maintain and repair; easy to adjust to new component designs requiring movable joints; and not expensive.

An industrial example of mechanical assembly can be found in cutting tools where the active part in cemented carbide is clamped to the steel holder more ductile, less hard and less expensive.

Figure 2 shows examples of mechanically clamped WC inserts in cutting tools.

These inserts can have different geometries and dimensions according to the tool characteristics as depicted in the above figure.

The major advantage of mechanical clamping lies in the facility to replace a damaged element, but it is limited in geometry. In addition, for several industrial components such as dies, punches, plungers, seal rings, valves, high-temperature devices, etc. with complex shapes, where several cemented carbides elements need to be joined, where the cemented carbide is a small part of a whole piece, or even for cemented carbides components repair, mechanical clamping can be inadequate. In these cases, more permanent long lifetime components are required (Schwartz, 1990).

The most common method of mechanical fastening uses bolts, nuts, screws and rivets inserted into holes in the parts to clamp. These holes can be drilled or produced during powder processing of cemented carbide. Nevertheless, holes are weak points in the structure, prone to stress concentration and strength reduction. So, proper treatment is required to induce compressive stresses on the hole surface and guarantee uniform dimensional characteristics.

Most mechanical assemblies are structural (load-bearing) components and may be subjected to shear and tensile stresses, so that the joint has to be designed to resist these stresses.

1.19.2.2 Diffusion Bonding

Diffusion bonding is a solid-state process where the parts are placed in close contact under an applied load at a temperature o– while maintaining a low risk of flammability of about 0.5 T_m, where T_m is the melting temperature of the base material. The overall strength of the joint is achieved by plastic deformation of the interface and atomic diffusion across it.

Filler material can be added to improve materials compatibility in dissimilar joints. Interlayers are usually selected because of the existing differences in linear expansion thermal coefficients, especially in butt joints. These differences in the thermal conductivity and thermal expansion coefficients induce distortions and residual stresses. The use of a ductile interlayer allows accommodating mechanical stresses reducing residual stress level.

Since this is a thermally activated process, it is usually slow and time consuming and the applied pressures can lead to crack formation in the cemented carbides. Therefore, these are operational parameters to control. On increasing the temperature and time of the weld thermal cycle, diffusion is promoted and elements diffuse potentially creating undesirable precipitates or inclusions on the interface that act as crack nucleation sites weakening the joint. Bonding temperature determines to a great extent diffusion processes across the bonding interface, being a more influential variable than the bonding time (Barrena, Gómez de Salazar, & Matesanz, 2010).

Figure 2 Examples of cutting tools with different mechanically clamped WC inserts.

Interlayers play a key role as far as weld resistance and soundness are concerned and these are selected on the basis of the materials to join, the overall mechanical and corrosion resistances and maximum working temperature. Barrena et al. (Barrena, Matesanz, & Gomez de Salazar, 2009) reported the effect of temperature and time when diffusion welding WC–Co to a 90MnCrV8 cold work tool steel with a 20 μm interlayer of Ni–Cu electroplated. The same research team joined WC–Co to Ti6Al4V using silver as interlayer and WC–Co to high-strength steel (Gomez de Salazar, Barrena, Merino, & Matesanz, 2006). Other research teams used nickel, cobalt, or even steel, which may be used preplaced between the parts before being heated.

The parts are introduced in a furnace under controlled atmosphere and temperature–time cycle to prevent chemical reaction with surrounding atmosphere and avoid rapid phase transformations.

Diffusion bonding is a commonly used industrial process due to the high resistance of the joints.

1.19.2.3 Brazing and Soldering

Brazed joints, especially for tool manufacturing applications, are also widely used in industry in furnace (continuous or discontinuous) under controlled atmosphere or in vacuum. A recent variant is to use laser beam as the heating source in a more precise and highly localized process.

The process consists of preplacing an interlayer with a melting temperature below that of the base materials between the parts. The application of external heat to melt the interlayer promotes the atomic diffusion in the interface, joining the parts.

Brazing has been proved to be a good approach for cemented carbides with low binder concentration or silicon nitride. AgCuTi active braze has been employed as filler metal to reduce thermally induced stresses due to the fact that both silicon nitride and cemented carbide cannot be wetted by conventional brazes (Martens, Tillrnann, Lugscheider, & Ziegler, 1996). Microstructural and mechanical analyzes revealed that interface interactions are significant for the joint quality. Although the use of interlayers is an effective approach to reduce thermally induced stresses in bimaterial joints, the influence of microstructural effects within the joint cannot be neglected. Copper- and nickel-based brazing alloys are the most used in industry for joining WC–Co to steel (Xu, 2011).

Brazing cemented carbide to carbon steel with multiple layers of Cu and Ni alloys as insert metal was investigated (Lee, Kwon, & Jung, 2006), and they showed that, when brazing time increased, brittle intermetallic phases and coarsening of WC grains were produced, with degradation of the joint strength. Joining WC-Co to carbon steel using double-layered Cu alloy and amorphous Ni alloy as inert metal was also investigated with an oil cooling method after brazing (Lu & Kwon, 2002). No cracks and voids were reported and the authors concluded that double-layered insert metals and oil cooling minimized the residual stress near the bonded zone after brazing. The shear strength of the joints decreased with increasing bond time eventually due to the shape of the interface, formation and growth of brittle intermetallic compounds, and coarsening of WC particles near the bond zone. The maximum shear strength of the joints was 310 MPa under 0.6 ks bonding time for WC with 8% Co. Brazing WC–Co to stainless steel with Cr–Ni interlayers was also researched (Lee, Kwon, & Jung, 2004).

1.19.2.4 Laser Welding

1.19.2.4.1 Basics of Laser Welding

The basic principle of laser welding is that a laser beam radiation produced in a resonator cavity is focused on the material surface through an optical system. Figure 3 presents a schema of the process. The effectiveness of the beam coupling depends on the laser wavelength and the optical properties of the material including the surface condition. Polished surfaces are more reflective of laser light and must be avoided either by roughening the surface or by darkening it (Steen, 2003).

Two distinct welding modes have been identified in laser welding: conduction and keyhole (Duley, 1999).

The absorption of the laser beam increases if the energy is transferred to the material, so that the temperature increases according to classical thermal conduction theory. If the energy absorbed is below a threshold value, the material conducts the heat into adjacent regions leading to a wide and low-penetrant molten pool similar to tungsten inert gas welding. This is a conduction laser welding mode observed in highly reflective materials or low-power lasers. If the energy absorbed by the material is above the threshold value, which is roughly the energy required to melt a unit volume of material, it evaporates forming highly absorbent plasma which transmits the heat into depth. This column of plasma is sustained by the surrounding molten metal. The

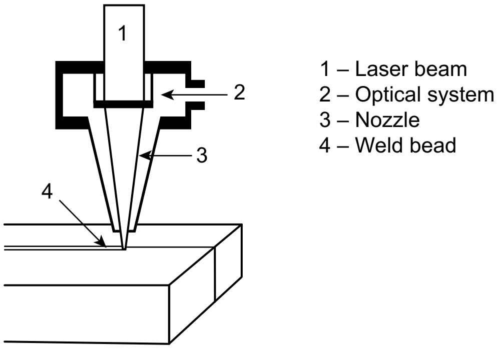

Figure 3 Schema of the basic principle of laser welding.

resultant weld has a small aspect ratio, that is, the weld width to the weld penetration ratio is less than 1. Figure 4 shows a schema of the conduction and keyhole laser welding modes. The molten metal motion is ruled by the forces exerted on the pool, namely, the Marangoni effect, which depend on the existing phase density and the thermal gradients in the weld pool (Duley, 1999).

Among the operating factors influencing the shape and properties of the molten pool and, consequently the properties of the weld, absolute and relative factors can be identified. The absolute factors are related to:

- laser beam: wavelength, power, power distribution, operating mode, spot size;
- materials: chemical composition, thermophysical properties, microstructure, geometry and dimensions;
- shielding gas: composition, flow rate, flow configuration; and
- filler material: chemical composition, thermophysical properties, type and dimensions.

The relative factors are:

- relative position of laser beam, welding materials, shielding gas and filler material and
- welding speed, filler material and feeding rate.

1.19.2.4.2 Types of Lasers

The two most industrially used lasers are carbon-dioxide and Nd:YAG lasers (Ready, 2001). The former is a gas laser emitting at a wavelength of 10.6 μm that has high output powers, efficiencies around 20% (higher than Nd:YAG lasers), good beam quality, and is easy to focus but requires complex and robust manipulation systems since the light cannot be transmitted via optical fiber. These lasers have high output powers (up to 50 kW).

Nd:YAG lasers are solid-state lasers emitting at 1.06 μm in a range of wavelengths where the metallic materials are most absorbent, that is, for the same weld penetration, the required power is lower for Nd:YAG laser than for CO_2 laser. However, they have poor energy conversion efficiency (around 5%), limited output powers

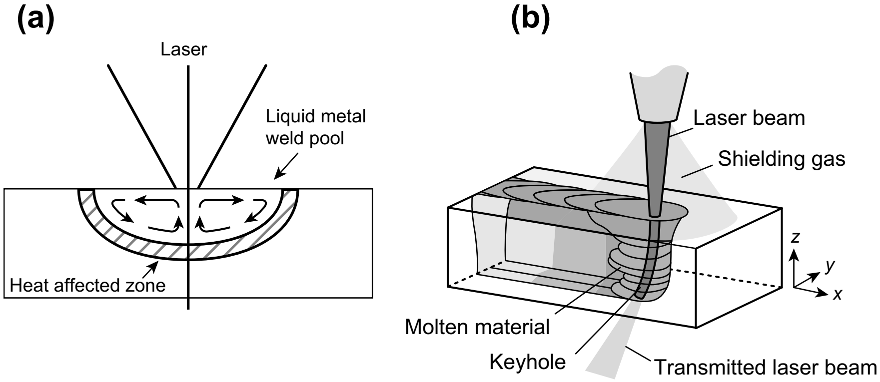

Figure 4 Schema of laser welding modes: a) conduction; b) keyhole.

and high running costs specially due to maintenance. The possibility of being transported via optical fiber improves the system flexibility.

Diode lasers and diode pumped lasers had innovative developments in the past decades. They use the same principles as a diode so that they are classified as solid-state lasers.

Disk lasers are a new generations of solid-state lasers. The active element of disk lasers is a thin disk of YAG crystal, 150–300 μm thick and approximately 12–15 mm in diameter. Usually, the crystal is doped with ytterbium (Yb:YAG) and the disk is mounted on a copper radiator dissipating the heat produced during lasing with a wall plug efficiency of about 25%.

Together with disk lasers, multikilowatt fiber lasers emerged in the past few years and have been introduced for materials processing up to 30 kW (Quintino et al., 2007). High-power fiber lasers have multiple advantages, including high efficiency, highly compact design with minimum footprint area, good beam quality with small beam focus diameter, and a robust setup for mobile applications.

The active medium is the core of a silica fiber doped with a rare earth: erbium, ytterbium, neodymium or thallium, the active fiber. The pumping process uses multimode diodes rather than diode bars. The laser beam is emitted longitudinally along the fiber. Two Bragg gratings inscribed on the fiber limit the wavelength of the emitted beam. The resonator cavity is constituted by the fiber itself, either the core, as in single-mode lasers, or the inner cladding around this core, as in double-clad fiber laser. The outer cladding is made of a polymeric material with low refractive index to minimize attenuation. The resulting laser beam is essentially diffraction limited and when fitted with an integral collimator, produces a beam that is extremely parallel.

Typically, ytterbium-doped multiclad fiber has an emission wavelength of 1.07–1.08 μm. Fiber lasers can be modular, and although the beam is no longer single mode, the resulting beam quality is better than for the same power in Nd:YAG lasers. A 6 kW laser can deliver a beam via a 200–300 μm fiber. Ytterbium fiber laser has a wall plug efficiency of 16–20%.

1.19.2.4.3 Laser Welding of Cemented Carbides

Laser welding has been extensively studied by several R&D groups (Deng & Wang, 1996) due to its particular characteristics, namely, very low heat input and high precision. Both CO_2 and Nd:YAG lasers have been researched to join cemented carbides and the effect of weld thermal cycle on mechanical properties (Costa, Miranda, & Quintino, 2006, 2004; Miranda et al., 2008). It was seen that Nd:YAG in continuous wave (CW) mode gave the best results, although there was a significant drop in mechanical resistance.

The high energy density allows confining the weld metal to a localized narrow zone with small amount of heat being conducted away from the molten pool, leading to a narrow heat-affected zone. The process is very precise and clean and the resulting phase transformations are minimized due to the rapid weld thermal cycle.

Laser welding has several characteristics adequate for welding cemented carbides; the most relevant being the high precision and the low heat input, which minimize microstructural modifications, residual stresses, and distortions (Pelletier & Robin, 1993). Previous work (Barbatti, Garcia, Liedl, & Pyzalla, 2007; Costa, Quintino, & Greitmann, 2003; Sandig, Wiesner, Greitmann, & Deutschmann, 1995) showed that sound welds of WC–Co to steel can be produced by an adequate control of both the heat input and the horizontal focal point position (tw). This parameter is the distance between the center of the laser beam spot and the materials interface, or the weld line, measured on the material's upper surface. In similar welds, the laser beam is always focused on the weld line, aiming at a homogeneous thermal cycle and dilution on both parts to be joined. In dissimilar welds, where the materials have distinct chemical and physical properties, namely, thermal conductivity and thermal expansion coefficient, it may be beneficial to shift laterally the laser beam to reduce the heat input in the material with limited capacity to accommodate thermal stresses induced by the weld thermal cycle. The heat input affects the phase transformations on heating and cooling. The horizontal focal point position affects dilution, that is, the amount of steel melted incorporated in the fusion zone, the maximum temperature, and the cooling rate in the cemented carbides. Considering heat transfer theory from Rosenthal, when the laser beam is positioned on the hardmetal/steel boundary ($tw = 0$ mm), the maximum temperature in the hardmetal is higher than when the laser beam interaction area is displaced to the steel side.

Overheating of the cemented carbides has two major effects:

1. Increase of cobalt volatilization, as it has a boiling temperature of 3143 K.
2. Increase of the carbon content in the weld metal. Tungsten carbide easily decomposes at high temperatures.
   Because both materials equally contribute to the formation of the fusion zone, carbon resulting from the

carbide decomposition migrates to the fusion zone, increasing the carbon equivalent. On cooling, this zone enriched in carbon transforms into martensite (Costa et al., 2006) and a poor-quality join is observed.

Several types of defects in laser weld of cemented carbides were identified and these were:

1. Misalignments: These are due to the different thermal expansion coefficients of the base materials. Hardmetal has a lower thermal expansion coefficient ($5.5–5.9 \times 10^{-6}$ k^{-1}) than steel (Brookes, 1996). To avoid this macrodefect, proper fixing has to be designed.
2. Excessive melt-through: This is usually due to the very high laser power and low travel speed.
3. Porosities: Pores are due to cobalt vaporization. Cobalt has a low boiling temperature and vaporizes at high energy densities.
4. Cracking in the hardmetal: Because the material has poor ductility and ability to accommodate thermal stresses, cracking can be observed because of both structural transformation and residual stresses. When observing the welds under the optical microscope, it was noticed that the shape of the weld metal is highly affected by the absorbed energy and the heat conduction mode. At high heat inputs, as those produced by the Nd:YAG laser in pulsed wave mode, the fusion zone presents a V shape, suggesting the welds were produced by conduction, whereas at lower heat inputs, as observed in CW Nd:YAG laser and in CO_2 laser, the fusion zone has a cylindrical shape, characteristic of a keyhole welding mode (Figure 5).

By observing a weld cross-section, it is seen that the fusion zone presents a cellular dendritic structure with a eutectic phase in the interdendritic spaces (Figure 6). The extent of this eutectic phase depends on the position of the laser beam (tw), interaction area, and on the hardmetal carbon content.

Solidification starts by epitaxy with iron in a cellular dendritic structure, due to the ratio between thermal gradient and solidification speed. Close to the hardmetal interface, carbon resulting from tungsten carbide decomposition migrates enriching the liquid phase in this element. On cooling, the liquid transforms into a eutectic mixture of a carbon-rich phase and austenite, which occupies interdendritic spaces of primary iron dendrites, with possible formation of complex intermetallic carbides (eta phase). Figure 7 shows the structures observed in different zones of a welded sample. Figure 8 shows qualitative analysis obtained by Energy Dispersive Spectroscopy (EDS) is the structure observed in the interface fusion zone/hardmetal for a K10 specimen (Costa et al., 2004).

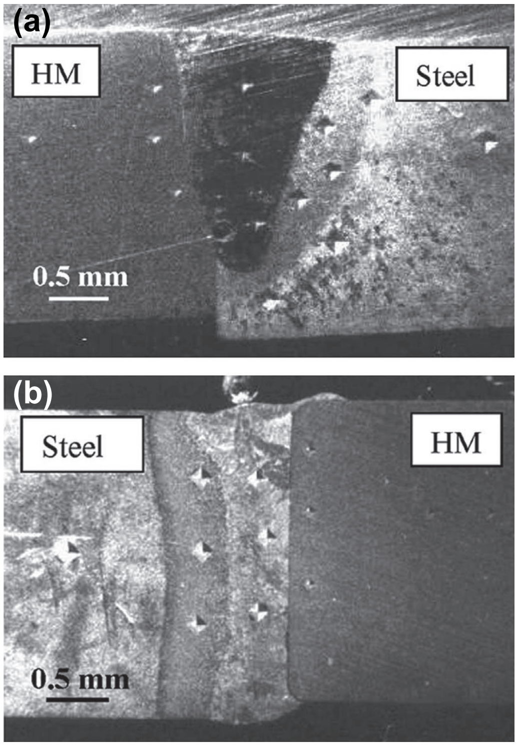

Figure 5 Weld beads geometry: (a) conduction mode and (b) keyhole mode. HM denotes Hardmetal in the figure.

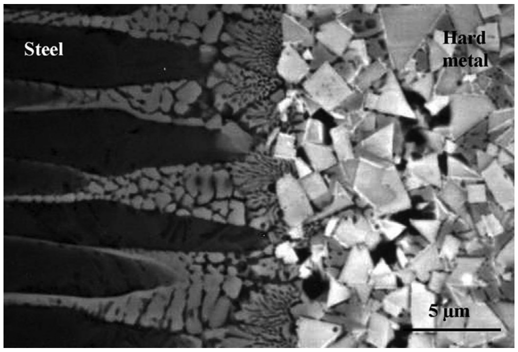

Figure 6 Scanning electron microscopic image of a CW Nd:YAG laser weld specimen showing dendrites formation in the weld bead and multiple carbides in the interdendritic spaces.

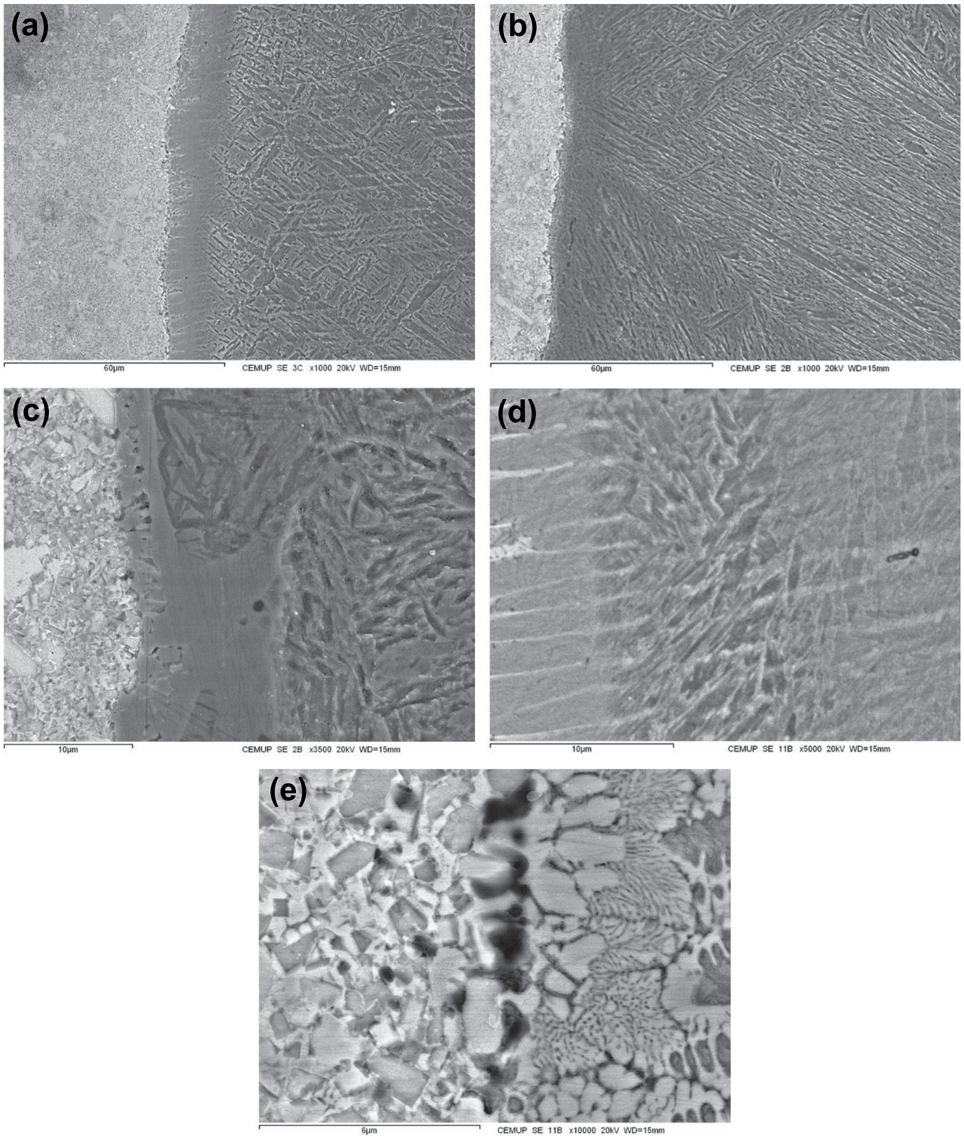

Figure 7 Microstructures observed in different zones of dissimilar welded samples. (a) K40 weld heat input, 40 J/mm; tw = 0.25 mm; preheating, 400 °C. (b) Fusion zone in K40 heat input, 44 J/mm; tw = 0.15 mm. (c) Same sample as in (b) at higher magnification. (d) Heat Affected Zone (HAZ) in K40 heat input, 40 J/mm; tw = 0.15 mm. (e) Fusion zone in K40 sample showing porosity in the fusion line. Heat input: 40 J/mm; tw = 0.15 mm.

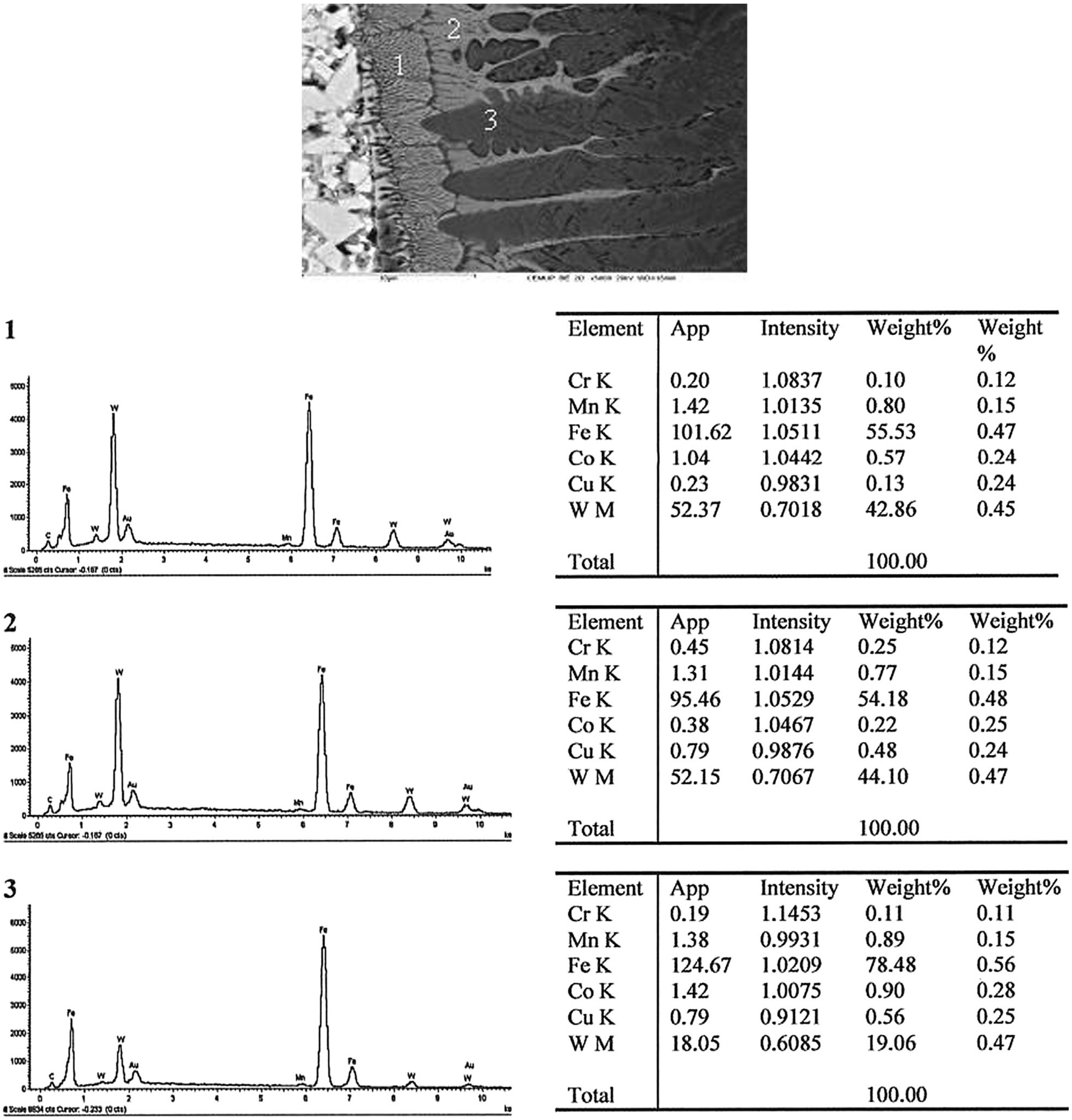

1

Element	App	Intensity	Weight%	Weight %
Cr K	0.20	1.0837	0.10	0.12
Mn K	1.42	1.0135	0.80	0.15
Fe K	101.62	1.0511	55.53	0.47
Co K	1.04	1.0442	0.57	0.24
Cu K	0.23	0.9831	0.13	0.24
W M	52.37	0.7018	42.86	0.45
Total			100.00	

2

Element	App	Intensity	Weight%	Weight%
Cr K	0.45	1.0814	0.25	0.12
Mn K	1.31	1.0144	0.77	0.15
Fe K	95.46	1.0529	54.18	0.48
Co K	0.38	1.0467	0.22	0.25
Cu K	0.79	0.9876	0.48	0.24
W M	52.15	0.7067	44.10	0.47
Total			100.00	

3

Element	App	Intensity	Weight%	Weight%
Cr K	0.19	1.1453	0.11	0.11
Mn K	1.38	0.9931	0.89	0.15
Fe K	124.67	1.0209	78.48	0.56
Co K	1.42	1.0075	0.90	0.28
Cu K	0.79	0.9121	0.56	0.25
W M	18.05	0.6085	19.06	0.47
Total			100.00	

Figure 8 Qualitative analysis obtained by EDS is the structure observed in the interface fusion zone/hardmetal for a K10 specimen in points 1, 2 and 3.

Hardness tests show a significant increase of hardness in the fusion zone, due to two main factors: the high cooling rate (characteristic of high-energy-density processes), which leads to martensitic structures, and the formation of complex carbides in the fusion zone (due to the presence of tungsten, iron and carbon), which have high hardness. Pulsed laser welding procedures produce a tungsten carbide detachment from the hardmetal, which flows to the melting pool with a consequent increase of the fusion zone hardness. The heat-affected zone in the steel side shows a supersaturated martensitic structure, while in the hardmetal side, hardness is in the range of 1600–1800 HV2, as observed in Figure 9.

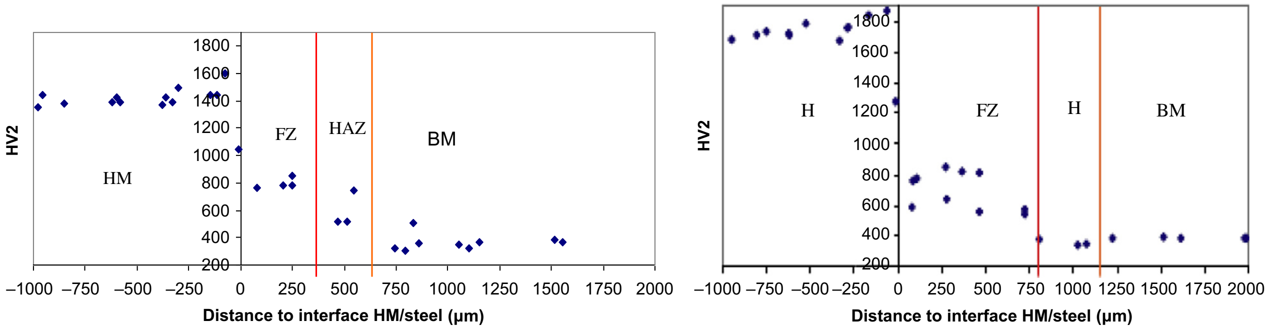

Figure 9 Vickers hardness profiles for two different samples welded with heat input of 40 J/mm. (a) K40 and (b) K10.

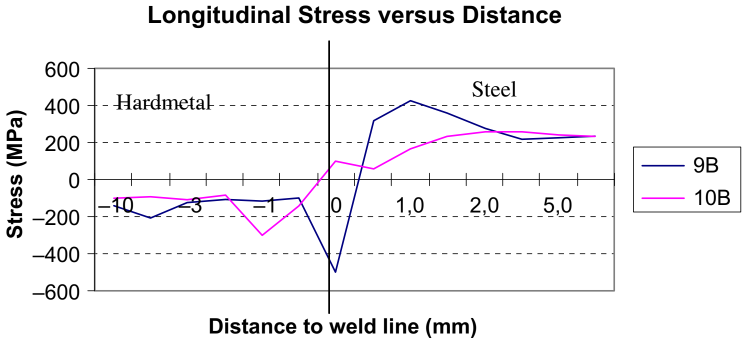

Figure 10 Evolution of residual stresses measured by X-ray diffraction for dissimilar welds of K40 samples welded with different welding parameters. 9B: heat input, 44 J/mm; tw = 0.2 mm; 10B: heat input, 40 J/mm; tw = 0.2 mm.

Residual stresses measured by X-ray diffraction in the longitudinal direction are plotted in Figure 10 for two samples welded in different conditions. These figures, however, have to be analyzed qualitatively, but a major indication is that hardmetal is subjected to compressive stresses, while the steel is under tensile stresses.

Figure 11 depicts the bending test results for the dissimilar joints involving K10 and K40 hardmetals, for the different lasers tested, showing the influence of the "tw" parameter on the maximum bending load. In all tested samples, fracture was observed in the hardmetal. In several welded specimens, fracture was observed around the load application area far from the weld bead ($\geq$1.5 mm). Fracture has never occurred in the heat-affected zone. Dissimilar welds involving K40 quality hardmetal showed a higher load than those involving K10 hardmetals, which is in agreement with base materials properties of hardmetals.

In fact, transversal bending stresses obtained according to ISO 3327 for hardmetals K10 and K40 from the manufacturers are 1600 and 2300 MPa, respectively. Maximum loads were attained for CW Nd:YAG laser when "tw" is in the range of 0.1–0.2 mm. CO_2 laser welds show an optimum load value for tw = 0.4 mm. However, for "tw" higher than 0.2 mm, bonding between base materials is reduced (Costa et al., 2004; Miranda et al., 2008).

The high load supported is probably related to a decrease in the residual stresses in the hardmetal, when the laser is moved more to the steel part.

Barbatti et al. (Barbatti et al., 2007) joined cemented carbides to steel with CW Nd:YAG laser using pre- and post heat treating minimizing defects as pores and cracks and reducing the amount of intermetallics, thus improving mechanical resistance.

Although laser welding is a well-established process in industry, it has still limited applications when applied to cemented carbides due to the high costs of the process.

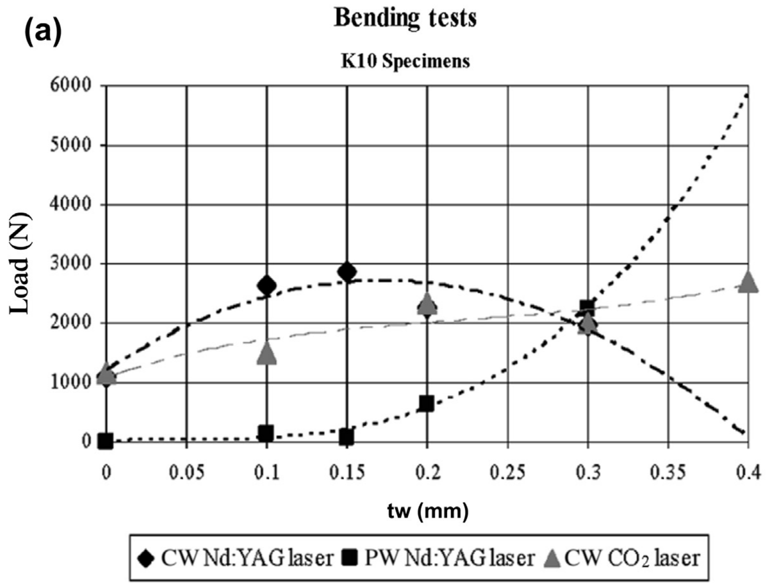

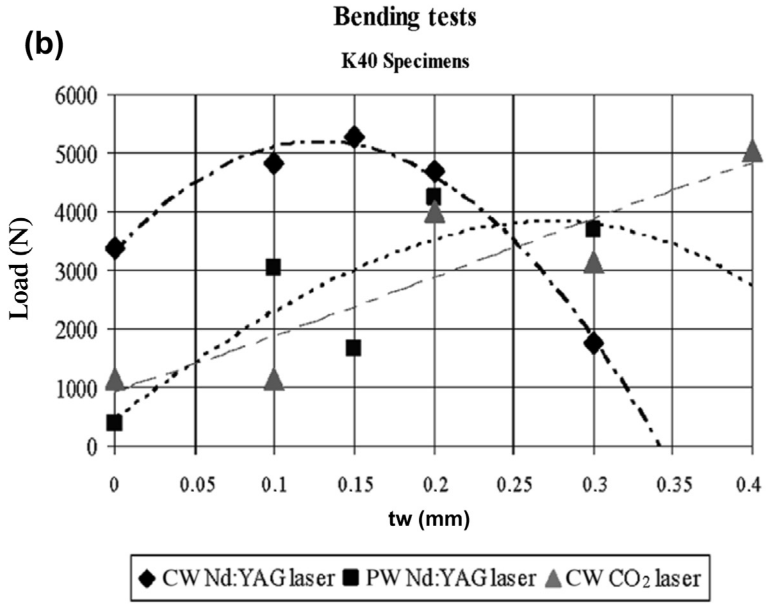

Figure 11 Bending test results. (a) K10 hardmetal and (b) K40 hardmetal.

Summary

Cemented carbides are widely used in increasing applications due to the particular characteristics they exhibit. Main weldability problems have been identified and discussed. Welding processes were presented, both the ones used in industry such as mechanical fastening, diffusion and brazing and recent research work specially for dissimilar welding of cemented carbides to steels. An intense research community works in developing and understanding basic phenomena associated with the use of interlayers and new welding procedures aiming to minimize residual stresses and to improve mechanical strength of joints at high temperature.

Aknowledgments

The author acknowledges the Portuguese Science and Technology Foundation for funding of TECDUR project, as well as colleagues L. Quintino and A. Costa.

References

Barbatti, C., Garcia, J., Liedl, G., & Pyzalla, A. (2007). Joining of cemented carbides to steel by laser beam welding. *Materialwissenschaft und Werkstofftechnik, 38*(11), 907–914.

Barrena, M. I., Gómez de Salazar, J. M., & Matesanz, L. (2010). Interfacial microstructure and mechanical strength of WC–Co/90MnCrV8 cold work tool steel diffusion bonded joint with Cu/Ni electroplated interlayer. *Materials and Design, 31*(7), 3389–3394.

Barrena, M. I., Matesanz, L., & Gomez de Salazar, J. M. (2009). Al_2O_3/Ti6Al4V diffusion bonding joints using Ag–Cu interlayer. *Material Characterization, 60*, 1263–1267.

Brookes, K. (1996). *World directory and handbook of hardmetals and hard materials* (6th ed.). International Carbide Data. Metal Powder Industry, UK.

Costa, A., Quintino, L., & Greitmann, M. (2003). Laser beam welding hard metals to steel. *Journal of Materials Processing Technology, 141*, 163–173.

Costa, A., Quintino, L., & Miranda, R. (November 2004). Microstuctural aspects of laser dissimilar welds of hardmetals to steels. *Journal of Laser Applications, 16*(4), 206–211.

Costa, A., Miranda, R., & Quintino, L. (2006). Materials behaviour in laser welding of hardmetals to steel. *Materials and Manufacturing Processes, 21*, 457–463.

Deng, S.-S., & Wang, S. C. (1996). *Study of laser molten welding of cemented carbides and steel*. In *Proc. SPIE laser processing of materials and industrial applications, 2888*, 185.

Duley, W. W. (1999). In *Laser welding*. John Wiley & Sons, Inc.

Gomez de Salazar, J. M., Barrena, M. I., Merino, N., & Matesanz, L. (2006). Diffusion welding of WC–Co (hardmetal)/high strength steels. *Materials Science Forum, 514–516*, 1526–1530.

Lee, W. B., Kwon, B. D., & Jung, S. B. (2004). Effect of bonding time on joint properties of vacuum brazed WC–Co hard metal/carbon steel using stacked Cu and Ni alloy as insert metal. *Materials Science and Technology, 20*(11), 1474–1478.

Lee, W., Kwon, B., & Jung, S. (2006). Effect of Cr_3C_2 on the microstructure and mechanical properties of the brazed joints WC–Co and carbon steel. *International Journal of Refractory Metals and Hard Materials, 24*(3), 215–221.

Lu, S., & Kwon, O. (2002). Microstructure and bonding strength of WC reinforced Ni-base allow brazed composite coating. *Surface and Coatings Technology, 153*, 40–48.

Martens, L., Tillrnann, W., Lugscheider, E., & Ziegler, G. (1996). Strength and microstructure of brazed cemented carbide and silicon nitride joints. *Journal of Materials Processing Technology, 58*, 13–23.

Miranda, R., Quintino, L., Costa, A., Pina, J. C., Rosa, T., Catarino, P., et al. (2008). Analysis of different laser welding processes for joining hardmetals to steel. *Welding in the World, 52*(7/8), 42–51.

Pelletier, J., & Robin, M. (1993). Metal-ceramic joining by laser. *Journal de Physique, IV*, 3 (Colloque C7, Supplément au Journal de Physique III).

Quintino, L., Costa, A., Miranda, R., Yapp, D., Kumar, V., & Kong, C. J. (2007). Welding with high power fiber lasers – a preliminary study. *Materials and Design, 28*(4), 1231–1237.

Ready, J. F. (2001). *LIA handbook of laser material processing*. Magnolia Publishing, Inc.

Sandig, S., Wiesner, P., Greitmann, M., & Deutschmann, G. (1995). Technological aspects of laser joining of steel and hard metal components. *Proceedings of ICALEO*.

Schwartz, M. (1990). Ceramic joining. In ASM, J. Fernie, P. Threadgill, & M. Watson (Eds.), *Progress in Joining of Advanced Materials, Welding and Metal Fabrication, May 1991*.

Steen, W. M. (2003). In *Laser material processing* (3rd ed.). Springer Verlag.

Stevenson, R. (1984). *Metals handbook–powder metallurgy cemented carbides* Vol. 7. ASM.

Welding handbook, Vol. 1-Welding science and technology, 9th ed., (ISBN 0-87171-657-7).

Xu, P. Q. (2011). Dissimilar welding of WC–Co cemented carbide to $Ni_{42}Fe_{50.9}C_{0.6}Mn_{3.5}Nb_3$ invar alloy by laser–tungsten inert gas hybrid welding. *Materials and Design, 32*, 229–237.